Dan Lubin
Robert Massom

Polar Remote Sensing

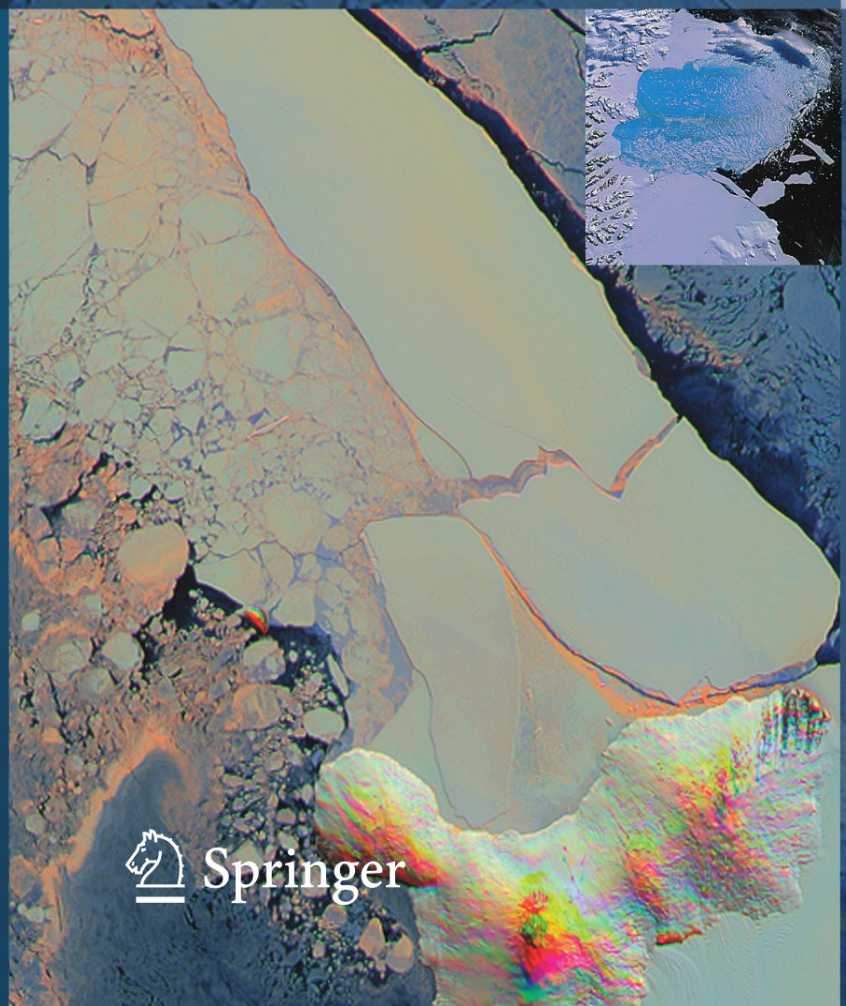

Volume I
Atmosphere and Oceans

Springer

PRAXIS

Polar Remote Sensing

Volume I: Atmosphere and Oceans

Dan Lubin and Robert Massom

Polar Remote Sensing

Volume I: Atmosphere and Oceans

Springer

Published in association with
Praxis Publishing
Chichester, UK

PRAXIS

Dr. Dan Lubin
Research Physicist and Senior Lecturer
Scripps Institution of Oceanography
University of California, San Diego
La Jolla
California
USA

Dr. Robert Massom
Senior Research Scientist
Antarctic Climate and Ecosystems Cooperative Research Centre
University of Tasmania
Private Bag 80
Hobart
Tasmania
Australia

SPRINGER–PRAXIS BOOKS IN GEOPHYSICAL SCIENCES
Published in association with Antarctic Climate and Ecosystems Cooperative Research Centre, Australia
SUBJECT *ADVISORY EDITOR*: Dr. Philippe Blondel, C.Geol., F.G.S., Ph.D., M.Sc., Senior Scientist, Department of Physics, University of Bath, Bath, UK

ISBN 3-540-43097-0 Springer-Verlag Berlin Heidelberg New York

Springer is part of Springer-Science + Business Media (springeronline.com)

Bibliographic information published by Die Deutsche Bibliothek

Die Deutsche Bibliothek lists this publication in the Deutsche Nationalbibliografie; detailed bibliographic data are available from the Internet at http://dnb.ddb.de

Library of Congress Control Number: 20059276101

Cover design: Jim Wilkie
Project management: Originator Publishing Services, Gt Yarmouth, Norfolk, UK

Printed on acid-free paper

Contents

Preface ix
List of figures xv
List of tables xxix
List of abbreviations xxxi
About the authors xli
Publisher credits xliii

1 Introduction 1
1.1 NASA in the 19th century: the great U.S. Exploring Expedition discovers Antarctica 2
1.1.1 Holes in the poles 3
1.1.2 The dawn of big government science 7
1.1.3 The seventh continent 21
1.1.4 Epilogue 36
1.2 Introduction to satellite remote sensing of polar regions 39
1.3 NASA in the 21st century: the Earth Observing System 44
1.3.1 Terra, Aqua, and Aura 46
1.3.2 Smaller EOS missions 49
1.3.3 NPOESS 53
1.4 European Space Agency 54
1.5 Russian missions 55
1.6 Japanese missions 56
1.7 Indian missions 56
1.8 Chinese missions 57
1.9 Satellite data availability and utilization 57
1.10 References 59

2 Satellite imaging and radiometry 61
2.1 Introduction 61
2.2 The polar-orbiting spacecraft 62
2.3 Radiometric quantities 66
2.3.1 Intensity and flux 66
2.3.2 Reflectance and albedo. 69
2.3.3 Scattering and absorption 74
2.3.4 The radiative transfer equation 84
2.3.5 Thermal radiation 86
2.3.6 Managing the radiative transfer equation 88
2.4 Scanning 92
2.5 Detectors 98
2.6 Spectral band selection 108
2.7 Calibration. 109
2.8 Microwave radiometry 112
2.9 Spectral radiometry 119
2.9.1 Dispersing spectrometers 120
2.9.2 Fourier transform spectrometers. 123
2.9.3 Microwave spectrometers 127
2.10 References 129

3 The polar stratosphere 133
3.1 The springtime Antarctic ozone decrease 134
3.2 The Total Ozone Mapping Spectrometer 143
3.2.1 The TOMS instrument and algorithm 144
3.2.2 The Curse of Captain Wilkes 151
3.3 Ozone retrieval from infrared sounders 153
3.4 The Polar Ozone and Atmospheric Measurement program 157
3.4.1 Instrument description 159
3.4.2 Retrieval principles 162
3.5 Remote sensing of polar stratospheric clouds 168
3.5.1 Occultation experiments 169
3.5.2 Imager studies 173
3.6 Polar mesospheric clouds 176
3.7 Arctic ozone depletion 177
3.8 The ozone hole, solar ultraviolet radiation, and Antarctic ecology 179
3.9 References 184

4 Polar climate and meteorology 193
4.1 Introduction 193
4.2 The Antarctic automatic weather station program 195
4.3 Satellite meteorology 199
4.3.1 Polar lows 201
4.3.2 Katabatic winds 205
4.3.3 Wind vectors from polar orbiter data 207

4.4 Cloud detection and classification . . . 213
4.4.1 Contrasting spectral signatures. . . . 217
4.4.2 Automated texture recognition. . . . 221
4.5 Cloud radiative properties . . . 226
4.5.1 Cloud phase discrimination . . . 230
4.5.2 Cloud optical depth and effective radius . . . 235
4.5.3 Uncertainties . . . 241
4.5.4 Comparison with *in situ* and ground-based measurements 244
4.6 Surface albedo and temperature . . . 249
4.6.1 Field measurements and theoretical studies. . . . 250
4.6.2 Remote sensing of sea ice albedo . . . 256
4.6.3 Remote sensing of ice surface temperature . . . 260
4.7 Satellite investigation of the polar radiation budget . . . 262
4.7.1 Sensitivity studies . . . 264
4.7.2 Use of Earth radiation budget sensors . . . 274
4.7.3 Aerosols . . . 277
4.8 The Polar Pathfinder dataset—example of a successful high-latitude adaptation. . . . 282
4.9 Modern experimental programs . . . 291
4.10 References . . . 295

5 Sea ice . . . 309
5.1 Introduction . . . 309
5.2 Sea ice formation processes (and the life of brine) . . . 316
5.3 Polar contrasts . . . 321
5.4 The profound impact and role of sea ice . . . 323
5.4.1 Physical and biogeochemical significance . . . 323
5.4.2 Ecological significance of sea ice . . . 328
5.5 Recent observations and simulations of rapid change, and current uncertainties . . . 331
5.6 The growth, decay, and heat budget of sea ice—dynamics versus thermodynamics . . . 343
5.6.1 The surface energy balance of a sea-ice-covered ocean . . 344
5.6.2 Sea ice dynamic processes. . . . 352
5.7 Basic remote-sensing principles relating to the measurement of sea ice and its snow cover . . . 356
5.7.1 Optical properties of sea ice and its snow cover 358
5.7.2 Thermal infrared remote sensing of sea ice and its snow cover . . . 364
5.7.3 Microwave properties. . . . 368
5.8 Major sensor classes and their attributes as sea ice research tools 380
5.8.1 Passive microwave sensors . . . 380
5.8.2 Active microwave . . . 385
5.9 Key geophysical parameters from satellite data . . . 420
5.9.1 Ice concentration . . . 422

5.9.2 Ice extent and ice edge characteristics 443
5.9.3 Fast ice distribution and behavior 462
5.9.4 Polynyas 466
5.9.5 Sea ice motion, dynamics, and kinematics 487
5.9.6 Sea ice thickness and its distribution. 507
5.9.7 Sea-ice-type discrimination (classification). 528
5.9.8 Snow cover thickness. 560
5.9.9 Ice/snow surface roughness characteristics 564
5.9.10 Floe size distribution 568
5.9.11 Sea ice/snow skin surface temperature. 571
5.9.12 Sea ice temperature 580
5.9.13 Sea ice albedo 582
5.9.14 Snow surface grain size and impurities 590
5.9.15 Detection of ice/snow melt and refreezing 591
5.9.16 Wave–ice interaction, and ice edge processes 604
5.9.17 Operational ice observation, analysis, and forecasting 609
5.10 References 616

Appendix: Parameters of synthetic aperture radar missions 729

Index 737

Preface

The objective of this book is to survey one of the most challenging and at the same time most necessary applications of satellite remote sensing: geophysical sciences in the Earth's polar regions. Much has happened in this field over the past decade. In addition to dedicated satellite instruments and programs that have monitored critical manifestations of climate and atmospheric change, such as the retreat of Arctic sea ice, the motion of the great Antarctic ice sheets, and the evolution of the ozone "hole" in both polar regions, many serendipitous applications of satellite remote sensing have arisen for polar research. In recent years, numerous imaginative researchers have adapted remote-sensing instruments for high-latitude investigations in ways that were never envisioned by the sensors' designers. A survey of polar remote-sensing accomplishments is particularly useful at this point in time, as the Earth Science community is experiencing a transition to a new generation of satellite remote-sensing instruments with an order of magnitude greater capability than their predecessors.

This two-volume set is subdivided into major geophysical disciplines related to climate change, and the intent is to introduce the physical principles involved with remote-sensing derivation of important geophysical quantities in the polar regions. After an introductory chapter, the first technical chapter provides a general background in shortwave, longwave, and microwave remote sensing, along with some radiative transfer fundamentals, as a self-contained reference point for the subsequent disciplinary chapters. We have divided our writing tasks according to the disciplines with which we have the most research experience. Dan provided the chapters on the stratosphere and on climate/meteorology. Rob provided the chapters on sea ice, radar interferometry, and glaciology, with an introductory chapter (in Volume 2) on ice sheets. The material on oceanography, both physical and biological, was written jointly.

The first part of the introduction, "NASA in the Nineteenth Century", was written by Dan, in the tradition we polar researchers maintain for keeping alive

the stories of history's great expeditions. This story should resonate in some way with anyone who has been involved with a major space agency. A juxtaposition of modern-day NASA with the United States Exploring Expedition of 1838–42 may have its irreverent moments where politics and bureaucracy are concerned, but we assure the reader that this section was written with the highest regard for NASA's scientists and astronauts.

On a more specific level, many individuals have played important roles in the recent growth and vitality of polar satellite remote sensing. In particular, we acknowledge Mr. Robert Whritner of the Scripps Institution of Oceanography. In the late 1980s, Bob recognized the need to archive the telemetry collected by polar orbiter tracking equipment then just installed at McMurdo and Palmer Stations by the U.S. National Science Foundation, for the benefit of the greater scientific community. Not only did he accomplish this, but in establishing the Arctic and Antarctic Research Center at Scripps, he also made his vast experience as a Navy meteorologist freely available to researchers interested in using the data. It is no exaggeration to state that Bob has helped hundreds of researchers worldwide, on an individual basis, to incorporate satellite remote sensing into their programs. Dr. Robert L. Bernstein, founder and now Chief Technical Officer of the SeaSpace Corporation, has also played a major role. SeaSpace, which in many respects sets the industry standard in Earth satellite tracking and scientific data processing, got its start with the NSF Antarctic contracts. The challenging Antarctic environment was a factor in the immediate technical excellence of the SeaSpace products, and these high standards in turn ensured that polar satellite data have been steadily available to a great many researchers and field expeditions, not only at fixed land-based stations but also from satellite-tracking equipment aboard polar research vessels. We also acknowledge the extraordinary contribution of Dr. Joey Comiso of the NASA Goddard Space Flight Center, and of many other colleagues who are too numerous to mention here. Their immense contribution in shaping the development of polar remote sensing will become fully apparent in the text and references. Writing a book is a major responsibility, and we only hope that we have done justice to their excellent work.

On a personal as well as professional level, Rob would like to extend heartfelt thanks to a number of special colleagues who have given extraordinary help, encouragement and much-valued friendship during his quarter century in polar research. These are Ted Scambos (NSIDC, University of Colorado), Joey Comiso and Claire Parkinson (NASA Goddard Space Flight Center), Mark Drinkwater (European Space Agency), Mark Rosenberg (Antarctic Climate and Ecosystems [ACE] CRC), Mark Curran (ACE CRC and Australian Antarctic Division), Mike Pook (CSIRO Division of Marine and Atmospheric Research, Australia), Andrew Cowan (formerly Scott Polar Research Institute), Vernon Squire (University of Otago), Gareth Rees (Scott Polar Research Institute), Peter Wadhams (University of Cambridge), Matthew Sturm (U.S. Cold Regions Research and Engineering Laboratory), and Steve Ackley (Clarkson University).

Dan would like to extend heartfelt thanks to colleagues and mentors who have given him so much encouragement, friendship, and so many outstanding

opportunities as a research physicist. These are John Frederick and Doug MacAyeal (University of Chicago), Catherine Gautier (University of California Santa Barbara), V. Ramanathan, Richard Somerville, Francisco P. J. Valero, Greg Mitchell, Osmund Holm-Hansen, Wolf Berger, Charles Kennel (Scripps Institution of Oceanography), Sally Ride, David Tytler, James Arnold (University of California San Diego), Knut Stamnes (Stevens Institute of Technology), David Bromwich (Byrd Polar Research Center), Charles R. Booth (Biospherical Instruments, Inc.), and Moshe J. Lubin (Laboratory for Laser Energetics, University of Rochester).

Many people have unselfishly and kindly given of their energy and precious time to contribute to this book by providing papers, expert comments and diagrams. These include Ted Scambos, Terry Haran, Florence Fetterer, Mark Serreze, Julienne Stroeve, Nancy Geiger Wooten, and Ken Knowles (all U.S. National Snow and Ice Data Center, University of Colorado); Helen Fricker (Scripps Institution of Oceanography); Ian Joughin (University of Washington [formerly of NASA Jet Propulsion Laboratory]); Mark Drinkwater and Evert Attema (European Space Agency); Joey Comiso, Claire Parkinson, Thorsten Markus, Bob Bindschadler, Dorothy Hall, Kimberley Casey, Nick DiGirolamo, Christopher Shuman, Jay Zwally, Rich McPeters, Ashwin Mahesh, and Patricia Vornberger (all NASA Goddard Space Flight Center); Henrik Steen Andersen (Danish Meteorological Institute); Mark Fahnestock (University of New Hampshire, U.S.A.); Klaus Grosfeld (University of Bremen, Germany); David Long (Brigham Young University, U.S.A.); Ian Boyd (University of St. Andrews, Scotland); Kevin Arrigo and Howard Zebker (Stanford University, U.S.A.); Frank Rau (University of Freiburg, Germany); Tony Liu (NASA Goddard Space Flight Center and U.S. Office of Naval Research, U.S.A.); Anne Nolin (Oregon State University, U.S.A.); Benoît Legrésy and Frédérique Rémy (LEGOS [CNES–CNRS–UPS], France); Eric Rignot, Ron Kwok, Ben Holt, and David Diner (NASA Jet Propulsion Laboratory, U.S.A.); Seelye Martin, Dale Winebrenner, Robert Drucker, Yanling Yu, and Ron Lindsay (all University of Washington); Bob Jacobel (St. Olaf's College, U.S.A.); Hermann Engelhardt (California Institute of Technology); Konrad Steffen, Russell Huff, and Chuck Fowler (University of Colorado); Leif Toudal Pedersen (Danish Centre for Remote Sensing); Wolfgang Rack (Alfred Wegener Institute, Germany); Helmut Rott (University of Innsbruck); Mike Manore, Dean Flett, and Katherine Wilson (Canadian Ice Service); Tavi Murray (University of Leeds, England); Cheryl Bertoia (COSPAS–SARSAT Secretariat, England); Yunhe Zhao (Caelum Research Corporation, U.S.A.); Harry Keys (Dept. of Conservation, New Zealand); David Vaughan (British Antarctic Survey); Jia Wang (IARC, University of Alaska Fairbanks); Jörg Haarpaintner (Norwegian Meteorological Institute); Massimo Frezzotti (ENEA CLIM–OSS, Italy); Baerbel Lucchitta (USGS, U.S.A.); Wolfgang Dierking (Alfred Wegener Institute, Germany); Christophe Genthon and Olivier Torinesi (LGGE CNRS, France); Miguel Angel Morales Maqueda (New York University); Kazutaka Tateyama (Kitami Inst. of Technology, Japan); Jon Bamber (University of Bristol, England); Pedro Skvarca (Instituto Antárctico Argentino, Argentina); LeenKiat Soh (University of Nebraska, U.S.A.); Gennady

Belchansky (IARC, University of Alaska Fairbanks); Bill Pichel (NOAA/NESDIS, U.S.A.); David Douglas (USGS Alaska Science Center, U.S.A.); Sheldon Drobot (National Academies, Washington D.C.); Jørgen Dall (Danish Centre for Remote Sensing); Laurence Gray (Canada Centre for Remote Sensing); Rick Forster (University of Utah, U.S.A.); Johan Mohr (Technical University of Denmark); Bob Onstott (General Dynamics–Advanced Information Systems, U.S.A.); Birgitte Furevik (Nansen Environmental and Remote Sensing Center, Norway); Seymour Laxon (University College London, England); Hernán De Angelis (University of Stockholm, Sweden); Laurie Padman (Earth and Space Research, U.S.A.); Berndt Scheuchl (University of British Columbia, Canada); Sylviane Surdyk and Yan Ropert-Coudert (National Institute of Polar Research, Tokyo); Steve Rintoul (CSIRO Marine Research); Warren White (Scripps Institution of Oceanography, U.S.A.); Volkmar Wismann (IFARS, Germany); Roland Warner and Neal Young (Antarctic Climate and Ecosystems Cooperative Research Centre [ACE CRC] and Australian Antarctic Division); Susan Solomon (NOAA Aeronomy Laboratory); Mike Fromm (U.S. Naval Research Laboratory); Cora Randall (LASP, University of Colorado); Kathy Pagan (NASA Ames Research Center); Ray Smith (University of California, Santa Barbara); Stephen Warren, Thomas Grenfell, and Bonnie Light (University of Washington); Von Walden (University of Idaho); Don Perovich (U.S. Army Cold Regions Research and Engineering Laboratory); David Bromwich (Byrd Polar Research Center); Jennifer Francis (Rutgers University); Jeff Key (NOAA/NESDIS); Janet Intrieri (NOAA ETL); Matthew Lazzara and Shelly Knuth (University of Wisconsin); and Tom Charlock (NASA Langley Research Center). This book would not exist without the inestimable help and input of these people.

Grateful thanks are extended by Rob to Glenn Hyland (ACE CRC and Australian Antarctic Division) for reviewing Chapter 2 of Volume 2, to Roland Warner, Vin Morgan, and Tas Van Ommen (ACE CRC and AAD) for their helpful comments regarding the ice sheet mass balance section of Volume 2, Petra Heil (ACE CRC and AAD) for reviewing the sea ice modeling section, and to Mark Rosenberg (ACE CRC) for his inestimable help in editing references.

Rob is also grateful to his many wonderful colleagues at the Antarctic Climate and Ecosystems Cooperative Research Centre (CRC) in Hobart, Tasmania (Australia) and the previous Antarctic CRC. For Rob, this work was supported by the Australian Government's Cooperative Research Centres Programme through the Antarctic Climate and Ecosystems Cooperative Research Centre (ACE CRC). He is very grateful for this support.

Dan is grateful to Gabrielle Ayres for invaluable editorial support, to Jo Griffith for excellent illustrations, and to Steve Hart and Rob Wittenmyer for assistance with satellite data processing.

Last but not least, we are extremely grateful to Philippe Blondel (University of Bath), who carried out the onerous task of scientifically reviewing the book with extreme diligence, thoughtfulness, and good humour. All of his comments have been highly beneficial. We are equally grateful to Clive Horwood (Praxis Publishing) for inviting us to write this book, and for his patience and encouragement as this project

evolved, and to Neil Shuttlewood and his team at Originator for outstanding editorial and production work.

This book is dedicated to Dan's wife Lorri, and Rob's wife Yuko and his beautiful daughter Adelle Yuki. This project would not have been possible without our spouses' love and unstinting support throughout, and little Adelle was a wonderful bonus for Rob during the writing.

Figures

1.1	*USS Vincennes*, flagship of the United States Exploring Expedition	3
1.2	John Cleves Symmes, Jr., the Newton of the West	4
1.3	The Honorable Mahlon Dickerson	14
1.4	Examples of mainstream American media attention given to major national scientific endeavors	20
1.5	Lieutenant Commander Charles Wilkes	22
1.6	Lieutenant William L. Hudson	25
1.7	The imminent collision between the disabled *USS Peacock* and a huge tabular iceberg	29
1.8	Sightings of the Antarctic continent by *USS Vincennes* and *USS Peacock*, drawn by Wilkes and Hudson for the official U.S government publication	31
1.9	Map of the section of Antarctic coastline surveyed by the U.S. Exploring Expedition	35
1.10	NASA's Earth Observing System Aqua spacecraft	color
1.11	NASA's ICESat spacecraft	color
1.12	Timeline of the expected transition between "heritage" Earth remote-sensing missions and the new generation of remote sensors offering an order of magnitude more capability, and using high-density X-band telemetry	color
2.1	Geometry of the Keplerian orbit	63
2.2	Equatorial coordinate system most commonly used for describing the motion of Low Earth Orbit spacecraft	64
2.3	Polar coordinate system used for describing radiometric quantities	68
2.4	Examples of Bidirectional Reflectance Distribution Functions for a cloudy atmosphere and four solar zenith angles	72
2.5	Example of the BRDF measured over an Antarctic snow surface, for two large solar zenith angles	73
2.6	Idealized potential well diagram for the diatomic molecule	75
2.7	The absorption cross section of ozone	77
2.8	Modes of vibration for diatomic and triatomic molecules, examples being CO_2 and H_2O, respectively	78

2.9 The scattering phase functions for various types of ice crystals, along with those from a spheroid and a sphere 82
2.10 Wavelength dependence in the single scattering albedo 83
2.11 Diagram of the Advanced Very High Resolution Radiometer 94
2.12 The Landsat Thematic Mapper scanning mechanism 95
2.13 The pushbroom scanning configuration 96
2.14 Diagram of a p–n junction 99
2.15 Diagram of a photomultiplier tube 101
2.16 Diagram of a Charge Coupled Device 102
2.17 Diagram of the typical spectral responsivity for Si and InGaAs 104
2.18 Detectivity D^* for Si and HgCdTe 107
2.19 Spectral responsivities of the NOAA-15 AVHRR channels 108
2.20 Example of deterioration in responsivity for the AVHRR sensor over time, as determined by monitoring selected clear-sky Earth scenes 113
2.21 A typical zenith opacity in the spectral region used for passive-microwave remote sensing 114
2.22 The extinction coefficient in the microwave for liquid water clouds of varying water content ($g\,m^{-3}$), at temperature 0°C 115
2.23 Schematic representation of a microwave antenna's power pattern, in polar and rectangular plots 118
2.24 Schematic diagram of a dispersing spectrometer 122
2.25 Schematic diagram of a Michelson interferometer 124
2.26 Schematic diagram of a superheterodyne radiometer 127
2.27 Emission lines of ClO (a key player in the Antarctic ozone "hole") over northern and high southern latitudes during September 128
3.1 Global climatology of atmospheric ozone as a function of latitude and season 135
3.2 Examples of ozone concentration as a function of altitude 136
3.3 The first report of springtime Antarctic ozone decrease, from ground-based spectrophotometer measurements 139
3.4 The first large-scale satellite maps of the springtime Antarctic ozone decrease, made by the Nimbus 7 Total Ozone Mapping Spectrometer 140
3.5 The column abundance of OClO measured at McMurdo Station, Antarctica, using visible wavelength spectroscopy 142
3.6 Schematic diagram of the mechanisms behind the springtime Antarctic ozone decrease 143
3.7 Schematic diagram of the Earth Probe TOMS, showing both the instrument optics and the orientation of the instrument in the spacecraft 145
3.8 Total ozone abundance as a function of transmittance in the 9.6-μm channel of the HIRS2 156
3.9 A comparison of TOVS/HIRS2 and TOMS total column ozone retrievals over Antarctica on September 15, 1987 158
3.10 Diagram of the POAM II instrument: (a) instrument orientation in spacecraft; (b) radiometer assembly 161
3.11 Time series of the tangent point latitudes in the Northern and Southern Hemispheres, seen by the POAM II instrument 162
3.12 Solar occultation viewing geometry 163
3.13 The slant path optical depth as a function of altitude, for major atmospheric constituents, in POAM channels 1, 4, 6, and 9 167

3.14 Two-week average ozone mixing ratio profiles and NO_2 mixing ratio profiles inside the 1994 Southern Hemisphere polar vortex 169
3.15 The first geographically extensive observations of polar stratospheric cloud extinction, made by NASA's SAM II instrument 170
3.16 Examples of Southern Hemisphere POAM aerosol extinction profiles at 1,060 nm 171
3.17 Southern Hemisphere polar map showing locations of POAM PSC detections between May 1 and November 30, 1995 172
3.18 Time series of POAM measurements and related information demonstrating dehydration in the Antarctic lower stratosphere 174
3.19 Radiative transfer simulation of the Brightness Temperature Difference in Kelvin between AVHRR channels 4 and 5 175
3.21 AVHRR composite image of Antarctica for August 31, 1992 . . . . . color
3.20 Summary of radiative transfer results 175
3.22 Examples of PMC signatures seen in POAM II 448-nm extinction profiles . . . 177
3.23 Examples of Microwave Limb Sounder measurements during the 1992 Arctic winter. . . . . color
3.24 Time series of UARS-measured ozone mixing ratio at 20 km. 180
3.25 The local noon UV-B flux (integral 280–315 nm) reaching the Antarctic and Southern Ocean surface on October 5, 1979 (top) and 1992 (bottom), derived from a radiative transfer retrieval algorithm that uses TOMS data to specify total column ozone and cloud effective optical depth, and SSM/I data to specify sea ice concentration . . . . . color
3.26 Illustration of the complexities involved in retrieving Antarctic chlorophyll *a* pigment concentrations from satellite ocean color data 183
3.27 SeaWiFS-derived map of chl *a* surface biomass abundance throughout the Southern Ocean, averaged over all available austral spring (September–November) data . . . . . color
4.1 Schematic diagram of the ice-albedo feedback 194
4.2 The Automatic Weather Station installation at Uranus Glacier being serviced with the help of a British Antarctic Survey Twin Otter aircraft 196
4.3 Location of Antarctic AWS sites as of 2002. . . . . color
4.4 Schematic diagram of a University of Wisconsin Antarctic Meteorology Research Center AWS system. 197
4.5 The Composite Annual Pressure Anomaly and Composite Annual Temperature Anomaly before and after a Southern Oscillation Index mininum 199
4.6 Composite of mid-IR imagery from AVHRR and GOES spacecraft covering nearly all of Antarctica and the Southern Ocean . . . . . color
4.7 Comparison of a mesoscale model prediction of weather conditions in the vicinity of McMurdo Station at 06:00 UTC January 15, 2001 with a contemporaneous AVHRR channel-4 image 202
4.8 AVHRR infrared images of mesoscale cyclones near 62°S and 68°S along the 80°W meridian, approaching the Antarctic Peninsula at 22:40 UTC on July 22, 1999. 203
4.9 Classification scheme for high-latitude mesoscale cyclone formation, maturity, and dissipation 204
4.10 The time–mean airflow over Antarctica during winter. 206
4.11 Schematic diagram of the katabatic wind confluence zone near the Siple Coast, which lends itself to satellite data analysis 207

4.12 NOAA-9 AVHRR mid-IR image at 03 : 38 UTC on June 5, 1988 showing a katabatic wind surge propagating from the Transantarctic Mountains all the way across the Ross Ice Shelf 208
4.13 DMSP Operational Linescan System visible image at 0.5 km resolution showing blowing snow in a katabatic wind 209
4.14 Example temperature weighting functions for three bands frequently used in the CO_2-slicing technique 211
4.15 The frequency of time differences between successive overpasses of the MODIS instrument 212
4.16 Example of wind vectors derived by applying an automated cloud tracking and CO_2-slicing algorithm to a sequence of MODIS images over Antarctica . . . . . color
4.17 A comparison of mean monthly cloud amounts in the high Arctic (north of 80°N) from two multiyear satellite datasets, the ISCCP-D2 and TOVS Path-P, and a climatology of surface-based observations 213
4.18 Schematic diagram of class clustering in a two-dimensional feature space 215
4.19 Schematic diagram of a multi-layer perceptron with two hidden layers, a neural network configuration frequently used in satellite remote-sensing algorithms . . 216
4.20 NOAA-14 AVHRR channel-1 image over part of West Antarctica at 20 : 17 UTC on December 1, 1997 . . . . . color
4.21 Image of the brightness temperature difference between channels 3 and 4, for the data of Figure 4.19 . . . . . color
4.22 Scatter diagrams of the brightness temperature differences 219
4.23 Illustration of the spatial coherence method for retrieving sub-pixel cloud fraction over a warm ocean surface in mid-IR imagery from AVHRR or similar sensors 221
4.24 Demonstration of how the Ebert (1987) cloud classification scheme utilizes both textural and multispectral features to identify low clouds (left panels) and high clouds (right panels) in full-resolution (LAC) AVHRR images from the SHEBA field experiment . . . . . color
4.25 Spectral intensity at a zenith angle of 75° measured by a Fourier Transform infrared spectroradiometer at the South Pole on May 1, 1992 227
4.26 The imaginary component of the index of refraction, for ice and for liquid water, in the wavelength range covered by AVHRR channels 3–5 229
4.27 Radiative transfer simulations of the brightness temperature difference between AVHRR channels 3 and 4 231
4.28 The single scattering albedo for several liquid and ice water clouds, and an illustration of how the single scattering albedo governs the AVHRR channel 3 (3.7 μm) cloud reflectance as a function of scattering angle 232
4.29 Validation of the cloud particle phase estimated from AVHRR data by the depolarization lidar system deployed at SHEBA 234
4.30 Discrete-ordinate-method radiative transfer simulation of reflected intensity from a cloud top 236
4.31 Simulated AVHRR channel-3 intensities as a function of cloud optical depth 237
4.32 Simulated brightness temperature in AVHRR channel 4 above a cloud top . . 238
4.33 Simulated AVHRR channel-2 and channel-3 intensity over a cloud top 239
4.34 Simulation of the AVHRR channel-2 intensity over a cloud top 240
4.35 Radiative transfer simulation showing the variation of the AVHRR channel-3 reflectance as a function of channel-2 reflectance 242

4.36 Cloud droplet size distribution spectra measured in ice-free or nearly ice-free clouds during seven research aircraft flights over the Beaufort Sea during June 1995 . . . 245
4.37 Variability in the microstructure of an Arctic stratocumulus cloud along a 40-km flight track . . . 246
4.38 As in Figure 4.37, but for a mixed phase cloud . . . 247
4.39 Histograms of cloud base heights over the South Pole derived from ground-based FTIR data during 1992. . . . 248
4.40 Histograms of ice-cloud-particle-effective radius r_e above the South Pole obtained from FTIR data during 1992 . . . 249
4.41 Histograms of cloud ice water path and shortwave optical depth derived from FTIR data during 1992 . . . 250
4.42 Sea ice albedos measured by Dr. Tom Grenfell (University of Washington) near Barrow, Alaska . . . 251
4.43 Meltponds at SHEBA, July 1998 . . . 252
4.44 Development of meltponds at SHEBA during summer, 1998. . . . 253
4.45 Evolution sequence of first-year ice albedo measured near Barrow, Alaska . . . color
4.46 Radiative transfer simulations of the spectral emissivity of snow throughout the near- and mid-IR . . . 254
4.47 The spectral albedo of Antarctic sea ice in various stages of development . . . color
4.48 The shortwave spectral albedo of continental Antarctic snow, showing observations and radiative transfer simulations for representative grain sizes . 255
4.49 The effect of sediment particulates on the albedo of sea ice . . . 256
4.50 Anisotropic reflectance factor $\xi_I(x, y)$ for a snow surface with solar zenith angle 70° . . . 258
4.51 Comparison of the sensitivity in satellite-derived net surface radiative flux to expected uncertainties in surface temperature T_s, surface albedo α_s, total column ozone O_3, precipitable water vapor PW, aerosol optical depth τ_h, and vertical temperature profile $T(z)$, for clear-sky conditions during summer over both snow and openwater . . . 267
4.52 As in Figure 4.51, but for clear-sky conditions during winter . . . 268
4.53 Comparison of the sensitivity in satellite-derived net surface radiative flux to expected uncertainties in surface temperature T_s, surface albedo α_s, total column ozone O_3, precipitable water vapor PW, aerosol optical depth τ_h, vertical temperature profile $T(z)$, cloud particle effective radius r_e, cloud top height Z_c, cloud amount A_c, and shortwave cloud optical depth τ_c, for cloudy-sky conditions during summer and winter over snow . . . 268
4.54 Comparison of AVHRR-derived downwelling shortwave flux at the surface at Barrow, Alaska during 1992–93 with co-located surface pyranometer (broadband shortwave radiometer) measurements . . . 269
4.55 Comparison of AVHRR-derived downwelling longwave flux at the surface at Barrow, Alaska during 1992–93 with co-located surface pyrgeometer (broadband longwave radiometer) measurements . . . 270
4.56 Comparison of AVHRR-derived net surface flux with co-located surface measurements from Barrow, Alaska during 1992–93 270
4.57 Satellite determination of the trends in surface temperature and broadband surface albedo for four seasons and for the annual mean, covering the time period 1982–99 and the entire Arctic north of 60° . . . 271
4.58 As in Figure 4.57, but for the cloud amount and precipitable water. . . . 272

4.59 As in Figure 4.57 but for the surface shortwave cloud forcing, longwave cloud forcing, and net cloud forcing, with the S and P values also listed in this order 273
4.60 Top-of-atmosphere shortwave albedo measured by ERBE as a function of downwelling shortwave flux divided by the solar zenith angle cosine μ, for 66 co-located measurements having $0.38 < \mu < 0.40$ 274
4.61 Monthly means of the shortwave absorption at the top-of-atmosphere, the outgoing longwave radiation, net radiation at the top-of-atmosphere, net shortwave flux, net longwave flux, and the net (shortwave plus longwave) flux at the surface for Syowa Station 276
4.62 As in Figure 4.61, but for the South Pole during 1987–88 276
4.63 Top-of-atmosphere absorbed shortwave radiation from a summertime simulation by the NCAR Community Climate Model version 3, and from a seasonal average of ERBE data 278
4.64 As in Figure 4.63, but for the Antarctic summer 279
4.65 Examples of temperature profiles retrieved using the original mid-latitude TOVS Pathfinder algorithm compared with co-located radiosonde data from CEAREX 287
4.66 The error in MSU channel-1 brightness temperature as a function of nadir-viewing angle, determined from sequential satellite overpasses overlapping the same region 288
4.67 Cloud amount observed during CEAREX compared with satellite-retrieved cloud amount using the original midlatitude TOVS Pathfinder algorithm and the modified Polar Pathfinder algorithm following Table 4.12 290
4.68 Annual mean (1980–1993) precipitable water vapor flux vectors derived by combining TOVS Polar Pathfinder water vapor profiles with National Center for Environmental Prediction reanalysis data for upper-level winds 291
4.69 The mean and r.m.s. uncertainties in TOVS Polar Pathfinder retrievals of the vertical temperature profile, compared with natural variability, for three seasons during SHEBA 292
4.70 Comparison of total column water vapor from the Polar Pathfinder algorithm with radiosonde measurements from SHEBA 293
5.1 Maps of the Arctic and Antarctic, with locations frequently referred to in the text marked 311
5.2 Schematic showing the network of information collected through bio-logging science (red connectors) that links the individual organism and its functions to the environment (biosphere, right and biotope, left) . . . . . color
5.3 A schematic of components of the Arctic marine system and the global climate systems 316
5.4 A schematic of the idealized sequence of formation (evolution) of thin sea ice 318
5.5 Photographs of different ice types and thicknesses for the Antarctic, with terminology based on the standard World Meteorological Organization sea ice classification . . . . . color
5.6 Photograph from the central section of the East Antarctic sea ice zone in winter showing the intense heat and water vapor loss that occurs from leads in the sea ice cover, where seawater with a temperature approximating $-1.8°C$ is exposed to a significantly colder atmosphere . . . . . color
5.7 Schematic of the impact of intense atmosphere–ocean–sea ice interactions on watermass characteristics of the high-latitude Southern Ocean . . . . . color

5.8 A schematic of the transport of ice and freshwater near the surface of the Arctic Ocean, and the thermohaline circulation associated with brine transport of the marginal shelves and deep overturning in the Greenland Sea 326
5.9 A schematic representation of features and spatial and temporal scales, increasing from left to right, of sea ice characteristics matched with part of the Antarctic foodweb 329
5.10 A schematic representation of (a) the sea ice albedo–ocean feedback loop, and (b) some of the key fluxes affecting the Arctic system, overlaying a satellite-derived ice concentration/extent map of the perennial ice cover at its summertime minimum in 2002 . . . . . color
5.11 A photograph of a vertical profile through a typical dry snowcover on Antarctic first-year ice in winter 348
5.12 The electromagnetic spectrum, with the major sensor classes discussed in this and other chapters marked. Microwave bands are also marked. A plot of *atmospheric transmission* as a function of wavelength 357
5.13 The complex refractive index $(n + ik)$ of pure ice and water as a function of wavelength (0.25–2.5 μm) 359
5.14 The spectral directional–hemispherical reflectance R_S of pure, deep, and dry snow (semi-infinite depth) over the spectral region 0.4–2.5 μm, as a function of grain radius r (50 to 1,000 μm). The spectral directional–hemispherical reflectance R_S of pure, deep, and dry snowcover (of semi-infinite depth) over the spectral region 0.25–2.5 μm as a function of illumination angle θ_0 (30°, 60°, and 75°) and grain size radius r (200 to 1,000 μm) 360
5.15 The spectral albedo of sea ice with a density of 880 kg m^{-3}, and as a function of thickness. 363
5.16 Theoretical penetration depth at microwave frequencies as a function of frequency, temperature, and salinity for Arctic first-year and multiyear ice . . . 372
5.17 Wet snow (a) dielectric constant (permittivity) ε'; and (b) dielectric loss factor ε'', at volume fractions of water of 0–12% and with a constant snow density of 250 kg m^{-3}. (c) The frequency dependence of microwave penetration depth (frequency range 1–37 GHz) as a function of snow liquid water volume 374
5.18 Schematic diagram of the seasonal dependence of physical and radiative characteristics of Arctic first-year and multiyear ice at 18 and 37 GHz (V-pol) over an annual cycle 376
5.19 Schematic representation of the seasonal response of radar backscatter measured by the ERS C-band VV-polarization SAR to changes in physical characteristics of Arctic first-year and multiyear ice over an annual cycle 377
5.20 A schematic of idealized radar backscatter interactions with smooth openwater, smooth first-year ice, pressure ridges, floe edges, and Arctic multiyear ice. . . . 378
5.21 Schematic of the scattering behavior of electromagnetic radiation at X- and L-band frequencies incident on smooth, rough, and very rough snow/ice surfaces 379
5.22 Frequency dependence of the microwave emissivity of Arctic first-year and multiyear ice and calm open ocean for both H and V polarizations 384
5.23 The general scanning configuration and geometry for side-looking synthetic aperture radar, in this case left-looking 387
5.24 A schematic of the operating modes and observation geometry of the Envisat ASAR 391
5.25 An image mosaic of Antarctica generated from Envisat ASAR data acquired by the Global Monitoring Mode over the period April to May 2004 393

5.26 A schematic of the operating modes and observation geometry of the ALOS PALSAR 394
5.27 Imaging modes of the Radarsat-2 SAR 396
5.28 Characteristics of four spaceborne radar scatterometers flown onboard Seasat (SASS), ERS-1 and −2 (ESCAT), ADEOS-I (NSCAT), and QuikSCAT (SeaWinds or QSCAT) 401
5.29 Representative radar altimeter waveforms from (a) an ice sheet surface, (b) sea ice, and (c) open ocean 404
5.30 An example of an Envisat Medium Resolution Imaging Spectrometer image, of sea ice conditions in East Greenland 412
5.31 A composite of two photographic scenes of the Mertz Glacier region of East Antarctica 413
5.32 Landsat Thematic Mapper images of coastal Antarctic sea ice conditions offshore from Cape Batterbee (~64.5°S, 55°E), from (a) March 27, 1989, and (b) November 24, 1989 . . . . . color
5.33 Scatterplot of AMSR-E V1937 brightness temperature (T_B) data for the Antarctic for August 13–26, 2002 429
5.34 Color-coded BBA Antarctic ice concentration maps for (a) the austral summer (March 1992) and (b) winter (August 2002), and (c) and (d) equivalent maps derived using the ABA algorithm . . . . . color
5.35 Flowchart of the NT2 algorithm 432
5.36 A daily map of Arctic sea ice concentration in early June 2002 retrieved from Aqua AMSR-E data using the NT2 algorithm . . . . . color
5.37 Color-coded monthly anomaly maps of Arctic ice concentration for each September (the annual ice minimum extent) from 1981 to 1999 . . . . . color
5.38 Maps of ice concentration anomalies in (a) the Arctic, and (c) the Antarctic for September 2003 . . . . . color
5.39 Composites of Antarctic ice edge/concentration anomalies for 1982 to 1998, derived from SMMR and SSM/I data during the three possible phases of the Southern Oscillation Index (SOI) . . . . . color
5.40 (a) A Landsat MSS scene (170 × 180 km) of sea ice in the Amundsen Sea, Antarctica in December 1990; and (b) the same image classified using the tie-point method applied to channel-4 (0.8–1.1 μm) data . . . . . color
5.41 MODIS sub-scene images and ice concentrations compared with passive-microwave (NRTSI) derived values for the same area and day 441
5.42 A cloud-free MODIS image of the Bering Sea, Bering Strait, and Chukchi Sea acquired on May 7, 2000 442
5.43 Maps of mean monthly sea ice concentration and extent from (a and b) the Arctic, and (c and d) the Antarctic, from March and September 1992 . . . . . color
5.44 Color-coded, daily ice concentration maps of the Arctic from the approximate freezeup period, on October 12 in (a) 1996, (b) 1997, and (c) 1998 . . . . . color
5.45 Plots of anomalies in mean monthly (a) ice extent, (b) actual ice area, and (c) ice concentration for the Arctic, with results of trend analyses, for the period 1979 to 2000 inclusive 446
5.46 Comparison of anomalies and linear trends in sea ice extent, area covered by ice and ice concentration for the Bellingshausen–Amundsen Seas sector of Antarctica (a–c) and the entire Southern Ocean sea ice cover (d–f) from 1978 to 2002 447

5.47 A map of monthly mean Arctic sea ice extent and concentration anomalies (in %) for September 2002 derived from near-real time SSM/I data and relative to NASA-Standard-Team-algorithm-derived mean values for the period 1988–2000 . . . . . color
5.48 Maps of Arctic mimimum summertime sea ice concentration and extent derived from consistent processing of Nimbus-7 SMMR and DMSP SSM/I data . . . . color
5.49 Time series of Arctic multiyear sea ice areal extent in winter, derived from Nimbus-7 SMMR and DMSP SSM/I data 449
5.50 Maps of sea ice extent anomalies in (a) Southern Ocean, and (b) the Northern Hemisphere for September 2003 . . . . . color
5.51 A simplified schematic summary of interannual variations in atmospheric sea level pressure, sea surface temperature, meridional wind stress (denoted by τ), and sea ice areal extent, together with the mean course of the Antarctic Circumpolar Wave . . . . . color
5.52 A composite ocean color image of the Southern Ocean produced from data from the SeaWiFS sensor onboard the SeaStar satellite, for the period September 1997 to August 2000 . . . . . color
5.53 (a) Average length of the ice season (in days) for the period 1979 to 1999, using a 15% ice concentration cutoff; and (b) trends in the average ice season length over the same period and with the same concentration cutoff . . . . . color
5.54 Examples of enhanced resolution (SIRF) *A* and *B* images of both polar regions, generated from 6 days of NSCAT data (H-pol) in 1996 458
5.55 Schematic of an algorithm to derive improved ice edge information from QuikSCAT data, using (a) Active Polarization Ratio (APR), (b) APR_{abs} images as the main input variables, (c) HH-backscatter $\sigma_{0'}$, (d) VV-backscatter σ_0, and (e) the VV/HH ratio of the daily standard deviation per pixel $STD_{/'}$ as secondary variables to eliminate ocean noise to obtain (f) the total ice cover and ice edge delineation 459
5.56 Maps of Antarctic sea ice derived from weekly averaged cloud-free AVHRR channel-1 (0.6 μm) global area coverage (4-km resolution) data from (a) late March 1989 and (b) late November 1989. (c) and (d) are corresponding maps of ice concentration/extent derived from DMSP SSM/I data. Note the polynyas along the East Antarctic coastline in (b) . . . . . color
5.57 An example of MODIS sea ice image products produced by the NASA MODIS Project and archived at the U.S. National Snow and Ice Data Center, from the Baffin Bay region of the Eastern Arctic and acquired on May 5, 2001 . . . . . color
5.58 Maps of (a) fast ice extent and (b) fast ice type derived from Radarsat ScanSAR Wide data, for the East Antarctic coastal sector from 125 to 150°E 464
5.59 A Terra MODIS image showing fast ice and pack ice in the Ross Sea, February 23, 2004 (18 : 20 GMT) 466
5.60 A schematic representation of physical processes occurring in, and responsible for, the formation of shelfwater and deepwater polynyas . . . . . color
5.61 Passive-microwave 3-day composite ice concentration images derived from Nimbus-5 ESMR data showing the extraordinary Weddell Polynya (marked WP) that occurred in the winters of (a) 1974, (b) 1975, and (c) 1976 . . . . . color
5.62 A map of coastal polynya locations in East Antarctica, derived from analysis of DMSP SSM/I ice concentration data (1987–1994) 473
5.63 A comparison of imagery of the Chukchi polynya adjacent to the Chukchi Sea coast of Alaska collected on March 12, 2000 . . . . . color

5.64 Results from the Polynya Signature Simulation Method, showing (a) an SSM/I-based retrieval of polynya areas in the Weddell Sea on November 16 (day 321), 1992, and (b) a DMSP OLS visible band image acquired at 11 : 28 GMT on the same day for comparison 475
5.65 (a) A map of the percentage of ice-free days around Antarctica derived from SSM/I ice concentration data over the period 1997–2001, using data from only June to October each year. (b) 37 polynyas identified and numbered . . . . . color
5.66 Part of a Radarsat ScanSAR image of the Mertz Glacier polynya, East Antarctica, on August 4, 1999 477
5.67 An HLS image of the St. Lawrence Island polynya region, from January 9, 1999 color
5.68 A sequence of geophysical products derived from cloud-free AVHRR imagery of the St. Lawrence Island polynya on February 6, 1999. . . . . color
5.69 Net annual salt flux to the Odden region of the Greenland Sea for the period 1988–89 to 1996–97 . . . . . color
5.70 A comparison of seasonal changes in post-polynya area (estimated from SSM/I data) and daily primary production 483
5.71 An AVHRR channel-4 image of the Mertz Glacier polynya region, June 14, 1999 (16 : 57 UTC) 485
5.72 A Radarsat ScanSAR image of the Mertz Glacier polynya region (East Antarctica), March 8, 1998 (~10.24 GMT), illustrating the effect of the grounded iceberg barrier in the region in steering the encroaching pack ice northwards away from the coast. 486
5.73 A 250-m resolution NASA EOS Terra MODIS image of the grounded iceberg B-15A in the Ross Sea, Antarctica, on October 26, 2003 (20 : 50 GMT) 488
5.74 Mid-December distributions of sea ice (gray) from DMSP SSM/I and chlorophyll concentrations from SeaWiFS for (a) 1998, (b) 1999, and (c) 2000 color
5.75 Map of monthly mean ice motion superimposed on a monthly mean map of ice concentration (both derived from SSM/I data) for the George V Land and Adélie Land coasts of Antarctica, July 1999 . . . . . color
5.76 Map of anomalies in SSMR- and SSM/I-derived sea ice drift and sea ice concentration combined for October 1999, for the George V Land and Adélie Land coasts of Antarctica . . . . . color
5.77 An example of a daily composite ice motion vector map from the NSIDC, for the Arctic for April 20, 2000 496
5.78 Map of the mean sea ice motion in the Antarctic in winter based on satellite observations from 1979 to 2003 497
5.79 Monthly mean maps of Antarctic sea ice (a) drift velocity, (b) drift divergence, (c) drift vorticity, and (d) drift shear . . . . . color
5.80 Daily sea ice drift maps of the Arctic for December 18, 1996 derived from wavelet analysis of (a) ADEOS NSCAT data with a grid-cell size of 100×100 km, and (b) SSM/I 85-GHz radiance data 500
5.81 A Radarsat ScanSAR Wide image (100-m resolution) from April 13, 1998 (12 : 02 GMT) of the Smith Sound/North Water Polynya region between NW Greenland and Ellesmere Island, with ice motion vectors overlaid 503
5.82 Ice divergence, vorticity, shear, and general ice motion for the central Arctic Basin from the period December 16 to 22, 1996. . . . . color

5.83 (a) Average shear deformation of Lagrangian elements, with dimensions of $\sim 10 \times 10$ km, over a 6-day period in the Arctic Ocean, based on small-scale ice motion data derived from the Radarsat Geophysical Processor System. (b) Sea ice shear/fractures simulated with a viscous–plastic sea ice model and an isotropic rheology where spatial domain is discretized with a sufficiently high spatial resolution (10 km) . . . . . color

5.84 (a) Map of the average Arctic winter sea ice thickness from October 1993 to March 2001 derived from ERS-1 and -2 radar altimeter data. (b) Mean boreal winter (October to March) ice thickness anomaly for the period 1993–2001. (c) Changes in ice thickness between consecutive winters (circles) and melt season length (triangles) during the intervening summer period . . . . . color

5.85 Schematic illustration of the concept of the CryoSat SIRAL altimeter instrument, which is (a) to use beam forming in the along-track direction to improve on the signal-to-noise ratio and pulse-limited resolution, while (b) using across-track interferometry in regions of undulating terrain (e.g., ice sheet margins) to determine the across-track source of the scattered energy 514

5.86 Two near-coincident ICESat GLAS and Radarsat SAR datasets from the regions of the Arctic Ocean marked in the small inset maps (a, f). The upper Radarsat SAR image in (b) is from March 10, 2003 ($\sim$21 : 00 GMT), while the lower image shows the same region 5 days later (on March 15 at $\sim$15 : 00 GMT), with the ICESat GLAS groundtrack (at $\sim$23 : 00 GMT) superimposed as a yellow dashed line (flight from left to right). In (g), the upper Radarsat SAR image is from 12 March (20 : 00 GMT), while the lower image is from 15 March ($\sim$15 : 00 GMT) with an ICESat groundtrack from $\sim$05 : 00 GMT superimposed. (c, h) ICESat freeboard profile and estimated ice draft (snow = light blue, ice = dark blue). (d, i) Along-track profile of uncorrected GLAS reflectivity. (e, j) The estimated thickness distribution with three different snow cover thicknesses superimposed (red is the climatological mean +10 cm, black the mean, and green the mean −10 cm). The inset plot in (i) shows the sigmoidal function for applying snow depth. . . . . color

5.87 Ice thickness distributions over the Arctic Ocean basin on December 22, 1996 color

5.88 (a) An example of the relationship between sea ice thickness in the Sea of Okhotsk and the co-polarization power ratio $\gamma_{HH/VV}$ derived from measurements by the Japanese L-band Pi-SAR aircraft system 521

5.89 (a) AVHRR-derived *IST*, (b) its frequency distribution, (c) estimated ice thickness and (d) its cumulative distribution over a 150×150-km region of the Beaufort Sea on December 1, 1990 . . . . . color

5.90 Composite image of AVHRR-derived ice thickness h_T superimposed on a near-simultaneous Radarsat C-band SAR data, for January 9, 1999 . . . . . color

5.91 Time series of (a) ice thickness and (b) ice volume in the Sea of Okhotsk (7-day running mean), both derived from DMSP SSM/I data, compared with (c) the Cold Air Mass Index at 57.5°N, 167.5°E, derived from NCEP/NCAR reanalysis data, during the boreal winters (December–April) of 1991/2–2001/2 526

5.92 Monthly averaged maps of Arctic multiyear sea ice concentration . . . . . color

5.93 Frequency dependence, determined theoretically, of the σ^0 of Arctic first-year and multiyear ice at an incidence angle of 40° and under (a) normal/winter and (b) extreme/summer melt conditions. (c) Schematic plot of the summer dependence of the radar backscatter of the Arctic Ocean measured at C-band and VV-polarization 532

5.94 Sea ice in the Beaufort Sea imaged simultaneously at P-band ($\lambda = 60$ cm), L-band ($\lambda = 25$ cm), and C-band ($\lambda = 5$ cm) by the NASA JPL airborne SAR on March 11, 1988 535
5.95 An airborne CV-580 SAR (C-band) image of a mix of undeformed and highly deformed (rubble field) first-year ice (the left side of each frame) and multiyear ice (the right side) acquired near Resolute Bay, Canada, on May 3, 1993 at (a) HH-pol and (b) HV-pol 546
5.96 C-band images of sea ice in the Greenland Sea from March 24, 1995, recorded by the Danish aircraft EMISAR . . . . . color
5.97 Coincident images of (a) entropy H, (b) anisotropy A, and (c) α-angle for first-year sea ice conditions in the Labrador Sea off the coast of Newfoundland . . 548
5.98 Envisat ASAR Alternating Polarisation (AP) mode scenes (beam IS4: 31–36° incidence) acquired on February 7, 2003 in the Gulf of St. Lawrence, Canada color
5.99 Total power images of data collected by the NASA JPL AIRSAR polarimetric SAR system in (a) C-band, (b) L-band, and (c) P-band . . . . . color
5.100 Maps of the January, mean, Arctic, multiyear sea ice concentration estimates for the period 1988–2001 . . . . . color
5.101 Estimates of annual mean multiyear sea ice area and linear trends (1988–2001) obtained by five different methods of SSM/I passive-microwave analysis 553
5.102 Classified Arctic images of (a) SSM/I ice concentration derived using the NASA Team algorithm where multiyear ice is set at concentrations $\geq$36%, and (b) NSCAT SIRF data using the *k*-means classifier 555
5.103 Daily Seawinds QuickSCAT VV-backscatter maps of the Arctic with boundaries of the perennial sea ice zone overlain for January 3, February 15, and April 15 for the years (a) 2000, (b) 2001, (c) 2002, and (d) 2003 . . . . . color
5.104 Maximum a posteriori ice classification of combined active–passive microwave image series from 1996. . . . . color
5.105 An example of a cloud-free NOAA AVHRR thermal infrared (channel 4) image from East Antarctica, showing complex pack and fast ice conditions in the vicinity of the Mertz Glacier Polynya 558
5.106 Maps of sea ice classification in coincident (a) Radarsat SAR and (b) EOS Terra MISR images in the Beaufort Sea on March 19, 2001 . . . . . color
5.107 Maps of snow depth on sea ice for (a) the Arctic (on March 10, 2003), and (b) the Antarctic (on August 10, 2003) . . . . . color
5.108 A map of the surface roughness of the Arctic sea ice cover at a 10-km length-scale derived from ICESat elevations, compared with coincident QuikSCAT radar scatterometer backscatter data . . . . . color
5.109 An illustration of the floe classification procedure . . . . . color
5.110 (a) An example of a cloud-free Terra MODIS ice surface temperature (*IST*) product (MOD29) derived from data collected on March 12, 2003 (18 : 45 GMT) in the Fram Strait region of the NE Greenland Sea. (b) An Aqua AMSR-E 89-Ghz vertically polarized brightness temperature image of the Arctic from the same day. . . . . color
5.111 Mean monthly AVHRR-derived *IST* anomaly maps of the Arctic for all Septembers from 1981 to 1999 . . . . . color
5.112 Color-coded *IST* trend maps derived from NOAA AVHRR data over the period 1981–2003 for the Arctic in (a) autumn (SON), (b) winter (DJF), (c) spring (MAM), and (d) summer (JJA). . . . . color

5.113 Color-coded maps of the NOAA AVHRR-derived mean surface temperature (*IST*) of the Arctic . . . . . color
5.114 Monthly mean maps of T_I derived from AMSR-E brightness temperature data for (a) the Arctic in March 2003, and (b) the Antarctic in September 2003 . . . color
5.115 Color-coded anomaly maps of annual albedo in the Arctic from 1987- to 1998-derived AVHRR data . . . . . color
5.116 Map of the mean surface albedo for each RGPS cell for the Beaufort and Chukchi Seas, April 20, 1997 589
5.117 An example of snow/ice products from cloud-free ADEOS-II GLI imagery acquired from April 7 to May 7, 2003 . . . . . color
5.118 (a) Map of mean sea ice melt onset dates in the Arctic derived from passive-microwave satellite data, 1979–1998. (b) Standard deviation in melt onset dates, 1979–1998. (c) Linear trend per grid cell in the annual melt onset date, 1979–1998 . . . . . color
5.119 Maps of average sea ice melt onset date, freeze onset date, and melt season duration in the Arctic Ocean and surrounding seas during the low-index Arctic Oscillation (AO) period (1979–1988) and high-index AO period (1989–2001) . color
5.120 Change in the mean (a) melt onset, (b) freeze onset, (c) melt season duration (days), from 1979–1988 to 1989–2001 . . . . . color
5.121 Maps of the sea ice melt onset dates for (a) Antarctica (1996/7), and (b) the Arctic (1997), derived from NSCAT data . . . . . color
5.122 A time series of daily images of ADEOS NSCAT σ^0_{40} data of the Arctic sea ice cover acquired through the spring of 1997, clearly showing the spatio-temporal decrease in normalized backscatter with the progression of snowmelt onset . . 597
5.123 A map of NSCAT-derived melt onset dates across the Arctic sea ice zone in 2001 598
5.124 (a) U.S. military reconnaissance satellite image of sea ice in the Arctic Ocean from June 18, 1998 (the image strip is ~7.8 km across). The square marks the location of the Canadian icebreaker *CCGS Des Groseilliers* (length ~100 m). (b) A close-up view of the square. The ship is ~100 m long, and the dark regions are meltponds, as shown in the oblique aerial photograph from August 3, 1998 in (c). (d) Detail of a surface-type map. The image at upper right shows the 10-km^2 surface-type product. Open water is dark, ice is light, and ponds are gray. (e) Image of an area corresponding to the box in (d) and showing a higher level of detail, with meltponds clearly visible 601
5.125 (a) A subscene (width 25 km) of a Landsat 7 ETM+ true-color image (bands 3, 2, and 1) of sea ice in Baffin Bay on June 26, 2000. (b) A "blow-up" of the boxed region in (a). (c) Difference map of bands 3 and 2 for the area shown in (b). (d) Classified image of the same area . . . . . color
5.126 Schematic of the Landsat analysis method to derive the meltpond fraction of Arctic sea ice from Landsat ETM+ band-1 (0.450–0.515 μm), -2 (0.525–0.605 μm), and -3 (0.630–0.690 μm) data, at a spatial resolution of 30 m 602
5.127 Use of Seasat L-band SAR data to study and model the propagation of ocean waves in pancake/frazil ice in the Chukchi Sea 606
5.128 ERS-1 SAR image strips from (a) January 13, 1992 and (b) January 16, 1992, showing rapid ice edge variability in the Greenland Sea–Fram Strait region as a result of strong off-ice winds 608
5.129 (a) A map of surface wind speed and direction retrieved from two ERS SAR scenes (100 km across) from the marginal ice zone (MIZ) in the Barents Sea,

May 7, 1999 (10 : 08 UTC). (b) A linear profile of the wind speed, along the bold white line in (a), running from north (left) to south (right) . . . . . color
5.130 (a) Mosaic of Radarsat-1 ScanSAR Wide imagery from the Canadian Arctic, February 1–4 2001. (b) The Regional Ice Analysis Chart derived by the Canadian Ice Service from (a) . . . . . color
5.131 A possible framework for a sea ice data assimilation scheme. 614
5.132 Ice motion in the eastern Arctic on March 18, 1993 derived from (a) SSM/I 85-GHz data (12.5-km resolution), (b) a sea ice model, and (c) the data assimilation 615
5.133 (a) A range-normalized daily composite mosaic of Envisat ASAR data over the Arctic on January 8, 2005. (b) An experimental Envisat ASAR-derived ice motion product from Christmas Day (2004), with a grid size of 50 km superimposed on the SAR amplitude image (2-km resolution). 615

Tables

1.1 The spectral range of divisions of the electromagnetic spectrum exploited by satellite remote sensing 39

1.2 Important atmospheric transmission windows exploited in satellite remote sensing of the Earth's surface 41

2.1 Frequently used imagers operational during the 1990s and early 21st century . 97

3.1 The wavelength triplets used in the Earth Probe TOMS ozone retrieval algorithm 148

3.2 Total ozone errors for TOVS middle-infrared retrievals 157

3.3 POAM II measurement channels 160

4.1 The ranges in directionally dependent reflectances 224

4.2 The 18 scene categories used in the Ebert (1987) classification algorithm for Arctic AVHRR data, along with an estimate from the Warren et al. (1988) atlas of the a priori climatological probability of each category over the central Arctic Ocean. 224

4.3 The category means and standard deviations for all 18 categories and 8 spectral features used in the Ebert (1987) Arctic cloud classification method. 225

4.4 Relationships between surface temperature T_S and AVHRR channel-4 brightness temperature T_4 used for initial cloud phase discrimination by Key and Intrieri (2000) 233

4.5 Error in the retrieval of shortwave cloud optical depth τ and droplet effective radius r_e (μm) when the true cloud amount f is smaller than the value of unity assumed in the single-pixel approximation 243

4.6 Coefficients in Eq. (4.47) for retrieving Arctic ice surface temperature from NOAA-11 AVHRR data, along with the r.m.s. error for the difference between the satellite-retrieved temperatures and the actual surface temperatures used to derive the algorithm 261

4.7 Sensitivities in downwelling and net surface fluxes for clear skies during the Arctic summer, over snow and over open water. 265

4.8 Sensitivities in downwelling and net longwave surface fluxes for clear skies during winter, over snow and over open water. 266

4.9 Sensitivities in downwelling shortwave, longwave, and net surface fluxes for cloudy skies during summer over snow 266
4.10 Sensitivities in downwelling longwave and net surface flux for cloudy skies during winter over snow 267
4.11 The combined uncertainty in estimating surface fluxes 269
4.12 Cloud effectiveness, or cloud forcing for 100% cloud cover, and other radiation budget components 275
4.13 HIRS-2 channels, the exact wavelength ranges for which vary slightly with spacecraft 284
4.14 Cloud detection tests in the original midlatitude TOVS Pathfinder algorithm, and modifications made for the Arctic by Francis (1994) 289
5.1 Broadband solar albedos as a function of ice type (thickness), measured *in situ* during East Antarctic cruises in the austral spring and covering the spectral range 0.3–2.8 μm 363
5.2 Characteristics of the EOS Terra MISR instrument 417
5.3 Summary of sea-ice-related applications of major satellite sensor classes. 421
5.4 Gridded (level 3) T_B and sea ice products available from the Aqua AMSR-E 428
5.5 Microwave emissivities measured *in situ* for surface conditions in summer . . . 434
5.6 Optimal radar parameters for a given classification task, based on C- and L-band data from a given Arctic region 549
5.7 Angular emissivities of snow modeled at the wavelengths of AVHRR channels 4 (10.3–11.3 μm) and 5 (11.5–12.5 μm) for the NOAA 7 satellite 574
5.8 Angular emissivities of snow modeled for the ERS-1 ATSR thermal infrared channels 576
5.9 A summary of the spatial and temporal sea ice information requirements as defined by the Canadian Ice Service for the Canadian Arctic. 610

Abbreviations

AARC	Arctic and Antarctic Research Center
AABW	Antarctic Bottom Water
AATSR	Advanced Along-Track Scanning Radiometer
ABA	AMSR Bootstrap Algorithm
AC	Atmospheric Corrector
ACC	Antarctic Circumpolar Current
ACSYS	WCRP Arctic Climate SYStem Study
ACW	Antarctic Circumpolar Wave
ADCP	Acoustic Doppler Current Profiler
ADEOS	Japanese ADvanced Earth Observing Satellite
ADM	Angular Dependence Model
AGCS	Antarctica and the Global Climate System
AGOs	Automated Geophysical Observatories
AHRA	Advanced Horizontal Range Algorithm
AIRS	Atmospheric InfraRed Sounder
AIRSAR	Airborne SAR system
ALI	Advanced Land Imager
ALOS	Advanced Land Observing Satellite
AMI	ERS Active Microwave Instrument
AMPS	Antarctic Mesoscale Prediction System
AMRC	University of Wisconsin's Antarctic Meteorology Research Center
AMSR	Advanced Microwave Scanning Radiometer
AMSR-E	Advanced Microwave Sounding Radiometer-EOS
AMSU	Advanced Microwave Sounding Unit
ANARE	Australian National Antarctic Research Expedition
AO	Arctic Oscillation
AOI	Arctic Oscillation Index
AP	Alternating Polarization mode

APR	Active Polarization Ratio
APT	Automatic Picture Transmission
ARM	U.S. Department of Energy Atmospheric Radiation Measurement
ASAR	Advanced SAR
ASCAT	Advanced SCATterometer
ASF	Alaska Satellite Facility
ASPeCt	Antarctic Sea Ice Processes and Climate project
ASTER	Advanced Spaceborne Thermal Emission and Reflection Radiometer
ATMOS	Atmospheric Trace MOlecule Spectroscopy
ATSR	Along-Track Scanning Radiometer
AUV	Autosub-2 Autonomous Underwater Vehicle
AVHRR	Advanced Very High Resolution Radiometer
AVN	NCEP AViatioN Model
AVNIR	Advanced Visible/Near Infrared Radiometer
AWiFS	Advanced Wide Field Sensor
AWS	Automatic Weather Station
BAS	British Antarctic Survey
BBA	Bootstrap Basic Algorithm
BEST	Bering Ecosystem STudy
BRDF	Bidirectional Reflectance Distribution Function
BTD	Brightness Temperature Difference
BUV	Backscatter UltraViolet
BYU	Brigham Young University (U.S.A.)
CALIOP	Cloud–Aerosol Lidar with Orthogonal Polarization
CALIPSO	Cloud–Aerosol Lidar and Infrared Pathfinder Satellite Observations
CAPA	Composite Annual Pressure Anomaly
CART	Cloud And Radiation Testbed
CASES	Canadian Arctic Shelf Exchange Study
CASPR	Cloud and Surface Parameter Retrieval system
CAST	Chinese Academy for Space Technology
CATA	Composite Annual Temperature Anomaly
CCD	Charge Coupled Device
CCM3	NCAR Community Climate Model Version 3
C-CORE	Centre for Cold Ocean Resources Engineering (Canada)
CE	Cloud Effect
CEAREX	Coordinated Eastern ARctic Experiment
CERES	Clouds and Earth's Radiant Energy System
CHL	Cold Halocline Layer
CIS	Canadian Ice Service
CLAES	Cryogenic Limb Array Etalon Spectrometer
CLIC	CLImate and Cryosphere Project
CLIVAR	CLImate VARiability and Predictability Program
CMIS	Conical-scanning Microwave Imager/Sounder

CNES	Centre National d'Etudes Spatiales (France)
CRYSYS	Canadian CRYosphere SYStem
CSA	Canadian Space Agency
CTD	Conductivity Temperature Density
CZCS	Coastal Zone Color Scanner
DAAC	Distributed Active Archive Center
DABUL	Depolarization And Backscatter Unattended Lidar
DCS	Data Collection System
DISORT	Discrete Ordinate Radiative Transfer; DIScrete ORdinaTes method in FORTRAN
DISP	Declassified Intelligence Satellite Photography program
DKP	Differential Kinematic Parameter
DLR	Deutsche Forschungsanstalt für Luft und Raumfahrt (German aerospace agency)
DMS	dimethylsulphide
DMSP	dimethylsulfoniopropionate; U.S. Defense Meteorological Satellite Program
DORIS	Doppler Orbitography and Radiopositioning Integrated by Satellite
DSCOVR	Deep Space Climate ObserVatoRy
EASE	Equal Area Scalable Earth (grid)
ECMWF	European Centre for Medium-range Weather Forecasts
EM	ElectroMagnetic
EMI	Electro Magnetic Induction
EMISAR	ElectroMagnetics Institute Synthetic Aperture Radar (Denmark)
EMR	ElectroMagnetic Radiation
ENSO	El Niño–Southern Oscillation
EO	Earth Observing spacecraft
EOF	Empirical Orthogonal Function
EORC	Earth Observation Research Center
EOS	Earth Observing System
EOSDIS	EOS Data and Information System
EPIC	Earth Polychromatic Imaging Camera
ERB	Earth Radiation Budget
ERBE	Earth Radiation Budget Experiment
EROS	Earth Resources Observation and Science
ERS	Environmental Research Satellite
ERTS	Earth Resources Technology Satellite
ESA	European Space Agency
ESCAT	ERS wind SCATterometer system
ESMR	Electrically Scanning Microwave Radiometer
ETM	Enhanced Thematic Mapper
ETM+	Enhanced Thematic Mapper Plus
FASCOD	Fast Atmosphere Signature CODe
FDD	Freezing Degree Days

FMI	Finnish Meteorological Institute
FOV	Field Of View
FTIR	Fourier Transform InfraRed
FWHM	Full Width at Half Maximum
GAC	Global Area Coverage
GCM	General (or Global) Circulation Model
GIFOV	Ground Instantaneous Field Of View
GIN	Greenland–Iceland–Norwegian Seas
GIS	Geographic Information System
GLAS	Geoscience Laser Altimeter System
GLDV	Gray Level Difference Vector
GLI	GLobal Imager
GLOBEC	Southern Ocean GLOBal ECosystem Dynamics Program
GMM	Global Monitoring Mode (Envisat)
GOES	Geostationary Operational Environmental Satellite
GOME	Global Ozone Monitoring Experiment
GOMOS	Global Ozone Monitoring by Occultation of Stars
GPS	Geophysical Processor System
GR	Gradient Ratio
GTS	Global Telecommunications System
H	horizontally polarized
HALOE	HALogen Occultation Experiment
HDF-EOS	Hierarchical Data Format for the Earth Observing System
HFOV	Horizontal Field Of View
HIRDLS	HIgh Resolution Dynamics Limb Sounder
HIRS	High-resolution InfraRed Sounder
HITRAN	HIgh-resolution TRANsmittance model
HLS	Hue–Lightness–Saturation technique
HPBW	Half Power Beam Width
HRPT	High Resolution Picture Telemetry (or Transmission)
HRV	High Resolution Visible
HSB	Humidity Sounder from Brazil
HYDROS	NASA's HYDROsphere State mission
IABP	International Arctic Buoy Program
iAnZone	International Antarctic Zone (SCAR)
IASI	Infrared Atmospheric Sounding Interferometer
IB	Iceberg
ICEMON	European ICE MONitoring in the Polar Regions initiative
ICESat	Ice, Cloud, and land Elevation Satellite
ICP	Ice Crystal Precipitation
IDL	Interactive Data Language
IF	Intermediate Frequency
IFOV	Instantaneous Field Of View
ILAS	Improved Limb Atmospheric Spectrometer
INDOEX	INDian Ocean EXperiment

IPAB	International Program for Antarctic Buoys
IPCC	International Panel on Climate Change
IPS	Ice Profiling Sonars
IRIS	InfraRed Interferometer Spectrometer
IRS	Indian Remote Sensing satellite
ISCPP	International Satellite Cloud Climatology Project
ISL	Ice Season Length
ISRO	Indian Space Research Organisation
IST	Ice Surface Temperature
JAXA	Japanese Aerospace eXploration Agency
JERS	Japanese Earth Resources Satellite
JGOFS	Joint Global Ocean Flux Study
JPL	NASA's Jet Propulsion Laboratory
KMSS	Multichannel Spectral Imaging System (Russia)
LAC	Local Area Coverage
LBLRTM	Line-by-Line Radiative Tranfer Model
LEO	Low Earth Orbit
LISS	Linear Imaging Self Scanner
LLLS	Low Level Light Sensor
LOS	Line Of Sight
LOWTRAN	LOW-resolution TRANsmittance model
LRR	Laser Retro Reflector
LTE	Local Thermodynamic Equilibrium
LTER	U.S. Palmer Long-Term Ecological Research Program
MAS	MODIS Airborne Simulator
MCC	Maximum Cross Correlation
McIDAS	Man-computer Interactive Data Access System
MCT	mercury cadmium telluride
MERIS	MEdium Resolution Imaging Spectrometer
MESSR	Multispectral Electronic Self-Scanning Radiometer
MetOp	Meteorological Operational satellite
MIPAS	Michelson Interferometer for Passive Atmospheric Sounding
MISR	Multi-angle Imaging Spectro Radiometer
MIZ	Marginal Ice Zone
MLS	Microwave Limb Sounder
MM5	Polar MM5, a version of the fifth-generation Pennsylvania State University–NCAR
MO	Melt Onset
MODIS	MODerate resolution Imaging Spectrometer
MODTRAN	MODerate-resolution TRANsmittance model
MOPITT	Measurements Of Pollution In The Troposphere
MPLNET	NASA Goddard Space Flight Center's MicroPulse Lidar NETwork
MRIN	More Research Is Necessary(!!)
MSA	Methanesulfonic acid

MSL	Melt Season Length
MSMR	Multi-channel (or -frequency) Scanning Microwave Radiometer
MSPPS	NOAA Microwave Surface and Precipitation Products System
MSS	Landsat Multi Spectral Scanner
MSU	Microwave Sounding Unit
MSU-E	High-Resolution Multi-Spectral Scanner with Electronic Scanning (Russia)
MSU-MR	Low-Resolution Multi-Spectral Scanner (Russia)
MVISR	Multichannel Visible and IR Scan Radiometer
MWR	MicroWave Radiometer
NADW	North Atlantic Deep Water
NAM	Northern Annular Mode
NAO	North Atlantic Oscillation
NASA	National Aeronautics and Space Administration
NASDA	National Space Development Agency of Japan
NCAR	National Center for Atmospheric Research
NCEP	National Center for Environmental Prediction
NDSI	Normalized Difference Sea Ice Index
NEΔT	Noise Equivalent Difference Temperature
NEMS	Nimbus-E Microwave Spectrometer
NEP	Noise Equivalent Power
NER	Noise Equivalent spectral Radiance
NESDIS	NOAA National Environmental Satellite, Data, and Information Service
NIC	National Ice Center
NIST	National Institute for Standards and Technology
NISTAR	NIST Advanced Radiometer
NIVR	Netherlands Agency for Aerospace Programs
NOAA	National Oceanic and Atmospheric Administration
NORSEX	NORwegian Remote Sensing EXperiment
NPOESS	National Polar Orbiter (or Orbiting) Environmental Satellite System
NPP	NPOESS Preparatory Project
NRTSI	NSIDC's Near Real Time DMSP SSM/I
NSA	North Slope of Alaska
NSCAT	NASA SCATterometer
NSIDC	U.S. National Snow and Ice Data Center
NT	NASA Team (algorithm)
NTBC	Narrow To Broadband Conversion
NTM	National Technical Means
O&SI SAF	European EUMETSAT Ocean and Sea Ice Satellite Application Facility project
OCM	Ocean Color Monitor
OCO	Orbiting Carbon Observatory
OCTS	Ocean Color and Temperature Scanner

OLR	Outgoing Longwave Radiation
OLS	Operational Linescan System
OMI	Ozone Monitoring Instrument
OMPS	Ozone Mapping and Profiler Suite
OPP	Office of Polar Programs (USAP)
OPS	OPtical Sensor
PALSAR	Phased Array-type L-band Synthetic Aperture Radar
PAN	PANchromatic camera; pancake ice
PAR	Photosynthetically Active Radiation
PARASOL	Polarization and Anisotropy of Reflectances for Atmospheric Sciences coupled with Observations from a Lidar (French instrument derived from the POLDER instrument)
PCA	Principal Component Analysis
PDO	Pacific Decadal Oscillation
PER	Antarctic multiyear ice
PIZ	Perennial Ice Zone
PMC	Polar Mesospheric Cloud
PMT	PhotoMultiplier Tube
PMW	Passive MicroWave
PNC	Pancake ice
POAM	Polar Ozone and Atmospheric Measurement
POES	Polar-orbiting Operational Environmental Satellite
POLDER	POLarization and Directionality of the Earth's Reflectances
POLES	POLar Exchange at the Sea Surface dataset
PR	Polarization Ratio
PRI	???
PRISM	Panchromatic Remote-sensing Instrument for Stereoscopic Mapping
PSC	Polar Stratospheric Cloud
PSSM	Polynya Signature Simulation Method
p.s.u.	Practical salinity units
r.m.s.	root-mean-square
RA	Radar Altimeter
RAR	Real Aperture Radar
RC	Resistance–Capacitance (capacitor charging)
READER	REference Antarctic Data for Environmental Research
RF	Radio Frequency
RFY	Rough First Year class
RGPS	Radarsat Geophysical Processor System
RKA	Russian Space Agency
RLSBO	Side-Looking Real-Aperture Radar (Russia)
RMSE	Root Mean Square Error
ROAVERRS	Research on Ocean–Atmosphere Variability and Ecosystem Response in the Ross Sea
SAGE	Stratospheric Aerosols and Gas Experiment

SAM	Southern Annular Mode; Stratosphere Atmospheric Measurement
SAO	Semi Annual Oscillation
SAOCOM	SAtellite for Observation and COMmunications
SAR	Synthetic Aperture Radar
SASS	SeaSat-A Scatterometer
SBDART	Santa Barbara DISORT Atmospheric Radiative Transfer
SCAR	Scientific Committee on Antarctic Research
SCIAMACHY	SCanning Imaging Absorption spectroMeter for Atmospheric ChartographY
SCICEX	SCientific ICe EXpeditions
SCOR	Scientific Committee on Oceanic Research
SCP	Scatterometer Climate Pathfinder
SEARCH	Study of Environmental ARctic CHange
SeaWiFS	Sea-viewing Wide Field of View Spectrometer
SFY	Smooth First Year class
SHEBA	Surface Heat and Energy Balance of the Arctic experiment
SICH	Satellite named after the Ukrainian for "owl"
SIR	Shuttle Imaging Radar
SIR-C	Shuttle Imaging Radar-C mission
SIRAL	Synthetic aperture Interferometric Radar ALtimeter
SIRF	Scatterometer Image-Reconstruction and Filtering algorithm
SLR	Side-Looking Radar
SME	Solar Mesosphere Experiment
SMMR	Scanning Multichannel Microwave Radiometer
SMOS	ESA Soil Moisture and Ocean Salinity mission
SNR	Signal to Noise Ratio
SOI	SO_2 Index; Southern Oscillation Index
SOLAS	Surface Ocean–Lower Atmosphere Study
SOLSTICE	SOLar STellar Irradiance Comparison Experiment
SPOT	Système Pour l'Observation de la Terre
SRTM	Shuttle Radar Topography Mission
SSEC	Space Science and Engineering Center
SSIZ	Seasonal Sea Ice Zone
SSM/I	Special Sensor Microwave/Imager
SSM/T	Special Sensor Microwave/Temperature
SSMIS	Special Sensor Microwave Imager Sounder
SSMT	Special Sensor Microwave Temperature/Humidity sounder
SST	Sea Surface Temperature
SSU	Stratospheric Sounding Unit
TES	Thermal Emission Spectrometer
THIR	Temperature Humidity Infrared Radiometer
TIGR	Thermodynamic Initial Guess Retrieval
TIR	Thermal InfraRed
TIROS	Television and Infrared Observation Satellite
TM	Thematic Mapper

TOA	Top Of Atmosphere
TOMS	Total Ozone Mapping Spectrometer
TOVS	TIROS-N Operational Vertical Sounder
TRMM	Tropical Rainfall Measuring Mission
UARS	Upper Atmosphere Research Satellite
UAV	Unmanned Aerial Vehicle
UKMO	United Kingdom Meteorological Organization
ULS	Upward-Looking Sonar
USAP	U.S. Antarctic Program
UV	UltraViolet
V	vertically polarized
VFOV	Vertical Field Of View
VHRR	Very High Resolution Radiometer
VIIRS	Visible/Infrared Imager/Radiometer Suite
WAP	Western Antarctic Peninsula
WCRP	World Climate Research Program
WiFS	Wide Field Sensor
WINDII	WIND Imaging Interferometer
WMO	World Meteorological Organization

About the authors

DAN LUBIN

Dan Lubin is a veteran of three Antarctic and two Arctic field campaigns, including the National Ozone Expedition, the 1994 Arctic Ocean Section, and the Surface Heat Budget of the Arctic (SHEBA) program. After his bachelor's degree in Physics from Northwestern University, Dan earned an M.S. in Astronomy and Astrophysics in 1988 and a Ph.D. in Geophysical Sciences in 1989 from the University of Chicago. He joined the Scripps Institution of Oceanography (SIO) in 1990 as a postdoc, and has been affiliated with SIO as a Research Physicist since 1993. In addition to maintaining research interests in polar field instrumentation, remote sensing, and astronomy, Dan also serves as an Engineering Duty Officer in the U.S. Navy Reserve. Dan lives in San Diego, California, with his wife Lorri and stepson Jacob.

ROB MASSOM

Rob Massom has participated in nine Antarctic and three Arctic sea ice research campaigns, including the Arctic Marginal Ice Zone Experiment (MIZEX, 1983–84) and the First Winter Weddell Sea Project cruise of 1986. After his bachelor's degree in Physical Geography from London University, Rob earned a Ph.D. in Glaciology/Remote Sensing in 1989 from the Scott Polar Research Institute (University of Cambridge). After that, he spent three years at NASA Goddard Space Flight Center as a U.S. National Research Council postdoc (working with Joey Comiso), before joining the Antarctic Cooperative Research Centre (CRC) in Hobart (Tasmania, Australia) in 1992 as a sea ice research scientist. He is currently a senior research scientist with the Antarctic Climate and Ecosystems CRC in Hobart. Rob's research interests include remote sensing, sea ice and polar oceans and their ecological significance, precipitation over the Antarctic Ice Sheet, and the impact of modes of large-scale anomalous atmospheric circulation on sea ice and ecology. Rob lives in Hobart with his wife Yuko and daughter Adelle. Even after 25 years' involvement in polar research, Rob is still drawn by the magical lure of polar regions, driven by the fact that the more he learns, the more he realizes he doesn't know.

Publisher credits

The following publishers have given their kind permission to reprint or adapt materials that appear in the following figures. In addition, we have attempted to reach the senior authors to obtain their permission as well; we trust that those we have not been able to reach will not object to their work being shown and discussed herein as advances in the field. Complete citations of these sources are given in the reference sections at the end of the respective chapters.

Publisher	*Figure No.*
A. Deepak	5.8
Academic Press	2.11, 4.1
Alaska SAR Facility	5.23
American Academy for the Advancement of Science	3.15, 4.57, 4.58, 4.59, 5.49
American Geographical Society	1.9
American Geophysical Union	2.5, 2.7, 2.27, 3.5, 3.8, 3.9, 3.10, 3.11, 3.12, 3.13, 3.14, 3.16, 3.17, 3.18, 3.19, 3.20, 3.22, 3.24, 3.25, 3.26, 3.27, 4.5, 4.11, 4.12, 4.17, 4.23, 4.25, 4.48, 4.49, 4.51, 4.52, 4.53, 4.54, 4.55, 4.56, 4.65, 4.66, 4.67, 4.68, 4.69, 4.70, 5.1, 5.4, 5.11, 5.15, 5.16, 5.17, 5.22, 5.28, 5.32, 5.37, 5.40, 5.41, 5.44, 5.45, 5.47, 5.56, 5.60, 5.63, 5.64, 5.65a, 5.70, 5.74, 5.75, 5.76, 5.83, 5.86, 5.89, 5.90, 5.92, 5.93, 5.100, 5.101, 5.103, 5.108, 5.109, 5.111, 5.127.
American Institute of Physics	5.10, 5.48, 5.113
American Meteorological Society	2.4, 2.10, 4.7, 4.10, 4.14, 4.18, 4.26, 4.27, 4.28, 4.29, 4.30, 4.31, 4.32, 4.33, 4.34, 4.35, 4.39, 4.40, 4.41, 4.46, 4.47, 4.50, 4.52. 4.60, 4.61, 4.62, 4.63, 4.64, 5.39, 5.46, 5.112, 5.119, 5.120

Publisher	*Figure No.*
Applied Physics Laboratory at Johns Hopkins University	5.24, 5.29
Artech House	2.21, 2.22, 2.23, 2.26
Australian Commonwealth	5.7, 5.82, 5.87
Cambridge Journals	5.72, 5.105
Canadian Space Agency and Radarsat International	5.27, 5.58, 5.66, 5.67, 5.95
Dayton Daily News	1.4
Elsevier Publishing	2.11, 4.1, 5.126
European Space Agency	5.25, 5.96, 5.98, 5.99, 5.121, 5.133
Gainesville Sun	1.4
General Dynamics Advanced Information Systems, Inc.	2.18
Institute of Electrical and Electronics Engineers	5.8a, 5.33, 5.34, 5.35, 5.36, 5.54, 5.55, 5.85, 5.97, 5.102, 5.104, 5.106, 5.110, 5.121, 5.129
International Glaciological Society	5.31, 5.53, 5.62, 5.69, 5.71, 5.80, 5.81, 5.91, 5.115, 5.116, 5.122, 5.123, 5.125, 5.131, 5.132
Japan Aerospace Exploration Agency	5.26, 5.117
Japan National Institute for Polar Research	5.2
John Wiley & Sons	5.14
Joint Oceanographic Institutions, Inc.	5.3
National Aeronautics and Space Administration	1.10, 1.11, 5.12, 5.13, 5.20, 5.52, 5.59, 5.73
National Oceanographic and Atmospheric Administration	5.21, 5.128, 5.130
National Snow and Ice Data Center	5.77, 5.78
Nature magazine	3.3, 3.4, 3.23, 5.51, 5.84
New York Historical Society	1.2, 1.3
Newark Star-Ledger	1.4
Oxford University Press	2.9, 2.12
Royal Meteorological Society	4.36, 4.37, 4.38
Scientific American	5.61
Scripps Institution of Oceanography Library Special Collections	1.1, 1.5, 1.6, 1.7, 1.8
Smithsonian Institution Division of Domestic Life	1.4
Springer Science and Business Media	3.1, 3.2, 4.42, 5.9, 5.19
Taylor & Francis, Ltd.	2.20, 4.9
Universität Karlsruhe	5.79
World Meteorological Organization	5.8

1

Introduction

The polar regions, perhaps more than any other places on Earth, give the geophysical scientist a sense of exploration. This sensibility is genuine, for not only is high-latitude fieldwork arduous with many locations seldom or never visited, but there remains much fundamental knowledge yet to be discovered about how the polar regions interact with the global climate system. The range of opportunities for new discovery becomes strikingly clear when we realize that the high latitudes are not one region but are really two vastly different worlds. The high Arctic is a frozen ocean surrounded by land, and is home to fragile ecosystems and unique modes of human habitation. The Antarctic is a frozen continent without regular human habitation, covered by ice sheets taller than many mountain ranges and surrounded by the Earth's most forbidding ocean.

When we consider global change as applied to the Arctic, we discuss impacts to a region whose surface and lower atmospheric temperatures are near the triple point of water throughout much of the year. The most consistent signatures of climate warming have occurred at northern high latitudes (IPCC, 2001), and the potential impacts of a few degrees increase in surface temperature include a reduction in sea ice extent, a positive feedback to climate warming due to lowering of surface albedo, and changes to surface runoff that might affect the Arctic Ocean's salinity and circulation. When we consider global change and the Antarctic, we discuss how changes in global atmospheric circulation might alter both the mass balance of the great ice sheets and the distribution of the highly seasonal sea ice concentration, and how delicate marine ecosystems might be affected by local climate warming and by ultraviolet radiation stresses arising from springtime ozone depletion. These are just a few of the issues, and it is becoming increasingly clear that both the Arctic and Antarctic need to be studied as entire systems, with major advances in our understanding being realized when we consider the coupling of atmospheric, oceanic, cryospheric, and biological processes. At the same time, individual mechanisms within each of these disciplines—cloud physics and radiative transfer, meteorology

of katabatic winds, sea ice dynamics, marine bio-optical properties, to name a few—have yet to be fully understood in the polar regions. Hence there is ample opportunity for future exploration and discovery.

This book treats one of the most important vantage points for studying the polar climate systems and their components: the space-based remote sensing platform. In terms of exploration, the polar regions and space have many parallels. For scientific advancement the use of space-based remote sensing is essential. Although *in situ* experimental work is necessary in all areas of Earth science, the logistical challenges of polar fieldwork limit detailed experimental work in the high Arctic, the Southern Ocean, and on the Antarctic continent to only a few locations and to relatively short timeframes. Remote sensing is required to generalize results from field programs to larger geographic areas and longer timescales.

There are other parallels. Polar biology is often studied and discussed in terms of "life in extreme environments", as a starting point for considering possible life elsewhere in the solar system. NASA has often regarded remote Antarctic field camps as analogues of space habitation, and has carried out psychological studies of personnel stationed in Antarctica. In addition to the similarities in group dynamics, polar fieldwork can be extremely demanding physically and often involves hazards to which an explorer can succumb within minutes if there is a mishap. The experiences of a polar researcher in the field—for example, an Antarctic meteorologist working in the face of hurricane force katabatic winds beneath a trans-Antarctic mountain range pass—rival those of a spacewalker.

For the remote-sensing researcher too, the sense of polar exploration continues with a new generation of space-based instruments now operational. These are the instruments with NASA's Earth Observing System (EOS), and similar programs from Europe, Japan, and India. Most Earth science missions are designed primarily for the study of tropical and middle latitudes, and one of the most rewarding aspects of research in polar remote-sensing research involves discovering how data from these missions can further polar science objectives as well. In this book we will cover many examples showing how data from existing and well-established remote-sensing missions, or "heritage" instruments (as they are called in space program vernacular), have been adapted for use over the Arctic and Antarctic. If, after going through such examples, the reader is motivated to find new ways to use EOS or similar next-generation datasets, this book will have served its purpose.

1.1 NASA IN THE 19TH CENTURY: THE GREAT U.S. EXPLORING EXPEDITION DISCOVERS ANTARCTICA

We start with some history. Massom (1991) reviews how remote sensing has made vital contributions to the modern era of polar research in the 20th century. In this section we go back yet another century before forging ahead into the 21st. All polar researchers are familiar with the exploits of such giants as Nansen, Amundsen, Scott, Shackleton, Mawson, and Byrd. In her monograph on Captain Robert Falcon

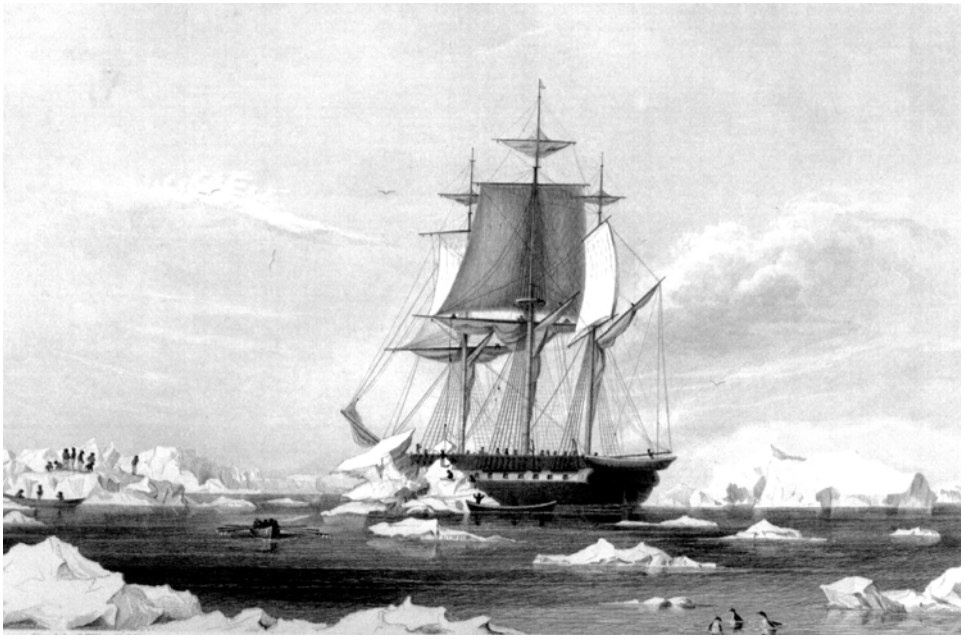

Figure 1.1. *USS Vincennes*, flagship of the United States Exploring Expedition.
From Wilkes (1845a), *Narrative*, **2**. Special Collections, Scripps Institution of Oceanography Library.

Scott's attempt at the South Pole, Solomon (2001) has shown just how vulnerable these early-modern explorers were in the harsh polar environment despite their experience and meticulous planning, and how a single climate anomaly could bring disaster. In fact, human survival at high latitudes is so fragile and vulnerable to the climate that every great expedition of the past can have some instructional value to the modern researcher. Here we review one that is both relevant to remote sensing, and also quite entertaining.

The reader familiar with various aspects of a national space program will recognize in the early history of polar exploration an episode with hauntingly familiar themes. Four books tell the story of the U.S. Exploring Expedition (Figure 1.1) in vivid and often humorous detail: Stanton (1976), Viola and Margolis (1985), Gurney (2000), and Landis (2001). Most of what follows in this section is abstracted from them. In this tale, there is a lesson for those who attempt to study the polar regions from space-based platforms.

1.1.1 Holes in the poles

The tale begins in 1825 with the nationwide lecture tour of John Cleves Symmes, Jr. (1780–1829), a self-styled natural philosopher from the Missouri Territory (Figure 1.2). Symmes had served as a captain of infantry during the War of 1812,

Figure 1.2. "I declare that the Earth is hollow and habitable within." John Cleves Symmes, Jr. (1780–1829), the Newton of the West (sketch by Audubon).

Courtesy: The New York Historical Society.

earning distinction at the battle of Lundy's Lane, and had afterward trained himself as a scientific gentleman. He eventually proved eccentric and glib enough to acquire the nickname "The Newton of the West". The source of Symmes' fame was his grand unified theory of geophysics, which contained three arguments: (1) the Earth is hollow and habitable within, being made up of "concentrick spheres"; (2) the center of the Earth can be reached through giant holes in the North or

South Pole; and (3) the United States should be the country to make this momentous discovery. To be fair to Symmes, he wasn't a solitary lunatic. This was an age when many a leading natural philosopher was proposing his own "Theory of the Earth"—supposedly comprehensive, mostly hand-waving. Symmes not only proposed his theory, but in a proper "hands on" American spirit offered to lead a polar expedition to prove it. He sent copies of his first "circular" describing his theory to governments around the world, and the appendix to this paper contained a certificate of his sanity. At a time of rough egalitarianism, when there were few American institutions of higher learning and when formal scientific peer review barely existed, numerous testimonials to Symmes' theory of polar holes began to originate in the western states and territories and make their way to Congress during the early 1820s. Even some respectable scientists such as the Cincinnati mathematician Thomas J. Matthews, who regarded Symmes' theory as rubbish, saw the groundswell of popular support as a possible means of persuading Congress to start funding scientific exploration.

Publicity for the theory of polar holes grew by leaps and bounds once it caught the attention of a young, ambitious, and well-educated Ohio journalist named Jeremiah Reynolds (1799–1859). Reynolds had a vision of the United States—the only nation governed by the people and also fundamentally a maritime nation—sending forth a great scientific expedition round the world, one whose exploits and discoveries would rival those of Halley, Cook, Bougainville, and other European giants. He saw Symmes' theory as a means to this end, and with great organizational skill and eloquent writing in the popular press, he put together and promoted a nationwide lecture tour. So successful was Symmes when addressing the Pennsylvania State Legislature at Harrisburg that 50 members of that body endorsed a petition to Congress declaring Symmes' justification for a polar expedition "quite as reasonable as that of the great Columbus" and "better supported by facts". Throughout the United States enthusiasm grew for dispatching an expedition to the Antarctic seas, to find the great hole in the South Pole leading to the center of the Earth.

Why the South Pole and not the North? Well, Reynolds had become quite crafty in his lobbying. Recognizing that Congress might never fund an overseas scientific enterprise on intellectual merit alone, he kept the private sector in mind. By shifting the emphasis of his proposed expedition from the North to the South Polar regions, he enlisted considerable support from the New England states whose legislators recognized the obvious commercial spinoffs: a government expedition to chart the Southern Ocean could greatly benefit the whaling industry.

In fact, the New England whaling and sealing industries already had a substantial history of commercial Antarctic exploration (Bertrand, 1971). A noteworthy example is the Fanning–Pendleton sealing fleet of 1820, which sailed to the newly discovered South Shetland Islands. One member of this expedition was 21-year-old Nathaniel B. Palmer, skipper of the tiny 47-foot sloop *Hero*. In November 1820 Palmer detached from the fleet and made an exploratory cruise to the south, sighting the mainland of the Antarctic Peninsula. In early 1821 Palmer made another exploratory cruise, during which he encountered the Russian Navy

frigates *Vostok* and *Mirny* commanded by Thaddeus von Bellingshausen. Various sources credit either Palmer or von Bellingshausen with being the first to sight the Antarctic mainland, and accounts of this meeting at sea are both sketchy and controversial. The controversies are mainly due to a language barrier, because both were fundamentally honest men. Palmer claimed that he had given the Russian commodore charts that enabled the frigates to extricate themselves from danger. What is more likely is that von Bellingshausen courteously examined the young man's charts and then went about his business. A second Fanning–Pendleton expedition went in search of new fur seal rookeries in late 1821–1822, as it became apparent that animals on the South Shetlands had been hunted to near extinction. During this expedition Nathaniel Palmer again played a major role, discovering the South Orkney Islands in collaboration with a British sealer, George Powell. There were many other voyages by Americans to the Southern Ocean during these years, the activities of which we can only divine from terse entries in the captains' logs that have survived. Most of the territorial discoveries made by the early sealing captains were kept secret, for obvious commercial reasons.

As Reynolds' lecture tour progressed throughout the eastern states, he gradually realized the need for a shift in emphasis. Although audiences were entertained, it was clear that eccentric theories about polar holes were never going to secure enough public and official support for an expedition. Reynolds, who never entirely believed in polar holes, tried to convince "Professor" Symmes that the primary objective of their travels should be to garner assistance in "testing the truth of the theory"—in other words, a polar expedition. To accomplish this, Reynolds insisted that he would need to speak and write more generally about the polar regions and the South Pacific, and introduce other points of view. Symmes would have none of this and, as his own health was beginning to fail, he cut short his participation in the lecture tour and returned home.

Reynolds, now on his own and enjoying considerable public relations momentum from his own writings, began advocating the notion of an open polar sea in the Southern Hemisphere. He poured over volumes of the *Transactions of the Royal Society*, and transcripts of voyages to the South Pacific, and found ample evidence of ice-free conditions at southern high latitudes. At that time, the record for progress toward the South Pole was held by English sealer James Weddell, who had reached an impressive $74°15'$ and had found open ocean. The general opinion among European scientists was that, because the Southern Hemisphere contained less land mass than the Northern, and because sea ice formed primarily in the presence of land (or so they believed), there should be fewer obstacles to polar exploration in the south than in the north. Moreover, southern high latitudes were almost entirely unknown in comparison with the north, as the Antarctic Circle had never been approached from regions encompassing $340°$ of longitude. There was plenty of glory left to be won in Antarctic exploration. By early 1828, Reynolds' labors for a national exploring expedition began to bear fruit. The House Committee on Naval Affairs had received so many favorable testimonials that they were persuaded to invite Reynolds to Washington to make a presentation to Congress.

1.1.2 The dawn of big government science

Reynolds' presentation was very skillful. He perceived that to enlist federal support a merger was necessary between scientific exploration and commerce. He reported that the sealing industry was already in decline, as seven million skins had already been taken by Americans and the known seal rookeries were nearly wiped out. The whaling fleets of New Bedford and Nantucket were bringing home four million barrels of oil annually from the South Seas, and the entire industry might soon be in jeopardy unless new stocks of animals were located. The Boston sandalwood trade was also in danger of excessive harvesting. Only comprehensive, government-sponsored scientific exploration could chart the Pacific and Southern Oceans with sufficient breadth and detail to maintain these vital American industries.

Many in Congress were sympathetic. Nearly all northern Whigs, and even a few southern Democratic-Republicans, supported the idea of an expedition to the South Pacific. At a dinner party, Reynolds met President John Quincy Adams and the two established an instant rapport. Adams liked the prospect of the United States following the European example of scientific exploration, and perhaps even doing better. However, the trouble lay in politics. Adams' administration was in its final year, and everyone including Adams expected his presidency to last only a single term. Democratic-Republicans, who had chosen Andrew Jackson as their champion, were already gearing up for the election of 1828 by labeling Adams as "artificial" and "aristocratic", and the concept of a naval exploring expedition emulating Europe fell under this stigma. The best the Adams administration could do was to push through a resolution in the House, on May 21, 1828, requesting that the Navy dispatch a small ship to the South Pacific to explore "coasts, islands, harbors, shoals, and reefs" if such a voyage could be accomplished without a special appropriation". Adams confided to Reynolds that he was delighted with even this penny-pinching resolution, and that it was the most satisfying piece of legislation to emerge from that particular session of Congress.

Even though the Adams administration had only a few months to run, the May 1828 resolution provided a mandate to start planning an exploring expedition. President Adams appointed Reynolds to the Navy Department as a "Special Agent for the Pacific and South Seas", and instructed him to prepare a detailed report about the extent of American trade in those regions. Reynolds carried out this assignment with characteristic enthusiasm and thoroughness. He traveled throughout New England to interview every whaling and sealing captain he could find, and his research resulted in the first proper survey of these industries. He also found that the gaps in geographical knowledge of high southern latitudes were larger than previously believed. Most sightings of land reported by American mariners were either improperly charted or described only in brief log entries. Hence there were many opportunities for rigorous scientific exploration. Most influential on Reynolds was his meeting with the Connecticut merchant captain Edmund Fanning (1769–1841), whom he described as "the Father of all Sealers". Fanning was probably the most experienced Antarctic mariner to date, and he shared

Reynolds' views that much of the southern polar sea remained open, and beyond that sea lay an undiscovered continent.

Reynolds also realized what would be necessary to maximize the scientific achievement of an exploring expedition. His travels and researches had taught him how much science had changed since the days of Captain Cook. By the early 1800s, scientific knowledge had increased to the point where specialization was necessary. No longer was it possible to embark a "natural philosopher" à la Sir Joseph Banks, who would make important contributions to all branches of science simply from the ship sailing to unknown lands. It had become impossible for any one scientist to be an expert in everything, and Reynolds insisted that the expedition should embark zoologists, botanists, geologists, technical artists, and an astronomer. In short, the expedition would need a *science team*.

On learning of Adams' and Reynolds' plans, Dr. James Ellsworth De Kay, head of the New York Lyceum of Natural History, volunteered to join the expedition as naturalist. So did the respected Albany geologist James Eights, naturalist-painter Titian R. Peale, and astronomer Robert Treat Paine. A very distinguished science team began to materialize. Enthusiasm was growing from outside the scientific community as well. President Adams allocated the Navy's sloop-of-war *USS Peacock* for the expedition, and many Navy officers volunteered. From the merchant marine, many experienced sealing captains applied for berths as ice pilots. When in December of 1828 the House of Representatives passed a resolution that surpassed the previous one of May and appropriated $50,000, a delighted Reynolds wrote that the world would now see "the first American Expedition of discovery—the first to go to the South Pole, and the first from any Republican Government; three grand points that can never happen again!"

Then, just as it was gathering headway, the United States Exploring Expedition ran aground in the Senate. Despite the expedition's merit, most southern Democratic-Republicans couldn't bring themselves to vote for an enterprise that might preferentially benefit the New England states. The leader of the naysayers was Senator Robert Y. Hayne of South Carolina, who was unfortunately the chairman of the Senate Committee on Naval Affairs. When the appropriations bill reached the Senate, Hayne went on the offensive. In a long-winded speech he argued that geographic discoveries would be "fraught with the most serious evils" such as defense expenditures and emigration, and that the Exploring Expedition would signal an "abandonment of the fundamental principles" which had so far kept the United States from becoming entangled in "unnecessary connections abroad". Furthermore, it would be "altogether superfluous to attempt the discovery of unknown lands" while so much of North America remained unexplored. As for American science, it should be regarded in the same light as agriculture, and be "safely left to the enterprise of individuals, which, with an instinctive sagacity, that puts to shame the assumed wisdom of governments, is invariably directed to the pursuits most profitable to themselves, and most to the welfare and honor of the country."

Most of this was hypocrisy. Despite the Jeffersonian mantra they chanted on the virtues of agrarian self-sufficiency, southern Democratic-Republicans weren't above

dipping into the federal purse to build roads, canals, and other infrastructure so that the South could better compete with the more industrialized North. And within 20 years, southern desire for more slave territories would involve the United States in one of the most vicious foreign entanglements in its history: war with Mexico. Nevertheless, Senator Hayne's message carried the day. All the Whigs but one voted for the appropriation, but in that session they were the minority. By February 1829 the Exploring Expedition was dead in the Senate and Democratic-Republicans rejoiced that the "South Sea Bubble" had burst.

Reynolds, though disappointed, wouldn't give up. He turned immediately to the merchant marine and with the help of his mentor Edmund Fanning organized a "South Sea Fur Company and Exploring Expedition". One of the original science team members signed on, geologist James Eights. In October 1829, the brigs *Annawan* and *Seraph*, commanded by the venerable Nathaniel Palmer and Benjamin Pendleton, respectively, and the schooner *Penguin*, commanded by Palmer's younger brother, set sail for the South American sector of the Antarctic. The little expedition cruised in the vicinity to the west of the Antarctic Peninsula (which was then known only as a series of landfalls and not as part of a continent), and explored the southern islands of Chile. But it soon ran into serious trouble. Scientific exploration and seal hunting were incompatible objectives. As the ships made lengthy transects across the open Southern Ocean looking for an unknown continent, the merchant seamen, who had signed on for shares in the seal catch, began to suffer from scurvy and became disaffected. Seeing that the expedition leaders weren't trying their best to catch seals, sailors deserted in droves every time the flotilla touched land in South America. Finally, the skippers had to insist on turning back to the United States while they still had enough men to work their ships. Reynolds tried hard to "inspire these men, with the feeling, that there is something worth living for, besides money", but he failed, and went ashore himself at Santa María, Chile. It took him 2 years to return to the United States.

Intellectually, this private expedition wasn't a total loss. James Eights made the most of his visit to the Antarctic Peninsula region, and was able to publish papers on oceanography, geology, and zoology. Reynolds, ever the journalist, had spent his long hours in the open sea transcribing sailors' yarns. One of these he later wrote up and published in a literary magazine called *The Knickerbocker*. It was called "Mocha Dick, the White Whale of the Pacific" and it caught the attention of Eights' fellow New Yorker Herman Melville. Still, both the scientific community and the merchant investors were disappointed.

In the spring of 1834 Reynolds returned to Washington and found a very different political situation, one he saw as encouraging. Andrew Jackson and his party had been firmly in power for several years. They had come to power on a platform of rough and natural egalitarianism that ultimately increased American patriotism and a belief that the young republic was a match for any European nation in any endeavor. As a result, the Jackson administration was able to institute new programs and technical reforms that under Adams would have been labeled "aristocratic". President Jackson ordered the standardization of weights and measures throughout the country, and a coastal survey for improving and

standardizing navigational charts. The Jackson administration even went so far as to dispatch two naval vessels—one of them *USS Peacock*—to Asia to uphold U.S. trading interests in the Pacific and to make commercial treaties. At the height of the Cold War, only Nixon could go to China. In the republic's early days, only an administration that extolled the virtues of log cabins and hard cider could involve the government in programs that might help make northeastern merchants rich. Furthermore, John Quincy Adams was now serving in the House of Representatives, and his former Navy Secretary, Samuel Southard of New Jersey, was in the Senate. When Reynolds again took up the cause of an Exploring Expedition, he could count on substantial congressional support.

Both the maritime and scientific communities again sent testimonials to Congress urging exploration, and again Reynolds became their spokesman. He addressed the House of Representatives in April 1836, and this time he was much better prepared than in 1828–29. In his travels he had seen and heard many things. He had seen, off the Chilean coast, a research vessel from of all places *Prussia*—a nation that had "scarcely a hundred tons of shipping" in the entire Pacific Ocean. Yet that nation was doing more than the United States at scientific exploration. He had heard sailors' yarns about a faraway place called the "Fee-Jee Islands", where on several occasions shipwrecked American sailors had been massacred by cannibals. If the United States was to increase its trade with Asia, then surely the twin beacons of Christian mercy and representative government must be brought to such savage places. Reynolds went beyond simply listing commercial advantages and actually turned Jeffersonian agrarianism on its head. *That* philosophy, he argued, was the true artifact of Old World colonialism and aristocracy. Its disciples insisted that Americans should remain on the farm "and suffer other nations to come and take the productions of our soil in exchange for their own manufactures".

Yet Reynolds' most enthusiastic testimony was on behalf of science. He answered those who doubted the practical benefit of scientific exploration with remarkable insight. Its "utility cannot be computed in advance", he said. He cited Great Britain's attempts to find the northwest passage, and how these voyages of discovery had resulted in the Hudson Bay fur trade, the whaling industry in Davis Strait, and the cod fisheries of Newfoundland; "yet not one of these rewards of enterprise was anticipated, or formed an element in the calculation, when her Cabot, her Davis, her Hudson and Baffin, were dispatched on their perilous voyages." Reynolds described his grand vision for a United States Exploring Expedition. It would "throw back on Europe, with interest and gratitude, the rays of light we have received from her", and would "wipe off, at one glorious effort, the taunting imputation so long cast upon the American character". The expedition's scientific charter would be enormous: "to collect, preserve, and arrange every thing valuable in the whole range of natural history, from the minute madrapore to the huge spermaceti, and accurately to describe that which cannot be preserved; to secure whatever may be hoped for in natural philosophy; to examine vegetation, from the hundred mosses of the rocks, throughout all the classes of shrub, flower, and tree, up to the monarch of the forest; to study man in his physical and mental

powers, in his manners, habits, and disposition, and social and political relations; and above all, in the philosophy of his language, to examine the phenomena of winds and tides, of heat and cold, of light and darkness ... in fine, there should be science enough to bear upon every thing that may present itself for investigation.'' And how would such a grand science plan be carried out? ''By an enlightened body of naval officers, joined harmoniously with a corps of scientific men, imbued with the love of science'', who by their dedication would ''like stars in the milky-way, shed a lustre on each other, and all on their country! ... Cast anchor on that point where all the meridians terminate, where our eagle and star-spangled banner may be unfurled and planted, and left to wave on the axis of the Earth itself!'' Modernize this language a bit, and you get material that resembles NASA's websites.

With the help of Southard, a new bill for an Exploring Expedition was approved overwhelmingly by the Senate. This time the more serious opposition was in the House of Representatives, where Democratic-Republicans rallied around Congressman Albert Gallatin Hawes of Kentucky. Hawes came from a wealthy family of Virginia landed gentry, but he affected many of the ''Davy Crockett'' mannerisms then popular among politicians. In the House debate, he declared that he would not stand to see taxpayers' money ''wrested from the hands of the American people'' for a ''chimerical and harebrained notion'' to ''take the vessels and seamen of the United States, and send them to the South Seas, exposing them to all the diseases, hurricanes, and mishaps of that climate''. But this time the naysayers' arguments couldn't overcome Reynolds' combination of intellectual vision, commercial promise, and flag-waving. President Jackson himself supported the idea of an expedition, and on May 9, 1836 the bill passed by a small majority in the House.

It was Reynolds' finest hour. The government of the United States had voted to support scientific exploration on a grand scale. Congress appropriated an extraordinary sum of $300,000, which was the same percentage of the federal budget as all of NASA is today.

President Jackson appointed a commanding officer, fellow War of 1812 veteran Commodore Thomas ap Catesby Jones. In the Louisiana theater of operations, the then-Lieutenant Jones had commanded the naval delaying action at Lake Borgne, which had given General Jackson time to concentrate his troops for the Battle of New Orleans; so naturally Jones was Old Hickory's first choice to lead a scientific expedition. He was in fact a highly respected officer, and was also very enthusiastic about the Exploring Expedition's charter. The size and scope of the expedition envisioned by both Jones and Reynolds was something never before seen. Americans like to think big: instead of following the European model of deploying two ships, Commodore Jones suggested that *six* should be used—a flagship assisted by two slightly smaller vessels, two pilot boats or schooners for detailed coastal surveys, and a storeship to carry most of the expedition's provisions and supplies. President Jackson approved this configuration, which would be the largest scientific expedition yet to sail under any flag. The plans also called for a science team of at least 25 civilian investigators. The first science team member was appointed by the president himself: Jackson sent a memorandum to his Navy

Secretary stating that Reynolds should be given the post of historiographer. ''It will be proper that Mr. Reynolds go with the expedition,'' he wrote, ''this the publick expect.'' Reynolds' lifelong dream was becoming reality.

There were still many obstacles on the path to reality. If Congress had once been befuddled by the concept of a national expedition for science and discovery, so too was the institution that would carry it out: the United States Navy. By 1836, the U.S. Navy had established a proud fighting tradition based on many successful single-ship and squadron actions during the War of 1812, and on successful blockade operations during the Barbary wars. However, from a global perspective, the U.S. Navy of the early 19th century could best be described as a second-rate copy of the Royal Navy. It possessed some four dozen small- to medium-sized warships, some of advanced design and construction (*USS Constitution*), some built on the cheap (*USS Adams*), and some improperly armed (*USS Essex*). Officers fought duels over trivial provocations, violent hazing was rampant among midshipmen, and enlisted men were punished by flogging as late as 1850 and were placated by a daily ration of spirits as late as 1862. The U.S. Navy lacked a solid working relationship with the scientific community, of the kind the Royal Navy had forged with the Royal Society over a period of more than 100 years and which had yielded the voyages of Halley, Cook, and Darwin. Even the Navy's strategic vision was quite limited. Despite some diplomatic tension with France during the 1830s, which resulted in a few line-of-battle ships being added to the assortment of frigates, sloops, and brigs, U.S. Navy doctrine remained firmly centered on one goal: protection of commerce. Overall, this was a hidebound and parochial organization from which one wouldn't expect recruitment and training of world-class explorers.

Nevertheless, one talented scientific explorer did emerge. Charles Wilkes (1798–1877) went to sea at age 15 to become a naval officer. A fair-skinned, artistically inclined, and mathematically gifted lad, he received more than his share of beatings from bullies in the midshipmen's berth. As a junior officer he was assigned to the frigates *USS Guerrière* and *USS Franklin*, which took him on overseas cruises to Russia, Sweden, the Mediterranean, and South America between 1818 and 1822. On these visits to foreign ports, Wilkes took every opportunity to learn about the lifestyles, economy, and governments of the local populations, and to visit their art museums. However, in addition to his intellectual prowess, his shipmates and superiors noted in Wilkes a degree of arrogance and obstinacy, and a tendency to insist that things be done only his way.

After his cruises as a junior officer, several years passed while Wilkes waited for his promotion to lieutenant and further orders. During this time ashore he found his true calling as a naval officer. He resolved to bring a high level of scientific competence to the Navy, and he set himself on a course of advanced study in all the physical sciences. He sought out instruction in mathematics and advanced navigation from Nathaniel Bowditch (author of the *American Practical Navigator*, still used today). Wilkes' brother-in-law, James Renwick, was a professor of natural history at Columbia and was then regarded as the country's most respected engineer. Renwick gave Wilkes ample instruction in such cutting-edge subjects as geomagnetism. Wilkes had hoped to sail as an astronomer during the

Exploring Expedition paper project of 1828. When it failed to materialize, he took command of the brig *USS Porpoise* and conducted surveys of the Atlantic coast as part of President Jackson's initiative to improve navigational charts. In 1836, when the Exploring Expedition was finally funded, Wilkes volunteered to go to Europe to purchase an extensive and modern collection of scientific instruments. He willingly took on this overseas duty with no guarantee that he would even sail with the Exploring Expedition, let alone command any vessel attached to it.

For a stark contrast in personality and work habits to those of Wilkes, we turn to the man responsible for organizing, funding, and staffing the Exploring Expedition. The Secretary of the Navy, the Honorable Mahlon Dickerson (1770–1853), lived proudly by his motto: "Be cautious not to attempt too much business in one day." The archetypal Washington insider (Stanton, 1976), Dickerson began his career as a young man marching with the federal army to help put down the Whiskey Rebellion. Later, after earning a law degree from Princeton, he inherited the New Jersey Suckassunny Iron Works and learned to live comfortably on an uninterruptible stream of income. He built a great manor house next to his iron works, and following the colonial patrician custom gave this estate a name: "Ferromonte". He served a term in the U.S. Senate, where he promoted certain politically correct views on tariffs that made him attractive as a cabinet member after Andrew Jackson won the election of 1828. As a middle-aged Navy Secretary in the Jackson administration (Figure 1.3), he proved to be a phlegmatic individual with only enough energy for three activities: (1) working in his garden, (2) trading gossip at dinner parties, and (3) managing his favorite defense acquisition program, a small steamboat for coastal protection. For a national overseas expedition for science and discovery Dickerson cared not a whit, and he did his best to ignore the project in the hope that it would go away. Early on, he tried to kill the expedition in a cabinet meeting by reminding the president that it was the brainchild of those despicable members of the opposition: John Quincy Adams and the Whigs. President Jackson replied that the Whigs could be allowed to have one good idea, and ordered Dickerson to continue the preparations.

Preparations began in earnest, despite Dickerson's lethargy. Defense contractors were eager to equip the Navy's next expedition with the latest advances in ship design. The Navy's newest frigate, *USS Macedonian*, had just been completed and was assigned to the expedition as flagship. It was envisioned that she would provide spacious accommodation for most of the science team members and their laboratories, as well as a splendid floating embassy in which to receive dignitaries from distant lands. Additionally, should any inhabitants of *Terra Australis Incognita* prove hostile, the frigate could lay down a withering covering fire from 36 eighteen-pounder guns.

The Navy also contracted for a vessel specifically engineered for polar exploration, but without bothering to consult merchant whaling and sealing captains already experienced at high latitudes. The result was a bark christened *USS Pioneer* and launched at Boston in October 1836 under the watchful eye of Commodore Jones. Of course, this new-fangled ship couldn't be sent to the other side of the world without first undergoing sea trials on a shorter maiden voyage. No

Figure 1.3. "Be cautious not to attempt too much business in one day." The Honorable Mahlon Dickerson (1770–1853), U.S. Secretary of the Navy during the Jackson administration.

Courtesy: The New York Historical Society.

sooner did *USS Pioneer* enter commissioned service than the State Department found a mission for her maiden voyage that was wholly in keeping with her charter as a ship of exploration and discovery. The mission was to embark the exiled Mexican dictator Santa Ana, sail to Vera Cruz, and return him to Mexican soil, whereupon it was hoped he would meddle with and weaken the government of

Mexico and thereby make it easier for the United States to annex Texas. This 1837 maiden voyage of *USS Pioneer* proved an embarrassment for two reasons. First, most Americans regarded Santa Ana as an unsavory character. Second, her skipper and crew reported that the *Pioneer* exhibited dangerously erratic sailing qualities, and that the technologically advanced anthracite galley stoves had nearly set the ship on fire. Edmund Fanning took one look at the *Pioneer* and muttered that she would be "dismasted by the Woollies". Rumors began to circulate that the Navy had purchased a brand new ship of exploration that couldn't keep the sea. The Navy could neither confirm nor deny these rumors.

The selection and organization of the science team began along similar lines. It was ultimately Dickerson's responsibility, and he preferred to look for people with advanced technical training from within the ranks of the Navy. Finding none but Wilkes, who was in Europe purchasing laboratory equipment, he began forming committees to study the issue. Fortunately Reynolds stepped in and did most of Dickerson's job for him. There was no shortage of applicants, but Reynolds wanted to recruit men of a suitably young age who were also highly recommended by leading institutions. His friend De Kay was unable to go this time, but recommended in his place a young botanist named Asa Gray (aged only 25). Yale University recommended an even younger geologist, James Dwight Dana (age 23). There was also a recent Harvard graduate in medicine named Charles Pickering, who by age 30 had established a reputation in zoology. Physicist Walter R. Johnson (age 42) gave up his faculty appointment at Philadelphia's Franklin Institute to join the expedition. For the position of philologist (linguist), Harvard University recommended a promising student named Horatio Hale. Although still an undergraduate, Hale was already known in the field of linguistics for several things, including a paper on the Algonquin Indian dialect, and also for the fact that his mother was the author of a nursery rhyme called "Mary Had a Little Lamb". Other science team members included James Eights and Titian Peale from before, and a marine life specialist (or "conchologist") named James Couthouy. With the addition of several other botanists and zoologists, and a staff of technical artists, a well-rounded science team began once again to materialize. Reynolds didn't fully realize it, but he was bringing together America's first generation of modern professional scientists.

Dickerson eventually declared himself "satisfied" with the list of science team members, but in fact he didn't really care. After an official reception to meet the science team appointees, the only remark Dickerson made in his diary about the event was that he had been served a "delightful" strawberry cobbler.

These first-generation professional scientists had to endure great financial hardship just to participate in the expedition. Their nominal salary was $2,000 for each principal investigator. However, the Navy Department, to save money, delayed placing the science team on the payroll until well into the fiscal year of 1837 and also refused them advances on their pay. Faced with projected departure dates only months away, and with numerous preparations for an enterprise that could make or break their careers, many science team members simply borrowed what money they needed. Couthouy, in particular, borrowed heavily so that he could build his

specialized sampling apparatus. When Dickerson learned of this, he moved to have Couthouy dismissed from the science team on the ground that the Navy Department shouldn't employ a debtor. The crisis was resolved when Couthouy pledged his entire personal specimen collection as credit.

In January 1837, Wilkes returned from Europe with $20,000 worth of scientific apparatus. It was the largest collection of scientific equipment ever acquired for exploration, and it included telescopes, theodolites, scores of chronometers, meteorological and hydrographic instruments, a giant pendulum for studying variations in the Earth's gravitational field, and even an early image-rendering device called a camera lucida. The science team members, however, were disappointed with this collection because it had clearly been conceived from the vantage point of the physical rather than the life sciences: Wilkes had forgotten to buy microscopes.

That omission was minor in comparison with the eventual state of the expedition's naval organization. Under Dickerson's management, there were delays with the appointment of officers, delays with modifications to the hulls and rigging, and delays with issuing contracts for provisions and supplies. And, at regular intervals, Dickerson would convene committee meetings of the Board of Navy Commissioners to inquire about the squadron's overall state of readiness, which caused further delays. By May of 1837, Reynolds and Commodore Jones became genuinely alarmed by all these delays once news arrived from Europe that their mission now had serious competition from France. The French were fitting out a naval expedition to attempt the South Pole, under the command of the formidable *Capitaine de Vaisseau* Jules-Sébastien-César Dumont d'Urville (1790–1842).

Dumont d'Urville's early career was similar in many ways to that of Wilkes. He was a precocious child, mastering seven languages before joining the French Navy at age 17. As a midshipman, he like Wilkes pursued studies in all the sciences to a level far above that of his peers. In 1819, while an ensign stationed in the eastern Mediterranean, he witnessed the unearthing of a famous statue we know today as the *Venus de Milo*. Immediately recognizing this sculpture's artistic value, he secured its possession for France and arranged for its eventual delivery to the Louvre. As one might expect in France, he was rewarded for that exploit by promotion to lieutenant. After this promotion, Dumont d'Urville then logged some serious sea time. Beginning in 1822 he took part in a two-and-a-half-year scientific expedition aboard the corvette *Coquille*, which took him throughout the South Atlantic, along the Australian coast, and throughout the tropical western Pacific. From 1826 until 1829, he commanded the same ship, renamed *L'Astrolabe*, in a follow-on circumnavigation that was even more successful. He discovered two new islands in the Fijian archipelago, discovered the shipwreck remains of the ill-fated 1788 La Pérouse expedition, and compiled so many charts and anthropological surveys of the western Pacific that for the first time three major ethnic groups were recognized: Polynesians, Melanesians, and Micronesians. By 1836 copies of Dumont d'Urville's monograph on these discoveries, *Voyage de la Corvette L'Astrolabe*, had reached the United States, and both Jones and Reynolds were nervously aware of this man's extraordinary abilities.

Even more alarming were reports from Paris about the great enthusiasm throughout France for Dumont d'Urville's next expedition. Some of the wealthiest noblemen had volunteered to go before the mast as ordinary seamen. King Louis Philippe had promised a bonus of 100 gold francs to each expedition member if they reached 75°S (and beat James Weddell's record), and an additional 20 gold francs for each degree of latitude they reached farther south. And if they raised the tricolor at the South Pole itself, they could name any reward they desired. Two corvettes, *L'Astrolabe* and *Zélée*, were being rapidly prepared for the rival nation's Antarctic mission. The French, it should be mentioned, were just as nervous about the American effort: they assumed that the lengthy American delays were due to meticulous planning for every contingency by the best and brightest of a great seafaring nation (little did they know...).

The Honorable Mahlon Dickerson, true to his character, saw the recent French successes as an opportunity to reduce the size and scope of his own country's expedition. With a rare burst of energy, he carried all seven volumes of Dumont d'Urville's *Voyage de la Corvette L'Astrolabe* to the White House to show the president how much exploration and discovery could be accomplished with just one ship. President Jackson replied that if so much could be accomplished with one ship, a great deal more could be expected from six ships, and he ordered Dickerson to continue the preparations.

By the middle of 1837 the preparations were a shambles. Delays and cost overruns pervaded every aspect of the expedition's planning. In a congressional investigation of the expedition's management, one Ohio congressman declared that Dickerson's "imbecilities" had made the United States a global laughing stock. An exasperated Reynolds tried to prod the Navy Department along by resorting to one of the publicity tricks common in the republic's early days: publishing in the newspapers critical "anonymous" letters whose authorship was obvious. The results of these appeals to public outrage were mixed. He succeeded in achieving a level of public indignation over the expedition's lack of progress. But, although Reynolds had a dreamer's grasp of the "big picture", he was naive about the Byzantine details of national politics, and didn't reckon on the petulance often displayed by the wise men in Washington.

For example, Dickerson's reasons for dithering went beyond incompetence and phlegm. Dickerson was a northern Democratic-Republican, and genuinely believed in strictly limited government. Moreover, the expedition's chief congressional supporter had been his arch-rival in New Jersey politics, Samuel Southard. Dickerson regarded the expedition's existence as a personal political defeat, an illegitimate government function, and an imposition on his time. There were also many senior people in the Navy Department who regarded the Exploring Expedition as an insult to the service; either because the expedition's non-standard officer selection process went against the sacred tradition of seniority, or because they feared that in such an enterprise Navy officers would be mere ship drivers while civilian scientists reaped all the glory. Reynolds' letters in the popular press only made such bad feelings worse. He felt secure in his personal science team appointment from President Jackson, and failed to realize the extent to which his public

letters were jeopardizing his own participation in the expedition. He couldn't imagine, for example, that the expedition's sailing might be delayed so far into the Van Buren administration that his science team appointment from Jackson would be worthless.

By September of 1837, enough of the preparations were complete that Commodore Jones felt confident in mustering the squadron for an imminent departure. He sent for the scientific equipment, dispatched the ships to New York for installation of a heating apparatus designed by Dr. Johnson, and read an encouraging speech to the crews. However, he soon encountered morale difficulties among the enlisted men. The delays had gone on so long that many of the sailors had already served one-third of their contractual obligation. They could rightfully insist on being returned home in the middle of the mission, from the Antarctic or wherever. Jones' solution was to offer 3 months' bonus pay in cash to all who would sign new enlistment papers when the squadron reached New York. Nearly all the sailors did and, as soon as the ships reached New York, 155 of them promptly took their cash bounties and deserted. Thus there was yet another problem to solve.

After a few more weeks, Dickerson had felt enough pressure from public scorn that on 9 November he issued sailing orders to Commodore Jones. These orders were quite detailed as to both the final list of personnel assigned to the squadron and the geographic regions the squadron was to explore. The orders even included useful reports from the advisory committees of several leading scientific and maritime institutions. Commodore Jones was to set sail from New York as soon as all of the scientific apparatus had arrived from Washington and had been installed on board. Everyone breathed a sigh of relief. Finally, it looked like the United States Exploring Expedition would get underway!

Not so fast: a careful look at the bureaucratic aspects of Dickerson's sailing orders revealed that they weren't orders to sail at all, but were merely lengthy and convoluted instructions to do absolutely nothing. Dickerson knew perfectly well that the scientific equipment wouldn't arrive from Washington for many weeks. Moreover, in the sailing orders he made personnel appointments he knew Jones would find objectionable and would protest. Even more exasperating was the revelation that Wilkes' scientific equipment purchases were no longer even in one place in Washington. Some of the instruments had been borrowed by Wilkes himself for use aboard *USS Porpoise*, and by his mentor Professor Renwick. The chronometers were essential for accurate determination of longitude and hence cartography, but all their calibration data sheets were missing. Dickerson had surreptitiously lent many other instruments to various naval officers. The science team's physicist, Dr. Johnson, did his best to collect and calibrate most of the instruments. However, once most of the instruments had been collected it soon became clear that there wasn't enough room for them aboard ship, even in *USS Macedonian*. Some of the flagship's guns would need to be removed to make additional laboratory spaces.

Fed up with the constant bungling Commodore Jones resigned his command, declaring that he could no longer serve as an effective commanding officer in the face of the Navy Department's "procrastination the most extraordinary". The Exploring

Expedition was now without a leader and came to a complete standstill. Two days after Commodore Jones' resignation, news arrived from Europe that the French Antarctic expedition under Dumont d'Urville had set sail from Toulon with "wine for two years".

Dickerson offered the expedition's command to three senior captains, but the whole project had become an embarrassment and one after another they refused. By this time President Van Buren began transferring responsibilities for the expedition to his Secretary of War Joel Poinsett, while giving lip service to Dickerson's "ill health". Poinsett offered the command to two other senior officers, who both refused. There was only one officer left who could be seriously considered. In April 1838, command of the expedition passed almost by accident to the one naval officer most qualified by training to lead it: Lieutenant Commander Charles Wilkes.

By the time Wilkes took command, the United States Exploring Expedition was 10 years late. It had spent more than $250 million in today's dollars without unfurling a sail. Pundits were calling it the "Deplorable Expedition". Old John Quincy Adams finally harrumphed that he didn't want to hear anything more about the expedition except that it had set sail. In fact, Wilkes and Poinsett had found themselves in a predicament faced by many a NASA program manager a century and a half later—that of overseeing a continuously slipping schedule on a fixed congressional appropriation (Figure 1.4). Various mission objectives would have to be descoped accordingly. The resulting cuts fell heaviest on the science team, which was reduced in number from 25 to 9 members.

Poinsett was desperate to keep the entire project from collapsing, and he gave Lt. Comdr. Wilkes a free hand with reorganization. This was another reason the civilian science team suffered. Wilkes was gifted scientifically, but he was also an arrogant and overbearing man. His particular vision for the expedition's science was simple and unshakeable: it should all be done by the Navy. He therefore appointed himself as the expedition's physicist and science team leader. In his reorganization plan he insisted that "All the duties appertaining to Astronomy, Surveying, Hydrography, Geognosy, Geodesy, Magnetism, Meteorology, and Physics generally to be exclusively confined to the Navy Officers", for there were none "so well qualified to perform them". By this, he meant himself as the physicist, with junior officers and midshipmen serving him as research assistants. As for the life sciences, he was forced to retain some of the civilians because of their unique expertise, but he continued to regard their participation as one of Reynolds' public relations stunts.

Thus, the axe fell heavily and frequently during the spring of 1838. Johnson was cut from the science team because Wilkes didn't want a civilian physicist along. Geologist Eights was cut because he too was too much of a physical scientist, and the vast experience he already had with Antarctic research probably made Wilkes self-conscious. The younger geologist Dana was retained, however, because Wilkes liked him. Wilkes tried to eliminate Hale, declaring philology the "most useless" of the disciplines, but Hale's mother intervened. Influential in American literary circles as editor of *Lady's Magazine*, Sarah Josepha Hale bombarded Washington with letters. The Secretary of War, not wanting to tangle with an angry woman,

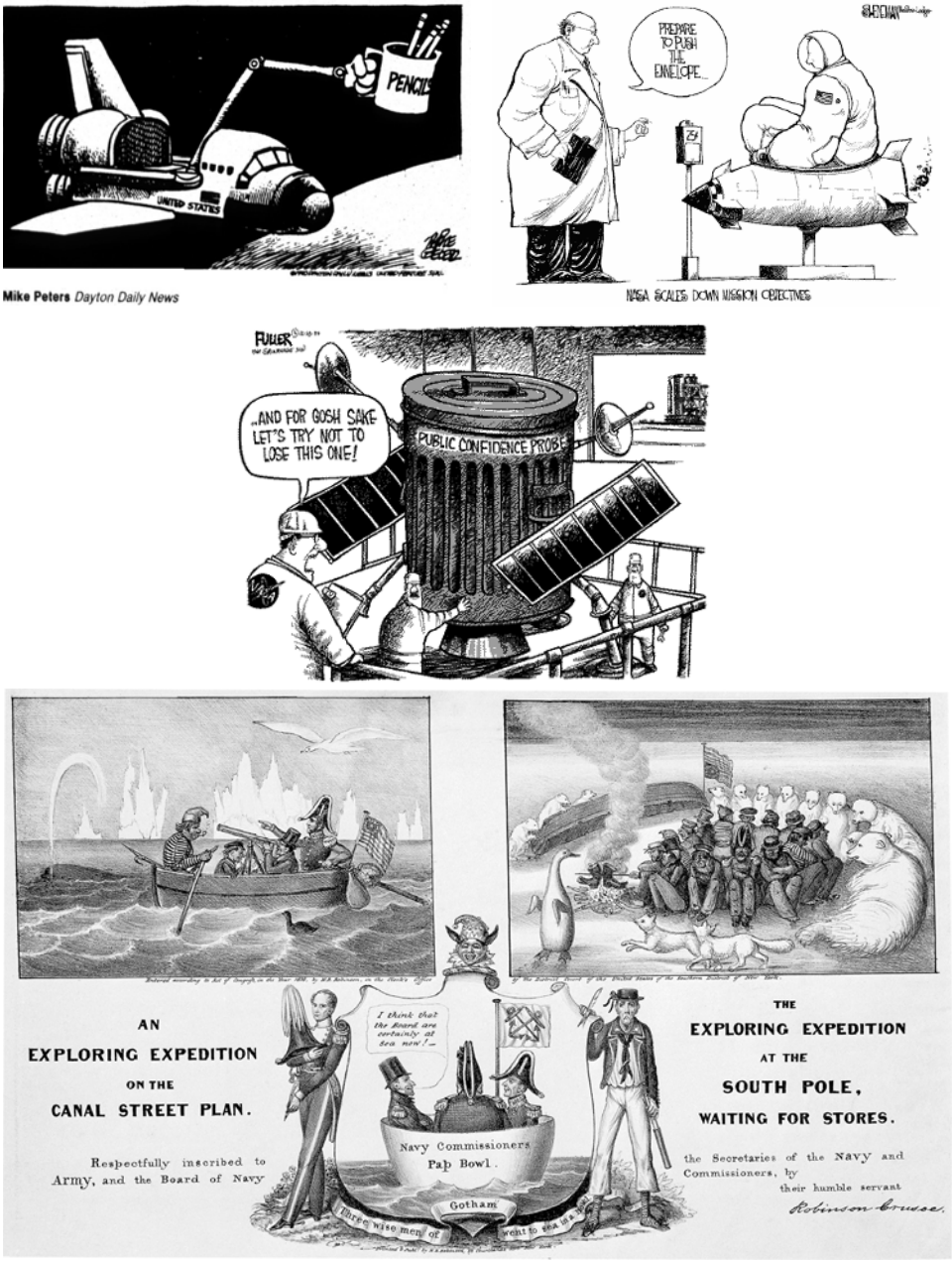

Figure 1.4. Examples of mainstream American media attention given to major national scientific endeavors: *top panel*—NASA during the 1990s; *bottom panel*—the Great U.S. Exploring Expedition of 1838.

Courtesy (top panel): *Dayton Daily News*, *Newark Star-Ledger*, *Gainesville Sun*. *Courtesy (bottom panel)*: Peters Collection, Division of Domestic Life and Social History, Smithsonian Institution.

overruled Wilkes on Hale's dismissal. Other science team members were dismissed based on summary judgments that they were "not agreeable", were "out of their senses", or their "habits were not the best". Asa Gray, the most talented of all, saw the carnage around him and became discouraged. He resigned from the science team, stating that the expedition had now strayed too far from its original intellectual vision. Gray would go on to become the founding father of American botany and taxonomy, and his absence from the expedition was an incalculable loss.

In a final act of unfairness, Jeremiah Reynolds—the visionary who had championed the expedition's cause from the backwoods lectures of "Professor" Symmes through congressional approval—was cut from the science team. Wilkes wanted to write the Exploring Expedition's story himself. Navy higher-ups, still smarting from Reynolds' criticism in the popular press, were more than happy to endorse Wilkes' desire for self-aggrandizement.

While Wilkes was busy dashing the hopes of many aspiring young civilian scientists, he was at the same time making practical adjustments to the squadron's composition. He rejected the frigate *USS Macedonian* as too large and unwieldy for exploration, and chose for his flagship the 24-gun ship-rigged sloop *USS Vincennes*. He discarded the hapless *USS Pioneer* in favor of the handy brig *USS Porpoise*, a ship familiar to him from his earlier coastal survey work. *USS Peacock* and the supply ship *USS Relief* had always been part of the expedition and were retained. Following Jones' original configuration, the schooners *USS Sea Gull* and *USS Flying Fish* were added for coastal surveys. Ironically, this particular selection of ships actually increased the squadron's overall tonnage above that previously selected by Commodore Jones. At a time when Poinsett and other high officials were insisting that program cuts were necessary due to budget restrictions, geologist Dana remarked dryly that this increase in squadron tonnage represented a "singular kind of reduction". Dana recognized that science had lost the political battle with the Navy.

Lt. Comdr. Wilkes, who as a squadron commander could now be called "Captain" by courtesy, was ultimately an efficient organizer. During the summer of 1838 he completed in 2 months the preparations that Dickerson had let drag on for 2 years. Finally in the morning of August 18, 1838, to the accompanying sounds of bosuns' whistles, clanking capstans, and a fanfare from an indifferent bugler, the six ships of the United States Exploring Expedition departed Hampton Roads, Virginia, stood out to sea, and headed south.

1.1.3 The seventh continent

As the squadron made its way south to Rio, Captain Wilkes' overbearing personality loomed over everything (Figure 1.5). Wilkes would later write with a touch of pride that in his command style he affected "the manner of a martinette", as this fostered "discipline and obedience to command". During the Atlantic passage he would frequently require the individual ships to sail alongside his flag, so that their crews could be mustered out on deck to stand at attention for his inspection. Carefully observing their ranks and officers through his spyglass, he would shout into his

Figure 1.5. "Stand up straight, you rascals!" Lieutenant Commander Charles Wilkes (1798–1877), the Exploring Expedition's commanding officer and physicist. Portrait by Thomas Sully.

From Wilkes (1845a), *Narrative*, **1**. Special Collections, Scripps Institution of Oceanography Library.

speaking trumpet such things as "That third man, Mr. Bacon, his legs are dirty sir! That next man's head has not been combed! Look at that lubber's neckerchief! Stand up straight, you rascals!" Wilkes was an overly strict and bad-tempered commander, even by the standards of his day. His harsh upbringing as a midshipman and ensign had made him hard when his turn came to lead other men. His attitude toward most of his officers involved paranoia. Always fearful of imagined conspiracies against his authority, he would occasionally reorganize the entire squadron's chain of command, transferring officers back and forth among the

ships. Some officers he fired or demoted when he became too suspicious of them. He maintained discipline among the enlisted ranks by liberal application of corporal punishment. After completing the survey work at Tierra del Fuego, he even went so far as to dismiss an entire ship from the expedition, the slow-sailing *USS Relief*, whose commanding officer he despised. Only one aspect of Wilkes' personality saved him from outright mutiny: the men saw that he drove himself harder than he drove them. He spent every waking moment of every day either managing the squadron or making scientific observations. As the men observed the behavior of their strange, humorless workaholic of a commander, they gradually came to believe that their expedition might be doing something important for their country.

The nine civilian science team members did their best to adapt to the spit-and-polish military environment fostered by Wilkes. These nine who had survived the draconian cuts included geologist Dana, zoologist Pickering, conchologist Couthouy, and linguist Hale. Naturalist-painter Titian R. Peale led a team of two talented technical illustrators: Joseph Drayton and Alfred Agate. The discipline of botany was represented by an amateur named William Rich, and a skilled Scottish gardener named William Brackenridge. Rich had been an early and unavoidable science team appointee, because he was one of Dickerson's garden club cronies. This botany team was a far cry from the genius of Asa Gray, but Gray had courteously given Rich as much training as possible before the squadron's departure. Brackenridge actually proved quite adept at managing specimens, and earned Wilkes' grudging approval on several occasions.

The civilian science team members, referred to as the "Scientifics" by their uniformed companions, found scientific work aboard ship very difficult. Because of naval quarterdeck etiquette and watchstanding procedure, it was inconvenient to do any serious work out on the open decks. Laboratory space below was extremely limited, and the odors emanating from dissections often caused Wilkes to order the laboratory work stopped. Priority for use of the small boats was given first to Wilkes' physical observations and squadron logistics, second to crew liberty, and a distant third to specimen collection and surveys by the Scientifics.

Even this third priority represented an extra workload for the coxswains and deck department, and the sailors often found the Scientifics' presence burdensome. The enlisted men also blamed the Scientifics, incorrectly and unfairly, for Wilkes' standing order that all items obtained in foreign lands by expedition personnel be handed over as government property. This order interfered with sailors' longstanding tradition of adding souvenirs from distant places to their meager possessions. Relations between the Scientifics and the enlisted men weren't all bad. Some of the Scientifics had brought along musical instruments, which provided very welcome entertainment on the fo'c'sle. Moreover, the civilians weren't strictly bound by 19th century wardroom protocols, and mingled freely with the sailors.

Relations between the Scientifics and the officers were also uneven. The junior officers were generally enthusiastic about the expedition's intellectual charter, and many showed a keen interest in the civilians' work. Some senior officers, however, felt displaced as the usual fount of all knowledge and wisdom aboard ship. This feeling had some grounding, for the Scientifics had a much higher level of education,

and some of them—particularly Dana and Couthouy—were more skilled at navigation than most of the officers. Some officers were less than enthusiastic about helping the Scientifics with their data collection, as the civilians might gain individual fame and recognition for their findings while the officers would probably remain in their anonymous military roles as ship drivers. Wilkes, when convenient for him, would accommodate the Scientifics' requests to transfer between vessels for scientific opportunities, but he would never alter the squadron's plans to further the civilians' research programs. From Valparaíso, Chile, Dana wrote to his colleague Asa Gray congratulating him on avoiding "Naval servitude".

As early as the passage to Rio, equipment problems began to plague the expedition. The long organizational delays between 1836–38 had left the ships in less than ideal condition. *USS Peacock* in particular leaked badly, desperately needed caulking, and had rusted-out pumps. Fortunately her skipper, Lt. William L. Hudson, was one of the Navy's best (Figure 1.6). His exemplary seamanship would keep the dilapidated sloop-of-war afloat in many perilous situations. Wilkes decided on an extended stay at Rio to make necessary repairs before the squadron could attempt to round Cape Horn. Ever impetuous, he crated the rusted pieces of the *Peacock*'s pumps and sent them via a northbound merchantman directly back to the Navy Department in Washington, to call attention to the incompetence of the Norfolk shipyard. Far from being chastened, the Board of Navy Commissioners thought this "a great piece of impertinence on the part of so young an officer".

Between January 25 and February 19, 1839, the squadron rounded the Horn and conducted cartographic and hydrographic surveys throughout the southern part of Tierra del Fuego. This was a valuable contribution to navigation in those days, when so many ships had no choice but to round the Horn, but Wilkes wasn't satisfied. He was aware that Dumont d'Urville had been in the Straits of Magellan the previous year and had declared an intention of heading south along the course of James Weddell. Although the austral summer was nearly over, Wilkes reorganized and provisioned the squadron for an attempt at the Antarctic. There was some gloom and trepidation because of the late departure and also because of the constant friction between Wilkes and many of the officers. However, some comic relief was provided by the expedition's spaced-out chaplain. Reverend Elliott had a knack for preaching inept and irrelevant sermons, and on the Sunday before the squadron was to sail from the end of the Earth into the frozen Antarctic darkness, he lectured the men on Belshazzar's Feast and the "sin of intemperate revelry".

For efficiency's sake, Wilkes left *USS Vincennes*, *USS Relief*, and all of the science team save Peale at Orange Harbor, Tierra del Fuego, and took command of the squadron's soundest vessel, *USS Porpoise*. To maximize his chances for an important discovery, he divided his southbound command. The *Porpoise* and *Sea Gull* set sail for Palmer's land (the Antarctic Peninsula), while the *Peacock* and *Flying Fish* took a course further west into what is today called the Bellingshausen Sea. Heavy weather persisted from the beginning of this cruise. The *Porpoise* and *Sea Gull* sighted the Antarctic Peninsula on March 3, but sea ice concentrations were too great for Wilkes to reach the shore. The constant squalls coated the rigging with ice and made the schooner nearly unmanageable. With no southerly progress possible

Figure 1.6. Lt. William L. Hudson (1794–1862), skipper of *USS Peacock* and the Exploring Expedition's second in command, acclaimed by his crew as "one who for Nautical Skill has not his superior in the service."

From Wilkes (1845a), *Narrative*, **2**. Special Collections, Scripps Institution of Oceanography Library.

beyond 63°10′, and nothing else to be gained in these increasingly dangerous conditions, Wilkes ordered his two ships back to Orange Harbor on March 5.

Lt. Hudson in the *Peacock* and Lt. Walker commanding the *Flying Fish* were more successful, although they were separated by squalls on their second day out of Orange Harbor. The tiny schooner *Flying Fish*, steered by a tiller in an open cockpit, made steady progress as far 70°S, 101°11′W, while being battered by gales that split both mainsail and jib and smashed the boats. The size of the bergs encountered by Lt. Walker and his crew made their schooner seem like "a mere skiff in the moat of a giant's castle". On March 23 they turned back only when daylight became perilously short and the increasingly unavoidable collisions with sea ice threatened to cut

through the hull's copper sheathing, but not before they sighted discolored bergs that hinted at the nearby presence of land. One hundred miles beyond their farthest point south, the Walker Mountains and Cape Flying Fish are named for their remarkable cruise. On their way back north they rejoined the *Peacock*, which had reached 68°08′S, 97°58′W, but was nearly disabled by her taller square rig being iced over and her bows clogged with ice (although, ironically, this stopped the ship from leaking). Upon receiving Lt. Walker's report of sea ice conditions farther south, Lt. Hudson reluctantly but sensibly ordered both ships to return in company to Orange Harbor.

Thus the Exploring Expedition's first Antarctic cruise was abortive, but it gave the senior officers experience at ice navigation that would serve them well during their major Antarctic cruise the next year. Wilkes didn't realize it, but Dumont d'Urville's foray into western Antarctic Peninsula waters the previous year had been equally abortive, and the French explorer would spend 20 months between his Antarctic cruises completing ethnographic research in the South Pacific. As the Exploring Expedition made its own way into the Pacific toward Valparaíso, a major tragedy struck. Somewhere along the way, in bad weather, *USS Sea Gull* disappeared with all hands.

After repair in Valparaíso and Callao, the squadron set sail for Sydney on July 12. The intention was to survey as many South Pacific islands as practical along the way, but Wilkes was anxious to make New South Wales in plenty of time for Antarctic exploration during the following austral summer. The expedition visited the Tuamotu Islands, Napuka and Tepoto in the Disappointment Islands, then divided to survey numerous other islands before regrouping at Matavai, Tahiti on September 10. At Samoa they learned that Dumont d'Urville's expedition had been there a year ahead of them, and also that a British expedition under Captain James Clark Ross, commanding *HMS Erebus* and *HMS Terror*, was on its way to the Antarctic. With Wilkes in haste, the routine at all these various South Pacific islands was essentially the same. The Scientifics were allowed a few hours to conduct exploratory surveys, but never enough time to do what they considered a proper job. Wilkes would carry out his geophysical research program by dispatching solitary junior officers to remote locations to carry out impossible data collection tasks—like taking hourly readings from networks of thermometers or offshore tidal staves for days on end—and then would be angry when gaps appeared in the time series due to the poor fellows' need for sleep. On the eve of departure, deserters would be rounded up and flogged, and then the ships would proceed to the next island.

They arrived at Sydney on November 29, and immediately began preparations for the major Antarctic cruise. The local residents of this already bustling international port of call, who had seen many well-prepared ships depart for the Southern Ocean, marveled at the courage of these "foolhardy and reckless" Americans who thought they could survive an Antarctic cruise in their used-up warships. The American squadron appeared as ill-prepared as could be. There were no watertight compartments in the hulls for flotation in case of ice damage. The hulls themselves, being pierced for gunports, were too frail to withstand

constant battering by the sea ice. The heating systems were inadequate, and there was no room for a full year of provisions in case of a forced winterover.

Beneath these outward appearances, things were even worse. *USS Peacock* still leaked like a sieve, and the structure supporting the spar deck had decayed to such an extent that it couldn't be counted on to support the boats except in calm weather. Nevertheless, Lt. Hudson stoically accepted these difficulties rather than insist on a major overhaul that would delay the Antarctic cruise by another year. As the departure date approached there were understandably more deserters than usual, but the Sydney police were accustomed to such things and rounded most of them up in good time. To keep any Antarctic discovery entirely a Navy accomplishment, Wilkes ordered the entire civilian science team ashore to explore Australia as they saw fit. Despite the numerous defects, the entire squadron could present a suitable martial appearance when necessary. When they finally set sail for the Antarctic in the morning of December 26, the *Sydney Herald* noted that "In their passage outwards, they were not merely beautiful, but grand".

Wilkes' plan called for the squadron to stay together as long as possible. If separated, they were to individually pause for 48 hours at Macquarie Island (some 500 nautical miles south of Sydney) in an attempt to regroup. Together or individually, the squadron was to proceed as far south as possible (hopefully reaching a continent), then head west to a longitude of 105°E, and begin a return leg to either Sydney or New Zealand before March 1. The ships became separated almost immediately in bad weather. They all dutifully stopped at Macquarie Island, but the crews were all anxious to strike out on their own to maximize their exploring time in Antarctic waters. The three larger ships would meet a few times in the ice, but the Exploring Expedition's major Antarctic cruise of 1840 was largely a series of adventures by individual vessels.

The greatest adventures marked the voyage of *USS Peacock* under Lt. Hudson. After gales in early January, the crew delighted in calm weather and ice-free conditions upon crossing 65°S. By January 16, however, they encountered first brash and floe ice and then ice blink on the horizon, which foretold an immense ice barrier and dashed their hopes for an easy continental discovery. For 2 days they cruised along the edge of the ice barrier in the company of the *Porpoise*, before the brig vanished in a fog bank. Now on their own, the *Peacock*'s crew were the first to see land. Two midshipmen, Henry Eld and William Reynolds (no relation to the expedition's founder), were aloft helping to con the ship through the ice. Midshipman Reynolds, himself a talented journalist, wrote in his personal log of a perspective experienced by every visitor to Antarctica to this day: "... went to the Masthead: we wanted to obtain a good view of the field of Ice, that Spread away beneath us ... to look over such a vast expanse of the frozen Sea, upon which human Eye nor foot had Ever rested, and which presented an impassable boundary to the Mysterious region beyond, filled us with feelings, Which we were powerless to utter."

Then they saw something they were certain wasn't sea ice. Midshipman Eld made an entry in his log that day, in a rambling style that evokes his youthful excitement: "Mr. Reynolds and myself almost at once Exclaimed this as land, but not trusting the Naked Eye went on deck for a Spy Glass, which only Confirmed

what we had before felt sure of, so unlike the usual appearance of the barrier was it that burst upon with the utmost Vividness and we unhesitatingly pronounced it the Southern Continent. The Mountains could be seen distinctly towering over the field Ice and Berg's in the back ground stretching to the S & W as far as we could discern any thing. Two peaks in particular were very distinct running up to an immense height in a conical form and others the lower parts quite as distinct but their summits lost in a light fleecy cloud tho few of which were to be seen in that quarter for the weather was remarkably clear and the sun shining brightly ridge after ridge with their sides partially bare connecting the Emminences that I have just spoken of which Must be from one to two thousand feet in height and alone is Enough to Establish its identity, for no berg or Ice Island Ever seen was one quarter of its Altitude.'' The ship's position was 65°18′S, 157°36′38″E, and Messrs. Eld and Reynolds had indeed seen two peaks on the George V Coast that today bear their names. Three days later, on January 19, the entire crew had an even more convincing sighting, of ''great height . . . rounded uneven Summit, and broken sides'', which was recorded in the ship's log as the first official landfall.

By January 23, the leadsman reported sea floor soundings at 320 fathoms, and his line was coming up coated with mud. Here was even more evidence that land was very near. Lt. Hudson, greatly encouraged, was determined to set foot on the Antarctic continent itself and at 05:00 the next morning steered into a promising opening in the pack ice. Once inside, he found a little too much floe ice for comfort, but the wind was light and steady and the ship could maneuver. By breakfast time, however, there was too much ice in every direction. Tacking a square-rigged ship takes considerable sea room, and it became impossible to avoid hitting the ice. At one point the ship came about to avoid one piece of ice, but as she crossed to the other tack she got sternway and slammed rudder-first into another piece. The steering gear was temporarily disabled, and the rudder slammed into the ice again and was nearly torn off. The carpenters went over the transom on a platform to inspect the casualty, and reported that the rudder was completely useless and would have to be unshipped. The Exploring Expedition possessed spare rudders, one of which at this point might have given the Peacock full use of her helm in a matter of minutes. However, the spares were safely stored in the hold of *USS Relief*, which had been detached the previous year to rid the expedition of officers Wilkes disliked. The situation was now critical. The *Peacock* drifted further into a greater concentration of sea ice. The crew attempted to steer using the headsails, but there wasn't enough room for this imprecise maneuvering and collisions with the ice became more frequent. To make matters worse, they were now drifting at a steady 3 knots toward a huge tabular berg 6 miles wide and 100 feet high.

Only by getting on the opposite tack could they avoid the giant berg. The only way to accomplish this now was to send out boats with ice anchors, in the hope of making fast to a smaller floe so that they could use the capstan to bring the ship around. There was so much ice that the boats' crews spent more time fending than rowing, but twice they succeeded in planting an anchor. The first time, another piece of ice drifted in the way, fouled the hawser, and pulled the anchor loose before the capstan could tighten it. The second time, the hawser was tightened, but as the crew

began to strain at the capstan to save their ship the anchor suddenly dragged. Now the collision was only minutes away. Aside from furling all canvas to slow their drift, there was nothing more they could do. As Midshipman Eld recorded, at that moment there was "no alternative but to await our fate; it was inevitable that we Must fetch up against the immense Ice Island that was towering over our head's... We Many of us had wives, and children, and all had dear & near relatives, Mothers, Sisters, & brothers, & almost Certain death stared us in the face."

They were out of options but not out of luck. Just as NASA today entrusts the maneuvering of its space shuttles to its most experienced pilots, someone in Jackson's Navy Department had found the consideration to see that the Exploring Expedition's second-in-command was a master ship handler. At that moment of impending doom a less disciplined crew might have panicked, but not the men under Lt. William Hudson. He methodically ordered every sailor to his station, keeping all the yards manned should the recoil from the collision place them on a useful tack, and he also ordered the mainmast reinforced by a spare topsail yard. Midshipman Eld wrote that everyone was "Calm and collected as possible, orders were issued & carried into Effect the same as usual. No blustering or unnecessary Noise, but cooly awaited the Event & the preparations Made for Making sail if she did not go down, & should cant the right way."

In the last few seconds before the collision the ship swung round so that she was drifting stern-first toward the berg (Figure 1.7). The officer of the deck called out "Look out for the Mizzen Mast, stand from under or we shall have it on our heads!"

Figure 1.7. "No choice but to await our fate..." The imminent collision between the disabled *USS Peacock* and a huge tabular iceberg. Sketch by science team artist Alfred Agate.
From Wilkes (1845a), *Narrative*, **2**. Special Collections, Scripps Institution of Oceanography Library.

The collision threw everyone off their feet, smashed the stern boat into splinters, snapped the spanker boom "like a pipe stem", and made the masts sway "like coach whips". Small ice fragments began to fall from an overhang on the giant berg that loomed above the mizzenmast. If those countless tons of ice fell before the ship cleared, the hull would be crushed.

But Lt. Hudson was ready to capitalize on their one small stroke of luck. The ship recoiled from the collision at such an angle that if they made sail immediately they could gather enough headway to clear the giant berg. Hudson gave the order to the men he had sensibly ordered to their stations, and first the jib and then the topsails were set within seconds. *USS Peacock* started moving ahead "and shot clear of this ugly customer" just moments before the ice overhang fell with a terrifying crash in her wake.

She wasn't out of danger yet. The opening in the pack ice, so inviting that morning, was nearly closed. The only way out was a half-mile-long but narrow channel next to the giant berg, through which she would have to be steered using the sails alone. Lt. Hudson expertly accomplished this despite badly damaged rigging, and the channel led to some more ice floes that could be navigated using ice anchors and the capstan. To keep up morale, Lt. Hudson ordered dinner piped at the usual time, and in the afternoon the damage control team managed to unship the rudder and begin repairs. By 19 : 00 the *Peacock* reached open water.

The next day Lt. Hudson assembled his officers and explained the extent of the damage. A jury-rigged rudder had been shipped, but it was nowhere near as strong as the original. Aloft there was serious damage to all three spars and their shrouds. The ship leaked more than ever. Near the waterline, the ice reinforcements had been stripped from the bows, and Hudson's instinct told him that there was even more extensive unseen damage below the waterline. Repairs could only be made at Sydney and would take at least a month, after which the season would be too late for further Antarctic exploration. Should they turn back for Sydney, or should they continue their present cruise for a few more days or even weeks? He called for a vote. One senior lieutenant, a plank-owner, had unlimited confidence in the old sloop-of-war. However, the rest of the officers agreed with their skipper that, with three other ships still in the field, the most sensible course was for the shipyard at Sydney. "And so Ended our attempt South!" wrote Midshipman Reynolds, "so vanished our bright hopes ... true we had seen the land afar off, and had touched the bottom with lead but this was a lame tale to tell." In the long run it wasn't a lame tale, and the early January 19 sightings of land by *USS Peacock*'s crew would later save America's priority in Antarctic discovery.

Meanwhile *USS Vincennes* was cruising alone along the edge of the icy barrier, having last been in contact with the *Peacock* on the morning of January 19. Her officers and crew didn't have the same confidence in her skipper as the *Peacock*'s company had in theirs. For although Captain Wilkes was intellectually gifted and a highly trained navigator, his seamanship wasn't in the league of Lt. Hudson's. Moreover, his aloof and paranoid command style was firmly establishing him as the Queeg of the Antarctic. Ironically, the somber wardroom atmosphere aboard the *Vincennes* became a kind of survival asset for this particular exploration. Because

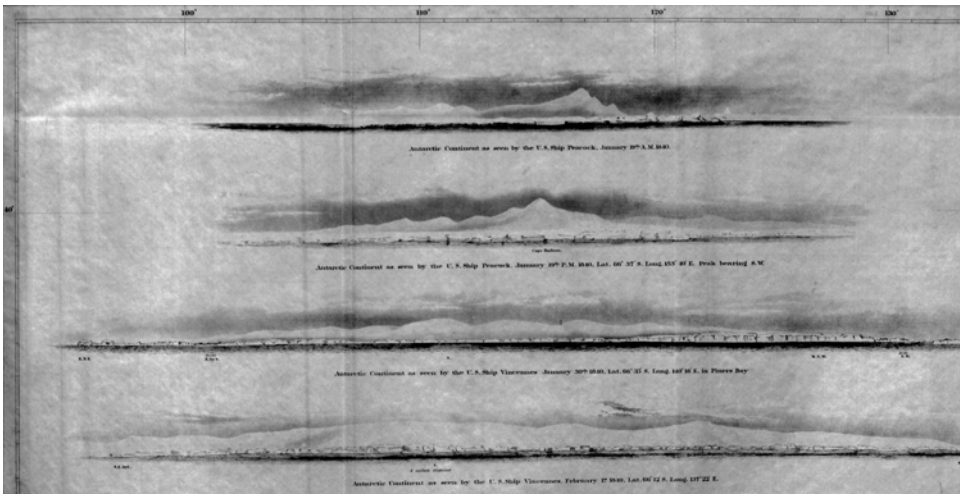

Figure 1.8. Sightings of the Antarctic continent by *USS Vincennes* and *USS Peacock*, drawn by Wilkes and Hudson for the official U.S government publication.
From Wilkes (1845b). Special Collections, Scripps Institution of Oceanography Library.

Wilkes so mistrusted his officers, the *Vincennes* was a much more timid ship than the *Peacock* during the Antarctic cruise. She largely avoided forays into openings in the pack ice, of the kind that had beckoned and nearly doomed the *Peacock*. Instead, she cruised steadily westward along the ice boundary for the next 30 days, and her crew made numerous reports of land from the highest masthead in the squadron (Figure 1.8).

Wilkes ignored the first of these reports. In the morning of January 19 the officer of the deck, Lt. Alden, heard water breaking on a nearby ice floe that was invisible in the fog, and sent for the captain. Wilkes emerged on the quarterdeck in one of his frequent foul moods, and ordered Lt. Alden to stand farther out to sea from the barrier. Lt. Alden, peering through gaps in the fog to the south, suddenly called out "There's something there that looks like land, Sir!" Wilkes, not believing such a thing possible yet, ignored him and walked away muttering "something about proper management of the ship".

The first sighting of land recorded by Wilkes occurred on January 28, when the ship's position was 66°35′S, 140°30′E. Before the *Vincennes* could make an attempt to reach it, a sudden squall forced her to stand clear of the ice barrier. Another sighting was made on January 30, along with an encouraging sounding of a rocky sea floor at only 35 fathoms, but again the weather became foul and a landing had to be aborted. Further sightings were made on February 2, 5–8, 12, 13, and 17. As the ship progressed westward the sightings gradually appeared closer, to the point where the crew could make out "all the ravines and separate hills", but in their wooden ship they were confined to the other side of the pack ice. The *Vincennes* made some attempts to find openings in the ice, and occasionally stopped at large bergs where

the crews had some ice liberty and collected drinking water (Figure 1.1), and where Wilkes and his officers conducted magnetic observations, but she was never able to get close enough to shore so that Americans could set foot on *terra firma*. Finally on February 21, with daylight hours diminishing, 30 men on the sick list, and the ship having reached its stated goal of 105°E, Wilkes decided that he had gathered enough evidence of an Antarctic continent. He thanked the crew for their good conduct (with the exception of some "disloyal" officers) and ordered the helm put up for Sydney. He had in fact made steady sightings of land along a 1,500-mile transect from the Adélie Coast to the Shackleton Ice Shelf, and had proved for the first time that the Antarctic landmass had continental dimensions.

USS Porpoise made a few, less confident sightings of land. Her skipper, Lt. Ringgold, was the most faithful to Wilkes' standing order that the ships should sail together whenever possible. At one point he transferred the carcasses of two freshly killed elephant seals to the *Peacock* for scientific preservation. He managed to keep the brig in the company of one of the larger sloops for some of the time, but sight of the other ships was easily lost in either fog or squalls. On January 30, the brig was alone and her position was 64°50′S, 135°27′W. Lt. Ringgold caught sight of two vessels under light canvas on the horizon. He assumed that they were the *Vincennes* and *Peacock*, and made more sail to catch up with them. On closer approach the ships were clearly foreign, and the crew guessed that they must be the Ross expedition. Lt. Ringgold immediately ordered the colors hoisted and eagerly prepared to salute the Englishman who had discovered the North magnetic pole. In reply, the strange ships hoisted the French tricolor and a commodore's pennant. It was Dumont d'Urville, the dreaded French competition. Ringgold continued his course toward the strangers, intending to salute the great French explorer and perhaps speak with him. Dumont d'Urville had the same thing in mind, and he set more canvas so that his corvettes could keep pace with the Americans as they rapidly approached.

Suddenly, in the variable wind, the French corvettes surged ahead under full sail, widening the distance between them and the American brig. Ringgold took this for a rebuff and, assuming the French were ill-mannered, abruptly hauled down his colors and bore up on his original course. Dumont d'Urville, making the same conclusion about the Americans, didn't bother to pursue the encounter and went his own way. When Wilkes learned of this incident, he wrote furiously that "by refusing to allow any communication . . . [Dumont d'Urville] not only committed a wanton violation of all proper feeling, but a breach of the courtesy due from one nation to another." It was typical of that age that naval officers found time for such puffings about etiquette while navigating fragile wooden ships in the world's most dangerous ocean. The idea that the botched encounter might have been a misunderstanding before the brig and the corvettes were within hail never occurred to anyone, French or American, and the farcical incident further soured relations between the two countries.

The schooner *USS Flying Fish* had the most miserable ordeal. She was only a converted fore-and-aft rigged pilot boat with a crew of ten, and after half a world of hard use was no match for the Southern Ocean's turbulence. On the way south from

Sydney, she suffered rigging damage and almost immediately lagged way behind the larger ships. She did reach the ice barrier by January 21, but by that time only four of her crew were fit for duty. The rest were either injured or sick from poorly cooked meals. Lt. Pinkney, her skipper, did his best to investigate large bergs for discolorations that might signify the presence of land. He even caught a fleeting glimpse of land on February 3. But four men, and eventually just three, weren't enough to work the ship in such high seas, and after a few days it was all they could do to stand watch. The officer of the deck, by now either Lt. Pinkney or his sailing master, could only keep a steady watch for bergs by lashing himself to the foremast. The crew's quarters were rendered uninhabitable by the freezing water constantly washing over the spar deck. The men could keep only one stove lit in the officers' quarters, and only sporadically. Lt. Pinkney ordered all the coal shifted aft in a partially successful effort to damp the schooner's pitching, and he allowed all of the ship's company to move into the slightly drier officer's quarters, but by February 5 even these measures weren't enough. The entire crew, in terrible health and fearing for their lives, wrote a formal letter to LT Pinkney requesting that they terminate the cruise. Lt. Pinkney agreed, and the *Flying Fish* turned north and reached New Zealand on March 10.

On March 11 *USS Vincennes* arrived at Sydney. As members of the reunited squadron exchanged stories, one warrant officer remarked that the expedition's sailing into the ice with the spare rudders in the storeship was like a man traveling the highway "with his pistols in his trunk". The fair-minded Lt. Hudson found some time to write to Jeremiah Reynolds, congratulating him on his now apparently correct theory about an Antarctic continent.

Wilkes was under orders to keep details of any major discovery secret until Washington could be notified, but he regarded the local U.S. consul as sufficient notification. The next day the ambassador came aboard to help prepare a statement for the press, stating that the United States Exploring Expedition had discovered the Antarctic continent. On that same day, however, a ship arrived with news that Dumont d'Urville had returned to Hobart, announcing that his expedition had discovered land on January 19, at 66°S, 130°E. Wilkes suddenly regretted his mistrust of Lt. Alden that very same morning, but there were *USS Peacock*'s reports to save him. Lt. Hudson had logged a report of land on January 19, and two of his midshipmen had made personal log entries on January 16 (which Hudson doubted at the time, but later believed). Thus the Americans had at least tied if not beaten the French, and had done better by proving that the land was a continent.

The French, to their credit, had actually reached land. After sighting it on the 19th, Dumont d'Urville navigated his well-equipped corvettes into the pack ice on January 21, dodging massive bergs whose "sheer walls were much higher than our masts ... The spectacle ... was both magnificent and terrifying. One could imagine oneself in the narrow streets of a city of giants." Far enough in, his crew could make out a surf and some rocky islets. Dumont d'Urville ordered two boats launched, and he and several of his crew reached *terra firma* 2 hours later. They pushed aside the penguins and planted the tricolor. Lt. Dubouzet wrote, "Following the ancient custom ... we took possession of [Antarctica] in the name of France ... To the glory of France ... we emptied a bottle of the most generous of her wines. Never

was a Bordeaux wine called upon to play a nobler role; never was a bottle emptied more appropriately.'' Dumont d'Urville named this outcropping Geology Point, after the boatload of mineral samples the men collected, and he named the land they had reached Adélie Land in honor of his wife. As for the penguins, he named the most numerous species Adélie again in honor of his wife. After several more days attempting further exploration in ferocious gales that shredded his sails and iced up his rigging, Dumont d'Urville returned to Hobart.

Clear minds could sort out the French and American accomplishments, and realize that there was plenty of credit to go around. However, a much more serious challenge to the U.S. Exploring Expedition's discovery came from the British 1 year later. In 1837, while in Europe procuring scientific equipment for the expedition, Wilkes had met Captain Ross, and the veteran polar explorer had given Wilkes some encouragement and advice. From Sydney in 1840, Wilkes decided to return the compliment. Ignoring his sailing orders' admonitions to secrecy, Wilkes wrote a letter to Ross that contained a summary of his Antarctic discoveries and magnetic observations. He imagined that he was doing Ross a favor, as one world-class explorer to another. Indeed he did Ross a favor, for the Englishman decided to revise his plans for 1841 and explore Antarctic regions east of where the Americans and French had been in 1840. In January 1841, *HMS Erebus* and *HMS Terror*, the best designed and best equipped polar exploring ships of the age, penetrated the ice barrier at 69°15′S, 176°E, entered an open sea that is today named after Captain Ross, and charted new lands as far south as 78°04′. They caught sight of something amazing, an erupting volcano towering above the frozen sea, and named it Mt. Erebus. Farther south, they encountered a sheer wall of ice rising two hundred feet above the sea surface and extending to the east and west as far as the eye could see. Captain Ross named this astonishing feature Victoria Barrier. Today it is known as the Ross Ice Shelf. For the sheer variety in discoveries and experiences, the British cruise is the most significant of the three nations' efforts between 1840 and 1841.

It was the British return leg that caused Wilkes grief. In early March on the way back to Hobart, Captain Ross decided to verify some of the landfalls reported by the U.S. Exploring Expedition at the eastern end of its transect. None could be found. Ross later wrote that he had ''sailed over'' the locations Wilkes had reported as land, and that the ''Antarctic Continent'' proclaimed by Wilkes probably didn't exist. According to Ross, Wilkes had probably just seen large icebergs surrounded by extensive low cloud and fog banks. To make matters worse, news of Ross' counterclaim reached the United States before the Exploring Expedition returned home, and the American explorers were greeted by controversy instead of accolades.

What had gone wrong? Wilkes, though conceited and overbearing, was an officer and a gentleman and would not have fabricated his data or exaggerated his claims. He was also a first-rate navigator. Had he somehow completely botched his reckoning? Had Ross? The answer lies in one of the unique aspects of polar meteorology. No one in the 19th century realized it, but the lower troposphere near the Antarctic coastline is subject to frequent temperature inversions. These

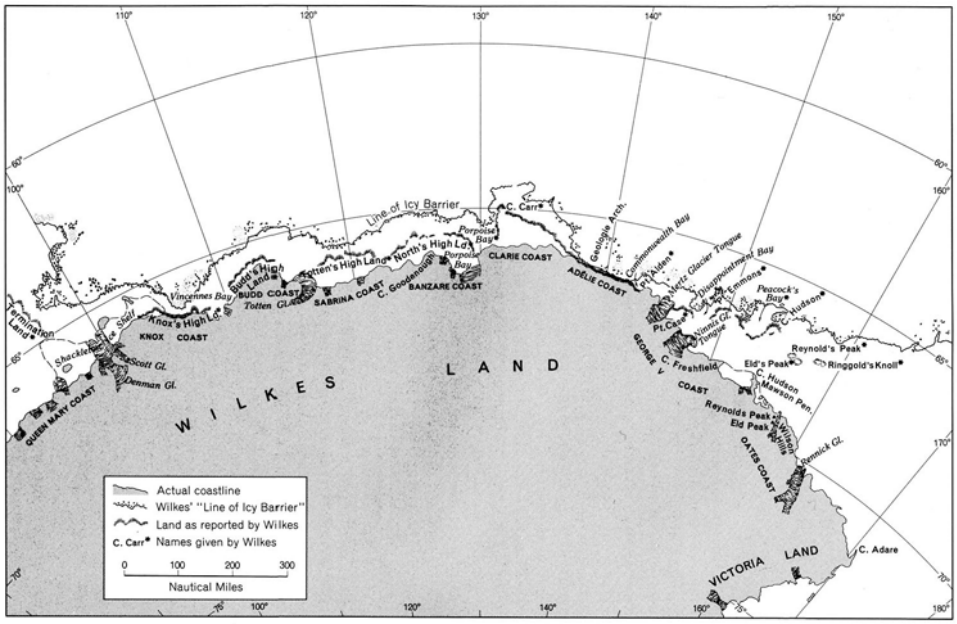

Figure 1.9. Map of the section of Antarctic coastline surveyed by the U.S. Exploring Expedition, showing the actual coastline and the sightings of land reported by Wilkes.
From Bertrand (1971). *Courtesy*: the American Geographical Society.

inversions cause the vertical density gradient, and hence refractive index, to decrease more than usual. The result is that optical ray paths are refracted significantly toward the ground, and distant objects below the horizon can appear above the horizon (Humphreys, 1940). This type of mirage is known as "looming". If the distant object is close enough to be above the horizon, the same refraction will make it appear taller and closer, an effect known as "towering". Evidently, these mirages afflicted Wilkes throughout most of his 1840 cruise, but affected Ross to a lesser extent the following year.

In 1958–59, the Australian National Antarctic Research Expedition (ANARE) conducted detailed aerial surveys of the route traveled by *USS Vincennes*. ANARE confirmed that all of Wilkes' reported landfalls were genuine, but that most were displaced tens of nautical miles too far north (Figure 1.9). The errors are the worst (more than 100 nautical miles) at the eastern end of Wilkes' route, indicating some extreme refraction events that might have been comparatively rare and not experienced by Ross. Thus, Wilkes was posthumously vindicated in his discovery of the Antarctic continent. But in his day the controversy raged, and many Europeans regarded the American claim as, while not dishonest, perhaps just wishful thinking. So heated did the debate become during the 1840s, and so haughty was Ross in dismissing Wilkes' accomplishments, that eventually even the French press and public began to side with the Americans.

This ordeal over the credit for Antarctica's discovery provides a lesson for today's remote-sensing scientists. Wilkes was one of the most highly trained navigators of his day, and he used the most advanced techniques in position-finding and cartography. Yet he was foiled by an atmospheric phenomenon uniquely extreme in the Antarctic. A similar fate awaits the modern researcher who is too confident when examining high-latitude satellite data. The polar regions are full of surprises that can confound both image interpretation and retrieval of geophysical quantities. Satellite remote-sensing algorithms designed for mid-latitudes usually won't work. The sources of the confusion are varied: they may be in the atmospheric structure, in unique properties of cloud cover, in the water column, or in the unique textures and albedos of high-latitude surface features. In any discipline, the researcher using space-based remote-sensing data must carefully consider the unique physical properties of the polar scene being studied. More than one major remote-sensing effort has needed to be redone entirely because of a unique polar phenomenon not fully understood or accounted for at first. Our story just told, of NASA's 19th century prototype, suggests a name for these recurring aspects of polar remote sensing, and perhaps of satellite remote sensing in general: the Curse of Captain Wilkes.

1.1.4 Epilogue

After the Antarctic cruise, the Exploring Expedition conducted scientific work in the Fiji Islands, Hawaii, and the Pacific Northwest, before recrossing the Pacific and returning to the United States via the Indian Ocean. While exploring the Oregon coast, on July 18, 1841 *USS Peacock* ran aground on an uncharted bar at the mouth of the Columbia River. Lt. Hudson saved his entire crew, but the ship was wrecked. In California (then part of Mexico), Wilkes purchased a merchant brig as a replacement, fitted her with two guns, and renamed her *USS Oregon*. At Singapore, the *Flying Fish* was judged too dilapidated to survive the voyage home and was sold into the opium trade. After nearly 4 years abroad, *USS Vincennes* arrived at Sandy Hook on June 10, 1842. The other two surviving ships reached the United States by July 4.

In assessing the Antarctic discoveries of that decade, one French reporter observed that "There was glory enough for all: Dumont d'Urville discovered the land, Wilkes explored it to the greatest extent, and Ross visited the portion nearest the Pole." This gentlemanly division of credit brought to a close the first great age of Antarctic exploration. To this triumvirate we should add the Russian Thaddeus von Bellingshausen and his 1819–21 Antarctic circumnavigation, which crossed the Antarctic Circle six times and was the first national expedition to see part of the Antarctic mainland. The second great age of Antarctic exploration would begin more than 50 years later with de Gerlache and Amundsen's 1898 winterover in the *Belgica*, and would end with high drama in both the race to the South Pole and Shackleton's *Endurance* adventure. Today, the section of Antarctic coast between longitudes 100°E and 145°E is known as Wilkes Land.

At this point, the reader might ask a valid question: if there are so many parallels, amusing or otherwise, between the U.S. Exploring Expedition and

modern day NASA, why do so few people today remember that the former ever took place? There is one important difference between the two: today's NASA maintains a multi-million dollar public relations infrastructure to promote and protect itself. In 1842, no such publicity machine was available to recount the heroic seamanship of Lieutenants Hudson and Walker, or the scientific accomplishments of Wilkes and Dana. Even the outstanding journalistic skills of Jeremiah Reynolds were unavailable. Having spent 13 years of his young adult life pursuing a dream, only to have it abruptly snatched from him, Reynolds had completely lost interest. In the 1840s Americans were concerned with other things, such as holding the increasingly fractious union together amidst the controversy over slavery, and realizing the Manifest Destiny by marching armies to the Rio Grande for an invasion of Mexico. At home the Exploring Expedition was quickly forgotten, and Wilkes spent many years trying to persuade Congress to fund a proper publication of the expedition's findings (Wilkes, 1845a, b).

However, the Exploring Expedition did score one major public relations coup: it made the United States respectable in the eyes of European scientists. The science team, unevenly qualified afterthought though it was by the time of sailing, had pulled its weight. The sheer volume of specimens and data gathered by the Scientifics from around the world was undeniably important to natural history, and the competent efforts at publishing by Dana, Couthouy, and Wilkes greatly enhanced America's international scientific reputation. In one ironic epilogue to this tale, Wilkes was awarded the Founder's Medal by the Royal Geographical Society for his scientific circumnavigation, and at the same time faced a court martial by his own Navy for his conduct as commander.

In addition to the controversy over his Antarctic sightings, Wilkes had returned with one of the most disgruntled officer corps that had ever been afloat. Many officers from the *Vincennes* and *Relief* filed numerous charges against him, and Wilkes filed countercharges against many of them. A general court martial was convened. Throughout the hearings nearly all of the charges against Wilkes collapsed. His mannerisms in command had certainly been "violent, overbearing, insulting, taxing forbearance to the last degree", according to Lt. Walker, and "exceedingly overbearing and offensive to a gentleman" according to Lt. Alden, but he had violated no regulations with respect to his officers. Furthermore, the hearings established that Wilkes' sightings of Antarctica were fundamentally honest. Only one charge couldn't be avoided—that of excessively flogging the enlisted men. U.S. Navy regulations at the time allowed for a maximum penalty of ten lashes for serious shipboard offenses, and only after a formal captain's mast hearing. Wilkes had often ordered summary punishments of 40. The court martial ordered a public reprimand placed in Wilkes' service record. This reprimand didn't end Wilkes' naval career, however. During the Civil War he commanded the steam-frigate *USS San Jacinto*, and in 1861 was briefly a hero when he intercepted the British mail packet *Trent* and arrested the Confederate Commissioners Mason and Slidell on their way to Europe (although President Lincoln reportedly reacted to that incident by saying "Let's fight one war at a time"). In 1862 Wilkes was promoted to commodore and in 1866 to rear admiral

on the retired list. He spent the rest of his life writing up his geophysical findings from the Exploring Expedition.

The star of the science team, James Dwight Dana, went on to become a world leader in geology. Dana made the Exploring Expedition's most enduring contributions to science. He discovered the relationship between Pacific island volcanism, subsidence, and the origin of coral islands, which confirmed and expanded on a hypothesis by Darwin (Dana, 1875). He also made another significant discovery that reef-forming corals are highly temperature-sensitive. One of his most insightful discoveries was that of an age progression along a specific direction, for every Pacific volcanic island chain he visited. These observations foreshadowed the theory of plate tectonics (Dana, 1890).

The huge collection of specimens acquired by the Exploring Expedition's science team played a controversial role in the establishment of the Smithsonian Institution, the national museum where so many of NASA's artifacts are exhibited today. The Smithsonian Institution was established in 1846, by a congressional act to properly manage the bequest of English philanthropist James Smithson. Its first director was physicist Joseph Henry, one of the few Americans with an international scientific reputation. Henry's vision for the Smithsonian was that it should serve, first, as a funding agency for research (much like today's National Science Foundation) and, second, as a data and specimen archive for selected material on which research was still being done. He had no objection to public museums, but he feared that such a charter for the Smithsonian would lead to permanent allocations of most of its funding and forestall the support of new research. The trouble for Henry was that the Exploring Expedition's collections, temporarily stored at the Patent Office, were so large that there was no other place to keep them on a permanent basis. By 1853 Henry had to acquiesce to government pressure, and the Smithsonian took charge of the Exploring Expedition's legacy. Henry's successors later expanded the role of the Smithsonian Institution as the national museum.

The Honorable Mahlon Dickerson retired from public office in June of 1838, content that he had done something for the future of the U.S. Navy by procuring the steamboat *USS Fulton 2*, and happy to leave the scene before there could be yet another congressional investigation of the Exploring Expedition's management. He died at Ferromonte in 1853, leaving behind numerous letters and diaries that are preserved today by the New Jersey Historical Society as the "Mahlon Dickerson Papers". These documents provide valuable insight into that transitional period in American history immediately after the founding fathers, when most national politicians were mediocrities.

The man who really made the Exploring Expedition happen, Jeremiah Reynolds, eventually settled in Texas and became a banker. Always philosophical, he wrote shortly before his death in 1859: "It's a pretty fair sort of world ... and if you don't expect too much you'll find many fine fellows in it." What did the United States Exploring Expedition, a great and often amusing 19th century prototype for NASA, really accomplish? It certainly proved the existence of the seventh continent, and made some significant contributions to natural history and geophysics. Perhaps more importantly, according to Stanton (1976), its conception and eventual

successful conclusion put the young and rough-hewn American democracy through one of its most demanding tests: that of supporting intellectual activity as one way to define national character. And, despite this voyage being the first time American naval officers and scientists would work together on something of national importance, there is some evidence that at least one of the officers understood and sympathized with the career of a scientist. After watching the Scientifics dissect a fish one day, Midshipman Reynolds wrote in his personal log: "All they did was Greek to us, but ... here's success to them, may they have a large book to publish when we return."

1.2 INTRODUCTION TO SATELLITE REMOTE SENSING OF POLAR REGIONS

The basis of satellite remote sensing of the Earth's surface is the detection and measurement of ElectroMagnetic Radiation (EMR) reflected by, or emitted from, surface objects or materials, and the atmosphere. Remote sensing exploits specific portions of the continuum of electromagnetic energy forming the ElectroMagnetic (EM) spectrum (Table 1.1). While passive systems detect reflected solar radiation (shortwave radiation) or thermal emissions (middle infrared and microwave) from the surface, active sensors transmit their own electromagnetic signal and measure the intensity and characteristics of the echo scattered back or reflected from the target surface. In principle, the information recorded can then be used to infer the physical properties and composition of objects within the field-of-view of the sensor. This

Table 1.1. The spectral range of divisions of the electromagnetic spectrum exploited by satellite remote sensing. Note that lidar (light detection and ranging) devices such as the GLAS sensor onboard the NASA ICESat are active sensors operating at visible to near-IR wavelengths.

Spectral range	Wavelength range	Quantity measured
Visible		
Blue	0.4–0.5 μm	Reflectance
Green	0.5–0.6 μm	Reflectance
Red	0.6–0.73 μm	Reflectance
Infrared (IR)		
Near-IR	0.7–1.3 μm	Reflectance
Mid-IR	1.3–3.0 μm	Reflectance + Thermal emission
Thermal IR	3.0–5.0 μm and 8.0–14.0 μm	Thermal emission
Microwave	1 mm–1 m	
Active		Reflectance
Microwave		Thermal emission

requires an understanding both of satellite instrument and viewing parameters and how EMR interacts with both the surface and the intervening atmosphere.

Remote-sensing science involves examining the "fate" of EM radiation that is incident on the Earth–atmosphere system (hitherto referred to as *incident radiation*). This can be in the form of solar radiation (in which case it is often termed *insolation*) or pulses of radiation transmitted by a laser or radar. On encountering the Earth–atmosphere system, the radiation is *reflected*, *absorbed*, and *transmitted* in varying proportions. These proportions depend upon: (1) the wavelength/frequency of the incident radiation; (2) the angle at which it impinges upon the atmosphere and surface (dependent upon both the look angle of the sensor and the geometry of the surface relative to the incident radiation); and (3) the composition and physical properties of the atmosphere and surface media. One of the basic premises, and strengths, of remote sensing is that an object can therefore be characterized by detecting these relative proportions of radiation at each wavelength or band of wavelengths (generally, the narrower the band, the higher the sensitivity to detecting differences).

Electromagnetic radiation traveling through the atmosphere is modified by complex interactions (Jensen, 2000; Kidder and Vonder Haar, 1995). Absorption occurs mainly through the presence of water vapor, carbon dioxide, oxygen, ozone and nitrogen; this leads to warming of the lower atmosphere. Radiation is reradiated, or emitted, at longer wavelengths. Atmospheric scattering occurs by three processes, namely *Rayleigh* and *Mie scattering* (both wavelength-dependent) and *non-selective scattering* (wavelength-independent). Rayleigh, or molecular, scattering is caused primarily by nitrogen and oxygen molecules, with dimensions at least 0.1 times smaller than the wavelength impacted, and the amount of scattering is inversely proportional to the fourth power of the wavelength. Mie, or non-molecular, scattering, on the other hand, occurs due to the presence of particles which are 0.1 to 10 times the given wavelength, including aerosol particles in the stratosphere and troposphere. These particles have an enormous variety in composition and origin, including volcanic, natural sea salt, natural dust, organics, biomass burning, soot, and other anthropogenic processes. The third mechanism, non-selective scattering, is a large-particle limit of Mie scattering. It occurs in the terrestrial atmosphere when larger particles are present in the form of cloud liquid water droplets and ice crystals and water droplets, for which the diameters or effective dimensions are ≥ 10 times larger than the wavelength. This non-selective, or wavelength-independent, situation arises at wavelengths $<\sim 1\,\mu m$ for most terrestrial clouds. At longer wavelengths, wavelength dependence is introduced because cloud particles begin to absorb as well as scatter radiation. In contrast to clouds, most terrestrial aerosol particles (smaller than cloud particles) both absorb and scatter radiation throughout the shortwave part of the EM spectrum. In all cases, the extent to which these atmospheric processes affect the radiation received at the satellite also depends on the atmospheric pathlength. In remote sensing, detailed understanding of these atmospheric scattering interactions is required, to either (1) correct for atmospheric attenuation or distortion of the signal from a desired surface property, or (2) quantify properties of clouds,

Table 1.2. Important atmospheric transmission windows exploited in satellite remote sensing of the Earth's surface.

Wavelength, λ (μm)	Spectral region
0.3–1.1	UV, visible, near-infrared
1.5–1.8	Near-infrared
2.0–2.4	Near-infrared
3.0–5.0	Middle-infrared
8.0–14.0	Middle-infrared
10.5–12.5	Middle-infrared
>0.6 cm	Microwave

After Jensen (2000). UV = ultraviolet.

aerosols, and precipitation directly to further the study of climate. The branch of theoretical physics that treats these EM interactions, *radiative transfer*, is reviewed in Chapter 2, and more detailed treatments can be found in the references therein. Radiative transfer plays a prominent role not only in understanding atmospheric influences on EMR, but also in understanding the remote-sensing signatures of the unique surface types in polar regions. In subsequent chapters, it will become clear how snow cover and sea ice must be studied and modeled as physical systems involving scattering centers and absorbing media, so that satellite data can be properly interpreted.

Spectral regions exploited by satellite remote sensing to study the Earth's surface rely upon the existence of *atmospheric windows*, or transmission bands. These are defined as regions of the electromagnetic spectrum within which specific wavelengths can pass relatively unimpeded through the atmosphere. Important atmospheric windows exploited by Earth-observing satellite sensors are given in Table 1.2. A number of broad rules of thumb apply. For example, the "transparency" of atmospheric windows decreases with an increase in air humidity. Fortunately, the atmosphere at high latitudes is generally very cold and therefore relatively dry, particularly over the Antarctic Ice Sheet interior, but this is not always the case. Maximum atmospheric gas absorption occurs at wavelengths $<0.3\,\mu m$, whereas the minimum impact occurs at microwavelengths $>0.6\,cm$ (Jensen, 2000). Importantly from a global warming perspective also, clouds absorb much of the longwave radiation emitted from the Earth's surface. Fortunately, microwave sensors operating at wavelengths $>0.9\,cm$ are capable of penetrating cloud.

Even within the atmospheric windows, variable atmospheric effects do still contribute to satellite-derived surface measurements acquired and often require correction. These effects are, however, minimal compared with those outside the transmission windows, where EMR–atmosphere interactions have a dominant impact on the radiation measured by the satellite sensor. Note that satellite systems designed to measure atmospheric constituents operate within both absorption bands and atmospheric windows (Kidder and Vonder Haar, 1995). The visible region of the electromagnetic spectrum (0.4–0.7 μm) resides within an atmospheric window in the wavelength range of about 0.32–0.90 μm while emitted

energy from the Earth's surface is sensed through windows at 3–5 μm and 8–14 μm. Radar and passive-microwave systems operate through a window region of 1 mm to 1 m.

The first civilian satellite remote sensing of polar regions occurred with the launch of TIROS-1 (Television and Infrared Observation Satellite-1) on April 1, 1960. This satellite carried a vidicon system, essentially a modified TV camera that scanned 500 lines containing 50 pixels to create a simple image. Although relatively crude by today's standards, these early research and development meteorological satellites, in the TIROS and Nimbus series, laid the foundation for the development of the sophisticated suite of tools that we now take for granted. In its infancy, the new technology provided scientists with tantalizing glimpses of polar surface phenomena and processes from sensors that were designed to monitor global cloud/weather patterns for synoptic meteorological forecasting purposes. The immense potential of satellites to monitor sea ice was first demonstrated when TIROS-2 monitored the spring ice breakup in the Gulf of St. Lawrence, Canada, in 1961 (Gloersen and Salomonson, 1975). As far as we know, the first useful ice sheet research-related information came in 1963/4, when a TIROS instrument provided images of a large iceberg calving event from the Amery Ice Shelf, albeit at a poor resolution (Massom, 1991).

However, it was the launch of the first Earth Resources Technology Satellite (ERTS-1) in 1972 (renamed Landsat-1 in 1975) that provided the first multispectral map of the Earth's surface and began the modern revolution in polar remote sensing. Subsequent dates stand out as heralding new ages in satellite remote sensing of polar snow and icemasses, including: the launches of the first civilian Synthetic Aperture Radar (SAR), together with a radar altimeter and scatterometer, onboard SeaSat in 1978; the Scanning Multichannel Microwave Radiometer (SMMR) and the Total Ozone Mapping Spectrometer (TOMS) onboard Nimbus-7 in the same year (these extraordinary sensors operated until 1987 and 1993, respectively, way beyond their expected lifetimes); the commencement in 1979 of the still operational NOAA (National Oceanic and Atmospheric Administration) polar orbiter series with the well-known Very High Resolution Radiometer (VHRR) and then the Advanced VHRR (AVHRR); the high-resolution radar altimeter onboard ERS-1 in 1991; the wide-swath ScanSAR onboard Radarsat-1 in 1995; the launch of NASA's EOS flagship Terra in 1999. Recently, the polar research community started to benefit from the launch of Aqua, Envisat and ADEOS-II (ADvanced Earth Observing Satellite-II) in 2002—a bumper year indeed!

In the course of studying faraway regions that are notoriously inhospitable, dangerous and logistically challenging, not to mention expensive, to visit, glaciologists soon realized the immense benefits that satellite remote sensing had to offer compared to *in situ* measurement, in the wake of Landsat-1. First and foremost, remote sensing enabled instantaneous coverage of large regions, providing a cost-effective means of extending *in situ* measurements that were both spatially and temporally limited. Moreover, it yielded regular repetitive coverage in a systematic fashion and over long time periods, enabling detection and monitoring of change. Over the last 30 years, Earth remote-sensing technology has evolved to include

increasingly sophisticated sensors operating at higher spectral and spatial resolutions, improved calibration and satellite-tracking accuracy, longer mission lifetimes, with more emphasis on the importance of data continuity with the launch of follow-ons to extend increasingly important time series. Remote sensing has now reached a level of maturity whereby it is an indispensable research tool.

Generally speaking, Earth satellite sensors are not specifically designed for polar research. Over the past 40 years, useful polar data and related science has been a byproduct. However, as our understanding of the central importance of polar regions in the global climate system has gathered momentum, so has the realization that satellite remote sensing is an absolutely essential polar research tool. As a result, missions dedicated to polar research are now being launched (e.g., ICESat). At the same time, most Earth remote sensors are intrinsically valuable for polar research because they are deployed in high inclination, or "polar" orbits (see Chapter 2). Because their ground tracks converge spatially at high latitudes, most polar regions benefit from more frequent coverage by the sensors, and polar processes can often be studied on a greater variety of spatial and temporal scales than those at mid- and tropical latitudes.

No ideal, all-purpose remote sensor exists. Rather, scientists now have a choice of a range of datasets, each with its own set of inherent attributes, strengths and limitations. The choice of an optimal dataset, or datasets, for a given application depends upon the scale and nature of the problem being investigated and the satellite dataset characteristics. Tradeoffs exist—for example, between coverage/revisit interval and spatial resolution. Due to telemetry bandwidth, scanning configurations, and other technological limitations, high-resolution sensors tend to offer limited spatial coverage over a narrow swath (generally $\leq$100 km), with ultra-high-resolution (<5 m) sensors generally operating over swaths of only ~10–20 km). Medium- to coarse-resolution (>250 m) sensors, on the other hand, typically operate over much wider swaths (>1,500 km). This is an important consideration, if true complete polar coverage is required, as most geosynchronous satellites orbit to a latitudinal limit of 81.6°. Moreover, the swathwidth and orbital configuration determine the interval between repeat passes—the wider the swath, the shorter the revisit interval at high latitudes. Again, this is a major consideration in process studies requiring fine temporal resolution—e.g., studies of sea-ice dynamics, which recent research suggests should ideally resolve semi-diurnal tidal and inertial forcing effects. Other considerations for the aspiring user relate to whether data are available in near-real time (a major consideration for the operational community), and cost. Commercialization of remote sensing is growing. In all cases, the synergistic combination of data from different yet complementary sources invariably yields greater levels of information and insight than can be derived from individual sensor data sources alone.

Moreover, satellite remote sensing captures the public imagination, nowhere more so than in dramatic images of immense iceberg calvings or "cataclysmic" short-term events such as the Larsen-B Ice Shelf disintegration. The Antarctic Meteorology Research Center (AMRC) at the University of Wisconsin has often made this type of imagery available to the public in recent years. For the polar field

researcher, remote sensing has immense operational value, for (1) planning research activities at a given location with due attention to historical climatic conditions, as can be discerned in a multiyear satellite data record, (2) maximizing scientific productivity and safety within a given field program by using satellite imagery to guide the field party away from hazardous conditions, or toward preferred conditions. One example may be found within the United States Antarctic Program (USAP), which maintains satellite-tracking antennas at McMurdo and Palmer Stations. The NOAA and U.S. Air Force (Defense Meteorological Satellite Program, DMSP) data tracked at McMurdo are used in real time for operational weather forecasting and flight planning (even routine resupply flights from New Zealand to McMurdo are intrinsically hazardous due to the severe shortage of alternative landing sites). After real time use, the USAP McMurdo data are archived onto magnetic tape and sent in duplicate to the AMRC and the Arctic and Antarctic Research Center (AARC) at the Scripps Institution of Oceanography. Both centers make the data available for retrospective basic research and environmental assessment for expedition planning; the former specializes in meteorological applications while the latter specializes in oceanographic applications. For example, DMSP data at the AARC are frequently used to provide near-real-time sea ice maps to Antarctic research vessels from several nations. From the standpoint of conducting safe and productive field research, one is hard-pressed to cite a geophysical research community having a greater need for satellite remote sensing than polar researchers.

1.3 NASA IN THE 21ST CENTURY: THE EARTH OBSERVING SYSTEM

Satellite remote sensing is in a period of enormous transition. For the past 25 years, the geophysical science community has had access to a capable and indispensable suite of Earth-observing instruments. The observational capabilities of these instruments have included:

(1) Global imaging at spatial resolutions of 1–5 km, with 1–3 bands in the visible and near-infrared, and 1–2 bands in the middle-infrared (examples include the AVHRR, and the DMSP Operational Linescan System, OLS).
(2) Higher resolution imaging of selected phenomena at some financial cost to the researcher, with spatial resolutions of 30–300 m, using half a dozen spectral bands (examples include the Landsat Thematic Mapper and Multispectral Scanner).
(3) Profiling of stratospheric ozone with a vertical resolution of several kilometers and spatial resolution of order 100 km, and global mapping of the atmospheric ozone column with spatial resolution of order 50 km (examples include the Backscatter UltraViolet, BUV, and the Total Ozone Mapping Spectrometer, TOMS).
(4) Atmospheric temperature and humidity soundings with a vertical resolution of several kilometers and spatial resolution of order 100 km (for example, the High-resolution InfraRed Sounder, HIRS).

(5) Passive microwave imaging of the Earth's surface with a spatial resolution of order 30 km (examples include the SMMR and the DMSP Special Sensor Microwave Imager, SSM/I).

These are some of the continuous observations whose time series now spans more than two decades. There have been several highly successful geophysical observatories flown in space, such as the Nimbus 4 and Nimbus 7 satellites, the Earth Radiation Budget (ERB) satellite, and the Upper Atmosphere Research Satellite (UARS). There have also been deployments of advanced techniques such as SAR aboard European and Japanese spacecraft, and aboard NASA's space shuttle, during the 1990s.

Active microwave techniques can be regarded as a transition between "heritage" and next-generation remote sensors, or even as the leading edge of the latter. SARs offer high-resolution measurements over a relatively narrow swath, while radar scatterometers enable the routine measurement of surface backscatter characteristics over large areas, albeit at a relatively coarse spatial resolution of 5–50 km. To date, polar-orbiting operational wind scatterometer missions have flown onboard the ERS-1 and -2, QuickScat, ADEOS, ADEOS-II, and Envisat spacecraft discussed below. Importantly, these sensors have provided global data in a routine and almost uninterrupted fashion since 1991.

The applications of many of these "heritage" remote-sensing missions to polar science will be discussed throughout this book. While reading through these examples, the reader should keep in mind that times are changing. Instead of observing meteorological phenomena at 1-km spatial resolution in five bands, we can now observe at half that resolution in dozens of bands and in some cases at multiple viewing angles. High spatial resolution (tens of meters) will become increasingly available to the researcher at reduced cost. The spatial footprint of passive-microwave imaging will improve to the order of 10 km, and several sources of 10-m resolution SAR data will become available. Instruments with high spectral resolution will enable not only the mapping and profiling of stratospheric ozone, but the simultaneous retrieval of many trace gas column abundances that are relevant to ozone chemistry. Instead of a single reference climatology of chlorophyll from an instrument shut down many years ago (the Nimbus 7 Coastal Zone Color Scanner—CZCS), we will now have abundant ocean color data from instruments beginning in 1997 with NASA's SeaWiFS (Sea-viewing Wide Field of View Spectrometer) program and continuing with instruments flown by several nations. These various advances in technology and commitment on the part of NASA and other space agencies have been eagerly awaited by the Earth science community for many years, and they are now actually flying or are awaiting launch.

The extraordinary new capabilities of interferometric SAR are discussed in Chapter 2 of Volume 2 of this book. Another exciting emerging technology is spaceborne SAR polarimetry. As discussed in Chapter 3 of Volume 2 of this book and Chapter 5 of this volume, a polarimetric SAR measures the backscattering properties of a target, including both the phase and amplitude information. The scattering matrix can be formed from data for the four linear polarization modes (HH, VV,

HV, and VH), from which the corresponding backscattering coefficient for any polarization combination can be obtained. Dominant backscattering surfaces of the targets can then be determined by comparing the polarimetric data with theoretical polarization signatures (van Zyl et al., 1987). Examples are the forthcoming Japanese Phased Array-type L-band Synthetic Aperture Radar (PALSAR; launch scheduled for 2005) and Radarsat-2 (launch scheduled for 2006).

At the same time as these new space remote-sensing technologies emerge, there are myriad scientific questions to address. Walsh et al. (2001) have reviewed climate change issues in the polar regions in the context of available remote-sensing datasets from NASA. This review is structured as a series of questions, some of which are capable of motivating a dedicated remote-sensing mission, and all of which are capable of motivating significant remote-sensing projects and are excellent topics for doctoral dissertations. For example, are there changes in the polar troposphere involving changes in precipitation rates, perhaps in response to changes in the hydrologic cycle? How is the radiation balance of the polar regions changing? What are the mechanisms behind the recent decrease in the overall mass of the Greenland Ice Sheet? Are there similar occurrences with the Antarctic Ice Sheet and ice streams? How do changes in Arctic precipitation and surface runoff influence the Arctic Ocean's salinity, sea ice extent, and circulation? Are there changes in high-latitude ocean primary production? Are there changes in the hydrology and distribution of permafrost in the Arctic? What is the importance of the ice–albedo feedback and the cloud–radiation feedback, and how might these mechanisms change in a warming climate? How do large-scale decadal and interannual modes of atmospheric variability, such as the El Niño–Southern Oscillation, the North Atlantic Oscillation, and the Arctic Oscillation, influence polar ocean circulation? And many others. The following sections of this chapter summarize the new remote-sensing missions that may help answer many of these questions. Additional new satellite instruments are discussed throughout the book. Chapter 2 gives more detailed definitions of the remote-sensing terminology introduced here.

1.3.1 Terra, Aqua, and Aura

The flagships of the EOS program are the *Terra* and *Aqua* spacecraft (Figure 1.10, see color section), with 10 : 30 a.m. and 1 : 30 p.m. equator crossings, respectively. Terra was launched in December, 1999, and Aqua in May, 2002. As the names suggest, the major thrust of the morning satellite mission is terrestrial and tropospheric processes for which cloud-free viewing is needed, while the afternoon satellite is intended mainly to study the global hydrological cycle and energy balance in which clouds play an essential role.

There are two instruments common to both Terra and Aqua: the Moderate Resolution Imaging Spectrometer (MODIS) and the Clouds and Earth's Radiant Energy System (CERES) experiment. MODIS, already widely used by many researchers, is a multi-purpose imaging radiometer with 36 spectral bands throughout the visible, near-infrared, and middle-infrared parts of the spectrum. The spatial

resolutions of these channels range from 250 m to 1 km. The applications of MODIS include monitoring glaciers, retrieval of cloud and aerosol optical properties, total column water vapor retrieval, synoptic meteorology, cloud climatology, sea surface temperature observation, monitoring terrestrial vegetation, and many others. CERES has a specific mission—to make highly accurate measurements of the Earth's radiation budget using broadband shortwave and longwave radiometers, with a spatial resolution of 20 km at nadir. CERES consists of two instruments, each having three broadband channels: (1) 03–5.0 μm, (2) 8–12 μm, and (3) 0.3–50 μm. One instrument is a cross-track scanner that provides limb-to-limb coverage; the other has a rotating azimuth scan plane to provide angular sampling. There are actually three CERES instruments; the first was deployed aboard the Tropical Rainfall Measuring Mission (TRMM) satellite in November, 1997.

There are three additional instruments aboard Terra that take advantage of the morning equator crossing. The Advanced Spaceborne Thermal Emission and Reflection Radiometer (ASTER) is the high spatial resolution instrument—15–90 m^2 per pixel. It consists of three telescopes, one each for visible, near-infrared, and middle-infrared radiation, which together provide 14 spectral bands. ASTER does not collect data continuously, but instead collects approximately 8 minutes of data per orbit from selected targets. ASTER also has the ability to change viewing angles so as to produce stereoscopic images. Another instrument whose specialty is changing viewing angles is the Multi-angle Imaging Spectro-Radiometer (MISR). MISR consists of nine pushbroom imagers, each with four spectral bands: blue, green, red, and near-infrared. One imager looks in the nadir direction, while the other eight are fixed to look forward and backward with viewing angles 26.1°, 45.6°, 60.0°, and 70.5°. MISR is intended to measure the bidirectional reflectance of all types of Earth scenes, a critical need for understanding radiant energy balance and for interpreting other types of remote-sensing data. Chapter 2 of Volume 2 of this book highlights some of MISR's unique applications for polar remote sensing. The MOPITT (Measurements Of Pollution In The Troposphere) instrument is designed to monitor global sources and sinks of carbon monoxide and methane. It uses a novel technique called gas correlation spectroscopy, in which light entering the sensor passes through onboard gas cells containing both gases.

The four additional instruments aboard Aqua each have as a major part of their mission some aspect of the Earth's hydrological cycle. The Atmospheric InfraRed Sounder (AIRS) is a middle-infrared spectroradiometer having a spatial resolution of 13.5 km. With 2,378 channels at wavelengths ranging from 3.74 to 15.4 microns, AIRS will be able to provide atmospheric temperature and water vapor profiles with a vertical resolution of 1 km. The spectral resolution of this instrument will also be useful for the study of cloud optical and microphysical properties. The atmospheric profiling capability of AIRS ends at the cloud top, and the Humidity Sounder from Brazil (HSB), a five-band passive-microwave radiometer (150–183 GHz) having a nadir spatial resolution of 13.5 km, is intended to help correct humidity profiles in the presence of clouds. The Advanced Microwave Sounding Unit (AMSU) is a passive-microwave radiometer operating in 15 spectral bands between 50 and

89 GHz, and a nadir spatial resolution of 40 km. It is intended to provide temperature and water vapor soundings over both clear-sky and cloudy scenes. There is already one AMSU in operation, aboard the NOAA-15 polar orbiter that was launched in May, 1998. The Advanced Microwave Sounding Radiometer-EOS (AMSR-E) is a general-purpose passive-microwave imager engineered by the National Space Development Agency of Japan (NASDA, renamed the Japan Aerospace Exploration Agency, JAXA), and will measure Earth scene brightness temperatures at 6.925, 10.65, 18.7, 23.8, 36.5, and 89.0 GHz. The spatial footprint varies with frequency, ranging from 6×4 km at 89.0 GHz to 75×43 km at 6.925 GHz. For passive-microwave studies of sea ice climatology, AMSR-E offers a dramatically increased spatial resolution over heritage sensors. Other applications for AMSR-E include measurement of precipitation rates, cloud liquid water content, total column water vapor, sea surface winds, sea surface temperature, and soil moisture.

The *Aura* mission (launched in June 2004) is studying the stratosphere and upper troposphere, with four complimentary instruments. Two of them are limb sounders, meaning that they look not down but toward the edge of the Earth's disk, in order to sample a long optical path through the atmosphere. The HIgh Resolution Dynamics Limb Sounder (HIRDLS) is a middle-infrared instrument with 21 bands in the wavelength range 6.12 to 17.76 microns. Its primary objective is to provide temperature soundings of the upper troposphere, stratosphere, and mesosphere. By using a limb-sounding variation of the "CO_2-slicing" technique (see Chapters 3 and 4), HIRDLS will provide profiles of temperature as a function of atmospheric pressure. From the retrieved height of the geopotential surfaces, upper atmosphere winds and potential vorticity can be determined. At the same time, the instrument's spectral resolution will enable the retrieval of total column abundances of ozone, water vapor, methane, N_2O, NO_2, HNO_3, N_2O_5, CFC-11, CFC-12, and $ClONO_2$. The importance of these trace gases in polar ozone depletion are explained in Chapter 3. HIRDLS will also be valuable for locating Polar Stratospheric Clouds (PSCs). The Microwave Limb Sounder (MLS) was first flown on the successful Upper Atmosphere Research Satellite (UARS) of the 1990s (see Chapter 5), and the Aura version of MLS has additional capabilities. The Aura MLS operates in five bands: (1) 118 GHz, for temperature and pressure profiling; (2) 190 GHz, for H_2O and HNO_3 abundances; (3) 240 GHz, for O_3 and CO; (4) 640 GHz, for N_2O, HCl, ClO, HOCl, BrO, HO_2, and SO_2; and (5) 2.5 THz, for OH. The MLS provides key observations of water vapor in the upper troposphere, which are important for studies of both climate variability and atmospheric chemistry.

The Ozone Monitoring Instrument (OMI), engineered by the Netherlands Agency for Aerospace Programs (NIVR) in collaboration with the Finnish Meteorological Institute (FMI), is a combination ozone mapper and ozone profiler. OMI is an imaging spectrograph that has 740 wavelength bands and a nominal spatial resolution of 13×24 km. The vertical ozone profiles derived from OMI will have a spatial resolution of 36×48 km. For special events such as urban pollution sources, the spatial resolution of the total column ozone maps can be

improved to 13×13 km. OMI's hyperspectral capability will also allow for retrieving total column abundances of NO_2, SO_2, BrO, and OClO, as well as distinguishing between various aerosol types (smoke, dust, sulfates). Aura will also carry a Fourier transform infrared spectrometer called the Thermal Emission Spectrometer (TES). TES will sample the middle infrared from 3.2 to 15.4 microns with a spectral resolution of $0.025\,cm^{-1}$. This high spectral resolution will enable linewidth measurement of many tropospheric trace gases that have middle-infrared absorption features. TES can be pointed toward any target within 45° of the local vertical, and can make both limb and nadir observations. This suite of Aura observations will come at a critical time when we should begin to detect stratospheric ozone recovery as a result of the Montreal Protocol.

1.3.2 Smaller EOS missions

In addition to the "flagships", there will be a number of smaller missions offering unique capabilities for polar science. One of them—the Ice, Cloud, and land Elevation Satellite (*ICESat*)—is already dedicated to high-latitude work (Figure 1.11, see color section). The launch of the Geoscience Laser Altimeter System (GLAS) onboard ICESat heralded a new era of ice sheet measurement from space. For one thing, it is the first satellite mission dedicated to ice sheet research. The sensor is designed to measure ice sheet elevations and temporal changes in elevation along profiles or narrow swaths (Zwally et al., 2002), as well as atmospheric aerosol and cloud properties. These unique data will create a benchmark against which to measure change. The aim is to measure seasonal and interannual variations in surface elevation, then to use the data in energy balance models and to verify the output of atmospheric circulation and ice sheet models.

ICESat was launched in January 2003 and, after some instrumental difficulties were addressed, began conducting a regular observing schedule in February 2004. The technology behind GLAS is called *lidar*, or light detection and ranging. Lidar is a distance-measuring system similar to radar, except that instead of radiowaves it uses pulses of laser light for range finding. A lidar system determines precise distances by measuring the amount of time necessary for a short-duration pulse of light to leave an emitter, hit a target, and return (Measures, 1984). The measured surface elevation is determined from the altitude of the satellite orbit above the Earth minus the range to the surface measured by GLAS. The range is corrected for delays caused by atmospheric refraction. Variations in the Earth's surface elevation caused by ocean, solid, atmospheric load, and polar tides are calculated to obtain the surface signals of interest.

ICESat is the first lidar mission dedicated to continuous Earth observations. GLAS has two principal components, namely a nadir-pointing laser transmitter and a telescope receiver. It measures the time interval for the laser pulse to travel a roundtrip from the instrument to the reflecting surface and back again, which is then converted into a distance. These short pulses (5 nanoseconds) of near-infrared light (1,064 nm) are used for the measurement of surface topography while

backscattered light in the visible-green light (532 nm) is used for measurement of the vertical distribution and characterization of aerosols and clouds. Ice sheet elevation profiles consist of the centroid elevations of ~70-m diameter laser footprints spaced at 172 m along-track, with a predicted vertical accuracy of ~15 cm (Zwally et al., 2002). Using a sophisticated onboard star tracker camera system and global positioning system, the spacecraft orbit and the laser direction and position in space are known very accurately (radial orbit determinations to better than 5 cm, and footprints located to 6 m horizontally) (Zwally et al., 2002). By controlling the spacecraft roll attitude, the laser footprint precisely follows the identical reference groundtrack ("exact repeat mode") for each cycle.

Laser altimetry has the unique capability of measuring the vertical distribution of surfaces within a single ground resolution element (i.e., laser footprint). This result is achieved by digitizing the complex, time-varying return pulse energy (waveform) that comes from the reflection of a single laser pulse from the target surface. This waveform is a measure of the vertical distribution of surface components weighted by projected area, reflectivity, and the spatial distribution of laser energy across the footprint. Compared with conventional radar altimetry, the much shorter wavelengths of lidar enable observation at greater detail, but cannot penetrate optically thick atmospheric layers such as clouds.

ICESat is designed to operate for 3–5 years and should be followed by successive missions to measure ice changes for at least 15 years (an ICESat follow-on mission is planned in the 2010 timeframe). The time series of elevation changes will enable determination of the current ice sheet mass balance, seasonal, interannual and longer term changes in icemass, causes of mass balance changes (e.g., precipitation patterns, ice flow deceleration/acceleration, icemelt), and estimation of the present and future contributions of changes in ice sheet mass and volume to global sea level rise (Zwally et al., 2002). Long time series are required to better understand the "background" variability of processes determining elevation change and to enable assessment of the causes of observed change. These are essential prerequisites to developing a predictive understanding of ice sheet variations (Walsh et al., 2001). ICESat will also make unique measurements of cloud heights and the vertical structure of clouds and aerosols, which may help improve the understanding of precipitation and blowing snow over the ice sheets and the surface energy balance. ICESat data should also yield a climatology for PSCs (Polar Stratospheric Clouds), which provide the mechanism for the severe springtime polar ozone depletion (Chapter 3). Other potential measurements include sea ice roughness and thickness.

CloudSat will fly in formation with Aqua, and will measure vertical profiles of clouds using a 94-GHz radar. Launch is planned for January 2005. The vertical resolution will be 500 m, and the horizontal cross-track resolution is 1.2 km. In conjunction with the Aqua instruments, these active microwave measurements will provide a thorough description of cloud microphysical properties such as liquid water and ice content, effective particle size, opacity, occurrence of precipitation, and geometrical properties. This should provide closure to many questions regarding cloud–climate feedback. CloudSat should also provide insight into the "indirect radiative effect" of tropospheric aerosols—in which aerosol particles within a

cloud seed more droplets for a given total water content, reducing the effective droplet radius and making the cloud more reflective (Chapter 4). ICESat measurements should show the importance of this effect on a global basis.

Landsat 7, launched in April 1999, continues the venerable time series of high-spatial-resolution visible and infrared imagery that, among many other accomplishments, revolutionized the field of glaciology during the early 1970s. This spacecraft carries the eight-band Enhanced Thematic Mapper Plus (ETM+). The spatial resolution of ETM+ is improved over previous Landsat instruments by more than a factor of 2. Its panchromatic band (0.50–0.86 μm) offers a spatial resolution of 15 m. The spatial resolution of the visible/near-IR and thermal IR bands are 30 m and 60 m, respectively.

The *SeaStar* spacecraft, carrying SeaWiFS, was launched in August, 1997. Although originally intended to be a short-duration mission whose scientific objectives would be taken over by MODIS, SeaWiFS has remained operational throughout 2003 and into 2004 due to the oceanographic community's demand for its high-quality ocean color imagery in an uninterrupted time series. SeaWiFS is an advanced ocean-color-monitoring system consisting of eight narrow spectral bands over the region 0.402–0.855 μm. Two modes are available for each band: a higher resolution option of 1.1-km resolution (at nadir) over a 2,800-km swath, and a degraded resolution mode of 4.5-km resolution over a 1,500-km swath. It is specifically designed to detect and monitor a range of ocean processes and phenomena, including primary production and phytoplankton processes. While over-ice applications are limited, the data from ocean color sensors are of immense importance in enabling a better understanding of the complex relationships between sea ice behavior and phytoplankton distribution (McClain et al., 1998; O'Reilly et al., 1998).

The *Earth Observing-1* (EO-1) spacecraft is part of a NASA program that intends to test advanced instruments and spacecraft systems. EO-1 was launched in November 2000, and tested three remote sensors that represent a significant improvement in land surface remote sensing. *Hyperion* is a hyperspectral instrument that resolves the full EM visible and near-IR spectrum backscattered from the Earth–atmosphere system, in 220 bands from 0.4 to 2.5 μm. The spatial resolution is 30 m, and the ground swath is 7.5×100 km. Hyperspectral imaging, or imaging spectroscopy, involves scanning hundreds of very narrow and closely spaced spectral bands to create continuous spectral response curves for each pixel. In other words, images are simultaneously acquired in multiple spectral bands, and are inherently co-registered. Hyperion was intended for low-latitude remote-sensing applications in agriculture, forestry, geology, and mining, by providing detailed surface classification via the full spectral resolution. However, this type of measurement also has profound implications for mapping the time evolution of sea ice, where the spectral signature is highly variable depending on ice type and concentration (Chapter 5). EO-1 also carries an Advanced Land Imager (ALI), which is intended as a testbed for future generation Thematic Mapper instruments. In comparison with ETM+, the ALI offers a similar spatial resolution and multispectral capability, but with mass and power consumption reduced by a factor of 4, and payload volume reduced by a

factor of 7. The third EO-1 instrument is the Atmospheric Corrector (AC), which is a hyperspectral imager covering 0.89–1.58 μm with moderate spatial resolution. The AC is designed to characterize the scattering and absorbing properties of aerosols, and to correct for atmospheric water vapor, so that the signal from atmospheric variability can be subtracted from a surface reflectance measurement.

A second NASA lidar instrument will be flown aboard a Langley Research Center mission called Cloud–Aerosol Lidar and Infrared Pathfinder Satellite Observations (*CALIPSO*). CALIPSO is scheduled for launch in 2005. The Cloud–Aerosol Lidar with Orthogonal Polarization (CALIOP) is, like GLAS, a two-wavelength lidar system operating at 532 and 1,064 nm. As with GLAS, timing the intensity of the returned laser pulses will yield information about the vertical profile of stratospheric and tropospheric aerosols. CALIOP's supplemental capability is the measurement of two polarized radiation components at 532 nm. This will yield information about cloud particle phase (liquid water or ice, see Chapter 4). CALIOP will be bore-sighted with an Imaging Infrared Radiometer (IIR) that will measure at three mid-IR window wavelengths: 8.7, 10.5, and 12.0 μm. As discussed in Chapter 4, this type of multispectral measurement yields information about cloud particle size.

NASA's Earth Observing System is making intelligent use of formation flying with its spacecraft. The EO-1 spacecraft flies 1 minute behind Landsat 7, so that its testbed instruments can be compared with contemporaneous ETM+ imagery. There is a larger formation known as the "A-train" which, when fully deployed, will consist of Aqua followed by CALIPSO, CloudSat, PARASOL (a French instrument derived from the POLDER instrument discussed below, that makes passive measurements of polarized light backscattered by the Earth–atmosphere system), and finally Aura. This type of formation flying is a welcome evolution in a program that began in the early 1990s with gigantic spacecraft buses carrying all the instruments at once. Formations such as the A-train reduce the risk to the overall Earth science mission, and allow flexibility to insert either new or replacement instruments as needed.

There is an additional NASA Earth-observing spacecraft having potentially useful polar applications that has been ready to fly since 2001: the Deep Space Climate ObserVatoRy (*DSCOVR*). Unlike most polar orbiters that fly at altitudes of order 700 km, and observe the Earth–atmosphere system in groundtracks, DSCOVR is meant to be deployed at the Lagrange-1 (L1) point, a location approximately 1 million miles (~1.6 million kilometers) from Earth where a spacecraft will experience the same gravitational attraction from the Sun as it does from the Earth. This results in the spacecraft's orbital period about the Sun being identical to that of Earth. With the spacecraft deployed in a stable "halo" orbit about the L1 point, the entire Earth disk can be imaged by a telescopic radiometer called the Earth Polychromatic Imaging Camera (EPIC). The EPIC instrument, developed by a collaboration between the Scripps Institution of Oceanography and the NASA Goddard Space Flight Center, has 10 spectral bands covering the wavelength range 0.318–0.905 μm, and will have an equatorial spatial resolution of order 8 km. The multispectral capability will allow the retrieval of total column ozone

and water vapor, retrieval of aerosol optical properties over low-albedo surfaces, and imaging of atmospheric dynamics on a global scale. The unique aspect of this measurement is the combination of high time resolution (one image every 15 minutes) with full Earth disk imaging, enabling large-scale dynamics of both the troposphere and stratosphere to be observed directly (the latter via ozone abundance), rather than stitched together from sequences or composites of polar orbiter and geostationary images. A second broadband radiometer similar to CERES, built by the U.S. National Institute for Standards and Technology and called the National Institute for Standards and Technology Advanced Radiometer (NISTAR), will measure the total shortwave energy backscattered from and total longwave energy emitted by the Earth's atmosphere system. This will lead to the first direct estimate of the Earth's planetary albedo. The halo orbit planned for DSCOVR will favor Arctic observation during the boreal summer, such that major dynamical interactions between the Arctic and lower latitudes might be investigated directly using EPIC. DSCOVR is currently awaiting a launch opportunity in the wake of the *Columbia* disaster of February 2003.

1.3.3 NPOESS

From the 1970s through the 1990s, the National Oceanic and Atmospheric Administration and the U.S. Air Force have been operating polar-orbiting meteorological satellites independently of one another. NOAA's well-known polar orbiter series carries the AVHRR imager and the HIRS. The U.S. Air Force DMSP polar orbiters carry the OLS imager and the SSM/I and SSM/T (Special Sensor Microwave/Temperature) passive-microwave instruments. The NOAA High Resolution Picture Telemetry (HRPT) has been available in direct broadcast mode (line of sight) to any suitable tracking antenna. Throughout most of the 1990s, the DMSP direct broadcast data were encrypted, and were available only to U.S. Government receiving stations. Robert Whritner, of the Scripps Institution of Oceanography, arranged with the U.S. Air Force for DMSP data over the Antarctic to be unencrypted during the 1990s.

The NOAA and DMSP polar orbiter spacecraft are now coming together into one program, called the National Polar Orbiter Environmental Satellite System (NPOESS). The final versions of the independent NOAA and DMSP spacecraft have incrementally improved heritage sensors, but an entirely new suite of instruments is planned for the NPOESS spacecraft. The timeline for the transition to the Polar Operational Environmental Satellites (POESs) is shown in Figure 1.12 (see color plates).

The successor to AVHRR and OLS will be the Visible/Infrared Imager and Radiometer Suite (VIIRS). It will have several bands in the wavelength range 0.3–14 microns, and a spatial resolution of 400 m at nadir and 800 m at the edge of the swath. The successor to SSM/I will be the Conical Microwave Imager/Sounder (CMIS), which will provide passive-microwave imagery at spatial resolution varying between 15 and 50 km, depending on band frequency. The successor to HIRS will be the Cross-track Infrared Sounder (CrIS), which will have 20 infrared

bands each with calibration accuracies of 2–3 K. CrIS should enable profiling with a vertical resolution of 1 km, with nadir spatial resolutions for temperature, water vapor, and pressure profiles of 18.5, 15, and 55 km, respectively. NPOESS will also deploy an Ozone Mapping and Profiler Suite (OMPS).

1.4 EUROPEAN SPACE AGENCY

The European Space Agency's Earth-observing "flagship" is Envisat, launched in February 2002. Envisat carries active microwave, high-resolution visible and infrared, and hyperspectral imagers that compliment the EOS instruments. Some of these instruments are improved versions of those flown on the Environmental Research Satellite (ERS-1 and ERS-2) missions of the 1990s. The Envisat spacecraft orbital position is monitored with an accuracy of a few centimeters using its Doppler Orbitography and Radiopositioning Integrated by Satellite (DORIS) payload. DORIS processes range rate measurements of signals from an extensive network of beacons on the ground.

The Advanced SAR (ASAR) is a polarization-sensitive active microwave instrument operating in the C-band. ASAR will have widespread utility for sea ice mapping. The Global Ozone Monitoring by Occultation of Stars (GOMOS) provides vertical profiles of temperature, water vapor, ozone, NO_2, NO_3, and OClO, with day and night measurement capability, with a vertical resolution of 1.7 km. The Michelson Interferometer for Passive Atmospheric Sounding (MIPAS) has a spectral resolution sufficient for retrieving the column abundances of ozone, methane, N_2O, HNO_3, and chlorofluorocarbons, and will also provide temperature, pressure, and water vapor soundings. The MEdium Resolution Imaging Spectrometer (MERIS) has similar objectives to those of MODIS, but operates in a pushbroom as opposed to a scanning configuration (see Chapter 2). MERIS has a spatial resolution of 300 m, and operates with 15 bands that are programmable in both width and spectral location. The MicroWave Radiometer (MWR) makes global total column water vapor and cloud liquid water content measurements. The Radar Altimeter version 2 (RA-2) measures sea surface height and the marine geoid, sea surface wave height and wind speed, and also measures the height of sea ice floes and ice sheets. The Advanced Along-Track Scanning Radiometer (AATSR) provides sea surface temperature measurements (with an accuracy of better than 0.3 K). Envisat has an advanced spectroscopic capability with the SCanning Imaging Absorption spectroMeter for Atmospheric ChartographY (SCIAMACHY) payload.

ESA is also beginning a polar-orbiting series in cooperation with the U.S. NPOESS program, called MetOp. MetOp will comprise a series of spacecraft beginning in 2005. These spacecraft will carry some NOAA heritage sensors such as AVHRR and HIRS, and will also carry new European instruments including a second-generation Global Ozone Monitoring Experiment (GOME-2), an Infrared Atmospheric Sounding Interferometer (IASI) for higher resolution soundings of temperature and moisture in the troposphere and lower stratosphere, and an

Advanced SCATterometer (ASCAT) for measuring wind velocities over the world's oceans. The goals of MetOp are similar to those of NPOESS, being more directed at operational meteorology than the archival of data for global climate change research, although these instruments will certainly contribute to the latter.

The European and Canadian space programs are at the forefront of one of the most powerful tools for polar remote sensing—synthetic aperture radar (see Chapter 5 of this volume and Chapters 1–3 of Volume 2 of this book). Following the Canadian success with Radarsat 1 (launched 1995), and its anticipated follow-up Radarsat 2 (launch planned for 2006), ESA will launch TerraSAR-L, and the German aerospace agency (DLR) will launch TerraSAR-X before the end of the decade. The Appendix (p. 731) gives the technical specifications for the progression of major SAR missions, for 1978 up to the present.

1.5 RUSSIAN MISSIONS

Since the 1960s, Russia's Earth remote-sensing program has paralleled that of the United States, and very early on the Soviet Union tailored this program toward operational environmental and geophysical monitoring using a series of spacecraft carrying similar instrumentation in successive generations to generate multi-decadal climatologies. This contrasts somewhat with NASA's Earth observation programs, many of which aim to demonstrate the latest technology and then hand the multidecadal applications over to another agency (e.g., NOAA). One major Russian achievement has been the Meteor-2 and Meteor-3 spacecraft series, which are analogous to the NOAA polar orbiter series but which often carried more advanced instrumentation. With increasing post-Cold-War cooperation with Russian scientists, some of these advanced measurements from earlier decades should be useful for filling gaps in our collective Earth observation time series. A noteworthy example is the Meteor-2 Fourier transform infrared spectro-radiometer data collected during the late 1970s (Liou, 1992). During the early 1990s, cooperation between NASA and the Russian Space Agency enabled a TOMS instrument to fly on a Meteor-3 spacecraft. This provided a critical piece in the global time series of total column ozone observations, immediately after the failure of Nimbus-7 and before successive TOMS instruments could be launched on American spacecraft.

The early Russian focus on continuous environmental monitoring was need-based; nowhere more so than in the Arctic where observation of sea ice concentration is required along their enormously long coastline, which is a major Russian shipping route. The Russian ice remote-sensing program, which predates NASA's by several years, has featured the Okean spacecraft series. These spacecraft have pioneered Side-Looking Radar (SLR) sensors, which offer all-weather sea ice mapping with a spatial resolution of 1–2 km. The Okean-01 series was unique in offering a three-sensor approach to sea ice mapping: passive-microwave, SLR, and optical. Chapter 5, and Chapter 3 of Volume 2 of this book, give more examples of Russian polar remote-sensing efforts, including their forays into Synthetic Aperture

Radar (SAR) during the late 1980s. These accomplishments are also discussed by Kondratyev et al. (1994).

1.6 JAPANESE MISSIONS

In February, 1992, NASDA began operating advanced Earth remote-sensing instruments with the launch of the Japanese Earth Resources Satellite (JERS-1). JERS carried a SAR and an OPtical Sensor (OPS). OPS was a seven-band visible and near-infrared imager that could provide stereoscopic views by looking both at nadir and 15° forward of nadir. NASDA launched the first of the modern Earth-observing "flagships" in August 1996, the ADvanced Earth Observing Satellite or ADEOS. ADEOS unfortunately operated for only 10 months before becoming silent because of structural damage to one of its solar arrays. However, enough data were collected from ADEOS to prove many of the mission's new remote-sensing concepts, and NASDA launched the ADEOS-II mission in December 2002. ADEOS-II carried two versatile imagers, the Advanced Visible/Near Infrared Radiometer (AVNIR) and the GLobal Imager (GLI), a more advanced version of the successful Ocean Color and Temperature Scanner (OCTS) flown on ADEOS. The POLarization and Directionality of the Earth's Reflectances (POLDER) instrument, developed by CNES, provides unique surface remote-sensing capabilities. ADEOS-II also carried an AMSR, a limb-sounding instrument, the Improved Limb Atmospheric Spectrometer (ILAS-II), and a scatterometer (Sea Winds) developed by NASA Jet Propulsion Laboratory. ADEOS-II unfortunately ceased operation in December 2003.

The Japan Aerospace eXploration Agency (JAXA), successor to NASDA, is preparing a new Earth-observing flagship. The Advanced Land Observing Satellite (ALOS) will carry the PALSAR instrument described above, a new version of AVNIR, and a stereoscopic imager analogous to MISR, called the Panchromatic Remote-sensing Instrument for Stereoscopic Mapping (PRISM). PRISM consists of three imagers having a 2.5-m spatial resolution. One imager is nadir-viewing, and the other two view fore and aft at nadir angles of $\pm 24°$. PRISM's main objective is to use this high spatial resolution and stereoscopic viewing capability to produce highly accurate digital elevation maps. It can be expected that PRISM will also have applications in glaciology (Chapter 3 of Volume 2 of this book).

1.7 INDIAN MISSIONS

ISRO (Indian Space Research Organisation) is making important contributions to ocean and climate sciences with the IRS-P4 Oceansat spacecraft, launched in 2001. The Ocean Color Monitor (OCM) instrument offers a spatial resolution of 360 m in eight bands between 400 and 885 nm. With this spatial resolution, OCM provides detailed images of phytoplankton blooms as well as global maps of ocean chlorophyll concentration. The Multi-frequency Scanning Microwave Radiometer (MSMR) operates in four bands (6.6, 10.65, 18, and 21 GHz) with both vertical

and horizontal polarization. Over the ocean, MSMR will provide measurements of total column water vapor, cloud liquid water content, sea surface temperature, and sea surface wind speed.

1.8 CHINESE MISSIONS

The Chinese Academy for Space Technology (CAST) and China's National Satellite Meteorological Center have successfully operated a series of Earth-observing satellites beginning in March, 1988. The Fen-Yung-1 (FY-1) series are polar orbiters, and the FY-2 series (beginning 1997) are geostationary spacecraft. The main instrument on the most recent two FY-1 spacecraft is the Multichannel Visible and IR Scan Radiometer (MVISR), which has a nadir spatial resolution of 1.1 km. The first six MVISR channels are very similar in wavelength coverage to the current generation of AVHRR instruments. Additional versatility is provided by three additional channels for ocean color, and a 900–965 nm channel for water vapor retrieval. The FY-1 telemetry is highly compatible with NOAA's HRPT system, making this spacecraft a versatile addition to operational environmental research programs. A new polar orbiter series with more advanced instrumentation, FY-3, is planned for launch beginning in 2006.

1.9 SATELLITE DATA AVAILABILITY AND UTILIZATION

The question of primary interest to the researcher is: Where can I obtain high-latitude satellite data? The overall situation regarding satellite data availability has been gradually improving over the past decade. The World Wide Web has made the search for satellite datasets much easier. Most national polar research programs collect satellite data with their own tracking systems. The extent to which these datasets are properly catalogued and archived varies, but, with forthright efforts at making contact, a researcher can usually obtain satellite datasets from the various national programs in exchange for genuine collaboration. Many ice-reinforced research vessels, including the U.S. Coast Guard cutters *Polar Sea*, *Polar Star*, and *Healy*, the United States Antarctic Program's *Nathaniel B. Palmer*, the Australian icebreaker R/V *Aurora Australis*, the Canadian Coast Guard ship *Des Groseilliers*, the Japanese icebreaker *Shirase*, and Germany's *Polarstern*, carry polar-orbiter-tracking equipment that gives a researcher real-time access to satellite data during a field campaign. One important consideration here is that with the increased capabilities of Earth remote sensors, requiring higher data transmission rates, current environmental satellites transmitting at L-band frequencies ($\sim$2 GHz) are gradually being phased out and replaced by satellites transmitting in the X-band ($\sim$8 GHz). This will require substantial satellite-receiving equipment upgrades at many key facilities.

In the United States, NASA's Global Change Master Directory is continuously being updated with references to new polar datasets, including satellite data products. NASA's EOS Data and Information System (EOSDIS), based upon Distributed Active Archive Centers (DAACs), has demonstrated significant

improvements in data distribution capability over the past 5 or so years. At present, most EOS data and data products can be obtained from a DAAC within a few days of collection (Parkinson and Greenstone, 2000). However, real-time data access in the field will probably always require dedicated line-of-sight tracking antennas in the field. The DAAC that specializes in polar applications is the National Snow and Ice Data Center (NSIDC), located in Boulder, Colorado. NSIDC archives an enormous variety of polar field data, and also hosts satellite data products (known as "pathfinder" products) that are very well-suited for climate change studies. These NSIDC data products have been rigorously developed with proper attention to the unique remote-sensing challenges in polar regions, and the chapters that follow give examples of how their data analysis techniques successfully avoid the Curse of Captain Wilkes.

Both JAXA and ESA now support data distribution centers that are as capable as the NASA DAACs. These are called the Earth Observation Research Center (EORC) and the ESA Earth Observation User Services portal, respectively. Their Web-based data browse and related capabilities are very extensive. For basic research applications, data are usually available at minimal cost. However, in contrast to NASA, these agencies usually call for a more formal collaboration to obtain data free or at reproduction cost. Otherwise data must be obtained at commercial rates (several tens of dollars per scene at JAXA, several hundred from ESA). Usually this collaboration is established by a short proposal reviewed by an agency advisory panel. NASA also requires something similar for DAAC access, but mostly for purposes of identification and legitimacy as basic research and not to evaluate potential significance. We have found that if one has an interesting and timely basic research program, both JAXA and ESA are generally very open to establishing the collaboration necessary for most data access.

Two smaller U.S. operations, which specialize in providing satellite data, customized remote-sensing retrievals, and near-real-time satellite data products, are the AMRC and AARC, discussed above. These centers have direct access to the USAP-supported satellite-tracking antennas at McMurdo and Palmer Stations, and can therefore provide direct assistance with satellite remote-sensing applications to researchers in the field. The emphasis of AMRC and AARC services are centered around meteorology and oceanography, respectively, but data for any research or operational purpose can be obtained from either site. At the AMRC and AARC, data are available at essentially no cost to a researcher; one exception being requests for very large data volumes that can't be distributed over the Internet, in which case the requestor is asked to provide the magnetic media for copying.

With respect to data acquisition costs, most EOS data is also cost-free. However, there have been suggestions to institute a cost recovery system for access to certain high-spatial-resolution instruments, as has often been done in the past by some government agencies. If implemented, this would be a regrettable step backward: in principle, taxpayer-supported scientific data acquisition should be freely available to the research community.

Once a satellite data source has been located, the next task (usually more challenging) is to acquire the computer equipment to visualize and analyze the

imagery. Fortunately, most high-end PCs are presently capable of performing basic satellite data processing and display; the major hardware costs involve data storage. However, a steep "learning curve" is often experienced when trying to master the various binary formats used for storing both satellite telemetry and finished data products. These various formats are too numerous to discuss in detail here. Suffice it to say that some training is required, and the more helpful satellite data centers usually provide "reader" source codes in standard programming languages that allow a researcher to at least ingest the data for manipulation in those standard languages. The EOS standard is the Hierarchical Data Format (HDF-EOS), which contains not only the satellite imagery, but also "metadata" files describing the imagery. With respect to software for satellite data analysis, there are many options depending on one's individual needs and computer-programming ability. For a researcher with substantial programming experience, it may be cost-effective to work with a standard general-purpose scientific software package such as the RSI (Inc.) Interactive Data Language (IDL). Current versions of IDL contain useful subroutines for assistance with satellite remote sensing, such as geographic databases and color contour mapping functions. EOSDIS distributes many basic source codes in IDL, C, and FORTRAN, for reading and initial image processing.

For a researcher or expedition planner who wishes to acquire a range of satellite data analysis skills and capabilities, without the steep learning curve involved with becoming a master computer programmer, one of the high-end satellite data analysis software packages is the best alternative. Two industry standards are the TeraScan and TeraVision package developed by the SeaSpace Corporation (San Diego, California), and the McIDAS (Man-computer Interactive Data Access System) package developed by the University of Wisconsin Space Science and Engineering Center (SSEC). Software of this caliber is capable of ingesting either raw satellite telemetry, or data products in most of the myriad binary formats, and with a few keystrokes and mouse clicks bring up displays and animations of calibrated and geo-located satellite images, apply many standard retrieval algorithms for deriving geophysical variables, and prepare publication quality graphics. This type of software is also usually flexible for basic research purposes, allowing data export to other programming languages, ingestion and co-location of other data types (e.g., field observations), addition of new remote-sensing retrieval algorithms, and inspection of individual steps within a geophysical retrieval process.

1.10 REFERENCES

Bertrand, K. J. (1971). *Americans in Antarctica 1775–1948*. American Geographical Society, New York, 554 pp.

Dana, J. D. (1875). *Corals and Coral Islands*. Sampson Low, Marston, Low & Searle, London, 348 pp.

Dana, J. D. (1890). *Characteristics of Volcanoes: With Contributions of Facts and Principles from the Hawaiian Islands*. Dodd-Mead, New York, 399 pp.

Gloersen, P. and W. Salomonson (1975). Satellites—New global observing techniques for ice and snow, *Journal of Glaciology*, **15**, 373–389.

Gurney, A. (2000). *The Race to the White Continent*. W. W. Norton, New York, 320 pp.

Humphreys, W. J. (1940). *Physics of the Air*. McGraw-Hill, New York, 676 pp.

IPCC (2001). *Climate Change 2001: The Scientific Basis* (International Panel for Climate Change). Cambridge University Press, Cambridge, 881 pp.

Kidder, S. Q. and T. H. Vonder Haar (1995). *Satellite Meteorology: An Introduction*. Academic Press, San Diego, 446 pp.

Kondratyev, K. Ya., O. M. Johannessen, and V. V. Melentyev (1994). *High Latitude Climate and Remote Sensing*. Wiley–Praxis, Chichester, 200 pp.

Jensen, J. R. (2000). *Remote Sensing of the Environment: An Earth Resource Perspective*. Prentice Hall, Upper Saddle River, NJ, 544 pp.

Landis, M. J. (2001). *Antarctica: Exploring the Extreme*. Chicago Review Press, Chicago, 395 pp.

Liou, K. N. (1992). *Radiation and Cloud Processes in the Atmosphere*. Oxford University Press, New York, 487 pp.

Massom, R. (1991). *Satellite Remote Sensing of Polar Regions*. Lewis, Boca Raton, FL, 307 pp.

Measures, R. M. (1984). *Laser Remote Sensing: Fundamentals and Applications*. John Wiley & Sons, New York, 510 pp.

McClain, C. R., M. L. Cleave, G. C. Feldman, W. W. Gregg, S. B. Hooker, and N. Kuring (1998). Science quality SeaWiFS data for global biosphere research. *Sea Technology*, **39**, 10–16.

O'Reilly, J. E., S. Maritorena, B. G. Mitchell, D. A. Siegel, K. L. Carder, S. A. Garver, M. Kahru, and C. McClain (1998). Ocean color chlorophyll algorithms for SeaWiFS. *Journal of Geophysical Research*, **103**, 24937–24953.

Parkinson, C. L. and R. Greenstone (2000). *EOS Data Products Handbook*. EOS Project Science Office, NASA Goddard Space Flight Center, Code 900, Greenbelt, MD, 256 pp.

Solomon, S. (2001). *The Coldest March*. Yale University Press, New Haven, CT, 419 pp.

Stanton, W. (1976). *The Great United States Exploring Expedition of 1838–1842*. University of California Press, Berkeley, 433 pp.

van Zyl, J., H. Zebker, and C. Elachi (1987). Imaging radar polarization signatures: Theory and observation, *Radio Science*, **22(4)**, 529–543.

Viola, H. J. and C. Margolis (eds.) (1985). *Magnificent Voyagers: The U.S. Exploring Expedition, 1838–1842*. Smithsonian Institution Press, Washington, DC, 303 pp.

Walsh, J. E., J. Curry, M. Fahnestock, M. C. Kennicutt, A. D. McGuire, W. B. Rossow, M. Steele, C. J. Vorosmarty, and R. Wharton (2001). *Enhancing NASA's Contributions to Polar Science: A Review of Polar Geophysical Data Sets*. National Academy Press, Washington, DC, 124 pp.

Wilkes, C. (1845a). *Narrative of the United States Exploring Expedition: During the Years 1838, 1839, 1840, 1841, 1842*. Lea & Blanchard, Philadelphia, 434 pp. (Volume 1), 476 pp. (Volume 2).

Wilkes, C. (1845b). *Chart of the Antarctic continent shewing the icy barrier attached to it: discovered by the U.S. Ex. Ex./Charles Wilkes Esq. Commander, 1840*, engraved by Sherman & Smith, New York.

Zwally, H. J. et al. (2002). ICESat's laser measurements of polar ice, atmosphere, ocean, and land. *Journal of Geodynamics*, **34**, 405–445.

2

Satellite imaging and radiometry

2.1 INTRODUCTION

The Arctic and Antarctic present unique challenges for space-based remote sensing. As we will see throughout this book, there are many instances where radiometric contrast is small between scene types, where atmospheric influences are not straightforward, or where instruments may be operating at their performance limits. It is important to have a basic understanding of how satellite instruments work before embarking on a serious remote-sensing research project in the polar regions. Most of the material in this chapter has been adapted from some excellent general textbooks on remote sensing, including Rees (1993), Kidder and Vonder Haar (1995), and Schott (1997), and is included here to provide a self-contained introduction to the subsequent chapters that discuss applications of satellite data to individual polar disciplines.

In this chapter, we consider the deployment in orbit of an instrument designed to measure solar backscattered (*shortwave*) or thermally emitted (*longwave*) intensity from the Earth–atmosphere system. We begin with the spacecraft itself—with the nomenclature of polar orbits and a discussion of how spacecraft motion determines image parameters. This knowledge is important for determining what types of data (sensors, platforms) are suitable for a given research task. Also important are the definitions of radiometric quantities—those being measured by the satellite instrument and those inferred from models or algorithms. We should also understand standard detector configurations for visible, near-infrared, and middle-infrared radiation, along with spectral bandwidth selection and radiometric calibration issues.

One should always bear in mind the type of data involved with satellite remote sensing—photon counts from an orbiting radiometer. The phenomenon the radiometer detects and records is a specific intensity of radiation at the top of the Earth's atmosphere. Many researchers have become accustomed to using satellite

"data products", in which satellite-measured shortwave or longwave radiation has been interpreted by algorithms to yield estimates of geophysical quantities. These satellite-derived geophysical "products", usually developed by major space agencies, are often compared with other information that may be more familiar to the researcher—for example, field measurements, climate model output or meteorological reanalysis. However, for the polar regions there are fewer satellite "data products" available from major national space programs. Furthermore, many algorithms developed for use over mid-latitudes prove less accurate when applied to polar satellite data, even when adjustments are made for high latitudes. Therefore, the researcher may be on his or her own to interpret a high-latitude satellite image in terms of geophysical phenomena. To succeed at this endeavor, and avoid the Curse of Captain Wilkes, one must first understand the fundamentals of the experimental apparatus.

Because this chapter will cross several disciplines, some mathematical symbols will appear to represent more than one quantity. To make this book easier to use in conjunction with more detailed texts on individual disciplines (e.g., radiative transfer, astrodynamics), the most common mathematical notation for each discipline is preserved here even though some symbols are used twice within this chapter.

2.2 THE POLAR-ORBITING SPACECRAFT

The polar orbit, or more accurately, near-polar orbit, has been the most frequently used satellite deployment for Earth remote sensing because it offers a Low Earth Orbit (LEO) satellite the greatest possible coverage of the Earth's surface. Over the Arctic and Antarctic, virtually all useful satellite data come from polar-orbiting spacecraft. Geostationary sensors offer too limited and distorted a view of the polar regions, and are useful for some polar research applications only if their imagery is merged with imagery from polar orbiters. In the near future, we may see some contributions to polar research from spacecraft in unusual orbits. For example, NASA's Deep Space Climate ObserVatoRy (DSCOVR), intended for deployment at the Lagrange (L-1) point, will enable an imager to view northern high latitudes with high time resolution during summer. There is also the theoretical possibility of using a solar sail to keep a spacecraft stationary above a pole (McInnes, 1999). However, the standard LEO configuration is the most relevant at present.

Figure 2.1 shows the standard geometry of an elliptical orbit. In polar coordinates with the Earth as the origin, the equation for the ellipse is given by:

$$r = \frac{a(1-\varepsilon^2)}{1+\varepsilon\cos\theta} \tag{2.1}$$

where a is the semi-major axis and ε is the eccentricity. The satellite's point of closest approach to the Earth is the *perigee*, which is always one end of the semi-major axis. The *true anomaly* θ is the angle between the satellite's radius vector $\mathbf{r}$ and the perigee,

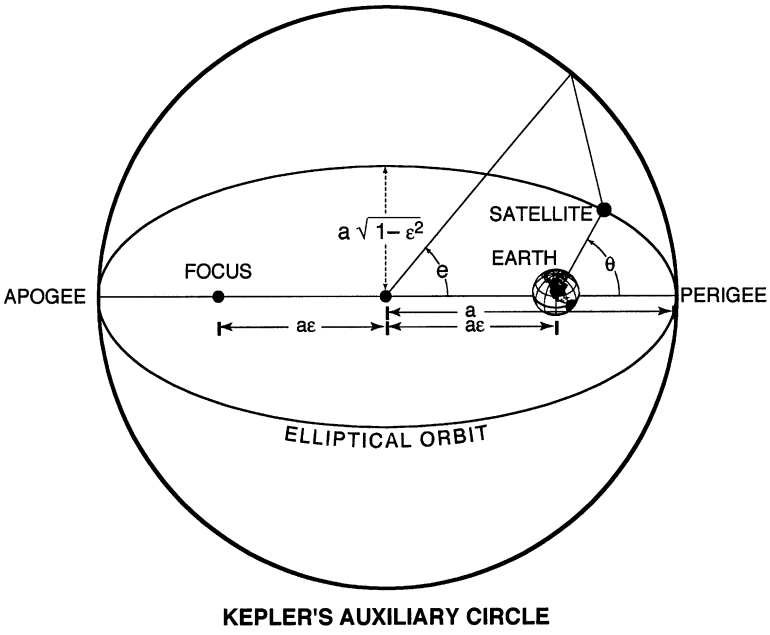

Figure 2.1. Geometry of the Keplerian orbit.

and is always measured counter-clockwise. It is related to the *eccentric anomaly* e, shown in Figure 2.1, by:

$$\cos\theta = \frac{\cos e - \varepsilon}{1 - \varepsilon \cos e} \tag{2.2}$$

Recall Kepler's three laws of planetary motion for a two-body orbital configuration with one body having very small mass compared with the other: (1) the orbit of the smaller body about the larger one is an elliptical path with the larger body at one focus; (2) the radius vector from the larger to the smaller body sweeps out equal areas in equal times; (3) the ratio of the square of the orbital period to the cube of the semi-major axis is the same for all small bodies revolving around the larger one. From Kepler's second law, the position of the satellite as a function of time is determined by:

$$M = n(t - t_p) = e - \varepsilon \sin e \tag{2.3}$$

where t_p is the time the satellite passes through perigee, and M is the *mean anomaly*. Now the period T of the satellite's orbit is related to its orbital velocity v by $T = 2\pi r/v$, and so from Newtonian mechanics the *mean motion constant*:

$$n = \frac{v}{r} = \frac{2\pi}{T} = \left(\frac{Gm_e}{a^3}\right)^{1/2} \tag{2.4}$$

where G is the universal constant of gravitation and m_e is the mass of the Earth.

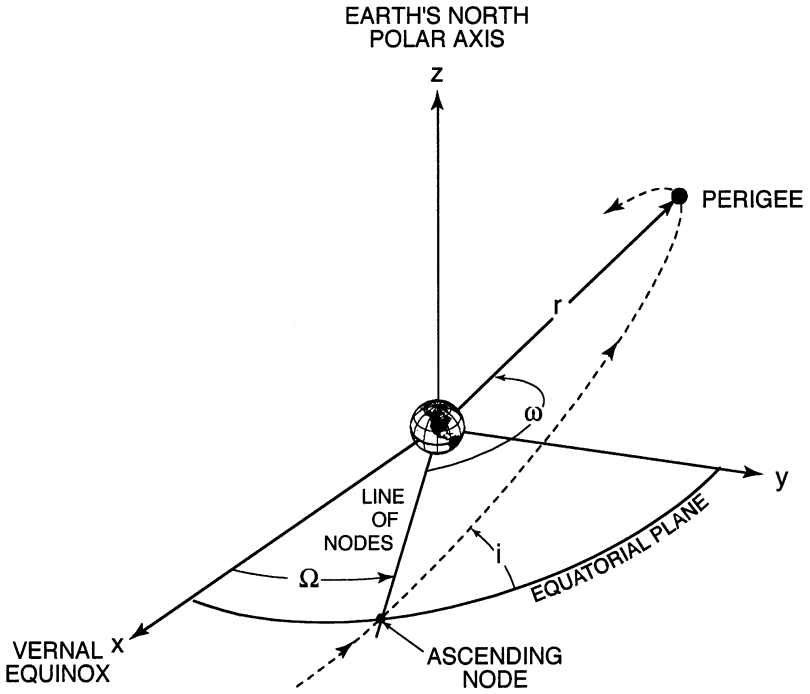

Figure 2.2. Equatorial coordinate system most commonly used for describing the motion of Low Earth Orbit (LEO) spacecraft.

Figure 2.2 shows the standard *equatorial coordinate system* most commonly used to describe Earth-orbiting spacecraft. The x–y plane passes through the Earth's equator, and the positive x-axis is chosen to lie along the line from the Earth to the Sun at the *March equinox*. The positive z-axis (polar axis) is aligned with the North Pole. The satellite's orbit, elliptical in general but in practice nearly circular, lies in a plane that intersects the Earth's equatorial (x–y) plane through the *line of nodes*. The orbital *inclination* i denotes the angle between the satellite's orbital plane and the Earth's equatorial plane. If the inclination $i < 90^\circ$, the satellite's revolution about the Earth is in the direction of the Earth's rotation, and the orbit is said to be *prograde*. If the inclination $i > 90^\circ$, the satellite's motion is in the opposite direction of the Earth's rotation and the orbit is said to be *retrograde*. A near-polar orbit is referred to as a *high-inclination* orbit, because i is somewhere near 90°. The point on the orbit where the satellite crosses the equator from south to north is referred to as the *ascending node*, and the angle between the March equinox and this point is referred to as the *right ascension of the ascending node* Ω. This angle is always measured in the x–y plane. We can also define the *descending node* as the point on the orbit where the satellite crosses the Equator from north to south. The angle ω measured in the orbital plane between the ascending node and the perigee is the

argument of perigee. The satellite's distance from the center of the Earth is denoted by the radius vector **r**. The instantaneous latitude and longitude of the satellite's position as projected onto the Earth's surface, or *subsatellite point*, are denoted by b and l, respectively.

Six of the geometrical quantities illustrated in Figures 2.1 and 2.2 together completely specify the location of a satellite in a simple Keplerian orbit, and these are known as the *classical orbital elements*. These six quantities are the semi-major axis a, the eccentricity ε, the inclination i, the argument of perigee ω, the right ascension of the ascending node Ω, and the mean anomaly M. A complete discussion of orbital elements, their determination, and their reference to a specific epoch time, can be found in Kidder and Vonder Haar (1995), Montenbruck and Gill (2000), Prussing and Conway (1993), Wiesel (1997), or other references on astrodynamics.

One of the most useful forms of a high-inclination orbit is the *Sun-synchronous* orbit, in which the spacecraft will cross a given latitude at the same local (solar) time each day. Here "local time" is defined as the geographic local time (LT):

$$LT = UTC + l/15^\circ \tag{2.5}$$

where UTC is the universal coordinated time in hours; this is different from the "local time" in a given time zone. The Sun-synchronous orbit makes use of the Earth's non-sphericity, which induces a precession of the satellite's orbital plane about the polar axis. The Earth is an oblate spheroid, and the gravitational potential of the Earth can be expanded in Legendre polynomials $P_k(\cos\phi)$:

$$U = \frac{Gm_e}{r}\left[1 - \sum_{k=2}^{\infty}\left(\frac{R}{r}\right)^k J_k P_k(\cos\phi)\right] \tag{2.6}$$

where G is the universal gravitational constant, R is the Earth's equatorial radius, ϕ is the *colatitude* (90° *latitude*) and the J_k are the constant coefficients of the expansion as determined by the actual shape of the Earth. Here the longitudally (azimuthal) varying component to the Earth's departure from sphericity is neglected. The first term in (2.6) represents the standard central force potential, and the terms that follow represent perturbations. The first perturbation term, the J_2 term, is three orders of magnitude larger than any subsequent terms, and has the value $J_2 = \sim 1.082\,63 \times 10^{-3}$. Thus the perturbation can be expressed as:

$$U_{J_2} = -\frac{Gm_e}{r}\left(\frac{R}{r}\right)^2 J_2 P_2(\cos\phi) = -\frac{Gm_e R^2}{r^3} J_2\left[\tfrac{1}{2}\left(2 - 3\sin^2\phi\right)\right] \tag{2.7}$$

It can be shown (e.g., Prussing and Conway, 1993) that this perturbation induces a precession of the satellite's orbital plane that has an angular speed of:

$$\dot{\Omega} = -\frac{3}{2} J_2 \left(\frac{Gm_e}{a}\right)^{1/2}\left(\frac{R^2}{a^3}\right)\frac{\cos i}{(1-e^2)^2} \tag{2.8}$$

Now the revolution of the Earth about the Sun appears, when viewed from above the North Pole, to be counterclockwise, and has a period of 1 year ($\sim 3.1558 \times 10^7$ s). If we want the spacecraft's crossing to occur at the same local time each day, then the

angular speed of the orbital precession $d\Omega/dt$ must be equal to the apparent angular speed of the Sun's motion in the sky with reference to the "fixed" stars, $d\omega_S/dt = 2\pi/3.1558 \times 10^7\,\mathrm{s} = 1.991 \times 10^{-7}\,\mathrm{rad\,s^{-1}}$. This can be accomplished by adjusting the inclination, semi-major axis, and eccentricity in (2.8). If we do so, it becomes apparent that the inclination must be greater than 96° (for the semi-major axis to be larger than the Earth's equatorial radius), and thus Sun-synchronous orbits are retrograde orbits.

The Sun-synchronous orbit is clearly appropriate for any remote-sensing mission that utilizes shortwave (solar backscattered) radiation. It also has advantages for spacecraft operation, including orientation of solar panels and standardizing the solar heating cycle of onboard instruments. The crossing time of a given latitude in a Sun-synchronous orbit can be chosen to suit the particular mission. An Equator crossing in the morning will maximize a remote sensor's utility for land and ocean surface viewing at low latitudes, because the diurnal cycle in cloud cover at low latitudes tends to peak during the afternoon. For example, the Landsat 7 descending node is at 10 a.m., which corresponds to an ascending node of 10 p.m. An Equator crossing near local noon will maximize solar illumination, and hence signal-to-noise ratio, over most lower latitudes (e.g., the Total Ozone Mapping Spectrometer—TOMS—discussed in Chapter 3). For deploying instruments to study clouds and their influence on climate, the Earth Observing System (EOS) Aqua spacecraft utilizes an early afternoon (1 : 30 p.m.) ascending node.

2.3 RADIOMETRIC QUANTITIES

A satellite imager samples electromagnetic radiation emitted or backscattered from the Earth–atmosphere system. The branch of theoretical physics known as *radiative transfer* is therefore central to satellite remote sensing. Most atmospheric scientists and astrophysicists consider the original modern treatment of radiative transfer theory to be that of Chandrasekhar (1960). Although there have since been numerous recent advances in the applications of radiative transfer theory to Earth science, Chandrasekhar (1960) contains rigorous derivations of the governing integro-differential equations, and introduces many of the mathematical techniques for obtaining analytic solutions in various useful approximations. This monograph should be on every remote-sensing researcher's bookshelf. For a researcher interested in using satellite data to study the Earth's polar regions, another essential companion to this book should be one or more of the thorough modern texts on radiative transfer theory applied to the Earth's atmosphere; for example, Goody and Yung (1989), Lenoble (1985), Liou (1980; 1992), Stephens (1994), or Thomas and Stamnes (1999).

2.3.1 Intensity and flux

The quantity actually sampled by a remote sensor is the *specific intensity* of radiation. This refers to the increment of electromagnetic energy dE_λ in the

infinitesimally narrow wavelength range $d\lambda$ crossing a unit area dA in time dt, traveling in direction **s** and diverging into an increment of solid angle $d\omega$. We can think of this as a "beam" of radiation traveling in a specific direction. Maxwell's electromagnetic theory provides a full description of this beam of radiation in terms of the electric field vector **E** and the magnetic field vector **B** (Jackson, 1975; Landau and Lifschitz, 1975), and it will be important to revisit classical electrodynamics when discussing the microwave remote sensing of sea ice. However, for the present discussion of shortwave and longwave radiation we can envision this beam of radiation as a stream of photons, each having an energy:

$$e = h\tilde{\nu} = \frac{hc}{\lambda} \tag{2.9}$$

where h is Planck's constant, ν is the corresponding frequency, and c is the speed of light in a vacuum.

Because we are referring to photons having a specific wavelength (all wavecrests in the electric and magnetic fields having equal distances), we are here defining the *monochromatic* or *spectral* specific intensity. For the shortwave, meteorological and climate researchers usually specify wavelength in microns ($1\,\mu\text{m} = 10^{-6}\,\text{m}$). Researchers in photobiology, and researchers in terrestrial or ocean color remote sensing (who frequently use specific wavelength bands in the visible part of the spectrum), more often specify wavelength in nanometers ($1\,\text{nm} = 10^{-9}\,\text{m}$). Astronomers are more accustomed to Ångstroms ($1\,\text{Å} = 10^{-10}\,\text{m}$). In the longwave, units of wavelength (μm) are often used for qualitative discussion, but for quantitative work the reciprocal of the wavelength, or *wavenumber* $\nu = 1/\lambda$ is more commonly used. The units of wavenumber are *inverse centimeters* (e.g., $10\,\mu\text{m} = 10^4\,\text{cm}^{-1}$). In the microwave, units of frequency ν (Gigahertz) are most frequently used to describe spectral dependence, although one sometimes sees wavelength expressed in centimeters (cm).

Figure 2.3 shows the standard polar coordinate system used to specify radiometric quantities. Referring to this coordinate system, it is evident that the increment of energy crossing a unit area depends on its angle of incidence with the unit area; i.e.:

$$\frac{dE_\lambda}{dA\,dt\,d\lambda\,d\omega} \propto \cos\theta$$

and so we need to define the specific intensity as:

$$I_\lambda(s,\theta,\phi) \equiv \frac{dE_\lambda}{dA\,dt\,d\lambda\,d\omega\cos\theta} \tag{2.10}$$

where the increment of solid angle is given by:

$$d\omega = \sin\theta\,d\theta\,d\phi \tag{2.11}$$

The spectral specific intensity is normally expressed in units of Watts (Joules per second) per square meter per steradian (unit of solid angle) per micron (unit of wavelength).

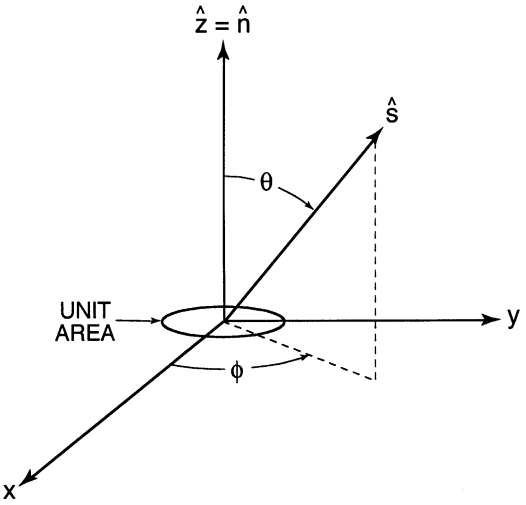

Figure 2.3. Polar coordinate system used for describing radiometric quantities.

Suppose we are instead interested in the total energy crossing a unit area, from all directions. This is the increment of spectral *flux*:

$$dF_\lambda = \frac{dE_\lambda}{dA\, dt\, d\lambda} = I_\lambda \cos\theta\, d\omega \tag{2.12}$$

and the *net flux* is the integral over all solid angles:

$$F_\lambda = \int_0^{2\pi} I_\lambda(\theta, \phi) \cos\theta\, d\phi = \int_0^{2\pi} \int_0^{\pi} I_\lambda \cos\theta \sin\theta\, d\theta\, d\phi \tag{2.13}$$

It is common to define $\mu = \cos\theta (-d\mu = \sin\theta\, d\theta)$ so that:

$$F_\lambda = \int_0^{2\pi} \int_{-1}^{1} I_\lambda(\mu, \phi)\mu\, d\mu\, d\phi \tag{2.14}$$

In the Earth sciences, we conventionally represent the net flux as the difference between the hemispheric fluxes in the downward and upward directions, or *downwelling* and *upwelling* fluxes:

$$F_\lambda = \int_0^{2\pi} \int_{-1}^{0} I_\lambda(\mu, \phi)\mu\, d\mu\, d\phi + \int_0^{2\pi} \int_0^{1} I_\lambda(\mu, \phi)\mu\, d\mu\, d\phi \tag{2.15}$$

One important example is the net shortwave flux at the top of the Earth's atmosphere, which is a measure of the solar energy absorbed by the Earth–atmosphere system, integrated over all wavelengths having energetic significance. For shortwave radiation at the top of the Earth's atmosphere, the downwelling flux is the extraterrestrial solar flux at the wavelength of interest, $F_{\lambda 0}$ weighted by the cosine of the solar zenith angle θ_0: $F_{\lambda 0} \cos\theta_0$. For most shortwave radiation, the upwelling flux consists of all solar photons at the wavelength of interest that have

entered the atmosphere, have avoided absorption by atmospheric constituents or by the Earth's surface, and have been scattered by the surface and/or atmosphere back to space. One important exception occurs for wavelengths between 3 and 4 microns, where there is a small thermally emitted component to the upwelling radiation. We will see later on how this exception is very useful for remote sensing in the polar regions. The spectral flux as given by (2.13)–(2.15) has units of Watts per square meter per micron (or some other unit of wavelength). If we are considering flux integrated over some large wavelength range (e.g., all visible radiation or the total shortwave radiation), then we are referring to a *broadband* flux having units of Watts per square meter.

In nature, the specific intensity of radiation nearly always depends on direction. However, suppose we have a physically idealized case in which the intensity is *isotropic* (independent of direction). Then the flux is:

$$F_\lambda = I_\lambda \int_0^{2\pi} \int_{-1}^{0} \mu \, d\mu \, d\phi = \pi I_\lambda \tag{2.16}$$

Here the expression has been written for the downwelling flux, but it also applies to the upwelling flux. This isotropic approximation is quite useful for making the governing equation of radiative transfer more manageable analytically. However, its application to real situations in the Earth–atmosphere system should be made with caution.

A final word about intensity and flux: they are often called by a variety of names. In Earth science, the term *radiance* (denoted by the symbol L) is often used for intensity, and the terms *radiant excitance* (M) and *irradiance* (E) are often used for flux. The lack of conformity in this nomenclature can be confusing. One will often see the terms *intensity* and *radiance* used interchangeably without any logical distinction. One convention specifies that *irradiance* should refer to flux incident on an area while *excitance* refers to flux emerging from an area (Kidder and Vonder Haar, 1995). In atmospheric science "vernacular" we often find the term *irradiance* used among researchers working in ultraviolet (UV) and photosynthetically active solar radiation, and related photo-biological applications, while the term *flux* is most often used by climatological researchers who are interested in the balance between total shortwave and total longwave radiation in the atmospheric energy budget. In this book, we will use the original astrophysical terms, *intensity* and *flux*, from now on.

2.3.2 Reflectance and albedo

Now we move on to a fundamental phenomenon for remote sensing—the reflection of energy from a surface or medium. Consider a surface that can reflect downwelling radiation incident upon it into any number of directions in the upward 2π steradians. For example, we might imagine a planet without an atmosphere, in which case the downwelling flux incident on the planet's surface at a given wavelength would be $F_{\lambda 0} \cos\theta_0$. Some fraction r_λ of the incident energy will be reflected by the surface and

the remaining fraction $(1 - r_\lambda)$ is absorbed by the surface. The radiation not absorbed by the surface may be reflected into any number of directions in the upward 2π steradians. If the surface is made of an idealized material that reflects incident radiation equally into all directions, such that the upwelling intensity is isotropic, then the reflected energy flux and the upwelling specific intensity of radiation are related by:

$$r_\lambda = \frac{\pi I_\lambda^\uparrow}{F_{\lambda 0} \cos\theta_0} \tag{2.17}$$

Such an idealized reflecting surface is known as a *Lambertian* surface. In nature there are very few Lambertian surfaces, and the specific intensity of radiation reflected into one direction (θ, ϕ) will generally be different from that reflected into other directions. We must therefore consider the *directional reflectance* of the surface, in which the fraction of radiant energy reflected into the direction (θ_r, ϕ_r) depends on the direction of the radiant energy incident upon the surface (θ_i, ϕ_i). An important principle applies here, the *Helmholtz principle of reciprocity*, which states that directional reflectance does not change if we interchange the directions of incident and reflected radiation; i.e.:

$$r_\lambda(\mu_r, \phi_r; \mu_i, \phi_i) = r_\lambda(\mu_i, \phi_i; \mu_r, \phi_r) \tag{2.18}$$

If the surface is illuminated by a general, non-uniform radiation field described by an intensity distribution $I_\lambda(\mu_i, \phi_i)$, then the intensity reflected into a given direction is:

$$I_{\lambda r}(\mu_r, \phi_r) = \int_0^{2\pi} \int_0^1 I_{\lambda i}(\mu_i, \phi_i) r_\lambda(\mu_i, \phi_i; \mu_r, \phi_r) \mu_i \, d\mu_i \, d\phi_i \tag{2.19}$$

For our example of a planetary surface illuminated by the Sun (with no intervening atmosphere), we can represent the incident intensity distribution by a Dirac delta function:

$$I_{\lambda 0}(\mu_i, \phi_i) = F_{\lambda 0} \, \delta(\mu - \mu_0) \, \delta(\phi - \phi_0) \tag{2.20}$$

where $\mu_0 = \cos\theta_0$, and the product of the two delta functions has units of sr^{-1}. In this case the intensity reflected into a given direction is:

$$I_{\lambda r}(\mu_r, \phi_r) = \mu_0 r_\lambda(\mu_r, \phi_r; \mu_0, \phi_0) F_{\lambda 0} \tag{2.21}$$

For a Lambertian surface, $r_\lambda(\mu_r, \phi_r; \mu_0, \phi_0) = r_\lambda$ in (2.21), with a constant $r_\lambda \leq 1$. The opposite idealized case to that of a Lambertian surface is the *specular* reflector. A perfect specular reflector is essentially a mirror—the directional reflectance can be represented by a Dirac delta function:

$$r_\lambda(\mu_r, \phi_r; \mu_i, \phi_i) = r_\lambda \, \delta(\mu - \mu_0) \, \delta[\phi - (\phi_0 + 180^\circ)] \tag{2.22}$$

such that the radiation is reflected only into the direction having solar zenith angle cosine μ_0 and a relative azimuth of 180 degrees opposite the Sun. As reflectors, ocean, ice, and snow surfaces are actually much more specular than Lambertian, and this has important implications for polar remote sensing.

Of course, we are really interested in a planet with an atmosphere: solar radiation incident at the top of the atmosphere will in general be attenuated by

some combination of scattering and absorption by the atmosphere (discussed in more detail below). Some of this radiation will reach the surface, which will have a directional reflectance $r_{\lambda s}(\mu_r, \phi_r; \mu_0, \phi_0)$. The radiation reflected by the surface into direction (μ_r, ϕ_r) will undergo further scattering and/or absorption by the atmosphere before some of it re-emerges to space. The intensity that emerges at the top of the atmosphere in direction (μ_r, ϕ_r), and the upwelling flux (cosine-weighted intensity integrated over all upward directions), both depend on the scattering and absorbing properties of the entire surface–atmosphere column. Similarly, we can think of a specific Earth surface—say, an ocean surface or a snowpack—as being a scattering and absorbing medium in which photons incident upon it are redirected or absorbed, and from which some photons emerge in the upward direction. With these considerations in mind, the proper term that describes the reflectance of a natural medium is the *albedo*, which is defined as the ratio of upwelling flux to downwelling flux. We can speak of the spectral albedo A_λ of the entire Earth–atmosphere system, where the downwelling flux is the extraterrestrial solar flux:

$$A_\lambda = \frac{\int_0^{2\pi} \int_0^1 I_\lambda^\uparrow(\mu, \phi) \mu \, d\mu \, d\theta}{\mu_0 F_{\lambda 0}} \tag{2.23}$$

and I_λ is the intensity emerging at the top of the atmosphere, or we can speak of the albedo of a surface type such as an ocean surface or a snowpack:

$$A_\lambda = \frac{\int_0^{2\pi} \int_0^1 I_{\lambda s}(\mu, \phi) \mu \, d\mu \, d\phi}{\int_0^{2\pi} \int_{-1}^0 I_{\lambda s}(\mu, \phi) \mu \, d\mu \, d\phi} \tag{2.24}$$

where $I_{\lambda s}(\mu, \phi)$ represents the intensity distribution at that surface. Now, earlier we described a surface in terms of its directional reflectance. For a medium or system that scatters and absorbs radiation, the concept is the same, only the most commonly used term is the *bidirectional reflectance distribution function* $R(\mu_r, \phi_r; \mu_0, \phi_0)$. Consider the entire Earth–atmosphere system. Its albedo is:

$$A_\lambda(\mu_0, \phi_0) = \frac{\mu_0 F_{\lambda 0} \, \delta(\mu - \mu_0) \, \delta(\phi - \phi_0) \int_0^{2\pi} \int_0^1 R_\lambda(\mu_r, \phi_r; \mu_0, \phi_0) \mu_r \, d\mu_r \, d\phi_r}{\mu_0 F_{\lambda 0}} \tag{2.25}$$

Note that the albedo of the Earth–atmosphere system is *a function of solar direction*. This is also true for the albedo of an ocean surface, snowpack, and most other natural surfaces. One convenient representation of the bidirectional reflectance distribution function is the *anisotropic reflectance factor* ξ_λ:

$$\xi_\lambda(\mu_r, \phi_r; \mu_i, \phi_i) \equiv \frac{\pi}{A_\lambda} R_\lambda(\mu_r, \phi_r; \mu_i, \phi_i) \tag{2.26}$$

where A_λ is the real (non-Lambertian) albedo. This illustrates the departure of the natural intensity distribution from isotropy; $\xi > 1$ in directions where the medium

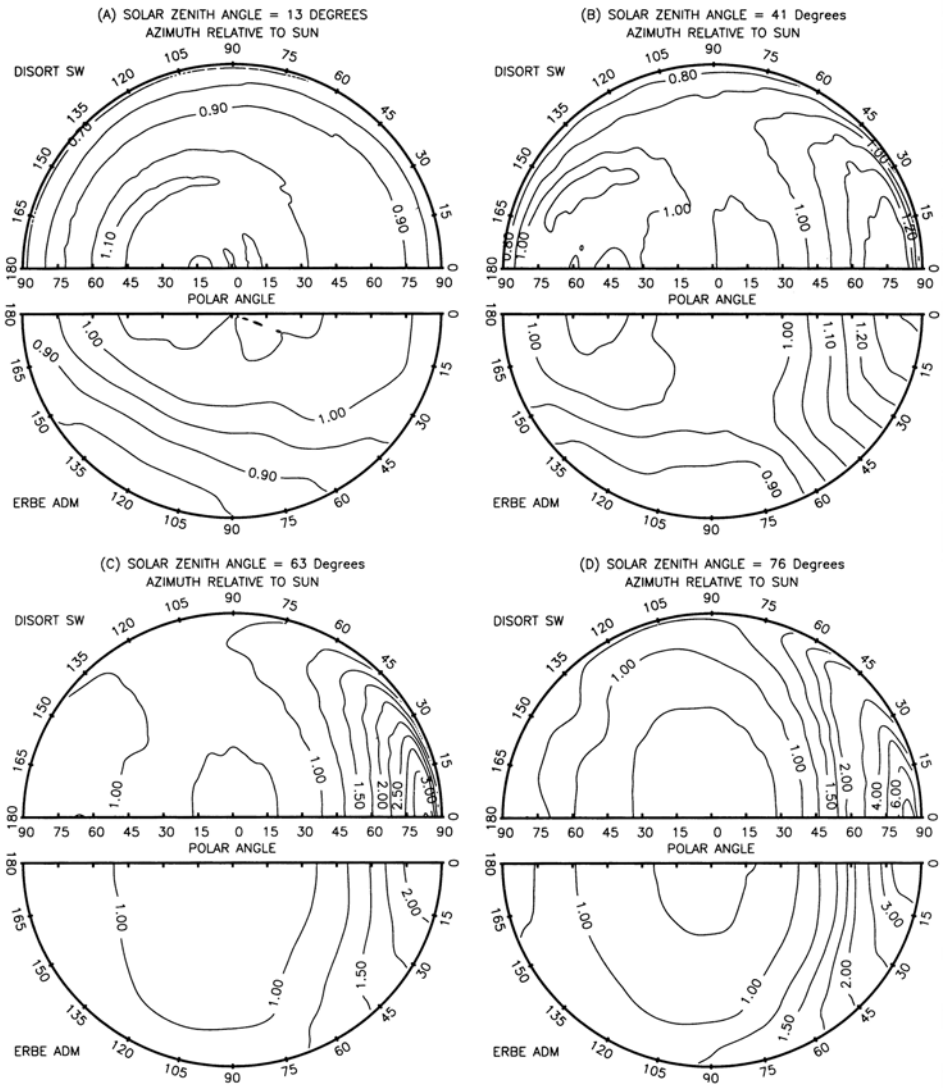

Figure 2.4. Examples of Bidirectional Reflectance Distribution Functions (BRDFs), also known as Angular Dependence Models (ADMs), for a cloudy atmosphere and four solar zenith angles. The upper semicircles depict the BRDF calculated using a plane-parallel discrete ordinate radiative transfer model. The lower semicircles depict empirical BRDFs based on extensive compilations of satellite intensity measurements, used with the Earth Radiation Budget Experiment (ERBE) (Suttles et al., 1989). In this figure, a relative azimuth of 0° refers to the direction opposite the sun (the direction of specular reflection).
From Lubin and Weber (1995).

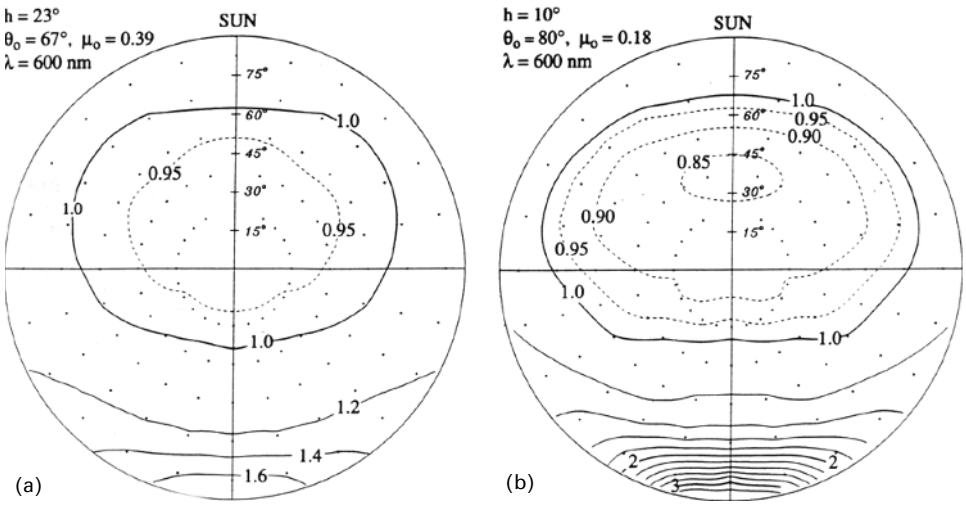

Figure 2.5. Example of the BRDF measured over an Antarctic snow surface, for two large solar zenith angles. These plots are based on intensity measurements taken in zenith and azimuth angle increments of 15°, from a tower at Amundsen–Scott Station, South Pole. The solar direction is at the top of the plot, the direction of specular reflection is at the bottom. Solid contours represent $R(\mu_r, \phi_r; \mu_0, \phi_0) > 1$, in increments of 0.2. Dotted contours represent $R(\mu_r, \phi_r; \mu_0, \phi_0) < 1$, in increments of 0.05.

reflects more than a Lambertian surface, and vice versa. Figure 2.4 gives an example of the bidirectional reflectance distribution function for a cloudy atmosphere, and Figure 2.5 gives an example of the bidirectional reflectance distribution function measured over Antarctic snow. These figures demonstrate the large variability in solar backscattered intensity from natural Earth–atmosphere scenes, and the need for detailed radiative transfer methods in order to interpret such intensities for retrieval of geophysical quantities.

Why belabor these points about directional reflectance and albedo? Well, many systems for displaying satellite imagery obscure them for convenience. For example, when data from visible or near-infrared wavelength imagers are manipulated by satellite data reduction algorithms and displayed on a monitor, the units given might be called "albedo" or "reflectance" (e.g., Kidwell, 1991, for the Advanced Very High Resolution Radiometer—AVHRR). These units are really defined in the data-processing algorithm as:

$$A_\lambda = \frac{100\pi I_\lambda^\uparrow(\mu, \phi)}{F_{\lambda 0}} \tag{2.27}$$

In other words, they have the built-in assumption that the scene being viewed is Lambertian, which is almost never true. Notice that these units also omit the important step of weighting the extraterrestrial solar flux by the cosine of the

solar zenith angle μ_0. These "albedo" units frequently displayed on computer screens are nothing more than a convenient way of scaling the intensity into a range of approximately 0–100%, for rapid inspection and animation of satellite images. However, the first step in utilizing shortwave satellite imagery for retrieval of geophysical phenomena is to make sure that the data are properly expressed in terms of a specific intensity in Watts per square meter per steradian (and per unit wavelength if applicable). The relevant albedos and bidirectional reflectance distribution functions can then be factored in from empirical tables (e.g., Suttles et al., 1988; Taylor and Stowe, 1984), or modeled using radiative transfer theory.

2.3.3 Scattering and absorption

To further develop a basic understanding of radiative transfer theory, let's consider the processes of scattering and absorption in a little more detail. These processes apply to solar photons reaching the Earth's atmosphere and to thermally emitted photons from within the Earth–atmosphere system, although their relative importance changes in different portions of the electromagnetic spectrum. There are several ways in which an atmospheric molecule can absorb (destroy) a photon, converting the photon's energy into some form of molecular kinetic energy. At the shortest UV wavelengths ($\lambda < 100\,\text{nm}$), solar photons have enough energy to *photoionize* molecules, or strike electrons from them. This is most relevant to the upper atmosphere and the formation of the ionization layer. At less energetic UV wavelengths ($100 < \lambda < 1{,}100\,\text{nm}$), solar photons break apart, or photo-dissociate, many atmospheric constituents.

The most important example of photo-dissociation is involved in the maintenance of the stratospheric ozone layer. In the "pure oxygen atmosphere" (Brasseur and Solomon, 1984), UV-C photons having wavelengths $\lambda < 242\,\text{nm}$ break apart oxygen molecules:

$$O_2 + h\nu \rightarrow O + O(\lambda < 242\,\text{nm}) \tag{2.28}$$

and the resulting atomic oxygen is able to recombine in a three-body reaction to create ozone:

$$O + O_2 + M \rightarrow O_3 + M \tag{2.29}$$

where the presence of the third molecule M in the collision (most frequently nitrogen) stabilizes the oxygen combination. The ozone molecule itself is photo-dissociated by sunlight in the wavelength having wavelengths $\lambda < 1{,}100\,\text{nm}$:

$$\left.\begin{aligned} O_3 + h\nu &\rightarrow O_2 + O \quad (\lambda < 1{,}100\,\text{nm}) \\ O + O_3 &\rightarrow O_2 + O_2 \\ O + O + M &\rightarrow O_2 + M \end{aligned}\right\} \tag{2.30}$$

The availability of UV-C radiation to generate atomic oxygen through photo-dissociation decreases with distance from the top of the atmosphere (as photons are scattered and absorbed), while the number of oxygen molecules available for

photo-dissociation increases exponentially with depth in the atmosphere. The result is a pronounced local maximum in the number density of ozone molecules, which we call the ozone "layer". This maximum is located at altitudes between 20 and 40 km at mid-latitudes, and between 15 and 30 km in the polar regions. The kinetic energy imparted to molecular oxygen through photo-dissociation elevates the atmosphere's temperature at these altitudes, resulting in the middle atmosphere layer we call the stratosphere because of its stability against the vertical motion of air parcels. The "pure oxygen atmosphere" of 2.28–2.30 is only one part of the ozone story. The actual concentration of ozone at any geographic location and altitude, although established to first order by 2.28–2.30, depends on numerous sources and sinks—some dynamical (transport by stratospheric winds), some from natural photochemistry, and some anthropogenic, as will be discussed in Chapter 3. In this chapter we are concerned with the important examples of photo-dissociation as they affect the intensity of radiation reaching a satellite sensor.

In this respect, the *wavelength dependence* of molecular photo-dissociation is the most important thing to bear in mind. A thorough introduction to the quantum-mechanical theory of atmospheric spectroscopy can be found in Brasseur and Solomon (1984), Wayne (2000), and other texts on atmospheric chemistry, and the original reference is Herzberg (1950). Here, we can briefly describe the wavelength dependence qualitatively by means of an idealized energy diagram for a diatomic molecule (Figure 2.6). The lower curve in this figure depicts the potential "well" that exists when two ground state atoms are bound together as a molecule—i.e., the potential energy as a function of distance between atomic nucleii. There is an equilibrium internuclear distance d_{eq} that represents the lowest energy state and

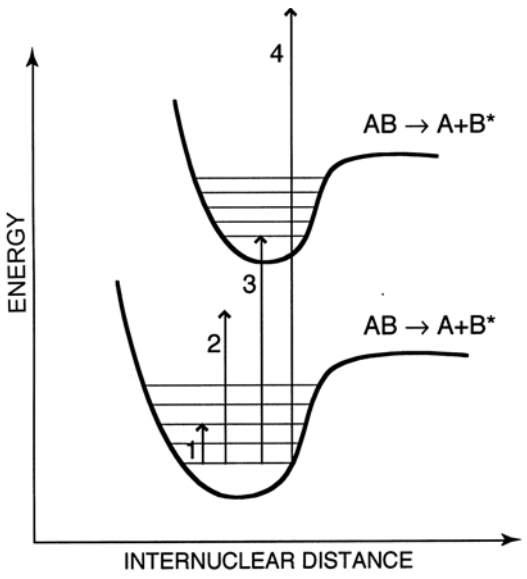

Figure 2.6. Idealized potential well diagram for the diatomic molecule.

maximum stability of the molecule. At smaller distances than d_{eq}, the electrical force between the atoms is repulsive, as indicated by a steep increase in the potential energy. At larger distances than d_{eq}, the electrical force between atoms is attractive, as indicated by another increase in the potential. However, this attractive side of the potential well does not increase infinitely with increasing internuclear distance, but remains constant (D) for large distances. If a photon having energy $e = hc/\lambda > D$ strikes the molecule, the attractive forces between the atoms may be overcome, and the molecule AB will have been dissociated into atomic constituents A and B. As shown in Figure 2.6, there can be a family of curves for a given molecule, corresponding to one of the atoms being in various excited electronic states. If one atom is in an electronically excited state, the molecule may still be bound, but its lowest energy state has a larger value than that for the molecule having both atoms in the ground electronic state. Within the potential well, there are a number of quantized energy levels that the molecule can assume, and these correspond to the molecule's *vibrational* modes. A photon striking the molecule, having an energy equal to the difference between two vibrational modes, may take the molecule from one vibrational state to a more energetic vibrational state.

Note in Figure 2.6 that there are four possible outcomes of a photon striking a diatomic molecule. A photon having relatively small energy may change the molecule's vibrational state. A photon having more energy may dissociate the molecule, or may transform the molecule from a ground electronic state to a molecule with one atom in an excited electronic state. If the photon is energetic enough, the molecule may be dissociated with one atom placed in an electronically excited state. In all cases the photon is absorbed (destroyed) by the molecule. In atmospheric spectroscopy, there are other possible outcomes that, together with those of Figure 2.6, can make the absorption a complicated function of wavelength. However, for this discussion the important points are: (1) that vibrational transitions occur at lower, quantized, energy levels and hence at discrete wavelengths, and (2) that photo-dissociation occurs at higher energies and is generally not quantized (to dissociate a molecule, the photon needs only to have energy greater than D). Thus, the strength by which a molecule may absorb photons by dissociation is generally a continuous function of wavelength. We describe this strength of absorption by photo-dissociation in terms of the molecular *absorption cross section* $\sigma_{a\lambda}$, which has units of cm^2, and generally varies by orders of magnitude as a function of wavelength. Figure 2.7 shows the absorption cross section of ozone.

A diatomic molecule has one mode of vibration, while triatomic molecules have several modes of vibration, as illustrated in Figure 2.8. In the Earth's atmosphere, most vibrational transitions are associated with near-infrared and middle-infrared wavelengths. The rotational state of a molecule is also quantized, and purely rotational transitions are relevant in the far-infrared and microwave parts of the spectrum. However, vibrational transitions can be accompanied by many rotational transitions. For a given vibrational transition associated with a particular wavelength, there may be a large number of rotational transitions allowed by quantum-mechanical selection rules. The result is a complicated band structure for absorption involving a large number of discrete wavelengths. One important

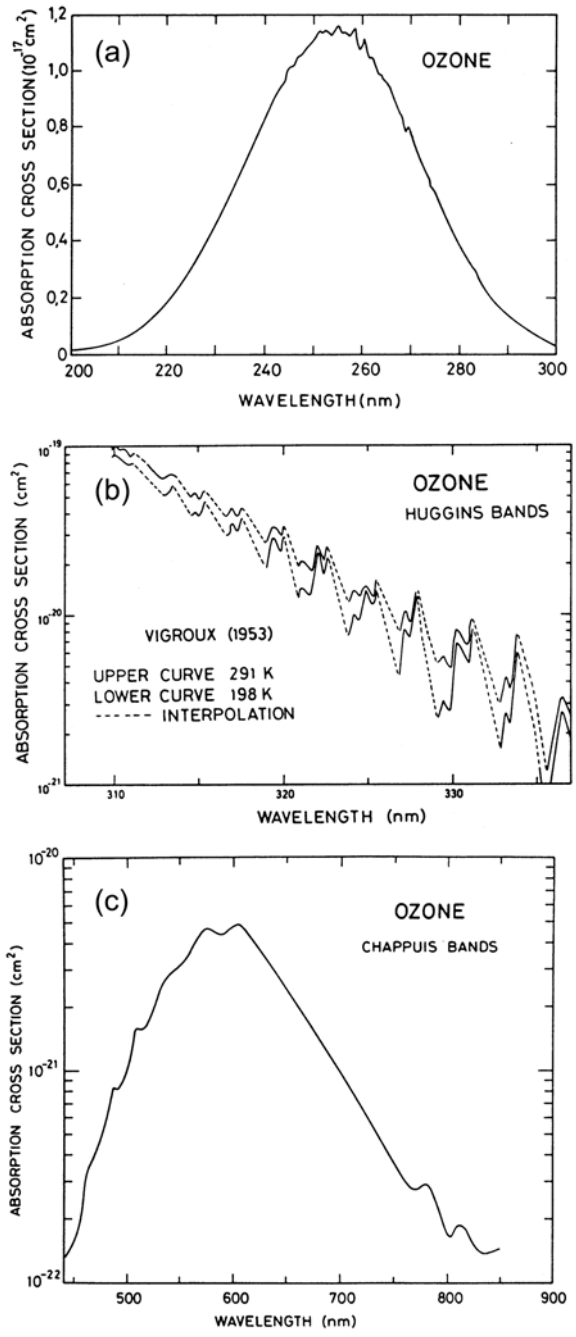

Figure 2.7. The absorption cross section of ozone.

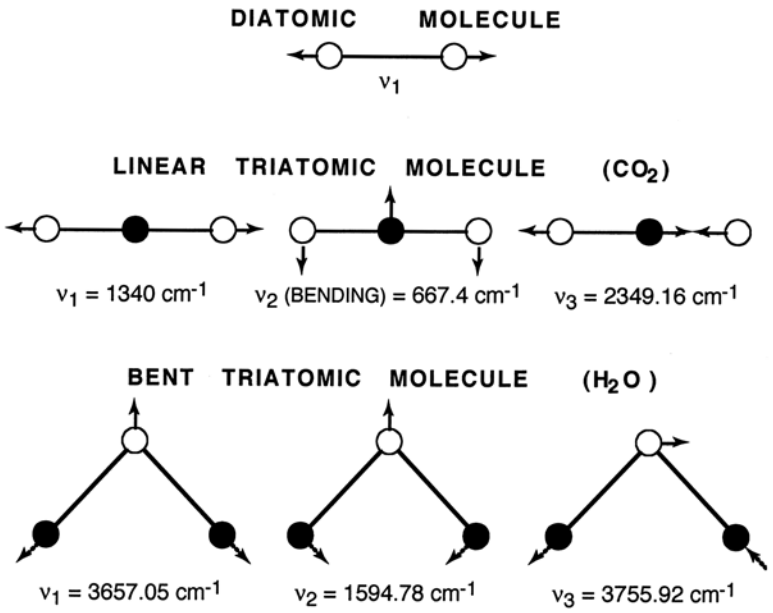

Figure 2.8. Modes of vibration for diatomic and triatomic molecules, examples being CO_2 and H_2O, respectively.

example for the Earth's atmosphere, the middle-infrared bending vibration mode of CO_2, is shown in Figure 2.8. For absorption involving vibrational and rotational transitions, we normally describe the strength of absorption in terms of the *mass absorption coefficient* k_ν in units of $m^2\,kg^{-1}$. For a discrete quantum-mechanical transition at wavenumber ν_0, the mass absorption coefficient is normally written as the product of a line strength S and a line shape factor f:

$$k_\nu = Sf(\nu - \nu_0) \tag{2.31}$$

with the shape factor normalized to unity such that:

$$S = \int_{-\infty}^{\infty} k_\nu \, d\nu \tag{2.32}$$

Consideration of the shape factor is necessary because, in the real atmosphere, physical processes involving the motion and collisions of molecules enable a quantum-mechanical transition occurring at wavenumber ν_0 in the restframe to actually be possible in a small range of wavenumbers centered about ν_0. Three shape factors are relevant to the Earth's atmosphere. The *Lorentz* profile, which pertains to collisionally broadened absorption lines, is given by:

$$f_L(\nu - \nu_0) = \left(\frac{\gamma_L}{\pi}\right) \frac{1}{(\nu - \nu_0)^2 + \gamma_L^2} \tag{2.33}$$

The Lorentz half-width at half-maximum of the line shape, γ_L, is inversely proportional to the mean free time τ_c between molecular collisions, and is normally expressed as a function of pressure and temperature in the form:

$$\gamma_L = \frac{1}{2\pi\tau_c} = \gamma_0 \frac{P}{P_0}\left(\frac{T_0}{T}\right)^n \tag{2.34}$$

In this expression γ_0 is the reference half-width for standard temperature T_0 and pressure P_0, and is typically of order 0.1 cm^{-1} (e.g., Tiwari, 1978). The classical value of the exponent n is 1/2, although n is somewhat larger for most atmospheric trace gases. Some of these Lorentz line-shape parameters are tabulated in Liou (1992).

In the rarified upper atmosphere, the motion of individual molecules induces Doppler shifts in the apparent wavenumber of quantum transitions, and the result is the Doppler broadening lineshape given by:

$$f_D(\nu - \nu_0) = \frac{1}{\gamma_D\sqrt{\pi}} \exp\left[\frac{-(\nu - \nu_0)^2}{\gamma_D^2}\right] \tag{2.35}$$

The Doppler width γ_D is:

$$\gamma_D = \frac{\nu_0}{c}(2R_g T)^{1/2} \tag{2.36}$$

where T is the temperature and R_g is the individual gas constant.

In the troposphere and lower stratosphere (surface to ~20 km), collisional broadening generally dominates over Doppler broadening, and the Lorentz shape factor is usually the most applicable. In the mesosphere and thermosphere (above ~50 km), Doppler broadening dominates over collisional broadening. In most of the stratosphere, both line-broadening processes have approximately equal importance, and a convolution of the two is needed. This convolution accounts for a redistribution by Doppler broadening of the Lorentz-broadened line at wavenumber ν to wavenumber ν', and yields a shape factor known as the Voigt profile:

$$f_\nu(\nu - \nu_0) = \frac{1}{\pi^{3/2}} \frac{a}{\gamma_D} \int_{-\infty}^{\infty} \frac{\exp(-y^2)}{a^2 + (x - y)^2}\, dy \tag{2.37}$$

where $a = \gamma_L/\gamma_D$, $x = (\nu - \nu_0)/\gamma_D$, and $y = (\nu' - \nu_0)/\gamma_D$. Here Doppler broadening redistributes the Lorentz line at wavenumber ν' to wavenumber ν. The Voigt profile is the most commonly used shape factor in line-by-line radiative transfer calculations (see Section 2.3.6), as it tends to the limiting cases of Lorentz and Doppler broadening for dense and rarefied atmospheres, respectively.

In addition to the monochromatic cases described by the lineshape factors above, the mass absorption coefficient k_ν may be calculated as an average quantity over many transitions (lines) within a spectral interval, using some form of band model approximation (for example, see chap. 4 of Goody and Yung, 1989 or chap. 2 of Liou, 1992).

Consider an infinitesimally thin atmospheric layer of thickness dz in which there are absorbing molecules. An intensity I_λ crossing this layer will decrease by dI_λ.

This decrease is proportional to the intensity, according to the principle known as *Bouger's* or *Beer's law*. We can express the change in intensity as:

$$-dI_\lambda = \frac{\sigma_{a\lambda} n_a(z) I\lambda}{\mu} \tag{2.38}$$

where $n_a(z)$ is the number density of the absorber (cm^{-3}). The increment of *optical depth* is defined as:

$$d\tau_\lambda = \sigma_{a\lambda} n_a(z)\, dz \tag{2.39}$$

and we normally refer to the optical depth as pertaining to a particular atmospheric layer, or the total atmospheric column:

$$\tau_\lambda = \int_{z_1}^{\infty} \sigma_\lambda n(z)\, dz \tag{2.40}$$

For an atmosphere of finite thickness, we expect the number density to vary in the vertical direction, but note that the absorption cross section (or mass absorption coefficient) may also vary across a thick enough atmospheric layer. One example is the ozone absorption cross section, which has considerable temperature dependence (Molina and Molina, 1986). In terms of the mass absorption coefficient, the optical depth is:

$$\tau_\lambda = \int_{z_1}^{\infty} k_\nu(z)\rho_a(z)\, dz \tag{2.41}$$

where $\rho_a(z)$ is the absorber density. From (2.38) and (2.39), we obtain the traditional way to express Beer's law for absorption:

$$I_\lambda(z) = I_{\lambda 0}\, e^{-\tau_\lambda(z)/\mu} \tag{2.42}$$

where $I_{\lambda 0}$ is the intensity incident on the atmospheric layer. While not a rigorous solution to most atmospheric radiative transfer problems, (2.42) can be useful for "back of the envelope" estimates when considering atmospheric absorbers.

The other important form of atmospheric attenuation is *scattering*, or redirection of radiation. Atmospheric constituents of all sizes—molecules, aerosol particles, cloud droplets, ice crystals—scatter radiation, and therefore there are several important types of scattering in the Earth–atmosphere system. The three important considerations with scattering are (1) the scattering strength of the particle, (2) the way in which the particle redirects radiation, and (3) whether or not the particle absorbs as well as scatters radiation. At a fundamental level, these three considerations are addressed by classical electrodynamics—solving the equations for a plane electromagnetic wave incident on a scattering particle (van de Hulst, 1981). The scattering strength of a particle can be expressed in terms of a *scattering cross section* σ_s. The redirection of radiation is expressed in terms of a *scattering phase function* $P(\theta', \phi', \theta, \phi)$ which specifies the fraction of the radiation incident from direction (θ', ϕ') that is scattered into direction (θ, ϕ). The phase function is usually expressed in terms of the scattering angle Θ,

$$\cos\Theta = \cos\theta\cos\theta' + \sin\theta\sin\theta'\cos(\phi - \phi') \tag{2.43}$$

and is normalized such that:

$$\frac{1}{4\pi}\int_0^{2\pi}\int_0^{\pi} P(\Theta)\sin\theta'\,d\theta'\,d\phi' = 1 \tag{2.44}$$

If the characteristic particle dimension is much smaller than the wavelength of incident radiation, as in the case of atmospheric molecules and shortwave radiation, Rayleigh scattering applies. The Rayleigh scattering cross section (see Kidder and Vonder Haar, 1995; Liou, 1980) exhibits the familiar, inverse fourth power of the wavelength:

$$\sigma_{s\lambda} = f\frac{32\pi^3 w_m \rho}{3\rho_0^2 N_A \lambda^4}(m_0 - 1) \tag{2.45}$$

where m_0 and ρ_0 are the index of refraction and density of air at sea level, ρ is the air density at the altitude being evaluated, N_A is Avogadro's number, w_m is the molecular weight of dry air, and $f = 1.061$ is a factor to correct for the anisotropic behavior of air molecules. An approximation for the sea level value of m_0, as a function of wavelength, is given by Liou (1980):

$$(m_0 - 1)\times 10^6 = 64.328 + \frac{29{,}498.1}{146 - \lambda^{-2}} + \frac{255.4}{41 - \lambda^{-2}} \tag{2.46}$$

where the wavelength λ is in microns. The Rayleigh scattering phase function is:

$$P(\Theta) = \tfrac{3}{4}(1 + \cos^2\Theta) \tag{2.47}$$

which specifies that equal fractions of incident radiation are scattered in the forward and backward 2π directions.

For particles such as aerosols or cloud droplets, in which the wavelength of incident radiation is comparable with or smaller than the particle size, Mie theory can be used to calculate the phase function and scattering strength in spherical particle approximation (e.g., van de Hulst, 1981). If an exact scattering phase function is needed for a non-spherical particle—for example, an ice crystal—the electromagnetic planewave equation must be solved for radiation incident on the particular geometry (Liou, 1992). In contrast to the simple symmetrical Rayleigh scattering phase function, the phase functions from larger particles are quite complicated; they generally involve pronounced redistribution of radiation into the direction directly forward (forward scattering "peak"), a much smaller secondary maximum in the direction directly backwards, and numerous "side lobes" that are smaller still. The derivation and parameterization of scattering phase functions for non-spherical particles is a current area of research in radiative transfer with direct application to the Earth's polar regions. Figure 2.9 illustrates the scattering phase function for various ice crystals.

If all radiation incident on a particle is scattered and none is lost, the scattering is said to be *conservative* or *elastic*. Depending on the medium's refractive index, the particle size, and the wavelength of the incident radiation, a particle may absorb some fraction of incident radiation in addition to redirecting the fraction not absorbed.

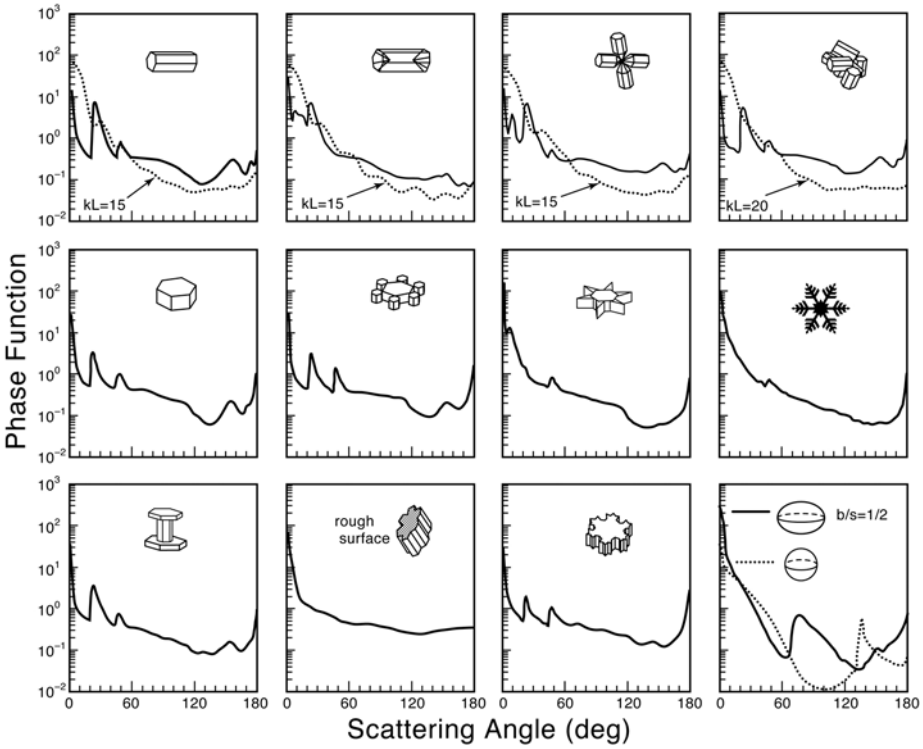

Figure 2.9. The scattering phase functions for various types of ice crystals, along with those from a spheroid and a sphere. Depending on satellite viewing geometry, these subtle differences in phase function can strongly influence the backscattered intensity from a polar Earth–atmosphere scene.

This is *non-conservative* or *inelastic* scattering. For example, a pure liquid water droplet of a typical size 10 microns scatters conservatively for wavelengths shorter than 1 micron, and absorbs radiation at longer wavelengths. The same is true for pure ice crystals. Aerosol particles may or may not absorb radiation at UV and visible wavelengths, depending on their composition. The quantity used to describe partial absorption by a scattering particle is the *single-scattering albedo* ϖ_λ, which specifies the probability that a photon striking the particle will be scattered rather than absorbed ($\varpi_\lambda = 1$ for conservative scattering). The single-scattering albedo is computed from the scattering and extinction cross sections that result from solution of Maxwell's equations for an electromagnetic planewave incident on the particle (e.g., Liou, 1992). Figure 2.10 illustrates the single-scattering albedo for typical maritime cloud droplets and for an Arctic cloud microphysical model.

Although a complete quantitative discussion of scattering by clouds and aerosols is beyond the scope of this chapter, one model phase function is worth mentioning. The *Henyey–Greenstein* phase function (Henyey and Greenstein, 1941) provides a

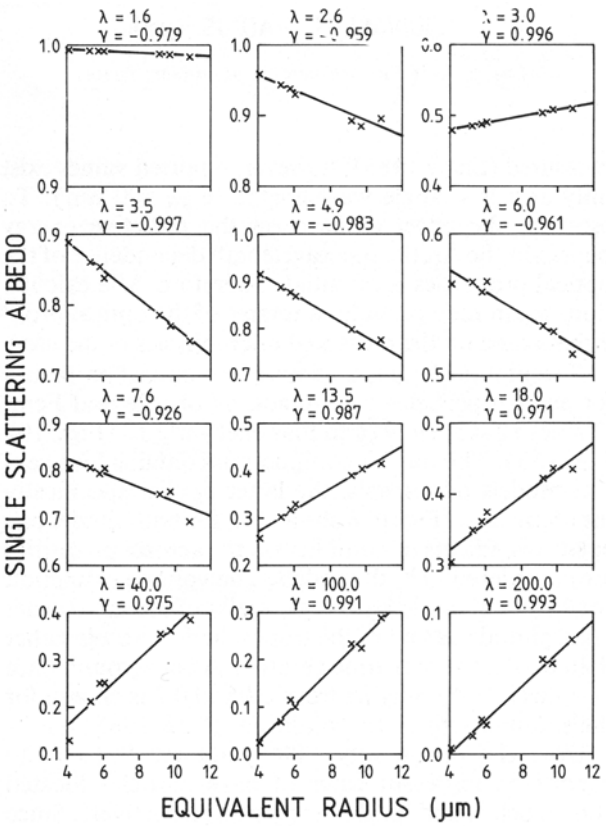

Figure 2.10. Wavelength dependence in the single-scattering albedo.
Example from Tsay et al. (1989).

useful approximation for highly anisotropic scattering. This phase function is:

$$P_{HG}(\Theta) = \frac{(1 - g^2)}{(1 + g^2 - 2g\cos\Theta)^{3/2}} \tag{2.48}$$

where g is the asymmetry factor. The asymmetry factor specifies the fraction of incident radiation scattered into the forward direction. The value $g = 0.5$ denotes equal amounts of energy scattered forward and backward, while $g = 1.0$ denotes the limiting case of all radiation being forward scattered. A typical value for a liquid water cloud, for wavelengths less than 1.0 micron, is $g = 0.85$. The asymmetry factor is a function of wavelength, and is calculated from electromagnetic theory along with the single scattering albedo. However, when using the Henyey–Greenstein phase function, g and ϖ_λ can be taken from applicable tables in the literature and used directly. The Henyey–Greenstein phase function is an acceptable approximation for many remote-sensing applications.

2.3.4 The radiative transfer equation

Consider a volume element across which a monochromatic beam of radiation propagates a distance $d\mathbf{s}$. In this volume element there are both scatterers and absorbers that can change the specific intensity along $d\mathbf{s}$. We first consider wavelengths at which thermal emission from the medium is negligible. In this case, there are three possible ways in which the intensity can change: (1) radiation can be absorbed by the medium, (2) radiation can be scattered out of the beam, and (3) radiation can be scattered into the beam from other directions. Expressing this quantitatively:

$$\frac{dI_\lambda(\vec{s})}{ds} = -\sigma_{a\lambda} n_a - \sigma_{s\lambda} n_s + j^s_\lambda(\vec{s}) \tag{2.49}$$

where n_a and n_s are the number densities (cm^{-3}) of the absorbers and scatterers, respectively, and where the source term representing radiation scattered into the beam makes use of the scattering phase function in an integral over solid angle:

$$j^s_\lambda(\vec{s}) = \sigma_{s\lambda} \oint \frac{d\omega}{4\pi} P(\vec{s}\,', \vec{s}) I_\lambda(\vec{s}\,') \tag{2.50}$$

In the general case, we could have radiation scattered not only from one direction $\mathbf{s}'$ to another direction $\mathbf{s}$, but we could also have radiation scattered from one wavelength λ' to another λ (e.g., Raman scattering). For most problems in satellite remote sensing, the wavelength remains constant throughout the scattering interaction (coherent scattering).

Also, note in (2.49) that Beer's law applies to radiation scattered out of the beam, just as it does for absorption. Now because $\mathbf{s}$ is an arbitrary direction, the change along this direction is given by:

$$\frac{d}{ds} \equiv \vec{s} \cdot \nabla = (\sin\theta)(\cos\theta)\frac{\partial}{\partial x} + (\sin\theta)(\cos\theta)\frac{\partial}{\partial y} + \cos\theta \frac{\partial}{\partial z} \tag{2.51}$$

In other words, a fully rigorous determination of the specific intensity as a function of distance requires three dimensions. However, in the Earth's atmosphere we can often assume that the scattering and absorbing properties are horizontally homogeneous ($d/dx = d/dy = 0$), and that significant spatial variation occurs only in the vertical direction. This approximation is acceptable for Rayleigh scattering, most atmospheric absorption, and extinction by aerosols. It is an acceptable first-order approximation for horizontally extended clouds, although we will see in subsequent chapters how this approximation is limited in the polar regions. With this *plane-parallel* approximation:

$$\mu \frac{dI_\lambda(\mu, \phi, z)}{dz} = n_s j^s_\lambda(\mu, \phi, z) - [\sigma_{s\lambda} n_s(z) + \sigma_{a\lambda} n_a(z)] I_\lambda(\mu, \phi, z) \tag{2.52}$$

As in (2.39), we can define the increment of optical depth as:

$$d\tau_\lambda \equiv -[\sigma_{s\lambda} n_s(z) + \sigma_{a\lambda} n_a(z)]\, dz \tag{2.53}$$

The convention is that the optical depth is zero at the top of the atmosphere ($z = \infty$), and that the total optical depth from some altitude z to the top of the atmosphere is:

$$\tau_\lambda(z) = \int_z^\infty [\sigma_{s\lambda} n_s(z) + \sigma_{a\lambda} n_a(z)]\, dz \tag{2.54}$$

Note that optical depth is a dimensionless quantity.

Above, we described the single-scattering albedo of an individual particle. Similarly, the single scattering albedo for the medium is:

$$\left.\begin{aligned} &\varpi_\lambda(\tau_\lambda) = \frac{\sigma_{s\lambda} n_s(\tau_\lambda)}{\sigma_{s\lambda} n_s(\tau_\lambda) + \sigma_{a\lambda} n_a(\tau_\lambda)} \\ &0 \le \varpi_\lambda(\tau_\lambda) \le 1 \end{aligned}\right\} \tag{2.55}$$

and this specifies the probability that a photon traversing the increment of optical depth $d\tau_\lambda$ will be scattered rather than absorbed. We further define the *source function for scattering* as:

$$S^s_\lambda(\tau_\lambda, \mu, \phi) \equiv \frac{\varpi_\lambda(\tau_\lambda) j^s_\lambda(\tau_\lambda, \mu, \phi)}{\sigma_{s\lambda}} \tag{2.56}$$

From (2.50) to (2.56), we arrive at the traditional representation of the radiative transfer equation for monochromatic shortwave radiation in the Earth's atmosphere:

$$\mu \frac{dI_\mu(\tau_\lambda, \mu, \phi)}{d\tau_\lambda} = I_\mu(\tau_\lambda, \mu, \phi) - S^s_\lambda(\tau_\lambda, \mu, \phi) \tag{2.57}$$

For an atmosphere illuminated by an extraterrestrial solar flux $F_{\lambda 0}(\mu_0, \phi_0)$, the source function has two terms:

$$\begin{aligned} S^s_\lambda(\tau_\lambda, \mu, \phi) = &\frac{\varpi_\lambda}{4\pi} \int_0^{2\pi} \int_{-1}^{1} I_\lambda(\tau_\lambda, \mu', \phi') P(\mu', \phi'; \mu, \phi)\, d\mu'\, d\phi' \\ &+ \frac{\varpi_\lambda}{4\pi} F_{\lambda 0} P(-\mu_0, \phi_0; \mu, \phi)\, e^{-\tau_\lambda/\mu_0} \end{aligned} \tag{2.58}$$

Although the change in the intensity distribution as governed by the radiative transfer equation is expressed in terms of total optical depth (2.54), it is often convenient to represent total optical depth as a sum of optical depths for each source of attenuation present in the medium. For example, in an atmospheric layer between altitudes z_1 and z_2, with J gaseous absorbers, Rayleigh scattering, and inelastic scattering by cloud droplets, we would have:

$$\tau_\lambda = \sum_{j=1}^{J} \int_{z_1}^{z_2} \sigma_{a\lambda j} n_{aj}(z)\, dz + \int_{z_1}^{z_2} \sigma_{r\lambda} n(z)\, dz + \int_{z_1}^{z_2} \sigma_{s\lambda} n_s(z)\, dz \tag{2.59}$$

where $\sigma_{s\lambda}$ and $n_s(z)$ are the scattering cross section and number density of the cloud droplets. In this case, the total single-scattering albedo of the medium can

be written as:

$$\varpi_\lambda = \frac{\tau_{r\lambda} + \varpi_s \tau_{s\lambda}}{\tau_\lambda} \tag{2.60}$$

where $\tau_{r\lambda}$ is the optical depth of the Rayleigh scatterers, ϖ_s and $\tau_{s\lambda}$ are the single scattering albedo and optical depth, respectively, for the cloud droplets, and τ_λ is total optical depth (for Rayleigh scattering, the single-scattering albedo is unity). This representation is convenient if the single scattering albedo for a particular type of cloud or aerosol particle is taken from the literature instead of being computed directly.

Note that all of the important quantities—the number densities of scatterers and absorbers, and the single scattering albedos—vary significantly in the vertical direction. Even the cross sections of important absorbers can vary with altitude if there is significant temperature dependence (see, for example, Molina and Molina, 1986, for ozone absorption). Practical solution of the radiative transfer equation therefore usually involves modeling the real atmosphere as a sufficient number of geometrically thin, vertically homogeneous layers. There will be two boundary conditions for the resulting system of equations. The upper boundary condition is the extraterrestrial solar flux in the shortwave or absence thereof in the longwave. The lower boundary condition might be the specification of (1) a Lambertian surface albedo in the case of simpler radiative transfer methods, (2) a parameterization for surface bidirectional reflectance in the case of more elaborate radiative transfer formulations, or (3) a model for the surface as a scattering and absorbing layer of very large optical depth, to simulate surface bidirectional reflectance properties from first principles.

2.3.5 Thermal radiation

Any material at a given temperature emits electromagnetic radiation, the intensity of which is a function of both temperature and wavelength. In general, thermal emission must be included as an additional source function term in the radiative transfer equation. We commonly refer to an idealized material, known as a *blackbody*, that absorbs all electromagnetic radiation incident upon it (reflectance $r = 0$), and emits electromagnetic radiation with perfect efficiency. For a blackbody, *Planck's law* states that the specific intensity resulting from the material's thermal emission is given by:

$$B_\nu(T) = \frac{2hc^{-2}\nu^3}{\exp\left(\dfrac{h\nu}{kT}\right) - 1} \tag{2.61}$$

or

$$B_\lambda(T) = \frac{2hc^2\lambda^{-5}}{\exp\left(\dfrac{hc}{\lambda kT}\right) - 1} \tag{2.62}$$

where h is *Planck's constant* and k is *Boltzmann's constant*. These equations are known as the wavenumber and wavelength forms of the *Planck function*. The wavelength corresponding to the maximum in thermally emitted intensity is determined by differentiating (2.62), yielding:

$$\lambda_m T = 2{,}987.9\,\mu\text{m K} \tag{2.63}$$

This is known as *Wien's displacement law*, and shows that the intensity maximum shifts toward shorter wavelengths as temperature increases. Integrating the Planck function over all wavenumbers, we obtain the flux emitted by a blackbody:

$$\pi B(T) = \pi \int_0^\infty B_\nu(T)\, d\nu = \sigma T^4 \tag{2.64}$$

which is known as the *Stefan–Boltzmann law*, and the constant σ is known as the Stefan–Boltzmann constant.

For real materials, the thermal emission will generally be less than that of an ideal blackbody, and this departure from perfect emission is generally a function of wavelength. A real material is characterized by its spectral *emissivity*:

$$\varepsilon_\nu = (\text{Radiation emitted at wavenumber } \nu)/B_\nu(T) \tag{2.65}$$

If the material is in *Local Thermodynamic Equilibrium* (LTE), meaning that one thermodynamic temperature applies throughout the volume element under consideration, then Kirchhoff's law applies. Kirchhoff's law states that a body is as good an emitter as it is an absorber, so that the *absorptance* a_ν is equal to the emissivity ε_ν. The absorptance is defined as the ratio of the radiation absorbed at frequency ν to that incident at frequency ν. LTE applies to most of the Earth's atmosphere; although above 100 km molecular collisions are rare enough that different gases can have different thermodynamic temperatures. The LTE condition, which in general does not apply to the atmospheres of stars or the gas giants, greatly simplifies infrared radiative transfer theory applied to the Earth's atmosphere. As a consequence of LTE, the spectral reflectance of a medium is:

$$r_\nu = 1 - \varepsilon_\nu \tag{2.66}$$

In satellite remote sensing, one frequently encounters the term *brightness temperature*. The strict definition of brightness temperature applies to microwave radiation. In the microwave (centimeter and millimeter wavelengths), $hc/\lambda kT \ll 1$. The exponential term in (2.62) can therefore be expanded, and the Planck function reduces to the *Rayleigh–Jeans approximation*:

$$B_\lambda(T) = \frac{2ckT}{\lambda^4} \tag{2.67}$$

Because the intensity is simply proportional to the temperature, the convention in microwave remote sensing is to divide the intensity by $2ck\lambda^{-4}$ to yield the brightness temperature T_b of the scene being observed. This type of effective scene temperature is much more physically intuitive than units of intensity, and it is frequently used in the middle-infrared as well. However, at middle-infrared wavelengths (4–50 μm) the

Rayleigh–Jeans approximation does not apply. One must determine the effective scene temperature T_b by inverting the Planck function (in the monochromatic case), or for a sensor with finite spectral bandwidth $\Delta\nu$, by a suitable integration of the Planck function over the bandwidth (taking into account the spectral responsivity of the sensor as discussed below). For the middle-infrared, this type of effective scene temperature is more correctly called the *equivalent blackbody temperature*, but it is commonly referred to as the brightness temperature.

2.3.6 Managing the radiative transfer equation

The generalized plane-parallel form of the radiative transfer equation is:

$$\mu \frac{dI_\lambda(\tau_\lambda, \mu, \phi)}{d\tau_\lambda} = I_\lambda(\tau_\lambda, \mu, \phi) - S_\lambda(\tau_\lambda, \mu, \phi),$$

$$S_\lambda = \frac{\varpi_\lambda(\tau_\lambda)}{4\pi} \int_0^{2\pi} d\phi' \int_{-1}^{1} P_\lambda(\tau_\lambda, \mu, \phi; \mu', \phi') I_\lambda(\tau_\lambda, \mu', \phi')\, d\mu' + [1 - \varpi_\lambda(\tau_\lambda)] B_\lambda[T(\tau_\lambda)] \tag{2.68}$$

which includes a thermal source term based on the Planck function. In the Earth's atmosphere, this entire equation applies only to a wavelength range of approximately 3–5 microns. At shorter wavelengths, thermal sources have a negligible contribution at terrestrial temperatures, and the applicable radiative transfer equation is (2.57)–(2.60). At longer wavelengths, the extraterrestrial solar flux becomes negligible. Equation (2.68) is straightforward to derive, but difficult to solve for a realistic terrestrial atmosphere, even with the simplifications of LTE and plane-parallel geometry. It is an integro-differential equation that lends itself to analytic treatment only for simple approximations that have very limited applicability to current climate and remote-sensing research. The practical complications with managing accurate atmospheric radiative transfer calculations vary with wavelength region, as scattering and absorbing properties vary in both importance and complexity.

In the UV-C (200–280 nm), UV-B (280–315 nm), UV-A (315–400 nm), and much of the visible, we have perhaps the most straightforward and easily managed form of the radiative transfer equation. Absorption by photo-dissociation usually involves continuous functions that can be represented directly by absorption cross sections. The Rayleigh scattering cross section and phase function is well known and relatively simple. Cloud scattering is conservative, and in many cases can be treated with scattering phase functions from Mie theory. Most aerosol extinctions can also be addressed by Mie theory, using refractive indices appropriate to a given region's aerosol composition (e.g., d'Almeida et al., 1991). Hence the radiative transfer equation can be solved monochromatically, with resulting intensities and fluxes summed over wavelength bands as needed. In the UV-C, solar radiation effectively never reaches the ground, and so one doesn't need to accurately specify a lower boundary condition representing the Earth's surface. Although the radiative

transfer equation is most easily managed at these wavelengths, the researcher must ensure that all processes represented in them are based on the most current literature. Also, some processes—for example, scattering in cirrus or other ice clouds—are inevitably complicated at any wavelength. For larger particles (micron or 10–100 μm size particles) at these wavelengths, particle shape will strongly influence the scattering phase function and hence will have a noticeable impact on intensities backscattered to space (although these influences on fluxes are smaller).

In the near- and middle-infrared, the major complication involves a suitable representation for tens of thousands of important molecular transitions (each at a discrete wavelength). Monochromatic calculations using a line-by-line radiative transfer formulation (e.g., Clough et al., 1981; 1992) are possible in principle, but are very cumbersome for most remote-sensing and climate research applications unless done offline to generate lookup tables. Many practical applications require a parameterization for gaseous absorption that reduces the number of wavelength intervals to something manageable. Rayleigh scattering is relatively unimportant for wavelengths longer than 1 micron, and is negligible in the middle-infrared. Cloud and aerosol extinction both need to be treated rigorously at all wavelengths. In the near-infrared, cloud scattering is a large part of the total extinction, and cloud particle shape should be accounted for in phase function computations. In the middle-infrared, scattering contributes several percent to the total extinction by clouds (e.g., Curry and Herman, 1985) and therefore cloud extinction should be treated at least by approximations from Mie theory. Aerosol extinction is generally smaller in the longwave than in the shortwave; however, in the longwave aerosol optical depth varies much more strongly with relative humidity (Blanchet and List, 1983). This is an important consideration during the Arctic spring when extensive aerosol layers are present (Shaw, 1982).

The radiative transfer equation can be greatly simplified if we only need to compute fluxes. Fluxes are often sufficient for climate modeling applications, or for estimating the surface UV radiation environment for applications in photobiology and ecology. For computing fluxes, the radiation field can be divided into two parts—all energy propagating in the downward direction and all radiation propagating in the upward direction. By integrating the intensities over the lower and upper 2π steradians, one can derive from (2.63) a pair of equations for the upwelling and downwelling flux. For a multi-layered model atmosphere with appropriate boundary conditions, the result is a system of coupled upwelling and downwelling flux equations that lend themselves to analytic treatment and can be solved either by matrix inversion or by straightforward numerical integration. Various approaches that use this or similar concepts include the standard two-stream model (Meador and Weaver, 1980), the Eddington approximation and delta-Eddington approximation (Joseph et al., 1976), and two-stream finite difference techniques (Frederick and Lubin, 1988). The delta-Eddington approximation is widely used in climate modeling and related applications (Briegleb, 1992), because it can provide an excellent representation highly anisotropic cloud scattering in conjunction with the Henyey–Greenstein phase function. There are two important

considerations with these simplified radiative transfer formulations. First, their applicability to satellite remote sensing is extremely limited. A satellite remote sensor looks in a specific direction, and to accurately simulate its signal we need to compute intensities. For some cases where the top-of-atmosphere radiation field is approximately isotropic—for example, upwelling middle-infrared radiation measured from a near-nadir viewing direction—flux calculations can provide some order-of-magnitude estimates to guide the researcher. However, they should not be used for rigorous algorithm development or image interpretation. Furthermore, the fluxes calculated by two-stream methods have noticeable errors in many limiting cases such as large solar zenith angles or particular ranges of optical depth, when compared with fluxes calculated by more rigorous radiative transfer formulations.

A researcher serious about using satellite remote sensing will eventually need to acquire some computational tools for radiative transfer, and these tools must be rigorous enough for calculations of specific intensity. Fortunately, radiative transfer is such an essential part of Earth science that many useful algorithms are available in the literature and throughout the research community. For computing intensities, the *discrete ordinates* method of Stamnes et al. (1988) is widely used. In the discrete ordinates method, the full angular dependence of the radiation field (4π steradians) is approximated by a suitable number of intensity streams, each for a specific angle. Analytic solutions are obtained for an atmospheric layer by expansion of these discretized intensities in Legendre polynomials. A computer code for the discrete ordinates method (called DISORT, in FORTRAN) can be obtained from Professor Knut Stamnes (Stevens Institute of Technology) or Dr. Si-Chee Tsay (NASA Goddard Space Flight Center). Other useful methods for solving the radiative transfer equation for specific intensities are the *adding–doubling* method (Lenoble, 1984), and the *Feautrier* method (Mihalas, 1978).

To explicitly calculate the absorbtion by individual molecular transitions, there is a complete database of absorption line strengths and half-widths called HITRAN (Clough et al., 1981; 1992). Two radiative transfer algorithms designed to work with database are the Fast Atmosphere Signature CODe (FASCOD) and the Line-by-Line Radiative Transfer Model (LBLRTM). These models are excellent for highly accurate computations in narrow wavenumber bands where absorption is important. For example, design of a temperature-sounding algorithm utilizing the edge of the 15-μm CO_2 band (discussed in Chapter 4) can benefit from calculations that reference HITRAN. However, radiative transfer calculations that treat every individual absorption line individually are very time-consuming. Most practical remote-sensing algorithm development requires that molecular absorption be parameterized to a lower spectral resolution for more rapid computations. Two algorithms that accomplish this very well throughout the infrared are the LOWTRAN and MODTRAN models developed by the U.S. Air Force Geophysics Laboratory (Kniezs et al., 1987; Berk, 1992) and are very useful. These models, which resolve the entire shortwave and longwave into spectral intervals of $20\,\mathrm{cm}^{-1}$ and $2\,\mathrm{cm}^{-1}$ respectively, also include several choices for the numerical treatment of scattering (the most recent versions include DISORT), along with numerous lookup tables containing parameterizations for cloud and aerosol extinction.

For the researcher who needs to build a custom radiative transfer code from scratch, one useful method for parameterizing gaseous absorption is the method of *exponential sum fitting of transmissions* (Wiscombe and Evans, 1977). In this method, the absorption by one or more atmospheric constituents in a desired large wavenumber interval is calculated as a function of absorber concentration at a constant pressure, using a detailed model such as LOWTRAN or FASCOD. This absorption function is then parameterized as a sum of a relatively small number M of exponential terms:

$$\left.\begin{aligned} \tilde{T}(u) &= \sum_{j=1}^{M} w_j \, e^{-b_j u} \\ \sum_{j=1}^{M} w_j &= 1 \end{aligned}\right\} \tag{2.69}$$

where T is the band transmission function, u is the absorber concentration and a_j and b_j are parameterization constants. Each term $b_j u$ is therefore a pseudo-optical depth for absorption that can be combined with optical depths for various types of scattering in a detailed radiative transfer calculation. This method offers the advantage of reducing hundreds or thousands of monochromatic calculations for individual molecular transitions to only M (typically 10 to 20) pseudo-monochromatic calculations for a spectral interval that can be arbitrarily chosen. The intensities calculated using these pseudo-optical depths are then summed according to the weights a_j to yield the actual intensity (Watts per square meter per steradian) in the entire spectral interval. Some coefficients a and b_j are published in the literature (e.g., Slingo and Schrecker, 1982). The generalized version of exponential sum fitting is the *k-distribution* method (Fu and Liou, 1992). Dr. Jeffrey Key (National Oceanic and Atmospheric Administration—NOAA) has designed a radiative transfer algorithm with the polar regions in mind called "Streamer", which combines exponential sum fitting for gaseous absorption with the discrete ordinates method of Stamnes et al. (1988). Another similar publicly available algorithm is the SBDART model of Ricchiazzi et al. (1998).

It is generally not necessary to use parameterizations such as exponential sum fitting, or band models such as LOWTRAN, for radiative transfer calculations at UV and visible wavelengths. At wavelengths where photodissociation is responsible for absorption, it is better to use the original absorption cross sections, since these are continuous functions that can be input directly into the radiative transfer model with a manageable number of monochromatic calculations. For the most important photochemically active gases in the Earth's atmosphere, the absorption cross sections are often measured directly in the laboratory with periodic improvements in accuracy as required by the research community (e.g., Molina and Molina, 1986).

For cloud and aerosol scattering, an efficient Mie scattering algorithm has been developed by Dr. Warren Wiscombe of the NASA Goddard Space Flight Center

(Wiscombe, 1980). For scattering by ice crystals that make up cirrus clouds, considerable work has been done by Professor Kuo-Nan Liou of the University of California, Los Angeles (e.g., Liou et al., 2001). Scattering particles of arbitrary shape can often be treated by the discrete dipole approximation (Draine and Flatau, 1994).

Finally, there are many situations where even the fully rigorous plane-parallel radiative transfer equation (2.68) is too crude an approximation. Such situations include broken cloud fields, spatial inhomogeities within clouds, large discontinuities in surface albedo, and solar zenith or scene viewing angles less close to 90 degrees. For large Sun or viewing angles, the Earth's sphericity matters. The optical pathlength for radiation incident at large angles is very different from the plane-parallel case, and should be treated by a radiative transfer equation derived for spherical geometry (e.g., Bush and Chakrabarti, 1995). For two- and three-dimensional radiative transfer problems, some analytical approaches are available (e.g., Stephens, 1986; and see numerous articles in the *Journal of Quantitative Spectroscopy and Radiative Transfer*). However, it is more common to use Monte Carlo simulations in three-dimensional situations because they can be tailored to the specific geometry (Marchuk et al., 1980; Ricchiazzi and Gautier, 1998).

2.4 SCANNING

We now discuss how a specific intensity backscattered or emitted from the Earth–atmosphere system can be sampled by an orbiting electro-optical device. Generally speaking, an electro-optical instrument consists of four major components: (1) a telescope or similar imaging device; (2) a detector assembly in the telescope's focal plane, which may also include filters or other devices for wavelength selection; (3) a calibration assembly that allows the detector's photon response to be interpreted in radiometric units (e.g., $\mathrm{W\,m^{-2}\,sr^{-1}\,\mu m^{-1}}$); and (4) an analog–digital converter that allows the instrument's observations to be encoded into the spacecraft's telemetry and broadcast back to Earth. To form an image, an orbiting remote sensor must sample a large number of intensities using a combination of the spacecraft's motion in one direction and some mechanical apparatus for projecting the detector elements at numerous locations in the direction perpendicular to that of the spacecraft's motion. These two directions are known as the *along-track* and *cross-track* directions, respectively. The length of the image along-track is, in principle, one planetary circumference, unless there is some mission requirement or limitation with telemetry that truncates it. For example, the NOAA polar-orbiting satellites continuously broadcast their highest resolution data to Earth as the data are collected. To collect high-resolution NOAA polar orbiter data for a given region, one must have a tracking antenna in the region that will acquire and then lose the spacecraft's signal as it rises above and descends below the horizon. The telemetry sample thus recorded, typically 15 minutes long, will contain an image of the order of 2,000 kilometers in the along-track direction. The cross-track width of the image may

range from a few tens of kilometers to more than a thousand kilometers, depending on the mission and design of the sensor. Crosstrack sampling can be achieved by mechanically scanning the telescope, by using a fixed array of detectors in the focal plane of a widefield telescope, or by a combination of both.

Three quantities that characterize the image formed by an electro-optical device are the *Field Of View* (*FOV*), the *Instantaneous Field Of View* (*IFOV*), and the *Ground Instantaneous Field Of View* (*GIFOV*). The FOV is defined as the angular extent of the sensor's entire cross-track swath, and this varies considerably depending on the mission. The AVHRR aboard the NOAA polar orbiters is designed for synoptic and mesoscale weather imaging at a spatial resolution of 1.1 km (nadir), and it has a large *FOV* of ± 55.4 degrees corresponding to a cross-track swath of order 2,400 km. The Landsat Thematic Mapper (TM) is designed to image terrestrial features at high spatial resolution (10–30 meters), and its *FOV* is only 14.9 degrees, corresponding to a cross-track swath of order 185 km. The *IFOV* is defined as the angular extent of an individual detector element, as projected through the telescope. The projection of the detector onto the scene (Earth surface or desired atmospheric layer) is the *GIFOV*, which is also known as the sensor's *ground spot*. At nadir:

$$GIFOV = h \times IFOV = h \times a/f \tag{2.70}$$

where h is the spacecraft's altitude, and f is the focal length of the optical system. The minimum spatial resolution is estimated as the larger of one of two quantities, either (2.70) or the *diffraction limit*. The diffraction limit is determined by the diameter D of the first obstruction encountered by the radiation before it reaches the detector, which is typically the telescope's objective mirror or lens. In a diffraction-limited system:

$$GIFOV_{\min} \cong 1.22\lambda h/D \tag{2.71}$$

The *GIFOV* is a useful first-order estimate of a sensor's spatial resolution, but the practical spatial resolution is often somewhat different. Where high-quality imaging is required, one must also consider the *modulation transfer function* of the entire optical system (see Schott, 1997 or Chen, 1997).

The most basic device for orbital electro-optical imaging is the *line scanner*. For each wavelength band, a single detector is mechanically scanned in the cross-track direction. A signal is read out from the detector each time the detector projects an additional *GIFOV* in the cross-track direction, creating a line of intensity measurements. The cycle repeats when the spacecraft advances approximately one *GIFOV* along-track, and the resulting adjacent lines of intensity measurements form an image as the spacecraft advances along-track. The time that the detector is allowed to sample the scene intensity before being read out is the *integration time* or *dwell time*. Generally speaking, a longer integration time results in a higher *Signal-to-Noise Ratio SNR* (exceptions are discussed below), and for a given type of detector, a smaller *GIFOV* (higher spatial resolution) requires a longer integration time to achieve a particular *SNR*. The simplest scanning mechanism is a rotating mirror, as is used in the AVHRR (Figure 2.11). While this offers the advantage of a

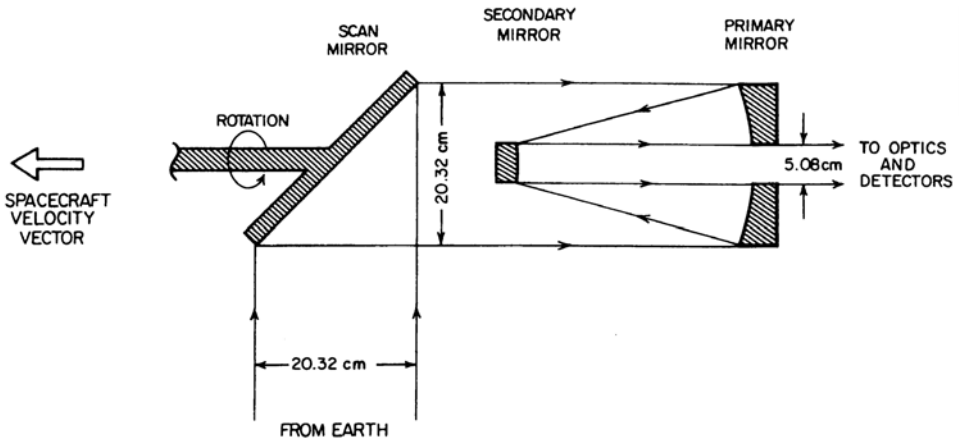

Figure 2.11. Diagram of the Advanced Very High Resolution Radiometer (AVHRR).
From Kidder and Vonder Haar (1995). Copyright 1995 with permission from Elsevier.

relatively simple apparatus, it has the disadvantage of an increasing *GIFOV* toward the edge of a wide cross-track (proportional to $1/\cos\theta$, θ being the nadir angle). Image elements near the edge of the AVHRR's cross-track are greatly elongated and distorted. The Operational Linescan System (OLS) aboard the U.S. Defense Meteorological Satellite Program (DMSP) spacecraft overcomes this problem in two ways. First, the *IFOV* is switched to a smaller value once the scanner reaches a certain angular distance from nadir. Second, the scanner oscillates with a sinusoidal motion that increases the detector's integration time toward the edge of the cross-track so that a consistent SNR can be realized with the smaller *IFOV*.

The major limitation with simple line scanner systems is that a single detector is used to form the entire image. The integration time is therefore relatively short, and this places a limitation on the spatial resolution available from a given type of detector. One way to overcome this limitation is to place a small linear array of N detector elements in the telescope's focal plane, aligned along track. As the telescope scans across track, it will create N scanlines at once, and the integration time can be increased by a factor of N. A scanner with this configuration is known as a *whiskbroom* scanner, the analogy being that of a broom continuously sweeping data elements to one side into the datastream. The Landsat Multi-Spectral Scanner (MSS) series of instruments is one example. A further refinement involves an oscillating scanning telescope that takes data in both crosstrack directions, thus taking advantage of all the useful scan time. The scene coverage scanned in this manner will be oversampled in some areas and will have gaps in coverage in other areas. To correct for this, a scanline corrector consisting of a pair of rotating mirrors is included between the telescope and the focal plane. These mirrors adjust the projection of the detector elements onto the scene such that back-and-forth cross-track scanlines are parallel. Because the trace of the image projection through the scanline corrector resembles a pair of triangles joined at their vertices, this type of

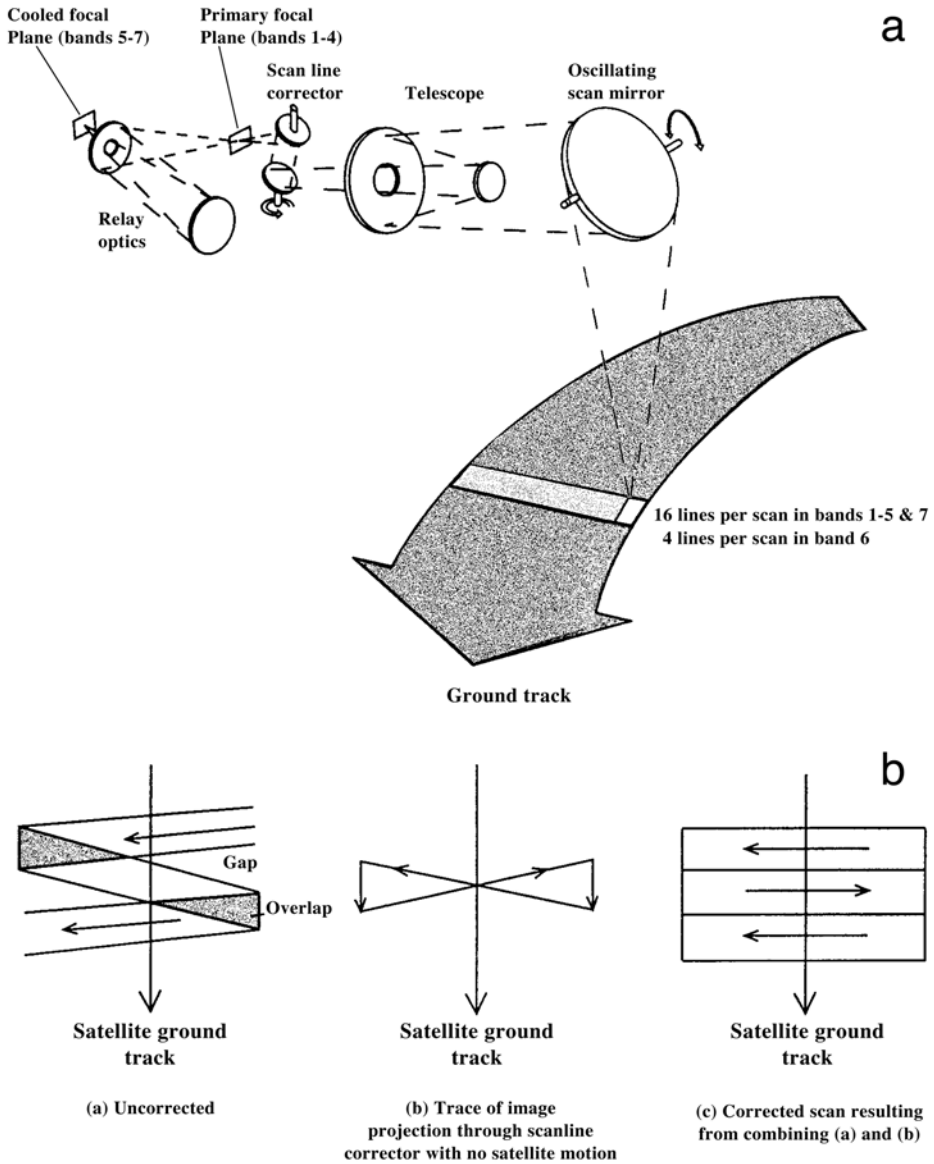

Figure 2.12. The Landsat Thematic Mapper scanning mechanism.

From Schott (1997), *Remote Sensing*, adapted from figs. 5.25 and 5.26. Copyright 1997 by Oxford University Press. Used by permission of Oxford University Press..

scanner is commonly called a *bow tie* imager. The most famous example of a bow tie imager is the TM aboard Landsat 5 and Landsat 7 (Markham and Barker, 1985). A diagram of the Landsat 5 TM scanning mechanism is shown in Figure 2.12. The increased integration time available from bow tie scanning allows the TM to achieve

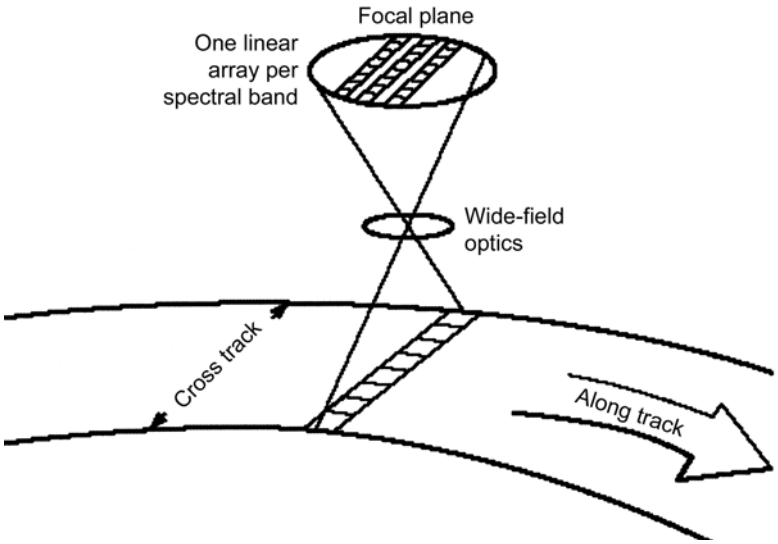

Figure 2.13. The pushbroom scanning configuration.

more than twice the spatial resolution of the older MSS (30-m *GIFOV* in the visible wavelength bands versus 79 m).

Another elegant solution to the problem of optimizing scanning integration time is to use a linear array of detectors to collect an entire cross-track scanline at once. In this *pushbroom* configuration (Figure 2.13), an individual detector element samples only at one angular distance across-track, and integration time can be greatly increased as compared with mechanical scanning systems. This potentially larger SNR, combined with the lack of moving parts, makes the pushbroom configuration very attractive for high-spatial-resolution imaging where a long design lifetime is also required. The French *Système Pour l'Observation de la Terre* (SPOT) is a well-known example of a pushbroom instrument. With detector technology comparable with that of TM, SPOT achieves a *GIFOV* of 10 m in its panchromatic band and 20 m in its spectral bands. There are some complications and drawbacks to the pushbroom configuration. For radiometric calibration, the large number of detector elements requires more effort and expense than is normally the case for a simple line scanner. Wide field-of-view optics are required in the cross-track dimension, yet the cross-track swath of a pushbroom sensor is typically much smaller than that of any scanning instrument (for example, SPOT's 60 km versus TM's 185 km). This makes comprehensive geographical coverage more of a challenge. This challenge can be met by using a cross-track pointing mirror to shift the *FOV* to one side of the spacecraft's ground track, as is done with SPOT. However, the instrument's user community still needs to make choices regarding target selection.

Table 2.1 compares the operational parameters of the imager configurations discussed so far: AVHRR, OLS, SeaWiFS (Sea-viewing Wide Field of View

Table 2.1. Frequently used imagers operational during the 1990s and early 21st century.

Sensor	Sensor configuration	Band wavelengths	Nadir *GIFOV*
NOAA Advanced Very High Resolution Radiometer (AVHRR)	Line scanner	1. 0.58–0.68 μm	1,100 m
		2. 0.72–1.02	1,100
		3. 3.5–3.9	1,100
		4. 10.2–11.4	1,100
		5. 11.4–12.5	1,100
Defense Meteorological Satellite Program (DMSP) Operational LinescanSystem (OLS)	Line scanner with cross-track *IFOV* adjustment	1.	500
		2.	500
NASA Sea-Viewing Wide Field-of-View Sensor (SeaWiFS), line scanner	Line scanner	1. 0.402–0.422	1,100
		2. 0.433–0.453	1,100
		3. 0.480–0.500	1,100
		4. 0.500–0.520	1,100
		5. 0.545–0.565	1,100
		6. 0.660–0.680	1,100
		7. 0.745–0.785	1,100
		8. 0.845–0.885	1,100
NASA Landsat 5 Multi-Spectral Scanner (MSS)	Whiskbroom imager	1. 0.50–0.60	80
		2. 0.60–0.70	80
		3. 0.70–0.80	80
		4. 0.80–1.10	80
		5. 10.41–12.60	237
NASA Landsat 7 Extended Thematic Mapper (ETM+), bowtie imager	Bow tie imager	1. 0.45–0.52	30
		2. 0.52–0.60	30
		3. 0.63–0.69	30
		4. 0.76–0.90	30
		5. 1.55–1.75	30
		6. 10.4–12.5	60
		7. 2.08–2.35	30
		8. 0.50–0.90	15
French Système Pour l'Observation de la Terre (SPOT 5) high-resolution imager	Pushbroom imager	1. 0.48–0.71	5
		2. 0.50–0.59	10
		3. 0.61–0.68	10
		4. 0.78–0.89	10
		5. 1.58–1.75	20

Spectrometer), Landsat MSS, Landsat TM, and SPOT. These are examples of basic ("heritage") electro-optical sensor configurations that serve specific remote-sensing missions very well. However, they are not the last word in sensor design. As discussed in Chapter 1, various instruments with the EOS, Envisat, and ADEOS (ADvanced Earth Observing Satellite) programs take these configurations further

with multiangle viewing to achieve diverse research objectives. These days, nearly every major Earth remote-sensing instrument has a dedicated World Wide Web site, at which specific instrumental configuration and engineering details are posted.

With any electro-optical instrument, the intensities sampled by the detector array need to be assembled into an image by means of detailed geometric corrections. In a linescanner or whiskbroom configuration, the spacecraft steadily advances as the detectors are scanned across-track, necessitating one type of geometric transformation in the data-processing algorithm. In addition, the rotation of the Earth under the spacecraft causes an apparent east or west drift in the ground track, which skews the image. For the most part, the investigator interested in climate change and related disciplines does not need to worry about these details with the data processing. Modern satellite data-processing software packages, such as the SeaSpace (Inc.) TeraScan and TeraVision systems, or the Man-computer Interactive Data Access System (McIDAS) developed at the University of Wisconsin, are generally adept at reducing images from raw telemetry. However, an investigator must always be concerned about image *Earth location*, or *geolocation*. This has to do with sensor-pointing errors or inaccuracies with the spacecraft's onboard clock. Most polar-orbiting spacecraft are tracked by ground radars (for example, at the United States Space Command) only often enough to periodically update knowledge of their orbital elements. Revised orbital elements are then distributed to the user community. Given a set of orbital elements, the spacecraft's location along the ground track can be retrieved from the telemetry as a function of the time recorded by the spacecraft's clock. Hence the geographic location of every intensity sample in the datastream is also known as a function of this time, and a latitude and longitude can be assigned to each image element. However, if there are small pointing errors in the sensor's scanning device, or small drifts in the accuracy of the spacecraft's clock, the actual ground location of the image element can be different from that retrieved from the telemetry by as much as several kilometers. Before using an image for research, an investigator must compare geographic features in the image with a reference database and make necessary corrections. Coastlines and islands are particularly useful for this. Most modern satellite data-processing packages have straightforward algorithms for correcting image Earth location.

2.5 DETECTORS

Detectors for shortwave and longwave radiation fall into two broad categories: *thermal detectors* and *photon detectors*. Examples of thermal detectors include devices such as bolometers, thermocouples, Golay cells, and pyroelectric devices. What all of these devices have in common is that radiation incident upon them causes a readily measurable change in one of their electrical properties, such as resistance. Thermal detectors are not often used in space remote-sensing systems

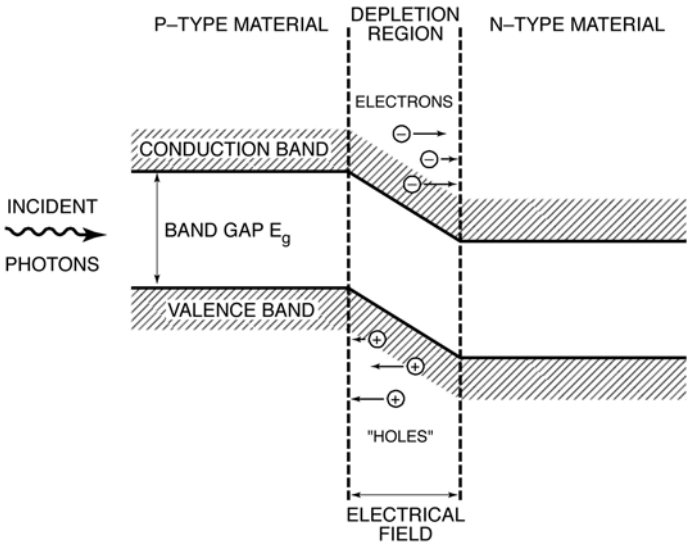

Figure 2.14. Diagram of a p–n junction.

(particularly imagers), primarily because of their long response time. In photon detectors, incident radiation releases electrons in some fashion within the sensing element, resulting in a measurable current proportional to the number of incident photons. Three modes of photon detector operation are the *photoconductive*, *photovoltaic*, and *photoemissive* modes. A thorough discussion is given in Adonovic and Uttamchandani (1989), Dereniak and Crowe (1984), and Schlessinger (1995).

The photoconductive and photovoltaic modes apply to semiconductors. Photons incident on the semiconductor material cause electrons to jump from the fully occupied valence band across the quantum-mechanically forbidden bandgap E_g to the conduction band. The actual device consists of a *p–n junction*, formed by adjoining sections of the semiconductor crystal (Figure 2.14). One section has been adjusted, or "doped" with impurities, to have a slight excess of electrons in the valence band (n-type material). The other section has been adjusted to have a slight deficit of electrons, or excess of positive "holes" (p-type material). Each section by itself is electrically neutral, as the charge of excess free current carriers is balanced out by the corresponding lack of charge in the impurities that give rise to them. When the two sections are brought in contact, electrons diffuse from the n-type material to the p-type side. Conversely, a diffusion of positively charged "holes" occurs in the opposite direction. The result is a local loss of charge neutrality at the junction. Near the junction, the impurities in the n-type material that have donated the diffused electrons remain ionized, and the impurities in the p-type material that have "accepted" electrons retain a slightly negative charge. Hence a potential gradient exists across the junction. Almost immediately after the junction is formed, this potential gradient takes effect and impedes further movement of charge. There is a region at the junction, encompassing part of both the n-type

and p-type sections, in which free charge carriers are swept away by the potential gradient. This is known as the *depletion region*. In some semiconductors such as silicon, a photon having enough energy can excite an electron from the conduction band to the valence band, creating an electron–hole pair. Electron–hole pairs thus formed are quickly swept out of the depletion region by the potential across the p–n junction, resulting in either a measurable voltage or current depending on how the device is biased.

The photovoltaic mode, in its simplest form, involves an unbiased device. The potential at the p–n junction sweeps out photo-excited electron–hole pairs, and the resulting electromotive force drives a current in an external circuit. In the photo-conductive mode a reverse bias is applied to the device, and the photo-excitation of electron–hole pairs increases the conductivity of the device. The photo-conductive mode offers the faster response time—a few nanoseconds—with the tradeoff of needing a relatively high bias voltage. The photovoltaic mode has a response time of only a few microseconds, but offers the advantages of having no dark current, and having very modest power requirements (applied voltages can typically be at logic levels). The lack of a dark current offers an advantage for low d.c. radiation signals. Photovoltaic devices are the most commonly used form of detector. However, in space remote sensing the choice between modes needs to be made based on the required integration time or other engineering parameters.

The three most commonly used semiconductor detector materials are silicon (for wavelengths $\lambda < 1\,\mu m$), indium gallium arsenide (InGaAs, for the near-infrared, wavelengths 2–5 μm), and mercury cadmium telluride (HgCdTe or MCT, for the middle-infrared, wavelengths 5–20 μm). In the infrared, the detector usually needs to be cooled to cryogenic temperatures so that the radiation signal can be detected above thermally induced noise from within the device. The SNR of visible wavelength detectors can often be improved as well by cryogenic cooling. If the required detector operating temperature is above 70 K, a space remote-sensing device can easily be cooled by multistage passive radiators (Chen, 1985). Between operating temperatures of 40–70 K, it becomes more complicated to design a passive radiator, and sometimes closed-cycle cryogenic refrigerators are preferred. Below 40 K some form of open-cycle or closed-cycle cryogenic refrigerator is necessary, and this has an impact on the spacecraft's power consumption and on the design lifetime of the sensor.

Photo-emissive devices offer the greatest sensitivity to visible and near-infrared radiation. In this type of detector, an incident photon ejects electrons from photo-sensitive material called a "photocathode". The free electrons, dislodged into a vacuum, can then be accelerated across a large electric field to form a current that can in principle be measured in an external circuit. A current will only be generated if the incident photons have an energy hc/λ greater than the work function of the photocathode. A metal photocathode will only respond to photons having wavelengths shorter than 300 nm. To detect visible and near-infrared radiation, semiconductors are most often used as photocathodes. In practice, a solitary photocathode will not produce enough electrons to be easily measured using realistic bias voltages. The practical application of photo-emission is the *PhotoMultiplier Tube* (PMT),

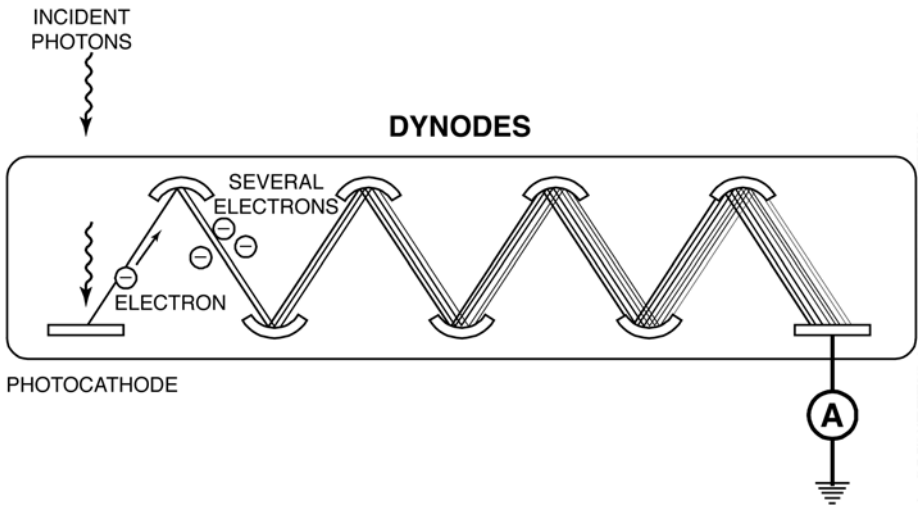

Figure 2.15. Diagram of a PhotoMultiplier Tube (PMT).

shown schematically in Figure 2.15. A single electron dislodged from the photocathode is accelerated across a potential difference toward the first dynode. Upon striking the dynode, the kinetic energy of this accelerated electron dislodges several electrons from the dynode, which are accelerated across another potential difference toward a second dynode. A much larger number of electrons are thus dislodged from the second dynode, which are accelerated toward a third, and so on. A gain of order 10^5 can be achieved with 10 or 11 dynodes, resulting in an easily measurable current. For space-based remote sensing, the biggest limitations with the PMT are (1) large biases and hence a large power source is required, and (2) arrays of these devices are clumsy. However, the very high sensitivity and large linear dynamic range of operation of the PMT (of order 10^8), has allowed this device to be the detector of choice in several critical remote-sensing missions of the 1970s and 1980s. Two examples are the Landsat MSS and the TOMS instruments. The PMT is always an attractive option when one needs to detect low-level monochromatic radiation from a grating or prism spectrometer (TOMS being one example).

This section wouldn't be complete without a description of the detector that is now ubiquitous in popular photography—the Charge-Coupled Device (CCD). The optical and electrical engineering requirements of a CCD for a space remote sensor are naturally much more demanding than those of a pocket digital camera, and in previous decades CCDs were often too difficult or expensive to manufacture and calibrate for space-based applications. Today, however, CCDs are at the heart of many Earth remote-sensing missions. Strictly speaking, the term CCD refers not to the detector itself but to an electronic device for holding and then reading out charges from an array of semiconductor detector elements. Figure 2.16 illustrates this schematically. A discrete charge created by either the photovoltaic or photoconductive effect is introduced into a conducting layer of material, and is

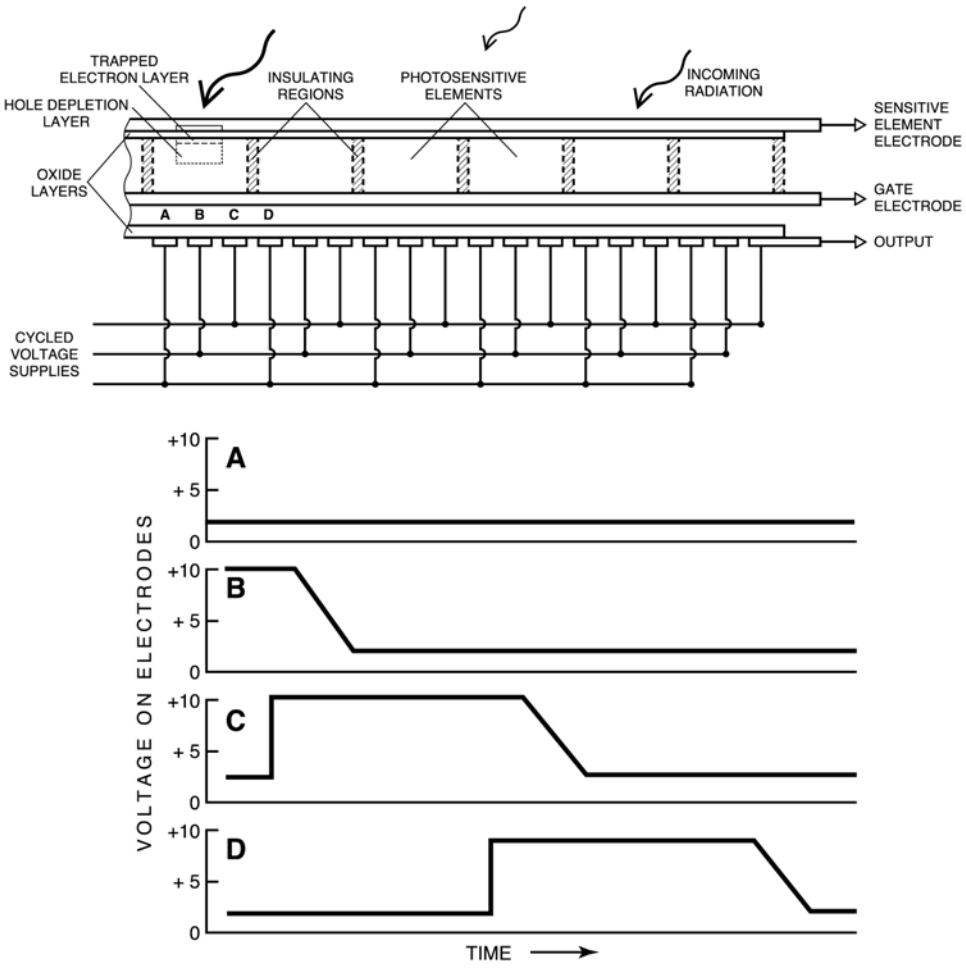

Figure 2.16. Diagram of a Charge Coupled Device (CCD).

kept there by an insulating layer. The charge is kept spatially isolated by a series of electrodes which set up potential wells that keep the charge from moving horizontally. Conceptually, one can imagine three such electrodes making up one charge isolation element for each detector element. After the detector elements in the array have been allowed to integrate (accumulate charges) for a specified period, the polarities of the electrodes are reversed in a sequence of pulse-trains that allows the charge from each detector element to migrate horizontally, one element at a time to the end of its line, and be read out. CCDs are usually made from semiconductors, and can be used merely to store and transfer charges from detector elements of another photo-sensitive semiconductor (for example, a hybrid mid-IR device consisting of an array of HgCdTe detector elements and silicon CCD underneath for efficient charge transfer). However, the CCD itself can also be made

photosensitive, as is often done with visible and near-infrared wavelength silicon detectors.

From common consumer use of CCDs we are familiar with the term *pixel*, referring to one detector element and hence one very small element of a digital image. In remote sensing "vernacular", the term "pixel" often refers to one image element as displayed on a computer monitor, irrespective of how the particular intensity was sampled (mechanical scanning device or photodiode array).

Let us consider the absorption of radiation within a semiconductor device, in order to introduce some detector figures of merit. If we make the approximation that the p-region is very thin, then the power (in Watts) at a given wavelength $P_{0\lambda}$ absorbed by a depletion region of width d can be estimated as:

$$P_\lambda(d) = P_{0\lambda}(1 - r)(1 - e^{-\alpha d}) \tag{2.72}$$

where r is front-surface reflectance (usually negligible due to anti-reflection coatings), and α is the material's absorption coefficient. If each electron–hole pair produced by a photon contributes a single electronic charge $e(= 1.6 \times 10^{-19}$ Coulombs) to the photocurrent, then an expression can be written for the photocurrent i_p (Johnstone, 1989):

$$i_p = \left(\frac{e\lambda}{hc}\right) P_{0\lambda}(1 - e^{-\alpha d}) \tag{2.73}$$

The number of electron–hole pairs produced per incident photon is called the *quantum efficiency* η which can be estimated as:

$$\eta = \frac{\left(\frac{i_p}{e}\right)}{\left(\frac{P_{0\lambda}}{hc}\right)} \tag{2.74}$$

This brings us to the first important detector figure of merit, *spectral responsivity*, which is the ratio of detector output photocurrent to incident radiative power:

$$R_\lambda = \frac{i_p}{P_{0\lambda}} = \frac{\eta e\lambda}{hc} \tag{2.75}$$

All semiconductors exhibit the same general behavior in their spectral responsivity, as shown in Figure 2.17 for Si and InGaAs. The long wavelength limit is determined by the energy bandgap E_g of the material. Photons having energies greater than the bandgap will produce charge carriers, while photons having energies less than the bandgap will not. The result is a sharp cutoff in spectral responsivity at the long wavelength limit. Toward shorter wavelengths, the number of photons per unit of incident radiation flux decreases, resulting in a nearly linear decrease in responsivity with decreasing wavelength. The material's absorption coefficient is typically large at the shortest wavelengths, resulting in noticeably less efficient production of charge carriers in the depletion region, and hence the spectral responsivity begins to

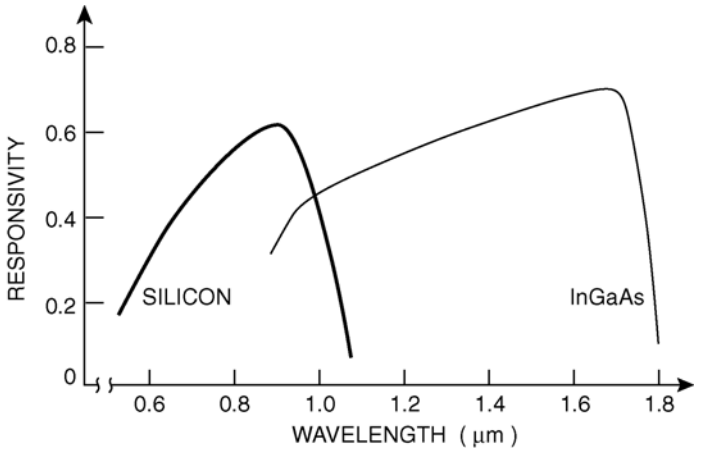

Figure 2.17. Diagram of the typical spectral responsivity for Si and InGaAs.

decrease nonlinearly at the shortest wavelengths. In a remote-sensing instrument, we are usually concerned less with spectral responsivity than with the effective responsivity over a given sensor spectral bandwidth:

$$R = \int_0^\infty R_\lambda \frac{F_\lambda}{\int_0^\infty F_\lambda \, d\lambda} d\lambda \tag{2.76}$$

where F_λ is incident spectral flux. Note that, although detectors in imaging devices are configured to measure intensities by the optics that precede them, at the level of the detector surface itself we describe the responsivity in terms of either the incident flux (Watts per square meter) or the incident power (Watts). The performance of the detector is characterized in terms of Watts per square meter per ampere (or volt), while the entire instrument is radiometrically calibrated in terms of Watts per square meter per steradian per digitized increment of current or voltage.

At a given wavelength, the current or voltage response of a photodetector is generally linear with the incident flux. However, once the incident flux increases to a certain point, no additional charge-carrying electron–hole pairs are created. At this flux level the detector is said to be *saturated*. In a good sensor design, the saturation level of the detector lies just above the maximum intensity expected from the scene (with a suitable margin for error), so that the sensor's *dynamic range* exactly encompasses the range of intensities expected from the scene.

In addition to the spectral response, we need to know the *frequency response*, or *bandwidth* Δf of a detector. This refers to how rapidly a signal can be read from a detector, and is an important consideration when choosing the integration time in the design of a scanning instrument. Three factors that influence the frequency response are (1) the time it takes for photo-generated charge carriers to cross the depletion region, (2) the capacitor-charging (RC) time constant (electrical frequency response) of the detector and its associated circuitry, and (3) the contribution to the

photocurrent of charge carriers generated outside the depletion region. The bandwidth is an important factor in evaluating various sources of detector noise. For an integration time t, the noise equivalent bandwidth is $\Delta f = 1/2t$.

Quantum noise is an irreducible form of noise related to the statistical nature of photon detection (Poisson statistics). Because of the unavoidable randomness in the number of photons per second impinging on the detector, quantum noise (uncertainty) is proportional to the magnitude of the resulting photocurrent, and the noise can be expressed as:

$$i_q = (2e\Delta f)^{1/2} \tag{2.77}$$

A similar form of noise within the detector is *shot noise*. Carrier generation also has a fundamental statistical nature, and the resulting noise current can be expressed as in (2.77). If the only source of current in the detector is signal photons, the shot noise and quantum noise are one and the same. However, there may also be *dark current shot noise*, if there is current flowing in the detector when it is not illuminated. Another form of noise arising within the detector is *generation–recombination noise*, which is the result of random thermal generation of current carriers and their recombination after a short lifetime. This is more of a concern in infrared detectors. *Johnson noise*, also known as *Nyquist noise*, results from the random thermally induced motion of charge carriers (Yariv, 1976). This type of noise is present in any resistive element, and the Johnson noise current has magnitude:

$$i_j = \left(\frac{4kT\Delta f}{\rho}\right)^{1/2} \tag{2.78}$$

where k is Boltzmann's constant, T is the temperature (Kelvin), and ρ is the resistance. There is one form of noise whose explanation is still elusive—$1/f$ noise. The name refers to the power spectrum, which is nearly inversely proportional to the frequency. The cause is known to be related to electrical connectivity between the detector material and its electrodes, and to the presence of carrier traps at the detector surface. However, the magnitude of this noise must be measured, and it can vary considerably between manufacturing lots of the same type of detector. This type of noise (also known as modulation, contact, or current noise) can become the dominant type of noise in the lower frequency range 10–1,000 Hz. When considering all of these sources of noise, we must bear in mind that they apply, first, to the detector element itself, and, second (of equal practical importance), to the early stages of signal amplification (the pre-amplifier circuitry). The pre-amplifier circuitry will inevitably make use of capacitances, particularly for frequency bandwidth selection, and will therefore have an associated *dielectric loss noise*.

The above sources of noise pertain to all photon detectors. CCDs have additional sources of noise. *Transfer noise* occurs when the parcels of charge are moved through the device on readout, and result when a parcel leaves behind a small fraction of charge ξ_1 at one element while perhaps picking up a small fraction of charge ξ_2 at the next element that was left behind by the parcel ahead. Statistical fluctuations in these imperfections at charge transfer result in noise. *Readout noise*

can result from the resetting of the CCD between samples (integration times), although there are several techniques to minimize or eliminate it. If the detector is a hybrid using one material for photodetection and another for charge transfer, then *injection noise* can result when the detectors' charges are inserted into the CCD.

All of the above sources of noise are considered very carefully by optical engineers designing a remote-sensing instrument, and all factor into the instrument's *SNR* in each spectral band. For the user of remote-sensing data, the most important concept to bear in mind is that every remote-sensing instrument is designed for a specific mission or set of missions, and the system *SNR* is optimized accordingly. While we generally expect that less noise—and higher *SNR*—is better, there are practical limits to what can be achieved when one needs to balance spatial resolution (smaller intensities for smaller targets) and wavelength band selection (smaller intensities for smaller spectral intervals). To ascertain whether a particular remote-sensing instrument is suitable for a given research task, the investigator must become familiar with the instrument's original mission and how the *SNR* and dynamic range are optimized for that mission.

Another useful way to describe detector noise is by means of radiometric units. *Noise Equivalent Power*, $NEP(\lambda)$, is the increment in flux at a given wavelength that will change the signal level by an amount equal to the noise. If i_N is the total noise current, then:

$$NEP(\lambda) = \frac{i_N}{R(\lambda)} \tag{2.79}$$

Variations in incident flux must be greater than the *NEP* level before they can be detected. The reciprocal of the *NEP* is called the detectivity $D(\lambda)$. To enable performance comparisons between detectors, we define the specific detectivity $D^*(\lambda)$ by normalizing the detectivity to unit area and bandwidth:

$$D^*(\lambda) = D(\lambda)(A_d \Delta f)^{1/2} = \frac{(A_d \Delta f)^{1/2}}{NEP(\lambda)} \tag{2.80}$$

where Δf is the bandwidth and A_d is the detector area. Examples of D^* for Si and HgCdTe detectors are shown in Figure 2.18. Specific detectivity is the most commonly used figure of merit, because it allows both spectral responsivity and frequency bandwidth to be compared among detector types.

Along the lines of detector noise equivalent power, we can speak of the *Noise Equivalent spectral Radiance*, $NER(\lambda)$ for the entire sensor. This takes into account the optical throughput of the entire system Θ, which to a first approximation is the product of the transmittances or reflectivities of all the optical components (telescope, collimating or scanline-correcting optics, bandwidth selection optics). The *NER* can be estimated as:

$$NER(\lambda) = \frac{NEP(\lambda)}{A_d}\Theta \tag{2.81}$$

The $NER(\lambda)$ is the increment in scene intensity that will change the detector output by an amount equal to the detector's noise level. This is a common and useful

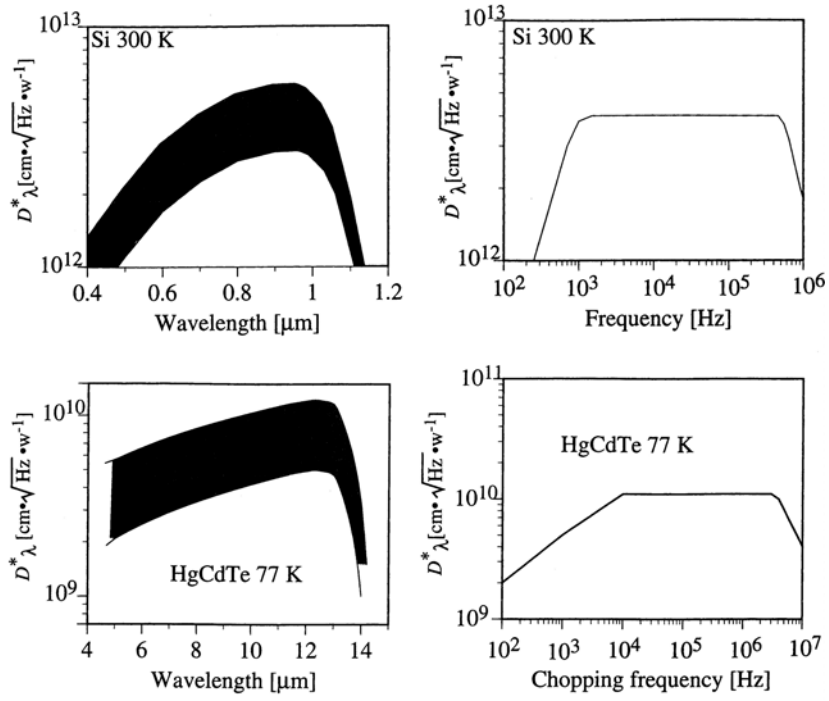

Figure 2.18. Detectivity D^* for Si and HgCdTe.
From Schott (1997). Used with permission of General Dynamics Advanced Information Systems, Inc.

specification. When planning a remote-sensing mission, the science steering committee will usually specify values of *NER*, effective for (integrated over) each channel's spectral bandpass, which the optical engineers must use for design purposes. Self-respecting optical engineers will usually try to beat these specifications. To make the *NER* more intuitive, we sometimes see a noise-equivalent change in reflectance ($NE\Delta r$, for visible and near-IR instruments) or a noise-equivalent change in temperature ($NE\Delta T$, for mid-IR instruments):

$$\left.\begin{aligned} NE\Delta r &= NER\frac{\Delta r}{\Delta I} \\ NE\Delta T &= NER\frac{\Delta T}{\Delta I} \end{aligned}\right\} \tag{2.82}$$

where $(\Delta r/\Delta I)$ is the change in scene intensity in the spectral band corresponding to a change in reflectance of 1% (see Section 2.3.2 for the assumptions that must be built into this specification), and $(\Delta T/\Delta I)$ is the change in scene intensity in the spectral band corresponding to a change of equivalent blackbody temperature by 1 K.

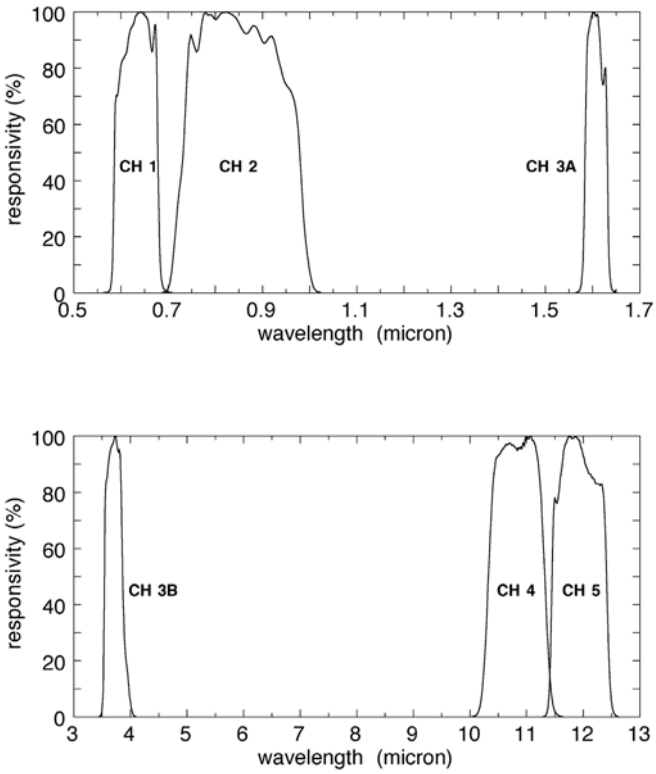

Figure 2.19. Spectral responsivities of the NOAA-15 AVHRR channels.

2.6 SPECTRAL BAND SELECTION

So far, we have discussed most of our radiometric concepts in terms of monochromatic intensities and fluxes, while noting that for most imaging devices the intensities are sampled as integrals over discrete bandpasses (2.76). The width of a particular interval is determined by the task at hand. Generally, one wants as wide an interval as possible to maximize *SNR*, but many applications that utilize absorption features in the atmosphere or water column require relatively narrow intervals of order 10–50 nm. Most imagers accomplish band selection by placing spectral filters at the focal plane, in front of the detectors. In the case where a sensor needs to measure visible and infrared radiation simultaneously using different detector types, a beamsplitter is used after the telescope to send these portions of the electromagnetic spectrum to their respective filter/detector assemblies. To create spectral intervals wider than 100 nm, optical engineers have a large number of high-pass or low-pass filters to choose from. These are similar to the color filters that can be ordered from optical laboratory suppliers such as Newport or Melles-Griot (Inc.), but are manufactured to higher standards for durability in the harsh space environment. For narrower spectral intervals,

interference filters are often used. With either filter type, responsivity within the band will never be perfectly constant with wavelength. Figure 2.19 shows the spectral responsivities of the NOAA-14 AVHRR channels. When designing a remote-sensing retrieval algorithm, intensities should be simulated by a radiative transfer model using enough monochromatic increments to capture the basic shape of the band's spectral responsivity in a weighted integration; e.g.:

$$I_{\text{band}} = \int_0^\infty R(\lambda) I_\lambda(\theta_0, \theta, \phi)\, d\lambda \tag{2.83}$$

This weighted integration yields an intensity in Watts per square meter per steradian. Because most remote sensor bandwidths are relatively narrow and are chosen for a particular spectroscopic feature, it is more common to see sensor intensities expressed in a "monochromatic" form (Watts per square meter per steradian per micron) by dividing the result of (2.83) by an effective width of the spectral response function. In a middle-infrared band, the effective blackbody temperature measured from space, T_B, is the value that satisfies:

$$\int_0^\infty R(\nu)[B_\nu(T_B) - I_\nu(T_S, \tau_\nu)]\, d\nu \tag{2.84}$$

where $I(T_S, \nu)$ is the measured intensity from a scene with characteristic temperature T_S.

2.7 CALIBRATION

Radiometric calibration, the referencing of photon detector counts to recognized standards of spectral irradiance, is one of the most challenging tasks in experimental physics. This challenge is particularly great for a sensor in orbit, beyond all laboratory control. If the changes in intensity measured throughout an image are to be interpreted by radiative transfer algorithms to yield estimates of geophysical quantities, then the standards of radiometric calibration for the instrument must be understood in detail. A detector can always be expected to exhibit gradual changes in responsivity with use, and in the harsh space environment (e.g., bombardment by high-energy particles), responsivity generally deteriorates over time. The spectral throughput of band selection filters can also change over time, due to such processes as vacuum outgassing. These potential changes need to be monitored by regular calibration exercises.

For wavelengths longer than 3 microns, radiometric calibration of Earth remote sensors is generally more reliable because blackbody sources can be used. A blackbody source is an area of very high and spectrally invariant emissivity maintained at one or more fixed temperatures. The reference intensity is the Planck function evaluated at the operating temperature and weighted by the spectral response function for the band. At least two temperatures are required for a complete two-point linear calibration, and this is most often achieved by two

separate blackbody sources. At frequent intervals during data collection the sensor will view the blackbody sources to enable registration of detector photon counts in radiometric units. A passable blackbody source can be made by coating a flat, roughened metal plate with specially designed non-reflecting material. However, in most practical systems a cavity design is used to trap incoming photons and increase the emissivity even more. In the middle-infrared it is straightforward to operate a blackbody source at a range of temperatures that brackets the intensities expected from the Earth–atmosphere system. An important concern in the middle-infrared is that HgCdTe detectors usually exhibit a nonlinearity in their responsivity that cannot be neglected when high radiometric accuracy is needed (e.g., Weinreb et al., 1990). This nonlinearity should be determined at least by published prelaunch calibration procedures, and some missions include a plan for monitoring changes in detector nonlinearity throughout the sensor's lifetime. The researcher should make certain that detector nonlinearity is properly incorporated in data reduction algorithms.

Radiometric calibration in the shortwave is more challenging than in the longwave because the practical shortwave equivalent of a blackbody source is a lamp. In the best of laboratory conditions, the absolute radiometric accuracy of calibration activities using lamps is poorer than those using blackbodies (an uncertainty of $\pm 2.5\%$ is considered good), because there is much more variability associated with hot, glowing filaments. Nevertheless, the best shortwave radiometric calibration is achieved using a tungsten lamp whose spectral output is directly traceable to the National Institute for Standards and Technology (NIST). In practice, only the largest and most expensive remote-sensing missions use such calibration lamps onboard the spacecraft (e.g., MODIS, Landsat 7, CERES). The power requirements are considerable, and the operational lifetime of a calibration lamp is short (typically, in 200 hours of operation the filament will have degraded to the point where the lamp's spectral output is no longer traceable to NIST). In addition, when turning an entire sensor or major part of the sensor to view the internal calibration source (necessary with a staring configuration such as pushbroom), there is the risk of mechanical failure that might leave the instrument jammed in a non-imaging status. Hence, internal calibration sources using lamps are generally used sparingly, as periodic checks on more frequent radiometric calibrations made using a diffuser or vicarious methods. For more modest remote-sensing missions, a solar or lunar diffuser can provide an adequate calibration. In this setup, the solar disk is allowed to fill the sensor's *IFOV* by means of a non-specular surface whose bidirectional reflectance properties are very well-characterized. The degradation rate of this reflecting surface is expected to be very small in the space environment. For a scanning instrument such as SeaWiFS, the rotating or oscillating scanning mirror can be easily configured to view the diffuser in a position outside the *FOV*. For a pushbroom or CCD array scanner, it is more difficult to design a diffuser mechanism. The wide field-of-view optics with these systems make it challenging to design a compact diffuser that will produce a uniform intensity field for all the detectors. If the illumination from the diffuser is not uniform, then not only will a calibration error exist between individual

detector elements, but this error may also be serious enough to cause striping or shading in the image. Although the ideal calibration device is one that lies outside the entire optical path of the sensor, so that the performance of the sensor as a whole is monitored, this cannot always be achieved in a satellite instrument design. Sometimes illumination from a calibration source must be introduced between the telescope and the detector focal plane assembly. For radiometric applications, the researcher needs to understand the sensor's calibration procedure and the associated accuracy and precision.

All shortwave remote sensors are given thorough prelaunch calibration and response characterization using a laboratory integrating sphere. An integrating sphere is a hollow spherical cavity whose interior is coated with a highly reflective, spectrally uniform, and nearly Lambertian material such as Spectralon®. The sphere has one circular aperture allowing light to escape. At various points on the sphere's circumference, away from the line of sight of the aperture, NIST-traceable lamps are mounted to illuminate the interior of the sphere. Multiple reflections within the sphere result in a nearly uniform intensity field at the aperture. If the aperture is large enough to fill the collection aperture of a remote-sensing instrument, the instrument will receive an excellent calibration from a spatially uniform light source. To achieve a high degree of uniformity in the intensity field, the sphere's diameter must be much larger than its exit aperture. Integrating spheres used for calibrating satellite instruments are therefore large devices (more than 2 m in diameter) with their own dedicated laboratory. The flux output of a NIST-traceable lamp cannot be varied. Its operating current must be not only fixed but also carefully monitored. This is why several lamps, typically 10–12, are needed within the sphere. Turning on successive lamps increases the intensity at the aperture such that a responsivity curve can be determined for the instrument being calibrated. With the instrument placed at the sphere's aperture, detector element d in band B will measure an intensity:

$$I_{B,d,n} = \int_0^\infty R_d(\lambda) I_n(\lambda)\, d\lambda \tag{2.85}$$

where $I_n(\lambda)$ is the known spectral radiance of the sphere with n lamps illuminated. The n discrete intensity measurements $I_{B,d,n}$ are used to fit a linear gain function with a slope $Q(B,d)$ and an intercept $b_{B,d}$ (the latter representing a dark current offset):

$$I_{B,d} = Q_{B,d} I_{B,d,n} + b_{B,d} \tag{2.86}$$

The relative spectral responsivity of the instrument $R_{B,d}(\lambda)$, and the wavelength dependence in the integrating sphere's output $I_n(\lambda)$ are both carefully determined using a monochromator.

Some space remote-sensing programs utilize relatively low-cost instruments that are intended to be replaced every 2–3 years. From a programmatic perspective, this can be a reliable way to keep a set of basic Earth remote-sensing measurements in operation from one decade to the next, with frequent redundancy among spacecraft as some of them outlast their design lifetime. One familiar program that has

functioned this way is the NOAA series of polar orbiters. Data from the AVHRR instruments aboard these spacecraft are of immense value to climate change research because they comprise a continuous near-global time series spanning more than two decades. The AVHRR is a straightforward, reliable multispectral imager which lacks complete onboard radiometric calibration. The three infrared channels are calibrated by onboard blackbody sources, but there is neither a diffuser nor an internal lamp apparatus to calibrate the visible and near-IR wavelength channels. The only direct calibration of these channels occurs before launch, per (2.85) and (2.86). To enable radiometric applications of these channels, vicarious calibration procedures have been developed using images of certain Earth scenes that are spatially uniform enough to serve as useful calibration standards (Brest and Rossow, 1991; Masonis and Warren, 2000; Rao and Chen, 1996). The most frequently used scenes are the Libyan desert, White Sands (New Mexico), and the Greenland Ice Sheet (Masonis and Warren, 2000). Examples are shown in Figure 2.20. These vicarious calibration programs have been able to monitor the steady deterioration in AVHRR shortwave channel responsivity, and have produced time-dependent radiometric corrections. Beginning with the NOAA-14 AVHRR, NOAA has provided updated radiometric corrections to the research community (Rao and Chen, 1996) on a regular basis. For earlier NOAA polar orbiter data, the researcher will need to rely on publications by the above-mentioned authors. The International Satellite Cloud Climatology Project (ISCCP), based at the NASA Goddard Institute for Space Studies (GISS), has provided a useful set of vicarious calibrations for earlier AVHRR channel 1 data (Brest and Rossow, 1991). However, there is as yet no complete set of vicarious radiometric corrections for both channels 1 and 2 in the entire AVHRR series. The researcher using some older data may need to perform his or her own calibration using vicarious techniques. Although the ISCCP, NOAA, and similar calibration programs for AVHRR have improved the utility of this sensor considerably, there are important uncertainties related to true spatial uniformity of the scenes and to attenuation by the intervening atmosphere. The radiometric accuracy of the AVHRR shortwave channels can never be as good as that of a sensor with onboard calibration.

2.8 MICROWAVE RADIOMETRY

Microwave radiometry is indispensable in polar satellite remote sensing, because the surface throughout many high-latitude regions is so often obscured by cloud cover. While higher and colder terrains, such as the Greenland Ice Sheet and the Antarctic Plateau, are often cloud-free, the polar oceans experience a higher cloud amount than many other regions on Earth (Warren et al., 1986; 1988). Highly energetic weather systems in the Southern Ocean bring about extensive cloud cover over Antarctic waters year-round. The Arctic Ocean experiences a minimum in cloud amount during winter, but during spring through autumn extensive stratus and stratocumulus clouds are the norm. When a high-latitude scene is cloud-free,

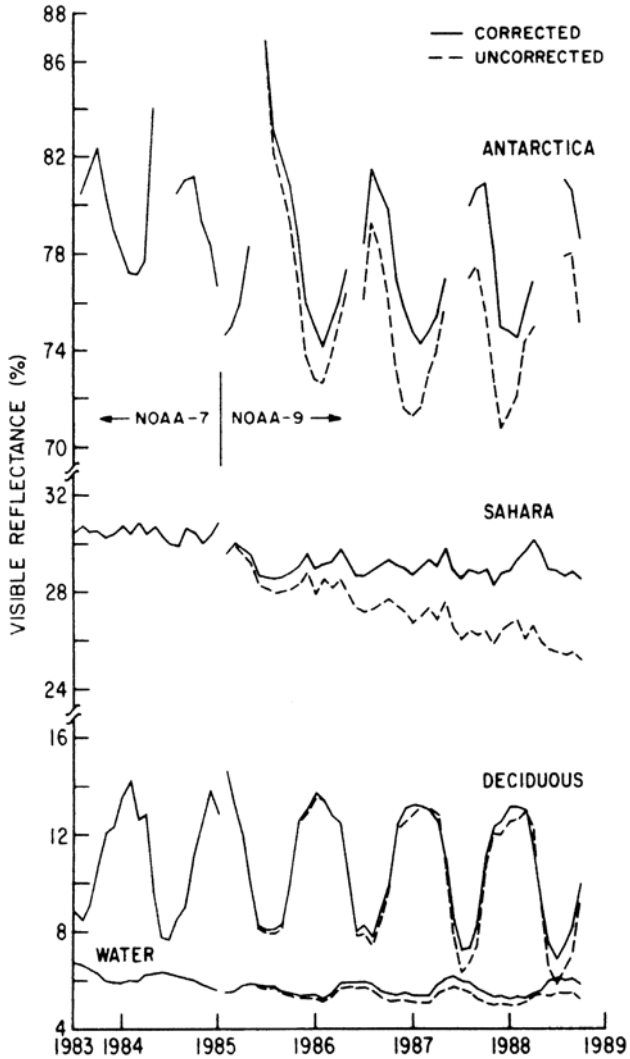

Figure 2.20. Example of deterioration in responsivity for the AVHRR sensor over time, as determined by monitoring selected clear-sky Earth scenes. This type of time series is used in the "vicarious" calibration technique, to derive time-dependent corrections—the radiometric calibration coefficients for sensors such as AVHRR.

From Brest and Rossow (1992), used with permission of Taylor & Francis Ltd. (*http://www.tandf.co.uk*).

spectacular structure is observed in ice streams and sea ice cover, even with "heritage" meteorological satellite imagery having a spatial resolution of only 0.5–1 km. Over continental areas, enough clear-sky imagery can sometimes be collected to enable climatological studies; for example, motion of ice streams (see Chapter 3 of Volume 2 of this book). Over most maritime conditions, cloud-free satellite images are few and far between. Regular observation of sea surface properties can only be

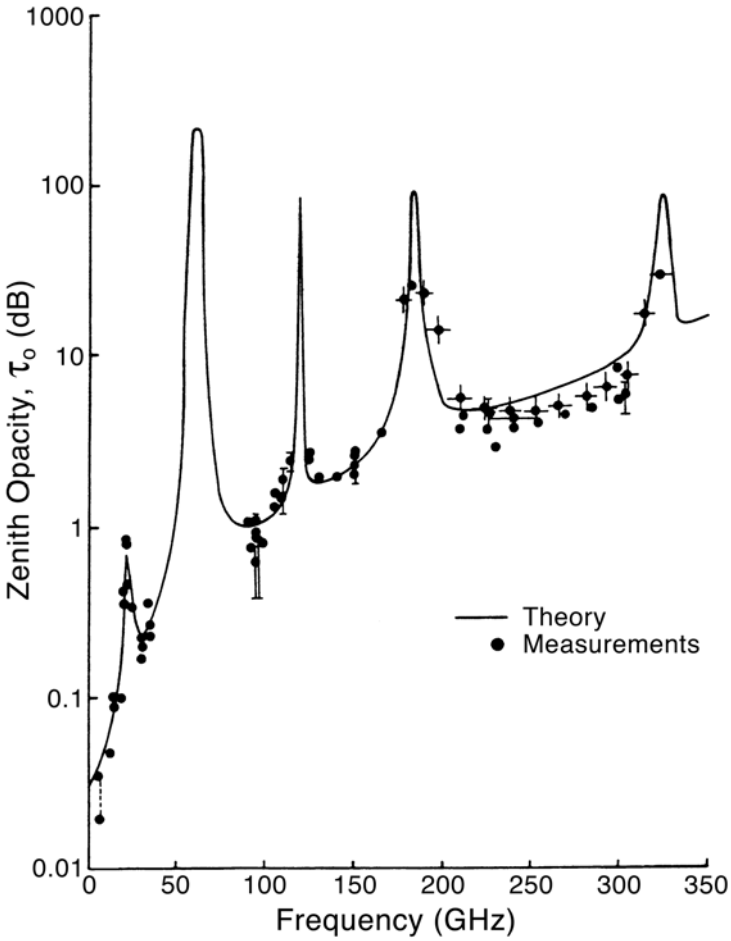

Figure 2.21. A typical zenith opacity in the spectral region used for passive-microwave remote sensing. Local maxima in opacity are from H_2O and O_2 absorption lines (alternating in this plot), starting with H_2O absorption at 22.24 GHz.

From Ulaby et al. (1981). Copyright 1981 by Artech House, Inc.

done at wavelengths where clouds are nearly transparent—in the microwave. Figure 2.21, from Ulaby et al. (1981) shows the opacity of the clear atmosphere and cloud liquid water throughout the wavelength range used in polar microwave remote sensing.

Recalling the Rayleigh–Jeans approximation (2.67), we can see in this case that specific intensity is directly proportional to temperature, and we can cast the radiative transfer equation directly in terms of the medium's effective radiating temperature. In the Rayleigh–Jeans limit, the medium's effective radiating temperature is therefore referred to as the *brightness temperature*, which is directly

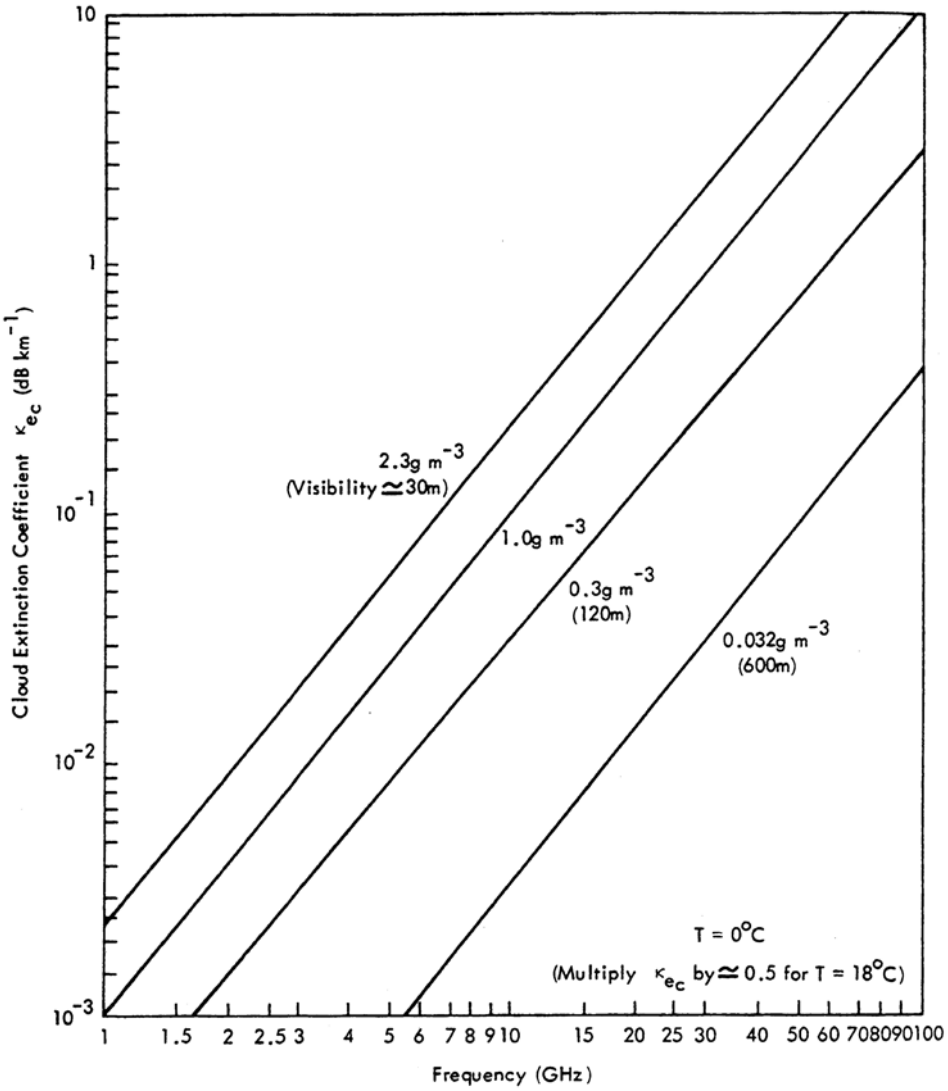

Figure 2.22. The extinction coefficient in the microwave for liquid water clouds of varying water content ($g\,m^{-3}$), at temperature 0°C.

From Ulaby et al. (1981). Copyright 1981 by Artech House, Inc.

related to the physical temperature T by the spectral emissivity:

$$T_b = \varepsilon_\lambda T \tag{2.87}$$

In addition to $hc/\lambda kT \ll 1$, another criterion for (2.87) being valid is that the radiation is due entirely to thermal emission. There are many astrophysical systems where radiation is not thermal (e.g., radio emission from active galaxies, caused by acceleration of elementary particles and following a power spectrum

rather than the Planck function), but from the Earth's natural surface these simple and useful expressions apply.

As with the near- and middle-infrared, certain wavelength ranges correspond to strong rotation bands—particularly 22.2 GHz and 183.3 GHz for water vapor and 60.0 GHz and 118.8 GHz for molecular oxygen (Figure 2.22). The atmosphere is opaque near these frequencies. Elsewhere in the microwave, the atmosphere is as transparent as any of the most useful shortwave or middle-infrared windows. Some of the EOS microwave instruments have bands centered on or near the opaque water vapor rotation features so that atmospheric water vapor profiling can be done. It remains to be seen how well such techniques would work over the polar oceans, where surface microwave brightness temperatures are so variable due to the presence of sea ice. In most polar remote sensing, we are concerned with the microwave frequencies at which one can easily see the Earth's surface from space, even through most cloud cover. These frequencies are generally less than 40 GHz (Figure 2.22), although frequencies as high as 90 GHz can be used with care (Garrity et al., 2002; and see Chapter 5).

Microwave techniques fall into two broad categories—*passive* microwave remote sensing, in which one detects radiation emitted by the scene, and *active* microwave remote sensing, in which a signal is generated by a transmitter and the information is obtained from the reflection of this signal from the scene. Some fundamentals of passive-microwave radiometry are given here, with applications to sea ice covered in Chapter 5. Active microwave techniques for polar remote sensing are discussed in Chapters 2 and 3 of Volume 2 of this book.

In visible and infrared imaging, we discussed sensors in which an optical system allows a specific intensity of radiation from a given *IFOV* to be brought to a detector apparatus at the sensor's focal plane. The detector then registers this radiation into an electrical signal by a quantum-mechanical or solid state process, such as the generation of an electron via the photoelectric effect, or the generation of an electron–hole pair in a semiconductor. For this to work, a photon must have enough energy to jump a semiconductor bandgap, or more energy than the work function of a photocathode. In practice, microwave photons lack this energy, and are detected in the same fashion as most radio signals—with an antenna. An antenna is made of an electrically conducting material, and the arriving photons (electromagnetic waves) induce a fluctuating current in the antenna which is then filtered in frequency ("tuned in"), amplified, and rectified using suitable Radio Frequency (RF) electronics.

A critical concept in antenna design for remote sensing is directional sensitivity. "Classical" antennas in RF theory, such as the half-wave dipole or the quarter-wave vertical, detect electromagnetic radiation efficiently from many directions; large angular ranges perpendicular to the antenna in the former, omnidirectionally perpendicular to the antenna in the latter. For remote sensing, where we want to construct an image from thermal microwave emission, we want the opposite: an antenna that detects electromagnetic radiation from as small a solid angle range as possible. Ideally, all of the antenna's sensitivity would be confined to one narrow solid angle range, or *main lobe*. In practice, all highly directional antennas

have the desired main lobe, but several *side lobes* also exist in which the antenna is again somewhat sensitive (Figure 2.23). As with most relative quantities in RF theory, the sensitivity ratio R_S between the main lobe and side lobes is usually expressed in decibels (dB):

$$R_S = 10 \log_{10}\left(\frac{I_1}{I_2}\right) \tag{2.88}$$

where I_1/I_2 is the ratio of two specific intensities (Watts per square meter per steradian). In this case, if a side lobe is sensitive enough to receive $I_1\,\mathrm{W\,m^{-2}\,sr^{-1}}$, then the main lobe would receive $I_2\,\mathrm{W\,m^{-2}\,sr^{-1}}$, and R_S is the relative sensitivity of the side lobe in dB. For properly designed highly directional antennas $R_S < -20\,\mathrm{dB}$, as referenced to the nominal direction of the main lobe where the power detected is $P_{\max}$.

The directional sensitivity function, as illustrated in Figure 2.23, is known as the power pattern. It specifies the relative sensitivity of the antenna's detection capability as a function of polar and azimuthal angles θ and ϕ, and is normalized to unity in the direction of $P_{\max}$:

$$P_n(\theta, \phi) = \frac{P(\theta, \phi)}{P_{\max}(\theta, \phi)} \tag{2.89}$$

The main lobe is characterized by a *Half Power Beam Width* (HPBW), which is the range in polar angle within which $P_n \geq 0.5$. The antenna's beam solid angle is the integral of the power pattern over 4π steradians:

$$\Omega_A = \int_{4\pi} P_n(\theta, \phi)\, d\Omega \tag{2.90}$$

From the power pattern, we also have the definition of the antenna's *directivity*:

$$D = \frac{4\pi}{\displaystyle\int_{4\pi} P_n(\theta, \phi)\, d\Omega} \tag{2.91}$$

Note that the above description of an antenna's reception requires that the source of the radiation be at a distance greater than the Fresnel distance $d^2/2\lambda$, where d is the antenna diameter, such that the incoming rays of electromagnetic energy can be regarded as parallel. Inside this distance Fresnel diffraction theory must be used to describe the antenna detection pattern.

From the Rayleigh–Jeans approximation (2.67) we can see that flux detected by an antenna is:

$$F_\nu = \frac{2kT_b\, d\Omega}{\lambda^2} \quad (\mathrm{W\,m^{-2}\,Hz^{-1}}) \tag{2.92}$$

and if the scene at which the antenna is pointed contains a range of brightness temperatures $T_b(\theta, \phi)$ the average flux detected by the antenna is:

$$F_\nu = \frac{2k}{\lambda^2} \int_{4\pi} T_b(\theta, \phi) P_n(\theta, \phi)\, d\Omega \tag{2.93}$$

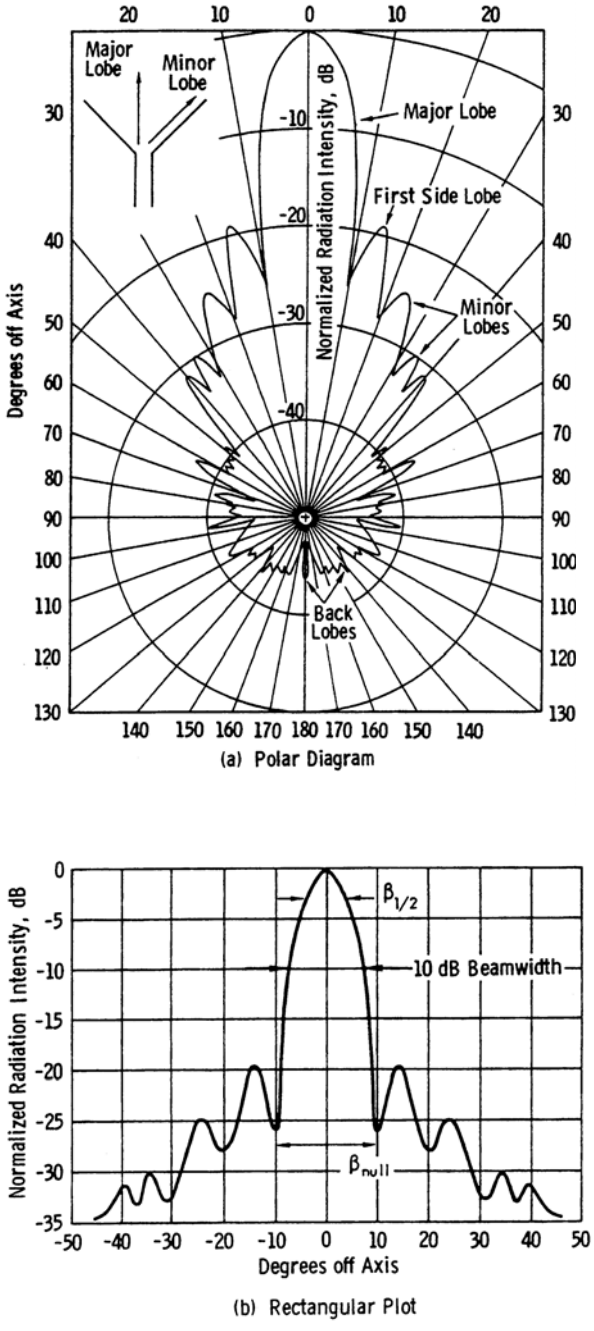

Figure 2.23. Schematic representation of a microwave antenna's power pattern, in polar and rectangular plots.

From Ulaby et al. (1981). Copyright 1981 by Artech House, Inc.

The effective area A_e of the antenna is related to the directivity:

$$D = \frac{4\pi}{\lambda^2} A_e = \frac{4\pi}{\lambda^2} \eta_a A_p \tag{2.94}$$

where A_p is the physical aperture and η_a is an aperture efficiency ($0 \leq \eta_a \leq 1$). From this relationship with the power pattern, we see that an antenna becomes more directive (smaller *GIFOV*) as its aperture area increases.

A fundamental aspect of microwave radiometery is the interpretation of the signal's *polarization*. Polarization refers to the orientation of the electric field vector **E** in an electromagnetic plane wave. If the electric field oscillates in time such that **E** maintains a fixed orientation, the wave is linearly polarized. If instead the tip of the vector **E** traces a circle or an ellipse, the wave is said to be circularly or elliptically polarized. In general, natural scattering processes at any wavelength change the polarization of incident radiation; the radiation field is more rigorously described by a vector consisting of the four Stokes parameters, and scattering is specified by a phase function that is actually a 4×4 matrix (Liou, 1980). To date, the vast majority of shortwave and longwave Earth remote-sensing experiments have neglected polarization, and simply measured total energy intensity as a function of viewing geometry. This is changing, however, with experiments such as the French Polarization and Directionality of the Earth's Reflectances (POLDER) instrument, which can exploit measurements of polarization to study tropospheric aerosol and surface reflectance properties, and which was first flown on the Japanese ADEOS spacecraft in 1996.

In the microwave, measurement of polarization is fundamentally important to remote sensing, as we will see in Chapter 5 (Sea ice). Two polarization components are measured by modern passive-microwave sensors, termed the *horizontal* and *vertical* polarizations. The definition of the horizontal polarization is that component of the vector **E** that oscillates in a plane parallel to the Earth's surface, and perpendicular to the line between the spacecraft and its ground spot. Vertical polarization refers to the component of **E** perpendicular to the horizontal component, and to the line joining the spacecraft to its ground spot. Measurement of these individual components is vital for passive-microwave sea ice mapping. Over open water, measured brightness temperatures are very different for horizontal and vertical polarizations, whereas they are much closer over most sea ice types (Carsey, 1992).

2.9 SPECTRAL RADIOMETRY

Most "heritage" remote sensors have relied on spectral band selection by means of filters or similar methods as described in Section 2.6, and relatively wide bands have been chosen to sample the basic properties of the Earth–atmosphere system, such as surface emission/reflection in atmospheric "windows", fundamental signatures of vegetation or in-water chlorophyll, or radiative properties of clouds and surfaces that depend primarily on the changes in the refractive index of ice and water that

vary slowly with wavelength. Filter-type radiometers are also useful for a few spectroscopic applications, such as the "CO_2-slicing" technique for atmospheric temperature sounding on the edge of the very wide 15-mm CO_2 band (Chapter 4). However, for most spectroscopic applications involving the retrieval of trace gas abundances, filtered radiometers cannot resolve the required individual absorption lines (i.e., for most molecules of interest to stratospheric chemistry) or rapid spectral shifts in absorption bands (e.g., the Hartley and Huggins bands of ozone). For these applications, the intensity scanned by the sensor must be resolved into a spectrum. There are three basic categories of spectrometers used in remote sensing, dispersing spectrometers for the shortwave, interferometers for the longwave, and heterodyne radiometers for the microwave. There are a few notable exceptions to this categorization, as optimal designs for individual instruments are chosen based on specific optical engineering requirements. Nevertheless, the following introduction to spectrometers illustrates how each type is most useful in its particular wavelength range.

It is in this subject area that the term *hyperspectral* applies. This term is most commonly used to describe an instrument that not only records a continuous solar backscatter or thermal emission spectrum, over a relatively large wavelength range (several hundred nanometers in the shortwave, or several microns in the longwave), from a given ground spot, but that also achieves a relatively high *GIFOV* of 1 km or better. One example is NASA's Hyperion experiment launched on the EO-1 spacecraft in November 2000. Spectrometers that record a continuous intensity spectrum but at coarse spatial resolution (tens of km), or instruments that sample monochromatically but not continuously over a given wavelength range, are usually not called hyperspectral.

2.9.1 Dispersing spectrometers

At most shortwave wavelengths, particularly in the visible, sampled radiances are usually large enough that a dispersing element can be used to spread incoming polychromatic radiation into a spectrum in the instrument's focal plane. In modern remote sensors, this is preferred because there are usually no moving parts within the spectrometer apparatus. The spectrum can be recorded directly on a linear detector array in the focal plane. A schematic representation of a dispersing spectrometer is shown in Figure 2.24. After collection by the remote sensor's scanning optics, light enters the spectrometer by an entrance slit, which works in conjunction with a collimating lens or mirror to send parallel rays of light to the dispersing element. In most practical spectrometers, the dispersing element is a reflection grating rather than a prism or transmission grating, because of the former's higher optical efficiency. Following the dispersing element is an imaging lens or mirror that places the spectrum in the focal plane. In the focal plane, the spectrum is composed of an infinite number of adjacent monochromatic images of the entrance slit. For a slit width s, the width W of one

of these images is:

$$W = s\left(\frac{f_i}{f_c}\right) \tag{2.95}$$

where f_i is the imaging element's focal length and f_c is the collimator's focal length.

A thorough text in applied optics (e.g., Hecht, 1990; Kitchin, 1984) will review how a diffraction grating disperses light into many spectra of different orders. The grating consists of a very large number of apertures, which through the principles of Fraunhofer diffraction create many principal maxima in intensity, or fringe patterns, at different angular distances along the image plane for different wavelengths. The grating creates a large number of useful intensity maxima that, combined with the wavelength dependence in their location along the image plane, form numerous *orders* of spectra. These orders, in principle, represent numerous individual spectra resolved in an infinitely wide image plane. In practice, the maxima from various orders quickly overlap such that few orders are useful for spectroscopy. For a given order of integer number m, the angular positions θ_m of the principle maxima are:

$$\theta_m = \sin^{-1}\left(\frac{m\lambda}{d}\right) \tag{2.96}$$

where d is the width of the grating's individual apertures, and λ is the wavelength. The angular width of a principal maximum, defined as the angular distance θ between the zeros in intensity on either side of it, is:

$$W = \frac{2\lambda}{Nd\cos\theta} \tag{2.97}$$

where N is the total number of apertures. The larger the number of apertures, the narrower the principal maxima. Rayleigh's criterion for the resolution of two fringe patterns with approximately equal intensity calls for the coincidence of the principal maximum of one with the first zero of the other. Thus the criterion for resolving maxima of two different wavelengths is:

$$W_m = \frac{\lambda}{Nd\cos\theta} \tag{2.98}$$

and this requires that the spectrometer's entrance slit have a width no larger than:

$$s = \frac{\lambda f_1}{Nd\cos\theta} \tag{2.99}$$

to preserve the grating's spectral resolving power $\lambda/\Delta\lambda$.

Equation (2.96) specifies the basic form of the grating equation:

$$d\sin\theta_m = m\lambda \tag{2.100}$$

The $m = 0$ order contains an original polychromatic view of the source. Typically, one of the lower orders ($m = 1$ or 2) is the desired spectrum for imaging in the focal plane. As shown schematically in Figure 2.24, the incident light is not normal to the grating, but arrives at an angle of incidence θ_i which results in a more general grating

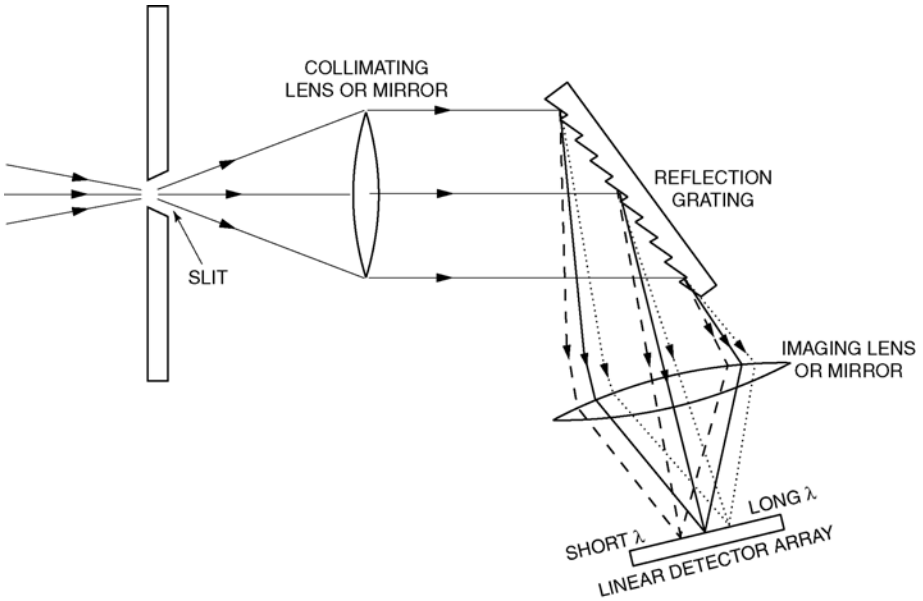

Figure 2.24. Schematic diagram of a dispersing spectrometer.

equation:

$$d(\sin\theta_m - \sin\theta_i) = m\lambda \tag{2.101}$$

The resolving power of the grating is:

$$\frac{\lambda}{\Delta\lambda} = \frac{Nd(\sin\theta_m - \sin\theta_i)}{\lambda} = mN \tag{2.102}$$

which signifies that the higher the order, the better the spectral resolution. The tradeoff is that the higher the order the lower the intensity of the principle maxima, and the larger orders also usually overlap and are useless. In current Earth remote-sensing spectrometers, the resolving power $\lambda/\Delta\lambda$ is typically in the range 1,200–1,500.

In a practical reflection grating, the angle of incidence θ_i isn't arbitrary. The grating's individual apertures are actually small facets set at an angle to the normal, such that at a certain θ_i most of the reflected light is concentrated into a single desired order m. The geometry of these facets is referred to as the grating's *blaze*. In most remote-sensing applications, the blaze is shallow (facets displaced at a relatively small angle from the grating's plane) so that up to 90% of the reflected light can be concentrated into a single lower order. However, in astronomical applications the blaze can be more pronounced, resulting in concentration of the light into several overlapping higher order spectra. These orders must then be separated by a second dispersing element of lower resolution, perpendicular to the first. This device is called an *echelle spectrograph*, and is frequently used with the

largest telescopes to produce spectra with very high resolving power ($\lambda/\Delta\lambda$ up to 60,000). It is conceivable that an echelle spectrograph may find its way into atmospheric remote-sensing applications requiring a greater number of trace gas abundance or profile retrievals.

One additional, important consideration with dispersing spectrometers is the instrument response function, here often called the *slit function*. Although the device reports spectral intensity monochromatically (e.g., Watts per square meter per steradian per nanometer), the spectral resolution is actually finite (2.98). An energy measurement at an exact location θ in the focal plane will contain not only the monochromatic intensity specified by (2.102), but also contributions from adjacent wavelengths on either side, according to a response function that depends on the exact geometry of the spectrometer's entrance slit. This response function is analogous to the broadband examples of Figure 2.19, but is at least an order of magnitude narrower in wavelength. When carrying out radiative transfer calculations to interpret measured spectra, one should normally use a wavelength resolution at least ten times that of the instrument, and then calculate weighted "monochromatic" intensities at the nominal wavelengths using the slit function (analogous to (2.83); also see the TOMS ozone retrieval algorithm in Chapter 3). The slit function is usually available in technical reports on the instrument; where it is not, Gaussian or even triangular approximations of appropriate half-width can often give adequate results.

As mentioned above, one modern advantage of a dispersing spectrometer is the instantaneous recording of a spectrum, with no moving parts required. ESA's Global Ozone Monitoring Experiment (GOME) is one example. In heritage instruments such as the TOMS (Chapter 3), when linear detector arrays were not yet available and PMTs had to be used, a mechanical scanning device such as a chopper had to be used to orient the detector toward selected wavelengths from the grating. Even with this additional mechanical burden, at UV wavelengths a dispersing spectrometer was the only practical option for achieving adequate spectral resolution. Today, with high-sensitivity HgCdTe detector arrays available, there is at least one dispersing spectrometer operating in the longwave, the EOS Atmospheric InfraRed Sounder (AIRS). Traditionally, however, the more common device for achieving spectral resolution in the longwave has been the Michelson interferometer.

2.9.2 Fourier transform spectrometers

The Fourier transform spectrometer, like the diffraction grating spectrometer, makes use of constructive and destructive optical interference, but as a function of time rather than space. A schematic diagram of the most common type, the Michelson interferometer, is shown in Figure 2.25. Light incident from the remote sensor's scanning optics is passed through a beamsplitter, and the two resulting paths are reflected back to the beamsplitter from two different mirrors. These two ray paths are recombined by the beamsplitter and sent to the detector. One mirror is fixed, and the other is allowed to move. If the distances between each mirror and the beamsplitter are at first equal, then as one mirror moves a path difference ΔP

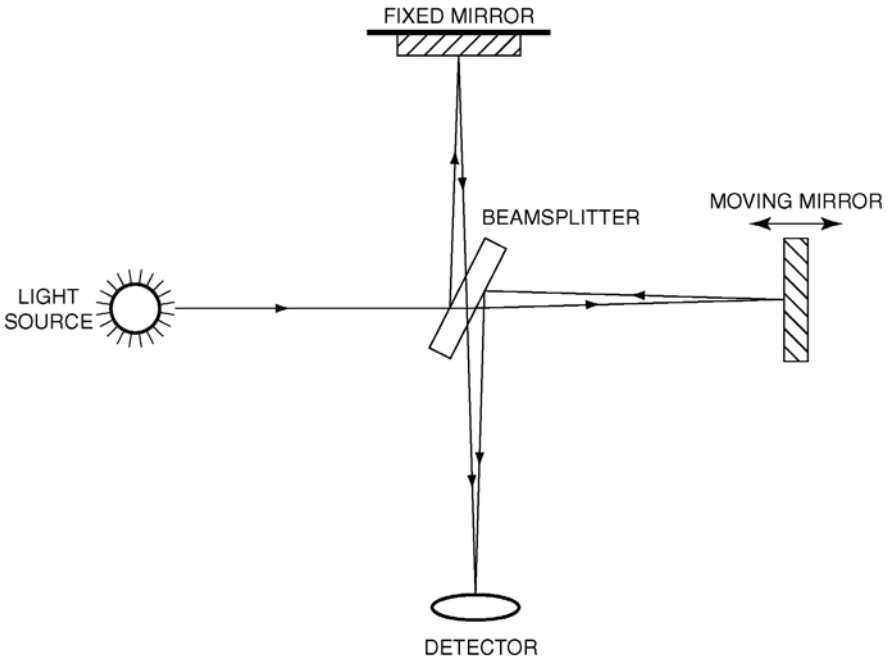

Figure 2.25. Schematic diagram of a Michelson interferometer.

results, which is twice the distance the moving mirror travels. If incident radiation $I_{0\lambda}$ is monochromatic, then the intensity I_d measured by the detector is:

$$I_d = I_{0\lambda}\left[1 + \cos\left(\frac{2\pi\Delta P}{\lambda}\right)\right] \tag{2.103}$$

As the mirror moves and the path difference ΔP changes, the measured intensity oscillates in time sinusoidally through zero and $I_{0\lambda}$ as the light waves interfere with each other constructively and then destructively. Suppose the source consists of two wavelengths. Then two sinusoidal intensity variations with different periods are superimposed and the detector will record the resulting beat frequency. Add more wavelengths and the intensity measured by the detector as a function becomes more complicated, but is interpretable as the Fourier transform of the incident radiation spectrum.

For a monochromatic source, we can express the total intensity measured by the detector in terms of a time-invariant mean intensity and a time-varying term dependent on the path difference ΔP created by the moving mirror:

$$I_d = \int_0^\infty CI(\lambda)\, d\lambda + \int_0^\infty CI(\lambda)\cos\left(\frac{2\pi\Delta P}{\lambda}\right) \tag{2.104}$$

where $C(<1)$ is a constant specifying the optical efficiency of the system. The

time-varying term can be expressed in terms of wavenumber (frequency):

$$I_\nu(\Delta P) = \int_0^\infty I(\nu)\cos(2\pi\Delta P\nu)\,d\nu \tag{2.105}$$

For a polychromatic source, integration over wavenumber yields:

$$\begin{aligned} I_d &= \int_0^\infty I_\nu(\nu)\,d\nu = C_\nu \int_0^\infty [1+\cos(2\pi\Delta P\nu)]I_\nu(\Delta P)\,d\nu \\ &= C_\nu I_0 + \int_0^\infty \cos(2\pi\Delta P\nu)I_\nu(\Delta P)\,d\nu \end{aligned} \tag{2.106}$$

which is in fact applying an inverse Fourier cosine transform to the incident spectrum. Recall that the Fourier transform $F(u)$ of a function $f(t)$ is:

$$\begin{aligned} F(u) &= \frac{1}{\sqrt{2\pi}}\int_{-\infty}^\infty f(t)\exp(-iut)\,dt \\ &= \frac{1}{\sqrt{2\pi}}\int_{-\infty}^\infty f(t)\cos(ut)\,dt - \frac{i}{\sqrt{2\pi}}\int_{-\infty}^\infty f(t)\sin(ut)\,dt \end{aligned} \tag{2.107}$$

where the real part is specified by the cosine transform. A full treatment of Fourier transform spectrometry principles is given by Griffiths and de Haseth (1986).

The spectral resolving power of the Michelson interferometer is:

$$\frac{\lambda}{\Delta\lambda} = \frac{2x}{\lambda} \tag{2.108}$$

where x is the distance traveled by the moving mirror (ΔP ranges from 0 to $2x$, and we use the average value of ΔP).

The intensity recorded by the detector as a function of time, or, equivalently, ΔP, is called an interferogram. It generally consists of a "centerburst" or "white light fringe" that results when ΔP is zero, followed by complicated oscillations that result from increasing ΔP, and that gradually decay to zero. There are two types of interferograms. A one-sided interferogram is generated when the moving mirror travels from zero ΔP out to its maximum distance x. From (2.107), this yields the highest spectral resolution. However, in real instruments it is usually necessary to record a two-sided interferogram, in which the mirror begins at $-x/2$, travels through zero ΔP, and stops at $+x/2$. The resulting intensity pattern consists of a centerburst with nearly identical complicated oscillation patterns decaying to zero on either side. This interferogram achieves only half the maximum possible spectral resolving power; its utility lies in providing information about the phase of the measured interferogram, which permits corrections for optical misalignment (Revercomb et al., 1988). A one-sided interferogram is analogous to the Fourier cosine transform, and transforms back to a real spectrum. A two-sided interferogram transforms to a complex spectrum because it contains two data points (measurements at the same ΔP) per wavenumber. In an optically perfect instrument, both measured intensities for the same ΔP would always be equal, the interferogram would be exactly symmetrical about the centerburst, and the Fourier transform

would be real. In a real instrument, small discrepancies between measurements for the same ΔP yield a slightly asymmetric interferogram that results in an imaginary (phase) component in the Fourier transform.

To achieve the spectral resolving power of (2.107), it can be shown (Griffiths and De Haseth, 1986) that the sampling interval Δx between individual positions of the moving mirror is approximately:

$$\Delta x = \frac{(\lambda_1 + \lambda_2)^2}{16(\lambda_1 - \lambda_2)} \tag{2.109}$$

where λ_1 and λ_2 are the short and long wavelength limits of the desired spectrum. With this expression, we see that sampling intervals typically become smaller than 1 micron at visible and UV wavelengths, while they are tens of microns in the infrared. This mechanical constraint has resulted in Fourier transform spectrometers being used mostly in the infrared, hence the common name Fourier Transform InfraRed (FTIR) spectrometer for this device.

There is an important advantage to using the Fourier transform spectrometer in the infrared, where overall radiance levels are much smaller than in the visible. In a dispersing spectrometer, each detector element records an intensity at essentially one wavelength. In a Fourier transform spectrometer light at all wavelengths contributes to every reading by the detector. This is called the multiplex advantage. Furthermore, the spectral resolution of a Michelson interferometer does not need to be maintained by an entrance slit, and this ultimately allows even more light to fall on the detector. Spectral measurements of longwave radiation emitted by the Earth–atmosphere system were made surprisingly early, by NASA's InfraRed Interferometer Spectrometer (IRIS) aboard the Nimbus-3 and Nimbus-4 spacecraft flown between 1969 and 1972. A modern descendant is the Michelson Interferometer for Passive Atmospheric Sounding (MIPAS), launched on ESA's Envisat in March 2002.

As with dispersing spectrometers, there is an instrument response function that needs to be considered in data analysis. This instrument response function results mainly from finite aperture size and geometry. Another significant source of instrumental error occurs when the moving mirror accelerates from rest or decelerates to a stop. This adds artificial secondary maxima to the far wings of the interferogram. Similarly, abrupt spectral changes in incident intensity, of the same order as the instrument's theoretical resolution, can add to the far wings of the interferogram. To deal with these sources of error, one usually applies an *apodization function* to the interferogram before applying the Fourier transform to retrieve the spectrum. This apodization (or "removing the feet") corrects these errors, but also degrades the spectral resolution. The instrument response function, and the proper apodization function, should both be found in a suitable technical report on the instrument. Their application to data analysis is somewhat different than for a dispersing spectrometer. The desired algorithm's radiative transfer calculations should be performed at a spectral resolution typically two orders of magnitude finer than the instrument's, using a line-by-line algorithm; then this theoretical spectrum is Fourier-transformed to yield a theoretical interferogram. The instrument

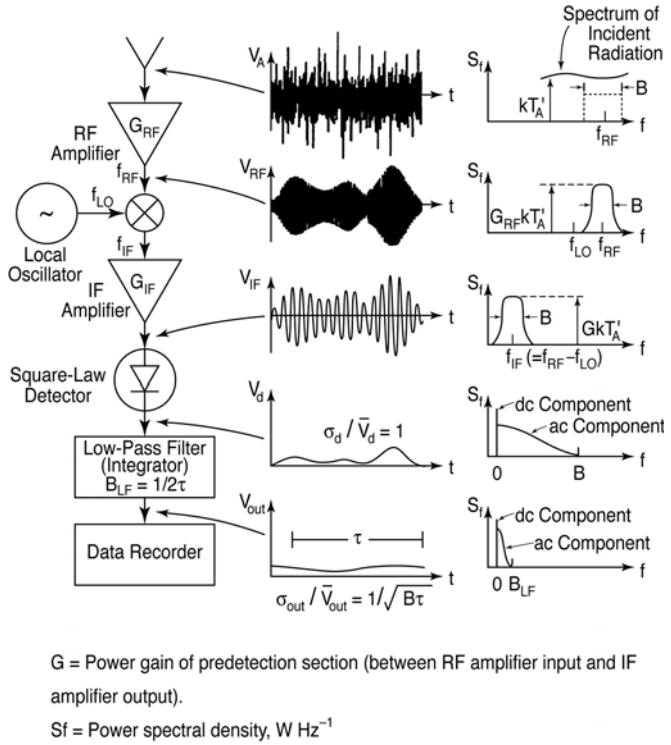

Figure 2.26. Schematic diagram of a superheterodyne radiometer.
From Ulaby et al., 1981. Copyright 1981 by Artech House, Inc.

response and apodization functions are applied to the theoretical interferogram, which is then transformed back into wavenumber space to yield a theoretical spectrum that can be directly compared with the data.

2.9.3 Microwave spectrometers

Above (in Section 2.8) it was casually mentioned that microwave radiometry lies more in the realm of RF as opposed to optical techniques. This is a big understatement, as microwave components are arguably the most challenging RF devices to design and characterize. A complete description of devices such as Gunn oscillators, waveguides, feedhorns, Schottky varactors, and the like is beyond the scope of this chapter. For a comprehensive introduction to microwave radiometry, the reader is referred to Ulaby et al. (1981, chap. 6). One can also gain a basic understanding of microwave techniques from references on modern satellite sensors such as the NASA Microwave Limb Sounder (MLS) instrument (Barath et al., 1993; Waters et al., 1999). There is one technique, common to a great many microwave spectroscopic and radiometric applications, with which the reader should be familiar: the *superheterodyne receiver*.

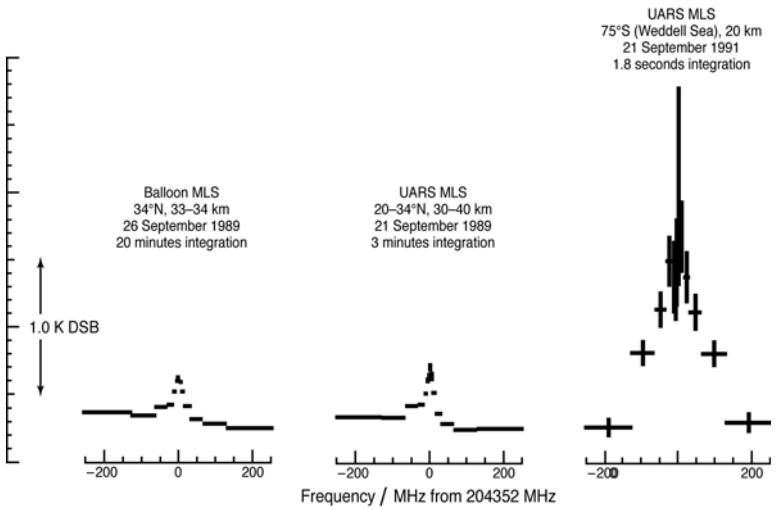

Figure 2.27. Emission lines of ClO (a key player in the Antarctic ozone "hole") over northern and high southern latitudes during September, recorded by the MLS 15-channel filter bank for 205 GHz, showing how this measurement resolves the lineshape such that trace gas abundance can be retrieved with reference to line-by-line radiative transfer calculations.

Superheterodyning has been a standard technique for improving the frequency selectivity of radio receivers since the 1920s, and it remains indispensable for microwave applications. The prefix "super" may be an artifact of early radioset salesmanship, as it ironically refers to reducing rather than increasing the operating frequency. However, the operative term is *heterodyning*—the mixing of two frequencies to produce beat frequencies that are the sum and difference between them. With a suitably designed local oscillator, a signal can be generated that can be heterodyned with the signal from the antenna, in a mixing circuit, to produce an Intermediate Frequency (*IF*) much lower than that from the antenna. This *IF* is then amplified and rectified to extract information. A block diagram is given in Figure 2.26. In basic radio reception, reducing the frequency from the carrier frequency incident on the antenna to an *IF* increases the frequency selectivity of a receiving circuit with a fixed bandwidth. For a fixed receiver bandwidth (%), signals with frequencies close to the one desired might pass through and interfere if left at the carrier frequency, but if the carrier frequency is reduced to a suitable *IF*, the same fixed receiver bandwidth will block the interference. This is known as arithmetic selectivity, and it is an important consideration in the microwave as well. What is more important about heterodyning in the microwave is the ability to transform the signal from a very difficult frequency range in which to design detector components (e.g., 50–200 GHz) to frequency ranges where detector electronics are straightforward and can be very well-characterized (several hundred MHz). Spaceborne instruments, from NASA's pioneering Nimbus-5

Nimbus-E Microwave Spectrometer (NEMS) through the EOS MLS, have inevitably used superheterodyning (Barath et al., 1993; Sabatini, 1972).

In the MLS, spectroscopy in three spectral bands—63, 183, and 205 GHz—is required to remotely-sense the vertical profiles of ozone, ClO, water vapor, H_2O_2, HNO_3, temperature, and pressure. Three radiometers, with local oscillators operating very near these band frequencies, and mixers followed by diplexers, convert the antenna signal into six separate *IF* signals centered at 400 MHz and with a 510-MHz bandwidth. The intermediate-stage amplification of these six 400-MHz signals can be very well-characterized. A second set of local oscillators provides additional heterodyning to convert these *IF* signals into six different new *IF* bandwidths (overall range 90–3,120 MHz) that each encompass a given atmospheric spectroscopic feature. These second *IF* signals are then sent to individual filter banks that split each signal into 15 contiguous spectral channels, thus resolving the desired spectroscopic feature. An example of an MLS spectroscopic detection of ClO in the Antarctic ozone "hole" (Chapter 3) is shown in Figure 2.27.

2.10 REFERENCES

Adonovic, I. and D. Uttamchandani (eds.) (1989). *Principles of Modern Optical Systems*. Artech House, Norwood, MA, 608 pp.

Barath, F. T., M. C. Chavez, R. E. Cofield, D. A. Flower, M. A. Frerking, M. B. Gram, W. M. Harris, J. R. Holden, R. F. Jarnot, W. G. Kloezeman et al. (1993). The Upper Atmosphere Research Satellite Microwave Limb Sounder Experiment. *Journal of Geophysical Research*, **98(D6)**, 10751–10762.

Berk, A., L. S. Bernstein, and D. C. Robertson (1989). *MODTRAN: A Moderate Resolution Model for LOWTRAN 7* (Report GL-TR-89-0122). Air Force Geophysics Laboratory, Hanscom AFB, MA, 38 pp.

Blanchet, J.-P. and R. List (1983). Estimation of optical properties of Arctic haze using a numerical model. *Atmosphere–Ocean*, **21**, 444–465.

Brasseur, G. and S. Solomon (1984). *Aeronomy of the Middle Atmosphere*. D. Reidel, Dordrecht, The Netherlands, 441 pp.

Brest, C. L. and W. B. Rossow (1992). Radiometric calibration and monitoring of NOAA AVHRR data for ISCCP. *International Journal of Remote Sensing*, **13**, 235–273.

Briegleb, B. P. (1992). Delta-Eddington approximation for solar radiation in the NCAR Community Climate Model. *Journal of Geophysical Research*, **97**(D7), 7603–7612.

Bush, B. C. and S. Chakrabarti (1995). Analysis of Lyman alpha and He I 584-Å airglow measurements using a spherical radiative transfer model. *Journal of Geophysical Research*, **100**(A10), 19609–19626.

Carsey, F. D. (ed.) (1992). *Microwave Remote Sensing of Sea Ice* (Geophysical Monograph 68). American Geophysical Union, Washington, DC, 462 pp.

Chandrasekhar, S. (1960). *Radiative Transfer*. Dover, New York, 393 pp.

Chen, H. S. (1985). *Space Remote Sensing Systems: An Introduction*. Academic Press, Orlando, FL, 257 pp.

Chen, H. S. (1997). *Remote Sensing Calibration Systems*. A. Deepak, Hampton, VA, 238 pp.

Clough, S. A., F. X. Kneizys, L. S. Rothman, and W. O. Gallery (1981). Atmospheric spectral transmittance and radiance: FASCOD1B. *Proceedings of the Society of Photo-optical Instrumentation Engineers*, **277**, 152–166.

Clough, S. A., M. J. Iacono, and J.-L. Moncet (1992). Line-by-line calculation of atmospheric fluxes and cooling rates: Application to water vapor. *Journal of Geophysical Research*, **97**(D8), 15761–15785.

Curry, J. A. and G. F. Herman (1985). Infrared radiative properties of summertime Arctic stratus clouds. *Journal of Climate and Applied Meteorology*, **24**, 525–538.

d'Almeida, G. A., P. Koepke, and E. P. Shettle (1991). *Atmospheric Aerosols: Global Climatology and Radiative Characteristics*. A. Deepak, Hampton, VA, 559 pp.

Dereniak, E. L. and D. G. Crowe (1984). *Optical Radiation Detectors*. John Wiley & Sons, New York, 320 pp.

Draine, B. T. and P. J. Flatau (1994). Discrete dipole approximation for scattering calculations. *Journal of the Optical Society of America*, **11**, 1491–1499.

Frederick, J. E. and D. Lubin (1988). The budget of biologically active ultraviolet radiation in the Earth–atmosphere system. *Journal of Geophysical Research*, **93**(D4), 3825–3832.

Fu, Q. and K. N. Liou (1992). On the correlated *k*-distribution method for radiative transfer in nonhomogeneous atmospheres. *Journal of the Atmospheric Sciences*, **49**, 2139–2156.

Garrity, C., D. Lubin, S. Kern, and L. T. Pedersen (2002). Linescan camera evaluation of SSM/I 85.5 GHz sea ice retrieval. *Remote Sensing of Environment*, **83**, 472–487.

Goody, R. M. and Y. Yung (1989). *Atmospheric Radiation: Theoretical Basis*. Oxford University Press, New York, 519 pp.

Griffiths, P. R. and J. A. de Haseth (1986). *Fourier Transform Infrared Spectrometry*. John Wiley & Sons, New York, 656 pp.

Hanel, R. A., B. J. Conrath, V. G. Kunde, C. Prabhakara, I. Revah, V. V. Salomonson, and G. Wolford (1972). The Nimbus 4 infrared spectroscopy experiment: 1. Calibrated thermal emission spectra. *Journal of Geophysical Research*, **77**, 2629–2641.

Hecht, E. (1990). *Optics* (2nd edn). Addison-Wesley, Reading, MA, 676 pp.

Henyey, L. G. and J. L. Greenstein (1941). Diffuse radiation in the galaxy. *Astrophysical Journal*, **93**, 70–83.

Herzberg, G. (1950). *Spectra of Diatomic Molecules*. Van Nostrand, Princeton, NJ, 658 pp.

Jackson, J. D. (1975). *Classical Electrodynamics*. John Wiley & Sons, New York, 848 pp.

Johnstone, W. (1989). Optical Detection. In: I. Adonovic and D. Uttamchandani (eds.), *Principles of Modern Optical Systems*. Artech House, Norwood, MA, pp. 99–128.

Joseph, J. H., W. J. Wiscombe, and J. A. Weinmann (1976). The delta-Eddington approximation for radiative flux transfer. *Journal of the Atmospheric Sciences*, **33**, 2453–2459.

Kidder, S. Q. and T. H. Vonder Haar (1995). *Satellite Meteorology: An Introduction*. Academic Press, San Diego, 466 pp.

Kidwell, K. B. (1991). *NOAA Polar Orbiter Data User's Guide*. National Oceanic and Atmospheric Administration, Boulder, CO.

Kitchin, C. R. (1984). *Astrophysical Techniques*. Adam Hilger, Bristol, 438 pp.

Kniezs, F. X., E. P. Shettle, L. W. Abreu, J. H. Chetwynd, G. P. Anderson, W. O. Gallery, J. E. A. Selby, S. A. Clough, and R. W. Fenn (1988). *User's Guide to LOWTRAN 7* (Report AFGL-TR-88-0177). Air Force Geophysics Laboratory, Hanscom AFB, MA, 137 pp.

Landau, L. D. and E. M. Lifschitz (1975). *The Classical Theory of Fields*. Pergamon Press, Oxford, UK, 402 pp.

Lenoble, J. (1985). *Radiative Transfer in Scattering and Absorbing Atmospheres: Standard Computational Procedures*. A. Deepak, Hampton, VA, 300 pp.

Liou, K. N. (1980). *An Introduction to Atmospheric Radiation*. Academic Press, New York, 392 pp.

Liou, K. N. (1992). *Radiation and Cloud Processes in the Atmosphere*. Oxford University Press, New York, 487 pp.

Liou, K. N., Y. Takano, P. Yang, and Y. Gu (2001). Radiative transfer in cirrus clouds: Light scattering and spectral information. In: D. Lynch (ed.), *Cirrus*, Oxford University Press, New York, pp. 265–296.

Lubin, D. and P. G. Weber (1995). The use of cloud reflectance functions with satellite data for surface radiation budget estimation. *Journal of Applied Meteorology*, **34**, 1333–1347.

Marchuk, G. I., G. A. Mikhailov, M. A. Nazaraliev, R. A. Darbinjan, B. A. Kargin, and B. S. Elepov (1980). *The Monte Carlo Methods in Atmospheric Optics* (Springer Series in Optical Science, Volume 12). Springer-Verlag, New York.

Markham, B. L. and J. L. Barker (1985). Spectral characterization of the Landsat Thematic Mapper Sensors. *International Journal of Remote Sensing*, **6(5)**, 697–716.

Masonis, S. J. and S. G. Warren (2000). Gain of the AVHRR visible channel tracked using bidirectional reflectance of Antarctic and Greenland snow. *International Journal of Remote Sensing*, **22**, 1495–1520.

McInnes, C. L. (1999). *Solar Sailing: Technology, Dynamics, and Mission Applications*. Springer-Praxis, Chichester, UK, 296 pp.

Meador, W. E. and W. R. Weaver (1980). Two-stream approximations to radiative transfer theory in planetary atmospheres: A unified description of existing methods and a new improvement. *Journal of the Atmospheric Sciences*, **37**, 630–643.

Mihalas, D. (1978). *Stellar Atmospheres*. W. H. Freeman & Co., New York, 632 pp.

Molina, L. T. and M. J. Molina (1986). Absolute absorption cross sections of ozone in the 185- to 350-nm wavelength range. *Journal of Geophysical Research*, **91**(D13), 14501–14508.

Montenbruck, O. and E. Gill (2000). *Satellite Orbits: Models, Methods, and Applications*. Springer-Verlag, Berlin, 369 pp.

Penndorf, R. (1957). Tables of the refractive index for standard air and the Rayleigh scattering coefficient for the spectral region between 0.2 and 20 micrometers and their application to atmospheric optics. *Journal of the Optical Society of America*, **47**, 176–182.

Prussing, J. E. and B. A. Conway (1993). *Orbital Mechanics*. Oxford University Press, New York, 194 pp.

Rao, C. R. N. and J. Chen (1996). Post-launch calibration of the visible and near-infrared channels of the Advanced Very High Resolution Radiometer on the NOAA-14 spacecraft. *International Journal of Remote Sensing*, **17**, 2743–2747.

Rees, W. G. (1993). *Physical Principles of Remote Sensing*. Cambridge University Press, Cambridge, UK, 247 pp.

Revercomb, H. E., H. Buijs, H. B. Howell, D. D. LaPorte, W. L. Smith, and L. A. Sromovsky (1988). Radiometric calibration of IR Fourier transform spectrometers: Solution to a problem with the High Spectral Resolution Interferometer Sounder. *Applied Optics*, **27**, 3210–3218.

Ricchiazzi, P. and C. Gautier (1998). Investigation of the effect of surface heterogeneity and topography on the radiation environment of Palmer Station, Antarctica, with a hybrid 3-D radiative transfer model. *Journal of Geophysical Research*, **103**(D6), 6161–6176.

Ricchiazzi, P., S. Yang, and C. Gautier (1989). SBDART: A practical tool for plane-parallel radiative transfer in the Earth's atmosphere. *Bulletin of the American Meteorological Society*, **79**, 2101–2114.

Sabatini, R. R. (1972). *The Nimbus-5 User's Guide*. NASA Goddard Space Flight Center, U.S. Government Printing Office, Washington, DC, 162 pp.

Schlessinger, M. (1995). *Infrared Technology Fundamentals*. Marcel Dekker, New York, 462 pp.

Schott, J. R. (1997). *Remote Sensing: The Image Chain Approach*. Oxford University Press, Oxford, UK, 394 pp.

Shaw, G. E. (1982). Atmospheric turbidity in the polar regions. *Journal of Applied Meteorology*, **21**, 1080–1088.

Slingo, A. and H. M. Schrecker (1982). On the shortwave properties of stratiform water clouds. *Quarterly Journal of the Royal Meteorological Society*, **108**, 407–426.

Stamnes, K., S.-C. Tsay, W. Wiscombe, and K. Jayaweera (1988). Numerically stable algorithm for discrete-ordinate-method radiative transfer in multiple scattering and emitting layered media. *Applied Optics*, **27**, 2502–2508.

Stephens, G. L. (1986). Radiative transfer in spatially heterogeneous two dimensional anisotropically scattering media. *Journal of Quantitative Spectroscopy and Radiative Transfer*, **36**, 51–67.

Stephens, G. L. (1994). *Remote Sensing of the Lower Atmosphere*. Oxford University Press, Oxford, UK, 544 pp.

Suttles, J. T., R. N. Green, G. L. Smith, B. A. Wielicki, I. J. Walker, V. R. Taylor, and L. L. Stowe (1989). *Angular radiation models for the earth–atmosphere system*: Vol. I, *Shortwave Radiation* (NASA Reference Publication RP-1184). NASA Langley Research Center, Hampton, VA.

Taylor, R. V. and L. L. Stowe (1984). Reflectance characteristics of uniform Earth and cloud surface derived from Nimbus-7 ERB. *Journal of Geophysical Research*, **89**(D3), 4987–4996.

Thomas, G. E. and K. Stamnes (1999). *Radiative Transfer in the Atmosphere and Ocean*. Cambridge University Press, Cambridge, UK, 517 pp.

Tiwari, S. N. (1978). Models of infrared atmospheric radiation. *Advances in Geophysics*, **20**, 1.

Tsay, S.-C., K. Stamnes, and K. Jayaweera (1989). Radiative energy budget in the cloudy and hazy Arctic. *Journal of the Atmospheric Sciences*, **46**, 1002–1018.

Ulaby, F. T., R. K. Moore, and A. K. Fung (1981). *Microwave Remote Sensing: Active and Passive* (Vol. I). Artech House, Norwood, MA, 456 pp.

van de Hulst, H. C. (1981). *Light Scattering by Small Particles*. Dover, New York, 470 pp.

Warren, S. G., C. J. Hahn, J. London, R. M. Chervin, and R. L. Jenne (1986). *Global Distribution of Total Cloud Cover and Cloud Type Amounts over Land* (NCAR Tech. Note NCAR/TN-273+STR). National Center for Atmospheric Research, Boulder, CO.

Warren, S. G., C. J. Hahn, J. London, R. M. Chervin, and R. L. Jenne (1988). *Global Distribution of Total Cloud Cover and Cloud Type Amounts over the Ocean* (NCAR Tech. Note NCAR/TN-317+STR). National Center for Atmospheric Research, Boulder, CO.

Warren, S. G., R. E. Brandt, and P. O'Rawe Hinton (1998). Effect of surface roughness on bidirectional reflectance of Antarctic snow. *Journal of Geophysical Research*, **103**(E11), 25789–25807.

Waters, J. W., W. G. Read, L. Froidevaux, R. J. Jarnot, R. E. Cofield, D. A. Flower, G. K. Lau, H. M. Pickett, M. L. Santee, D. L. Wu et al. (1999). The UARS and EOS Microwave Limb Sounder (MLS) experiments. *Journal of the Atmospheric Sciences*, **56**, 194–218.

Wayne, R. P. (2000). *Chemistry of Atmospheres*. Oxford University Press, Oxford, UK, 808 pp.

Weinreb, M. P., G. Hamilton, and S. Brown (1990). Nonlinearity corrections in calibration of Advanced Very High Resolution Radiometer infrared channels. *Journal of Geophysical Research*, **95**(C5), 7381–7388.

Wiesel, W. E. (1997). *Spaceflight Dynamics*. McGraw-Hill, Boston, 331 pp.

Wiscombe, W. J. (1980). Improved Mie scattering algorithms. *Applied Optics*, **19**, 1505–1509.

Wiscombe, W. J. and J. W. Evans (1977). Exponential-sum fitting of radiative transmission functions. *Journal of Computational Physics*, **24**, 416–444.

Yariv, A. (1976). *Introduction to Optical Electronics*. Holt, Rinehart, & Winston, New York, 438 pp.

3

The polar stratosphere

Throughout the greater scientific community, and the general public, Antarctica is known for the "ozone hole" first reported in the mid-1980s. Many people, including scientists and engineers, ask the same questions today that were asked by atmospheric scientists when the phenomenon was first discovered. Why does it happen over Antarctica when the chlorofluorocarbons that supposedly cause it are released far away in the industrialized world? Is it spreading? Is there an "ozone hole" over our heads right now? One of the major success stories in modern science involves how quickly the mechanism for the springtime Antarctic ozone depletion was realized and demonstrated. Even though we now have a very thorough understanding of the heterogeneous chemistry that dramatically depletes stratospheric ozone abundances at high latitudes during spring, there are many remaining issues to understand. For example, is there a relationship between stratospheric ozone depletion and climate warming manifested in the lower troposphere (e.g., Thompson and Solomon, 2002)? Under what circumstances might ozone depletion during the Arctic spring approach the severity of that in the Antarctic? What is the climatology of the various types of polar stratospheric clouds? Given the implementation of the Montreal Protocol, when can we expect polar stratospheric ozone to recover? Satellite remote sensing has an important role to play in addressing all of these questions.

The polar stratosphere is one of the Earth's most unique meteorological regimes, and topics in polar stratospheric chemistry, cloud physics, and dynamics provide some of the most interesting satellite remote-sensing applications. These applications include retrieving the column abundances of exotic trace gases, and unique case studies in cloud microphysics. Since the discovery of springtime polar ozone depletion, several remote-sensing missions have been deployed specifically to research this phenomenon, or have been reconfigured to better understand it. After briefly reviewing the ozone depletion issue, this chapter discusses some of these missions and key remote-sensing techniques, some roles that heritage

instruments such as AVHRR can play, and some of the techniques that will be available from next-generation remote-sensing missions.

3.1 THE SPRINGTIME ANTARCTIC OZONE DECREASE

The "pure oxygen atmosphere" as first proposed by Chapman (1930) was introduced in Section 2.3.3. The abundance of a trace gas can be conceptualized as a balance between sources and sinks or, equivalently, production and loss terms in a continuity equation. In the case of the Chapman chemistry, the chemical sources are (1) the photo-dissociation of O_2 to yield atomic oxygen, and (2) the three-body reaction that combines an oxygen atom with an oxygen molecule to yield an ozone molecule. The chemical sinks are (1) the photo-dissociation of an ozone molecule to yield atomic and molecular oxygen, (2) another three-body reaction that binds two oxygen atoms together, and (3) a two-body reaction in which an oxygen atom and an ozone molecule are transformed into two oxygen molecules. The importance of the various production and loss terms in the continuity equation, related to these processes, are determined by the rates (efficiencies) with which each reaction takes place. In the real atmosphere, additional sources and sinks result from large-scale transport and eddy diffusion.

There is one piece of chemical nomenclature to introduce here: when a molecule contains one atomic constituent plus an odd number of oxygen atoms, it is referred to as an "odd" atom. Thus, atomic oxygen and ozone in 2.26–2.28 are forms of "odd oxygen", NO is a form of "odd nitrogen", and so forth.

The natural climatology of stratospheric ozone is discussed in Brasseur and Solomon (1984). An illustration is given in Figure 3.1. The total ozone column abundance is usually expressed in milli-atmosphere-centimeters, or Dobson units (DU). Because the local ozone concentration varies by orders of magnitude with altitude (maximum in the stratosphere), as shown in Figure 3.2, it is convenient to imagine the total thickness of the atmospheric ozone column condensed to standard temperature and pressure. A typical thickness over mid-latitudes is 0.35 cm or 350 DU. One Dobson unit is the equivalent of 2.6×10^{16} ozone molecules in the entire ozone column overhead. The global and seasonal variability in total ozone abundance shown in Figure 3.1 is due mainly to stratospheric dynamics. The rate of ozone production is greater near the Equator due to greater insolation, but in the stratosphere poleward transport processes are strong and total column abundances are generally the smallest near the Equator. Note that the climatology of Figure 3.1 was compiled before the discovery of springtime Antarctic ozone depletion.

A thorough review of anthropogenic ozone depletion chemistry is given by Solomon (1999). The important concept is the addition of large sinks through *catalytic cycles*, which result in a smaller equilibrium ozone concentration. In a catalytic cycle, one type of atom or molecule—the catalyst—induces a sequence of chemical reactions from which it ultimately emerges intact. The catalyst is then free to start the sequence of reactions all over again. The first catalytic cycles related to

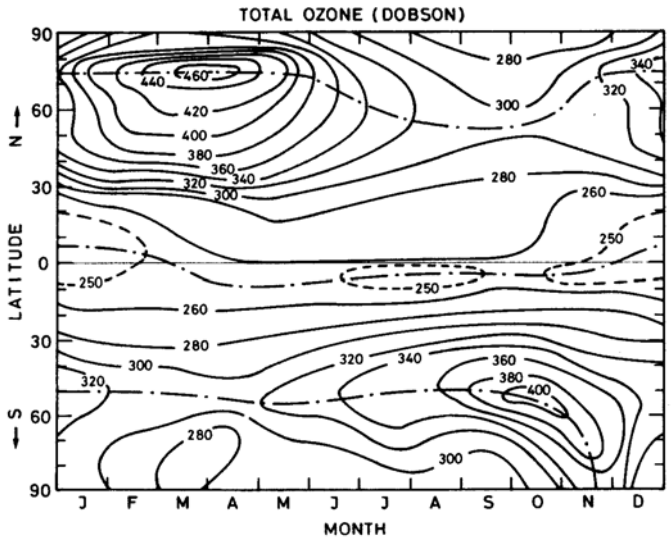

Figure 3.1. Global climatology of atmospheric ozone as a function of latitude and season. This climatology primarily represents the effects of natural photochemistry and stratospheric transport processes, and does not show results of anthropogenic ozone destruction.

From Brasseur and Solomon (1984), *Aeronomy of the Middle Atmosphere*, fig. 5.6, p. 214. Copyright 1984 with kind permission of Springer Science and Business Media.

ozone chemistry were discovered to be hydrogen (Bates and Nicolet, 1950):

$$\left.\begin{aligned} &\mathrm{O} + \mathrm{OH} \rightarrow \mathrm{O_2} + \mathrm{H} \\ &\mathrm{H} + \mathrm{O_2} + M \rightarrow \mathrm{HO_2} + M \\ &\mathrm{O} + \mathrm{HO_2} \rightarrow \mathrm{O_2} + \mathrm{OH} \\ &\overline{\qquad\qquad\qquad\qquad} \\ \text{Net:}\ &\mathrm{O} + \mathrm{O} + M \rightarrow \mathrm{O_2} + M \\ \\ &\mathrm{OH} + \mathrm{O_3} \rightarrow \mathrm{HO_2} + \mathrm{O_2} \\ &\mathrm{HO_2} + \mathrm{O_3} \rightarrow \mathrm{OH} + 2\mathrm{O_2} \\ &\overline{\qquad\qquad\qquad\qquad} \\ \text{Net:}\ &2\mathrm{O_3} \rightarrow 3\mathrm{O_2} \end{aligned}\right\} \tag{3.1}$$

and nitrogen oxide (Crützen, 1970, 1971; Johnston, 1971):

$$\begin{aligned} &\mathrm{NO} + \mathrm{O_3} \rightarrow \mathrm{NO_2} + \mathrm{O_2} \\ &\mathrm{O} + \mathrm{NO_2} \rightarrow \mathrm{NO} + \mathrm{O_2} \\ &\overline{\qquad\qquad\qquad\qquad} \\ \text{Net:}\ &\mathrm{O} + \mathrm{O_3} \rightarrow 2\mathrm{O_2} \end{aligned} \tag{3.2}$$

The first concern about human impact on the ozone layer involved odd nitrogen injection directly into the lower stratosphere by high-altitude aircraft, particularly the supersonic passenger transports that were anticipated during the early 1970s.

The major discovery related to human impact on the ozone layer came with the realization that chlorine is a highly effective catalyst (Stolarski and Cicerone, 1974),

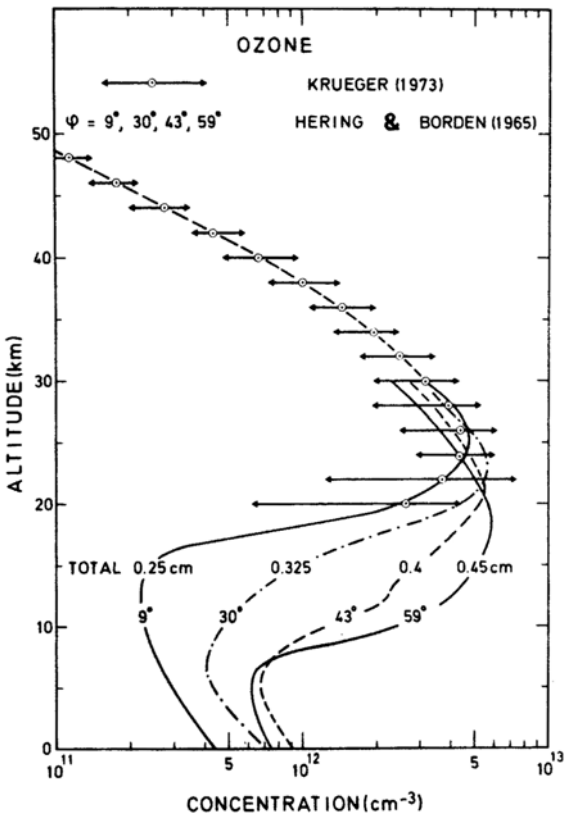

Figure 3.2. Examples of ozone concentration as a function of altitude.

From Brasseur and Solomon (1984), *Aeronomy of the Middle Atmosphere*, fig. 5.7, p. 215. Copyright 1984 with kind permission of Springer Science and Business Media.

and that industrial chlorofluorocarbons are an inevitable source of chlorine in the stratosphere (Molina and Rowland, 1974; Rowland and Molina, 1975). The catalytic cycles are:

$$\left.\begin{array}{l} \mathrm{Cl} + \mathrm{O_3} \rightarrow \mathrm{ClO} + \mathrm{O_2} \\ \mathrm{ClO} + \mathrm{O} \rightarrow \mathrm{Cl} + \mathrm{O_2} \\ \hline \text{Net: } \mathrm{O} + \mathrm{O_3} \rightarrow 2\mathrm{O_2} \end{array}\right\} \qquad \left.\begin{array}{l} \mathrm{Cl} + \mathrm{O_3} \rightarrow \mathrm{ClO} + \mathrm{O_2} \\ \mathrm{ClO} + \mathrm{ClO} + M \rightarrow \mathrm{Cl_2O_2} + M \\ \mathrm{Cl_2O_2} + h\nu \rightarrow \mathrm{Cl} + \mathrm{ClO_2} \\ \mathrm{ClO_2} + M \rightarrow \mathrm{Cl} + \mathrm{O_2} + M \\ \hline \text{Net: } 2\mathrm{O_3} \rightarrow 3\mathrm{O_2} \end{array}\right\} \qquad (3.3)$$

A coupling between bromine and chlorine also occurs (McElroy et al., 1986; Tung et al., 1986), leading to an additional catalytic cycle:

$$\left.\begin{array}{l} \mathrm{Cl} + \mathrm{O_3} \rightarrow \mathrm{ClO} + \mathrm{O_2} \\ \mathrm{Br} + \mathrm{O_3} \rightarrow \mathrm{BrO} + \mathrm{O_2} \\ \mathrm{BrO} + \mathrm{ClO} \rightarrow \mathrm{Br} + \mathrm{ClO_2} \\ \mathrm{ClO_2} + M \rightarrow \mathrm{Cl} + \mathrm{O_2} + M \\ \hline \text{Net: } 2\mathrm{O_3} \rightarrow 3\mathrm{O_2} \end{array}\right\} \tag{3.4}$$

The implication of (3.3) and (3.4) is that a single chlorine atom can catalytically destroy $\sim 10^6$ ozone molecules before being bound in some form of non-reactive molecule and settling out of the stratosphere. There are many natural sources of chlorine, but natural chlorine compounds are generally water-soluble and do not reach the lower stratosphere in a high enough concentration to cause significant ozone destruction. Even hydrochloric acid (HCl) emitted from volcanic eruptions is efficiently removed from the stratosphere (Tabazadeh and Turco, 1993).

In contrast, the chlorofluorocarbons, such as CFC-11 and CFC-12 ($CFCl_3$ and CF_2Cl_2, respectively) were intended for use in refrigeration, and were therefore specifically designed to be highly stable and virtually insoluble in water. These properties make their atmospheric residence times very long. They do not rain out, nor do they react with any chemical species in the troposphere. Measurements from many locations (e.g., Montzka et al., 1996, and references therein) have shown that CFCs are well-mixed in the troposphere, meaning that their concentration does not change appreciably with latitude or longitude. In other words, their lifetimes in the troposphere are long enough that they are transported from their points of release all the way around the globe. As discussed in Andrews et al. (1987) and in Holton et al. (1995), a small fraction of tropospheric air is continually injected into the stratosphere. CFCs carried along with this airmass will cycle through the upper stratosphere over a timescale of $\sim$5 years. The cycling of air between the troposphere and stratosphere constitutes a meridional dynamical cell known as the *Brewer–Dobson circulation*. Volz et al. (1978) summarizes measurements of both CFC-11 and CFC-12 to altitudes as high as 40 km.

As the CFCs circulate to the upper atmosphere, they are exposed to high fluxes of UV-C radiation which photo-dissociate them and release free chlorine. After some catalytic destruction of ozone molecules, the free chlorine becomes bound in "reservoir compounds", so-called because they do not cause ozone depletion. Some of the important reactions leading to reservoir compounds are:

$$\left.\begin{array}{l} \mathrm{ClO} + \mathrm{NO} \rightarrow \mathrm{Cl} + \mathrm{NO_2} \\ \mathrm{Cl} + \mathrm{CH_4} \rightarrow \mathrm{HCl} + \mathrm{CH_3} \\ \mathrm{HO_2} + \mathrm{ClO} \rightarrow \mathrm{HOCl} + \mathrm{O_2} \\ \mathrm{ClO} + \mathrm{NO_2} + M \rightarrow \mathrm{ClONO_2} + M \\ \mathrm{OH} + \mathrm{NO_2} + M \rightarrow \mathrm{HNO_3} + M \end{array}\right\} \tag{3.5}$$

The most common reservoir compound is hydrochloric acid (HCl), which eventually returns to the troposphere and rains out. A commonly asked question is: How long

will it take the ozone layer to recover from chlorine-induced catalytic depletion once CFCs are phased out? As explained by Solomon (1999), the stratosphere contains ~10% of the mass of the atmosphere, while the troposphere contains the other ~90%. Thus the Brewer–Dobson circulation must cycle through at least ten times before the entire tropospheric CFC loading is destroyed, which implies a recovery time of ~50 years. This ozone recovery concept and timescale is supported by recent chemical modeling and statistical analyses (Weatherhead et al., 2000). This assumes that most of the CFC molecules are photo-dissociated once they reach the upper troposphere, which is generally true for CFC-11. For other CFC variants the photo-dissociation rates are slower and their lifetime in the stratosphere will be longer.

The ozone depletion mechanism just described (Reactions 3.3) is known as *gas-phase ozone depletion*, because it involves only the various chlorine and oxygen compounds themselves in the stratospheric environment. The most important thing to note about gas-phase ozone depletion is that, because the free chlorine is released by photo-dissociation in the upper stratosphere, the ozone layer is depleted from the top down. Most gas-phase ozone depletion occurs at altitudes above the midlatitude maximum in ozone concentration (Harris et al., 1998). Thus, the magnitude of total column ozone depletion due to gas-phase chemistry is relatively small—only a few percent per decade. Nevertheless, these small trends have been measured by satellite instruments and they show considerable zonal and meridional variability (Niu et al., 1992).

The major concern over industrially caused ozone depletion has been concurrent increases in biologically harmful UV-B fluxes at the Earth's surface. The increases in UV-B surface flux related to gas-phase ozone depletion are for the most part relatively small; for example, they are equivalent to moving ~100 miles closer to the Equator. If left unchecked, gas-phase ozone depletion can lead to upward trends in surface UV-B flux that are likely to exceed the natural interannual variability in cloud opacity within 1–2 decades at most midlatitude locations (Lubin and Jensen, 1995). However, the stratospheric ozone layer is expected to recover on a timescale of 50–60 years as most nations accede to the Montreal Protocol. At present it is difficult to establish a direct link between health effects such as skin cancer and gas-phase catalytic ozone destruction.

The Antarctic stratosphere provided a dramatic contrast, beginning in the early 1980s. As one example of the useful atmospheric monitoring programs deployed in Antarctica since the International Geophysical Year (1957), the British Antarctic Survey (BAS) has continuously operated Dobson spectro-photometers at their research stations. The Dobson spectro-photometer (Dobson, 1957) measures total column ozone using the technique of *differential absorption spectroscopy* at UV wavelengths (discussed in Section 3.2). By 1985, BAS scientists had noticed that October column ozone abundances over Halley Bay Station were in a significant decline from one year to the next (Figure 3.3). The Japanese Antarctic Program was also recording low springtime column ozone abundances from Syowa Station (Chubachi and Kajiwara, 1986). Between 1978 and 1985, the backscattered UV intensities associated with the low springtime ozone abundances were being measured by NASA's Total Ozone Mapping Spectrometer (TOMS) instrument.

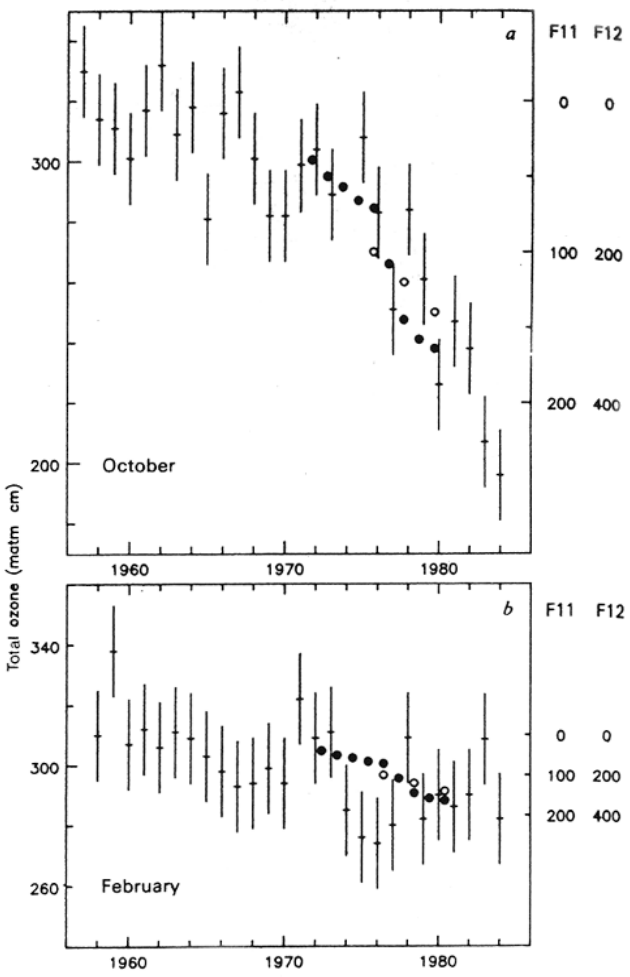

Figure 3.3. The first report of springtime Antarctic ozone decrease, from ground-based spectrophotometer measurements at the British Antarctic Survey's Halley Bay and Argentine Islands research stations.

From Farman et al. (1985). Copyright 1985, *Nature* magazine.

Of these three activities, the BAS scientists are most frequently given the credit for discovering springtime Antarctic ozone depletion, because in their paper they recognized both the importance of the observation and that its likely cause was some form of chlorine chemistry (Farman et al., 1985). As soon as the observations of Farman et al. (1985) were reported the TOMS science team quickly confirmed that springtime Antarctic ozone decrease appeared in their UV backscatter observations and was also a continental-scale phenomenon (Stolarski et al., 1986). An example of the first TOMS observations of the phenomenon is shown in

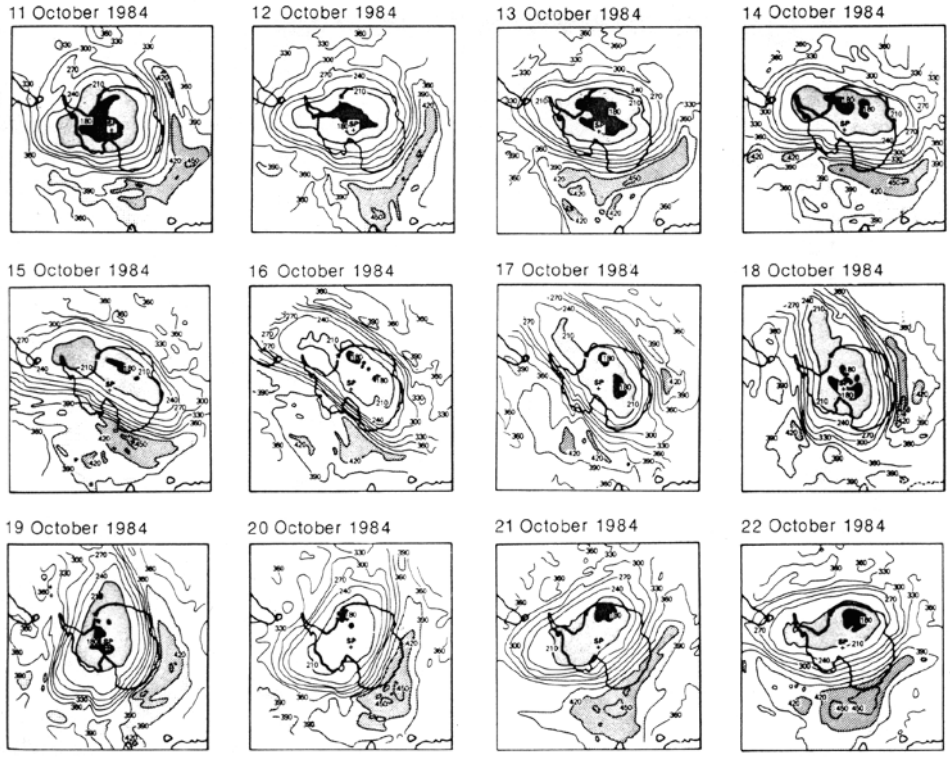

Figure 3.4. The first large-scale satellite maps of the springtime Antarctic ozone decrease, made by the Nimbus 7 Total Ozone Mapping Spectrometer (TOMS).
From Stolarski et al. (1986). Copyright 1986, *Nature* magazine.

Figure 3.4. At the same time, the phenomenon was confirmed by visible wavelength and infrared spectroscopy (Farmer et al., 1987; Mount et al., 1987), thus providing reassurance that the observation was not some local artifact of the UV differential absorption technique. The colloquial expression "Antarctic ozone hole" came about because TOMS observations showed that throughout the early 1980s the phenomenon had been growing in both geographic extent and severity of the ozone decrease. At the time, it wasn't clear that the phenomenon would remain confined to high latitudes.

In 1985–86 there were few detailed observations of the Antarctic stratosphere, and several imaginative hypotheses were proposed to explain the ozone hole. Some were dynamical, while others were related to solar proton events. These hypotheses were compiled in a special edition of *Geophysical Research Letters* published in late 1986 (e.g., Mahlman and Fels, 1986; Tung et al., 1986). The three U.S. National Ozone Expeditions of 1986–1988 quickly provided the observations that supported a mechanism related to human industrial activity. The biggest clue was the set of vertical ozone profile measurements, provided by *in situ* chemical ozone sondes

(e.g., Chubachi, 1984; Hoffman et al., 1987). These observations showed large local minima in ozone concentration in the middle of the stratosphere (12–25 km), as opposed to the monotonic decrease in ozone concentration in the upper stratosphere that would be expected from gas-phase chemistry. These pronounced local minima appeared to correlate with the presence of *Polar Stratospheric Clouds* (PSCs). PSCs have been known to explorers of the Antarctic continent since the days of Captain R. F. Scott, and detailed satellite observations of them were reported by McCormick et al. (1981, 1982). Solomon et al. (1986) hypothesized that heterogeneous chemistry might take place on the surfaces of PSCs, removing chlorine from reservoir compounds.

During the Antarctic winter, the stratosphere over the continent becomes dynamically isolated from stratospheric air at lower latitudes. The absence of insolation for weeks on end leads to cooling of the entire atmosphere column as the Antarctic Earth–atmosphere system radiates to space. Temperatures in the Antarctic stratosphere fall to the lowest recorded anywhere on Earth, sometimes as low as ~180 K. This extremely cold environment is required for PSCs to form. PSCs are classified into two types based on their size and composition. *Type-1* PSCs grow from background stratospheric aerosols and have smaller, sub-micron particle sizes. Ground-based lidar observations have shown that type-1 PSCs can be either liquid or solid, as interpreted from the polarization of the laser backscatter (Browell et al., 1990; Toon et al., 1990). The solid particles (depolarizing) are known as type-1a PSCs, and the liquid particles (non-depolarizing) are known as type-1b PSCs. Early on, Crützen and Arnold (1986) and Toon et al. (1986) suggested that type-1 PSCs might be composed of nitric acid trihydrate (NAT) crystals. The presence of nitric acid in PSCs was confirmed by *in situ* observations by Fahey et al. (1989) and by Gandrud et al. (1989). However, later observations of infrared spectra showed inconsistency with NAT composition (Toon and Tolbert, 1995). Observed size distributions as a function of temperature (Dye et al., 1992; Tabazadeh et al., 1994) have been more consistent with supercooled liquid ternary solutions of HNO_3–H_2SO_4–H_2O, which can remain liquid at temperatures as cold as 188K. Our present understanding of type-1 PSCs is that they are liquid much of the time, and it is actually the freezing mechanism of these particles, at temperatures above the frost point, that is not yet clear (Santee et al., 1998; Tabazadeh et al., 1996). In contrast, the mechanism of *type-2* PSCs (ice–water–cloud) formation at temperatures below the frost point is straightforward (Poole and McCormick, 1988a, b). Type-1a or -1b PSC particles grow from background stratospheric aerosols, which grow further into type-2 PSCs if temperatures fall below the frost point.

Shortly after the ozone "hole" was discovered, an important set of observations from ground-based microwave remote sensing (de Zafra et al., 1987, 1989) and airborne *in situ* resonance fluorescence techniques confirmed the presence of greatly enhanced active chlorine species in the springtime Antarctic stratosphere around 20 km. In particular, the observed abundance of ClO was of the order of 1 ppbv, 100 times larger than that expected from gas-phase chemistry. Satellite observations, discussed below, later confirmed the geographic extent of the enhanced ClO abundances, which could only be explained by the substantial

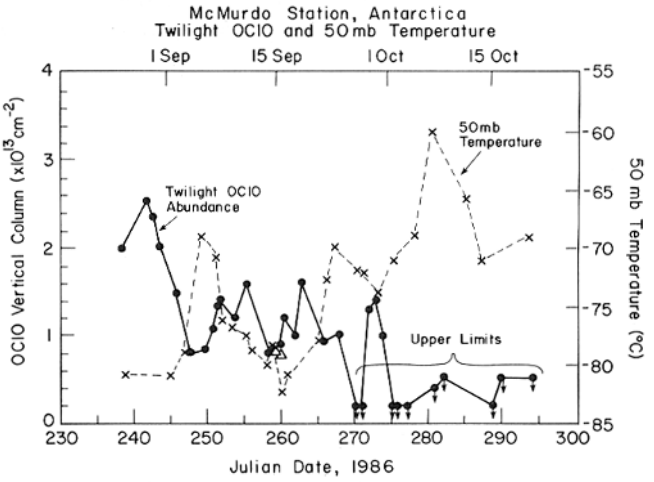

Figure 3.5. The column abundance of OClO measured at McMurdo Station, Antarctica, using visible wavelength spectroscopy.

From Solomon et al. (1987a). Copyright 1987 American Geophysical Union. Reproduced by permission of American Geophysical Union.

release of chlorine from the reservoir compounds HCl and $ClONO_2$. Measurements of the HCl column abundance also suggested conversion to active chlorine (Coffey et al., 1989; Farmer et al., 1987). The visible spectroscopy of column OClO abundance (Solomon et al., 1987a) further demonstrated the gigantic enhancements in active chlorine, and also demonstrated their seasonal cycle—a decrease between August and October (Figure 3.5). Thus, less than three years after the discovery of the springtime Antarctic ozone decrease, the scientific community had a robust set of measurements that were consistent with massive chlorine activation for catalytic ozone destruction due to the presence of PSCs. The major heterogeneous reactions that occur on PSC surfaces to activate chlorine are:

$$\left.\begin{aligned} &HCl + ClONO_2 \rightarrow HNO_3 + Cl_2 \\ &N_2O_5 + H_2O \rightarrow 2HNO_3 \\ &ClONO_2 + H_2O \rightarrow HNO_3 + HOCl \\ &HCl + HOCl \rightarrow H_2O + Cl_2 \\ &BrONO_2 + H_2O \rightarrow HNO_3 + HOBr \\ &HCl + BrONO_2 \rightarrow HNO_3 + BrCl \\ &HCl + HOBr \rightarrow H_2O + BrCl \end{aligned}\right\} \quad (3.6)$$

We now know that heterogeneous chlorine activation chemistry can occur on all types of PSC particles found in the polar regions, regardless of particle phase, at altitudes around 20 km for temperatures below ~198 K. At altitudes 12–14 km, the heterogeneous chemistry can occur at temperatures as warm as 200–210 K.

To summarize, the mechanism for the ozone "hole" involves both human influence and the unique meteorology of the polar stratosphere, as illustrated in Figure 3.6. During the Antarctic winter, the stratosphere over the continent and

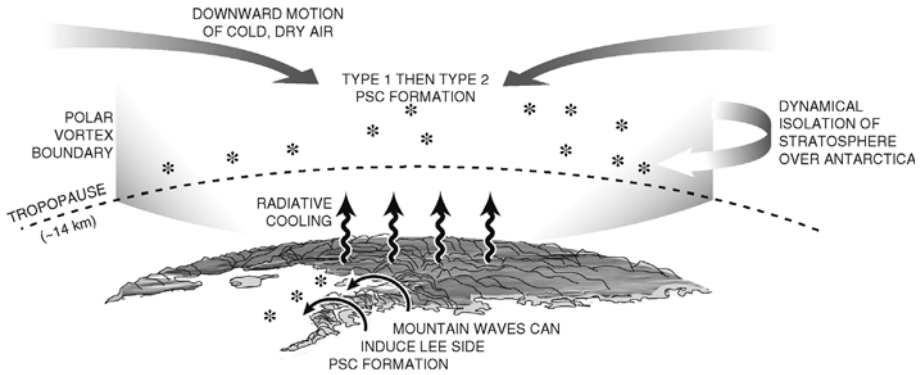

Figure 3.6. Schematic diagram of the mechanisms behind the springtime Antarctic ozone decrease.

part of the Southern Ocean becomes dynamically isolated from lower latitudes and cools radiatively to space, creating the "polar vortex". As the temperature decreases, first type-1 and then type-2 PSCs form. The polar vortex persists into September and October, as dynamical isolation continues and as the net downward motion of stratospheric air does not cause enough adiabatic warming to dissipate the PSCs. The heterogeneous chemistry (3.6) removes chlorine from the reservoir compounds and places it into photochemically active compounds such as Cl_2 and HOCl. As the sunlight returns in September, photo-dissociation releases atomic chlorine which catalytically destroys the stratospheric ozone column over Antarctica. At 20 km, all of the ozone is destroyed within 40–60 days after the Sun rises. A process which enhances this ozone destruction is *denitrification*. This refers to the removal of reactive nitrogen (necessary to restock the reservoir compounds) from the stratosphere by the settling out of PSC particles containing nitric acid (Toon et al., 1986). Early on, it was believed that denitrification was essential in allowing ozone depletion to persist throughout the spring. Because heterogeneous chlorine activation chemistry can occur on liquid type-1b PSCs and at warmer temperatures than previously realized, we now realize that denitrification enhances ozone destruction but is not essential for its persistence during spring. During late spring, the polar vortex breaks down and ozone-rich air from lower latitudes replenishes the depleted stratospheric column over Antarctica. During the 1990s, Antarctic ozone "hole" events became as severe as possible, with all stratospheric ozone being wiped out at some altitudes over much of the continent and part of the Southern Ocean, and with the depletion lasting into early December.

3.2 THE TOTAL OZONE MAPPING SPECTROMETER

Perhaps the most important stratsopheric quantity that can be studied by remote sensing is total column ozone abundance. Retrieval of total column ozone from

space can be achieved with high accuracy using the method of *differential absorption spectroscopy*. This method can be used for column retrievals of many trace gases from space or from the ground (e.g., Solomon et al., 1987b). For ozone, the method takes advantage of the large variability in the ozone absorption cross section throughout the UV-B and UV-A parts of the spectrum (Figure 2.7). Since a measured intensity or flux depends approximately exponentially on the product of the absorption cross section and column density (i.e., optical depth), a ratio or difference in intensities or fluxes measured at different wavelengths having significantly different values of the absorption cross section will be a strong function of the absorber column amount. This function can be calculated using a radiative transfer model. This method has been applied since the 1930s, when Dobson spectro-photometers were first developed (Dobson, 1957). The method is conceptually straightforward, yet it can be difficult to implement in practice with a space-based instrument. The TOMS program is discussed in detail here to illustrate one highly successful application.

3.2.1 The TOMS instrument and algorithm

The TOMS series began operation on November 1, 1978, with an instrument aboard NASA's Nimbus 7 spacecraft. The Nimbus 7 TOMS was a remarkably durable instrument that provided near-continuous useful data until May 6, 1993. A follow-on TOMS was deployed on the Russian Meteor-3 spacecraft, and provided data from 22 August, 1991 until 24 November, 1994. Meteor-3 TOMS analysis was complicated somewhat by that spacecraft's non-Sun-synchronous orbit. Another TOMS instrument was deployed aboard the Japanese ADEOS (ADvanced Earth Observing Satellite) spacecraft, which provided data between July 25, 1996 and June 28, 1997. At present, the Earth Probe TOMS has been operating since July 25, 1996. Eventually, the total column ozone measurements made by TOMS will be taken up by NPOESS (National Polar Orbiter Environmental Satellite System), while NASA incorporates total column ozone retrieval into the list of data products provided by newer instruments such as the Earth Polychromatic Imaging Camera (EPIC) aboard the DSCOVR (Deep Space Climate ObserVatoRy) spacecraft, and the Ozone Monitoring Instrument (OMI) aboard Aura.

Here we discuss the current version of TOMS, the Earth Probe instrument (McPeters et al., 1998). An optical diagram is shown in Figure 3.7. It is designed to provide maps of total column ozone abundance, at local noon, covering all sunlit parts of the globe. The final gridded ozone product ("level-3" data) has a spatial resolution of 1 degree of latitude by 1.25 degrees of longitude, but to provide reliable measurements on this grid the instrument must sample at a higher spatial resolution so that several retrievals can be averaged within a level-3 grid cell. Initially, the Earth Probe instrument had a *GIFOV* (Ground Instantaneous Field Of View) of 26 km from an altitude of 500 km. However, after the failure of the ADEOS TOMS, the Earth Probe spacecraft's altitude was raised to 739 km, yielding a *GIFOV* of 39 km, so that the single instrument could provide better global coverage. The instrument's scanning mirror samples at thirty-five 3° intervals in the cross-track direction, from

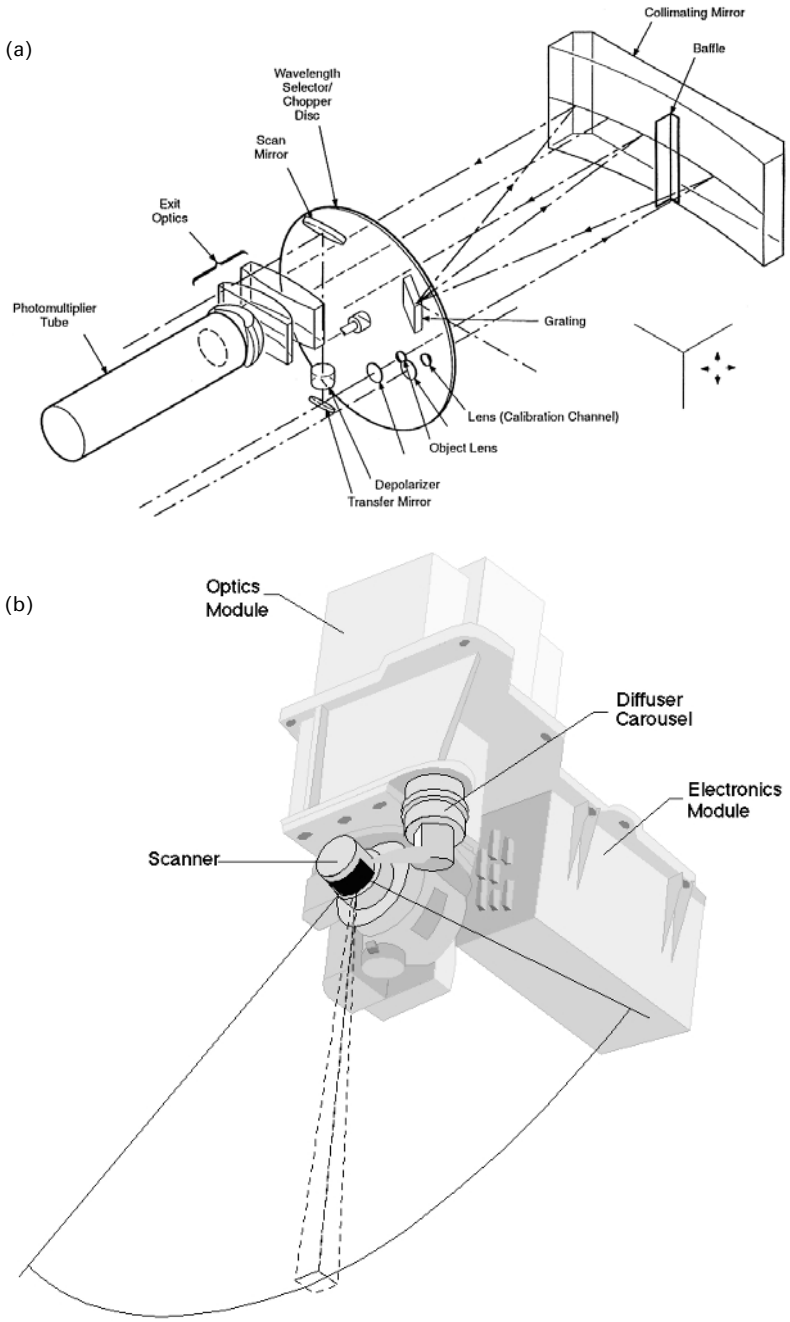

Figure 3.7. Schematic diagram of the Earth Probe TOMS, showing both the instrument optics and the orientation of the instrument in the spacecraft.

Courtesy of Dr. R. D. McPeters, NASA Goddard Space Flight Center.

51° to the left of nadir to 51° to the right. The scanning mirror sends backscattered intensity into a single monochromator that is fixed to sample six UV-B and UV-A wavelengths: 308.6, 313.5, 317.5, 322.3, 331.2, and 360.4 nm. This wavelength selection is effected by means of a chopper wheel with openings at six separate radial distances, which allow the detector (a photomultiplier tube) to sample at six different positions along the monochromator's exit slit. The slit function is triangular with a 1-nm bandwidth. Because the intensities at the three shortest wavelengths are strongly absorbed by stratospheric ozone, the TOMS instrument is placed in a Sun-synchronous orbit near local noon to maximize scene illumination and SNR (Signal-to-Noise Ratio).

The measured quantity required for ozone retrieval is the ratio of backscattered intensity I_λ to extraterrestial solar flux $F_{0\lambda}$. To measure $F_{0\lambda}$ the scan mirror views a solar diffuser near the northern terminator during each orbit. The photomultiplier tube operates in three different gain ranges, the least sensitive of which is used for sampling $F_{0\lambda}$. The backscattered solar intensity may be measured in any of the gain ranges depending on the scene, and thus a gain range correction must be factored into the determination of $I_\lambda/F_{0\lambda}$. In terms of radiometric calibration, the measured backscattered intensity can be written:

$$I_\lambda(t) = C_{i\lambda} k_{i\lambda} G_i f_\lambda(t) \tag{3.7}$$

where $C_{i\lambda}$ are the detector counts in backscatter-viewing mode, $k_{i\lambda}$ is a calibration constant for intensity, $G_{i\lambda}$ is a gain range correction factor, and $f_\lambda(t)$ is a correction for time-dependent instrument changes. The measured extraterrestrial solar flux is:

$$F_{0\lambda}(t) = \frac{C_{f\lambda} k_{f\lambda} G_f f_\lambda(t)}{g(t) r(\theta, \phi)} \tag{3.8}$$

where $C_{f\lambda}, k_{f\lambda}, G_f$ are quantities corresponding to (3.7) but for flux-viewing mode, $r(\theta, \phi)$ is the diffuser's directional reflectance, and $g(t)$ is a time-dependent correction for changes in the diffuser's reflectivity. The ratio of these measured quantities becomes:

$$\frac{I_\lambda(t)}{F_{0\lambda}(t)} = \frac{C_{i\lambda}}{C_{f\lambda}} K \frac{G_i}{G_f} g(t) r(\theta, \phi) \tag{3.9}$$

where K is a combined calibration constant determined before launch. The gain range correction factors G (which are of order 10) are determined before launch and can also be monitored in flight. Note that any changes in instrument sensitivity affecting both backscatter and solar flux measurements ($f_\lambda(t)$) cancel this ratio. An internal mercury–argon lamp is used for periodic wavelength calibration in flight.

The radiative transfer model used to calculate $I_\lambda/F_{0\lambda}$ represents the backscattered intensity emerging at the top of the atmosphere as:

$$I^{\text{meas}}(\lambda, \theta, \theta_0, \Omega, p_0, R_\lambda) = I_a(\lambda, \theta, \theta_0, \Omega, p_0) + I_s(\lambda, \theta, \theta_0, \Omega, p_0, R_\lambda) \tag{3.10}$$

where the I_a term represents atmospheric backscatter, and the I_s term represents backscatter from a surface of reflectivity R_λ. The column ozone amount is Ω and p_0 is the pressure level of the reflecting surface. Two separate reflecting surfaces are

actually used in this model, one for cloud tops and one for the Earth surface. The measured intensities are compared with values calculated separately for 100% cloud cover and 100% Earth surface viewing to determine the fractional contribution of each. The surface reflection term can be written:

$$\left.\begin{aligned} I_{s\lambda}(\lambda,\theta,\theta_0,\Omega,p_0,R_\lambda) &= \frac{R_\lambda \mathbf{X}(\lambda,\theta,\theta_0,\Omega,p_0)}{1-R_\lambda S_b(\lambda,\Omega,p_0)} \\ X(\lambda,\theta,\theta_0,\Omega,p_0) &= I_d(\lambda,\theta,\theta_0,\Omega,p_0)\beta(\lambda,\theta,\theta_0,\Omega,p_0) \end{aligned}\right\} \tag{3.11}$$

where S_b is the fraction of radiation reflected from the surface that the atmosphere scatters back to the surface, I_d is the sum of the direct and diffuse intensity reaching the surface at p_0, and β_λ is the fraction of the intensity reflected toward the satellite that reaches the sensor. The denominator in this expression represents the multiple reflection of photons between the surface and the atmosphere.

The algorithm actually calculates the ratios as "N-values":

$$N = -100\log_{10}\left(\frac{I}{F_0}\right) \tag{3.12}$$

which give the calculated backscattered intensities a scaling comparable with total column ozone. The N-values are calculated offline and stored in a large set of lookup tables for the full ranges of total column ozone, vertical ozone profile, solar and viewing angles, and pressure levels for reflecting surfaces, relevant to the Earth–atmosphere system. The retrieval of total column ozone is a two-step process. First, an initial ozone estimate is made using a pair of N-values at different wavelengths—a shorter wavelength very sensitive to ozone and a longer one much less sensitive to ozone. This removes any dependence on instrumental uncertainties such as zero-point calibration. Second, the radiative transfer model is used to calculate N-values at all measured wavelengths using the initial ozone estimate. These N-values will generally be different than the measured values used to derive the initial estimate. The differences between the measured and calculated N-values in this step are called the *residues*. The residues are used for an appropriate triplet of wavelengths, to solve for a correction to the first ozone estimate and also for an intensity correction that is due to a combination of possible wavelength dependence on scene (Earth surface) reflectivity and changes in instrument calibration. The triplet consists of the original wavelength pair plus 360.4 nm. Three different triplets are used in the algorithm to refine the ozone estimate, depending on the optical path $\sec\theta_0 + \sec\theta$ (Table 3.1).

The intensities are calculated monochromatically in 0.05-nm intervals, and are integrated over the 1-nm instrument bandpass:

$$A(\lambda_b) = \frac{\int A(\lambda)F(\lambda)S(\lambda)\,d\lambda}{\int F(\lambda)S(\lambda)\,d\lambda} \tag{3.13}$$

Table 3.1. The wavelength triplets used in the Earth Probe TOMS ozone retrieval algorithm.

Pair/Triplet designation	Ozone-sensitive wavelength	Ozone-insensitive wavelength	Reflectivity wavelength	Range of optical path s
A	312.6 nm	331.3 nm	360.4 nm	$s \leq 1$
B	317.6	331.3	360.4	$1 < s \leq 3$
C	322.4	331.3	360.4	$3 < s$

From McPeters et al. (1998).

where $A(\lambda) = I(\lambda)/F(\lambda)$ are the monochromatic values of backscattered intensity and extraterrestrial solar flux, and $S(\lambda)$ is the triangular instrument response function. The wavelength dependence of the extraterrestrial solar flux is taken from SOLSTICE (SOLar STellar Irradiance Comparison Experiment) measurements from the UARS (Upper Atmosphere Research Satellite) mission. The calculated intensities are then corrected for rotational Raman scattering (the ring effect) following Joiner et al. (1995).

The radiative transfer model must account for the fact that large contributions to the backscattered intensity can come from both the Earth surface and cloud. For the surface, information on snow cover is provided by the U.S. Air Force Global Weather Center, and terrain height (which affects the Rayleigh scattering optical depth) is included. Climatological cloud top heights are provided by the International Satellite Cloud Climatology Project (ISCCP, Chapter 4). Reflectivity is determined from 360.4-nm measurements, which are not influenced by ozone absorption. For the given viewing geometry, an intensity I_g is calculated for clear skies using a surface reflectivity of 0.08, and a second intensity I_c is calculated using the climatological cloud top height and a cloud top reflectivity of 0.80. If $I_g \leq I_{\text{meas}} \leq I_c$, and snow/ice are not present, then an effective cloud amount α_C is estimated:

$$\alpha_C = \frac{I_{\text{meas}} - I_g}{I_c - I_g} \tag{3.14}$$

If snow/ice are present, then α_C is divided by 2, under the assumption that there is a probability of 0.5 that reflectivity arises from cloud. If α_C is so reduced, (3.14) is solved to yield a revised estimate of I_g and surface reflectivity is recalculated using (5.11). The effective scene reflectivity is:

$$R = R_g(1 - \alpha_C) + \alpha_C R_C \tag{3.15}$$

where $R_g = 0.08$ in the absence of snow/ice, or is the recalculated value if snow/ice are present. This scene reflectivity is included among the TOMS data products. For ozone retrievals, intensities are calculated assuming that a fraction α_C of the measured intensity comes from the cloud top with reflectivity 0.80, and the remaining fraction $(1 - \alpha_C)$ comes from the surface. If the measured intensity is less than the calculated I_g, radiation is assumed to come entirely from the surface with a reflectivity less than 0.08. If the measured intensity is greater than I_c, radiation is assumed to come entirely from cloud with reflectivity greater than 0.80. In either

extreme case, the revised surface or cloud top reflectivity is determined from the combination of (3.10) and (3.11); that is:

$$R = \frac{I - I_a}{X + S_b(I - I_a)} \tag{3.16}$$

The initial ozone estimate is made using the B-pair from Table 3.1, and 360.4-nm reflectivity by interpolation over a large set of intensity lookup tables that account for viewing geometry, latitude, cloud top height, terrain height, cloud fraction, and meridionally varying ozone vertical profile. Two tabulated column ozone amounts are selected whose B-pair N-values bracket the measured N-value difference. Linear interpolation between these values yields the initial estimate. The initial ozone estimate is then used to calculate a new set of N-values at all measured wavelengths, using appropriate climatological ozone profiles. In general, these recalculated N-values will not be the same as the measured N-values. The initial ozone estimate is based on the assumption that surface reflectivity is independent of wavelength, which is not true for many scenes including desert or sea glint. There can also be wavelength-dependent artifacts in instrument calibration. The error in ozone that results from these factors will contribute to the discrepancy between the measured N-value N_m and the value N_0 calculated from the initial ozone estimate. The TOMS algorithm assumes that the difference between the initial ozone estimate and the true column ozone abundance is small enough that it can be represented in a Taylor expansion. The algorithm further assumes that the wavelength-dependent contribution to the residue from spectral reflectivity and instrumental uncertainties is linear in wavelength—i.e., $a + b\lambda$. Then the residue at wavelength λ can be expressed as:

$$N_m = N_0 + (\Omega - \Omega_0)\left(\frac{dN}{d\Omega}\right)_0 + a + b\lambda \tag{3.17}$$

and if we define:

$$\left.\begin{aligned} r_\lambda &\equiv (N_m - N_0)_\lambda \\ s_\lambda &\equiv \left(\frac{dN}{d\Omega}\right)_\lambda \end{aligned}\right\} \tag{3.18}$$

then:

$$r_\lambda = s_\lambda(\Omega - \Omega_0) + a + b\lambda \tag{3.19}$$

where r_λ is the residue at wavelength λ. At 360.4 nm, the intensity is insensitive to ozone, so that $(dN/d\Omega)_{360.4} = 0$, and $r_{360.4} = 0$ because the reflectivity was derived at this wavelength. Therefore, for the other wavelengths:

$$r_\lambda = s_\lambda(\Omega - \Omega_0) + b(\lambda - 360.4) \tag{3.20}$$

If we define $\Delta\lambda_i = \lambda_i - 360.4$, then we can use the measurements at two other wavelengths λ_1 and λ_2 to solve for the column ozone abundance Ω:

$$\Omega = \Omega_0 + \frac{r_1\Delta\lambda_2 - r_2\Delta\lambda_1}{s_1\Delta\lambda_2 - s_2\Delta\lambda_1} \tag{3.21}$$

This expression uses the residues to transform the initial ozone estimate into a refined ozone estimate, and is applied at each pixel using two vertical ozone profiles that bracket the pixel location geographically.

The final ozone measurement is determined from the refined ozone estimates for the two profiles:

$$\Omega = \left(1 - f_{\text{prof}}\right)\Omega_{\text{low}} + f_{\text{prof}}\Omega_{\text{high}} \tag{3.22}$$

where the subscripts "low" and "high" refer to quantities derived from the lower and higher latitude ozone profiles, and f_{prof} is the weight given to the higher latitude profile. For latitudes lower than 15° or higher than 75°, only one profile is used (tropical or polar), and $f_{\text{prof}} = 0$. At mid-latitudes and an optical path less than 1.5, f_{prof} is specified by simple interpolation:

$$f_{\text{prof}} = \frac{|\text{Latitude}| - |\text{Latitude}|_{\text{low}}}{|\text{Latitude}|_{\text{high}} - |\text{Latitude}|_{\text{low}}} \tag{3.23}$$

For longer optical paths, f_{prof} is determined using the residues for the B-triplet and 313-nm channel (optical paths between 1.5 and 3.0) or the C-triplet and the 318-nm channel (optical paths longer than 3.0), by:

$$f_{\text{prof}} = \frac{r'(\text{low})}{r'(\text{low}) - r'(\text{high})} \tag{3.24}$$

where the triplet residue r' is defined as:

$$r'_\lambda = r_\lambda + \frac{\lambda - 360.4}{331.2 - 360.4} r_{331.2} \tag{3.25}$$

The justification for this approximation is that the triplet residue of a shorter wavelength can help specify the combination of ozone profiles that best explain the intensities measured at all wavelengths.

Once the final ozone retrieval has been determined for a given *IFOV* (Instantaneous Field Of View), it is subjected to several validity checks. If any residue is larger than 12.5 in units of *N*-value, the measurement is flagged as unreliable. Residues this large usually result from a corrupted data stream leading to incorrectly reported intensity, or very unusual atmospheric conditions outside the assumptions built into the algorithm. Retrievals that pass this residue test are then checked for sulfur dioxide contamination. An SO_2 Index (SOI) is defined by:

$$r = SOI\left[\frac{dN}{d(\text{SO}_2)}\right] + \Delta\Omega\left(\frac{dN}{d\Omega}\right) + b(\lambda - 360.4) \tag{3.26}$$

This is the same formulation as (3.19), with an additional term for SO_2 contamination, and contains the assumption that the discrepancy between calculated and measured intensity has a contribution from SO_2 in addition to the abovementioned

factors. Three wavelengths are used in (3.26), 317.5, 322.3, and 331.2 nm, yielding three equations that are solved for the SOI as a function of the residues, sensitivities, and wavelengths. If the SOI is greater than 12.5, the measurement is flagged as being contaminated by sulfur dioxide. As separate projects, TOMS measurements have been used to derive SO_2 column abundance (Krotkov et al., 1997; Krueger et al., 1995), but in the ozone algorithm only a contamination index is evaluated.

There are additional validity checks for triplet consistency, to determine if the measured values of I/F are consistent with the algorithm's linear corrections. If a single triplet was used to determine the ozone, the triplet residue of (3.23) is evaluated at the ozone-sensitive wavelength not used in ozone determination (317.5 nm in the case of the A-triplet, 313.5 for the B-triplet). If this triplet residue exceeds a maximum value (N-value of 1.1 at 317.5 nm for the A-triplet and 0.9 at 313.5 nm for the B-triplet), ozone retrieval is flagged as unreliable. If a second triplet was used to determine the ozone profile via (3.22), then ozone retrieval is flagged as unreliable if $f_{\text{prof}} > 3.5$ or $f_{\text{prof}} < 0.5$. A final check is done on the residue at 331.2 nm. If this residue exceeds 4 in N-value units, the retrieval is flagged as unreliable. Additionally, ozone retrievals are identified for which the solar zenith angle $\theta_0 > 84^\circ$, and these retrievals are not used in level-3 gridded data products.

The TOMS level-2 data product contains all ozone retrievals at the spatial resolution of the original *IFOV*. The level-3 product, using grid cells of 1° in latitude by 1.25° in longitude, is constructed from weighted averages of all level-2 retrievals overlapping the cells that have no error flags from the above-mentioned validity checks. When plotting the level-3 ozone product, one notices a discontinuity at the 180° meridian (international dateline). This is because the data product is not synoptic. "Local noon" ozone is determined over the Western Pacific near the beginning of the GMT day, and over the Eastern Pacific near the end of the GMT day.

The TOMS algorithm just described provides an instructive example of how radiative transfer theory is used in satellite remote-sensing retrieval. Although the retrieval principle—UV differential absorption spectroscopy—is conceptually straightforward, the algorithm must be designed to account for post-launch instrument changes and uncertainties. As satellite data collection progresses, remote-sensing scientists must diagnose the inevitable changes in instrument performance and continuously update the retrieval algorithms to account for these changes. The user of a remote-sensing data product should be aware of the large amount of "detective" work that goes into the production of a high-quality satellite data product. The TOMS algorithm has gone through several evolutions in response to both sensor performance changes and optical engineering improvements to later models of the spectrometer, and the current edition of the TOMS total column ozone product is version 8.

3.2.2 The Curse of Captain Wilkes

The BAS is generally credited with discovering the springtime Antarctic ozone decrease, using Dobson spectro-photometer measurements made at their research

stations on a regular basis for several decades. Their insightful paper (Farman et al., 1985) was the first to report this phenomenon in the commonly available literature. Because NASA's TOMS instrument had been operating since late 1978, NASA scientists are sometimes criticized for having "missed" the ozone "hole" with their expensive satellite instrument, while BAS made the discovery with two simple and reliable ground-based instruments. Such criticisms are unjustified, because they are based on the assumption that large new datasets can be easily understood in their entirety rightaway. In the early 1980s, TOMS was a brand new instrument charged with two demanding tasks: (1) making the first high-spatial-resolution maps of total column ozone from space and (2) searching for small ozone depletion trends anticipated from midlatitude gas-phase chlorine chemistry. Most of the TOMS science team effort at the time was directed toward careful intercalibration of satellite ozone retrievals with ground-based (Dobson) and *in situ* (electrochemical ozonesonde) measurements (McPeters and Labow, 1996).

In retrospect, the TOMS series of instruments is one of the most successful geophysical experiments ever flown in space. The nearly continuous time series has revealed the presence and geographic distribution of small gas-phase ozone depletion trends at midlatitudes (Stolarski et al., 1991; Weatherhead et al., 2000). The detection of these small trends is a remarkable feat for a series of complex optical systems in orbit beyond any laboratory control.

There's an old yarn, still occasionally bandied about at conferences, that a single line of FORTRAN code somewhere in the tens of thousands of lines of TOMS data-processing software rejected the anomalously low Antarctic ozone values as "bad data", and that's why NASA "missed it". That tale isn't true. NASA scientists noticed the low ozone values early on, but were reluctant to publish them until they were fully confident with their instrument's performance and validation. There's an old adage that applies here: *Nobody believes a theoretical model except the modeler, and everybody believes an experimenter's data except the experimenter*. A remote-sensing scientist might first attribute strange low values in a retrieved quantity over Antarctica to a subtle change in instrument performance, perhaps due to thermal regulation problems when crossing the terminator. From the standpoint of good science, the TOMS science team was correct to put off publishing their Antarctic ozone retrievals until the validation studies had been completed to their satisfaction. However, once the BAS made their 1985 report, the TOMS science team quickly examined their Antarctic data which revealed (1) the enormous geographic extent of the springtime Antarctic ozone decrease and (2) the close connection to the dynamics of the polar vortex. TOMS therefore played a key role in the rapid discovery of the mechanism behind the ozone "hole".

This story is interesting in terms of what Professor Eugene N. Parker (Department of Astronomy and Astrophysics, University of Chicago) calls the "Sociology of Science". Satellite remote sensing, which provides retrieved values of geophysical quantities via the interpretation of photons scattered, absorbed, or emitted by the Earth–atmosphere system, cannot tell us everything about a given problem in Earth science. Remote sensing can sometimes provide only first-order estimates of important quantities, or ancillary observations, and detailed fieldwork is required

to reveal the substantive details. Yet the enormous geographical and temporal coverage available from space-based remote sensors can often give a superficial *appearance* of revealing everything important about the Earth–atmosphere system. And, to be sure, NASA's publicity machine occasionally oversells a "Mission to Planet Earth" or "Earth Science Enterprise" in this respect. Consequently, there are many scientists, including some of the best field researchers, who look down their noses at satellite remote sensing. To them, remote sensing is best for making "pretty pictures" and an occasional "scoop" in *Science*, *Nature*, or the newspapers, in order to justify a multimillion dollar government program. Scientists with such a viewpoint were naturally amused when NASA "missed" the ozone "hole", and one of the most venerable organizations for fieldwork—the BAS—made the great "scoop" for atmospheric science during the 1980s.

Such snickering misses the point. The 1985 BAS discovery of the ozone "hole" was made by first-rate scientists. The ability of NASA remote-sensing programs to quickly provide critical large-scale interpretation and guidance was also due to first-rate researchers working at that organization, and NASA's suite of atmospheric science missions being well-conceived throughout the 1970s. Current problems in atmospheric science are complex enough to require the combined efforts of experimenters, remote-sensing scientists, and theoreticians. Moreover, as atmospheric science involves the study of our climate and biosphere, most current issues have direct societal connections and a related sense of urgency. The key to success lies in recognizing what each mode of investigation—remote sensing, fieldwork, laboratory experiments, and theoretical work—can bring to a given problem.

One hundred and fifty years before the ozone "hole", Charles Wilkes took command of a large, expensive, and bureaucratically burdened expedition, and led it across the Southern Ocean. Prevented by the pack ice from reaching terra firma in his wooden ships, he was forced to survey the Antarctic coastline from a distance. He meticulously charted ~1,500 km of previously unknown territory, but was unaware of a unique polar phenomenon (strong temperature inversions and related mirages) that rendered his charts inaccurate. As a result, the British and French received most of the credit for the Antarctic discoveries of that era. The first reports of the Antarctic ozone "hole" follow a hauntingly similar storyline. However, the most important historical aspect is this: once Farman et al. (1985) made their report, NASA had the measurements on hand—both in total ozone and PSC climatology—that immediately provided crucial insight in a global context. So NASA scientists didn't really "miss" the ozone "hole" at all. They merely fell under the Curse of Captain Wilkes, as do all remote-sensing researchers eventually.

3.3 OZONE RETRIEVAL FROM INFRARED SOUNDERS

There is a set of heritage instruments that provide soundings of tropospheric temperature, pressure, and water vapor profiles. These soundings are useful for extrapolating wind vectors at various altitudes. The most familiar of these

sounding systems is the TIROS-N Operational Vertical Sounder (TOVS), which has flown regularly aboard the NOAA (National Oceanic and Atmospheric Administration) polar orbiters. One of the three instruments in this system, the High-resolution InfraRed Sounder (HIRS2) contains 20 infrared channels. The center wavelengths of these channels are selected to exhibit maximum sensitivity in measured intensity to emission from particular altitude ranges in the troposphere and stratosphere. Some of these channels exploit the large variation in atmospheric opacity due to CO_2, between 500–800 cm^{-1}, such that the emission due to the CO_2 column at various optical depths is most sensitive to temperature at various altitudes. This is the "CO_2-slicing" method, discussed in more detail in Chapter 4 (Smith et al., 1979). Other channel wavelengths are centered in the mid-IR window region, so that the lower boundary condition to the sounding problem can be established. For retrieving stratospheric temperatures, one channel is centered on the 9.6-μm ozone emission band. The brightness temperature measurements in this channel can also be used to estimate total column ozone abundance. These mid-IR measurements offer the advantage of ozone mapping during the polar night, when there is no solar UV radiation available for instruments such as TOMS.

One method for retrieving total column ozone from TOVS data was developed by Lefèvre et al. (1991). In addition to the HIRS2 channel centered on the mid-IR ozone band (channel 9), the algorithm uses channels 2, 6, and 8 centered at 14.7, 13.7, and 11.1 μm, respectively. Satellite-measured intensities in channels 2 and 6 are most sensitive to emission from atmospheric pressure levels of 60 and 800 millibars, respectively. Channel 8 is located in the mid-IR window. Transmittance of the 9.6-μm ozone band is ~0.5, so the intensity measured by the satellite instrument contains a component due to emission from the Earth's surface. In this band, there is also substantial absorption due to water vapor, so transmittance must be written:

$$\chi_9 = \chi_{9,H_2O} + \chi_{9,O_3} \tag{3.27}$$

where χ_{9,O_3} and χ_{9,H_2O} are the ozone and water vapor transmittances within the channel's spectral interval. In general, the applicable form of the radiative transfer equation for a sounding instrument is:

$$I(\nu) = B(\nu, T_S)\chi(\nu, p_s) + \int_{p_s}^{0} B[\nu, T_p] \frac{d\chi(\nu, p)}{dp} dp \tag{3.28}$$

where $I(\nu)$ is the intensity at wavenumber ν, $B[\nu, T_p]$ is the Planck function evaluated at the temperature corresponding to pressure level p, p_s is the atmospheric pressure at the Earth's surface, and $\chi(\nu, p)$ is the column transmission from pressure level p to the top of the atmosphere. For the 9.6-μm channel, the equation becomes:

$$I_9 = B_9(T_s)\chi_9 + \int_{s}^{0} B_9(T)\, dt_9 \tag{3.29}$$

The separation of band transmittance into ozone and water vapor components allows us to reformulate (3.27) in terms of components from two different altitude regions. Most water vapor emission comes from tropospheric altitudes with

pressures greater than 400 millibars. At the same time, the contribution of tropospheric ozone emission to a space-based mid-IR measurement is very small. Above 400 millibars, we can therefore make the approximation that $\chi_{9,H_2O} = 1$, and that $\chi_{9,O_3} = \chi_{9,H,O_3}$. The radiative transfer equation can now be approximated by a lower atmosphere term, for pressure levels greater than 400 millibars, and an upper atmosphere term for pressure levels below 400 millibars:

$$I_9 = \left[B_9(T_s)\chi_{9,H_2O} + \int_s^{400} B_9(T)\, d\chi_{9,H_2O}\right]\chi_{9,H,H_2O} + \int_{400}^{s} B_9(T)\, d\chi_{9,O_3} \tag{3.30}$$

To evaluate the lower atmosphere term, we need an estimate of the water vapor emission in the 9.6-μm band. Channel-averaged water vapor emission in the HIRS2 9.6-μm and 11.1-μm channels are similar enough that the brightness temperature measured in channel 8, $T_{11.1\,\mu m}$ can be used to evaluate the lower atmosphere term. The radiative transfer equation then becomes:

$$I_9 = B_9(T_8)\chi_{9,H,O_3} + \int_{400}^{0} B_9(T)\, d\chi_{9,O_3} \tag{3.31}$$

where $B_{9.6\,\mu m}(T_{11.1\,\mu m})$ represents the Planck function evaluated in the wavelength range of channel 9, using the brightness temperature measured by channel 8.

The upper atmosphere term is evaluated by defining a model "ozone layer temperature", T_{O_3}, which is the temperature of an isothermal atmosphere between 400 and 0 millibars having the same 9.6-μm emission as the real atmosphere in this pressure range. With this approximation, we have:

$$\left.\begin{aligned} I_9 &= B_9(T_8)\chi_{9,H,O_3} + \left(1 - \chi_{9,H,O_3}\right)B_9(T_{O_3}) \\ \chi_{9,H,O_3} &= \frac{I_9 - B_9(T_{O_3})}{B_9(T_8) - B_9(T_{O_3})} \end{aligned}\right\} \tag{3.32}$$

At this point, a very thorough set of independent (offline) radiative transfer calculations is needed to express T_{O_3} in terms of the intensities measured by HIRS2. If channel 9 is used for retrieval of ozone, then another measurement of stratospheric temperature must be introduced. This is provided by channel 2. In addition, there is some ozone emission from the warmest part of the lower troposphere that will introduce errors in ozone retrieval from channel 9. The algorithm must use channels 6 and 8 to correct for these errors. Lefèvre *et al.* (1991) therefore developed a parameterization for T_{O_3}:

$$T_{O_3} = a_1 T_2 + b_1 T_6 + c_1 T_8 + d_1 T_9 + e_1 \tag{3.33}$$

The regression coefficients a_1–e_1 are determined by independent radiative transfer calculations in which the various channel brightness temperatures are simulated over the full range of ozone and temperature profiles observed in the global atmosphere. This is done using a line-by-line radiative transfer model (Scott and Chedin, 1981). These radiative transfer equations are also used in the final parameterization for total column ozone abundance:

$$\Omega = -a_2 \ln(\chi_{9,H,O_3}) + b_2 T_{O_3} + c_2 \tag{3.34}$$

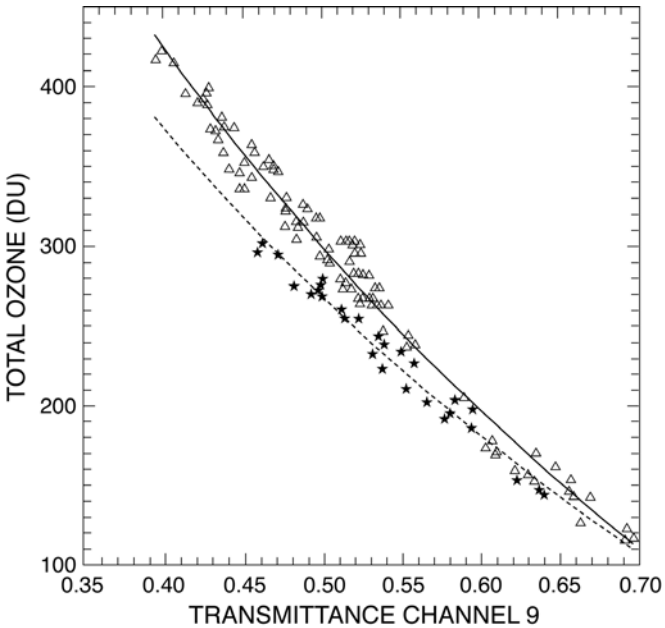

Figure 3.8. Total ozone abundance as a function of transmittance in the 9.6-mm channel of the HIRS2.

From Lefèvre et al. (1991). Copyright 1991 American Geophysical Union. Reproduced by permission of American Geophysical Union.

Figure 3.8, an example from these line-by-line radiative transfer calculations, shows how the total column ozone amount is related to transmission in HIRS2 channel 9. Climatological tropospheric ozone column values (25 DU on average) must be added to the total column value retrieved from 3.34.

The algorithm presented above contains many approximations, each of which introduce uncertainty in the retrieved total ozone abundance. Because the algorithm is based on a large but finite set of line-by-line calculations, the assumptions will also have a detrimental effect on the retrieval precision (repeatability). There are some Earth scenes over which the algorithm will not work at all. If there are high tropospheric clouds or optically thick PSCs in the instrument's *IFOV*, the measured T_8 ceases to be an accurate measure of lower atmosphere water vapor emission. For clouds below 400 millibars, the algorithm still works, but the total column ozone will be underestimated by $\sim$10 DU. Over some parts of the Antarctic Plateau, certain very cold near-isothermal tropospheric conditions may exist that introduce large uncertainties in the 9.6-μm-based retrieval. Lefèvre et al. (1991) give a thorough discussion of the biases and uncertainties inherent in their algorithm, and they are summarized here in Table 3.2. Although the uncertainties with mid-IR ozone retrieval are generally larger than those of a UV differential absorption method, TOVS-based retrievals generally compare well with those from TOMS (Figure 3.9). Because NOAA polar orbiter data can be readily tracked worldwide, some satellite

Table 3.2. Total ozone errors for TOVS middle-infrared retrievals.

Source	Error (DU)	Comment
Measurement noise	4	Result of the errors given by the constructor, introduced in simulation with test profiles
Algorithm error	12–14	Given by the comparisons of real and calculated column, for regression and test profiles
Tropospheric ozone variability	10	Error due to the parameterization of the ozone column below 400 hPa (25 DU)
Total clear sky	16–18	Quadratic sum of three errors above
Clouds in low troposphere	Bias of −13	Given by cloud simulations in test and regression profiles
Clouds in high troposphere	Total ozone not calculated	Computation avoided when $T_8 - T_{O_3} < 20°K$
Type-2 PSCs	Underestimation >50 DU or ozone not calculated	When ozone is retrievable (see above), measurement of the column above the PSC

From Lefèvre et al. (1991).

data analysis software packages, such as the TeraScan and TeraVision systems from the SeaSpace Corporation, include the TOVS ozone retrieval algorithm.

3.4 THE POLAR OZONE AND ATMOSPHERIC MEASUREMENT PROGRAM

The Polar Ozone and Atmospheric Measurement (POAM) program is discussed here to introduce the remote-sensing technique of *solar absorptive occultation*. In the solar occultation technique an instrument views the Sun, through the atmosphere, as it rises and sets in the satellite's frame of reference. By using a detailed radiative transfer model that describes both atmospheric attenuation and refraction of solar flux along the extended optical path, vertical profiles of atmospheric absorbers, scatterers, and temperature can be derived. This technique has two advantages for measuring the vertical dependence in atmospheric composition, and related long-term trends. First, high *SNR* is possible with a light source as bright as the Sun. Second, using the Sun as a direct light source (without a reflecting diffuser) makes the technique self-calibrating, and therefore insensitive to long-term changes in detector performance. Several successful atmospheric remote-sensing missions have used the occultation technique, including the SAGE (Stratospheric Aerosols and Gas Experiment) program whose PSC discoveries are discussed above, the Stratosphere Atmospheric Measurement (SAM II) program (McCormick et al., 1979), the

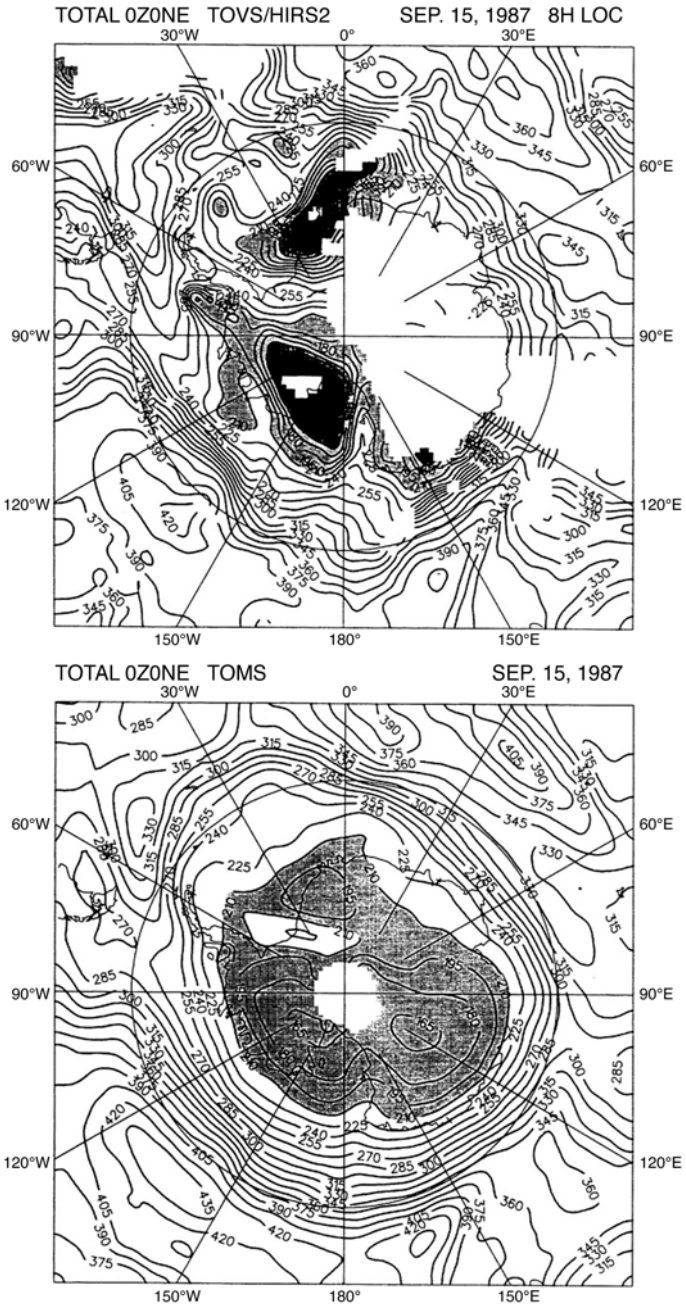

Figure 3.9. A comparison of TOVS/HIRS2 and TOMS total column ozone retrievals over Antarctica on September 15, 1987.

From Lefèvre et al. (1991). Copyright 1991 American Geophysical Union. Reproduced by permission of American Geophysical Union.

HALogen Occultation Experiment (HALOE, discussed below), and the Atmospheric Trace MOlecule Spectroscopy (ATMOS) experiment (Gunson, 1992).

The geometrical considerations are slightly different from those of a downward-looking instrument. The *Vertical Field Of View* (VFOV) refers to the angular field of view in the direction perpendicular to the Earth's horizon, and the *Horizontal Field Of View* (HFOV) is perpendicular to the VFOV. The *vertical resolution* is defined by the Full Width at Half Maximum (FWHM) of the sensor's vertical point spread function P_α where α is the displacement from the center of the VFOV. Along the instrument's *Line Of Sight* (LOS) through the atmosphere, the *tangent point* is the point closest to the Earth's surface. To locate the tangent point exactly, atmospheric refraction must be accounted for. A solar occultation instrument must be mounted in a two-axis gimbal with a Sun tracker.

In the early 1990s, the U.S. Ballistic Missile Defense Organization supported a satellite program designed to characterize atmospheric opacity at major laser wavelengths (primarily 353 and 1,060 nm). This program had important spinoffs in basic atmospheric science, in that the science team headed by the U.S. Naval Research Laboratory has made many useful contributions in the area of polar stratospheric ozone depletion. The POAM II and POAM III instruments are nine-channel visible/near-IR radiometers deployed aboard the French SPOT 3 and SPOT 4 spacecraft, respectively. POAM II was launched on September 26, 1993 and operated into November, 1996 when the SPOT 3 spacecraft failed. POAM III was launched in March, 1998 and, after the hardware was allowed to outgas for a few weeks, began data collection on April 24, 1998. The SPOT (Système Pour l'Observation de la Terre) spacecraft are in Sun-synchronous polar orbits of inclination 98.7°, mean altitude 833 km, orbital period 101.5 minutes, and descending node Equator crossing time 10 : 30 LT. Viewed from the spacecraft, the Sun rises in the Arctic and sets in the Antarctic 14.2 times per day.

3.4.1 Instrument description

The POAM II/III instrument measures direct-beam solar intensity, through a near-horizontal atmospheric optical path, in nine spectral bands using nine separate radiometer assemblies (Glaccum *et al.*, 1997). The nine wavelength bands are given in Table 3.3, and are chosen to sample the vertical profiles of Rayleigh scattering efficiency and molecular oxygen number density (and hence temperature), ozone, water vapor and NO_2 number density, and aerosol loading. There are small differences in the wavelength selection between POAM II and POAM III, but the purposes of each band remain the same (Lucke et al., 1999). Water vapor, NO_2, and O_2 are measured by differential absorption spectroscopy, with two closely-spaced bands on the relative minimum and maximum of useful absorption features. The Chappuis band of ozone in the visible (Brasseur and Solomon, 1984) is used for ozone retrieval (peak near 601 nm).

Each radiometer assembly (Figure 3.10) consists of an objective plano-convex lens that images the Sun onto a fieldstop. The fieldstop is a long horizontal aperture oriented parallel to the Earth's horizon. This aperture in the objective's focal plane

Table 3.3. POAM II measurement channels.

Channel	Center wavelength (nm)	FWHM (nm)	SNR (at launch)	Primary purpose
1	352.3	4.4	400	Rayleigh/aerosol
2	441.6	2.0	1,700	NO_2 offband/aerosol
3	448.1	2.1	2,800	NO_2 onband
4	601.4	14.3	3,800	O_3
5	761.2	2.2	5,000*	O_2 onband
6	781.0	16.7	3,000	O_2 offband/aerosol
7	921.0	2.1	4,500	H_2O offband/aerosol
8	936.4	2.3	3,500	H_2O onband
9	1,060.3	11.1	4,500	Aerosol

From Lumpe et al. (1997).

subtends angles of 0.014° in elevation by 1.5° in azimuth. At spacecraft altitude the instrument's vertical resolution, defined by the FWHM at the Earth's limb, is ~0.8 km. The horizontal resolution perpendicular to the LOS is determined by the solar diameter, and is approximately 30 km. The horizontal resolution along the LOS is approximately 200 km. Behind the horizontal aperture, an interference filter is used to select the narrow spectral interval, and a photodiode is used for the detector. The nine radiometers are carefully coaligned to within 0.015° before launch.

The radiometers are also coaligned with a Sun tracker. The Sun tracker consists of four detectors operating near 700 nm. The signals from these four detectors are used to generate elevation and azimuth corrections, which are applied in a feedback loop to drive motors to enable active tracking on the center brightness of the solar disk. The instrument tracks the Sun between tangent altitudes of 200 km and a minimum altitude defined by the tracking threshold. This threshold is set at 3–5% of the unattenuated solar signal. The resulting minimum tangent altitude lies between 8 and 15 km, depending on stratospheric aerosol loading. At high-tangent altitudes, the center brightness and geometric center of the solar disk are the same, but they begin to diverge at tangent altitudes lower than ~40 km due to differential attenuation of the intensity across the solar disk. This has implications for altitude location of the datastream, as discussed by Lumpe et al. (1997). The normal data collection procedure for a single occultation event takes 120 s and consists of two steps, an atmospheric sounding step and a Sun scan step. The atmospheric sounding step begins shortly after sunrise, when the instrument begins to track the Sun once the Sun tracker signal exceeds the threshold. The data collection progresses through higher tangent altitudes, until the tangent altitude reaches ~105 km. At this point the Sun scan step begins. The Sun tracker's elevation correction is turned off, and the elevation controller first slews the intrument ahead of the Sun's apparent motion and then holds the instrument fixed in elevation. Tracking in azimuth continues while the Sun drifts through the *FOV* of each radiometer. This allows each radiometer to sample several points throughout the solar disk. The Sun scan step provides a

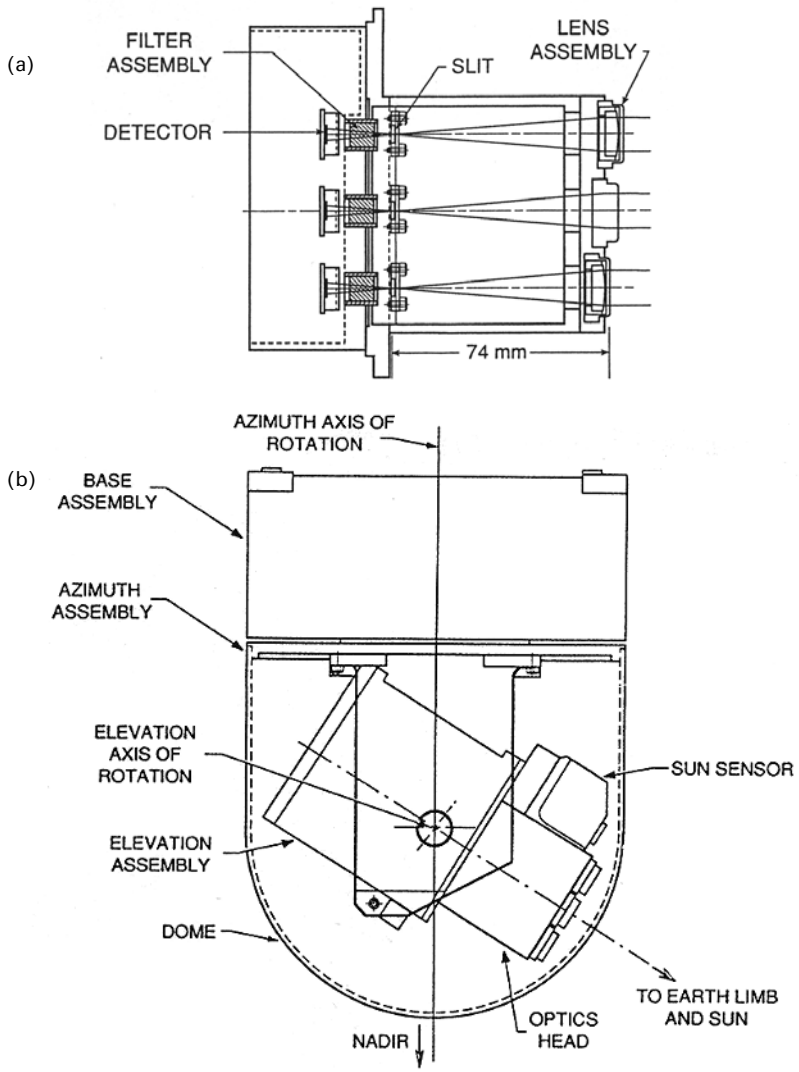

Figure 3.10. Diagram of the POAM II instrument: (a) instrument orientation in spacecraft; (b) radiometer assembly.

From Glaccum et al. (1997). Copyright 1997 American Geophysical Union. Reproduced by permission of American Geophysical Union.

robust measurement of the unattenuated solar signal, which is necessary for calculating atmospheric transmissions along the LOS. As the spacecraft reaches southern high latitudes, the Sun begins to set in the instrument's frame of reference and the two-step data collection procedure is reversed.

The near-polar orbit of the SPOT spacecraft ensures that the sunrises and sunsets seen by the instrument occur within 40° latitude of the poles. Figure 3.11

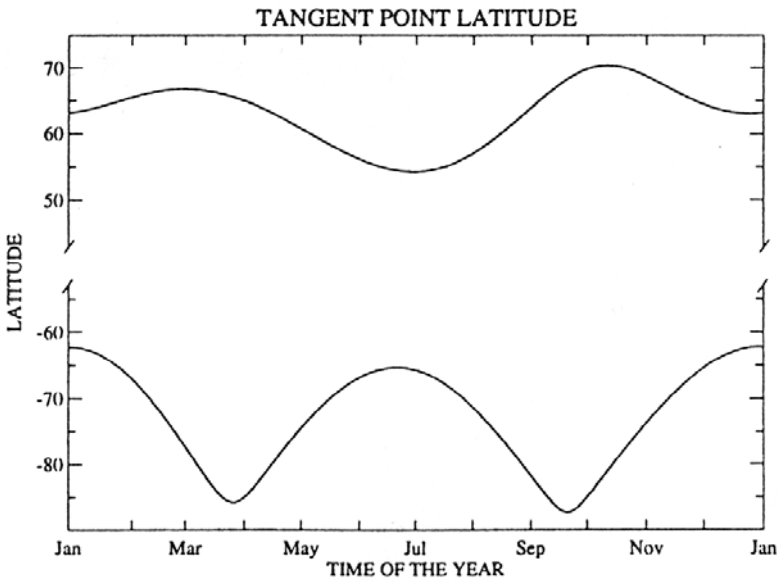

Figure 3.11. Time series of the tangent point latitudes in the Northern and Southern Hemispheres, seen by the POAM II instrument.

From Glaccum et al. (1997). Copyright 1997 American Geophysical Union. Reproduced by permission of American Geophysical Union.

shows that the latitudes of sunrises and sunsets vary slowly throughout the year, due to the Sun-synchronous orbit. Sunrises occur in the latitude range 54°–71°N, and sunsets occur in the latitude range 63–88°S. Each successive sunrise or sunset is displaced westward from the previous one by 25.4° in longitude, which corresponds to displacements of 900–1,700 km for sunrises and 100–1,300 km for sunsets, depending on latitude.

3.4.2 Retrieval principles

The radiative transfer model used with the solar occultation technique is somewhat different from the basic one-dimensional formulation outlined in Chapter 2, because at stratospheric altitudes and long optical paths both the Earth's sphericity and atmospheric refraction must be included. Figure 3.12 shows the geometry for the solar occultation radiative transfer problem. As with the TOMS algorithm, radiative transfer calculations are performed monochromatically for very small wavelength steps—of order 0.05 nm—and are then integrated over each radiometer's spectral interval with a weighting for the radiometer's spectral responsivity. For water vapor and O_2, which have discrete vibrational absorption features, the monochromatic calculations must have a fine enough wavenumber step to resolve these features (typically $5 \times 10^{-3}\,\mathrm{cm}^{-1}$). In the model, the atmosphere is taken to be spherically symmetric. A specific direct beam solar intensity traced through the atmosphere for a

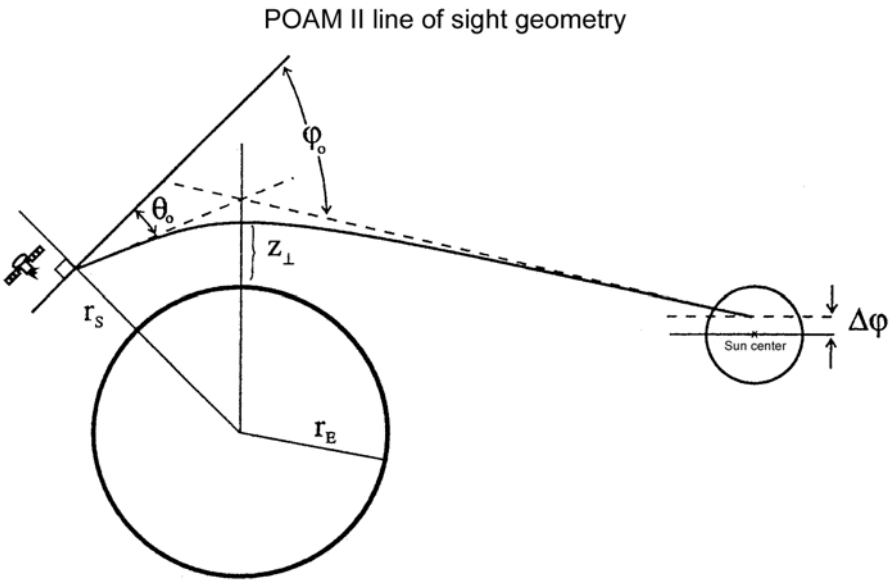

Figure 3.12. Solar occultation viewing geometry.

From Lumpe et al. (1997). Copyright 1997 American Geophysical Union. Reproduced by permission of American Geophysical Union.

given LOS is defined by its tangent point altitude $z_\perp$. The monochromatic slant path transmittance at wavelength λ can be expressed as the product of transmittances for all individual extinction components α, including Rayleigh scattering, aerosol scattering and absorption, and absorption by O_2, O_3, NO_2, and water vapor:

$$\chi_\lambda(z_\perp) = \prod_\alpha \chi_{\lambda\alpha j}(z_\perp) \tag{3.35}$$

From Beer's law, the monochromatic transmission in terms of the slant path optical depth is:

$$\chi_{\lambda j}(z_\perp) = \exp\left[-\tau_{\lambda j}(z_\perp)\right] \tag{3.36}$$

where the optical depth $\tau_{\lambda j}$ is calculated by integrating along the entire refracted optical path:

$$\tau_{\lambda j}(z_\perp) = \int_{z_\perp} \sigma_{\lambda j}(T(s), P(s)) n_j(s)\, ds \tag{3.37}$$

where ds is the slant path increment, $n_j(s)$ is the number density, $\sigma_{\lambda j}$ is the absorption or scattering cross section, and $P(s)$ and $T(s)$ are pressure and temperature. For aerosols:

$$\tau_{\lambda,\text{aer}} = \int_{z_\perp} k_{\lambda,\text{aer}}(s)\, ds \tag{3.38}$$

where $k_{\lambda,\text{aer}}$ is the aerosol scattering extinction coefficient calculated from aerosol microphysical information using a Mie scattering algorithm (e.g., Wiscombe, 1980).

In calculating the slant path optical depths for water vapor and O_2, we run into a computational obstacle with their absorption features. In (3.37) the absorption cross section must in general remain within the integral because it can vary with both pressure and temperature. Thus integration must be done separately for each wavelength step. To resolve the vibration absorption line features of O_2 and water vapor, this requires very high spectral resolution and a prohibitive computation time. What is often done in this situation is to define an effective pressure $P(z_\perp)$ and temperature $T(z_\perp)$ for each atmospheric path, so that the cross section can be taken outside the integral in (3.37) and the number of computations can remain manageable. The resulting approximation is:

$$\tau_{\lambda j}(z_\perp) \cong \sigma_{\lambda j}\big(\tilde{T}_j(z_\perp), \tilde{P}_j(z_\perp)\big) \int_{z_\perp} n_j(s)\, ds \equiv \sigma_{\lambda j}\big(\tilde{T}_j(z_\perp), \tilde{P}_j(z_\perp)\big)\Omega_j(z_\perp) \tag{3.39}$$

where $\Omega_j(z_\perp)$ is the column absorber amount. Various approximations for the effective pressure and temperature are discussed in Goody and Yung (1989) or Liou (1992). One useful example is the Curtis–Godson approximation:

$$\left.\begin{aligned} \tilde{T}_j(z_\perp) &\equiv \frac{1}{\Omega_j(z_\perp)} \int_{z_\perp} n_j(s) T(s)\, ds \\ \tilde{P}_j(z_\perp) &\equiv \frac{1}{\Omega_j(z_\perp)} \int_{z_\perp} n_j(s) P(s)\, ds \end{aligned}\right\} \tag{3.40}$$

This approximation is easier to use when temperature dependence is relatively weak, as is the case for ozone in the Chappuis band. However, (3.40) must be evaluated with care for O_2 and water vapor, because there are strong temperature and pressure dependencies which in some cases include saturation of the vibrational lines. In the POAM algorithm, equations (3.37)–(3.40) are evaluated in a model atmosphere consisting of spherical shells 1 km thick, as described in detail by Lumpe et al. (1997).

A solar occultation instrument has a more complex viewing geometry than a traditional nadir-looking remote sensor, and it is important to be able to simulate the measured signal in order to derive reliable retrieval algorithms. In particular, the POAM II/III instruments sample direct beam solar intensity with a frequency of 18 Hz, and for a given radiometer this time-dependent signal $I(t)$ is a spectrally and spatially weighted integration of the solar source and atmospheric transmission:

$$I_j\big(\theta_0^j(t)\big) = \int_{\Delta\lambda_j} \int_{\Delta\theta_j} \int_{\Delta\psi_j} K_j(\lambda) H_j\big(\theta - \theta_0^j(t)\big) t(\lambda, \theta) F_0(\lambda, \theta, \psi)\, d\lambda\, d\theta\, d\psi \tag{3.41}$$

where $K_j(\lambda)$ is the normalized interference filter transmission as a function of wavelength, which defines an effective radiometer bandpass $\Delta\lambda$. Here we have defined two new geometric variables, θ and ψ, which denote viewing elevation and azimuth angles, respectively. The angle $\theta_0(t)$ is the elevation angle that defines the center of the radiometer's FOV. A simple way to think of $\theta_0(t)$ is that it is the elevation angle that would be read out from the instrument's pointing controller. However, we must consider the effective VFOV and LOS that results from refraction, and refraction becomes more significant at lower altitudes which are of

the greatest scientific interest. We must therefore make a coordinate transformation and define an angle φ as the elevation angle relative to the refracted ray (Figure 3.12). This results in a transformation of variables, such that the time-dependent signal is:

$$I_j\left(\varphi_0^j(t)\right) = \int_{\Delta\lambda_j}\int_{\Delta\varphi_j}\int_{\Delta\psi_j} K_j(\lambda)\frac{\partial\theta}{\partial\varphi}(\varphi)H_j\left(\varphi-\varphi_0^j(t)\right)\chi(\lambda,\varphi)F_0(\lambda,\varphi,\psi)\,d\lambda\,d\varphi\,d\psi \tag{3.42}$$

where the refractive compression factor $\partial\theta/\partial\varphi$ is unity above the atmosphere and decreases to $\sim$0.2 near the Earth surface. If we make the assumption that atmospheric transmission and instrument FOV functions depend on elevation angle only (a good approximation for the POAM instrument), then the only azimuthal dependence comes from limb darkening on the solar disk. The horizontal dimension of the POAM radiometers' focal plane apertures subtend an angle of 1.5°, so the instrument samples the entire solar disk in the horizontal. The limb-darkening law can be represented by a polynomial form (Pierce et al., 1976):

$$F_0(\lambda,\phi) = F_0'(\lambda)\sum_{k=0}^{M} a_k(\lambda)\mu^k \tag{3.43}$$

where $\mu = \cos\phi$, ϕ is the angular displacement from the Earth–Sun vector, and $F_0'(\lambda)$ is the solar flux at disk center ($\phi = 0$). With this, we can write a final expression for the time-dependent signal:

$$\left.\begin{aligned} I_j\left(\varphi_0^j(t)\right) &= \int_{\Delta\varphi_j} H_j\left(\varphi-\varphi_0^j(t)\right)\Gamma(\varphi-\varphi_c(t))\langle\chi(\varphi)\rangle_j \\ \langle\chi(\varphi)\rangle_j &\equiv \int_{\Delta\lambda_j} K_j(\lambda)F_0'(\lambda)\chi(\lambda,\phi) \\ \Gamma^j(\varphi-\varphi_c(t)) &= \Phi_S\sum_{k=0}^{M}\left[1-\left(\frac{\varphi-\varphi_c(t)}{\Phi_S}\right)^2\right]^{(k+1)/2} B\left(\frac{1}{2},\frac{k}{2}+1\right)a_k^j \end{aligned}\right\} \tag{3.44}$$

where $\langle\chi(\varphi)\rangle$ is the spectrally averaged transmission, the quantities a_k^j are spectrally averaged limb-darkening coefficients, B is the beta function, Φ_S is the solar half-angle, and $\varphi(t)$ is the elevation angle for the LOS to the center of the solar disk. With (3.42)–(3.44) it is possible to simulate such things as the effect of Sun tracking and pointing errors on measurement uncertainties.

The measured signal I_j in each channel is used to calculate the transmission in each channel:

$$\chi_j(z_\perp) = \frac{I_j(z_\perp)}{I_j^0(\Delta\varphi(z_\perp))} \tag{3.45}$$

where the intensities are then interpreted using a forward retrieval model to derive trace gas and aerosol concentrations as a function of altitude. The forward retrieval

model utilizes the multiplicative property of the transmittance:

$$\begin{aligned}\langle\chi(z_\perp)\rangle_j &= \int_{\Delta\lambda_j} K_j(\lambda)F_0'(\lambda)\,d\lambda \prod_\alpha \chi_\alpha(\lambda, z_\perp) \\ &\cong \prod_\alpha \int_{\Delta\lambda_j} K_j(\lambda)F_0'(\lambda)\chi_\alpha(\lambda, z_\perp)\,d\lambda \\ &\equiv \prod_\alpha \langle\chi(z_\perp)\rangle_j \end{aligned} \tag{3.46}$$

In the second step of (3.46), the transmittance components are assumed to be separable in the integrand, which is valid if there is no spectral correlation between absorbing gases across the radiometer's bandpass. The measured slant path optical depth reduces to a sum over components:

$$\tau_j^{\text{meas}}(z_\perp) \equiv -\ln\langle\chi(z_\perp)\rangle_j = -\sum_\alpha \ln\langle\chi(z_\perp)\rangle_j \tag{3.47}$$

For each contribution to the optical depth we can define an effective cross section:

$$\sigma_\alpha^j(z_\perp) \equiv \frac{-\ln\langle\chi_\alpha(z_\perp\rangle_j}{\Omega_\alpha(z_\perp)} \tag{3.48}$$

and thus the aerosol contribution to total optical depth is separated from those of the absorbers:

$$\tau_j^{\text{meas}}(z_\perp) = \sum_{\alpha\neq\text{aer}} \sigma_\alpha^j(z_\perp)N_\alpha(z_\perp) + \tau_{\text{aer}}(\lambda_0^j, z_\perp) \tag{3.49}$$

with the approximation that:

$$-\ln\langle\chi_{\text{aer}}(z_\perp)\rangle_j \cong \langle\tau_{\text{aer}}(z_\perp)\rangle_j \cong \tau_{\text{aer}}(\lambda_0^j, z_\perp) \tag{3.50}$$

The aerosol optical depth is effectively constant across any of the radiometer channel spectral intervals, and can be evaluated at the center of the bandbass. It is important to note the difference between the "retrieval" cross sections of (3.48) and the cross sections as first defined in (3.39). The latter are monochromatic, whereas the former include spectral integration over a bandpass. The definition of (3.48) normalizes out most of the dependence on total absorber amount, and these "retrieval" cross sections are nearly constant with altitude and independent of season for O_3 and NO_2. For O_2 and water vapor, they must be calculated more carefully on a 1-km tangent altitude grid.

Figure 3.13 shows how the optical depth varies with altitude differently in four different POAM channels, and thus illustrates how this instrument can be used to simultaneously retrieve several vertical profiles. In each channel a different source of direct beam extinction is the major contributor to the optical depth. In channels 1 and 4, Rayleigh scattering and O_3 absorption are the dominant contributors to optical depth. The optical depth in channel 9 is dominated by aerosol extinction at lower altitudes and by Rayleigh scattering at higher altitudes. Channel 6, the

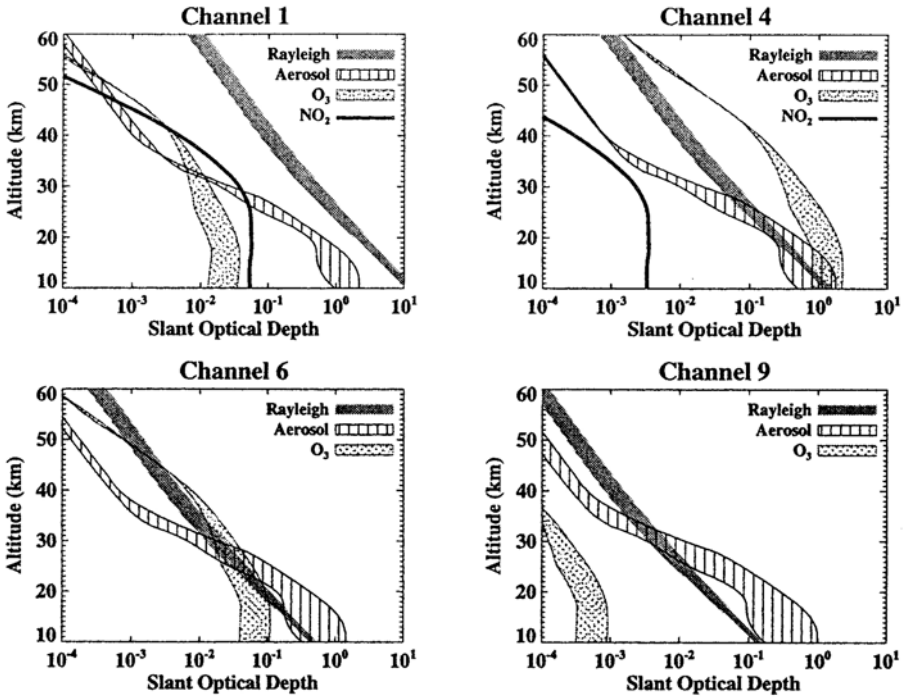

Figure 3.13. The slant path optical depth as a function of altitude, for major atmospheric constituents, in POAM channels 1, 4, 6, and 9. The spread in the curves for Rayleigh scattering, ozone absorption, and aerosol extinction represents natural variability with season and latitude. The curve for NO_2 represents a fixed vertical profile used in the radiative transfer model.

"O_2 off-band" channel, is primarily sensitive to Rayleigh scattering and aerosols, but also to O_3 at higher altitudes.

Details of the POAM retrieval, including corrections for instrument-pointing offsets and specific model atmosphere formulations, are described by Lumpe et al. (1997). The two important steps are *spectral inversion* and *limb inversion*. In spectral inversion, the total optical depth is partitioned into individual contributions from each gas and aerosol component. For each of the trace gases, the effective cross sections of (3.48) define the spectral dependence. In general, aerosol optical depth also has a spectral dependence, which must be retrieved along with the trace gas components, and which must first be treated as an unknown quantity in each radiometer channel. A nonlinear parameterization for the aerosol optical depth contribution is required:

$$\ln \tau_{\text{aer}}^{j} = \beta_0 + \beta_1 \ln \lambda_j + \beta_2 \left(\ln \lambda_j\right)^2 \tag{3.51}$$

where λ_j is the channel central wavelength of channel j, and β_k are coefficients to be retrieved by the algorithm. Combining (3.51) and (3.49) yields:

$$\tau_j^{\text{meas}} = \exp\left[\beta_0 + \beta_1 \ln \lambda_j + \beta_2 (\ln \lambda_j)^2\right] + \left(\sigma_{\text{Ray}}^j + w\sigma_{\text{O}_2}^j\right)\Omega_{\text{TOT}} + \sigma_{\text{O}_3}^j \Omega_{\text{O}_3} + \sigma_{\text{NO}_3}^j \Omega_{\text{NO}_2} + \sigma_{\text{H}_2\text{O}}^j \Omega_{\text{H}_2\text{O}} \quad (3.52)$$

Note that a constant mixing ratio w is used to combine the Rayleigh scattering and O_2 absorption terms. With (3.52) we have nine equations for seven unknowns, which can be solved simultaneously using a nonlinear optimal estimation technique (Rodgers, 1976). To start the inversion procedure, initial estimates of all retrieved number densities must be specified. If these are well-chosen from climatology and are held constant, the retrieved profiles should be independent of these choices. Retrieved vertical profiles are derived by solving equations (3.52) sequentially at each tangent altitude level in the model atmosphere. The final step is limb inversion, in which the slant path absorber column densities and aerosol extinctions derived from (3.52) are converted to true vertical profiles. This effectively requires inversion of the linear path integral of (3.37). With a spherical shell model atmosphere in which trace concentrations and aerosol extinction are allowed to vary linearly with altitude across each shell, this inversion procedure involves the solution of a linear matrix equation.

Randall et al. (1998) used POAM II retrievals of NO_2 and ozone vertical profiles to support the hypothesis that downward transport of NO_x, formed in the mesosphere and thermosphere, can contribute to ozone loss within the polar vortex via reactions (3.2) (Rusch et al., 1981). According to theory, NO is produced year-round in the upper atmosphere, but only during the polar night, in the absence of photo-dissociation, can enough NO survive a descent all the way to the stratosphere. An increase in NO abundance should result in both an increase in NO_2 abundance and a decrease in ozone abundance, as suggested by (3.2). Figure 3.14, from Randall et al. (1998), shows a convincing example of this scenario. In this time series of ozone and NO_2 profiles observed within the 1994 Southern Hemisphere polar vortex, we see a downward-moving maximum in NO_2 mixing ratio corresponding to a local minimum in ozone abundance as the seasons progress from winter into spring.

3.5 REMOTE SENSING OF POLAR STRATOSPHERIC CLOUDS

Satellite studies of Polar Stratospheric Clouds (PSCs) are likely to be rewarding endeavors for the foreseeable future. From the remote-sensing perspective, they are a challenging problem for both detection and retrieval of microphysical properties. In the global change perspective, the climatology and microphysical evolution of PSCs are intimately linked to changes in lower atmosphere dynamics due to climate warming, and to the anticipated recovery of stratospheric ozone over the next 50 years. The important satellite work to date on PSCs falls into two categories, occultation experiments and imager studies.

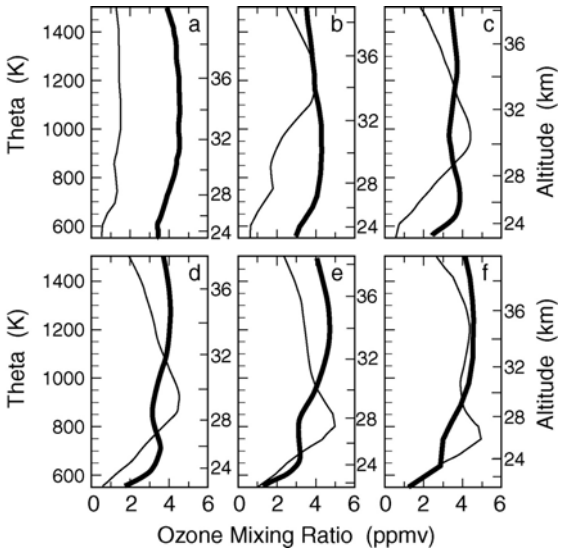

Figure 3.14. Two-week average ozone mixing ratio profiles (thick line) and NO_2 mixing ratio profiles (thin line) inside the 1994 Southern Hemisphere polar vortex, as measured by POAM II, for (a) July 1–15, (b) August 1–15, (c) September 1–15, (d) September 16–30, (e) October 1–15, and (f) October 16–31. The vertical axis on the left is the potential temperature.

3.5.1 Occultation experiments

The first study to demonstrate the large-scale significance of PSCs was accomplished by NASA's SAM II program. From late 1978 through 1979, this single-band (1 μm) occultation instrument collected enough data to demonstrate that PSCs are a major stratospheric phenomenon during the polar winter (McCormick et al., 1982). The results of this study made the atmospheric science community aware of PSCs once the Antarctic ozone "hole" was discovered a few years later. The fundamental, first-order properties of PSCs were reported by the SAM II science team, and are shown in Figure 3.15: (1) that elevated aerosol extinctions are pervasive at most polar latitudes during the winters of both hemispheres, (2) that these enhanced extinctions correlate with stratospheric temperatures, and (3) that the related stratospheric optical depths are an order of magnitude larger over the Antarctic than over the Arctic.

Fromm et al. (1997) developed a reliable algorithm for detecting and mapping Antarctic PSCs using POAM data. As shown in Figure 3.16, a typical clear-sky POAM aerosol extinction profile begins at approximately 2 km above the tropopause, and then decreases monotonically with altitude through 30 km. PSCs appear in the form of local maxima in aerosol extinction somewhere in this altitude range. In POAM data, reliable PSC detection was obtained using an aerosol extinction anomaly threshold of four standard deviations (4σ) above the clear-sky

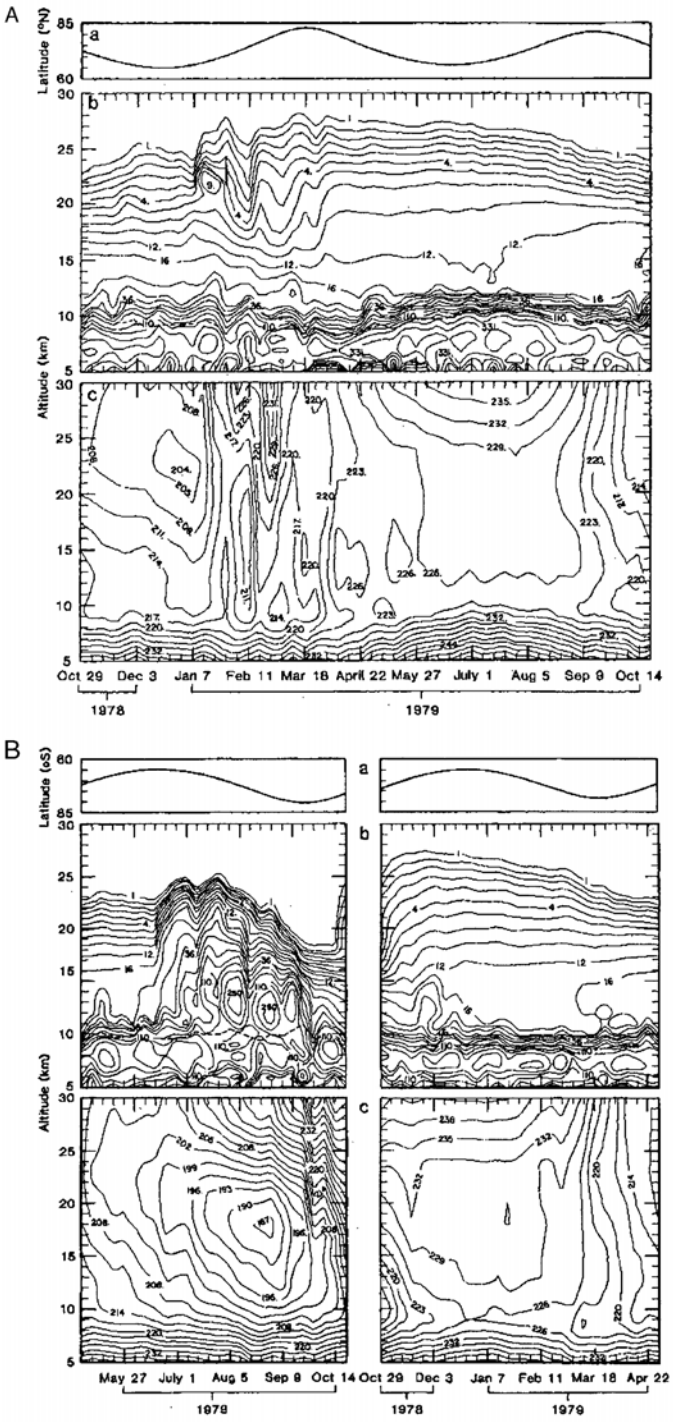
A
Latitude (°N)
Altitude (km)
a
b
c
Oct 29 Dec 3 Jan 7 Feb 11 Mar 18 April 22 May 27 July 1 Aug 5 Sep 9 Oct 14
1978
1979
B
Latitude (oS)
Altitude (km)
a
b
c
May 27 July 1 Aug 5 Sep 9 Oct 14 Oct 29 Dec 3 Jan 7 Feb 11 Mar 18 Apr 22
1978
1978
1979

◄ **Figure 3.15.** The first geographically extensive observations of polar stratospheric cloud extinction, made by NASA's SAM II instrument. The figures show time series of weekly average values. The top three panels show (a) the latitude of the measurement, (b) 1,000-nm aerosol extinction in units of $10^{-5}\,km^{-1}$, and (c) temperature profile in Kelvin from meteorological reanalysis data, for the Northern Hemisphere. The lower six panels show the same information for the Southern Hemisphere. In the lower panels, the figures have been split into two time series plots so that the seasonal progression coincides with that of the Northern Hemisphere plots.

average. In addition, PSCs at lower altitudes were found to cause the POAM Sun tracker to cease tracking early (or start tracking late). The additional PSC opacity in the lower stratosphere prevents the tracker from acquiring the Sun until the instrument reaches tangent altitudes several kilometers above the tropopause. The reliability of both these criteria for identifying PSCs was established by coincident lidar data. Using these criteria, Fromm et al. (1997) were able to make climatological maps of PSC distribution, examples of which are shown in Figure 3.17.

The multispectral information available from instruments such as POAM and NASA's SAGE II has enabled researchers to study the microphysical properties of PSCs and other stratospheric aerosol particles (Massie et al., 1998; Randall et al., 2000; Steele et al., 1999a). Using the refractive indices of molecules believed to be

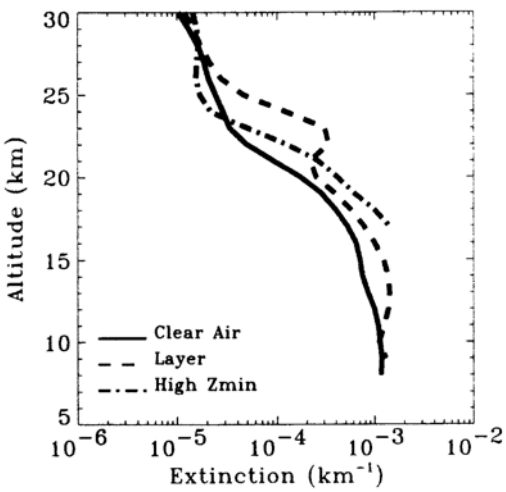

Figure 3.16. Examples of Southern Hemisphere POAM aerosol extinction profiles at 1,060 nm, for clean air (solid line, July 12, 1995), a distinct PSC layer between 21–26 km (dashed line, July 11, 1995), and a profile aborted at high altitude (17 km) due to PSC opacity reducing the solar intensity below the Sun tracker's detection threshold (July 26, 1994).

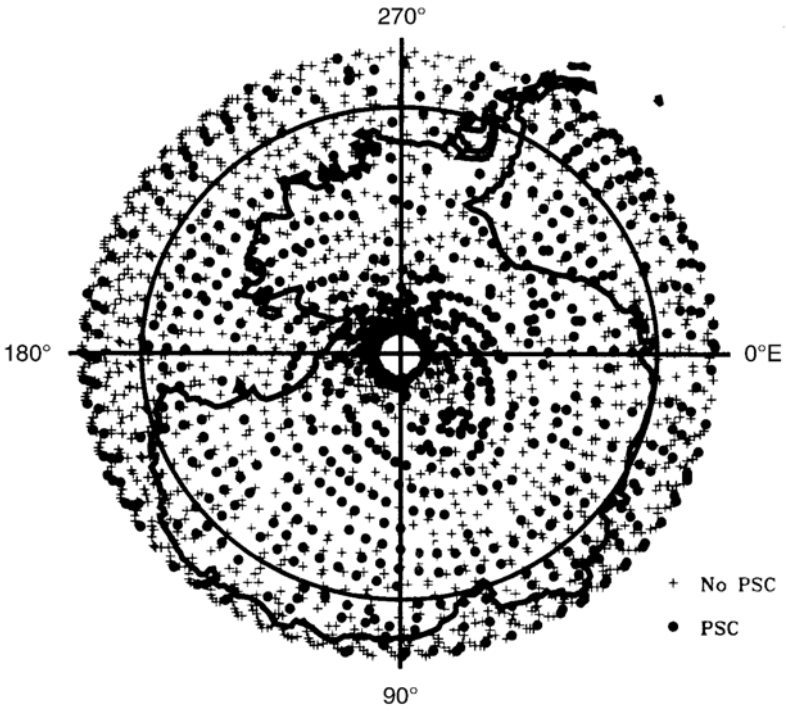

Figure 3.17. Southern Hemisphere polar map showing locations of POAM PSC detections between May 1 and November 30, 1995. Crosses represent locations where no PSC was detected, dots represent a PSC detection. The latitude line is 70°S.

part of PSCs, and PSC particle size distributions inferred from field data, one can use Mie theory to compute the wavelength dependence in the volume extinctions on various types of hypothetical PSC particles. With a radiative transfer model configured for the occultation geometry, one can then iterate to find the type of PSC that best fits the observed spectral measurements from the sensor. This must be done carefully, however, to avoid spurious solutions due to error amplification in the inversion. The most promising technique for this type of retrieval appears to be Principal Component Analysis (PCA: Twomey, 1974). Aerosol extinction is given by:

$$k_{\text{aer}}(\lambda) = \int \pi r^2 Q_{\text{ext}}(\lambda, r) \frac{dn}{dr} dr = \int \frac{3Q_{\text{ext}}(\lambda, r)}{4r} \frac{dV}{dr} dr = \int C(\lambda, r) \frac{dV}{dr} dr \qquad (3.53)$$

where $C(\lambda, r)$ is the kernel function, and is the result of a complex set of Mie calculations. In PCA, the kernel function is expanded in a set of functions (principal components) that capture the essential variation of the kernel in all its independent variables with the fewest possible terms. Truncation of this expansion,

to eliminate higher order functions, can effectively exclude noise from the solution. For a given set of extinction measurements $k_i(\lambda)$ at wavelengths λ_i, the expansion takes the form:

$$\frac{dV}{dr} = C^*(r)U\Lambda^{-1}U^*k \tag{3.54}$$

where $C^*(r)$ is the transpose of the kernel matrix $C(\lambda_i, r_j)$, U is the matrix of eigenvectors, and Λ is the diagonal matrix of eigenvalues. The largest eigenvalues in Λ correspond to the eigenvectors in U that capture the kernel's essential variability. As shown by Steele et al. (1999a), various properties of the size distribution dV/dr, such as particle area density and volume density, can be evaluated by using (3.54) to construct the appropriate linear combination of extinction measurements.

Satellite occultation measurements have proven powerful enough to trace the microphysical evolution of PSCs. By tracking air parcels coincident with individual POAM II observations, Steele et al. (1999b) used a detailed aerosol microphysical model (Drdla, 1996) to simulate the types of PSC particles expected in the instrument's field of view. Comparison of the theoretical spectral extinctions of the modeled PSC particles with the POAM II spectral extinction measurements provided useful constraints on current theoretical formulations of PSC chemistry and microphysics. With the POAM III program (Lucke et al., 1999), water vapor profiles were added as a retrieval product. This enabled direct observation of dehydration in the stratosphere and its correlation with PSC extinction observations (Nedoluha et al., 2000). An example is shown in Figure 3.18.

3.5.2 Imager studies

The multispectral capability of many infrared imagers enables identification and mapping of PSCs composed of larger particles. Some imagers such as AVHRR provide a time history of data going back two decades, which enables climatological study of PSC formation and dissipation. Occasionally, a PSC has sufficient optical thickness that the mid-IR brightness temperature appears in the range expected for the polar stratosphere (Garcia et al., 1995; Pagan, 1996). Hervig et al. (2001a) showed that the spectral dependence on ice–cloud extinction throughout the mid-IR can be used to detect a larger number of type-2 PSCs. They simulated the expected difference in brightness temperature between channels 4 and 5 of AVHRR (center wavelengths 11 and 12 μm, respectively), for a full range of microphysical scenarios relevant to PSCs. Over most tropospheric liquid water clouds, this brightness temperature difference is small (<2–3 K). However, Hervig et al. (2001a) showed that for stratospheric ice particles this brightness temperature difference could be as large as 20 K (Figure 3.19), and that in some cases PSCs can be distinguished from tropospheric cirrus clouds (Figure 3.20). Figure 3.21 (see color section) gives an example of how this brightness temperature difference signature is used to identify a geographically extensive PSC to leeward of the Antarctic Peninsula. Orographic forcing of the prevailing westerlies by the peninsula makes this region ripe for PSC formation in the lower stratosphere. Note that cold channel

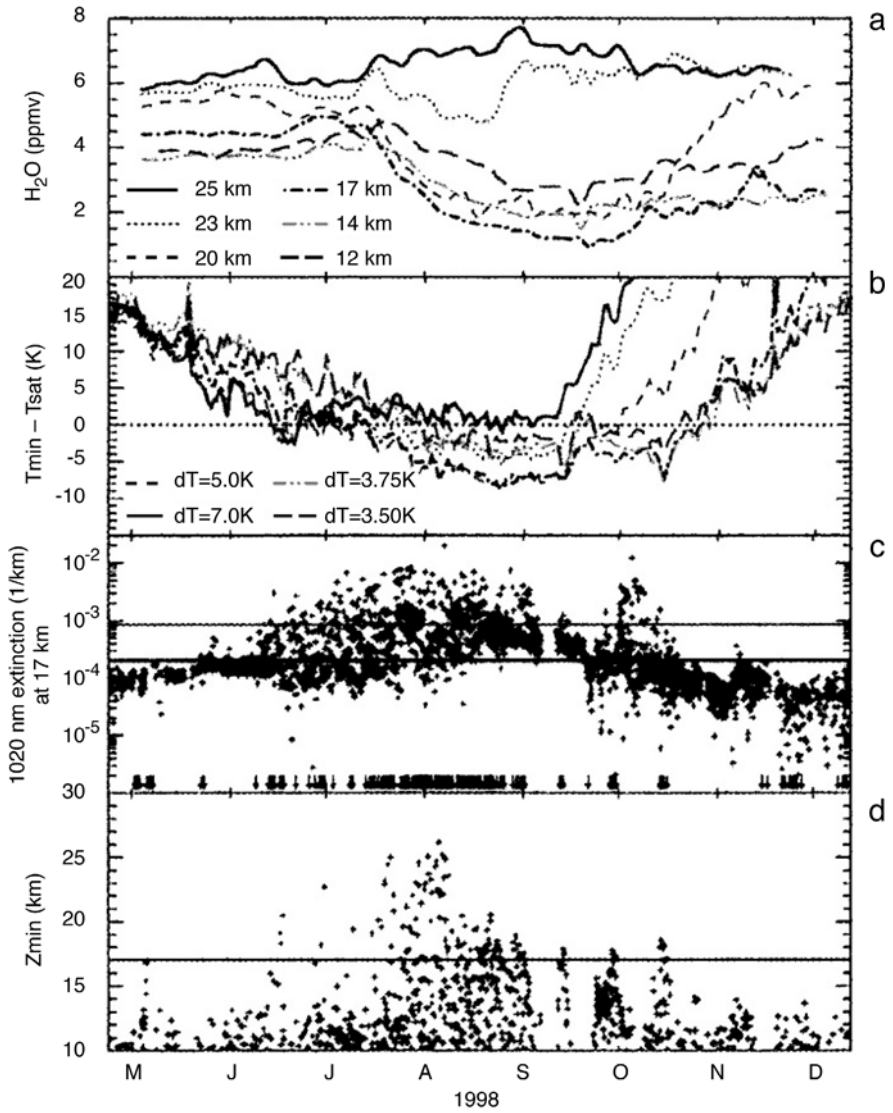

Figure 3.18. Time series of POAM measurements and related information demonstrating dehydration in the Antarctic lower stratosphere. The top panel (a) shows measured water vapor mixing ratios at six different altitudes. Panel (b) shows the difference between the minimum daily temperature of the POAM measurements and the freezing point temperature, calculated using a pre-dehydration (June 24–26 average) water vapor profile. Panel (c) shows the 1,020-nm extinction from individual POAM measurements. Arrows indicate extinction values below $10^{-6}\,km^{-1}$. The bottom panel (d) shows the minimum altitude at which POAM measurements could be made when Sun tracking was cut off above 10 km.

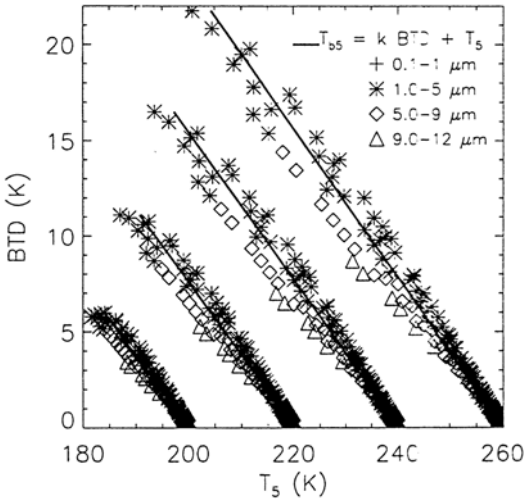

Figure 3.19. Radiative transfer simulation of the Brightness Temperature Difference (BTD) in Kelvin between AVHRR channels 4 and 5, as a function of the brightness temperature in channel 5, for four different PSC microphysical models (symbols) and a linear fit to the results (line). Four different model lower boundary temperatures T_b are used, corresponding to the four scatterplots (200, 220, 240, and 260 K, with $T_b(\text{ch4}) = T_b(\text{ch5})$), and the cloud temperature is 180 K. This plot shows how a very large BTD can appear for the smallest particles over the coldest surfaces.

From Hervig et al. (2001a). Copyright 2001 American Geophysical Union. Reproduced by permission of American Geophysical Union.

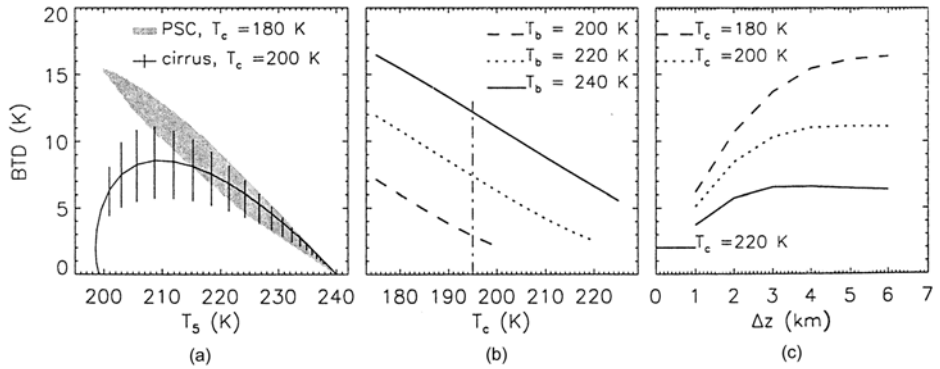

Figure 3.20. Summary of radiative transfer results, showing (a) how the BTD signature for PSCs can differ from that of cirrus clouds in the upper troposphere, (b) the maximum BTD as a function of cloud temperature for values of T_b indicated (the vertical line represents the maximum frost point temperature in the stratosphere), and (c) the maximum BTD as a function of cloud thickness Δz, calculated for the cloud temperatures indicated and $T_b = 240$ K.

From Hervig et al. (2001a). Copyright 2001 American Geophysical Union. Reproduced by permission of American Geophysical Union.

5 (12 μm) brightness temperatures over the continental interior in the top panel most likely represent the cold surface, as the corresponding brightness temperature difference (lower panel) is near zero over the continent, while consistent with Hervig et al. (2001a) over the Weddell Sea.

One limitation with using mid-IR imagery is that type-1 PSCs have particle size distributions with mode radii so small that no radiative signature can be detected in mid-IR imager data. Thus, imagers such as AVHRR and MODIS are at present limited to studying the evolution and dispersal of mature PSC systems. Another limitation is that much of the PSC season occurs during the polar night, when additional solar scattering information in the near-IR is not available for satellite measurement. However, the long historical database from imagers, and the ease of tracking airmasses in imager data, make studies of PSCs with these instruments highly valuable from a climatological perspective.

3.6 POLAR MESOSPHERIC CLOUDS

A polar phenomenon conceptually similar to PSCs are noctilucent clouds, or Polar Mesospheric Clouds (PMCs: Avaste, 1993; Thomas, 1989). These clouds can be observed from the ground, and occur during summer near the mesopause. PMCs have been observed in a variety of satellite experiments since the early 1970s (Donahue et al., 1972; Olivero and Thomas, 1986; Thomas, 1984; Thomas and Olivero, 1989). Recent evidence indicates that PMCs are composed of ice water particles (Hervig et al., 2001b). An example of an occultation observation of PMC extinction is shown in Figure 3.22, from Debrestian et al. (1997). This figure shows vertical profiles of the residual slant path optical depth measured by POAM II at 448.1 nm. The term "residual" refers to the optical depth profile after background Rayleigh scattering optical depth has been subtracted. Superimposed on these plots are calculations from a spherical shell radiative transfer model in which PMCs are represented by Mie scattering particles having log-normal size distributions with mode radii in the range 20 to 100 nm. Recent satellite instruments such as POAM, and the WIND Imaging Interferometer (WINDII) aboard UARS are gradually providing a comprehensive climatology of PMCs. Comparison of PMC events recorded by WINDII and POAM shows an increase in their number as compared with Solar Mesosphere Experiment (SME) measurements made a decade earlier (Shettle et al., 2002). This is consistent with ground-based observations that suggest an upward trend in Northern Hemisphere PMC occurrence over the past three decades (Gadsden, 1998). This increasing trend in PMC occurrence may be a manifestation of increasing abundances of atmospheric CO_2 and CH_4, which in the upper atmosphere result in cooler temperatures and higher water vapor abundances (Thomas, 1996).

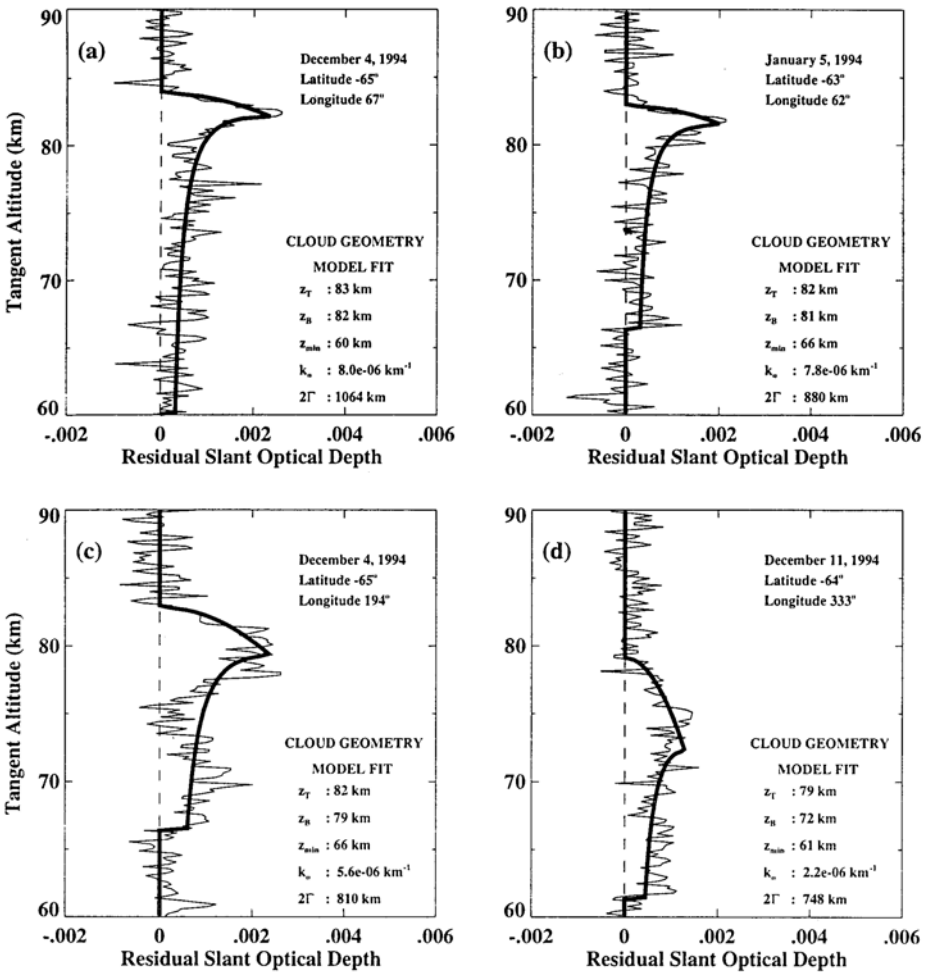

Figure 3.22. Examples of PMC signatures seen in POAM II 448-nm extinction profiles. The term "residual" slant path optical depth refers to the optical depth after background Rayleigh scattering has been subtracted. The solid curves depict results from various radiative transfer model simulations.

From Debrestian et al. (1997). Copyright 1997 American Geophysical Union. Reproduced by permission of American Geophysical Union.

3.7 ARCTIC OZONE DEPLETION

Generally speaking, springtime ozone depletion occurs in the Arctic stratosphere to a lesser extent than over the Antarctic. Arctic ozone "holes" cover a smaller area, and have appeared in some years but not others (Newman et al., 1997). Our first-order understanding of springtime Arctic ozone depletion is that it should be less severe because the Arctic stratosphere is generally warmer than the Antarctic during winter

and spring. Occasions when Arctic stratospheric temperatures fall to the range required for PSC formation are less frequent, and often do not last long enough into the spring for the related photochemical ozone loss to become severe. While not as dramatic in appearance, Arctic stratospheric ozone depletion is as important a geophysical problem as the Antarctic ozone "hole". In terms of ecological effects, enhanced levels of UV-B radiation reaching the Earth's surface through a springtime Arctic ozone decrease can reach terrestrial ecosystems and some human populations. In terms of atmospheric science, the variable nature of Arctic ozone depletion constitutes an interesting and complex problem involving both chemistry and dynamics.

There are two major dynamical considerations that limit ozone depletion in the Arctic stratosphere as compared with the Antarctic. First, greater atmospheric wave activity, ultimately related to the greater continental landmass in the Northern Hemisphere, results in a less isolated Arctic polar vortex, and brings about an earlier vortex breakdown and earlier transport of ozone-rich air from lower latitudes during spring. The less frequent episodes of extremely cold temperatures are also related to the smaller Arctic polar vortices. Second, in the Arctic upper stratosphere during winter there is a greater downward motion of air. This leads to both a warmer stratosphere due to diabatic heating, and a seasonal increase in stratospheric ozone abundance of more than 100 DU. Chlorine-catalyzed ozone destruction during early spring therefore acts against this background climatological ozone increase. Nevertheless, during the 1990s several winter/spring seasons were colder than the climatological mean (Coy et al., 1997; Zurek et al., 1996), resulting in significant ozone depletion events.

Satellite remote sensing has helped unravel many of the complexities associated with Arctic ozone depletion. During the 1990s, NASA's UARS program played a major role (Dessler et al., 1998), and UARS instruments were used to describe the details of the Arctic polar vortex during the cold seasons of the 1990s (Manney et al., 1997; Santee et al., 1996; Zurek et al., 1996). The individual UARS instruments have been discussed in Chapter 4. Early on in the UARS program, Microwave Limb Sounder (MLS) measurements showed the correlation between enhanced ClO concentrations and ozone depletion within the Arctic vortex during January (Schoeberl et al., 1993; Waters et al., 1993), demonstrating that extensive chlorine activation takes place in the Arctic (Figure 3.23, see color section). However, Cryogenic Limb Array Etalon Spectrometer (CLAES) measurements of HNO_3 and $ClONO_2$ (see reactions 3.5) during the same Arctic winter showed (1) localized depletions of both compounds coincident with the coldest stratospheric temperatures and (2) generally high concentrations of HNO_3 within the Arctic vortex (Roche et al., 1994). These CLAES measurements suggest a much smaller rate of denitrification in the Arctic vortex.

Manney et al. (1995a) employed a technique for tracing air parcel trajectories, in combination with passive tracer (chemically long-lived compounds) measurements from UARS (H_2O from MLS, N_2O and CH_4 from CLAES). Air parcels were identified using United Kingdom Meteorological Organization (UKMO) meteorological assimilation data (Manney et al., 1994), and a Lagrangian model is used to

follow air parcel trajectories in three dimensions. The calculations are initialized by assigning to each air parcel a tracer mixing ratio measured by UARS. As the Lagrangian model is run for subsequent days, evolution of the geographic distribution in tracer mixing ratios is compared with subsequent UARS observations. A successful comparison of the modeled and measured mixing ratio distributions throughout the simulation validates the use of a particular passive tracer for following air parcel trajectories. By examining the evolution of a chemically active species, such as ozone, along the air parcel trajectories identified by the passive tracers, one can gain insight into the balance between chemistry and dynamics in governing the distribution of the active species. For example, if the passive tracer mixing ratio is conserved along a trajectory but the active species mixing ratio changes, this indicates a chemical rather than a dynamical mechanism for the change in the active species mixing ratio. This Lagrangian analysis is subject to some sources of error, particularly (1) inaccuracies in the meteorological reanalysis data (typically worse in the Southern Hemisphere than in the Northern, due to fewer meteorological observations to initialize the reanalysis models), and (2) gridding errors with satellite trace gas measurements made at coarse spatial resolution. Nevertheless, Lagrangian analysis has been a useful tool for studying springtime Arctic ozone depletion. Manney et al. (1995b) concluded from this type of analysis that dynamical effects offset 20–35% of the chemical ozone depletion during the 1993 Arctic spring. Using a similar analysis for the 1991–92 Arctic winter, Müller et al. (1996) reported that ~60 DU of Arctic ozone were depleted on constant CH_4 surfaces, reinforcing the conclusion that heterogeneous chemistry plays a major role in Arctic ozone loss.

An example of the interannual variability in Arctic ozone loss is shown in Figure 3.24. Dynamical processes, primarily downward motion of stratospheric air, tend to add ozone to the lower stratosphere within the vortex. In the spring of 1994, heterogeneous chemistry caused a rate of ozone loss that only canceled out vertical transport, resulting in a nearly constant ozone mixing ratio at 20 km as observed by UARS. In the spring of 1996, vertical transport was slightly weaker, and heterogeneous chemistry more pronounced within the vortex, resulting in a net loss of ozone during that season. As both NASA and ESA will maintain major stratospheric remote-sensing programs in the coming years (e.g., the EOS Aura spacecraft), there will be many opportunities for investigating springtime Arctic ozone in the context of expected gradual recovery from anthropogenic ozone depletion.

3.8 THE OZONE HOLE, SOLAR ULTRAVIOLET RADIATION, AND ANTARCTIC ECOLOGY

The scientific community's initial concerns about the ecological effects of the Antarctic ozone "hole" are reviewed by Karentz (1991). The Antarctic ecosystem is overwhelmingly a marine ecosystem, and is characterized by a very short foodchain. The base of the foodchain involves primary production by

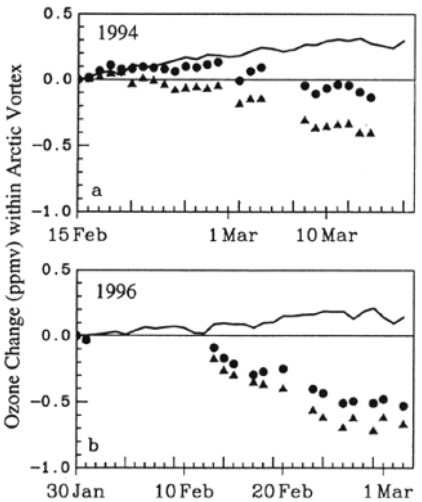

Figure 3.24. Time series of UARS-measured ozone mixing ratio at 20 km, within the Arctic polar vortex (dots), (a) for 1994, (b) for 1996. Also shown by the solid curve is the time series that would result if the ozone mixing ratio was governed only by transport (estimated from Langrangian analysis), and the magnitude of the chemical contribution to ozone loss (triangles), estimated from the difference between the satellite observations and the Lagrangian model.

phytoplankton and grazing by Antarctic krill (*Euphausia superba*), which in turn are a staple for all the higher predators. During spring, phytoplankton are particularly vulnerable as they are released from their overwinter habitat as the sea ice retreats. Due to lower salinity near the edge of the melting and retreating sea ice, the upper several meters of the water column into which the phytoplankton are released are relatively stable against vertical mixing, implying that the organisms are trapped in a regime where light levels are higher. If these light levels consist of spectral UV and Photosynthetically Active Radiation (PAR) under which the organisms have evolved, then this is a favorable situation for rapid phytoplankton growth, or algal "blooms" (e.g., Arrigo and McClain, 1994). If, on the other hand, this stratified water column is exposed to elevated UV-B fluxes under the ozone "hole", the organisms will be at risk of DNA damage and inhibition of photosynthesis (Holm-Hansen et al., 1993; Smith et al., 1992). Ecologists have been concerned that any significant impacts of enhanced UV-B on Antarctic primary production could have immediate and serious consequences up the relatively short foodchain.

Immediately after the ozone "hole" discovery, the U.S. Antarctic Program initiated a program to measure and monitor spectral UV radiation at Palmer Station, McMurdo Station, the South Pole, and Ushuaia, Argentina (Booth et al., 1994). The resulting network of scanning spectro-radiometers quickly confirmed that the ozone "hole" brings about greatly enhanced UV-B fluxes at the Antarctic Earth

surface (e.g., Lubin et al., 1989). By the late 1980s, several robust biological field experiments were gathering valuable information about the response and adaptation of Antarctic marine organisms to UV radiation, including quantifying protective pigments, DNA damage and repair mechanisms, the balance between inhibition of photosynthesis caused by UV-B and UV-A, and rates of photosynthesis under ambient PAR fluxes. Much of this research is discussed in Weiler and Penhale (1994). The very comprehensive Icecolors cruise in the Western Antarctic Peninsula (WAP) region (Smith et al., 1992) was able to carry out biological experiments on samples in the water column as the polar vortex edge passed back and forth over the ship's research stations. This provided natural "control" conditions under climatological UV and PAR fluxes, alternating with enhanced UV-B under the ozone "hole". First-order extrapolation of the Icecolors field results to the larger region suggested that the effect of the ozone "hole" was to reduce primary production by 6–12%. Other field experiments yielded more conservative estimates of less than 1% (Holm-Hansen et al., 1993). It remains unclear whether these reductions have had an immediate effect on higher trophic levels, or if the Antarctic ecosystem has undergone more subtle changes in the form of population shifts in favor of those phytoplankton species more resilient to UV-B exposure.

Part of the difficulty in making these ecological assessments lies in the nature of the fieldwork itself: the highest quality and most comprehensive measurements are few and far between. Robust field experiments, such as Icecolors, on natural organisms are indispensable for elucidating and quantifying the actual response of individual plankton species to both normal and enhanced UV-B. However, there remains the difficulty of generalizing these findings to an entire region. This is where satellite remote sensing can play an important role. The TOMS data have mapped the extent of the Antarctic ozone "hole" since 1979. If TOMS or other satellite instruments can provide information about the other important factors that regulate UV and PAR flux at the Antarctic surface—particularly sea ice and cloud optical depth—then it is possible to use appropriate radiative transfer models to retrieve the climatology of UV and PAR throughout Antarctica and the Southern Ocean. Chapters 4 and 5 discuss in depth the ways in which cloud optical properties, sea ice concentration, and sea ice albedo can all be retrieved from appropriate satellite data. Presently there have been some successful efforts to map UV radiation throughout Antarctica based on remote sensing (e.g., Krotkov et al., 2001; Lubin and Morrow, 2001; Lubin et al., 1994; Nunez et al., 1997). Some of the radiative transfer methods have attained a high degree of sophistication, and are able to treat multi-dimensional radiative transfer effects that lead to radiation enhancements over the open water by multiple reflection of photons from an adjacent high-albedo coastline (Ricchiazzi and Gautier, 1998).

An example of satellite-based UV-B mapping is shown in Figure 3.25 (see color section). These retrievals use the TOMS reflectivity product for estimating cloud effective optical depth, and a parameterization for ultraviolet sea ice albedo, for sea ice of any concentration, derived by Lubin and Morrow (2001). Satellite retrievals of this type have been validated by United States Antarctic Program (USAP) UV Monitor (spectro-radiometer) measurements at Palmer Station

(Arrigo et al., 2003). Compared with 1979, the local noon UV-B surface fluxes on October 5, 1992 are elevated by a factor of 2 or more over half of the Antarctic coastline, due to a geographic bias in the polar vortex on that day which placed low total column ozone amounts (<150 DU) over West Antarctica, the WAP region, the Weddell Sea, and the Indian Ocean sector of the Southern Ocean. At lower latitudes, there are some large differences in surface UV-B flux due to interannual variability in cloud cover.

Satellite remote sensing can map not only sources of physical forcing to an ecosystem, such as UV and PAR, but also fundamental properties of the ecosystem itself. A prime example is the SeaWiFS (Sea-viewing Wide Field of View Spectrometer) ocean color program, and its predecessor the Nimbus 7 Coastal Zone Color Scanner (CZCS), which, by measuring backscattered radiance from the cloud-free ocean–atmosphere system at selected wavelengths over a range where chlorophyll differentially absorbs (see Table 2.1), enables space-based mapping of surface chlorophyll *a* which is an indicator of phytoplankton biomass. The standard (midlatitude) algorithms for chlorophyll *a* retrieval are discussed by Gordon (1997), O'Reilly et al. (1998), and references therein. An alternative approach based on rigorous, coupled ocean-atmosphere, discrete ordinates radiative transfer modeling has been proposed by Stamnes et al. (2003). If the phytoplankton biomass can be mapped by satellite, along with UV and PAR as influenced by the real ozone layer and troposphere, then there is the potential for multi-sensor satellite assessment of the ozone hole's ecological impact throughout the Southern Ocean.

There are two major challenges with deriving the climatological distribution of Antarctic phytoplankton biomass from ocean color satellite data. First, the Southern Ocean is one of the cloudiest regions on Earth (Warren et al., 1988), and in many sectors it can take years of satellite overpasses to obtain enough cloud-free scenes for ocean color analysis. Second, the bio-optical properties of Antarctic phytoplankton are quite different from their mid-latitude counterparts, and application of the standard SeaWiFS or CZCS algorithms will yield hopelessly unrealistic results. Figure 3.26 shows the essence of chlorophyll pigment concentration retrieval based on empirical relationships between chlorophyll *a* abundance and satellite-measured reflectance ratios, but clearly demonstrates (1) the "global" algorithms are at odds with bio-optical data from the Ross Sea, and (2) there can be substantial disagreement between algorithms developed from different Antarctic bio-optical datasets. This particular study (Arrigo et al., 1998) concludes that no single satellite parameterization will apply to the three taxonomically distinct phytoplankton blooms that appear in the Ross Sea. Similarly, Dierssen and Smith (2000) have shown that a regionally specific ocean color algorithm is required for Antarctic Peninsula waters. At present, ocean color algorithms designed for the Antarctic are beginning to yield an accurate climatological distribution of phytoplankton surface biomass, and there is potential for satellite-based ecological studies (Figure 3.27, see color section). More discussion is given in Chapter 5 on the relationship between primary production and Antarctic sea ice, and the role that satellite remote sensing can play.

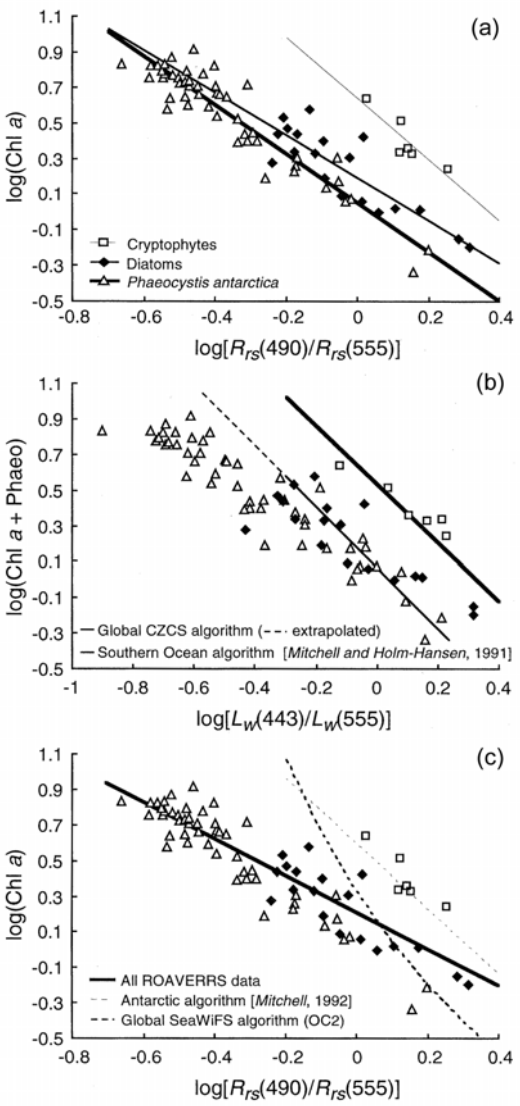

Figure 3.26. Illustration of the complexities involved in retrieving Antarctic chlorophyll *a* pigment concentrations from satellite ocean color data. (a) Empirical relationship between Chl *a* and the ratio of reflectances at 490 and 555 nm, for research stations dominated by three different species compositions; lines are least-squares regressions. (b) Empirical relationship between Chl *a*+ phaeopigment and the ratio of reflectances at 443 and 555 nm; lines represent predictions based on a Southern Ocean algorithm based on other bio-optical data (thick) and the global CZCS algorithm (thin). (c) As in (a) but with all data fitted to a single regression (thick solid), a prediction based on another Antarctic algorithm (thin dashed), and a prediction based on the global SeaWiFS algorithm (thick dashed).

Arrigo et al. (2003) made the first attempt to combine ocean color maps of phytoplankton biomass with surface UV and PAR flux retrievals to assess the ecological impact of the ozone "hole". The surface fluxes derived from TOMS and SSM/I (Special Sensor Microwave/Imager) data were propagated into the water column, and a numerical model of phytoplankton growth as a function of light availability and temperature was used to estimate primary production. This model included a parameterization for UV-B-induced inhibition of photosynthesis, based on fieldwork by Neale et al. (1998). This study was conducted as a numerical simulation experiment for the entire Southern Ocean, for the 1992 ozone hole, with 1979 TOMS ozone values also used as a "control" case (all other radiative transfer parameters held constant). The simulation yielded good agreement with ICECOLORS results for the upper water column near the Antarctic Peninsula. However, when primary production losses were integrated to the 0.1% light depth, the loss attributable to excess UV-B due to ozone depletion was $<0.25\%$ for August through December. Although this result suggests a negligible impact of the ozone hole on the Antarctic marine ecosystem, it is probably not the final result. The year 1992 saw a deep ozone hole (<100 DU much of the time), but most of the lowest ozone abundances were confined over the Antarctic continent; in contrast to the late 1990s when much more of the Southern Ocean lay under ozone abundances $\sim$100–150 DU during spring. Furthermore, this type of study has yet to take advantage of improved radiative transfer formulations that yield enhancements near the sea ice edge (Ricchiazzi and Gautier, 1998), and fully rigorous radiative transfer coupling between the atmosphere and ocean (Jin and Stamnes, 1994). This type of multisensor approach to marine ecology is new to remote sensing in general, and applications to the polar regions are particularly compelling.

3.9 REFERENCES

Andrews, D. G., J. R. Holton, and C. B. Leovy (1987). *Middle Atmosphere Dynamics*. Academic Press, San Diego, 489 pp.

Arrigo, K. R. and C. R. McClain (1994). Spring phytoplankton production in the western Ross Sea. *Science*, **266**, 261–263.

Arrigo, K. R., D. H. Robinson, D. L. Worthen, B. Schieber, and M. P. Lizotte (1998). Bio-optical properties of the southwestern Ross Sea. *Journal of Geophysical Research*, **103**(C10), 21683–21695.

Arrigo, K. R., D. Lubin, G. L. van Dijken, O. Holm-Hansen, and E. Morrow (2003). Impact of a deep ozone hole on Southern Ocean primary production. *Journal of Geophysical Research*, **108**(C5), DOI: 10.1029/2001JC001226-23-1-19.

Avaste, O. (1993). Noctilucent clouds. *Journal of Atmospheric and Terrestrial Physics*, **55**, 133–143.

Bates, D. R. and M. Nicolet (1950). Atmospheric hydrogen. *Publications of the Astronomical Society of the Pacific*, **62**, 106–110.

Booth, C. R., T. B. Lucas, J. H. Morrow, C. S. Weiler, and P. A. Penhale (1994). The United States National Science Foundation's polar network for monitoring ultraviolet radiation. *American Geophysical Union Antarctic Research Series*, **62**, 17–37.

Brasseur, G. and S. Solomon (1984). *Aeronomy of the Middle Atmosphere*. D. Reidel, Boston, 441 pp.

Browell, E. V., C. F. Butler, S. Ismail, P. A. Robinette, A. F. Carter, N. S. Higdon, O. B. Toon, M. R. Schoeberl, and A. F. Tuck (1990). Airborne lidar observations in the wintertime Arctic stratosphere: Polar stratospheric clouds. *Geophysical Research Letters*, **17**, 385–388.

Chapman, S. (1930). On ozone and atomic oxygen in the upper atmosphere. *Philosophical Magazine*, **10**, 369–383.

Chubachi, S. (1984). Preliminary result of ozone observations at Syowa Station from February, 1982 to January, 1983. *Memoirs of the National Institute for Polar Research of Japan*, Special Issue, **34**, 13–20.

Chubachi, S. and R. Kajiwara (1986). Total ozone variations at Syowa, Antarctica. *Geophysical Research Letters*, **13**, 1197–1199.

Coffey, M. T., W. G. Mankin, and A. Goldman (1989). Airborne measurements of stratospheric constituents over Antarctica in the austral spring, 1987, 2: Halogen and nitrogen trace gases. *Journal of Geophysical Research*, **94**(D14), 16597–16613.

Coy, L., E. R. Nash, and P. A. Newman (1997). Meteorology of the polar vortex: Spring 1997. *Geophysical Research Letters*, **24**, 2693–2696.

Crützen, P. J. (1970). The influence of nitrogen oxide on the atmospheric ozone content. *Quarterly Journal of the Royal Meteorological Society*, **96**, 320–327.

Crützen, P. J. (1971). Ozone production rates in an oxygen–hydrogen–nitrogen atmosphere. *Journal of Geophysical Research*, **76**, 7311–7327.

Crützen, P. J. and F. Arnold (1986). Nitric acid cloud formation in the cold Antarctic stratosphere: A major cause for the springtime "ozone hole". *Nature*, **324**, 651–655.

Debrestian, D. J., J. D. Lumpe, E. P. Shettle, R. M. Bevilacqua, J. J. Olivero, J. S. Hornstein, W. Glaccum, D. W. Rusch, C. E. Randall, and M. D. Fromm (1997). An analysis of POAM II solar occultation observations of polar mesospheric clouds in the southern hemisphere. *Journal of Geophysical Research*, **102**(D2), 1971–1981.

Dierssen, H. M. and R. C. Smith (2000). Bio-optical properties and remote sensing ocean color algorithms for Antarctic Peninsula waters. *Journal of Geophysical Research*, **105**(C11), 26301–26312.

Dessler, A. E., M. D. Burrage, J.-U. Grooss, J. R. Holton, J. L. Lean, S. T. Massie, M. R. Schoeberl, A. R. Douglass, and C. H. Jackman (1998). Selected science highlights from the first 5 years of the Upper Atmosphere Research Satellite (UARS) program. *Reviews of Geophysics*, **36**, 183–210.

de Zafra, R. L., M. Jaramillo, A. Parrish, P. Solomon, B. Connor, and J. Barnett (1987). High concentrations of chlorine monoxide at low altitudes in the Antarctic spring stratosphere: Diurnal variation. *Nature*, **328**, 408–411.

de Zafra, R. L., M. Jaramillo, J. Barnett, L. K. Emmons, P. M. Solomon, and A. Parrish (1989). New observations of a large concentration of ClO in the springtime lower stratosphere over Antarctica and its implication for ozone-depleting chemistry. *Journal of Geophysical Research*, **94**(D9), 11423–11428.

Dobson, G. M. B. (1957). Observer's handbook for the ozone spectrometer. *Annals of the International Geophysical Year*, **5**, 46–81.

Donahue, T. M., B. Guenther, and J. E. Blamont (1972). Noctilucent clouds in daytime: Circumpolar particulate layers near the summer mesopause. *Journal of the Atmospheric Sciences*, **30**, 515–517.

Drdla, K. (1996). Applications of a model of polar stratospheric clouds and heterogeneous chemistry. Ph.D. thesis, University of California Los Angeles.

Dye, J. E., D. Baumgartner, B. W. Gandrud, S. R. Kawa, K. K. Kelly, M. Loewenstein, G. V. Ferry, K. R. Chan, and B. L. Gray (1992). Particle size distributions in Arctic polar stratospheric clouds, growth and freezing of sulfuric acid droplets, and implications for cloud formation. *Journal of Geophysical Research*, **97**(D8), 8015–8034.

Fahey, D. W., K. K. Kelly, G. V. Ferry, L. R. Poole, J. C. Wilson, D. M. Murphy, M. Loewenstein, and K. R. Chan (1989). In situ measurements of total reactive nitrogen, total water and aerosol in a polar stratospheric cloud in the Antarctic. *Journal of Geophysical Research*, **94**(D9), 11299–11315.

Farman, J. C., B. G. Gardiner, and J. D. Shanklin (1985). Large losses of total ozone in Antarctica reveal seasonal ClO_x/NO_x interaction. *Nature*, **315**, 207–210.

Farmer, C. B., G. C. Toon, P. W. Shaper, J. F. Blavier, and L. L. Lowes (1987). Stratospheric trace gases in the spring 1986 Antarctic atmosphere. *Nature*, **329**, 126–130.

Fromm, M. D., J. D. Lumpe, R. M. Bevilacqua, E. P. Shettle, J. Hornstein, S. T. Massie, and K. H. Fricke (1997). Observations of Antarctic polar stratospheric clouds by POAM II: 1994–1996. *Journal of Geophysical Research*, **102**(D19), 23659–23672.

Gadsden, M. (1998). The north-west Europe data on noctilucent clouds: A survey. *Journal of Atmospheric and Terrestrial Physics*, **60**, 1163–1174.

Gandrud, B. W., P. S. Sperry, L. Sanford, K. K. Kelly, G. V. Ferry, and K. R. Chan (1989). Filter measurement results from the Airborne Antarctic Ozone Experiment. *Journal of Geophysical Research*, **94**(D9), 11285–11297.

Garcia, O., K. L. Pagan, P. G. Foschi, S. Gaines, and R. S. Hipskind (1995). Detection of polar stratospheric clouds over Antarctica using AVHRR images obtained at Palmer Station during August 1992. *Polar Record*, **31**, 211–226.

Glaccum, W., R. L. Lucke, R. M. Bevilacqua, E. P. Shettle, J. S. Hornstein, D. T. Chen, J. D. Lumpe, S. S. Krigman, D. J. Debrestian, M. D. Fromm et al. (1997). The Polar Ozone and Aerosol Measurement instrument. *Journal of Geophysical Research*, **101**(D9), 14479–14487.

Goody, R. M. and Y. Yung (1989). *Atmospheric Radiation: Theoretical Basis*. Oxford University Press, New York, 519 pp.

Gordon, H. R. (1997). Atmospheric correction of ocean color imagery in the Earth Observing System era. *Journal of Geophysical Research*, **102**(D14), 17081–17106.

Gunson, M. R. (1992). The Atmospheric Trace Molecular Spectroscopy (ATMOS) experiment: The ATLAS 1 mission. In: *Optical Methods in Atmospheric Chemistry* (SPIE 1715). Society for Photo-optical Instrumentation Engineers, pp. 513–519.

Harris, N., R. Hudson, and C. Phillips (eds.) (1998). *Assessment of Trends in the Vertical Distribution of Ozone* (SPARC [Stratospheric Processes And their Role in Climate] Report 1, Ozone Research and Monitoring Project Report 43). World Meteorological Organization, Geneva.

Hering, W. S. and T. R. Borden (1965). *Ozone Sonde Observations over North America* (Vol. 3, Report AFCRL-64-30(3)). Air Force Cambridge Research Laboratories, Bedford, MA.

Herman, J. R., P. K. Bhartia, J. Ziemke, Z. Ahmad, and D. Larko (1996). UV-B increases (1979–1992) from decreases in total ozone. *Geophysical Research Letters*, **23**, 2117–2120.

Hervig, M. E., K. L. Pagan, and P. G. Foschi (2001a). Analysis of polar stratospheric cloud measurements from AVHRR. *Journal of Geophysical Research*, **106**(D10), 10363–10374.

Hervig, M., R. E. Thompson, M. McHugh, L. L. Gordley, J. M. Russell III, and M. E. Summers (2001b). First confirmation that water ice is the primary component of polar mesospheric clouds. *Geophysical Research Letters*, **28**, 971–984.

Hoffman, D. J., J. W. Harder, S. R. Rolf, and J. M. Rosen (1987). Balloon-borne observations of the development and vertical structure of the Antarctic ozone hole in 1986. *Nature*, **326**, 59–62.

Holm-Hansen, O., E. W. Helbling, and D. Lubin (1993). Ultraviolet radiation in Antarctica: Inhibition of primary production. *Photochemistry and Photobiology*, **58**, 567–570.

Holton, J. R., P. H. Haynes, M. E. McIntyre, A. R. Douglass, R. B. Rood, and L. Pfister (1995). Stratosphere–troposphere exchange. *Reviews of Geophysics*, **33**, 403–439.

Jin, Z. and K. Stamnes (1994). Radiative transfer in nonuniformly refracting media: Atmosphere-ocean system. *Applied Optics*, **33**, 431–442.

Johnston, H. S. (1971). Reduction of stratospheric ozone by nitrogen oxide catalysts from supersonic transport exhaust. *Science*, **173**, 517–522.

Joiner, J., P. K. Bhartia, R. P. Cebula, E. Hilsenrath, R. D. McPeters, and H. Park (1995). Rotational Raman scattering (Ring effect) in satellite backscatter ultraviolet measurements. *Applied Optics*, **34**, 4513–4525.

Karentz, D. (1991). Ecological considerations of the Antarctic ozone hole. *Antarctic Science*, **3**, 3–11.

Klenk, K. F., P. K. Bhartia, A. J. Flieg, V. G. Kaveeshwar, R. D. McPeters, and P. M. Smith (1982). Total ozone determination from the Backscattered UltraViolet (BUV) experiment. *Journal of Applied Meteorology*, **21**, 1672–1684.

Krotkov, N. A., A. J. Krueger, and P. K. Bhartia (1997). Ultraviolet optical model of volcanic clouds for remote sensing of ash and sulfur dioxide. *Journal of Geophysical Research*, **102**(D18), 21891–21904.

Krotkov, N. A., J. R. Herman, P. K. Bhartia, V. Fioletov, and Z. Ahmad (2001). Satellite estimation of spectral surface UV irradiance, 2: Effects of homogeneous clouds and snow. *Journal of Geophysical Research*, **106**(D11), 11743–11759.

Krueger, A. J. (1973). The mean ozone distributions from several series of rocket soundings to 52 km at latitudes from 58°S to 64°N. *Pure and Applied Geophysics*, **1271**, 106–108.

Krueger, A. J., L. S. Walter, P. K. Bhartia, C. C. Schnetzler, N. A. Krotkov, I. E. Sprod, and G. J. S. Bluth (1995). Volcanic sulfur dioxide measurements from the Total Ozone Mapping Spectrometer instruments. *Journal of Geophysical Research*, **100**(D7), 14057–14076.

Lefèvre, F., D. Cariolle, S. Muller, and F. Karcher (1991). Total ozone from the TIROS Operational Vertical Sounder during the formation of the 1987 "ozone hole". *Journal of Geophysical Research*, **96**(D7), 12893–12911.

Liou, K. N. (1992). *Radiation and Cloud Processes in the Atmosphere*. Oxford University Press, New York, 487 pp.

Lubin, D. and E. Jensen (1995). Effects of clouds and stratospheric ozone depletion on ultraviolet radiation trends. *Nature*, **377**, 710–713.

Lubin, D. and E. Morrow (2001). Ultraviolet radiation environment of Antarctica, 1: Effect of sea ice on top-of-atmosphere albedo and on satellite retrievals. *Journal of Geophysical Research*, **106**(D24), 33453–33461.

Lubin, D., J. E. Frederick, C. R. Booth, T. Lucas, and D. Neuschuler (1989). Measurements of enhanced springtime ultraviolet radiation at Palmer Station, Antarctica. *Geophysical Research Letters*, **16**, 783–785.

Lubin, D., C. Gautier, P. Ricchiazzi, and R. H. Whritner (1994). A method for mapping Antarctic surface ultraviolet radiation using multispectral satellite imagery. In: C. W. Weiler and P. A. Penhale (eds.), *Ultraviolet Radiation in Antarctica: Measurements and Biological Effects* (AGU Antarctic Research Series No. 62, pp. 53–81). American Geophysical Union, Washington, DC.

Lucke, R. L., D. R. Korwan, R. M. Bevilacqua, J. S. Hornstein, E. P. Shettle, D. T. Chen, M. Daehler, J. D. Lumpe, M. D. Fromm, D. Debrestian et al. (1999). The Polar Ozone and Aerosol Measurement (POAM) III instrument and early validation results. *Journal of Geophysical Research*, **104**(D15), 18785–18799.

Lumpe, J. D., R. M. Bevilacqua, K. W. Hoppel, S. S. Krigman, D. L. Kriebel, D. J. Debrestian, C. E. Randall, D. W. Rusch, C. Brogniez, R. Ramananaherisoa et al. (1997). POAM II retrieval algorithm and error analysis. *Journal of Geophysical Research*, **102**, 23593–23614.

Mahlman, J. D. and S. B. Fels (1986). Antarctic ozone decrease: A dynamical cause? *Geophysical Research Letters*, **13**, 1316–1319.

Manney, G. L., L. Froidevaux, J. W. Waters, R. W. Zurek, W. G. Read, L. S. Elson, J. B. Kumer, J. L. Mergenthaler, A. E. Roche, A. O'Neill et al. (1994). Chemical depletion of ozone in the Arctic lower stratosphere during winter 1992–93. *Nature*, **370**, 429–450.

Manney, G. L., L. Froidevaux, J. W. Waters, and R. W. Zurek (1995a). Evolution of microwave limb sounder ozone and the polar vortex during winter. *Journal of Geophysical Research*, **100**(D2), 2953–2972.

Manney, G. L., R. W. Zurek, L. Froidevaux, J. W. Waters, A. O'Neill, and R. Swinbank (1995b). Lagrangian transport calculations using UARS data, Part I: Passive tracers. *Journal of the Atmospheric Sciences*, **52**, 3049–3068.

Manney, G. L., R. W. Zurek, L. Froidevaux, J. W. Waters, A. O'Neill, and R. Swinbank (1995c). Lagrangian transport calculations using UARS data, Part II: Ozone. *Journal of the Atmospheric Sciences*, **52**, 3069–3081.

Manney, G. L., L. Froidevaux, J. W. Waters, M. L. Santee, W. G. Read, D. A. Flower, R. F. Jarnot, and R. W. Zurek (1996a). Arctic ozone depletion observed by UARS MLS during the 1994–95 winter. *Geophysical Research Letters*, **23**, 85–88.

Manney, G. L., M. L. Santee, L. Froidevaux, J. W. Waters, and R. W. Zurek (1996b). Polar vortex conditions during the 1995–96 Arctic winter: Meteorology and MLS ozone. *Geophysical Research Letters*, **23**, 3203–3206.

Manney, G. L., L. Froidevaux, M. L. Santee, R. W. Zurek, and J. W. Waters (1997). MLS observations of Arctic ozone loss in 1996–97. *Geophysical Research Letters*, **24**, 2697–2700.

Massie, S. T., D. Baumgardner, and J. E. Dye (1998). Estimation of polar stratospheric cloud volume and area densities from UARS, stratospheric aerosol measurement II, and polar ozone and aerosol measurement II extinction data. *Journal of Geophysical Research*, **103**(D5), 5773–5783.

McCormick, M. P., P. Hamill, T. J. Pepin, W. P. Chu, T. J. Swissler, and L. R. McMaster (1979). Satellite studies of the stratospheric aerosol. *Bulletin of the American Meteorological Society*, **60**, 1038–1046.

McCormick, M. P., W. P. Chu, G. W. Grams, P. Hamill, B. M. Herman, L. R. McMaster, T. J. Pepin, P. B. Russell, H. M. Steele, and T. J. Swissler (1981). High latitude stratospheric aerosols measured by the SAM II satellite system in 1978 and 1979. *Science*, **214**, 328–331.

McCormick, M. P., R. E. Veiga, W. P. Chu, and T. J. Swissler (1982). Polar stratospheric cloud sightings by SAM II. *Journal of the Atmospheric Sciences*, **39**, 1387–1397.

McElroy, M. B., R. J. Salawitch, S. C. Wofsy, and J. A. Logan (1986). Reductions of Antarctic ozone due to synergistic interactions of chlorine and bromine. *Nature*, **321**, 759–762.

McPeters, R. D. and G. J. Labow (1996). An assessment of the accuracy of 14.5 years of Nimbus 7 TOMS version 7 ozone data by comparison with the Dobson network. *Geophysical Research Letters*, **23**, 3695–3698.

McPeters, R. D., P. K. Bhartia, Arlin J. Krueger, R. Jay, and G. Herman (1998). *Earth Probe Total Ozone Mapping Spectrometer (TOMS) Data Products User's Guide* (NASA Tech. Pub. 1998-206895). NASA Goddard Space Flight Center, Greenbelt, MD, 64 pp.

Mitchell, B. G. (1992). Predictive bio-optical relationships for polar oceans and marginal ice zones. *Journal of Marine Systems*, **3**, 91–105.

Mitchell, B. G. and O. Holm-Hansen (1991). Bio-optical properties of Antarctic Peninsula waters: Differentiation from temperate ocean models. *Deep Sea Research I*, **38**(8/9), 1009–1028.

Molina, M. J. and F. S. Rowland (1974). Stratospheric sink for chlorofluoromethanes: Chlorine atom catalyzed destruction of ozone. *Nature*, **249**, 810–814.

Montzka, S. A., J. H. Butler, R. C. Myers, T. M. Thompson, T. H. Swanson, A. D. Clarke, L. T. Lock, and J. W. Elkins (1996). Decline in the tropospheric abundance of halogen from halocarbons: Implications for stratospheric ozone depletion. *Science*, **272**, 1318–1322.

Mount, G. H., R. W. Sanders, A. L. Schmeltekopf, and S. Solomon (1987). Visible spectroscopy at McMurdo Station, Antarctica, 1: Overview and daily variations of NO_2 and O_3, austral spring, 1986. *Journal of Geophysical Research*, **92**(D7), 8320–8328.

Müller, R., P. J. Crutzen, J.-U. Grooß, and C. Brühl (1996). Chlorine activation and ozone depletion in the Arctic vortex: Observations by the Halogen Occultation Experiment on the Upper Atmosphere Research Satellite. *Journal of Geophysical Research*, **101**(D7), 12531–12554.

Neale, P. J., R. F. Davis, and J. J. Cullen (1998). Interactive effects of ozone depletion and vertical mixing on photosynthesis of Antarctic phytoplankton, *Nature*, **392**, 585–589.

Nedoluha, G. E., R. M. Bevilacqua, K. W. Hoppel, M. Daehler, E. P. Shettle, J. H. Hornstein, M. D. Fromm, J. D. Lumpe, and J. E. Rosenfield (2000). POAM III measurements of dehydration in the Antarctic lower stratosphere. *Geophysical Research Letters*, **27**, 1683–1686.

Newman, P. A., J. F. Gleason, R. D. McPeters, and R. S. Stolarski (1997). Anomalously low ozone over the Arctic. *Geophysical Research Letters*, **24**, 2689–2692.

Niu, X. F., J. E. Frederick, M. L. Stein, and G. C. Tiao (1992). Trends in column ozone based on TOMS data: Dependence on month, latitude, and longitude. *Journal of Geophysical Research*, **97**(D13), 14661–14669.

Nunez, M., K. Michael, D. Turner, M. Wall, and C. Nilsson (1997). A satellite-based climatology of UV-B irradiance for Antarctic coastal regions. *International Journal of Climatology*, **17**, 1029–1054.

Olivero, J. J. and G. E. Thomas (1986). Climatology of polar mesospheric clouds. *Journal of the Atmospheric Sciences*, **43**, 1263–1274.

O'Reilly, J. E., S. Maritorena, B. G. Mitchell, D. A. Siegel, K. L. Carder, S. A. Garver, M. Kahru, and C. McClain (1998). Ocean color chlorophyll algorithm for SeaWiFS. *Journal of Geophysical Research*, **103**(C11), 24937–24953.

Pagan, K. L. (1996). Detection of polar stratospheric clouds over Antarctica using AVHRR satellite imagery. M.S. thesis, San Francisco State University.

Pierce, A. K., C. D. Slaughter, and D. Weinberger (1976). Solar limb darkening in the interval 7404–24018 Å. *Solar Physics*, **52**, 179–189.

Podgorny, I. and D. Lubin (1998). Biologically active insolation over Antarctic waters: Effect of a highly reflecting coastline. *Journal of Geophysical Research*, **103**(C2), 2919–2928.

Poole, L. R. and M. P. McCormick (1988a). Polar stratospheric clouds and the Antarctic ozone hole. *Journal of Geophysical Research*, **93**, 8423–8430.

Poole, L. R. and M. P. McCormick (1988b). Airborne lidar observations of Arctic polar stratospheric clouds: Indications of two distinct growth stages. *Geophysical Research Letters*, **15**, 21–23.

Randall, C. E., D. W. Rusch, R. M. Bevilacqua, K. W. Hoppel, and J. D. Lumpe (1998). Polar Ozone and Aerosol Measurement (POAM) II stratospheric NO_2, 1993–1996. *Journal of Geophysical Research*, **103**(D21), 28361–28371.

Randall, C. E., R. M. Bevilacqua, J. D. Lumpe, K. W. Hoppel, D. W. Rusch, and E. P. Shettle (2000). Comparison of Polar Ozone and Aerosol Measurement (POAM) II and Stratospheric Aerosol and Gas Experiment (SAGE) II aerosol measurements from 1994–1996. *Journal of Geophysical Research*, **105**(D3), 3929–3942.

Ricchiazzi, P., and C. Gautier (1998). Investigation of the effect of surface heterogeneity and topography on the radiation environment of Palmer Station, Antarctica, with a hybrid 3-D radiative transfer model. *Journal of Geophysical Research*, **103**(D6), 6161–6176.

Roche, A. E., J. B. Klumer, J. L. Mergenthaler, R. W. Nightingale, W. G. Uplinger, G. A. Ely, J. F. Potter, D. J. Wuebbles, P. S. Connell, and D. E. Kinnison (1994). Observations of lower-stratospheric $ClONO_2$, HNO_3, and aerosol by the UARS CLAES experiment between January 1992 and April 1993. *Journal of the Atmospheric Sciences*, **51**, 2877–2902.

Rodgers, C. D. (1976). Retrieval of atmospheric temperature and composition from remote measurements of thermal radiation. *Reviews of Geophysics and Space Physics*, **14**, 609–624.

Rowland, F. S. and M. J. Molina (1975). Chlorofluoromethanes in the environment. *Reviews of Geophysics*, **13**, 1–35.

Rusch, D. W., J.-C. Gerard, S. Solomon, P. J. Crutzen, and G. C. Reid (1981). The effect of particle precipitation events on the neutral and ion chemistry of the middle atmosphere, 1: Odd nitrogen. *Planetary and Space Science*, **29**, 767–774.

Santee, M. L., G. L. Manney, W. G. Read, L. Froidevaux, and J. W. Waters (1996). Polar vortex conditions during the 1995–96 Arctic winter: MLS ClO and HNO_3. *Geophysical Research Letters*, **23**, 3207–3210.

Santee, M. L., A. Tabazadeh, G. L. Manney, R. J. Salawitch, L. Froidevaux, W. G. Read, and J. W. Waters (1998). UARS Microwave Limb Sounder HNO_3 observations: Implications for polar stratospheric clouds. *Journal of Geophysical Research*, **103**(D11), 13285–13313.

Schoeberl, M. R., R. S. Stolarski, A. R. Douglass, P. A. Newman, L. R. Lait, J. W. Waters, L. Froidevaux, and W. G. Ready (1993). MLS ClO observations and Arctic polar vortex temperatures. *Geophysical Research Letters*, **20**, 2861–2864.

Scott, N. A. and A. Chedin (1981). A fast line-by-line method for atmospheric absorption computations: The automatized atmospheric absorption atlas. *Journal of Applied Meteorology*, **20**, 802–812.

Shettle, E. P., G. E. Thomas, J. J. Olivero, W. F. J. Evans, D. J. Debrestian, and L. Chardon (2002). Three satellite comparisons of polar mesospheric clouds: Evidence for long-term change. *Journal of Geophysical Research*, **107**(D12), DOI: 10.1029/2001JD000668—AC12-1-18-.

Smith, R. C., B. B. Prezelin, K. S. Baker, R. R. Bidigare, N. P. Boucher, T. Coley, D. Karentz, S. MacIntyre, H. A. Matlick, D. Menzies et al. (1992). Ozone depletion: Ultraviolet radiation and phytoplankton biology in Antarctic waters. *Science*, **255**, 952–959.

Smith, W. L., H. M. Woolf, C. M. Hayden, D. Q. Wark, and L. M. McMillin (1979). The TIROS-N operational vertical sounder. *Bulletin of the American Meteorological Society*, **60**, 1177–1187.

Solomon, S. (1999). Stratospheric ozone depletion: A review of concepts and history. *Reviews of Geophysics*, **37**, 275–316.

Solomon, S., R. R. Garcia, F. S. Rowland, and D. J. Wuebbles (1986). On the depletion of Antarctic ozone. *Nature*, **321**, 755–758.

Solomon, S., G. H. Mount, R. W. Sanders, and A. L. Schmeltekopf (1987a). Visible spectroscopy at McMurdo Station, Antarctica, 2: Observations of OClO. *Journal of Geophysical Research*, **92**(D7), 8329–8338.

Solomon, S., A. L. Schmeltekopf, and R. W. Sanders (1987b). On the interpretation of zenith sky absorption measurements. *Journal of Geophysical Research*, **92**(D7), 8311–8319.

Stamnes, K., W. Li, B. Yan, H. Eide, A. Barnard, W. S. Pegau, and J. J. Stamnes (2003). Accurate and self-consistent ocean color algorithm: Simultaneous retrieval of aerosol optical properties and chlorophyll concentrations. *Applied Optics*, **42**, 939–951.

Steele, H. M., J. D. Lumpe, R. P. Turco, R. M. Bevilacqua, and S. T. Massie (1999a). Retrieval of aerosol surface area and volume densities from extinction measurements: Application to POAM II and SAGE II. *Journal of Geophysical Research*, **104**(D8), 9325–9336.

Steele, H. M., K. Drdla, R. P. Turco, J. D. Lumpe, and R. M. Bevilacqua (1999b). Tracking polar stratospheric cloud development with POAM II and a microphysical model. *Geophysical Research Letters*, **26**, 287–290.

Stolarski, R. S. and R. J. Cicerone (1974). Stratospheric chlorine: A possible sink for ozone. *Canadian Journal of Chemistry*, **52**, 1610–1615.

Stolarski, R. S., A. J. Krueger, M. R. Schoeberl, R. D. McPeters, P. A. Newman, and J. C. Alpert (1986). Nimbus 7 satellite measurements of the springtime Antarctic ozone decrease. *Nature*, **322**, 808–811.

Stolarski, R. S., P. Bloomfield, R. D. McPeters, and J. R. Herman (1991). Total ozone trends deduced from Nimbus 7 TOMS data. *Geophysical Research Letters*, **18**, 1015–1018.

Sullivan, C. W., K. R. Arrigo, C. R. McClain, J. C. Comiso, and J. Firestone (1993). Distributions of phytoplankton blooms in the Southern Ocean. *Science*, **262**, 1832–1837.

Tabazadeh, A. and R. P. Turco (1993). Stratospheric chlorine injection by volcanic eruptions: HCl scavenging and implications for ozone. *Science*, **260**, 1082–1086.

Tabazadeh, A., R. P. Turco, K. Drdla, M. Z. Jacobson, and O. B. Toon (1994). A study of type I polar stratospheric cloud formation. *Geophysical Research Letters*, **21**, 1619–1622.

Tabazadeh, A., O. B. Toon, B. L. Gary, J. T. Bacmeister, and M. R. Schoeberl (1996). Observational constraints on the formation of type Ia polar stratospheric clouds. *Geophysical Research Letters*, **23**, 2109–2121.

Thomas, G. E. (1984). Solar mesosphere explorer measurements of polar mesospheric clouds (noctilucent clouds). *Journal of Atmospheric and Terrestrial Physics*, **46**, 819–824.

Thomas, G. E. (1989). Mesospheric clouds and the physics of the mesopause region. *Reviews of Geophysics*, **29**, 553–575.

Thomas, G. E. (1996). Global change in the mesosphere–lower thermosphere region: Has it already arrived? *Journal of Atmospheric and Terrestrial Physics*, **58**, 1629–1656.

Thomas, G. E. and J. J. Olivero (1989). Climatology of polar mesospheric clouds, 2: Further analysis of Solar Mesosphere Explorer data. *Journal of Geophysical Research*, **94**(D12), 14673–14681.

Thompson, D. W. J. and S. Solomon (2002). Interpretation of recent Southern Hemisphere climate change. *Science*, **296**, 895–899.

Toon, O. B. and M. Tolbert (1995). Spectroscopic evidence against nitric acid trihydrate in polar stratospheric clouds. *Nature*, **375**, 218–221.

Toon, O. B., P. Hamill, R. P. Turco, and J. Pinto (1986). Condensation of HNO_3 and HCl in the winter polar stratosphere. *Geophysical Research Letters*, **13**, 1284–1287.

Toon, O. B., E. V. Browell, S. Kinne, and J. Jordan (1990). An analysis of lidar observations of polar stratospheric clouds. *Geophysical Research Letters*, **17**, 393–396.

Tung, K. K., M. K. W. Ko, J. M. Rodriguez, and N. D. Sze (1986). Are Antarctic ozone variations a manifestation of dynamics or chemistry? *Nature*, **333**, 811–814.

Twomey, S. (1974). Information content in remote sensing. *Applied Optics*, **13**, 942–945.

Volz, A., D. H. Ehhalt, and H. Cosatto (1978). The vertical distribution of CFM and related species in the stratosphere. *Pure and Applied Geophysics*, **116**, 545–553.

Warren, S. G., C. J. Hahn, J. London, R. M. Chervin, and R. L. Jenne (1988). *Global Distribution of Total Cloud Cover and Cloud Type Amounts over the Ocean* (NCAR Tech. Note NCAR/TN-317+STR). National Center for Atmospheric Research, Boulder, CO.

Waters, J. W., L. Froidevaux, W. G. Read, G. L. Manney, L. S. Elson, D. A. Flower, R. F. Jarnot, and R. S. Harwood (1993). Stratospheric ClO and ozone from the Microwave Limb Sounder on the Upper Atmosphere Research Satellite. *Nature*, **362**, 597–602.

Weatherhead, E. C., G. C. Reinsel, G. C. Tiao, C. H. Jackman, L. Bishop, S. M. H. Frith, J. DeLuisi, T. Keller, S. Oltmans, E. Fleming et al. (2000). Detecting the recovery of total column ozone. *Journal of Geophysical Research*, **105**(D17), 22201–22210.

Weiler, C. S. and P. A. Penhale (eds.) (1994). *Ultraviolet Radiation in Antarctica: Measurement and Biological Effects* (ADU Antarctic Research Series No. 62, 257 pp.). American Geophysical Union, Washington, DC.

Wiscombe, W. J. (1980). Improved Mie scattering algorithms. *Applied Optics*, **19**, 1505–1509.

Zurek, R. W., G. L. Manney, A. J. Miller, M. E. Gelman, and R. M. Nagatani (1996). Interannual variability of the north polar vortex in the lower stratosphere during the UARS mission. *Geophysical Research Letters*, **23**, 289–292.

4

Polar climate and meteorology

4.1 INTRODUCTION

Our concern about the Earth's changing climate guarantees that there will always be applications for satellite-based study of the polar troposphere. At present, there are many new research opportunities arising from (1) the need to fully develop, refine, and validate procedures for retrieving important quantities such as polar cloud optical properties and radiation budget components, and (2) the polar regions being in the forefront of some important climate change issues. As an example of the latter, Global Climate Model (GCM) simulations have long suggested that climate warming due to anthropogenic greenhouse gas increases should have an early and pronounced manifestation at northern high latitudes, particularly during winter. Observations of both surface temperature trends *in situ* (Overland et al., 2002; Rigor et al., 2000) and Arctic sea ice concentration from satellite (Cavalieri et al., 1997; Johannessen et al., 1999) show consistency with GCM predictions.

For many years, high-latitude climate warming has been expected as a result of classical climate "feedback" mechanisms involving surface albedo, solar and terrestrial radiation, and cloud cover (Crane and Barry, 1984; Curry and Webster, 1999; Ledley, 1993; Somerville and Remer, 1984). In *ice albedo feedback* (Figure 4.1), which should be significant at temperatures close to the triple point of water, a warming induces a localized melting of snow or ice, which reduces surface albedo (Section 4.6.1). This reduced albedo leads to more shortwave radiation absorption by the surface, which accelerates the melting rate and further decreases the albedo. The result is a reduction in shortwave radiation backscattered to space by the Earth–atmosphere system, a concomitant increase in shortwave absorption by the surface, and a decrease in snow/ice cover, which together constitute a strong positive feedback to a climate-warming scenario. A warming scenario may also allow the atmosphere to hold more water vapor, and this water vapor will partially close infrared windows such that atmospheric longwave emission warms the surface to

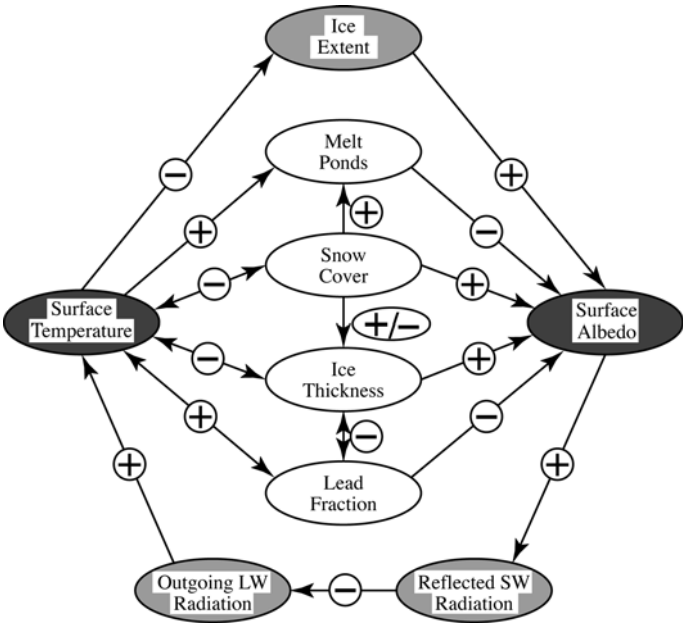

Figure 4.1. Schematic diagram of the ice albedo feedback.
Reproduced from Curry and Webster (1999). Copyright 1999, with permission from Elsevier.

a greater extent. This *water vapor feedback* is another potentially important positive feedback at high latitudes (Curry et al., 1995). There is a general *cloud–radiation feedback* (Curry and Webster, 1999), through which changes in atmospheric precipitable water may bring about various changes in cloud amount, vertical distribution, optical depth, thermodynamic phase, effective droplet radius or ice particle size, and temperature. The present consensus is that the net of these feedback mechanisms should be positive at high latitudes, although recent satellite trend analysis has challenged this conclusion (Wang and Key, 2003). In contrast to these positive feedbacks, a negative feedback can arise if there is increasing precipitation on sea ice resulting from a warming atmosphere containing more moisture (Ledley, 1993). In this scenario, snow cover buildup (1) increases the surface albedo, thus decreasing the absorbed shortwave radiation, and (2) decreases the turbulent energy flux transfer from the ocean to the atmosphere.

Recent research in atmospheric dynamics has introduced a new perspective on high-latitude climate change. Thompson and Wallace (1998) identified the Arctic Oscillation (AO), a persistent mode of variability in atmospheric circulation, as a major regulator of Arctic surface temperature. Today, the AO and the North Atlantic Oscillation (NAO) index (known for several decades) are often considered part of the same dynamical phenomenon known as the Northern Annular Mode (NAM), although this classification remains somewhat controversial (Moritz et al., 2002). The NAM is manifest as an oscillation in the strength of counter-clockwise

zonal flow at temperate and high latitudes. In the positive phase of this oscillation, stronger flow isolates colder air to the north, allowing Arctic temperatures at many locations to become warmer. In the negative phase, with weaker zonal flow, colder air is allowed to move farther south at most longitudes. During the past two decades, there has been a shift toward a positive phase in the NAM, and this may be the direct cause of much of the observed warming (Thompson and Wallace, 1998).

Although the NAM appears to lessen the role of direct greenhouse and similar forcings in high-latitude warming, these anthropogenic factors may still have a prominent indirect role. Current GCM simulations are beginning to reproduce the NAM (Moritz et al., 2002), and some GCM work suggests that a strengthening of the AO may result from anthropogenic greenhouse forcing (Shindell et al., 1999). Furthermore, a similar annular mode has been discovered at southern high latitudes, having a similar positive index bias in recent decades (Thompson and Solomon, 2002; Thompson and Wallace, 2000), and this bias may be related to the onset of the Antarctic ozone "hole" in the stratosphere. The stratospheric cooling associated with springtime ozone depletion may strengthen southern high-latitude westerlies, suppressing cold air outbreaks over the Bellingshausen Sea and leading to a gradual warming of the western Antarctic Peninsula region.

The Annular Modes are the present focus for studying climate dynamics at high latitudes, although substantial efforts have also been made at understanding the relationship between Antarctic climate and the El Niño–Southern Oscillation (ENSO). Studies of large-scale circulation at high latitudes will always require substantial use of satellite data, at any stage of our understanding. This chapter reviews many of the useful tasks that satellite remote sensing can accomplish in the areas of polar meteorology and climatology.

4.2 THE ANTARCTIC AUTOMATIC WEATHER STATION PROGRAM

The Antarctic continent's meteorology is as diverse as that of any other continent (King and Turner, 1997; Schwerdtfeger, 1984), and exhibits unique features—katabatic winds, for example—rarely found anywhere else. Yet Antarctica has the most sparse *in situ* meteorological sampling of any continent. Hence the need for satellite observations; but before discussing applications of satellite remote sensing we first introduce a different type of satellite-based observation. Automatic Weather Stations (AWSs) transmit data out of Antarctica by satellite telemetry. The scientific community owes an enormous debt to the researchers who have persevered over the years to maintain AWS equipment in Antarctica. Important Antarctic AWS installations have been supported by BAS (British Antarctic Survey), ANARE (Australian National Antarctic Research Expedition), the German, Italian, and Finnish Antarctic research programs, and the U.S. Antarctic Program (USAP). A history of these programs is given in King and Turner (1997), who also give a thorough review of the difficulties with meteorological observations and sampling in the harsh polar environment. Here we introduce the USAP-supported AWS program headed since 1980 by Professor Charles Stearns of the University of

Figure 4.2. The Automatic Weather Station installation at Uranus Glacier being serviced with the help of a British Antarctic Survey Twin Otter aircraft.
Courtesy: Matthew Lazzara and Shelley Knuth (University of Wisconsin).

Wisconsin at Madison. These AWS observations, maintained and archived at their host organization—the University of Wisconsin's Antarctic Meteorology Research Center (AMRC)—qualify as a form of satellite exploration in their own right. The logistical effort, and genuine hazards, involved with deploying and maintaining Antarctic AWS equipment are reminiscent of the *in situ* probes NASA has been sending to the Martian surface in recent years (Figure 4.2).

Figure 4.3 (see color section) shows the locations of Wisconsin, Australian, and Italian AWS installations, as of 2002. In addition to the AWS locations, the map shows the locations of Automated Geophysical Observatories (AGOs) deployed by BAS and USAP and operated by Augsburg College of Minnesota, which carry similar meteorological instrumentation. The standard Wisconsin AWS installation (Stearns et al., 1993) consists of a 3-m tower, at the top of which air temperature, humidity, wind speed, and wind direction are measured. Near the mid-point of the tower, the station's data-logging enclosure also houses a transducer for measuring air pressure. On some installations, the air temperature difference is measured between the top of the tower and 2.5 m down from the top, and/or an array of eight temperature sensors extending to a depth of 4 m in the snowpack. A schematic is shown in Figure 4.4.

The Wisconsin AWS instrument and calibration standards are rigorous, given the logistical challenges involved with servicing the stations (which can take place only during the austral summer, between November and February). The pressure transducer is a Parascientific Digiquartz model, having a frequency range of 40 kHz at a nominal 0 hPa to 36 kHz at 1,000 hPa, with a pressure resolution of 0.05 hPa. Calibration in the field is accomplished using a reference aneroid barometer at McMurdo Station and a reference mercury barometer at Scott Base, and the

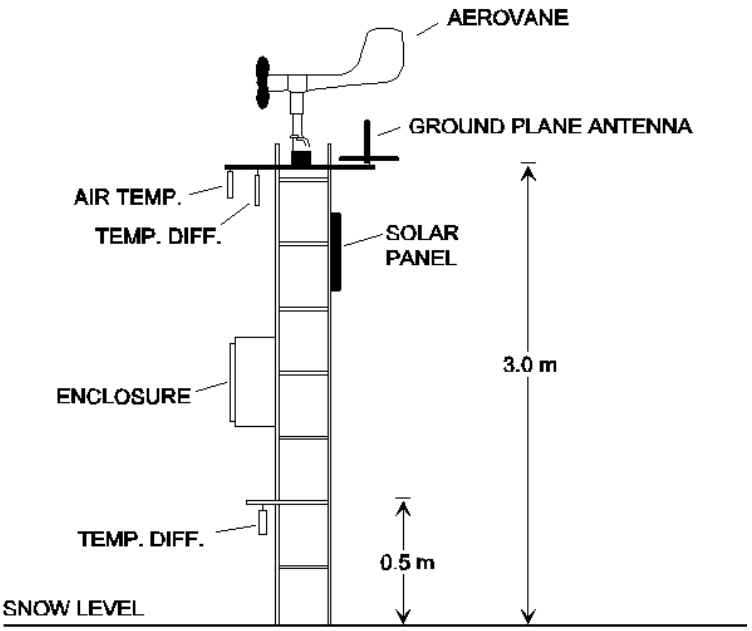

Figure 4.4. Schematic diagram of a University of Wisconsin Antarctic Meteorology Research Center (AMRC) AWS system.
Courtesy: Matthew Lazzara and Shelley Knuth (University of Wisconsin).

calibrations are nominally within ± 0.2 hPa. Wind speed and direction are measured using a Belfort aerovane. During field checks, the wind direction is reset with reference to solar position, if necessary. The wind speed is calibrated by spinning the vane at a reference 1,800 r.p.m., corresponding to a reference wind speed of $39.8\,\mathrm{m\,s^{-1}}$, and checking the tachometer voltage and load resistance. The Vaisala HMP-31UT or HMP-35A humidity sensor is calibrated by referencing saturated salt solutions with known relative humidities. Sodium chloride (75%) and lithium chloride (12%) provide a two-point calibration for the linear response of this sensor. The offset (0% relative humidity) is also checked, by forcing an inert gas over the sensor element. The humidity sensors have a resolution of 1%, and drift by about 2–3% per year in the field. The air temperature difference between two tower positions is measured by a pair of junction thermocouples having an output of between 60 and 78 μV per degree difference between the thermocouples in the temperature range -80 to 0°C. This output is sent to a differential amplifier having a gain of ~425, with zero output set at 0.4 V. This setup yields a signal range 0–1 V for a temperature difference range of -6°C to $+9^{\circ}$C, with a resolution of 0.05°C. Calibration is accomplished using reference voltages at the differential amplifier input.

Each AWS transmits data to the Argos (Inc.) global data telemetry and geo-positioning service Data Collection System (DCS) aboard the NOAA (National

Oceanic and Atmospheric Administration) polar orbiters (Schwalb, 1978). The AWS computer transmits the data as 256-bit words in 1 s, every 200 s, at the Argos frequency of 401.650 MHz. AWS data logging occurs in 10-minute intervals (updates). In each dataword transmitted to the satellite, the data logger includes the current measurements, and also the difference between successive readings of pressure and temperature for the previous four readings, along with the previous four readings of wind speed and wind direction. This provides redundancy in case of a loss in satellite reception, although at high latitudes there is usually a satellite within line-of-sight to each AWS every 50 minutes (assuming two NOAA polar orbiters are operational).

The AWS data are used in near real time for meteorological reanalyses by the European Centre for Medium-range Weather Forecasts (ECMWF) and the U.S. National Center for Environmental Prediction (NCEP). The data have also been used for validating the atmospheric models used for reanalysis (Bromwich et al., 1999). The American Geophysical Union's *Antarctic Research Series* has published a volume illustrating the versatility of the AWS data for climatological studies in Antarctica (Bromwich and Stearns, 1993, and references therein). Bromwich and Stearns's volume includes AWS applications for the study of katabatic winds, sensible and latent heat flux estimates, an Antarctic kernlose winter (an episode of no systematic temperature change for several months), tropospheric aerosol concentrations over the Antarctic plateau, and nanoclimate studies in the McMurdo Dry Valleys.

Of particular interest in the Bromwich and Stearns (1993) volume is a study of the dynamic link between the ENSO and Antarctic climate (Smith and Stearns, 1993). By combining all available AWS data, the authors derived composite maps of the anomalies in temperature and pressure over the entire continent. Analyzing both the complete dataset (Figure 4.5), and the pressure and temperature anomalies before and after individual Southern Oscillation Index (SOI) minima, the authors discovered that both the pressure and temperature anomalies exhibit very pronounced sign changes when transitioning through an SOI minimum, throughout the continent. The pressure anomalies tend to switch from positive to negative across the SOI minimum, over most of the continent, while the behavior in the temperature anomalies is more regional. In contrast, examining the composites of climate anomalies on either side of the midpoint between two SOI minima did not reveal such coherent sign changes. Constructing a hypothesis that involved extrapolating these anomalies, surrounding the SOI minimum, to changes in 500-hPa heights, the authors suggest that the anomalies should strengthen both a ridge over Wilkes Land and a trough over the Ross and Amery Ice Shelves. This enhanced pressure gradient, related to Antarctic topography, is consistent with a large-scale flow known to involve a blocking ridge in the New Zealand region (Trenberth, 1980; Mo et al., 1987). This New Zealand block may in turn influence the western branch of the Southern Oscillation. The authors conclude that the ENSO is therefore influenced by the climate of Antarctica. Satellite imagery covering Antarctica and the Southern Ocean, some databases of which now span more than two decades, offer ample opportunities for further investigation of such teleconnections.

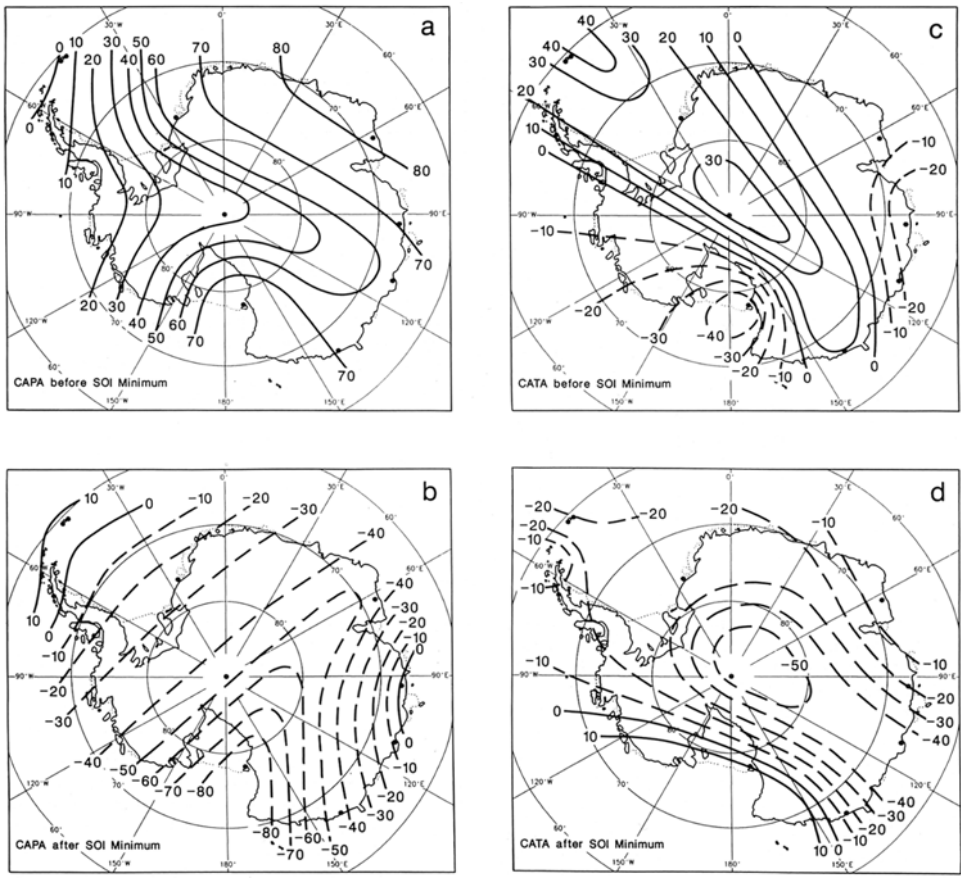

Figure 4.5. The Composite Annual Pressure Anomaly (CAPA) and Composite Annual Temperature Anomaly (CATA) before and after a Southern Oscillation Index (SOI) minimum, as mapped using the continental network of AWS installations. Pressures are contoured in increments of 10 mbar and temperatures in increments of 10°C. Dashed curves represent negative anomalies.

4.3 SATELLITE METEOROLOGY

The potential uses of satellite imagery for studies of high-latitude meteorology are enormously diverse, ranging from synoptic-scale case studies involving unique geography to hemispheric climatological research. To give the reader a sample of some important polar applications, three topics are introduced here: polar lows, katabatic winds, and the tracking of wind vectors in cloud drift and water vapor imagery.

We first mention one highly useful data product for large-scale studies: a composite of polar orbiter and geostationary imagery (Stearns and Lazzara, 1999). Since 1992, the AMRC has been producing composite satellite images in which NOAA polar orbiter AVHRR (Advanced Very High Resolution Radiometer) images over Antarctica (obtained several times per day) are merged with contemporaneous Geostationary Operational Environmental Satellite (GOES) imagery obtained over lower latitudes (obtained four times per hour). GOES imagery is used to generate the satellite weather maps with which we are all familiar, and their obvious advantages are large geographical coverage and high time resolution. However, these sensors view the Equator near nadir, and their observations become useless poleward of 60° latitude. By merging GOES data with polar orbiter data that become increasingly frequent at higher latitudes as the latters' orbits converge, it is possible to generate composite images covering most longitudes poleward of 60°, with a time resolution of approximately 3 hours. A sample AMRC composite image is shown in Figure 4.6 (see color section). An animated "loop" of such hemispheric composite images clearly shows meteorological teleconnections between Antarctica and lower latitudes. As the time history of these composites grows longer, they become increasingly valuable.

On a more local scale, satellite imagery is indispensable for aviation safety at high latitudes. During the regular field season, the USAP operates regular aircraft flights between Christchurch, New Zealand and McMurdo Station. NOAA and DMSP (Defense Meteorological Satellite Program) data collected by USAP-supported line-of-sight tracking antennas at McMurdo Station are used on a daily basis to help determine if a given flight should be attempted. The hazards to aviation include stronger winds than expected in a region where there are virtually no alternate airfields, and severely impaired visibility upon approach and landing in Antarctica. Indeed, weather over the Ross Sea can change so quickly that the latest polar orbiter overpass briefed to a flight crew might no longer be relevant. Hence there is a need to not only observe the meteorological conditions along a flightpath but also to predict them as best one can in the near term. To this end, the USAP has recently supported an Antarctic Mesoscale Prediction System (AMPS), in which a mesoscale model is modified for the polar environment for use in improving Antarctic weather forecasting (Bromwich et al., 2003).

AMPS utilizes a mesoscale model known as the Polar MM5, which is a version of the fifth-generation Pennsylvania State University–National Center for Atmospheric Research (NCAR) Mesoscale Model (MM5) that has been modified for use over extensive ice sheets. The goal is to provide twice daily synoptic forecast products that meet the unique requirements of forecasters at McMurdo. The Polar MM5 contains several important high-latitude adaptations, including improvements to the representation of ice condensation nuclei, a radiation code that includes ice cloud optical properties, calculations of latent heat flux using the latent heat of sublimation, assumption of ice saturation when calculating surface saturation mixing ratios, and explicit inclusion of the unique thermal properties of a sea ice surface (Bromwich et al., 2001; Cassano et al., 2001; Guo et al., 2003). This model operates with three nested forecast domains: most of the Southern Ocean at 90-km

grid spacing, the Antarctic continent at 30-km grid spacing, and the western Ross Sea centered about McMurdo at 10-km grid spacing. The model is initialized with as many data as is practicable, including AWS and AGO observations, rawinsonde data from McMurdo, and NCEP upper-level reanalysis, and first-guess fields are provided by an earlier forecasting model, the NCEP AViatioN Model (AVN). Even with these refinements, the AMPS program is a demanding application for the MM5 model, which is expected to simulate katabatic (downslope) winds and barrier winds (easterlies redirected by the Transantarctic Mountains), and accurately forecast the tracks of depressions. Analysis of satellite imagery has been valuable for assessing Polar MM5 performance. Figure 4.7 shows an instant in a cyclogenesis case study by Bromwich et al. (2003), where two depressions exist (the one in the middle of the panels being more evident in the satellite image, the northerly one inferred from *in situ* data), and where the MM5 has predicted the existence of both lows, but not their precise strength or location. Furthermore, the MM5 predicts a third low toward the lower right of the test region, which does not appear in the satellite image. The actual dynamical situation in this case study was complex, but not uncommon. Ongoing investigations of such case studies are required to suggest improvements to mesoscale model physics.

4.3.1 Polar lows

The satellite data record is now extensive enough for multidecadal climatological studies of polar lows, which are important both for understanding local meteorology (as in the case study discussed above) and teleconnections between polar and lower latitudes. The European Geophysical Society Polar Lows Working Group in 1994 defined a polar low as a maritime cyclonic vortex that develops poleward of a polar front, having a horizontal scale $<$1,000 km, and surface wind speeds in excess of $15\,\mathrm{m\,s^{-1}}$ (Carrasco et al., 2003). This definition does not strictly apply to all mesoscale systems at southern high latitudes, some of which can develop much farther south than the open ocean. A more general term is *polar mesoscale cyclone*.

Carleton (1991) provides a comprehensive review of satellite-based studies in meteorology and climatology, including work on Arctic polar mesoscale cyclones from the 1980s. Infrared imagery having a spatial resolution of order 1 km (e.g., AVHRR, OLS, MODIS) is very well-suited for observing these systems, because their structure and development are well-resolved (Figure 4.8) and, with frequent polar orbiter data availability at high latitudes, their tracks can be followed with precision. A classification scheme that represents the developmental stages of polar mesoscale cyclone formation is described in Carleton (1991) and Carleton and Carpenter (1990). This classification scheme is shown in Figure 4.9 for the Northern Hemisphere. For the Southern Hemisphere, these same cloud patterns have clockwise rather than counterclockwise rotation (Figure 4.8).

Stage 1 in this scheme (panel 1 in Figure 4.9) represents frontal cyclogenesis, seen as a bulge on an existing cloud band. In this stage the cloud band may also become brighter as its thickness and hence optical depth increases due to convergence and ascent in the lower troposphere. In the second stage (panels 4

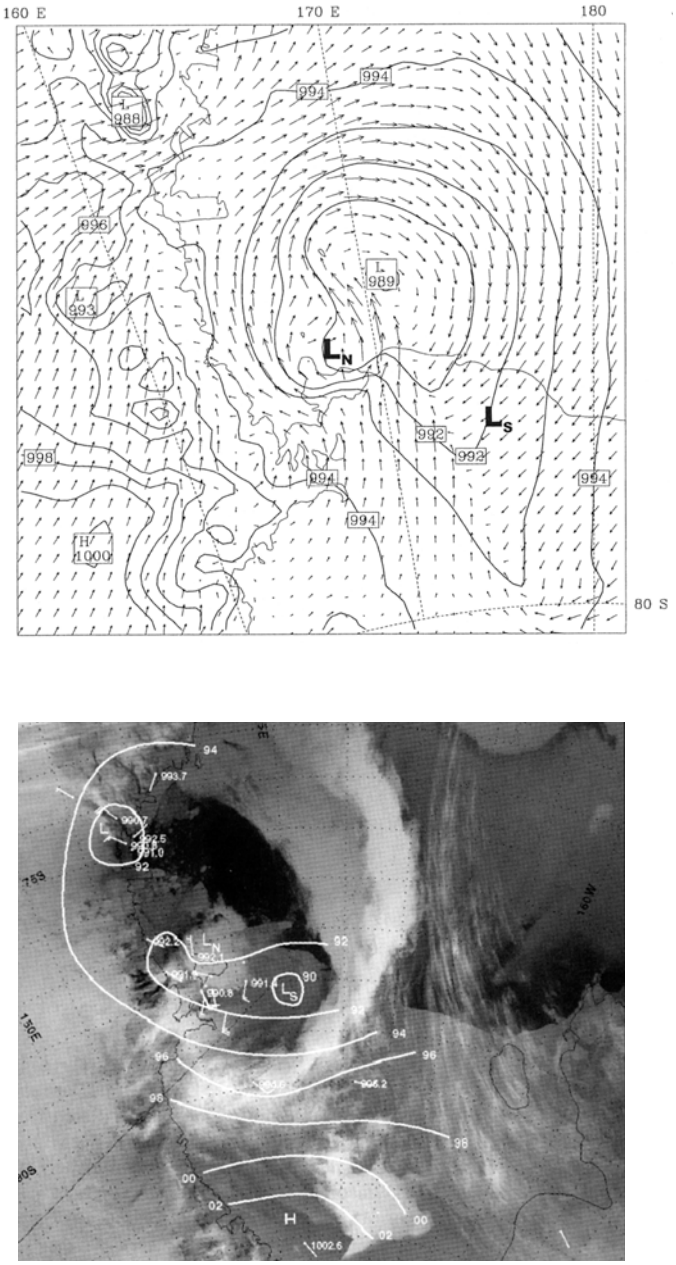

Figure 4.7. Comparison of a mesoscale model prediction of weather conditions in the vicinity of McMurdo Station at 06 : 00 UTC January 15, 2001 (top panel) with a contemporaneous AVHRR channel-4 image (07 : 00 UTC). Surface weather information from the AWS network is annotated on the AVHRR image.

From Bromwich *et al.* (2003).

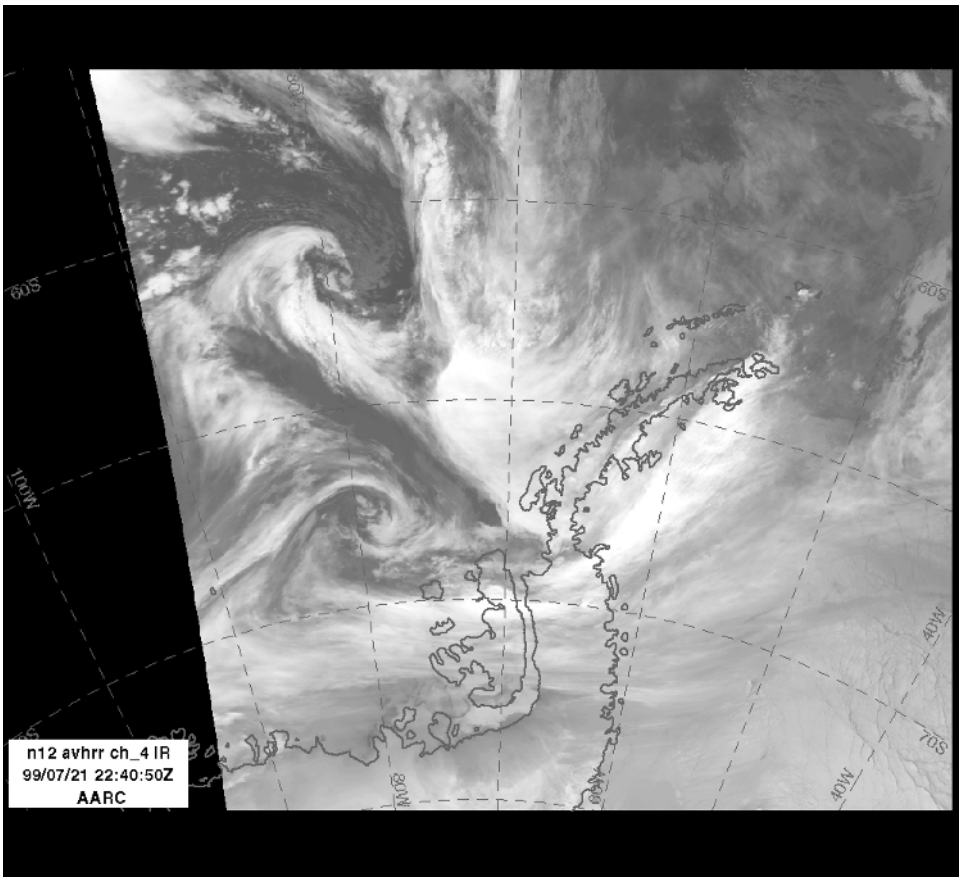

Figure 4.8. AVHRR infrared images of mesoscale cyclones near 62°S and 68°S along the 80°W meridian, approaching the Antarctic Peninsula at 22 : 40 UTC on July 22, 1999.
Data from the Arctic and Antarctic Research Center at the Scripps Institution of Oceanography.

and 5), one sees a "dry slot" of clear air on the poleward side of the cloud system, near the bulge. This is an area of subsidence, which eventually penetrates the cloud system, yielding a "comma" and then the familiar spiral. At this point the cyclone is nearing maximum intensity. This phase is depicted as stages (panels) 7 and 8 in the Carleton (1991) scheme, the difference between these two stages being determined by the extent of the dry slot's penetration (a "hook" in 7 and a clear-air spiral in 8). The extent of this penetration, as manifested in the satellite imagery, is related to cyclones' vertical structure. The deeper cyclones, having lower sea level pressure and 500- and 300-millibar heights, are associated with stage 7. The onset of dissipation is indicated by stages 9 and 10, which show a gradual fattening of the spiral arms and then a loss of spiral structure. This is often the longest phase, with images 12 or more hours apart sometimes showing very little change. In the final stage of

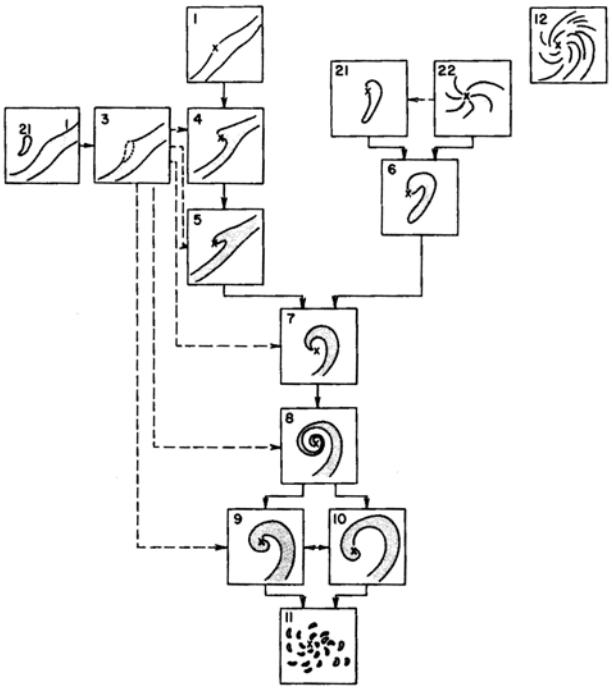

Figure 4.9. Classification scheme for high-latitude mesoscale cyclone formation, maturity, and dissipation, developed for use with satellite imager data of order 1 km resolution by Carleton and Carpenter (1989). The schematic shown here is a Northern Hemisphere perspective. See text for explanations of the different panels.

From Carleton (1991), *Satellite Remote Sensing in Climatology*. Copyright 1991, used with permission of Taylor & Francis Ltd. (*http://www.tandf.co.uk*)..

dissipation (stage 11), the frontal cloud band is lost. New polar air vortices may arise from stage 11. The classification scheme also includes variants leading to the mature stages of 7 and 8, including incipient spirals and comma clouds (stages 12 then 22, and 21 then 6, respectively), followed by a developed comma cloud with a dry slot. Fusion of a comma cloud and a frontal cloud band may also occur (stage 3).

The Southern Hemisphere mesocyclone climatology of Carleton and Carpenter (1990), covering the years 1977–82, demonstrated a relationship between the frequency and location of these events and the ENSO. During a warm ENSO event (1981), more polar lows were seen in the southeast Pacific sector (below Australia and New Zealand). Carleton and Song (1997) used satellite imagery to identify teleconnections between mesocyclonic activity south of Australia/New Zealand and in the South America/Antarctic Peninsula region. The Polar Meteorology Group at the Byrd Polar Research Center (Ohio State University) has conducted extensive satellite investigations of the seasonal and zonal variability in Southern Hemisphere polar mesocyclones (Bromwich et al., 1996; Carrasco and Bromwich, 1996a, b, 1997; Carrasco et al., 1997a, b, 2003). These studies have

provided insight into the various physical forcings for cyclogenesis, including (1) extensive sea ice cover in the Weddell Sea region (a damping influence); (2) cold air outbreaks from the continent over the Bellingshausen Sea, resulting in instability and more frequent and deeper mesocyclones over the western Antarctic Peninsula region, and (3) the prominent role of katabatic winds in Ross Sea cyclogenesis.

4.3.2 Katabatic winds

Katabatic winds have an enormous influence on the climate and meteorology of Antarctica, and are also significant over much of Greenland. Over extensive elevated ice sheets, net radiative flux is negative for most of the year due to the high surface albedo. This radiative cooling near the surface yields strong temperature inversions. On a sloping ice sheet with these temperature inversions, a near-surface air parcel is colder than an adjacent air parcel over a lower point on the slope but at the same height above sea level. This leads to a gravitational acceleration of near-surface air down the slope. Forces that oppose this "negative buoyancy" force include surface friction, the Coriolis force, and larger scale pressure gradients. A balance between the "negative buoyancy" force and these opposing forces yields a steady state katabatic flow. Near the coast there are often confluence zones and mountain passes, where katabatic flows can be "funneled" into very strong winds (of order $20\,\mathrm{m\,s^{-1}}$). The physical mechanisms behind katabatic winds, first modeled by Ball (1956, 1960), are reviewed in detail by King and Turner (1997). The continental-scale airflow pattern (Figure 4.10) has been described by Parish and Bromwich (1987). Not surprisingly, many AWS installations have been located to study regions of strong katabatic winds, both at the coast and upslope (Breckenridge et al., 1993; Bromwich et al., 1993; Wendler et al., 1993). The confluence zones at the coast have important meteorological impacts. One example involves Marie Byrd Land, discussed by Bromwich and Liu (1996), Carrasco et al. (1997a), and Liu and Bromwich (1997), and illustrated in Figure 4.11. In this confluence zone, a cold katabatic flow from East Antarctica persists from the surface to about 500 m. Overlying this is another, warmer, katabatic flow from West Antarctica. The time-averaged low in the Amundsen Sea brings about an additional easterly flow above both katabatic streams. The result of these three adjacent air streams is a strong low-level temperature gradient in southern Marie Byrd Land that produces baroclinic instability. This is therefore a region of persistent mesoscale cyclogenesis. During 1991, for example, satellite analysis revealed between one and two mesoscale cyclones per week, with even higher cyclonic activity during March (Carrasco et al., 1997a).

The unique signature of katabatic winds in high resolution mid-IR imagery was observed early on (D'Aguanno, 1986; Godin, 1977; Swithinbank, 1973). The path of a katabatic wind can appear warmer than the surrounding areas by up to 15 K. Satellite imagery can therefore show the trajectories of katabatic winds for distances of 1,000 km or more. Figure 4.12 shows an example of a katabatic flow—discussed by Carrasco and Bromwich (1993)—that originates in West

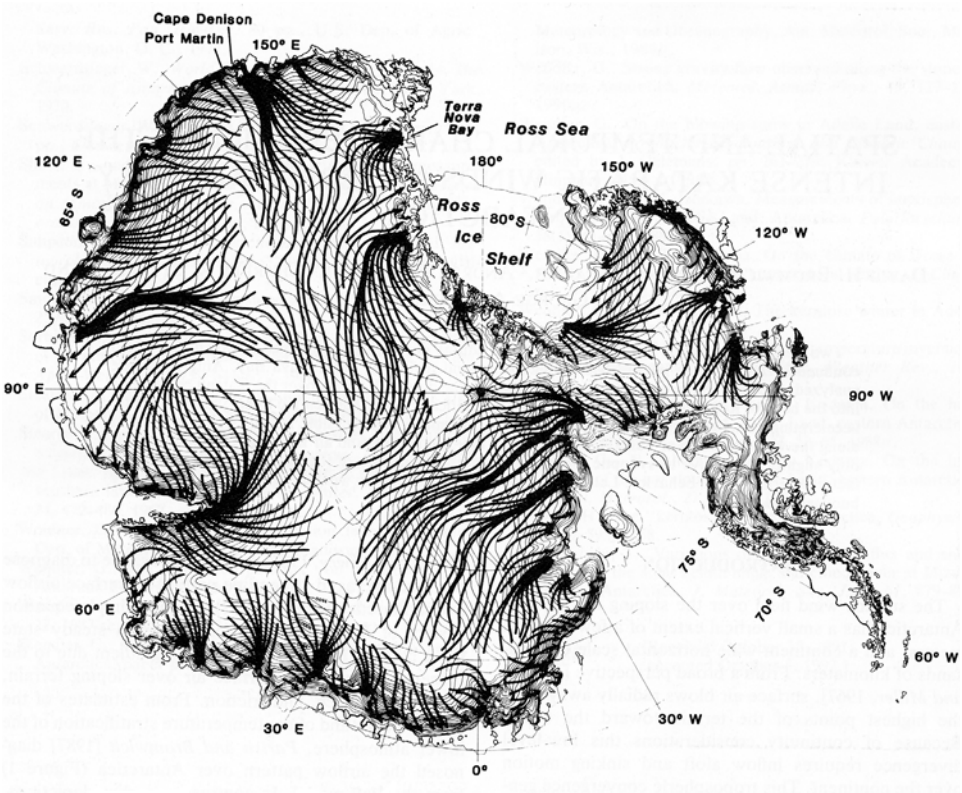

Figure 4.10. The time–mean airflow over Antarctica during winter.
From Parish and Bromwich (1987).

Antarctica, traverses the Ross Ice Shelf, and opens a polynya at the edge of the Ross Ice Shelf. The warm signature of katabatic winds in mid-IR imagery seems paradoxical at first, given that the winds themselves consist of colder air than their surroundings. Indeed, the low temperature of the katabatic flow itself, relative to its surrounding environment has been measured directly by Parish and Bromwich (1989). A resolution to this paradox has been suggested by Bromwich (1989a, b). The fast-moving airflow disrupts the local low-level temperature inversion and produces vertical mixing, and also carries drifting snow in the boundary layer. The result of these processes is warmer air just above the surface, underneath the colder katabatic flow. In visible wavelength imagery with spatial resolution finer than 1 km, such as OLS (0.5 km), this near-surface mixing and blowing snow can sometimes be observed directly (Figure 4.13). Thus, at present, katabatic winds can be readily identified and their intensity judged qualitatively in satellite imagery. In future, with larger volumes of higher spatial resolution visible and mid-IR imagery, it may be possible to derive quantitative relationships between the various satellite signatures and the katabatic wind strength.

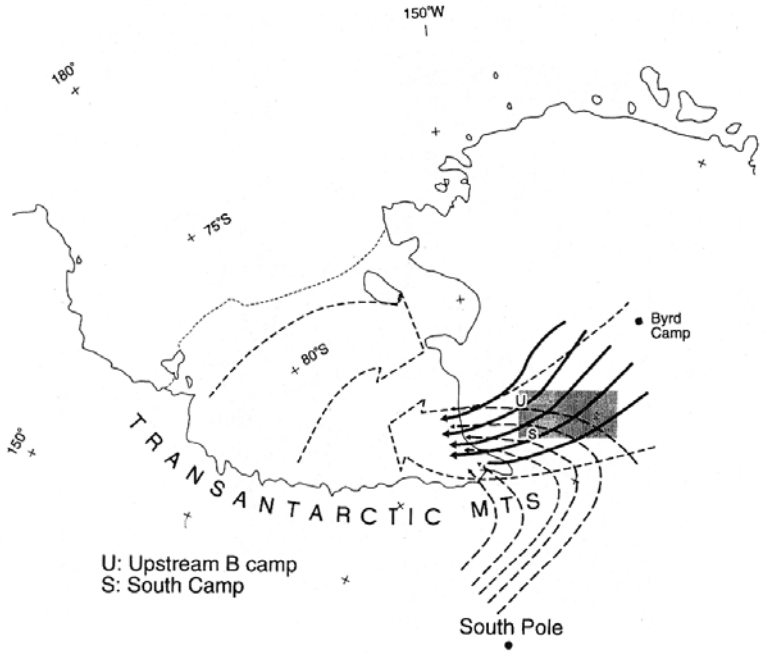

Figure 4.11. Schematic diagram of the katabatic wind confluence zone near the Siple Coast, which lends itself to satellite data analysis. The scale of this entire figure is approximately 2,000 km (east to west). The heavy vectors represent streamlines of near-surface winds from West Antarctica. These are undercut by near-surface winds from East Antarctica (dashed vectors). The dashed arrow from West Antarctica denotes warm air advection that may enhance the baroclinic zone. The dashed arrow originating from the Transantarctic Mountains (propagating over the Ross Ice Shelf) denotes cold air advection.

From Carrasco et al. (1997a). Copyright 1997 American Geophysical Union. Reproduced by permission of American Geophysical Union.

4.3.3 Wind vectors from polar orbiter data

Geostationary satellites, which produce images covering 60°S to 60°N and approximately 120° of longitude every 30 minutes, have been used for automated wind vector identification since their inception in the 1960s. With their high-time-resolution imagery, cloud or water vapor features tend to persist coherently for several images in a row, such that they can be automatically identified and tracked. At high latitudes, polar orbits converge in space such that time sampling over a given location often becomes useful for wind vector determination, with the same principles as those used for geostationary data.

Both geostationary satellite remote sensing and wind vector tracking are reviewed in detail by Kidder and Vonder Haar (1995). The essential principle was described by Leese et al. (1971). Let us suppose we have a cloud field resolved in relatively high-spatial-resolution (*GIFOV* of order 10 km or less) mid-IR imagery, or a two-dimensional total column water vapor distribution retrieved from 6.7-μm

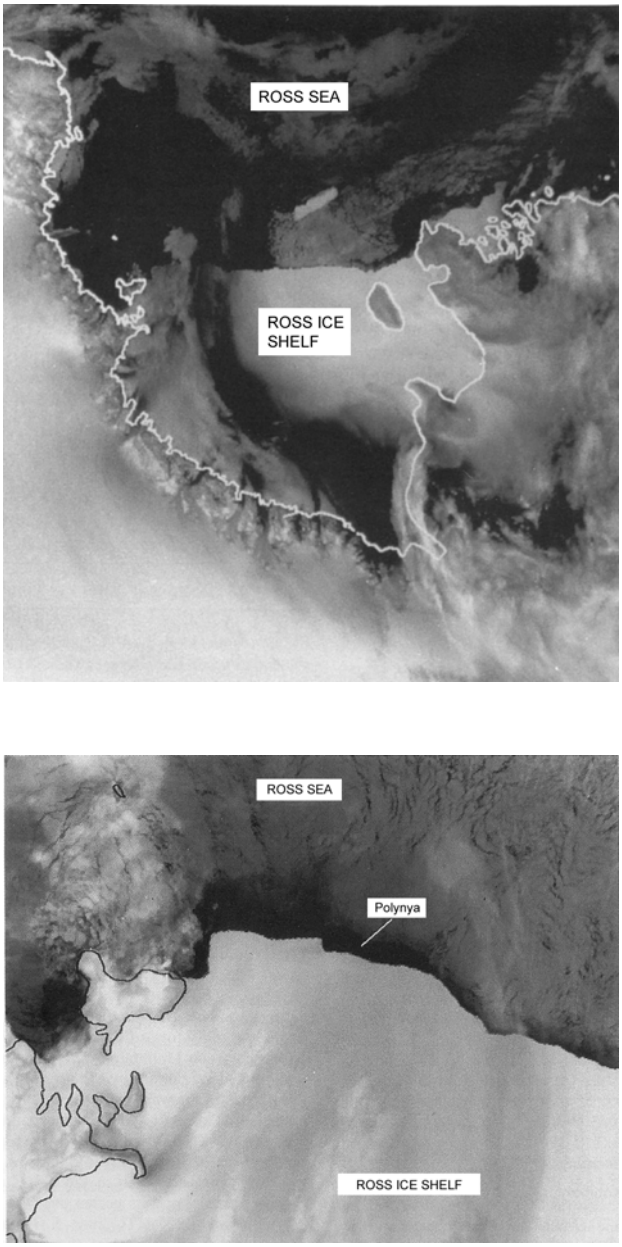

Figure 4.12. NOAA-9 AVHRR mid-IR image at 03 : 38 UTC on June 5, 1988 showing a katabatic wind surge propagating from the Transantarctic Mountains all the way across the Ross Ice Shelf (dark region). The lower panel is a closeup of the subsequent image at 06 : 52 UTC, showing the polynya being opened by the katabatic wind.

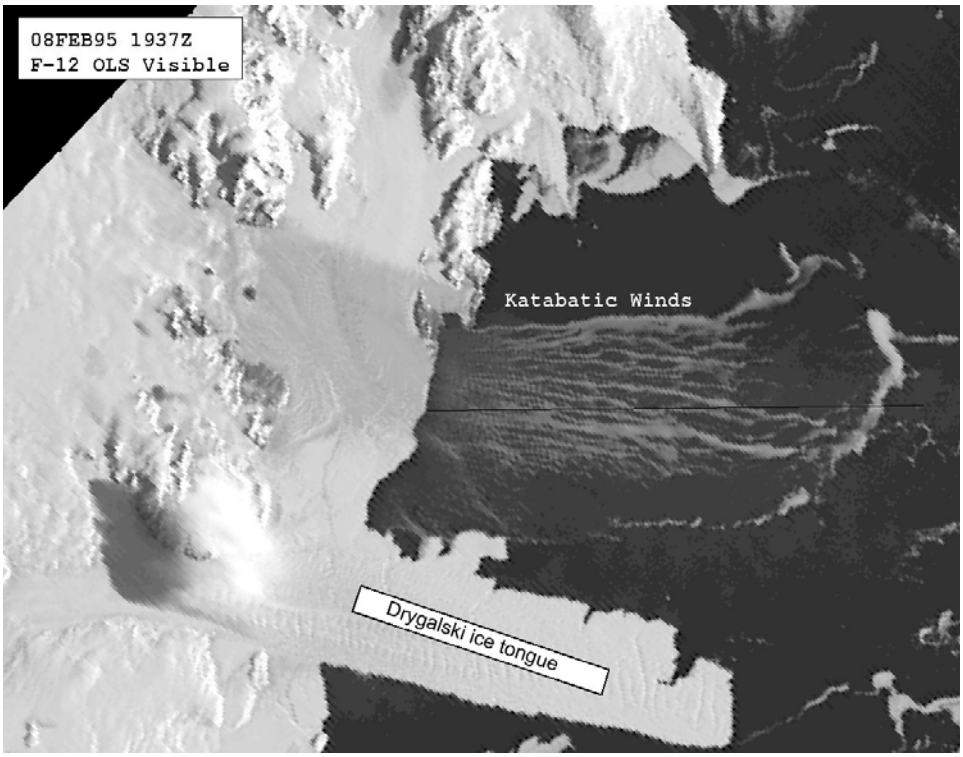

Figure 4.13. DMSP Operational Linescan System (OLS) visible image at 0.5 km resolution showing blowing snow in a katabatic wind.

Courtesy: MST1 David Hutchison, U.S. Coast Guard, data from the Arctic and Antarctic Research Center at the Scripps Institution of Oceanography.

imagery (e.g., Morel et al., 1978). If either type of image is rendered in a range of digital grayscale counts (0–255), and if a subsequent image is close enough in time that atmospheric dynamics have not yet distorted the essential spatial structure, then pronounced features can usually be identified in both images, and their change in geographic location used to construct a wind vector. A *target array* of $m \times m$ grayscale pixels, $\boldsymbol{G}_{t0}$, is chosen in the first image (time t_0), and a *search array* of $2m \times 2m$ pixels is identified in the second image (time t_1), centered about the geographic location of the target array $\boldsymbol{G}_{t0}$. Within the search array, the target array is repositioned to each of $m+1$ lag positions. These lag positions are indexed in one direction by p and in the orthogonal direction by q. Each repositioning constitutes a trial target array $\boldsymbol{G}_{t1}(p,q)$. A cross-correlation coefficient $X(p,q)$ is calculated for each of these lag positions:

$$X(p,q) = \frac{\mathrm{Cov}(p,q)}{\sigma_{t0}\sigma_{t1}} \tag{4.1}$$

where $\mathrm{Cov}(p,q)$ is the covariance between the original target array $\boldsymbol{G}_{t0}$ and the trial target array $\boldsymbol{G}_{t1}$ at lag position p,q ($-m < p < +m$ in one direction; $-m < q < +m$ in the orthogonal direction). The quantities σ_{t0} and σ_{t1} are the root mean square variations of $\boldsymbol{G}_{t0}$ and $\boldsymbol{G}_{t1}$, respectively. The lag position where $X(p,q)$ is a maximum, $X(p',q') = \max[X(p,q)]$, is identified as the location of the target array in the second image. For an east–west pixel width Δx and north–south pixel width Δy, the magnitude V and direction θ of the wind vector $\boldsymbol{V}$ are then determined as:

$$\left.\begin{aligned} |V| &= \frac{\left[(p'\Delta x)^2 + (q'\Delta y)^2\right]}{\Delta t} \\ \theta &= \arctan\left(\frac{p'\Delta x}{q'\Delta y}\right) \end{aligned}\right\} \tag{4.2}$$

Early on, fast Fourier transforms were introduced to speed up the calculations of cross-correlation coefficients (Leese et al., 1971).

Later, Menzel et al. (1983) introduced the *CO_2-slicing technique* (Smith et al., 1970) to assign cloud top heights to the tracked features. Current mid-IR sounding instruments on both geostationary and polar-orbiting spacecraft provide several bands displaced slightly from the center of the strong 15-μm CO_2 band. For example, the GOES sounder includes bands at 14.71, 14.37, 14.06, 13.64, and 13.37 μm. The HIRS/2 instrument, discussed in Chapter 3 for IR column ozone retrieval, offers measurements at 14.95, 14.71, 14.49, 14.22, 13.97, 13.64, and 13.35 μm. The effective bandwidth of such channels is in the range 10–15 cm^{-1}. As the wavelength decreases away from the fully opaque band center at 15 μm, the atmosphere becomes more transparent, and the majority of the thermal emission measured at each subsequent shorter wavelength comes from an altitude farther down in the atmosphere. This is typically expressed in terms of a temperature profile weighting functions $W_\lambda(\chi_\lambda, T, p)$ for the band at wavelength λ:

$$W_\lambda(\chi_\lambda, T, p) = \left[\frac{\partial B_\lambda(T)}{\partial T}\right]\left[\frac{\partial \chi_\lambda}{\partial \ln p}\right] \tag{4.3}$$

where $\chi_\lambda(p)$ is the atmospheric transmission at wavelength λ, $\ln p$ is the natural logarithm of the atmospheric pressure p, and $B_\lambda(T)$ is the Planck function. Examples of these weighting functions are given in Figure 4.14. These curves represent the sensitivity of the space-measured radiance in each band to variations in atmospheric temperature in cloud-free conditions. The CO_2-slicing method was in fact designed first for tropospheric temperature sounding (Kidder and Vonder Haar, 1995). The advent of sounders having a *GIFOV* (Ground Instantaneous Field Of View) of order 10 km offered the possibility of altitude assignment to cloud-tracked wind vectors.

When clouds are present, they may or may not appear in the various CO_2-slicing sensor channels depending on their altitude. Referring to Figure 4.13, we can visualize how this principle is used. At a wavelength closer to the CO_2 band center, say 14.2 μm, only high clouds (above 350 hPa) will appear in the imagery. At a slightly shorter wavelength, say 14.0 μm, both high- and mid-level clouds

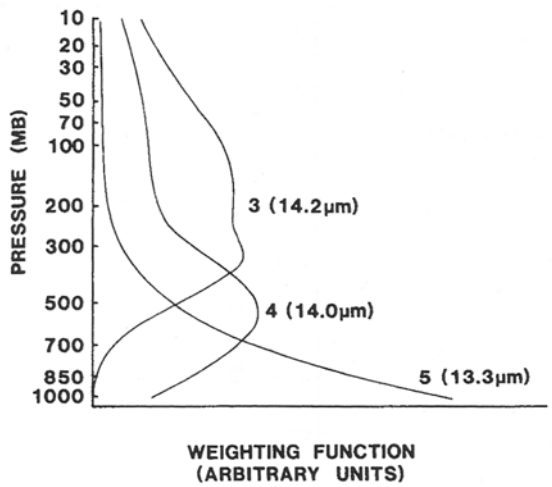

Figure 4.14. Example temperature weighting functions (4.3) for three bands frequently used in the CO_2-slicing technique.
From Menzel et al. (1983).

(around 500 hPa) will appear in the imagery. Simultaneous feature tracking in both 14.0-μm and 14.2-μm imagery will reveal vectors that do not appear in the latter, and can thus be identified as belonging to mid-level clouds. At an even shorter wavelength, say 13.3 μm, low-level clouds will appear in the imagery in addition to the mid-level and high clouds. Simultaneous feature tracking at all three wavelengths will reveal vectors in the 13.3-μm imagery that do not appear on either of the longer wavelength images, and these can be identified with low-level clouds. Once a cloud has been identified, its pressure level (and hence altitude) can be estimated by considering the ratio of two intensities from among the bands used:

$$\frac{I_{\lambda 1} - I_{\lambda 1}^{CLR}}{I_{\lambda 2} - I_{\lambda 2}^{CLR}} = \frac{\varepsilon_1 \int_{p_s}^{p_c} \chi_{\lambda 1}(p) \dfrac{dB_{\lambda 1}[T(p)]}{dp}}{\varepsilon_2 \int_{p_s}^{p_c} \chi_{\lambda 2}(p) \dfrac{dB_{\lambda 2}[T(p)]}{dp}} \tag{4.4}$$

Here $I_{\lambda 1}$ and $I_{\lambda 2}$ are the measured intensities for the two bands, and $I_{\lambda 1}(CLR)$ and $I_{\lambda 2}(CLR)$ are the equivalent clear-sky intensities. The latter are usually determined from radiative transfer calculations using climatological profiles. The cloud emissivity is ε_1 in the first band and ε_2 in the second. Because the two band center wavelengths are close, we usually have $\varepsilon_1 = \varepsilon_2$, and (4.4) can be solved for an effective cloud top pressure. After incorporation of CO_2-slicing, numerous other practical improvements were made to the geostationary automatic wind vector tracking techniques (reviewed by Nieman et al., 1997; Menzel, 2001; Velden et al., 1997). In 1996, fully automated GOES wind vector tracking became reliable enough

to serve as a routine source of information for numerical models used by the U.S. NCEP.

In the polar regions, many of the same principles have been applied to successive polar orbiter images, taking advantage of the convergence of orbits. Cloud drift wind vectors have been produced using AVHRR images (Herman, 1993; Turner and Warren, 1989), and co-located HIRS/2 (High-resolution InfraRed Sounder) data have been used to add the CO_2-slicing method (Herman and Nagle, 1994). Presently, MODIS (Moderate Resolution Imaging Spectrometer) offers the best opportunity for polar wind vector tracking, due to its higher spatial resolution, the availability of a 6.7-μm water vapor band for use in cloud-free scenes or when the presence of cloud in the imagery is ambiguous (see Section 4.4), the availability of four CO_2-slicing bands (bands 33–36, centered at 13.34, 13.64, 13.94, and 14.24 μm, respectively) and the deployment of MODIS aboard both the Terra and Aqua spacecraft (Key et al., 2001). Figure 4.15 shows the frequency of time differences

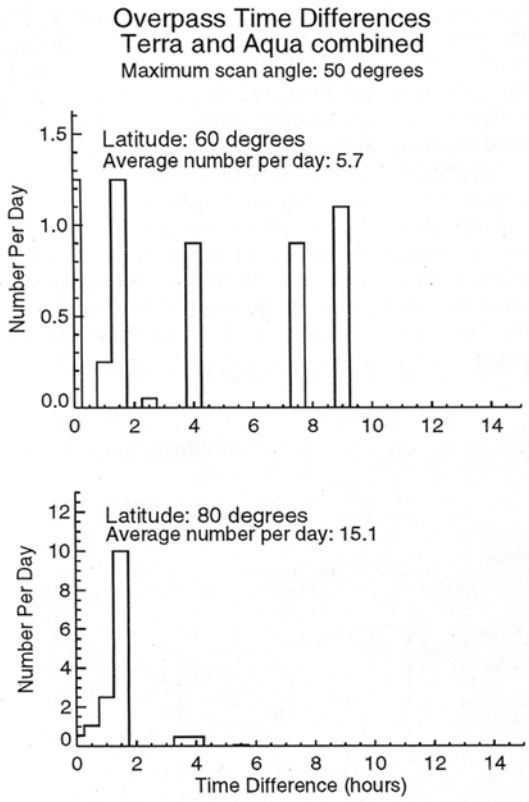

Figure 4.15. The frequency of time differences between successive overpasses of the MODIS instrument, at 60°S (top) and at 80°S (bottom), when both the Terra and Aqua spacecraft are considered, and when the nadir-viewing angle is restricted to 50° or smaller.

Courtesy Dr. Jeffrey Key, NOAA/NESDIS.

between successive overpasses of the MODIS sensor, considering both Terra and Aqua. At higher latitudes (80° versus 60°) there are more available overpasses and in principle the wind vectors should be more reliable. Figure 4.16 (see color section) shows an example of MODIS wind vectors produced by NOAA's Polar Satellite Meteorology project.

4.4 CLOUD DETECTION AND CLASSIFICATION

The above discussion of automated feature tracking leads to a challenging topic that represents a major difference between Earth remote sensing at high versus low latitudes. Over tropical and temperate latitudes, most types of cloud cover are readily identified in high-resolution satellite imagery (*GIFOV* of order 1 km or finer). This is not at all true at high latitudes. While scene features that likely represent cloud can often be identified and tracked in sequences of images to derive wind vectors, accurate cloud classification and cloud fraction determination are much more difficult (Figure 4.17).

Over snow and ice surfaces, this is a "white on white" problem. At visible wavelengths, and at many near-infrared wavelengths selected for lower latitude satellite remote-sensing applications, there is often too little contrast in backscattered specific intensity between a cloud top and a snow or ice surface. At mid-IR wavelengths, frequent temperature inversions in the lower troposphere can render temperature discrimination between the surface and cloud top ineffective. In addition, over some polar scenes the lower intensity levels are at the bottom of some sensors' dynamic range, resulting in a lower *SNR* (Signal-to-Noise Ratio). The problem is more difficult over extensive, pristine snow surfaces on the

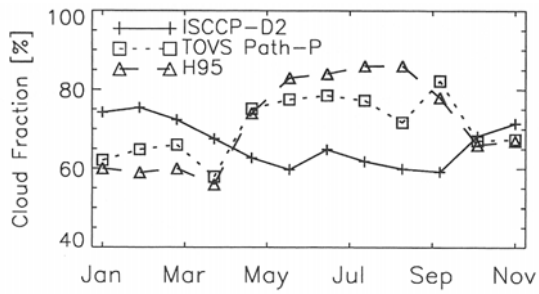

Figure 4.17. A comparison of mean monthly cloud amounts in the high Arctic (north of 80°N) from two multiyear satellite datasets, the ISCCP-D2 and TOVS Path-P, and a climatology of surface-based observations made by Hahn et al. (1995). Satellite cloud climatologies such as that from ISCCP cloud are generally more reliable at lower latitudes. The complexities involved with polar cloud detection and classification usually take longer to address in the development of global climatological products. Subsequent versions of the ISCCP dataset are known to perform better against validation data.

Antarctic Plateau and Greenland Ice Sheet. These surfaces have the highest albedos. For many sea ice types, surface albedo is noticeably lower such that some useful intensity contrast between surface and cloud top remains. In addition, spatially non-uniform sea ice surfaces, particularly during summer, have a different texture than the tops of stratocumulus or cirrus clouds, and thus cloud and sea ice are more easily distinguished both manually and with automated techniques.

Despite the fundamental complication with intensity contrasts, there are several strategies available for polar cloud detection and classification. A trained satellite meteorologist can recognize clouds over most high-albedo surfaces, and manual nephanalysis has long been useful for compiling high-latitude cloud climatologies (e.g., Crane and Barry, 1984; and the meteorological case studies discussed above). The obvious drawback is that this is labor-intensive. In the analysis of large satellite datasets, one desires a reliable automated algorithm. The first-order problem, the discrimination of clouds from cloud-free scenes, is often called "cloud masking". More detailed investigation involves identifying basic cloud types such as stratus, stratocumulus, cirrus, and multi-layered cloud decks, or "classification". Automated algorithms have been proposed in the literature for both cloud masking and classification, and are now used to help generate high-latitude data products for the International Satellite Cloud Climatology Project (ISCPP), MODIS, and other programs. However, before publishing an analysis of such satellite data products, the researcher should examine the original cloud mask with all images used, for confidence in its validity.

Cloud detection and classification algorithms are usually developed using detailed analysis of representative satellite data subsets called "training data". The properties, or "features", of the various desired scene types are derived quantitatively from the training data (see Key, 1990; Key and Barry, 1989). The training data are first analyzed manually by a skilled satellite meteorologist to locate the various desired scene types throughout the images (e.g., stratus cloud, cirrus cloud, sea ice, open water, etc.). Once an algorithm is developed, it is tested first with the training data, to determine its skill score with reference to the original manual classification. Then it is tested against manual interpretation of different data, or "validation" data. There are two types of cloud "features" that are generally exploited for cloud detection and classification: (1) the contrasting spectral signatures of clouds and underlying surfaces, and (2) contrasting textures. In an automated algorithm, these features must be represented numerically such that there are representative quantitative values for the desired classification categories. Given a set of such representative values for the categories, usually expressed as a matrix of means and standard deviations, two numerical classifying techniques have been used in the literature: (1) standard Bayesian decision techniques, and (2) neural networks.

For the traditional Bayesian classifier, Figure 4.18 illustrates the classification problem schematically. If N features are used to classify data into M categories, these properties must be chosen from the data such that a representative mean value for each feature emerges that appears to be unique to a given category, with a usefully small standard deviation. We represent the set of features as an

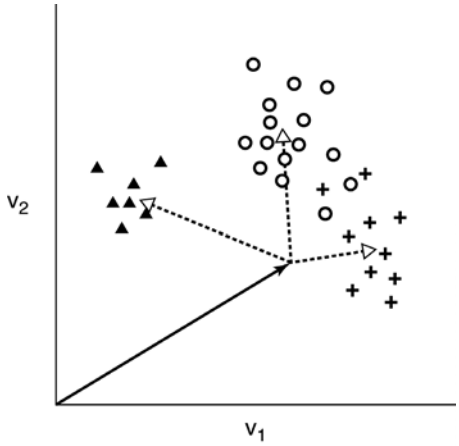

Figure 4.18. Schematic diagram of class clustering in a two-dimensional feature space. The solid vector denotes an observation, and the dashed arrows are the vector distances between the observation and the centers of the class clusters.
After Ebert (1987).

N-dimensional vector $\mathbf{v}$, which is used to classify a given observation into one of M categories: $C_1, C_2, \ldots, C_M$. The observation is classified into the category C_k whose "cluster" (mean and standard deviation of the feature values derived from the training data) lies closest to the observation's feature values, in N-dimensional feature space. In notation, we express this shortest distance as the maximum in the product of the probability density function of $\mathbf{v}$, $p(\mathbf{v}|C_j)$, and the a priori probability $P(C_j)$ that category C_k exists in nature; that is:

$$p(\mathbf{v}|C_k)P(C_k) > p(\mathbf{v}|C_j)P(C_j) \quad \text{for all } j \neq k \tag{4.5}$$

Designing the classification algorithm is equivalent to determining all of the $p(\mathbf{v}|C_j)$ and $P(C_j)$ from the training data. Some attention should be given to the a priori probability for the existence of each category in nature, although successful results can often be obtained by assuming that all scene categories are equally probable. An example of a successful cloud classification scheme using the Bayesian decision method, and the concept of (4.5) and Figure 4.17, is discussed below.

The concept of a neural network is sketched in Figure 4.19. In a computer code, an array of "nodes" is constructed, nodes being analogues of neurons in the human brain. Each node discharges a signal to nodes farther along in the array when input signals upon it reach a certain threshold. As diagrammed in Figure 4.18, the nodes are typically arranged in layers. The threshold is calculated using a nonlinear-bounded, monotonically increasing "activity" function incorporating the weighted sum of all input signal values x_i incident upon it; for example:

$$y = f\left(\sum_{i=0}^{L-1} w_i x_i - k\right) \tag{4.6}$$

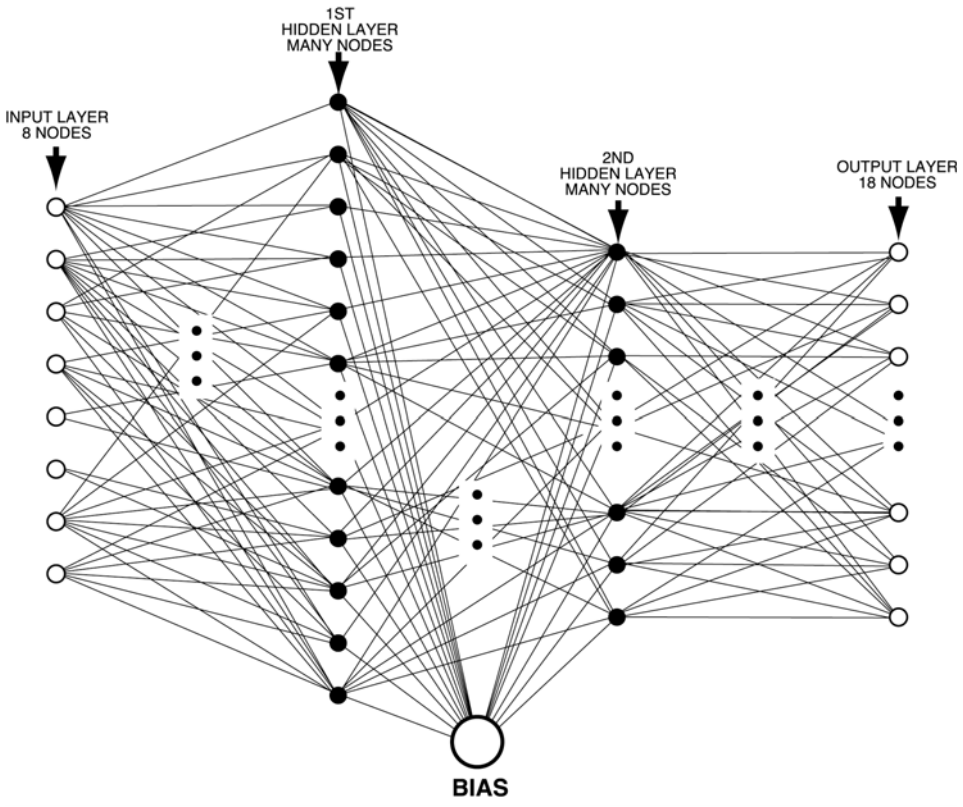

Figure 4.19. Schematic diagram of a multi-layer perceptron with two hidden layers, a neural network configuration frequently used in satellite remote-sensing algorithms.

where w_i are the weights of all L nodes in the preceding layer. Sometimes a constant k is included to better define a threshold for node activation. "Training" the neural network involves determining the appropriate weights w_i for all the nodes.

An input layer having N nodes receives the vector $\mathbf{v}$ containing the feature values. The output layer contains M nodes and represents the desired classification categories. One or more intermediate layers contain nodes each having a different threshold in its activity function. Each receives an input signal from every node in the preceding layer and, when its activation threshold is reached, sends a signal to every node in the following layer. To configure this computer code as a classifier, the training data are introduced at the input layer and the weights of all the nodes in the intermediate layers are adjusted until correct classifications appear at the output layer (e.g., a value of unity at the node representing the correct classification, zero for all other nodes). This description is merely an introduction to the large and diverse topic of neural network programming (Hecht-Nielsen, 1990). More details, with application to polar cloud classification, are given by Key et al. (1989) and Welch

et al. (1992); the latter report slightly better performance with neural network classifiers versus a Bayesian discriminator.

4.4.1 Contrasting spectral signatures

Yamanouchi and Kawaguchi (1992) demonstrated how some very useful polar cloud detection can be accomplished using the thermal infrared channels of the AVHRR. The AVHRR was designed in the 1970s primarily for weather imaging, and has been flown regularly on the NOAA polar orbiters. It is a straightforward line scanner (Chapter 2) having a nadir *GIFOV* of 1.1 km. With the simple circular scanning mechanism, *GIFOV* increases as the instrument sweeps out toward the edge of the crosstrack. The major advantage of working with AVHRR is the long time series of data from these instruments that now spans more than two decades. Careful analysis of this imagery may yield information about trends in polar meteorological phenomena, and at present research is only just beginning with such long time series of satellite data (e.g., Wang and Key, 2003).

Most AVHRR instruments have five channels, each with identical spatial resolution, and with the following nominal spectral bandwidths: channel 1 (0.58–0.68 mm), channel 2 (0.73–1.1 μm), channel 3 (3.5–3.9 μm), channel 4 (10.3–11.3 μm), and channel 5 (11.5–12.5 μm). The earliest versions of this instrument lacked channel 5; this second mid-IR band was added primarly to allow for atmospheric water vapor correction when retrieving surface temperature. The most recent versions have channel 3 switch between a 3.7-μm measurement at night and a 1.6-μm measurement during the day. As discussed in Chapter 2, the AVHRR channels 1 and 2 are radiometrically calibrated only before launch. Without onboard calibration, vicarious methods must be used to make these channels radiometrically useful (Section 2.7). For channels 3, 4, and 5, a blackbody calibration source is available onboard the spacecraft, and with proper data reduction techniques that account for the nonlinearities in detector response (e.g., Weinreb et al., 1990), data from these thermal channels can be used directly for both radiometric and image analysis.

For polar cloud detection, the three AVHRR thermal infrared channels are the most useful. Over most high-albedo surfaces, channel 1 will show too little radiometric contrast between the surface and cloud, although the cloud texture can often be distinguished from surface textures in this visible wavelength channel as discussed below. AVHRR channel 2 is marginally useful for showing radiometric contrast between cloud tops and underlying sea ice surfaces, as discussed below for retrieving cloud optical depth, but over the highest albedo surfaces, such as the Antarctic Plateau or Greenland Ice Sheet, radiometric contrast between surface and cloud is not much more useful than in channel 1. The useful quantities for cloud detection are the brightness temperature difference between channels 3 and 4, $\Delta T_{34} = T_3 - T_4$, and the brightness temperature difference between channels 4 and 5, $\Delta T_{45} = T_4 - T_5$.

For a typical natural snowpack, infrared emissivity is near unity, but has some spectral variability such that in a clear-sky scene over snow the AVHRR will show

$\Delta T_{45} \approx 0.5$, the exact value depending on viewing angle, and the effective size of the snow grains. According to the model of Dozier and Warren (1982), the dependence of a snow brightness temperature measurement T_b on nadir-viewing angle θ may be represented as:

$$T_b - T = \frac{C_0 + C_1\mu}{1 + D_1\mu} \tag{4.7}$$

where $\mu = \cos\theta$, and T is the physical temperature. For the NOAA-7 spacecraft, Dozier and Warren (1982) give coefficients $C_0 = -1.3117$, $C_1 = 1.1019$, and $D_1 = 1.6805$ for AVHRR channel 4, and $C_0 = -3.3526$, $C_1 = 2.7279$, and $D_1 = 1.6266$ for AVHRR channel 5. Specific coefficients must be derived for a particular spacecraft sensor, or with enough cloud-free satellite data an analagous expression can be derived empirically. Real AVHRR cloud-free data over pristine snow usually lie fairly close to the values predicted by (4.7). The emissivity of snow or ice is also close to unity in AVHRR channel 3, and snow surfaces, which usually consist of ice particles with effective radius larger than 25 μm, also backscatter a small fraction of incident solar radiation at 3.7 μm. The result is that ΔT_{34} typically lies in the range 5–20 K for most snow and ice surfaces. Liquid water or ice clouds, in contrast, usually backscatter much more radiation to space in this wavelength range. The primary reason is that the clouds are composed of much smaller liquid water droplets (effective radius of order 10 μm), or in the case of ice clouds: (1) the effective radius of the cloud particles is also often smaller than that of surface snow grains, and (2) the smaller optical depths (generally <5) yield a moderate emissivity and hence a reflectance that contrasts with the underlying snow surface. Yamanouchi and Kawaguchi (1992) demonstrated this using radiative transfer calculations, and also showed that many polar clouds can be readily detected using a scatter diagram of ΔT_{34} versus T_4.

Figure 4.20 (see color section) shows a region of the Siple Coast in Antarctica, in AVHRR channel 1. Some contrasting texture is evident between clouds and underlying snow, but automating an algorithm to recognize this texture alone would be unreliable. Figure 4.21 (see color section) shows the corresponding image of ΔT_{34}. Figure 4.22 (top panel) shows a scatter diagram of ΔT_{34} versus T_4 for a representative sample of pixels in the same image. Two branches appear in this scatterplot: a lower branch where $\Delta T_{34} < 10$ K for all T_4, and a higher "arc" where ΔT_{34} shows a wide range of larger values. This scatter diagram allows us to define a threshold of $\Delta T_{34} = 10$ K, below which a pixel is identified as cloud-free and above which a pixel is identified as containing cloud cover in some fraction. This straightforward method for cloud detection is very effective, but subject to two limitations. First, it is useful only in the sunlit part of the year. In the polar winter, with no solar backscatter, and the channel 3 detector operating near the lower limit of its performance, ΔT_{34} is useless for cloud detection. Second, there is no single threshold for cloud detection using ΔT_{34}. Over a broken sea ice surface, ΔT_{34} might be as small as 0 K. Over a high ice sheet with pristine snow cover, and with large solar zenith- and nadir-viewing angles, ΔT_{34} might be larger than 30 K for cloud-free conditions. Assigning arbitrary climatological thresholds is always dangerous in satellite

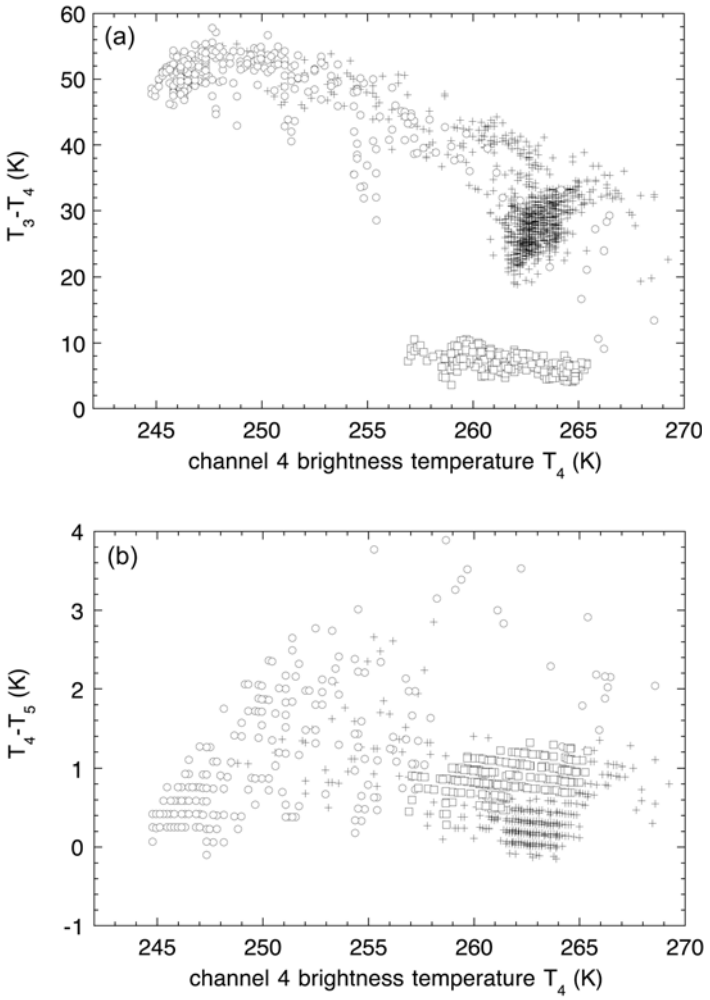

Figure 4.22. Scatter diagrams of the brightness temperature differences (a) channel 3 and channel 4, (b) channel 4 and channel 5, versus the channel-4 brightness temperature, for the data of Figure 4.19. Crosses refer to measurements north of −73°S. Circles refer to measurements between −73°S and −74°S. Squares refer to measurements below −76°S.

meteorology, but more so over the polar regions where the radiative transfer involving surface and cloud is more complicated. At present, the most modern cloud-masking techniques for AVHRR and similar data use radiative transfer calculations to help choose the threshold ΔT_{34} (or its analog with other sensors) for a variety of snow surfaces and viewing geometries (Minnis et al., 2001).

Even when detection thresholds are defensibly chosen from physical fundamentals, there remains an issue of sub-pixel variability. A given threshold value in, say, ΔT_{34} might be used to classify a pixel as clear or cloudy, but what if the actual

cloud fraction within that *GIFOV* is somewhere between 0 and 1? The spatial coherence method (Coakley and Bretherton, 1982) described below addresses this issue for clouds over a warmer surface, but to date no analog has been developed for the polar regions. An analytical treatment of subpixel-scale variability, in the context of threshold detection techniques, has been given by Key (1994). Such an analytical approach might prove useful in some situations where the cloud amount needs to be retrieved with the highest accuracy; for example, when analyzing smaller images with relatively large pixel sizes. Generally speaking, threshold detection techniques must be used with great care in any satellite remote-sensing research, but with even more caution over the polar regions.

During the polar winter, Yamanouchi and Kawaguchi (1992) suggest that the AVHRR mid-IR brightness temperature difference ΔT_{45} might also be useful for cloud detection. Many polar clouds are optically thin, yielding more spectral dependence in their emissivity between 800 and 1,200 cm^{-1}, and hence a larger ΔT_{45} than a snow surface. An optically thick cloud may behave nearly like a blackbody and hence have ΔT_{45} slightly smaller than that of a snow surface. Over some clouds, ΔT_{45} might be negative, depending on complexities involving thermodynamic phase and/or temperature contrasts with the surface. Figure 4.21 (lower panel) shows the scatter diagram of ΔT_{45} versus T_4 for the same images as Figures 4.19 and 4.20. A small range in ΔT_{45} appears for pixels previously identified by ΔT_{34} as cloud-free, suggesting a range of 0.5–1.2 K for clear-sky scene identification. However, a scatter diagram of ΔT_{45} versus T_4 is usually not as reliable as that for ΔT_{34}, the main reason being that a wide range in polar cloud optical and radiative properties (liquid/ice water path, effective particle radius, temperature) will yield ΔT_{45} very similar to that of a snow or ice surface. This is evident in Figure 4.21, where we see that cloudy-sky pixels that have ΔT_{45} in the range 0.5–1.2 K for $T_4 < 257$ K and $T_4 > 266$ K.

These spectral threshold techniques using scatter diagrams are reminiscent of the spatial coherence technique developed by Coakley and Bretherton (1982). Over a uniformly warm midlatitude ocean there is often enough thermal contrast between the sea surface and cloud tops that two ranges of datapoints from an AVHRR channel 4 or 5 image can be identified: one associated with completely cloud-free pixels and one associated with entirely cloud-covered pixels. If one groups individual pixels into "superpixels" of, say, 16×16 original pixels, and computes the standard deviation σT_4 of T_4 for each cluster, then a scatter diagram of this standard deviation versus T_4 itself will often show smaller σT_4 for the cloud-free and entirely cloudy superpixels, and larger σT_4 for superpixels with partial cloud cover. An example is shown in Figure 4.23. Having identified these limiting cases, these and the intermediate values of T_4 can be converted from brightness temperature back to measured specific intensities, and the cloud fraction f for an individual original pixel's intensity I can be estimated using a linear relationship in intensity:

$$f = \frac{I - I_{CLR}}{I_C - I_{CLR}} \tag{4.8}$$

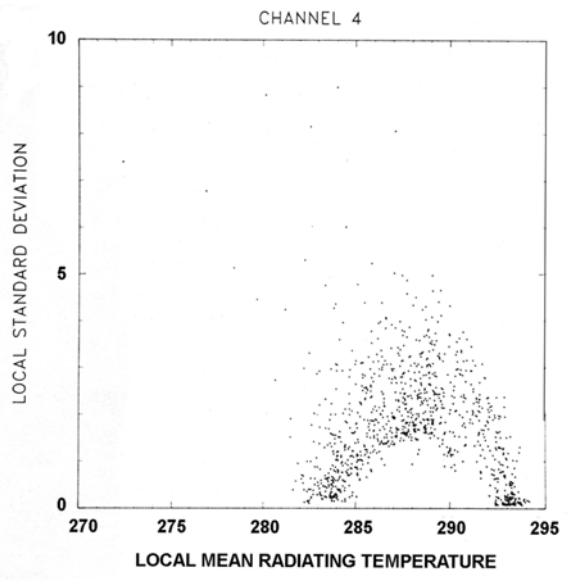

Figure 4.23. Illustration of the spatial coherence method for retrieving sub-pixel cloud fraction over a warm ocean surface in mid-IR imagery from AVHRR or similar sensors. The standard deviation in brightness temperature in a small cell is plotted against the mean brightness temperature for the cell. The warm (~293 K) cluster with near-zero standard deviation represents cloud-free cells. The colder (~283 K) cluster with near-zero standard deviation represents cells with 100% cloud cover. Intermediate temperatures, with higher standard deviations, represent partially cloudy scenes.

where I_{CLR} and I_C are the intensities corresponding to the mean brightness temperatures in the clusters for clear and cloudy skies, respectively. Thus, this spatial coherence method provides information about cloud amount at the subpixel scale. Over polar surfaces, with more complicated radiative transfer scenarios (e.g., optically thin ice clouds, temperature inversions, etc.), straightforward application of this spatial coherence technique is not obvious. However, in future it may be possible to use this technique, in conjunction with the multispectral techniques discussed above, to retrieve information about polar cloud amount within a single pixel. This will require in-depth understanding of the radiative transfer considerations with the type of scene being studied. In addition, future sensors will offer more near-IR and mid-IR channels than AVHRR, providing more opportunities to exploit spectral signatures.

4.4.2 Automated texture recognition

The spatial coherence technique of Coakley and Bretherton (1982) introduces texture recognition, automated techniques which have shown some success at identifying

and classifying polar cloud cover. The "texture", or spatial variability within a satellite image, can be quantified by means of *gray-level difference statistics* (Weszka et al., 1976), also known as the *Gray Level Difference Vector* (*GLDV*). To calculate these statistics, we express the pixel values (intensities or temperatures) as brightness levels B in a standard grayscale (values 0 to 255), and subdivide the image into large superpixels, or "cells" of dimension $I \times J$ original pixels. A gray-level difference $g(\varphi, d)$ is the difference in brightness B between two pixels separated by a fixed distance d, along a direction φ, from the point of origin at the center of the "cell". In most studies, $d = 1$, denoting calculations for adjacent pixels along a given direction, although larger separation distances can be considered. We then construct a histogram of these gray-level difference values, $h_{\varphi,d}(g)$, and normalize this histogram by the total number of gray-level differences H calculated for a given separation d and direction φ. From this normalized histogram $h_{\varphi,d}(g)/H$, several quantities can be computed that describe various aspects of texture within a cell. The mean is defined as:

$$\mathrm{MEAN}(\varphi, d) = \frac{1}{256} \sum_{g=0}^{255} g \frac{h_{\varphi,d}(g)}{H} \tag{4.9}$$

More complex measures of texture include the contrast:

$$\mathrm{CON}(\varphi, d) = \sum_{g=0}^{255} g^2 \frac{h_{\varphi,d}(g)}{H} \tag{4.10}$$

the angular second moment:

$$\mathrm{ASM}(\varphi, d) = \sum_{g=0}^{255} \left[\frac{h_{\varphi,d}(g)}{H}\right]^2 \tag{4.11}$$

and the entropy:

$$\mathrm{ENT}(\varphi, d) = -\sum_{g=0}^{255} \frac{h_{\varphi,d}(g)}{H} \ln\left[\frac{h_{\varphi,d}(g)}{H}\right] \tag{4.12}$$

Additional statistical measures are given by Welch et al. (1992). Adequate values of these statistical measures can usually be calculated for a cell size $I = J \sim 32$. These statistics can be calculated for any sensor channel, and often their behavior will be different from one channel to the next. The *GLDV* approach is not the only method for quantifying texture within an image. Other methods include the gray-level co-occurrence matrix (Haralick et al., 1973), and the gray-level runlength method (Connors and Harlow, 1980; Haralick, 1979). All of these methods are discussed in Welch et al. (1992).

Having computed the *GLDV* or similar statistics for all sensor channels in the training data, the next task is to determine which ones actually help classify a given cell into a given desired scene category. The first step is to determine a realistic list of categories that can be detected in the satellite data. For example, it is reasonable to

expect a discrimination between the textures of, say, marine stratocumulus cloud tops and broken sea ice cover. However, it may not be possible to distinguish between various cloud levels—say, low-level versus mid-level stratus. A preliminary list of categories can usually be complied from careful inspection of both textures and multispectral signatures in the training data. However, once the numerical iteration begins to configure the algorithm, it may appear that some categories cannot be discerned by machine in an automated fashion, even though they are evident to the trained satellite meteorologist. In this case, the list of categories will need to be revised to reflect what can actually be achieved by an automated algorithm.

Given a desired list of categories, the next step is to sort through all the computed features to determine which ones best make the classifications. From the training data, the means μ_i and standard deviations σ_i of all features must be calculated (to avoid confusion, note that in the case of Eq. 4.5, this means taking the mean of all *GLDV* "means" calculated from the training data for each category). To help determine which features are most unique for each category, and thus provide the best discrimination, Ebert (1987) suggests the use of a divergence parameter D_{ijk}:

$$D_{ijk} = \frac{|\mu_{ij} - \mu_{ik}|}{\sigma_{ij} + \sigma_{ik}} \tag{4.13}$$

where the indices j and k refer to categories C_j and C_k, and this parameter therefore measures the degree to which the feature v_i can discriminate between categories C_j and C_k.

In one successful example of an Arctic cloud classification algorithm, Ebert (1987) found that a combination of textural and multispectral features works best. Each of the *GLDV* features was computed for four directions—$\varphi = 0^\circ$, 45°, 90°, and 135°—with reference to a consistent direction in all the images, and both the maximum (MAX) and mean (MEAN) values over these directions were considered in algorithm development. In addition to these textural features computed from expressions (4.9) to (4.12), various ratios and differences of AVHRR channel intensities and brightness temperatures were considered. To examine the "albedo" in AVHRR channel 3, the thermal component to the intensity was estimated by evaluating the Planck function over the channel-3 spectral interval using the brightness temperature of channel 4. The directionally dependent reflectance r_3 (see Section 2.3.2) was then computed as the ratio of the solar backscatter component to extraterrestrial solar flux:

$$r_3 = \frac{I_3 - B_3(T_4)}{\dfrac{F_{03}\cos\theta_0}{\pi} - B_3(T_4)} \tag{4.14}$$

where I_3 is the measured channel-3 intensity, F_{03} is the extraterrestrial solar flux for channel 3 (see Section 2.6), and θ_0 is the solar zenith angle. Additional spectral features were created by computing the percentage of pixels within a cell that fall into the ranges listed in Table 4.1. Defining these spectral features, referred to as the LOW, MED, and HIGH percentages for channels 1, 3, and 4, comes dangerously

Table 4.1. The ranges in directionally dependent reflectances r_1 and r_3, for AVHRR channels 1 and 3 respectively, and the ranges in channel-4 brightness temperature T_4, used to define the LOW, MED, and HIGH features used in developing the multispectral and textural Arctic cloud classification algorithm of Ebert (1987).

Channel	Low	Medium	High
1	$r_1 < 40$	$40 < r_1 < 70$	$r_1 > 70$
3	$r_3 < 10$	$10 < r_3 < 30$	$r_3 > 30$
4	$T_4 < 245\,\mathrm{K}$	$245\,\mathrm{K} < T_4 < 265\,\mathrm{K}$	$T_4 > 265\,\mathrm{K}$

close to assigning arbitrary climatological thresholds, but their use is acceptable when they are only one potential part of the algorithm.

After examining a total of 66 multispectral and textural features using the divergence parameter (4.13), 8 features were identified that best classified Arctic AVHRR data into 18 categories (Table 4.2). The category means and standard deviations for all 8 features and 18 categories are given in Table 4.3. The Ebert (1987) method uses a classical Bayesian discriminator, where the feature means

Table 4.2. The 18 scene categories used in the Ebert (1987) classification algorithm for Arctic AVHRR data, along with an estimate from the Warren et al. (1988) atlas of the a priori climatological probability of each category over the central Arctic Ocean.

Category (j)	$P(C_j)$	Scene
1	0.00	Land without snow
2	0.00	Land with snow
3	0.97	Open water
4	0.97	Unbroken sea ice
5	0.97	Broken sea ice
6	0.00	Ice sheet
7	0.00	Mixed surface types
8	2.35	Cirrostratus/Altostratus over land/water
9	3.40	Cirrus/Cirrocumulus/Altocumulus over land/water
10	14.18	Stratus over land/water
11	14.18	Stratocumulus over land/water
12	2.55	Cumulus over land/water
13	2.35	Cirrostratus/Altostratus over snow/ice
14	3.40	Cirrus/Cirrocumulus/Altocumulus over snow/ice
15	14.18	Stratus over snow/ice
16	14.18	Stratocumulus over snow/ice
17	2.55	Cumulus over snow/ice
18	23.77	High cloud over low cloud

From Lubin and Morrow (1998).

and covariances are given by:

$$\left.\begin{aligned}\hat{\mu}_j &= \frac{1}{N_j}\sum_{n-1}^{N_j}\mathbf{v}_{jn} \\ \hat{\Sigma}_j &= \frac{1}{N_j}\sum_{n=1}^{N_j}(\mathbf{v}_{jn}-\hat{\mu}_j)^T(\mathbf{v}_{jn}-\hat{\mu}_j)\end{aligned}\right\} \tag{4.15}$$

and where the sums are over N_j samples for category j in the training data. A multivariate normal distribution is used for the probability density function:

$$p(\mathbf{v}|C_j) = \frac{1}{(2\pi)^{d/2}\left|\hat{\Sigma}_j\right|^{1/2}}\exp\left\{-\tfrac{1}{2}(\mathbf{v}-\hat{\mu}_j)^T\Sigma_j^{-1}(\mathbf{v}-\hat{\mu}_j)\right\} \tag{4.16}$$

where d is the dimensionality, or number of features in the feature vector $\mathbf{v}$. It actually proves more computationally stable to use the logarithm of this probability density function:

$$\log p(\mathbf{v}|C_j) = -\frac{d}{2}\log 2\pi - \frac{1}{2}\log\left|\hat{\Sigma}_j\right| - \frac{1}{2}(\mathbf{v}-\hat{\mu}_j)^T\Sigma_j^{-1}(\mathbf{v}-\hat{\mu}_j) \tag{4.17}$$

Using the category means and standard deviations from Table 4.3, the probability that a given unclassified feature vector $\mathbf{v}$ belongs to each category C_j is calculated using 4.16, and then the logical decision-making procedure of (4.5) is applied to make the classification.

Table 4.3. The category means and standard deviations (in parentheses) for all 18 categories and 8 spectral features used in the Ebert (1987) Arctic cloud classification method.

Category	alb(1)-alb(2)	low(3)	alb(3)/alb(1)	mean asm(3)	mean(1)	mean(4)	max ent(4)	max ent(1)
1	−4.0 (2.6)	0.93 (0.07)	0.30 (0.19)	0.76 (0.14)	12 (2)	283.5 (4.0)	1.50 (1.25)	1.70 (0.85)
2	3.0 (4.7)	0.85 (0.15)	0.26 (0.17)	0.34 (0.12)	27 (12)	275.0 (6.0)	3.70 (1.85)	5.30 (1.20)
3	1.8 (2.0)	0.90 (0.09)	0.19 (0.31)	0.63 (0.19)	10 (3)	276.5 (4.0)	1.60 (1.20)	2.65 (1.50)
4	12.8 (1.3)	0.94 (0.10)	0.05 (0.05)	0.62 (0.11)	56 (7)	270.0 (1.0)	0.30 (0.50)	2.95 (0.65)
5	6.9 (2.0)	0.94 (0.09)	0.09 (0.10)	0.60 (0.13)	29 (9)	271.0 (1.5)	0.80 (0.90)	5.00 (0.85)
6	7.5 (1.8)	0.99 (0.03)	0.04 (0.02)	0.33 (0.08)	61 (5)	257.5 (5.0)	0.70 (0.60)	0.95 (1.10)
7	5.3 (3.3)	0.95 (0.07)	0.08 (0.10)	0.52 (0.14)	26 (11)	273.0 (2.0)	2.10 (1.00)	4.10 (0.95)
8	−0.7 (1.5)	0.41 (0.26)	0.57 (0.37)	0.34 (0.09)	32 (9)	264.5 (11.0)	3.70 (0.65)	4.15 (0.50)
9	−0.2 (4.0)	0.66 (0.19)	0.42 (0.20)	0.41 (0.14)	22 (9)	271.0 (7.0)	4.10 (1.15)	4.20 (1.00)
10	4.0 (1.3)	0.14 (0.20)	0.55 (0.23)	0.61 (0.18)	35 (9)	271.5 (4.5)	1.70 (1.15)	4.25 (0.80)
11	2.3 (3.0)	0.25 (0.19)	0.69 (0.28)	0.36 (0.14)	30 (7)	272.0 (4.5)	3.50 (1.15)	5.50 (0.50)
12	−3.0 (2.5)	0.60 (0.19)	0.73 (0.16)	0.49 (0.14)	17 (4)	281.5 (4.5)	3.60 (0.95)	4.15 (0.90)
13	6.0 (2.7)	0.63 (0.34)	0.18 (0.10)	0.30 (0.05)	59 (6)	247.5 (5.0)	3.85 (0.90)	3.65 (0.65)
14	9.8 (2.6)	0.82 (0.17)	0.14 (0.08)	0.45 (0.13)	51 (13)	265.5 (4.0)	3.20 (0.80)	3.90 (0.60)
15	10.2 (2.0)	0.31 (0.26)	0.28 (0.11)	0.50 (0.13)	60 (11)	266.0 (4.0)	1.70 (0.90)	3.45 (0.75)
16	8.0 (1.7)	0.26 (0.25)	0.38 (0.12)	0.24 (0.05)	53 (7)	262.0 (4.0)	3.70 (0.55)	4.85 (0.40)
17	9.2 (1.0)	0.72 (0.14)	0.17 (0.09)	0.30 (0.09)	67 (12)	261.5 (3.5)	2.10 (1.10)	3.25 (1.10)
18	6.0 (3.2)	0.40 (0.24)	0.37 (0.17)	0.31 (0.10)	46 (14)	262.0 (6.0)	3.95 (0.75)	4.45 (0.70)

The algorithm was tested by Ebert (1987) against the original training data, and also with synthetic data generated using Monte Carlo calculations. The algorithm's success can be described by two metrics—a classification accuracy, A:

$$A = \frac{R}{T} \times 100 \tag{4.18}$$

where R is the number of correct classifications and T is the total number of classifications, and by a skill score, s:

$$s = \frac{R - E}{T - E} \times 100 \tag{4.19}$$

where E is the number of correct classifications one would expect from random chance. The skill score was also used in the optimization of the algorithm: feature combinations were tried, and categories redefined, until s converged to a maximum value. The final algorithm (Table 4.3) showed classification accuracies of 85.4% and 92.8% when tested with the original training data and synthetic data, respectively. The respective skill scores were 84.6% and 92.4%. When tested on independent AVHRR data, the accuracy was 83.9% and the skill score 83.0%. These numbers are typical for the performance of automated cloud classification algorithms applied to polar regions. Whether the implied inaccuracies are significant or not depends on the particular analysis of cloud climatology. The researcher should keep both the strengths and weaknesses of such algorithms in mind when analyzing high-latitude climatologies, and not be too comfortable using "data products".

Lubin and Morrow (1998) performed an independent assessment of the Ebert (1987) algorithm, using whole-sky photographs of cloud cover taken during the 1994 Arctic Ocean Section (Aagaard et al., 1996). The algorithm was shown to be fundamentally sound, and useful for both full-resolution "Local Area Coverage" (LAC, 1.1-km nadir) AVHRR data and the original sub-sampled 3×5-km resolution "Global Area Coverage" (GAC) data format with which the algorithm was originally developed. When tested against the whole-sky imagery, the skill score was improved slightly when a priori category probabilities $P(C_j)$ were taken from other baseline climatological cloud atlases (Warren et al., 1988, see Table 4.2). Figure 4.24 (see color section) shows an example of AVHRR LAC data classified by the Ebert (1987) algorithm.

4.5 CLOUD RADIATIVE PROPERTIES

The influence of clouds on the Earth's radiation budget has been successfully studied over tropical and midlatitudes using satellite data (Ramanathan et al., 1989). Near-global climatologies of fundamental cloud radiative properties have also been derived from sensors such as AVHRR (Rossow et al., 1996). In the polar regions, such retrievals are more difficult for many of the same reasons that automated cloud detection and classification are difficult. And yet, in the polar regions, the optical properties of clouds have a relatively larger influence on the radiation budget and

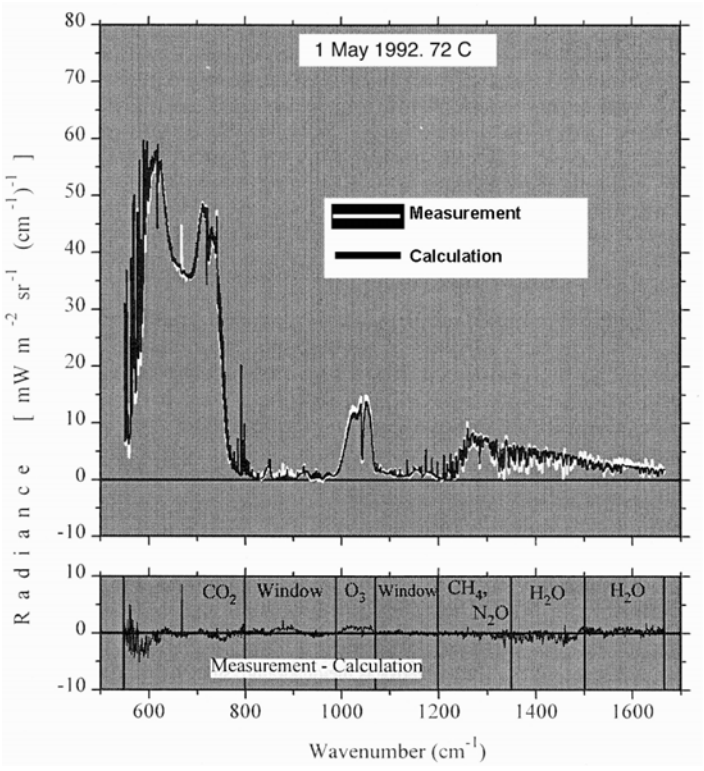

Figure 4.25. Spectral intensity at a zenith angle of 75° measured by a Fourier Transform InfraRed (FTIR) spectro-radiometer at the South Pole on May 1, 1992. The measurement is compared with a line-by-line radiative transfer calculation. Note the extremely low intensity in the mid-IR window, and the rapid decrease in intensity as wavenumber decreases below 600 cm^{-1}, signifying a very transparent second mid-IR window beyond the CO_2 band.

From Walden et al. (1998). Copyright 1998 American Geophysical Union. Reproduced by permission of American Geophysical Union.

climate than at lower latitudes, due to the diminished radiative influence of the important greenhouse gases—water vapor and CO_2—in the colder atmosphere (e.g., Walden et al., 1998). This is particularly true in the longwave, where the 8–12-μm "mid-IR" window is much more transparent, and, in the coldest atmospheres, a second window opens beyond 15 μm as both water vapor and CO_2 emission features lose their strength (Figure 4.25).

The cloud properties generally recognized as influencing climate through radiative processes are (1) the total cloud fraction and fractional cloud amount of various types and altitudes, (2) thermodynamic phase (the preponderance of liquid water, ice crystals, or radiatively important concentrations of both liquid water and ice in a "mixed phase"), (3) the optical depth, as a function of wavelength, and (4) size distributions of the liquid water droplets and/or ice crystals that make up the cloud. The three cloud components of plane-parallel radiative transfer calculation—

optical depth, single-scattering albedo, and a scattering asymmetry factor—depend ultimately on both thermodynamic phase and particle size distribution, as was shown in Figure 2.15. Real clouds are never composed of droplets or crystals all the same size, but a useful measure of a cloud's effective radiating particle size, or *effective radius*, is the ratio of the third to the second moment of particle size distribution:

$$r_e = \frac{\int r^3 n(r)\, dr}{\int r^2 n(r)\, dr} \tag{4.20}$$

Numerous *in situ* measurements of cloud particle size distribution can be found in the literature for temperate and tropical latitudes. For polar regions such measurements are still sparse, although useful information can be found in the references discussed in Section 4.5.4.

Examining Figure 2.15, it is clear that for terrestrial ice or liquid water clouds the single scattering albedo is near unity, and essentially independent of wavelength, for wavelengths shorter than about 1.0 μm. In this limiting case of conservative scattering, it can be shown (Liou, 1992; Stephens, 1978) that the cloud optical depth τ can be expressed as a straightforward relationship between the effective radius r_e and the liquid water path W:

$$\tau \cong \frac{3}{2}\frac{W}{r_e} \tag{4.21}$$

where r_e is in microns and W is the integral of the cloud's water content (LWC, $\mathrm{g\,m^{-3}}$):

$$LWC = \frac{4\pi\rho_w}{3}\int r^3 n(r)\, dr \tag{4.22}$$

over the cloud's vertical extent z_1 (cloud base) to z_2 (cloud top):

$$W = \int_{z_1}^{z_2} LWC(z)\, dz \quad (\mathrm{g\,m^{-2}}) \tag{4.23}$$

At wavelengths longer than 1.0 μm the optical depth τ varies with the wavelength.

The cloud properties used directly in a GCM are the optical depth $\tau(\lambda)$ and effective radius r_e. The GCM generally assigns values of these quantities based on parameterization schemes for predicting cloud phase and liquid water content. At present, GCM radiative transfer algorithms are plane-parallel (e.g., Briegleb, 1992). These algorithms include linear mixing schemes for handling fractional cloud cover, the cloud fraction at various altitudes being also generated from meteorological parameterizations. GCMs still exhibit their largest and most consistent errors at high latitudes (Briegleb and Bromwich, 1998). Attempting to improve and validate GCM predictions of polar clouds and radiation budget components is a natural application of satellite remote sensing. GCM output can be readily compared with

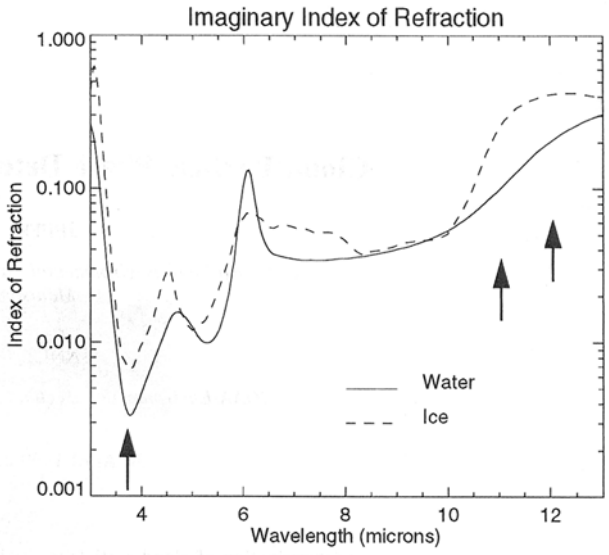

Figure 4.26. The imaginary component of the index of refraction, for ice and for liquid water, in the wavelength range covered by AVHRR channels 3–5. Arrows denote center wavelengths for these channels.

From Key and Intrieri (2000).

large-scale maps derived from satellite data showing time variation in cloud amount and type, cloud phase, optical depth, and effective radius.

The following discussion gives examples for how the latter three quantities can be estimated from AVHRR data. The physical basis for many of these techniques begins with the difference in imaginary refractive index between liquid water and ice. Figure 4.26 illustrates this for part of the near-IR and for the entire mid-IR window. The single scattering albedo, asymmetry factor, and volume extinction for a given particle composition and size distribution are ultimately determined from calculations describing the transition of electromagnetic radiation between two media with different refractive indices (i.e., from air to a liquid water droplet). Useful compilations of the complex refractive index have been prepared by Irvine and Pollack (1968) for liquid water and by Warren (1984a) for ice.

Introductions to this complex topic in radiative transfer can be found in Van de Hulst (1957) for liquid water and in Liou (1992) for ice crystals. One useful technique for computing radiative transfer parameters for arbitrary, non-spherical particles is the discrete dipole approximation (Draine and Flatau, 1994), for which Dr. Piotr Flatau (Scripps Institution of Oceanography) has prepared a FORTRAN code called DDSCAT. This approach works well for particles with size parameter $x_p = 2\pi\rho/\lambda$ in the small to medium range, up to 10–20 (here ρ is the particle radius and λ is the wavelength).

In many cases, the complexities involved in scattering by ice particles with complex shapes can be circumvented by using a suitable "equivalent sphere"

representation. Representing complicated ice crystals by spheres of equivalent volume or equivalent surface area will inevitably lead to errors when computing volume extinction, single scattering albedo, and asymmetry factor. However, Grenfell and Warren (1999) have shown that an ice crystal can often be well-represented by a collection of independent spheres having the same volume to surface area ratio as the original non-spherical particle. In radiative transfer calculations, the primary requirement is to conserve the total mass of the scattering and absorbing substance. There is no rigorous requirement that the total number of particles be conserved in a given representation, provided the total mass is conserved in such a way that the volume to surface area ratio remains the same as for the original particles. This is particularly true when modeling snow cover (Section 4.6.1), in which case the scattering centers are in contact with one another and their exact number is therefore ambiguous. Grenfell and Warren (1999) show that the "equivalent volume-to-surface-area sphere" approach works very well for simulating the scattering properties of randomly oriented, long, circular cylinders, throughout both the shortwave and longwave. Further research will clarify the utility of this approach for other non-spherical geometries. If an equivalent sphere approach can be adopted, radiative transfer computations for remote-sensing retrievals can be greatly accelerated on a given computer processor.

Finally, Dr. Jeffrey Key (head of NOAA's Polar Satellite Meteorology Project based at the University of Wisconsin's Space Science and Engineering Center) has developed two useful research tools that give a researcher a substantial headstart with polar cloud and radiation retrieval from satellite data: the *Streamer* and *FluxNet* radiative transfer software (Key and Schweiger, 1998), and a comprehensive software package called *Cloud and Surface Parameter Retrieval* (CASPR; Key, 1999).

4.5.1 Cloud phase discrimination

Key and Intrieri (2000) showed how the thermodynamic phase of Arctic clouds can be defensibly classified in AVHRR data. To understand this procedure, one must first recognize how AVHRR channel 3 is used differently during the polar winter versus summer. In the sunlit part of the year, there is large solar backscatter from clouds (exploited above for cloud detection and classification). During the Arctic night, AVHRR channel 3 will only measure the thermal emission component from clouds, and will record values of a similar magnitude as channels 4 and 5 but with a much lower *SNR* (recall the discussion in Section 2.5 about dynamic range; the dynamic range of AVHRR channel 3 has been optimized to encompass solar backscatter at low latitudes).

From thermal radiative transfer calculations, Key and Intrieri (2000) estimate the brightness temperature differences ΔT_{34} and ΔT_{45} for liquid water versus ice clouds, as a function of cloud optical depth (Figure 4.27). From this figure, it is evident that phase discrimination should be possible if the ice clouds are composed of particles substantially larger than those of liquid water clouds. Over most of the globe this situation prevails. For most terrestrial liquid water clouds, $4 < r_e < 12\,\mu\text{m}$.

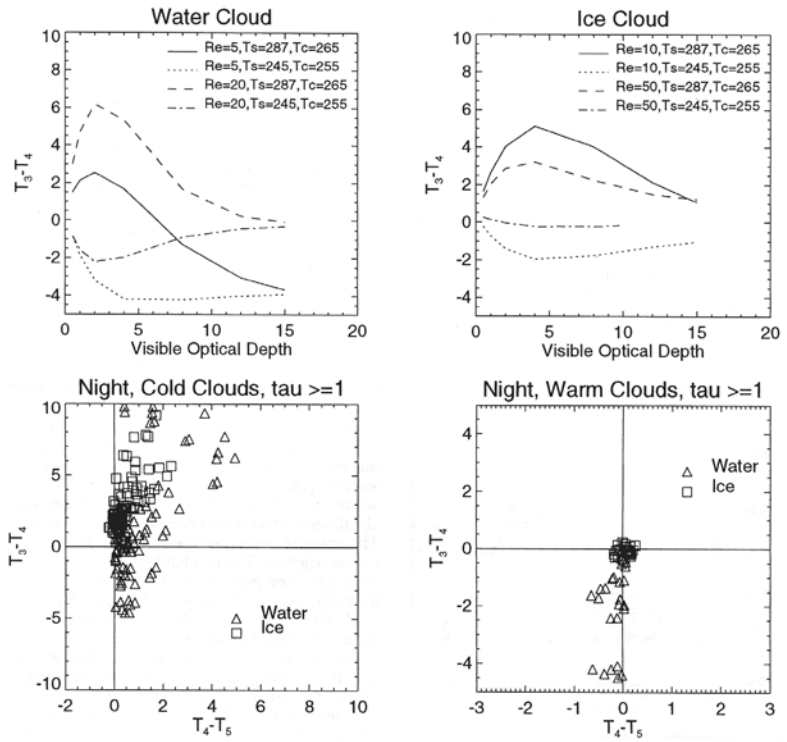

Figure 4.27. Radiative transfer simulations of the brightness temperature difference between AVHRR channels 3 and 4. The top panels show how this brightness temperature difference $T_3 - T_4$ varies with shortwave cloud optical depth, for liquid water and ice clouds. The bottom panels show how $T_3 - T_4$ varies with the brightness temperature difference $T_4 - T_5$, for various ice and liquid water clouds with shortwave optical depth greater than unity.
From Key and Intrieri (2000).

For most terrestrial ice crystal clouds, $20 < r_e < 200\,\mu\text{m}$, although r_e is usually in the lower part of this range in the polar regions. Calculations of the type—shown in Figure 4.26—led Key and Intrieri (2000) to a series of decision rules for cloud phase during the polar night, for various measured values of ΔT_{34} and ΔT_{45}. During the sunlit part of the year, differences in the channel-3 solar backscatter component between liquid water and ice clouds are quite pronounced, due to differences in the single scattering albedo (Figure 4.28). Defining channel-3 reflectance as in (4.14), Key and Intrieri (2000) show that r_3 is a strong function of the scattering angle Θ:

$$\Theta = 180 - \cos^{-1}(\cos\theta_0 \cos\theta + \sin\theta_0 \sin\theta \cos\phi) \tag{4.24}$$

as in Figure 4.27. From this relationship, a parameterization of the form:

$$\zeta = \exp\left(a + \frac{b}{\Theta^2}\right) + c \tag{4.25}$$

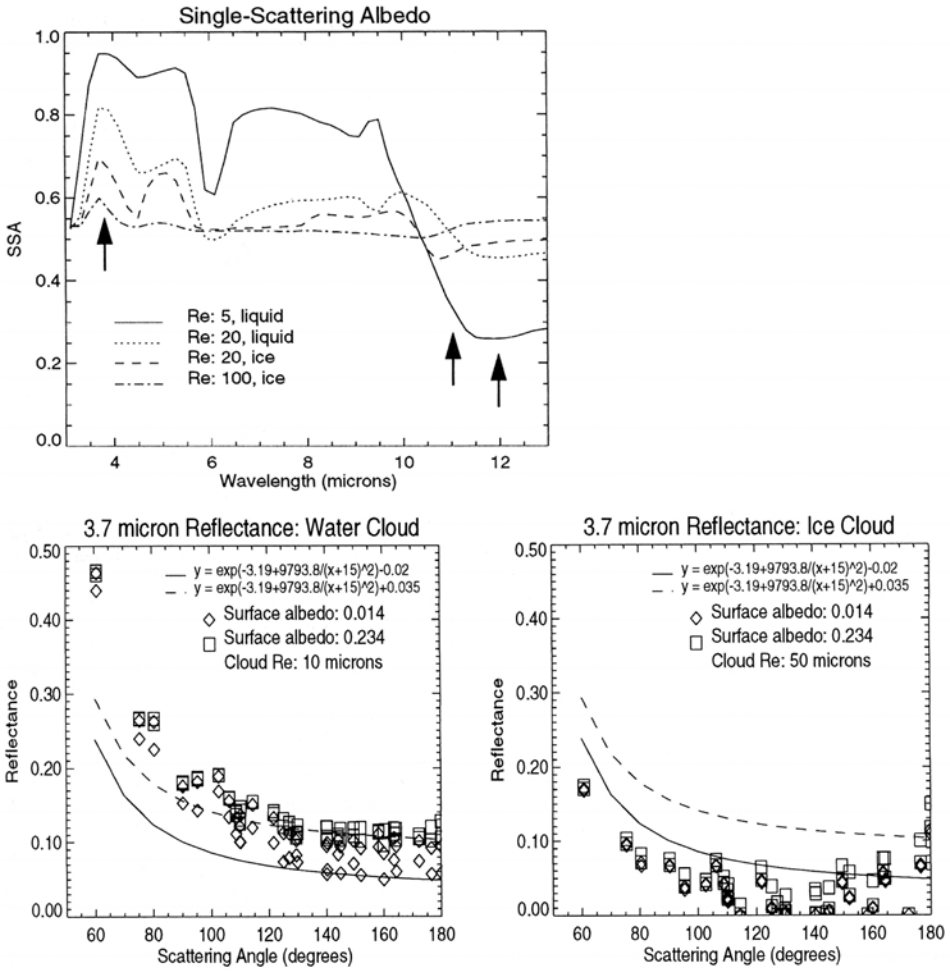

Figure 4.28. The single scattering albedo for several liquid and ice water clouds (top panel), and an illustration of how the single scattering albedo governs the AVHRR channel 3 (3.7 μm) cloud reflectance as a function of scattering angle.

From Key and Intrieri (2000).

can be used to specify thresholds ζ for the upper limit in ice cloud reflectance r_3 over various surface types. Constants a–c in (4.25) are given in Figure 4.27. For large Θ, and for optically thin clouds over snow, channel-3 solar backscatter does not provide useful discrimination between liquid water and ice clouds, but thresholds defined by (4.25) should be valid for $\Theta < 150^\circ$.

The first step in the Key and Intieri (2000) phase discrimination algorithm is to classify as many pixels as possible according to channel-4 brightness temperature thresholds, as depicted in Table 4.4. This requires an assumption that a threshold value γ_{min} exists in nature below which all clouds are likely to be entirely ice. A value

Table 4.4. Relationships between surface temperature T_S and AVHRR channel-4 brightness temperature T_4 used for initial cloud phase discrimination by Key and Intrieri (2000).

Condition	Phase
$T_S - \delta < \gamma_{max}$ and $T_4 > \gamma_{max}$	Liquid
$T_S - \delta < \gamma_{max}$ and $T_4 > T_S$	Liquid
$T_S - \delta < \gamma_{min}$ and $T_4 < \gamma_{min}$	Ice
$T_S - \delta < \gamma_{min}$ and $T_4 < T_S$	Ice

$\gamma_{min} = 243.16\,\mathrm{K}$ ($-30^{\circ}\mathrm{C}$) is consistent with current understanding of cloud physics and recent fieldwork, but for very clean (low aerosol) and cold environments liquid water might exist in environments as cold as $-40^{\circ}\mathrm{C}$. An upper threshold for all liquid water clouds of $\gamma_{max} = 273.16\,\mathrm{K}$ is probably sound, but might also deserve some scrutiny in cases of rapidly moving airmasses. This step requires an estimate of the surface temperature, which might come from clear-sky pixels within the satellite dataset, or from meteorological reanalysis. If clear-sky satellite data are used, then the small correction δ ($\sim 2\,\mathrm{K}$) is needed to account for the surface temperature being slightly colder under cloud cover during the day and slightly warmer under cloud during the polar night.

The second step is to classify pixels not treated by the previous step using the radiative transfer theory depicted in Figures 4.26 and 4.27. At night, if $\Delta T_{34} < -0.5\,\mathrm{K}$ the pixel is classified as liquid water cloud; if $\Delta T_{34} > +1\,\mathrm{K}$ and $0 < \Delta T_{45} < 1\,\mathrm{K}$ the pixel is classified as optically thick ice cloud. During the day, the threshold functions of (4.25) are used on pixels for which $\Theta < 150^{\circ}$ and $\Delta T_{45} < 1\,\mathrm{K}$. The latter precaution is necessary to avoid optically thin clouds, for which phase discrimination is ambiguous. For surface types not treated explicitly by Key and Intrieri, one could interpolate between their snow and vegetation functions (4.25) as suggested by the authors, although it might be better to generate a specific functional form analagous to Figure 4.27 for the specific scene type and meteorological conditions being studied. The final step is to classify pixels not treated by either of the above steps, by applying a single channel-4 brightness temperature threshold of $258.16\,\mathrm{K}$ ($-15^{\circ}\mathrm{C}$), below which the pixel is classified as ice cloud and above which the pixel is classified as liquid–water cloud.

This algorithm was validated against data from a unique lidar instrument deployed with the Surface HEat Budget of the Arctic (SHEBA) experiment (Perovich et al., 1999; Uttal et al., 2002). This instrument, the Depolarization And Backscatter Unattended Lidar (DABUL), transmits 523-nm laser pulses upward. Its receiver measures the resulting backscatter from the atmosphere, the strength and timing of which indicates the height of cloud cover, and often its geometrical thickness. The receiver also measures the polarization of the backscattered light, which provides information about cloud phase. Liquid–water droplets, mainly spherical in shape, do not change the polarization of the incident laser light. The presence of ice crystals, in contrast, introduces internal reflections to the scattering physics such that the polarization of the incident laser light is rotated at random, and

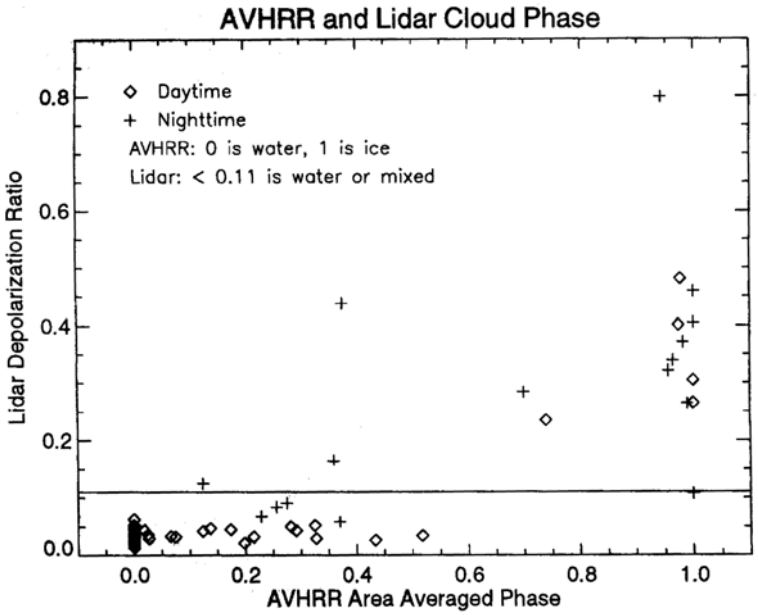

Figure 4.29. Validation of the cloud particle phase estimated from AVHRR data by the depolarization lidar system deployed at SHEBA. A lidar depolarization ratio of 0.11 or less signifies liquid water or mixed phase clouds. The area-averaged phase from the AVHRR data is expressed as zero for entirely liquid water and one for entirely ice.
From Key and Intrieri (2000).

the backscattered beam is depolarized. Thus, with collocated satellite and DABUL data, we have two independent measures of cloud phase. Figure 4.29 shows how the AVHRR algorithm performed against the lidar depolarization ratio (the ratio of backscattered laser beam intensities polarized in the perpendicular and parallel directions) for the highest cloud layer detected by the DABUL system. A depolarization ratio smaller than 0.11 indicates liquid water. The comparison is mostly favorable, with all clouds identified in AVHRR data as entirely liquid water and entirely ice correlated with consistent values of the lidar depolarization ratio. Intermediate values of area-averaged cloud phase from AVHRR also show some encouraging consistency.

This AVHRR cloud phase discrimination algorithm demonstrates that radiative transfer principles can be successfully applied to this task. Even more successful algorithms should be possible when designed for more capable sensors, such as MODIS and VIRSS. There are two cautions, however, with this type of algorithm. First, there is the general caution about using arbitrary thresholds. This can be addressed by customizing an algorithm to a given time and meteorological condition using specific radiative transfer calculations. Second, there is the actual dynamic range of AVHRR channel 3 or similar sensors. The nighttime component of the Key and Intrieri (2000) algorithm should be sound over much

of the Arctic, but over the much colder nighttime Antarctic continent AVHRR channel 3 does not yield a useful *SNR*. Key and Intrieri allude to this limitation by suggesting that any cloudy pixels showing channel-4 brightness temperatures less than 230 K be automatically labeled as ice cloud.

4.5.2 Cloud optical depth and effective radius

The principles for estimating simultaneously the cloud optical depth and effective radius using multispectral satellite imagery over mid-latitudes have been well-established (see, e.g., Han et al., 1994; King, 1987; Nakajima and King, 1990; Nakajima et al., 1991). For a conservative scattering wavelength, $\lambda < 1\,\mu m$, the backscattered intensity is primarily a function of cloud optical depth as given by (4.21). For longer wavelengths in the near-IR, the backscattered intensity begins to show strong dependence on effective radius. These properties, again related ultimately to the spectral dependence of the imaginary index of refraction for either liquid water or ice, have been used on a near-global basis at lower latitudes (e.g., Han et al., 1994). They apply directly to the polar regions if the surface albedo is low—for example, over open ocean or tundra. Figure 4.30 illustrates how AVHRR channels 1 and 3 can be used to estimate cloud optical depth and effective radius, respectively, over tundra. Over tundra, the broadband surface albedo is approximately 0.2, as suggested by Han et al. (1999). Assuming that AVHRR channel 1 has a suitable vicarious radiometric correction applied (Section 2.7), useful estimates of both quantities can be obtained from this pair of intensity measurements.

Note, however, that there is no straightforward set of parameterizations or lookup tables for performing these retrievals. The researcher must customize a radiative transfer model to simulate the expected intensities for the specific meteorological conditions, wavelengths, and viewing geometry. For liquid water clouds, this is simplified by a Mie scattering parameterization developed by Hu and Stamnes (1993), in which the volume extinction coefficient β_{ext}, single scattering albedo, and asymmetry factor are shown to have the functional forms:

$$\frac{\beta_{ext}}{LWC} = a_1 r_e^{b_1} + c_1 \tag{4.26}$$

$$1 - \varpi = a_2 r_e^{b_2} + c_2 \tag{4.27}$$

$$g = a_3 r_e^{b_3} + c_3 \tag{4.28}$$

and the cloud optical depth is:

$$\tau = \int_{z_1}^{z_2} \beta_{ext}(z)\, dz \tag{4.29}$$

Hu and Stamnes (1993) give a table of wavelength-dependent coefficients a_i–c_i that can replace lengthy Mie scattering computations, and their parameterization is representative of most droplet size distributions in terrestrial liquid water clouds.

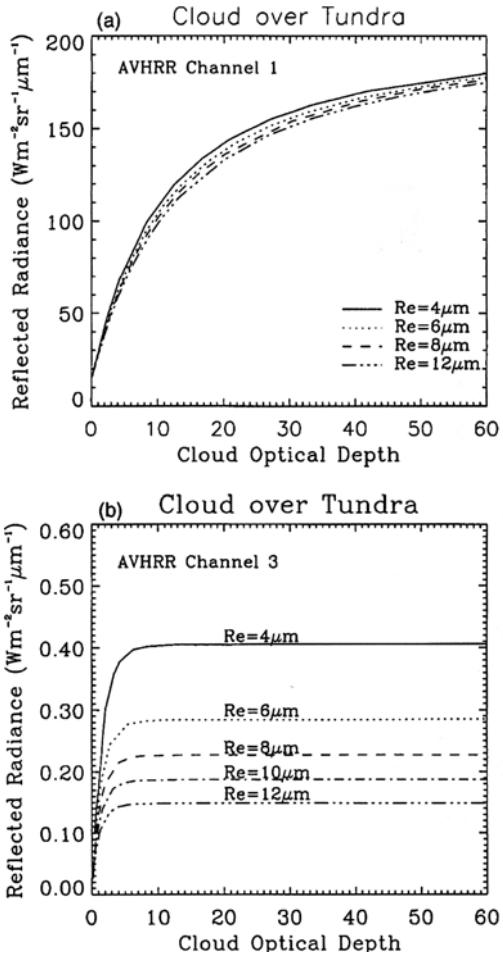

Figure 4.30. Discrete-ordinate-method radiative transfer simulation of reflected intensity from a cloud top for (a) AVHRR channel 1, and (B) AVHRR channel 3, for several values of effective droplet radius r_e, as a function of cloud optical depth. The Lambertian surface albedo is 0.1. The solar zenith, nadir-viewing, and relative azimuth angles are 60°, 10°, and 50°, respectively.

From Han et al. (1999).

When calculating intensities in the AVHRR channel-3 spectral interval, the thermal emission component must be included. This is demonstrated in Figure 4.31, which shows how the satellite-measured intensity evolves when one adds the thermal emission from the ground and cloud separately, and then together. For cloud optical depths smaller than 10, the surface thermal emission is noticeable through the cloud. Note that the AVHRR channel-3 reflectance function shown in Figure 4.30 does not include the thermal component.

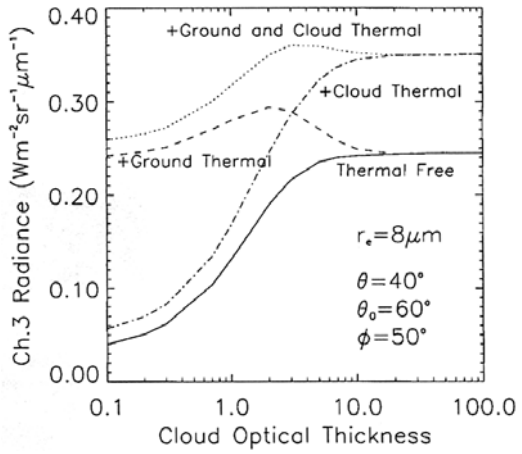

Figure 4.31. Simulated AVHRR channel-3 intensities as a function of cloud optical depth, showing the components (1) with no thermal radiation (backscattered solar only), (2) with only thermal radiation from the ground added to the solar backscatter, (3) with only thermal radiation from the cloud added to the solar backscatter, and (4) with both ground and cloud thermal radiation added to the solar backscatter. The surface temperature is 288.2 K, the cloud top temperature is 275.2 K, and the surface albedo is zero.
From Han et al. (1999).

To estimate the thermal component in AVHRR channel 3, one often uses the channel-4 brightness temperature, as in (4.14). This is not always straightforward, as shown in Figure 4.32. This figure illustrates how the measured brightness temperature can be quite different from the physical cloud temperature, in cases of small cloud optical depth and effective radius, with a large temperature difference between cloud and surface. Therefore, before beginning a lengthy set of cloud optical property retrievals, one needs to perform a series of radiative transfer sensitivity studies to fully understand the applicability of the retrieval method to the scenes being studied.

Over sea ice, matters become more complicated. In the wavelength range of AVHRR channel 1, the albedo of most snow and ice surfaces is at a maximum (see Section 4.6). Over most well-developed sea ice coverage, and over snow surfaces, the high albedo renders the backscattered solar intensity insensitive to the optical depth of overlying cloud cover. One solution to this problem is to use the slightly longer wavelength range of AVHRR channel 2, in which many high-latitude surface albedos begin to decrease. Figure 4.33 illustrates how AVHRR channels 2 and 3 can be used to simultaneously retrieve cloud optical depth and effective radius. Care must be taken over the highest surface albedos, however. As shown in Figure 4.32, the variability in AVHRR channel-2 backscattered intensity over a high-albedo surface, as a function of cloud optical depth, may only be of order 10–15% over the range of cloud optical depths found in nature. If there is a substantial radiometric calibration uncertainty (often the case with AVHRR), the

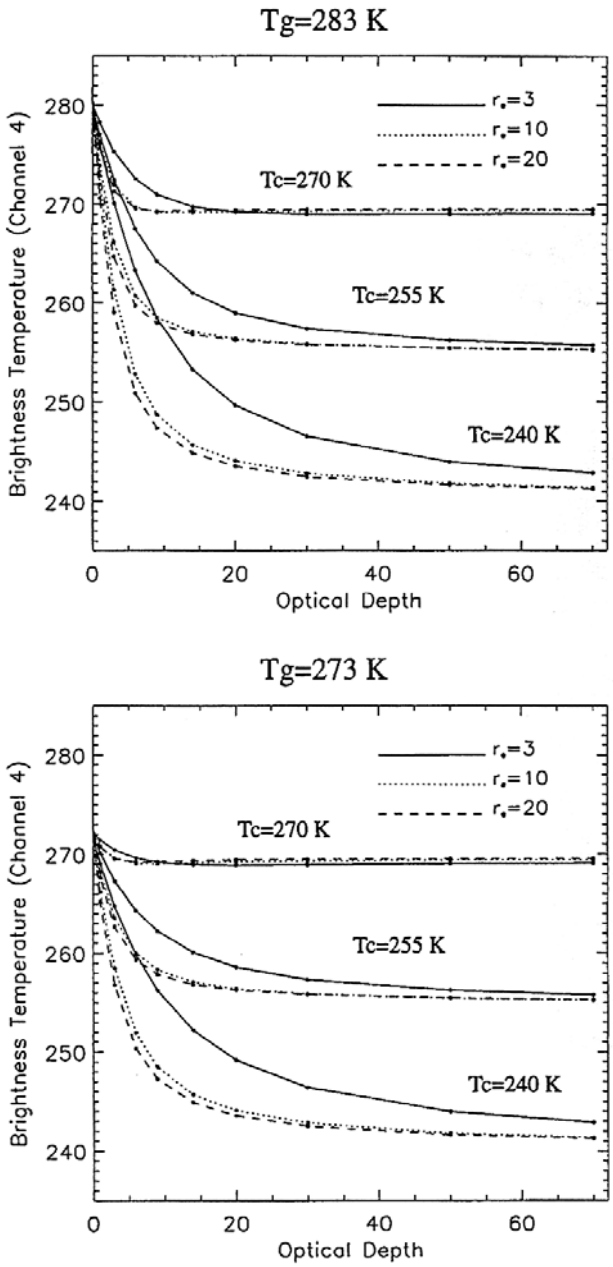

Figure 4.32. Simulated brightness temperature in AVHRR channel 4 above a cloud top, for several values of cloud temperature T_c and effective radius r_e, as a function of shortwave cloud optical depth. The surface temperatures T_g are 283 K and 273 K in the upper and lower panels, respectively.

From Han et al. (1999).

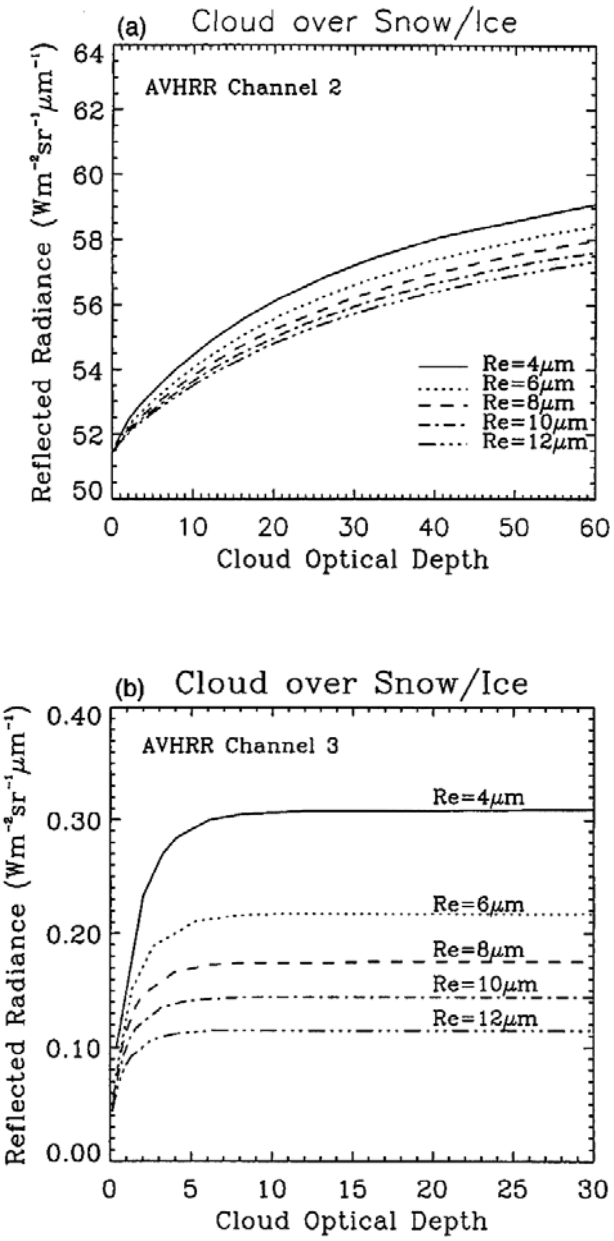

Figure 4.33. Simulated AVHRR channel-2 (a) and channel-3 (b) intensity over a cloud top, for several values of effective radius r_e, as a function of shortwave cloud optical depth. The surface is modeled as snowpack with effective grain size 100 mm, yielding a visible wavelength albedo of 0.95. The solar zenith, nadir-viewing, and relative azimuth angles are 70°, 10°, and 50°, respectively.

From Han et al. (1999).

value of retrieved cloud optical depths may be more qualitative than quantitative. Xiong et al. (2002a) compared Arctic AVHRR retrievals with those from collocated aircraft-borne MODIS Airborne Simulator (MAS) data (the latter having NIST-traceable radiometric calibration for each flight), and showed that AVHRR-based retrievals of effective radius were more reliable than those for cloud optical depth. This is most likely related to the use of channel 3 for effective radius, which has onboard radiometric calibration from a blackbody source.

One additional fundamental aspect of cloud property retrieval at high latitudes concerns representation of the surface *BRDF* (Bidirectional Reflectance Distribution Function). Over a low-reflectance surface such as the ocean at small nadir and solar zenith angles, the surface can often be acceptably modeled as Lambertian. Over high-latitude scenes, where both the surface albedos and solar/viewing angles are usually larger, a Lambertian surface will introduce noticeable errors for smaller cloud optical depths. Often the intensity solution as a function of cloud optical depth will not even be single-valued, as in Figure 4.34. This is an important consideration at high latitudes, because with the lower liquid water contents often

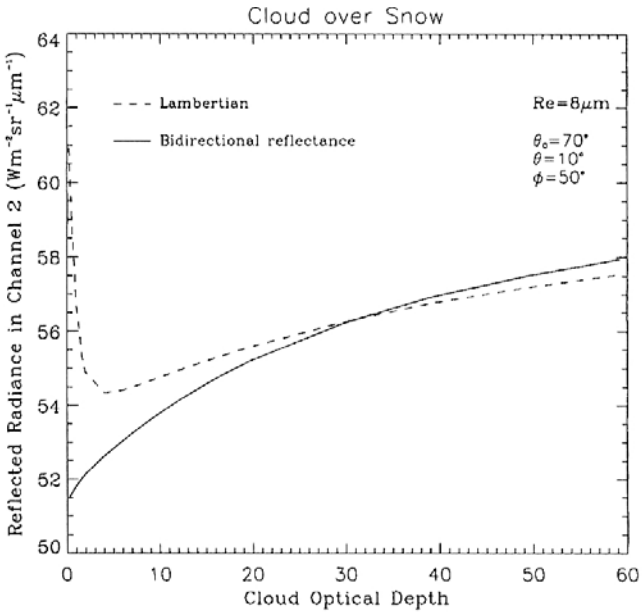

Figure 4.34. Simulation of the AVHRR channel-2 intensity over a cloud top, for the viewing geometry of Figure 4.32, and a cloud effective droplet radius of 8 μm. The snow-effective grain size is 100 μm, which yields an average albedo of 0.87 in the AVHRR channel-2 spectral interval. The solid curve shows the intensity as a function of cloud optical depth when the snow surface is modeled with an appropriate BRDF. The dashed curve shows the corresponding intensity when a Lambertian approximation is used instead of a realistic BRDF. Note that in the Lambertian case, the intensity as a function of cloud optical depth is not single-valued. From Han et al. (1999).

expected in colder atmospheres, one must expect that the real cloud optical depth may often be less than 10. In the radiative transfer model for cloud property retrieval, the snow or ice surface must be treated more rigorously than a simple Lambertian approximation. A realistic representation of the surface *BRDF* must be included. For snow, Han et al. (1999) treated the snow surface as an optically thick scattering layer at the bottom of the model atmosphere, in a discrete ordinates model. This approach for snow has a rigorous physical basis (e.g., Warren and Wiscombe, 1980). For bare ice, where an aggregate of individual scattering centers are not a true representation of the way incident light is redirected upward from the surface, an atmospheric radiative transfer model based on a method such as discrete ordinates must be able to incorporate a realistic surface BRDF specified from measurements or offline calculations from ice-specific radiative transfer or ray-tracing calculations.

4.5.3 Uncertainties

In remote-sensing science, there regularly emerges a consensus that a given type of satellite retrieval is possible. Nevertheless, critical sensitivity studies are needed to reveal the strengths and limitations of the accepted retrieval techniques. Satellite remote sensing depends strongly upon radiative transfer modeling of the Earth–ocean–atmosphere system, but nature will always offer more complexities than a given radiative transfer formulation can fully simulate. Hence there will always be uncertainties related to the physical approximations used in the retrieval technique. Critical examinations of these uncertainties sometimes reveal that a given remote-sensing technique is not so robust as previously believed. However, in the long run such analyses lead to improvements and strengthen the science rather than detract from it.

At present there is a consensus that standard remote sensors such as AVHRR can be used over the Arctic to retrieve the radiative properties of liquid water clouds relevant to GCM simulations—optical depth and effective radius—with an accuracy suitable for large-scale radiation budget studies (e.g., Key et al., 1997). The basic concepts for simultaneous retrieval of τ and r_e described by Nakajima and King (1990) should be applicable to the Arctic provided that a long enough wavelength can be used for retrieving τ such that the surface albedo is low enough to allow measurable backscattered intensity variation as a function of τ (e.g., Han et al., 1999; Platnick et al., 2001). Xiong et al. (2002b) examined the validity of these concepts with a set of sensitivity studies to account for (1) radiometric calibration uncertainty, (2) vertical inhomogeneity in cloud microphysical properties, and (3) partial cloud cover.

For radiometric calibration uncertainty, it is straightforward to examine the expected intensities in AVHRR channels 2 and 3, as functions of τ and r_e, respectively, and estimate how these retrievals would change if the measured intensity is subject to a given uncertainty. An example is given in Figure 4.35. Here we see that if both measured intensities are decreased by 10%, then an actual value of $r_e = 8\,\mu\text{m}$ would be retrieved as $r_e = 9\,\mu\text{m}$, and actual cloud

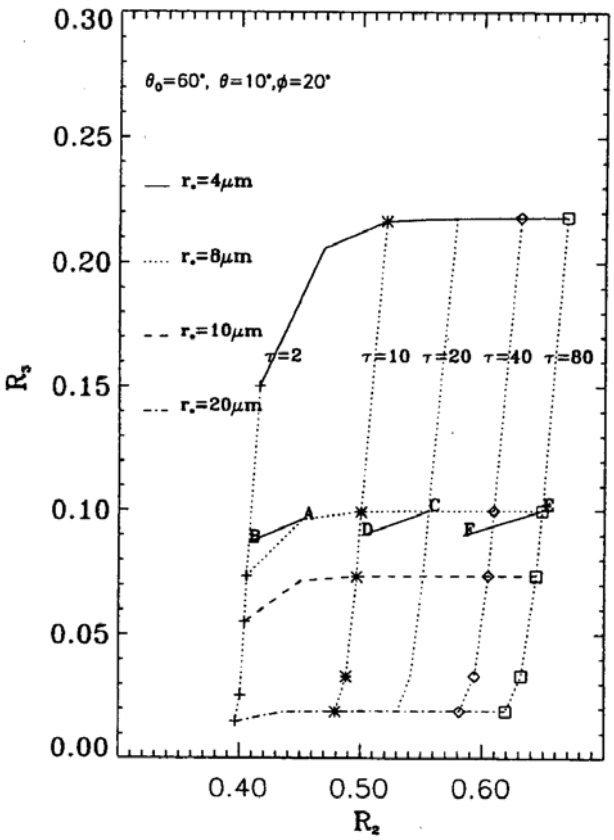

Figure 4.35. Radiative transfer simulation showing the variation of the AVHRR channel-3 reflectance as a function of channel-2 reflectance, for several shortwave cloud optical depths (τ) and effective droplet radii (r_e). The solar zenith, nadir-viewing, and relative azimuth angles are 60°, 10°, and 20°, respectively, over a model snowpack with an effective grain size of 1,000 μm. For a 10% decrease in the reflectance for both channels, points A, C, and E change to points B, D, and F, respectively.

From Xiong et al. (2002).

optical depth values of 5, 20, and 80, would be retrieved as 2.2, 10.3, and 32, respectively. Hence the error in retrieved r_e is of order 10%, while the error in retrieved τ_c is of order 50–60% for the same measurement uncertainty in channels 2 and 3. In practice, we would expect 10% to be an upper limit to the channel-3 uncertainty, because of this channel's onboard radiometric calibration. However, with only vicarious calibration for channel 2, we should expect calibration uncertainties of 10% or greater. This has implications for the validity and usefulness of high-latitude τ_c retrieval, particularly in older AVHRR data whose channel-2 degradation rates have not been given as much attention as those for NOAA-14 and later spacecraft.

Table 4.5. Error in the retrieval of shortwave cloud optical depth τ and droplet effective radius r_e (μm) when the true cloud amount f is smaller than the value of unity assumed in the single-pixel approximation. The final column is the error in downwelling shortwave flux F_{SW} estimated from cloud optical depth retrieval, for the $\tau = 30$ case.

f	$r_e = 10\,\mu m$	$\tau = 15$	$\tau = 30$	F_{SW} for $\tau = 30$
0.5	15.4 (54%)	8.7 (42%)	12.9 (57%)	5.6 (81%)
0.8	12.1 (21%)	12.4 (17%)	21.7 (28%)	15.5 (48%)
0.9	11.0 (10%)	13.7 (9%)	25.9 (14%)	21.4 (29%)

From Xiong et al. (2002b).

The retrieval uncertainties related to partial cloud cover can be estimated by approximating the measured intensities in channels 2 and 3 as linear functions of the cloud fraction f within a hypothetical pixel:

$$\left.\begin{aligned} r_2 &= r_{2CLD} f + r_{2CLR}(1-f) \\ r_3 &= r_{3CLD} f + r_{3CLR}(1-f) \approx r_{3CLD} f \end{aligned}\right\} \tag{4.30}$$

where r_{CLD} and r_{CLR} are the TOA (Top Of Atmosphere) reflectances for entirely cloudy and entirely clear scenes, respectively. Note that the surface reflectance in the channel-3 wavelength region is small enough that it can be neglected in this type of analysis. By linearly mixing plane-parallel radiative transfer calculations for the cloudy and clear cases according to (4.30), one can estimate how the satellite-measured intensity would decrease for various values of $f < 1$, and the resulting error in τ and r_e. Some examples from Xiong et al. (2002b) are shown in Table 4.5, and these demonstrate that the percentage error in both retrieved τ and r_e are approximately proportional to the percent difference in true subpixel cloud fraction from the single-pixel approximation $f = 1$.

Actual vertical inhomogeneity in cloud cover introduces uncertainties both within a single cloud layer and from undetected multiple cloud layers. Generally speaking, the effective radius r_e of a liquid water stratiform cloud increases with height above the cloud base (e.g., Slingo et al., 1982; Stephens and Platt, 1987), the exception being an optically thin entrainment region at the cloud top (Harrington et al., 1999; Nakajima and King, 1990; Olsson et al., 1998; Tsay et al., 1989). This difference between r_e near the cloud top and cloud base can be as large as a factor of 2. Modeling a cloud layer with a single value of r_e is an obvious source of error. This was considered in the early theoretical development of satellite cloud property retrieval (Nakajima and King, 1990), and the Arctic uncertainty analysis of Xiong et al. (2002b) shows that a two-channel cloud retrieval algorithm may have an error in retrieved τ_c as large as 20% with a vertically homogeneous assumption, while the retrieved r_e will be 10–20% smaller than the r_e at the cloud top.

A frequent multilayer cloud occurrence in the Arctic involves optically very thin cirrus ($t < 1$) overlying a low-level stratiform cloud. The stronger absorption of ice versus liquid water, most importantly in AVHRR channel 3 but also slightly in

channel 2, results in smaller backscattered intensities measured in both channels when the cirrus cloud is present. If the optically thin cirrus cloud is not detected by some other means and is ignored in the retrieval algorithm, the retrieved liquid water cloud r_e will be too large by 35–50%, and the cloud optical depth will be underestimated by up to 70–80%. The additional spectral channels available on MODIS and VIIRS (Visible/Infrared Imager and Radiometer Suite) may offer an independent means for detecting optically thin cirrus so that cloud property retrieval algorithms can be adjusted accordingly.

4.5.4 Comparison with *in situ* and ground-based measurements

When conducting any remote-sensing study of cloud properties, familiarity with *in situ* observations is critical. Sometimes one is fortunate enough to have satellite imagery covering a rigorous field program. More often, field observations are used to develop the regionally specific radiative transfer models suitable for remote-sensing retrieval (e.g., Tsay et al., 1989). At the very least, familiarity with the range of cloud properties, and governing mechanisms, observed in nature will allow determination of whether remote-sensing retrievals are reasonable.

With respect to cloud properties, there is more published field information for the Arctic than for the Antarctic. Detailed investigations of Arctic cloud liquid–water content and droplet size distribution, from aircraft measurements, have been reported by Herman and Curry (1984) and Tsay and Jayaweera (1984). Both of these references give droplet size distributions suitable for radiative transfer modeling. When interpreting these measured size distributions in terms of the effective radius, most r_e are of order 8 μm in clouds with base heights between 500 and 1,000 m. Higher cloud layers tend to have smaller r_e, in the range 4–6 μm. There is also a tendency for r_e to increase with altitude within the cloud in most of these measurements. A detailed compilation of cloud micro-physical properties, which emphasizes the importance of the mixed phase, can be found in Hobbs and Rangno (1998). The persistence of a given phase in Arctic clouds can be surprising. For example, Hobbs and Rangno (1998) found cloud liquid water at temperatures as cold as −31°C, and a general tendency for concentrations of ice particles to increase with increasing temperature across the range −30 to −4.5°C. Another aircraft study emphasizing the importance of the mixed phase has been reported by Pinto (1998). Examples of liquid water droplet distributions are shown in Figure 4.36.

Another aspect of cloud properties as observed in nature involves spatial variability. Figures 4.37 and 4.38 illustrate how clouds that appear morphologically as ideal "plane-parallel" layers, perhaps most suitable for remote-sensing retrieval, can actually exhibit enormous variability in liquid and ice water content over relatively small spatial scales. Measurements of shortwave radiation fluxes at high time resolution under polar stratiform clouds often show large variability on small timescales, indicating large local variability in optical depth (e.g., Lubin et al., 2002a, b). The remote-sensing implications of such natural variability on smaller, subpixel scales may require serious consideration, especially if remotely-sensed cloud properties are used for local process studies.

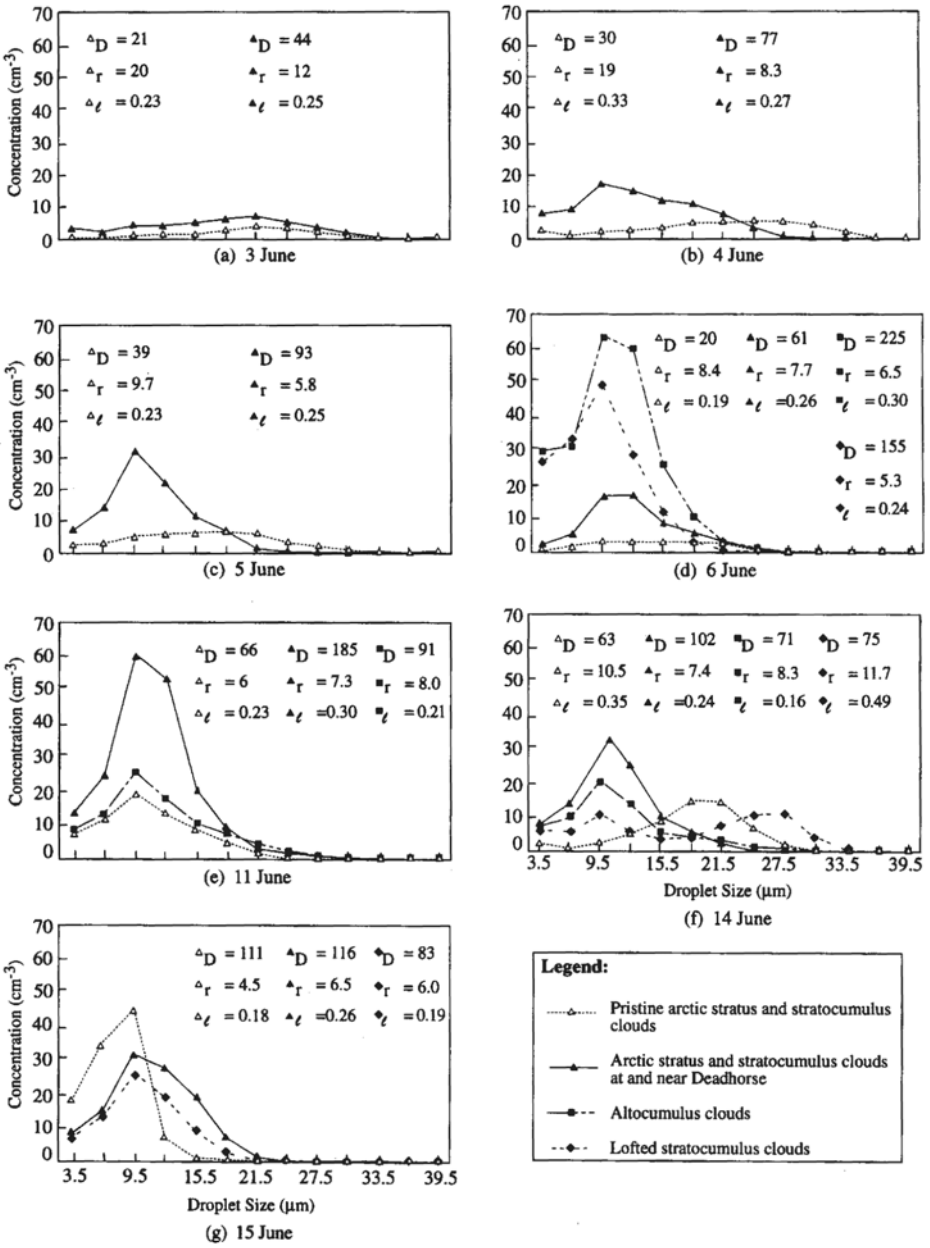

Figure 4.36. Cloud droplet size distribution spectra measured in ice-free or nearly ice-free clouds during seven research aircraft flights over the Beaufort Sea during June 1995. The symbols D, r, and l, denote the average droplet concentration (cm^{-3}), the effective cloud droplet radius (μm), and the liquid water content ($g\,m^{-3}$), respectively, in the various cloud types denoted by the different symbols.

From Hobbs and Rangno (1998). Copyright: Royal Meteorological Society.

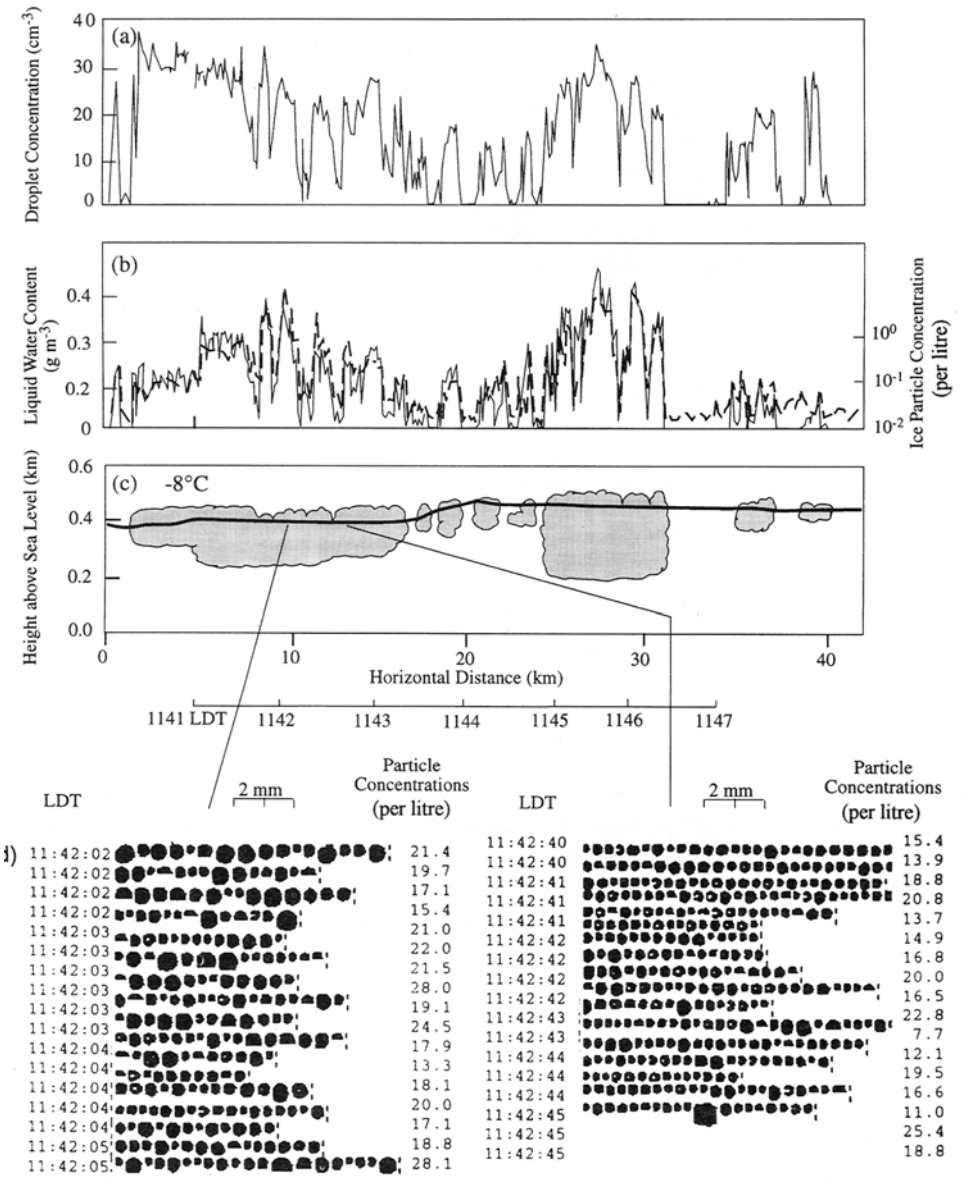

Figure 4.37. Variability in the micro-structure of an Arctic stratocumulus cloud along a 40-km flight track, measured from a research aircraft over the Beaufort Sea on June 3, 1995: (a) droplet concentration, (b) liquid–water content measured by two different probes (no ice particles were observed on this transect), (c) aircraft flight path, (d) short sequences of cloud micro-probe images at high time resolution showing the small-scale variability in cloud droplet size.

From Hobbs and Rangno (1998). Copyright: Royal Meteorological Society.

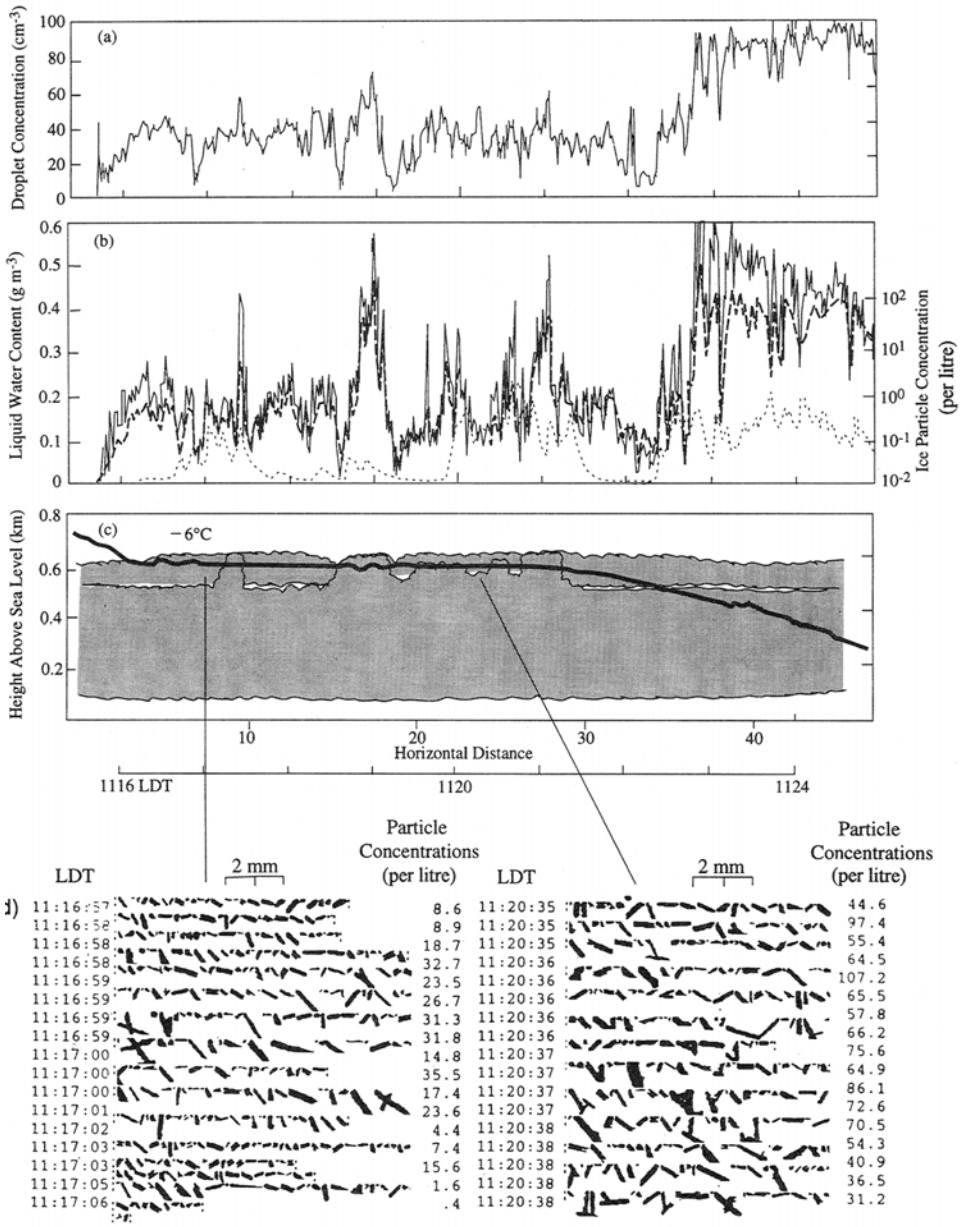

Figure 4.38. As in Figure 4.37, but for a mixed phase cloud. Here, ice–water content is depicted by the dotted curve in (b).

From Hobbs and Rangno (1998). Copyright: Royal Meteorological Society.

At present there is much less published fieldwork available on Antarctic clouds. Morley et al. (1989) deployed an elastic backscatter lidar on a resupply aircraft transiting between McMurdo Station and the South Pole, and the lidar returns show a transition between primarily liquid water clouds over the Ross Ice Shelf to primarily ice clouds over the Antarctic Plateau. Saxena and Ruggiero (1990) took advantage of a rare opportunity to deploy cloud micro-probes on a C-130 research aircraft, and made useful measurements of liquid water cloud micro-physical properties over the Ross Sea during late spring. These measurements revealed liquid water contents ranging from 0.06 to 0.18 $g\,m^{-3}$, and $r_e \sim 9\,\mu m$, for cloud base temperatures in the range -19° to $-5^\circ C$. Lubin (1994) analyzed ground-based FTIR (Fourier Transform InfraRed) measurements from Palmer Station, and showed that most downwelling emission spectra were consistent with liquid water clouds having $r_e \sim 10\,\mu m$. These FTIR data also provided some estimates of mid-IR cloud emissivity for the maritime Antarctic.

Over the Antarctic Plateau, Stone (1993) analyzed wintertime radiometersonde data, and with a radiative transfer model determined that the measured flux divergences were consistent with ice particles having a small $r_e \sim 10\,\mu m$. Mahesh et al. (2001a, b) deployed an FTIR spectro-radiometer at the South Pole for all of 1992. From this unique dataset, cloud base height was retrieved using a ground-based version of the CO_2-slicing technique (Figure 4.39). Using an ice–cloud radiative transfer model, cloud effective particle size (Figure 4.40) and optical

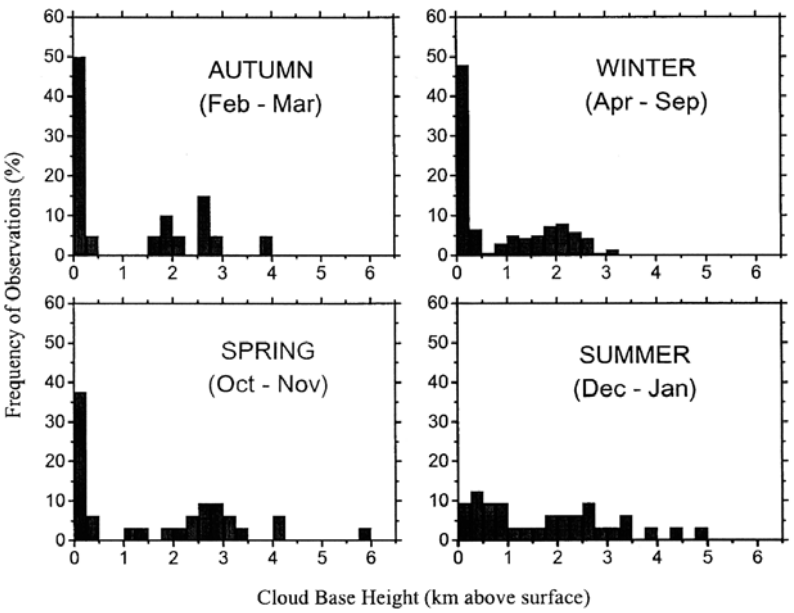

Figure 4.39. Histograms of cloud base heights over the South Pole derived from ground-based FTIR data during 1992.

From Mahesh et al. (2001a).

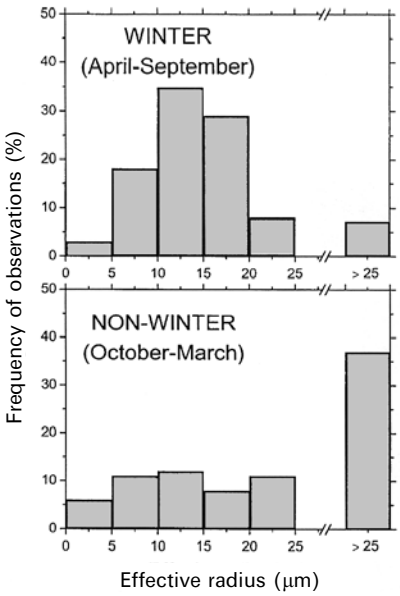

Figure 4.40. Histograms of ice-cloud-particle-effective radius r_e above the South Pole obtained from FTIR data during 1992.
From Mahesh et al. (2001b).

depth (Figure 4.41) were retrieved by exploiting the spectral dependence in ice particle extinction within the mid-IR window. The spectral dependence in extinction, while ultimately based on the refractive index (Figure 4.26), is also a function of both ice water path and effective particle size, and is noticeable for ice water paths smaller than $\sim 40\,\mathrm{g\,m^{-2}}$. The radiative transfer methods discussed by Mahesh et al. (2001a, b) and Lubin (1994) may be applicable to the next generation of space-based mid-IR spectroradiometers such as AIRS, although the space-based measurements will have the added complication of surface temperature and emissivity being part of the signal.

4.6 SURFACE ALBEDO AND TEMPERATURE

The measurement of surface albedo and temperature are fundamental remote-sensing applications for climate study. We have already seen how knowledge of the underlying surface albedo is critical for studies of cloud climatology and cloud properties. To develop useful remote-sensing methods, we require knowledge about the surface scattering and absorbing properties that govern spectral and directional reflectance and emissivity. In general, there is a progression in albedo ranging from (1) low values for open water and tundra to (2) intermediate values for sea ice in various stages of formation to (3) high values for snow and glacial ice surfaces, and high concentrations of sea ice covered by snow to (4) decreasing albedo as melting

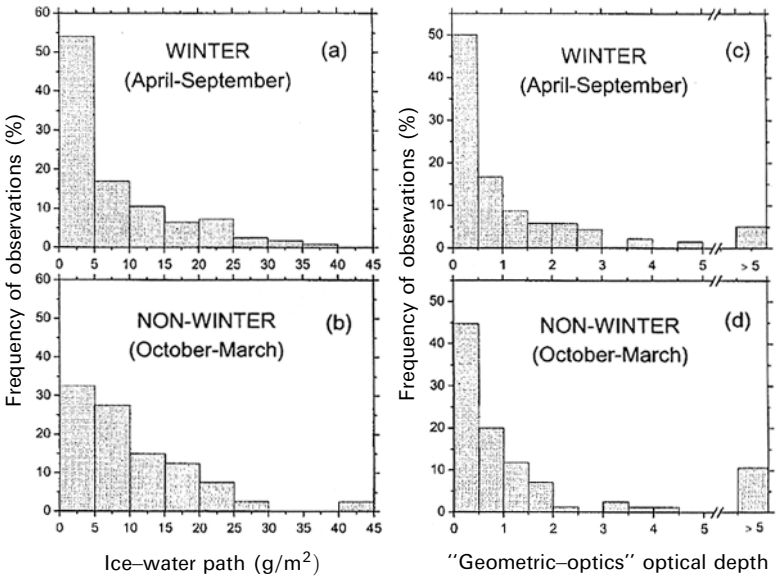

Figure 4.41. Histograms of cloud ice water path and shortwave optical depth derived from FTIR data during 1992.

From Mahesh et al. (2001b).

processes begin on the sea ice surface. There is also considerable spectral dependence in most polar surface albedos, and also considerable contrast between the Arctic and the Antarctic. Our knowledge about ice and snow infrared emissivities has evolved from theoretical studies on shortwave albedo, as well as longer wavelength emissivity for microwave applications.

4.6.1 Field measurements and theoretical studies

The canonical measurements of Arctic surface albedo were made by Grenfell and Perovich (1984). These measurements covered a wide variety of surfaces, including dry snow, melting snow, snow-covered first-year sea ice, bare first-year ice, meltponds, refrozen meltponds, lake ice, and tundra. Figure 4.42 shows some of these measurements that are most widely used in remote-sensing applications. For snow and ice surfaces, albedo remains the highest in the visible portion of the spectrum, only decreasing significantly as the wavelength approaches 1 μm. We have seen how this causes difficulty with many midlatitude remote-sensing techniques for cloud identification and optical property retrieval, and how we must use near-infrared rather than visible wavelength channels for such retrievals.

The albedo of Arctic sea ice often exhibits great complexity on small spatial scales. Figure 4.43 gives an example of surface conditions at the SHEBA Ice Camp during summer. Here the surface contains bare white ice, and significant areas of both dark and light meltponds, all within approximately 1 km. Figure 4.44 shows

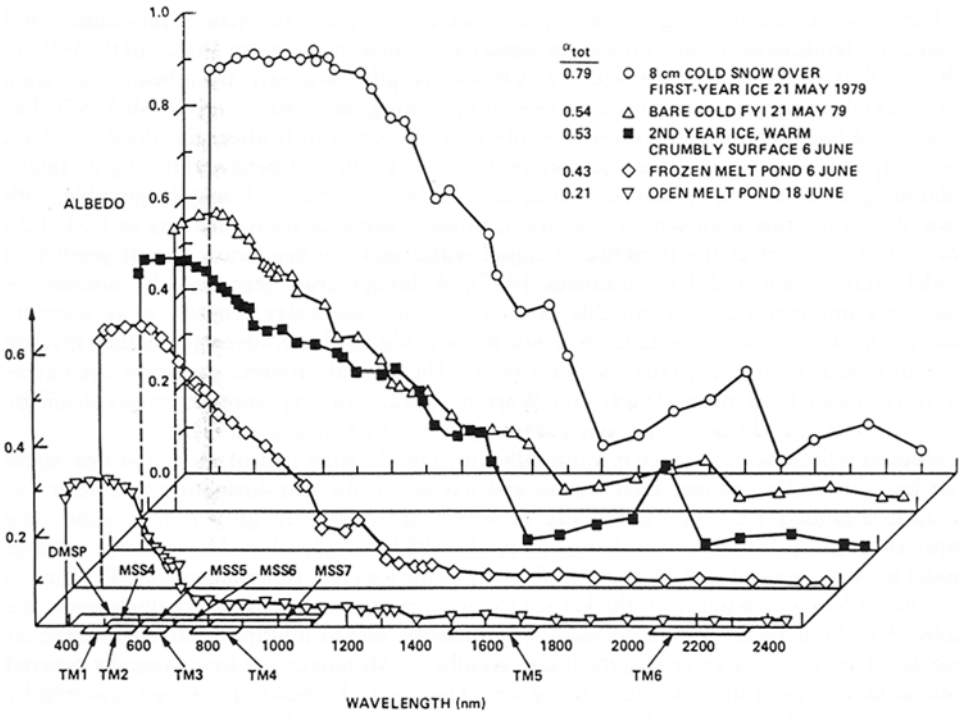

Figure 4.42. Sea ice albedos measured by Dr. Tom Grenfell (University of Washington) near Barrow, Alaska. These values represent samples as no effort has been made to generalize by season or region. Some heritage sensor bands are shown (DMSP OLS, Landsat MSS, and TM).

From Carsey and Zwally (1986), fig. 1, p. 1028. Copyright 1986. With kind permission of Springer Science and Business Media.

how the surface albedo evolved at the SHEBA Ice Camp from late spring to late summer. Figure 4.45 (see color section) gives an example of the evolutionary sequence in spectral surface albedo for first-year ice near Barrow, Alaska. These figures, on the one hand, suggest that satellite remote sensing is able to monitor significant changes in surface albedo over seasonal and interannual timescales, but also illustrate the difficulties due to subpixel-scale variability, on the other hand.

Professor Stephen G. Warren (University of Washington) and his collaborators have made tremendous contributions to our understanding of high-latitude surface radiative processes. Wiscombe and Warren (1980) developed a detailed radiative transfer model to examine the spectral albedo of snow, and demonstrated how many of the spectral signatures in Figures 4.43 and 4.44 arise from fundamental principles of multiple scattering and absorption in ice particles. Warren and Wiscombe (1980) extended this model to consider small concentrations of absorbing impurities in a snowpack, and showed how snow albedo can decrease dramatically with their presence. Dozier and Warren (1982) used a similar

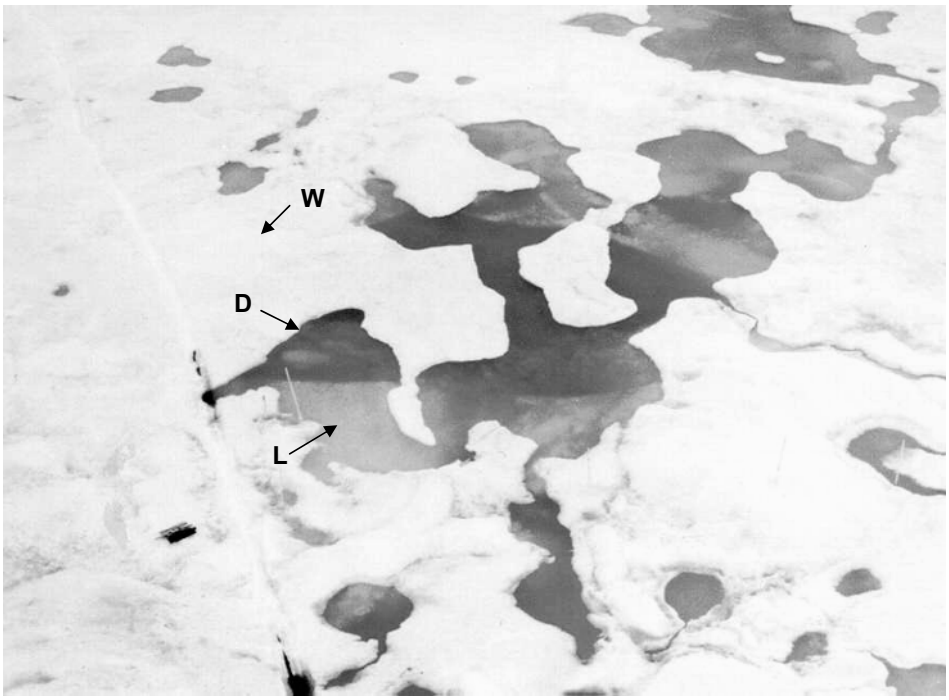

Figure 4.43. Meltponds at SHEBA, July 1998. W points to bare white ice, D a dark pond, and L a light pond. The water depth in the pond was the same for D and L, indicating the importance of the underlying ice on pond albedo.

Courtesy: Dr. Donald K. Perovich, U.S. Army Cold Regions Research and Engineering Laboratory.

radiative transfer formulation to examine the infrared emissivity of snow. Figure 4.46, reproduced from Dozier and Warren's paper, illustrates how the emissivity is markedly different from unity at many wavelengths relevant to climatic processes and remote sensing, and also varies with the nadir-viewing angle. Warren (1982) reviewed the status of the community's understanding of radiative processes in snow, as of the early 1980s. At that time, this knowledge was quite substantial in terms of the basic principles, and included some information about the snow BRDF. These four papers are required reading for anyone seriously interested in remote sensing of the Earth's polar regions.

The Southern Ocean exhibits some important contrasts with the Arctic in sea ice albedo, because the Antarctic is primarily a marginal ice zone. Antarctic sea ice advances and retreats with the seasons, exhibiting a factor of 4 change in total area, and there is very little multiyear ice. At maximum extent, Antarctic sea ice cover is generally much thinner than its Arctic counterpart, typically of order 1m in thickness. Meltponds are a much less prevalent feature on Antarctic sea ice. Spectral albedo measurements for Antarctic sea ice reported by Warren et al. (1997) and Brandt et al. (1999) show the progression in spectral albedo from open water to

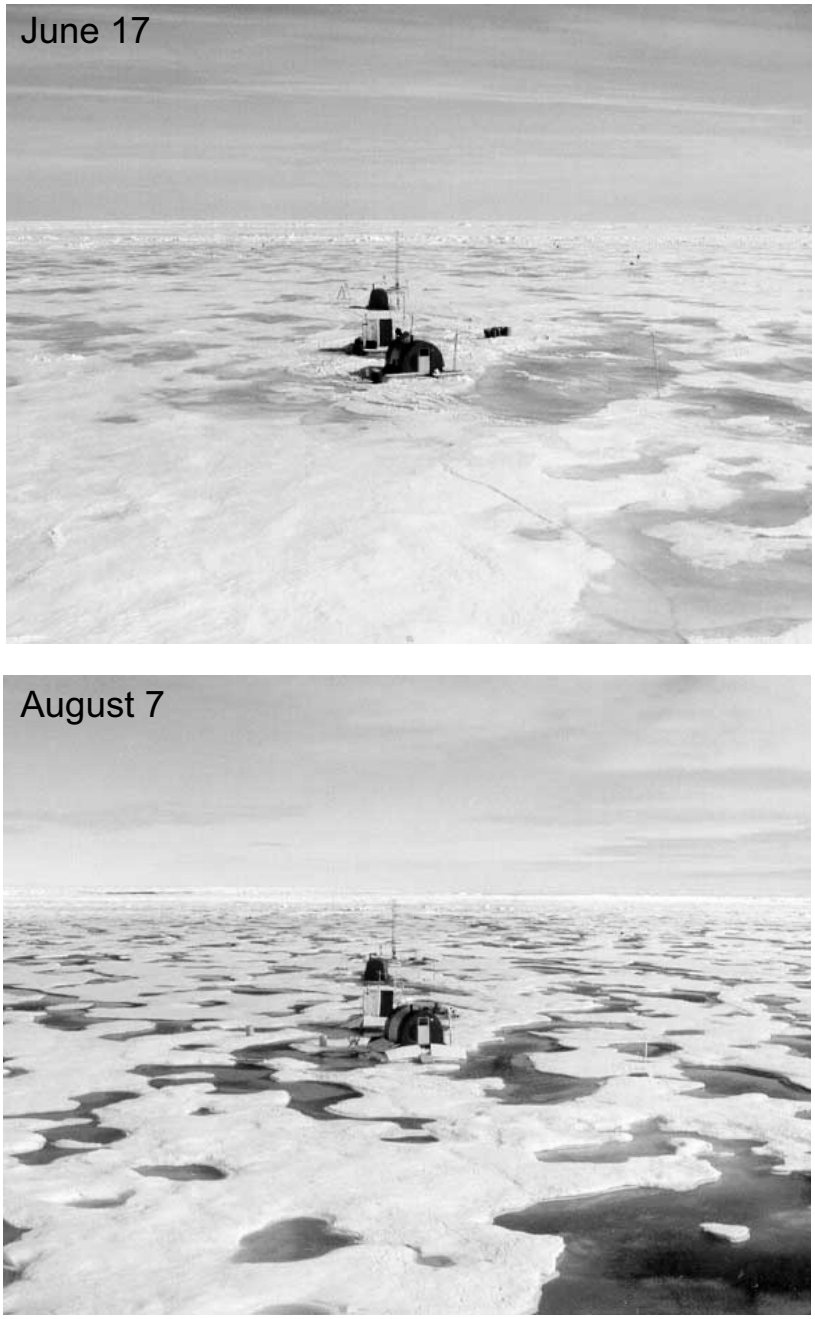

Figure 4.44. Development of meltponds at SHEBA during summer, 1998. Also note how the bare ice looks the same, even though there was 50 cm of surface ablation.

Courtesy: Dr. Donald K. Perovich, U.S. Army Cold Regions Research and Engineering Laboratory.

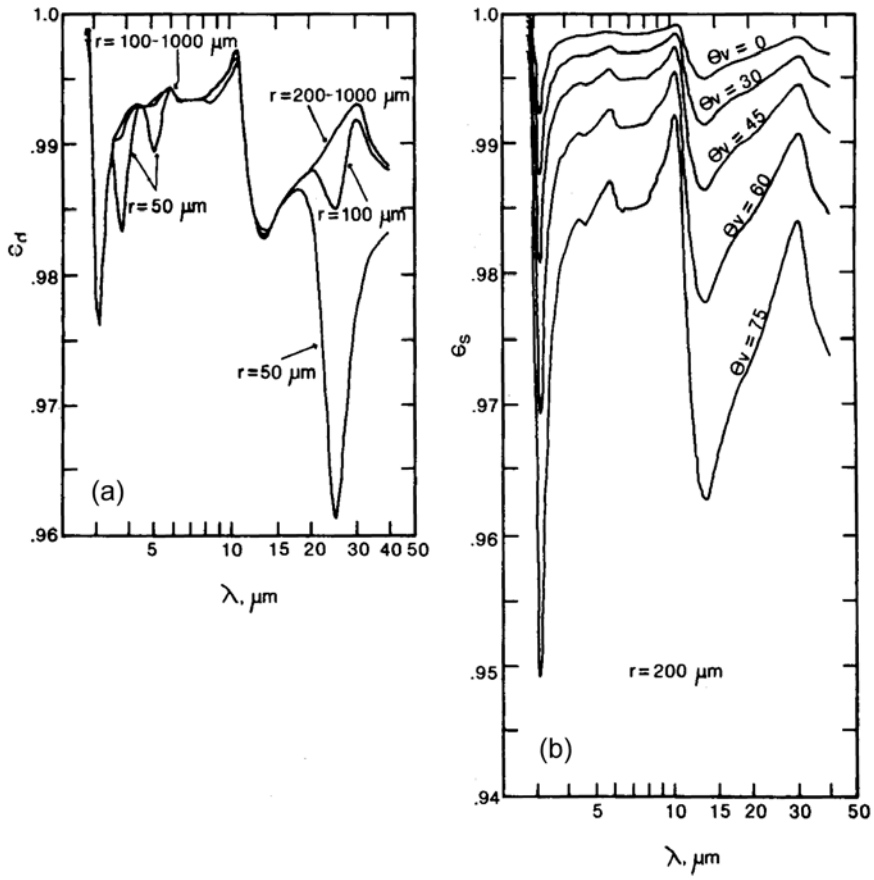

Figure 4.46. Radiative transfer simulations of the spectral emissivity of snow throughout the near- and mid-IR: (a) emissivity averaged over the upward 2π steradians for snow-effective grain sizes r ranging from 50 to 1,000 μm, (b) directional emissivity for snow-effective grain size $r = 200$ μm and nadir-viewing angles between 0 and 75°.

From Dozier and Warren (1982).

nilas (young ice) to a fully developed first-year ice cover with varying types of snow cover. Examples from these measurement programs are shown in Figure 4.47 (see color section).

Over the Antarctic Plateau, the great Antarctic Ice Shelves, and the interior of Greenland, are found the Earth's highest albedos. Grenfell et al. (1994) report measurements on spectral snow surface albedos from South Pole and Vostok stations, an example of which is shown in Figure 4.48. At visible wavelengths, the albedos of such pristine surfaces are very close to unity. In the near-infrared, Grenfell et al. (1994) show that the albedo is sensitive to the effective snow grain size (see Volume 2 of this book). The effective snow grain size is in turn related to the age of the snowpack and the nature of snow precipitation. Larger particles exhibit

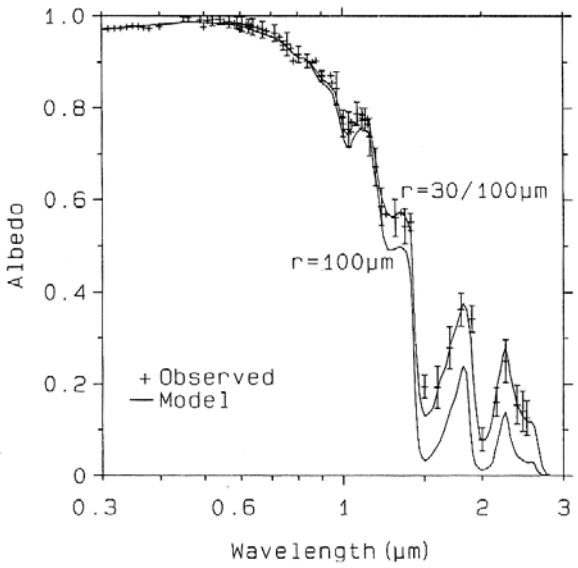

Figure 4.48. The shortwave spectral albedo of continental Antarctic snow, showing observations and radiative transfer simulations for representative grain sizes. $r = 30/100\,\mu m$ refers to a thin layer of smaller grains above larger grains. The Antarctic Plateau and the Greenland Ice Sheet exhibit Earth's highest surface albedos.

From Grenfell et al. (1994). Copyright 1994 American Geophysical Union. Reproduced by permission of American Geophysical Union.

noticeably more absorption, and hence a lower albedo for wavelengths longer than 1 μm. This offers the potential for observing important changes in snow cover from satellite instruments having adequate near-infrared channels. Berque et al. (2004) have shown that AVHRR channel 3 can be used for this purpose during the Antarctic summer, although there are some limitations with the very low snow reflectance beyond 3 μm. With longer time series from instruments such as MODIS, offering channels between 1 and 3 μm, reliable observation of major snow accumulation events may be possible.

Grenfell et al. (1994), Warren (1984b), Warren and Clarke (1990), and Warren and Wiscombe (1980) discuss the impact of impurities on snow albedo. The major albedo reductions occur at visible wavelengths. The relevant consideration in satellite remote sensing involves an awareness of possible sources of widespread snow contamination by soot or other aerosol particles from industrial sources, or from volcanic ash, when interpreting high-latitude surface observations. Light et al. (1998) have shown how particulate impurities also affect the spectral albedo of sea ice. In the case of sea ice, impurities frequently result from natural entrainment of sediments, algal cells, detrital particles, and other organics, as the ice forms over shallow Arctic shelf regions. Figure 4.49, from Light et al. (1998), illustrates how ice albedo can decrease noticeably with even modest concentrations of entrained particulates.

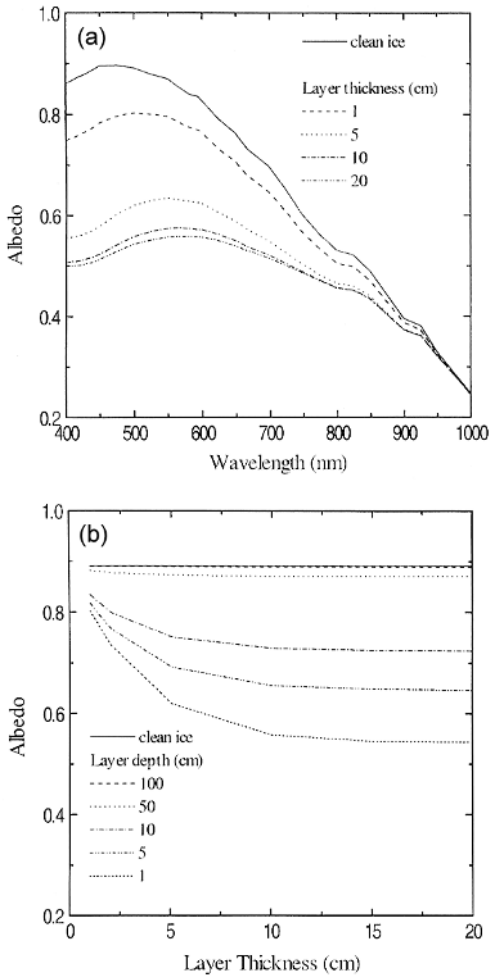

Figure 4.49. The effect of sediment particulates on the albedo of sea ice: (a) spectral albedo for various particle layer thicknesses beginning 1 cm below the ice surface, (b) albedo at 500 nm as a function of particle layer thickness for various depths below the ice surface. In these radiative transfer simulations the particle concentration is fixed at $100\,\mathrm{g\,m^{-3}}$ and the effective particle size is 9 μm.

From Light et al. (1998). Copyright 1998 American Geophysical Union. Reproduced by permission of American Geophysical Union.

4.6.2 Remote sensing of sea ice albedo

Section 2.3.2 discussed the definitions of reflectance and albedo, and from (2.23) to (2.27) one can see how to relate a satellite-measured specific intensity to a hemispheric flux and hence albedo. A method that puts these principles into practice was developed by Lindsay and Rothrock (1994a), who derived the

seasonal cycle in Arctic sea ice albedo from AVHRR data. Their method works upward from the raw detector counts, and is thus an excellent example of a polar remote-sensing application, complete with appropriate qualifications and discussions of uncertainties. The sea surface albedo retrieval method is applied to data that have already been identified as cloud-free. It begins with the linear relationship between detector counts d_i in channel i ($i = 1$ or 2 of AVHRR) and AVHRR narrowband channel-specific intensity I_i, discussed previously in Section 2.7:

$$I_i = \frac{d_i - b_i}{q_i} \tag{4.31}$$

where q_i is the instrument gain (counts per $\mathrm{W\,m^{-2}\,sr^{-1}\,\mu m^{-1}}$) and b_i is the dark offset (in counts). As discussed in Section 2.7, the absolute value of the albedo derived from this specific intensity is subject to the large uncertainties in knowing the post-launch values of the calibration coefficients q_i and b_i. Hence Lindsay and Rothrock (1994a) choose fixed gains q_i such that the mean derived albedos are 0.80 in March and April (for the year 1989) over the brightest (95th-percentile) floes. This fixing of the post-launch gain limits the method to deriving the seasonal cycle in albedo, rather than absolute albedos for studying interannual variability. With more modern sensors such as MODIS, having more reliable monitoring of the radiometric calibration, an application of the Lindsay and Rothrock (1994a) procedures may not have this limitation.

The specific intensity derived from (4.31) is transformed to a narrowband reflectance $r_i(\theta_0, \theta, \phi)$ following the definitions of Section 2.3.2:

$$r_i(\theta_0, \theta, \phi) = \frac{\pi w_i I_i}{F_{0i} \cos\theta_0} \tag{4.32}$$

where F_{0i} is the extraterrestrial solar flux in channel i, and w_i is the equivalent width of channel i, derived from the channel's spectral response function (Kidwell, 1991). From the narrowband reflectance, the TOA narrowband albedo $\alpha_{i,TOA}(\theta_0)$ is computed using the BRDF, $R_i(\theta_0, \theta, \phi)$:

$$\alpha_{i,TOA}(\theta_0) = \frac{1}{\pi} \int_0^{\pi/2} \int_0^{2\pi} R_i(\theta_0, \theta, \phi) \cos\theta \sin\phi \, d\theta \, d\phi \tag{4.33}$$

or, equivalently, the anisotropic reflectance factor $\xi_i(\theta_0, \theta, \phi)$:

$$\xi_i(\theta_0, \theta, \phi) = \frac{R_i(\theta_0, \theta, \phi)}{\alpha_{i,TOA}(\theta_0)} \tag{4.34}$$

For their analysis, Lindsay and Rothrock (1994a) used an empirical anisotropic reflectance factor for sea ice derived from a variety of satellite data by Taylor and Stowe (1984), and adapted this empirical function into a smoothed and parameterized form such that:

$$\alpha_{i,TOA}(\theta_0) = \frac{r_i(\theta_0, \theta, \phi)}{\xi_i(\theta_0, \theta, \phi)} \tag{4.35}$$

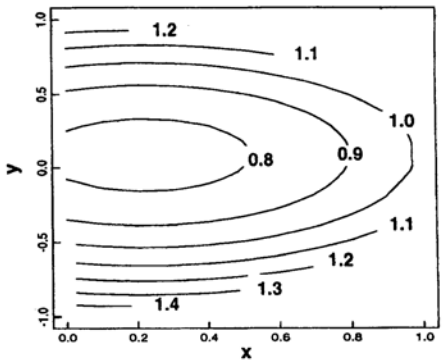

Figure 4.50. Anisotropic reflectance factor $\xi_l(x, y)$ for a snow surface with solar zenith angle 70°, parameterized from the empirical analysis of Taylor and Stowe (1984). The parameterization variables x and y appear in (4.39).

From Lindsay and Rothrock (1994).

which relates a single AVHRR-measured reflectance $r_i(\theta_0, \theta, \phi)$ to an AVHRR-derived albedo $\alpha_{i,TOA}(\theta_0)$, via a parameterized form for $\xi_i(\theta_0, \theta, \phi)$:

$$\left.\begin{aligned} \xi(x, y) &= a_0 + a_1 x + a_2 y + a_3 \mu_0 + a_4 x^2 + a_5 y^2 + a_6 y \mu_0 \\ x &= \sin\theta \cos(\pi/2 - \phi) \\ y &= \sin\theta \sin(\pi/2 - \phi) \\ \mu &= \cos\theta_0 \end{aligned}\right\} \tag{4.36}$$

The coefficients a_i result from weighted least squares regression, and have the values $a_0 = 0.681$, $a_1 = -0.185$, $a_2 = -0.222$, $a_3 = 0.310$, $a_4 = 0.413$, $a_5 = 0.608$, and $a_6 = 0.338$. An excerpt from this parameterized anisotropic reflectance factor f is shown in Figure 4.50. In this method, the function $\xi_i(x, y)$ is assumed to be applicable to both AVHRR channels 1 and 2.

After deriving the TOA narrowband albedo, the atmospheric attenuation by absorption and scattering must be "removed" to yield an estimate of the narrowband surface albedo. In general, this requires detailed radiative transfer calculations to determine how the albedo as observed at TOA differs from the actual surface albedo as a function of solar zenith angle, absorber abundance (e.g., ozone for AVHRR channel 1, water vapor for AVHRR channel 2), Rayleigh scattering, and aerosol extinction. Lindsay and Rothrock (1994a) use a parameterized form of such radiative transfer calculations derived by Koepke (1989):

$$\alpha_i(\theta_0) = \frac{\alpha_{i,TOA}(\theta_0) - c_i(\theta_0)}{d_i(\theta_0)} \tag{4.37}$$

where the coefficients $c_i(\theta_0)$ and $d_i(\theta_0)$ are taken directly from tabulations in Koepke (1989) and given representative values for the Arctic of total column ozone, water vapor, and aerosol burden. Here a typical Arctic aerosol optical depth is taken as 0.2

in the spring and 0.05 in summer, a typical Arctic water vapor column is taken as $0.5\,\mathrm{g\,m^{-2}}$ in spring and fall and $1.0\,\mathrm{g\,m^{-2}}$ in summer, and ozone climatology is adopted following Figure 3.1.

The final step involves an estimation of the broadband shortwave surface albedo from the two AVHRR-channel narrowband albedos using Narrow-To-Broadband Conversion (NTBC) coefficients. The manner in which the narrowband albedos can be combined to yield a broadband albedo depends on the spectral dependence in the surface albedo, the spectral dependence in extraterrestrial solar flux, and details of atmospheric attenuation. Based on a useful compilation of Antarctic sea ice albedo data by Allison et al. (1993), Lindsay and Rothrock (1994a) use an NTBC parameterization:

$$\alpha(\theta_0) = 0.43\alpha_1(\theta_0) + 0.47\alpha_2(\theta_0) \tag{4.38}$$

Xiong et al. (2002c) have reviewed various NTBC coefficients derived for polar regions, including one from the Greenland Ice Sheet reported by Stroeve et al. (1997):

$$\alpha(\theta_0) = 0.041 + 0.655\alpha_1(\theta_0) + 0.216\alpha_2(\theta_0) \tag{4.39}$$

and one by Li and Leighton (1992) for TOA albedo over snow surfaces:

$$\alpha(\theta_0) = 0.0453 + 0.389\alpha_1(\theta_0) + 0.452\alpha_2(\theta_0) \tag{4.40}$$

Xiong et al. (2002c) made further refinements to the NTBC approach, deriving a parameterization for Arctic sea ice based on both SHEBA data and radiative transfer simulations for a snowpack:

$$\left.\begin{aligned} \alpha(\theta_0) &= 0.28(1 + 8.26\gamma)\alpha_1(\theta_0) + 0.63(1 - 3.96\gamma)\alpha_2(\theta_0) + 0.22\gamma - 0.009 \\ \gamma &= \frac{\alpha_1(\theta_0) - \alpha_2(\theta_0)}{\alpha_1(\theta_0) + \alpha_2(\theta_0)} \end{aligned}\right\} \tag{4.41}$$

The factor γ parameterizes the change in spectral albedo as a function of snowmelt and/or the presence of meltponds (Figures 4.42–4.44). No single NTBC parameterization is applicable to the entire Arctic or Antarctic. The NTBC parameterization should be chosen with care for the particular scenes being studied, and modern radiative transfer algorithms often allow these parameterizations to be calculated directly (e.g., Xiong et al., 2002c).

The above steps yield retrieval of an instantaneous surface albedo, which is a strong function of solar zenith angle. To make a large number of such retrievals comparable with one another, they must all be normalized to a common solar zenith angle. Lindsay and Rothrock (1994a) choose $\theta_0 = 70^\circ$, being near the median value of solar zenith angles encountered in their study, to minimize the magnitude of the normalization correction. Normalization is made using:

$$\alpha = \alpha(\theta_0)\left[\frac{h(70^\circ)}{h(\theta_0)}\right] \tag{4.42}$$

where $h(\theta_0)$ is the mean ice surface albedo at solar zenith angle θ_0, as parameterized from Antarctic snow data reported by Liljequist (1956):

$$h(\theta_0) = 0.85 - 0.075 \cos \theta_0 \tag{4.43}$$

Lindsay and Rothrock (1994a) also discuss the effects of local spatial inhomogeneity when analyzing Arctic surface albedos in a climatological sense. Among a large number of satellite retrievals, there can be spatial gradients due to subpixel-scale sea leads, variability in snow accumulation on the sea ice, and variability in tropospheric aerosol. An effort should be made to understand these factors before climatological conclusions are drawn.

4.6.3 Remote sensing of ice surface temperature

Ice surface temperature can be retrieved from mid-IR satellite imagery, and better results are obtained if two or more channels are available so that atmospheric water vapor absorption can be taken into account. Key and Haefliger (1992) developed a practical method for retrieving Arctic ice surface temperature from the AVHRR thermal channels 4 and 5. In order to account for atmospheric water vapor absorption, a surface temperature retrieval algorithm must explicitly include the nadir-viewing angle θ (McClain et al., 1985). Key and Haefliger (1992) use the expression:

$$T_{\text{ice}} = a + bT_4 + cT_5 + d[(T_4 - T_5) \sec \theta] \tag{4.44}$$

where T_{ice} is the retrieved ice surface temperature, T_4 and T_5 are the brightness temperatures measured by AVHRR channels 4 (11 μm) and 5 (12 μm), and coefficients *a–d* result from detailed radiative transfer calculations. Key and Haefliger (1992) used the LOWTRAN 7 radiative transfer model (Kneizys et al., 1988) to account for trace gas absorption and extinction by Arctic tropospheric aerosols (Blanchet and List, 1983).

In radiative transfer calculations for this purpose, there are two important considerations. First, directional emissivity $\varepsilon(\theta)$ of the surface must be included, as it can depart significantly from unity if the surface is snow-covered (Figure 4.45). For a given sensor-spectral responsivity $R_i(\lambda)$, the directional emissivity $\varepsilon_i(\theta)$ must be calculated from a radiative transfer model of the snowpack:

$$\varepsilon_i(\theta) = \frac{\int_{\lambda_1}^{\lambda_2} \varepsilon(\lambda, \theta) R_i(\lambda)\, d\lambda}{\int_{\lambda_1}^{\lambda_2} R_i(\lambda)\, d\lambda} \tag{4.45}$$

Second, thermal radiative transfer calculations require the use of rawinsonde data to specify the vertical tropospheric temperature and relative humidity profiles, and rawinsonde data must be used with care. Rawinsondes are usually prepared for launch inside a shelter, and the near-surface air temperature within the shelter

may be significantly different from the actual surface temperature (by up to 10 K). If there is no independent measurement of the surface temperature, the rawinsonde data must be interpreted with the help of an energy balance model to derive a range of representative surface temperatures. Given the range of shelter temperatures and observed wind speeds in their particular dataset, Key and Haefliger (1992) used an energy balance model after Maykut (1982):

$$(1-\alpha)F_{SW} - F_{\text{ice}} + F_{LW} + \varepsilon\sigma T_{\text{ice}}^4 + F_l + F_e + F_c = 0 \tag{4.46}$$

where α is the broadband shortwave albedo, ε is the broadband longwave emissivity, σ is the Stefan–Boltzmann constant ($\text{W m}^{-2}\,\text{K}^{-4}$), F_{ice} is the flux of shortwave radiation that penetrates the ice and does not heat the surface, F_{SW} is the downwelling shortwave flux, F_{LW} is the downwelling longwave flux, F_l is the latent heat flux, F_e is the sensible heat flux, and F_c is the conductive heat flux. The sensible and latent heat fluxes are functions of air temperature, wind speed, and T_{ice}. With this model, Key and Haefliger (1992) calculated a range of T_{ice} (maximum, minimum, and mean) for each rawinsonde profile, based on ± 1 standard deviation of variability in the relevant environmental parameters.

With the considerations of surface directional emissivity and rawinsonde data interpretation thus accounted for, the LOWTRAN 7 model was used to calculate T_4 and T_5 as functions of T_{ice}, θ, and tropospheric composition. A least squares regression procedure was then used to determine the coefficients *a–d* in (4.44), as a function of spacecraft and season. Table 4.6 lists these coefficients for the NOAA-11 AVHRR sensor. Key and Haefliger (1992) report that the root-mean-square errors in retrieved T_{ice} involved with applying coefficients for the wrong spacecraft can be as large as 1 K. When this type of method is derived and applied properly, the two-channel water vapor correction approach is of order ± 0.1 K in all seasons. However, Key and Haefliger (1992) do caution that the atmospheric data used should only be considered valid for the central Arctic region in which they were collected, and wintertime clear-sky precipitation (diamond dust) could introduce errors as large as ± 2 K.

Table 4.6. Coefficients in (4.47) for retrieving Arctic ice surface temperature from NOAA-11 AVHRR data, along with the r.m.s. error for the difference between the satellite-retrieved temperatures and the actual surface temperatures used to derive the algorithm. These coefficients pertain only to NOAA-11 data, and considerable errors can result from not considering the specific spacecraft instrument.

Season	*a*	*b*	*c*	*d*	r.m.s. (K)
Winter	−5.394 36	5.468 00	−4.452 33	−1.458 53	0.071
Transition	−5.354 87	4.479 13	−3.462 85	−0.971 28	0.053
Summer	−1.768 99	3.665 54	−2.662 49	−3.396 76	0.053

From Key and Haefliger (1992).

4.7 SATELLITE INVESTIGATION OF THE POLAR RADIATION BUDGET

In Section 4.5 we discussed uncertainties related to retrievals of individual atmospheric parameters such as cloud optical depth and effective droplet radius. However, in climate research one often requires knowledge about the shortwave and longwave components of the Earth's radiation budget either at the surface or TOA. Satellite remote sensing is the best way to acquire such knowledge on a global basis. At TOA, shortwave and longwave radiation fluxes can be observed directly from spacecraft, as has been done by the ERBE, SCARA-B, and CERES programs (e.g., Ramanathan et al., 1989). However, there is one important remote-sensing retrieval involved with such TOA measurements. A remote sensor viewing the Earth–atmosphere system measures a specific intensity of radiation from a given solid angle and over a particular spectral interval. A model for the *BRDF* must be applied to this intensity measurement to convert the intensity to a flux. For Earth radiation budget measurement programs, these *BRDF*s are usually constructed with great care using a large volume of empirical data as well as detailed radiative transfer calculations (e.g., Suttles et al., 1988 for ERBE). However, one should bear in mind that Earth radiation budget "data products" are not pure radiation flux measurements, but do contain remote-sensing retrieval involving *BRDF* assumptions and related uncertainties. Lubin and Weber (1995) discuss the effect of contrasting *BRDF* assumptions—the empirical *BRDF*s used by NASA's ERBE program versus plane-parallel radiative transfer calculations for a cloudy atmosphere—on uncertainties with shortwave radiation budget estimation.

For the surface radiation budget, one must use satellite data as input to either a rigorous or a parameterized radiative transfer algorithm to compute surface radiation fluxes. Over mid-latitudes, this has been done successfully for many years (e.g., Li et al., 1993a, b). For the polar regions, there are specific uncertainties related to the highly variable surface albedo, and the challenges with retrieving the various atmospheric parameters discussed above.

In climate research it is important to distinguish between *downwelling*, *upwelling*, and *net* radiation fluxes at the surface and TOA. The net surface shortwave flux $F_{SWN,SFC}$ is defined as the difference between the downwelling and upwelling fluxes at the surface:

$$F_{SWN,SFC} = F^{\downarrow}_{SW,SFC} - F^{\uparrow}_{SW,SFC} \tag{4.47}$$

Conceptually, the upwelling shortwave flux at the surface is:

$$F^{\uparrow}_{SW,SFC} = \int F^{\downarrow}_{SW,SFC}(\lambda)\alpha(\lambda)\, d\lambda \tag{4.48}$$

where $\alpha(\lambda)$ is the spectral surface albedo.

Similarly, the net surface longwave flux is defined as:

$$F_{LWN,SFC} = F^{\downarrow}_{LW,SFC} - F^{\uparrow}_{LW,SFC} = \varepsilon_S F^{\downarrow}_{LW,ATM} - \varepsilon_S \sigma T_S^4 \tag{4.49}$$

i.e., the difference between downwelling longwave flux from the atmosphere and the thermal radiative flux emitted by the surface at temperature T_S. More precisely, instead of a broadband surface emissivity ε_S, the final term in (4.49) can be written:

$$F^{\uparrow}_{LW,SFC} = \int B_\lambda(T_S)\varepsilon_S(\lambda)\, d\lambda \tag{4.50}$$

and the downwelling longwave flux from the atmosphere also has enormous spectral dependence, ranging from fluxes comparable with those from the surface in the middle of major greenhouse gas bands to fluxes orders of magnitude smaller in window regions.

The net shortwave flux at TOA is the difference between extraterrestrial solar flux and the flux backscattered to space by the Earth–atmosphere system:

$$F_{SWN,TOA} = \mu_0 F_0 - F^{\uparrow}_{SW,TOA} \tag{4.51}$$

where μ_0 is the cosine of the solar zenith angle. For the broadband shortwave, F_0 is referred to as the *solar constant* ($F_0 = 1{,}370 \pm 4\,\mathrm{W\,m^{-2}}$).

Similarly, net longwave flux at TOA is defined as:

$$F_{LWN,TOA} = -F^{\uparrow}_{LW,TOA} \equiv OLR \tag{4.52}$$

based on the extraterrestrial solar longwave flux being negligibly small for purposes of climate study, and $F_{LWN,TOA}$ is commonly known as the Outgoing Longwave Radiation OLR.

Net surface radiative flux is defined as:

$$F_{N,SFC} = F_{SWN,SFC} + F_{LWN,SFC} \tag{4.53}$$

and, similarly, net TOA radiative flux is:

$$F_{N,TOA} = \mu_0 F_0 - F^{\uparrow}_{SW,TOA} + OLR \tag{4.54}$$

There is sometimes confusion in terminology, where this sum of longwave and shortwave components is loosely called either "net flux", "total flux", or "global radiation". For clarity in papers and presentations, the term "net" should be used to specify a difference between upwelling and downwelling, and "radiative" or "total" should be used to specify the sum of shortwave and longwave. At any given location, the net surface radiative flux represents the energy absorbed by the surface, and the net TOA radiative flux represents the energy absorbed by the entire Earth–atmosphere column immediately below. Thus net fluxes are often of greater interest to climate researchers than the individual upwelling and downwelling components.

Generally, we consider the broadband shortwave and longwave fluxes, and so the above equations are given without spectral subscript notation. However, in climate system research it is becoming more important to identify radiation budget components in specific spectral intervals. For example, over snow or ice the surface albedo is high for wavelengths shorter than 1 μm, and a large fraction of surface insolation is reflected back to the atmosphere. For the near-IR

($1\,\mu m < \lambda < 4\,\mu m$, representing about 40% of the Sun's energy), snow or ice surfaces have a much smaller albedo averaged over this spectral interval, and a relatively small fraction of near-IR surface insolation is reflected back to the atmosphere. When we consider that the absorbing properties of atmospheric constituents (clouds and trace gases) have considerable spectral dependence, with the greatest contrast between the visible and near-IR, we realize that radiative transfer in the Earth–atmosphere system involves a complex repartitioning of energy in both the spectral and spatial domains. Consequently, GCM radiation codes have been evolving to divide the shortwave and longwave into a greater number of spectral intervals for greater accuracy despite the need for great computational speed with such algorithms.

From (4.47)–(4.54), other commonly used expressions have been derived. The atmospheric longwave *greenhouse effect* G_{LW} is defined as:

$$G_{LW} = \varepsilon_S \sigma T_S^4 - OLR \tag{4.55}$$

Cloud forcing (C), for either the shortwave or the longwave, is defined as:

$$C = F_{N,CLR} - F_N = f(F_{N,CLR} - F_{N,OVC}) \tag{4.56}$$

where F_N refers to the net flux in a cloudy atmosphere with cloud amount f, and $F_{N,CLR}$ refers to the net flux in an equivalent cloud-free atmosphere (all other atmospheric parameters the same). For cloud fraction f, C can be expressed in terms of equivalent clear and equivalent overcast fluxes ($F_{N,OVC}$). A negative value of cloud forcing represents a cooling effect of clouds on a given component of the climate system, while a positive value represents a warming effect. When we speak of the total greenhouse effect, or total cloud forcing, we mean the sum of the shortwave and longwave components, as in (4.54).

4.7.1 Sensitivity studies

To determine if a given satellite remote-sensing method can provide maps of net flux suitable for analysis of long-term trends, it is necessary to perform sensitivity studies to evaluate the errors that arise due to uncertainties in individual satellite-retrieved quantities such as surface albedo and cloud microphysical properties (Key et al., 1997). Generally speaking, if we have a quantity F, such as net flux, that is a function of two variables x and y, with errors (standard deviations) σ_x and σ_y, then these errors propagate such that the uncertainty in F is:

$$\sigma F = \sqrt{\left(\frac{\partial F}{\partial x}\sigma_x\right)^2 + \left(\frac{\partial F}{\partial y}\sigma_y\right)^2 + \frac{\partial F}{\partial x}\frac{\partial F}{\partial y}2\sigma_{xy}} \tag{4.57}$$

The final term under the radical sign is the covariance between the variables x and y. If x and y are independent, this covariance term disappears. Often the data specifying the covariance between two variables is not available. If the covariance cannot be determined, then we can still provide an upper limit to the uncertainty in

Table 4.7. Sensitivities in downwelling and net surface fluxes for clear skies during the Arctic summer, over snow and over openwater. The solar zenith angle is 70°. Surface temperature is T_s, surface albedo is α_s, O_3 is the total column ozone abundance, PW is precipitable water, τ_h is aerosol optical depth, and $T(z)$ is the tropospheric temperature profile.

Parameter	Reference value	Error, ±	Shortwave down		Longwave down		Net	
			Difference (%)	$\Delta F/\Delta x$	Difference (%)	$\Delta F/\Delta x$	Difference (%)	$\Delta F/\Delta x$
SNOW								
T_s, K	272	1	0.0	0.00	<0.1	<0.01	4.3	−4.51
α_s at 0.6 μm	0.6	0.05	0.4	30.30	—	—	11.9	−250.80
O_3, DU	334	5	0.01	−0.011	<0.1	0.006	<0.1	0.05
PW, mm	11.9	2.4	0.7	−1.01	0.7	0.70	0.1	−0.053
τ_h	0.08	+0.22	9.4	−144.50	1.8	19.36	10.2	−48.96
$T(z)$, K	—	2–3	0.4	−0.50	4.1	3.20	8.4	2.96
WATER								
T_s, K	271.4	1	0.0	0.00	<0.1	<0.01	2.0	−4.48
α_s at 0.6 μm	0.07	0.01	0.1	25.00	—	—	1.3	−301.50
O_3, DU	334	5	<0.1	−0.009	<0.1	0.006	0.01	−0.15
PW, mm	11.9	2.4	0.7	−1.00	0.7	0.70	0.2	−0.23
τ_h	0.08	+0.22	10.8	−158.96	1.8	19.36	12.3	−128.64
$T(z)$, K	—	2.3	0.5	−0.52	4.1	3.20	3.5	2.68

From Key et al. (1997).

F, which will never exceed (Taylor, 1982):

$$\sigma_F \leq \left|\frac{\partial F}{\partial x}\right|\sigma_x + \left|\frac{\partial F}{\partial y}\right|\sigma_y \tag{4.58}$$

The two expressions above can easily be generalized to a larger number of variables.

Key et al. (1997) have evaluated the sensitivity in retrieved Arctic net surface flux to the uncertainties in atmospheric surface parameters that arise in the remote-sensing methods described above. The variables considered in this sensitivity study are the surface temperature T_s, surface albedo α_s, total column ozone, precipitable water PW, aerosol optical depth τ_h, tropospheric vertical temperature profile $T(z)$, cloud droplet effective radius r_e, cloud top height Z_c, cloud fraction A_c, and cloud optical depth τ. Climatological reference values for these quantities were chosen for winter and summer, over open water and over snow, and for clear and cloudy skies. Errors σ_i in these quantities were assigned based on expected uncertainties from satellite retrieval, or if satellite retrieval is not feasible (e.g., for aerosol optical depth), from climatological variability. Tables 4.7–4.10 give these reference values and their assigned errors, and the effects of these errors on the surface downwelling and net fluxes. In these tables, the solar zenith angle is 70° (summer). For summer, the model cloud type is taken to be stratus with liquid water content 0.2 g m^{-3}. For winter, the model cloud type is taken to be a cirroform cloud with an ice water content of 0.03 g m^{-3}. The sensitivity in net surface flux to all quantities considered is

Table 4.8. Sensitivities in downwelling and net longwave surface fluxes for clear skies during winter, over snow and over open water. Variable definitions are as in Table 4.7.

Parameter	Reference value	Error, ±	Longwave down		Net	
			Difference (%)	$\Delta F/\Delta x$	Difference (%)	$\Delta F/\Delta x$
SNOW						
T_s, K	242	3	<0.1	<0.01	16.6	−3.18
O_3, DU	337	17	0.1	0.004	0.1	0.005
PW, mm	2.0	0.4	1.5	5.03	3.49	5.00
τ_h	0.08	+0.22	4.4	27.45	10.4	27.14
$T(z)$, K	—	2–3	5.4	2.11	12.7	2.08
WATER						
T_s, K	272	1	<0.1	<0.01	2.6	−4.51
O_3, DU	337	17	0.1	0.005	<0.1	0.004
PW, mm	2.0	0.4	1.5	5.01	1.2	5.00
τ_h	0.08	+0.22	4.5	27.91	3.5	27.64
$T(z)$, K	—	2–3	5.4	2.11	4.2	2.09

From Key et al. (1997).

Table 4.9. Sensitivities in downwelling shortwave, longwave, and net surface fluxes for cloudy skies during summer over snow. These calculations assume a stratus cloud with a liquid water content of $0.2\,\mathrm{g\,m^{-3}}$. The cloud effective droplet radius is denoted by r_e, the cloud top height by Z_c, the cloud fraction by A_c, and the cloud optical depth by t.

Parameter	Reference value	Error, ±	Shortwave down		Longwave down		Net	
			Difference (%)	$\Delta F/\Delta x$	Difference (%)	$\Delta F/\Delta x$	Difference (%)	$\Delta F/\Delta x$
T_s, K	268	4	0.0	0.0	0.1	0.05	16.2	−4.26
α_s at 0.6 μm	0.6	0.5	2.5	104.8	—	—	5.9	−123.50
O_3, DU	334	5	<0.1	−0.008	<0.1	0.001	<0.1	−0.002
PW, mm	11.9	2.4	0.6	−0.48	0.2	0.17	0.4	−0.18
$T(z)$, K	—	2–3	0.5	−0.31	4.3	4.22	11.5	4.02
r_e, μm	8	2	0.9	0.95	0.1	0.20	1.3	0.69
Z_c, m	1,500	500	0.3	−0.001	0.4	−0.002	1.44	−0.003
A_c	0.8	0.08	6.4	−166.5	2.0	73.8	1.7	−22.56
τ	10	5	13.7	−5.64	0.5	0.30	13.7	−2.89

From Key et al. (1997).

also depicted in Figures 4.51, 4.52, and 4.53. In these figures, we see that the errors in surface temperature, vertical temperature profile, cloud amount, and cloud optical depth are consistently the largest sources of uncertainty in net surface flux estimation from satellite data. Table 4.11 summarizes the combined uncertainty in retrieving surface radiation fluxes, based on (4.57) and (4.58).

Table 4.10. Sensitivities in downwelling longwave and net surface flux for cloudy skies during winter over snow. Variable definitions are as in Table 4.9. A cirrus cloud is assumed with an ice water content of $0.03\,g\,m^{-3}$.

Parameter	Reference value	Error, ±	Longwave down		Net	
			Difference (%)	$\Delta F/\Delta x$	Difference (%)	$\Delta F/\Delta x$
T_s, K	247	4	<0.1	0.01	33.0	−3.37
O_3, DU	337	17	<0.1	0.002	0.1	0.002
PW, mm	2.0	0.4	0.5	2.28	2.2	2.25
$T(z)$, K	—	2–3	5.2	2.50	21.2	2.47
r_e, μm	40	10	1.0	0.18	4.3	0.17
Z_c, m	6000	1000	2.6	−0.004	10.6	−0.004
A_c	0.6	0.09	2.9	55.33	12.1	54.78
τ	5	2.5	5.0	3.37	20.4	3.33

From Key et al. (1997).

Key et al. (1997) also discuss surface validation exercises. It is common to compare satellite estimates of the surface radiation budget with surface radiation measurements by means of a scatter diagram, as in Figures 4.54, 4.55, and 4.56. These figures compare fluxes estimated from AVHRR data over Barrow, Alaska, with surface radiation measurements from the NOAA Climate Modeling and Diagnostics Laboratory (Stone et al., 1996). In such scatterplots, one can perform a regression and obtain a linear correlation coefficient r, a bias, and a Root-Mean-Square Error ($RMSE$). If these statistics are small, or are within the expected range

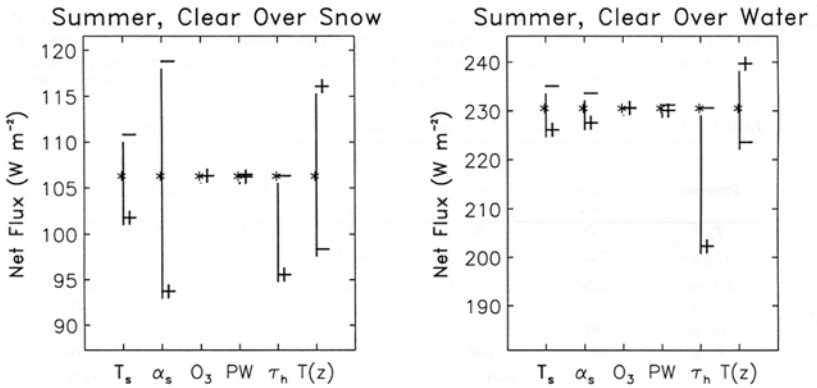

Figure 4.51. Comparison of the sensitivity in satellite-derived net surface radiative flux to expected uncertainties in surface temperature T_s, surface albedo α_s, total column ozone O_3, precipitable water vapor PW, aerosol optical depth τ_h, and vertical temperature profile $T(z)$, for clear-sky conditions during summer over both snow and open water.

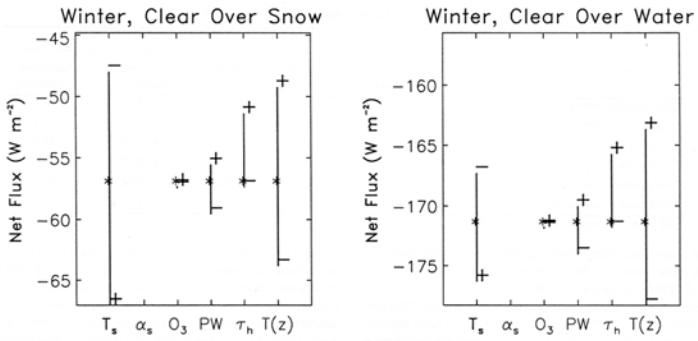

Figure 4.52. As in Figure 4.51, but for clear-sky conditions during winter.

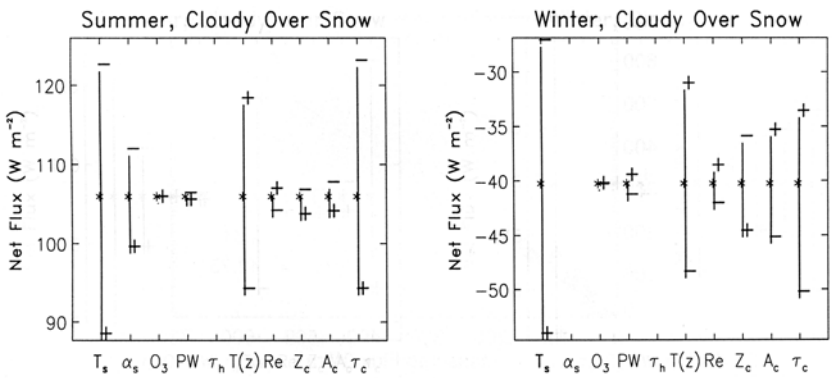

Figure 4.53. Comparison of the sensitivity in satellite-derived net surface radiative flux to expected uncertainties in surface temperature T_s, surface albedo α_s, total column ozone O_3, precipitable water vapor PW, aerosol optical depth τ_h, vertical temperature profile $T(z)$, cloud particle effective radius r_e, cloud top height Z_c, cloud amount A_c, and shortwave cloud optical depth τ_c, for cloudy-sky conditions during summer and winter over snow.

of uncertainties, one generally concludes that the satellite retrieval performance is acceptable. However, one important caution with such scatter diagrams is that this performance assessment applies only to the *largest* timescales. For example, Figures 4.54–4.56 contain several months of data. Although one might conclude from these figures that the AVHRR-based method used is performing within acceptable uncertainty limits, there is no guarantee that *every single* satellite retrieval will be within those limits. As one hypothetical example, consider the four "outlier" points in Figure 4.54, where the surface-measured fluxes (horizontal axis) are between 470 and 550 $W\,m^{-2}$, and where the AVHRR-retrieved fluxes are $\sim$100 $W\,m^{-2}$ smaller. If those four points happen to be consecutive, from a given 4-day period, then the

Table 4.11. The combined uncertainty in estimating surface fluxes. σ(ind) is the uncertainty assuming the uncertainties in the individual variables are independent (4.57), and σ(max) is the maximum uncertainty per (4.58). These uncertainties are given in watts per square meter.

	Shortwave down		Longwave down		Net	
Conditions	σ(ind)	σ(max)	σ(ind)	σ(max)	σ(ind)	σ(max)
Clear summer over snow	32.0	37.2	10.6	15.6	19.3	36.8
Clear summer over water	35.1	39.2	10.6	15.6	29.9	44.4
Clear winter over snow	—	—	9.7	15.5	13.6	24.9
Clear winter over water	—	—	9.8	15.6	10.7	20.0
Cloudy summer over snow	31.7	51.4	14.1	22.3	26.3	54.9
Cloudy winter over snow	—	—	14.0	29.3	19.3	42.4

From Key et al. (1997).

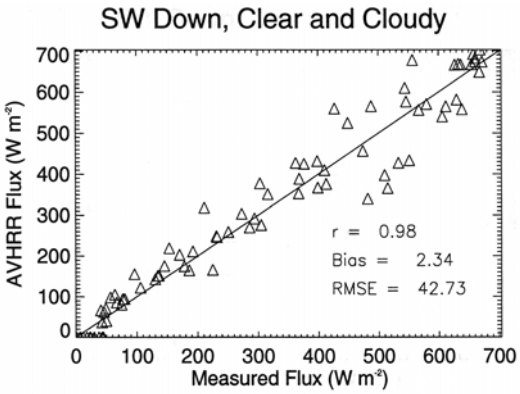

Figure 4.54. Comparison of AVHRR-derived downwelling shortwave flux at the surface at Barrow, Alaska during 1992–93 with co-located surface pyranometer (broadband shortwave radiometer) measurements.

From Key et al. (1997). Copyright 1997 American Geophysical Union. Reproduced by permission of American Geophysical Union.

satellite retrieval algorithm is performing very poorly for the meteorological conditions that prevail during that particular time period. If in such a period a significant climatic event occurs, such as the onset of sea ice melting, then the satellite retrievals are erroneous enough to be irrelevant to that particular climatic event. Generally speaking, the utility of satellite radiation budget retrievals improves when one considers longer timescales. Key et al. (1997) conclude that current methods using imager data such as AVHRR are acceptable at monthly timescales. Further improvements are needed to achieve universal reliability for high-latitude meteorological conditions that change from day to day.

Despite the inherent uncertainties just discussed, estimation of surface and TOA radiation budget components using meteorological and surface properties derived

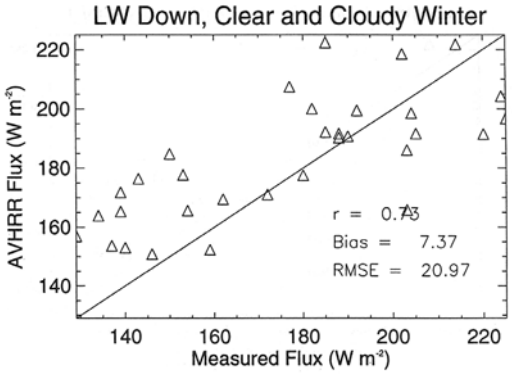

Figure 4.55. Comparison of AVHRR-derived downwelling longwave flux at the surface at Barrow, Alaska during 1992–93 with co-located surface pyrgeometer (broadband longwave radiometer) measurements.

From Key et al. (1997). Copyright 1997 American Geophysical Union. Reproduced by permission of American Geophysical Union.

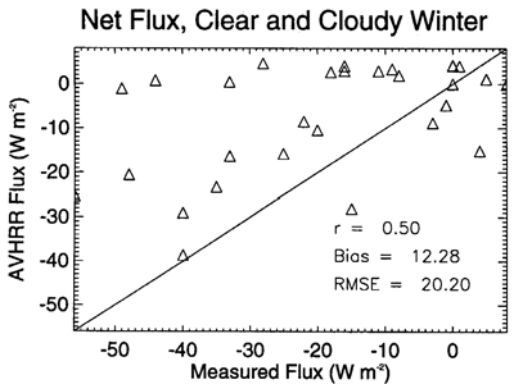

Figure 4.56. Comparison of AVHRR-derived net surface flux with co-located surface measurements from Barrow, Alaska during 1992–93.

From Key et al. (1997). Copyright 1997 American Geophysical Union. Reproduced by permission of American Geophysical Union.

from imager data, as in Key et al. (1997), can be a valuable strategy for investigating high-latitude radiation budgets. The practical advantage in this approach lies in the availability of a continuous time series in "heritage" imager data that now spans more than 20 years. Once the retrieval uncertainties are understood, the long time series lends itself to analysis of climatological trends. For example, Wang and Key (2003) have analyzed satellite-derived trends in Arctic surface temperature, surface albedo, cloud fraction, and cloud forcing in the context of trends in the NAM (Figures 4.57, 4.58, and 4.59). These analyses reveal trends in cloud amount and opacity that appear to function as a negative feedback during summer: a long-term

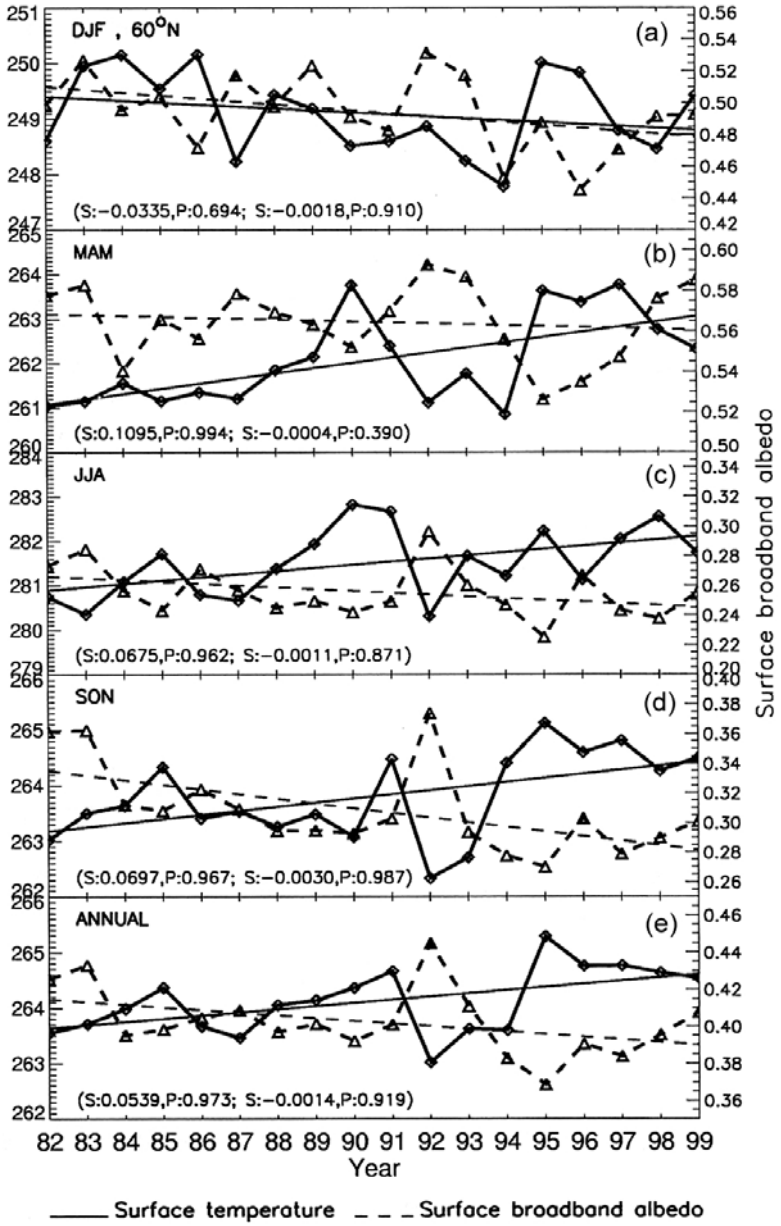

Figure 4.57. Satellite determination of the trends in surface temperature and broadband surface albedo for four seasons and for the annual mean, covering the time period 1982–99 and the entire Arctic north of 60°. The numbers on each panel are the trend slope per year (S), and the F-test confidence level (P); the first pair pertains to surface temperature (solid line) and the second pair to surface albedo (dashed).

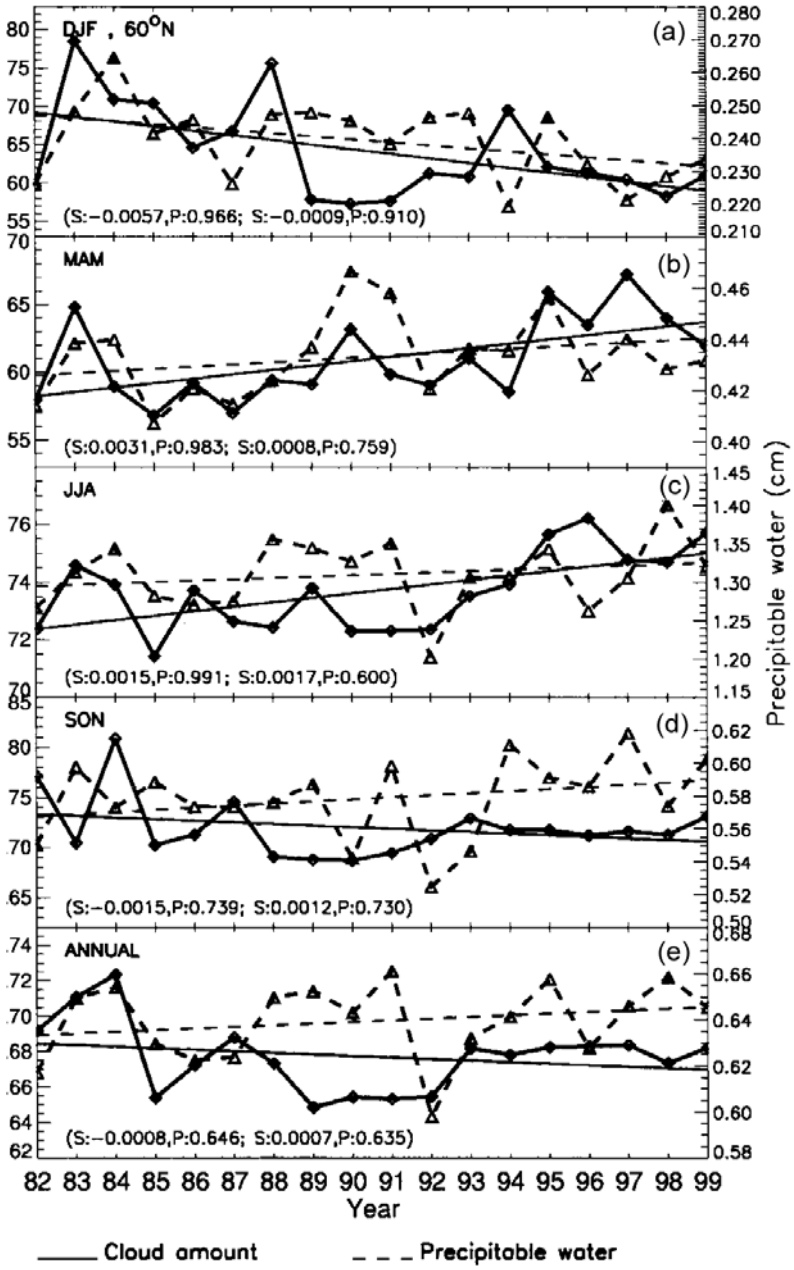

Figure 4.58. As in Figure 4.57, but for the cloud amount (solid) and precipitable water (dashed). The first pair of S and P values pertains to the cloud amount and the second to the precipitable water.

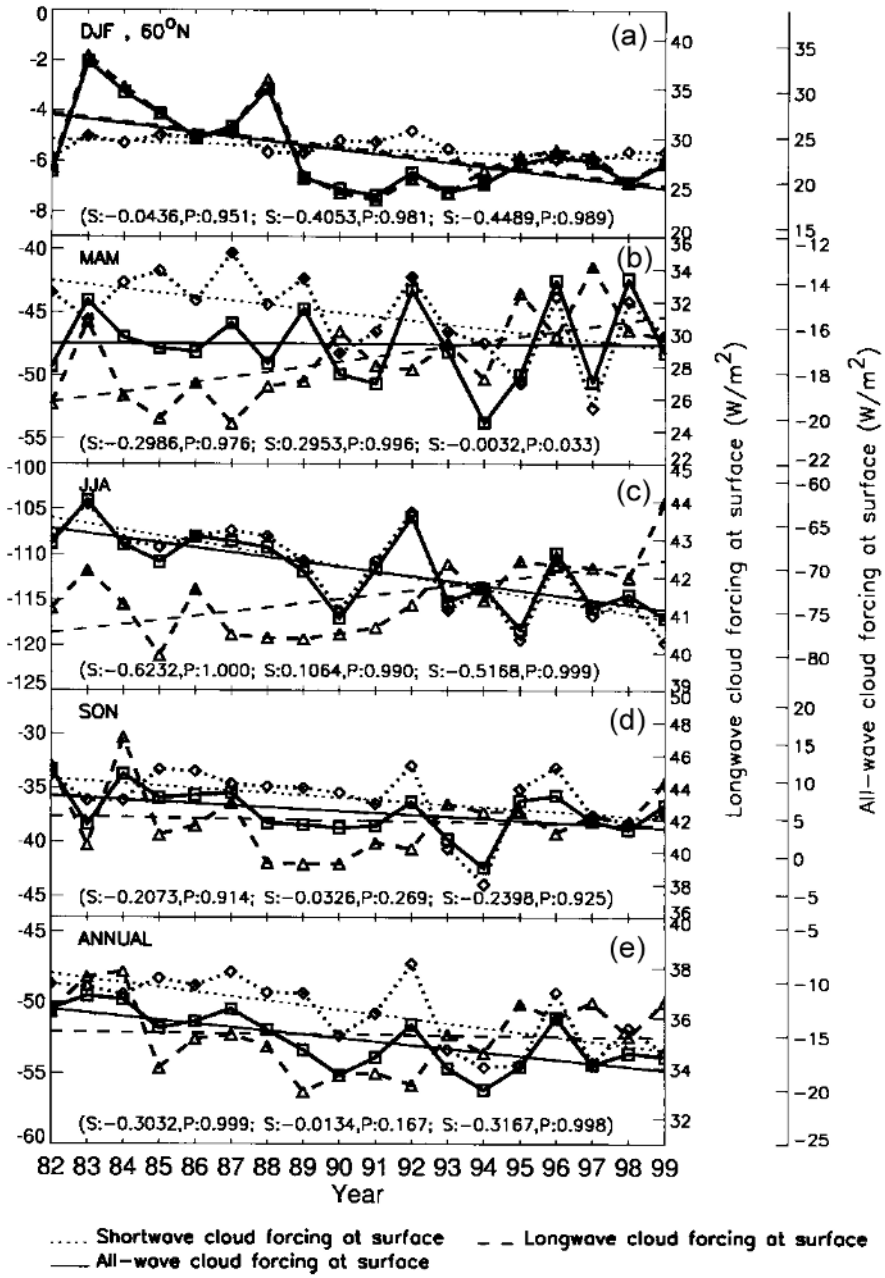

Figure 4.59. As in Figure 4.57 but for the surface shortwave cloud forcing (dotted), longwave cloud forcing (dashed), and net (all-wave) cloud forcing (solid), with the S and P values also listed in this order.

increase in cloud cooling of the climate (negative cloud radiative forcing, as shown in Figure 4.59) implies that Arctic climate warming would have been even larger over the past two decades had cloud properties not also changed in response to the NAM.

4.7.2 Use of Earth radiation budget sensors

A second valuable strategy for investigating high-latitude radiation budget involves using Earth radiation budget instrument data directly. This eliminates many of the uncertainties involved in calculating radiation components with radiative transfer models and satellite-derived meteorological variables. As mentioned above, the only substantial remote-sensing retrieval with Earth radiation budget instruments is the conversion of measured intensities to fluxes using models for the *BRDF*. One important complication involves scene identification at high latitudes. Earth radiation budget instruments are designed primarily to have very high radiometric accuracy and precision, and to achieve the desired *SNR* these instruments typically have a *GIFOV* of order tens of kilometers, and measure over very large spectral intervals (e.g., total shortwave, total longwave, all solar near-IR). It is therefore very difficult to differentiate between clear and cloudy scenes over high-albedo surfaces. This requires that Earth radiation budget data be co-located either with other satellite data for scene identification, or with surface radiometer data. Nemesure et al. (1994) co-located ERBE (Earth Radiation Budget Experiment) data with shortwave surface flux measurements at the South Pole, and showed that cloud cover increases the TOA shortwave albedo, even over the very high albedo of the snow cover at the South Pole, as shown in Figure 4.60.

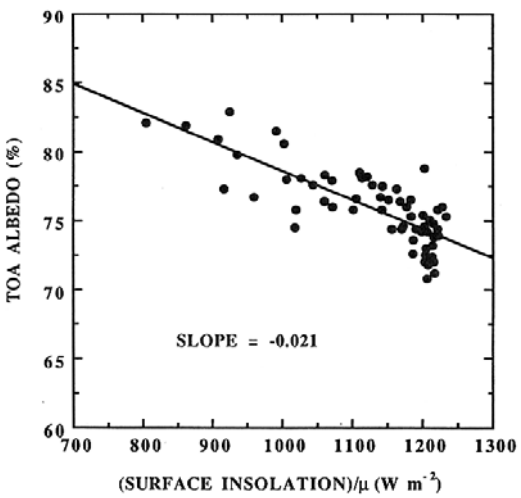

Figure 4.60. Top-of-atmosphere shortwave albedo measured by ERBE as a function of downwelling shortwave flux divided by the solar zenith angle cosine μ, for 66 co-located measurements having $0.38 < \mu < 0.40$.

From Nemesure et al. (1994).

Table 4.12. Cloud Effectiveness (CE), or cloud forcing for 100% cloud cover, and other radiation budget components, derived from ERBE data and surface radiation measurements at Syowa Station and the South Pole. Columns are TOA shortwave albedo α_{SW}, CE for albedo, shortwave absorption A_{SW}, shortwave CE ($W\,m^{-2}$), outgoing longwave radiation OLR ($W\,m^{-2}$), longwave CE ($W\,m^{-2}$), net flux under clear skies $F_{N,CLR}$ ($W\,m^{-2}$), and radiative (shortwave plus longwave) CE ($W\,m^{-2}$).

	α_{SW}	CE(α)	A_{SW}	CE(SW)	OLR	CE(LW)	$F_{N,CLR}$	CE(rad)
Syowa								
July 1987								
TOA					172.4	12.7	−172.4	12.7
ATM					112.2	−18.2	−112.2	−18.2
SFC					60.2	30.9	−60.2	30.9
January 1988								
TOA	42.6%	13.0%	266.2	−54.6	229.7	21.5	36.5	−33.1
ATM			143.5	11.2	135.1	−48.8	8.4	−37.6
SFC	67.2	7.35	122.7	−65.8	94.6	70.3	28.1	4.5
South Pole								
July 1987								
TOA					105.4	−5.2	−105.4	−5.2
ATM					88.9	−10.4	−88.9	−10.4
SFC					16.5	5.2	−16.5	5.2
January 1988								
TOA	70.1	6.21	152.2	−32.9	196.0	4.3	−43.8	−28.6
ATM			57.7	−0.4	107.5	−45.5	−49.8	−45.9
SFC	79.2	2.31	94.5	−32.5	88.5	49.8	6.0	17.3

From Yamanouchi and Charlock (1995).

Yamanouchi and Charlock (1995) examined both the shortwave and longwave radiation budget components using ERBE data co-located with surface radiation measurements and observations of sky conditions at both the South Pole and at Syowa Station (69°00′S, 39°35′E). Table 4.12 gives these components as evaluated from one winter and one summer month, in terms of the TOA and surface fluxes, and the flux absorbed by the atmosphere. The fluxes are given for clear-sky conditions, and then cloud forcing is given in the case of 100% cloud cover. In Yamanouchi and Charlock (1995), the term *Cloud Effect* (CE) is used to specify cloud forcing for 100% cloud cover, as distinct from the standard definition of cloud forcing which applies to the naturally occurring cloud fraction (Ramanathan et al., 1989). An annual cycle in radiation budget components, from ERBE and surface measurements, is shown in Figure 4.61 for Syowa Station and in Figure 4.62 for the South Pole. In summer, clouds cool the Antarctic Earth–atmosphere column as measured at TOA, but warm the surface. In winter there is a contrast between this coastal station and the South Pole. At Syowa Station, the longwave cloud forcing is positive at TOA and at the surface, and negative in the atmosphere. At the South Pole during winter the longwave cloud forcing is negative

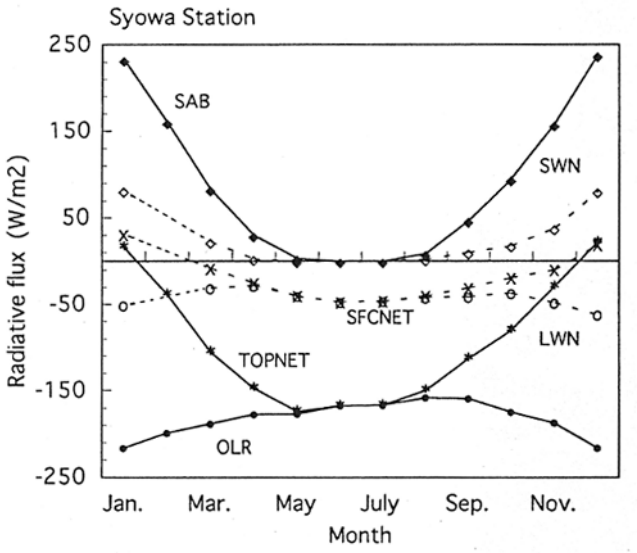

Figure 4.61. Monthly means of the shortwave absorption at the top-of-atmosphere (SAB), the outgoing longwave radiation (OLR), net radiation at the top-of-atmosphere (TOPNET), net shortwave flux (SWN), net longwave flux (LWN), and the net (shortwave plus longwave) flux at the surface (SFCNET) for Syowa Station (Antarctica) during 1987–88, derived from co-located ERBE and surface pyranometer and pyrgeometer measurements. Positive values are downward fluxes, negative values are upward fluxes.

From Yamanouchi and Charlock (1995).

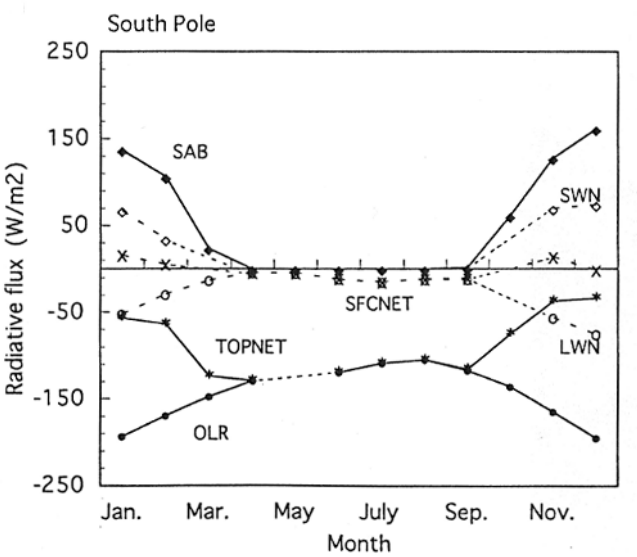

Figure 4.62. As in Figure 4.61, but for the South Pole during 1987–88.

From Yamanouchi and Charlock (1995).

both at the TOA and in the atmosphere, and positive at the surface. This results from the strong lower troposphere temperature inversion over the very cold surface of the Antarctic Plateau during winter.

Another useful application of Earth radiation budget data lies in the direct validation of GCM performance. Given that one major interest in climate model simulation is the prediction of global climate change in response to various warming scenarios (e.g., CO_2 increases), a satellite evaluation of how a GCM simulates present-day shortwave and longwave radiation budget components is a particularly useful test of the GCM simulation's validity. Briegleb and Bromwich (1998) evaluated the net shortwave flux at TOA and the OLR at TOA, as simulated by the NCAR Community Climate Model Version 3 (CCM3) by direct comparison with ERBE measurements from 1985 to 1989. It was found that the TOA net shortwave flux in the GCM is too small by about $20\,W\,m^{-2}$ in both polar regions (Figures 4.63 and 4.64), and that the annual polar net TOA radiation is smaller than ERBE measurements by 5–$10\,W\,m^{-2}$. The seasonal amplitude in OLR in the GCM is $40\,W\,m^{-2}$, versus $\sim 60\,W\,m^{-2}$ in ERBE measurements. Detailed analysis of GCM output fields revealed that these discrepancies could be related to GCM deficiencies in the simulation of cloud water path and winter low cloud amount, artificial discontinuities in cloud particle size at high-latitude coastlines, and a simplistic GCM representation of sea ice albedo that neglects the effects of meltponds. Overall, it was found that the polar radiation budgets simulated by CCM3 were degraded in quality as compared with ERBE data, from those simulated by the earlier version of this GCM (CCM2), despite numerous changes to the paramaterizations for cloud and atmospheric physics that are recognized as being important at lower latitudes. Studies such as Briegleb and Bromwich (1998) can serve to focus the atmospheric science community on polar processes in GCM simulations, which from a climate system perspective are just as important as processes at tropical and mid-latitudes. In addition to GCM radiation budget validation, Earth radiation budget sensor data can also be used to validate other satellite radiation budget estimations from imager data (Schweiger and Key, 1994).

4.7.3 Aerosols

There is a well-known anthropogenic aerosol burden in the Arctic troposphere, known as the "Arctic haze" (Shaw, 1982). It is now recognized that tropospheric aerosols play an important role in regional climate forcing (Kiehl and Briegleb, 1993). In the Arctic, tropospheric aerosols have an opacity that is sufficient to directly affect shortwave radiative fluxes and tropospheric heating rates (Pilewskie and Valero, 1993; Tsay et al., 1989; Valero et al., 1984, 1988).

On a global basis, five climatic effects of tropospheric aerosol are now recognized. The *direct shortwave effect* refers to the attenuation of insolation at the Earth's surface due to aerosol scattering and absorption. This effect has the largest magnitude, sometimes many tens of watts per square meter at the highest aerosol opacities (Meywerk and Ramanathan, 1999). In addition, recent satellite studies (e.g., Kaufmann et al., 1998; Mischenko et al., 1999; Rajeev and

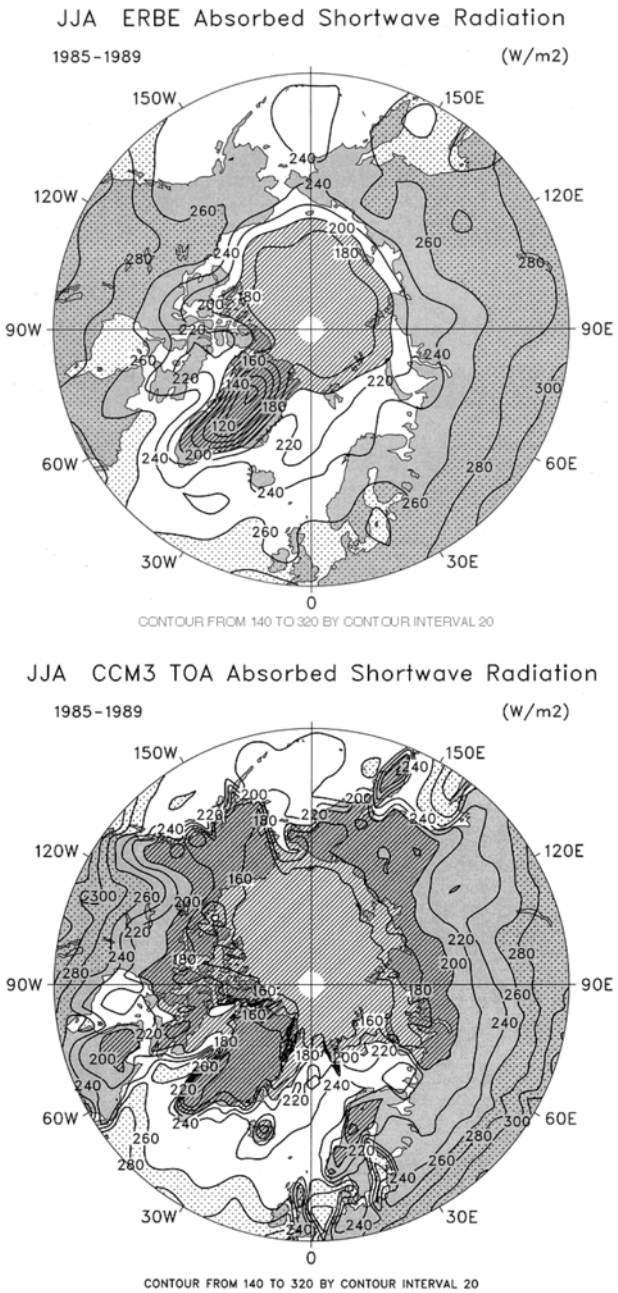

Figure 4.63. Top-of-atmosphere absorbed shortwave radiation from a summertime (JJA) simulation by the NCAR Community Climate Model version 3 (CCM3) (top panel), and from a seasonal average of ERBE data (bottom panel).

From Briegleb and Bromwich (1998).

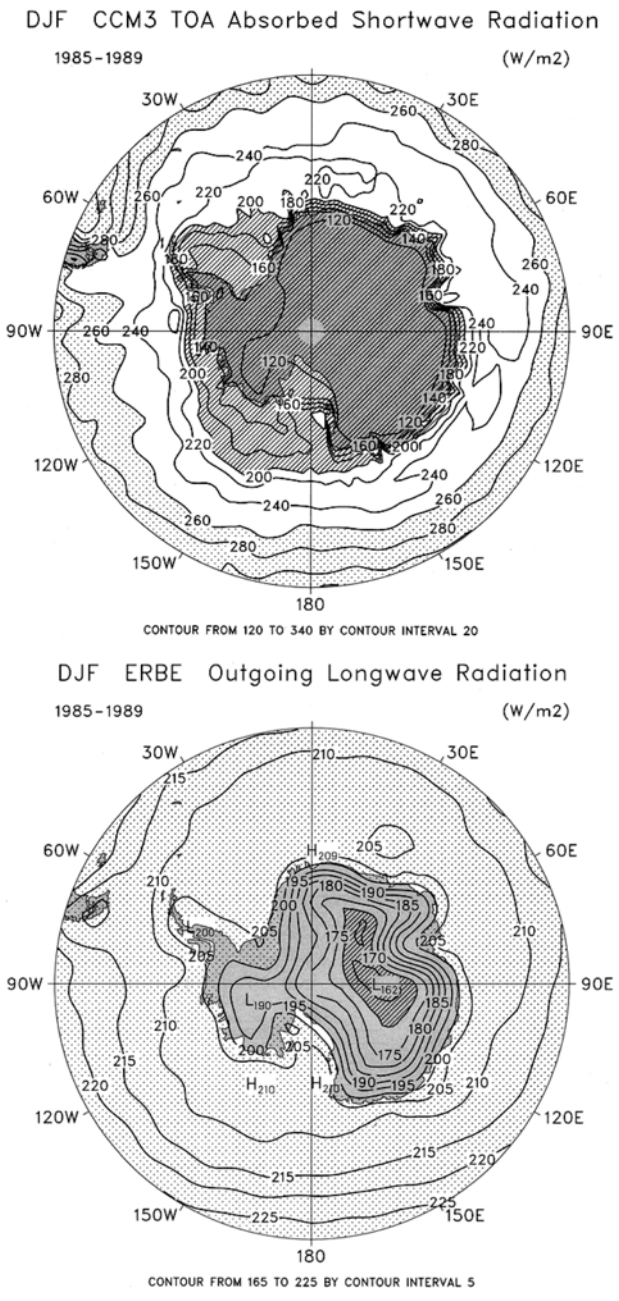

Figure 4.64. As in Figure 4.63, but for the Antarctic summer.
From Briegleb and Bromwich (1998).

Ramanathan, 2001] and model simulations (Collins et al., 2001; Kiehl and Briegleb., 1993; Kiehl et al., 2000) suggest that the geographic extent of this effect may be much larger than previously believed. Smaller aerosol particles having longer tropospheric lifetimes can cause significant attenuation of shortwave radiation at great distances from their source. The *direct longwave effect* refers to heating of the Earth's surface by aerosol particle emission in the mid-IR window, and concomitant cooling of the lower troposphere if the aerosol column extends significantly above the boundary layer. The magnitude of the longwave effect is much smaller than that of the direct shortwave effect (i.e., generally $<5\,\mathrm{W\,m^{-2}}$), but it is comparable with the radiative forcings of greenhouse gas increases, and it persists during the nighttime. The direct longwave effect has been measured under urban aerosol using a Fourier transform infrared spectro-radiometer (Lubin and Simpson, 1994) and has been predicted as a persistent phenomenon in aerosol compositions relevant to large-scale climate warming (Lubin et al., 2002b).

The *first indirect*, or "*Twomey effect*" refers to the relationship between the number concentration of aerosol particles and the precipitable water vapor abundance (Twomey, 1977). For a constant abundance of water vapor available to condense into cloud droplets, an increase in the number of aerosol particles represents an increase in the number of available cloud condensation nuclei. The result is a decrease in the effective radiating radius of cloud droplets, which makes the clouds more reflective to shortwave radiation. This effect has been observed in the recent INDian Ocean EXperiment (INDOEX) by McFarquar and Heymsfield (2001). Evidence for the first indirect effect has also been seen in the Arctic (Dong et al., 2001; Garrett et al., 2002). From first-order radiative transfer calculations, we can describe the "susceptibility" S_{SW} of the shortwave cloud albedo α as a change in droplet concentration N_c at fixed cloud liquid water constant and geometrical thickness (Platnick and Twomey, 1994):

$$S_{SW} = \frac{d\alpha}{dN_C} \approx \frac{\alpha(1-\alpha)}{3N_C} \tag{4.59}$$

A similar longwave cloud susceptibility, S_{LW}, can be derived to describe the change in spectrally averaged cloud emissivity ε:

$$S_{LW} = \frac{d\varepsilon}{dN_C} \approx -\frac{(1-\varepsilon)\ln(1-\varepsilon)}{3N_C} \tag{4.60}$$

The *second indirect effect* is closely related to the first: an increase in the number of cloud condensation nuclei leads to slower formation rates of large droplets, which suppresses precipitation. A suppression of precipitation leads to increased cloud lifetime, and higher liquid water content, both of which serve to increase shortwave planetary albedo. This second indirect effect has been observed in satellite studies (Rosenfeld, 2000) and aircraft studies (Albrecht, 1989). The *semi-direct effect* refers to a result of shortwave attenuation by the direct effect: absorption of shortwave radiation by aerosol warms the troposphere and increases the evaporation of cloud droplets, leading to shorter cloud lifetimes and smaller cloud fractions. This is particularly prevalent in tropical trade cumulus (e.g., Ackerman

et al., 2000). Climatological results of this semi-direct effect can include an alteration of the hydrological cycle. The atmospheric science community is only just beginning to assess the magnitude and sign of these aerosol effects on a global basis. Over the Indian Ocean, Ramanathan et al. (2001) determined that the direct shortwave effect and both indirect effects had a net cooling effect (negative climate forcing), while the semi-direct effect and the direct longwave effect had a smaller net warming effect. Determining the relative magnitudes, signs, and time histories of these effects is of primary importance in climate studies for the near future.

A second issue of vital importance concerns the chemical composition of tropospheric aerosol. The radiative properties of aerosol particles vary enormously with composition. This variability is further enhanced by the relatively small size of aerosol particles (of order 0.1–1 μm), which from Mie theory signifies that they absorb as well as scatter shortwave radiation. Between various aerosol types there is also differential sensitivity in aerosol radiative properties—*single scattering albedo* $\varpi_a(\lambda)$, *asymmetry factor* $g_a(\lambda)$, and *volume extinction coefficient* $\beta_a(\lambda)$—to relative humidity. The earliest climate studies involving aerosol used radiative properties typical of sulfates, which are ubiquitous and relatively non-absorbing (IPCC, 2001). Nowadays, we realize the climatic importance of aerosol types with radiative properties very different from those of sulfates, including black carbon (which is much more absorbing than sulfate—e.g., Haywood and Ramaswamy, 1998), mineral dust (e.g., Sokolik and Toon, 1999; Tegen et al., 1996), sea salt (e.g., O'Dowd and Smith, 1993), natural biogenic aerosol (Charlson et al., 1987), and products of biomass burning (e.g., Hobbs et al., 1997; Kaufmann et al., 1998). Of primary importance to climate studies is that the chemical composition of aerosol particles, and hence their radiative properties, vary with geographic region depending on their source (natural, anthropogenic–industrial, biomass burning, etc.). A valuable reassessment of "characteristic" aerosol types has been provided by d'Almeida et al. (1991).

The physical properties of a given aerosol distribution, such as size distribution and mixing state, also have profound effects on their radiative properties and hence on their climatic effects. For climatic effects, smaller aerosol particles in *accumulation mode* (particle diameter range 0.1–1 μm) are the most significant. These smaller particles have the largest scattering efficiency, and also the longest lifetimes in the troposphere. However, larger particles in *coarse mode* are also important radiatively. For a given composition, the single scattering albedo will be smaller for a larger particle, and hence its absorption will be more efficient. Also, the larger particles begin to exert a significant direct longwave effect (Lubin et al., 2002b). The mixing state of multi-component aerosol adds considerable uncertainty in determining radiative forcings. An *external mixture* refers to a mixture of various chemically homogeneous aerosol particle types: in radiative transfer analysis, $\varpi_a(\lambda)$, $g_a(\lambda)$, and $\beta_a(\lambda)$ are evaluated separately for each chemical component, and are then combined in the formulation of the radiative transfer equation. An *internal mixture* refers to aerosol particles which themselves are aggregates of several chemical components. To evaluate the radiative properties of an internal mixture, a model for mixing the refractive indices of the discrete components must be devised

and validated (e.g., Sokolik and Toon, 1999). For strongly absorbing aerosol particles, uncertainty in mixing state can lead to large uncertainties in radiative forcing (Haywood and Shine, 1995). A third physical property of tropospheric aerosol distribution involves the growth of particles with increasing relative humidity (Nilsson, 1979; d'Almeida et al., 1991). Some aerosols are non-hygroscopic (e.g., dust), while most aerosol particles exhibit a growth factor with relative humidity which varies widely with chemical composition.

To date, most of our knowledge about the geographic and temporal variability in Arctic haze has come from a handful of ground stations (e.g., Polissar et al., 1998; Shaw, 1982). Alaska has proven to be a useful location for these studies, because Alaska is affected alternately by Arctic and Pacific airmass systems. In the Pacific airmass system, aerosol chemical composition is characterized by enrichment in elements related to sea salt. In the Arctic airmass system, pollutants such as excess sulfates are transported over long distances to Alaska. The abundance of these excess sulfates has been shown to exhibit a general negative gradient from northwestern to southeastern Alaska, indicating a long-distance source to the northwest of Alaska (e.g., industrial activity in or near the Russian Arctic). A review of aerosol studies in the Russian Arctic is given by Kondratyev et al. (1996).

The overall seasonal cycle in the Arctic haze involves a maximum tropospheric aerosol burden during late winter and spring, with a decrease toward a minimum during midsummer due primarily to removal by increased precipitation. In addition to atmospheric radiative effects, deposition of aerosol particles on pristine snow cover may decrease the surface albedo, which by ice albedo feedback may amplify an existing warming trend. For future climate study, it will be important to (a) better characterize the temporal and spatial variability in aerosol opacity with a better resolution than is available from a handful of ground stations, and (b) identify possible transport pathways.

Direct satellite observations of aerosol opacity are much more difficult at high latitudes than anywhere else, because the high surface albedo eliminates the contrast between intensities from aerosol-laden versus clean atmospheres. Although excellent aerosol remote-sensing programs exist using imager data over tropical and temperate regions (e.g., Rajeev and Ramanathan, 2001), polar aerosol remote sensing remains a challenge for future generations of researchers. The task may fall to missions such as ICESat and CALIPSO, which feature lidar. Alternatively, limb-sounding instruments such as SAGE II may provide useful space-based observations of Arctic aerosol (Thomason et al., 2003). Because of the recognized climatic implications of increases in anthropogenic aerosol, this remains an important topic for remote sensing.

4.8 THE POLAR PATHFINDER DATASET—EXAMPLE OF A SUCCESSFUL HIGH-LATITUDE ADAPTATION

So far we have introduced in a piecemeal fashion how the remote-sensing signatures of meteorological and climatological parameters—including cloud amount, cloud

optical properties, surface albedo and temperature, radiation budget components—are influenced by the unique polar environment. At this point it is useful to describe a remote-sensing research program that has successfully dealt with many high-latitude challenges and has produced a multidecadal data product that is useful for many climate studies. The TOVS (TIROS-N Operational Vertical Sounder) Polar Pathfinder dataset (Francis and Schweiger, 2000), in addition to providing climatological information from 1979 to the present, serves as an excellent example for avoiding the Curse of Captain Wilkes. The procedures used in adapting a "heritage" multispectral sensor for high-latitude use should serve as a model for future remote-sensing projects using next-generation sensors.

The Polar Pathfinder project utilizes the TOVS instrument suite, first introduced for total column ozone retrieval in Chapter 3. Its three instruments—the Stratospheric Sounding Unit (SSU), the Microwave Sounding Unit (MSU), and the HIRS-2—are discussed in detail by Smith et al. (1979) and by Kidder and Vonder Haar (1995).

Briefly, the SSU operates at three wavenumbers within $50\,cm^{-1}$ of the center of the 15-μm CO_2 emission band. Discrimination of the stratospheric CO_2 signal is accomplished by the method of *gas correlation spectroscopy*. The optical path of each channel includes a cell containing CO_2 whose mean pressure is set to the approximate atmospheric pressure at the desired stratospheric altitude (100, 35, and 10 millibars for the three channels). The instrument modulates the pressure within the cells at a frequency of 40 Hz, such that the absorption features resulting from the gas within the cells alternately become wider and then narrower than the emission features from the atmosphere. Hence the atmospheric signal is alternately blocked from the detectors and passed to the detectors at a frequency of 40 Hz, and the amplitudes of this 40-Hz oscillation on detector signals contain information on how the actual stratospheric pressure varies from the mean pressure in each of the cells, thus enabling reconstruction of the stratospheric temperature profile. The SSU is not used in the Polar Pathfinder project, but the method of gas correlation spectroscopy is interesting to bear in mind in the context of future space missions.

The HIRS-2 is a 20-channel multispectral scanner, with 19 channels at center wavelengths between 3.76 and 14.95 μm and one visible channel (0.69 μm). Channels 1–7 cover 13.35–14.95 μm and are intended for tropospheric temperature profiling by covering the transition between the 15-μm CO_2 band and the mid-IR window. Channels 8 and 19 (11.11 and 3.76 μm, respectively) measure surface temperature through two infrared windows. As discussed in Chapter 3, channel 9 is designed for ozone measurement. Channels 10–12 cover the water vapor emission band between 6.72 and 8.16 μm, and are intended for atmospheric moisture retrieval. Channels 13–18 cover the CO_2 emission band between 4.00 and 4.57 μm, and are intended to improve the sensitivity of temperature retrievals in warmer atmospheres. The purpose of the visible wavelength channel 20 is to provide unambiguous cloud detection for the sounding algorithms. These channels are summarized in Table 4.13. The *GIFOV* is 18.5 km in diameter at nadir, increasing to 32 km along-track by 63 km crosstrack at the scan edge. As discussed by Kidder and Vonder Haar (1995), the HIRS-2 and similar sounding instruments do not produce images.

Table 4.13. HIRS-2 channels, the exact wavelength ranges for which vary slightly with spacecraft.

Channel	Description	Central wavenumber (cm^{-1})	Central wavelength (μm)	Half-power bandwidth (cm^{-1})
1	15 μm CO_2	669	14.95	3
2	15 μm CO_2	680	14.71	10
3	15 μm CO_2	690	14.49	12
4	15 μm CO_2	703	14.22	16
5	15 μm CO_2	716	13.97	16
6	15 μm CO_2	733	13.64	16
7	15 μm CO_2	749	13.35	16
8	Window	900	11.11	35
9	O_3	1,030	9.71	25
10	H_2O	1,225	8.16	60
11	H_2O	1,365	7.33	40
12	H_2O	1,488	6.72	80
13	4.3 μm CO_2	2,190	4.57	23
14	4.3 μm CO_2	2,210	4.52	23
15	4.3 μm CO_2	2,240	4.46	23
16	4.3 μm CO_2	2,270	4.40	23
17	4.3 μm CO_2	2,360	4.24	23
18	4.3 μm CO_2	2,515	4.00	35
19	Window	2,660	3.76	100
20	Window (visible)	14,500	0.69	1,000

From Kidder and Vonder Haar (1995).

Instead, the detector integration times are adjusted to be somewhat longer than those used on imagers, by moving the cross-track scanning mirror in steps, such that there are gaps of order 10 km between the individual 18.5-km ground footprints (scanspots) along a scanline. In addition, the sensor goes into calibration mode after each scanline, alternately viewing space, and then cold and warm internal calibration sources, each for a duration equivalent to one scanline. This results in alongtrack gaps of order 150 km between scanlines as projected onto the Earth's surface. These longer integration and calibration times, and the coarser spatial resolution versus an imager (AVHRR), are required to provide adequate *SNR* and radiometric accuracy for atmospheric profiling.

The MSU is designed to provide supplemental temperature soundings in the presence of cloud cover, using three channels in the 55-GHz O_2 emission band and one nearby window channel. The MSU frequencies are 50.03, 53.74, 54.96, and 57.95 GHz for channels 1–4, respectively. Although this instrument can "see through" clouds, the tradeoff is a much coarser spatial resolution (110 km at nadir), per the discussion in Section 2.8.

These NOAA polar orbiter sensor data have been cleverly processed into a valuable multi-decadal data product called the TOVS Pathfinder Path-B Dataset

(Scott et al., 1999). The remote-sensing algorithms used therein have steadily increased in sophistication over the project's duration, and these algorithms are now very instructive as to retrieving meteorological variables from multispectral and multi-band satellite data. The TOVS Pathfinder Path-B Dataset now comprises reliable retrievals of temperature and virtual temperature (K) at nine pressure intervals, total column precipitable water vapor (cm), precipitable water vapor above the pressure levels of 850, 700, 500, and 300 millibars, surface temperature, total cloud amount, cloud amounts between five different pressure intervals, and cloud top pressure and temperature. These retrievals are available on a $1^\circ \times 1^\circ$ latitude/longitude grid for all tropical and temperate latitudes. Here we discuss how these robust algorithms needed modification for application to the Arctic (Francis, 1994).

Conceptually, retrieval of most meteorological variables involves an inversion of the radiative transfer equation. Numerical methods must be chosen with care, as the associated collinearities among variables can be quite subtle, and spurious solutions are possible when analyzing real data with finite measurement uncertainties. An iterative inversion technique typically requires an intelligent "initial guess". The TOVS Pathfinder project accomplishes this on a near-global basis using a library of 2,300 model atmospheres derived from 150,000 radiosondes. A line-by-line radiative transfer model (Scott and Chédin, 1981) is used to calculate weighting functions (4.3), clear-sky transmittances, and specific intensities for all TOVS sensor bands, for 10 nadir-viewing angles between 0° and 60°, for 19 values of surface pressure to account for terrain elevation, and for land and sea. This massive volume of model atmosphere and radiative transfer simulation is collectively referred to as the Thermodynamic Initial Guess Retrieval (TIGR) dataset. For application to satellite data, the TIGR dataset is sorted into five airmass classes (one tropical, two mid-latitude, and two polar) for assigning initial guesses to individual observations.

At tropical and mid-latitudes, cloud detection over a warm and dark surface is relatively straightforward, using standard threshold and spatial coherence techniques (see, for example, Coakley and Bretherton, 1982; Stubenrauch et al., 1999), as compared with the polar challenges discussed above. However, given that the global mean cloud amount is $\sim$60%, it is not sufficient to simply eliminate cloudy pixels from analysis and attempt to derive a robust climatological dataset based only on cloud-free scenes. Some important meteorological variability would be missed. Fortunately, the combination of MSU measurements (which are basically insensitive to cloud) with the HIRS-2 measurements, allows for decontamination of many cloudy-sky intensity measurements. This is known as "cloud clearing". Individual HIRS-2 and MSU channels are paired based on mutual sensitivity to the same range in atmospheric pressure. The MSU brightness temperature, along with the initial first guess in specific intensity from the TIGR dataset, allows estimation of the intensity that would be measured by the corresponding HIRS-2 channel if the scene were cloud-free. Details of this procedure are given by Chédin et al. (1985). With either cloud-free or cloud-cleared data, an initial guess for the temperature profile is chosen by comparing the observation with intensity simulations from the appropriate

atmosphere class in the TIGR dataset, and constructing a trial atmosphere from the mean of model atmospheres corresponding to the closest simulated intensities.

For temperature profile retrieval, experience has taught that standard numerical approaches, such as a least squares minimization technique, can yield spurious solutions. Better results are obtained by using a priori knowledge to refine the minimization technique—in other words, Bayesian statistics. The TIGR dataset provides this a priori knowledge; from this dataset differential covariance matrices are calculated for each condition of observation, including surface pressure, nadir-viewing angle, surface type, clear or cloudy flag, atmosphere class, etc. Once the temperature profile has been retrieved, cloud top pressure and cloud amount are estimated using the CO_2-slicing technique (Wahiche et al., 1986). After clouds have been located in this manner, further cloud clearing is done for the HIRS-2 channels that are sensitive to both water vapor and temperature (channels 7, 8, 10–13, 18, 19). Surface temperature is retrieved from various HIRS-2 mid-IR window channels using knowledge of the emissivity properties of the various lower tropical and midlatitude surface types (land, open ocean). The final retrieval, for the precipitable water vapor profile, involves challenging nonlinearities that actually lend themselves well to a neural network approach (Figure 4.19). A neural network with one hidden layer of 15 nodes was found to be trainable by the TIGR dataset, such that the input layer consisting of four moisture-sensitive HIRS-2 channels (8, 10–12) and six 15-μm CO_2 band channels (2–7, for supplemental information on the temperature profile) could be reliably identified with an output layer consisting of precipitable water vapor contents in five layers. These water vapor retrievals are then transformed into the total column water vapor above the surface and the four pressure levels listed above. This is only a brief description of mid-latitude retrieval methods, given to illustrate the sophistication based on investigators' years of experience. Details can be found in the related references.

Despite the sophistication of the original (lower latitude) TOVS Pathfinder method, and its successful validation against independent meteorological data (Scott et al., 1999), initial application of the algorithms to Arctic data gave unsatisfactory results. Figure 4.65 compares the midlatitude algorithm temperature profile retrieval with co-located radiosonde data from the Coordinated Eastern ARctic Experiment (CEAREX Drift Group, 1990). The satellite algorithm completely misses near-surface temperature inversions, which are a key feature of polar meteorology. Francis (1994) set about adapting TOVS Pathfinder algorithms for Arctic application by taking steps to improve discrimination between open ocean and sea ice, cloud detection, and ice surface temperature retrieval.

The original algorithm attempted to identify sea ice using the 50.3-GHz (channel-1) measurement from MSU, given that sea ice has higher emissivity than open water at this frequency. Two techniques were used to estimate surface emissivity: (1) regression of MSU channel 1 against MSU channel 2, and (2) regression of MSU channel 1 against an HIRS-2 IR window channel (channel 8 during daylight, channel 18 at night). Over sea ice, Francis (1994) found that these techniques introduce an artificial nadir-viewing angle dependence in the retrieved emissivity, which invalidates most retrievals far from nadir. At the cross-track edge,

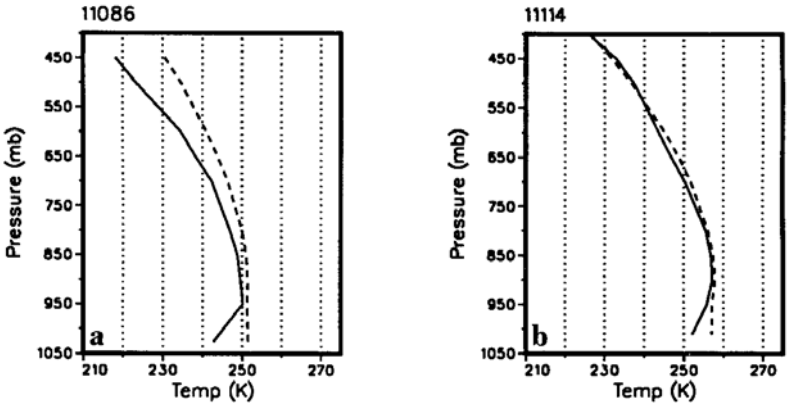

Figure 4.65. Examples of temperature profiles retrieved using the original mid-latitude TOVS Pathfinder algorithm (dashed curve) compared with co-located radiosonde data from CEAREX (solid). The retrieved and measured profiles are within 30 min and 50 km of each other.

From Francis (1994). Copyright 1994 American Geophysical Union. Reproduced by permission of American Geophysical Union.

emissivities estimated over areas known to be ice-covered were as low as ~0.7, which is the threshold for identifying open ocean. By inspecting numerous overlapping satellite passes of the central Arctic Ocean, the MSU channel-1 brightness temperature T_{B1} measured at a given location near nadir could be compared with another measurement from a preceding or following orbit, at the same location but with a larger nadir angle. A least squares regression of these co-located brightness temperature differences against nadir angle (Figure 4.66) yielded an empirical correction factor C_{MSU1} for the MSU channel-1 brightness temperature:

$$C_{MSU1} = -0.076\,514\theta + 0.003\,424\theta^2 \tag{4.61}$$

With this correction factor, more realistic emissivities are derived which allow for more accurate discrimination between sea ice and open water. First-year ice generally has a higher emissivity than multiyear ice (see Chapter 5), and a threshold emissivity of 0.88 is used to distinguish between them. Francis (1994) notes that one unavoidable source of error, even with this refinement, involves clouds with a significant ice phase or frozen precipitation. These clouds may fool the algorithm into identifying sea ice where there is open water.

In the original algorithm, there is a series of tests for cloud identification that are mutually reinforcing (Wahiche et al., 1986). Francis (1994) found that five of these tests needed to be modified or eliminated. These tests, and their Arctic modifications, are listed in Table 4.14. Two tests which utilized local spatial variability in small clusters of scan footprints were eliminated altogether. Over mid-latitudes, these tests work well over a warm surface with considerable spatial temperature uniformity. However, Arctic sea ice can exhibit considerable surface temperature variability on scales comparable with HIRS-2 footprints, due to variability in ice concentration,

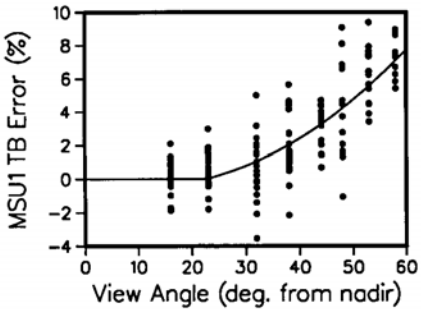

Figure 4.66. The error in MSU channel-1 brightness temperature as a function of nadir-viewing angle, determined from sequential satellite overpasses overlapping the same region. From Francis (1994). Copyright 1998 American Geophysical Union. Reproduced by permission of American Geophysical Union.

ice thickness, and the presence of leads. Thus the tests can yield erroneous discriminations between clear and cloudy skies, or vice versa, throughout the marginal ice zone. The normally effective technique of differencing MSU channel-2 brightness temperatures against a pseudo-MSU channel-2 measurement simulated using a regression of HIRS-2 channels 3–8 (pseudo-measurement is higher over cloudy skies) needed modification to its cloud detection threshold. Whereas a brightness temperature difference of 2 K was an adequate threshold over midlatitudes, a threshold of 0.8 K was found necessary in the Arctic. This latter threshold was chosen with reference to co-located AVHRR and OLS thermal images. Finally, the original algorithm contains several multispectral threshold tests that exploit brightness temperature differences in the mid-IR and 3.7-μm windows. Francis (1994) found that these needed to be modified for the Arctic along the lines of Yamanouchi and Kawaguchi's (1992) work on the Antarctic (Section 4.4.1). These refinements to Arctic cloud detection are evident in a comparison with CEAREX cloud observations (Figure 4.67).

The original algorithm missed low-level temperature inversions (Figure 4.67) primarily because its surface temperature retrievals over sea ice were too high. Francis (1994) traced this problem to a tendency of the algorithm to overestimate total column water vapor in the Arctic, which was an artifact of the simultaneous retrieval of both surface temperature and water vapor in an earlier version of the algorithm before the neural network was used (Chédin et al., 1985). If the "initial guess" model atmosphere contained too much water vapor in the mid- to upper troposphere, the resulting specific intensity in the window channels was too low compared with the measurements. Over the Arctic, the algorithm had a tendency to compensate for this by artificially raising the surface temperature. In clear skies, it was found that direct satellite measurements of the surface temperature were necessary, using HIRS-2 channels 18 and 19 (4.0 and 3.7 μm, respectively) during night and channel 8 (11.1 μm) during daylight, with appropriate corrections for surface emissivity and climatological water vapor. Validation against field measurements revealed r.m.s. errors of the order of 2 K with these direct

Table 4.14. Cloud detection tests in the original mid-latitude TOVS Pathfinder algorithm, and modifications made for the Arctic by Francis (1994).

Cloud test in 3I	Original test (brightness temperatures in K)	Modifications to cloud test for polar regions
3: Window channels test	Spot declared cloudy if Day: |HIRS18c − HIRS8c| > 12.0 Night: HIRS18c − HIRS8c > 2.5 or HIRS8c − HIRS18c > 4.0 or HIRS19c − HIRS18c > 3.0 or HIRS18c − HIRS19c > 4.0 (HIRS18c is HIRS18 corrected for water vapor and surface emissivity)	Spot declared cloudy if Sea ice day: HIRS19 − HIRS18 > 8.0 Sea ice night: HIRS19 − HIRS8c < 1.0 or HIRS19 − HIRS8c > 2.0 Cold land (HIRS8 < 260) day: HIRS19 − HIRS18 > 8.0 Cold land (HIRS8 < 260) night: HIRS19 − HIRS8c < −1.5 or HIRS19 − HIRS8c > 0.5 Warm land and open water same as original
4: Inter-channel regression test	Compares observed MSU2 T_B to MSU2 T_B computed by regression with HIRS 3, 4, 5, 6, 7, and 8. Spot declared cloudy if difference > 2.	Spot declared cloudy in polar and winter mid-latitude air masses if difference in observed and computed MSU2 > 0.8
6: HIRS8 − HIRS19 test	Spot declared cloudy if Night only: HIRS8 − HIRS19 > −0.5	Spot declared cloudy if Night only: HIRS8 − HIRS19 > −0.5 or HIRS8 − HIRS19 < −4.0
7: Adjacent spots test	Compares IR window channel T_Bs in two adjacent spots—if $\Delta T_B > 1.5$, spot declared cloudy	Test not performed over sea ice because leads may cause difference in T_Bs that is due to surface temperature differences rather than cloud cover differences
9: Maximum value test	Compares IR window channel T_B of each HIRS spot in a box to the max. T_B in the entire box – if $\Delta T_B > 4.0$, declared cloudy	Test not performed over sea ice for same reason given in number 7

observations, much better than the ~8-K discrepancies of Figure 4.66. Over cloudy skies, the HIRS-2 window channels cannot be used, and microwave data must be used instead. Comparing MSU measurements against CEAREX field observations, Francis (1994) discovered a nearly linear relationship between MSU channel-2 brightness temperature and surface temperature:

$$T_{ice} = -3.548\,369 T_{B2} + 0.019\,686 T_{B2}^2, \quad T_{B2} < 236\,\mathrm{K} \tag{4.62}$$

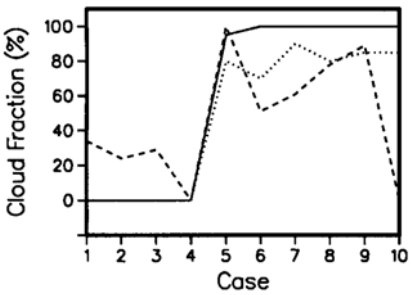

Figure 4.67. Cloud amount observed during CEAREX (solid) compared with satellite-retrieved cloud amount using the original mid-latitude TOVS Pathfinder algorithm (dashed) and the modified Polar Pathfinder algorithm following Table 4.12 (dotted).

which yields a useful satellite estimate of ice surface temperature T_{ice}. It is important to note that only ~10% of the MSU channel-2 signal comes directly from the ice. What makes this measurement correlate well with T_{ice} is the regulation of the T_{ice} by the downward-radiating warm atmospheric layer at the top of the temperature inversion (Overland and Guest, 1991), to which the MSU channel-2 measurement is quite sensitive. Thus (4.62) is an empirical result that is not valid when T_{B2} exceeds 236 K (in warmer conditions sensible heat transfer offsets surface heating by downwelling longwave radiation), and cannot be used in daylight (the surface is warmed significantly by insolation). Nevertheless, (4.62) allows for interpretation of large volumes of TOVS data.

The application of the Francis (1994) algorithms to more than two decades of atmospheric sounder data yields a wealth of exciting possibilities for Arctic climate research. As discussed by Francis (1994), useful retrievals of both surface temperature and tropospheric temperature profile enable estimates of surface heat and momentum transfer. Using the temperature, moisture, and cloud profiles as input data to a radiative transfer model, it is possible to extend the Pathfinder dataset to include retrievals of downwelling longwave fluxes (Francis, 1997). More recent analysis of the TOVS Polar Pathfinder dataset has yielded information about transport pathways for tropospheric water vapor into the high Arctic from lower latitudes (Figure 4.68; Groves and Francis, 2002). The SHEBA field campaign of 1998, mentioned several times already, provided a unique opportunity to validate the Polar Pathfinder dataset against rawinsonde and numerous other observations (Schweiger et al., 2002). This validation effort revealed that temperature profile retrievals are generally accurate to within 3 K (Figure 4.69), as are surface temperature retrievals. Total column water vapor was found to be accurate to within 2 mm annually (Figure 4.70). These uncertainties in temperature and moisture retrieval are smaller than intra-seasonal variability at all times of year. When compared with surface-based cloud amount measurements from lidar, the accuracy and validity of satellite-retrieved cloud amount increases with increasing timescales and is best for 5-day averages.

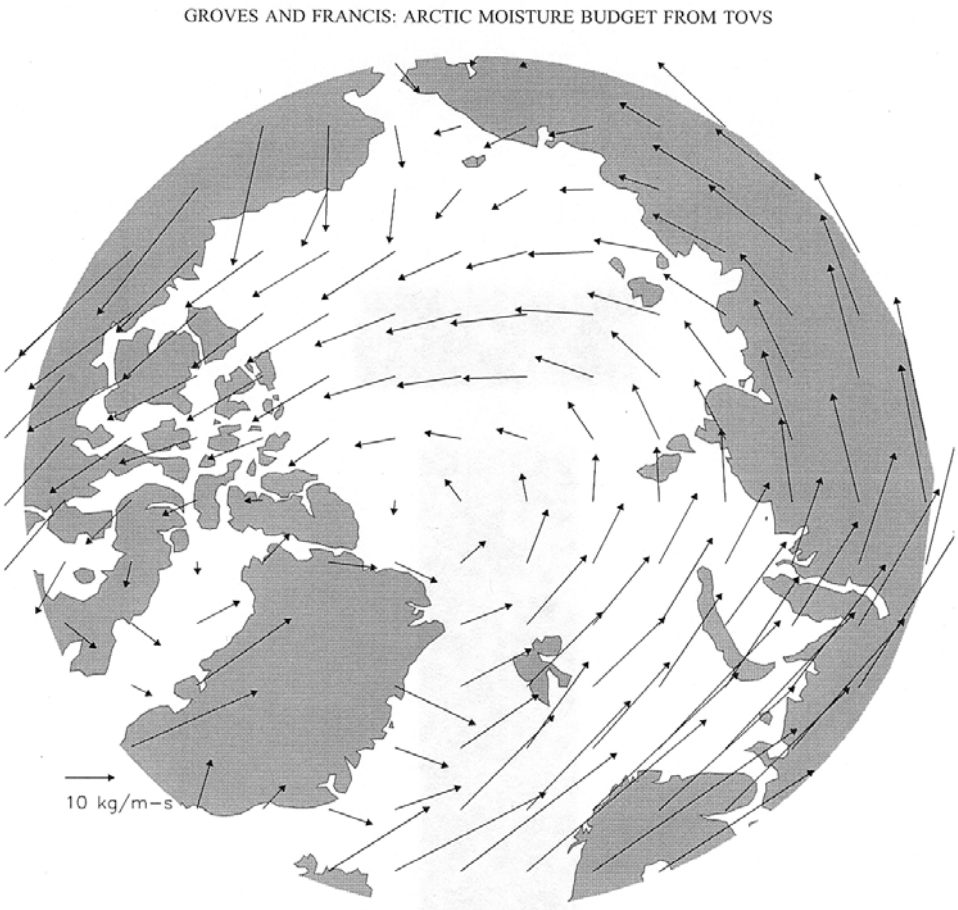

Figure 4.68. Annual mean (1980–1993) precipitable water vapor flux vectors derived by combining TOVS Polar Pathfinder water vapor profiles with National Center for Environmental Prediction (NCEP) reanalysis data for upper-level winds.

4.9 MODERN EXPERIMENTAL PROGRAMS

Successful validation of the Polar Pathfinder dataset brings us to a final but important discussion related to remote sensing for studies of polar meteorology and climate. Chapter 1 of this book noted how satellite remote sensing is in a period of transition to sensors with markedly improved capabilities. In the climate sciences, there has in recent years been a parallel transition in surface-based and *in situ* experimental programs. The complexity of the anthropogenic "global warming" issue, in which radiative flux changes of a few watts per square meter must be discerned from much larger radiative forcings due to tropospheric aerosols and

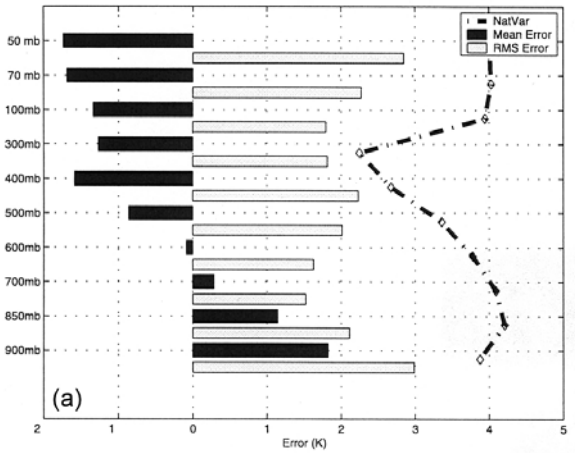
NatVar
Mean Error
RMS Error
50 mb
70 mb
100mb
300mb
400mb
500mb
600mb
700mb
850mb
900mb
(a)
2 1 0 1 2 3 4 5
Error (K)

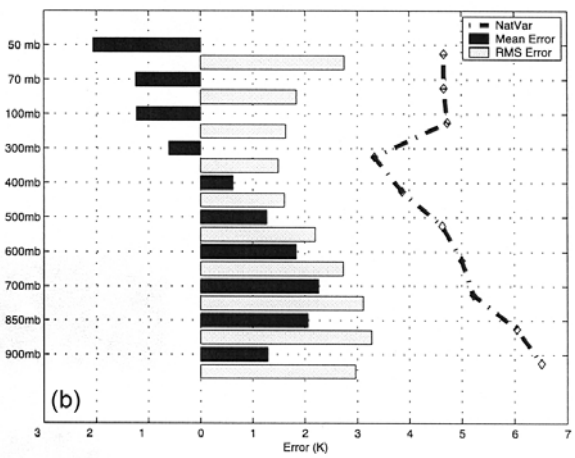
NatVar
Mean Error
RMS Error
50 mb
70 mb
100mb
300mb
400mb
500mb
600mb
700mb
850mb
900mb
(b)
3 2 1 0 1 2 3 4 5 6 7
Error (K)

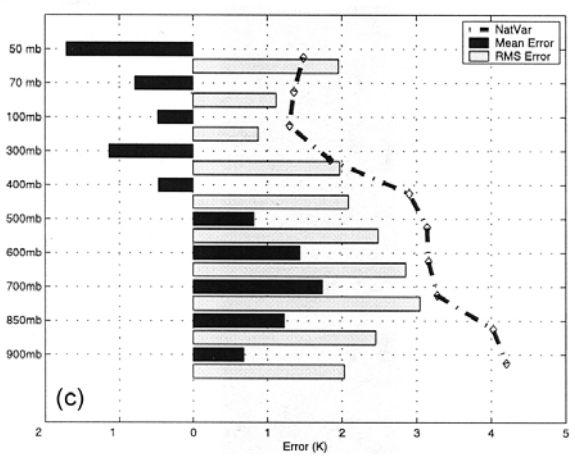
NatVar
Mean Error
RMS Error
50 mb
70 mb
100mb
300mb
400mb
500mb
600mb
700mb
850mb
900mb
(c)
2 1 0 1 2 3 4 5
Error (K)

◄ **Figure 4.69.** The mean and r.m.s. uncertainties in TOVS Polar Pathfinder retrievals of the vertical temperature profile (solid and shaded bars, respectively), compared with natural variability (heavy dashed line), for three seasons during SHEBA: (a) winter (DJF), (b) spring (MAM), (c) summer (JJA). During autumn there were too few measurements available to yield meaningful statistics.

clouds, has motivated a variety of rigorous experimental programs. The goals of these programs range from direct observation of specific phenomena, such as the climatic effects of aerosols as quantified by INDOEX (Ramanathan et al., 2001), to developing better representations of complex atmospheric and cloud physics in GCM simulations, which is a stated objective of the U.S. Department of Energy Atmospheric Radiation Measurement (ARM) program (Ackerman and Stokes, 2003). Often, the most robust of these experimental programs fulfill multiple scientific objectives, as when ARM program data were used to confirm the existence of the "cloud excess absorption" phenomenon (Valero et al., 2000), currently an issue of fundamental physical importance to atmospheric science (Cess et al., 1995; Ramanathan et al., 1995). For the remote-sensing scientist, these experimental programs offer high-quality measurements of atmospheric and cloud properties relevant to climate that can serve as validation data for remote-sensing methods.

For the polar regions, there are presently several surface-based measurement programs of interest. The ARM program established a "North Slope of Alaska" (NSA) site at Barrow, Alaska, in 1998 (Stamnes et al., 1999). The experimental concept behind the ARM sites is to construct a "Cloud And Radiation Testbed" (CART) by deploying state-of-the-art instrumentation at a central location, and

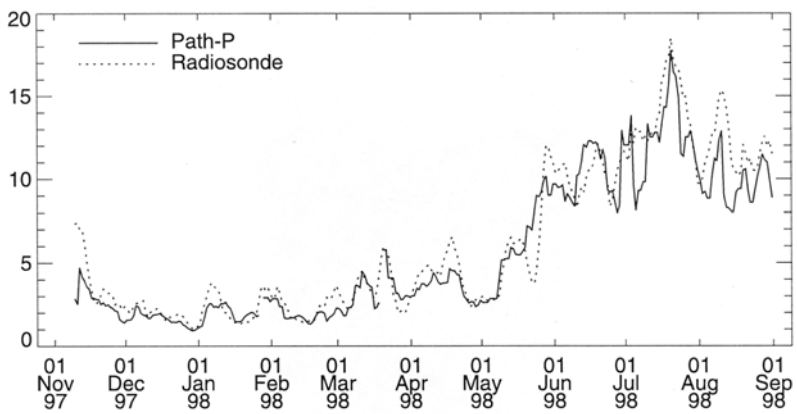

Figure 4.70. Comparison of total column water vapor from the Polar Pathfinder algorithm (solid curve) with radiosonde measurements (dotted) from SHEBA. Data are smoothed using a 5-day running mean.

subsets of this instrumental suite at surrounding remote locations, so that the entire measurement network resembles a GCM grid cell as closely as is practical. At the main location, the standard ARM measurements include a variety of broadband and multispectral shortwave radiometers, FTIR spectro-radiometers, whole-sky imagers, cloud radars, a backscatter lidar, and a microwave radiometer. These are supplemented by standard meteorological measurements including synoptic rawinsondes. At remote sites, broadband radiometers and meteorological instruments are typically deployed. The ARM program is presently using a combination of these various sensors to retrieve climatically relevant cloud properties with high accuracy. As the NSA site was being established, a parallel effort occurred in the SHEBA experiment (Perovich et al., 1999; Uttal et al., 2002). During SHEBA, many standard ARM instruments were deployed aboard the Canadian Coast Guard Ship *Des Groseilliers*, which was frozen into the ice pack in the Canadian Arctic during October 1997, and subsequently drifted in both west and northerly directions through the Beaufort Sea until October 1998. Several times during the SHEBA deployment, cloud properties were measured by overflying research aircraft (Curry et al., 2000). The SHEBA dataset will undoubtedly have lasting value for validating and refining satellite remote-sensing techniques using "heritage" sensors (Dong et al., 2001; Intrieri et al., 2002; Minnis et al., 2001). Similarly, ARM NSA data will be a primary validation source for the EOS (Earth Observing System) generation of remote sensors.

In Antarctica there is presently no surface-based measurement program as robust and multidisciplinary as ARM, but there are noteworthy efforts that should have considerable value for remote-sensing validation. In recent years, Professors S. G. Warren (University of Washington) and V. P. Walden (University of Idaho) have been expanding upon the FTIR measurement program that commenced at the South Pole during 1992 (Mahesh et al., 2001a, b). This program includes a new set of FTIR measurements, backscatter lidar measurements of cloud geometry and extinction in collaboration with NASA Goddard Space Flight Center's MicroPulse Lidar NETwork (MPLNET; Spinhirne, 1993), and direct microphysical observations of tropospheric ice particles (Walden et al., 2003). These measurements are supplemented by ongoing broadband radiation measurements at the South Pole (Dutton et al., 1991). Similarly, the British Antarctic Survey is commencing cloud microphysical observations on the Antarctic Peninsula, a location where orographic effects might influence cloud physics. Finally, the U.S. National Science Foundation has since 1988 maintained a network of solar UV spectro-radiometers at high latitudes in response to the springtime ozone decrease (Booth et al., 1994). These instruments can provide long time series retrievals of cloud optical depth and surface shortwave radiation components, suitable for satellite validation, following Leontyeva and Stamnes (1994), Lubin and Frederick (1991), and Stamnes et al. (1990).

In recent years, the World Wide Web (WWW) has greatly facilitated not only community awareness of experimental programs, but also access to their data. For example, in experimental programs supported by the U.S. National Science Foundation, it is now standard procedure for a central data repository and

archive to be established offering WWW data access, into which experimenters are required to migrate their data as soon as the data have been suitably quality checked. This trend is a significant improvement over the situation in past decades, where so much of the best experimental data remained "proprietary" among individual principal investigators and insider groups. Remote-sensing researchers can look forward to an increasingly versatile and readily accessible body of experimental data for algorithm validation in both polar regions.

4.10 REFERENCES

Aagaard, K., L. A. Barrie, E. C. Carmack, C. Garrity, E. P. Jones, D. Lubin, R. W. Macdonald, J. H. Swift, W. B. Tucker, P. A. Wheeler et al. (1996). U.S., Canadian researchers explore Arctic Ocean. *EOS Transactions of the American Geophysical Union*, **77**, 209.

Ackerman, A. S., O. B. Toon, D. E. Stevens, A. J. Heymsfield, V. Ramanathan, and E. J. Welton (2000). Reduction of tropical cloudiness by soot. *Science*, **288**, 1042–1047.

Ackerman, T. P. and G. M. Stokes (2003). The Atmospheric Radiation Measurement Program. *Physics Today*, **56**, 38–44.

Albrecht, B. A. (1989). Aerosols, cloud microphysics, and fractional cloudiness. *Science*, **245**, 1227–1230.

Allison, I., R. E. Brandt, and S. G. Warren (1993). East Antarctic sea ice: Albedo, thickness distribution, and snow cover. *Journal of Geophysical Research*, **98**(C7), 12417–12429.

Ball, F. K. (1956). The theory of strong katabatic winds. *Australian Journal of Physics*, **9**, 373–386.

Ball, F. K. (1960). Winds on the ice slopes of Antarctica. In: *Antarctic Meteorology, Proceedings of the Symposium, Melbourne, 1959*. Pergamon Press, New York, pp. 9–16.

Berque, J., D. Lubin, and R. C. J. Somerville (2004). Infrared radiative properties of the Antarctic Plateau from AVHRR data. Part I: Effect of the snow surface. *Journal of Applied Meteorology*, **43**, 350–362.

Blanchet, J.-P. and R. List (1983). Estimation of optical properties of Arctic haze using a numerical model. *Atmosphere–Ocean*, **21**, 444–465.

Booth, C. R., T. B. Lucas, J. H. Morrow, C. S. Weiler, and P. A. Penhale (1994). The United States National Science Foundation's polar network for monitoring ultraviolet radiation. *American Geophysical Union Antarctic Research Series*, **62**, 17–37.

Brandt, R. E., C. S. Roesler, and S. G. Warren (1999). Spectral albedo, absorptance, and transmittance of Antarctic sea ice. *Proceedings of the 5th Conference on Polar Meteorology and Oceanography*. American Meteorological Society, Boston, pp. 456–459.

Breckenridge, C. J., U. Radok, C. R. Stearns, and D. H. Bromwich (1993). Katabatic winds along the Transantarctic Mountains. In: D. H. Bromwich and C. R. Stearns (eds.), *Antarctic Meteorology and Climatology: Studies Based on Automatic Weather Stations* (AGU Antarctic Research Series No. 61). American Geophysical Union, Washington, DC, pp. 69–92.

Briegleb, B. P. (1992). Delta-Eddington approximation for solar radiation in the NCAR Community Climate Model. *Journal of Geophysical Research*, **97**(D7), 7603–7612.

Briegleb, B. P. and D. H. Bromwich (1998). Polar radiation budgets of the NCAR CCM3. *Journal of Climate*, **11**, 1246–1269.

Bromwich, D. H. (1989a). Satellite analyses of Antarctic katabatic wind behavior. *Bulletin of the American Meteorological Society*, **70**, 738–749.

Bromwich, D. H. (1989b). Satellite observations of katabatic winds blowing from Marie Byrd Land onto the Ross Ice Shelf. *Antarctic Journal of the United States*, **24**(5), 218–221.

Bromwich, D. H. and Z. Liu (1996). An observational study of the katabatic wind confluence zone near Siple Coast, West Anarctica. *Monthly Weather Review*, **124**, 462–477.

Bromwich, D. H. and C. R. Stearns (eds.) (1993). *Antarctic Climatology and Meteorology: Studies Based on Automatic Weather Stations* (AGU Antarctic Research Series No. 61). American Geophysical Union, Washington, DC, 207 pp.

Bromwich, D. H., T. R. Parish, A. Pellegrini, C. R. Stearns, and G. A. Weidner (1993). Spatial and temporal characteristics of the intense katabatic winds at Terra Nova Bay, Antarctica. In: D. H. Bromwich and C. R. Stearns (eds.), *Antarctic Meteorology and Climatology: Studies Based on Automatic Weather Stations* (AGU Antarctic Research Series No. 61). American Geophysical Union, Washington, DC, pp. 47–68.

Bromwich, D. H., J. F. Carrasco, and J. Turner (1996). A downward developing mesoscale cyclone over the Ross Ice Shelf during winter. *The Global Atmosphere and Ocean System*, **4**, 125–147.

Bromwich, D., Z. Liu, A. Rogers, and M. L. Van Woert (1998). Winter atmosphere forcing of the Ross Sea Polynya. In: *Ocean, Ice and Atmosphere: Interactions at the Antarctic Continental Margin* (AGU Antarctic Research Series No. 75). American Geophysical Union, Washington, DC, pp. 101–133.

Bromwich, D. H., R. I. Cullather, and R. W. Grumbine (1999). An assessment of the NCEP operational global spectral model forecasts and analyses for Antarctica during FROST. *Weather and Forecasting*, **14**, 835–850.

Bromwich, D. H., J. J. Cassano, T. Klein, G. Heinemann, K. M. Hines, K. Steffen, and J. E. Box (2001). Mesoscale modeling of katabatic winds over Greenland with the Polar MM5. *Monthly Weather Review*, **129**, 2290–2309.

Bromwich, D. H., A. J. Monaghan, J. G. Powers, J. J. Cassano, H.-L. Wei, Y.-H. Kuo, and A. Pellegrini (2003). Antarctic mesoscale prediction system (AMPS): A case study from the 2000–01 field season. *Monthly Weather Review*, **131**, 412–434.

Carleton, A. M. (1991). *Satellite Remote Sensing in Climatology*. CRC Press, Boca Raton, FL, 291 pp.

Carleton, A. M. and D. A. Carpenter (1989). Intermediate-scale sea ice–atmosphere interactions over high southern latitudes in winter. *Geo*, **18**, 87–101.

Carleton, A. M. and D. A. Carpenter (1990). Satellite climatology of "polar lows" and broadscale climatic associations for the Southern Hemisphere. *International Journal of Climatology*, **10**, 219–246.

Carleton, A. M. and Y. Song (1997). Synoptic climatology, and interhemispherical associations, of cold air mesocyclones in the Australasian sector. *Journal of Geophysical Research*, **102**(D12), 13873–13887.

Carrasco, J. F. and D. H. Bromwich (1993). Satellite and automatic weather station analyses of katabatic surges across the Ross Ice Shelf. In: D. H. Bromwich and C. R. Stearns (eds.), *Antarctic Meteorology and Climatology: Studies Based on Automatic Weather Stations* (AGU Antarctic Research Series No. 61). American Geophysical Union, Washington, DC, pp. 93–180.

Carrasco, J. F. and D. H. Bromwich (1996a). Mesoscale cyclone activity near Terra Nova Bay and Byrd Glacier, Antarctica, during 1991. *The Global Atmosphere and Ocean System*, **5**, 43–72.

Carrasco, J. F. and D. H. Bromwich (1996b). A study of mesoscale cyclone activity near the Antarctic Peninsula. *Serie Científica Instituto Antárctico Chileno*, **46**, 83–101.

Carrasco, J. F. and D. H. Bromwich (1997). A survey of mesocyclones near the Antarctic Peninsula using digital satellite imagery collected near Palmer Station. *Serie Científica Instituto Antárctico Chileno,* **47**, 39–57.

Carrasco, J. F., D. H. Bromwich, and Z. Liu (1997a). Mesoscale cyclone activity over Antarctica during 1991, 1: Marie Byrd Land. *Journal of Geophysical Research*, **102**(D12), 13923–13937.

Carrasco, J. F., D. H. Bromwich, and Z. Liu (1997b). Mesoscale cyclone activity during 1991, 2: Near the Antarctic peninsula. *Journal of Geophysical Research*, **102**(D12), 13939–13954.

Carrasco, J. F., D. H. Bromwich, and A. J. Monaghan (2003). Distribution and characteristics of mesoscale cyclones in the Antarctic: Ross Sea eastward to the Weddell Sea. *Monthly Weather Review*, **131**, 289–301.

Carsey, F. and H. Zwally (1986). Remote sensing as a research tool. In: N. Untersteiner (ed.), *The Geophysics of Sea Ice*. Plenum Press, New York, pp. 1021–1098.

Cassano, J. J., J. E. Box, D. H. Bromwich, L. Li, and K. Steffen (2001). Verification of Polar MM5 simulations of Greenland's atmospheric circulation. *Journal of Geophysical Research*, **106**(D24), 33867–33890.

Cavalieri, D. J., P. Gloersen, C. L. Parkinson, J. C. Comiso, and H. J. Zwally (1997). Observed hemispheric asymmetry in global sea ice changes, *Science*, **278**, 1104–1106.

CEAREX Drift Group (1990). CEAREX drift experiment (Coordinated Eastern ARctic EXperiment). *EOS Transactions of the American Geophysical Union*, **71**, 1115–1118.

Cess, R. D., M. H. Zhang, P. Minnis, L. Corsetti, E. G. Dutton, B. W. Forgan, D. P. Garber, W. L. Gates, J. J. Hack, E. F. Harrison et al. (1995). Absorption of solar radiation by clouds: Observations versus models. *Science*, **267**, 496–499.

Charlson, R. J., J. E. Lovelock, M. O. Andreae, and S. G. Warren (1987). Ocean phytoplankton, atmospheric sulfur, cloud albedo and climate. *Nature*, **326**, 655–661.

Chédin, A., N. A. Scott, C. Wahiche, and P. Moulinier (1985). The improved initialization inversion method: A high resolution physical method for temperature retrievals from satellites of the TIROS-N series. *Journal of Climate and Applied Meteorology*, **24**, 128–143.

Coakley, J. and C. Bretherton (1982). Cloud cover from high-resolution scanner data: Detecting and allowing from partially filled fields of view. *Journal of Geophysical Research*, **87**(C7), 4917–4932.

Collins, W. D., P. J. Rasch, B. E. Eaton, B. Khattatov, J.-F. Lamarque, and C. S. Zender (2001). Simulating aerosols using a chemical transport model with assimilation of satellite aerosol retrievals: Methodology for INDOEX. *Journal of Geophysical Research*, **106**(D7), 7313–7336.

Connors, R. W. and C. A. Harlow (1980). A theoretical comparison of texture algorithms. *IEEE Transactions on Pattern Analysis and Machine Intelligence*, **PAMI-2**, 204–222.

Crane, R. G. and R. G. Barry (1984). The influence of clouds on climate with a focus on high latitude interactions. *Journal of Climatololgy*, **4**, 71–93.

Curry, J. A. and P. J. Webster (1999). *Thermodynamics of Atmospheres and Oceans*. Academic Press, San Diego, 471 pp.

Curry, J. A., J. L. Schramm, M. C. Serreze, and E. E. Ebert (1995). Water vapor feedback over the Arctic Ocean. *Journal of Geophysical Research*, **100**(D7), 14223–14229.

Curry, J. A., P. V. Hobbs, M. D. King, D. A. Randall, P. Minnis, G. A. Isaac, J. O. Pinto, T. Uttal, A. Bucholtz, D. G. Cripe et al. (2000). FIRE Arctic Clouds Experiment. *Bulletin of the American Meteorological Society*, **81**, 5–29.

D'Aguanno, J. (1986). Use of AVHRR data for studying katabatic winds in Antarctica. *International Journal of Remote Sensing*, **7**, 703–713.

D'Almeida, G. A., P. Koepke, and E. P. Shettle (1991). *Atmospheric Aerosols: Global Climatology and Radiative Characteristics*. A Deepak, Hampton, VA, 559 pp.

Dong, X., G. G. Mace, P. Minnis, and D. F. Young (2001). Arctic stratus cloud properties and their impact on the surface radiation budget; Selected cases from FIRE ACE. *Journal of Geophysical Research*, **106(D14)**, 15297–15312.

Dozier, J. and S. G. Warren (1982). Effect of viewing angle on the infrared brightness temperature of snow. *Water Resources Research*, **18**, 1424–1434.

Draine, B. T. and P. J. Flatau (1994). Discrete dipole approximation for scattering calculations. *Journal of the Optical Society of America*, **A11**, 1491–1499.

Dutton, E. G., R. S. Stone, D. W. Nelson, and B. G. Mendonca (1991). Recent interannual variations in solar radiation, cloudiness, and surface temperature at the South Pole. *Journal of Climate*, **4**, 848–858.

Ebert, E. (1987). A pattern recognition technique for distinguishing surface and cloud types in the polar regions, *Journal of Climate and Applied Meteorology*, **26**, 1412–1427.

Francis, J. A. (1994). Improvements to TOVS retrievals over sea ice and applications to estimating Arctic energy fluxes. *Journal of Geophysical Research*, **99**(D5), 10395–10408.

Francis, J. A. (1997). A method to derive downwelling longwave fluxes at the Arctic surface from TIROS operational vertical sounder data. *Journal of Geophysical Research*, **102**(D2), 1795–1806.

Francis, J. A. and A. J. Schweiger (2000). A new window opens to the Arctic. *EOS Transactions of the American Geophysical Union*, **81**, 77–83.

Garrett, T. J., L. F. Radke, and P. V. Hobbs (2002). Aerosol effects on cloud emissivity and surface longwave heating in the Arctic. *Journal of the Atmospheric Sciences*, **59**, 769–778.

Godin, R. H. (1977). An investigation of synoptic and associated mesoscale patterns leading to significant weather days at McMurdo Station, Antarctica. M.S. thesis, Naval Postgraduate School, Monterey, CA, 114 pp.

Grenfell, T. C. and D. K. Perovich (1984). Spectral albedos of sea ice and incident solar irradiance in the Southern Beaufort Sea. *Journal of Geophysical Research*, **89**(C3), 3573–3580.

Grenfell, T. C., S. G. Warren, and P. C. Mullen (1994). Reflection of solar radiation by the Antarctic snow surface at ultraviolet, visible, and near-infrared wavelengths. *Journal of Geophysical Research*, **99**(D9), 18669–18684.

Grenfell, T. C. and S. G. Warren (1999). Representation of a nonspherical ice particle by a collection of independent spheres for scattering and absorption of radiation. *Journal of Geophysical Research*, **104**(D24), 31697–31709.

Groves, D. G. and J. A. Francis (2002). Moisture budget of the Arctic atmosphere from TOVS satellite data. *Journal of Geophysical Research*, **107**(D19), DOI: 10.1029/2001JD001191—ACL11-1-21.

Guo, Z., D. H. Bromwich, and J. J. Cassano (2003). Evaluation of Polar MM5 simulations of Antarctic atmospheric circulation. *Monthly Weather Review*, **131**, 384–411.

Han, Q., W. B. Rossow, and A. A. Lacis (1994). Near-global survey of effective droplet radius in liquid water clouds using ISCCP data. *Journal of Climate*, **7**, 465–497.

Han, W., K. Stamnes, and D. Lubin (1999). Remote sensing of surface and cloud properties in the Arctic from AVHRR measurements. *Journal of Applied Meteorology*, **38**, 989–1012.

Haralick, R. M. (1979). Statistical and structural approaches to texture. *Proceedings of the IEEE*, **67**, 786–804.

Haralick, R. M., K. S. Shanmugan, and I. Dinstein (1973). Textural features for image classification. *IEEE Transactions on Systems, Man and Cybernetics*, **SMC-3**, 610–621.

Harrington, J. Y., T. Reisin, W. R. Cotton, and S. M. Kreidenweis (1999). Cloud resolving simulations of Arctic stratus. Part II: Transition-season clouds. *Atmospheric Research*, **51**, 45–75.

Haywood, J. M. and V. Ramaswamy (1998). Global sensitivity studies of the direct radiative forcing due to anthropogenic sulfate and black carbon aerosols. *Journal of Geophysical Research*, **103**(D6), 6043–6058.

Haywood, J. M. and K. P. Shine (1995). The effect of anthropogenic sulfate and soot aerosol on the clear sky planetary radiation budget. *Geophysical Research Letters*, **22**, 603–606.

Hecht-Nielsen, R. (1990). *Neurocomputing*. Addison-Wesley, 430 pp.

Herman, G. F. and J. A. Curry (1984). Observational and theoretical studies of solar radiation in Arctic stratus clouds. *Journal of Climate and Applied Meteorology*, **23**, 5–24.

Herman, L. D. (1983). High frequency satellite cloud motion at high latitudes. *Proceedings of the 8th Symposium on Meteorological Observations and Instrumentation, American Meteorological Society, Anaheim, CA, 17–22 January*, pp. 465–468.

Herman, L. D. and F. W. Nagle (1994). A comparison of POES satellite derived winds techniques in the Arctic at CIMSS. *Proceedings of the 7th Conference on Satellite Meteorology and Oceanography, American Meteorological Society, Monterey, CA, 6–10 June*, pp. 444–447.

Hobbs, P. V. and A. L. Rangno (1998). Microstructures of low and middle-level clouds over the Beaufort Sea. *Quarterly Journal of the Royal Meteorological Society*, **124**, 2035–2071.

Hobbs, P. V., J. S. Reid, J. D. Herring, J. D. Nance, R. E. Weiss, J. L. Ross, D. A Hegg, R. D. Ottmar, and C. A. Liousse (1997). Particle and trace-gas measurements in the smoke from prescribed burns of forest products in the Pacific Northwest. In: J. S. Levine (ed.), *Biomass Burning and Global Change*. MIT Press, Cambridge, MA, pp. 697–715.

Hu, Y. X. and K. Stamnes (1993). An accurate parameterization of the radiative properties of water clouds suitable for use in climate models. *Journal of Climate*, **6**, 728–742.

Intrieri, J. M., C. W. Fairall, M. D. Shupe, P. O. G. Persson, E. L. Andreas, P. S. Guest, and R. E. Moritz (2002). An annual cycle of Arctic surface cloud forcing at SHEBA. *Journal of Geophysical Research*, **107**(C10), DOI: 10.1029/2000JC000439—SHE13-1-14.

IPCC (2001). *Climate Change 2001: The Scientific Basis* (International Panel on Climate Change). Cambridge University Press, New York, 881 pp.

Irvine, W. M. and J. B. Pollack (1968). Infrared optical properties of water and ice spheres. *Icarus*, **8**, 324–360.

Johannessen, O. M., E. V. Shalina, and M. W. Miles (1999). Satellite evidence for Arctic sea ice cover in transformation. *Science*, **286**, 1937–1939.

Kaufmann, Y. J., L. P. V. Hobbs, V. W. J. H. Kirchhoff, P. Artaxo, L. A. Remer, B. N. Holben, M. D. King, D. E. Ward, E. M. Prins, K. M. Longo et al. (1998). Smoke, clouds, and radiation-Brazil (SCAR-B) experiment. *Journal of Geophysical Research*, **103**(D24), 31783–31808.

Key, J. R. (1990). Cloud cover analysis with Arctic Advanced Very High Resolution Radiometer data, 2: Classification with spectral and textural measures. *Journal of Geophysical Research*, **95**(D6), 7661–7675.

Key, J. R. (1994). The area coverage of geophysical fields as a function of sensor field-of-view. *Remote Sensing of Environment*, **48**, 339–346.

Key, J. R. (1999). *The Cloud and Surface Parameter Retrieval (CASPR) System for Polar AVHRR*. Cooperative Institute for Meteorological Satellite Studies, University of Wisconsin, Madison, WI, 59 pp.

Key, J. R. and R. G. Barry (1989). Cloud cover analysis with Arctic AVHRR data, 1: Cloud detection. *Journal of Geophysical Research*, **94**(D15), 18521–18535.

Key, J.R. and M. Haefliger (1992). Arctic ice surface temperature retrieval from AVHRR thermal channels. *Journal of Geophysical Research*, **97**(D5), 5885–5893.

Key, J. R. and J. M. Intrieri (2000). Cloud particle phase determination with the AVHRR. *Journal of Applied Meteorology*, **39**, 1797–1804.

Key, J., J. A. Maslanik, and A. J. Schweiger (1989). Classification of merged AVHRR and SMMR Arctic data with neural networks. *Photogrammetric Engineering and Remote Sensing*, **55**, 1331–1338.

Key, J. and A. J. Schweiger (1998). Tools for atmospheric radiative transfer: Streamer and FluxNet. *Computers & Geoscience*, **24**, 443–451.

Key, J. R., A. J. Schweiger, and R. S. Stone (1997). Expected uncertainty in satellite-derived estimates of the surface radiation budget at high latitudes. *Journal of Geophysical Research*, **102**(C7), 15837–15847.

Key, J. R., C. S. Velden, and D. Santek (2001). High-latitude cloud-drift and water vapor winds from MODIS. *American Meteorological Society 6th Conference on Polar Meteorology and Oceanography*, 5B.7.

Kidder, S. Q. and T. H. Vonder Haar (1995). *Satellite Meteorology*. Academic Press, San Diego, 466 pp.

Kidwell, K. B. (1991). *NOAA Polar Orbiter Data User's Guide*. NOAA/NESDIS/NCDC (availiable from NOAA/NESDIS, 4401 Suitland Road, rm. 2069, Suitland, Maryland 20233).

Kiehl, J. T. and B. P. Briegleb, (1993). The relative roles of sulfate aerosols and greenhouse gases in climate forcing, *Science*, **260**, 311–314.

Keihl, J. T., T. L. Schneider, P. J. Rasch, M. C. Barth, and J. Wong (2000). Radiative forcing due to sulfate aerosols from simulations with the National Center for Atmospheric Research climate model, version 3. *Journal of Geophysical Research*, **105**(D1), 1441–1457.

King, J. C. and J. Turner (1997). *Antarctic Meteorology and Climatology*. Cambridge University Press, Cambridge, 409 pp.

King, M. D. (1987). Determination of the scaled optical thickness of clouds from reflected solar radiation measurements. *Journal of the Atmospheric Sciences*, **44**, 1734–1751.

Kneizys, F. X., E. P. Shettle, L. W. Abreu, J. H. Chetwynd, G. P. Anderson, W. O. Gallery, J. E. A. Selby, and S. A. Clough (1988). *User's Guide to LOWTRAN 7* (Rep. AFGL-TR-88-0177, Environmental Research Paper No. 1010). Air Force Geophysics Laboratory, Bedford, MA, 137 pp.

Koepke, P. (1989). Removal of atmospheric effects from AVHRR albedos. *Journal of Applied Meteorology*, **28**, 1341–1348.

Kondratyev, K. Ya., O. M. Johannessen, and V. V. Melentyev (1996). *High Latitude Climate and Remote Sensing*. Wiley/Praxis, Chichester, UK, 200 pp.

Ledley, T. S. (1993). Variations in snow on sea ice: A mechanism for producing climate variations. *Journal of Geophysical Research*, **98**(D6), 10401–10410.

Leese, J. A., C. S. Novak, and B. P. Clark (1971). An automated technique for obtaining cloud motion from geosynchronous satellite data using cross correlation. *Journal of Applied Meteorology*, **10**, 118–132.

Leontyeva, E. and K. Stamnes (1994). Estimations of cloud optical thickness from ground-based measurements of incoming solar radiation in the Arctic. *Journal of Climate.*, **7**, 566–578.

Li, Z. and H. G. Leighton (1992). Narrowband to broadband conversion with spatially autocorrelated reflectance measurement. *Journal of Applied Meteorology*, **31**, 421–433.

Li, Z., H. G. Leighton, and R. D. Cess (1993a). Surface net solar radiation estimated from satellite measurements: Comparisons with tower observations. *Journal of Climate*, **6**, 1764–1772.

Li, Z., H. G. Leighton, K. Masuda, and T. Takashima (1993b). Estimation of SW flux absorbed at the surface from TOA reflected flux. *Journal of Climate*, **6**, 317–330.

Light, B., H. Eicken, G. A. Maykut, and T. C. Grenfell (1998). The effect of included particulates on the spectral albedo of sea ice. *Journal of Geophysical Research*, **103**(C12), 27739–27752.

Liljequist, G. H. (1956). *Energy Exchange of an Antarctic Snow Field: Short-wave Radiation (Maudheim 71°03′S, 10°56′W), Volume 2, Part 1A: Norwegian–British–Swedish Antarctic Expedition, 1949–52, Scientific Results*. Norsk Polarinstitutt, Tromsø, Norway, 304 pp.

Lindsay, R. W. and D. A. Rothrock (1994a). Arctic sea ice albedo from AVHRR. *Journal of Climate*, **7**, 566–578.

Lindsay, R. W. and D. A. Rothrock (1994b). Arctic sea ice surface temperature from AVHRR. *Journal of Climate*, **7**, 174–183.

Liou, K. N. (1992). *Radiation and Cloud Processes in the Atmosphere*. Oxford University Press, New York, 487 pp.

Liu, Z. and D. H. Bromwich (1997). Dynamics of the katabatic wind confluence zone near Siple Coast, West Antarctica. *Journal of Applied Meteorology*, **36**, 97–118.

Lubin, D. (1994). Infrared radiative properties of the maritime Antarctic atmosphere. *Journal of Climate*, **7**, 121–140.

Lubin, D. and J. E. Frederick (1991). The ultraviolet radiation environment of the Antarctic Peninsula: The roles of ozone and cloud cover. *Journal of Applied Meteorology*, **30**, 478–493.

Lubin, D., and E. Morrow (1998). Evaluation of an AVHRR cloud detection and classification method over the central Arctic Ocean. *Journal of Applied Meteorology*, **37**, 166–183.

Lubin, D. and A. S. Simpson (1994). The longwave emission signature of urban pollution: Radiometric FTIR measurement. *Geophysical Research Letters*, **21**, 37–40.

Lubin, D. and P. J. Weber (1995). The use of cloud reflectance functions with satellite data for surface radiation budget estimation. *Journal of Applied Meteorology*, **34**, 1333–1347.

Lubin, D., P. Ricchiazzi, A. Payton, and C. Gautier (2002a). The significance of multidimensional radiative transfer effects measured in surface fluxes at an Antarctic coastline. *Journal of Geophysical Research*, **107**(D19), 4387, DOI: 10.1029/2001JD002030—AAC10-1-9.

Lubin, D., S. K. Satheesh, G. McFarquar, and A. J. Heymsfield (2002b). The longwave radiative forcing of Indian Ocean tropospheric aerosol. *Journal of Geophysical Research-Atmospheres*, **107**(D19), 4387, DOI: 10.1029/2001JD001183.

Mahesh, A., V. P. Walden, and S. G. Warren (2001a). Ground-based infrared remote sensing of cloud properties over the Antarctic Plateau, Part I: Cloud-base heights. *Journal of Applied Meteorology*, **40**, 1265–1278.

Mahesh, A., V. P. Walden, and S. G. Warren (2001b). Ground-based infrared remote sensing of cloud properties over the Antarctic Plateau, Part II: Cloud optical depths and particle sizes. *Journal of Applied Meteorology*, **40**, 1279–1294.

Maykut, G. A. (1982). Large-scale heat exchange and ice production in the central Arctic. *Journal of Geophysical Research*, **87**(C10), 7971–7984.

McClain, E. P., W. G. Pichel, and C. C. Walton (1985). Comparative performance of AVHRR-based multichannel sea surface temperatures. *Journal of Geophysical Research*, **90**(C6), 11587–11601.

McFarquar, G. J. and A. J. Heymsfield (2001). Parameterizations of INDOEX microphysical measurements and calculations of cloud susceptibility: Applications for climate studies. *Journal of Geophysical Research*, **106**, 28675–28698.

Menzel, W. P. (2001). Cloud tracking with satellite imagery: From the pioneering work of Ted Fujita to the present. *Bulletin of the American Meteorological Society*, **82**, 33–47.

Menzel, W. P., W. L. Smith, and T. R. Stewart (1983). Improved cloud motion wind vector and altitude assignment using VAS. *Journal of Climate and Applied Meteorology*, **22**, 377–384.

Meywerk, J. and V. Ramanathan (1999). Observations of the spectral clear-sky aerosol forcing over the tropical Indian Ocean. *Journal of Geophysical Research*, **104**(D20), 24359–24370.

Minnis, P., V. Chakrapani, D. R. Doelling, L. Nguyen, R. Palikonda, D. A. Spangenberg, T. Uttal, R. F. Arduini, and M. Shupe (2001). Cloud coverage during FIRE ACE derived from AVHRR Data. *Journal of Geophysical Research*, **106**(D14), 15215–15233.

Mischenko, M. I., I. V. Geogdzhayev, B. Cairns, W. B. Rossow, and A. A. Lacis (1999). Aerosol retrievals over the ocean by use of channels 1 and 2 AVHRR data: Sensitivity analysis and preliminary results. *Applied Optics*, **38**, 7325–7341.

Mo, K. C., J. Pfaendtner, and E. Kalnay (1987). A GCM study on the maintenance of the June 1982 blocking in the Southern Hemisphere. *Journal of the Atmospheric Sciences*, **44**, 1123–1142.

Morel, P., M. Desbois, and G. Szewach (1978). A new insight into the troposphere with the water vapor channel of Meteosat. *Bulletin of the American Meteorological Society*, **59**, 711–714.

Moritz, R. E., C. M. Bitz, and E. J. Stieg (2002). Dynamics of recent climate change in the Arctic. *Science*, **297**, 1497–1502.

Morley, B. M., E. E. Uthe, and W. Viezee (1989). Airborne lidar observations of clouds in the Antarctic troposphere. *Geophysical Research Letters*, **16**, 491–494.

Nakajima, T. and M. D. King (1990). Determination of the optical thickness and effective particle radius of clouds from reflected solar radiation measurements, Part I: Theory. *Journal of the Atmospheric Sciences*, **47**, 1878–1893.

Nakajima, T., M. D. King, J. D. Spinhirne, and L. F. Radke (1991). Determination of the optical thickness and effective particle radius of clouds from reflected solar radiation measurements, Part II: Marine stratocumulus observations. *Journal of the Atmospheric Sciences*, **48**, 728–750.

Nemesure, S., R. D. Cess, E. G. Dutton, J. J. DeLuisi, Z. Li, and H. G. Leighton (1994). Impact of clouds on the shortwave radiation budget of the surface–atmosphere system for snow-covered surfaces. *Journal of Climate*, **7**, 579–585.

Nieman, S. J., W. P. Menzel, C. M. Hayden, D. Gray, S. T. Wanzong, C. S. Velden, and J. Daniels (1997). Fully automated cloud-drift winds in NESDIS operations. *Bulletin of the American Meteorological Society*, **78**, 1121–1133.

Nilsson, B. (1979). Meteorological influence on aerosol extinction in the 0.2-40-μm wavelength range. *Applied Optics*, **18**, 3457–3473.

O'Dowd, C. D. and M. H. Smith (1993). Physico-chemical properties of aerosols over the Northeast Atlantic: Evidence for wind-speed-related sub-micron sea salt aerosol production. *Journal of Geophysical Research*, **98**(D1), 1137–1149.

Olsson, P. Q., J. Y. Harrington, G. Feingold, W. R. Cotton, and S. M. Kreidenweis (1998). Exploratory cloud-resolving simulations of boundary-layer Arctic stratus clouds, Part I: Warm-season clouds. *Atmospheric Research*, **48**, 573–597.

Overland, J. E. and P. S. Guest (1991). The Arctic snow and air temperature budget over sea ice during winter. *Journal of Geophysical Research*, **96**(C3), 4651–4662.

Overland, J. E., M. Wang, and N. A. Bond (2002). Recent temperature changes in the Western Arctic during spring. *Journal of Climate*, **15**, 1702–1716.

Parish, T. R. and D. H. Bromwich (1987). The surface windfield over the Antarctic ice sheets. *Nature*, **328**, 51–54.

Parish, T. R. and D. H. Bromwich (1989). Instrumented aircraft observations of the katabatic wind regime near Terra Nova Bay. *Monthly Weather Review*, **117**, 1570–1585.

Perovich, D. K., E. L. Andrews, J. A. Curry, H. Eiken, C. W. Fairall, T. C. Grenfell, P. S. Guest, J. Intrieri, D. Kadko, R. W. Lindsay et al. (1999). Year on ice gives climate insights. *EOS Transactions of the American Geophysical Union*, **80**, 481–486.

Pilewskie, P. and F. P. J. Valero (1993). Optical depths and haze particle sizes during AGASP III. *Atmospheric Environment*, **27A**, 2895–2899.

Pinto, J. O. (1998). Autumnal mixed-phase cloudy boundary layers in the Arctic. *Journal of the Atmospheric Sciences*, **55**, 2016–2038.

Platnick, S. and S. Twomey (1994). Determining the susceptibility of cloud albedo to changes in droplet concentration with the AVHRR. *Journal of Applied Meteorology*, **33**, 334–347.

Platnick, S., J. Y. Li, M. D. King, H. Gerber, and P. Hobbs (2001). A solar reflectance method for retrieving the optical thickness and droplet size for liquid water clouds over snow and ice surfaces. *Journal of Geophysical Research*, **106**(D14), 15185–15199.

Polissar, A. V., P. K. Hopke, W. C. Malm, and J. F. Sisler (1998). Atmospheric aerosol over Alaska, I: Spatial and seasonal variability. *Journal of Geophysical Research*, **103**(D15), 19035–19044.

Rajeev, K. and V. Ramanathan (2001). Direct observations of clear-sky aerosol radiative forcing from space during the Indian Ocean Experiment. *Journal of Geophysical Research*, **106**(D15), 17221–17235.

Ramanathan, V., R. D. Cess, E. F. Harrison, P. Minnis, B. R. Barkstrom, E. Ahmad, and D. Hartmann (1989). Cloud-radiative forcing and climate: Results from the Earth Radiation Budget Experiment. *Science*, **243**, 57–63.

Ramanathan, V., B. Subasilar, G. J. Zhang, W. Conant, R. D. Cess, J. T. Kiehl, H. Grassl, and L. Shi (1995). Warm pool head budget and short-wave cloud forcing: A missing physics? *Science*, **267**, 499–503.

Ramanathan, V., P. J. Crutzen, J. Lelieveld, A. P. Mitra, D. Althausen, J. Anderson, M. O. Andreae, W. Cantrell, G. R. Cass, C. E. Chung et al. (2001). Indian Ocean experiment: An integrated analysis of the climate forcing and effects of the great Indo-Asian haze. *Journal of Geophysical Research*, **106**(D22), 28371–28398.

Rigor, I. G., R. L. Colony, and S. Martin (2000). Variations in surface air temperature observations in the Arctic, 1979–97. *Journal of Climate*, **13**, 896–914.

Rosenfeld, D. (2000). Suppression of rain and snow by urban and industrial air pollution. *Science*, **287**, 1793–1796.

Rossow, W. B., A. W. Walker, D. E. Beuschel, and M. D. Roiter (1996). *International Satellite Cloud Climatology Project (ISCCP) Documentation of New Cloud Datasets*. World Meteorological Organization, Geneva, 115 pp.

Saxena, V. K. and F. H. Ruggiero (1990). *Antarctic Coastal Stratus Clouds: Microstructure and Acidity* (AGU Antarctic Research Series No. 50). American Geophysical Union, Washington, DC, pp. 7–18.

Schwalb, A. (1978). *The TIROS-N/NOAA A-G Satellite Series* (NOAA Tech. Memo. NESS-95). U.S. Department of Commerce, Washington, DC, 95 pp.

Schweiger, A. J. and J. R. Key (1994). Arctic Ocean radiative fluxes and cloud forcing estimated from the ISCCP C2 cloud dataset, 1983–1990. *Journal of Applied Meteorology*, **33**, 948–963.

Schweiger, A. J., R. W. Lindsay, J. R. Key, and J. A. Francis (1999). Arctic clouds in multiyear satellite data sets. *Geophysical Research Letters*, **26**, 1845–1848.

Schweiger, A. J., R. W. Lindsay, J. A. Francis, J. Key, J. M. Intrieri, and M. D. Shupe (2002). Validation of TOVS Path-P data during SHEBA. *Journal of Geophysical Research*, **107**(C10), DOI: 10.1029/2000JC000453—SHE17-1-20.

Schwerdtfeger, W. (1984). *Weather and Climate of the Antarctic*. Elsevier, Amsterdam, 261 pp.

Scott, N. A. and A. Chédin (1981). A fast line-by-line method for atmospheric absorption computations: The "4A" Automatized Atmospheric Absorption Atlas. *Journal of Applied Meteorology*, **20**, 801–812.

Scott, N. A., A. Chédin, R. Armante, J. Francis, C. Stubenrauch, J.-P. Charboneau, F. Chevalier, C. Claud, and F. Cheruy (1999). Characteristics of the TOVS Pathfinder Path-B Dataset. *Bulletin of the American Meteorological Society*, **80**, 2679–2701.

Shaw, G. E. (1982). Atmospheric turbidity in the polar regions. *Journal of Applied Meteorology*, **21**, 1080–1088.

Shindell, D. T., R. L. Miller, G. A. Schmidt, and L. Pandolfo (1999). Simulation of recent northern winter climate trends by greenhouse-gas forcing. *Nature*, **399**, 452–455.

Slingo, A., S. Nicholls, and J. Schmetz (1982). Aircraft observations of marine stratocumulus during JASIN. *Quarterly Journal of the Royal Meteorological Society*, **108**, 833–856.

Smith, S. R. and C. R. Stearns (1993). Antarctic climate anomalies surrounding the minimum in the Southern Oscillation Index. In: D. H. Bromwich and C. R. Stearns (eds.), *Antarctic Climatology and Meteorology: Studies Based on Automatic Weather Stations* (AGU Antarctic Research Series No. 61). American Geophysical Union, Washington, DC, pp. 149–174.

Smith, W. L., H. M. Woolf, and W. L. Jacob (1970). A regression method for obtaining real-time temperature and geopotential height profiles from satellite spectrometer measurements and its application to Nimbus-3SIRS observations. *Monthly Weather Review*, **98**, 604–611.

Smith, W. L., H. M. Woolf, C. M. Hayden, D. Q. Wark, and L. M. McMillin (1979). The TIROS-N operational vertical sounder. *Bulletin of the American Meteorological Society*, **60**, 1177–1187.

Sokolik, I. N. and O. B. Toon (1999). Incorporation of mineralogical composition into models of the radiative properties of mineral aerosol from UV to IR wavelengths. *Journal of Geophysical Research*, **104**(D8), 9423–9444.

Somerville, R. C. J. and L. A. Remer (1984). Cloud optical depth feedbacks in the CO_2 climate problem. *Journal of Geophysical Research*, **89**(D6), 9668–9672.

Spinhirne, J. D. (1993). Micro pulse lidar. *IEEE Transactions on Geoscience and Remote Sensing*, **31**, 48–55.

Stamnes, K., J. Slusser, M. Bowen, C. R. Booth, and T. Lucas (1990). Biologically effective ultraviolet radiation, total ozone abundance, and cloud optical depth at McMurdo Station, Antarctica, September 15, 1988 through April 15, 1989. *Geophysical Research Letters*, **17**, 2181–2184.

Stamnes, K., R. G. Ellingson, J. A. Curry, J. E. Walsh, and B. D. Zak (1999). Review of science issues, deployment strategy, and status for the ARM North Slope of Alaska—Adjacent Arctic Ocean Climate Research Site. *Journal of Climate*, **12**, 46–63.

Stearns, C. R. and M. A. Lazzara (1999). Six years of composite infra-red images south of Forty South at three hourly intervals. *Abstracts, IUGG 99 Conference, Birmingham, UK*. International Union of Geodesy and Geophysics, Boulder, CO, p. B119.

Stearns, C. R., L. M. Keller, G. A. Weidner, and M. Sievers (1993). Monthly mean climatic data for Antarctic automatic weather stations. In: D. H. Bromwich and C. R. Stearns (eds.), *Antarctic Climatology and Meteorology: Studies Based on Automatic Weather Stations* (AGU Antarctic Research Series No. 61). American Geophysical Union, Washington, DC, pp. 1–21.

Stephens, G. L. (1978). Radiation profiles in extended water clouds, II: Parameterization schemes. *Journal of the Atmospheric Sciences*, **35**, 2123–2132.

Stephens, G. L. and C. M. R. Platt (1987). Aircraft observations of the radiative and microphysical properties of stratocumulus and cumulus cloud field. *Journal of Applied Meteorology*, **26**, 1243–1269.

Stone, R., T. Mefford, E. Dutton, E. Longenecker, B. Halter, and D. Endres (1996). *Barrow Surface Radiation Balance Measurements, January 1992 to December 1994* (NOAA Data Report ERL CMDL-11). U.S. Department of Commerce, Washington, DC, 81 pp.

Stone, R. S. (1993). Properties of austral winter clouds derived from radiometric profiles at the South Pole. *Journal of Geophysical Research*, **98**(C7), 12961–12971.

Stroeve, J., A. Nolin, and K. Steffen (1997). Comparison of AVHRR-derived and *in situ* surface albedo over the Greenland ice sheet. *Remote Sensing of Environment*, **62**, 262–276.

Stubenrauch, C. J., W. B. Rossow, F. Cheruy, N. A. Scott, and A. Chédin (1999). Clouds as seen by satellite sounders (3I) and imagers (ISCCP), Part I: Evaluation of cloud parameters. *Journal of Climate*, **12**, 2189–2213.

Suttles, J. T., R. N. Green, P. Minnis, G. L. Smith, W. F. Staylor, B. A. Wielicki, I. J. Walker, D. F. Young, V. R. Taylor, and L. L. Stowe (1988). *Angular Radiation Models for Earth–Atmosphere System, Vol. I: Shortwave Radiation* (NASA Reference Publication No. 1184). National Aeronautics and Space Administration, Washington, DC, 144 pp.

Swithinbank, C. (1973). Higher resolution satellite pictures. *Polar Record*, **16**, 739–751.

Taylor, J. R. (1982). *An Introduction to Error Analysis*. University Science Books, Mill Valley, CA, 270 pp.

Taylor, V. R. and L. L. Stowe (1984). *Atlas of Reflectance Patterns for Uniform Earth and Cloud Surfaces (Nimbus-7 ERB-61 days)* (NOAA Tech. Rep. NESDIS No. 10). National Oceanic and Atmospheric Administration, Silver Spring, MD, 66 pp.

Tegen, I., A. A. Lacis, and I. Fung (1996). The influence on climate forcing of mineral aerosols from disturbed soils. *Nature*, **380**, 419–422.

Thomason, L. W., A. B. Herber, T. Yamanouchi, and K. Sato (2003). Arctic study on tropospheric aerosol and radiation: Comparison of tropospheric aerosol extinction

profiles measured by airborne photometer and SAGE II. *Geophysical Research Letters*, **30**, 1328–1331.

Thompson, D. W. J. and S. Solomon (2002). Interpretation of recent Southern Hemisphere climate change. *Science*, **296**, 895–899.

Thompson, D. W. J. and J. M. Wallace (1998). The Arctic Oscillation signature in the wintertime geopotential height and temperature fields. *Geophysical Research Letters*, **25**, 1297–1300.

Thompson, D. W. J. and J. M. Wallace (2000). Annular modes in the extratropical circulation, Part I: Month-to-month variability. *Journal of Climate*, **13**, 1000–1016.

Thompson, D. W. J. and J. M. Wallace (2001). Regional climate impacts of the Northern Hemisphere annular mode. *Science*, **293**, 85–89.

Trenberth, K. E. (1980). Planetary waves at 500 mb in the Southern Hemisphere. *Monthly Weather Review*, **108**, 1378–1389.

Tsay, S.-C. and K. Jayaweera (1984). Physical characteristics of Arctic stratus clouds. *Journal of Applied Meteorology*, **23**, 584–596.

Tsay, S.-C., K. Stamnes, and K. Jayaweera (1989). Radiative energy budget in the cloudy and hazy Arctic. *Journal of the Atmospheric Sciences*, **46**, 1002–1018.

Turner, J. and D. E. Warren (1989). Cloud track winds in the polar regions from sequences of AVHRR images. *International Journal of Remote Sensing*, **10**, 695–703.

Twomey, S. (1977). The influence of pollution on the short wave albedo of clouds. *Journal of the Atmospheric Sciences*, **34**, 1149–1152.

Uttal, T., J. A. Curry, M. G. McPhee, D. K. Perovich, R. E. Moritz, J. A. Maslanik, P. S. Guest, H. L. Stern, J. A. Moore, R. Turenne et al. (2002). Surface heat budget of the Arctic Ocean. *Bulletin of the American Meteorological Society*, **83**, 255–275.

Valero, F. P. J., T. P. Ackerman, and W. J. Y. Gore (1984). The absorption of solar radiation by the Arctic atmosphere during the haze season and its effects on the radiation balance. *Geophysical Research Letters*, **11**, 465–468.

Valero, F. P. J., T. P. Ackerman, W. J. Y. Gore, and M. L. Weil (1988). Radiation studies in the Arctic. In: *Aerosols and Climate*. A. Deepak, Hampton, VA.

Valero, F. P. J., P. Minnis, S. K. Pope, A. Bucholtz, B. C. Bush, D. R. Doelling, W. L. Smith Jr., and X. Dong (2000). Absorption of solar radiation by the atmosphere as determined using satellite, aircraft, and surface data during the Atmospheric Radiation Measurement Enhanced Shortwave Experiment (ARESE). *Journal of Geophysical Research*, **105**(D4), 4743–4758.

van de Hulst, H. C. (1957). *Light Scattering by Small Particles*. Dover, New York, 470 pp.

Velden, C. S., C. M. Hayden, S. J. Nieman, W. P. Menzel, S. Wanzong, and J. S. Goerss (1997). Upper-tropospheric winds derived from geostationary satellite water vapor observations. *Bulletin of the American Meteorological Society*, **78**, 173–195.

Wahiche, C., N. A. Scott, and A. Chédin (1986). Cloud detection and cloud parameters retrieval from satellites of the TIROS-N series. *Ann. Geophys.*, **4**, 207–222.

Walden, V. P., S. G. Warren, and F. J. Murcray (1998). Measurements of the downward longwave radiation spectrum over the Antarctic Plateau and comparisons with a line-by-line radiative transfer model for clear skies. *Journal of Geophysical Research*, **103**(D4), 3825–3846.

Walden, V. P., S. G. Warren, and E. Tuttle (2003). Atmospheric ice crystals over the Antarctic Plateau in winter. *Journal of Applied Meteorology*, **42**, 1391–1405.

Wang, X. and J. R. Key (2003). Recent trends in Arctic surface, cloud, and radiation properties from space. *Science*, **299**, 1725–1728.

Warren, S. G. (1982). Optical properties of snow. *Reviews of Geophysics and Space Physics*, **20**, 67–89.

Warren, S. G. (1984a). Optical constants of ice from the ultraviolet to the microwave. *Applied Optics*, **23**, 1206–1223.

Warren, S. G. (1984b). Impurities in snow: Effects on albedo and snowmelt. *Annals of Glaciology*, **5**, 177–179.

Warren, S. G. and A. D. Clarke (1990). Soot in the atmosphere and snow surface of Antarctica. *Journal of Geophysical Research*, **95**(D2), 1811–1816.

Warren, S. G. and W. J. Wiscombe (1980). A model for the spectral albedo of snow, Part II: Snow containing atmospheric aerosols. *Journal of the Atmospheric Sciences*, **37**, 2734–2745.

Warren, S. G., S. C. Roesler, and R. E. Brandt (1997). Solar radiation processes in the East Antarctic sea ice zone. *Antarctic Journal of the United States (Annual Review)*, **32**, 185–187.

Warren, S. G., C. J. Hahn, J. London, R. M. Chervin, and R. L. Jenne (1988). *Global Distributions of Total Cloud Cover and Cloud Type Amounts over the Ocean* (NCAR TN-317+STR). National Center for Atmospheric Research, Boulder, CO, 288 pp.

Weinreb, M. P., G. Hamilton, and S. Brown (1990). Nonlinearity corrections in calibration of Advanced Very High Resolution Radiometer infrared channels. *Journal of Geophysical Research*, **95**(C5), 7381–7388.

Welch, R. M., S. K. Sengupta, A. K. Goroch, P. Rabindra, N. Rangaraj, and M. S. Navar (1992). Polar cloud and surface classification using AVHRR imagery: An intercomparison of methods. *Journal of Applied Meteorology*, **31**, 405–420.

Wendler, G., J. C. André, P. Pettré, J. Gosnik, and T. Parish (1993). Katabatic winds in Adélie Coast. In: D. H. Bromwich and C. R. Stearns (eds.), *Antarctic Meteorology and Climatology: Studies Based on Automatic Weather Stations* (AGU Antarctic Research Series No. 61). American Geophysical Union, Washington, DC, pp. 23–46.

Weszka, J. S., C. R. Dyer, and A. Rosenfeld (1976). A comparative study of texture measures for terrain classification. *IEEE Transactions on Systems, Man and Cybernetics*, **SMC-6**, 2269–2285.

Wiscombe, W. J. and S. G. Warren (1980). A model for the spectral albedo of snow, Part I: Pure snow, *Journal of the Atmospheric Sciences*, **37**, 2712–2733.

Xiong, X., W. Li, D. Lubin, and K. Stamnes (2002a). Evaluating the principles of cloud remote sensing with AVHRR and MAS imagery over SHEBA. *Journal of Geophysical Research*, **107**(C10), 8036, DOI: 10.1029/2000JC000424—SHE10-1-13.

Xiong, X., D. Lubin, W. Li, and K. Stamnes (2002b). A critical examination of satellite cloud retrieval from AVHRR in the Arctic using SHEBA data. *Journal of Applied Meteorology*, **41**, 1195–1209.

Xiong, X., K. Stamnes, and D. Lubin (2002c). Surface albedo over the Arctic Ocean derived from AVHRR and its validation with SHEBA data. *Journal of Applied Meteorology*, **41**, 413–425.

Yamanouchi, T. and T. P. Charlock (1995). Comparison of radiation budget at the TOA and surface in the Antarctic from ERBE and ground surface measurements. *Journal of Climate*, **8**, 3109–3120.

Yamanouchi, T. and S. Kawaguchi (1992). Cloud distribution in the Antarctic from AVHRR data and radiation measurements at the surface. *International Journal of Remote Sensing*, **13**, 111–127.

5

Sea ice

5.1 INTRODUCTION

Sea ice is awesomely beautiful, ever varying. It has long captured the imagination—as well as the ships—of intrepid explorers. Once encountered, never forgotten. Beyond the poetic domain, the vast and variable sea ice cover of the polar oceans occupies a unique and critical niche not only in the high-latitude but also the global climate system, and plays a dominant role in shaping polar–marine ecosystems. The polar oceans remain, however, among the most complex and least understood regions of the planet, notorious for their remoteness and inhospitality and data-sparse in the extreme.

Sea ice is a dominant feature of polar oceans, and one that clearly differentiates them from all other oceans. Indeed, it is a pivotal and highly sensitive component and modulator of the global climate system and polar marine ecosystems. It is also a sensitive indicator of possible climate change. The sheer scale of its coverage is phenomenal. At its annual maximum extent, sea ice covers approximately 8% of the Southern Hemisphere—equivalent to an area 50% larger than the Antarctic continent (Zwally et al., 1983) and comprising ~40% of the Southern Ocean area (Lizotte, 2001)—and 5% of the Northern Hemisphere (Gloersen et al., 1992). Importantly from both climatic and ecological perspectives, it exhibits a strong seasonality (Gordon, 1981), with the annual advance (growth) and retreat (decay) cycle representing one of the greatest and most spectacular geophysical changes on Earth. The areal extent of Antarctic sea ice alone varies annually by a factor of ~5, from a maximum of $18–20 \times 10^6\,km^2$ in September–October to $3–4 \times 10^6\,km^2$ each February (Comiso, 2003a; Gloersen et al., 1992). In contrast, the Mediterranean-like configuration of the Arctic Ocean about the North Pole (see Section 5.3) and the atmospheric and oceanic circulation regimes of it and its marginal seas result in a sea ice cover that exhibits much less seasonal variability: i.e., by a factor of only about 2—from a maximum of $14–16 \times 10^6\,km^2$ each February–March to

8–9.5 $\times 10^6$ km^2 each August (Comiso, 2003a; Gloersen et al., 1992; Parkinson and Cavalieri, 2002; Parkinson et al., 1987). As such, up to $\sim$35 $\times 10^6$ km^2, or $\sim$13%, of the world's surface area is covered and affected by a seasonal sea ice cover at some time during the year, and $\sim$7% at any one time (Parkinson and Gloersen, 1993). Some areas remain perennially ice-covered. In terms of areal extent, sea ice accounts for $\sim$65–70% of the Earth's permanent ice cover, but only a minuscule fraction of its volume (estimated to be $\sim$0.1% by Horner et al., 1992). Whereas sea ice is also an important seasonal feature in certain water masses at lower latitudes, including the Sea of Okhotsk (Kimura and Wakatsuchi, 2004), the Baltic Sea (Launiainen and Vihma, 2001) and the Black Sea, the Gulf of St. Lawrence, and the Caspian and Aral Seas (Kouraev et al., 2003), we concentrate mainly on the polar ice covers in this chapter. Maps of both polar regions are shown in Figure 5.1.

Sea ice information is available from a number of sources, some more reliable than others and all with different spatial resolutions, sampling frequencies (temporal resolutions), and degrees of continuity (Eicken and Lemke, 2001). In the pre-satellite era—i.e., in effect prior to the early 1970s—these mainly relate to ice extent, and include historical whaling and sealing and other records. These entail ice charts that extend back centuries (de la Mare, 1997; Laxon et al., 2004; Shapiro et al., 2003; Vinje, 2001a), paleo-records of winter and summer maxima and minima from ocean sediment cores extending back many thousands of years (Armand and Leventer, 2003; Burckle and Mortlock, 1998; Crosta et al., 2004; Keeling and Stephens, 2001), and proxy high-resolution measurements from ice sheet firn cores that resolve annual variability over decadal through centennial periods (Curran et al., 2003). While important, modern *in situ* measurements of sea ice parameters provide limited temporal and/or spatial coverage, given the vast areal extent and highly-variable nature of sea ice. Over the past 30 years, polar-orbiting satellites have revolutionized the study of sea ice by providing unprecedented views of the vast frozen oceans from which detailed regional and global climatologies can be constructed and important processes examined. While early meteorological satellites operating at visible to Thermal InfraRed (TIR) wavelengths provided tantalizing glimpses of the magnitude and variability of sea ice in the 1960s (Massom, 1991), they were seriously limited by polar darkness and cloud cover—a ubiquitous feature of polar and sub-polar oceans. Indeed, it has been estimated that clouds or fog obscure the Arctic sea ice edge about 70% of the time, for example (Pichel et al., 2003), with the summer months being most badly affected. It was not until the launch of microwave systems, including the Electrically Scanning Microwave Radiometer (ESMR) onboard Nimbus-5 in 1972, that cloud and darkness were penetrated to reveal the first global view of sea ice distribution and its extraordinary patterns of variability (Gloersen and Salomonson, 1975)—note that the first satellite with microwave sensors was Kosmos-243, launched in 1968 (Basharinov and Gurvich, 1970; Kondratyev and Melentyev, 1994). This marked the dawn of the modern satellite era. Considerable improvements have since occurred in sensor performance and coverage. Exciting new science-driven missions carrying innovative sensor packages have recently been launched, or are about to be launched or are planned, and some for the first time in space. These include multi-polarization and

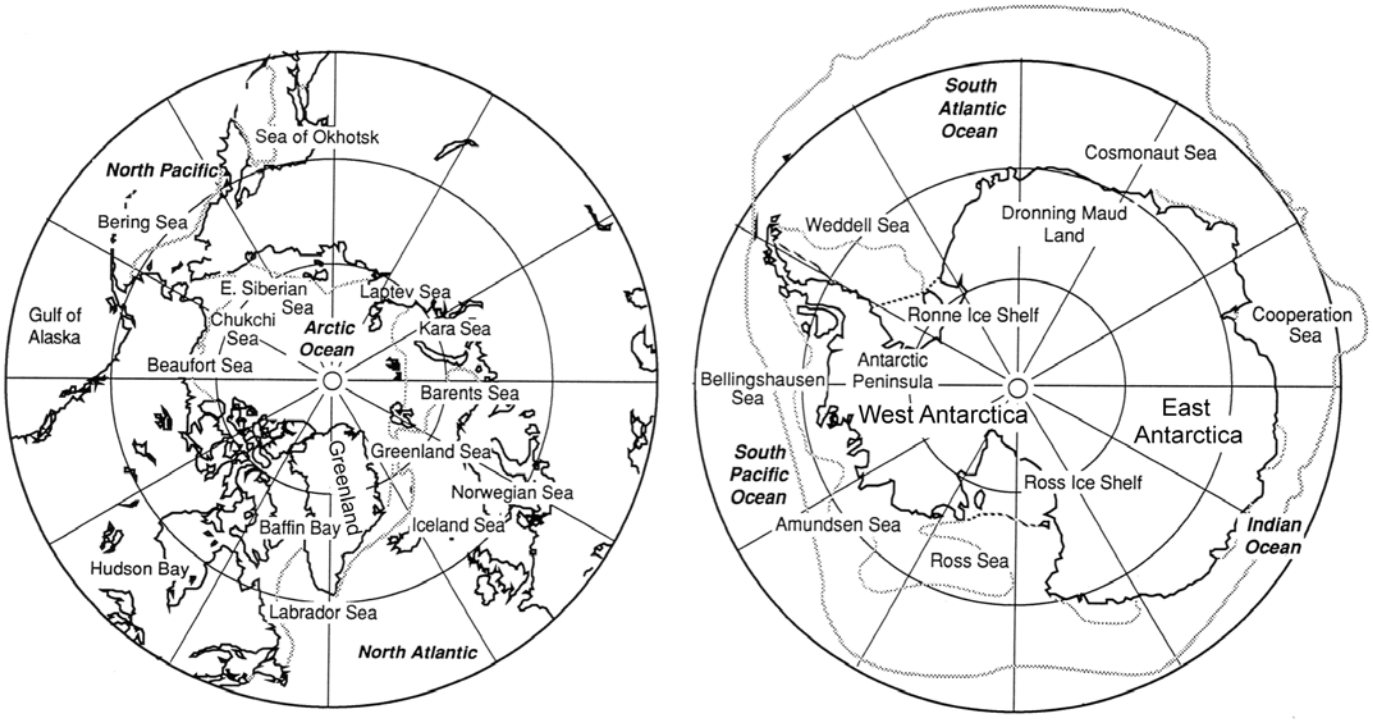

Figure 5.1. Maps of the Arctic and Antarctic, with locations frequently referred to in the text marked. The dotted lines show the locations of the minima and maxima in ice extent for 1989. Determined from US Defense Meteorological Satellite Program (DMSP) Special Sensor Microwave/Imager (SSM/I) passive-microwave data.

fully polarimetric Synthetic Aperture Radars (SARs) (not only single but also in constellations), hyperspectral imagers, improved passive-microwave radiometers, multi-angular spectro-radiometers, the first spaceborne laser altimeter, and a new-generation radar altimeter (onboard ESA's CryoSat mission)—the latter to directly measure sea ice thickness from space for the first time. The trend has been towards improved spatial and spectral/radiometric resolution.[1] Innovative data-processing techniques are also being devised to extract new geophysical products from existing data, which in some cases date back ~30 years.

Major advances have since taken place not only in satellite platform and sensor technology but also in the ground sector, not least in the processing, storage, and dissemination of the vast volume of data that has rained down from space. The emergence of the Internet has made a huge contribution in this respect. Realizing the immense value of archival data, satellite agencies have also put considerable resources into reprocessing archival data, where possible, using state-of-the-art algorithms to produce more consistent and user-friendly time series—e.g., the NOAA/NASA Polar Pathfinder programs (Armstrong and Brodzik, 1995; Maiden et al., 1996). As a result, satellite remote sensing has become an indispensable but constantly evolving sea ice research tool, a major challenge being to maintain key, lengthening time series in a consistent fashion for reliable climate studies. Modern researchers can now access diverse satellite-derived information from their personal computers, ranging from low-level satellite data to high-level data products. It is the latter that we look at in this chapter. Once again, a great deal is owed to the major space agencies for having the foresight to establish key data archival facilities that offer a superb service and to encourage the development of improved algorithms with which to produce important geophysical data products. As we will see, many of these time series, although relatively short, are reaching a level of maturity whereby climate variability and change can be resolved. Satellite remote sensing is also an increasingly important operational workhorse, providing key information in near-real time to aid a range of activities in ice-infested waters—e.g., navigation and fisheries. Such is the diversity of data available, and the rate of development, that the field can appear somewhat daunting. The aim of this chapter is to hopefully dispel some of this "daunt", and to show what can and cannot be achieved with modern satellite data and techniques when applied to sea-ice-related problems. The perspective throughout is not only physical but also biological.

Our approach is to first provide a brief description of the formation processes

[1] *Spatial resolution* is defined as a measure of the smallest object that can be resolved by a given sensor, and is commonly expressed as the most closely spaced line pairs per unit distance that can be distinguished in an image. *Spectral resolution* is the sensitivity of a sensor to respond to a specific frequency range, where the discrete frequency/wavelength range that a sensor is able to detect and measure is called a *band*. *Radiometric resolution* refers to the number of possible brightness values in each band of data and is determined by the number of bits into which the recorded energy is divided. In 8-bit data, for example, the brightness values can range from 0 to 255—i.e., 256 total possible gray-level values.

and unique physical characteristics of sea ice—what makes it such an interesting and challenging remote-sensing target. We then move on to background information on the profound and wide-ranging impact and role of sea ice in the high-latitude biosphere and atmosphere–ocean interaction system, and indeed the global climate system. There follows an evaluation of recent and somewhat alarming predictions and observations of large-scale environmental change and variability in polar oceans, the important part that sea ice plays in such change, and how sea ice can be used as a sensitive bellwether of change. An aim of this and the previous section is to place subsequent discussion of satellite remote sensing into context. This section also examines key uncertainties in our current understanding of polar oceans and in the predictive capabilities of numerical models. It sets the scene for an assessment of the critical role being played by satellites (in concert with *in situ* measurement campaigns, modeling, and emerging data assimilation techniques) in helping to reduce these uncertainties and improve our knowledge base. The next section outlines our current understanding, from a modeling perspective, of the physics of the growth, decay, and heat budget of sea ice—as a primer to where and how individual satellite-derived geophysical data products fit into the complex big picture. Improved simulations of sea ice dynamics and thermodynamics are required to (i) more accurately predict fields of ice extent, motion, and thickness, and (ii) to incorporate sea ice into global circulation models in a realistic fashion (Gordon and O'Farrell, 1997; O'Farrell, 1998). There follows a brief summary of the major satellite sensor classes available, and the basic principles of remote sensing as they apply to sea ice. We then embark upon a review of the satellite-derived geophysical parameters themselves. This section includes information on techniques (algorithms) used, and case study examples of applications to illustrate how the issues and uncertainties raised in earlier sections are being addressed. The overall focus of the chapter is on developments over the past decade or so. For information on older satellite sensors and data sources, and their application to polar oceans research, the reader is referred to Carsey (1986), Comiso (1991), Hall and Martinec (1985) and Massom (1991, 1995). The provision of detailed information on the characteristics of the different satellite and sensor systems is beyond the scope of this book, and the reader should consult Kramer (2002) for this information. Similarly, an overview of digital image processing for remote sensing is provided by Jensen (2004).

In this field, as in the others outlined in this book, satellite remote sensing is not (and never will be) a universal panacea. It is a very powerful research and operational tool, but one that demands careful use. Many challenges exist, both in the interpretation of signatures from ice-covered oceans and in algorithm development and the validation of key, derived geophysical parameters. Satellite remote sensing will never entirely replace *in situ* measurement in the sea ice zone. The latter continues to be extremely important, both in terms of providing (i) detailed information with which to calibrate and validate satellite-derived geophysical parameters and drive process studies, and (ii) key information that cannot be measured directly from space—e.g., on the three-dimensional structure of the ocean, and changes therein (Rintoul et al., 2001a). Surface observational programs

in sea ice zones are, however, logistically challenging and expensive. They also result in datasets that are spatially and temporally sparse. Satellites alone can measure and monitor the vast polar oceans in a reliable, systematic, repetitive, and cost-effective fashion and on a variety of scales, from fine to global. Importantly, satellites offer the only means of obtaining sustained, long-term, basin-wide observations needed to develop consistent climatologies of key parameters that are comparable with output from numerical models. Combined with models and emerging data assimilation techniques, these will be the tools that enable assessment and understanding of trends and variability, and also application to the study of important regional processes nested within the bigger picture. It should be noted here that satellites also play a key role in transmitting important information from sensor packages deployed on ice floes (e.g., automatic weather stations and a variety of ice beacons and buoys), in the ocean and attached to marine mammals and birds (Figure 5.2, see color section). An up-to-date treatise on the important emergent field of "bio-logging science" is provided by Naito (2004).

While this chapter concentrates on polar-orbiting satellites, mention should be made of the important role played by Unmanned Aerial Vehicles (UAVs), and most notably the Aerosonde (Holland et al., 2001; ⟨*http://www.aerosonde.com*⟩). With a payload capacity of 7 kg (including fuel) and a maximum range of 3,000 km, this UAV has been extensively used to measure sea ice and atmospheric/meteorological parameters in the Beaufort Sea region of Alaska (Curry et al., 2004). Measurements from sensors onboard Aerosondes (i.e., TIR radiometers and digital cameras) have included surface-radiative fluxes and surface sea ice characteristics—e.g., surface temperature, lead, and pressure ridge characteristics, and meltpond fraction. These measurements have been used to validate algorithms for sea ice concentration retrieval from satellite passive-microwave data. Instruments under consideration for future deployment on Aerosondes include a laser altimeter, short- and long-wave radiometers, and even a passive-microwave radiometer (Curry et al., 2004). While geostationary satellites provide important information on weather conditions skirting the polar regions (Lazzara et al., 2003; Turner and Pendlebury, 2004), images of ice features tend to be geometrically distorted.

Such is the broad scope and complexity of the field of sea ice remote sensing that it is impossible to do it full justice here. Rather, an aim is to gather information together from a wide range of sources to illustrate how and where remote sensing from polar-orbiting satellites is making an immense and often revolutionary contribution. For the reader requiring additional information, important remote-sensing texts with a focus on sea ice are by Carsey (1992), Haykin et al. (1994), Ikeda and Dobson (1995), Kondratyev et al. (1996), Li (2000), and Tsatsoulis and Kwok (1998a), and references therein (see also Bamber and Kwok, 2004 and Laxon et al., 2004). Remote-sensing measurement of global climate change in general is covered by Cracknell (2001). Detailed information on sea ice physical properties relevant to remote sensing is given by Hallikainen (1992), Hallikainen and Winebrenner (1992), and Tucker et al. (1992), and on the modeling of sea ice electromagnetic characteristics by Golden et al. (1998a, b) and Winebrenner et al. (1992). For more complete descriptions of sea ice growth processes, structure, and properties, and polar

contrasts, the reader is encouraged to refer to the excellent reviews by Ackley (1996), Eicken (2003a), Haas (2003), Maykut (1985, 1986), Weeks and Ackley (1986), Weeks (1998), and Wettlaufer (1998). Key sea ice texts are Jacobs and Weiss (1998), Jeffries (1998), Johannessen et al. (1994a), Smith (1990), Thomas and Dieckmann (2003), Leppäranta (1998a, 2005), Untersteiner (1986), and Wadhams (2000). Wadhams (2004) provides information on *in situ* measurement techniques. The critical role of sea ice as a pivotal element of the global cryosphere and global climate, and its potential response to global change, is covered in detail by Allison et al. (2001), Everett and Fitzharris (2001), Fitzharris (1996), Goodison et al. (1999), and Houghton et al. (2001). Optical properties of sea ice are reviewed by Perovich (1996), while Maykut (1986) provides a thorough treatment of sea ice energy and mass balance, with Yen et al. (1991) providing a summary of snow and sea ice thermophysical properties. Steele and Flato (2000) review ice growth models, Dempsey and Shen (2001), Hibler (2004), and Leppäranta (2005) ice mechanics and dynamics, Pritchard (2001) ice dynamics models, and Flato (2004) and Häkkinen (1990) sea ice models in general. The role of sea ice in structuring polar marine ecosystems is discussed by Ackley and Sullivan (1994), Eicken (1992), Horner (1985), Horner et al. (1992), and Smith et al. (1998a, b). Up-to-date discussions on sea ice primary production, macrobiology, and microbiology are provided by Lizotte and Arrigo (1998) and Smith et al. (2001, 2003a), Arrigo (2003), Arrigo and Thomas (2004), Fritsen and Sullivan (1999), Schnack-Schiel (2003), Smetacek et al. (2004), Smith and Lancelot (2004), Stewart and Fritsen (2004), and Lizotte (2001), respectively, while the role of sea ice as a habitat for marine birds and mammals is treated by Ainley and DeMaster (1990) and Ainley et al. (2003). Sea ice biochemistry is reviewed by Thomas and Papadimitriou (2003). The key role of sea ice in delivering particulate flux to the ocean is reviewed by Leventer (2003). The paleoclimate perspective is reviewed by Armand and Leventer (2003). Polar oceanography is addressed by Carmack (1990), Cattle et al. (2001), the CLIVAR Scientific Steering Group (1995), Godfrey and Rintoul (1998), Rintoul (2000), Rintoul et al. (2001a), Siedler et al. (2001), Smith and Grebmeier (1995), Spezie and Manzella (1999), Tomczak and Godfrey (2003), and meteorology by Barry and Chorley (2003), Bromwich and Parish (1998), Karoly and Vincent (1998), King and Turner (1997), Serreze (2003). and Turner and Pendlebury (2004). Historical observations of Antarctic meteorological variables are available online from the SCAR (Scientific Committee on Antarctic Research) READER (REference Antarctic Data for Environmental Research) project at: ⟨*http://www.antarctica.ac.uk/met/READER/*⟩. An excellent text on the physics of climate is Peixoto and Oort (1992). Last but not least, Martin (2004) and Robinson (2004) provide up-to-date information on remote sensing of the global ocean.

While this chapter focuses on sea ice, it should be noted that the sea ice–ocean–atmosphere system also interacts with, affects, and is affected by other elements of the global cryosphere, hydrosphere, and climate system. Examples include Arctic hydrology through the effect of river inflow on the freshwater budget (Macdonald et al., 1999; Peterson et al., 2002; WCRP, 1999), sediment and nutrient regimes of the Arctic Ocean (Bareiss et al., 1999; Dean et al., 1994; Eicken

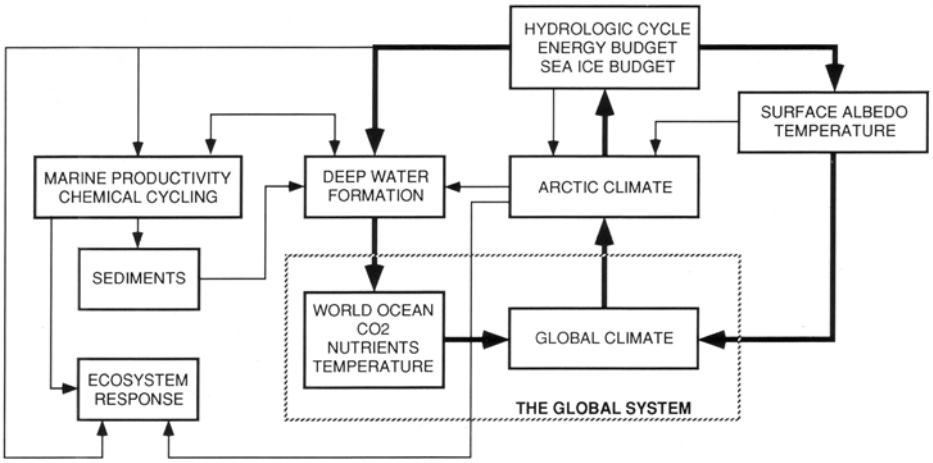

Figure 5.3. A schematic of components of the Arctic marine system (solid lines) and the global climate systems (dashed lines). Thin arrows indicate causal linkages, while bold arrows denote feedback loops.

From Moritz et al. (1990).

et al., 1995a; Frey et al., 2003; Searcy et al., 1996); the role of ocean–ice sheet interaction in ocean water mass modification and formation (see Volume 2 of this book), and the influence of ice shelf melting on sea ice (Hellmer, 2004), as well as the role of ice sheets in atmospheric circulation and precipitation patterns over the ocean, and the impact of changing ice concentrations on precipitation patterns over the ice sheets (Weatherly, 2004). These and other issues relating to the complexity of intra-cryosphere interactions are largely outside the scope of this chapter, and are more fully discussed in Allison et al. (2001). One important cross-elemental interaction that will be examined here is the impact of icebergs on sea ice distribution and primary production. Some of the interactions are illustrated from an Arctic perspective in Figure 5.3.

5.2 SEA ICE FORMATION PROCESSES (AND THE LIFE OF BRINE)

Before embarking on an assessment of the profound role of sea ice, we present a brief summary of the main formation processes, large-scale morphological features, and polar contrasts (please see the references in Section 5.1 for a more complete description). An aim is to give insight into the complexity of sea ice as a remote-sensing target, and to provide a basic grounding before consideration of satellite-derived geophysical parameters. Terminology adheres throughout to the standard sea ice classification scheme of the World Meteorological Organization (WMO, 1970), which is based upon its formation and developmental stage and thickness (this is available online at: ⟨*http://www.aari.nw.ru/gdsidb/gdsidb_2.html*⟩). An illustrated glossary of Antarctic sea ice types, based upon the WMO classification, is

available online at: ⟨*http://www.antcrc.utas.edu.au/aspect/seaiceglossary.html#frazil*⟩, while Steffen (1986) and Eicken (2003a) provide excellent photographic glossaries of Arctic sea ice types. Another excellent glossary of snow and ice terminology (for both sea ice and ice sheet environments) is that of Armstrong et al. (1973). The evolutionary sequence of the formation of "thin" sea ice, up to and including first-year ice, is depicted schematically in Figure 5.4 as a function of calm and less calm conditions. Note that polar contrasts are evaluated in the next section.

The main stages of ice formation are as follows (photographs are given in Figure 5.5, see color section). Initial ice formation occurs in the ocean surface layers when they reach a temperature of $\sim -1.86^{\circ}$C (at a salinity of 34 p.s.u.), in the form of randomly oriented ice crystals, individually ~3–4 mm in diameter and termed *frazil ice*. These crystals, which may also form at some depth in supercooled water and float to the surface, coalesce to form a soup-like mixture on the ocean surface termed *grease ice*. This is typically herded downwind in openings in the ice known as leads and polynyas (for a description of the latter, see Section 5.9.4). Under moderately turbulent conditions due to ocean swell and wave action—i.e., in the outer pack and in polynyas/large leads—the ice crystals rapidly freeze together to form near-circular 5–10 cm-scale discs on the ocean surface (Lange et al., 1989; Shen et al., 2001; Wadhams et al., 1986). These *pancakes* subsequently raft and freeze together to form aggregates meters across, which damp the short-period wave energy and eventually form a consolidated ice cover tens of centimeters thick.

Where very calm oceanic and atmospheric conditions prevail—e.g., within the interior pack and with surface wind speeds of ~5 m s^{-1}—ice crystals aggregate into a uniformly thin sheet of ice termed *nilas*. The rate of thermodynamic ice growth slows considerably once a sheet of ice forms, either as nilas or pancake ice, due to the insulative effect of the ice. Once the ice consolidates and attains a thickness of ~0.5 m, it also promotes a more quiescient upper-ocean environment for ice growth by damping the energy of short-period ocean waves (Shen and Squire, 1998). The overall effect in both cases is to diminish frazil ice formation but promote the slow growth of long, columnar crystals onto the underside of the existing ice layer in the form of *congelation ice*.

The description above is of idealized ice growth cycles. In reality, a certain amount of ice-type overlap tends to occur due to constant synoptic-scale cycling between calm and turbulent (wavy) conditions (Grenfell et al., 1992; Weeks, 1976). For example, nilas can be broken into small fragments that form pancake ice, while grease ice can rapidly develop into nilas if the waves subside. Moreover, sea ice is highly mobile, drifting and deforming rapidly in response to synoptic-scale changes in winds (Massom, 1992; Thorndike and Colony, 1982; Thorndike et al., 1992; Zubov, 1943) and high-frequency inertial and tidal forcing (Heil and Hibler, 2002; Kowalik and Proshutinsky, 1994). On monthly and longer timescales, sea ice drift patterns correspond to large-scale prevailing wind and ocean current regimes (Nansen, 1902). Highly dynamic and changeable conditions result in a complex ice cover that is constantly "reworked" by cyclical synoptic-scale patterns of divergence and convergence (Massom, 1992). Divergent conditions create open-water regions known as *leads* if they are linear and ephemeral, and *polynyas* if they are more

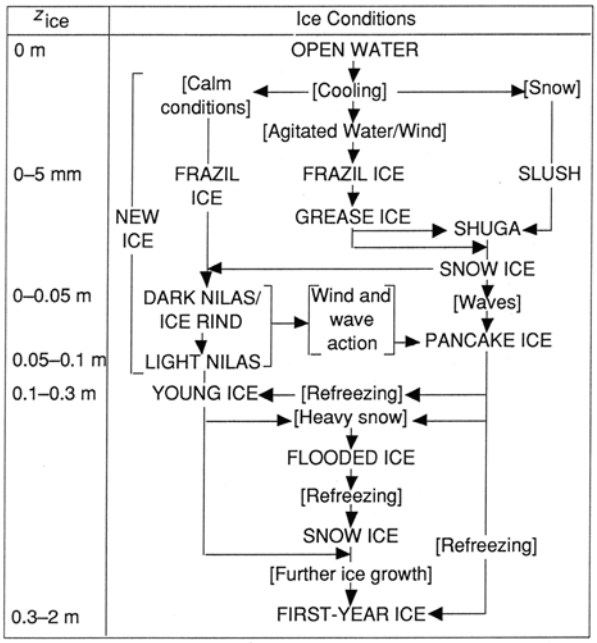

Figure 5.4. A schematic of the idealized sequence of formation (evolution) of thin sea ice. Ice types are depicted in capital letters, while related environmental processes are enclosed in square brackets. *Young ice* is subdivided into *gray ice* ($h = 0.1$–0.15 m) and *gray–white ice* ($h = 0.15$–0.30 m). The thicker the young ice, the more likely it is to ridge than raft (the process whereby one ice plate overrides another). *First-year ice* ($h = 0.3$–2.0 m), which is, ice of not more than one winter's growth, is typified by bulk salinities of 4–8 p.s.u. Note that first-year ice can attain thicknesses of much greater than 2 m in the vicinity of pressure ridges where floes collide. Ice that survives an annual summer melt season becomes *second-year ice*, whereas *multiyear ice* is *old ice* that has survived at least two summers' melt. *Old ice* is characterized by a thickness of >2 m in the WMO (1970) classification, with bulk salinities of the order of 2–4 p.s.u. in the Arctic and an increase in the size and number of gas bubbles in the ice volume. Multiyear ice can attain thicknesses of a few tens of meters in pressure ridges in the central Arctic (Hibler et al., 1972). See Ackley (1996), Weeks (1998), and Weeks and Ackley (1986) for further details, and for an assessment of polar contrasts. For information on snowcover thickness and characteristics, see Warren et al. (1999) and Sturm et al. (2002a) for the Arctic, and Massom et al. (2001a) and Sturm et al. (1998) and references therein for the Antarctic.

persistent and recurrent. Convergence, on the other hand, leads to ice deformation and the thickening of ice beyond its thermodynamic equilibrium thickness by *pressure ridge* formation and/or *rafting*, the latter process entailing the overriding of one section of a floe by another (Parmeter, 1975). Ridging occurs where floes collide or the internal ice stress builds up to the point of fracture and the ice breaks up into blocks (Parmeter and Coon, 1972). These pile on top of each other to form

long, linear features characterized by a deep "keel" below the surface and a shallower "sail" on the surface. In the Arctic, ridges can attain thicknesses of tens of meters, while smaller dimensions are more typical over much (though not all) of the Antarctic sea ice zone. Such is the widespread occurrence of ridging and rafting in both polar regions that few expanses of level sea ice are typically encountered or persist. The surface manifestation of rafting is much less pronounced than it is for ridging.

In response to variable wind, current and ocean wave forcing, sea ice is broken up into fragments called *floes*, the diameters of which range from meters to tens of kilometers depending on conditions and ice thickness. Sea ice distribution (areal extent and concentration), thickness and other properties are determined by the complex interplay of a variety of dynamic and thermodynamic processes—e.g., motion, redistribution and deformation, freezing and melting (these are laid out in more detail in Section 5.6). As a result, pack ice comprises a highly variable substrate, characterized by variability in concentration, properties, thickness, floe sizes, snow cover thickness and properties, and roughness characteristics, all of which exhibit strong seasonal variation—a truly challenging remote-sensing target! The state of the ice cover, its variability, and thus its role in modulating exchanges between ocean and atmosphere, and its response to, and impact upon, climate change/variability are determined by the net effect of these processes on the geophysical scale (Allison et al., 2001).

In spite of this apparent chaos, large-scale morphological patterns are apparent in the ice cover (Massom et al., 1999). On the regional scale, the sea ice cover of both polar oceans in winter comprise a series of zones or major sea ice morphological regimes, each having distinct physical characteristics that depend on broad-scale climatological patterns. Each zone also differs in terms of its biological significance. The following is a brief overview of these major zones in Antarctica, working equatorward from the coast. *Fast ice* is an annual, and in places perennial, feature along certain coastal margins, and forms a band typically kilometers to tens of kilometers wide. This is sea ice which remains largely stationary or "fast" (attached) to the coast, as distinct from *pack ice* which by definition constantly drifts in response to winds, ocean currents, and other forces. The region forming the transition between the fast ice zone or coastline is typically characterized by a band of highly deformed and very rough ice formed by shearing and convergence of the pack's motion, and known as the *shear zone*. Fast ice and pack ice may also be separated by elongated and narrow areas of recurrent open water termed *flaw leads* (Dmitrenko et al., 2001). Coastal margins in certain locations are also characterized by large areas of openwater which persist for weeks to months and recur from year to year. These are known as *polynyas*—a Russian word meaning lake. As we will see in Section 5.9.4.3, these play a profound role as the "ice factories" of the pack and as sites of major watermass modification and, in places, enhanced biological activity.

Beyond the shear and polynya zones lies the central pack ice zone. This may be from hundreds to a thousand or so kilometers wide, depending upon the geographical sector. Finally, the outer extremities ($\sim$10–300 km) of the pack are greatly affected by proximity to the open ocean and particularly the effects of intense ocean wave energy—i.e., wave–ice interaction processes (Fox and Haskell,

2001; Squire, 1995; Squire et al., 1995; Wadhams, 1986, 2000). The resultant region of broken ice is known as the *Marginal Ice Zone* (*MIZ*). This is a highly dynamic region, and the site of intense atmosphere–ice–ocean interaction processes (see Squire, 1998 for an excellent review). It also plays an important role in ocean primary production and the carbon cycle (Savage et al., 1996). Ocean wave and swell-induced floe collisions lead to floe pulverization and breakdown into ice fragments known as *brash ice*. Brash ice fragments separated by interstitial frazil "slush" can cover the ocean, but are unconsolidated and characterized by a wet and typically snow-free surface due to wave-overwashing effects. As we will see, this can lead to ambiguous sea ice retrievals using satellite microwave data. This ice can reconstitute under calm conditions. By attenuating wave energy (Wadhams et al., 1988), ice in the MIZ effectively impacts sea ice growth, melt, and mechanical destruction processes in the inner pack. The outer margin of the MIZ—i.e., the ice edge region—can be either compact or diffuse and extending over tens of kilometers as a series of bands (Martin et al., 1983; Wadhams, 1986), depending upon the wind direction. Such variability complicates the use of ice extent alone as a climate parameter/indicator. Due to their freedom of movement, floes in this region can trace out the location and behavior of important oceanic features such as eddies, enabling their tracking in time series of high- to medium-resolution satellite images to give proxy information on ocean circulation and boundaries (Fukamachi et al., 1998; Shuchman et al., 2004; Wakatsuchi et al., 1990). With typical diameters of 20 to 100 km, ocean eddies are of great importance in momentum and heat transport, and probably play a key role in controlling the strength of the Antarctic Circumpolar Current (ACC), for example. Ice edge location is determined by climatological air temperature and wind speed and direction as they affect ice drift, formation and melt, and can exhibit considerable synoptic-scale variability.

All regions that melt back annually are collectively termed *seasonal ice zones* (see Wadhams, 1986 for an excellent review), as distinct from regions of perennial or *multiyear ice* that survive the summer melt period. Quite distinctive seasonal changes occur in the surface morphology and properties of Arctic ice in summer (Perovich et al., 2001; Tucker et al., 1999), with a dominance of bare ice and meltponds, and a weathering of surface roughness features such as pressure ridges to create a more undulating topography (the surface of Antarctic sea ice is generally more angular or blocky). Given their vast scale, these morphological zones can once again only be studied and monitored from space. Monitoring changes in their large-scale distribution and characteristics may provide another sensitive indication of climate variability and/or change (Johannessen et al., 2004). Ecological implications are discussed below.

On the micro-scale—important from the perspective of the interaction with electromagnetic radiation at wavelengths exploited by satellite sensors and the colonization of the ice by micro-organisms—sea ice is a complex composite material comprising pure ice and brine and gas inclusions, the size and geometry of which depend on ice crystal structure, temperature, and bulk salinity (Eicken, 2003a; Golden et al., 1998a, b; Perovich and Gow, 1996; Light et al., 2003a, b; Tucker et al., 1992; Weeks and Ackley, 1986). Typical dimensions in first-year ice

are 0.1–1 mm, depending on the growth history of the ice. In effect, its bulk material and microstructural properties respond dramatically over a small temperature range. During the growth period, sea salt ions are concentrated in the liquid phase rather than being incorporated into the sea ice crystal lattice, and form long, narrow channels of entrapped brine (Eicken, 2003a; Weeks, 1998). The initial amount of salt trapped in the ice depends both on seawater salinity and the ice growth rate, and is greater for frazil ice than congelation ice (Cox and Weeks, 1988; Maykut, 1985). Rather than remaining stationary, brine moves vertically within the ice column by brine channel migration, upward and downward brine expulsion, gravity drainage and flushing (by meltwater percolating downwards through brine drainage channels). While a small fraction of this brine remains in small pockets (a few hundredths to tenths of millimeters in size) within the ice (Weeks and Ackley, 1986), most is subsequently expelled into the ocean, where its enhanced density induces deepening of the mixed layer and thermohaline convection (Carmack, 1986). Further changes occur in the ice salinity and microscale structure as it ages and thickens. Moreover, sea ice older than a few days also accumulates a snow cover, which itself evolves with time and has a major impact on the development of the ice and its remote-sensing signature. For example, temperature-gradient metamorphism leads to changes in snow grain size and density with time (Colbeck, 1982; Colbeck et al., 1990). The variable role of the snow cover is discussed in Section 5.6.1.2. For detailed information on the snow cover properties of sea ice, see Granberg (1998), Iacozza and Barber (1999), Massom et al. (1998a, 2001a), and Sturm et al. (1998, 2002a, b).

5.3 POLAR CONTRASTS

Major large-scale differences exist between the sea ice cover of the two polar regions due to their contrasting geographical settings and the environmental conditions therein. The Arctic Ocean is a deep, permanently ice-covered basin (mean depth ~1,800 m) skirted by broad continental shelves and shallow marginal seas that are seasonally ice-covered (Wadhams, 2000). It is in effect a Mediterranean-like sea centered on the North Pole—i.e., mostly surrounded by land masses, with "outlets" for the exchange of ice masses and water masses only through the Bering Strait, Fram Strait (the region between NE Greenland and Svalbard), and the Canadian Arctic Archipelago. Due to the persistent anticyclonic circulation in the Beaufort Gyre, sea ice may reside in the Arctic Basin for years before becoming caught up in the Transpolar Drift and drifting southwards through Fram Strait. This is a major contributing factor to the thickness of ice in the Arctic. This same pattern of ice drift pushes ice from the Russian Arctic towards the Canadian Arctic Archipelago and the northern coast of Northern Greenland to create some of the thickest and most highly deformed ice in the Arctic. The enclosed nature of the Arctic Basin leads to a compact ice cover, with ice movement and deformation being affected by high internal stresses (particularly in winter). Between ~50 and 90% of the overall sea ice cover is perennial (Gloersen et al., 1992; Parkinson et al., 1987), with a thickness of >2 m (Horner et al., 1992; Maykut, 1985). Water and ice exchange is

mainly with the North Atlantic, with an estimated 10% of the ice cover drifting out of the basin each year, largely through Fram Strait (Aagaard and Carmack, 1994). The latitudinal range of Arctic sea ice is from the pole to ~44°N (in the Sea of Japan).

The Southern Ocean, on the other hand, is a circumpolar ocean bounded at its southern extremity by a vast frozen continent, and covered by a band of largely seasonal sea ice that extends from a maximum southerly extent of ~75°S northwards as far as ~55°S at maximum extent (Gloersen et al., 1992). The width of this band is highly variable, ranging from a few hundred kilometers in the Indian Ocean sector to ~1,600 km in the Weddell Sea. Given the narrow width of the continental shelves, a large proportion of the Antarctic ice cover occurs over deep ocean, where it is exposed to a zone of strong cyclone activity (King and Turner, 1997) and ocean waves and swell. Climatological atmospheric and oceanic circulation patterns, including the Antarctic Circumpolar Current (Olbers et al., 2004), combined with a lack of restrictive land boundaries to the north and within the zone of freezing, result in an ice cover that is largely divergent and much less constrained than its Arctic counterpart (Allison, 1997). As a result, ice drift speeds tend to be significantly higher than they are in the Arctic. Together with relatively high vertical ocean heat fluxes of as great as $30\,W\,m^{-2}$ (Gordon and Huber, 1990; Launiainen and Vihma, 1994; Lytle et al., 2000; Martinson, 1993; McPhee et al., 1999; McPhee and Martinson, 1994) compared with an annual average in the Arctic of $\sim 2\,W\,m^{-2}$ (Wadhams, 2000), this results in an ice cover that is thinner on average than in the Arctic (~1 m versus ~3 m). Similarly, rafting is more common in Antarctica, with pressure ridges in general being more blocky and irregular than they are in the Arctic. The Antarctic has a high proportion—i.e., ~80%–of first-year ice that melts back each summer, compared with <50% for the Arctic (Comiso, 2003a). The residence time of sea ice is up to 5–7 years in the Arctic Ocean, compared with 1–2 years in the Southern Ocean (Dieckmann and Hellmer, 2003). The rapidity and extent of the seasonal meltback of Antarctic sea ice results from its constant northward movement, exposure to rough, warm waters and storms around its circumpolar periphery, and its coverage of relatively low latitudes (at maximum extent). A significant polar contrast also exists in the relative lengths of the annual sea ice growth and decay seasons (Gloersen et al., 1992, 1999). While that of the Arctic follows a symmetrical pattern with ice extent maxima and minima occurring approximately 6 months apart, the Antarctic cycle is asymmetrical, with the autumn–winter growth period being longer than the spring–summer decay period.

Antarctic sea ice in summer is much less affected by surface melt and meltponds are largely absent, due to the combined effects of a colder, drier, and windier atmosphere in the Antarctic (compared with the Arctic) (Andreas and Ackley, 1981) and smaller concentrations of soot and other impurities which affect the snow albedo (Eicken, 2003b). Meltponds are a ubiquitous feature of Arctic sea ice in the summer, with surface melt and weathering processes leading to the "rounding off" of blocky surface features on Arctic sea ice that survives the summer melt. In contrast, Antarctic sea ice tends to retain a more "blocky" and angular topographic appearance (Wadhams and Davis, 2001).

Major differences are also apparent in ice microscale textural characteristics,

with significant implications for the microwave properties of the two ice covers. Due to more turbulent ice growth conditions in the Southern Ocean, the Antarctic ice cover comprises a higher proportion (i.e., 50–60%) of frazil ice (Lange et al., 1989) compared with columnar ice (Gow et al., 1982). The opposite is true in the Arctic Ocean—i.e., only 5–20% frazil ice (Spindler, 1990; Tucker et al., 1987). These estimates come from sea ice core analyses. As a result, Antarctic sea ice tends to be more saline overall. Generally, the more rapid the ice growth rate, the higher the sea ice salinity. Another important difference is the ubiquitous formation of snow/ice in Antarctica (Adolphs, 1998; Eicken et al., 1994; Jeffries et al., 1994, 2001; Kawamura et al., 1997; Lange et al., 1990), but not in the Arctic (this is expanded upon in Section 5.6.1.2). Snow/ice forms by the flooding and freezing of the snow cover, which is generally thicker in the Antarctic. It is similar in texture to frazil ice, but comprises a large meteoric component that is distinguishable by oxygen isotope analysis (Eicken et al, 1994; Eicken, 1998, 2003a; Jeffries et al., 1998). Different hemispheric melt conditions are discussed in Section 5.6.1.3.

In the Arctic, multiyear ice is significantly less saline than first-year ice, due to the strong evolution of its salinity and micro-structural properties, largely in response to downward percolation of meltwater from meltponds. The latter may cover 50–60% of the ice surface in summer (Maykut, 1985). This percolation occurs via interconnecting brine drainage channels and tubes, which coalesce as the ice warms (Golden, 2001; Golden et al., 1998c). As a result, brine is flushed out of the ice, and brine pockets are gradually replaced over time by millimeter- to submillimeter-scale air bubbles, which act as scattering centres for electromagnetic radiation. As we will see in Section 5.7.1, these differences affect the microwave properties of the different ice types, and thus their characteristics as remote-sensing targets. This provides a means of classifying Arctic sea ice in the satellite data.

Other physical hemispheric differences in the sea ice fields include the presence of sediments from river runoff and suspension freezing, and eolian precipitates—e.g., soot (Clarke and Noone, 1985; Grenfell et al., 2002)—in the Arctic, compared with the relatively pristine nature of Antarctic sea ice and its snow cover (Dieckmann and Hellmer, 2003). Such differences affect the optical properties of the respective ice cover and snow cover. Moreover, the input of river discharge also contributes to the overall freshwater budget of the Arctic (Macdonald et al., 1999)—a factor that is lacking in Antarctica. Biological differences and similarities are reviewed by Dieckmann and Hellmer (2003) and Spindler (1990).

5.4 THE PROFOUND IMPACT AND ROLE OF SEA ICE

5.4.1 Physical and biogeochemical significance

Although relatively thin—i.e., centimeters to meters thick—sea ice has a profound and highly variable impact on high-latitude ocean–atmosphere interactions, biological, biogeochemical, and sedimentological processes, and human activities. Indeed, the impact of sea ice is extraordinarily far-reaching. Sea ice is recognized as a key component of the global cryosphere and climate system (Allison et al., 2001; Goodison et al., 1999), and is prominent in reports by the Intergovernmental Panel

on Climate Change (Fitzharris, 1996; Houghton et al., 2001). Primarily, patterns of sea ice growth, movement, and eventual decay affect the energy and mass balances and properties of the polar ocean system in a complex and profound fashion. The major impacts (both physical/environmental and biogeochemical—the two intimately tied together by the "biological pump") can be summarized as follows:

- Due to its high but variable albedo—i.e., to >0.85 compared with ~0.07 for an ice-free ocean (Allison et al., 1993; Barry, 1996; Warren, 1982; Grenfell and Maykut, 1977; Grenfell and Perovich, 1984)—snow-covered sea ice greatly modifies the surface radiation balance, reflecting a large fraction of the incoming shortwave (solar) radiation back into space to greatly limit its capacity to illuminate and heat the ocean surface (Barry et al., 1993; Maykut, 1986). Albedo describes the ratio of all outgoing to incident radiation for a given surface area.
- By virtue of its low thermal conductivity of $\sim 2.0\,W\,m^{-1}\,K^{-1}$ (Schwerdtfeger, 1963; Untersteiner, 1961), even a thin layer of sea ice forms an insulative barrier that greatly inhibits heat exchange between the relatively warm ocean (at $\sim -1.8^{\circ}C$) and cold atmosphere in winter (Maykut, 1982, 1986). The effect of sea ice and its growth and decay cycle on the heat budget of polar regions is strongly determined by the thickness of the ice, which is linked to its age.
- Where breaks do occur (as shown in Figures 5.5 and 5.6, see color section), heat fluxes are up to two orders of magnitude larger over a polynya or refreezing lead in winter than over the surrounding pack ice (Andreas et al., 1979; Badgley, 1966; Glendening, 1995; Glendening and Burk, 1992; Ledley, 1988; Maykut, 1978, 1982), leading to intense heat loss and rapid rates of thermodynamic ice formation and brine rejection. For this reason, even a small fraction of open water can dominate the total regional energy transfer between ocean and atmosphere (Maykut, 1986).
- Sea ice intercepts snowfall, affecting the ocean freshwater budget by delaying its entry into the upper ocean. As it accumulates, the snow cover itself plays a major, complex, highly variable, and often subtle role in modifying the impact of the sea ice on ocean–atmosphere interactions (Eicken et al., 1995b; Ledley, 1991, 1993). It has a first-order effect on the surface albedo, increasing the latter for new thin ice in particular (Allison et al., 1993; Grenfell and Maykut, 1977; Warren et al., 1997). Moreover, the thermal conductivity of snow (i.e., ~0.1 to $0.4\,W\,m^{-1}\,K^{-1}$ depending upon snow type) is an order of magnitude lower than that of sea ice (Sturm et al., 1997, 1998, 2002b; Massom et al., 1998a, 2001a), making it an even greater thermal insulator and modulating the rate of ice thermodynamic growth. In Antarctica, however, snow also contributes to sea ice growth by the process of snow/ice formation (see below). Snow is also characterized by a high latent heat.
- Sea ice forms a physical barrier that acts to modulate the exchanges of momentum and matter between atmosphere and ocean (Aagaard and Carmack, 1994; Andreas, 1980), effectively decreasing the exchange of gases—e.g., carbon dioxide (CO_2), oxygen, and water vapour. Regarding CO_2, the uptake rate by the ocean is controlled not only by sea ice but also by the CO_2

difference across the air–sea interface and the wind forcing of the ocean surface. The impact on water vapour may affect regional cloud cover distribution and precipitation rates (Weatherly, 2004), while regulation of carbon uptake by the ocean affects atmospheric greenhouse gas levels (Allison et al., 2001; Anderson and Kaltin, 2001; Follows and Oguz, 2004; Matear and Hirst, 1999; Sabine et al., 2004). Both affect the Earth's overall radiation balance.

- In autumn–winter, surface heat and brine fluxes—the latter associated with salt rejection and brine drainage during sea ice growth—deepen and destabilize the ocean mixed layer to initiate deep ocean convective overturning (Aagaard and Carmack, 1989; Martinson, 1991) and ventilation (Anderson et al., 1999; Martinson, 1990; Muench and Hellmer, 2002; Orsi et al., 1999). Again, heat losses and concomitant new sea ice formation rates and associated salinity fluxes are particularly large in leads and polynyas. In certain key Antarctic locations, these processes, and associated supercooling beneath ice shelves and glacier tongues, lead to the formation of dense, cold, Deep Water and Bottom Water (Fahrbach et al., 1994; Gordon, 1998; Gordon et al., 1993, 2000; Grumbine, 1991; Rintoul, 1998). As such, sea ice plays a fundamental role in the thermohaline "conveyor belt" circulation of the global ocean (Aagaard and Carmack, 1994; Carmack, 1986; Goosse and Fichefet, 1999; Weaver et al. 1999), which constitutes a major mechanism for the poleward transport of oceanic heat and the sequestering of atmospheric CO_2 into the deep ocean (Goodison et al., 1999). In the Arctic, brine input helps to maintain the halocline (Aagaard et al., 1981; Rudels et al., 1996; Steele et al., 1995) and drive secondary upper-ocean circulation (Morison et al., 1992). Looking to the south, water encountered at abyssal and intermediate depths at low latitudes rises towards the surface in the Southern Ocean (Rintoul and Church, 2002). Where these layers reach the surface, their characteristics are modified by intense interactions between the ocean, sea ice, ice shelves (see Volume 2 of this book), and atmosphere (Figure 5.7, see color section).
- Upon melting in spring–summer, the sea ice, with a typical bulk salinity of 5 p.s.u.—in Antarctica, for example (Eicken and Lange, 1989a)—introduces relatively fresh water into the water column to stabilize the mixed layer and decrease its depth (Timmermann et al., 2001). This acts to moderate deep-ocean convection and play a major role in stabilizing large-scale and long-term ocean thermohaline circulation patterns—e.g., in the North Atlantic (Aagaard and Carmack, 1989; Mauritzen and Häkkinen, 1997) and Southern Ocean (Martinson and Iannuzzi, 1998). Due to its large-scale drift in response to climatological ocean–surface current and wind regimes—e.g., at rates of up to $>20\,\mathrm{km\ day^{-1}}$ around Antarctica (Heil and Allison, 1999; Kottmeier et al., 1992)—sea ice melt can occur thousands of kilometers from its point of initial formation. As such, given regions are dominated by net seasonal surface fluxes of saltwater or freshwater—i.e., positive or negative freezing rates, respectively (Allison et al., 2001; Lewis et al., 2000; Steele and Flato, 2000). The timing and location of these phase changes can affect the variability and ultimate fate of freshwater fluxes and, as we will see, are of major concern in a climate change

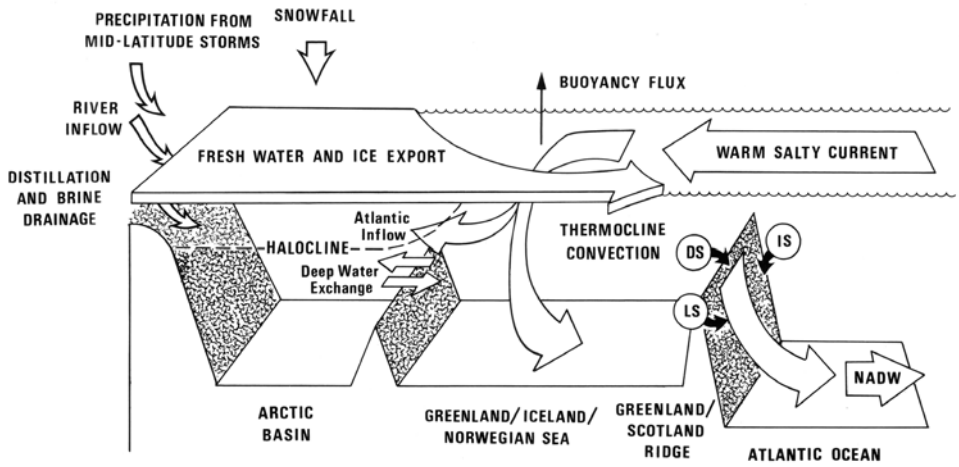

Figure 5.8. A schematic of the transport of ice and freshwater near the surface of the Arctic Ocean, and the thermohaline circulation associated with brine transport of the marginal shelves and deep overturning in the Greenland Sea. Decreasing latitude is from left to right, and NADW is North Atlantic Deep Water.

From Untersteiner and Carmack (1990). Reprinted with permission of the World Meteorological Organization.

scenario. The freshwater balance of the Arctic Ocean and the marginal Greenland–Iceland–Norwegian (GIN) Seas, for example, plays a major role in the climate system (Steele et al., 1996). Net ice growth in the Arctic Ocean is balanced by southward export through Fram Strait and net ice melt in the GIN Seas, where warmer North Atlantic waters are encountered (Aagaard and Carmack, 1989; Aagaard et al., 1991; Moritz et al., 1990). The transport of freshwater through the Arctic marine system is illustrated in Figure 5.8.

- Sea ice formation in autumn–winter and ablation in spring–summer affect the export of both sensible and latent heat[2] between the ocean and atmosphere (Moritz and Perovich, 1996).
- Sea ice is not only affected by large-scale atmospheric circulation (Carleton, 1989; Harangozo, 1997; Yuan, 2004; Yuan and Martinson, 2000) but also has a substantial impact on it (Godfred-Spelling and Simmonds, 1996; Menendez et al., 1999a, b; Raphael, 2003; Yuan et al., 1999). In so doing, it affects water isotope transport and accumulation on the ice sheets (affecting ice core interpretation) (Noone and Simmonds, 2004). It follows that changes in sea ice distribution may have an impact on hemispheric patterns of atmospheric circulation (Murray and Simmonds, 1995). Seasonal and interannual variations in sea ice distribution are thought to impact the weather and climate of

[2] *Sensible heat* is defined as the energy transferred (heat absorbed or released) by a substance during a change of temperature which is not accompanied by a change of state. *Latent heat* is the energy transferred (i.e., heat released or absorbed) by a substance per unit mass when it changes its physical phase at constant temperature.

lower-latitude regions, through atmospheric and oceanic teleconnections[3] in ways that are not well-understood (Carleton, 2003; Liu et al., 2002a, b).

- In the Arctic, sea ice also plays a role in the entrainment and transport of pollutants/contaminants (Davis, 1996; Krembs et al., 2002; Lange, 2002; Pfirman et al., 1995; Rigor and Colony, 1997), sediments (Eicken et al., 1997, 2000; Lisitzin, 2003; Reimnitz et al., 1995a; Stierle and Eicken, 2002), and the cycling and transport of terrestrial organic matter (Eicken, 2003b).
- The ocean plays a key role in the global carbon cycle with 50 times more carbon in the ocean than in the atmosphere (Richard Matear of CSIRO, pers. commun., 2005). The presence of sea ice cover, and associated ice–ocean–atmosphere interaction processes, affect the air–sea exchange of carbon dioxide and the storage of carbon in the ocean. The air–sea exchange of CO_2 is driven by three main processes (Allison et al., 2001), all of which are affected in some fashion by sea ice (at high latitudes): (i) the "biological pump", whereby planktonic biota take up CO_2 and then release it upon dying, decaying, and sinking into the deep ocean (Honjo, 2004); (ii) the "solubility pump", whereby the colder the ocean is, the more CO_2 it can sequester in near-surface waters; and (iii) Deep Water formation and entrainment, whereby CO_2 in surface and intermediate waters is transported directly to deeper layers where it is stored for long periods. While a large proportion of the total ocean uptake of CO_2 occurs in the mid-latitude band of the Southern Ocean (Liss et al., 2004a, b; Sabine et al., 2004), the ocean at higher southern latitudes is thought to be a net source of CO_2 to the atmosphere, as the result of upwelling of carbon-rich Deep Water. Recent research—e.g., by Hoppema (2004a) in the Weddell Sea—has shown it to be a modern major sink of CO_2 also. By playing a pivotal role in the nutrient chemistry and physics of high-latitude oceans, and by forming a physical lid on the ocean, the presence (characteristics) and dynamics of sea ice defines patterns of ocean primary production (see Section 5.5) and openwater CO_2 exchange (Arrigo et al., 1999; Stoll et al., 2002). Sea ice affects the flux of carbon from the atmosphere to the deep ocean by modifying biological and physical processes (Hoppema, 2004b). By comparison, carbon budgets for the Arctic Ocean have indicated that it is not at present a major sink region (Anderson et al., 1998a, b), although recent results challenge this—e.g., Miller et al. (2002) and Semiletov et al. (2004). An up-to-date review of the carbon cycle in the Arctic Ocean is given by Stein and Macdonald (2003).

Attempts to predict the future global environment depend on a comprehensive understanding of how biogeochemical cycling in the oceans affects the climate system, and how changes in climate influence the structure and functional properties of oceanic ecosystems. The basin-scale impact of the Southern Ocean on the level of atmospheric CO_2 is determined by competition between the biological pump and

[3] Remote connections between two parts of the world, or between two different processes in different places. Teleconnection is commonly used to describe the phenomenon by which weather patterns in one region influence those in a distant location.

physical processes (Honjo, 2004)—i.e., ocean upwelling, horizontal transport, and Antarctic Bottom Water formation. The Southern Ocean and its sea ice cover also play an important role in the global cycle of related biogenic elements—i.e., iron, nitrogen, phosphorus, and silicon. See SCAR (1993) for background information on the impact of the Antarctic sea ice zone on feedbacks and interactions within the global geosphere–biosphere system. Issues and current uncertainties relating to the role of the Southern Ocean and its sea ice cover in carbon release/uptake, and the role of high-latitude biological productivity in the transfer of carbon to the deep ocean, are discussed by Matear (2001), McNeil et al. (2001, 2003), Orr et al. (2001), and Trull et al. (2002). Of concern is a prediction by climate models of a decrease in the uptake of CO_2 by the Southern Ocean due to changes in ocean stratification, upwelling, and circulation caused by enhanced greenhouse warming, creating another positive climate change feedback (Sarmiento et al., 1998). Changes in the extent to which sea ice limits air–sea exchange may also affect the future atmospheric concentration of CO_2, as is believed to have occurred in the past (François et al., 1997; Sigman et al., 2004). Coordinated research into these important issues is taking place within a number of large multidisciplinary and international programs—e.g., the Joint Global Ocean Flux Study (JGOFS—see ⟨*http://www.uib.no/jgofs/jgofs.html*⟩ and Smith and Anderson, 2003) and the current Surface Ocean Lower Atmosphere Study (SOLAS) study (Liss et al., 2004b). Such programs are reliant on satellite remote sensing to extend surface measurements. See Field and Raupach (2004) for a modern review of the global carbon cycle.

A critical factor is that many of the important atmosphere–ocean–ice–biogeochemical interaction processes, and the complex feedbacks involved, are currently poorly quantified, and represent a major source of uncertainty in climate (and ecological) models and their predictions. While climate models predict large changes in global sea ice extent in response to increasing greenhouse gas concentrations in the atmosphere, the spatial characteristics and magnitude of the predicted response vary substantially between models (ACIA, 2004; Houghton et al., 2001). These inconsistencies relate in large part to differences in the representation of sea ice dynamics and thermodynamics, and the oversimplistic representation of sea ice and its snow cover, which in turn relate to incomplete knowledge. Satellites have a unique and key role to play in terms of reducing current uncertainties, both in furnishing improved data for (i) models and process studies, and in (ii) detecting and monitoring change and/or variability. Issues relating to scale are covered by Eicken (2003a) and McNutt and Overland (2003).

5.4.2 Ecological significance of sea ice

Covering such a vast area of the world's ocean, and forming an important habitat for a wide range of organisms specifically adapted to its presence, sea ice is also of immense ecological significance. It plays a dominant defining role in structuring high-latitude marine ecosystems (Ackley and Sullivan, 1994; Alexander, 1980; Brierley and Thomas, 2002; Constable et al., 2003; Eicken, 1992; Horner et al., 1992; Lizotte, 2001; Ross et al., 1996; Smith et al., 1995a, 1998a, b), and on a variety of scales (Figure 5.9). On the hemispheric scale, sea ice cover in winter

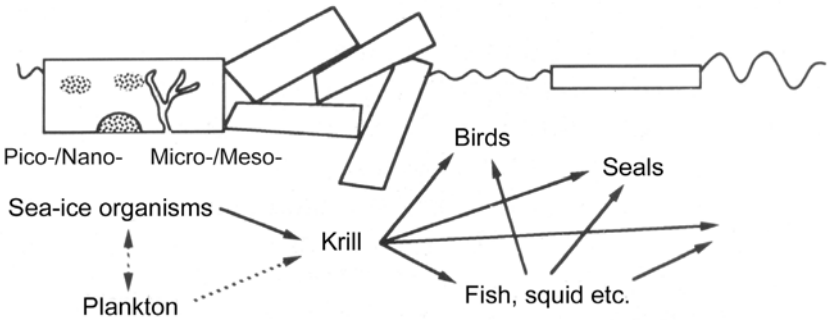

Feature	Primary porosity	Secondary porosity	Crevasses & ridges	Leads	Floes	Polynyas
Size	µm - mm	mm - dm	dm - m	m - km	10s m - 10s km	km - 100s km
Time Scale	min - d	d - 10s d	h - 100s d	h - 10s d	d - 100s d	d - 100s d

Figure 5.9. A schematic representation of features and spatial and temporal scales, increasing from left to right, of sea ice characteristics matched with part of the Antarctic foodweb (based on Murphy et al., 1988). Timescale in this case refers to the approximate temporal framework within which features change in appearance, h is hour and d is day. In the scale, dm is decimeter.

From Eicken (1992). With kind permission of Springer Science and Business Media.

interacts with key oceanic and biological boundaries such as the continental shelf break, the southern boundary of the Antarctic Circumpolar Current (Tynan, 1998) and the Antarctic Divergence, the latter being an important zone of upwelling. Polar marine ecosystems are characterized by strong seasonal cycles and major foodweb differences which are intimately related to the sea ice growth–decay cycle and conditions as well as associated nutrient availability and water density (Garrison and Mathot, 1996; Legendre et al., 1992; Lizotte, 2001). Also important are the impact of periodic fluctuations in sea ice distribution and characteristics associated with large-scale atmospheric circulation phenomena, such as El Niño–Southern Oscillation (ENSO).

Sea ice is home to thriving and diverse communities of micro-organisms, including algae and bacteria (Arrigo and Thomas, 2004; Dieckmann et al., 1998; Garrison, 1991; Lizotte, 2001; Palmisano and Garrison, 1993). As Brierley and Thomas (2002) point out, biological activity is associated with all physical components of the sea ice system—namely, the sea ice surface, its internal matrix, and brine channel system (microstructure), its underside, and the waters in the vicinity of sea ice that are modified by its presence. Sea ice plays a key role in polar marine primary production (Arrigo and Thomas, 2004), with the seasonal sea ice zone making a major contribution to the biological pump of CO_2 at high latitudes (OASIS, 2004; SCAR, 1993). This in turn has a potentially important impact on global climate. Sea ice algae form an important food source for a wide range of zooplankton predators, and certain deepwater fish species migrate to shallow depths beneath sea ice to exploit the resultant elevated concentrations of zooplankton there (Brierley and Thomas, 2002). Phytoplankton production also exerts an important control on the distribution and composition of marine sediments (Armand, 2000).

Sea ice microalgae also increase the internal heating and melting of the ice by enhancing light absorption (Zeebe et al., 1996)

Salt rejection during ice growth retards phytoplankton and algal growth in the ocean and sea ice limits the availability of Photosynthetically Active Radiation (PAR) in the upper ocean (Tilzer et al., 1985). The ice itself, however, forms a stable, nutrient-rich substrate with sufficiently high light levels for net growth of algae with a suite of physiological adaptations to the strong gradients in salinity, temperature, nutrients, and visible and ultraviolet radiation therein (Arrigo and Thomas, 2004; Eicken, 1992; Nöthig et al., 1991). This results in a concentration of algae (and bacteria and grazers) in the thin ice layer to create standing stocks that are typically significantly higher than those which occur in the upper tens of meters of the underlying water column, although species' diversity is lower (Brierley and Thomas, 2002; Schnack-Schiel, 2003). This represents an important food source for a wide range of organisms (Schnack-Schiel, 2003), including Antarctic krill (*Euphausia superba*) (Quetin et al., 1996; Ross et al., 1996). Antarctic krill also exploit interstitial gaps in sea ice as a refuge from surface and sub-surface predators during their larval stages (Frazer et al., 1997). Krill in turn is the pivotal species in the marine ecosystem, forming a critical food source for a range of apex predators including seabirds, seals and whales, which also have preferential adaptations for different ice conditions (Hofmann and Murphy, 2004). They also support a major fishery (Croxall and Nicol, 2004).

In spring–summer, sea ice melt releases particulate and dissolved organic matter into the water column (Leventer, 2003). This not only plays a major role in biogeochemical cycling, but it also "seeds" the water column with phytoplankton. Meltwater input stabilizes the upper ocean to enhance phytoplankton growth within the shallow mixed layer, leading in certain locations to algal blooms at the receding ice edge (Smith and Nelson, 1985, 1986; Smith and Grebmeier, 1995; Sullivan et al., 1993). In fact, the ice edge is typically the focus of enhanced biological activity (Falk-Petersen et al., 2000; Smith et al., 1988) and as such plays an important role in the carbon cycle (Savage et al., 1996). It has also long been the focus of the Southern Ocean whaling industry. Another important factor, in the light of ozone holes (see Chapter 4), is that the presence of snow-covered sea ice dramatically decreases the penetration of potentially harmful UV radiation into the upper water column, with snow cover greatly diminishing UV penetration into the ice cover (Davidson and van der Heijden, 2000; Smith et al., 1992; Weiler and Penhale, 1994).

For marine mammals and birds, sea ice forms a relatively stable platform on which to rest and breed, and provides a refuge from predators and access to specialist food (Ainley et al., 2003). It can also form a variable barrier to access to the atmosphere for breathing, and the ocean for feeding and migrating (Bornemann et al., 2000; Kasamatsu et al., 1998). Emperor penguins (*Aptenodytes forsteri*) rely on stable fast ice for breeding, but also require ready access to open water nearby for feeding (Ancel et al., 1992). As a result, their breeding success is dependent upon suitable ice conditions, and exhibits high interannual variability as a result. Areas of openwater in the form of ephemeral leads and recurrent flaw leads and polynyas enable marine mammals and birds to survive and migrate within the sea ice zone

(Massom, 1988; Stirling, 1980; Stirling and Cleator, 1981; Thiele and Gill, 1999). They can also be sites of enhanced primary production and even phytoplankton blooms in spring–summer (Arrigo and van Dijken, 2003a), and may play a role in primary production by also acting as skylights for transmitting higher levels of PAR to the ice underside and upper water column. In essence, PAR is the portion of the electromagnetic radiation used for photosynthesis (i.e., 0.4–0.7 μm), and corresponds to mainly the blue and green regions. There is widespread concern that ecosystem change may be induced by changes in sea ice extent. Indeed, sensitive ecosystem responses to sea ice changes are becoming increasingly apparent (Fraser et al., 1992; Fraser and Trivelpiece, 1996; Ross et al., 1996; Smith et al., 1999, 2003b). Sea ice also has a number of direct impacts on *Homo sapiens*. It has played a significant role in the lifestyle of native peoples in the Arctic for thousands of years (Dunbar and Dunbar, 1972), and also forms a major hazard to polar operations—e.g., shipping and hydrocarbon operations.

It should also be noted that very high concentrations of dimethylsulfoniopropionate (DMSP, not to be confused with the satellite series!) occur in both pack and fast ice, due to high production by ice algal communities (Curran and Jones, 2000; Curran et al., 1998; Liss et al., 2004b; Turner et al., 1995). These concentrations can attain values of >1,500 nM, compared with values for seawater of 0–50 nM (Trevena et al., 2003). This is of considerable climatic significance, in that DMSP is a precursor of dimethylsulphide (DMS), which is the main source of ocean-derived sulfates and thus affects cloud condensation nuclei and solar insolation (Buckley and Mudge, 2004; Liss et al., 2004b). Indeed, Trevena et al. (2003) concluded that such is the size of the reservoir of DMSP in the Antarctic sea ice zone that considerable fluxes of DMS occur to the atmosphere during the annual meltback, having a potentially important effect on both localized and global weather and climate patterns. It follows that any change in sea ice coverage and characteristics will potentially also affect weather and climate via this path through concomitant change in the distribution patterns of sea ice algae (Liss et al., 2004b). Please see OASIS (2004) for an assessment of our current understanding of the impact of air–snow–ice–ocean and biosphere–snow–ice–atmosphere interactions on atmospheric composition, the feedbacks involved, current research questions, and possible impacts of changing sea ice and snow cover conditions.

Another recent line of research has unearthed the considerable potential of exploiting cold-adapted organisms found in sea ice in a range of biotechnological applications. For example, attention has focused on sea ice microbes as a source of products for medical, agricultural, domestic, and industrial purposes (Cavicchioli et al., 2002; Nichols et al., 1999). These applications are reviewed in Arrigo and Thomas (2004).

5.5 RECENT OBSERVATIONS AND SIMULATIONS OF RAPID CHANGE, AND CURRENT UNCERTAINTIES

Importantly, sea ice is both an integrator and modulator of key ocean–atmosphere interaction processes within the high latitude and global climate systems (Barry and

Key, 1994; Barry and Maslanik, 1989; Eicken and Lemke, 2001; Schmidt and Hansen, 1999). Moreover, it is a sensitive indicator of anomalous behavior in atmospheric and oceanic regimes. It also constitutes a key agent of change through complex feedback mechanisms involving the coupled atmosphere–ice–ocean system (Allison et al., 2001; Goodison et al., 1999; Ledley, 1991; Simmonds and Jacka, 1995; Walsh and Timlin, 2003), as depicted in Figure 5.10 (see color section). Indeed, sea ice is a critical yet poorly understood and parameterized element in assessments of current conditions and predicted climate change. Although there is general agreement on the evidence of global warming (in both the sea ice and ice sheet domains), much debate rages and uncertainty exists on the regional pattern and magnitude of the response of ice masses to climate change. In this section, we examine observations and numerical model simulations of recent change and the uncertainties involved, leading into the critical importance of accurate satellite observations in helping to reduce these uncertainties.

A consistent feature of General (or Global) Circulation Model (GCM) and coupled model simulations is a polar amplification of the predicted increase in mean global air temperature forced by a gradual increase in atmospheric greenhouse gas concentrations (Holland and Bitz, 2003; Kattenberg et al., 1996; Manabe and Stouffer, 1993; Manabe et al., 1991, 1992). This high-latitude sensitivity has been attributed to positive feedback mechanisms involving surface albedo and reduced sea ice extent and thickness (see pp. 193–194), whereby an increase in heating decreases sea ice coverage and albedo by melting, which in turn further reduces the albedo and leads to additional heating (Curry et al., 1995; Ingram et al., 1989; Rind et al., 1995, 1997; Shine et al., 1984). In the Arctic, a number of models have, as a result, predicted a decreasing trend in Arctic sea ice extent and thickness, and even an almost complete disappearance of the summer ice cover over the current century (Johannessen and Miles, 2000) under a typical increasing greenhouse gas scenario—e.g., Gordon and O'Farrell (1997) (see Allison et al., 2001 and Houghton et al., 2001 for reviews). The climatic, ecological, cultural, social and economic implications of these changes are profound (ACIA, 2004; Houghton et al., 2001; Rapley et al., 2004). Looking on the bright side, Brigham et al. (2003) suggest that significant changes in sea ice distribution may lead to new opportunities for the shipping and offshore industries in the Arctic. Less encouraging are predictions of enhanced Arctic coastal erosion and possibly a change in patterns of cyclogenesis (Lynch et al., 2004; Walsh and Timlin, 2003). The impact on Inuit communities is also likely to be immense (Huntington, 2000), and is indeed being felt (Gearheard, 2004; Nichols et al., 2004; Oozeva et al., 2004). Current concerns and issues regarding the role of Arctic sea ice in the climate system, and its potential response to climate change, are summarized in Aagaard et al. (1999), ACIA (2004), and ACSYS (2003a, b).

Recent observations, many of which are based on satellite data analysis, provide strong evidence that substantial change has indeed been taking place at high latitudes and, in recent decades, most notably in the Arctic climate system (Morison et al., 2001; Polyakov et al., 2002, 2003), and that sea ice is central to this change. The observed Arctic changes, which are unprecedented in recent times in their rapidity, include:

- A recent decrease in atmospheric sea level pressure (Walsh et al., 1996).
- A change in patterns of Arctic Ocean circulation (Morison et al., 1998; Tremblay and Mysak, 1998), with a weakening of the Beaufort Gyre (an important element of ocean circulation in the Arctic Ocean) (Drobot and Maslanik, 2003; Proshutinsky et al., 2002) and a migration of the Transpolar Drift Stream (I. Rigor, pers. commun., 1999, cited in Kwok and Holt, 1999; Kwok, 2000). Particularly startling was an apparent rapid movement of warm Atlantic Water into the Arctic Ocean in the late 1980s to 1990s (Morison et al., 2000; Steele and Boyd, 1998). These observations are backed up by model simulations showing major regime shifts in general surface ocean circulation (Johnson et al., 1999; Maslowski et al., 2001; Proshutinsky and Johnson, 1997; Zhang et al., 1998a, b).
- An apparent decrease in sea ice thickness of ~40% in the Arctic Ocean since the late-1950s, observed in submarine sonar data collected along repeat tracks (Rothrock et al., 1999, 2003; Wadhams, 1994; Wadhams and Davis, 2000).
- A major decline of ~75% in the incidence (concentration) of submarine sonar-derived deep pressure ridges in the Eurasian Basin of the Arctic Ocean between 1976 and 1996 (Wadhams and Davis, 2000), suggesting that a change in regional ice dynamics has taken place (as modeled by Makshtas et al., 2003).
- A net decrease in overall Arctic sea ice extent of ~2–3% per decade over the last 20 years or so (Cavalieri et al., 1997; Comiso, 2003a; Johannessen et al., 1999; Parkinson and Cavalieri, 2002; Parkinson et al., 1999; Serreze et al., 2000).
- A recent decrease in sea ice extent in the Bering Sea (Niebauer, 1998; Niebauer et al., 1999).
- A decrease in the areal extent of thick multiyear ice in both winter and summer over the past 30 years (Johannessen et al., 1999; Maslanik et al., 1996, 1999), with a record minimum ice extent in the Arctic Basin in the summer of 2002 (Comiso, 2002a; Serreze et al., 2003) followed by a near-record minimum in 2003 (Comiso, 2003b) and yet another in 2004 (Stroeve et al., 2005).
- A 33% reduction in overall ice extent in the Nordic Seas in April over the last 135 years, determined from analysis of historical and latterly satellite data (Vinje, 2001a).
- A shortening of the sea ice season by ~25 days per decade over the period 1978–1996 in Arctic marginal seas (Parkinson et al., 1999).
- A recent increase in the length of the annual sea ice melt season for Arctic multiyear ice (Smith, 1998a).
- A recent loss of decades-old sea ice "plugs" between Canadian Arctic islands (Agnew et al., 2001; Jeffers et al., 2001).
- Changes in ice export from the Arctic Basin via Fram Strait (Harder et al., 1998; Hilmer and Jung, 2000; Hilmer et al., 1998; Kwok and Rothrock, 1999; Gerdes and Köberle, 2002; Kwok et al., 2004a).
- Associated large-scale changes in the near-surface structure of the ocean (Steele and Boyd, 1998; Morison et al., 1998), with a freshening of the mixed layer (Maslanik et al., 1996; McPhee et al., 1998) and a rapid freshening of deep layers of the North Atlantic accompanied by a decrease in water salinity (Dickson et al., 2002, 2003).

These changes have coincided with an observed decrease in mean sea level atmospheric pressure, changes in cloudiness (Wang and Key, 2003; Schweiger, 2004), and regional changes in air temperature (negative over Eastern North America and Greenland but positive over much of the Arctic) (Jones et al., 1999; Moritz et al., 2002; Serreze et al., 2000). Please see Aagaard et al. (1999), Cattle et al. (2001), and Morison et al. (1998; 2000), and the references therein, for a detailed review of oceanic processes in the Arctic, and recent changes observed therein. See also Bobylev et al. (2004) for an assessment of Arctic environmental change in the context of global change.

The implications of such changes, if sustained over periods of a few years to decades, are immense, and have motivated the establishment of the Study of Environmental ARctic CHange (SEARCH) initiative involving scientists, policy makers and scientists (Morison et al., 2001; ⟨*http://psc.apl.washington.edu/search/index.html*⟩). Of great concern, for example, is the observation by Steele and Boyd (1998) of an anomalous thinning and retreat in some areas of the Cold Halocline Layer (CHL), the upper-ocean layer characterized by a strong salinity gradient, from the Eurasian Basin of the Arctic Ocean in the 1990s. They attribute this to a large-scale shift in ice drift and upper-ocean circulation patterns forced by a strengthening of the Eurasian atmospheric low-pressure cell. The CHL is "normally" maintained by the advection of cold, saline water masses produced during sea ice growth on the continental shelves surrounding the Arctic basin, with polynyas on the Alaskan, Siberian, and Canadian coasts being considered important sources of this dense water (Aagaard et al., 1981; Chapman, 2000; Signorini and Cavalieri, 2002; Winsor and Björk, 2000). It has a major impact on the sea ice thickness distribution by insulating the ice cover from the heat stored within the underlying relatively warm Atlantic water. Removal of this protective layer would lead to strong vertical ocean heat fluxes (Martinson et al., 2000) and the depletion of the perennial sea ice cover (McPhee et al., 1998; Steele and Boyd, 1998). As noted previously, Steele and Boyd (1998) reported an increase in Atlantic-type water in the Eastern Arctic in the 1990s, while the temperature of Atlantic Water in the Arctic Ocean was found by Morison et al. (2000) to be the highest in 50 years of observation. Björk et al. (2002) and Martinson et al. (2000) reported that the CHL appeared to be re-establishing itself in the late-1990s, possibly in response to a reduction in the strength of the atmospheric circulation anomaly that first came into place about a decade earlier.

A major concern regarding these patterns, and as predicted by certain models, is that a change in Arctic sea ice-related processes may propagate downstream as a change in the ocean heat, saltwater and/or freshwater budgets (Häkkinen, 1995). The stratification of high-latitude oceans is highly sensitive to changes in the freshwater balance. These changes could result in the Arctic not only from changing sea ice regimes but also by higher input of freshwater through enhanced precipitation, river discharge (Peterson et al., 2002), and glacier/ice sheet meltwater runoff. Such changes may act to reduce or even block Deep Water formation in the North Atlantic, and could have a drastic impact on global thermohaline circulation and regional/global climate (ACIA, 2004; ACSYS, 2003a; Dickson et al., 2002, 2003), although the uncertainty is again high (Cattle et al., 2001; Wu et al., 2004). For

example, less tropical heat could be advected northwards by the Gulf Stream to moderate European winters (ACIA, 2004). In addition, a slowing of thermohaline circulation would impact the transport of carbon dioxide to the deep ocean (leading to a more rapid buildup in the atmosphere), and the availability of nutrients for marine life. These examples illustrate the fact that high-latitude changes will have global ramifications. The annual production of ice, its export to lower latitudes—e.g., via Fram Strait (Vinje and Finnekåsa, 1986)—and its eventual melt are poorly understood, requiring accurate information on ice motion, distribution, and thickness.

The major questions that revolve around observed sea-ice-related changes are abrupt shifts of climate regimes or part of a long-term trend related to anthropogenic global warming, manifestations of natural oscillatory cycles of climate variability (Lynch et al., 2001; Serreze et al., 2000; Walsh et al., 1996), or a complex combination of both. A warming trend has in fact been observed in recent times in the Arctic Ocean and sub-Arctic terrestrial regions (Comiso, 2003b; Dickson, 1999; Karcher et al., 2003; Martin et al., 1997), but this exhibits considerable regional variability in a manner that is poorly understood and with slight cooling occurring in some areas (Chapman and Walsh, 1993; Magnuson et al., 2000; Serreze et al., 2000; Vinnikov et al., 1999). Based upon a linear regression analysis of the National Oceanic and Atmospheric Administration (NOAA) Advanced Very High Resolution Radiometer (AVHRR)-derived TIR over the period 1981–2003 (Comiso and Parkinson, 2004), it appears that mean surface temperatures north of latitude 60°N have increased at a rate of ~0.54°C per decade over sea ice (see Section 5.9.11 for further discussion of regional and seasonal variability). Any interpretation of sea ice as a bellwether of climate variability is tempered by the fact that such variability is likely to be affected by the complex interplay of local and regional weather and climate (Stone, 1998).

Strong evidence is emerging that the major anomalies in Arctic pack ice distribution, heat and freshwater exchange, water mass structure and upper-ocean circulation outlined above are correlated with recently identified decadal-scale natural modes of variability in large-scale atmospheric circulation (Deser et al., 2000, 2002; Dukhovskoy et al., 2004; Goosse et al., 2001; Häkkinen, 2000; Moritz et al., 2002; Mysak, 1999; Mysak et al., 1996; Polyakov and Johnson, 2000; Proshutinsky and Johnson, 1997). Recently described modes of variability in high northern latitude wind fields include the Arctic Oscillation or AO (Gillett et al., 2002; Overland et al., 2002; Rigor et al., 2002; Thompson and Wallace, 1998, 2000; Wang and Ikeda, 2001), and the North Atlantic Oscillation or NAO (Dickson, 1999; Dickson et al., 2000; Hurrell, 1995; Hurrell and van Loon, 1997; Hurrell et al., 2003; Mysak and Venegas, 1998; Polyakov et al., 1999; Proshutinsky and Johnson, 1997; Serreze et al., 2000)—see pp. 194–195. The AO is defined as the leading Empirical Orthogonal Function (EOF) of the monthly, mean sea level pressure poleward of 20°N in winter. The AO/NAO remained positive from the late-1980s through the late-1990s, resulting in a weakening of the Beaufort Gyre and an increase in the advection of sea ice out of the Arctic Ocean and into the North Atlantic via Fram Strait (Kwok, 2000; Kwok and Rothrock, 1999). By

weakening the Beaufort High, this results in increased ice divergence and open-water fractions, decreased surface albedo, increased radiative heating and lateral ice melt, and freshening of the upper Beaufort Sea. Such a pattern is thought to have contributed to the observed recent reduction in the overall longevity and related volume of sea ice within the Arctic Basin. In addition, contemporary warming in Russia and northern Europe appears to be correlated with the AO. Recent modeling suggests that this shift in the behavior of the AO may be symptomatic of anthropogenic climate change—i.e., the AO is both a natural pattern of variability and a component of climate change.

Another example of resultant decadal variability in the ocean is the "Great Salinity Anomaly" of the late-1960s (Dickson et al., 1988), whereby enhanced sea ice melt in the sub-polar North Atlantic, resulting from increased ice export southward in the Greenland Sea, caused an ocean salinity decrease responsible for increasing stratification to interrupt deep vertical convection in the ocean (Haak et al., 2003; Häkkinen, 1993). While recent work has led to a much improved understanding of this natural variability, worrying evidence is emerging to indicate that the significant warming trend and decrease in sea ice extent in the Arctic over the past two decades cannot be explained by natural processes alone (Bengtsson et al., 2004; Johannessen et al., 2004). Given the feedbacks involved, there is even talk of an Arctic Ocean that is largely ice-free in the boreal summer by the end of this century (Johannessen et al., 2004). This—and a reduced ice cover in the intervening period—would have a profound impact on global thermohaline circulation and regional–global climate, and immense ecological and socio-economic implications. These necessitate improved knowledge of the complex physical processes and feedbacks involved.

It appears that the immense seasonal pulsation of Antarctic sea ice is also highly sensitive/responsive to, and interactive with, ocean–atmosphere heat and freshwater fluxes (Komuro and Hasumi, 2003; Timmermann et al., 2001) and associated ocean thermohaline overturning (Cattle et al., 2001). Significant shrinkage in the areal coverage of Antarctic sea ice has been predicted over the coming century by GCMs running with an increase in atmospheric CO_2—e.g., of 25% where the CO_2 increase is 1% per annum (Meehl et al., 2000) and 17–31% in response to a doubling of atmospheric CO_2 (Rind et al., 1997). Other GCMs predict that global warming may in fact lead to a thickening of Antarctic sea ice, due to an increase in precipitation (i.e., freshwater) input into the upper ocean (Manabe et al., 1992). This, the authors suggested, would act to stabilize the pycnocline and diminish the upward flux of deep-ocean heat available for ice basal melt, thereby counteracting enhanced surface melt. In a typical climate change scenario, model analyses by Wu et al. (1997), Wu and Budd (1998), and Hirst (1999) further predicted a decrease in ice formation combined with increases in precipitation minus evaporation and glacial meltwater from the ice sheet. These processes would increase the strength of the halocline and reduce deep-ocean convection and Bottom Water formation. According to Broecker et al. (1998), this would result in a slowdown in thermohaline circulation (a scenario also predicted by Hirst, 1999 and Manabe and Stouffer, 1993), and even a shutdown at high greenhouse gas concentrations in the atmosphere, with far-reaching global implications. Bi et al. (2001) also predicted the collapse and

reorganization of Southern Ocean overturning in response to global warming. Such a stagnation also has implications for deep-ocean ventilation and the uptake of atmospheric CO_2, although the overall extent to which ocean uptake of anthropogenic CO_2 will be affected by climate change is uncertain. Other models, which prescribe a fractional sea ice cover, produce contradictory results (see Cattle et al., 2001). Regarding the uptake of anthropogenic CO_2 by polar oceans, current model-derived estimates differ markedly in the pattern and magnitude of the uptake. Improved understanding of the marine carbon cycle is essential to assessing feedback between the oceanic uptake of carbon and climate change, balancing regional and global carbon budgets, and understanding potential impacts of climate change on marine ecosystems.

In contrast to the Arctic, Antarctic sea ice extent as a whole has increased slightly over the satellite era—i.e., the past 30 years (Cavalieri et al., 2003a; Parkinson, 2004; Watkins and Simmonds, 2000; Zwally et al., 2002a). Strong regional contrasts are, however, apparent in satellite passive-microwave time series. A positive ice extent trend has occurred in the Ross Sea—of $\sim 6.7 \pm 1.1\%$ per decade from 1979 to 1998 (Zwally et al., 2002a). On the other hand, the only Antarctic sector to have exhibited a strong negative trend over this period is that to the west of the Antarctic Peninsula (Comiso, 2003a; Smith and Stammerjohn, 2001; Smith et al., 1996; Jacobs and Comiso, 1993, 1997; Zwally et al., 2002a). Stammerjohn and Smith (1996, 1997) showed that this decrease has coincided with an extraordinary regional-scale warming trend of $>2^\circ$C since the 1940s (King et al., 2003; Vaughan et al., 2003), a phemonenon that is discussed in more detail in Section 5.9 and Volume 2 of this book. Warming over the Antarctic as a whole appears to have been $\sim 0.5^\circ$C over the last 50 years or so (Jacka and Budd, 1998), although certain regions have cooled in recent decades. Why the warming trend should be largely limited to the Antarctic Peninsula is not currently known.

Modeling studies by Wu and Budd (1998) and Wu et al. (1999a) indicated that Antarctic sea ice was more extensive in the last century, and reduced by 0.4–1.8° of latitude over the 20th century. de la Mare (1997) inferred that the summer Antarctic sea ice edge retreated southwards by 2.8° of latitude between the mid-1950s and the early-1970s, suggesting a decline of $\sim 25\%$ in the area covered by sea ice in summer. Ackley et al. (2003) question the uncertainties in this result, however, based upon the indirect nature of the ice edge location reconstruction by de la Mare (1997) using whaling records. A modeling perspective is provided by Fichefet et al. (2003a, b). Intriguing new results have emerged from an analysis by Curran et al. (2003) of methanesulfonic acid (MSA) in firn/ice cores from the coastal Law Dome on the East Antarctic Ice Sheet that seem to support the de la Mare (1997) findings. By resolving and dating seasonal variability in the MSA record, and comparing it with contemporary satellite data, Curran et al. (2003) discovered a close correspondence between MSA in ice cores from Law Dome and sea ice extent in the sector 80–140°E. This gave them confidence to use the MSA record as a proxy measure of regional sea ice extent in the pre-satellite era. By extending the analysis back to 1840, they also showed that sea ice extent is currently at an historical low, at least in the sector studied. Moreover, it appears that the ice edge has retreated by $>1^\circ$ of latitude since

1950. Such results and methods are yet to be tested in the wider geographical context.

Observation of water mass properties suggests that important oceanic changes may have occurred in the Southern Ocean over the past 30 years (Bindoff and McDougall, 2000; Gille, 2002; Jacobs et al., 2002; Johnson and Orsi, 1997; Wong et al., 1999). Examples are an apparent warming trend of both Weddell Sea Deep Water and Bottom Water masses that occurred, for example, in the 1990s (Robertson et al., 2002), followed by a cooling phase with apparent decadal-scale variations in water mass properties in response to changes in atmospheric forcing (Fahrbach et al., 2004). Such changes have important implications for Antarctic Bottom Water formation, sea ice mass balance, and the regional ocean–atmosphere heat transfer. Once again, the wider implications are immense, given that processes occurring in the Southern Ocean have a profound influence on regional and global ocean circulation and climate (Jacobs, 2004; Rintoul et al., 2001a, b). The warming trend noted in oceanographic data from the 1970s to 1990s is comparable with warming in satellite-derived ice surface temperature data observed in the Weddell Sea by Comiso (2000). Again, our understanding of mechanisms responsible for observed variability in high-latitude oceans in both hemispheres, and on timescales ranging from decadal to centennial and beyond, is minimal. Issues relating to climate variability and the Southern Ocean are assessed in the World Climate Research Program (WCRP) CLImate VARiability and Predictability Program CLIVAR (CLIVAR Scientific Steering Group, 1995), with its role in global processes being evaluated by Busalacchi (2004).

As with the Arctic, the emerging picture of atmospheric variability is immensely complex and far from fully understood. New studies based on improved meteorological data show evidence of significant oscillatory behavior in atmospheric circulation anomaly patterns over the Southern Ocean—on a range of scales and with teleconnections to lower latitude phenomena (Carleton, 2003; Liu et al., 2002a, b; White et al., 2002; Yuan and Martinson, 2000). The implication is that climate patterns in regions such as southern Australia, for example, may be affected by Antarctic sea ice distribution. Any anthropogenically driven change will form a backcloth to apparent natural climatic variability composed of elements which (i) are semi-annual—e.g., the Semi-Annual Oscillation or SAO (Enomoto and Ohmura, 1990; Meehl et al., 1998; Simmonds, 2003; Van den Broecke, 1998; van Loon, 1967); (ii) are interannual—e.g., El Niño/La Niña (Carleton et al., 2003; Kwok and Comiso, 2002a, b; Rind et al., 2001; Turner, 2004; Yuan, 2004); (iii) have an apparent period of 4 years—e.g., the propagating pattern of anomalies known as the Antarctic Circumpolar Wave (Connolley, 2002; Venegas and Drinkwater, 2001; Venegas et al., 2001; White and Peterson, 1996; White et al., 2004; Zhang and Semtner, 2001); and (iv) are longer term—i.e., decadal to centennial (Chen and Yen, 1997; Martinson et al., 1995) and beyond.

On the decadal scale, recent change has been observed in large-scale tropospheric circulation in the Southern Ocean in the form of a strengthening and contraction of the circumpolar vortex, and concomitant strengthening of the circumpolar westerlies (Gillett and Thompson, 2003; Hurrell and van Loon, 1994;

Thompson and Solomon, 2002). This is associated with the so-called Southern Annular Mode (SAM), or Antarctic Oscillation (Fyfe et al., 1999; Gong and Wang, 1999; Hall and Visbeck, 2002; Karoly, 1990; Kidson, 1988; Marshall et al., 2004; Thompson and Wallace, 2000). The SAM is analogous to the Arctic Oscillation, and is the dominant mode of variability in atmospheric circulation in the Southern Hemisphere. Changes in the SAM, and specifically an apparent trend towards its high (positive) index state, have been largely responsible for the observed broad-scale change in Antarctic climate in recent decades—e.g., strengthening of the westerly wind field, and increased Ekman (northward) transport of sea ice (i.e., enhanced regional ice extent) in the Pacific sector of the Southern Ocean (Liu et al., 2004a). Localized factors have also played a role in the Antarctic Peninsula region (Turner and Colwell, 2004). Thompson and Solomon (2002) suggested that the behavior of the SAM, and therefore its impact on atmospheric circulation and temperatures within and around Antarctica, is linked to seasonal and interannual variability in the stratospheric ozone hole. Other work—e.g., Cai et al. (2003) and Fyfe et al. (1999)—suggested a link between changes in the SAM and an enhanced greenhouse effect. Other dominant patterns of variability include the Pacific–South American mode and the Antarctic Dipole, which entails atmospheric anomalies of opposite sign in the southwest Atlantic and southeast Pacific Ocean sectors of the Southern Ocean (Liu et al., 2002b, 2004a; Yuan and Martinson, 2001). It is characterized by an out-of-phase relationship between ice and temperature anomalies in the two regions. For an evaluation of modes of variability in the Southern Hemisphere atmosphere, see Kidson (1999) and Simmonds (2003), while Simmonds and King (2004) evaluate hemispheric and global climate variations affecting the Southern Ocean.

Unravelling the mechanisms behind these modes of variability, their interconnectivity and teleconnections with lower latitudes (including possible inter-hemispheric), their impact on high-latitude climate and ecosystems, and the complex feedback processes involved—e.g., between modes of atmospheric variability and sea ice extent—presents a major and stimulating challenge. Only now are the implications of such variability on high-latitude sea ice distributions, ocean properties and circulation, and ecosystems starting to be addressed (Ainley et al., 2005; Oke and England, 2004). There is also a strong likelihood that a changing distribution of sea ice will affect the atmosphere in a complex fashion, given the strong coupling between atmosphere and ice-covered ocean (Alexander et al., 2004; Simmonds et al., in press; Zhang et al., 2004). Possible changes include the synoptic-scale patterns of atmospheric circulation and, particularly, cyclogenesis and the trajectories of cyclones, which will in turn feed back on the sea ice distribution. Liu et al. (2004a) provide an interpretation of the impact of patterns of anomalous atmospheric circulation on Antarctic sea ice variability, while Renwick (2002) examines the relationship between Southern Hemisphere circulation and sea ice, as well as sea surface temperature. However, the patterns of atmospheric variability exhibit high- and low-frequency variability for reasons that are not yet fully understood. Also poorly understood at present is their impact on sea ice.

Unfortunately, major discrepancies exist in different GCM simulations, leading to large and unacceptable uncertainties in climate predictions (Gates et al., 1996; Houghton et al., 2001; Kattenberg et al., 1996). As noted before, the snow/ice albedo feedback mechanism is a key issue in that it not only drives an amplification of predicted global warming at high latitudes, but also amplifies errors in the parameterization of the processes involved (Goodison et al., 1999). Other factors contributing to uncertainty include a model grid cell resolution that is too coarse to resolve many important processes and phenomena—e.g., coastal polynyas, and an oversimplified and incomplete representation of the physics involved (Allison et al., 2001; Randall et al., 1998). Modern standalone sea ice models and coupled atmosphere–ice–ocean models, on the other hand, operate at a finer resolution and parameterize sea-ice-related processes in greater detail (see Flato, 2004 for an excellent review). Significant discrepancies are again apparent in model performance, however (Kreyscher et al., 1997, 2000; Lemke et al., 1997; O'Farrell and Connolley, 1998; Proshutinsky et al., 2001). Clearly, differences in model simulations and predictions result from incomplete knowledge of the complex relationship(s) between sea ice, polar ocean circulation and the large-scale interannual to decadal (and longer) modes of atmospheric variability involved (Walsh et al., 2000), coupled with inadequate treatment of the physics involved. A critical challenge is to develop and implement a realistic sea ice model into GCMs (Stössel et al., 1996). Fortunately, the tide is turning, thanks to satellite remote sensing with its unique ability to provide time series of improved and consistent large-scale data with which to reconcile these differences and improve model performance. Such data are required to define and constrain key parameters and processes, and to validate and improve model performance (Goodison et al., 1999).

Also serious are the impacts of changing sea ice distribution and characteristics on the structure and function of polar ecosystems (Clarke and Harris, 2003), and the possibility of a resultant decrease in polar biodiversity. For example, a recent reorganization of penguin distributions in the Antarctic Peninsula has been attributed to the rapid regional warming encountered there (Fraser et al., 1992; Vaughan et al., 2001). While the population of chinstrap penguins (*Pygoscelis antarctica*), which require open water (a divergent ice cover), is increasing at Faraday Station, that of Adélie penguins (*Pygoscelis adeliae*) is decreasing. The latter species prefers access to winter pack ice, and heavier ice conditions in general (Ainley, 2002). Another apparent impact is on the prey species and their availability. This is just one of many examples of significant ecosystem change in response to environmental change that are emerging from both polar regions. While ecosystem structure and biogeochemical fluxes are thought to be particularly sensitive to climate warming and changes in sea ice circulation/distribution patterns (Smith et al., 1999), the scenario is again complex and fraught with uncertainty. Once again, there are many gaps in our knowledge of current physical conditions that compromise biological/ecological predictions. For example, reasons for the observed variability in the circumpolar distribution of ice edge phytoplankton blooms are largely unknown, and more realistic descriptions of ice edge conditions are required to improve coupled physical–biogeochemical models of the ice edge ecosystem (Buesseler et al., 2003).

In a global-warming scenario, reductions in sea ice concentration and extent are predicted to cause enhanced light availability in the upper water column, which will combine with higher surface water temperatures to increase algal production. Such a scenario may also increase carbon uptake from the atmosphere. On the other hand, a reduced sea ice cover may limit primary production and carbon uptake through reductions in (i) the input of freshwater and seeding of the ocean with ice algae and nutrients during seasonal melt, and (ii) nutrient inputs from the deep ocean due to a reduction in upwelling associated with a weakening of the ocean "conveyor belt" circulation (Arrigo et al., 1999; Lizotte, 2001; Walsh et al., 2000), while increasing the intensity of harmful UV radiation (Smith et al., 1992). Moreover, the predicted increase in circumpolar storminess may significantly impact the size and characteristics of biologically active marginal ice zones. How such scenarios will impact predators such as krill, fish, penguins, seals, and whales is largely unknown, but is the subject of intensive research (Arrigo and Thomas, 2004; Ross et al., 1996; Smith et al., 1995a). Recent research also suggests that associated changes in high-latitude ocean circulation and stratification could have a global impact on biological productivity and biogeochemical cycles (Sarmiento et al., 2004). For an assessment of the potentially serious impact of sea ice regime change on polar marine bird and mammal species, see Ainley et al. (2003, 2005), Croxall et al. (2002), Krajick (2001), Smith et al. (1999), Stirling and Derocher (1993), and Tynan and DeMaster (1997). Potential impacts of a changing sea ice cover on primary production are assessed by Arrigo and Thomas (2004). Information on climate variability and the ecological response of the marine ecosystem in the West Antarctic Peninsula region is given by Smith et al. (2003a, b, c). It is not just the areal extent of sea ice that affects the structure and function of high-latitude marine ecosystems. Other factors include the length of the ice season and the growth and decay seasons (Smith et al., 1999, 2003b), as well as the degree of ice compaction and deformation and the thickness of the snow cover (Massom et al., in press) and the relative sizes of the marginal ice zone compared with the inner pack (Arrigo and Thomas, 2004) and the seasonal versus the perennial ice zones.

New and continuing datasets from satellite sensors are enabling us to tackle key fundamental deficiencies in our knowledge base, with a critical need being to improve knowledge of large-scale time-varying distributions of the key physical (and chemical) characteristics of sea ice-covered oceans (Allison et al., 2001). Sea ice is a common factor in all of the processes and changes outlined. These deficiencies have severely limited our ability to accurately model current conditions, predict probable future conditions, and distinguish long-term trends from natural oscillatory variability with any level of confidence. Major scientific questions involving sea ice include:

- How does sea ice influence, and respond to, global climate variability and change?
- What are the current mean state, natural variability, and recent trends in sea ice characteristics, and what physical processes determine them?

- How are sea ice mass balance[4] and extent changing (Bamber and Kwok, 2004)?
- How does sea ice modulate and moderate surface fluxes, and what impact will changing sea ice regimes have on global ocean thermohaline circulation, the ice albedo feedback mechanism, and energy/moisture/boundary-layer exchange?
- What are the sea ice and other physical conditions regulating the spatio-temporal variability of high-latitude marine ecosystems, community composition, and structure?
- What are the interactions among the physical, biological, and chemical systems in polar oceans?
- How do spatial and temporal changes and variability in sea ice and its snow cover affect biological processes and human activities?
- What are the processes and sensitivities controlling the exchange of CO_2 between the ocean and atmosphere in polar regions and its subsequent sequestering in all layers from surface water to deep water, including the role of sea ice and the larger scale mechanisms and feedbacks controlling these processes?
- What are the links between and interactions, on all scales, between polar regions and the rest of the Earth, and what processes control them? This question is being addressed by the SCAR Antarctica and the Global Climate System (AGCS) initiative, for example (⟨*http://www.clivar.org/organization/southern/AGCS.pdf*⟩).

Further key questions, from a wider Southern Ocean perspective, are laid out by Busalacchi (2004). Addressing such questions will be the focus of intensive research as part of the International Polar Year in 2007–2008 (Rapley et al., 2004).

These questions are being addressed by the new scientific strategy for research on ocean–ice–atmosphere interactions laid out in a number of coordinated initiatives. These are both national—e.g., the Canadian CRYosphere SYStem (CRYSYS) (⟨*http://www.msc.ec.gc.ca/crysys/overview/crysys_whatis_e.cfm*⟩) and Canadian Arctic Shelf Exchange Study (CASES, ⟨*http://www.giroq.ulaval.ca/cases*⟩) programs—and international—e.g., the SCAR (Scientific Committee on Antarctic Research) Antarctic Sea Ice Processes and Climate project (ASPeCt) (⟨*http://www.antcrc.utas.edu.au/aspect/index.html*⟩), the WCRP Arctic Climate SYStem Study or ACSYS (WCRP, 1998), CLImate and Cryosphere (CLIC) projects (Allison et al., 2001; Barry et al., 2004; ⟨*http://clic.npolar.no*⟩) and CLImate VARiability and Predictability program (CLIVAR) (⟨*http://www.clivar.org/organization/index.htm*⟩) programs, Study of Environmental ARctic CHange (SEARCH) ⟨*http://psc.apl.washington.edu/search/index.html*⟩), and the Scientific Committee on Oceanic Research (SCOR) International Antarctic Zone (iAnZone) program (⟨*http://www.ldeo.columbia.edu/physocean/ianzone/*⟩; Muench and Hellmer, 2002). All stress the need for an integrated approach combining field observations, numerical modeling, and satellite remote sensing. The major sea-ice-related objectives of CLIC, for example, are (Allison et al., 2001):

[4] Mass balance is defined here as the difference between ice production and the sum of ice export and ablation.

- To derive a sustained and consistent climatological dataset describing the basic physical properties of sea ice cover.
- To improve understanding of the processes of interaction between sea ice and other components of the global climate system—e.g., processes of ice formation and decay, ice mass budget, ocean freshwater budget, water mass modification, ice margins, and the maintenance of polynyas.
- To validate, calibrate, and improve the parameterization of sea ice properties and processes in coupled ocean–ice–atmosphere models (Curry et al., 2002).

Sea ice research also forms a major component of key international ecological programs, including the U.S. Palmer Long-Term Ecological Research (LTER, Smith et al., 2003a), Southern Ocean GLOBal ECosystem Dynamics (GLOBEC) (Hofmann et al., 2002), and Bering Ecosystem STudy (BEST, ⟨*http://www.arcus.org/Bering/*⟩) programs.

While they sound simple on paper, the research strategy and scientific questions outlined above represent an immense challenge, given the highly dynamic nature of sea ice and the complexity of the processes and interactions involved, and over a wide range of spatial and temporal scales. Once again, satellite remote sensing clearly has a unique and critical contribution to make. It alone can provide the requisite observations on a long-term, sustained, large-scale, homogeneous, and consistent basis in order to resolve variability over its apparent range of timescales, from synoptic through seasonal and interannual to decadal and multi-decadal and beyond (Johannessen et al., 2004). Satellites also greatly extend detailed surface measurements. In turn, satellite measurements and derived geophysical measurements, from not only emerging but also established sensor technologies, require adequate validation using *in situ*, aircraft, and other satellite data. Validation in this sense refers to the independent estimation of error, and its importance cannot be overstressed.

5.6 THE GROWTH, DECAY, AND HEAT BUDGET OF SEA ICE—DYNAMICS VERSUS THERMODYNAMICS

We have seen how the distribution (areal extent and concentration), thickness and other properties of sea ice are determined by the complex interplay of a variety of dynamic (motion and deformation) and thermodynamic (freezing and melting) processes. From a modeling perspective, these are described by thermodynamic and dynamic formulations which are governed by (i) the surface energy balance (heat balance plus radiation balance), and (ii) the conservation laws of ice momentum and mass, respectively, with ice rheology and redistribution also playing central roles. In this section, we briefly examine the theory behind these important concepts, which form the basis of much of our current understanding of polar atmosphere–ice–ocean interactions and upon which predictions are based. An overall aim is again to illustrate how and where the satellite-derived geophysical products described later make a contribution to the parameterization of individual

terms, while underlining the complexity of the interrelationships and feedbacks involved.

5.6.1 The surface energy balance of a sea-ice-covered ocean

The rate of basal sea ice growth or melt is determined by thermodynamic processes which are controlled by the energy exchange at the upper and lower surfaces of the combined ice–snow layer (Holland et al., 1997a, b; Maykut and Untersteiner, 1971). Under freezing conditions, heat released both by the cooling of the interior of an existing sheet of ice and the freezing seawater onto its base is transferred upwards to the ice/snow surface and released to the atmosphere. For a given slab of sea ice, heat is advected to the base which remains at a constant temperature T_I —i.e., the melting point ($\sim -1.86^{\circ}$C for seawater). The upper surface radiates heat to achieve a temperature T_S. As heat conducts across the slab, from areas of high to low temperature and in the direction of the temperature gradient (following Fourier's law of heat conduction), the ice interior has a temperature between T_I and T_S. The rate of heat extraction is determined by the thermal properties of the snow and ice (i.e., their thermal conductivity and diffusivity[5]), and the energy balance at the upper and lower surfaces of the ice. Conservation of energy for surfaces in equilibrium with the atmosphere requires that the heat fluxes into and out of the ice are balanced as follows:

$$(1-\alpha)F_{sw} - I_{ice} + F_{lw}^{\Downarrow} - F_{lw}^{\Uparrow} + F_{lat} + F_{sens} + F_m = 0 - F_c \tag{5.1}$$

where F_{sw} is the shortwave (solar) radiative flux at the surface; α is the surface albedo and $(1-\alpha)$ denotes the proportion of incoming shortwave energy reflected back at the snow/ice surface; I_{ice} is the amount of shortwave energy that penetrates the snow/ice and does not directly heat the surface; $F_{lw}^{\Downarrow}$ is the downwelling longwave flux emitted by the atmosphere and clouds; $F_{lw}^{\Uparrow}$ is the outgoing longwave flux emitted by the surface; F_{lat} and F_{sens} are the latent and sensible heat fluxes, respectively; F_m is the heat flux due to surface freezing or melting; and F_c is the conductive heat flux through the ice (Eicken, 2003a; Maykut, 1982, 1986; Parkinson and Washington, 1979).

More specifically, and from a surface energy balance perspective, albedo is taken to be the ratio of irradiance (M) to exitance (E) over all solar-reflective wavelengths (typically spanning the shortwave region), and is equivalent to hemispherical reflectance—i.e., the reflectance integrated in all directions (Sun view geometries). Exitance is the radiant flux density leaving the surface in all directions per unit area and per unit time (in $\mathrm{W\,m^{-2}}$), and irradiance that is incident upon the surface per unit area per unit time (also in $\mathrm{W\,m^{-2}}$). Here, radiant flux density is the rate of energy transfer per unit area (in $\mathrm{W\,m^{-2}}$), where radiant flux is the rate of energy transfer in all directions per unit time (in W) (Slater, 1980).

In (5.1), F_{sw} depends on latitude, solar zenith angle, day of the seasonal cycle,

[5] *Thermal diffusivity* is a measure of the length of time it takes a heat pulse to travel a given distance.

atmospheric transparency, and cloud fraction and type, while I_{ice} depends on the state of the ice and its snow cover. Also, $F_{lw}^{\Uparrow} = \varepsilon\sigma T_{ice}^4$, where ε is the surface emissivity[6] integrated over all TIR wavelengths, σ is the Stefan–Boltzmann constant ($5.670\,51 \times 10^{-8}\,\mathrm{W\,m^{-2}\,K^{-4}}$), and T_{ice} is surface physical (absolute) temperature of the ice (in K). The concept of emissivity is examined in more detail in Section 5.7.2. The longwave components in models are generally affected by air temperature, humidity, and cloudiness. Computed latent and sensible heat fluxes depend, amongst other things, on accurate surface temperature and ice surface roughness information. The latter affect the bulk transfer coefficients via their impact on the surface drag coefficient (see below). Apart from $F_{lw}^{\Downarrow}$, all of the terms in (5.1) are dependent on surface temperature, both implicitly and explicitly. The shortwave spectrum is typically defined as the region of the electromagnetic spectrum from 0.2 to 2.5 μm. Conventionally, fluxes directed away from the surface are negative. Detailed information on the surface energy balance is given in Launiainen and Cheng (1998), Launiainen and Vihma (1994), Maykut (1986), and Steele and Flato (2000).

The rate of heat transfer between ocean and atmosphere determines the rate of thermodynamic ice growth or melt. At the ice–water interface—i.e., the ice base—the sum of the oceanic heat flux F_w and F_c is balanced by the release/consumption of the latent heat of freezing/melting L for a change in ice thickness h per timestep dt:

$$F_w + F_c + \rho_i L \frac{dh}{dt} = 0 \tag{5.2}$$

where ρ_i is the bulk ice density. Along with snow cover thickness (see below and Section 5.9.8), h controls the conductive heat flux F_c into and through the ice cover, and thus the ocean–atmosphere heat exchange. This in turn affects the thermodynamic ice growth/melt rate. For a sheet of ice under steady-state conditions and assuming that F_c is a linear function of the temperature difference across the ice, the flux is driven by the difference between the temperature of the floe surface (IST) and that of the underlying ocean—i.e., at the ice–water interface (T_{sea})—and can be approximated by the simple relationship:

$$F_c = (T_{sea} - IST)(k_{floe}/z_{floe}) \tag{5.3}$$

where k_{floe} is the bulk thermal conductivity of the floe (ice and snow combined) and z_{floe} is the floe thickness (Guest and Davidson, 1994). In general, therefore, the thicker the ice and snow cover, the lower the rate of basal ice formation. An important overarching factor is that extremely high rates of heat loss and ice growth can occur in openwater and thin ice areas in winter (Maykut, 1978). In reality, the steady-state assumption falls down due to constant changes in atmospheric forcing, necessitating the inclusion in sea ice thermodynamic models of a multi-layer time-dependent component (incorporating salinity effects) to

[6] Emissivity is defined as the ratio of radiative flux emitted by the material per unit solid angle per wavelength to that of a blackbody (perfect radiator) at the same physical temperature.

estimate T_{ice}—e.g., Semtner (1976), Maykut (1982), and Parkinson and Washington (1979). Note, however, that this quantity can now be routinely retrieved from satellite data (see Section 5.9.11). From this discussion, it can be seen that accurate large-scale estimates of the ice (and snow) thickness distribution are of fundamental importance to both initiate and validate such models, and to constrain model parameters.

As can be seen from (5.2), the ice growth rate and ultimately ice (thermodynamic) thickness are also highly sensitive to the ocean heat flux F_w. In fact, F_w has a highly variable impact on ice growth/melt, and can be a significant term in the Southern Ocean—i.e., of the order of tens of $\mathrm{W\,m^{-2}}$ in certain locations (Martinson and Ianunuzzi, 1998; Muench et al., 2001; Lytle et al., 2000). This has the net effect of limiting the "equilibrium" thermodynamic thickness (see Section 5.6.2.1) in winter to a maximum of 0.5–0.7 m (Heil et al., 1996; Martinson and Iannuzzi, 1998; Wadhams et al., 1987). Indeed, modeling studies highlight the sensitivity of Antarctic sea ice to oceanic heat flux and its variability (Wu et al., 2001). In the Arctic, on the other hand, significantly less deep ocean heat is entrained into the surface-mixed layer from below the halocline, with maximum values of F_w of a few $\mathrm{W\,m^{-2}}$ across most regions (Steele and Flato, 2000) and larger equilibrium ice thickness (Eicken, 2003a). Maykut and McPhee (1995) proposed that the seasonal cycle of F_w in the Arctic is controlled largely by the absorption of solar radiation in the upper ocean, with subsequent transferral of the stored heat to the ice base later in the season. A major current concern is the effect on the ice cover of recently observed changes in F_w in the Arctic, summarized in Section 5.5.

Oceanic heat flux is an example of an important climate variable that cannot be measured directly by spaceborne sensors in ice-covered oceans (McPhee, 1992). Developing an improved understanding of its spatio-temporal variability, that of other oceanic variables, and potential response to changing ocean conditions, will continue to rely upon *in situ* measurements from ships, moorings, and, increasingly, satellite-interrogated buoys and autonomous vehicles (e.g., Autosub: ⟨*http://www.soc.soton.ac.uk/aui/*⟩), Lagrangian drifters, gliders equipped with acoustic transceivers and Conductivity Temperature Density (CTD) sensors for navigation and ocean measurements, and ballast-controlled floats equipped with ice-profiling upward-looking sonars. Oceanographic measurement has benefited greatly from recent technological advances, as summarized by D'Asaro (2003) and Rintoul et al. (2001a), with new sensor packages such as Argo floats revolutionizing our ability to conduct sustained CTD-type measurements of water column structure and properties over vast and remote areas and at a density of coverage only dreamt of until recently (⟨*http://www.argo.ucsd.edu*⟩). Although such instruments are currently unable to operate under/through sea ice cover, work is underway to develop smart, neutrally buoyant floats and other sophisticated satellite-interrogated instrument packages for this purpose (Proshutinsky et al., 2004). See Rudnick and Perry (2003) for a review of autonomous and Lagrangian sensors and platforms. Satellite-tracked and -interrogated buoys also play a key role in providing real-time atmospheric pressure data to improve meteorological analyses in the sea ice zone, and are increasingly sophisticated in their transmission of sea ice and ocean properties (⟨*http://ioeb.whoi.edu/index.htm*⟩, Morison et al., 2002). An excellent example of a

suite of *in situ* satellite-interrogated sensors designed to yield long-term measurements with which to detect and monitor change is given by the North Pole Environmental Observatory (Morison et al., 2002). First established in 2000, this installation includes an automated drifting station consisting of a cluster of ice buoys and a deep-sea instrument mooring, supplemented by annual airborne hydrographic surveys. Other recent innovations include fitting deep-diving and ice-loving southern elephant seals (*Mirounga leonina*) with a new generation of Argos transmitters incorporating temperature, pressure, and salinity sensors for novel oceanographic measurements over data-sparse regions of the Southern Ocean, in addition to providing locational information (Fedak, 2004; Guinet, 2004). Data from these sensors can then be used to examine the preferential migration and feeding behavior of the animals in relation to the physical (oceanic and sea ice) variables involved.

Regarding the term I_{ice} in (5.1), additional information is needed on the fundamental optical properties of ice to quantify energy absorption within the ice and transmission to the underlying ocean (Ebert et al., 1995; Grenfell and Maykut, 1977; Perovich, 1996; Perovich et al., 1998a; Schlosser, 1988). Once again, this cannot currently be measured directly from space. This requires *in situ* measurement of the vertical profiles of downwelling irradiance (Light, 2001), from which spectral extinction coefficients for the ice and snow cover can be estimated. Such measurements essentially complement albedo data collected by satellites (see Section 5.9.13). In addition, the amount and spectral composition of shortwave radiation transmitted through sea ice strongly impacts primary productivity and biological activity in and under sea ice cover (Arrigo et al., 1993; Soo Hoo et al., 1987). Radiative fluxes into the ice and underlying ocean depend on ice concentration, its thickness and structure, and its snow cover (Trodahl et al., 1989; Perovich, 1990a, 1996). Absorption and backscatter within the ice—and the snow cover, in particular—greatly reduce the amount and spectral properties of light entering the ocean through the ice by a factor of 50 to 1,000 (Buckley and Trodahl, 1987; Perovich, 1990a). The optical properties of snow and ice are outlined in Section 5.7.1.

5.6.1.1 The key role of snow

Snow cover is an integral and highly variable component of the polar atmosphere–ice–ocean interaction system (Eicken, 2003a; Eicken et al., 1995b; Granberg, 1998; Iacozza and Barber, 1999; Ledley, 1991, 1993; Massom et al., 2001a; Sturm et al., 2002a). As the albedo of snow is significantly higher than that of bare ice—e.g., 0.85 for thick (0.7 m) first-year Antarctic ice with a thick snow cover versus 0.49 for the same ice thickness without snow (Allison et al., 1993; Brandt et al., 1999)—it dominates the surface shortwave energy exchange and the ice albedo feedback mechanism. In spring, it also acts to delay ice surface ablation due to its high albedo and low thermal diffusivity (Ledley, 1991), and may in places contribute to the survival of sea ice through the summer melt period—e.g., in certain regions of Antarctica (Eicken et al., 1995b). Rather than forming a uniform substrate, snow on sea ice is characterized by a high degree of variability and inhomogeneity in terms of

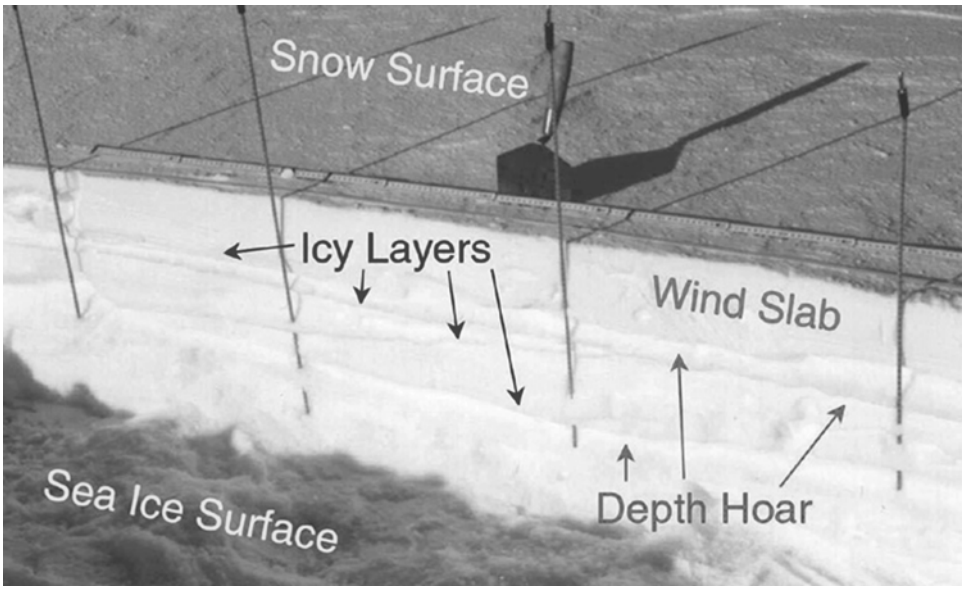

Figure 5.11. A photograph of a vertical profile through a typical dry snow cover on Antarctic first-year ice in winter (Amundsen Sea, September 1994). Snow depth is 0.25 m. Note the complex stratigraphy, which is constantly evolving and is caused here by different conditions during and after each snowfall, the burial of surface crusts, and subsequent depth–hoar formation. The latter occurs by temperature–gradient metamorphism (Colbeck, 1982), in response to steep vertical temperature gradients that typically occur across the snow layer in winter (Granberg, 1998; Massom et al., 2001a; Sturm et al., 1998, 2002b). This has the effect of transforming layers originally comprising small, fragmented, and tightly packed snow grains into low-density horizons of faceted crystals which can grow to a centimeter in diameter (by comparison, newly fallen snow grains are typically sub-millimeter in the minimum dimension). Such layers are characterized by different densities, grain size and shape, and therefore by different thermal conductivities (Massom et al., 2001a; Sturm et al., 1998). Even in the absence of flooding and under cold conditions, snow-basal layers in Antarctica are invariably saline (>5–10 p.s.u.) and damp (Massom et al., 2001a; Sturm et al., 1998). As a result, snow has a variable and at times strong impact on sea-ice-reflected optical, thermal, and microwave properties, affecting the interpretation of satellite data.
From Massom et al. (2001a).

its thickness and physical properties (Figure 5.11). In spite of its overall significance, snow tends to be treated in a coarse and simplistic fashion in coupled ice–ocean–atmosphere models (Lemke et al., 1997).

Snow properties change over time with changing radiation, temperature, and wind conditions, to exert a large impact on the processes occurring within the snow (Sturm, 2002). By controlling both the nature of the snow crystal surface and bonds, snow metamorphism affects its thermal conductivity and permeability (Sturm et al., 1997, 2002b). Snow on sea ice and firn on ice sheets are highly dynamic and complex media (Sturm et al., 1998), and feedbacks in mass and heat transfer mechanisms

affect both the processes of change and the nature of the snow microstructure (Sturm, 2002).

By virtue of its low thermal conductivity (see above), snow has the net effect of greatly reducing F_c in (5.2), by as much as 50% (Eicken, 2003a; Eicken et al., 1995b). This results in a significant decrease in heat loss between ocean and atmosphere, ice basal thermodynamic growth rate and equilibrium thickness under freezing conditions (Maykut, 1978). Paradoxically, however, snow also contributes to thermodynamic ice thickening in Antarctica through snow/ice formation (Adolphs, 1998; Eicken et al., 1994; Jeffries et al., 2001; Lange et al., 1990; Massom et al., 1997, 2001a; Sturm et al., 1998). Due to the combined effects of a relatively thin seasonal ice cover (resulting from net divergence and relatively high F_w values) and high precipitation rates, the ratio of snow to ice thickness tends to be large enough in Antarctica to affect floe isostasy and depress the ice surface below sea level. Flooding then occurs by the lateral incursion of seawater from floe margins, and/or vertically up through the ice lattice by percolation. The latter is strongly dependent on ice salinity and temperature, with air/brine pockets and brine drainage channels tending to interconnect to form conduits between ocean and ice surface once levels of 5 p.s.u. and -5°C, respectively, have been attained (Golden et al., 1998c). Ephemeral warming events related to synoptic weather patterns occur over the Antarctic pack even in winter (Oelke, 1997; Massom et al., 1997), and contribute to these processes. The overall outcome is that over 50% of the surface can be flooded by seawater in some regions (Eicken et al., 1994; Jeffries et al., 1994; Massom et al., 2001a; Sturm et al., 1998), this estimate being based on limited *in situ* observations. The resultant slush layer subsequently freezes onto the existing sea ice surface to form a layer of meteoric or snow/ice (Maksym and Jeffries, 2001). By this process, it appears that snow/ice formation can to some extent compensate for basal ice melt in regions of high ocean heat flux (Drinkwater and Lytle, 1997; Jeffries et al., 2001). The implications under a global-warming scenario are intriguing, given that enhanced precipitation rates are predicted at high latitudes (Hunt et al., 1995), leading to the possible maintenance of ice growth under warming conditions through an increase in the contribution of snow/ice formation (Wu et al., 1999b). Moving into the annual melt period, the presence of a thick, insulative snow cover may also act to delay surface melt by maintaining a high surface albedo (Eicken et al., 1995b; Ledley, 1991; Massom et al., 2001a). Flooding, however, also raises the salinity and thus the melting point of the lower snow horizons.

The contribution of meteoric ice to the overall sea ice mass balance is negligible in the Arctic, due to the thicker ice relative to snow thickness (Eicken, 2003a), which is again a function of ocean heat flux and precipitation patterns that may be changing due to oscillations and/or long-term trends in atmospheric forcing noted earlier (in Section 5.5). In the Antarctic, on the other hand, meteoric ice makes a major contribution, accounting for a few percent to $>50\%$ of the total ice thickness (see Massom et al., 2001a and references therein), with an actual meteoric ice fraction of typically $<20\%$ (Eicken, 2003a). These estimates are based on oxygen isotope analysis of a limited number of samples that are widely scattered in space and time. Large-scale estimates of snow/ice formation have been made by models—

e.g., Fichefet and Morales Maqueda (1999) and Wu et al. (1999b)—but these remain largely unvalidated. It can be seen that accurate large-scale measurements of the thickness distribution of sea ice and its snow cover are essential to examine the distribution of this important process. A remote-sensing system that can unambiguously measure the distribution and evolution of flooding is also highly desirable.

Snow also plays a fundamental role in the ecology of ice-covered oceans, and at all trophic levels (Arrigo, 2003; Arrigo et al., 1998a; Eicken, 1992). In the Arctic, snow thickness distribution is a factor determining habitat selection by predators at the apex of the food chain such as the ringed seal (*Phoca hispida*) (Hammill and Smith, 1989) and polar bear (*Ursus maritimus*) (Ferguson et al., 2000; Mauritzen et al., 2003; Stirling and Derocher, 1993). The flooding process outlined above also brings nutrients, algae, and other micro-organisms onto the ice surface to form an "infiltration community" in a relatively stable environment with higher light levels for photosynthesis (Ackley and Sullivan, 1994; Arrigo et al., 1997, 1998a; Fritsen et al., 1998, 2001; Lizotte, 2001). Conversely, snow plays a major role in the extinction of downwelling PAR (0.4–0.7 μm) available to intra- and sub-ice algal communities (Eicken, 1992). As a result of the exponential nature of PAR extinction, small variations in snow thickness can have a major impact on total transmitted PAR (Iacozza and Barber, 1999). In addition, snow on Antarctic sea ice accumulates iron in the form of aerosols deposited from the atmosphere (Edwards, 2000; Ussher et al., 2004). Although levels are small, they may be large enough to play a role in stimulating phytoplankton growth in Antarctic shelf waters when released into the water column by melt (Sedwick and DiTullio, 1997).

Our current knowledge of snow properties and thickness emanates from sparse surface observations (Granberg, 1998; Iacozza and Barber, 1999; Jeffries and Adolphs, 1997; Jeffries et al., 1997a; Massom et al., 1997, 2001a; Sturm et al., 1998, 2002a; Warren et al., 1999). The lack of accurate large-scale measurements of snow thickness (and properties) creates considerable uncertainty in model simulations of current atmosphere–ice–ocean interaction processes and their response to predicted climate variability and change. Clearly, much improved information is again required. Information on snow parameters and processes is also required to reduce errors and uncertainties in satellite sea ice algorithms. As we will see in Sections 5.9.8 and 5.9.14, recent developments have occurred in the remote sensing of snow thickness, surface grain size, and impurity content from space.

5.6.1.2 Processes of melt

Each spring–summer, an extraordinary meltback of vast areas of sea ice occurs in both hemispheres, coinciding with the onset of warm weather and the seasonal peak in solar radiation. As shown in (5.1), ice and snow melt begin once the surface energy budget becomes positive, leading to a negative thermodynamic thickness balance (Eicken, 2003a; Haas, 2003; Maykut, 1986). Basal ice melt occurs when the ocean heat flux into the ice–water interface exceeds the conductive heat flux out of it. Sea ice melt in summer is strongly influenced by ice dynamics and incoming shortwave radiation entering the open ocean through low-albedo leads and polynyas (Maykut

and Perovich, 1987; Perovich and Maykut, 1990; Richter-Menge et al., 2001). This energy contributes both to lateral floe melting (Holt and Rio, 1998; Maykut and Perovich, 1987; Steele, 1992; Zubov, 1943) and basal ice melt. Important hemispheric contrasts are, however, apparent in the large-scale seasonal melt regimes. In the Arctic, surface melting is a dominant ablation process (Perovich and Tucker, 1997). It accounts for an estimated annual loss of 0.3–1.0 m of ice from the surface of the perennial ice region in the central Arctic (Eicken, 2003a). The fate of this meltwater plays a pivotal role in the overall energy and mass balance of the ice cover (Eicken, 2003a). Eicken et al. (2001a) estimated that ~25% runs off directly into the ocean, and as much as 50% percolates downwards into the ice column. The remainder accumulates on the ice surface in the form of meltponds, the appearance of which leads to a dramatic reduction in surface albedo. With an albedo of ~0.2–0.5, compared with >0.8 for snow to ~0.6 for snow-free ice of equivalent thickness (Curry et al., 2001; De Abreu et al., 1995; Eicken et al., 2001a; Grenfell and Maykut, 1977; Morassutti and LeDrew, 1996; Perovich, 1996, 1998), meltponds absorb significantly more shortwave energy than surrounding snow/ice surfaces (Haas, 2003). This positive feedback leads to enhanced localized melt rates (Perovich et al., 2001), contributing to a decrease in ice thickness and an increase in surface roughness. See Haas (2003) for further discussion on the net effect of small-scale melt processes on the seasonal sea ice ablation cycle. Given the importance of these processes, there is a critical need to better understand their large-scale distribution and evolution.

Sufficient soot is often present in Arctic (but not Antarctic) snow to reduce the spectrally averaged albedo by 1–2% (Warren and Clarke, 1986), thereby contributing to the absorption of shortwave radiation and hence melt (Eicken, 2003b). Importantly, from a microwave remote-sensing perspective, summer surface melting is short-lived in Antarctica, with little meltpond formation and associated downward freshwater percolation to desalinate the surviving ice. As a result, the ice remains relatively saline. The dramatic annual meltback of ~80% of the Antarctic sea ice cover is mainly driven by heat entrainment from the deep ocean (Gordon, 1981) and solar heating in leads and lateral floe melt (Nihashi and Ohshima, 2001; Ohshima et al., 1998). This effect is enhanced by the largely divergent nature of the pack. It should again be noted that melt in Antarctica is not confined to the summer melt season. Basal melt can occur throughout the year in certain regions due to high ocean heat fluxes (Launiainen and Vihma, 1994; Lytle et al., 2000; Martinson, 1993), and ephemeral surface melt related to transient storms transporting warm air over the pack in winter (Massom et al., 1997; Oelke, 1997). Accurate estimates of ice concentration and floe size distribution are required to effectively parameterize seasonal ice melt. New observations of apparent meltponds in the northern Weddell Sea (Drinkwater and Liu, 2000) may give a taste of change expected in a climate-warming environment (Eicken, 2003a). Our current knowledge of summer ice conditions in Antarctica is poor, being based on very few surface measurements—e.g., Haas (1998, 2003).

Of major concern is emerging evidence that ice basal melt is increasing in importance in the Arctic (Eicken, 2003a). For example, McPhee et al. (1998) and

Perovich et al. (2003) observed basal melt of up to 0.5 m over a single season. As only a small proportion of this melt is attributable to ocean heat flux, most is apparently due to solar heating in leads. Serreze et al. (2000) further suggested that decreasing ice extent and concentrations observed in the Arctic Ocean since the 1990s have resulted in an increase in the amount of solar energy stored in the upper ocean and apparently released during the summer to contribute to ice melt. Such hypotheses require further testing using accurate integrated measurements over a variety of scales. Also of concern are changes in the large-scale onset and progression of seasonal melt, which can be readily detected and monitored from space.

5.6.2 Sea ice dynamic processes

Not only does sea ice respond to the balance of heat fluxes at the ocean surface. It is also subjected to various forces that result in its motion (drift) and deformation (described by the spatial gradient of the ice velocity). A major defining characteristic of pack ice is that it is constantly drifting in response to wind and ocean currents—i.e., external forces—combined with mechanical stress gradients—i.e., internal forces of ice interaction. Free drift predominates away from obstacles and coasts, with drift speed and direction being closely correlated with geostrophic wind. In the Arctic, ice drifts at ~1% of the mean geostrophic wind speed when in free drift and at an angle to the right of ~18° (Colony and Thorndike, 1984; Serreze et al., 1989). In the Southern Ocean, corresponding values of 1.6% and 10–15° to the left have been measured in the Weddell Sea (Kottmeier et al., 1992). The contribution of internal stresses increases dramatically with increasing proximity to the coast and blocking features—e.g., grounded icebergs.

According to Hibler (1979, 1989) and Leppäranta (1998b), the physics of sea ice dynamics can be characterized by four elements, namely:

(1) A momentum balance, describing the response of the ice to water and air stresses, internal ice stress, inertial forces, ocean currents, and Coriolis force.
(2) An ice mass balance/redistribution function describing the dependence of ice thickness characteristics on ice growth, drift, and decay.
(3) An ice rheology relating ice stress to deformation and strength, known as the "constitutive law".
(4) And ice strength dependent on floe-size and ice-thickness distributions.

The reader is encouraged to consult Leppäranta (2005) for in-depth information on the drift of sea ice and the laws governing it.

5.6.2.1 Sea ice thickness distribution

An important descriptor of the ice cover, and its effect on atmosphere–ocean interaction processes and vice versa, is the ice thickness distribution (Babko et al., 2002; Haas, 2003; Rothrock, 1986; Thorndike et al., 1975, 1992). Accurate

information on the ice thickness distribution is essential for quantifying its mass balance. Following Thorndike et al. (1975), this is defined statistically as a probability density function $g(h)$ of the areal fraction (concentration) of ice with a given thickness $d(h)$ as:

$$g(h)\,dh = \frac{dA(h, h+dh)}{R} \tag{5.4}$$

where $dA(h, h+dh)$ is the areal fraction of region R covered by ice with a thickness between h and $(h+dh)$ (Thorndike et al., 1975). Thickness distribution is a fundamental quantity in sea ice models in that it describes the aggregate behavior of the pack, and is a function of time and position (Babko et al., 2002; Haapala, 2000). Indeed, it is critical to the calculation (in dynamic–thermodynamic models) of area-averaged albedo, the input of solar radiation into the ocean (Grenfell, 1979), surface temperature, compressive strength, and deformation, as well as the estimation of regional fluxes of heat, mass, freshwater and saltwater at the ocean surface, and light penetration and biological productivity. A complicating factor in the estimation of the ice thickness distribution and overall ice volume, from thickness measurements, is that pressure ridges can contain up to 30–80% of the total ice volume in a given region, depending on the degree of deformation (Dierking, 1995; Haas, 2003; Lytle and Ackley, 1991; Weeks et al., 1989). This represents the largest uncertainty in estimates of total ice volume (Koerner, 1973). Accounting for this factor requires a statistical representation of ridge size, shape, and spacing (Wadhams, 1994), although a universally applicable function has yet to be formulated. Satellite techniques addressing this issue are evaluated in Section 5.9.9.

In effect, $g(h)$ is maintained by a balance between not only thermodynamic (ice growth and melt) but also dynamic (mechanical) processes, and understanding and predicting this key distribution requires consideration of both processes and their intimate association (Hibler, 2004). Mechanical processes result from ice motion and deformation, a factor that is evaluated below and in Section 5.9.5.6. Following Thorndike et al. (1975) and Hibler (1980), the temporal evolution of the thickness distribution, $\partial g/\partial t$, is given by:

$$\frac{\partial g}{\partial t} = -\frac{\partial (f_g g)}{\partial h} - \nabla \cdot (\nu g) + \psi + F_L \tag{5.5}$$

where t is time; f_g is the ice thermodynamic (vertical) growth or melt (decay) rate of ice of thickness h; ν is the horizontal ice velocity vector; ψ is the mechanical redistribution function describing the rearrangement of the ice thickness distribution by open-water creation (divergence) and the transfer of ice from one thickness to another by rafting and pressure ridge formation (convergence) (Babko et al., 2002; Haas, 2003; Hibler, 2004); and F_L is the lateral ice melt rate (Hibler, 1980; Maykut and Perovich, 1987), where:

$$\int_0^\infty F_L\,dh = 0 \tag{5.6}$$

Although this theory has become a key integral component of several important sea ice models—e.g., Hibler (1980) and Flato and Hibler (1991, 1995)—it incorporates a

number of assumptions about poorly understood processes—e.g., the formation of leads and ridges (Babko et al., 2002). Babko et al. (2002) tested this theory and examined the redistribution function ψ in the Arctic Ocean, using submarine sonar-derived thickness data. Their conclusion was that modification of the theory to include rafting processes would provide a more realistic parameterization.

5.6.2.2 Ice drift/advection and deformation

It is apparent from (5.5) that ice dynamics play a major role in determining the ice thickness distribution through ice deformation and horizontal redistribution. Sea ice deformation results in the formation of leads, near-shore shear zones and pressure ridges. Shear zones form where one ice "plate" slides past another along a mechanical fracture, and are characterized by a zone of intense deformation with heavy ice rubble formation to create a very rough surface on the meter to decameter scale. Leads formed under divergent conditions are loci of rapid ice formation, with subsequent convergence causing enhanced ice thickening by ridging and rafting. This mechanism accounts for the thickest ice observed and is responsible for ice thickening beyond the equilibrium thickness that would be attained through thermodynamic processes alone. In Antarctica, cyclical synoptic-scale divergence and convergence (Massom, 1992) plays a primary role in thickening the sea ice beyond an equilibrium thermodynamic thickness of $\sim$0.5–1.0 m (Heil et al., 2001a; Wadhams, 2000; Worby et al., 1998). As noted earlier, a key source of uncertainty in mass balance estimates relates to the fact that a large but unknown proportion of sea ice volume is contained in ridges (Koerner, 1973). In a warming environment, dynamic (deformation) processes of ice thickening may to some extent compensate for thermodynamically driven ice thinning. Clearly, an improved understanding of patterns of deformation, and lead and ridge formation, is critical in the larger analysis of ocean–ice–atmosphere interactions and their role in the climate system.

The ice redistribution function term ψ in (5.5) describes how thin ice is transformed into thicker ice classes when deformation due to convergence occurs. Not only is this term critical, but it is also complex and poorly understood (Haas, 2003). It depends both on ice fracture mechanics and on deformation energy and lengths and friction effects (Haas, 2003; Hopkins, 1996). These factors are in turn strongly dependent on parameters such as ice thickness, as well as external forcing. The ridging process entails a deformational energy sink, while both ridging and lead formation are important contributing factors to the overall rheological response of an ice cover to external forcings by wind and currents (Li et al., 1998). Ice deformation also modifies the roughness characteristics of the ice surface and base, by ridging and rafting. Pressure ridge sails are typically up to a few meters in elevation, while keels can extend downwards into the ocean by up to ten times as much (Wadhams, 2000). As shown below, these features play an important role in determining the degree of aerodynamic and hydrodynamic coupling between the atmosphere, ocean, and ice (Garbrecht et al., 1999, 2002; Launiainen and Vihma,

1994; Li et al., 1998; Mai et al., 1996; Vihma et al., 2003). Given the persistence of eolian snow redistribution, ice surface roughness features also act as loci for both enhanced snow accumulation and deflation—i.e., sastrugi and dune formation—which in turn modify the surface roughness (Adolphs, 1999; Massom et al., 2001a; Sturm et al., 1998, 2002a; Tin and Jeffries, 2001). Sastrugi are linear snow dunes formed by wind erosion and deposition (Armstrong et al., 1973). Along with dunes, they are a major determinant of the large, localized variability in snow thickness typically encountered across individual ice floes.

On the regional scale, the ice thickness distribution can be obtained by solving the momentum balance equation (Haas, 2003; Hibler, 2004). This describes the main forces acting on a unit area of sea ice that determine its drift and deformation, and is given by:

$$Ma = \sum F = \tau_a + \tau_w + F_i + F_c + F_t \tag{5.7}$$

where the force of mass M times acceleration a balances the sum of the main forces; τ_a and τ_w are the body forces per unit area due to air (wind) and water stresses, respectively (where τ_w is assumed to include frictional drag due to the relative motion between ocean and ice); F_i represents internal ice forces/stresses; F_c is the Coriolis force ($\sim 10^{-4}\,\mathrm{s}^{-1}$ at high latitudes); and F_t is the force due to sea surface tilt. Inertial motions driven by strong coupling via turbulence within the ocean boundary layer induce variations in sub-daily deformation (Hibler, 2004; McPhee, 1978).

The stress exerted by a surface wind field on an ice-covered ocean depends both on the hydrodynamic roughness of "flat" open water and sea ice surfaces (termed *skin drag*) and the resistance of larger geometric features such as pressure ridges and floe edges (*form drag*) (Mai et al., 1996). Generally, τ_a and τ_w are dominant terms, by more than an order of magnitude (Haas, 2003). The momentum transferred from atmosphere to sea ice depends on the atmospheric stability, the surface wind velocity, and the aerodynamic roughness of the surface (Guest and Davidson, 1991). The latter is generally expressed as a roughness length parameter z_0 or a neutral drag coefficient (Arya, 1975; Banke and Smith, 1973; Guest and Davidson, 1987; Joffre, 1983; Mai et al., 1996). Drag coefficients relate turbulent fluxes of heat and momentum to atmospheric temperature and wind, and depend on both surface structure and atmospheric conditions. Drag coefficients as a function of ice type have also been published—for example, by Andreas (1995), Andreas and Claffey (1995), Andreas et al. (1993), Guest and Davidson (1991), Martinson and Wamser (1990), Overland (1985), and Overland and Davidson (1992). According to Banke et al. (1980), differences in ice surface geometry can change the drag coefficient by up to a factor of 2. Sea ice models require an accurate parameterization of drag coefficients, which relate the turbulent fluxes of momentum and heat to atmospheric wind and temperature (Cheng et al., 2001; Launiainen and Cheng, 1998; Maykut, 1986; Tin and Jeffries, 2001; Wefelmeier and Etling, 1991). Ice-basal roughness can be measured by submarine and moored ice-profiling (upward-looking) sonars, and is beyond the scope of this chapter (see Melling and Riedel, 1995 and McPhee, 2002 for

information). The incorporation of a more realistic drag parameterization into the momentum balance component of sea ice models requires improved observations of ice roughness, and its variability (Steiner, 2001).

In sea ice models, mean ice thickness for each grid cell is generally derived by solving (5.6) for ice motion, then distributing the ice volume that drifted into each individual cell equally over the cell area. This is based on the assumption that the evolution of the ice drift field must satisfy the conservation of ice mass. For single-thickness models, see Hibler (1979, 1986), Leppäranta (1998b), and Thorndike (1986). New multiple thickness category models have also been developed. These range from simple thin and thick ice plus open water—e.g., Heil and Hibler (2002)—to multi-thickness ice—e.g., Flato and Hibler (1995), Bitz et al. (2001), and Lipscomb (2001). They solve the equations for each ice category and then derive the component ice thickness/mass for the grid cell. See Hibler (2004) for in-depth information on the governing equations in sea ice dynamics.

It is clear from (5.7) and the ice redistribution term ψ in (5.5) that *ice strength* and *ice rheology* are key terms. The rheology of sea ice is an unsolved issue, and internal ice stress is the most complex and least understood force acting on the ice cover. Modern sea ice dynamics models utilize enhanced elastic–viscous–plastic rheologies (Hunke and Dukowicz, 1997), harnessing the power of parallel computing. The development of improved ice rheologies is the subject of intensive current research using laboratory experiments (Schulson et al., 1999) and satellite data (see Section 5.9.5.6). For in-depth discussion of ice deformation, see Fily and Rothrock (1990), Hibler (2004), Lindsay (2002), McNutt and Overland (2003), Rothrock (1986), and Thorndike et al. (1975). The formulation of a more accurate model representation of the sea ice momentum balance requires data with which to test and improve key parameters such as compressive strength, shear, and drag coefficients.

The ice velocity field is often described in terms of its kinematics. This differs from ice dynamics in that it is only concerned with the manifestation of the forces at work, rather than the forces themselves or their manifestation by the ice cover (Thorndike, 1986). It is crucial to have an accurate statistical description and a clear conceptual model of regional sea ice kinematics, as it will be recalled from (5.5) that both internal ice stress and processes affecting heat and mass balance depend on spatial differences in the ice motion field. Once again, satellite remote sensing has a key role to play, and is making a revolutionary contribution.

5.7 BASIC REMOTE-SENSING PRINCIPLES RELATING TO THE MEASUREMENT OF SEA ICE AND ITS SNOW COVER

Satellite signatures over sea ice are typically complex, and require careful interpretation and processing to extract useful and accurate geophysical parameters. As we will see, considerable challenges remain in many cases. An important

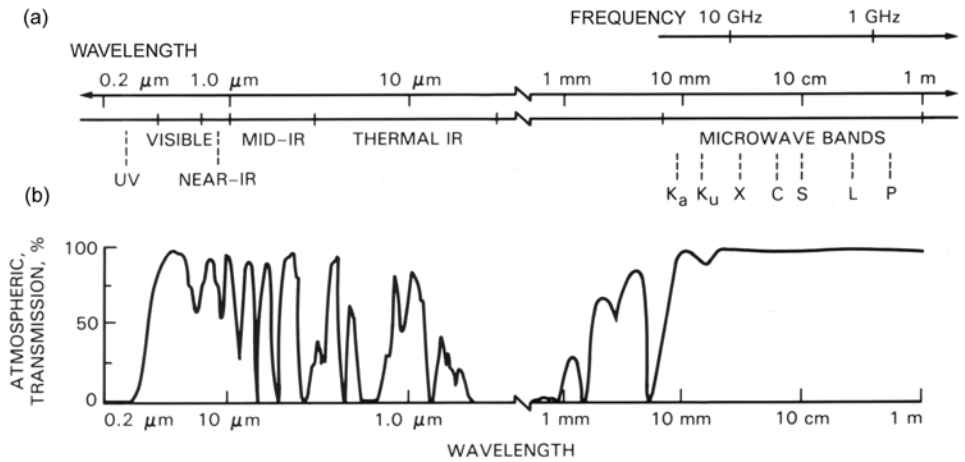

Figure 5.12. (a) The electromagnetic spectrum, with the major sensor classes discussed in this and other chapters marked. UV is ultraviolet and IR is infrared. Microwave bands are also marked. (b) A plot of *atmospheric transmission* as a function of wavelength. Regions of high atmospheric transmission equate to *atmospheric windows* through which the Earth's surface can be sensed, whereas absorption bands are represented by areas of low transmission. Radiation in these bands is absorbed by atmospheric gases such as water vapour, carbon dioxide, and ozone (depending on the wavelength). Frequency/wavelength details of radar bands K_a through P are given in Table A.1 in the Appendix.
After Carver (1989).

prerequisite to the interpretation of satellite-derived signatures of sea ice is an understanding of the interaction of electromagnetic radiation measured by satellite sensors with the snow and ice layers (and ocean), and its dependence on both surface properties and instrument parameters—e.g., wavelength, polarization, and incidence angle (see Kong, 2000 for background information on electromagnetic wave theory). In this section, we provide a brief overview of the theoretical fundamentals of the satellite measurement of sea ice and its snow cover as a function of broad sensor class. The major sensor classes evaluated are marked on the electromagnetic spectrum shown in Figure 5.12, along with the position of atmospheric transmission windows. For more in-depth information, the reader is encouraged to consult Askne (2003), Eppler et al. (1992), Grenfell et al. (1992), Hallikainen and Winebrenner (1992), Onstott (1992), Onstott and Shuchman (2004), Shuchman and Onstott (1990), and Ulaby et al. (1981, 1982, 1986a). For further information on the dielectric and other microwave properties of snow and ice, see Barber et al. (1998a), Comiso (1995a), Matsuoka et al. (1997), Mätzler (1985, 1998, 2001), Mätzler and Wegmüller (1987), Moore and Fujita (1993), Vant et al. (1974), and Warren (1984). Lewis et al. (1994) and Tucker et al. (1992) provide in-depth information on the physical properties of sea ice relevant to remote sensing, including hemispheric contrasts.

5.7.1 Optical properties of sea ice and its snow cover

The solar-radiant exitance that is incident upon and illuminates the Earth's surface is mainly limited to the optical portion of the electromagnetic spectrum. This refers to the shortwave region within which reflection processes dominate over thermal emission processes. For Earth-remote-sensing purposes, this region is typically taken to be 0.4 μm to 2.5 μm or 3.0 μm. This can be subdivided into the visible (0.4 μm to 0.70 μm) and reflected IR (0.70 μm to 3.00 μm) regions, with the near-IR occupying the 0.70 μm to 1.30 μm band and the middle (shortwave) IR region from 1.30 μm to 3.00 μm. The relative proportions of incident shortwave radiation that are reflected, transmitted, and absorbed by a given surface are a function of the unique physical characteristics of that surface and the wavelength (or suite of wavelengths) at which it is observed. This provides a potential means of deriving information on the composition and state of the surface from multi-spectral satellite data, but requires knowledge of the wavelength-dependent radiative properties of that surface (as well as the highly variable effect of the intervening atmosphere on the signal measured at the satellite). In this section, we briefly outline the optical properties of snow and sea ice, as a primer to understanding the information on snow and ice geophysical parameters that can be derived from satellite optical measurements—this is covered in later sections—such as albedo and snow grain size. For more detailed information on the optical properties of sea ice, see Perovich (1996). Choudhury (1981), Mobley et al. (1998), Warren (1982) and Dozier (1989) provide a more complete review of snow optical properties, while Asrar (1989) provides important background information on optical remote sensing in general.

Understanding the reflectance, transmittance, and absorptance of shortwave radiation by sea ice and its snow cover is a key to interpreting data acquired by satellites operating at these wavelengths. It is also critical to a number of key processes and problems, including those relating to ice thermodynamics (Section 5.6.1), algal ecology/primary production, and polar climatology—e.g., the albedo–temperature feedback mechanism. Transmittance is the relationship between the energy transmitted by a surface to that incident upon it, while absorptance is the relationship between energy absorbed by a surface to that incident upon it. In this section we concentrate on reflectance, as this can be measured by satellites (see Perovich, 1996 and Fuhrhop et al., 1998) for information on radiative transfer through the ice). Reflectance is defined as the ratio of the intensity of reflected radiation to that incident on the surface. When properly processed, the surface-spectral reflectance measured by satellite visible to near-IR sensors provides key information on the large-scale spatial and temporal variability of the albedo of polar oceans—cloud permitting (see Section 5.8.2.4.1). The total (all-wavelength) albedo is defined as the spectrally integrated hemispheric reflectance over the solar (shortwave or optical) part of the ElectroMagnetic (EM) spectrum—i.e., ~0.25 μm to 3.00 μm (Perovich, 1996; Warren, 1982). By definition, this type of remote sensing requires solar illumination, and is therefore inoperable at night and during periods of polar darkness at high latitudes.

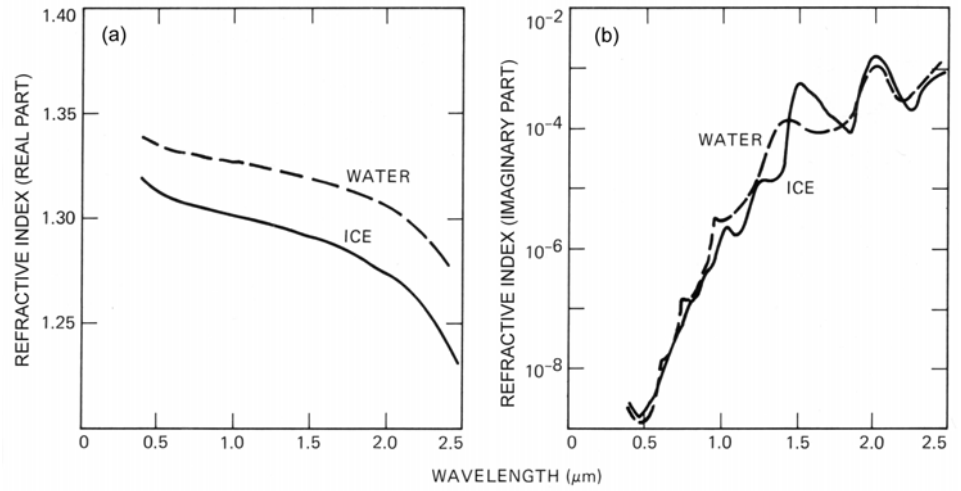

Figure 5.13. The complex refractive index $(n + ik)$ of pure ice and water as a function of wavelength (0.25–2.5 μm), where (a) is the real part n, and (b) the imaginary part k.

Data for water are from Hale and Querry (1973), and data for ice from Warren (1984). From NASA (1987). Image courtesy of NASA.

As noted previously, knowledge of the optical properties of snow and ice is also important from the perspective of the surface energy budget and biological activity both within and under the sea ice–snow cover substrate. The bulk optical properties of water and ice are similar at visible to near-IR wavelengths—i.e., 0.4–1.3 μm (Dozier, 1989; Li, 2000; Warren, 1982). The reflectance and transmittance characteristics of the snow cover depend upon the variation with wavelength of the refractive index of ice, grain size distribution, density and depth, the absence/presence (size and amount) of impurities, and liquid-water content. The refractive index is expressed as a complex number $n + ik$, where n is the real part and k the imaginary part (or absorption coefficient). These are shown as a function of wavelength for ice and water in Figure 5.13. While the spectral variation of the real part n is small and the difference between ice and water minimal, the absorption coefficients of clean water and pure ice are similar (Grenfell and Perovich, 1981). Importantly, k varies by seven orders of magnitude over the spectral range 0.4–2.5 μm (Warren, 1982; Dozier, 1989). This is the key optical property of ice, and one that mainly causes large observed spectral variations in snow and ice reflectance. Note that k attains a minimum value at a wavelength λ of $\sim$0.46 μm (Bolsenga, 1983; Warren, 1982)—i.e., pure ice is largely transparent to shortwave radiation at this wavelength. It becomes moderately absorptive in the near-IR, with absorption increasing with wavelength (Dozier, 1989; Goetz, 1987; O'Brien and Munis, 1975).

We noted earlier that dry, cold snow is a collection of air and ice grains, the size, density, and geometry of which vary depending on conditions during deposition, the degree of eolian redistribution, and *in situ* metamorphism (Colbeck, 1982; Massom

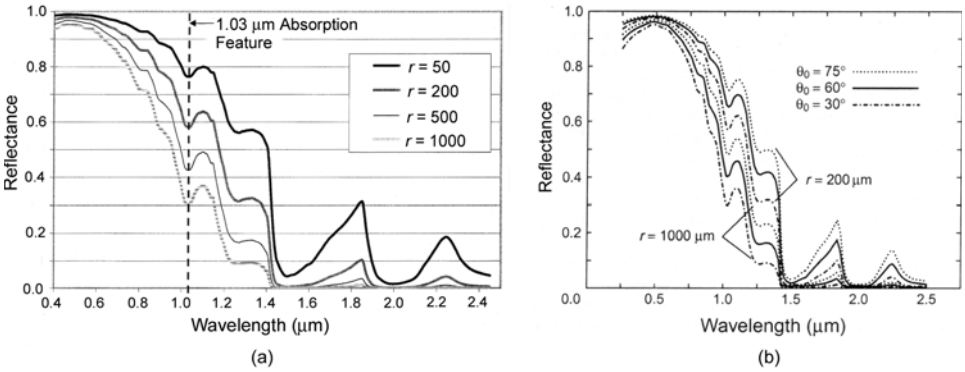

Figure 5.14. (a) The spectral directional–hemispherical reflectance R_s of pure, deep, and dry snow (semi-infinite depth) over the spectral region 0.4–2.5 μm, as a function of grain radius r (50 to 1,000 μm). The dashed vertical line indicates the location of the 1.03-μm absorption feature. (b) The spectral directional–hemispherical reflectance R_s of pure, deep, and dry snowcover (of semi-infinite depth) over the spectral region 0.25–2.5 μm as a function of illumination angle θ_0 (30°, 60°, and 75°) and grain size radius r (200 to 1,000 μm).

(a) From Nolin and Dozier (2000). (b) From Dozier (1989). Reprinted with permission of John Wiley & Sons, Inc.

et al., 2001a; Sturm et al., 1998). Figure 5.14 shows the equivalent values of the directional–hemispherical reflectance R_s of dry, pure, and deep snow as a function of (a) grain size and (b) illumination angle and grain size. These values were computed using radiative transfer-based snow models, namely the *Discrete Ordinate Radiative Transfer* (*DISORT*) model of Stamnes et al. (1988) in (a) and the model of Warren and Wiscombe (1980) and Wiscombe and Warren (1980) in (b). A typical approach to characterizing the spectral reflectance of snow as a function of grain size involves using (i) Mie theory to calculate the absorbing and scattering properties of individual ice grains, then (ii) a radiative transfer model to calculate reflectance from the volume of ice grains (Nolin and Dozier, 2000). As scattering can be treated more simply in models using spherical particles rather than other shapes, "equivalent spheres" are generally used to represent non-spherical snow grains (see Grenfell and Warren, 1999 for details). Typical grain sizes are ~50 μm for fresh, cold snow to > 1,000 μm (> 1 mm) for aged snow, grain clusters, or wet snow (Massom et al., 2001a; Nolin and Dozier, 2000; Sturm et al., 1998). Grain size also tends to increase with depth (Warren et al., 1982), due to the effects of snow metamorphism (Colbeck, 1982; Colbeck et al., 1990). Indeed, grains of up to a few millimeters in diameter and even greater can occur within horizons of depth hoar in older snowpacks on sea ice (and elsewhere) (Granberg, 1998; Massom et al., 2001a; Sturm et al., 1998).

In the spectral region below ~0.7 μm, snow reflectance is largely insensitive to grain size (as ice is largely transparent to visible radiation—see Figure 5.14), but is sensitive to finite depth and the presence of absorbing impurities (Grenfell et al., 1981; Warren, 1982; Wiscombe and Warren, 1980). Warren and Wiscombe (1980) showed that soot concentrations as low as 0.1 parts per million by weight (p.p.m.w.) are sufficient to perceptibly reduce snow reflectance. This is more of a factor for

Arctic than Antarctic snow, due to the proximity of the former to industrial centers (Clarke and Noone, 1985; Grenfell et al., 2002). In the near-IR, on the other hand, even pure ice is moderately absorptive and the reflectance is sensitive to grain size, with the sensitivity being greatest at ~0.9–1.3 μm (Aoki et al., 2000; Dozier et al., 1981; Warren and Wiscombe, 1980). The angular dependence shown in Figure 5.14b—i.e., an increase in R_s with increasing illumination angle—occurs because ice grains are strongly forward-scattering at near-IR wavelengths (particularly for larger grains). It can be seen from these plots that, while new and uncontaminated snow represents one of the most reflective (brightest) targets of all natural substances in the visible part of the EM spectrum, it is also amongst the darkest in the shortwave IR (Dozier, 1989). Please see Section 5.9.15 for discussion on the optical effects of an increase in snow wetness. Dozier and Painter (2004) provide a review of snow properties from the perspective of multi-spectral and hyperspectral remote sensing.

Other factors affecting the optical properties of snow are its density and physical depth (Perovich, 1996). Density does not have a direct impact on the spectral albedo of snow, but rather affects the relationship between geometric and optical depth (Bohren and Beschta, 1979; Nolin and Dozier, 2000). Optical depth τ is a dimensionless coordinate that for snow is given by (Nolin and Dozier, 2000):

$$\tau = \frac{3\rho_{snow} d Q_{ext}}{4 r \rho_{ice}} \tag{5.8}$$

where ρ_{snow} is snow density; d is geometric depth; and Q_{ext} is the Mie extinction efficiency, which in turn depends on the complex refractive index of ice, wavelength λ, and grain radius r.

In snow, light transmission decays exponentially across depth d as $\exp(-4\pi k d/\lambda)$ (Bohren and Barkstrom, 1974), and the distance over which transmittance is reduced to $1/e$ (or ~37% of the incident solar irradiance)—i.e., the e-folding distance. This distance is expressed either as an optical depth τ or a geometric depth d, and is directly proportional to the number density of particles in the snow layer (Nolin and Dozier, 2000). For snow, it approximates >20 m at 0.4–0.5 μm but decreases to <1 mm at 1.6 μm (Dozier, 1989; Nolin and Dozier, 2000; Perovich, 1996; Warren, 1982). This is an important factor in that it represents the depth of the snow layer over which a given geophysical parameter is derived from satellite data—e.g., snow grain size (Section 5.9.14). Equivalent figures for ice are ~24 m at 0.47 μm through 2 m at 0.7 μm to <1 mm at 1.4 μm (Perovich, 1996). In effect, this indicates that it takes only a few centimeters of ice or snow to absorb most of the incident solar irradiance at wavelengths beyond ~1.0 μm, and that ice/snow are relatively transparent in the blue region of the EM spectrum. If the snow is sufficiently thick, then visible light eventually re-emerges upward from the surface (Warren, 1982).

The above relationships are for pure snow and ice. Sea ice differs in that it is saline and constitutes an intricate and heterogeneous structure, with additional complexity due to the presence of a snow cover (for older ice types) that is itself highly variable (Massom et al., 2001a; Perovich, 1996; Sturm et al., 1998). As a

result, the spectral albedo of sea ice is more challenging to model, not least due to the fact that columnar ice crystals (the size of which relates to the sea ice growth rate) cannot be approximated by equivalent spheres (Goetz, 1987). For the sea ice itself, reflectance is determined by the sum of (i) scattering and specular reflection at the surface, and (ii) scattering and absorption in the ice (and snow cover) volume (please see Perovich, 1996 for more in-depth coverage). Sea ice is a highly scattering medium in that it is composed of a high density of air bubbles and brine pockets, which scatter light strongly as they have different indices of refraction compared with the surrounding nearly pure ice (Grenfell, 1983, 1991; Perovich, 1996). Differences in the magnitude of sea ice optical properties result mainly from differences in scattering, while spectral variations are mainly due to absorption (Figure 5.13). On the simplest level, an absorption coefficient for sea ice k_{si} is determined from the combined absorption coefficients for the constituent components of ice k_i and brine k_b by:

$$k_{si} = \nu_i k_i + \nu_b k_b \tag{5.9}$$

where ν_i and ν_b are the volume fractions of ice and brine, respectively (Grenfell, 1983; Perovich, 1996). Absorption within air inclusions (bubbles) is negligible, and generally assumed to be zero. In reality, the situation is complicated by the presence of biogenic particulates (Arrigo et al., 1991; Roessler and Iturriaga, 1994), dissolved organic matter, precipitated salts and sediments (the latter mainly in the Arctic) (Light et al., 1998), and their optical properties should also be considered. These impurities are generally weakly scattering but strongly absorbing (Perovich, 1996). An important factor is not only the bulk volume of ice and inclusions but also their distributions (Light, 2001; Perovich, 1996). Please again see Perovich (1996) for a review of the radiative transfer models of sea ice albedo.

Fundamentally speaking, reflectance from sea ice in the optical part of the EM spectrum depends upon its age and thickness, the presence/absence of a snow cover, and the thickness and state of the snow for older (thicker) ice types. This provides a means of classifying the ice types present in terms of their stage of development (see Section 5.9.7.5). While the broadband albedo of an ice-free ocean is ~0.05–0.1, that of sea ice cover ranges from ~0.1 to ~0.9 (Allison et al., 1993; De Abreu et al., 1995; Grenfell and Maykut, 1977; Grenfell and Perovich, 1984; Key et al., 2001a; Perovich, 1990a, b, 1996; Schlosser, 1988; Zhou et al., 2001) (Table 5.1). This spans virtually the entire range encountered for planetary surfaces. Values are generally highest for thick snow-covered multiyear ice and lowest for thin or melting ice. To reiterate, the most important determinant of sea ice albedo is the presence or absence of snow cover (Brandt et al., 1999; Warren et al., 1997). For snow-free new/young sea ice, sunlight is both reflected from the upper surface and scattered from the ice volume, and the albedo is relatively low and determined by ice thickness and the size of air bubble and brine pocket inclusions and their effect on scattering and absorption (Grenfell, 1991). As shown in Figure 5.15, and is the case with snow, spectral reflectance as a function of ice type (thickness) attains a maximum value between ~0.4 to 0.55 μm, followed by a rapid decrease beyond ~0.6 μm—i.e., albedo in the near-IR is largely insensitive to ice thickness (Allison et al., 1993; Grenfell, 1983; Light et al., 1998; Perovich, 1996; Warren, 1982).

Table 5.1. Broadband solar albedos as a function of ice type (thickness), measured *in situ* during East Antarctic cruises in the austral spring and covering the spectral range 0.3–2.8 μm. The dramatic rise in albedo caused by adding even a thin snow layer, of only a few millimeters in thickness, to thick sea ice is discussed and explained by Warren et al. (1997).

Ice type	Snow-free	Thin snow, continuous, <3 cm	Thick snow ≥3 cm
Open water	0.07	–	–
Grease ice	0.09	–	–
Nilas, <0.1 m	0.16*	0.42	–
Young gray ice, 0.1–0.15 m	0.25	(0.52)	(0.70)
Young gray–white ice, 0.15–0.30 m	(0.35)	(0.62)	(0.74)
First-year ice, 0.3–0.7 m	(0.42)	(0.72)	0.77
First-year ice, >0.7 m	0.49	0.81	0.85

*Nilas albedo varies with ice thickness from 0.07 to 0.25; 0.16 is the middle of the range.
From Brandt et al. (1999), updated from Allison et al. (1993).

The relationship between ice thickness and albedo largely breaks down once the ice accumulates even a thin snow cover. The sensitivity of albedo to snow thickness occurs for snow layers thinner than a few centimeters (Allison et al., 1993) (Table 5.1), and also relates to stratigraphy. When the snow cover is thicker, it dominates the surface albedo. The latter then depends largely upon snow characteristics and state, as outlined above. It should be noted that wetness in the snow cover on sea ice is not limited to the melt season. It also occurs by the capillary wicking of brine upwards into the snow column leading to dampness, and also saturation due to

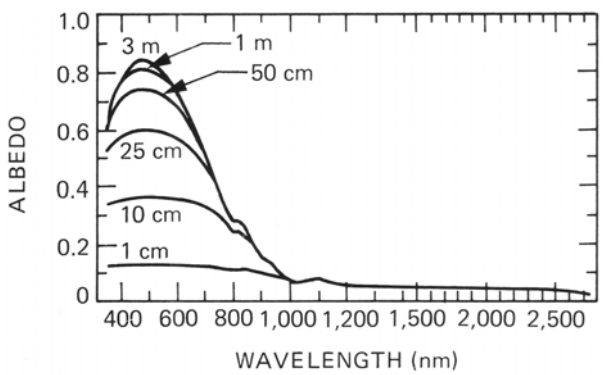

Figure 5.15. The spectral albedo of sea ice with a typical density of 880 kg m^{-3}, and as a function of thickness. In general, albedo increases with ice density, due to multiple scattering from bubbles, and albedo is higher for faster growing sea ice—e.g., frazil versus columnar ice (Goetz, 1987; Grenfell, 1983).

flooding by wave overwashing (in the MIZ), deformation and snow loading (Massom et al., 2001a). Other factors affecting the surface reflectance measured by satellites include surface topography and roughness (Warren et al., 1998), reflection angle, and solar zenith angle—i.e., an increase in albedo with a decrease in the solar elevation angle (Key et al., 2001a; Warren, 1982; Wiscombe and Warren, 1980). In order to compare albedo data from different locations and times, it is therefore necessary to normalize the albedo to a fixed solar zenith angle. Another determinant of sea ice albedo is cloud cover (total albedo increasing with an increase in cloud thickness), due to its effects on the spectral composition of the downwelling flux. For example, Grenfell and Maykut (1977) measured clear-sky total albedo values of 0.63 and 0.22 for melting, old Arctic snow and a mature meltpond, respectively, while equivalent values under cloudy skies were 0.77 and 0.29. This effect is most pronounced in the near-IR, as cloud particles are typically smaller than surface snow grains. As noted above, the reflectance of open ocean is generally different compared with snow and ice, enabling separation of ice and water. Care must be taken, however, where very thin ice is present, as its reflectance is very similar.

Importantly from the perspective of monitoring sea ice by optical remote sensing, spectral changes in ice and snow optical properties are directly related to changes in their structure and state. For example, larger albedos (and extinction coefficients) result from physical changes that enhance scattering, such as air bubble formation due to brine drainage in Arctic multiyear ice (Perovich, 1996). Regarding sensitivity to surface state, the appearance of liquid water in the snow volume or on a bare ice surface causes a substantial decrease in albedo, which is more pronounced at longer wavelengths. In the Arctic, the situation is further complicated in spring and summer by the appearance of surface meltponds. These evolve in areal extent and depth as a result of drainage and the absorption of shortwave radiation. These changes enable the determination of melt season onset and length from space, as discussed in Section 5.9.15. The measurement of snow and ice albedo by satellite sensors is evaluated in Section 5.9.13.

Even though satellite sensing of the Earth exploits atmospheric windows, three Top-Of-Atmosphere (TOA) components are received at the sensor under clear-sky conditions. These are: (i) ''direct'' (unscattered and surface-reflected), with TOA radiation modified by atmospheric transmittance along the solar path; (ii) ''skylight'', where the radiation is downscattered and surface-reflected; and (iii) ''path radiance'' (path-scattered). These must be accounted for to derive accurate geophysical parameters from the measured spectral reflectance.

5.7.2 Thermal infrared remote sensing of sea ice and its snow cover

Thermal infrared (TIR) data are widely used in the remote sensing of sea ice, both as a means of deriving ice surface temperature *IST* on the large scale and also of detecting and mapping sea ice distribution at times of polar darkness when visible/near-IR sensors are inoperable. Unfortunately, TIR data are again limited by their inability to penetrate cloud cover. Recalling earlier discussion, satellite remote sensing of the Earth's surface in the TIR region of the EM spectrum

(3–14 μm) typically exploits atmospheric transmission windows in two wavebands: 3–5 μm and 8–14 μm. These are separated by atmospheric water vapour absorption bands at 5–6 μm (Rees, 2001). The 8–14 μm band is most frequently used as the contribution of reflected sunlight is significantly less (Stewart, 1985). The intervening mid-wave IR spectral band (3–8 μm) contains contributions from both solar-reflected and thermally emitted radiation, and is most commonly used to distinguish clouds and snow/ice in daytime satellite images and to detect high-temperature sources—e.g., fires and volcanic eruptions. Thermal radiation dominates in the spectral range from 8 μm to 14 μm, emitted by objects on the Earth's surface as a function of their temperature and emissivity. The radiation measured by a sensor in space is again modified by propagation upwards through the intervening atmosphere. An additional component is thermal radiation emitted downwards by the atmosphere and reflected by surface objects (Rees, 2001).

The basis of TIR remote sensing is that every object with a physical temperature greater than absolute zero (0 K) thermally emits radiation that can be recorded by TIR radiometers—i.e., kinetic heat. TIR remote sensing involves measuring spectral radiance, as it does at visible and near-IR wavelengths. Under clear-sky conditions, TIR sensors in effect record the radiant temperature of the surface, which is correlated to the kinetic temperature and thermal properties of surface materials. In the case of snow and ice, these are complicated for two main reasons—namely, that phase changes occur within the media and also due to internal movement of moisture. Here, we briefly outline the main equations governing the measurement of TIR radiation, with a view to deriving the surface temperature from satellite measurements. The spectral radiance of this radiation I_λ (in $\mathrm{W\,m^{-2}\,sr^{-1}\,m^{-1}}$), which describes what the satellite sensor measures, is defined by *Planck's law* and given for a blackbody (i.e., perfect emitter) as:

$$I_\lambda = B_\lambda(T) = \frac{2hc^2}{\lambda^5(e^{hc/\lambda kT} - 1)} \tag{5.10}$$

where h is the *Planck constant* ($6.626\,075\,5 \times 10^{-34}$ J s), c is the speed of light *in vacuo* ($2.997\,924\,58 \times 10^{-8}\,\mathrm{m\,s^{-1}}$), λ is the wavelength of the radiation, k is the *Boltzmann constant* ($1.380\,658 \times 10^{-23}\,\mathrm{J\,K^{-1}}$), and T is the absolute temperature of the emitting material (body). *Radiance* is defined as the total exitance of energy in a given direction per unit area and solid angle of measurement (in $\mathrm{W\,m^{-2}\,sr^{-1}}$). The Planck function (5.10) is often written as:

$$I_\lambda = B_\lambda(T) = \frac{c_1\lambda^{-5}}{e\left(\frac{c_2}{\lambda T}\right) - 1} \tag{5.11}$$

where c_1 and c_2 are the first and second radiation constants ($1.191\,043\,9 \times 10^{-16}\,\mathrm{W\,m^2\,sr^{-1}}$ and $1.438\,769 \times 10^{-2}\,\mathrm{m\,K}$, respectively). As I_λ is independent of direction for isotropic radiation, the spectral-radiant exitance (flux) F_λ is given by:

$$F_\lambda = \pi I_\lambda \tag{5.12}$$

Following *Wien's displacement law*, emission from the Earth's surface (at a mean temperature of ~300 K) peaks at ~10.5 μm—i.e., in the TIR region. The total outgoing radiance I of a blackbody is given by integrating (5.10) with respect to wavelength as follows:

$$I = \int_0^\infty I_\lambda d\lambda \tag{5.13}$$

The total radiant exitance (from a blackbody) F as a function of temperature T is given by *Stefan's law*:

$$F = \int_0^\infty F_\lambda d\lambda = \frac{\pi^5}{15} c_1 c_2^{-4} T^4 = \sigma T^4 \tag{5.14}$$

where $\sigma = 5.670\,51 \times 10^{-8}\,\mathrm{W\,m^{-2}\,K^{-4}}$ is the *Stefan–Boltzmann constant*.

The above relationships hold for idealized blackbodies, and remote-sensing instruments are largely calibrated according to blackbody conditions. Natural surfaces, including snow and ice, are not blackbodies, however. Rather, they are characterized by wavelength-dependent *reflectance* or albedo (r_λ), *transmittance* (τ_λ) and *absorptance* (α_λ), whereby $r_\lambda + \tau_\lambda + \alpha_\lambda \equiv 1$ (5.15). By *Kirchoff's law*, $\varepsilon_\lambda \equiv \alpha_\lambda$ (5.16) for an opaque object in thermodynamic equilibrium, and (5.15) can thus be modified as $\varepsilon_\lambda + r_\lambda + \tau_\lambda = 1$ (5.17), where ε_λ is spectral emissivity. All also have an angular dependency. In order to derive the surface physical temperature from TIR measurements, one must incorporate information on the emissivity of that surface to account for the degree to which it deviates from the ideal of a blackbody. As noted earlier, spectral emissivity is defined as the ratio of energy radiated from a surface to that from a blackbody at the same physical temperature, the same wavelength, and under the same viewing conditions. It is a dimensionless number lying between 0 and 1, where 0 indicates a perfect reflector (white body) and 1 a perfect absorber (blackbody), with natural objects falling somewhere in-between—i.e., they are gray-bodies. In effect, emissivity expresses the ability of an object to emit radiation by thermal energy conversion relative to a blackbody at the same physical temperature. For snow and ice surfaces, the Planck function is therefore modified to:

$$I_\lambda = \varepsilon_\lambda B_\lambda(T) = \varepsilon_\lambda \frac{2hc^2}{\lambda^5 (e^{hc/\lambda kT} - 1)} \tag{5.18}$$

and Stefan's law to:

$$F = \varepsilon \sigma T^4 \tag{5.19}$$

In other words, the amount of thermal radiation emitted by an object for a given wavelength and temperature is directly proportional to the spectral emissivity of the object's surface.

The monochromatic brightness temperature T_B (i.e., the radiant temperature) measured by a radiometer is defined as the equivalent blackbody temperature, which assumes that the target emissivity is equal to 1.0 and that the radiant temperature

equals the physical temperature:

$$\frac{2hc^2}{\lambda^5(e^{hc/\lambda kT_B}-1)} = \varepsilon_\lambda \frac{2hc^2}{\lambda^5(e^{hc/\lambda kT}-1)} \tag{5.20}$$

where T_B is a function of λ. In effect, the brightness temperature of a target surface at wavelength λ is the temperature of a blackbody that emits the same amount of radiation at that wavelength as does the surface. Radiance data from satellite TIR channels can be converted to brightness temperature T_B (which is wavelength-dependent) by inverting the Planck function as follows:

$$T_B = \frac{hc}{k\lambda \ln\left(\dfrac{\varepsilon_\lambda + e^{hc/k\lambda T} - 1}{\varepsilon_\lambda}\right)} \tag{5.21}$$

Temperature T can then be found from:

$$T = \frac{hc}{k\lambda \ln(1-\varepsilon+\varepsilon e^{hc/k\lambda T_B})} \tag{5.22}$$

It is apparent from the above that the accurate remote sensing of surface temperature from satellite data requires knowledge of the spectral emissivity of that surface (Carsey and Zwally, 1986; Key et al., 1994a). Fortunately, the largest uncertainties in snow/ice emissivity occur beyond the 10.5–12.5-μm atmospheric window used by most systems (Dozier and Painter, 2004).

The brightness temperature T_B observed by a satellite TIR sensor, and converted from the radiance (emitted energy) received at the satellite by inverting the Planck function, consists of three main contributions (Yu, 1996; Yu et al., 1995):

$$T_B = \varepsilon I_{sfc}(IST)\tau + I_{atm} + (1-\varepsilon)I_{atm}\tau \tag{5.23}$$

where I_{sfc} is the radiance emitted from the surface at skin temperature IST; ε is the incidence angle-dependent surface emissivity; τ is the atmospheric transmittance; and I_{atm} is the radiance emitted by the atmosphere. With careful processing, IST can be derived from satellite T_B data (see Section 5.9.11). It can be seen from (5.22) and (5.23), however, that this requires: (i) a correction for atmospheric emission and absorption by water vapour, ozone (O_3), aerosols, and CO_2; and (ii) precise knowledge of the surface emissivity and its angular dependence (given that the satellite sensor scan angle typically varies) (Stroeve et al., 1996).

Whereas the emissivity of sea ice and snow exhibits a wide range at microwavelengths (see below), values are all >0.96 in the TIR for all grain sizes and viewing angles (Dozier and Warren, 1982; Warren, 1982). Indeed, an emissivity of 0.99 has often been assumed for many applications. That the TIR emissivity of snow is close to unity is due to the large absorptivity and low reflectivity of ice at wavenumbers below 10,000 cm^{-1} (Hobbs, 1974). Due to the strong absorption at IR wavelengths, ice and/or snow is infinitely thick at small depths in terms of absorption and emission of IR radiation (Dozier and Warren, 1982). Even where the snow or sea ice cover is only a few millimeters thick, the underlying surface does

not contribute to thermal emission. As a result, emissivity is unaffected by snow or ice thickness, and the temperature is sensed from the upper 1 mm or so of the surface at TIR wavelengths.

According to Warren (1982) and Dozier and Warren (1982), the IR emissivity of snow is quite insensitive to primary snowpack parameters such as density, grain size, and shape, and impurity and liquid water content in the atmospheric water vapour window from 8–14 μm—i.e., where most of the emitted radiation is concentrated. Emissivity is more sensitive to grain size in the 3.5–4.0 μm water vapour window, however, and especially for small grains (Berque et al., 2004; Dozier and Warren, 1982). Satellite split window techniques (Berque et al., 2004) use the former window. Spectral sensitivity also exhibits a dependence on the viewing geometry in both windows, and this should ideally be accounted for when using IR emission data to obtain the ice/snow surface temperature (Dozier and Warren, 1982; Rees and James, 1992). The angular and grain-size dependence of longwave ε is elaborated upon in Section 5.9.11. It should also be noted that a fairly wide spectrum of measured snow TIR emissivities has been reported. This ranges from significantly low values, of <0.8, reported for very cold Arctic snow by Rees (1993), to 0.98 (Kondo and Yamazawa (1986) and 0.99 (Griggs, 1968).

For a given snow/ice surface, the radiant temperature depends on other interrelated thermal properties of the surface in addition to emissivity. These include thermal capacity, conductivity, diffusivity, and inertia (see Holman, 2002; Wolfe and Zissis, 1989), which are dependent not only on the temperature but also the physical characteristics of the snow/ice surface including crystal and air-pocket size, density and liquid water content (Schwerdtfeger, 1963; Yen, 1981). While these properties cannot be remotely sensed, they can be inferred from spatial and temporal characteristics of satellite TIR images (this is more commonly carried out for geological applications). Due to these factors, and the effects of varying solar radiation with Sun elevation angle, wind and slope, etc., different surfaces warm and cool at different rates during nighttime and daytime conditions. This gives rise to a diurnal cycle of temperatures, with implications for the time of day at which satellite TIR observations are acquired. The amplitude of the temperature fluctuations is largely controlled by the thermal inertia of the snow/ice mass, which is a measure of how well a material retains heat. Detailed discussion of the thermal properties of snow and ice is beyond the scope of this chapter (see Schwerdtfeger, 1963 and Yen, 1981 for reviews). Brandt and Warren (1993) further discuss temperature characteristics and solar heating of Antarctic snow. The reader is referred to the text of Jensen (2000) for further information on thermal properties in general from a remote-sensing perspective.

5.7.3 Microwave properties

Passive microwave radiometers measure the intensity of natural thermal emissions from the surface, in a similar fashion to TIR radiometers (see Section 5.7.1) but at much longer (i.e., centimeter) wavelengths. Radars, on the other hand, transmit their own microwave signal and measure the reflection or backscatter (echo) received back

from the target as a function of frequency, polarization, and incidence angle. The challenge is to extract information, by inversion, on sea ice and snow cover physical characteristics and properties from their observed microwave signatures. This represents a complex problem, given that sea ice and snow are heterogeneous media that respond rapidly to changing environmental conditions. Major determinants of the microwave signature of sea ice are the dielectric and scattering properties of the ice and its surface, and understanding the basic microwave properties of sea ice is a prerequisite to interpreting satellite data and extracting useful geophysical parameters from them.

For satellite passive-microwave radiometers operating at wavelength λ and polarization *pol*, the intensity of the emission measured represents an average over the sensor pixel and is again converted to an equivalent brightness temperature T_B. This can be expressed in terms of the radiative transfer equation (Zwally et al., 1983), given by (Comiso et al., 2003a):

$$T_B = \varepsilon T_S\, e^{-\tau} + \int_0^{\tau} T(z)\zeta(z)\, e^{-\tau+\tau'(z)}\, d\tau'(z) + (1-\varepsilon)\kappa\, e^{-\tau} \int_0^{\tau} T(z)\zeta(z)\, e^{-\tau'(z)}\, d\tau'(z) \tag{5.24}$$

where ε is the wavelength-, angular- and polarization-dependent emissivity ($0 < \varepsilon \leq 1$); T_S is the physical temperature of that layer (in K); $\tau'(z)$ and τ are the atmospheric opacities from the surface to height z and to the satellite height, respectively; $T(z)$ is the physical temperature of the atmosphere at height z; κ is an estimate of the diffusiveness of the surface reflection; and $\zeta(z)$ is the atmospheric emittance at height z.

The dominant contribution in (5.24) is the first term, which represents radiation received directly from the Earth's surface. The second term is satellite-observed radiation contributed directly from the atmosphere, while the third term is downwelling radiation from the atmosphere which is reflected by the Earth's surface. An additional contribution, taking into account the contribution of reflected radiation from free space, is negligible and not included in (5.24).

For passive-microwave radiometry of targets at typical terrestrial temperatures, $hc/\lambda kT \ll 1$. In this case, the spectral radiance of a blackbody at physical temperature T is given by *Rayleigh–Jeans approximation to Planck's law*, whereby:

$$I_\lambda = 2kT/\lambda^2 \tag{5.25}$$

This relation provides an accurate and convenient description for spectral radiance for wavelengths which are much greater than the wavelength of the peak in the blackbody radiation formula. Assuming that atmospheric effects are negligible, the Rayleigh–Jeans approximation provides a simple linear relationship between measured spectral radiance and surface temperature as long as the emissivity of the surface ε is known. Equation (5.24) can then be simplified to give:

$$T_B(\lambda, pol, \theta_i) = \varepsilon(\lambda, pol, \theta_i) T_S \tag{5.26}$$

where *pol* is polarization (vertical or horizontal) and θ_i is the local incidence angle off-nadir. As we will see, this relationship forms the basis of algorithms designed to extract sea ice concentration and type information from satellite passive-microwave data.

Moving on to active microwave systems (radars), the intensity of the signal received back from a target is determined by the scattering properties of the illuminated area, and is termed "backscatter". The measure of the reflective "strength" of a given target is expressed as the backscattering cross-section σ in the direction toward the radar. The normalized measure of the radar return from a distributed target is expressed as the radar backscatter coefficient σ^0 (in dB), defined as the ratio of scattered power relative to isotropic scattering targets and a calibrated estimate of the return power of a radar pulse at the satellite. Note that the remaining fraction of the signal may be absorbed by the target and/or reflected and scattered away from the radar. The normalized backscatter coefficient is defined with respect to the nominally horizontal plane, and is a function of frequency (wavelength), incidence angle, and polarization, as well as the scattering (geometrical) and material (dielectric) properties of the illuminated target area (Elachi, 1988; Ulaby et al., 1982).

The microwave emissive and scattering characteristics of sea ice are determined by combinations of four parameters, again as a function of sensor wavelength, polarization, and incidence angle (Onstott and Shuchman, 2004). These are:

- the complex dielectric constant of the sea ice and its snow cover (both the real and imaginary parts);
- the presence of dielectric discontinuities or discrete scatterers—e.g., gas bubbles in the ice;
- the surface roughness (both small- and large-scale); and
- the orientation of the ice/snow and its surface features relative to the radar azimuth look angle.

The complex dielectric constant (relative complex dielectric permittivity) ε^* is a fundamental parameter that describes the basic electrical properties of a material, which determine EM wave propagation, scattering, reflection, attenuation, and (for passive sensors) emission (Mätzler, 1996; Onstott and Shuchman, 2004; Ulaby et al., 1981, 1982). Knowledge of ε^* is key to understanding the microwave remote-sensing signatures of polar snow and ice. It is a complex number defined as:

$$\varepsilon^* = \varepsilon_0(\varepsilon' - j\varepsilon'') \tag{5.27}$$

where ε_0 is the free-space dielectric constant, the real part ε' is referred to as the relative dielectric constant or relative permittivity, $j = \sqrt{-1}$, and ε'' is the relative imaginary part or dielectric loss factor (Hallikainen and Winebrenner, 1992; Onstott and Shuchman, 2004; Tiuri et al., 1984). Values of ε'' for dry snow, at both the C- and L-band, are of the order of 0.001 to 0.0001 (Rott et al., 2003). The real part ε' sets the absolute backscatter level—i.e., the degree of scattering by a medium is proportional to its dielectric constant—while the depth of the wavelength-dependent penetration of EM waves into the ice/snow layer is governed by the imaginary part ε''. The dielectric loss factor describes how much energy is lost in

the material volume once it passes across a dielectric interface (determined by permittivity), and is frequency- and temperature-dependent (Matsuoka et al., 1996; Ulaby et al., 1986a). For a given surface roughness, scattering from the sea ice surface increases with a higher permittivity in the surface layer (Nghiem et al., 1995a).

The loss that occurs when EM energy passes through a medium is commonly represented in terms of the loss tangent $\tan\delta$, where:

$$\tan\delta = \frac{\varepsilon''}{\varepsilon'} \tag{5.28}$$

In turn, $\tan\delta$ is related to the attenuation of microwave energy in the medium, and is used to determine the penetration depth δ_p—i.e., the depth at which the incident energy is reduced by $1/e$. In effect, δ_p indicates the maximum depth in the ice/snow medium at which scattering contributes to the observed brightness temperature or backscattering coefficient. Following Rott et al. (2003), it is given by:

$$\delta_p = \frac{\lambda_0\sqrt{\varepsilon'}}{2\pi\varepsilon''} \tag{5.29}$$

where λ_0 is the wavelength in free space. Penetration depth is governed by absorption and scattering of EM energy, and depends on (i) the incidence angle and frequency of the sensor, and (ii) the temperature and conductivity of the ice/snow layer (Hallikainen and Winebrenner, 1992; Vant et al., 1978). The latter relationships are shown in Figure 5.16. Factors affecting penetration depth in sea ice as a function of ice type are discussed below.

Sea ice is a complex heterogeneous substance. In terms of its dielectric properties, it is considered to be a three-phase medium comprising pure (freshwater) ice, air, and liquid brine (Weeks and Ackley, 1986). Its complex dielectric constant is determined by ice density, brine volume, and the dielectric properties of the ice and brine (Arcone et al., 1986; Onstott and Shuchman, 2004; Stogryn, 1971). Additional factors include the volume fraction of each constituent, and the geometry (size, shape, and orientation) of brine pockets and gas inclusions (bubbles) relative to the propagation direction of the EM wave (Hallikainen and Winebrenner, 1992). Many of these characteristics are temperature-dependent (Nghiem et al., 1996, 1998; Stogryn and Desargant, 1985), and, importantly, they also change with ice type (age). Moreover, the shape and concentration of brine pockets depends on the ice growth rate. Radar signatures also vary with other meteorological conditions (precipitation and wind conditions), region, and season.

Although its bulk salinity is typically only 4 to 10 p.s.u., first-year ice is very "lossy" at typical satellite sensor microwave frequencies (i.e., it is a strong absorber of EM radiation), which limits δ_p. In this case, ε' is largely determined by brine inclusions (Stogryn and Desargant, 1985), given that the relative dielectric constant of brine is typically 10–20 times that of pure ice (Shokr and Barber, 1994). The dielectric loss depends on the phase of the salt components in the liquid brine. As a result, the predominant scattering mechanism for first-year ice at the C-band, for example, is surface scattering (Onstott and Shuchman, 2004), from a topography

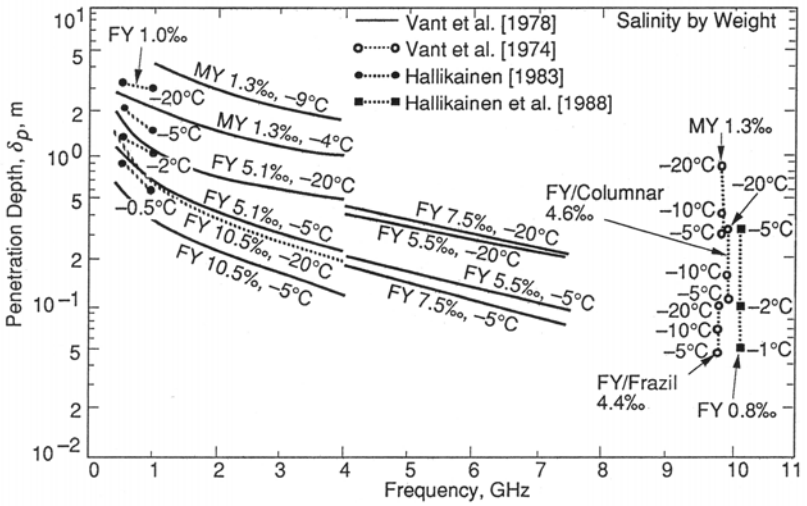

Figure 5.16. Theoretical penetration depth at microwave frequencies as a function of frequency, temperature (°C), and salinity (p.s.u.) for Arctic first-year (FY) and multiyear (MY) ice. As we will see, the frequency (and polarization) dependence of sea ice penetration depth and dielectric properties opens the door for enhanced differentiation of ice type using multi-frequency and multi-polarization satellite sensors.

From Hallikainen and Winebrenner (1992). Copyright 1992 American Geophysical Union. Reproduced by permission of American Geophysical Union.

that is generally sharp and angular with a moderate relief. In this case, the wavelength is ~6 cm and the frequency ~5 GHz. For Arctic multiyear ice, on the other hand, bulk salinities are relatively low in the freeboard layer due to desalination over time, and the value of ε' is correspondingly lower and indeed similar to that of pure ice (Lei et al., 1988; Ulaby et al., 1986a). Moreover, values of ε'' are lower (Shokr and Barber, 1994). This results in a greater penetration depth and a greater contribution from dielectric discontinuities and discrete scatterers—e.g., gas bubbles (to ~2 mm in diameter)—within the ice volume. As a result, the backscatter from Arctic multiyear ice under freezing conditions is dominated by volume scattering at C-band and higher frequencies, with the dimensions of voids and bubbles (Perovich and Gow, 1991, 1996) being within an order of magnitude of the wavelength of the EM radiation (Onstott and Shuchman, 2004). Volume scattering describes multiple scattering within a medium (Fung and Eom, 1982). As seen above, its intensity and relative contribution is determined by the physical properties of the target medium (principally the distribution and size of scatterers relative to λ), its dielectric properties, and the radar characteristics (Hallikainen and Winebrenner, 1992). Regarding the passive-microwave signature, multiple scattering both lowers the T_B for a given physical temperature and decreases the difference between vertically and horizontally polarized T_Bs (Hallikainen and Winebrenner, 1992). Hallikainen and Winebrenner (1992) review numerical relationships between sea ice physical properties and dielectric properties, and their frequency- and incidence-angular-

dependence. Antarctic sea ice exhibits significantly different physical properties and therefore backscatter characteristics (Drinkwater, 1998a, b; Drinkwater and Lytle, 1997; Drinkwater et al., 1998a, b; Hosseinmostafa et al., 1995; Morris et al., 1998).

While the discussion has so far largely focused on sea ice, its snow cover also makes a variable and at times first-order contribution to the microwave signature of ice-covered oceans measured from space (Barber et al., 1998a; Comiso et al., 1992; Drinkwater, 1988; Garrity, 1992; Grenfell and Lohanick, 1985; Tjuata et al., 1993, 1995). While dry snow constitutes a dielectric mixture of ice and air, its complex permittivity is determined by the combined dielectric properties of ice, snow crystal shape, and snow density (Hallikainen and Winebrenner, 1992; Kärkäs et al., 2002; Ulaby et al., 1986a). In fact, the dielectric constant of dry snow is mainly a function of its density (Hallikainen and Winebrenner, 1992; Hallikainen et al., 1986; Tiuri et al., 1984), which can vary significantly over short vertical scales on sea ice (Granberg, 1998; Massom et al., 1998a, 2001a; Sturm et al., 1998, 2002a). It should be noted that a snow cover has a number of other important and subtle impacts, even when dry. Working on Arctic first-year ice, Barber et al. (1998a) also noted a contribution of snow grain size to volume scattering at frequencies above ~37 GHz for passive systems and 5 GHz (C-band) for radars. This effect, of a decrease in passive-microwave emission and an increase in radar backscatter, is enhanced at horizontal compared with vertical polarization. Relationships between snow grain size and passive-microwave emission are discussed by Armstrong et al. (1993) and Foster et al. (1987). Dry snow also plays an indirect role, via the effect of its low thermal conductivity and diffusivity on the definition of vertical brine volumes, the distribution of the water phase present, and snow grain metamorphism. The complex permittivity at the snow/ice interface is significantly higher than for a snow-free ice surface, due to the warmer ice surface under snow cover. This increases the brine volume in the lower snow horizons to again create a "dielectrically rough" interface. The additional impact of diurnal thermal cycling is examined by Barber et al. (1992) and Nghiem et al. (1998).

Wet snow, on the other hand, is electromagnetically a three-component dielectric mixture of air, ice particles, and liquid water. Values of the dielectric constant for these three components (at 0°C) is air = 1, pure ice = 3.15, and water = 80 (Hallikainen, 1977). The frequency- and temperature-dependent dielectric constant of wet snow is strongly determined by the volume fraction of liquid water present (Arslan et al., 2001; Hallikainen and Winebrenner, 1992; Hallikainen et al., 1986; Tiuri et al., 1984). The appearance of even a small amount of free water (i.e., 2–3% by volume) in the snow cover leads to a high dielectric loss (Winebrenner et al., 1998), thereby increasing the snow absorption coefficient and dramatically affecting its reflectivity and decreasing its microwave penetration depth (Beavan and Gogineni, 1994; Drinkwater, 1995a; Onstott and Gogineni, 1985; Rott et al., 1988; Shi and Dozier, 1995). These relationships are shown in Figure 5.17. For snow cover on sea ice, liquid is commonly present in at least the lower horizons at temperatures well below freezing (Granberg, 1998; Massom et al., 1997, 2001a), and much higher dielectric constants are recorded—e.g., $\varepsilon' = 2.9$ by Kärkäs et al. (2002) in East Antarctica. This is due to both the upward capillary migration of brine from the

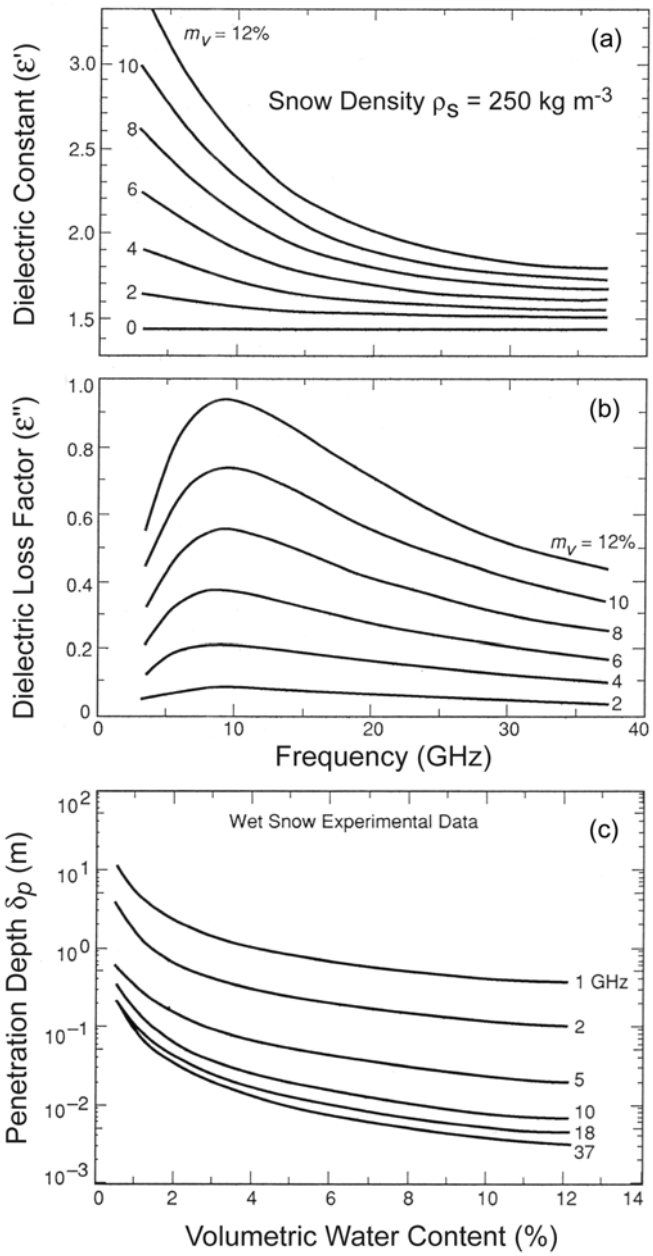

Figure 5.17. Wet snow (a) dielectric constant (permittivity) ε'; and (b) dielectric loss factor ε'', at volume fractions of water of 0–12% and with a constant snow density of 250 kg m^{-3}. (c) The frequency dependence of microwave penetration depth (frequency range 1–37 GHz) as a function of snow liquid water volume.

wet, underlying sea ice, flooding by wave action, ice deformation, the incorporation of highly saline frost flowers into the snow cover, and the overburden of the snow depressing relatively thin ice below sea level. Taken together, these processes result in a snow cover that is typically saline, thereby raising its melting point (Massom et al., 2001a). Wetness also modifies the grain size distribution and the degree of bonding between snow and underlying sea ice (Massom et al., 1998a). The impact of saline frost flowers, saline snow and slush on sea ice dielectric and emission/scattering properties is examined by Drinkwater and Crocker (1988), Eppler et al. (1992), Grenfell et al., 1992, Nghiem et al. (1997a), Onstott (1992), Shokr and Barber (1994), and Ulander et al. (1995). Frost flowers form on the surface of snow-free new ice by evaporative processes under clear, cold, and calm conditions. Their impact on TIR remote sensing is evaluated by Martin et al. (1996). With a salinity often in excess of 100 p.s.u., wind-transported frost flowers are a dominant source of sea salt to aerosols in the ice sheet of coastal Antarctica, providing a potential proxy means of determining Antarctic sea ice production from ice sheet ice core analysis (Wolff et al., 2003).

One of the main challenges to the unambiguous interpretation of satellite microwave data is that the sea ice and snow cover signatures evolve in response to dynamic and thermodynamic changes in the physical properties of the surface, and over a wide range of scales. Arctic sea ice in particular exhibits considerable seasonal variability that greatly affects analysis and geophysical parameter retrieval from microwave data (Cavalieri et al., 1990; Eppler et al., 1992; Grenfell et al., 1998; Soh et al., 1998). In early spring, diurnal and semi-diurnal fluctuations in σ^0 are associated with freeze–thaw cycles driven by oscillating air temperatures (Nghiem et al., 1998). Dramatic changes occur through the summer melt period. At the onset of melt, the appearance of liquid water in the snow cover has the effect outlined above, and attenuates the radar signal. Radar penetration depth decreases considerably and surface scattering becomes dominant (Hall, 1998). The most common outcome is a reduction in backscatter (Drinkwater and Liu, 2000; Forster et al., 2001; Haas, 2001; Kwok et al., 1998a; Long and Drinkwater, 1999; Winebrenner et al., 1994; Yueh and Kwok, 1998), resulting in a darkening of sea ice in the SAR image irrespective of ice type (Jeffries et al., 1997b). Periodic backscatter increases can also occur at this time (e.g., Barber et al., 1992; Forster et al., 2001). As the snow cover decays, an increase in wetness combined with surface roughness effects can increase the backscatter (Jeffries et al., 1997b), with the ephemeral appearance of a rough layer of superimposed ice at the floe surface (Gogineni et al., 1992; Haas et al., 2001; Onstott et al., 1987). A subsequent decrease in σ^0 coincides with the appearance of meltponds, which can cover up to 60% of the surface area of Arctic sea ice in summer (Jeffries et al., 1997b). For passive-microwave data, the net effect is to greatly decrease surface emissivity, thereby undermining the unambiguous distinction of actual open water from meltponds/saturated snow. The subsequent drainage of meltponds through the ice in late summer leaves behind a granular and highly porous ice surface, resulting in an increase in radar backscatter (Holt and Digby, 1985).

With a return to freezing conditions in autumn, the surviving ice cools, freewater freezes, and the dominant backscatter mechanism changes from surface to volume

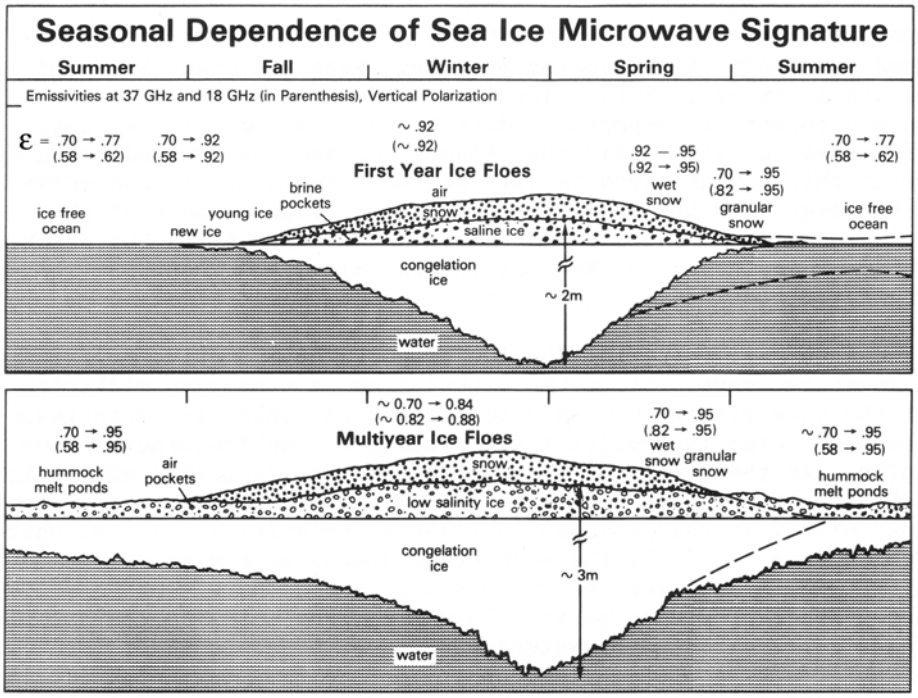

Figure 5.18. Schematic diagram of the seasonal dependence of physical and radiative characteristics of Arctic first-year and multiyear ice at 18 and 37 GHz (vertical polarization) over an annual cycle.

From Comiso (1985). Reprinted with permission of A. Deepak Publishing.

scattering, leading to a fairly rapid return of σ^0 to winter levels (Beavan and Gogineni, 1994; Carlström and Ulander, 1993; Jeffries et al., 1997b; Winebrenner et al., 1996). The seasonal change in ice conditions in the Arctic, and its effect on passive-microwave emissivities at 18 and 37 GHz, is illustrated schematically in Figure 5.18. The equivalent impact of seasonal change on observed backscatter at C-band and VV-polarization[7] is shown in Figure 5.19. For detailed information on summertime passive-microwave signatures and their evolution, the reader is referred to Carsey (1985), Cavalieri et al. (1990), Comiso (1990), Comiso and Kwok (1996), Comiso and Steffen (2001), Comiso et al. (1997), Dokken et al. (2000a), Eppler et al. (1992), Gohin et al. (1998), Grenfell (1992), Grenfell and Lohanick (1985), Onstott (1992), Onstott and Shuchman (2004), and Smith (1998b). Arctic wintertime sea ice emissivities at 89, 157 and 183 GHz are given by Hewison et al. (2002). Comiso et al. (1992) and Drinkwater (1995a) evaluated Antarctic seasonal considerations.

To summarize, a number of general relationships exist which enable the broad classification of ice types in microwave imagery, at least in the Arctic due to the

[7] See Section 5.7.3.1. for an explanation of the different types of polarization.

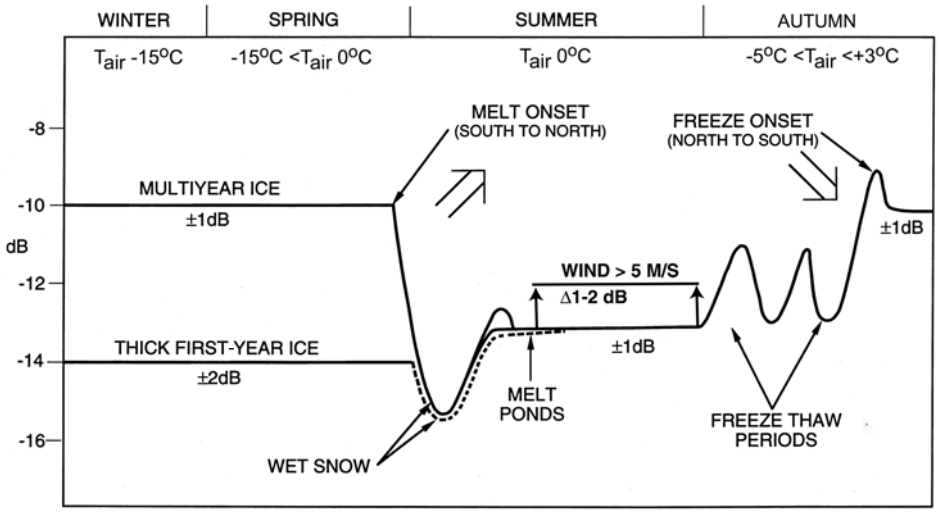

Figure 5.19. Schematic representation of the seasonal response of radar backscatter measured by the ERS C-band VV-polarization SAR to changes in physical characteristics of Arctic first-year and multiyear ice over an annual cycle (using data from Kwok and Cunningham, 1994a; and Winebrenner et al., 1994, 1996). Approximate ranges of backscatter and seasonal air temperature are given. Note the effect of an increase in wind speed on the backscatter of the surface during summer.

Courtesy: Ben Holt (NASA Jet Propulsion Laboratory), modified from Soh et al. (1998). Reprinted with kind permission of Springer Science and Business Media.

stronger contrast in the physical characteristics of the ice types compared with the Antarctic (see Section 5.3). For low-salinity Arctic multiyear ice under freezing conditions, volume scattering makes a significant contribution to σ^0 to create a bright target, whereas the dominant contribution from saline new and first-year ice, or a wet snow cover and/or flooded multiyear ice, is surface scattering (Gogineni et al., 1992). It follows that surface roughness has a major effect on radar scattering from saline ice (Dierking et al., 1997; Fung and Eom, 1982; Kim et al., 1985a), wet snow, and ice surfaces (Stiles and Ulaby, 1980). Importantly, from the perspective of microwave remote sensing of sea ice concentration, ice-free ocean surfaces have a high dielectric constant, with much of the incident radiation being reflected away from the sensor to create a relatively dark target in SAR imagery under calm conditions. Under windy conditions, however, the roughened ocean backscatter increases to overlap with that from consolidated ice types.

As stated earlier, the intensity of radar returns from sea ice (and snow and ice surfaces in general) is determined by the interaction of its electrical, micro-structural, and surface geometrical characteristics (Figure 5.20). The third of the backscatter determinants—surface roughness—is a measure of the irregularity of the surface (both vertical and horizontal) compared with the radar wavelength. Whether or not a surface appears rough to incident microwave energy depends on the incidence angle of the radar beam θ_i, its wavelength λ, and the variability of

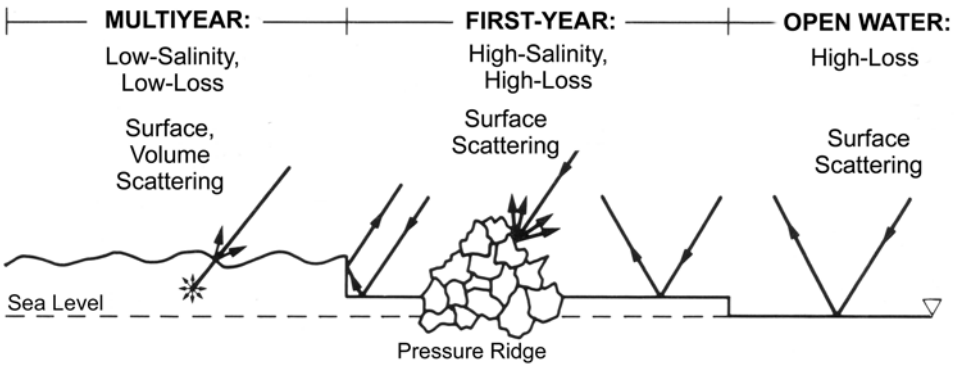

Figure 5.20. A schematic of idealized radar backscatter interactions with smooth open water, smooth first-year ice, pressure ridges, floe edges, and Arctic multiyear ice. Note that for Antarctic multiyear ice, the interactions are generally equivalent to those of Arctic first-year ice. Note also that, whereas new pressure ridges present sharp and angular targets, old pressure ridges on Arctic multiyear ice are typically weathered and more rounded.
From Carver (1989). Image courtesy of NASA.

height (standard deviation) of the surface Δh (Onstott and Shuchman, 2004). The incidence angle is the angle defined by the incident radar beam and the vertical (normal) to the intercepting surface. EM roughness can be characterized using the Rayleigh criterion, whereby a surface is said to be rough if $\Delta h > \lambda/(4.4\cos\theta_i)$ (5.30a) and smooth if $\Delta h < \lambda/(25\cos\theta_i)$ (5.30b). Taking European Remote-Sensing (ERS) satellite SAR data as an example—i.e., $\lambda = 6$ cm and $\theta_i = 23°$—a rough surface is one where the vertical displacement exceeds 1.41 cm, while a vertical displacement of <0.24 cm constitutes a smooth surface. Surface-scattering models generally use correlation length and root-mean-square (r.m.s.) parameters to define the horizontal and vertical components, respectively, of the surface geometry (Ulaby et al., 1982). Parameters commonly used to measure and describe the surface roughness characteristics of snow and ice are the standard deviation of small-scale surface elevation and the spatial autocorrelation function of the surface, from which the correlation length is derived (Drinkwater, 1988). See Paterson et al. (1991) for information on micro-scale surface roughness measurement in the field.

As a rule of thumb, rough surfaces tend to act as diffuse reflectors—i.e., they reflect a significant proportion of incident radiation back in the direction of illumination, resulting in a high backscatter and bright radar target. Smooth surfaces, on the other hand, act as specular reflectors, reflecting a significant proportion of radiation away from the direction of illumination, resulting in relatively low backscatter and a darker target. The wavelength- (frequency-) dependence of reflection characteristics, in this case for X- and L-band radars, is shown schematically in Figure 5.21.

Much of our current understanding of the backscattering behavior of sea ice and its snow cover comes from *in situ* and airborne campaigns in the Arctic. Little similar work has been carried out in the Antarctic, and relatively little is known about the

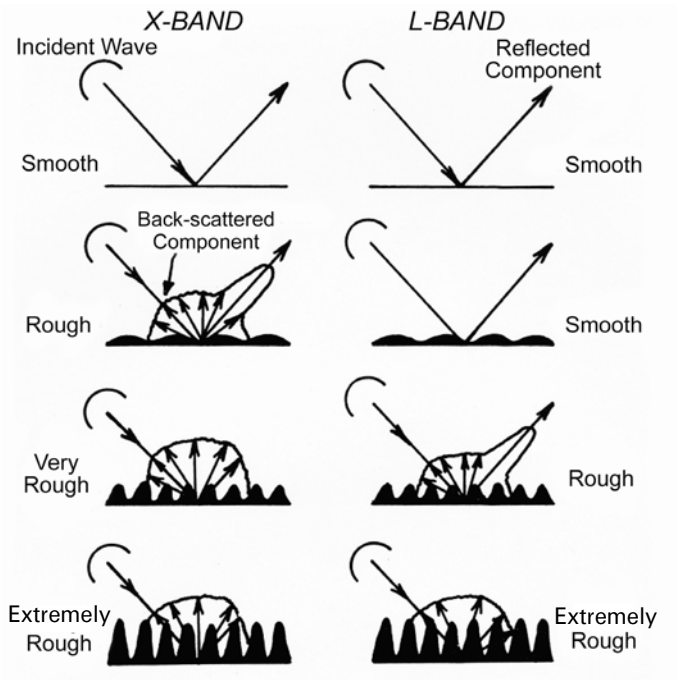

Figure 5.21. Schematic of the scattering behavior of electromagnetic radiation at X- and L-band frequencies ($\lambda = \sim 3$ and ~ 23 cm, respectively) incident on smooth, rough, and very rough snow/ice surfaces. These two frequencies form the end members of recent, current, and near-future spaceborne SARs (see Appendix). Scattering behavior at intermediate frequencies—e.g., C-band ($\lambda = 6$ cm)—will be somewhere in-between.

From Onstott and Shuchman (2004). Reprinted with permission of NOAA.

seasonal evolution of the sea ice backscatter signature there as a result (Drinkwater, 1995a). Once again, Antarctic sea ice represents a different target altogether (see Drinkwater, 1998a, b). Given the complexity and often poorly understood nature of these relationships, physical models have an important role to play in terms of providing theoretical explanations for the backscatter and emission characteristics involved (Fung and Eom, 1982; Kim et al., 1984, 1985a, b; Mätzler et al., 2000; Wang et al., 2000). Reviews of techniques, capabilities, and current uncertainties in EM modeling are provided by Dierking (1992), Barber et al. (1998a), Fung (1994), Golden et al. (1998a, b), Hallikainen and Winebrenner (1992), and Winebrenner et al. (1992). These are dependent on accurate information on the snow and ice micro-structure (Perovich and Gow, 1991, 1996; Tucker et al., 1992; Weeks and Ackley, 1986). Empirical observations are also making a major contribution, both in the field and under controlled conditions (Grenfell et al., 1994a; Jezek et al., 1998; Kwok et al., 1998a; Lohanick, 1990; Nghiem et al., 1998; Shokr and Barber, 1994; Swift et al., 1992). Moreover, polarimetric studies are laying the groundwork for the new generation of polarimetric SARs, with a view to improving the classification of

sea ice (see Section 5.9.7.3.2). Such work is essential in enabling us to better interpret and extract optimal and at times subtle sea ice geophysical information from multi-spectral and multi-polarization satellite data, both radar and passive-microwave. This is a critical consideration in the light of the new trend in spaceborne SARs towards multi-polarization and fully polarimetric capabilities (see Section 5.8.2.1).

5.7.3.1 Polarization

Polarization is an important property when discussing the propagation and scattering of microwave energy, and is a key determinant of both microwave backscatter and emission. Recalling Chapter 2, polarization describes the locus of the electrical field vector in the plane perpendicular to the direction of propagation (for a plane EM wave). Importantly, horizontally polarized (H) waves interact in a different manner with sea ice and snow than do vertically polarized (V) waves. This results in additional and complementary information to aid discrimination of various ice types (see Section 5.9.7). As we will see below, an exciting new development is the launch of satellite SARs with multi-polarization and full polarimetric capability, whereby both the amplitude and the phase information are available. A multi-polarization SAR is one which can have two or four possible polarizations, which are not necessarily simultaneous or phase-coherent, and may have only one channel which is switchable between polarizations. A fully polarimetric or quadrature polarization (quad pol) radar, on the other hand, has the ability to simultaneously collect data at HH, VV, HV, and VH polarizations. By convention, the first letter refers to the polarization transmitted and the second letter to that received. Importantly, a polarimetric SAR measures not only amplitude but also relative phase between channels (this may or may not be measured by conventional systems). Polarimetric passive-microwave systems are also being launched (WindSat in 2003—see below) and planned.

5.8 MAJOR SENSOR CLASSES AND THEIR ATTRIBUTES AS SEA ICE RESEARCH TOOLS

In this section, we introduce the major satellite sensor classes applied to polar ocean research. These are: (i) passive-microwave; (ii) synthetic aperture radar (SAR); (iii) radar scatterometer; (iv) radar altimeter; and (v) visible to thermal infrared (TIR). Microwave sensors are of key importance in being able to penetrate both polar cloud cover and darkness.

5.8.1 Passive microwave sensors

Passive microwave radiometers are collectively without doubt the ''workhorse'' among satellite sensors applied to sea ice research. Since the launch of the Nimbus-5 Electrically Scanning Microwave Radiometer (ESMR) in 1972, they have yielded the most consistent and detailed information on the large-scale characteristics and variability of the global sea ice cover on a virtually continuous

basis, uninterrupted by darkness and (largely) clouds. Given their poor (but improving) resolution of up to tens of kilometers but wide swath width, they are best suited to providing a broad-scale overview of sea ice distribution, with individual morphological features such as leads remaining unresolved. While ESMR provided the first consistent global view of sea ice, it operated a single channel only, and much-improved data became available with the launch of the first multichannel instrument, the Scanning Multichannel Microwave Radiometer (SMMR), onboard Nimbus-7 in 1978. This sequence continued with the advent of the U.S. Defense Meteorological Satellite Program (DMSP) Special Sensor Microwave/Imager (SSM/I) series (1987–present), with the addition of a higher resolution 85-GHz channel. The launch of almost identical Advanced Microwave Scanning Radiometers (AMSRs) onboard the Japanese ADvanced Earth Observing Satellite-II or ADEOS-II (AMSR, ⟨*http://sharaku.eorc.jaxa.jp/ADEOS2/index.html*⟩) and NASA's Earth Observing System (EOS) Aqua (AMSR-E) in 2002 marked the dawn of a new era of passive-microwave measurement (Kawanishi et al., 2003; Parkinson, 2003). Improvements include a higher spatial resolution (to ~5 km), a wider spectral range (enabling the measurement of additional parameters—e.g., ice temperature), and better temporal coverage. Moreover, the AMSR sensors reinstated the low-frequency channels present in SMMR but missing in SSM/I, enabling the retrieval of ice temperature (see Section 5.9.12). Unfortunately, a malfunction led to the early demise of the ADEOS-II AMSR in late 2003. Importantly, the new data are directly comparable with SSM/I data (Comiso, 2003c). As such, the multi-channel time series extends back over 25 years, and represents a key baseline for assessing the state of the ice cover and for evaluating variability and trends.

This sequence will continue into the future with the launch of the Conical-scanning Microwave Imager/Sounder (CMIS) onboard the National Polar Orbiting Environmental Satellite System (NPOESS) series in 2009 and launches planned right up to NPOESS-6 in ~2019 (⟨*http://www.ipo.noaa.gov/index.html*⟩). This sophisticated sensor is based upon the heritage of the SSM/I and AMSR, but merged with an atmospheric sounding capability. Data will also be available from the AMSR follow-on, scheduled for launch onboard the Japanese GCOM-B1 satellite in 2010. Data are also used from Advanced Microwave Sounding Unit (AMSU) sensors, but this is a secondary source as it is largely devoted to atmospheric sounding (Zhao and Weng, 2002). Improved spatial resolutions may become available in the future through the developing technology of synthetic aperture passive-microwave systems (Le Vine et al., 1990; Ruf et al., 1998).

The Russian sea ice surveillance program also has a long history in launching spaceborne passive-microwave radiometers, dating back to 1968. More recently, the Okean-O satellite carried an eight-channel sensor operating at wavelengths of 0.8, 1.35, 2.25, and 4.3 cm (dual-pol) and with a resolution of 20–100 km over a 1,130-km swath width (Belchansky and Douglas, 2000). The Okean-01 series, on the other hand, carried a 0.8-cm-wavelength (H-pol) sensor with a spatial resolution of 15 km over a 550-km swath width. Data are available from the Russian Hydrometeorological Centre. Other data are available from the MTVZA sensor onboard the Russian Meteor-M satellites (Cherny et al., 2002). This 26-channel sensor is

equivalent to the AMSU and DMSP Special Sensor Microwave Imager Sounder (SSMIS) sensors, operating at frequencies located both in atmospheric windows at 18.7, 33, 36.5, 42, 48, 91.65 GHz and also in absorbing lines of oxygen (52–57 GHz) and water vapour (22.235 and 183.31 GHz). First launched on satellite F-16 in October 2003, the SSMIS combines the attributes and capabilities of the SSM/I and the SSMT-1 and SSMT-2 (Special Sensor Microwave Temperature/Humidity sounder) sensors. For the MTVZA, data are collected over a swath width of 2,200 km at spatial resolutions ranging from 12 to 75 km, with the satellite flying in an orbit with an inclination of 99.63°, a local time ascending node of 9 : 15 a.m., and a revisit period of 3 days (Asmus, 2003; Bedritsky et al., 1999). Note that the scanning mechanism of the sensor onboard Meteor-3M N1 failed in May 2002. A modified sensor, the MTVZA-OK (Combined Microwave-Optical Imaging/Sounding Radiometer) was launched onboard the Russian–Ukrainian satellite SICH-1M in December 2004. This instrument combines an optical system (four bands from 0.37 to 0.78 μm and one band at 3.55–3.93 μm, spatial resolution 1.1 km) with a passive-microwave one (Cherny and Chernyavsky, 2001; Fournier-Sicre et al., 2003). The latter operates in 22 channels, from 6.9 to 183.31 GHz, at a spatial resolution ranging from 12 to 260 km. The swath width for both systems is ~2,000 km. Further information on earlier Russian satellite microwave remote sensing is given by Kondratyev and Melentyev (1994). See also ⟨*http://sputnik.infospace.ru/welcome.htm*⟩ for information on data availability.

A recent alternative (although again secondary) source of sea ice information is the Multi-channel Scanning Microwave Radiometer (MSMR) onboard the Indian Oceansat-1 (IRS-P4) satellite. Launched in 1999, this satellite makes dual (i.e., vertical and horizontal) polarization measurements at four frequencies (6.6, 10.65, 18, and 21 GHz) over a constant 49° incidence angle over a swath width of 1,360 km (Binyala et al., 2003; Narayanan and Sarkar, 2001; ⟨*www.nrsaftp.gov.in/msmr_help*⟩). This sensor provides complete global coverage once every 2 days, to a maximum latitude of 88° and at a frequency-dependent spatial resolution that ranges from 50 to 150 km.

The launch of the WindSat sensor onboard the U.S. Naval Research Laboratory's Coriolis mission on January 6, 2003 represents the emergence of a new technology in space. WindSat is the first spaceborne polarimetric microwave radiometer. Polarimetric microwave radiometers are designed to measure polarization information beyond conventional dual-polarized radiometers (Piepmeier and Gasiewski, 2001). This information is used to determine parameters of the Stokes vector or polarization ellipse, to characterize the polarization properties of surface microwave emissions. As its name implies, this sensor is specifically designed to measure surface wind vectors over open ocean (resolution ~30 km) to performance requirement accuracies of $\pm 2\,\mathrm{m\,s^{-1}}$ or 20% for wind speed and ±20° over the range of $3–25\,\mathrm{m\,s^{-1}}$ for wind direction (Gaiser et al., 2004). The WindSat radiometer, which will form a component of the NPOESS CMIS system, operates in discrete bands at 6.8, 10.7, 18.7, 23.8 and 37.0 GHz. While the 6.8- and 23.8-GHz channels are dual-polarized only (i.e., vertical and horizontal), the 10.7-, 18.7-, and 37.0-GHz channels are fully polarimetric. The pixel size ranges from 40×60 km at 6.8 km to

8×13 km at 37.0 GHz. WindSat offers an alternative source of operational information on global sea ice concentration and extent. As a polarimetric radiometer, this instrument can measure the full Stokes vector[8] (Gaiser et al., 2004; St. Germain et al., 2002), compared with the current generation of SSM/I and AMSR sensors which measure only the first two components of the four-element Stokes vector to enable retrieval of wind speed but not direction over open ocean. The exact benefits of these new capabilities to sea ice research and monitoring are currently unknown, although the potential exists for improved sea ice classification. Apart from direct measurement of sea ice, however, the availability of large-scale windfield products from this new sensor in near-real time will likely make a significant contribution to the operational modeling and nowcasting/forecasting of sea ice (although the wind data can only be acquired over open water regions, as is the case with radar scatterometers).

As we saw in Section 5.7.1, passive-microwave systems measure natural thermal emissions of EM radiation in the millimeter to centimeter range from the surface. At these wavelengths, a strong contrast exists between the emissivity of ice-free ocean and that of different ice types (Figure 5.22)—e.g., ~0.4 for open ocean, ~0.90 for first-year ice and ~0.70 for multiyear ice at 37-GHz horizontal (H) polarization—and in the Arctic in particular (Comiso, 1986; Comiso et al., 1984; Eppler et al., 1992; Svendsen et al., 1983). It is on this basis that passive-microwave radiometers constitute the primary source of global ice concentration and extent data, and also of information on the fraction of multiyear ice in the Arctic. This is achieved by combining brightness temperatures (T_Bs) measured at different frequencies—e.g., 19 and 37 GHz—and both H and vertical (V) polarization, resulting in the retrieval of total ice concentration at a ground resolution ranging from 12.5 to 25 km (for AMSR-E). Note that in the Antarctic, the different sea ice growth processes noted earlier lead to a much smaller contrast in the emissivities of first-year and multiyear ice (Comiso et al., 1992; Gloersen et al., 1992), enabling the extraction of total ice concentration only.

The overall advantages of passive-microwave sensors can be summarized as follows:

- ability to penetrate polar darkness and non-precipitating clouds (depending on frequency);
- excellent daily coverage of the complete global sea ice cover, ensured by the low data rate;
- stable instrument calibration; and
- a consistent time series dating back to 1978.

Disadvantages include:

- their large fields-of-view of ~6 to 50 km (depending on frequency)—i.e., inability

[8] A four-element real vector whose elements consist of the Stokes parameters (a set of four real numbers describing the state of polarization of an EM wave). It describes the polarization state of an EM wave in terms of the orthogonal components of the electric field of the wave.

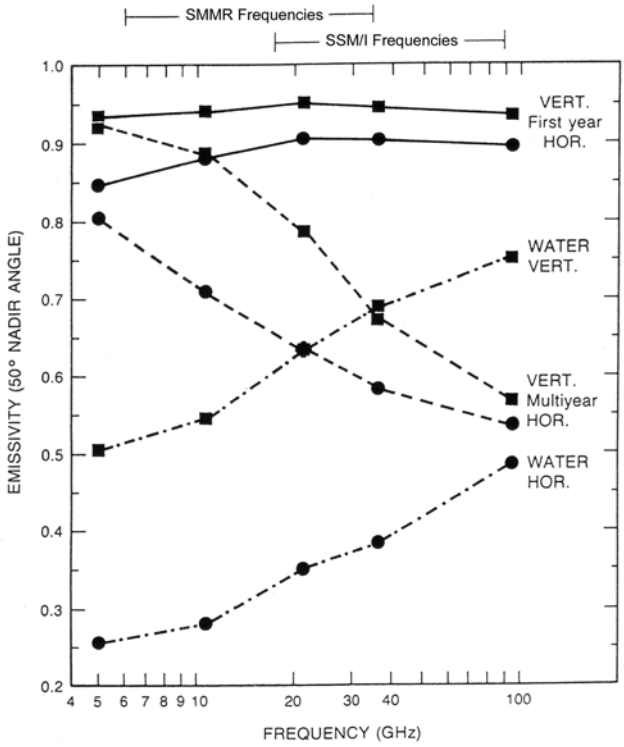

Figure 5.22. Frequency dependence of the microwave emissivity of Arctic first-year and multiyear ice and calm open ocean for both H and V polarizations.

Data are from surface measurements acquired by the NORwegian Remote Sensing EXperiment (NORSEX) group in September 1979 north of Svalbard. From Svendsen et al. (1983). Copyright 1983 American Geophysical Union. Reproduced by permission of American Geophysical Union.

to resolve individual morphological features such as leads (although some studies have combined high-frequency channel data with higher resolution satellite data to characterize large leads, e.g., Agnew et al., 1999);

- the mixed-pixel problem (common to all poor-resolution sensors), whereby the signatures of different ice types present within a pixel are averaged and cannot easily be unmixed;
- the large variability and uncertainty in sea ice (and snow cover) emissivity at microwavelengths (compared with TIR wavelengths) (Comiso et al., 1989, 1992; Grenfell et al., 1992, 1994a; Eppler et al., 1992), and during melt periods and in marginal ice zones in particular (Grenfell and Lohanick, 1985); and
- coastal contamination effects, whereby coastal pixels containing sea ice physically overlap with and contain a contribution from land/ice sheet.

Other strengths and weaknesses will become apparent later. In an effort to address these factors and provide consistently accurate sea ice information, modern satellite

passive-microwave radiometers provide simultaneous coverage at multiple frequencies and both V and H polarizations (Tables A.1–A.10 of the Appendix). An important tradeoff is that the higher the frequency, the better the spatial resolution but the greater the atmospheric contribution. Indeed, the latter can be significant beyond 37 GHz and, especially, at 85 GHz (St. Germain, 1994). This is a factor that should be taken into account when using these data to measure and monitor sea ice.

5.8.2 Active microwave

Three classes of radar sensor have been used to measure sea ice from space, uninterrupted by cloud and darkness: (i) SARs; (ii) radar wind scatterometers; and (iii) radar altimeters. Unlike visible and TIR imagers, radars penetrate the snow and ice surface to yield additional information on internal properties. This provides a tool capable of classifying sea ice, but comes at the cost of additional complexity in data interpretation and algorithm development, more limited coverage, and the need for dedicated receiving stations to ensure regular repeat coverage. Spaceborne Side Looking Radars (SLRs) have also been launched by the Russian program—e.g., the X-band payload onboard Kosmos Okean satellites (since 1983). These sensors use Real Aperture Radar (RAR) technology, whereby spatial resolution is a function of the physical size of the antenna in space and is therefore relatively poor (compared with the SAR). Specifications of the Okean SLR (in operation until 2000) are: $\lambda = 3.15$ cm, VV polarization, resolution 1.8 km (along-track) and 0.8–2.0 km cross-track, swath width 450 km, orbit altitude 600–650 km, and incidence angle 20–50°. Other satellites in this series have carried X-band SLRs with a spatial resolution of $\sim$1 km in the near range over two 700-km swath widths (Tsatsoulis and Kwok, 1998b). The follow-on Russian–Ukrainian SICH-1M series was launched in December 2004 with an Okean-type X-band SLR known as RLSBO ($\lambda = 3.14$ cm, frequency 9.7 GHz, resolution 1.7 to 2.8 km along-track and 0.7 to 1.3 km cross-track, swath width 450 km or 700 km, left-looking), into an elliptical orbit with an inclination of 82.57° (Fournier-Sicre et al., 2003). Alexandrov et al. (2000) used time series of Russian Okean SLR images, NOAA AVHRR images, and SSM/I data combined with a model to analyse sea ice drift patterns in the Laptev Sea (Russian Arctic) and ice exchange with the Arctic Ocean. Belchansky and Douglas (2002) further used Okean SLR and passive-microwave data to classify Arctic sea ice. While SLR data have been extensively used operationally in the Russian Arctic (Johannessen et al., 1997), their application to global sea ice research has been more limited. As such, we concentrate in this chapter on the other three radar classes, and on SAR and radar scatterometers in particular. It should be noted that the Russian Okean-01 polar-orbiting satellite series is unique for ice mapping because it carries three intermediate-resolution instruments that have the capability of simultaneously collecting passive-microwave, SLR, and optical imagery. The passive-microwave instrument (36 GHz, wavelength 0.8 cm, horizontal polarization, swath width 550 km), X-band SLR, and single-channel (0.8–1.1 μm) optical sensor provide imagery at spatial resolutions of 15 km, 1.2 km, and 1.0 km, respectively. Ice maps produced using

simultaneously acquired passive- and active-microwave Okean data have compared favourably with concurrent SSM/I and AVHRR ice classifications in several case studies of northern Russian seas (Belchansky and Douglas, 2000).

5.8.2.1 Synthetic aperture radar (SAR)

Since first being launched for Earth observation on Seasat in 1978, the spaceborne synthetic aperture radar (SAR) has emerged as an immensely powerful sea ice operational and research tool (Holt and Kwok, 2003; Katsaros and Brown, 1991; Shuchman and Flett, 2003; Stern, 1998). Although the Seasat L-band mission lasted for only 90 days, it collected a large volume of data (from the Arctic only, and at a spatial resolution of 25 m across a 100-km swath width). These data were used to clearly demonstrate the immense potential of SAR as a polar research tool (Fu and Holt, 1982). Importantly, SAR can provide quantitative measurements of key parameters to aid interpretation of observations of variability and processes on horizontal scales of tens of meters to hundreds of kilometers (Winebrenner et al., 1998), uninterrupted by cloud and darkness. It enables the researcher to focus on a given region of interest, and to resolve important features such as leads, polynyas, and even pressure ridges (Melling, 1998). The high spatial resolution largely avoids the mixed-pixel problem of poor-resolution sensors, such as passive-microwave instruments, but comes at the expense of data volume and complexity in processing and analysis.

The viewing geometry of a spaceborne side-looking SAR is shown in Figure 5.23. For a real-aperture radar system, the spatial resolution in azimuth depends on the antenna beamwidth, and is linearly proportional to the distance between the sensor and surface (Elachi, 1988). The spatial resolution in range, on the other hand, depends on the bandwidth of the transmitted radar pulse, with high resolution being achieved through pulse compression techniques. Bandwidth is a measure of the frequency-limiting stages in the system or the span of frequencies available in a signal. By the principle of SAR, an improvement in resolution in azimuth, from a value of the order of a kilometer to meters/tens of meters, is achieved by exploiting the along-track motion of the satellite to create (synthesize) a large aperture (antenna) in space. This technique is based on sampling the range and Doppler history of a given point on the surface from different along-track positions while it remains within the antenna footprint on the surface (i.e., the area on the ground affected by one transmitted radar pulse from which the backscattered signal is received). The radar signal in azimuth and range is then separated during processing to create a high-resolution image. The fact that SAR needs to record both the amplitude and phase of the returned signal in order to achieve aperture synthesis is also of key importance from the perspective of interferometry (see Chapter 2 of Volume 2 of this book). The azimuth resolution achievable is approximately equal to one-half the length of the actual (real) antenna and does not depend on platform altitude (distance above the surface). For a thorough treatment of the underlying principles of radar remote sensing, the reader is referred to references in the introductory section of Chapter 2 of Volume 2.

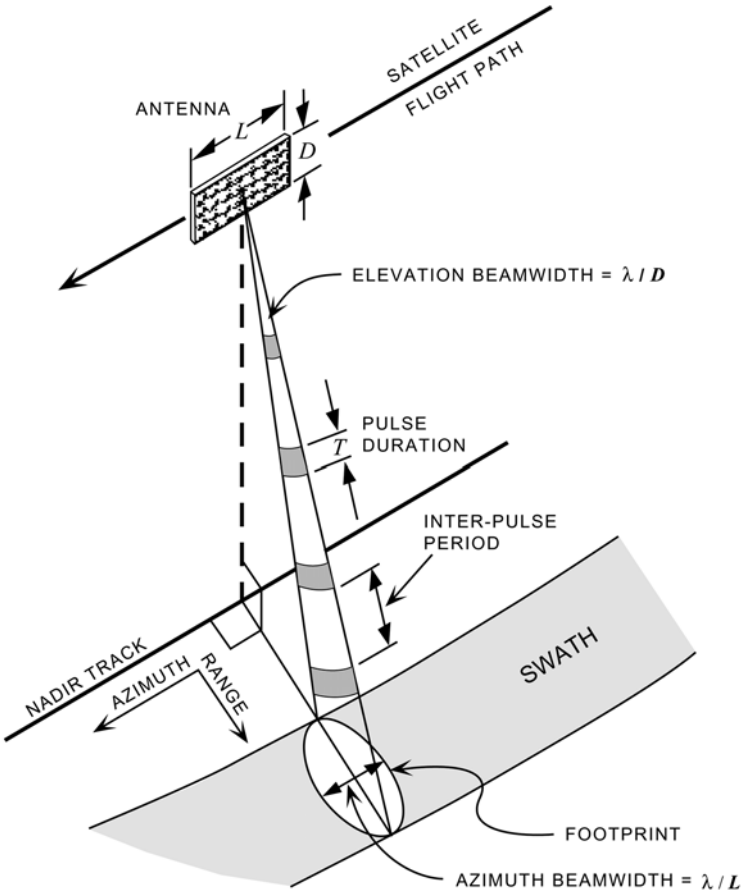

Figure 5.23. The general scanning configuration and geometry for side-looking synthetic aperture radar (SAR), in this case left-looking. Scanning in the along-track (azimuth) direction is provided by the forward motion of the satellite, while that in the cross-track (range) direction results from directing the radar beam to the side of the platform trajectory to map the ground surface.

From Olmsted (1993). Information obtained from the Internet online information page (*http://www.asf.alaska.edu/*) maintained by the Alaska Satellite Facility, University of Alaska Fairbanks (December, 2004).

The swath width of conventional SAR "stripmap" systems is limited primarily by the radar pulse repetition interval minus the pulselength—i.e., the lower the azimuth resolution, the wider the swath and the greater the ground coverage. As a result of this limitation, a high-resolution system such as TerraSAR-X has a narrow swath width of only 30 km (in its stripmap modes at 3–6 m resolution), compared with 100 km for ESA's ERS (launched in 1991: ESA, 1991) and Envisat (2002 launch) satellites, for example. Larger swaths can be achieved at the cost of azimuth resolution by operating the radar in bursts and stepping the antenna pointing repeatedly through different elevation angles. This mode is called "ScanSAR", and has become

a standard feature of modern satellite SAR remote sensing (see below) to greatly facilitate studies and operational applications requiring regional coverage.

A further key characteristic of not only SARs but all satellite sensors, and one that affects their applicability to the measurement/monitoring of given polar phenomena and processes, is revisit time (interval). Previous-generation SARs such as ERS-1/-2 and the Japanese Earth Resources Satellite (JERS-1) (1992–1998) operated with a fixed viewing geometry. Modern SARs, on the other hand, operate at variable look angles and even direction (left or right), thereby reducing imaging revisit interval and greatly increasing coverage flexibility to—in theory—better suit the needs of the user.

Another feature of modern SARs is that they are well-calibrated. With radiometric corrections applied, the absolute calibration of ERS SAR, for example, is at least ± 1 dB or better (Laur et al., 1998). In effect, a calibrated SAR image of an ice-covered ocean represents a "snapshot" map of the spatially varying intensity of the radar reflectivity, or normalized backscattering cross section σ^0, of the surface, and can be accurately geo-registered. Referring back to Section 5.7.1, the strength of return is strongly related to both physical (i.e., surface and near-surface roughness, morphology) and related electrical (i.e., dielectric constant, absorption) characteristics of the surface. It is also determined by the radar incidence angle, polarization, and frequency (wavelength). In an ideal case and under winter (freezing and dry) conditions, interpretation of single-polarization SAR imagery is based on a number of well-known relationships (Onstott and Shuchman, 2004). These can be briefly summarized as follows:

- Strong backscatter contrasts exist between calm open water (i.e., strong forward scatter, appearing dark in the SAR image), smooth new ice (i.e., moderate backscatter, appearing medium-bright), and thick deformed ice (i.e., a strong backscatter, resulting in a very bright return).
- For newer ice, the relatively high salinity limits the penetration of microwaves, leading to a dominance of surface roughness (at millimeter to decimeter scales) as a determinant of the backscatter.
- Ice desalination with age and increasing thickness leads to an increase in radar penetration and an enhanced contribution of volume scattering by inhomogeneities within the ice bulk—e.g., air bubbles (note that surface roughness remains an important factor). This provides a means of classifying the ice, which in itself is a proxy means of roughly estimating ice thickness, again most effectively in the Arctic.
- Special conditions occur in marginal ice zones, where ocean waves make a significant contribution to the sea ice radar signature (Dierking, 2001).

In spite of these known relationships, the interpretation of sea ice signatures in SAR data remains a challenging issue, given the often unpredictable and complex backscatter returns from different ice types and wind-roughened open water and their variability (Shuchman et al., 2004). In particular, large and abrupt variations are observed in sea ice and snow cover backscatter in response to changing environmental conditions to greatly limit the retrieval of accurate geophysical

parameters during the annual melt season. This is unfortunate, given the importance and lack of knowledge of large-scale atmosphere–ice–ocean interaction processes in summer (note that this limitation applies to all microwave sensors). As we will see, this information can, however, be used advantageously to detect and track melt and freeze-up across the sea ice cover. The main applications of SAR are the measurement of ice-type classification, ice edge delineation and detailed information on the configuration of the ice edge (e.g., the presence of eddies, etc. [Johannessen et al., 1994b, c]), open-water fraction, and thin-ice discrimination (leads and polynyas), ice surface roughness, ice motion, ice deformation, and the inference of ice thickness, floe size distribution, fast ice extent, wave–ice interaction, seasonal melt and freeze-up detection, and iceberg and ice island detection and tracking—a powerful combination for sea ice research. The role that SAR can play in surface energy flux measurements over sea ice was evaluated by Barber et al. (1998b) and Drinkwater (1995b). Secondary applications are ice concentration and ice extent. The data are also extensively used as a powerful operational tool (DMSG, 2000), lending themselves well to data assimilation and fusion (Section 5.9.17). The latter refers to the combination of information from different data sources to produce a better overall understanding of sea ice conditions.

The first generation of satellite SARs, including those flown onboard Seasat (L-band at 1.28 GHz, HH-pol, look angle $\theta_i = 23^\circ$), ERS-1 and -2 (C-band at 5.3 GHz, VV-pol, $\theta_i = 23^\circ$), and to a lesser extent JERS-1 (L-band, $\lambda = 23.5$ cm, $\theta_i = 35^\circ$), made an immense contribution to sea ice research. The JERS-1 SAR was not extensively used for polar applications due to its relatively poor noise floor (of approximately -18 dB), caused by persistent technical problems (Rosenqvist et al., 2003). The ERS Active Microwave Instrument (AMI) combines the function of a SAR for both image and wave modes (Johannessen et al., 1995b). When in image mode, it operates at 5-bit resolution (for raw data), which corresponds to a spatial resolution of about 30 m. For the majority of its mission (1991–2000), ERS-1 flew in a 35-day repeat orbit cycle, apart from (i) April 10, 1994–March 21, 1995 when it was in a 168-day repeat "geodetic phase"; and (ii) two periods when it was in a 3-day "ice phase" (December 28, 1991–March 30, 1992 and December 23, 1993–April 10, 1994). Launched in 1995, ERS-2 is in the same 35-day repeat orbit as ERS-1. Both satellites operated in a Sun-synchronous polar orbit with a 98.52° inclination. As noted previously, the ERS, JERS-1, and Seasat SARs were, however, limited to measurement at a fixed incidence angle (note the difference between ERS and JERS-1), frequency, and polarization combination, and yielded data over a narrow swath of 75–100 km. Note that other satellite SARs included Russian S-band (3.125 GHz, $\lambda = 9.6$ cm) and HH-polarization sensors onboard the low Earth-orbiting Kosmos 1870 (July 1987 to July 1989, 25–30-m spatial resolution, 20–35-km swath) and Almaz-1 (March 1991 to September 1992). Almaz-1 operated at an improved resolution (11–18 m, depending on swath width) over a wider adjustable swath of 40–280 km (Tsatsoulis and Kwok, 1998b). The orbital inclinations of Kosmos 1870 and Almaz-1 were 73°, precluding coverage of the central Arctic Ocean.

As noted above, a major advance in terms of coverage and flexibility came with the launch of ScanSAR technology onboard Radarsat-1 (C-band, $\lambda = 5.7$ cm,

HH-pol) in November 1995. With an electronically steerable beam, this enables data collection over a range of incidence angles and across a number of stripmap-imaging modes, which can be adjusted to suit the application while retaining the narrow swath width, fine-resolution capability by beam-steering (Mahmood et al., 1998). It also enables reduced-resolution coverage over a wider swath, to a maximum of ~300–500 km for modern ScanSAR systems. Data from the Radarsat-1 ScanSAR "Narrow" swath width of 300 km are at a resolution of 50 m, while those from the 500-km-wide ScanSAR "Wide" swath are at a 100-m resolution. This in turn enables shorter revisit intervals between data acquisitions. For example, while the nominal repeat period of Radarsat-1 is 24 days, repeat coverage can be obtained every 3 days of the western part of the Arctic Basin (within the Alaska Satellite Facility—ASF—reception range). This has opened up a number of important additional sea ice applications, including measurement of large-scale ice dynamics and deformation fields (see Section 5.9.56). Radarsat-1 was also launched to provide operational information on sea ice conditions (in the Arctic), and these data have become an important component of operational analyses—e.g., Ramsay et al. (1998, 2001)—see Section 5.9.17. Note that the spatial resolution, however, decreases with increasing swath width—i.e., to 100–200 m for the ScanSAR Wide mode (with a swath width of 450–510 km). When ordering data, note also that ScanSAR Wide A refers to data available only as a direct downlink to a dedicated ground station, whereas ScanSAR Wide B is tailored for storage on the onboard tape-recorder (see ⟨*http://www.rsi.ca/products/sensor/radarsat/cl_ra_sw.asp*⟩ for further details). General issues relating to SAR resolution and polar coverage were evaluated by Drinkwater (1995b).

Another exciting technological advance is the emergence of multi-polarization systems. Launched in March 2002, the C-band Advanced SAR (ASAR) onboard ESA's Envisat (Environmental satellite) mission is the first polar-orbiting SAR capable of acquiring data at different polarization combinations. This advanced capability is based upon an active phased array antenna, which allows independent control of the phase and amplitude of the transmitted radiators from different regions of the antenna surface (Zink et al., 2001). It also provides independent weighting of the received signal to each of these regions. This offers great flexibility in the generation and control of the radar beam, giving the ASAR instrument the capability to operate in a number of different modes at variable incidence angles between 15 and 45° to collect data using either conventional stripmap SAR or ScanSAR methods. In its unique Alternating Polarization (AP) mode, the ASAR provides one of three different channel combinations: (i) VV and HH; (ii) HH and HV; or (iii) VV and VH, the latter over a narrow (<100 km) swath only. This important sensor is based upon the heritage of the AMI SAR missions on ERS-1 and ERS-2, to extend the time series that began in 1991 but with these much-improved capabilities. It should be noted that the HH–VV phase for the Envisat AP mode is not meaningful due to the time lapse between measurements, and that the radiometric resolution of alternating-mode measurements is reduced compared with that of the high-resolution modes. While Envisat follows the 35-day repeat cycle of ERS-1 and -2, shorter repeat intervals are again possible due to the pointing capability of the antenna (Figure 5.24).

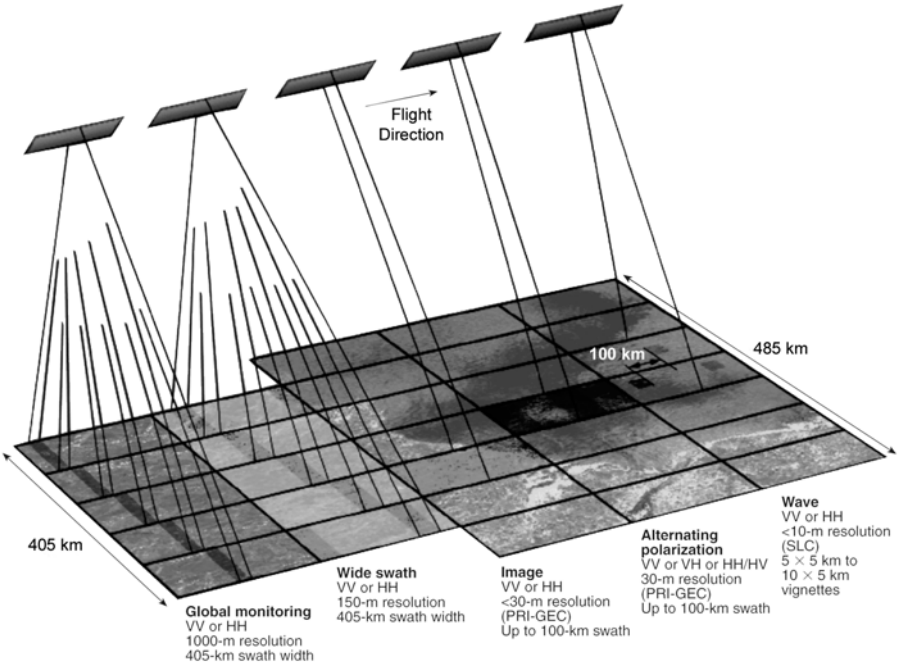

Figure 5.24. A schematic of the operating modes and observation geometry of the Envisat ASAR. PRI = precision image, GEC = geocoded image, and SLC = single-look complex image. The ASAR instrument can operate in 37 different and mutually exclusive, high-rate operating modes. These modes use two principal methods, operating as either a conventional stripmap SAR or as a ScanSAR. (a) *Stripmap* mode operates in either image mode or wave mode. In image mode, the ASAR operates as an imaging radar collecting data in one of seven predetermined but relatively narrow swaths (up to 100 km within a viewing area of about 485 km and designated IS1 to IS7) with a nominal high spatial resolution of 30 m. It provides continuous coverage over a single swath that can be pointed anywhere within the incidence angle range of 15–45°, with a choice of HH or VV polarization. In wave mode, imaging takes place of small areas of 5 km × 5 km (referred to as *vignettes*) at frequent intervals over alongtrack distances of 100 km for ocean surfaces. Wave mode uses the same swaths and polarizations as image mode. The intermittent operation provides a low data rate, such that the data can be stored onboard the satellite, rather than being downlinked immediately to a ground station. (b) The *ASAR ScanSAR* modes are alternating polarization, wide swath, and global monitoring. Alternating polarization mode provides a choice of HH or VV or cross-polarized imaging of the same scene, over narrow swaths of <100 km. Wide-swath mode offers continuous image coverage over a swathwidth of 405 km (or greater), divided into five sub-swaths ranging from 60 to 100 km in width. The spatial resolution is 150 m. Global monitoring mode provides continuous along-track sampling across a 405-km swath, with the ASAR operating at a reduced spatial resolution of 1,000 m (with a corresponding reduced data rate for onboard recording) (Sandven et al., 2003). For in-depth information on the various modes, see ⟨*http://envisat.esa.int/instruments/asar/descr/concept.html#asar%20stripmap%20modes*⟩.

Figure from Attema et al. (2000), courtesy of Evert Attema (ESA). Reproduced with permission © The Johns Hopkins University Applied Physics Laboratory.

Another important factor affecting the coverage capability of high data-rate SARs in remote polar regions is the presence or absence of an onboard solid-state recorder. Envisat has this facility, although it should be noted that data collection over polar regions is affected by the overall duty cycle of the satellite and the fact that simultaneous operation of different sensors onboard the same satellite cannot always be achieved. It also has a reduced-resolution Global Monitoring Mode or GMM (1-km resolution over a 420-km swath width), which has been operational since February 2004. This opens up the exciting prospect of directly comparing/fusing SAR data with medium-resolution visible to TIR data—e.g., from AVHRR and MODIS (MODerate resolution Imaging Spectrometer). ESA routinely acquires Antarctic- and Arctic-wide coverage of the ice pack and ice sheets, in a background ASAR mission planned to prioritize coverage of polar regions. An important potential by-product is the generation of regular, periodic mosaics or swath composites of the entire Antarctic sea ice zone and much of the outer part of the continental ice sheet for the first time. An example is shown in Figure 5.25. Given their relatively small data volume and good radiometry, GMM products are being made available to ESA-registered researchers via the Internet in near-real time—i.e., about 3 hours after acquisition. In general, near-real time refers to data that are provided within a maximum of 1 day from acquisition by the satellite, and are also referred to as fast-delivery products. The general Envisat data browse catalog can be accessed at ⟨*http://muis-env.esrin.esa.it/*⟩, while EnviView provides access to the data (Levrini and Brooker, 2001). The ASAR can also acquire imagery simultaneously with the MEdium Resolution Imaging Spectrometer (MERIS), thereby facilitating interpretation of the SAR data (see Section 5.8.2.4). The importance of synergy applies throughout this book, and cannot be stressed strongly enough. It is also a foremost consideration in the planning of modern satellite missions.

Adding icing to the cake, other satellite systems are about to be launched with full polarimetric capability, again for the first time in polar orbit.[9] With a launch in 2005 onboard the Japanese Aerospace eXploration Agency (JAXA, formerly NASDA) Advanced Land Observing Satellite (ALOS), the Phased Array L-band SAR (PALSAR) is capable of beam-steering, ScanSAR operation, and full polarimetry (Rosenqvist et al., 2003). The centre frequency is 1.270 GHz (wavelength 23.6 cm). The ScanSAR mode will offer coverage at single polarization (HH or VV) over a 250–350-km swath width (depending on the number of scans), again at the expense of spatial resolution—i.e., 100 m. Maximum latitudinal coverage is to approximately 81°, with an orbit repeat period of 46 days with a sub-cycle of 2 days. The nominal high-resolution operating mode will provide 10-m (two-look) resolution data in HH or VV/HH + HV or VV + VH modes, this time at the expense of coverage—i.e., over a swath of 70 km. Figure 5.26 provides information on the various scanning modes and observation geometry; detailed information on these modes is given in Table A.7 (Appendix). In full polarimetric mode, PALSAR can

[9] Note that a few fully polarimetric SAR scenes were collected from the outer margins of the Weddell Sea (Antarctica) by the NASA Space Shuttle during the Shuttle Imaging Radar-C (SIR-C) mission in 1994 (Eriksson et al., 1998).

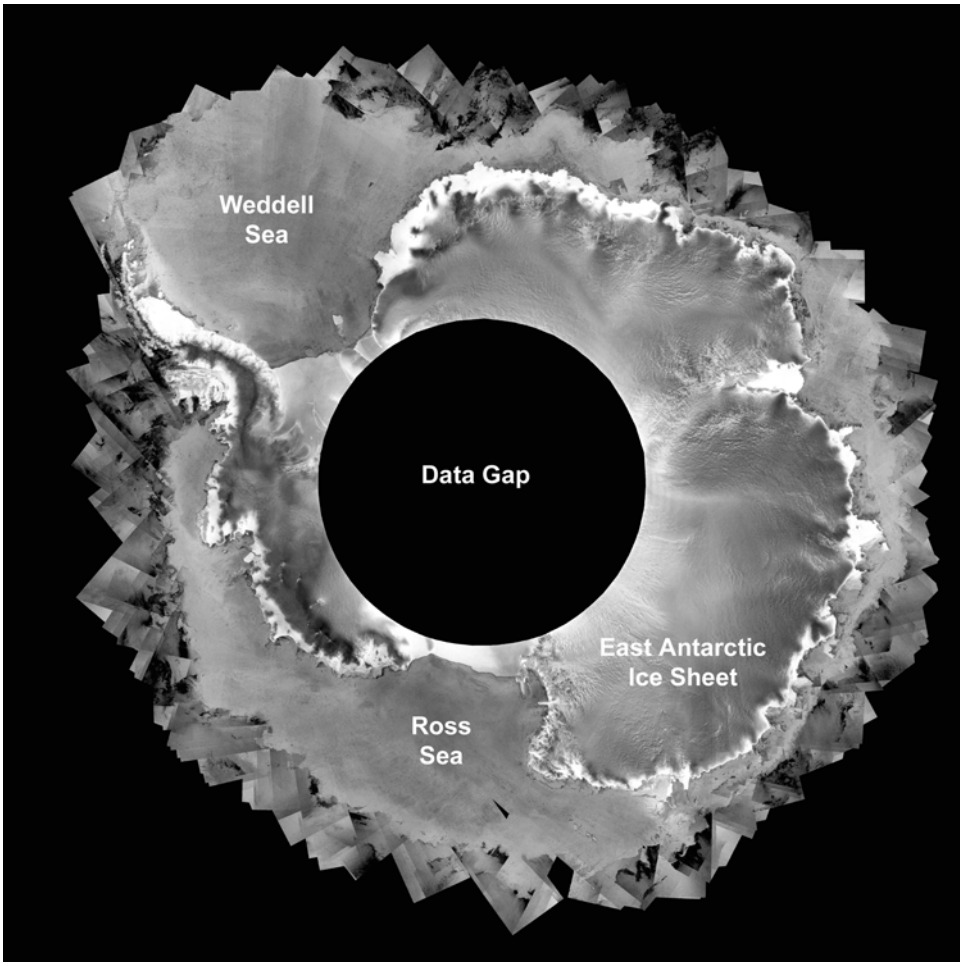

Figure 5.25. An image mosaic of Antarctica generated from Envisat ASAR data acquired by the Global Monitoring Mode (GMM) over the period April to May 2004. Such a mosaic takes about 200 GMM images to complete (Envisat acquires 14 new Antarctic images per day)—considerably less effort than is required to produce a similar product with high-resolution mode data. As such, the mosaic can be regularly updated.

Image courtesy of ESA, and copyright ESA 2004.

simultaneously collect backscatter amplitude data at HH, VV, HV, and VH polarizations, and also measures relative phase between channels. The scattering matrix can be formed from data for the four linear polarization combinations (HH, VV, HV, and VH), from which the corresponding backscattering coefficient for any polarization combination can be obtained (see Section 5.9.7.3). Dominant backscattering surfaces of the targets can then be determined by comparing the polarimetric data with theoretical polarization signatures (van Zyl et al., 1987). In

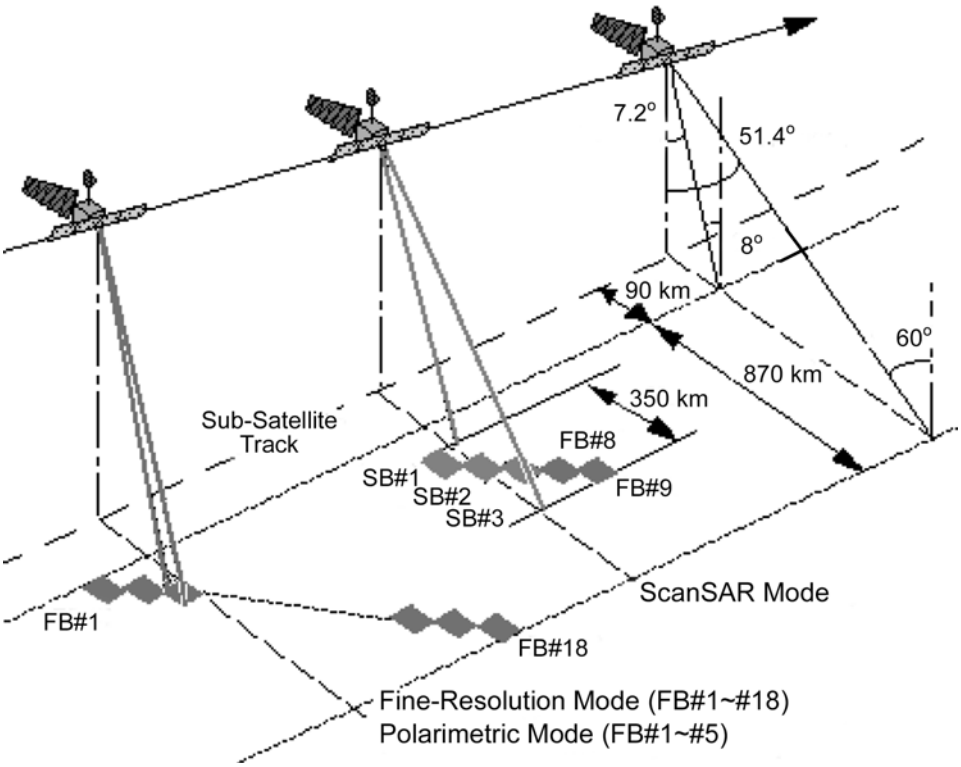

Figure 5.26. A schematic of the operating modes and observation geometry of the ALOS PALSAR. The PALSAR features four operational modes: *Fine*, *Direct Downlink*, and *ScanSAR* modes permit extended observation coverage of up to a 350-km swath width, and *Polarimetric* mode on an experimental basis. Polarization is changed in every pulse of the transmission signal, and dual-polarization signals are simultaneously received. The operation is limited to the lower incident angle in order to achieve higher performances. At the nominal off-nadir angle (21.5°), the swath width is 30 km with 30-m spatial resolution under the maximum data rate condition. The look angle is variable between 7° and 51° (8–60° incidence angle). Note that PALSAR and AVNIR-2 are able to operate simultaneously. SB = Scansar Mode.

Figure courtesy of JAXA, and obtained from ⟨*http://www.eorc.jaxa.jp/ALOS/about/palsar.htm*⟩.

principle, this provides the potential to significantly improve ice-type discrimination. As we will see in Section 5.9.7.3, the information content of polarimetric SAR data is not yet fully understood, but is the focus of increasing research and shows great promise. In practical terms, full polarimetric coverage will be limited by narrow swath coverage and the overall satellite duty cycle.

Other fully polarimetric SARs are to follow. The commercial follow-on to Radarsat-1—Radarsat-2 (launch 2006)—offers three polarimetric modes: (i) high-resolution (3 m) single-polarization (single-pol) channel (VV or HH), over a 10–20-km swath width; (ii) selective polarization (dual-pol) at HH + HV or

VH + VV; and (iii) a fully polarimetric mode (quad-pol) providing both amplitude and phase (Morena et al., 2004; Staples, 2003). By default, Radarsat-2 data products are one co-polarization channel (HH or VV) and the cross-polarization channel (HV). In practical terms, the commercial focus of the Radarsat-2 mission dictates the development of operational applications, and ultimately the extraction of information from the SAR data (Staples et al., 2004). While the Envisat ASAR AP modes offer limited coverage over narrow swath widths (<100 km) only, Radarsat-2 will acquire dual-polarisation ScanSAR data over a 500-km swath width (Scheuchl et al., 2004a). Quad-polarization coverage is limited to a 25-km swath width. Radiometric and geometric calibration will also be implemented to permit correlation of time series data for applications such as long-term change detection (Luscombe and Thompson, 2001). Other enhanced features of the new SARs include increased geometric accuracy.

Imaging modes of the Radarsat-2 SAR are shown in Figure 5.27 (with details given in Table A.6 in the Appendix). In addition to flying the same repeat cycle and ground track and supporting the SAR imaging modes/beams of Radarsat-1, Radarsat-2 has the additional flexibility of routinely being able to change its look direction from right to left (Radarsat-1 is mainly right-looking with the ability to switch on a limited number of occasions—see Chapter 3 of Volume 2 of this book). This will to some extent mitigate the tradeoff limitations of SAR sensors—i.e., high resolution at the expense of reduced spatial coverage, and increased spatial coverage at the expense of coarser resolution.

Plans are underway to continue the Radarsat program to at least 2012, with Radarsat-2 (⟨*http://www.radarsat2.info/rs2_satellite/overview.asp*⟩) and the future Radarsat-3 operating in a tandem mission which will focus on interferometric applications (Staples et al., 2004). Note that Radarsat-3, which is due for launch in 2007, is not a commercial satellite like its predecessor. The reader will also note that, while the mainline Canadian and European space programs continue with C-band SARs, the Japanese program persists with L-band systems. As we will see, both offer different advantages and disadvantages, and are indeed complementary. The frequency of the Radarsat-2 and -3 SARs is, at 5.405 GHz, marginally different from that of the Radarsat-1 SAR (5.3 GHz).

The TerraSAR program comprises two satellite polarimetric SAR systems flying in tandem for near-simultaneous and complementary observation of the target surface—namely, the German TerraSAR-X and European TerraSAR-L missions (operating at the X- and L-band, respectively). Planned for a 2006 launch, TerraSAR-X is a high-resolution X-band SAR satellite mission being developed within the scope of a private public partnership between the Deutsche Forschungsanstalt für Luft und Raumfahrt (DLR) and Astrium GmbH. It operates at 9.65 GHz ($\lambda = 3$ cm) and HH, VV, HV, and VH polarization. This will be the first polar-orbiting X-band system, being based on the heritage of two NASA Space Shuttle missions—namely, the Shuttle Radar Topography Mission or SRTM in 2000 (Werner, 2000) and the Spaceborne Imaging Radar C-/X-Band SAR mission (SIR-C/X-SAR) in 1994 (Evans and Plaut, 1996). It is both left- and right-looking and has multi-mode capabilities, operating in "spotlight" mode at 1–2-m resolution

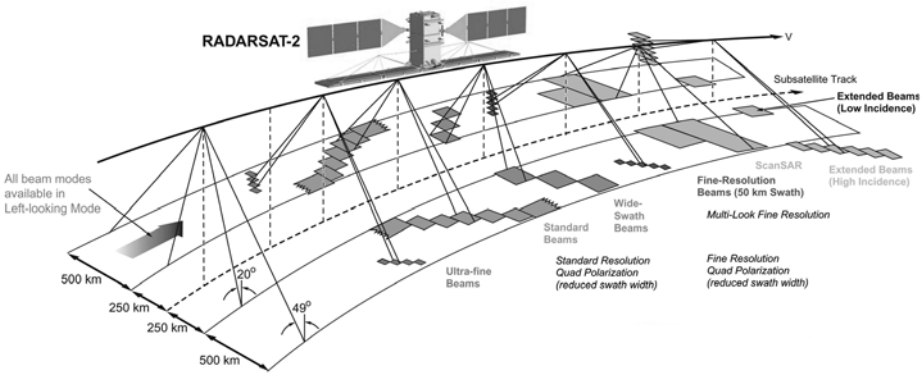

Figure 5.27. Imaging modes of the Radarsat-2 SAR. *Fine Beam* modes are intended for applications which require higher spatial resolution and lower swath coverage, and cover the incidence angle range from 30° to 50°. This imaging mode will be available in co-polarization, cross-polarization, dual-polarization, and quad-polarization. The *Triple Fine Resolution Beam* mode is the three-look version of Fine Resolution mode, therefore providing the same spatial resolution with improved radiometric resolution. *Ultra-Fine Beam* modes, with a 3-m resolution, are intended for applications which require very high spatial resolution. Data from both fine-resolution modes will be available in selective single-polarization (HH or VV). *Standard Beams* allow imaging over a wide range of incidence angles acquired in seven different modes, referred to as S1 to S7. The incidence angles range from 20° at the inner edge of S1, to 49° at the outer edge of S7. The Standard Beam mode generates image quality characteristics which provide a good compromise between spatial resolution, radiometric resolution, and image coverage. This imaging mode will be available in co-polarization, cross-polarization, dual-polarization, and quad-polarization. *Extended Beam* modes are divided into Low Incidence and High Incidence, both available in co-polarization, cross-polarization, and dual-polarization. An *Extended Low Incidence Beam* covers the incidence angle range from 10° to 23°, over a 170-km swath width. *High Incidence Beam* mode covers the incidence angle range of 49° to 60°. For both, the spatial resolution is the same as Standard Beams, with data being available in co-polarization, cross-polarization, and dual-polarization. *Wide-Swath Beams* enable coverage of a larger region than the Standard Beam at the expense of a slightly coarser spatial resolution. Three Wide-Swath Beams cover a range on incidence angles from 20° to 45°, with data available in co-polarization, cross-polarization, and dual-polarization. Finally, *ScanSAR* imagery is generated with a combination of single beams covering adjoining swaths. This provides the largest swath coverage available, but at the expense of spatial resolution. ScanSAR imaging mode data will be available in co-polarization, cross-polarization, and dual-polarization.

across a 5–10-km swath width, in "stripmap" mode (3-m resolution, 30-km swath), and "ScanSAR" mode (16-m resolution, 100-km swath width). For the innovative spotlight mode, the very high resolution is achieved in the range by increasing the bandwidth (to 300 MHz), and in azimuth by electronic azimuth beam-steering (Moreira, 2003). This is achieved at the expense of azimuth scene length (Bamler et al., 2003). The orbital inclination is 97.44°, with a nominal repeat period of 11

days, reducing to up to 4.5 days with antenna steering. TerraSAR-X also offers single-, dual-, and full-polarization modes. For further information on this commercial system, please see Lehner et al. (2004) and Moreira (2003). The ESA TerraSAR-L (launch ~2007) will operate at 1.257 GHz in three modes: (i) stripmap in single-, dual-. and quad-polarization; (ii) ScanSAR in single- and dual-polarization; and (iii) a wave mode (sampled stripmap, vignettes of 20×20 km acquired each 100 km). Spatial resolution varies from 5×9 km (azimuth and range) to 50×50 km, over a 20–200-km swath width, with a 14-day repeat period (Zink, 2003). The main performance requirements are summarized in Tables A.8 and A.9 (Appendix). The two spacecraft will operate in the same orbit but spaced approximately 12 minutes apart, to provide near-simultaneous observations. Key features are tight orbit control and high-precision orbit determination.

In addition, a four-satellite constellation of polarimetric multimode X-band SARs (right- and left-looking) is planned within the COSMO-SkyMed (Constellation of Small Satellites for Mediterranean basin Observation) program (*www.alespazio.it/program/tlr/cosmo/cosmo.htm*), developed by the Italian Space Agency and France's space agency—CNES (Rum, 2003). The planned orbital inclination is 97.9°, with a nominal repeat period of 14 days. With the first launch planned in 2005, COSMO-SkyMed will be coordinated with optical satellites and will feature revisit times of a few hours and operate at meter and sub-meter resolutions (i.e., in spotlight mode). Further planned polar-orbiting SARs are the Argentinian SAOCOM, an L-band (1.275 GHz) system with a 2006 launch (Giraldez, 2003) and combined L/C or L/X band systems onboard the NPOESS Ocean satellite (planned launch 2012) (Pichel et al., 2003). SAOCOM will operate in stripmap and ScanSAR modes, at resolutions of 10 and 100 m and swath widths of >65 km and >320 km, respectively, and in single- and dual-polarization modes. It also offers a quad-polarization mode, with a stripmap swath width of 30 km and a resolution of >30 km. The orbit repeat cycle will be 16 days. Further information is available at: ⟨*http://www.conae.gov.ar*⟩.

These advances lead to greatly enhanced potential in terms of ice classification, but add a new dimension of complexity to data processing and interpretation. The user now has a choice when requisitioning data, and is confronted with a need to understand something about the optimal sensor–parameter combination—i.e., polarization, frequency, and incidence angle, for a given sea ice application. This issue is discussed in Section 5.9.7, taking in information based on the analysis of data from laboratory experiments, aircraft campaigns, satellites, and theory (models).

Of immense importance are parallel advances in ground segment technology, enabling faster and more complex image processing. The development of the Radarsat Geophysical Processor System (RGPS), for example, has enabled the routine processing of Radarsat-1 Arctic image data into fields of geophysical variables (Kwok, 1998). This provides high-resolution repeat coverage of the entire Arctic Ocean every 3 days (the "Arctic Snapshot") using calibrated and geo-located ScanSAR Wide B backscatter images with a 500-km swath width and 100-m resolution. These data have been acquired and archived at the Alaska Satellite Facility (ASF) since November 1996. A data user's handbook for the RGPS is given

by Kwok and Cunningham (2000), with Kwok et al. (2000) providing RGPS product specifications. The following datasets are produced on a 10-km grid at weekly intervals: sea ice motion, sea ice age, sea ice thickness of young ice, sea ice deformation, open water fraction, and (twice/year) dates of melt onset and freeze-up. Similar coverage of the Southern Ocean by an Antarctic RGPS-like system does not exist, and is a high priority. This remains a difficult proposition, due to logistical reasons and the fact that Antarctic sea ice represents a relatively homogeneous radar target and is therefore more difficult to track in sequential images (Drinkwater, 1998a, b).

A major concern is the uncertainty in the continuation of the important RGPS time series after the demise of Radarsat-1, which is already operating well beyond its design lifetime. The characteristics of the Envisat ASAR wide-swath image mode, including resolution and frequency, provide excellent compatibility with RGPS input image requirements (Holt and Kwok, 2003). Negotiations are underway to continue RGPS-type mapping of the Arctic using Envisat ASAR and possibly other satellite SAR data (including ALOS PALSAR). This is crucial given the importance of the lengthening time series as a means of evaluating the observed environmental changes (Kwok and Holt, 1999). Operating in wide ($\sim$400 km) swath mode, the ASAR enables approximately complete coverage of the Arctic Basin once every 3 days—i.e., 12 mappings per 35-day orbit repeat cycle (Kwok and Holt, 1999). Several important calibration parameters will be improvements over Radarsat-1 data quality, which should translate to improved RGPS output (Holt and Kwok, 2003). These include a radiometric error of 0.2 dB, and an absolute location accuracy to 2 pixels—i.e., $\sim$150 m. Moreover, the availability of Envisat stripmap data will reduce data manipulation requirements within the RGPS. With dedicated and long-term mappings, these Arctic data would continue monitoring the climatic changes in Arctic sea ice cover. As noted above, the ASAR also offers a lower resolution Global Monitoring Mode—i.e., enhanced coverage at the expense of spatial resolution. While the Radarsat-2, ALOS PALSAR, and TerraSAR missions should be invaluable for sea ice investigations in general, the feasibility of these data for the continuous mapping required for ice motion and ice age via the RGPS is currently unclear (Holt and Kwok, 2003). The absence of a similar system to RGPS in Antarctica is a major defficiency, and one that should be rectified as soon as possible if the full power of SAR as a key sea ice tool is to be realized there. Currently, and indeed since the launch of ERS-1 in 1991, SAR coverage of the Antarctic sea ice zone tends to be "spotty" and irregular, and typically linked to individual research programs.

There are technological tradeoffs affecting the application of SAR in general. One relates to the relatively narrow swath width, which limits temporal coverage (resolution) and results in a data gap around the North Pole for non-ScanSAR sensors/modes. As a result, conventional satellite SARs are unsuitable for global operational applications. Moreover, the data volume of SAR imagery is immense. This is a diminishing issue given recent developments in data storage technology and computing power, but remains an issue nonetheless. Thankfully, facilities such as NASA EOS SAR Distributed Active Archive Center (DAAC) at the Alaska Satellite

(formerly SAR) Facility provide the user with streamlined access to data (Carsey et al., 1998; Kaupp and Holt, 1998). This is a superb resource, providing the user not only with online access to the data catalog but also a wide range of ancillary information, including data analysis tools (⟨*http://www.asf.alaska.edu*⟩). A review of NASA's DAAC facilities is provided by the National Research Council (1998). ESA's Envisat (⟨*http://envisat.esa.int*⟩) and JAXA's ALOS (⟨*http://www.eorc.nasda.go.jp/ALOS/index.html*⟩) sites are similarly superb facilities. Another major issue relates to geographical coverage. As ERS-1/-2 and JERS-1 were not equipped with onboard data recorders for SAR, data access is limited to regions of direct data broadcast to dedicated ground receiving stations—i.e., within the station data masks. No Seasat SAR data were acquired over Antarctica due to a lack of a dedicated SAR receiving station there in 1978. Radarsat-1 does have onboard recording but with limited storage capacity for ScanSAR wide-swath "Narrow" mode data for subsequent download. Details of operational satellite-specific SAR receiving stations are given in Drinkwater (1998a) for Antarctica and the ASF website (see above) for the Arctic. Note that modern spacecraft such as ALOS and Envisat have improved onboard data-recording capabilities, although the operational duty cycle of ALOS (concentrating largely on earthquake detection and vulcanism in Japan) may preclude regular large-scale data collection in polar regions.

5.8.2.2 Radar scatterometry

Radar scatterometers also transmit radar pulses and receive the energy backscattered from the surface. Unlike SARs, the return signal is measured by the scatterometer at several different angles. Although their primary purpose is to measure wind velocity over open ocean (Fetterer et al., 1998; Thomas and Minnett, 1986), they also provide useful information over ice-covered surfaces, where the return energy depends on both the roughness and dielectric properties of the surface. While the scatterometer is essentially a non-imaging sensor, recent advances in image generation enable images to be generated from orbital swath data (Drinkwater et al., 1993). Unlike SARs, modern scatterometers yield low bit-rate data that can be tape-recorded for subsequent downlink—i.e., they do not require dedicated ground receiving stations within areas of interest. Their frequent, wide-swath coverage allows investigation of sea ice thermodynamic state (Howell et al., 2005) distribution, properties, processes, and dynamics at regional to hemispheric scales on a near-daily basis (Drinkwater and Lin, 2000; Long et al., 2001; Wismann, 1998). This compares with the 35-day repeat cycle of the ERS SARs, for example. Offering continuous day–night operation, and a routine all-weather imaging capability over a wide swath and independent of sunlight, radar scatterometer backscatter images are being increasingly used as an effective means of monitoring the large-scale and seasonal characteristics of global sea ice cover (Long and Drinkwater, 1999). They provide data which are stable and accurately calibrated—e.g., to ± 0.2 dB for the ERS AMI in wind mode (ERS wind SCATterometer system—ESCAT). Importantly, these data are complementary to those from passive-microwave sources in their coverage and resolution, as they observe independent properties of the same ice structures at a similar resolution.

They also complement more detailed SAR measurements, at a fraction of the data volume while offering daily global coverage. An excellent review of satellite scatterometry in general is given by Moore and Jones (2004).

The brief flight of the Ku-band (14.6 GHz) SeaSat-A Scatterometer (SASS) in 1978 showed the potential of scatterometry as an important polar ocean research tool, albeit at a poor resolution of 50 km (Drinkwater and Carsey, 1991; Swift, 1999). It wasn't until the launch of the AMI ESCAT on ERS-1 in 1991, however, that operational measurement from space began. Operating at C-band (5.3 GHz) with VV-polarization, ESCAT illuminated the surface across a 500-km swath, with an alongtrack and crosstrack spatial resolution of ~50 km, and a processed pixel spacing of 25 km (Attema and Lecomte, 1998). For each pixel, the scatterometer measured the backscatter coefficient σ^0 of a target from three directions—i.e., 45° (fore-beam), 90° (mid-beam) and 135° (aft-beam) with respect to satellite flight direction. The fore- and aft-beams obtained data at near-identical incidence angles ranging from 25 to 59°, whereas the mid-beam obtains data at incidence angles of 18 to 47°. As a result, three independent values of σ^0 were obtained from three look directions at two different incidence angles. The large swath width of scatterometer data and orbital convergence at high latitudes leads to imaging of sea ice at given points almost daily, but with differing viewing geometries.

Subsequent missions have included an identical ESCAT system onboard ERS-2 (launch 1995), the NASA SCATterometer (NSCAT) onboard ADEOS-I (1996–1997: Naderi et al., 1991; Tsai et al., 1999), SeaWinds on QuikSCAT (1999–present: JPL, 2001; Spencer et al., 2000), and SeaWinds on ADEOS-II/Midori-2 (2002–2003) (⟨*http://www.nasda.go.jp/projects/sat/adeos2/index_e.html*⟩). SeaWinds is a 13.4-GHz (Ku-band) pencil beam scatterometer, with two beams that sweep across the surface in a circular fashion. The outer beam operates at VV-polarization, at an incidence angle of 55° and over an ~1,800-km swath, whereas the inner beam is HH-polarization at an angle of 47° over a swath of ~1,400 km (Leidner et al., 2000). Importantly, NSCAT and QuikSCAT offer wider coverage than ESCAT—i.e., 1,800 km for QuikSCAT, and a dual-polarization capability. The characteristics of four spaceborne scatterometers are compared in Figure 5.28. Scatterometer coverage is planned well into the future, with the launch of the Advanced Scatterometer (ASCAT) on ESA's MetOp-1 in 2005 (⟨*http://earth.esa.int/METOP.html*⟩, Figa-Saldaña et al., 2002; Quilfen, 1997). The ASCAT is a C-band real-aperture radar (5.255 GHz, VV-pol) based on the design of the ERS-1 and -2 scatterometers. It generates an operational product with a spatial resolution of 50 km on a nodal grid of 25 km. Common features include a fan beam geometry with antennae oriented at 45°, 90°, and 135° with respect to the satellite ground track. Further ASCAT launches are planned onboard MetOp-2 in 2007 and MetOp-3 in 2012.

Although the resolution of scatterometers is nominally poor (25–50 km), their effectiveness in polar research has been greatly enhanced by the development of techniques to improve the resolution of images created from σ^0 measurements—e.g., the Scatterometer Image Reconstruction with Filtering (SIRF) algorithm (Drinkwater et al., 1993; Early and Long, 1998, 2001; Long and Early, 1993;

SENSOR	SASS	ESCAT	NSCAT	SeaWinds
FREQUENCY	14.6 GHz	5.3 GHz	13.995 GHz	13.6 GHz
AZIMUTHS	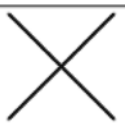			
POLARIZATION	V-H, V-H	V Only	V, V-H, V	V-Outer/H-Inner
BEAM RESOL.	Fixed Doppler	Range Gate	Variable Doppler	Pencil-Beam
SCI. MODES	Many	SAR, Wind	Wind Only	Wind/Hi-Res.
RESOLUTION	50/100 km	25/50 km	25/50 km	25 km/6 x 25 km
SWATH	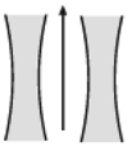	 500 km	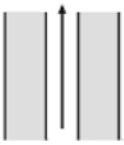 600 km 600 km	 1400, 1800 km
INCIDENCE ANG.	0° - 70°	18° - 59°	17° - 60°	48° & 54°
DAILY COVERAGE	Variable	< 41%	78%	92%
DATES	6/78 - 10/78	92-96, 96-	8/96 - 6/97	5/99 & 11/01

Figure 5.28. Characteristics of four spaceborne radar scatterometers flown onboard Seasat (SASS), ERS-1 and -2 (ESCAT), ADEOS-I (NSCAT), and QuikSCAT (SeaWinds or QSCAT).

Long, 2003; Long et al., 1993). The resulting enhanced resolutions are ~8–10 km for SASS and NSCAT, 25 km for ESCAT, and either 8–10 km or 5–6 km for SeaWinds (Long et al., 2001)—significantly better than the nominal resolutions shown in Figure 5.28. For a discussion on the limitations of the enhancement procedure for ERS data, see Walker (1997). Importantly, these sensors have provided global normalized backscatter (σ^0) data in a routine and almost uninterrupted fashion since 1991. The application of this unique time series to sea ice research has gained impetus in recent times (Drinkwater and Lin, 2000; Drinkwater and Liu, 1997, 2000; Long and Drinkwater, 1999; Long et al., 2001), and shows great potential for further development. An important factor is again their ready availability. Enhanced resolution data are available from the NASA Scatterometer Climate record Pathfinder (SCP) at Brigham Young University (⟨*http://www.scp.byu.edu/*⟩). The SCP datasets are based on a time series of images created using the SIRF algorithm, and combining multiple orbit passes to ensure the highest possible spatial resolution as well as full coverage. Two different datasets are produced from SASS, NSCAT, and ERS backscatter data for use in geophysical studies:

- Images of the backscatter coefficient in each pixel normalized at the 40° incidence angle (σ^0_{40}, generally termed dataset *A*), to mitigate variations in measured backscatter with radar incidence angle. The value of σ^0_{40} is intimately related to thermodynamically regulated snow and ice characteristics, and is extremely sensitive to differences in surface wetness or salinity and changes in the ice surface composition.
- The slope of σ^0 versus incidence angle in dB/° is known as dataset *B*. These values indicate the linear rate of decay of backscattering across the full-swath incidence angle range—e.g., of 20 to 60° for ESCAT.

For SeaWinds, images of σ^0 at the constant sensor incidence angle are produced for each beam—i.e., ~54.24° (VV-pol) or ~46.44° (HH-pol). In general, the dynamic range (the maximum signal-to-noise ratio) is higher at the lower incidence angle (Ezraty and Cavanié, 1999a, b; Voss et al., 2003). In addition, ancillary products are generated for all sensor data, including maps of sea ice extent and motion. Further details are available on the SCP website, and in Long et al. (2001). Specific characteristics of ESCAT images are described in further detail by Drinkwater (1998a, b), while Long and Drinkwater (1999) illustrate applications of SIRF scatterometer images to the study of polar ice. The dependence of sea ice backscatter on incidence angle for scatterometers is discussed by Frey et al. (2003).

Similar processing conventions are also followed by other research groups and processing/archiving institutions. The Centre ERS d'Archivage et de Traitement (CERSAT) French Processing and Archiving Facility (F-PAF), for example, offers weekly sea ice products of the backscatter incidence angle derivative at 28° of ESCAT (⟨*http://www.ifremer.fr/cersat/*⟩) from 1991 to 1996. In addition, CERSAT archives weekly sea ice products (also 1991–1996). A user manual by Gohin and Maroni (1998) is available online with documentation and tools. Ezraty and Poillé (2001) provide information on QuikSCAT daily products from CERSAT. Sheng et al. (2002) also provide 1-day, 3-day, and 7-day products of ERS backscatter in the Arctic for the period 1991–2000. Full resolution products and Web-based animations are available for scientific use from ⟨*http://merced.gis.ucla.edu/scatterometer/index.htm*⟩. Near real-time QuikSCAT data are also available for both polar regions from NOAA at ⟨*http://manati.orbit.nesdis.noaa.gov/cgi-bin/qscat_ice.pl*⟩. As such, scatterometer data are more readily available than SAR data, and are well-suited to temporal studies. Of concern is the fact that QuikSCAT is already operating beyond its designed lifetime, and a gap could in future exist in scatterometer measurements should this satellite fail (as a replacement could take several years to launch).

5.8.2.3 Radar altimetry

Although the primary polar application of radar altimetry is the measurement of ice sheet elevation (see Chapter 3 of Volume 2 of this book), useful data are also collected over the sea ice zone (Fetterer et al., 1992), with measurements dating back to Seasat (Ulander, 1987) and Geosat (Hawkins and Lybanon, 1989). Satellite radar altimeters transmit short pulses of microwave energy towards the

surface at nadir, then measure the time delay before the signal is reflected back from the surface and received at the satellite. Assuming that the satellite position is precisely known, this provides an accurate measure of the range or distance between satellite and surface, and thus a measure of surface elevation (averaged over the *pulse-limited footprint* on the ground, which for current conventional radar altimeters is >1.2 km). For the ERS-1 radar altimeter with a pulse repetition frequency of 1 kHz, packets of 50 consecutive pulses were averaged to reduce the waveform noise. This resulted in a recording rate of 20 Hz, and an alongtrack sampling interval of ~330 m. See Chapter 3 of Volume 2 for more detailed discussion of the operational characteristics of altimetry, which plays a major role in the measurement of sea surface height in the ice-free ocean and large-scale ocean circulation (e.g., Chelton et al., 2001; Fu and Cazenave, 2001). Chapter 3 of Volume 2 also contains more in-depth information on the basic principles of radar altimeter measurements, including the concepts of pulse-limited footprints, altimeter waveforms, and tracking, etc.

Radar altimeters operating over sea ice measure the time taken for a transmitted radar pulse to return to the satellite from the snow/ice interface, and are uninterrupted by cloud and darkness. In principle, this provides a measure of the ice freeboard—i.e., the elevation of the snow/ice interface above the sea surface, averaged over the pulse-limited footprint on the ground. The strength and characteristics of the return signal also contain information on the nature of the surface from which it was reflected. The contrasting signatures of open ocean and sea ice provide a measure of the transition from sea ice to open ocean, or vice versa—i.e., the ice edge and, *ipso facto*, ice extent. Examples of return waveforms from ice sheet, sea ice, and open ocean surfaces are shown in Figure 5.29. The return pulse shape of the reflection from sea ice is typically specular (rising to sharp peaks), whereas that from ice-free ocean or ice sheets tends to be diffuse (rising to a plateau value) (Drinkwater, 1991; Laxon, 1989). However, the variability of the range measurement is of the same order as that from the ocean and this surface can therefore generally be tracked using the altimeter ocean-tracking mode. However, the sampling capability of satellite altimeters involves a tradeoff between temporal resolution and spatial resolution. Due to the long repeat cycle of altimeter missions (typically tens of days, to ensure a close spacing of ground tracks) and the narrow footprint, global coverage of sea ice is far from instantaneous. As such, altimeters are very much a secondary source of ice extent information compared with passive-microwave radiometers.

Launched onboard ESA's Envisat in March 2002 and providing data since early 2003, the advanced dual-frequency (13.575 GHz at Ku-band and 3.2 GHz at S-band) Radar Altimeter-2 (RA-2) guarantees the continuity of ERS-1 and -2 observations begun in 1991 (Louet, 2001). The secondary, 3.2-GHz channel is operated to compensate the range error on altitude measurements caused by the variable propagation of radar signals through the ionosphere. See Benveniste (2002) for instrument characteristics. The RA-2 incorporates a MicroWave Radiometer (MWR) for atmospheric correction, and improved tracking of orbital parameters and retracking of the radar pulse over sea ice, and switches autonomously between three different range window widths to adapt to different surfaces and

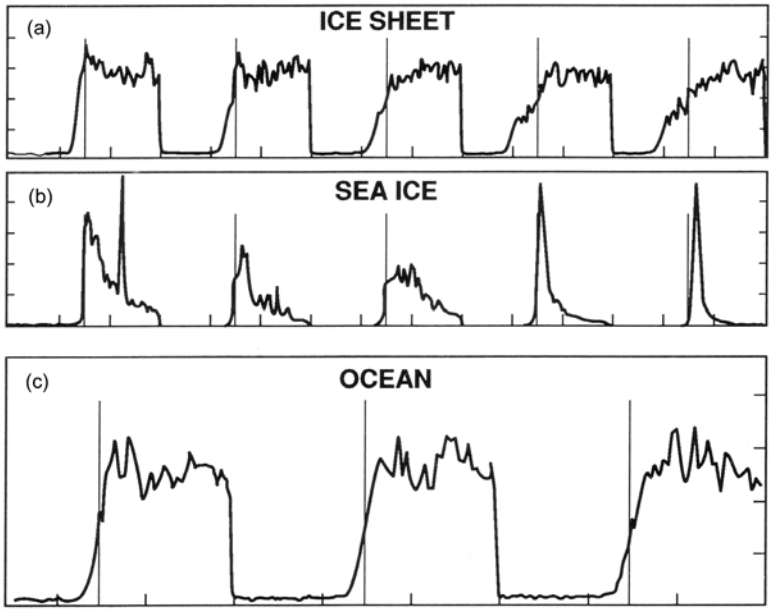

Figure 5.29. Representative radar altimeter waveforms from (a) an ice sheet surface, (b) sea ice, and (c) open ocean. The vertical lines mark the location on the waveform automatically "tracked" by the altimeter, and to which ranges (i.e., the distance between the sensor and surface) are measured. While automated tracking is effective over open ocean, measured ranges automatically tracked over sea ice and ice sheets are unreliable, and each waveform must be "retracked".

From Thomas (1995), after Zwally et al. (1987). Reproduced with permission © The Johns Hopkins University Applied Physics Laboratory.

avoid losing track (Benveniste, 2002; Benveniste et al., 2002). It also has the new capability of providing limited bursts of individual—i.e., non-averaged—Ku-band echoes at 1,800 Hz, for theoretical research on backscattering and precise monitoring of bright radar targets. These characteristics result in improved geophysical data products.

All Envisat RA-2 data are processed simultaneously by four different retrackers—namely, Ocean, Ice1, Ice2 and Sea-Ice—to enable users to choose the most suitable for their particular application (Benveniste, 2002). In other words, waveform data are fully processed in the ground processor to extract the geophysical parameters (note that previous systems have tended to carry out tracking onboard the satellite). Ice1 retracking is the range estimation technique for ice sheet echoes used on ERS data (Bamber, 1994), while Ice2 retracking is aimed at ocean-like echoes returned from continental ice sheet interiors. The latter is based on an idealized Brown-type model (Brown, 1977; Legrésy and Rémy, 1997). Improved retracking for the Envisat RA-2 sea ice product is optimized for specular echoes from ice-covered regions and associated "peaky" waveforms (Laxon, 1994a), with

parameters being supplied to distinguish returns from ice and water surfaces. The combination of these measurements enables the estimate of ice freeboard (for thick ice), from which sea ice thickness can theoretically be determined by assuming hydrostatic equilibrium and parameterizing the effects of seawater and ice density, and snow cover thickness and density (see Section 5.9.6.1). Users wishing to develop their own retracking algorithms can access the echo waveforms delivered alongside Geophysical Data Records, including brightness temperatures from the MWR. Conventional radar altimetry measurements will continue with the launch onboard NPOESS-1 (in 2009) of a sensor similar to the current Jason-1 (launched in December 2001). The latter carries a CNES Poseidon-2-type, dual C-band and Ku-band altimeter in an orbit covering the latitudinal band between 66°N and 66°S.

Of major interest is the innovative Ku-band (2.2-cm wavelength) Synthetic aperture Interferometric Radar ALtimeter (SIRAL), to be launched onboard ESA's CryoSat in 2005 (⟨*www.esa.int/livingplanet/cryosat*⟩; Drinkwater et al., in press). This is the first spaceborne altimeter specifically designed to measure sea ice thickness, driven by the need to accurately measure apparent changes in the thickness of Arctic multiyear ice (see Section 5.5). The SIRAL sensor combines three measurement modes, namely:

- low-resolution, for conventional altimetric measurements limited to the relatively flat relief of continental ice sheets;
- SAR mode, to provide high-resolution measurements of floating sea ice; and
- interferometric radar mode, to study sharper relief areas, such as the very active transition areas where ice fields meet the continental shelf.

The SAR mode operates as a nadir-looking unfocused SAR, providing a resolution cell of 0.25×1.0 km. This is a marked improvement over other spaceborne radar altimeters. During its "science orbit", CryoSat will operate in a 369-day repeat cycle and a 30-day pseudo-subcycle (ESA, 2001). Its high-inclination orbit of 92° will ensure coverage to 88° latitude, offering significantly greater coverage of the Arctic Ocean perennial ice zone compared with the pulse-limited radar altimeters onboard ERS-1 and -2 and Envisat, which are limited in their coverage to a maximum latitude of 81.5°. As with all satellites measurements, CryoSat data can only be scientifically useful if they are adequately calibrated and validated, and an extensive program is underway to verify the measurement uncertainty, or $\bar{\sigma}_m$, using contemporary, independent, and collocated *in situ* measurements (ESA and UCL, 2001; Forsberg et al., 2004; Haas, 2002; Wingham, 2004).

Launched in January 2003, the Geoscience Laser Altimeter System (GLAS) on NASA's ICESat is the first spaceborne Earth-observing laser altimeter. Although it is an optical sensor, GLAS measurements are similar to those of radar altimeters; it will be introduced here to aid comparison. While ICESat's primary mission is to measure changes in ice sheet elevation (see Chapter 3 of Volume 2 of this book), other scientific objectives include the global measurement of dense cloud heights and the vertical distribution of clouds and aerosols (see Chapter 4), and the measurement of sea ice thickness, surface roughness, and surface reflectivity. Detailed information is given by Zwally et al. (2002b). In elevation mode, laser altimeters work on the

same principle as radar altimeters—i.e., they measure the echo of a pulse transmitted towards the surface, but operate at much shorter visible to near-IR wavelengths, in this case at 1.064 μm (for the altimetry) and 0.532 μm (for cloud and aerosol vertical distributions). With precise knowledge of the orbital track and altitude of the satellite, in this case using an onboard GPS receiver and startrackers, the time delay between laser pulse transmission and echo reception can be used as a precise measure of the distance between the satellite and surface. This equates to surface elevation relative to a reference, which for sea-ice-covered regions is the open ocean surface exposed in leads. Here, surface elevation is a measure of the ice plus snow freeboard layer. The GLAS instrument transmits 40 laser pulses per second from an altitude of ~600km, illuminating an ellipsoidal footprint of ~60 m on the surface with an alongtrack spacing of 172 m. As such, the echo is carried out over a substantially smaller footprint than it is with ERS and Envisat radar altimeters—i.e., ~60 m versus ~1.2 km—leading to much-improved horizontal resolution. While the expected range precision of single-footprint measurements was 10 cm, the actual range precision has been shown to be better than 2–3 cm (Zwally, 2004a). The primary mission uses a 183-day repeat track, with coverage to a maximum latitude of 86°. This again entails significantly greater coverage compared with the radar altimeters onboard ERS-1/-2 and Envisat, which are limited to coverage equatorward of 81.5° latitude, and comparable with that of CryoSat (to latitude 88°). Unfortunately, problems were encountered with one of the laser transmitters not long after launch. However, the second of ICESat's lasers was subsequently activated, and data are acquired at approximately 33-day periods at 3- to 6-month intervals (Shuman, 2004; Zwally, 2004a, b). A major limitation compared with the radar missions is its inability to penetrate cloud cover. Data from this mission, including sea ice products, and documentation are available from the U.S. National Snow and Ice Data Center (NSIDC) DAAC EOS Data Gateway (⟨*http://nsidc.org/~imswww/pub/imswelcome/index.html*⟩), and further information from ⟨*http://icesat.gsfc.nasa.gov/index.html*⟩.

5.8.2.4 Visible to thermal infrared sensors

Sea ice detection at these wavelengths is based upon the large contrast between the albedos and temperature of sea ice and open water in the visible to near-IR and TIR, respectively. Temperature itself is an important geophysical parameter (see Section 5.9.11). Moreover, the measurement of intermediate albedos can yield additional information about the type of ice present, and whether or not it has a snow cover. Regarding the latter, near-IR radiation is sensitive to changes in snow grain size (see Section 5.7.2). Depending upon resolution and coverage, the main applications are the measurement of surface albedo (visible to near-IR channels), ice/snow skin surface temperature (TIR data), pack ice and fast ice extent, ice motion, iceberg detection, floe size distribution (for very high resolution data), ice-type discrimination, and the inference of ice thickness. Secondary applications are the estimation of ice concentration, seasonal melt detection, ice edge characterization, and the determination of snowgrain size and impurity content. Collectively, these sensors also play an important role in the validation and interpretation of poorer resolution

sensors, and in process studies. The wide-swath data are extensively used by operational agencies to produce ice analyses, along with passive-microwave and radar data (see Section 5.9.17). It should be noted that a major determinant of the quality of measurements obtained with optical sensors is absolute radiometric calibration. A key factor here is that instrument sensitivity generally changes and degrades with time. Although newer satellite sensors are equipped with onboard calibration devices, independent calibration based on natural targets is also required to validate the results. See Hagolle et al. (2004) for an assessment of the calibration characteristics of various modern satellite optical sensors.

5.8.2.4.1 Moderate-resolution visible to thermal infrared

Amongst moderate-resolution optical instruments, the NOAA Advanced Very High Resolution Radiometer (AVHRR) is another veritable workhorse in the polar remote-sensing stable, with coverage by at least one operational meteorological satellite from 1978 onwards and the data being freely available to the scientific community. Three series of AVHRR sensors have been launched as part of the NOAA POES (Polar-orbiting Operational Environmental Satellite) program. The first (AVHRR/1) was a four-channel radiometer which was initially carried on Television and Infrared Observation Satellite (TIROS-N) (launched in October 1978). This was subsequently improved to a five-channel instrument (AVHRR/2) that was initially carried on NOAA-7 (launched in June 1981). The latest version is AVHRR/3. This was first carried on NOAA-15 (launched in May 1998), and operates with six channels centered on 0.58–0.68, 0.725–1.00, 1.58–1.64, 3.55–3.93, 10.30–11.30, and 11.50–12.50 μm. The additional channel (3A) has been incorporated to improve the separation of clouds and snow/ice surfaces under daylight conditions. Currently operational satellites in the series are NOAA-16 (-L, launched September 21, 2000) and NOAA-17 (-M, launched June 24, 2002). The follow-on satellites in the series are planned for launch in 2004 and 2008, with the program switching to NPOESS in 2009. The aim of this program has been to maintain at least two operational satellites in complementary circular, Sun-synchronous orbits at any one time. The even-numbered satellites cross the Equator at local solar times of approximately 07 : 30 and 19 : 30, while the odd-numbered crossing times occur at approximately 02 : 30 and 14 : 30.

The data are digitized onboard the satellite to a 10-bit radiometric resolution (i.e., 1,024 gray values per pixel), and are readily available at two spatial resolutions: (i) direct-broadcast High Resolution Picture Transmission (HRPT) and Local Area Coverage (LAC) at 1.09 km at nadir (~2.5 km resolution at the swath edge), and (ii) Global Area Coverage (GAC) at ~4 km resolution (recorded onboard the satellite for subsequent download/transmission). While the reduced resolution data are recorded onboard the satellite, NOAA's data policy is such that the high-resolution data are available to anyone with a suitable receiving antenna. For additional information, please refer to Cracknell (1997), Hastings (1998), Hastings and Emery (1992), Kidwell (2000), Saitoh (1995), and ⟨*http://www2.ncdc.noaa.gov/docs/klm*⟩.

Disadvantages of the AVHRR are its relatively poor calibration, sensor drift over time for channel-1 and -2 data (Masonis and Warren, 2001), and poor navigation (geometric correction) and geo-location at high latitudes. At best, the

geo-location accuracy of AVHRR LAC is ~1.5 km (Emery et al., 1989). This deteriorates where few identifiable ground control points are available—e.g., over the sea ice zone. A further factor relates to the fact that AVHRR wavelength intervals are approximate only, as the sensors are imperfect filters and exhibit a certain response at a given wavelength. As a result, knowledge of the satellite-specific spectral response functions is required for image processing. Although the IR channels are calibrated in-flight using space and a view of a stable blackbody as references, no in-flight calibration is performed on the visible and near-infrared channels 1 and 2. Data from these channels must be calibrated using pre-launch and post-launch time-adjusted calibration (depending on the satellite). These coefficients are available from NOAA, as are the satellite-specific spectral response functions (see Kidwell, 2000 for details). In spite of these difficulties, the data are of sufficient quality for a range of polar applications, with excellent coverage of high latitudes over a 2,400-km swath width.

A number of processing steps must be carried out by the user prior to applying AVHRR data to geophysical studies—namely, image navigation, calibration, and atmospheric correction. The reader is referred to Hill (2000), Kidwell (2000), Saitoh (1995), Steffen (1995) and ⟨*http://www2.ncdc.noaa.gov/docs/klm*⟩ for further information and guidelines. Normalization of the satellite visible to near-IR radiances to the solar zenith angle is also typically carried out to enable direct comparison of scenes collected under different solar illumination conditions. Fortunately, processed polar data (twice-daily EASE–Grid composites) are available at three different resolutions (1.25, 5, and 25 km) from the NOAA/NASA AVHRR Polar Pathfinder Project (Hutchinson and Scambos, 1997; Maslanik et al., 1998a) at the NSIDC (⟨*http://nsidc.org*⟩). This dataset includes calibrated channel data and solar zenith angle, satellite elevation angle, Sun–satellite relative azimuth angle, surface-type mask, cloud mask, orbit mask, time of acquisition, and ice motion vectors. Data are composited onto two grids per day based on common local solar times and scan angle. Data are available poleward from 48.4°N and 53.2°S: (i) for the 1.25-km data from August 1993 through December 1998 for the Northern Hemisphere, and April 1992 through January 1996 for the Southern Hemisphere; and (ii) from July 1981 through August 1998 for the 5- and 25-km resolution (Fowler et al., 2001, 2002a, b; Scambos et al., 2002). The overall aim of the NOAA/NASA Polar Pathfinder Project has been to prepare long time series of calibrated, consistent, and easy-to-use gridded datasets. The reader is referred to Steffen (1995) and Steffen et al. (1993) for excellent overviews of the AVHRR and its polar applications.

An equivalent sensor is the Multi-channel Visible and Infrared Scan Radiometer (MVISR) onboard the Chinese Fengyun-1C (FY-1C) and FY-1D satellites (launched in May 1999 and May 2002, respectively). This sensor has ten spectral channels, between 0.43 and 12.5 μm, including three channels with ocean color capability (channels 7–9). Spatial resolution is ~1.1 km at nadir, and swath width ~2,250 km (Huixing et al., 1999; Jianping and Caiying, 2000). These satellites build on the heritage of FY-1B, which was launched carrying a five-channel visible to TIR sensor package in September 1990. Since 1988, China has launched four Sun-synchronous polar-orbiting satellites, with FY-1C and FY-1D being currently operational. These satellites transmit data continuously in analog format for

Automatic Picture Transmission (APT) and in digital format for HRPT, with signal formats compatible with NOAA satellite data. Information on the first-year program is available online from the Chinese National Satellite Meteorological Center at ⟨*http://nsmc.cma.gov.cn/*⟩. Operating in parallel, the Operational Linescan System (OLS) on the US DMSP satellites series has also been extensively used, particularly in operational analyses, and provides broadband data in the visible to near-IR (0.58–0.91 μm) and TIR (10.3–12.9 μm) at spatial resolutions of both 0.55 and 2.7 km which are maintained across the 3,000-km swath (⟨*http://dmsp.ngdc.noaa.gov/dmsp.html*⟩). Although OLS data are limited by poorer radiometric resolution—i.e., 8-bit (256 gray levels per pixel)—the visible channel tends to produce images with better sea ice and water contrast than either AVHRR channels 1 or 2 (which are quantized to 8-bit radiometric resolution). This effect arises because the broad spectral wavelength of the OLS suppresses optically thin clouds compared with surface features (Isaacs and Barnes, 1987). A similar but improved effect can be created for the AVHRR by differencing the visible and near-IR channel data (Lee et al., 1993). As is the case for the AVHRR, OLS data are easily downloaded by L-/S-band antenna reception facilities (outside encryption zones). Note that although DMSP data are broadcast in encrypted format, encryption is removed over Antarctica. Decrypted data are available from NOAA's National Geophysical Data Center (Boulder, Colorado). An excellent source of polar AVHRR and DMSP imagery is the Arctic and Antarctic Research Center (*http://arcane.ucsd.edu/*), which is an archive of more than 175,000 satellite passes that supplies data to the U.S. National Snow and Ice Data Center (NSIDC). Note that the OLS also has a unique Low Level Light Sensor (LLLS) capable of detecting visible radiation at night. A further sensor is the Vegetation instrument on the commercial Système Pour l'Observation de la Terre satellites (SPOT 4 and 5), operating in four bands from 0.43 to 1.75 μm at a resolution of ~1 km over a 2,250-km swath.

Since their launch in 1989, the Russian Meteor-3 series of polar-orbiting satellites has provided images from two visible scanning radiometers (MR-900B and MR-2000M) operating between 0.5 and 0.8 μm with a 2-km resolution, and an IR radiometer (Klimat) operating at 10.5–12.5 μm with 3-km resolution. The swath width is 3,100 km. Imagery from these satellites has been extensively used for operational purposes in the Northern Sea Route. The series began in 1969 with the launch of the Meteor-1 satellite, and has since run in parallel with the NOAA polar-orbiting program (Massom, 1991). As no data encryption is imposed, Meteor data are readily available to anyone with a suitable receiver. Indeed, visible images have been transmitted according to the international APT format since 1971, and are available on the following carrier frequencies: 137.300 MHz, 137.400 MHz, and 137.850 MHz (FM, +50 KHz bandwidth, at two lines per second). The follow-on Meteor-3M series began with the launch of Meteor-3M-N1 in December 2001. Satellites in this series carry payloads equivalent to those of the NOAA and MetOp satellites. The main imaging sensor is the MSU-MR, a six-channel sensor operating in the visible to TIR (0.5 to 12.5 μm) over a 3,000-km swath at a spatial resolution of ~1 km—i.e., equivalent to the NOAA AVHRR/3. A similar sensor, the MSU-M, was launched onboard Sich-1M in December 2004 (four

channels from 0.5 to 1.1 μm, resolution 1.7 km, swath 2,000 km). Another sensor, the KMSS multichannel scanning unit, is due to be launched onboard future satellites in the Meteor-3M series and will operate in four visible to near-IR channels (0.45–0.9 μm) at a medium resolution of 50–100 m across a 100-km swath. This will build upon the current MSU-E sensor onboard Meteor-3M-N1, a three-channel high-resolution multispectral imager (0.5–0.9 μm, resolution 38 m, swath width 76 km). The MSU-E, which was also flown on the Resurs-1 satellite series (1985–2000), has a cross-track pointing capability, providing a field-of-regard of 430 km. Data quantization is 8-bit. Further details are available in Asmus (2003).

Based on the heritage of the AVHRR, the Coastal Zone Color Scanner (CZCS) onboard Nimbus-7 (1978–1986) effectively proved that useful global ocean color data related to ocean primary production could be operationally acquired from space. Data from the CZCS are available at ⟨*http://daac.gsfc.nasa.gov/data/dataset/CZCS/*⟩. Launched in August 1997 onboard the OrbView-2 (SeaStar) satellite, the Sea-viewing Wide Field-of-view Sensor (SeaWiFS) operates in eight spectral bands in the visible to near-IR (0.402–0.855 μm), and was specifically designed to yield routine global ocean color measurements related to primary production and phytoplankton processes (Hooker et al., 1992; McClain et al., 2004). Two modes are available for each band: a higher resolution option of 1.1 km resolution (at nadir) over a 2,800-km swath, and a degraded resolution mode of 4.5 km resolution over a 1,500-km swath. The orbit repeat cycle is 16 days. Data from SeaWiFS, covering the period since September 1997, are available from: ⟨*http://daac.gsfc.nasa. gov/data/dataset/SEAWIFS/*⟩.

The MODIS sensors onboard the EOS Terra (with a 10 : 30 local time descending node) and Aqua (with a 1 : 30 pm local time ascending node) satellites view the entire surface of the Earth once every 1–2 days. They make observations in 36 discrete, narrow and co-registered bands over the spectral interval ~0.405 to 14.385 μm, and at three spatial resolutions (0.25 km for bands 1–2, 0.5 km for bands 3–7, and 1.0 km for bands 8–36) over a 2,330-km swath width (scan angle ±65°), and 12-bit quantization (i.e., 4,096 gray levels per pixel). This broad spectral range but high spectral and radiometric resolution represents a significant enhancement of previous data sources. Another key improvement, and one that characterizes all of the modern sensors coming online, is onboard calibration. For detailed information, see: ⟨*http://modis.gsfc.nasa.gov/*⟩. Although MODIS contains 20 visible to near-IR bands, bands 8–19 are specifically designed for the measurement of ocean color (related to the chlorophyll content of the upper ocean) and biogeochemistry (⟨*http://snowmelt.gsfc.nasa.gov/ MODIS_Snow/modis.html*⟩). Generally operating in high-gain mode, these channels are unsuitable for snow and ice studies due to sensor saturation over highly reflective surfaces (a problem previously suffered by CZCS channels). Ocean products from MODIS are available online for Terra at ⟨*http://daac. gsfc.nasa.gov/data/dataset/MODIS/*⟩ and for Aqua at ⟨*http://daac.gsfc.nasa.gov/data/dataset/MODIS-Aqua/*⟩. MODIS has great potential to improve automated ice and cloud analysis of the polar regions (⟨*http://modis.gsfc. nasa.gov/*⟩), although ice coverage is again seriously affected by cloud cover. Sea ice products are routinely available from the NSIDC at level-2 (swath) and level-3

(gridded) formats, and as daily, 8-day, and monthly composites (Hall et al., 2004a, b, in press). Browse image products are available in near real-time at: ⟨*http://landweb.nascom.nasa.gov/cgi-bin/browse/browse.cgi*⟩. The *MODIS Sea Ice Products User's Guide* (Riggs et al., 2003) is available from: ⟨*http://modis-snow-ice.gsfc.nasa.gov/userguides.html*⟩.

Envisat's MERIS is a MODIS-like instrument operating with 15 spectral bands in the visible and near-IR (0.413–0.900 μm), with 300-m ground resolution over a 1,150-km swath width (⟨*http://envisat.esa.int/instruments/meris/*⟩). As with MODIS, it offers superb quality data with substantially more detail on sea ice characteristics than was previously achievable using poorer resolution sensors (see Figure 5.30), but lacks the nighttime viewing capability. A primary aim of MERIS is again to provide large-scale ocean color measurements (see Section 5.9.2.1.3).

The GLobal Imager (GLI) was a similar sensor that flew onboard ADEOS-II from 2002 to 2003. As the successor to the Ocean Color and Temperature Scanner (OCTS) onboard ADEOS (1996–1997), the GLI collected data in 36 channels over the spectral range 0.38–12.0 μm over a 1,600-km swath (scan angle ±45°) and at a spatial resolution ranging from 0.25 to 1.0 km. Data and documentation are available from JAXA's EORC at ⟨*http://sharaku.eorc.jaxa.jp/ADEOS2/index.html*⟩. The GLI follow-on (SGLI) will be launched onboard GCOM-B1 in 2010. Ocean color data are also derived from the identical *POLarization and Directionality of the Earth's Reflectances* (*POLDER*) sensors launched onboard the Japanese ADEOS-I and -II satellites in 1996 and 2003, respectively (Breon et al., 2002) and the improved POLDER sensor onboard the ingeniously named European PARASOL (Polarization and Anisotropy of Reflectances for Atmospheric Sciences coupled with Observations from a Lidar) satellite in December 2004. POLDER is a wide-field-of-view imaging radiometer that has provided the first systematic, global measurements of spectral, directional, and polarized characteristics of the solar radiation reflected by the Earth–atmosphere system (⟨*http://smsc.cnes.fr/POLDER/*⟩). It achieves this by observing targets from 12 directions. Data from POLDER are available online at ⟨*http://parasol-polder.cnes.fr/en/index.htm*⟩.

PARASOL is the second in a series of Myriade micro-satellites developed by CNES (see ⟨*http://smsc.cnes.fr/PARASOL/*⟩ for further details). It flies in a Sun-synchronous orbit with an inclination of 98.21° and a local Equator-crossing time of 13 : 30. The PARASOL-P sensor acquires data in nine channels in the visible to near-IR (centered on 0.443–910 μm) over a scene of size ~1,600 km (along-track) × 2,200 km (cross-track) with a ground spatial resolution of 5.3 × 6.2 km at nadir. With an expected 2-year mission, PARASOL flies in formation with the EOS Aqua and Aura (NASA), Calipso (NASA/CNES), and CloudSat (NASA/CSA) missions as part of the so-called EOS "A-Train" (in a p.m. sequence). When combined and joined by NASA's Orbiting Carbon Observatory (OCO) in 2008, these satellites will entail the first-ever full suite of instruments in space for observing the Earth's clouds and aerosols, using payloads ranging from passive radiometers to active lidar and radar sounders.

The follow-on to both the AVHRR and OLS, and indeed the MODIS, will be the Visible/Infrared Imager/Radiometer Suite (VIIRS). This improved sensor will

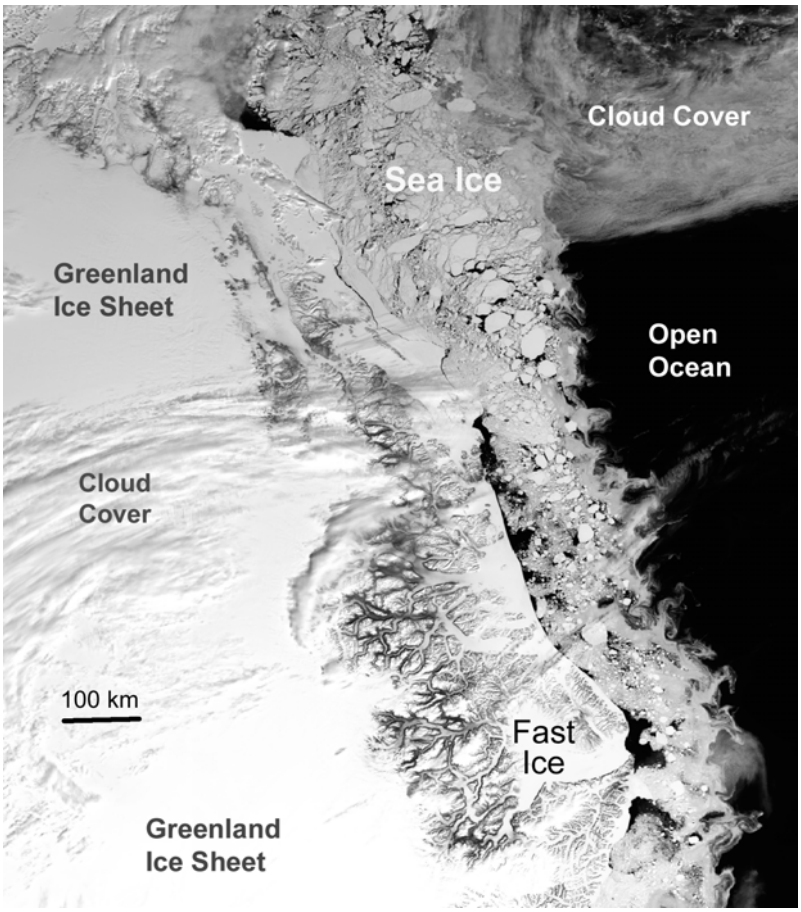

Figure 5.30. An example of an Envisat Medium Resolution Imaging Spectrometer (MERIS) image, of sea ice conditions in East Greenland. The image is a composite of data from the 0.443, 0.560, and 0.865-μm channels. Here, the near-IR channel (0.865 μm) enables a clear separation of atmospheric features and ice features. Ocean eddies and vortices are apparent in the ice edge region. The image was acquired on May 17, 2002 (orbit number 01109). The coordinates of the top left corner are 78°N, 26°W.

provide MODIS-like measurements, and will be launched onboard the NPOESS Preparatory Project (NPP) satellite in 2006 (10 : 30 a.m. descending node), then on the NPOESS series proper (starting in 2009). Attributes include no loss of resolution off-nadir (across a scan of $\pm 56^{\circ}$ and maximum swath of $\sim$3,000 km), onboard calibration, a unique scanning mechanism to optimize both spatial resolution and signal-to-noise ratio, and a large number of spectral bands to enable generation of improved products for both operational and research purposes (at a spatial resolution of $\sim$375 m to 800 m). Launches are then planned right up to NPOESS-6

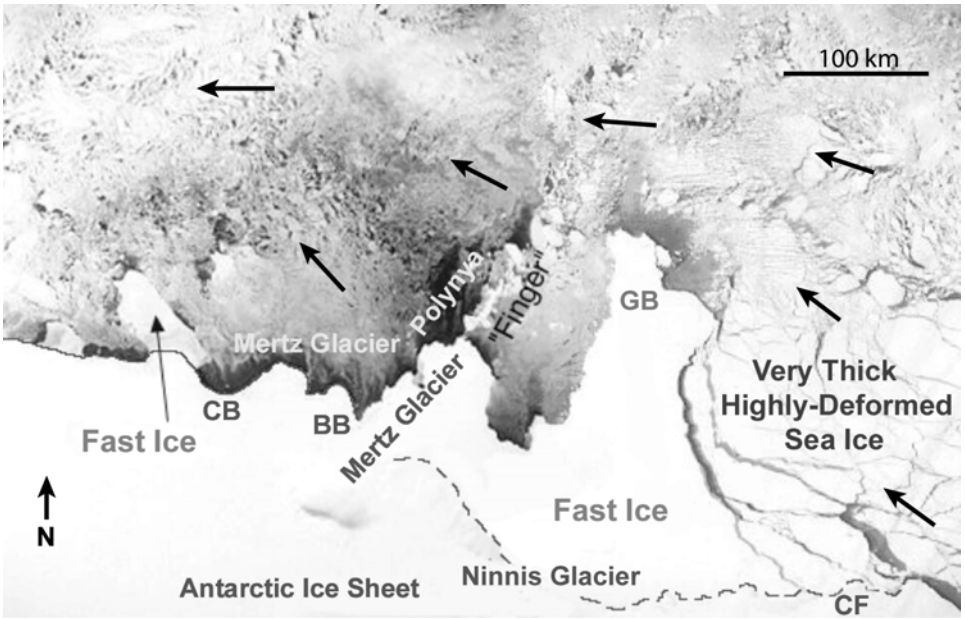

Figure 5.31. A composite of two photographic scenes of the Mertz Glacier region of East Antarctica (~140–152°E), collected by the Argon satellite on October 29, 1963. Spatial resolution is ~140 m. BB is Buchanan Bay, CB Commonwealth Bay, and CF Cape Freshfield, while GB demarcates a region of numerous, small grounded icebergs. Arrows indicate the approximate direction of prevailing sea ice drift in the region, within the coastal East Wind Drift. Massom et al. (2001b) compared fast and pack ice conditions in this image with those in 1998 and 1999 (derived from AVHRR, OLS, and ERS and Radarsat SAR data).

After Massom et al. (2001b). Imagery courtesy of USGS. Reprinted with permission of the International Glaciological Society.

(~2019). In effect, NPP is designed as a bridge between EOS and NPOESS. Plans are afoot to operationally retrieve sea ice temperature, albedo, age and edge motion (Appel et al., 2002). Major issues relating to changes affecting the direct download of these data are assessed by King (2003).

It should be noted that polar visible imagery is also available from the beginning of the space age—from the U.S. Declassified Intelligence Satellite Program (DISP), dating back to 1960 (MacDonald, 1995a, b). This program, which began with Corona, Argon, and Lanyard spacecraft, comprised fairly extensive high-resolution photographic (non-digital) coverage, but over a number of short periods, again limited by cloud. When cloud-free, however, these images give a tantalizing glimpse of past sea ice conditions over limited areas (Figure 5.31). These data are available in non-digital (hardcopy) format from the USGS EROS Data Center at ⟨*http://edcsns17.cr.usgs.gov/EarthExplorer/*⟩. Specifications of the Corona satellites are given at ⟨*http://leonardo.jpl.nasa.gov/msl/programs/corona.html*⟩.

5.8.2.4.2 Cloud cover—a delight to some, a curse to others

Polar sea ice zones are seldom cloud-free for any length of time. In Chapter 4, we saw how clouds act as important modulators of radiation in the Arctic and Antarctic (Curry and Ebert, 1992; Curry et al., 1993, 1996; Makshtas et al., 1999; Raschke, 1987; Rossow and Schiffer, 1999; Schweiger et al., 1999; Shine and Crane, 1984), sending climatologists into paroxysms of delight. Those interested in remotely sensing the polar surface from space using visible to TIR data, however, view cloud as a major contaminant. For the latter, the development of cloud detection and masking techniques that are effective over a snow/ice background is both a high priority and a major challenge (Key and Barry, 1989), given the similarity between clouds and snow/ice in terms of radiance, the small contrast in T_B (thermal characteristics) between polar surfaces and the troposphere, and exaggerated bidirectional effects at large zenith angles (Lubin and Morrow, 1998; Welch et al., 1992). Various procedures have been devised to overcome these difficulties, some automated and others manual (Key et al., 1994a; Lindsay and Rothrock, 1993; Sakellariou et al., 1993; Simpson and Keller, 1995; Welch et al., 1992, 1996; Yamanouchi and Seko, 1992; Yamanouchi et al., 1987, 2000). Neural network techniques have been applied in an effort to increase the effectiveness and efficiency of cloud-masking (McIntire and Simpson, 2002). For the AVHRR, cloud-masking is typically carried out by a thresholding technique using one of the visible to near-IR channels, or the difference between channels 3 (centred on 3.7 μm) and 4 (~11 μm) and/or 4 and 5 (~12 μm) (Kidder and Wu, 1984; Calvin et al., 2002), with other techniques using additional image-textural information (Ebert, 1989; Key and Barry, 1989; Welch et al., 1992). As the reflectance of clouds at 3.7 μm is in general greater than that from snow/ice, the T_B difference $T_{B3.7} - T_{B11}$ is higher for clouds than snow and can be used as a daytime discriminator of polar clouds (Kidder and Wu, 1984; Sakellariou et al., 1993; Yamanouchi and Kawaguchi, 1992). Note that instrumental noise contamination is a common problem in AVHRR channel-3 data (creating a so-called "herring bone" pattern), and the application of a noise reduction procedure, custom-designed by Simpson and Yhann (1994), is recommended before these data are used.

Improved daytime cloud detection against a snow/ice background is afforded by the addition of a channel at ~1.55–1.75 μm, as is the case with the AVHRR/3, ERS-1 Along Track Scanning Radiometer (ATSR), ERS-2 ATSR/2, Envisat Advanced ATSR (AATSR), Landsat Thematic Mapper (TM), and Enhanced Thematic Mapper+ (ETM+), SPOT Vegetation, the FY-1C MVISR (McIntire and Simpson, 2002), ADEOS-II GLI (Stamnes, 1999a), and MODIS (Gao et al., 2003). In this spectral region, ice is more absorptive while reflectance is most sensitive to icegrain size (Figure 5.14). Certain clouds, such as high-altitude cirrus, are more reflective at this wavelength than snow/ice as they are composed of ice crystals which are smaller than surface snow grains (Hori et al., 2001; Stroeve et al., 1996; Warren, 1982). Water clouds, on the other hand, have a higher reflectance than snow, as water droplets are less absorptive. The technique unfortunately becomes ineffective when thin cirrus clouds are present. Cloud-masking is greatly hampered during periods of darkness by the unavailability of 1.6 and 3.7 μm reflectance data (Scorer, 1989). Another

method, termed "daily-differencing" (Comiso, 1994), largely circumvents the difficulty of masking clouds in individual images by detecting clouds by their rapid movement compared with the background sea ice in closely spaced image time series, using a threshold based on the change in observed radiances. Comiso (2000) showed that the most effective method combines the daily-differencing method using AVHRR channel-4 data with the thresholding technique using the difference between channel-3 and -4 data (during daylight hours). Monthly averaging can significantly reduce such errors (Comiso, 2000; Shuman and Comiso, 2002). The MODIS cloud mask algorithm is described by Ackerman et al. (1997, 1998), with further information available at ⟨*http://modis-atmos.gsfc.nasa.gov/MOD35_L2/index.html*⟩. Information on nighttime polar cloud detection with MODIS is provided by Liu et al. (2004b). Similar detailed information on state-of-the-art cloud-masking for high-spatial-resolution imagery, as applied to Terra Advanced Spaceborne Thermal Emission and Reflection Radiometer (ASTER) data, is given by Welch et al. (1999). Polar cloud-masking algorithms for the MODIS and GLI are discussed by Ackerman et al. (1998) and Stamnes (1999a), respectively.

Even with all channels available and careful manual processing, subpixel-scale clouds—e.g., cirrus—can remain undetected to contaminate surface temperature and albedo retrievals. Moreover, thin clouds such as stratus are notoriously difficult to detect (Key et al., 1994a), as are low-level ice and water fogs—e.g., ice crystal precipitation, or "diamond dust"—under clear-sky conditions in winter and early spring (Curry et al., 1990; Key et al., 1994a). This problem is compounded by the fact that they typically occur within the low-level temperature inversion layer (Kahl et al., 1992), and their longwave and shortwave radiative properties are very similar to those of the surface (Key and Haefliger, 1992; Key et al., 1994a; Steffen et al., 1993). Persistent temperature inversions may cause clouds to appear warmer than the underlying ice/snow. Unfortunately, no one method is universally applicable, and unresolved cloud remains one of the largest error sources in the retrieval of geophysical parameters from satellite data collected at visible to TIR wavelengths. Multi-angular measurements from new-generation sensors such as the EOS Terra Multi-angle Imaging Spectro Radiometer (MISR) show great promise, however, as a means of distinguising thin cirrus cloud from snow/ice and for improving cloud characterization (Diner et al., 1999a; Nolin et al., 2002)—see below. The ATSR series also offers improved discrimination of clouds by virtue of their multiple scan angle capability.

5.8.2.4.3 Clear-sky atmospheric effects

Even under clear-sky conditions, the intervening atmosphere contaminates signals of the surface recorded by satellite sensors at visible to TIR wavelengths. In the optical region, atmospheric aerosols (airborne particles) and gases scatter and absorb solar radiation. As a result, they can modulate the radiation reflected by a body on the Earth's surface by changing its spatial distribution, attenuating it, and introducing radiation scattered from the atmosphere into the sensor Field Of View (FOV).[10]

[10] FOV is defined as the solid angle or area which can be viewed through a sensor.

Although the atmosphere is relatively transparent in the atmospheric windows typically used by Earth-observing satellite TIR instruments, absorption and re-emission of radiation by the atmosphere can make significant contributions to surface parameters (i.e., temperature) derived from satellite data (Wolfe and Zissis, 1989). Unfortunately, atmospheric effects are not a constant term that can simply be added to or subtracted from remotely sensed albedo or temperature retrievals. In the case of surface temperatures, they act to reduce the apparent thermal contrast. As a result, atmospheric corrections are required, and these are best applied on a case-by-case basis to account for the high degree of variability in atmospheric effects. Examples of corrections commonly applied will be outlined later (see Kaufman, 1989 for more in-depth coverage of both atmospheric effects and their correction).

5.8.2.4.4 Multi-angle optical–thermal infrared remote sensing

A technology with great potential in sea ice/snow cover research is near-simultaneous optical multi-angle remote sensing—i.e., multiangle observations recorded during a single data acquisition. Information on the change in reflection at different view angles affords an additional means of distinguishing different types of surface (under cloud-free conditions), atmospheric particles (aerosols), and cloud forms, as well as providing improved albedo information (see Section 5.9.13).

The first operational spaceborne sensor to fully exploit this technology was the ATSR launched onboard ERS-1 in 1991 (Prata et al., 1990), with the ATSR-2 on ERS-2 and the AATSR onboard Envisat following. These sensors exploit similar spectral channels to the AVHRR, but are equipped with onboard calibration and a radiometric precision of <0.1 K with 12-bit quantization. The Envisat AATSR is a seven-channel sensor (spectral range 0.55–12 μm) operating at a 1-km resolution over a 500-km swath. The ability to view the same surface area through a near-vertical atmospheric path, then through an inclined path a little later, enables the sensor to account for variations in atmospheric absorption due to different concentrations in all absorbing species. This results in an improved atmospheric correction. Taken together, these characteristics result in enhanced accuracies in surface parameter retrievals—e.g., of temperature and albedo. As the emphasis with multi-directional instruments is on spectral rather than spatial data acquisition, the detection channels are precisely calibrated.

Developing this concept further, the MISR, which was launched on Terra in December 1999, measures radiometrically and geometrically calibrated TOA radiances in four spectral bands (interval 0.443 to 0.865 μm) from each of nine pushbroom imaging cameras oriented at different view angles along-track (Diner et al., 1998). Spatial resolution varies from 0.275 to 1.1 km, across a 360-km swath. Sensor characteristics are given in Table 5.2. The 233 repeating orbits are called paths, with each path being divided into 180 blocks measuring 563.2 km (cross-track) $\times$ 140.8 km (along-track). The MISR observes the daylit Earth continuously, providing full global coverage between 82°N and 82°S in 2 to 9 days (depending on latitude). MISR data are available from the NASA Langley Atmospheric Sciences Data Center at ⟨*http://eosweb.larc.nasa.gov*⟩. The multi-angular

Table 5.2. Characteristics of the EOS Terra MISR instrument. Detailed information on the MISR project is given at ⟨*http://www–misr.jpl.nasa.gov/*⟩.

Parameter	Value
Spectral bands (solar-spectrum-weighted)	0.4464, 0.5575, 0.6717, and 0.8664 μm
Spectral bandwidths	0.0419, 0.0286, 0.0219, and 0.0397 μm
Camera view zenith angles at Earth's surface	0.0° (nadir), 26.1′, 45.6′, 60.0′, and 70.5′ (both fore and aft of nadir)
Swath width	360 km (9-day global coverage, 2-day repeat at the poles)
Cross-track × along-track pixel sampling	0.275 × 0.275 km 0.55 × 0.55 km 1.1 × 1.1 km 0.275 × 1.1 km

measurement capability of sensors such as the MISR and ASTER enables more complete characterization of the surface Bidirectional Reflectance Distribution Function (BRDF) and therefore albedo (see Section 5.9.13). For in-depth information on the Terra MISR, ASTER, and MODIS missions, their synergism and duty cycles, and products, see King et al. (2003b). Similar information on the Aqua AMSR-E, MODIS, and AMSU-A, and also the Landsat-7 ETM+ (see below) and QuikSCAT Seawinds, is given by Parkinson and Greenstone (2000).

5.8.2.4.5 High-resolution visible to thermal infrared

High-resolution visible to TIR systems have been less extensively used in modern sea ice research, due in part to their limited coverage over a narrow swath (typically <200 km wide), relatively long repeat interval and, for commercial systems—such as Landsat, SPOT, Ikonos, and QuickBird—cost. The Landsat and SPOT programs date back to 1972 and 1986, respectively (Massom, 1991). Once again, they are also unable to penetrate cloud cover and, for the visible to near-IR channels, polar darkness. Due to their accuracy when cloud-free and their ability to resolve morphological features such as individual floes and leads, however, they have made a significant contribution to the validation of coarser resolution satellite data products—e.g., Landsat imagery has been used in the validation of sea ice products from Nimbus-7 SMMR and DMSP SSM/I (Steffen and Maslanik, 1988; Steffen and Schweiger, 1990), and also in sea-ice algorithm comparisons (Comiso et al., 1997; Comiso and Steffen, 2001). They also have an important role to play in regional process studies requiring very-high-resolution coverage, and as a means of interpreting SAR data (with a similar spatial resolution).

Launched onboard Landsat-7 in April 1999, the ETM+ provides high-resolution measurements at visible to TIR wavelength bands (⟨*http://Landsat.gsfc.nasa.gov*⟩). It is an improved version of the TM onboard earlier Landsat-4 and -5 missions, incorporating a 15-m-resolution panchromatic band and an improved resolution for the TIR band, as well as 30-m resolution for the other bands. It operates eight spectral bands covering the range 0.45–12.5 μm, and

the latitudinal band to a maximum of 81°. The repeat cycle is 16 days. A science data user's handbook is provided by the Landsat Project Science Office (2003). The Landsat-7 orbit precedes Terra by 30 minutes along a common ground track, providing the opportunity for data fusion with data from MISR, ASTER, and MODIS sensors. Dating back to 1972, the Landsat series provides data at a resolution of 15–80 m in the visible and near-IR bands and 60–120 m in the TIR bands. Examples of the amount of detail that can be extracted from these images when cloud-free, albeit over a narrow area, are given in Figure 5.32 (see color section). While SPOT sensors offer higher resolution than their Landsat counterparts, the latter offer substantially greater coverage—i.e., 185×185 km versus 60×60 km. Moreover, SPOT sensors lack the nighttime-viewing capability of the TIR channels of the Landsat ETM+ and previous sensors. The SPOT system has been operational since the launch of SPOT 1 in 1986. This was followed by SPOT 2 in January 1990, SPOT 3 in September 1993, SPOT 4 in March 1998 and SPOT 5 in May 2002. System continuity will be assured by a constellation of new-generation minisatellites to be known as Pleïades from 2008 onwards (see ⟨*http://www.spot.com/html/SICORP/_401_.php*⟩ for details).

Since being first launched with Indian Remote Sensing satellite-1A (IRS-1A) in March 1988, India's civilian polar-orbiting satellite program has carried a series of Landsat- and SPOT-like sensors as well as other sensors. These have been specifically designed for application around the Indian sub-continent, but also have potential for polar research where the data are available. The two Linear Imaging Self Scanning (LISS-I and -II) sensors aboard IRS-1A and IRS-1B (launched in August 1991) provided data in four spectral bands in the visible and near-IR regions, with a spatial resolution of 36.5 m and 72.5 m and a repeat period of 22 days. See ⟨*http://www.nrsa.gov.in/engnrsa/sitemap.html*⟩ for a detailed description of the Indian EOS program. The imaging sensors on IRS-1C (launched in December 1995) and IRS-1D (launched in September 1997) are:

- a multispectral Linear Imaging Self Scanner (LISS-III) operating in two visible and one near-IR spectral bands with a spatial resolution of ~23.5 m and a shortwave IR band with a resolution of ~70.5 m, over swath widths of 141 km and 148 km, respectively;
- a PANchromatic (PAN) Camera with a resolution of ~6 m, a swath width of 70 km, and with a ±26° cross-track steering capability (relative to nadir). The latter attribute gives a stereo-viewing capability, and a revisit interval of 5 days for IRS-1C and 3 days for IRS-1D; and
- a Wide Field Sensor (WiFS) operating in two visible and near-IR bands with a spatial resolution of 188 m and a wide swath of around 810 km and a repeat coverage interval of 5 days.

Launched in October 1994, IRS-P2 carried a modified LISS-II camera, while IRS-P3 (launched in March 1996) carried a WiFS sensor similar to that onboard IRS-1C as well as a Modular Opto-electronic Scanner (MOS) provided by the DLR. Launched in 1999, IRS-P4 (Oceansat-1) carries a four-frequency MSMR and an Ocean Color Monitor (OCM). As its name suggests, the latter is designed to measure ocean

primary productivity, using eight narrow spectral bands in the visible and near-IR with a 350 m resolution over a 1,500 km swath (⟨*www.ioccg.org/general/ocm/ocm*⟩). IRS-P5 (Cartosat-1), which is due to be launched in 2005, carries two identical PAN cameras with a 2.5 m resolution. These collect data over a 30-km swath, with a fore–aft stereo-viewing capability.

Launched in October 2003, the IRS-P6 (Resourcesat) carries a three-band multispectral LISS-4 camera with a spatial resolution of better than 6 m and a swath of around 25 km with cross-track steerability ($\pm 26^\circ$) for selected area and stereo-monitoring (at 7-bit quantization). An improved LISS-III sensor will operate with four bands (red, green, near-IR, and SWIR), all at 23.5-m resolution and 140-km swath, and will also provide essential continuity to LISS-III (7-bit quantization). The IRS-P6 satellite also carries an Advanced Wide Field Sensor (AWiFS) operating in three bands in the visible to near-IR and one band in the shortwave IR, with a 56-m resolution and 1,400-km swath (10-bit quantization). The website of the Indian Remote Sensing Organization is ⟨*www.isro.org/irs-p4*⟩.

In addition, a number of new research-and-development sensors have recently been launched—e.g., the Terra ASTER and ADEOS-II Advanced Visible and Near Infrared Radiometer (AVNIR), which have the potential to provide important new data (Shirasaki et al., 1998). The ASTER operates in three visible to near-IR, six shortwave, and five TIR bands with 15, 30, and 90-m resolutions, respectively (Yamaguchi et al., 1998, 2001). Coverage is over a narrow swath of 60 km. ASTER can be used synergistically with MODIS and/or MISR, and its pointing capabilities are such that repeat coverage occurs once every 16 days in all 14 bands and once every 5 days in the 3 visible to near-IR bands. AVNIR-2 will be flown onboard the Japanese ALOS satellite in 2005 (Hamazaki, 1999). It operates in four spectral bands (from 0.42 to 0.89 μm), with a nadir ground resolution of 10 m over a 70-km swath width (8-bit quantization). Data from this sensor are enhanced by improved onboard calibration. Simultaneous operation of the ALOS AVNIR-2 and PALSAR sensors is possible, and the former will be of importance in helping to interpret complex polarimetric SAR images of sea ice from the latter.

The launch of EarlyBird (Earth Watch Inc.) in 1997, with a 3-m resolution panchromatic band, heralded a new era in very-high-resolution surveillance from space (Zhou et al., 2002). New ultra-high (meter to sub-meter) resolution optical sensors onboard commercial satellites—e.g., Ikonos-II (⟨*http://www.spaceimaging.com*⟩), Quickbird-2 (Toutin and Cheng, 2002; ⟨*http://www.digitalglobe.com*⟩) and EROS-A1 (⟨*http://www.imagesatintl.com*⟩), provide satellite images comparable in spatial resolution with mid-scale aerial photos. Once again, the high spatial resolution comes at the expense of areal coverage, with data being collected over a very narrow swath—e.g., 11 km for Ikonos and 16.5 km for QuickBird. Radiometric resolution is also high, at 11-bit (2,048 gray shades). Although these data have yet to be extensively used in sea ice studies, they show potential as a means of validating coarser resolution satellite data and gaining information on floe size distribution, for example. Big Brother is indeed now watching—during the daytime on a cloud-free day—if he can afford it, that is!

5.8.2.4.6 Hyperspectral sensors (imaging spectroscopy)

Another new, and as yet largely untapped, tool for sea ice research is the emerging technology of hyperspectral remote sensing. Whereas conventional imaging systems such as those onboard Landsat and SPOT satellites acquire images in a few separate bands of various widths, hyperspectral imaging (or imaging spectroscopy) refers to the simultaneous acquisition of images of the same area in many narrow and contiguous spectral bands. As such, each pixel has a continuous spectrum associated with it (Goetz, 1987). The NASA Earth Observing-1 (EO-1) spacecraft, which was launched in November 2000 into a Sun-synchronous orbit behind that of Landsat 7, carried two advanced technology sensors—namely, the Advanced Land Imager (ALI) and the Hyperion Imaging Spectrometer. The Hyperion was a high-resolution hyperspectral imager capable of resolving 220 calibrated spectral bands in 10-nm bandwidths (from 0.4 to 2.5 μm) with a 10–30 m resolution. The instrument could image a 7.75 km by 100 km area per image and provide detailed spectral mapping across all 220 channels with high radiometric accuracy (12-bit digitization—i.e., 4,096 gray levels per pixel). Further details are available online at ⟨*http://eo1.gsfc.nasa.gov*⟩. While such data have again yet to be extensively applied to sea ice studies, they show potential for the examination of the surface optical albedo and snow-grain-size properties (Dozier and Painter, 2004; Nolin et al., 2002), albeit in a localized fashion due to the narrow coverage—e.g., in support of field measurements, and once again with a view to validating other sensor products. Based upon their high spectral resolution, hyperspectral imagers have the potential to expand the capability of multi-spectral imagers in a number of ways, including sub-pixel detection and mixed pixel classification. As such, this emerging technology shows promise regarding the improved classification of sea ice types based upon subtle spectral contrasts. Cloud detection and masking remains a major limiting factor, as does polar darkness. Moreover, the enormous volume of data involved presents a new challenge. A common practice in this respect is to compress data prior to image analysis (see Du and Chang, 2004). See Chang (2003) for detailed information on hyperspectral imaging and image analysis.

5.9 KEY GEOPHYSICAL PARAMETERS FROM SATELLITE DATA

In this section, we examine the primary sea-ice-related variables that can be derived from satellite data. Some are routinely and operationally produced, while others are currently research-and-developmental. Information is given on techniques (algorithms) used, and case study examples to illustrate how the issues and uncertainties raised in earlier sections are being addressed. An effort is made throughout to highlight weaknesses as well as strengths, and to evaluate error sources and magnitudes where possible. A summary of satellite sensor classes used to measure these parameters is provided in Table 5.3, with the parameters listed in the order in which they are subsequently discussed in the text. While important parameters are presented individually for convenience, they are in reality intimately interrelated (as shown in Section 5.6). In all cases, the applicability and suitability of a satellite

Table 5.3. Summary of sea-ice-related applications of major satellite sensor classes. Vis is visible to near-infrared; TIR is thermal IR; Scatt is scatterometer; Alt is altimeter; # = cloud-affected (visible to near-IR sensors are also darkness-affected); P = primary data source; S = secondary data source; and R = research and development.

Parameter	Passive microwave	SAR	Low-res. Vis-TIR#	Hi-res. Vis-TIR#	Radar Scatt	Radar Alt	Laser Alt#
Sea ice concentration	P	S	S	S	–	–	–
Sea (pack) ice extent	P	S	S	S	P	S	R
Fast ice extent	–	P	P	P	–	–	–
Polynya size	P	P	P	P	–	–	–
Iceberg size/tracking	–	P	P	P	S	S	S
Ocean color (primary production)	–	–	P	–	–	–	–
Sea ice motion	P	P	P	S	P	–	–
Ice dynamic kinematic parameters	S	P	S	–	S	–	–
Sea ice thickness	R	R	R	–	–	R	R
Sea ice classification	P	P	S	S	S	–	–
Snowcover thickness	P/R*	–	–	–	–	–	–
Surface roughness	–	R	–	R	–	–	R
Floe size statistics	–	P	S	P	–	–	–
Surface "skin" temp.	–	–	P	S	–	–	–
Snow/ice interface temp.	P/R*	–	–	–	–	–	–
Broadband albedo	–	R	P	S	–	–	–
Snow grain size	–	–	P	–	–	–	–
Snow impurity content	–	–	P	–	–	–	–
Annual melt onset and freeze-up	P	P	S	S	R	–	–
Meltpond coverage	–	R	–	R	–	–	–
Wave–ice interaction	–	P	–	–	R	–	–
Ice edge characteristics	–	P	P	P	R	–	–

* Although operationally produced (with data from the EOS Aqua AMSR-E), these are new products that require validation. Icebergs are included as they have a significant effect on sea ice distribution, as is primary production because it is closely linked to sea ice distribution and melt.

sensor/dataset to the measurement of a given sea-ice-related parameter or process depends upon (i) the nature and scale of the parameter, and (ii) the attributes of the satellite sensor data. Important satellite-sensor parameters include swathwidth (area of coverage), revisit interval (frequency of coverage), wavelength/frequency, polarization, incidence angle, spatial resolution, spectral resolution, and radiometric resolution. Note that revisit interval differs from repeat period, in the sense that it is determined not only by the orbital repeat period but also by the sensor coverage characteristics and most notably swathwidth. An important tradeoff exists between detection capability (spatial resolution) and geographical coverage (swath). Another distinction, and one that affects the timeliness of data availability, is between

operational versus research-and-development sensors. As we will see, an important recent development has been in the synergistic application of different datasets, and even data fusion, to take advantage of complementary sensor attributes to derive additional geophysical information. In all cases, the approach is more powerful if ancillary data are available—e.g., meteorological data—to help interpret what are often complex signatures, given the complex nature of the target itself. To reiterate, not all important variables can be measured directly by spaceborne sensors, an example being the three-dimensional structure of the ocean and its variability.

5.9.1 Ice concentration

Sea ice concentration (defined as the areal fraction, or percentage, of sea ice present within a given area), and derived quantities including total ice area (the area of ice-covered ocean), ice extent (the area within the ice–ocean margin), and open-water area (the difference between ice extent and total ice area) are fundamental geophysical parameters describing sea ice distribution. Ice concentration is a major determinant of the mechanical properties of the pack and the surface energy balance of polar oceans, with changes in concentration (and extent) playing a major role in ocean–atmosphere fluxes of heat, moisture, and momentum (see Section 5.4). Ice concentration and thickness not only impact ocean–atmosphere interaction processes but also reflect the state of ocean and atmosphere circulation and heat and moisture fluxes. These variables also provide important feedbacks to the larger climate system by regulating the planetary heat balance and the formation of deepwater, for example (Walsh et al., 2000). Accurate estimates of ice concentration are crucial as errors of even a few percent in the open-water fraction in models can make a large difference in heat and salinity flux and ice production rate calculations (Maykut, 1978; Parkinson et al., 2001; Simmonds and Budd, 1990, 1991). For information on the sensitivity of climate models to the ice concentration/open-water fraction, please see Parkinson et al. (2001) and Flato and Ramsden (1997) and the references therein. To date, ice concentration has been measured using data from (i) visible to TIR radiometers; (ii) SARs; and, most importantly, (iii) passive-microwave radiometers. Microwave sensors have the prime advantage of being able to penetrate both cloud cover and polar darkness.

5.9.1.1 Passive microwave techniques

With a continuous time series dating back to 1978, multi-spectral passive-microwave data are the primary source of global ice concentration information. These in turn form the cornerstone of both process studies and long-term trend analyses, enabling investigation of the complex role of sea ice in, and response to, climate variability and change. While passive-microwave data are characterized by a poor spatial resolution—i.e., 12.5–25.0 km for current ice concentration products—they largely circumvent the need with high-resolution sensors to resolve all individual areas of openwater in order to compute concentration. In other words, the passive-microwave ice concentration product entails a single value integrated over the

area contained within each pixel and based on the T_B data. Moreover, these data are on a scale that is ideally suited to the validation of sea ice models and, increasingly, the assimilation into models (this exciting new development is evaluated in Section 5.9.17.1). Eppler et al. (1992) and Comiso (2003a) provide excellent introductions to characterizing sea ice with passive-microwave data.

The first consistent time series of ice concentration (and extent) came from the Nimbus-5 ESMR, which graced the skies from 1973 to 1976 (Gloersen et al., 1974). This sensor measured horizontally polarized (H-pol) radiation at a single frequency of 19.35 GHz ($\lambda = 1.55$ cm), and over a 1,400-km swath at a spatial resolution of $\sim$30 km. Ice concentration estimates were derived by applying a simple mixing algorithm that employed climatological surface temperature data to correct for temperature effects (Comiso and Zwally, 1982). Estimates of ice concentration could be made to an accuracy of $\sim$15% in regions of approximately homogeneous ice cover. This enabled the production of sea ice atlases of both Antarctica (Zwally et al., 1983) and the Arctic (Parkinson et al., 1987). These and similar data from Russian satellites (Massom, 1991) gave an extraordinary and truly eye-opening first view of the sheer scale of the global sea ice cover in its glorious entirety, and the seasonal and interannual variability.

Improved accuracy followed with the launch of the SMMR onboard Nimbus-7 in 1978 (Gloersen and Barath, 1977). In operation until 1987, the SMMR provided brightness–temperature (T_B) data at both H and V polarizations at five frequencies—i.e., 6.6, 10.7, 18, 21, and 37 GHz—with 21-GHz data being used for atmospheric water vapor correction purposes. The availability of these improved data led to the development of a number of sea ice algorithms making use of the frequency and polarization dependence of surface microwave emissivity. The SMMR provided global sea ice data every other day and also the fraction of multiyear ice cover in the Arctic (Gloersen et al., 1992). Algorithms include the NASA Team (NT) (Cavalieri et al., 1984; Gloersen and Cavalieri, 1986), the NASA Bootstrap (Comiso and Sullivan, 1986), the NORSEX (Svendsen et al., 1983), and others—e.g., Swift et al. (1985). The inner workings of the main SMMR and SSM/I algorithms are described and evaluated by Meier (2005) and Steffen et al. (1992), and weather effects on algorithm retrieval accuracy are evaluated by Maslanik (1992) (see also Section 5.9.1.2.1). Information on SMMR brightness–temperature data is provided by Njoku et al. (1998).

Starting in June 1987, the DMSP has flown the SSM/I (Hollinger et al., 1987, 1990). Operating at 19.35, 37, and 85.5 GHz (V-pol and H-pol) and 22.235 GHz (V-pol only), the SSM/I continues to offer complete daily coverage of both polar sea ice covers. Ice concentrations have been retrieved using improved versions of the NT (Cavalieri et al., 1990, 1999a, b) and Bootstrap Basic (Comiso, 1995b) algorithms. Other algorithms include the Bristol algorithm (Hanna and Bamber, 2001; Smith, 1996) the Cal/Val (AES-York) (Ramseier et al., 1988), and the U.S. National Ice Center (NIC) Hybrid algorithm (a fusion of the Cal/Val and NT algorithms: Partington, 2000). Recent reprocessing of SMMR data has produced a consistent and continuous time series dating back to 1978. This important time series is continuing with the launch of two AMSRs—namely, AMSR-E onboard Aqua in

May 2002 and AMSR on ADEOS-II in 2002. This new instrument, which was supplied by JAXA, combines the capabilities of the SMMR and SSM/I, but at an improved spatial resolution. This results in 12.5-km resolution sea ice products compared with 25 km for SMMR and SSM/I. Unfortunately, the ADEOS-II AMSR prematurely ceased operation in October 2003.

As they form the basis for current ice concentration retrievals from SSM/I and AMSR data, we will briefly describe the NT and Bootstrap algorithms. Applied to SMMR and SSM/I data, the Bootstrap uses the 37V and 37H channels in high concentration ($>90\%$) regions of the Arctic and the 19V and 37V channels in lower concentration regions of the Arctic and throughout the Antarctic (Comiso, 1995b). It is based upon the consistent tendency, in scatterplots of 37H versus 37V (or 19V versus 37V) T_B data, of open-water pixels to cluster around a point and consolidated ice pixels to cluster along a line of a given slope, with pixels of intermediate concentration falling somewhere in-between. The ice concentration for a given pixel (datapoint) is then determined by a linear interpolation between the openwater tiepoint and the line representing 100% ice. The algorithm employs seasonal tiepoints for both hemispheres, to account for seasonal variabilities in the sea ice surface properties and their effect on surface emissivity. In addition, a weather filter based on the 19V and 22V GHz channels is employed to remove spurious ice concentration retrievals over open ocean—i.e., equatorward of the ice edge.

The NT algorithm, on the other hand, is based on two ratios—the normalized T_B polarization difference (Polarization Ratio, or PR) and the Gradient Ratio (GR)—using the 19V, 19H, and 37V channels (see Section 5.9.1.1.3.3). The use of ratios minimizes the effect of surface temperature variability on ice concentration retrieval. While PR generally distinguishes between open water and ice, with open water having higher PR values, GR differentiates multiyear and first-year ice in the Arctic, with higher GR values corresponding to first-year ice. Spurious ice retrievals over open water due to wind, water vapor, and cloud–liquid water are removed by applying two weather filters. These are based on threshold values of GR(22V/19V) and GR(37V/19V). Other work has adapted circumpolar algorithms to regional sea ice conditions. Enomoto (1996), for example, developed coefficients specific to the Sea of Okhotsk for application with the NT algorithm (Cavalieri, 1994)—see also Cho et al. (1996).

Other SSM/I algorithms use 85-GHz data collected in a 16×14-km footprint to obtain sea ice concentrations at an improved spatial resolution—i.e., 12.5 km (Shokr and Agnew, 1999). Examples are the Sea Lion algorithm (Kern, 2001, 2004; Kern and Heygster, 2001) and the Artist algorithm (Kaleschke et al., 2001). The former uses the polarization ratio, while the latter uses the polarization difference. Moreover, Lubin et al. (1997) have successfully used SSM/I 85-GHz channel data to retrieve total ice concentrations in the Arctic under clear-sky conditions and during summer (see also Lomax et al., 1995). Compared with lower frequencies, 85-GHz data are somewhat limited by a larger atmospheric contribution that can at times compromise the retrieval of surface parameters (St. Germain, 1994). Other error sources include an increase in surface emissivity due to wind-roughening of the open ocean and an increase in sensitivity to variability in snow cover properties—e.g., layering, density, grain size distribution. These effects can result in a net

decrease of the polarization ratio at 85 GHz and thus an overestimate of ice concentration. As a result, algorithms designed to use 85-GHz data alone must incorporate means of minimizing such affects (Kern et al., 2003). In fact, the tiepoints for the Sea Lion algorithm reflect virtually clear-sky conditions, and the T_B data are explicitly weather-corrected by either radiative transfer calculations or using lower frequency SSM/I channel data. No such correction is required for the Artist algorithm as tiepoints empirically include the weather effect. For the SSM/I, the advantage of using these higher resolution (i.e., 85 GHz) data is that land contamination effects are smaller, and polynyas are better resolved (Kern et al., 2003). Such a need has, however, recently been circumvented by the launch of improved-resolution AMSR sensors.

5.9.1.1.1 Error sources in ice concentration retrieval

Comparisons of the performance of the NT and Bootstrap algorithms have been carried out, and results validated with independent data, by a number of workers, including Agnew and Howell (2002, 2003), Cavalieri (1992), Cavalieri et al. (1992), Comiso et al. (1997), Comiso and Steffen (2001), Meier (2005), Meier et al. (2001), Partington and Bertoia (1999), Steffen and Schweiger (1991), and Emery et al. (1994). While some error sources are algorithm-specific, most are common to both algorithms. Regarding the former, the Bootstrap algorithm is sensitive to ice temperature variability, although this is minimized by use of dual-polarized 37-GHz channel data. The NASA Team 2 (NT2) algorithm, on the other hand, has problems in regions of predominantly thin ice. Common error sources include:

- Unresolved ice types. For example, the presence of new and young ice within the sensor footprint results in a low concentration bias (Cavalieri, 1994; Cavalieri and Comiso, 2000; Grenfell et al., 1992; Wensnahan et al., 1993). In his comparison with Radarsat SAR data, Kwok (2002a) showed that overestimates of openwater fraction by about 3–5 times occurs in winter in the Arctic using Passive MicroWave (PMW) data.
- Unfiltered weather effects, particularly about the ice edge. Atmospheric opacity-related errors as large as 10% were reported by Oelke (1997) in SSM/I ice concentration retrievals during a warm moist air incursion across the NW Weddell Sea in Antarctica in winter.
- Surface melt effects during the late spring to summer melt period in the Arctic lead to significant overestimates of the open-water fraction (Cavalieri et al., 1990; Comiso and Kwok, 1996; Grenfell and Lohanick, 1985; Lohanick, 1993). Ephemeral synoptic-scale warming events can also occur during the autumn and winter in marginal seas, and throughout much of the Antarctic pack, in particular (Massom et al., 1997, 1998a).
- Surface wetness throughout the year, including flooding throughout the Antarctic pack due to the effect of snow on ice isostasy, and in the Marginal Ice Zones (MIZs) and adjacent to large leads and polynyas by wave–ice interaction processes. Particularly large concentration underestimates of up to tens of percent can occur in the MIZ, where wave overwashing and floe buffeting and deformation create an ice cover composed predominantly of brash ice with a wet

surface (Massom et al., 1999). This can in turn affect the accuracy of ice extent determinations using ice concentration thresholds—e.g., 15% (see Section 5.9.2).
- The contamination of coastal pixels with terrestrial/ice sheet signals.
- Frequency- and polarization-dependent temporal and spatial variations in microwave emissivity ε, as a function of thickness, age, salinity, temperature, structure, snow cover, and surface conditions overall (Comiso et al., 1989, 1992, 1997; Crane and Anderson, 1994; Eppler et al., 1992; Grenfell et al., 1994a). According to Comiso and Steffen (2001) and Comiso (2002a), this represents the largest source of error in sea ice concentration retrievals outside the melt season.

Overall ice concentration errors of up to 10–20% have been reported for SMMR and SSM/I data in the Arctic summer, dropping to an average of 5–15% in winter (Comiso and Kwok, 1996; Comiso and Steffen, 2001; Comiso and Sullivan, 1986; Comiso et al., 1991).

5.9.1.1.2 Data availability

Gridded sea ice concentrations produced by the NT and Bootstrap algorithms are available for the SMMR period (October 1978 through 1987) and since 1987 for the SSM/I from the NSIDC EOS DAAC at ⟨*http://nsidc.org*⟩. Three daily datasets are available—namely, the NT product, the NASA Boostrap product, and NSIDC's Near Real Time DMSP SSM/I (NRTSI) product. Monthly composite images are also available. Data are mapped to a standardized SSM/I polar stereographic grid (NSIDC, 1996). Daily near real-time ice concentration data are also available in two formats—namely, on the standard SSM/I grid (Cavalieri et al., 2003b) or the SSM/I EASE-grid (Nolin et al., 2003). Gridded daily average T_B data are also available, along with extensive documentation and supporting software. The standard data products appear on the NSIDC website/ftp site about 3–6 months after acquisition, whereas the near-real time products appear after about 1 day. Important additional ice concentration products available from the NSIDC (⟨*http://nsidc.org*⟩) include monthly mean ice concentrations derived using the NASA Bootstrap algorithm for each month from (currently) November 1978 through September 2002, spanning the Nimbus-7 SMMR and DMSP SSM/I datasets (⟨*http://nsidc.org/data/smmr_ssmi_ancillary/monthly_means.html*⟩). An associated and derived product is "ice persistence" (⟨*http://nsidc.org/data/smmr_ssmi_ancillary/persistence.html*⟩), whereby individual ocean pixels containing a minimum of 15% ice cover are summed throughout the time series. Such data can be readily applied to climatological or trend analyses. Note that Nimbus-5 ESMR data are also available from the NSIDC.

5.9.1.1.3 AMSR sea ice concentration algorithms

5.9.1.1.3.1 THE THEORETICAL BASIS OF CURRENT PASSIVE-MICROWAVE ICE CONCENTRATION ALGORITHMS Recall from (5.7) that the brightness temperature T_B measured by satellite passive-microwave systems can be expressed in terms of the radiative transfer equation. Current ice concentration algorithms are based on the

fact that satellite-received radiation emanates from open water and an ice- or snow-covered surface, or a combination of both. The measured T_B is expressed by a linear mixing formulation to account for the relative contribution from each surface type within the sensor Field Of View (FOV) as follows (Comiso et al., 2003a):

$$T_B = \sum_I C_I T_{BI} + \left(1 - \sum_I C_I\right) T_{BO} \tag{5.31}$$

where T_{BI} is the representative brightness temperature for the different ice types present, C_I is the corresponding fraction of each ice type within the sensor FOV, and T_{BO} is the average brightness temperature for ice-free ocean. A major challenge confronting ice concentration algorithms is the need to account for spatial and temporal changes in T_{BI} and T_{BO}, which are functions of surface emissivity (ε) and physical temperature (T_I) and atmospheric opacities (τ and τ'), as shown in (5.24). In addition, the emissivity of an ice cover and its snow cover changes in a frequency- (and polarization-) dependent manner as it evolves and ages. In an effort to account for and minimize these effects, the AMSR ice concentration algorithms described below use data from several channels.

Ice concentration products are retrieved from AMSR-E T_B data using three different algorithms that draw upon these basic premises (Comiso et al., 2003a), to account for the different ice conditions in the Arctic compared with the Antarctic discussed in Section 5.3 (Gloersen et al., 1992). Antarctic sea ice is composed predominantly of seasonal ice formed under relatively turbulent conditions—i.e., it largely comprises frazil ice and is more saline (Comiso et al., 1992). Arctic sea ice, on the other hand, contains a large proportion of older multiyear ice, composed of a higher proportion of lower salinity columnar ice. Importantly, snow cover thickness (h_S) and ice surface temperature (T_I) are for the first time derived from the same T_B dataset, using techniques described in Sections 5.9.8 and 5.9.12, respectively. It is anticipated that the availability of coincident ice concentration, T_I and h_S data will significantly improve model performance.

The AMSR-E algorithms, which are based on the heritage of the NT and Bootstrap algorithms described above, are:

- the enhanced NT2 algorithm (Markus and Cavalieri, 2000) in the Arctic (12.5- and 25-km-resolution products); and
- the Bootstrap Basic Algorithm (BBA: Comiso, 1995b; Comiso and Zwally, 1997) and the AMSR Bootstrap Algorithm (ABA: Comiso and Steffen, 2001; Comiso et al., 2003a) in the Antarctic (12.5- and 25-km-resolution products, respectively).

In addition, differences in ice concentrations produced from each algorithm are available for each hemisphere, essentially allowing a user to derive Bootstrap ice concentrations for the Northern Hemisphere and NT2 ice concentrations for the Southern Hemisphere. The BBA algorithm has also been used by the JAXA Earth Observation Center for generating standard sea ice data products from the similar AMSR system onboard the Japanese ADEOS-II satellite. Unfortunately, this satellite failed in late 2003, leaving only a short time series.

Table 5.4. Gridded (level 3) T_B and sea ice products available from the Aqua AMSR-E.

Parameter	Approximate resolution (km)	IFOV (km)	Grid resolution size (km)	Product temporal frequency
Sea ice Concentration (%)	–	–	25.0, 12.5	Daily Asc., Desc., and average
Snow cover depth (cm)	–	–	12.5	5-day average
Sea ice temperature (K)	–	–	25.0	Daily Asc., Desc., and average
T_B (6.925 GHz)	58	74×43	25.0	Daily Asc., Desc., and average
T_B (10.65 GHz)	37	51×30	25.0	Daily Asc., Desc., and average
T_B (18.7 GHz)	21	27×16	25.0, 12.5	Daily Asc., Desc., and average
T_B (23.8 GHz)	21	31×18	25.0, 12.5	Daily Asc., Desc., and average
T_B (36.5 GHz)	11	14×8	25.0, 12.5	Daily Asc., Desc., and average
T_B (89.0 GHz)	5	6×4	25.0, 12.5, 6.25	Daily Asc., Desc., and average

IFOV is Instantaneous Field Of View, and Asc. and Desc. refer to ascending and descending orbits, respectively. For further details, please see ⟨*http://nsidc.org*⟩. After Comiso et al. (2003a).

The following is a brief summary of each algorithm. Comiso et al. (2003a) provided more complete information on theoretical and empirical foundations, as well as preliminary results. Both the T_B and sea ice products are mapped to the standard SSM/I grid, with grid resolutions optimized to take advantage of the enhanced spatial resolution of the AMSR-E while providing continuity with SMMR and SSM/I data. Details of the gridded products, which are available from the NSIDC (⟨*http://nsidc.org*⟩), are given in Table 5.4.

5.9.1.1.3.2 THE AMSR-E BOOTSTRAP BASIC ALGORITHM (BBA) AND AMSR BOOTSTRAP ALGORITHM (ABA) Used to produce 12.5-km products for Antarctica, the BBA is based on a technique described above and by Comiso (1995b). In short, it is based on the calculation of tiepoints for open water and consolidated ice using 19V GHz and 37V GHz (V1937) data, thereby ensuring consistency with historical sea ice products (beginning with SMMR in 1978). Further details are given in Cavalieri and Comiso (2004) and Comiso et al. (2003a). The ABA (Cavalieri and Comiso, 2004; Comiso et al., 2003a), on the other hand, is a modified version that replaces T_B with ε, exploiting the availability of new AMSR-E 6.925-GHz channel data to reduce errors associated with variations in physical temperature T_I (Comiso and Zwally, 1997). Following Zwally et al. (1983), the first step is to compute an initial ice concentration, C_I, corresponding to an observed T_B, on a pixel-by-pixel basis,

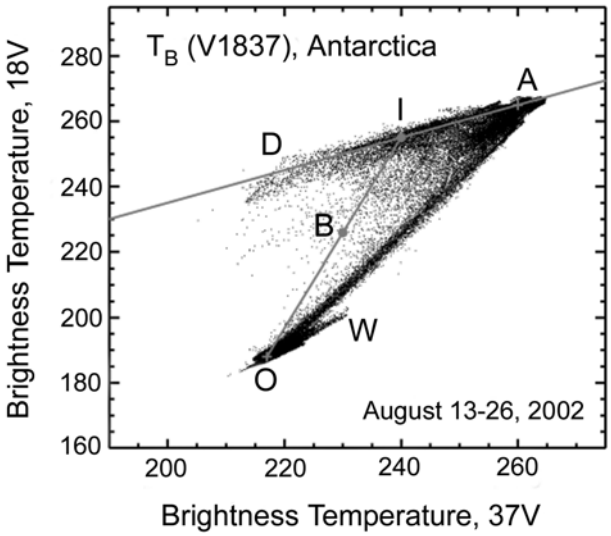

Figure 5.33. Scatterplot of AMSR-E V1937 brightness temperature (T_B) data for the Antarctic for August 13–26, 2002. The cluster of points about line AD represents consolidated (100%) ice, whereas that along OW belongs to open (ice-free) ocean. The ice concentration for any datapoint, here represented by B, is derived from the ratio of OB to OI, where I is the intercept of lines OW and AD. Line AD is determined by applying linear regression to the consolidated ice cluster then adding a small offset, of one standard deviation of the datapoints about the line, to account for some openwater in the 100% ice area. The ratio OB : OI is equal to the solution of (5.31) for ice concentration C (or $\sum_i C_I$).

From Comiso et al. (2003a). Reprinted with permission of the IEEE. © 2005 IEEE.

through the use of 6.925- and 36.5-GHz channel data at vertical polarization (7V and 37V):

$$C_I = (T_B - T_{BO})/(T_{BI} - T_{BO}) \tag{5.32}$$

where T_{BO} and T_{BI} are the T_Bs of ice-free ocean and sea ice, respectively, and atmospheric contributions are included in all terms (and assumed to be negligible). While T_{BO} remains relatively constant for open water within the ice pack, T_{BI} varies spatially with changes in ice ε and T_I. The success of this algorithm, which assumes a linear relationship between the fraction of ice cover and the observed T_B (Figure 5.33), depends on the accurate determination of T_I.

The next step involves calculating the effective emissivity of the surface within each pixel, ε_B, from:

$$\varepsilon_B = \varepsilon_I C_I + \varepsilon_O (1 - C_I) \tag{5.33}$$

where ε_I and ε_O are the emissivities of ice and ice-free open ocean, respectively, and are assumed to be constant. The ice surface physical temperature, T_P, within each pixel is determined by:

$$T_P = T_B(7\text{V})/\varepsilon_B(7\text{V}) \tag{5.34}$$

The surface emissivity at 18.7 and 36.5 GHz for a combination of V and H polarizations can then be derived from:

$$\varepsilon_B(19\mathrm{H}) = T_B(19H)/T_P \tag{5.35}$$

$$\varepsilon_B(19\mathrm{V}) = T_B(19V)/T_P \tag{5.36}$$

$$\varepsilon_B(37\mathrm{H}) = T_B(37H)/T_P \tag{5.37}$$

$$\varepsilon_B(37\mathrm{V}) = T_B(37V)/T_P \tag{5.38}$$

with the assumption that the physical temperature of the ice layer from which measured radiation is emitted is approximately frequency-independent between 7 and 37 GHz, and also equals T_P. Following Comiso (1995b), the tiepoint for a datapoint at B occurs at the intercept point $I(\varepsilon_{1I}, \varepsilon_{2I})$ of the line OB and the 100% ice line AD. The coordinates are calculated by:

$$\varepsilon_{1I} = \frac{(\varepsilon_{1A} - \varepsilon_{1O} - \varepsilon_{2A}S_{AD} + \varepsilon_{2O}S_{OB})S_{OB}}{(S_{OB} - S_{AD}) + \varepsilon_{1O} - S_{OB}\varepsilon_{2O}} \tag{5.39}$$

and

$$\varepsilon_{2I} = \frac{(\varepsilon_{1A} - \varepsilon_{1O} - \varepsilon_{2A}S_{AD} + \varepsilon_{2O}S_{OB})}{(S_{OB} - S_{AD})} \tag{5.40}$$

where S_{AD} and S_{OB} are slopes of lines AD and OB, respectively; $(\varepsilon_{1A}, \varepsilon_{2A})$ is any point along line AD; and $(\varepsilon_{1O}, \varepsilon_{2O})$ represents the reference emissivity of open water. The ice concentration for the datapoint at B is then derived from the ratio of distances OB and OI (see Figure 5.33) and given by:

$$C = \left[\frac{\left\{(\varepsilon_{1B} - \varepsilon_{1O})^2 + (\varepsilon_{2B} - \varepsilon_{2O})^2\right\}}{\left\{(\varepsilon_{2B} - \varepsilon_{2O})^2 + (\varepsilon_{1B} - \varepsilon_{1O})^2\right\}}\right]^{1/2} \tag{5.41}$$

As the initial calculation of emissivity at 6.925 GHz uses an ice concentration that has not been temperature-corrected, the emissivity is now recalculated using the more accurate result from (5.25). The final ice concentration is then estimated from a second iteration, starting with (5.17), and is given at both 12.5- and 25-km resolution. Examples of derived Antarctic ice concentration maps are given in Figure 5.34 (see color section).

5.9.1.1.3.3 THE ENHANCED NASA TEAM (NT2) ALGORITHM With the task of retrieving Arctic ice concentrations from AMSR-E data, the enhanced NT2 algorithm (Markus and Cavalieri, 2000) is based upon the NT algorithm outlined above (Cavalieri et al., 1984; Gloersen and Cavalieri, 1986). This approach is based upon two basic premises (Cavalieri et al., 1984):

- that the difference between H- and V-polarized radiances is typically small for both Arctic first-year and multiyear ice compared with that for the open (ice-free) ocean; and

- that the discrimination between first-year and multiyear ice increases with increasing frequency—i.e., decreasing wavelength.

These characteristics are parameterized in terms of two independent variables—namely, the previously mentioned PR and spectral GR—which are defined by:

$$\mathrm{PR}(\nu) = \frac{(T_B[\nu, V] - T_B[\nu, H])}{(T_B[\nu, V] + T_B[\nu, H])} \tag{5.42}$$

and

$$\mathrm{GR}(\nu_1, \nu_2, p) = \frac{(T_B[\nu_1, p] - T_B[\nu_2, p])}{(T_B[\nu_1, p] + T_B[\nu_2, p])} \tag{5.43}$$

where ν is the AMSR-E frequency in GHz, and p is the polarization. The use of T_B ratios circumvents the need to account for surface temperature variability. Applied extensively to SMMR and SSM/I data, the NT algorithm distinguishes two ice types in both hemispheres—i.e., first-year and multiyear ice in the Arctic, and types A and B in the Antarctic, requiring hemisphere-specific tiepoints (Gloersen et al., 1992). The NT2 algorithm (Markus and Cavalieri, 2000) was developed to reduce ice concentration biases resulting from snow layering and surface glaze effects and from the presence of thin ice types, as reported for the NT algorithm by Comiso et al. (1997). The NT2 algorithm addresses this problem by incorporating 89-GHz data, as these are less affected by variability in surface conditions than are 19-GHz data (Mätzler et al., 1984; Svendsen et al., 1987). The thin ice bias is reduced by resolving a third ice type, and also by using GR(37V/19V) and only two ice types (following Cavalieri, 1994). Due to the enhanced sensitivity of 89-GHz channels to variable atmospheric effects, the latter are quantified by computing T_Bs for each channel using a forward atmospheric radiative transfer model (Kummerow, 1993) for first-year ice, multiyear ice, total ice concentration, and openwater. By using the radiative transfer model, the algorithm calculates T_Bs for each channel and generates matrices of values containing all combinations of ice concentration (i.e., 0–100%) and atmospheric conditions. PRs and GRs are calculated from the observed and modeled T_Bs. The ice concentration for a given pixel is then determined where the difference between an observed and a modeled ratio is smallest (Figure 5.35). The algorithm eliminates spurious sea ice concentration retrievals over open ocean by employing weather filters originally developed for use with SSM/I data (Cavalieri et al., 1995). Ice concentrations for image pixels with GR(37/19) values greater than 0.05 and GR(22/19) values greater than 0.045 are set to zero. An example ice concentration image for the Arctic is shown in Figure 5.36 (see color section). For further algorithm details, see Cavalieri and Comiso (2004) and Comiso et al. (2003a).

The radiance ratios used in the current NT2 algorithm are $\mathrm{PR}_R(18.7)$, $\mathrm{PR}_R(89.0)$, GR(89.0, 18.7, H-pol), and GR(89.0, 18.7, V-pol), where subscript R refers to a rotation of axes (Cavalieri and Comiso, 2000; Comiso et al., 2003a). In short, this rotation is carried out in the NT algorithm PR(18.7)–GR(36.5, 18.7, V-pol) domain. The axes are rotated through an angle ϕ until the ice-type lines—i.e., the A–B line for Antarctica and the FY–MY ice line for the Arctic–run parallel

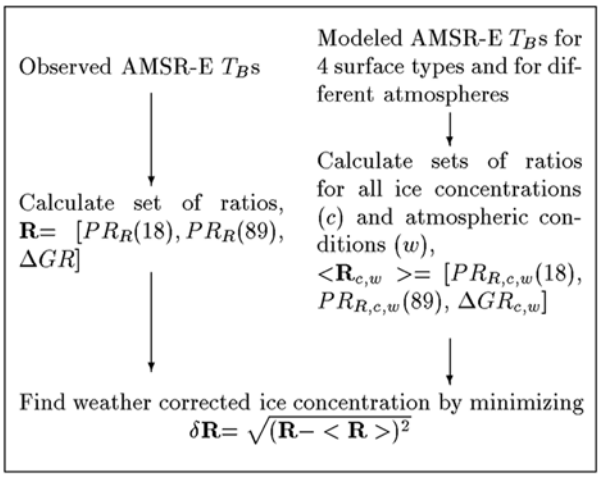

Figure 5.35. Flowchart of the NT2 algorithm.

From Markus and Dokken (2002). Reprinted with permission of the IEEE. © 2005 IEEE.

to the GR axis. Details of subsequent steps involved are laid out in Comiso et al. (2003a). Since the inception of the NT2 algorithm in Markus and Cavalieri (2000), modifications have been made in an attempt to account for the low-concentration bias associated with the presence of thin ice types, following Cavalieri (1994). Additionally, the NT2 algorithm employs a pair of weather filters (Cavalieri et al., 1995) to eliminate or greatly reduce spurious ice concentration retrievals over open ocean regions. Again, see Cavalieri and Comiso (2004) and Comiso et al. (2003a) for further algorithm details.

Daily level-2B and level-3 AMSR-E products have been available from the NSIDC since February 18, 2004. Weekly, 5-day, and monthly products have also been available since March and April 2004 (Cavalieri and Comiso, 2004). For more information and instructions for ordering these and other AMSR-E data products, including level-1A raw observation counts and level-2A brightness temperatures, please see ⟨*http://nsidc.org/data/amsr/*⟩. The NSIDC also distributes AMSR-E validation data via ⟨*http://nsidc.org/data/amsr_validation*⟩. Note that ADEOS-II AMSR data and products are available from the JAXA Earth Observation Center via their excellent website at ⟨*http://sharaku.eorc.jaxa.jp/AMSR/index_e.htm*⟩, together with documentation (including algorithm descriptions and a user's handbook—NASDA, 2003) and software tools.

The common error sources outlined above for SMMR and SSM/I ice concentration retrievals still apply. An assessment is underway of the uncertainty of AMSR-E sea ice products, within a NASA-coordinated international validation effort in both polar regions (⟨*http://eospso.gsfc.nasa.gov/validation*⟩; Steffen, 2003). A major challenge in the validation of satellite data is to obtain adequate *in situ* sampling of the geophysical variable(s) of interest that exhibit temporal and spatial variance at the subpixel scale of the satellite sensor. High-resolution

satellite data have an important role to play by extending limited *in situ* measurements. The overall aim for AMSR-E concentration retrievals is to achieve an accuracy of 4% during the cold dry winter months and 10% during late spring and summer (Cavalieri et al., 2002a), the lower level representing the approximate precision (Comiso et al., 2003a). For further discussion of important issues relating to error analysis and sensitivity studies, please refer to Comiso (2002b).

Markus and Dokken (2002) took a closer look at the impact of surface melt on Arctic ice concentration retrieval accuracy in the summer using the NT2 algorithm. Although a dry snow cover is largely transparent at frequencies of <37 GHz and likely has a minimal impact on ice concentration retrieval accuracies (Lohanick, 1990), this is not the case when it becomes wet—i.e., melts. We saw in Section 5.7 that when snow contains $\sim$3% liquid water by volume, it becomes opaque and surface emissivity approaches unity—i.e., it acts radiometrically like a blackbody, leading to a dramatic increase in observed T_Bs at all frequencies and an overestimate of ice concentration. The subsequent formation of meltponds has the opposite effect, leading to ice concentration underestimates, as the microwave emissivity of meltponds resembles that of ice-free ocean (Comiso and Kwok, 1996; Fetterer and Untersteiner, 1998a, b). These low-albedo features evolve through the season (Eicken, 2003a), can cyclically freeze and melt on semi-diurnal to diurnal timescales, and eventually melt downwards through the ice to either drain the surface or cause flooding by seawater (the mapping of meltponds from space is examined in Section 5.9.15). The overall impact of these physical changes in reducing the stability of the frequency- and polarization-dependent microwave emissivity of Arctic first-year ice under a range of summertime ice conditions is apparent in Table 5.5. Encouragingly, however, Markus and Dokken (2002) showed that the new NT2 algorithm can produce usable sea ice concentrations during the summer in the Arctic, and therefore represents an important improvement over the NT algorithm. Its ability to compensate for low-concentration biases caused by surface melt effects lies with its incorporation of 85-GHz data. This additional information enables the definition of a third ice type representing inhomogeneities and layering within the snow cover, to which the 19-GHz H-channel, in particular, is sensitive. It has been validated using ice concentrations derived from ERS and Radarsat SAR data convolved to the SSM/I antenna pattern. For an examination of error sources specific to Antarctica, please see Comiso and Steffen (2001) and Comiso et al. (1992).

Mention should be made of a secondary passive-microwave source of ice extent (and concentration data)—i.e., the NOAA's AMSU. This sensor, which was launched on NOAA-15 in May 1998 and on NOAA-16 in September 2000, contains 20 channels spread across two separate sensor packages: AMSU-A (15 channels, 23–89 GHz) and AMSU-B (5 channels, 89–183 GHz), with a resolution ranging from 16 to 48 km at nadir. Unlike the AMSR sensors, which operate with a conical scan geometry, AMSU has a cross-track scan geometry across a 2,200-km swathwidth. It also lacks polarization. Although the main purpose of this sensor is the operational measurement of tropospheric variables (Ferraro et al., 2002; Grody et al., 2001), broad-scale sea ice information is a useful by-product. These

Table 5.5. Microwave emissivities measured *in situ* for surface conditions in summer, measured in the Arctic as a function of microwave frequency and polarization for channels equivalent to the DMSP SSM/I, ADEOS-II AMSR, and EOS Aqua AMSR-E.

Surface Type	19V	19H	37V	37H	85V	85H
Winter first-year ice	0.936	0.905	0.932	0.903	0.928	0.900
Late spring[1]	0.950	0.905	0.920	0.845	0.890	0.760
Early summer[2]	0.950	0.905	0.950	0.920	0.945	0.935
Midsummer[3]	0.960	0.895	0.960	0.920	0.955	0.935
Late summer[4]	0.960	0.910	0.965	0.930	0.975	0.950
Rainy weather[5]	0.950	0.870	0.950	0.895	0.950	0.935
Moist snow[6]	0.955	0.895	0.960	0.910	0.955	0.940
Frozen crust in snow	0.960	0.950	0.925	0.910	0.740	0.705
Frozen meltpond	0.969	0.877	0.970	0.970	0.876	0.818

[1] The temperature of the ice and snow is ~0°C, the snow is moist, and there is a superimposed ice layer (i.e., refrozen meltwater) at the snow/ice interface.
[2] The air temperature approximates 0°C, and the snow cover is wet (~4% liquid water by volume).
[3] Considerable snowmelt has occurred, creating a slush layer.
[4] Extensive meltponds, and an icy crust on elevated snow surfaces.
[5] Saturation in the upper part of the snowpack.
[6] ~5% liquid water by volume.

From Markus and Dokken (2002), compiled from data collected by El Naggar et al. (1998) and Onstott et al. (1987).

data are produced from NOAA-15, -16 and -17 satellite data by the NOAA Microwave Surface and Precipitation Products System (MSPPS) in near-real time, and are available from the NOAA National Environmental Satellite, Data, and Information Service (NESDIS) at: ⟨*http://www.osdpd.noaa.gov/PSB/IMAGES/MSPPS_day2.html*⟩ (composites) and ⟨*http://orbit-net.nesdis.noaa.gov/arad2/MSPPS/index.html*⟩ (swath data). Details of the operational AMSU sea ice concentration algorithm, which uses 23.8-, 31.4-, and 50-GHz channel data, are given at the latter. The estimated accuracy (r.m.s.) is 15%. Measurements will continue with the launch of AMSU A-1/-2 onboard ESA's MetOp-1 satellite in 2005. Operating at frequencies equivalent to the SSM/I and AMSR-E minus the 89-Ghz channels, WindSat provides another alternative source of sea ice concentration data, but with an additional polarimetric capability (see Section 5.8.1). The advantage of this capability has yet to be determined.

5.9.1.1.4 Anomalies and trends in ice concentration

Ice concentration data derived from passive-microwave data are well suited to the analysis of anomalies and trends, and as such form the backbone of many modern studies of large-scale variability and change in polar oceans. The key issue of internal consistency in the different datasets making up the passive-microwave time series has been investigated by Stroeve (1998), Stroeve and Smith (2001), and Stroeve et al. (1998). With this in mind, considerable effort has been put into creating more seamless, internally consistent time series from multi-sensor datasets—e.g., from

the Nimbus 7 SMMR and DMSP SSM/I sensors (Cavalieri et al., 1999a). These data are available from the NSIDC.

Ice concentration anomaly maps are a very useful way of analysing and displaying change/variability. A recent example, taken from Comiso et al. (2003b), is shown in Figure 5.37 (see color section), depicting monthly anomalies in Arctic ice concentration for each September from 1981 to 1999 compared with the overall mean for all Septembers from 1981 to 1999. Each anomaly map was derived by taking the difference of each monthly mean and the overall mean. Monthly means are preferred to daily data due to the high degree of variability apparent in the latter in response to the synoptic-scale passage of cyclones. As can be seen, this tool gives excellent insight into interannual variability, and is particularly powerful when combined with other data sources. Comiso et al. (2003b) in fact combined these data with *in situ* hydrographic data, modeled wind fields from the European Center for Medium-Range Weather Forecasts (ECMWF), drifting buoys, and AVHRR-derived skin surface temperature maps (see Section 5.9.11.1) to detect large-scale change in the Arctic. This approach, of data fusion, is being taken by an increasing number of studies as these improved datasets become increasingly available. In this example, it enabled observed decreases in summer sea ice to be tied in with changes in surface temperature, atmospheric circulation, and upper-ocean temperature. An Antarctic example, constructed for monthly means for July over the period 1979–1998, is given in Comiso (2000).

The reader is encouraged to access an excellent new tool on the NSIDC website—namely, an index of monthly trends and anomalies in both sea ice concentration and extent (Fetterer and Knowles, 2002), which is accessible via ⟨*http://nsidc.org/data/seaice_index/*⟩ and updated on an ongoing basis. This site also provides documentation to help users comprehend trends in the context of natural variability. Ice concentration anomaly images are again produced by subtracting monthly mean concentration images from an image of the mean for the month in question. Both are derived from the standard NT dataset (Cavalieri et al., 2003b). An example, from September 2003, is shown in Figure 5.38 (see color section). The color bar (in percent) indicates how much the ice concentration for the month differs from the mean calculated for that month over the 1988–2000 time period, while the number gives the total anomaly for the entire hemispheric sea ice cover. It should be noted that an area may exhibit a positive anomaly for a given month while at the same time having a negative trend in concentration over time (Fetterer and Knowles, 2002).

Images of trends in ice concentration are also produced by the NSIDC Sea Ice Index to show how ice concentration has changed for a given month over the period from July 1987 to the present month, using data from the NT dataset (Cavalieri et al., 2003b) extended beyond 2000 with the NRTSI dataset (Cavalieri et al., 2002b). This is achieved by performing a least squares regression on the ice concentration time series on a pixel-by-pixel basis. Pixels with zero concentration are omitted. The slope of the linear regression gives the trend in concentration for that pixel, with a 95% confidence interval being used for significance—i.e., the null hypothesis that the slope of the fit line is zero is rejected with 95% confidence. Trends are typically

shown as a percentage change in concentration per decade. The result for September 2003 is shown in Figures 5.38b and 38d. Assumptions and limitations inherent to linear regression for trend analysis were evaluated by Fetterer and Knowles (2002). One issue relates to the fact that trend results can vary depending on the start and end points of the dataset used. Another is the difficulty in interpreting trends and anomalies during summer in the Arctic in particular, when significant ice concentration underestimates occur due to extensive surface melt. Fetterer and Knowles (2002) stressed that it is currently difficult to draw hard and fast conclusions about future patterns of ice concentration based upon the short time series of satellite-derived trends. It should be stated, however, that such data play a key role in assessing the performance of models, and that satellite passive-microwave coverage is confirmed for the next 15 years at least.

Such techniques are being increasingly applied to the study of large-scale patterns in sea ice distribution in response to cyclical variability and changes in patterns of atmospheric and oceanic forcing. In their analysis of the Antarctic passive-microwave sea ice record, Kwok and Comiso (2002a), for example, highlighted strong associations between sea ice anomalies, the Southern Oscillation (van Loon and Shea, 1985), and climate in the Southern Ocean (Figure 5.39, see color section). Gloersen and Mernicky (1998) applied a spectral analysis to ice concentration data from the interior Antarctic pack, using discrete Fourier analysis of a shorter satellite data time series filtered by a multiple-window technique. This resulted in phase distributions of two components observed in the El Niño–Southern Oscillation (ENSO) signal, with periods of ~2.4 and 4.2 years suggesting a propagating wave in the interior pack. See also Gloersen (1995), and a similar study in the Arctic by Gloersen et al. (1996). Watkins and Simmonds (2000) showed that Antarctic sea ice open-water area, extent, and ice area increased over the period 1987–96. They suggested that these changes result from modifications in the position and depth of the circumpolar trough, which could be linked to the major ENSO event of 1990–1995. In their analysis of SMMR and SSM/I data in Antarctica, Liu et al. (2004a) observed a major increase (decrease) in ice concentration (extent) in the central Pacific (Bellingshausen and N. Weddell Seas) sector of ~4–10% per decade over the period 1979–2002. Comparison with atmospheric data from the National Center for Environmental Prediction/National Center for Atmospheric Research (NCEP/NCAR) Reanalysis Dataset (Kalnay et al., 1996) showed a linkage between this change and polarities of the Antarctic Oscillation and ENSO. These are but a few of an ever-expanding corpus of multi-disciplinary studies based upon analysis of the key satellite passive-microwave dataset. Together, they are providing unique insight into extraordinary variability and change. Information on changes in sea ice extent are covered in Section 5.9.2.

5.9.1.2 Synthetic Aperture Radar (SAR) techniques

With their all-weather, day–night capability, satellite SARs are also used to measure ice concentration, but generally not in the operational sense as is the case with passive-microwave radiometers. With a high spatial resolution—e.g., 25 m for

ERS-2 (5.3 GHz, VV-pol)—individual leads can be resolved. As a result, SAR yields more realistic estimates of the fraction of open water and thin ice contained in leads than passive-microwave radiometers (Kwok, 2002a, b, c). As such, it has a major role to play in the validation of passive-microwave sea ice products. Its coverage is, however, limited to a narrow swath ranging from 75 km for JERS-1 to ~500 km for Radarsat in ScanSAR Wide mode. Temporal coverage is therefore sparse compared with that of current passive-microwave systems, which offer complete coverage poleward of 60° latitude on a daily basis. The revisit capability of spaceborne SARs has improved with the recent emergence of systems with the increased flexibility of programmable multi-imaging modes—e.g., Radarsat-1, Envisat-1 and ALOS. In addition, Radarsat-2 has the ability to routinely swath from left- to right-looking and vice versa (van der Sanden and Ross, 2001).

The ability of SARs to accurately discriminate between sea ice and open water is a function of operating frequency and polarization, radar incidence angle, and surface wind speed as they determine the backscatter contrast between ice and water (Nghiem and Bertoia, 2001; Shuchman and Flett, 2003). The automated retrieval of ice concentration from SAR data, and potentially single (like) polarization channels, is complicated by wind-roughening of ice-free ocean, which results in an increase in radar backscatter and a signature similar to that of an ice cover in data acquired by single-channel SARs (Furevik et al., 2002; Livingstone, 1994). Ocean clutter is generally greater at steeper incidence angles (van der Sanden and Ross, 2001). Clutter refers to random background noise in a radar image due to scattering from a surface with homogeneous roughness on a scale larger than the signal wavelength. Once again, the accuracy of SAR-derived ice concentration retrievals also drops off during melt periods (Cavalieri et al., 1990). Issues relating to the retrieval of ice concentrations from SAR data in summer are discussed by Kwok et al. (1996).

Under freezing conditions, openings and closings of leads can be detected and monitored from fine-scale sea ice motion fields derived from time-sequential SAR data. Such products, which rely upon the accurate co-registration of the image series, are routinely available for the central Arctic from the RGPS, which can be accessed at: ⟨*http://www.gi.alaska.edu/%7Ergps/index.htm*⟩ *and* ⟨*http://www.radar.jpl.nasa.gov/rgps/radarsat.html*⟩. Ice concentration can be computed from these data as the ratio of the difference between (i) the area and integrated openings within it, and (ii) the total area. The ice motion products themselves are evaluated in Section 5.9.5. Similar coverage is lacking outside the RGPS data acquisition mask—i.e., no RGPS-type system currently exists in Antarctica. The retrieval of ice concentration from SAR will be evaluated further in Section 5.9.4 on polynyas.

Other techniques are required where fewer images are available. One derives ice concentration (and extent) from SAR images using radiometric analysis of calibrated backscatter (σ^0) values. Dokken et al. (2000a), for example, developed an automated SAR ice discrimination algorithm known as Sica that is based on three different techniques—namely, (i) a local threshold, (ii) a mean ratio, and (iii) a wavelet method. Wavelet analysis is an efficient bandpass filter that provides an effective

means of separating processes at various scales and of showing their relative location/phase information (Liu and Peng, 1993a, 1998; Liu et al., 1997a, b; Ruskai et al., 1992). The choice of method used by Dokken et al. (2000a) depends on the SAR sensor polarization and wind conditions at the time of image acquisition. In the unsupervised, dynamic local threshold technique, pixels containing sea ice are distinguished by utilizing local thresholds between ice-covered and ice-free ocean. The mean ratio method discriminates sea ice coverage over a large area by relating measured σ^0 values to typical sea ice and openwater values. For the wavelet technique (see Section 5.9.5), ice coverage is derived through the detection and linking of edges around floes or assemblages of floes. According to Dokken et al. (2000a), Sica ice concentration retrievals agree with *in situ* observations to within $\pm 3\%$ in the Arctic. Another algorithm is described by Kern et al. (2003).

Another technique is a binary analysis scheme that discriminates open water from sea ice (Holt and Martin, 2001). This is based upon the incidence angle dependence of ice and ice-free ocean σ^0, and the variability of the latter with wind speed (see Section 5.9.7 for an explanation). The algorithm allows for linear adjustment of the σ^0 threshold between the two surfaces as a function of incidence angle in 0.1-dB steps (Comiso and Kwok, 1996). In their study in the western Arctic, Holt and Martin (2001) estimated the accuracy of ice–open-water separation to be $\sim 10\%$. The technique performed best under strong winds, when the backscatter of wind-roughened leads is uniformly brighter than that of ice. It is less successful under low wind speed conditions, and also in the MIZ, where highly variable and complex ice conditions—e.g., brash, interstitial slush and grease ice—result in a broad range of often-overlapping backscatter values for ocean and ice (Holt and Martin, 2001; Sandven et al., 1999). In the interior Antarctic pack, wind-roughened meltponds contribute to the uncertainty in summer (Comiso and Kwok, 1996). Other sources of uncertainty relate to the presence of sub-pixel resolution (<100 m) features, and the misclassification of strong returns from floe edges as open water (Holt and Martin, 2001). Again, this scheme has yet to be applied to the Antarctic sea ice zone. These examples illustrate the difficulty in implementing fully automated ice concentration algorithms using SAR data.

Polarimetric SAR shows great promise as a means of deriving improved ice–water discrimination (see Section 5.9.7.3.2). Enhanced ice–water contrast is possible using cross-polarization channel data (at HV) and the co-polarization ratio between HH and VV channel data from the new spaceborne polarimetric SARs (Scheuchl et al., 2001; van der Sanden and Ross, 2001). The enhanced contrast is based upon the fact that the cross-polarization backscatter response of open ocean is lower and relatively independent of wind-induced surface roughening (van der Sanden and Ross, 2001). Multi- and fully-polarimetric data are readily available from the advanced new SARs onboard Envisat-1, Radarsat-2, ALOS and TerraSAR-X and -L. For Radarsat-2, for example, the SDP and SSP modes will enable acquisition of cross-polarization data in all currently available Radarsat-1 modes, including ScanSAR (van der Sanden and Ross, 2001). Here, SDP refers to Selective Dual Polarization (HH + HV or VV + VH) while SSP is Selective Single Polarization

(HH or HV or VV or VH). The co-polarization ratio between the HH and VV channels has similar capabilities, but will only be acquired in narrow-swath fully polarimetric modes (see Section 5.9.7.3.2).

5.9.1.3 Visible to Thermal Infrared (TIR) techniques

Cloud-free visible to TIR data represent a secondary source of ice concentration information. Concentrations have been retrieved from both high-resolution data—e.g., from Landsat (Comiso and Steffen, 2001; Comiso and Zwally, 1982; Comiso et al., 1997; Steffen and Schweiger, 1990)—and at medium resolution—e.g., NOAA AVHRR (Emery et al., 1991a, 1994; Ishikawa et al., 1996; Kern et al., 2003; Massom and Comiso, 1994; Steffen, 1995; Zibordi et al., 1995)—DMSP OLS (Comiso and Steffen, 2001), and MODIS (Drue and Heinemann, 2004; Serreze et al., 2003). While most techniques are manual, automated algorithms have also been developed—e.g., an expert systems technique by Williams et al. (2002), and a neural networks scheme by McIntire and Simpson (2002), the latter applied to Chinese FY-1C satellite 1.6-μm data. Obvious limitations are cloud and darkness (for optical channel techniques). Refer to Chapter 4 and Section 5.8.2.4.2 for information on cloud-masking techniques.

Techniques used to derive ice concentration from AVHRR data generally exploit the radiance measured by channels 1 and 2 (wavelengths 0.58–0.68 and 0.725–1.10 μm, respectively), and/or the TIR brightness temperatures (T_{IR}) measured at channel 4 (10.3–11.3 μm). Under daylight conditions, channel-2 data are most useful due to the larger contrast in the reflectances of sea ice and openwater in the near-IR compared with the visible (Ito, 1985; Steffen, 1995). Two methods have been developed to derive ice concentration from channel-2 data on a pixel-by-pixel basis: (i) a tiepoint method relating the brightness value to a ratio of two surface types—e.g., ice and open water; and (ii) a threshold/maximum-likelihood classifier technique relating average brightness to a given ice type when more ice types are present (Steffen, 1995; Steffen and Schweiger, 1991). Developed for application to Landsat imagery (Comiso and Zwally, 1982; Steffen and Schweiger, 1991), the tiepoint procedure is based on the notion that only white ice and openwater are present in scenes from late spring into summer (Comiso and Zwally, 1982), and that brightness values in-between the end points (determined in training areas) represent ice concentrations at sub-resolution. Ice concentration C_I (in percent) is then given by:

$$C_I = [(Bx - B_{OW})/(B_{WI} - B_{OW})] \cdot 100 \tag{5.44}$$

where Bx is the brightness value of the pixel (representing ice concentration), B_{OW} is the value for openwater, and B_{WI} is the value for white ice minus one standard deviation. Tiepoints were located manually using training areas for open water and white ice floes. An example of a classified Landsat Multi Spectral Scanner (MSS) scene is given in Figure 5.40 (see color section).

The threshold method uses brightness value ranges determined from training areas for open water and different ice types—e.g., open water/nilas, gray/gray–white

ice, and white ice (WMO, 1970, Steffen, 1986). Ice concentration is then estimated as the sum of all ice types minus open water. Compared with the tiepoint method, this approach is limited by its inability to account for subresolution-scale leads and icefloes (Key et al., 1993; Steffen, 1995). According to Steffen (1995), extensive use of AVHRR and similar data for ice concentration retrieval is also limited by the difficulty in discriminating open water from thin ice, due in part to the effects of atmospheric water vapor and ice crystals in the vicinity of leads and polynyas in biasing radiance measurements from space. Nonetheless, these techniques provide a useful means of validating poorer resolution passive-microwave retrievals (Steffen and Schweiger, 1990).

TIR data are typically used under freezing conditions—i.e., during the winter and spring—when a high thermal contrast generally exists between ice and open ocean. Channel-4 data are generally used in preference to channel-5 (11.5–12.5 μm) due to their lower sensitivity to atmospheric water vapor effects (Kidder and Vonder Haar, 1995). Ice concentrations are generally estimated from tiepoints for openwater and consolidated ice—i.e., using an approach similar to that outlined above (Burns et al., 1992; Emery et al., 1991a, 1994). The processing sequence used to determine the tiepoints is laid out in Kern et al. (2003), and involves:

- the generation of maps of albedo from channel-1 and -2 data and brightness temperature from channel-4 data, using satellite-specific prelaunch slopes and intercept values and conversion coefficients provided by NOAA (Kidwell, 2000);
- cloud masking;
- identification of gray or gray–white ice (close to regions of openwater) in the channel-1 map, taking the average value of the channel-4 T_{IR} as the consolidated ice tiepoint $T_{IR,ic}$;
- identification of open water (in a region close to the ice edge) in the channel-1 map, taking the average value of the channel-4 T_{IR} as the open-water tiepoint $T_{IR,OW}$.

Ice concentration C_{AVHRR} is then calculated from the tiepoints by:

$$C_{AVHRR} = 100\% \text{ for } T_{IR} < T_{IR,ic} \tag{5.45}$$

$$C_{AVHRR} = \frac{T_{IR} - T_{IR,OW}}{T_{IR,ic} - T_{IR,OW}} \tag{5.46}$$

$$T_{IR,ic} \leq T_{IR} \leq T_{IR,OW} \tag{5.47}$$

$$C_{AVHRR} = 0\% \text{ for } T_{IR} > T_{IR,OW} \tag{5.48}$$

Certain limitations are inherent to this technique. One is due to the difficulty of masking all clouds and sub-pixel cloud (this problem applies to all techniques). Another relates to the lack of contrast between thermal signatures—i.e., surface temperatures, of ice and water when the air temperature approximates −1.8°C. This is a major problem during the melt season, but can occur at other times of the year in marginal Arctic seas and throughout much of the Antarctic pack (Massom et al., 1997). A further limitation again relates to the fact that sub-pixel

distributions of ice and open water cannot be resolved (Kern et al., 2003). Issues relating to the resolution of lead fraction with AVHRR data are discussed by Fetterer and Hawkins (1991), Key et al. (1994b), Lindsay and Rothrock (1994a, 1995), and Stone and Key (1993). A similar technique has been put forward by Ishikawa et al. (1996).

Improved ice concentration estimates are possible using MODIS data, by virtue of their higher spatial, spectral, and radiometric resolutions and improved calibration. Serreze et al. (2003) used MODIS in combination with SSM/I to examine the anomalously low Arctic sea ice extent and area in September 2002. Cloud-free images are shown in Figure 5.41, with computed ice concentrations from both the MODIS and coincident NRTSI data given. The MODIS algorithm used by Serreze et al. (2003) divides a bimodal brightness histogram into two

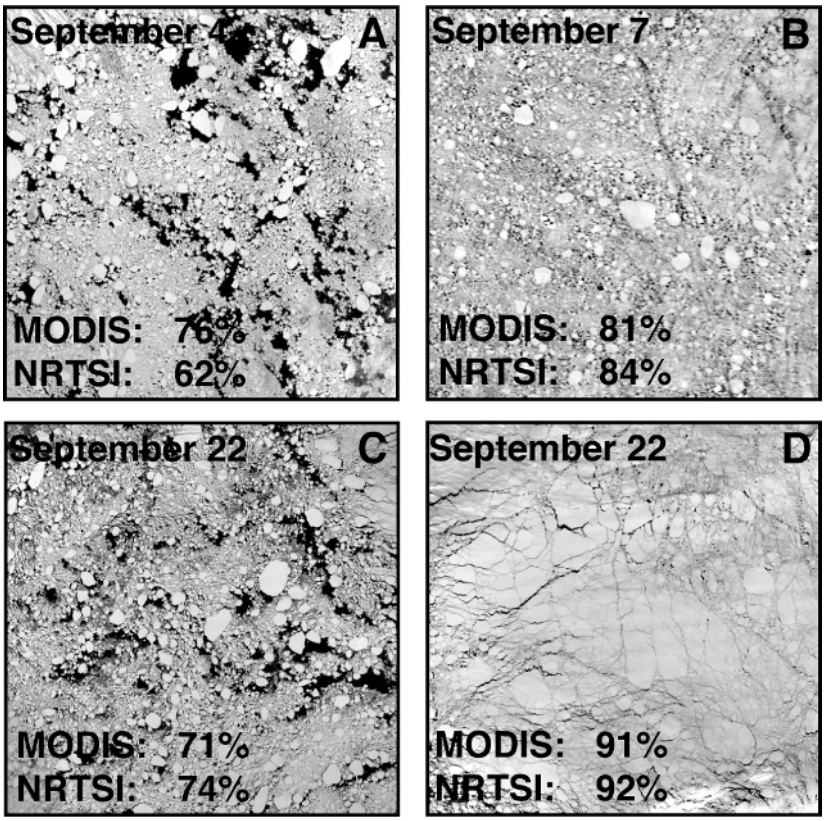

Figure 5.41. MODIS sub-scene images and ice concentrations compared with passive-microwave (NRTSI) derived values for the same area of the central Arctic Ocean and day in 2002 (see the next section). Each scene is 200 km by 200 km. These boxes correspond to the four boxes in the SSM/I image in Figure 5.47 (see color section).

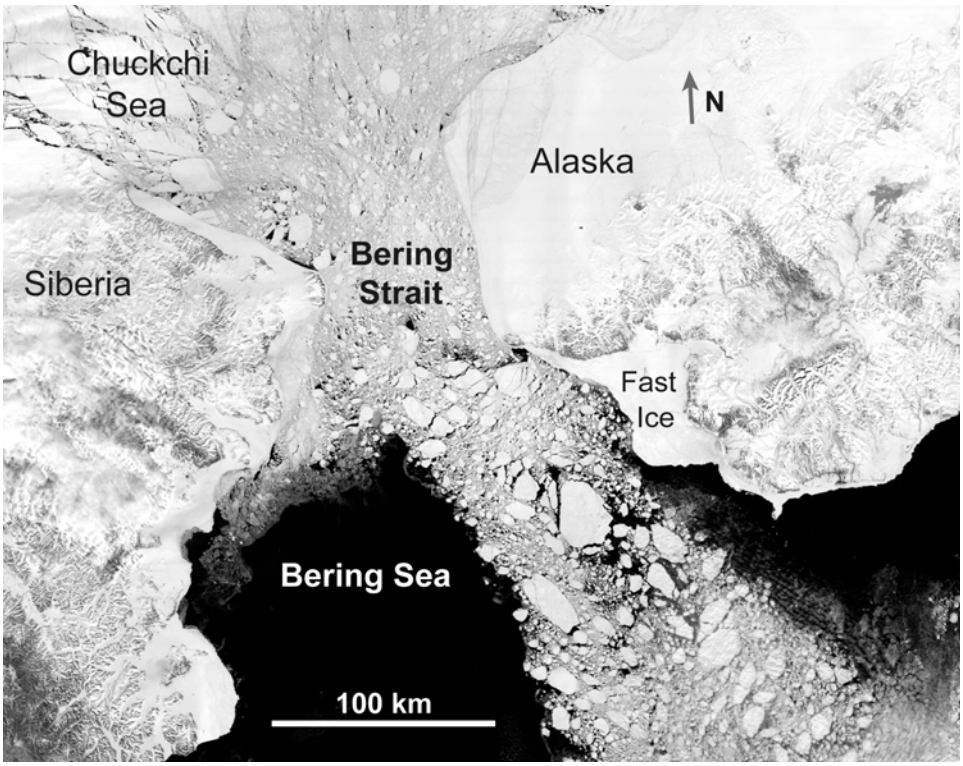

Figure 5.42. A cloud-free MODIS image of the Bering Sea, Bering Strait, and Chukchi Sea (southern Arctic Ocean) acquired on May 7, 2000. The image was generated from MODIS band 2 (0.85 μm) data at a 250-m spatial resolution. The detailed structure of the pack is apparent, with large floes and leads resolved. Ice flow is from north to south through the shallow Bering Strait (water depth 30–50 m). The Bering Sea and Strait are named after the Danish-born Russian explorer Vitus Bering, who crossed the strait in 1728.

Image courtesy of George Riggs (NASA Goddard Space Flight Center), and NASA.

classes—namely, open water and floes—and estimates the ice fraction contribution of mixed pixels by their intermediate brightness. Such techniques take advantage of the improved spatial resolution of MODIS, enabling more reliable estimates of lead fractions than is possible with the AVHRR. The algorithm of Drue and Heinemann (2004) uses surface temperature from MODIS data to derive high-resolution maps of ice concentration. Initial comparison of results with coincident aircraft observations from the Arctic suggests that ice concentration can be measured by this technique to an accuracy of about $\pm 10\%$. When not cloud-affected (and the visible to near IR channels darkness-affected), the data quality of MODIS is superb (Figure 5.42). Moreover, image navigation is significantly better than is possible with the AVHRR, which has a location error of approximately one to several kilometers,

the latter away from coastlines (Rosborough et al., 1994). Limitations are similar to those of the AVHRR, outlined above.

5.9.2 Ice extent and ice edge characteristics

Ice extent is widely viewed as a primary indicator of variability and change in atmospheric and oceanic circulation patterns, possibly related to global warming. It also represents a fundamental measure of the area of the ocean that is modified by sea ice in the manner described in Section 5.6, and is a key parameter within models. Ice edge location is also of major ecological significance, with the MIZ and adjacent ocean having long been recognized as a region of concentrated biological activity at all trophic levels (Ainley and Jacobs, 1981; Fraser and Ainley, 1986; Ribic et al., 1991; Smith and Nelson, 1986). Nihashi and Ohshima (2001) further speculate that interannual variability in sea ice extent (and concentration and thickness) can impact annual heat storage in the ocean, and as such will affect the patterns of ice advance and retreat in subsequent seasons and years (see also Comiso and Gordon, 1998). Routine daily estimates of sea ice extent are derived from passive-microwave-derived sea ice concentration data and, increasingly, from radar scatterometer data.

5.9.2.1 Passive microwave analyses

For the passive-microwave data, ice extent is the area within a specified minimum concentration, which is generally taken to be 15% (Cavalieri et al., 1991). Total ice extent is derived by summing the number of pixels with an ice concentration of at least 15% multiplied by the area per pixel. These parameters in turn form the basis of important trend and variability analyses of sea ice. Daily and monthly total sea ice extent and total ice-covered area data from 1978 onwards (SMMR and SSM/I data) are available from the NSIDC (⟨*http://nsidc.org/data/smmr_ssmi_ancillary/area_extent.html*⟩). Monthly mean data in this case are derived from monthly mean rather than daily ice concentration data, due to the high variability in ice edge behavior over short time periods. An example, showing annual minimum and maximum sea ice extents from both the Arctic and Antarctic in 1992, is shown in Figure 5.43 (see color section). Also available is a merged dataset of ESMR, SMMR, and SSM/I ice extent, covering the period from 1972 for the Arctic and 1973 for the Antarctic. In this case, the temporal gap between the demise of ESMR (1976) and the launch of SMMR (1978) is filled by sea ice climatological data based on weekly operational ice charts from the US National/Navy Ice Center for the Arctic (Dedrick et al., 2001) and a weekly ice extent time series for the Antarctic (Ropelewski, 1983).

Analysis of Antarctic passive-microwave, satellite-tracked buoy and meteorological data combined has shown that ice edge behavior can be divided into three phases: (i) a growth or ice advance phase (in autumn and winter), with patterns determined by climatological air temperature, wind, and ocean circulation regimes; (ii) an equilibrium phase around maximum ice extent, containing small episodes of advance and retreat; and (iii) a retreat/decay phase (in late spring and summer) (Massom, 1992). In an analysis of a full annual cycle of ice advance and

retreat in the Weddell Sea using Nimbus-7 SMMR ice concentration data combined with drifting buoy data, Massom (1992) showed that the regional advance and decay phases are rapid and relatively short, while the intervening equilibrium phase is prolonged. In other regions, the ice edge regime is largely thermodynamically controlled, resulting in relatively long advance and retreat phases separated by a short equilibrium phase (Allison et al., 2001). By comparing ice drift rates from the buoys with satellite passive-microwave data, Massom (1992) showed that ice edge advance in the Weddell Sea in autumn occurred largely by *in situ* freezing (in 1990). In other regions and at other times, ice dynamics plays a leading role in driving ice edge advance and maintaining ice edge location. As we will see, these patterns exhibit considerable interannual variability.

An alternative approach is to derive ice extent from T_B data rather than the ice concentration product. Hunewinkel et al. (1998), for example, developed a method to retrieve ice edge location from the 37- and 85-GHz channels of the SSM/I at an enhanced resolution. Errors in ice edge location were shown to be <5 km on average by comparison with high-resolution IR data. Martin and Drucker (1997) further showed that ice edge location is sensitive to the polarization ratio PR at 19 GHz:

$$PR = \frac{19V - 19H}{19V + 19H} \tag{5.49}$$

Holt and Martin (2001) applied this technique to a study of the impact of a storm on the outer margins of the sea ice covers of the Beaufort, Chukchi and East Siberian Seas in summer. Whereas accuracies in ice concentration methods diminish in summer due to surface melt effects (Steffen and Schweiger, 1991), PR is sensitive to the contrast between sea ice and open ocean and may provide a more accurate ice edge location. Holt and Martin (2001) defined the ice edge as a threshold where $PR = 0.16$, where sea ice values are <0.16 and open ocean values are >0.16. The disadvantage of this approach is the lower resolution at 19 GHz—i.e., 50 km.

The advent of higher resolution AMSR-E data will likely result in more accurate estimates of ice extent. An alternative source is the MSMR onboard the Indian Oceansat-1. Vyas et al. (2003) used brightness temperature data from the 18-GHz vertical polarization (18V) channel to map Antarctic sea ice extent from 1999 to 2001, as this sensor is equipped with neither 37-GHz nor 85.5-GHz channels. The method used is based on a threshold technique which takes the ice edge to be the location where brightness temperature gradients of >20 K occur. In general, the brightness temperature of open ocean at 18V falls in the range of 170 to 180 K, while sea ice ranges from 180 to 260 K (Vyas et al., 2003).

5.9.2.1.1 Analysis of trends and anomalies in ice extent

Intriguing results are emerging from this uniquely important dataset as it lengthens beyond 30 years (if ESMR data are included). Analysis has revealed both long-term trends and considerable interannual variability in regional and hemispheric sea ice distribution (Comiso et al., 2003a, b; Gloersen and Campbell, 1991; Parkinson, 1991, 1992, 2000a, b; Parkinson and Cavalieri, 1989). An example of interannual variability, from Comiso et al. (2003b), is shown in Figure 5.44 (see color section), in this case at the approximate median date of annual freezeup in the Arctic for three

consecutive years. Of these, 1996 is most typical of ice extent since 1973 (Gloersen et al., 1992; Parkinson et al., 1999). Note the extraordinary change apparent in the Beaufort Sea sector, for example. This region is generally covered in thick multiyear ice, and the observed change is therefore significant on a number of levels. By combining their passive-microwave analysis with data from drifting buoys, *in situ* oceanographic measurements, AVHRR-derived surface temperature data, and winds derived from ECMWF model runs, Comiso et al. (2003b) ascertained that observed changes in ice conditions related to both a warming and a change in regional patterns of atmospheric circulation—i.e., from mainly cyclonic in 1996 to anticyclonic in the following two years. While this example illustrates large-scale change, care should again generally be taken when using daily ice concentration images to determine ice extent, given the high degree of synoptic-scale variability in ice edge location. Indeed, this location can at any given longitude fluctuate by tens to hundreds of kilometers over a few days, particularly in the Southern Ocean (Massom, 1992). For this reason, monthly averages are most often used in trend analyses of ice extent.

Time series analyses of the passive-microwave ice concentration dataset have revealed that changes have occurred in global sea ice extent since 1978, and that these changes exhibit a marked hemispheric asymmetry. Although the time series is relatively short, certain trends are becoming apparent. They show that sea ice areal extent is decreasing at a mean rate of ~3% per decade in the Arctic compared with a slight overall increase of ~1.0–1.5% per decade in the Southern Hemisphere (see below), with strong interannual variability since the late-1970s (Bjørgo et al., 1997; Cavalieri et al., 1997, 2003a; Comiso, 2003a, b; Comiso and Steffen, 2001; Johannessen et al., 1999; Parkinson et al., 1999; Zwally et al., 2002a). Examples of anomaly plots of Arctic monthly mean ice extent, area, and concentration from the Arctic and for the period 1979–2000, again taken from Comiso et al. (2003b), are given in Figure 5.45. Superimposed on interannual variability is a clear negative trend, of $-2.0 \pm 0.3\%$ and $-3.1 \pm 0.3\%$—per decade for ice extent and ice area anomaly distributions, respectively. It is apparent from Figure 5.45(c) that the difference in trend values between the two parameters is due mainly to the accompanying negative trend in ice concentration of $-1.303 \pm 0.108\%$ per decade.

Cavalieri et al. (2003a) further revealed that apparent trends in the 30-year satellite record comprise different stages. While Arctic sea ice extent decreased overall by $0.30 \pm 0.03 \times 10^6$ km^2 per decade from 1972 through 2002, the decrease was $0.36 \pm 0.05 \times 10^6$ km^2 per decade from 1979 through 2002. This suggests an acceleration of 20% in the rate of decrease. In Antarctica, on the other hand, ice extent decreased dramatically over the period 1973–1977, then gradually increased (by $0.15 \pm 0.08 \times 10^6$ km^2 per decade). This apparent trend reversal is attributed to a large positive anomaly in Antarctic sea ice extent in the early 1970s, which Cavalieri et al. (2003a) suggest began in the late 1960s (based upon analysis of early visible and IR satellite images). This again highlights the fact that trends are necessarily affected by the end points chosen.

Current research has also revealed that overall hemispheric trends are made up of considerable regional variability (Parkinson, 2004). In their analysis of passive-microwave data from 1979 to 1998, for example, Zwally et al. (2002a) found that

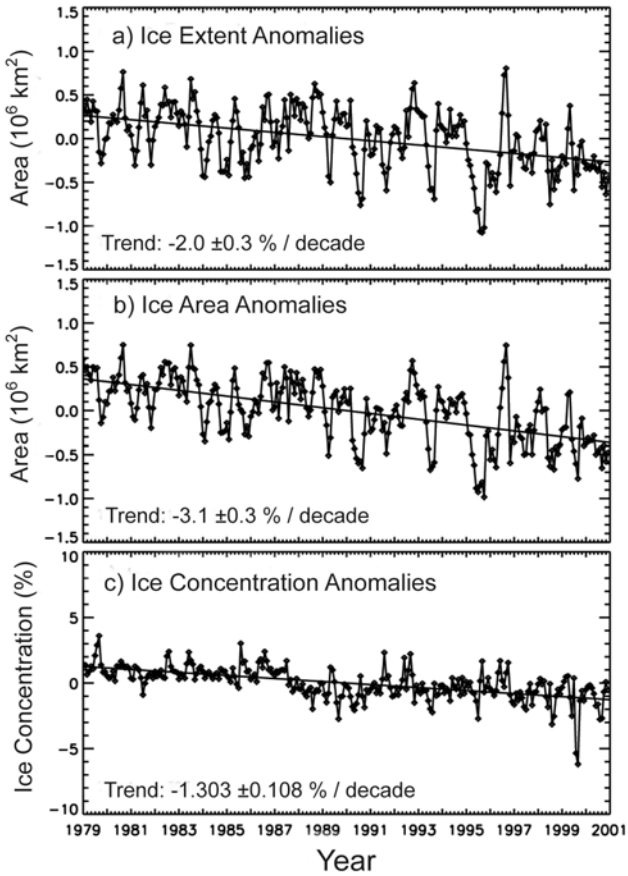

Figure 5.45. Plots of anomalies in mean monthly (a) ice extent, (b) actual ice area, and (c) ice concentration for the Arctic, with results of trend analyses, for the period 1979 to 2000 inclusive. The ice concentration data were derived from gridded Nimbus-7 SMMR and DMSP SSM/I T_B data (resolution 25 km) using the NASA Boostrap algorithm (Comiso et al., 1997).

trends in extent are positive in the Weddell Sea (1.4 ±0.9% per decade), Pacific Ocean (2.0 ±1.4% per decade), and Ross Sea (6.7 ±1.1% per decade) sectors, slightly negative in the Indian Ocean (−1.0 ±1.0% per decade), and strongly negative in the Bellingshausen and Amundsen Seas sector (−9.7 ±1.5% per decade). Plots of ice anomalies in ice extent, area, and concentration comparing this sector with the entire Southern Ocean are given in Figure 5.46 (updated from Kwok and Comiso, 2002a). While major regional variability occurs on an inter-annual basis (Cavalieri and Parkinson, 1981), the area to the west of the Antarctic Peninsula is the only sector to have exhibited a statistically significant negative trend

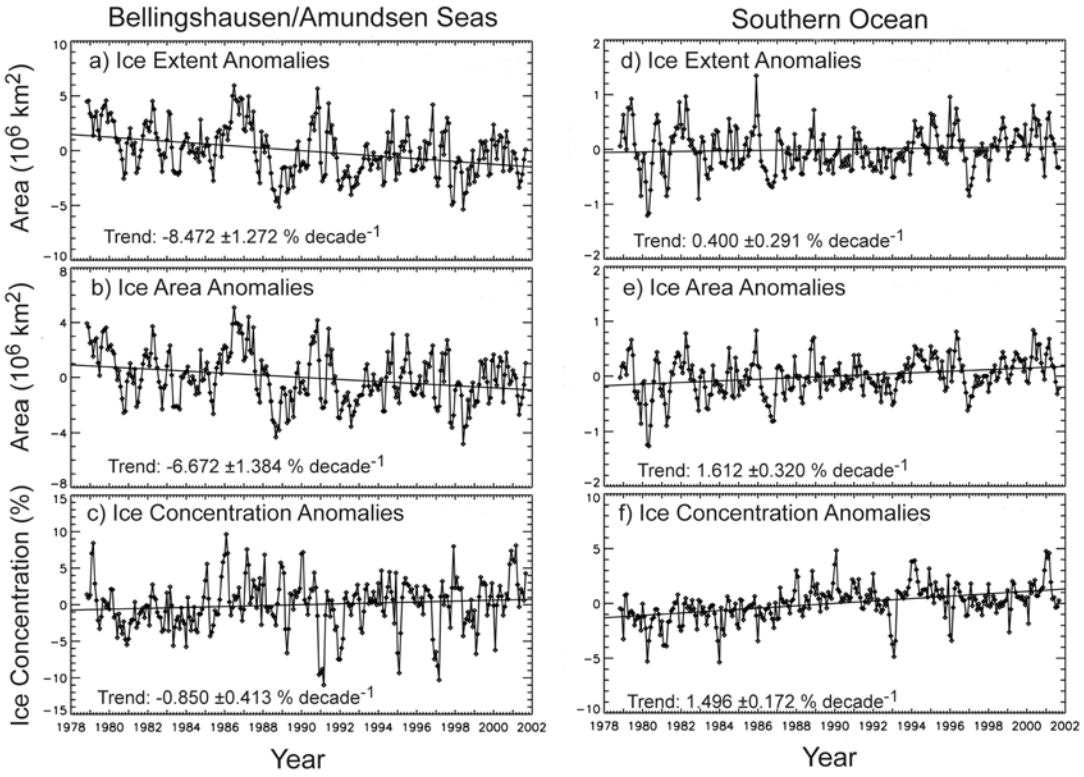

Figure 5.46. Comparison of anomalies and linear trends in sea ice extent, area covered by ice and ice concentration for the Bellingshausen–Amundsen Seas sector of Antarctica (a–c) and the entire Southern Ocean sea ice cover (d–f) from 1978 to 2002. These plots were derived from SMMR and SSM/I ice concentration data by taking each monthly average away from the average over the entire 1978 to 2002 time period. In these plots, the trends have not been removed. Note that anomalously low values occurred in both ice extent and area in the Bellingshausen–Amundsen Seas in 1983, 1987, 1992, and 1998, which were ENSO years.

Updated from Kwok and Comiso (2002a). Courtesy of Joey Comiso (NASA Goddard Space Flight Center). Reprinted with permission of the American Meteorological Society (AMS). © AMS 2005.

in sea ice extent over the past 30 years (Comiso, 2003a; Jacobs and Comiso, 1997; Kwok and Comiso, 2002b; Smith and Stammerjohn, 2001; Smith et al., 1996; Stammerjohn and Smith, 1996, 1997; Zwally et al., 2002a). Stammerjohn and Smith (1996) showed that this decrease has coincided with a warming trend in the peninsula of $>2^{\circ}$C since the 1940s (King et al., 2003a; Vaughan et al., 2003). Colwell and Turner (2003) also showed that a high correlation exists in this region between winter sea ice extent and air temperatures measured at stations on the western Antarctic Peninsula, with extent being closely linked to surface air pressure over the Bellingshausen Sea. Smith et al. (1999) further linked a shift in the population size and distribution of penguin species in the region to the observed sea ice changes (see also Wilson et al., 2001a). Due to their intimate relationship with sea ice distribution and conditions, certain species can be used as a proxy indicator of climate change—e.g., Adélie penguins (*Pygoscelis adeliae*) (Ainley, 2002).

In the Arctic, attention has recently focused on a continuing trend in decreasing summer ice extent (Comiso, 2003a, b; Johannessen et al., 1995a; Maslanik et al., 1996; Serreze et al., 1995, 2003). Studies of causal effects and relationships are benefiting greatly from not only satellite data but also the recent availability of improved atmospheric data fields, notably from the NCEP/NCAR Reanalysis Project (Kalnay et al., 1996). As Simmonds (2003) stated, we are now for the first time able to confidently document and understand the rich variety of modes of variability in and around both polar regions, as the sea ice trends/changes are part of a larger pattern of recent environmental change (see Section 5.5). The great sea ice masses are now under close scrutiny on a daily basis, thanks to the availability of NRTSI passive-microwave data from the NSIDC. Access to these data enabled the discovery that Arctic sea ice extent and area in September 2002 attained their lowest recorded levels since 1978 (Figure 5.47, see color section) (Comiso, 2003c; Serreze et al., 2003). Combined analysis of available satellite data and the NCEP/NCAR Reanalysis Project data led Serreze et al. (2003) to conclude that these anomalous ice conditions likely resulted from (i) persistent low-pressure and high-temperature patterns over the Arctic Ocean in summer, and/or (ii) anomalous warm southerly winds in spring, advecting ice poleward from the Siberian coast. Taken together, these patterns would promote ice divergence and rapid melt (Serreze et al., 2003). The extraordinary decrease in Arctic minimum summertime sea ice extent is shown in the comparison in Figure 5.48 (see color section) of decadal means from 1979–1990 and 1991–2002, derived from SMMR and SSM/I data (Comiso and Parkinson, 2004). The difference map, constructed to illustrate spatiotemporal change, is shown in Figure 5.48d, and the extreme minimum in 2003 in Figure 5.48c. Trend analysis using linear regression on the entire dataset indicated that the decline in the areal coverage of Arctic perennial ice has been fully $9.2 \pm 1.7\%$ per decade since 1979. These examples again illustrate the benefits of this important dataset as the primary source of global sea ice information dating back 25 years. Previous record minima in late-summer ice extent were also noted in 1990 in the Siberian Arctic, and in 1998 in the region north of Alaska (Maslanik et al., 1996, 1999). Who knows what future surprises may emerge from this extraordinary satellite time series as it lengthens?

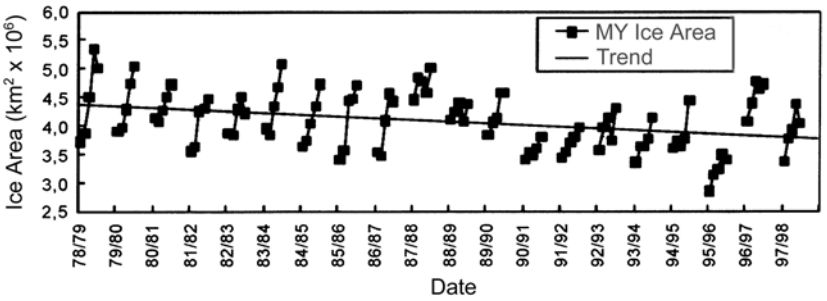

Figure 5.49. Time series of Arctic multiyear (MY) sea ice areal extent in winter, derived from Nimbus-7 SMMR and DMSP SSM/I data. The linear regression indicates a decrease of ~14% over the 20-year period, equivalent to an area of $\sim 0.61 \times 10^6$ km^2.

From Johannessen et al. (1999). Reprinted with permission of the American Academy for the Advancement of Science (AAAS). © 2005 AAAS.

Other studies—e.g., Comiso (2002a) and Johannessen et al. (1999)—have examined changes in the wintertime extent of Arctic multiyear ice (Figure 5.49). In this case, Johannessen et al. (1999) showed an apparent reduction of ~7% per decade in the areal extent of Arctic multiyear ice in winter from 1978 to 1998. As average multiyear ice extent and average ice thickness are strongly correlated, with multiyear ice being ~3 times thicker than seasonal (first-year) ice in the Arctic, the authors conclude that this decrease implies a decrease in the ice thickness distribution. As such, these results tie in with those from studies of submarine sonar data (see Section 5.5). Please note once again that a similar passive-microwave study of the wintertime extent of Antarctic multiyear ice is currently not possible due to the similarity in emissivity between first-year and perennial ice in the Southern Ocean (see Section 5.2). In Antarctica, the extent of multiyear ice is simply taken to be the area of ice remaining in passive-microwave images at the end of the annual melt season.

Images of ice extent anomalies and trends are available in near-real time and on an ongoing basis from the NSIDC (⟨*http://nsidc.org/data/seaice_index/*⟩), as a complement to the similar ice concentration products referred to in Section 5.9.1. Tools such as these again enable detection of anomalies in a timely fashion. The ice extent anomaly product shows the difference between the location of the median ice edge for a given month and the ice edge location for that month (Fetterer and Knowles, 2002). The total sea ice extent is also shown for that month. Figure 5.50 (see color section) shows an example from September 2003, equivalent to the ice concentration anomaly maps shown in Figure 5.38. Up-to-date information on ice extent anomalies is plotted as a time series of percentage differences between the total extent for a given month and the mean for that month (based on the 1988–2000 part of the NT dataset: Cavalieri et. al., 2003b). The trend (in percentage change per decade) is then computed by applying a least squares regression, with a 95% confidence interval for the resultant slope. In effect, the trend in anomaly maps illustrate how sea ice areal extent changes from year to year for a given month.

Please note that, due to the coarse resolution of the data and method of masking false sea ice detection due to land contamination, retrievals are biased low in an absolute sense but correct in a relative sense. An improved method of correcting for false sea ice detection around coasts is currently being implemented (Florence Fetterer, NSIDC, pers. commun., 2004).

It is clear from the above that exciting findings are emerging from analysis of the extraordinary and lengthening passive-microwave dataset. It is also apparent that care must be exercised in constructing trends and drawing conclusions from them. Assumptions and limitations inherent to linear regression for sea ice extent trend analysis, including the treatment of anomalous outliers and fitting regression lines to data with oscillatory characteristics, were evaluated by Fetterer and Knowles (2002). Difficulties arise due to the high interannual variability in ice extent; for example, Gloersen et al. (1999) reported that the annual variation of global sea ice area approximates 37% of the mean. Once again, the value of an ice extent trend and even its sign depends on the start and end point of the time series chosen. For example, Parkinson et al. (1999) observed a reduction in Arctic Ocean ice extent from 1978 to 1996, but an increase when only 1990 to 1996 is considered. Fetterer and Knowles (2002) concluded that simple linear regression is in a number of ways inadequate for describing changes in sea ice distribution. For example, the technique is based on the assumption that datapoints are independent samples, whereas ice conditions for a given month in fact depend on those from the previous month. They argued that an autoregressive model, whereby observations are modeled as a function of the values of prior observations, would be more appropriate. In their test of this assumption, Piwowar and LeDrew (2001) discovered, however, that autoregressive models are valid for only $\sim$60% of the Arctic, with rapidly changing weather patterns increasing variability elsewhere. Vinnikov et al. (2002) estimated that the autocorrelation timescale of observed daily ice extent is $\sim$50 days, suggesting that mean monthly ice extents are probably independent, although periodicity on a longer timescale cannot be ruled out (Fetterer and Knowles, 2002). Vinnikov et al. (2002) extracted seasonal cycles in ice extent trends from daily passive-microwave data using harmonic analysis, which is free from the assumption of linear analysis that the population of observations is stationary. Their finding was that monthly ice extent trends exhibit negative values for all 12 months in the Northern Hemisphere, based on the 20-year data record analysed. In summary, care should be taken when inferring long-term trends or natural oscillations from relatively short observational records of ice extent (Fetterer and Knowles, 2002).

Care should also be exercised in relating changes in sea ice extent to climatic change associated with thermodynamic variables—e.g., trends in air temperature—as much of the observed variability in sea ice extent may also be due to changes in patterns of ice transport and associated deformation related to wind. For example, Maslanik et al. (1999) commented that it is not clear whether the record retreat of sea ice in the Beaufort Sea in 1998 was due to an increase in icemelt or a change in ice advection patterns, or both. In another example, Massom et al. (in press) showed that an anomalously low ice extent in the west Antarctic Peninsula region was accompanied by both surface melt and extreme sea ice thickening (the latter by

dynamic processes—i.e., convergence). This strongly suggests that care should be taken when interpreting satellite-derived ice extent in isolation, and that more complete and realistic analysis of change should include consideration of ice thickness and motion/deformation. The key variable is ice volume, or the product of ice extent, concentration, and thickness, as we will see in Section 5.9.6.

5.9.2.1.2 Oscillatory patterns in sea ice extent

Harking back to Section 5.5, analysis of passive-microwave time series has shown that regional trends and oscillations are a major feature of the circumpolar Antarctic sea ice zone (Parkinson, 1995). A recent research focus has been on combining passive-microwave sea ice time series with improved atmospheric data to examine causal links between regional sea ice behavior and changes in dominant patterns of large-scale atmospheric circulation. In Antarctica, strong signatures of large-scale atmospheric circulation anomaly patterns and teleconnections—e.g., ENSO, AO, and SAO—have been identified in sea ice distribution patterns (Cavalieri and Parkinson, 1981; Comiso, 2003c; Hanna, 2001; Kwok and Comiso, 2002a; Jacobs and Comiso, 1997; Liu et al., 2004a; Parkinson, 1998; Rind, 2001; Simmonds and Jacka, 1995). Other discoveries have included the apparent existence of an Antarctic Circumpolar Wave (ACW) in anomalies of ice extent, sea surface temperature, sea level atmospheric pressure and meridional wind stress, which propagates around Antarctica with a period of 4–5 years and $\sim 180^{\circ}$ longitude zonal wavelength (White and Peterson, 1996). The ACW has been proposed as a possible mechanism for transmitting ENSO signals southwards. Baba and Wakatsuchi (2001) observed an associated eastward propagation of intra-seasonal variability in sea ice concentration in the circumpolar MIZ. Other studies have identified various modulations in sea ice extent anomalies—e.g., wavenumber-1, -2 and -3 patterns (Parkinson, 1994). Changes also appear to be linked to variability within the Antarctic Circumpolar Current and the windfield associated with the ACW (Figure 5.51, see color section) (Gloersen and Huang, 1998; Gloersen and White, 2001; White and Peterson, 1996). Possible feedback mechanisms between sea ice and the formation and strength of these large-scale modes of variability are poorly understood, but are the focus of new research based on combined analysis of meteorological and satellite passive-microwave data (Liu et al., 2004a). Please see Simmonds (2003) for a review of modes of variability in atmospheric circulation over the Southern Ocean.

In the Arctic Ocean, observed recent changes in sea ice extent, distribution, and thickness have been largely attributed to increases in the Arctic Oscillation Index or AOI (Morison et al., 2000; Parkinson, 2000b; Thompson and Wallace, 1998). Increases in the AOI lead to decreases in the strength of the Beaufort High (pressure system), which in turn affects the circulation patterns of the Arctic Ocean (Thompson and Wallace, 1998). The net impact of the positive phases of the AO is stronger than normal winds and relatively warmer conditions—i.e., increased ice advection and enhanced summer melt. The conceptual model is that the resultant reduction in convergence within the Beaufort Gyre leads to more openwater, increased ocean heating in summer, and therefore more extensive ice

melting (Morison et al. 2000). Another study, by Mysak et al. (1996), attributed anomalous ice extents in the eastern Arctic to simultaneous ENSO and NAO episodes. Recent changes in ice extent in the Bering Sea have been linked to switches in the dominance of El Niño over La Niña events since the late-1970s and a shift in the mean location of the Aleutian Low (pressure system), which may be explained by the influence of the Pacific Decadal Oscillation (PDO) (Niebauer, 1998). These are just a few examples of an expanding corpus of important information emerging from analyses of passive-microwave and other data (see Section 5.5 for other examples). Such studies are also dependent on other satellite-derived variables, such as ice motion fields, as we will see in Section 5.9.5. Clearly, this is a highly complex system, with the control of sea ice trends being determined by the interactions of physical processes over a range of temporal and spatial scales (Liu et al., 2004a). As such, the continued acquisition of passive-microwave data, and their careful analysis, is critical.

Results such as these have another role to play. They are also invaluable as a means of evaluating model performance by comparing satellite-derived anomalies in areal extent (and concentration) with hindcast model simulations extending back over the past 20 years. This approach has been adopted in both regional analyses—e.g., by Beckmann and Timmermann (2001); Holloway and Sou (2002); Kauker et al., 2003; Polyakov and Johnson (2000); and Zhang et al. (2000)—and also in analyses of the entire Arctic and Antarctic sea ice covers—e.g., by Fichefet et al. (2003a). Satellite-derived results are also being directly compared with longer term observational analyses from the Arctic in particular. For example, Vinje (2001a) suggests in his historical analysis in the nordic seas that ice extent has undergone a reduction of $\sim$33% over the past 135 years, superimposed upon pronounced decadal-scale oscillatory variations. Ice edge retreat has also been noted in the Barents Sea over the period 1850–2001 (Shapiro et al., 2003). Moreover, in their update of the analysis of historical data by Chapman and Walsh (1993), Folland et al. (2001) revealed the presence of spring and summer decreases in Arctic ice extent over the entire second half of the 20th century. Such decreases have been shown to be largely responsible for the overall negative trend in Arctic sea ice areal extent noted above in the satellite passive-microwave era (Parkinson et al., 1999). Folland et al. (2001) further revealed that only a slight and uncertain downward trend has occurred in autumn and winter Arctic extents since about 1970. These are examples of cases where satellite results are providing credence to other observations which are immensely important in their implications, and which place current observations within a longer temporal context.

Regional and interannual differences in ice extent also have a major but poorly understood impact on large-scale biological regimes (Constable et al., 2003; Thomas and Dieckmann, 2003). For example, a comparison of satellite-derived ice extent with *in situ* observations to the west of the Antarctic Peninsula has suggested that the zooplankton community is dominated by salps (*Salpa thompsonii*) after years of low extent with a reduction in krill (*Euphausia superba*) after winters of high extent (Siegel and Loeb, 1995; Loeb et al., 1997). The implication is that krill predators may suffer accordingly. Similar observations have been made in East Antarctica by

Nicol et al. (2000). Results are also emerging of a major decline in krill biomass across the SW Atlantic Ocean over the past 30 years (Atkinson et al., 2004), which the authors attribute to changes in sea ice extent in the austral winter.

The strong connection between krill distributions and sea ice has been further highlighted by Brierley et al. (2002), who used the Autosub-2 Autonomous Underwater Vehicle (AUV) to conduct long biological-sampling transects across the Antarctic ice edge. This study found approximately three times more krill under the ice compared with the adjacent open ocean, with the majority being encountered within a zonal band from 1 and 13 km inside the sea ice edge. These results are consistent with those of Nicol et al. (2000), and further suggest that, not ice extent *per se*, but rather the extent of the ice edge may be an important determinant of krill distribution. As an example, they show that a 25% decrease in sea ice area would in fact only equate to a 9% reduction in the overall length of the sea ice edge. Clearly, satellite and *in situ* data combined will play a key role in helping to unravel these and other important sea-ice-ecology-related questions.

5.9.2.1.3 Ice extent and ocean phytoplankton biomass

Ice extent also determines the location and timing of the annual freshwater flux at and within the receding ice edge in spring–summer, which in places appears to create conditions conducive to intense algal blooms (Smith and Nelson, 1985). As noted in Section 5.4.1, algae associated with sea ice and ice edge regions are an important component of the marine food chain. In addition, they play a major role in important geochemical processes, with their ability to convert dissolved carbon dioxide into organic compounds being of major interest regarding the global carbon cycle and climate change assessments. The causal link between variability in enhanced biological activity and seasonal ice edge retreat is largely unknown, but is thought to relate to the stratification of the mixed layer by freshwater from melt, "seeding" by algae released from the ice, increased light availability, and trace nutrient inputs—e.g., iron (Smith and Nelson, 1985; Sullivan et al., 1993). The areal extent, magnitude, and timing of such blooms can only be determined from satellite-derived ocean color data under cloud-free and solar illumination conditions (Comiso et al., 1990, 1993; Sullivan et al., 1993). Prior to satellite ocean color observations, large-scale distributions of phytoplankton, and their seasonal and interannual variability, were little known. Due to the limiting effect of cloud cover, many studies sacrifice high temporal resolution in favor of enhanced cloud-free coverage by combining multiple passes into monthly and longer term average composites—e.g., Figure 5.52 (see color section).

Ocean color sensors distinguish subtle variations in the ice-free ocean surface and near-surface color related to the concentration of chlorophyll, which is an index of phytoplankton biomass (Moore and Abbott, 2000). The magnitude of primary production can be derived from this information after careful processing, and based on the amount of solar radiation absorbed by phytoplankton chlorophyll in the upper water column. Key factors are accurate removal of the large atmospheric contribution to the measured radiance and the need for accurate calibration. Long-term estimates of ocean primary production from time series of satellite

ocean color measurements are required to better understand the role of polar and sub-polar oceans in the global carbon cycle. In particular, satellite ocean color observations can be combined with biological process studies in order to determine patterns of primary production and biological carbon export to the deep ocean. A remaining issue is that a number of ocean color algorithms exist, and these differ in certain key ways (Honjo, 2004).

In addition to their role in helping to quantify ocean carbon flux and understanding how it is controlled, ocean color sensors have two other broad thematic uses. These are (i) assisting with scientific management and analysis of fisheries, and (ii) providing an observational, synoptic link between the development of the ocean ecosystem and the physics of the ocean-mixed layer (Yoder, 1999). As phytoplankton control the optical turbidity of much of the ice-free ocean, they also determine and control the manner in which the mixed layer is heated up by incoming shortwave radiation. Excellent information on satellite ocean color data and their availability is given at ⟨*http://oceancolor.gsfc.nasa.gov/*⟩.

An increasing number of studies are using satellite-derived ocean color and ice concentration/extent data to examine the relationships between phytoplankton distribution/primary production and sea ice distribution. These build upon the earlier analyses using Nimbus-7 CZCS data. Arrigo et al. (1999), for example, combined SeaWiFS data with SSM/I data to analyse how variations in sea ice distribution affect primary production associated with an advancing or receding ice edge. Engelsen et al. (2004) exploited satellite measurements of near-surface chlorophyll *a*, ice concentration, and ice concentration history (from DMSP SSM/I data), and sea surface temperature (from NOAA AVHRR data) to identify three distinct bloom phases in the Barents Sea MIZ. The validation of satellite-derived ocean color data at high latitudes remains an issue. Techniques have also been developed to measure and map UV radiation in ice-covered polar regions using multispectral satellite imagery (Lubin et al., 1994; Nuñez et al., 1997). A major concern is the deleterious effect of increased dosages of UV radiation associated with high-latitude ozone holes on polar organisms, including phytoplankton (Davidson and van der Heijden, 2000; Perovich, 1995; Smith et al., 1992; Vernet et al., 1994). The satellite mapping of biologically active UV irradiance is covered in Chapter 4. Unfortunately, sea ice algal distributions and primary production in an ice-dominated environment cannot be monitored and measured by satellite remote sensing. As a result, our knowledge of this important contributor to the overall primary productivity of high-latitude oceans relies on *in situ* observations and is extremely patchy.

5.9.2.1.3 Analysis of the duration of the annual sea ice season

The availability of a lengthening time series of satellite passive-microwave data has also enabled monitoring and analysis of the annual sea Ice Season Length (ISL), defined by Parkinson (1992, 1994) as the number of days over a year when the ice concentration at a given location exceeds 15%. This is another parameter that may be highly sensitive to climate variability/change, and is intimately related to ice extent. Parkinson et al. (1999) observed an ISL shortening by 25 days per decade in Arctic marginal seas from 1978 to 1996. While the ISL appears to have diminished

for the Arctic as a whole since 1978, the pattern once again exhibits considerable spatial and temporal variability. Parkinson (2000a), for example, observed a decrease in the Arctic ISL in the Chukchi Sea, but a lengthening in the eastern Beaufort Sea and the Bering Sea. Work by Comiso and Gordon (1998) has revealed a possible relationship in some Antarctic sectors between above-average winter maxima in ice extent and subsequent below-average summer minima. The patterns of ISL variability have again been linked to patterns of anomaliesy in large-scale atmospheric circulation. Parkinson (1998) observed an eastward (clockwise) propagation for variations in the Antarctic ISL between 1988 and 1994, which she associated with the ACW (White and Peterson, 1996). Similarly, Baba and Wakatsuchi (2001) observed an eastward propagation of intraseasonal variability in sea ice concentration in the Antarctic circumpolar MIZ. Watkins and Simmonds (2000) also carried out an analysis of ISL in the Antarctic, over the periods 1979–1986 and 1989–1996.

Parkinson (2002) also analyzed the length of the Southern Ocean sea ice season to obtain trends in circumpolar sea ice coverage over the 21-year period from 1979 to 1999. The length of each annual sea ice season was again determined from sea ice concentration data by counting the number of days with ice coverage of at least 15% at each gridpoint. Additional comparative analysis was carried using 30% and 50% cutoffs, which yielded comparable results. The trend in ISL was determined at each gridpoint as the slope of the line of linear least squares fit through the entire season length dataset (see Parkinson, 2002 for further details). Results are shown in Figure 5.53 (see color section). Blue and green colors represent areas where the sea ice is lasting longer, while orange and red indicate a decrease in the number of days that the ocean remains frozen. While most of the Amundsen Sea and the entire Bellingshausen Sea has undergone a substantial shortening of the ice season, the opposite is true in the Ross Sea, with mixed signatures in the Weddell Sea (see also Parkinson, 2004). Overall, it appears that the area of the Southern Ocean undergoing a lengthening of the ice season by $\geq$1 day per annum (from 1979 to 1999) was $5.6 \times 10^6\,\mathrm{km}^2$, while $\sim 3.0 \times 10^6\,\mathrm{km}^2$ underwent a shortening of at least 1 day per annum. The larger area covered by longer lasting ice indicates an increase in the amount of Antarctic ice. These changes require further analysis to determine causal factors, as they likely result from a complex combination of both dynamic and thermodynamic processes.

Passive microwave analyses of sea ice season duration have formed the basis for analysis of the role of sea ice in the structure and function of the marine ecosystem—e.g., in the West Antarctic Peninsula (WAP) region through the Palmer Long Term Ecological Research (LTER) project (Smith et al., 2003a). Smith and Stammerjohn (2001) and Stammerjohn et al. (2003) have noted increased variability associated with the timing of sea ice advance and retreat in the WAP region since the 1990s. Underlying trends of later advance and earlier retreat translate into a decreasing trend in the length of the winter ice cover season. In other words, the decreasing trend in winter sea ice extent that has been observed in the WAP and greater Bellingshausen Sea regions is not so much due to a decrease in the magnitude but rather a decrease in the duration of winter sea ice extent. This has subtle yet important ecological implications, and changes in the timing and duration of the

sea ice season have been linked to observed changes in the regional marine ecosystem (Smith et al., 1999, 2003b). Such variations in sea ice coverage also have important implications for the radiation balance at the surface, given that an open ocean absorbs significantly more incoming shortwave radiation than an ice-covered ocean. In addition, a decreased spring sea ice extent would likely lead to changes in cyclone trajectories (Menendez et al., 1999a; Murray and Simmonds, 1995). Such complex feedback mechanisms require further study.

5.9.2.1.4 Possible discrepancies in passive-microwave-derived ice edge location

Of great importance is the need to assess the accuracy of ice extent and concentration retrievals from the different algorithms, given an observed discrepancy between the outputs. For example, while Cavalieri et al. (1997) computed a 1.3% per decade increase in mean ice extent in the Antarctic, as noted above and using the NT algorithm, the Norsex algorithm showed a decrease of 1.1% over the period 1978–1995 (Bjørgo et al., 1997). All estimates effectively come from the same input (brightness temperature) dataset. An important factor affecting the reliability of satellite-derived time series of ice extent is therefore the accuracy and consistency of detection of the ice edge location. While the threshold ice concentration value of 15% is generally used for this purpose, this is somewhat arbitrary and has never been fully validated. Using a 20% or 30% cutoff will give different values, although similar trends, for extent (Parkinson et al., 1999). Given its improved resolution, the AMSR-E should enable more accurate ice edge demarcation than the DMSP SSM/I. An issue remains, however, as to how appropriate the 15% ice concentration isoline is as a universally applicable threshold. This relates to the major question as to what constitutes an ice edge. At any given time, it can either be compact (e.g., due to on-ice winds), or diffuse (due to off-ice winds), or somewhere in-between. Diffuse ice edges can extend meridionally for tens of kilometers, in which case the satellite-derived ice edge can be substantially further poleward than the actual ice edge. Moreover, the ice edge region typically comprises wet and highly fragmented ice, with concentrations typically underestimated by spaceborne passive-microwave radiometers (Massom et al., 1999; see Section 5.2).

Parkinson and Cavalieri (1989) estimated an uncertainty of $\sim$30 km in ice edge location from passive-microwave data. Steffen and Schweiger (1991) further showed a seasonal dependence on the accuracy of sea ice extent and concentration retrievals, estimating that the total ice-covered area in the Arctic can be measured to within $\sim 0.3 \times 10^6$ km^2 using passive-microwave data. Worby and Comiso (2004) compared limited ship observations and Radarsat SAR estimates of Antarctic ice edge location with contemporary SSM/I-derived ice edge locations. Their findings indicate that a generally good agreement occurs between March and October (the freezeup months), with the 15% passive-microwave threshold providing a reasonable estimate of the actual ice edge location. In November and December (spring–summer), on the other hand, the SSM/I-derived ice edge was found on average to be 1.00–1.56° of latitude to the south of the observed ice edge. This clearly has important implications for interpretation of satellite ice extent data for climate studies, although more extensive comparisons are required—e.g., using high-

resolution satellite data. These and other issues are being addressed, with a coordinated international effort to validate new AMSR and AMSR-E sea ice products in both the Arctic and Antarctic (⟨*http://eospso.gsfc.nasa.gov/validation/*⟩).

5.9.2.3 Radar scatterometer and SAR measurement of sea ice extent

The detection of boundaries between sea ice and open water using radar data is based on the greater backscatter from sea ice compared with open ocean. The degree of backscatter contrast depends upon ice type, deformation and roughness, and the roughness of the water surface (ocean clutter). Ocean clutter is generally greater at steeper incidence angles (van der Sanden and Ross, 2001), and is related to wind speed. Given their ability to acquire data from entire sea ice covers on a daily basis and uninhibited by polar darkness and cloud cover, satellite radar scatterometers are also well-suited to the measurement and monitoring of circumpolar ice edge location. In fact, the temporal and spatial coverage of modern scatterometers—e.g., NSCAT and QuikSCAT—is comparable with that of passive-microwave radiometers, and provides a complementary view of the global sea ice cover (as noted in Section 5.8.2.2). Recent advances in processing techniques have produced significantly improved spatial resolutions—as fine as 4.45 km for QuikSCAT data (Early and Long, 2001). Issues relating to the use of Ku-band scatterometer data to map ice edges are discussed by Remund and Long (1999). Although gaps occur in the data, they extend back to the SASS onboard Seasat in 1978, and are therefore a potentially important climate research resource, and one that has until recently been largely underutilized. The polarization ratio, or ratio of vertically and horizontally polarized returns, at incidence angles of $>40^\circ$ is an effective discriminator of ice and open ocean in both hemispheres (Yueh and Kwok, 1998; Yueh et al., 1997, 1998). This technique was first applied to Seasat SASS data, then NSCAT data. Yueh and Kwok (1998) further found that Arctic ice extent derived from NSCAT data by applying a polarization threshold of 2 dB showed reasonable agreement with the 25% ice concentration isoline in coincident SSM/I-derived ice concentration data, but less so with the 15% contour. Scatterometer data remain a secondary source of ice extent information for research purposes behind passive-microwave techniques, but show great potential due to their ready availability, and they are now also routinely incorporated into operational ice analyses (Long et al., 2001) (Figure 5.54). Moreover, the normalized radar backscatter information contained in these images is highly complementary to the measurements of thermal emissions in the passive-microwave data, and may be less affected by atmospheric variability (Meier and Vermeychuk, 2003).

Unresolved issues again remain regarding the accuracy of derived ice edge locations. In a comparison of enhanced-resolution QuikSCAT SIR data and coincident Radarsat SAR and DMSP OLS data, Haarpaintner et al. (2004) have shown that the automated ice mask developed by Remund and Long (1999) and applied to QuikSCAT data tends to underestimate the Arctic ice edge location. They proposed a refinement of the current product that takes advantage of the linear dependence of the QuikSCAT Active Polarization Ratio (APR) on ice

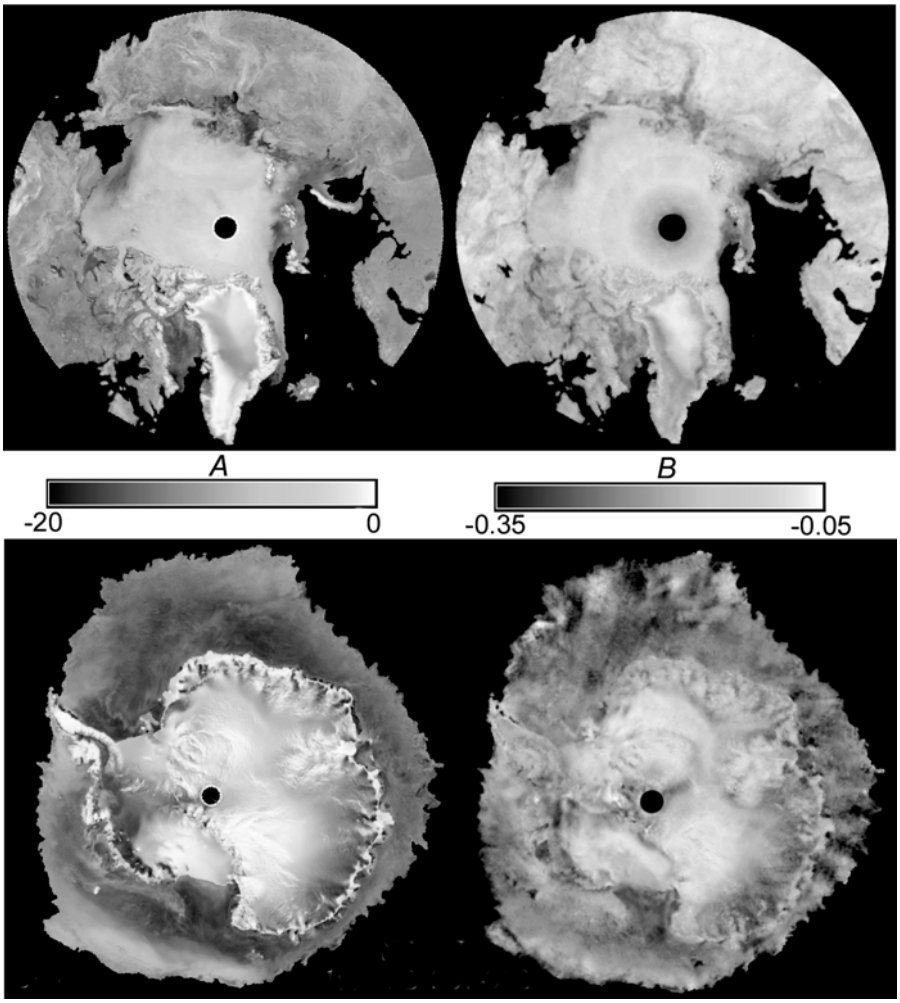

Figure 5.54. Examples of enhanced resolution (SIRF) *A* and *B* images of both polar regions, generated from 6 days of NSCAT data (H-pol) in 1996 and showing sea ice extent in the Arctic and Antarctic. Regions identified as open ocean are set to black using the technique outlined in Remund and Long (1999). *A* is the value of σ^0 at 40° (mid-swath), while *B* represents the dependence of σ^0 on incidence angle θ_i. Images such as these are available from the Scatterometer Climate Record Pathfinder facility at Brigham Young University (⟨*http://www.scp.byu.edu/data/Quikscat/SIR/Quikscat_sir.html*⟩).

From Long and Drinkwater (1999). Reprinted with permission of IEEE. © 2005 IEEE.

concentration, enabling definition of the APR threshold to a fixed value (of −0.02) to allow manual adjustment of the ice extent to different ice concentrations. Haarpaintner et al. (2004) further discussed the validity of the satellite-derived ice edge for near-real time applications in relation to ice motion in the MIZ over the integration time necessary to produce enhanced resolution images—i.e., 36 hours.

Comparison with coincident Radarsat SAR data showed that the new APR algorithm improves automatic global ice edge resolution by a factor of 2 when compared with SSM/I products, and as such could be used in both model initialization and data assimilation. An example is shown in Figure 5.55.

A new sea ice database is available from the Norwegian Meteorological Institute at ⟨*http://icemon.met.no/quikscat*⟩, showing the current (near-real time) Arctic ice edge, concentration, and drift information, derived from enhanced-resolution QuikSCAT/SeaWinds scatterometer data produced by NOAA's National Environmental Satellite, Data and Information Service (NESDIS) in conjunction with the Brigham Young University Microwave Earth Remote Sensing (MERS) Laboratory. The resolution of the ice edge product is 6.675 km. Details of the algorithm and data are given in Haarpaintner (2004). While the resolution of the ice concentration

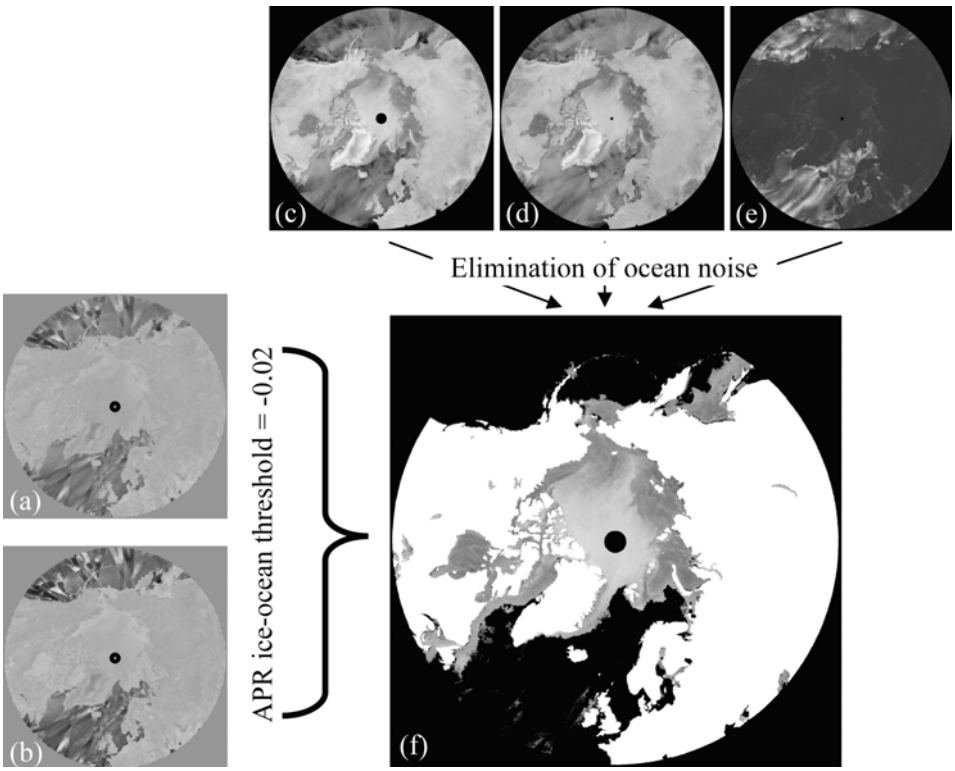

Figure 5.55. Schematic of an algorithm to derive improved ice edge information from QuikSCAT data, using (a) Active Polarization Ratio (APR), (b) APR_{abs} images as the main input variables, (c) HH-backscatter σ_{0H}, (d) VV-backscatter σ_{0V}, and (e) the VV/HH ratio of the daily standard deviation per pixel $STD_{V/H}$ as secondary variables to eliminate ocean noise to obtain (f) the total ice cover and ice edge delineation. The land mask is in white. The effective resolution of this product is 7 km. This example, from the Arctic, is from March 11, 2003.

From Haarpaintner et al. (2004). Original data NOAA/NESDIS/Brigham Young University. Reprinted with permission of IEEE. © 2005 IEEE.

product is also 6.675 km (pixel size), it has been averaged over 3×3 pixels (20 km). The 48-hour ice drift product has a resolution of 2.225 km (pixel size), with ice drift being calculated for every 25th pixel. Validation with International Arctic Buoy Program (IABP) buoy data showed an error standard deviation of about 4 km for the filtered results for a 2-day ice displacement—i.e., an accuracy of 2.5 cm s^{-1} in ice drift speed.

With its fine resolution and ability to penetrate cloud cover, satellite SAR is well-suited to detailed but more localized studies of ice edge configuration and processes—a factor first identified in Seasat data from 1978 (Carsey and Pihos, 1989). Particularly important has been the development of ScanSAR technology, enabling much wider swath coverage for current satellites—e.g., ~500 km for Radarsat-1 versus 100 km for ERS. Given its generally limited coverage and high data rate, SAR is less well-suited to routine monitoring of global ice edge location. It remains, however, a powerful tool in regional operational applications (Bertoia et al., 2004; Gill, 2001; Gill and Valeur, 1996; Gill et al., 2000), and is of great importance as a means of validating coarse-resolution passive-microwave estimates—e.g., Massom et al. (1999) and Worby and Comiso (2004). As an example of a regional application, Holt and Martin (2001) used ERS SAR data combined with SSM/I data to examine the impact of a major storm on ice edge regions of the western Arctic in summer. Another study, by Liu et al. (1997a), demonstrated the effectiveness of wavelet analysis as a means of automatically tracking the ice edge in SAR data (see Section 5.9.5 for further information on wavelet analysis). This method is particularly effective in the tracking of ice edge ocean eddies, whereby floes trace out the pattern of underlying ocean circulation features and has been used to measure marginal ice zone rheology (Drinkwater and Squire, 1989). According to van der Sanden and Ross (2001), HH-polarization data are preferable to VV-polarization for SAR ice edge applications, and shallow incidence angles minimize ocean clutter. Once again, wind-roughened open ocean can have a signature resembling consolidated ice. Polarimetric SAR again shows great promise in improved ice edge delineation (see Section 5.9.7.3.2). Scheuchl et al. (2001), for example, found that σ°_{HV} at the C-band is well-suited to ice edge detection. Referring back to Section 5.9.1.3, enhanced ice–water contrast is possible using cross-polarization channel data (at HV) and the co-polarization ratio between HH- and VV-channel data from new polarimetric SARs onboard Envisat-1 and, in the near future, Radarsat-2 and ALOS (van der Sanden and Ross, 2001). Again, the co-polarization ratio between the HH- and VV-channels has a similar ice edge detection capability, but will only be acquired in narrow-swath full-polarimetric modes (see Section 5.9.7.3.2).

5.9.2.4 Radar altimetry and ice extent

For reasons already outlined in Section 5.8.2.3, satellite radar altimeters are very much secondary sources of ice extent data, with the detection of sea ice based upon the different shape of the return pulse from ice compared with open ocean (Fetterer et al., 1992; Hawkins and Lybannon, 1989). Altimeter return signals typically exhibit a higher peak power and rate of power falloff with incidence for sea ice than ice-free

ocean, as sea ice tends to be relatively smooth and quasi-specular while open ocean is rougher and quasi-Lambertian in its scattering behavior (Drinkwater, 1991; Laxon, 1989). The response of the echo depends on the nature of the ice edge (Laxon, 1994a, b). Laxon (1989) developed an ice index from the average altitude/specular gate and automatic gain control signals, whereby the value ranges from >1 for ice to ~0.6 for ice-free ocean. Using Geosat data, Laxon (1990) demonstrated that the radar altimeter signal is sensitive to even low ice concentration. Laxon (1990, 1994b) used ERS-1 data to map sea ice extent, as a proof of concept. Unfortunately, large-scale maps of ice extent derived from altimeter data are difficult to interpret, given that it takes several days to collect sufficient data to gain complete circumpolar coverage. Sea ice boundary and extent information retrieved from radar altimeter data from the Seasat, Geosat, and ERS-1 and -2 missions is available from NASA at ⟨*http://icesat4.gsfc.nasa.gov/ia_home/AltDoc.html*⟩.

5.9.2.5 Medium-resolution visible to TIR radiometers and ice extent

Another less extensively used technique exploits the spectral characteristics of NOAA AVHRR data to discriminate between sea ice and open ocean and locate the ice edge, using a subjective threshold method (Emery et al., 1991a). Andersen et al. (2001), for example, use the bidirectional reflectance (the change in surface brightness with viewing angle) of channel-2 data and the estimated bidirectional reflectance of channel-3b data (the latter determined from the difference between channels 3b and 4). This builds upon the method of Gesell (1989). These data have also been used to study large ice edge ocean eddies traced by ice floes (Fukamachi et. al., 1998; Wakatsuchi et al., 1990). Another, more simple method uses averages of cloud-free data from a single channel (Figure 5.56, see color section). As already discussed, visible to near-IR techniques are seriously limited by cloud cover and darkness, and TIR techniques by cloud cover. Moreover, the latter are ineffective when the thermal contrast between ice surface temperature and ocean temperature is not strong—i.e., during melt periods.

The MODIS is another key source of sea ice information, operating at improved spatial and spectral resolutions compared with the AVHRR. Daily global sea ice extent maps (by swath) are routinely produced in an automated fashion using data from the Aqua and Terra MODIS TIR and solar-reflective bands. The daytime product is based on the Normalized Difference Sea Ice Index (NDSI), which detects sea ice by exploiting high reflectance at visible wavelengths—i.e., at 0.55 μm, band 4—but low reflectance at 1.6 μm (band 6)—i.e., NDSI = (band 4 − band 6)/(band 4 + band 6). A pixel is identified as containing sea ice if band-2 reflectance is >0.11, band-1 reflectance is >0.10, and NDSI is ≥0.4 (Hall et al., 2001; Riggs et al., 2003). Nighttime products use Ice Surface Temperature (*IST*) data computed from TIR channel data (see Section 5.9.11 for more details on the latter), and identify sea ice as any pixel where $IST = \leq 271.5$ K (the freezing point of seawater). The MODIS Icemap algorithm generates a binary ice/no-ice product, at a spatial resolution of 1 km (Riggs et al., 1999, 2001). An example is shown in Figure 5.57 (see color section). Gridded and swath data of sea ice extent from late 2000 onwards are available from the NSIDC DAAC at ⟨*http://nsidc.org/data/modis*⟩.

Sea ice products are processed to level-2 (swath) and level-3 (gridded) formats, and are available separately for both hemispheres and for day and night. The products are derived from daily, 8-day, and monthly composites. The MODIS cloud mask, which differs between day and night, is described by Ackerman et al. (1998). Information on MODIS ice (and snow) data and algorithms is available at ⟨*http://modis-snow ice.gsfc.nasa.gov/modis.html*⟩.

5.9.3 Fast ice distribution and behavior

So far, the discussion has focused on moving pack ice. Also important, though often largely overlooked, is landfast or fast ice, which is sea ice that remains fixed or "fast" along the coast for much of the winter or even perennially. It may be attached to grounded icebergs, the shore, an ice wall or an ice front (WMO, 1970). It also forms in sheltered coastal embayments, behind coastal protrusions such as floating glacier tongues and between islands. In the Arctic, fast ice tends to occur over shallower waters compared with the Antarctic (Kovacs and Mellor, 1974; Wadhams, 1986). Fast ice forms by two processes: *in situ* thermodynamic growth (Heil et al., 1996; Kawamura et al., 1997; Tison et al., 1998), and the interception of sea ice moving into a region by blocking features—e.g., assemblages of grounded icebergs (Massom et al., 2001b). It can also either be annual or perennial, the latter occuring in more sheltered locations. The breakout of annual fast ice typically occurs during storms (Heil, 2001), and/or by the effects of ocean swell penetration (Crocker and Wadhams, 1989; Langhorne et al. (2001)—often when the protective surrounding pack ice cover has dispersed. In this section, we examine the important role of remote sensing in mapping and monitoring fast ice, which covers an estimated $0.8 \times 10^6\,\mathrm{km}^2$, or 5% of the total sea ice cover, in the Antarctic (Fedotov et al., 1998), and a large though at present indeterminate area along Arctic coastal regions.

Developing an improved understanding of the distribution and long-term behavior of fast ice is important from a number of perspectives:

- Given the relative stability of fast ice, its behavior, and characteristics—i.e., extent, thickness, and date of formation/breakup may be of considerable value as an integral measure of climate variability and change, both local and regional (Divine et al., 2003; Murphy et al., 1995).
- It restricts navigation and offshore exploration, particularly in the Arctic (Divine et al., 2003; Wang et al., 2003a). It has played an important role in the lifestyle of coastal Inuit communities for millenia (ARCUS, 1997; Mahoney et al., 2002).
- Fast ice can grow to a considerable thickness, particularly in the case of perennial ice, thereby representing a considerable freshwater reservoir.
- In both polar regions, it forms an important interface between the land/ice sheet and the moving pack ice zone.
- Recurrent flaw leads form in many locations in the shear zone separating fast ice and moving pack ice. As discussed further in Section 5.9.4, these form *loci* of intense heat exchange between relatively warm ocean and cold atmosphere (in

winter), resulting in high rates of sea ice formation, brine rejection into the underlying ocean, thermohaline overturning, and dense water formation (Dethleff et al., 1998). Flaw leads also form key arteries along which marine mammals migrate—e.g., along the Alaskan Beaufort Sea coast.

- The fast ice itself is also ecologically highly significant, forming an important habitat for micro-organisms (Arrigo et al., 1993; Günther and Dieckmann, 2001; McMinn et al., 2000; Swadling et al., 2000) and a critically important stable breeding platform for various bird and mammal species—e.g., Weddell seals (*Leptonychotes weddellii*) and emperor penguins (*Aptenodytes forsteri*) (Kirkwood and Robertson, 1997; Kooyman and Burns, 1999; Reijnders et al., 1990; Wienecke and Robertson, 1997).
- Arctic fast ice entrains contaminants and particulate materials—e.g., sediments entering the Arctic Ocean from rivers—during its formation process, for example, in the Laptev Sea region (Eicken et al., 1995a; Reimnitz et al., 1995a).

While long-term *in situ* monitoring programs have been established at various locations in the North American and Siberian Arctic (Bilello, 1980; Brown and Cote, 1992; Flato and Brown, 1996; Reimnitz et al., 1995b; Zubov, 1943) and Antarctica (Murphy et al., 1995; Enomoto et al., 2002; Heil, 2001), satellites provide a much broader overview to complement and extend these detailed *in situ* studies. Current passive-microwave radiometers are unsuitable for this application due to their poor resolution and pixel contamination with land/ice sheet signatures in coastal regions. High-resolution visible to TIR sensors—e.g., the High Resolution Visible (HRV) instruments onboard SPOT 1 to 4 and the TM and ETM+ onboard Landsat satellites—have been used in a somewhat limited fashion due to their expense, narrow-swath coverage, and inability to penetrate cloud cover. Once again, such sensors are best suited to localized studies where high resolution is essential but broad-scale coverage is not—e.g., in support of studies of the impact of fast ice variability on specific penguin colonies. The launch of the modern satellite SAR era with ERS-1 in 1991 allowed monitoring of fast ice under cloudy conditions, though limited to a narrow data swath. Improved coverage came with the launch of the ScanSAR technology onboard Radarsat-1 in 1995. This and similar sensors—e.g., the Envisat ASAR and ALOS PALSAR—provide excellent regional-scale coverage over 400–500-km swathwidths. Although these high-resolution sensors are well-suited to measuring the distribution of fast ice, the latter is often indistinguishable from surrounding pack ice based upon analysis of normalized backscatter values alone in single snapshot images. Giles et al. (in preparation) addressed this ambiguity by adapting feature-tracking methods, designed to determine pack ice drift and outlined in Section 5.9.5, to delineate the fast ice–pack ice boundary in time series of carefully co-registered Radarsat ScanSAR Wide 100-m resolution images, based upon the fact that fast ice shows up as a stationary entity in such analyses. Using this technique, Giles et al. (in preparation) mapped the wintertime extent of fast ice across a large sector of the East Antarctic coastline (75–150°E) for the first time (Figure 5.58a), and examined interannual variability. This and similar ''snapshot'' datasets provide important

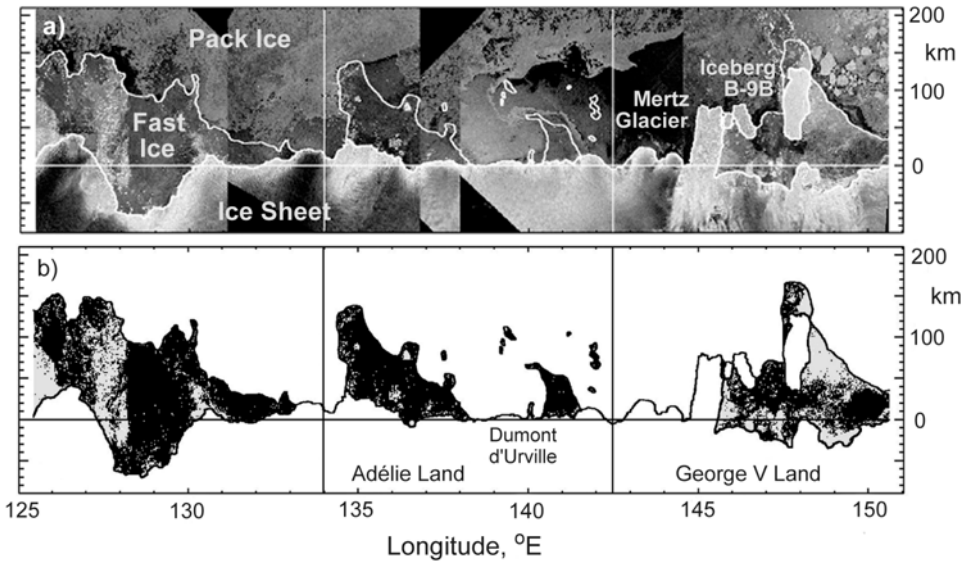

Figure 5.58. Maps of (a) fast ice extent and (b) fast ice type derived from Radarsat ScanSAR Wide data, for the East Antarctic coastal sector from 125 to 150°E.

After Giles *et al.* (in preparation). Radarsat data copyright Canadian Space Agency/Agence Spatiale Canadienne 1999, processed and distributed by the NASA Alaska Satellite Facility (ASF), used with permission.

baseline measurements against which to monitor future change. It is expected that such products will contribute to the development and validation of fine-scale fast ice models (Wang et al., 2003b). Such developments will greatly contribute to improving our understanding of the processes and interactions involved in fast ice formation, extent, and breakup, and their interannual variability and possible response to climate change.

Giles et al. (in preparation) further exploited the relatively stable characteristics of fast ice, in this case in East Antarctica, to monitor spatial variability in its radar backscatter signature. This information was then used to classify the ice into two broad categories based upon its mode of formation—namely, first-year and multiyear. The results are shown in Figure 5.58b. Cloud-free data from the Terra MISR may prove to be similarly useful, by enabling discrimination of fast ice types based upon their roughness characteristics (Nolin et al., 2002). Moreover, the new multi-polarization (Envisat ASAR) and polarimetric SAR data—e.g., ALOS PALSAR and Radarsat-2 SAR—are expected to improve discrimination of fast ice (see Section 5.9.7.3). While conventional repeat pass SAR interferometry is generally not applicable to pack ice research, due to the breakdown in coherence in such a dynamic environment, it has been applied to the study of the motion of fast ice, which presents a more stable and coherent target (Dammert et al., 1998; Li et al., 1996; Morris et al., 1999). Such interferograms are, however, difficult to interpret without supplementary information (Morris et al., 1999). See Chapter 2 of Volume 2 of this book for an in-depth discussion of SAR interferometry.

Further work has used Radarsat SAR, JERS-1 and ERS-1 and -2 SAR data combined with NOAA AVHRR data to focus in on a sub-sector of the East Antarctic region, to the east of the Mertz Glacier (Massom, 2003; Massom et al., 2001b). Strong links were found between the distributions of fast ice and grounded icebergs, which in turn have a profound impact on regional pack ice conditions:

- Assemblages of grounded bergs provide essential anchor points for fast ice growth, enabling it to extend hundreds of kilometers offshore. Comparison of data from 1999 with U.S. Declassified Intelligence Satellite Photographs (DISP) satellite data from 1963 (see Figure 5.31) showed a similarity in the morphology of the meridional fast ice promontory in October for each year (Massom et al., 2001b).
- The fast ice in turn appears to trap and hold ungrounded bergs for the duration of the ice season (in regions where ocean current velocities are low: Frezzotti et al., 1998; Massom, 2003), greatly limiting their drift for much of the year.
- The promontory intercepts sea ice advecting westwards within the near-coastal East Wind Drift. This leads to a major dynamic buildup and thickening of the promontory to create a major perennial ice feature in the region. Given an estimated thickness of >5 m, this fast ice lens contains a substantial volume of ice and forms a major regional freshwater reservoir (Massom, 2003).
- This promontory plays a major role in regional patterns of ice advection by steering ice drifting around the coast northwestwards to follow the continental shelf break—i.e., away from the key Mertz Glacier polynya to the west (see Section 5.9.4). As such, it has a major impact on the coastal climatological East Wind Drift.
- A major recurrent polynya forms on the leeside of the berg fast ice promontory (again see Section 5.9.4).

Analysis has also shown that, although the fast ice remains largely intact for much of the winter, periodic breakouts occur during intense storm events. Ice produced in this fashion joins the pack to the north to have a significant impact on regional ice dynamics and total sea ice mass in certain locations. This study illustrates the complexity of interactions between different components of the cryosphere. It further implies that possible changes in the number and distribution of grounded icebergs in response to global warming, and related to enhanced iceberg calving rates, will have an impact on fast ice and coastal pack ice distribution and thickness—and out to a distance of 300–400 km from the coast (Massom, 2003).

Cloud-free medium-resolution visible and TIR data from NOAA AVHRR and equivalent sensors (DMSP OLS and Russian Okean series sensors) have been fairly extensively used in fast ice studies. Regions of fast ice stand out in such imagery as being relatively featureless and homogeneous. Japanese scientists have used AVHRR data extensively to monitor Antarctic fast ice distribution in Lützow-Holm Bay, adjacent to Syowa Station, and along the nearby Prince Olav Coast (Yamanouchi and Seko, 1992). Enomoto et al. (2002) used higher resolution ADEOS AVNIR data to examine breakup and melt, also at Lützow-Holm Bay. Divine et al. (2003) investigated the spatial and temporal variability of Arctic fast ice extent in the NE

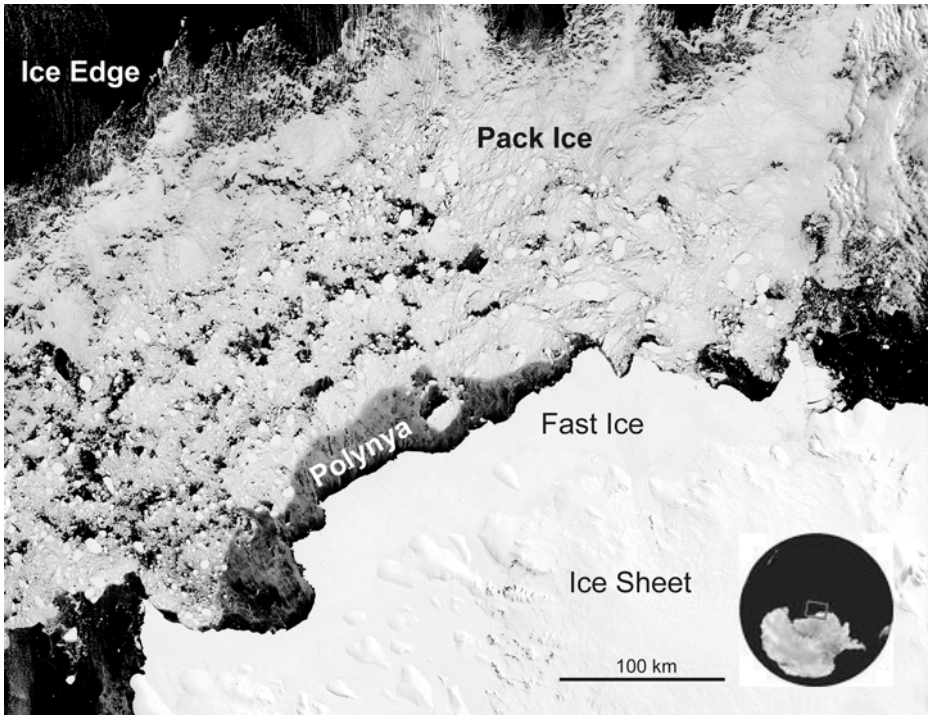

Figure 5.59. A Terra MODIS image showing fast ice and pack ice in the Ross Sea, February 23, 2004 (18 : 20 GMT). The location is marked on the inset map. The image, with a pixel size of 250 m, has been normalized for solar zenith angle. Note the significant increase in floe size with distance from the ice edge (open ocean), and the diffuse nature of the ice edge itself. Rather than forming a distinct boundary, the latter typically forms a low-concentration region comprising series of ice bands.

Image courtesy of NASA (obtained from the NASA MODIS Rapidfire website at ⟨*http://rapidfire.sci.gsfc.nasa.gov/gallery/*⟩).

Kara Sea over the period 1953–1990, using meteorological data and Russian ice charts that were latterly constructed using satellite visible and TIR data (Fetterer and Troisi, 1997). Mahoney et al. (2002) further combined AVHRR and *in situ* data to analyse anecdotal evidence from local concerned Inuit communities that the fast ice year is shortening in the vicinity of Barrow (Alaska). Such studies have observed considerable seasonal and interannual variability in areal extent, and the timings of formation and breakout. Undoubtedly, MODIS will revolutionize our ability to accurately delineate and monitor fast ice extent. An example is shown in Figure 5.59.

5.9.4 Polynyas

Nested within the large-scale atmosphere–ice–ocean system are a plethora of important processes and phenomena. Prominent among these is polynya

formation and maintenance. Polynyas are a common feature of the Antarctic continental perimeter and certain regions of the Arctic coastal margin. They are nonlinear openings, partially or totally ice-free, within the sea ice cover (WMO, 1970). They differ from leads in that they tend to recur and persist in the same locations over periods of weeks to months, and as such play an important role in regional air–sea ice interaction processes and, as we will see, even the global climate system. Polynyas have traditionally been classified according to their mode of formation and maintenance as either *latent heat* or *sensible heat* (Figure 5.60, see color section). *Latent heat polynyas* form where divergent ice motion conditions occur due to the prevailing wind and/or ocean current regimes—i.e., heat loss from the ocean surface is balanced by the latent heat of new ice formation. They are typically coastal, and often form in the lee of coastal promontories, grounded icebergs, fast ice, or islands, and are often associated with katabatic winds[11] (which are readily detectable by their strong thermal signature on the surface: Adolphs and Wendler, 1995; Bromwich and Geer, 1991; Bromwich and Kurtz, 1984). *Flaw polynyas*—e.g., in the Laptev Sea (Dethleff et al., 1998; Popov and Romanov, 2001)—form adjacent to fast ice. *Sensible heat polynyas*, on the other hand, result from the entrainment of sufficient oceanic sensible heat from below the pycnocline to prevent ice formation or melt existing ice (Comiso and Gordon, 1987). They usually, although not exclusively, occur away from the coast, typically as a result of the interaction between ocean currents and topographic features such as seamounts. A more realistic distinction is in fact between "shelf-water" and "deep-water" polynyas, given that certain polynyas often result from a combination of both sensible and latent heat processes (Morales Maqueda et al., 2004; Barber et al., 2001a, b).

Polynyas have the following key attributes and impacts:

- Although covering only a small areal fraction of the ice-covered ocean, polynyas (and leads) can dominate regional ocean–atmosphere heat exchanges in winter (Maykut, 1978, 1982). Heat fluxes of 500–1,000 $W\,m^{-2}$ have been measured over the St. Lawrence Island Polynya (SLIP) in the Bering Sea by Walter (1989), for example.
- Polynyas (and large leads) warm the atmosphere both above and downwind (Pinto et al., 1995, 2003; Roberts et al., 2001) to modify mesoscale atmospheric motion (Alam and Curry, 1995, 1998; Gallée, 1997; Kottmeier and Engelbart, 1992; Walter, 1989).
- Intense ocean surface cooling within polynyas results in ice formation rates which are much higher than those occurring in the surrounding pack ice (Cavalieri and Martin, 1985; Drucker et al., 2003; Ushio and Wakatsuchi, 1993; Zwally et al., 1985). For example, estimates of $\sim$5–25 $cm\,d^{-1}$ come from the Mertz Glacier Polynya (East Antarctica) in winter, depending on wind speed and air temperature (Bindoff et al., 2001; Lytle et al., 2001; Roberts et al., 2001). As such, coastal latent heat polynyas constitute major regional "ice factories"

[11] Katabatic wind is a wind that results from dense, cold air flowing downslope as a result of gravity, with the flow being typically channeled by the topography.

for the pack, with ice typically being advected away by winds and/or currents as it forms. This results in annual ice production rates of up to tens of meters (Roberts et al., 2001).

- Brine rejection during sea ice growth combines with ocean surface cooling to drive thermohaline convective overturning of the ocean (Mauritzen and Häkkinen, 1997; Schumacher et al., 1983), ventilation of the deep ocean (Muench and Hellmer, 2002), and water-mass modification. Downslope oceanic flows of cold, dense, and saline water contributes to Deep and Bottom Water formation in certain coastal polynyas in both the Arctic (Dethleff et al., 1998; Schauer, 1995; Schauer and Fahrbach, 1999; Signorini and Cavalieri, 2002; Swift et al., 1997; Weingartner et al., 1998; Winsor and Chapman, 2002) and Antarctic (Baines and Condie, 1998; Bindoff et al., 2000; Foldvik and Gammelsrød, 1988; Foldvik et al., 2004; Fukamachi et al., 2000; Gordon, 1982; Rintoul, 1998; Ushio et al., 1999), which in turn plays a central role in global ocean thermohaline circulation and therefore climate. Recent modeling studies have highlighted the critical importance of polynyas to the maintenance of oceanic thermohaline circulation, and the possible future impacts of global warming (Wu et al., 2003). Again, uncertainties are large, however, and the interannual variability in polynya contributions is poorly understood.
- In the Arctic, maintenance of the halocline is thought to be due to the advection of cold saline water formed in coastal polynyas in the Bering Sea and Arctic Ocean (Aagaard et al., 1981; Backhaus et al., 1997; Cavalieri and Martin, 1994; Martin and Cavalieri, 1989; Signorini and Cavalieri, 2002; Winsor and Björk, 2000). Siberian Shelf polynyas are estimated to produce between 20 and 60% of total Arctic Intermediate Water (Martin and Cavalieri, 1989).
- In late spring to summer, polynyas (and leads) transform into sites of enhanced shortwave radiation absorption and melt (Hunke and Ackley, 2001; Maykut and McPhee, 1995; Maykut and Perovich, 1987; Perovich and Richter-Menge, 2000). By this process, polynyas (and leads) play a major role in the annual meltback of the seasonal sea ice zone (Ohshima et al., 1998).
- Snow entering the ocean through polynyas and leads modifies the ocean freshwater balance.
- Polynyas (and flaw leads) greatly facilitate polar ship navigation (Brigham, 1991).
- Enhanced ocean–atmosphere moisture fluxes from leads and polynyas (Dare and Atkinson, 1999; Morales Maqueda et al., 2004; Pinto et al., 1995, 2003) may significantly impact local to regional cloud cover (Dethleff, 1994; Fett et al., 1997; Mailhot et al., 2002) and precipitation regimes, to affect the snow cover thickness distribution and surface energy balance. Cloud forcing effects on western Arctic polynyas were assessed by Key et al. (2001b), and on the North Water Polynya (NW Greenland) by Hanafin and Minnett (2001). Clouds also affect the surface albedo and energy budget.

Polynyas also play a major role in high-latitude ecological and biogeochemical processes, and have been likened to polar oases (Brown and Nettleship, 1981;

Dunbar, 1981; Grebmeier and Cooper, 1995; Massom, 1988; Smith and Gordon, 1997; Stirling, 1980, 1997; Stirling and Cleator, 1981):

- With leads, they enable marine mammals and birds to remain within the pack throughout the winter (Massom, 1988), and mammals to migrate.
- They strongly influence regional primary and secondary production. Major phytoplankton blooms can occur in polynyas in spring (Arrigo and van Dijken, 2003a; Arrigo et al., 1998b; Smith and Gordon, 1997).
- By virtue of enhanced biological activity and physico-chemical processes combined with vertical ocean mixing and convection, polynyas are thought to constitute major sinks of atmospheric CO_2 (Arrigo et al., 1999; Bates et al., 1998; Yager et al., 1995). As such, they have a profound impact on air–sea biogeochemical fluxes and ocean tracer transport.
- Major Arctic seabird colonies are directly associated with, and reliant upon, coastal polynyas (Falk et al., 2001; Gilchrist et al., 2001), and Antarctic penguin species are highly dependent on the close proximity of open water to breeding sites for ready access to food (Ainley et al., 2003).
- Polynyas have played an important role in the subsistence, lifestyle, and settlement patterns of Inuit peoples in the Arctic for thousands of years (Schlederman, 1980).

An excellent review of our current knowledge of atmosphere–polynya interactions, surface heat and moisture fluxes over polynyas, and observational and modeling studies is given by Morales Maqueda et al. (2004).

It follows that knowledge of the frequency and distribution of polynyas (and leads) is important in understanding large-scale high-latitude climate and biological processes. As a result of large uncertainties in the above processes, improved knowledge of the formation, maintenance, and interannual variability of polynyas is critical to better understand their complex role and possible response to climate variability/change (Martin, 2002; Smith et al., 1990). Moreover, polynyas are poorly represented in GCMs and most sea ice models, due in part to their typically small size relative to model grid scale. Considerable effort has recently been put, however, into constructing high-resolution models aimed at resolving individual polynyas—e.g., the Mertz Glacier Polynya in East Antarctica (Marsland et al., 2004) and the Cosmonaut Sea Polynya (Bailey and Lynch, 2000a, b).

The 2001 International Polynya Symposium (⟨*http://www.fsg.ulaval.ca/giroq/now/IPS2001/*⟩) highlighted four major themes in current polynya research:

- physical mechanisms responsible for the opening, maintenance, and closure of polynyas;
- the effects of these mechanisms and the environmental characteristics of polynyas on ecosystems and carbon cycling;
- intercomparison of the physics, chemistry, biology, and carbon cycling in polynyas; and

- interannual variability in the time of opening, extent, biological productivity, and carbon sequestration in sediments of polynyas, based on remote sensing (sea ice, ocean color, etc.) and sediment records.

To this can be added a major current concern about possible changes in polynya behavior related to climate change and their impact on global thermohaline circulation.

A number of major international field programs have recently focused on key polynyas—e.g., the Mertz Glacier Polynya in East Antarctica in 1999 (Bindoff et al., 2001; Lytle et al., 2001; Roberts et al., 2001; Wu et al., 2003), the North-East Water Polynya in Greenland (Minnett et al., 1997: ⟨*http://www.emi.dtu.dk/research/DCRS/seaice/new.html*⟩), the North Water Polynya in Baffin Bay/NW Greenland from 1997 to 1999 (Barber et al., 2001b, c; Deming et al., 2002; Ingram et al., 2002; Minnett et al., 1997: ⟨*http://www.fsg.ulaval.ca/giroq/now/wel.htm*⟩), and the Bathurst Island Polynya in the SE Beaufort Sea since 1990 (Macdonald et al., 2001; Melling and Riedel, 1995). All have relied heavily on satellite remote sensing not only to plan field measurements but also to provide a broad-scale overview and spatio-temporally extend surface measurements, which have in turn greatly enhanced interpretation of the satellite data. Such process studies are an essential prerequisite to the more realistic parameterization of polynyas in models. Major advances are being made in the latter, including the development of sophisticated high-resolution models for application to specific important polynyas—e.g., Bailey and Lynch (2000a, b), Bailey et al. (2001), Biggs and Willmott (2001), Biggs et al. (2000), and Marsland et al. (2001, 2004). Polynya models, as reviewed by Morales Maqueda et al. (2004), require improved observational data for both input and validation. For example, Walkington and Willmott (2004) have introduced sea ice concentration into a polynya flux model, a move that facilitates comparison between predicted and satellite-observed polynya areas. Satellites cannot provide all essential information, however. Oceanographic data in ice-covered regions, for example, can only be collected by *in situ* methods (Bindoff et al., 2001). The latter, however, are of key importance in providing fundamental information.

5.9.4.1 Determination of polynya size/extent

The most fundamental contribution of satellites to polynya research is in the detection, mapping, and monitoring of polynya extent and its variability. For sensible heat polynyas, extent is determined by the dimensions of the associated warm-water anomaly, while that of latent heat polynyas is a function of the balance between ice production and export (Morales Maqueda et al., 2004). Accurate estimates of ice concentration in these and other regions are again crucial as errors of even a few percent in open-water fraction within the sensor footprint can make a large difference in heat and salinity flux estimates (Maykut, 1978), which are a motivation for polynya research (see below). Factors controlling the exchange of sensible heat from polynyas (and leads) include air temperature, wind speed, and surface temperature. Moreover, polynya size affects the rate of energy transfer (Andreas and Murphy, 1986; Maslanik and Key, 1995).

Once again, the primary data source has been the passive-microwave radiometer time series, within which polynyas show up as areas of anomalously low ice concentration (Martin et al., 1992). Given their uninterrupted large-scale coverage, they are well-suited to analyses of polynya synoptic-scale opening and closing and interannual variability (Bohm et al., 1997). Most analyses have used the multi-frequency data available since 1978. Perhaps the most famous polynya discovery of all, however, occurred in single-channel ESMR data. With a maximum area of $\sim$350,000 km^2, the extraordinary deepwater Weddell Polynya, which occurred in the winters of 1974 to 1976 but was never measured *in situ* (Carsey, 1980), is the largest polynya encountered to date (Figure 5.61, see color section). Although this author (R.M.) has seen reference in a certain magazine beloved of US supermarket checkout counters to a Martian base under the pack as being the cause of this immense perturbation of ocean–atmosphere coupling, a more likely explanation is probably Earth-based. Various hypotheses have been put forward—e.g., Parkinson (1983), Holland (2001a, b), Martinson et al. (1981), Moore et al. (2002), as reviewed by Morales Maqueda et al. (2004). A polynya watch has been set up at the U.S. National Ice Center to detect Weddell Polynya formation if and when it occurs using near-real time satellite passive-microwave (DMSP SSM/I) data (⟨*http://science.natice.noaa. gov/polynya/polynya.htm*⟩).

Other important polynya studies using passive-microwave data include:

- The Cosmonaut Sea polynya in Antarctica and centered on $\sim$65°S, 40°E (Arbetter and Lynch, 2002; Arbetter et al., 2004; Bailey and Lynch, 2000a,b; Bailey et al., 2001; Comiso and Gordon, 1987, 1996; Gordon and Comiso, 1988; Takizawa et al. (1994). Significant variability was noted in polynya maximum area, of between $\sim$35,000 and 115,000 km^2, with open water accounting for 30–45% of the total polynya extent.
- The Ross Ice Shelf polynya (Bromwich et al., 1998; Budillon et al., 2002; Gloersen et al., 1992; Jacobs and Giulivi, 1998; Zwally et al., 1985). This is the largest recurrent Antarctic coastal polynya, with an average and maximum area of 27,000 and 50,000 km^2 respectively. It has a major impact on regional ice formation and melt and marine ecology, and also is an important site of Antarctic Bottom Water production (Koshlyakov and Tarakanov, 2003). Its formation is attributed to ice divergence forced by both katabatic (Bromwich et al., 1993) and synoptic winds (Jacobs and Comiso, 1989), combined with upwelling of relatively warm Circumpolar Deep Water (Pillsbury and Jacobs, 1985).
- The nearby Terra Nova Bay polynya, with a study by Van Woert et al. (2001a) using satellite data (NOAA AVHRR and DMSP OLS) and other observations to determine ocean-current regimes within the polynya.
- Deep-water polynyas in the Arctic e.g., the Kashevarov Bank Polynya in the Sea of Okhotsk (Alfultis and Martin, 1987; Martin et al., 1998), and the Odden/Nordbukta system in the East Greenland Sea (Comiso et al., 2001).
- Coastal polynyas in peripheral Arctic seas (Gloersen et al., 1992). Although small, these are important sites of new-ice formation and dense shelf-water

formation, which contributes to the production of Arctic Intermediate and Deep Water (Gladyshev et al., 2000; Golovin, 2002; Martin and Cavalieri, 1989; Swift et al., 1997). Driven by the need to determine the contribution of these polynyas to the maintenance of the cold Arctic Ocean halocline layer, a number of studies have used satellite data to assess their interannual variability and seasonality e.g., Cavalieri and Martin (1994), Martin and Cavalieri (1989), and Winsor and Björk (2000).

For more detailed information on these and other polynyas, please see Morales Maqueda et al. (2004) and the references therein.

Massom et al. (1998b) detected and monitored 28 polynyas along the East Antarctic coastline over the period 1987 to 1994 by applying a simple threshold to SSM/I ice-concentration data at 25 km resolution. Their map of the locations of these polynyas, which range in size from $\sim$1000 km^2 for the Cape Hudson polynya to $\sim$23,000 km^2 for the Mertz Glacier polynya, is shown in Figure 5.62. Combining the satellite analysis with ancillary data, Massom et al. (1998b) also determined the factors affecting polynya recurrence and maintenance. This study also observed significant interannual variability both in polynya maximum extent and its timing, which have important implications given the global significance of the Mertz Glacier polynya as a major source of Antarctic Bottom Water (Rintoul, 1998; Williams and Bindoff, 2003). Massom et al. (2003) further highlighted the key role played by certain Antarctic shelf polynyas in the seasonal (spring-summer) meltback of the pack, enabling ice decay to simultaneously occur from both the south and north. Ice production and deep-water entrainment processes within the polynyas to the west of the region in Breid and Lützow-Holm Bays was discussed by Ushio et al. (1999). Note that as much of the Antarctic pack is seasonal, many of its polynyas become global in extent in the austral summer!

Other studies have estimated open-water area within polynyas. An example of a time series of an openwater area derived from 25-km-resolution SSM/I ice concentration data, and for polynyas in the Weddell Sea (Antarctica), is given by Comiso and Gordon (1998). As Morales Maqueda et al. (2004) point out, however, the uncertainty in such estimates is large. Problems in applying passive-microwave data to polynya studies relate to coastal pixel contamination effects and their coarse resolution (Van Woert, 1999a), given that many important polynyas are small—e.g., dimensions of the order of 5 to 10 km—even compared with individual pixels. Other ambiguities stem from the difficulty in deriving accurate estimates of ice concentration in regions of predominantly new/thin ice (see Section 5.9.1). This raises an important issue concerning the definition of polynya extent. Polynya margins are typically indistinct, entailing a gradation from openwater and frazil ice in the polynya heart outwards to a gradually thicker (older) ice cover. The open-water fraction is often small compared with the overall polynya "regime", which includes ice newly formed within the polynya. Ambiguities remain in the determination of the boundary between the thin polynya ice and the thicker surrounding pack ice. As such, "polynya size" can be a somewhat misleading term if not qualified, a factor that affects the interpretation and comparison of polynya

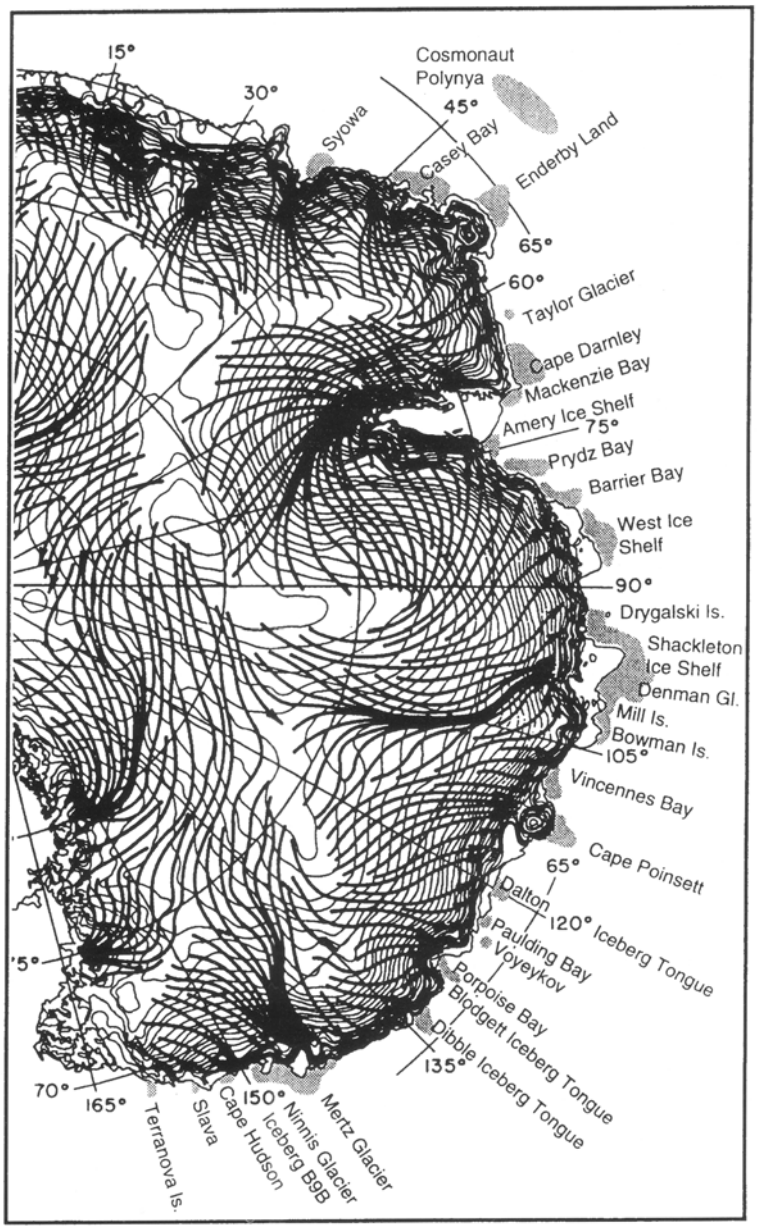

Figure 5.62. A map of coastal polynya locations in East Antarctica, derived from analysis of DMSP SSM/I ice concentration data (1987–1994). The gray shading indicates the approximate maximum areal extent of each polynya. Over the Antarctic Ice Sheet, thin lines denote contours of surface elevation, while thick lines represent streamlines of near-surface gravity drainage winds (from Parish and Bromwich, 1987).

From Massom et al. (1998b), after Potter (1995). Reprinted with permission of the International Glaciological Society (IGS). © 2005 IGS.

retrievals using satellite data collected at different resolutions (and wavelengths). An example of the different yet complementary information obtainable from different satellite sources and derived products, in this case SSM/I, AVHRR TIR, AVHRR-derived ice thickness and Radarsat SAR data, is given in Figure 5.63 (see color section). This again illustrates the considerable benefits to be gained from combining different datasets.

Budillon et al. (2002) partly addressed the resolution issue by studying opening and closing episodes of the Ross Sea polynya using meteorological data with daily SSM/I ice concentration data at a spatial resolution of 12.5 km. The latter were derived using the Sea Lion algorithm, which incorporates 85-GHz data (Kern, 2001, 2004; Kern and Heygster, 2001). The increased atmospheric water vapor contamination effects associated with this higher frequency were corrected for using a radiative transfer model, numerical weather prediction model data, and data from other SSM/I channels—i.e., 19, 22, and 37 GHz. This approach also corrects for the effects of wind-roughening of openwater on observed brightness temperatures. Non-application of these corrections would typically result in an overestimation of ice concentration—a key factor in polynya and other studies. Correlation of interannual polynya behavior was achieved by Budillon et al. (2002) through principal component analysis.

Another method, developed by Markus and Burns (1995), measures subpixel-scale polynyas in SSM/I data using 85- and 37-GHz T_B data successively, creating an enhanced resolution of ~6.25 km. Known as the Polynya Signature Simulation Method (PSSM), it takes advantage of the higher resolution at 85 GHz (~15 km) while using lower frequency data (at ~30-km resolution) to compensate for the sensitivity of 85 GHz to atmospheric effects. It is based upon the simulation of microwave images of polynya events by convolving an assumed brightness–temperature distribution with the satellite sensor antenna pattern. These images are compared with measured microwave data, and the polynya area is iteratively modified until the best agreement is attained. According to the authors, application of the technique to synthetic images produces maximum and mean errors of 200 km^2 and 80 km^2, respectively. An example of polynya area retrieval, from the Weddell Sea, is shown in Figure 5.64. Comparison of results with coincident TIR data has shown that the algorithm in fact yields not only the area of open water but also that of new ice (up to a thickness of ~0.06 m). If atmospheric effects can be properly accounted for, this likely produces a more realistic estimate of the area of a polynya "ice factory" than can be achieved with simple concentration thresholding techniques, which likely produce information on the wider polynya "regime" only. Using this enhanced resolution technique, Markus et al. (1998) derived open-water area values 20–40% lower than those estimated for the same region of the Weddell Sea by Comiso and Gordon (1998). They further applied their results to an assessment of the impact on ocean salinity. Renfrew et al. (2002) combined this enhanced resolution SSM/I dataset with meteorological data and physical models to assess the surface energy budget of coastal polynyas in the southern Weddell Sea. Such studies are important in that they provide data directly comparable with output from state-of-the-art high-resolution polynya models (see Morales Maqueda et al.,

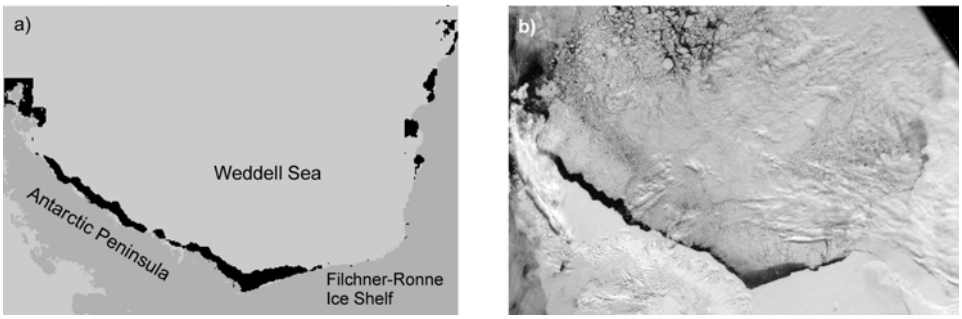

Figure 5.64. Results from the Polynya Signature Simulation Method (PSSM), showing (a) an SSM/I-based retrieval of polynya areas in the Weddell Sea on November 16 (day 321), 1992, and (b) a DMSP OLS visible band image acquired at 11 : 28 GMT on the same day for comparison. Polynya regions are marked in black in (a). The spatial resolution in (a) is 5 km. Good qualitative agreement is apparent in polynya size.

2004 for details of the latter). The application of polynya area retrievals to the study of primary production and the impact of vast icebergs are outlined in Sections 5.9.4.3 and 5.9.4.4, respectively. Further improvements are likely to result by applying this technique to improved resolution AMSR and AMSR-E data.

Arrigo and van Dijken (2003a) took a different approach based on that outlined above. They used PSSM-derived daily images of sea ice distribution to construct a circumpolar Antarctic map of the percentage of ice-free days that a given pixel remained ice-free over the June to October period from 1997 through 2001 (Figure 5.65a, see color section). Coastal regions with consistently low sea ice concentrations were then identified as polynyas, based on the qualifying threshold of 50% ice-free days in winter. By this method, they identified 37 polynyas around Antarctica, which are numbered in Figure 5.65b. The largest was the Ross Sea polynya (adjacent to the Ross Ice Shelf and centered on $\sim$75.51°S, 179.19°E) at $\sim$20,000 km^2, while the smallest was $\sim$130 km^2 (in the West Lazarev Sea at 69.94°S, 7.85°E). They also introduced the concept of ''post-polynyas''. While a polynya is strictly a region of open water or reduced sea ice cover that occurs in waters that would be expected to be ice-covered, post-polynyas occur each year after conventional wintertime polynya activity. The rationale is that these springtime features, while technically not polynyas, are biologically and biochemically important and are intimately related to winter polynyas. Using these criteria, the Ross Sea post-polynya expanded to a size of 396,500 km^2—i.e., in summer—while the West Lazerev Sea post-polynya remained the smallest at 1,040 km^2. Arrigo and van Dijken (2003a) also carried out a study of phytoplankton dynamics in these polynyas (see below).

Due to the different approaches used with the same dataset (but over different periods), the winter polynya areal extents reported by Arrigo and van Dijken (2003a) differ markedly from those reported by Massom et al. (1998b) for 27 East Antarctic

coastal polynyas. Equivalent polynya areas calculated by the former are in some cases an order of magnitude smaller. This is attributable to the fact that Arrigo and van Dijken (2003a) calculate the openwater area only, while calculation of polynya area using the ice concentration approach is sensitive to the concentration threshold used and is limited by poor resolution (Massom et al., 1998b). Moreover, Massom et al. (1998) did not include data from months when the polynya did not develop in their calculation of mean wintertime polynya area. As Arrigo and van Dijken (2003a) point out, however, the differences are largely operational and are based upon how a polynya is defined. In fact, the polynya locations determined by the two studies agree very well.

Higher resolution visible to TIR data—e.g., from the AVHRR—have been used to better resolve polynya areal extent. Such techniques are based upon the strong contrast in the albedo and surface temperature of open water/thin ice versus thick snow-covered ice. While these data have been extensively used to detect and monitor polynyas—e.g., Adolphs and Wendler (1995), Ishikawa et al. (1996), Kozo et al. (1990), Kurtz and Bromwich (1985), Massom et al. (2001b), Stringer and Groves (1991), Van Woert (1999a, b), Wendler et al. (1997), and Yamanouchi and Seko (1992)— they are again severely limited by cloud cover. Even under apparent "cloud-free" conditions in satellite visible to TIR data, two types of cloud can obscure polynya regions and bias polynya measurements using these data—namely, high thin clouds and ice fog (Martin et al., 2004). High cold thin clouds make the ice appear thicker and colder than its actual values, while warm ice fogs or sea smoke are generated by vapor flux from the polynya itself. In spite of these limitations, the ready availability of AVHRR and similar data makes them attractive to polynya studies, especially when combined with microwave satellite data (see below). Moreover, surface temperature derived from the thermal channels is itself an important parameter in the computation of ice growth rates (see Section 5.6.1). With their improved spatial and temporal resolution and higher accuracy, the Aqua and Terra MODIS sensors promise to deliver enhanced analyses. For further discussion on the satellite detection of thin ice, please refer to Sections 5.9.6 and 5.9.7.

Other studies have exploited the high resolution and all-weather, day–night capabilities of spaceborne SAR to study polynya opening and closing (Haarpaintner, 1999), based upon the backscatter distinction between openwater/frazil ice and consolidated ice or young gray ice and older ice. A high spatial resolution is desirable to both determine the open-water area proper within the polynya, the spatial distribution of ice thickness classes present, and the shape of the polynya and the nature of its boundary (Dokken et al., 2000b). The open-water "core" is the region of largest heat flux, ice production, and salt ejection (Roberts et al., 2001). Accurate information on polynya shape is required to understand the development process and its response to atmospheric and oceanic forcing (Darby et al., 1995). An example of SAR imagery of polynyas is shown in Figure 5.66. These data can be used to interpret coarser resolution data and to validate and fine-tune wind-driven polynya models (Haugan and Skogseth, 2003). Wilson et al. (2001b) have used time series of Radarsat-1 ScanSAR Wide imagery to derive ice kinematics in the North Water Polynya (see Section 5.9.5.5), gaining information on processes of polynya

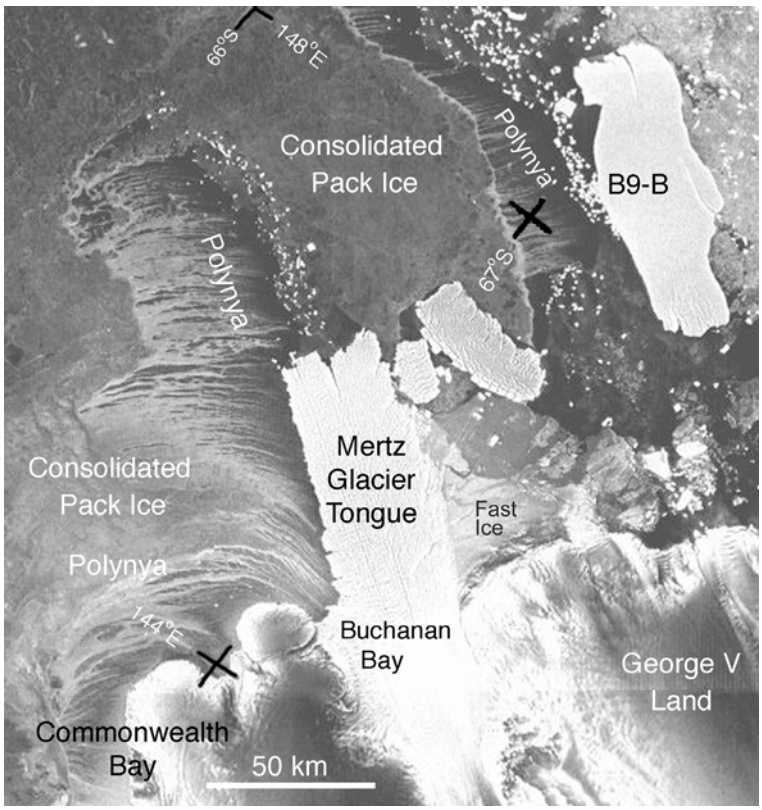

Figure 5.66. Part of a Radarsat ScanSAR image (resolution 100 m) of the Mertz Glacier polynya, East Antarctica, on August 4, 1999. This is one of the largest recurrent polynyas in Antarctica, and an important site for the formation of dense and cold Antarctic Bottom Water (Bindoff et al., 2000; Rintoul, 1998). Strong wind conditions on this day produced high rates of sea ice formation in the form of frazil ice streamers (the streaked regions in the polynya) which are aligned with the wind direction—classic polynya "ice factory" conditions. The important impact of the floating Mertz Glacier tongue and the associated line of small grounded icebergs to the north on polynya extent is clearly apparent. This polynya is formed by two different wind regimes: cold, strong, and unrelenting katabatic winds cascading seawards from the ice sheet into Buchanan and Commonwealth Bays, and winds related to the passage of storms farther to the north (Massom et al., 2001b). Synoptic-scale changes in the latter typically result in cyclical opening and closing of the larger polynya at a frequency of 3 to 7 days. Time series of images such as this are well-suited to monitoring polynya opening and closing in response to changing synoptic-scale wind conditions. Note also the recurrent polynya in the lee (i.e., downwind) of grounded iceberg B9-B and myriads of small grounded bergs to the north. The impact of grounded icebergs on ice conditions is discussed in Section 5.9.4.4. Commonwealth Bay to the lower left of the image is the site of Sir Douglas Mawson's classic tale of polar pluck and endurance, *The Home of the Blizzard* (Mawson, 1915).

From Massom (2002). Radarsat data © Canadian Space Agency/Agence Spatiale Canadienne 1999, processed and distributed by the Alaska Satellite Facility, used with permission.

formation and maintenance. Thomsen et al. (1998a, b) carried out an intensive study of the North East Water Polynya (NE Greenland) using ERS-1 SAR imagery. In their studies of the SLIP, Liu and Peng (1998) and Liu et al. (1997a) demonstrated that wavelet analysis of SAR imagery (in this case from ERS-1) can be employed to automatically delineate and track polynya boundaries. Dokken et al. (2000b) also developed a satellite SAR-based algorithm to detect and map Arctic coastal polynyas. This technique consists of three stages. The first two perform segmentation and classification based on image texture and backscatter information, or alternatively backscatter and irregularity. Segmentation is a process by which the number of surface-type classes is determined and each pixel is labeled accordingly. The third stage is based on wavelet analysis to detect the transition between ice classes—e.g., open water and surrounding ice. Errors are reduced by using three independent results, with a comparison being made with SSM/I results from the Markus and Burns (1995) PSSM method. Dokken et al. (2000b) further developed a routine to systematically identify and map Arctic polynyas by incorporating ERS SAR browse images (Laur and Dokken, 1997), the SSM/I PSSM technique (for large polynyas), and a numerical polynya model. Polynya shape and size were further characterized by applying wavelet analysis (Liu et al., 1997a) to higher resolution (25 m) and calibrated ERS SAR PRI data. The latter are available from ESA (⟨*http://earthnet.esrin.esa.it/*⟩) for the period August 1991 to August 1997, while SAR browse data are available from January 1994 to the present. This study shows the considerable advantages to be gained from SAR data with the polynya model in terms of characterizing polynya dynamics.

Polynya analyses using SAR data are limited to some extent by the fact that shelfwater polynyas typically occur in windy, turbulent environments. Wind-roughened open ocean is a strong scatterer of radarwaves, and yields a high backscatter which can resemble that from consolidated thick ice (Dokken et al., 2000a). Automated polynya characterization using single-frequency and single-polarization SAR is limited by the fact that the backscatter and textural characteristics of open water and ice will often overlap. As such, care should be taken when analysing individual SAR images. Such analysis should ideally include time series of closely spaced images and additional ancillary information—e.g., meteorological data. This problem can, however, be circumvented to some extent by combining the SAR data with near-coincident TIR satellite imagery by a co-registration procedure known as the Hue–Lightness–Saturation, or HLS, technique. This method has been applied to the SLIP (Drucker et al., 2003). In effect, it combines the strengths of both techniques to enhance the detection of newly forming ice and open water, and once again underlines the considerable benefits of combining different yet complementary satellite data. As described by Drucker et al. (2003), the SAR/AVHRR composite is constructed from near-concurrent images. Primarily, an AVHRR IST image is created using the technique outlined later (in Section 5.9.11). This and a near-contemporary calibrated Radarsat ScanSAR amplitude image are both processed to a common map projection and grid, with a 200-m grid size. An important step here is image co-registration, which is facilitated using landmarks identifiable in the imagery (if

available). Finally, a composite RGB (true color) image is created in HLS color space by (i) mapping IST values over the range of -30° to 0°C to hue values from 0 to 1 (according to a fixed map function), then (ii) mapping SAR backscatter values over the range of -25 to -10 dB to lightness/value (brightness) values from 0 to 1 according to a second mapping function. Drucker et al. (2003) set the third color dimension (saturation) to a fixed value of 70%. Finally, the HLS composite image is converted into RGB color space by applying an HLS to RGB transform function. This sequence is shown in Figure 5.67 (see color section).

Considerable improvements are again anticipated with the emergence of new polarimetric SARs onboard Envisat, ALOS, and Radarsat-2 (Dokken et al., 2000b). Of particular importance from a polynya detection and monitoring perspective is that these systems offer improved temporal resolution (based upon their programmable and flexible imaging modes) and the potential to greatly enhance discrimination of different ice types, albeit over narrow swaths. To this can be added the exciting prospect of enhanced detection of thin ice and open water using the polarimetric capabilities of the new SARs (see Section 5.9.7.3). Regarding temporal resolution, a major drawback of fixed incidence angle and narrow-swath sensors such as the SARs onboard ERS-1 and -2 is that their repeat cycle is long—i.e., 35 days—compared with the dynamic behavior of typical polynyas. The average opening–closing cycle of polynyas is of the order of 3–4 days (Dokken et al., 2000b; Massom et al., 2001b), in response to synoptic-scale atmospheric forcing.

5.9.4.2 Determination of ice production and brine rejection rates in polynyas

Estimates of ice and concomitant salt production rates within polynyas have been limited by large uncertainties associated with inaccurate mapping and monitoring of both the openwater and ice thickness distributions in and adjacent to polynyas (note that ice thickness is more fully discussed in Section 5.9.6). A more precise understanding of ice production rates and associated surface fluxes in polynyas is essential for accurate determination of the mass balance of sea ice, the energy budget of the atmosphere, and salt flux to the ocean (Morales Maqueda et al., 2004). One approach has been to estimate ice production and brine rejection rates and concomitant brine rejection rates by combining satellite-derived estimates of polynya area with meteorological data in simple thermodynamic ice growth models. Martin and Cavalieri (1989) and Cavalieri and Martin (1994) calculated polynya open-water area using passive-microwave data from satellites then performed a surface energy balance to estimate the ice growth rate. Estimates of mean ice growth were $\sim 10\,\mathrm{m\,yr^{-1}}$ with a 30% uncertainty for Eastern Arctic polynyas, and generally higher for Western Arctic polynyas, although these estimates may have been biased by the inherent inability of the microwave sensor to distinguish between open water and thin ice.

Kurtz and Bromwich (1985) used AVHRR-derived estimates of polynya extent, in this case for the Terra Nova Bay Polynya (Antarctica), to compute cumulative ice production over the winter period. Their estimate of $\sim$40–60 m of ice, equivalent to a volume of 50–80 $\mathrm{km^3}$, represents $\sim$10% of the annual ice production over the entire

continental shelf of the Ross Sea. Such "ice factory" conditions play a key role in the modification of the estimated ~1 Sverdrup of High-Salinity Shelf Water exported from the polynya (Budillon and Spezie, 2000; Buffoni et al., 2002; Van Woert, 1999b). Van Woert et al. (2001a) have further used satellite observations to determine ocean current regimes within the Terra Nova Bay polynya, Antarctica. Such studies illustrate the key role that satellite remote sensing is playing in improving our knowledge of the behavior of important polynyas, and their central role in air–sea ice interaction processes.

Following on from this work, attempts have been made to quantify salt fluxes—e.g., Haarpaintner et al. (2001a, b)—and dense-water production using sea ice information derived from satellite data—e.g., for all Arctic polynyas—by Cavalieri and Martin (1994), Martin and Cavalieri (1989), Martin et al. (1998), and Winsor and Björk (2000). As important sites of Antarctic Bottom Water formation (Broecker et al., 1998; Foldvik and Gammelsrød, 1988; Jacobs, 2004), coastal polynyas in the southern Weddell Sea have been under the spotlight. Satellite-based studies using passive-microwave data have determined that large heat losses over these polynyas—e.g., a winter monthly average of $400\,W\,m^{-2}$—create ice growth rates as large as ~10 to $12\,m\,a^{-1}$, fully a factor of 10 greater than equivalent rates in the central Weddell Sea (Cavalieri and Martin, 1985; Markus et al., 1998; Renfrew et al., 2002; Zwally et al., 1985). Renfrew et al. (2002) further noted a large interannual variability in total annual ice production, and estimated that southern Weddell Sea polynyas account for only ~0.2% of the total sea ice area in the Weddell Sea, but account for 2.5 to 9% of the total ice volume (Renfrew et al., 2002). Considerable uncertainty remains as to the source regions of Antarctic Bottom Water (Jacobs, 2004).

Ice and salt production-rate estimates such as those presented above must be treated with some caution, however, given current uncertainties in both observational data (particularly, the coarse-resolution satellite data and modeling tools available: Morales Maqueda et al., 2004). These relate to (i) large uncertainties associated with inaccurate mapping and monitoring of both the openwater and ice thickness distributions in and adjacent to polynyas (Gawarkiewicz and Chapman, 1995; Van Woert, 1999a); (ii) assumptions made about ocean salinity and temperature profiles within polynyas; and (iii) the poor spatial resolution and often low (though improving) reliability of meteorological data. Re-evaluations using improved resolution data—e.g., from the AMSR—and new techniques aimed at enhancing the resolution of DMSP SSM/I data—e.g., Markus and Burns (1995)—are promising, as noted above.

Recent studies have further underlined the considerable benefits of merging different datasets—i.e., data fusion (Beavan and Gogineni, 1998; Collins, 1992). Martin et al. (2000) used time series of SAR, AVHRR, and passive-microwave data with meteorological data to monitor the growth and decay of the SLIP in response to the passage of storms. The authors combined SAR-derived information on frazil ice, pancake ice and open-water distributions within the polynya with surface temperatures derived from the AVHRR to compute polynya heat transfer as a function of ice type. Drucker et al. (2003) examined the same polynya by combining AVHRR, Radarsat-1 SAR data, moored ice-profiling sonar and

salinity/temperature sensor data. The SLIP is a major regional "ice factory", and was the focus of a pioneering modeling study by Pease (1987). Her steady-state model describes polynya size in terms of four variables—namely, polynya width R, the solid ice equivalent h_C of the frazil accumulation thickness, the export velocity U_I of ice away from the polynya, and heat loss F_F from the region of new frazil ice formation. These are related by:

$$R = \frac{h_C U_I}{F_F} \tag{5.34}$$

Drucker et al. (2003) provided the means to directly measure the terms in (5.34). Polynya width is determined from single SAR images, based upon the distinctive signature of frazil/grease ice plumes and bands—i.e., bright linear streaks (Liu et al., 1997a). Frazil accumulation thickness can be estimated over a large area from clear-sky AVHRR data, using the technique laid out in Section 5.9.4, while IPS (Ice-Profiling Sonar) measurements permit point estimates of h_C. Drucker et al. (2003) reduced the frazil accumulation thickness to h_C following Martin and Kaufman (1981). Ice export velocity can be derived from successive SAR images, and F_F from AVHRR-derived surface temperatures combined with meteorological data. As such, direct comparison can be made between simulated and observed polynya width. Error sources and uncertainties of this technique, which represents a first validation of the steady-state relationship (5.34), are given in Drucker et al. (2003). The sequence for estimating ice thickness is laid out in Figure 5.68 (see color section). It is anticipated that such an approach, and its future refinement as improved satellite data become available—e.g., the use of MODIS rather than AVHRR data—will result in improved models of specific polynyas and an enhanced knowledge of their key role in ocean–atmosphere interaction processes.

Noting that water vapor and fog emanating from the polynya affect the accuracy of thin-ice thickness estimates using TIR data, Martin et al. (2004) developed a thin-ice algorithm that uses SSM/I 37-GHz data (V/H ratio). While this method is limited to a resolution of 25 km, it enables collection of near-daily information unaffected by cloud and water vapor effects. A detailed assessment of the strengths and weaknesses of various passive-microwave thin-ice algorithms—e.g., Cavalieri (1994), Cavalieri and Martin (1994), Markus and Burns (1995), Markus and Cavalieri (2000), and Weingartner et al. (1998)—is given by Martin et al. (2004). The latter applied their technique to a study of heat flux and thin-ice thickness for the large Chukchi Sea–Alaskan coast polynya over the period 1990–2001, validating the results with AVHRR-derived estimates (using the technique given in Drucker et al., 2003) and SAR data. This method is adaptable to use with improved AMSR-E data.

New research by Holt et al. (2003) is examining the variability of Arctic polynyas and their response to recent changes in large-scale atmospheric patterns. Holt et al. (2003) have developed a new technique to measure heat flux and ice thickness within polynyas using multisensor satellite data. Specifically, they combine SSM/I passive-microwave data, AVHRR data, Radarsat SAR data, and QuikSCAT radar scatterometer data to measure polynya opening and closing and monitor thin-ice

formation over time. It appears that the SSM/I polarization ratio V/H at 37 GHz is sensitive to thin ice to a thickness of 20 cm, enabling estimates of polynya activity on a daily basis. Such computations in turn enable estimates of salt flux, which can be compared with measured and modeled changes in the Arctic halocline described in Section 5.5. Regarding sea-ice-induced salt flux in the open ocean, Toudal and Coon (2001) developed a numerical model to relate the formation, advection and decay of frazil, grease, and pancake ice, as observed in SMMR and SSM/I data, to salt redistribution in the Odden region of the Greenland Sea for the period 1979–1997 (see Brandon and Wadhams, 1999; Carsey and Roach, 1994; Comiso et al., 2001; and Toudal et al., 1999 for further information on mapping and monitoring the Odden region from space). A subset of the results, in the form of maps of the total annual salt flux from 1988/89 to 1996/97, is shown in #Figure 5.69# (see color section). This promising melding of satellite and other data into a model requires further validation.

5.9.4.3 Primary production in polynyas

A focus of increasing research is the quantification of seasonal and interannual variability in upper-ocean chlorophyll *a* (chl *a*) concentration and primary production within major polynyas, as well as at the ice edge, using satellite ocean color data. These data can be used under cloud-free conditions in spring and summer due to the absence of contaminating sea ice (Arrigo et al., 1998b, c; Smith and Gordon, 1997). The latter tends to saturate ocean color sensors. Note that ocean color data are reliant on solar illumination, and are unobtainable at high latitudes in winter. For example, Arrigo (2000) used SeaWiFS data and 6.25-km resolution DMSP SSM/I data (enhanced using the PSSM technique of Markus and Burns, 1995) to characterize the relationship between the annual cycle of primary production and sea ice distributions within the Ross Sea polynya region (Antarctica) between 1997 and 1999.

Arrigo and van Dijken (2003a) extended this work to an analysis of 37 Antarctic coastal polynyas (see Section 5.9.4.1). They derived chl *a* concentrations from SeaWiFS 8-day composite level-3 binned files using the OC4v4 algorithm of O'Reilly et al. (1998). While constant with longitude (at 9.8 km), the spatial resolution of these images varies with latitude, ranging from 2.0 km at 78°S to 4.3 km at 63°S. Methods for deriving primary production are given in detail by Arrigo and van Dijken (2003a). Their results indicate high (i.e., enhanced) concentrations of mean polynya chl *a*, ranging from 0.16 to 2.2 mg m^{-3} and averaging 0.69 mg m^{-3} for the 37 polynyas identified and over the period of September through March inclusive (from 1997 to 2002). High but variable rates of primary production were also observed, with daily averages of 0.09 to 0.76 g C m^{-2} d^{-1} compared with mean annual rates ranging from 18 to 161 g C m^{-2} d^{-1}, with most coastal polynyas exhibiting annual rates of between 20 and 80 g C m^{-2}. Putting this into wider perspective, peak production in summer (January) averaged over all post-polynyas detected by Arrigo and van Dijken (2003a) is more than three times higher than the average for the entire offshore Southern Ocean. Arrigo and van Dijken

(2003a) noted a strong relationship between seasonal polynya area and primary production (Figure 5.70). They further observed that only 4 of the 37 polynyas studied—namely, the Ronne Ice Shelf, Ross Sea, Prydz Bay, and Amundsen Sea Polynyas—were together responsible for >75% of total phytoplankton production.

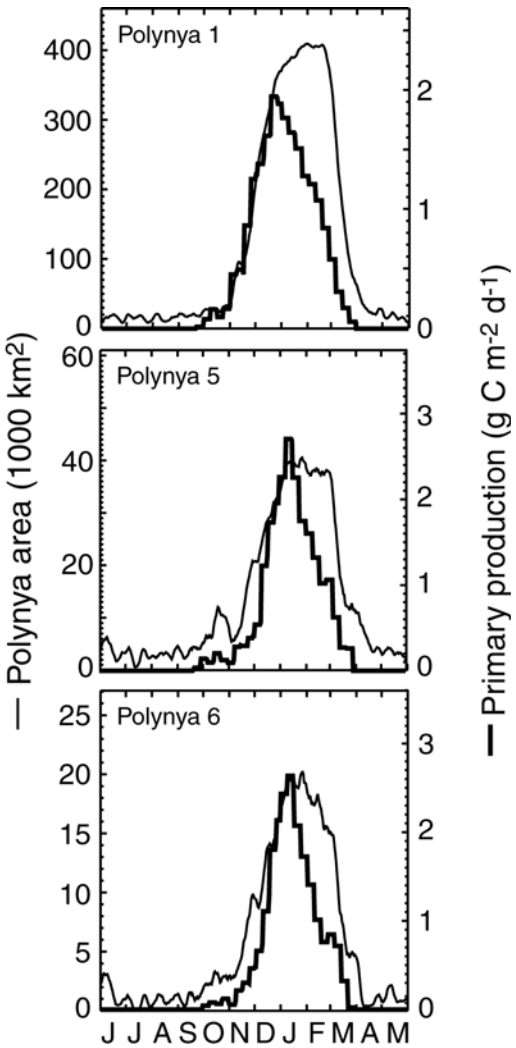

Figure 5.70. A comparison of seasonal changes in post-polynya area (estimated from SSM/I data) and daily primary production (estimated from SeaWiFS data), showing the characteristic early decline in production relative to the refreezing of the ocean within the three most biologically productive polynyas—i.e., (1) the Ross Sea, (5) the Amundsen Sea, and (6) Pine Island Bay.

Bélanger and Larouche (2001) have similarly shown that intense phytoplankton blooms occur in May/June in the North Water polynya (NW Greenland), again using SeaWiFS data. In another Arctic study, Arrigo and van Dijken (2004) combined SSM/I and SeaWiFS data to study the relationship between phytoplankton abundance and sea ice dynamics within the Cape Bathurst Polynya region (Canadian Arctic), and its response to recent changes in ice conditions.

With these new polynya-specific estimates of primary-production rates, it is possible for the first time to quantitatively assess the extent to which the magnitude of productivity within polynyas, and its variability, impacts population sizes and the ecology of upper-trophic-level organisms—e.g., penguins. Arrigo and van Dijken (2003a) found that in eastern Antarctica, where 91% of all Adélie penguin (*Pygoscelis adeliae*) rookeries are associated with coastal polynyas (Ainley, 2002), 65% of the variance in penguin colony size is explained by the magnitude of annual production in polynyas. This same relationship does not hold for West Antarctica, where only a quarter of the Adélie penguin colonies are closely associated with recurring post-polynyas (Ainley, 2002; Arrigo and van Dijken, 2003a).

While over-ice applications of satellite ocean color sensors are limited, their data are of immense importance in enabling a better understanding of the complex relationships between sea ice behavior and phytoplankton distribution/primary production. Compared with the earlier Nimbus-7 CZCS, SeaWiFS lacks the simultaneous sea surface temperature measurement capability—i.e., a TIR band. SeaWiFS data and information are available from the SeaWiFS Project at ⟨*http://seawifs.gsfc.nasa.gov/SEAWIFS.html*⟩. Other important current ocean color sensors include MODIS and the Envisat-1 Medium Resolution Imaging Spectrometer (MERIS). Routine global measurements will continue with the Visible Infrared Imager Radiometer Suite (VIIRS) through the NPOESS era.

5.9.4.4 The impact of icebergs on polynya formation and maintenance

Another emerging line of research is using satellite data to focus on the profound impact of large iceberg groundings on regional sea ice conditions and, *ipso facto*, marine ecology, in near-coastal areas. Icebergs are particularly abundant at high southern latitudes, and play a key role in polynya formation and maintenance when grounded (generally in water shallower than ~300–400 m). Analysis of AVHRR and Radarsat ScanSAR data by Massom (2003) and Massom et al. (2001b) has shown that not only large tabular icebergs but also myriads of small bergs (all grounded) and associated fast ice play an important and complex role in sculpting sea ice conditions and polynya formation and maintenance in the region of East Antarctica from ~140 to 155°E. This impact is both direct and indirect, as shown in Figures 5.71 and 5.72. With the ice drifting westwards around the Antarctic coast within the East Wind Drift, an immense buildup of highly deformed ice (to estimated thicknesses of >5 m) occurs on the upstream (eastern) side of the barrier, while polynya formation occurs downwind (on the west). In this way, the icebergs have a profoundly important impact on regional sea ice thickness distribution and

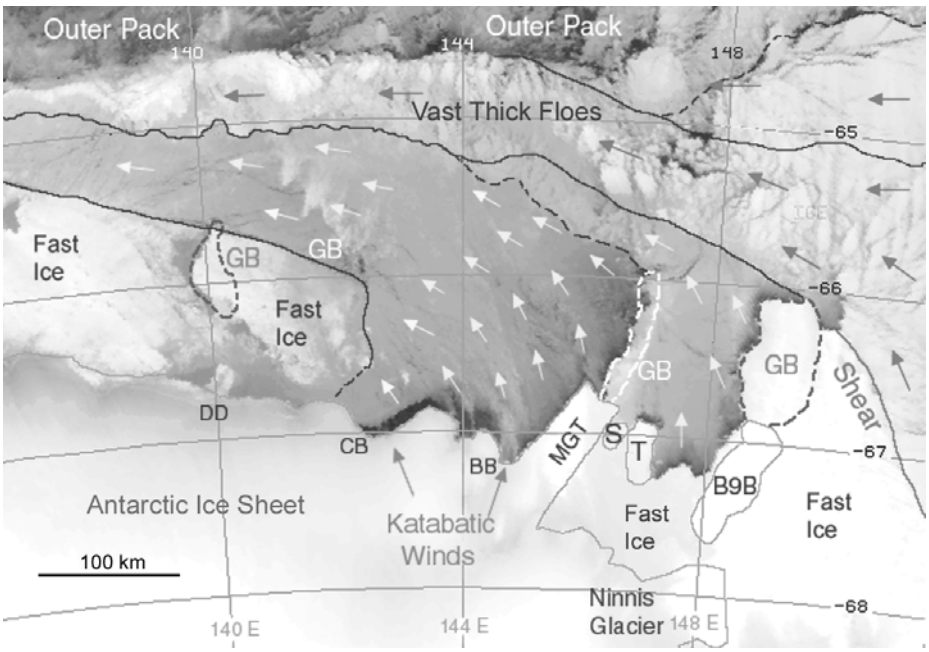

Figure 5.71. An AVHRR channel-4 image of the Mertz Glacier polynya region, June 14, 1999 (16 : 57 UTC), showing features referred to in the text. Together with the annual buildup of fast ice around grounded bergs to the west to form the "buttress", the "stream" effectively limits the outlet zone available for ice export away from the polynya "ice factory". Moreover, the eastern boundary of the buttress propagates eastwards to limit and decrease the westward extent of the polynya. By analysing time series of cloud-free AVHRR data and coincident meteorological data from a nearby automatic weather station, Massom et al. (2001b) showed that the overall effect of this complex interplay is to periodically limit the open-water area within the polynya, due to ice backfilling—i.e., the polynya producing ice more rapidly than it can be exported—while subsequent storms flush out and cyclically increase the polynya size.

The image was acquired at Casey Station by the Australian Bureau of Meteorology. After Massom et al. (2001b). Reprinted with permission of the International Glaciological Society (IGS). © IGS 2005.

rates of sea ice formation (and, *ipso facto*, brine rejection into the ocean). Note the different information obtainable in the AVHRR and SAR imagery, and how the two data sources complement each other. For example, bergs show up much more clearly in SAR imagery (see Chapter 3 of Volume 2 of this book), while the visible to TIR data represent an important means of interpreting the SAR data. These studies benefited further from the availability of meteorological data from automatic weather stations and *in situ* observations. Further analysis has shown that grounded icebergs, which have a long residence time of 10–20 years in the region to the east of the Mertz Glacier (Frezzotti et al., 1998), can exert a significant influence on the size of the Mertz Glacier polynya when they eventually escape but typically reground for a few months at the tip of the "finger" (Massom et al., 2003) (Figure 5.71). Impacts such as those outlined above are potentially important,

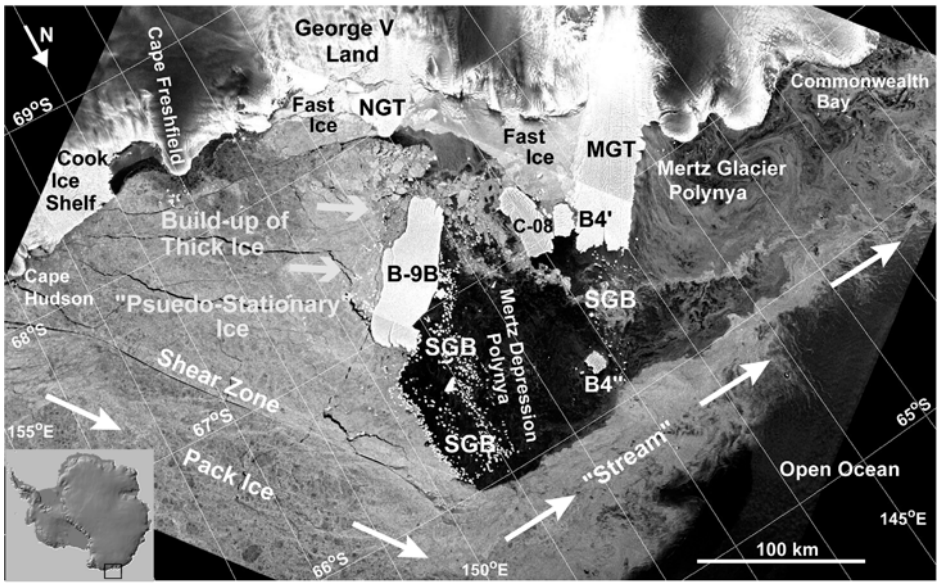

Figure 5.72. A Radarsat ScanSAR image of the Mertz Glacier polynya region (East Antarctica), March 8, 1998 (~10.24 GMT), illustrating the effect of the grounded iceberg barrier in the region in steering the encroaching pack ice northwards away from the coast. This barrier includes not only immense bergs but also myriads of small bergs (marked SGB), which emanate both from fragmentation of larger bergs and from regional glaciers. Iceberg B-9B, which calved from the Ross Ice Shelf in October 1987 (Keys et al., 1990), subsequently drifted westwards and has remained grounded in approximately its current position in East Antarctica (~67.4°S, 148.5°E) since June 1992. Although this image is from early in the annual growth season, it clearly shows the downstream impact of the resultant compact and westward-drifting ice "stream" in enclosing the Mertz Glacier polynya region; this effect continues through much of the year. Note the polynya on the leeward side of the grounded berg barrier. Note also the extraordinary linear shear zone separating the zone of highly deformed, psuedo-stationary sea ice from the drifting pack ice to the north, and long fractures in the former. These persistent and recurrent features stretch fully 300 km from the tip of B-9B to Cape Hudson and the Cook Ice Shelf.

MGT is Mertz Glacier tongue, and NGT Ninnis Glacier tongue. After Massom (2003). Radarsat data copyright Canadian Space Agency/Agence Spatiale Canadienne 1999, processed and distributed by Radarsat International, used with permission. © Radarsat International/Canadian Space Agency. Reprinted with permission of Cambridge University Press.

given that the Mertz Glacier Polynya has been identified as a major site of Antarctic Bottom Water production (Rintoul, 1998).

Arrigo et al. (2002) examined the ecological impact of a major iceberg grounding, of iceberg B-15 in the Ross Sea, using SSM/I data (processed to 6.25-km resolution using the Markus and Burns, 1995 algorithm), MODIS (0.25-km resolution data from the 0.62–0.67- and 4.433–4.498-μm bands), and SeaWiFS data (chlorophyll *a* concentrations at 4-km resolution). This gargantuan iceberg, with a length of 295 km and an area of ~10,000 km^2 (the size of Jamaica) calved

from the Ross Ice Shelf in March 2000 and broke into a number of pieces which drifted westwards (Young, 2001). Iceberg B-15A subsequently grounded in the Ross Ice Shelf Polynya adjacent to Ross Island (Figure 5.73). The presence of this immense barrier had an immediate impact on the normal climatological drift pattern of sea ice, resulting in a significantly heavier ice cover in spring/summer and an associated large reduction in both the area of open water suitable for phytoplankton growth and the length of the algal growing season (Figure 5.74, see color section). The outcome was a >40% reduction in regional primary productivity compared with the mean. Seibel and Dierssen (2003) reported on temporally and trophically cascading impacts of the depression in primary productivity on higher trophic levels in the McMurdo Sound region. The grounding of iceberg B-15A adjacent to important Adélie and emperor penguin colonies at Cape Crozier in July 2001, and the resultant abnormally heavy sea ice conditions, also had a disastrous effect on penguin breeding success (Wienecke, 2002). Arrigo et al. (2002) argue that such iceberg-driven changes in phytoplankton population structure and primary productivity will also alter key biogeochemical processes such as particle export (DiTullio et al., 2000), carbon drawdown (Arrigo et al., 1998b), and sedimentation (Dunbar et al., 1998). A similar study was carried out by Arrigo and van Dijken (2003b) on the impact of iceberg C-19 on primary production in the Ross Sea.

5.9.5 Sea ice motion, dynamics, and kinematics

As stressed earlier in Section 5.6, sea ice drift under the influence of winds, ocean currents, and floe–floe interaction redistributes pack ice and changes its concentration, areal extent, and thickness distribution, to have a strong impact on albedo, surface roughness, heat and moisture fluxes, ice growth and melt rates, and salinity fluxes. On scales of up to a few kilometers, sea ice motion involves the movement of individual floes and floe ensembles, and determines the opening of lead and ice deformation processes—e.g., pressure-ridging. Ice motion in effect controls the abundance of thin ice and therefore the intensive heat flux from the ocean to the atmosphere, ice production, and salinity flux. On larger scales of greater than a few hundred kilometers, ice motion in response to the climatological patterns of atmospheric and oceanic circulation provides the advective component of the icemass balance as well as a velocity boundary condition on the ocean surface. It follows that changes in circulation will impact ice extent, export, and regional mass balance (Kwok, 2000). By the same token, high-latitude climate is itself sensitive to changes in sea ice motion/dynamics (Vavrus and Harrison, 2003). Improved information on patterns of sea ice advection, thickness distribution, and melt is required to better understand the ocean heat and salinity/freshwater budgets. Recall from Section 5.6.2 that accurate parameterization of the ice velocity field, and the derived deformation rate, is critical to the realistic representation of sea ice in climate simulations and predictions (Lindsay et al., 2003). Accurate sea ice motion data are also required to monitor the transport of pollutants (Emery et al., 1997a), sediments, and radioactive waste (Eicken et al., 1997, 2000), which are entrained

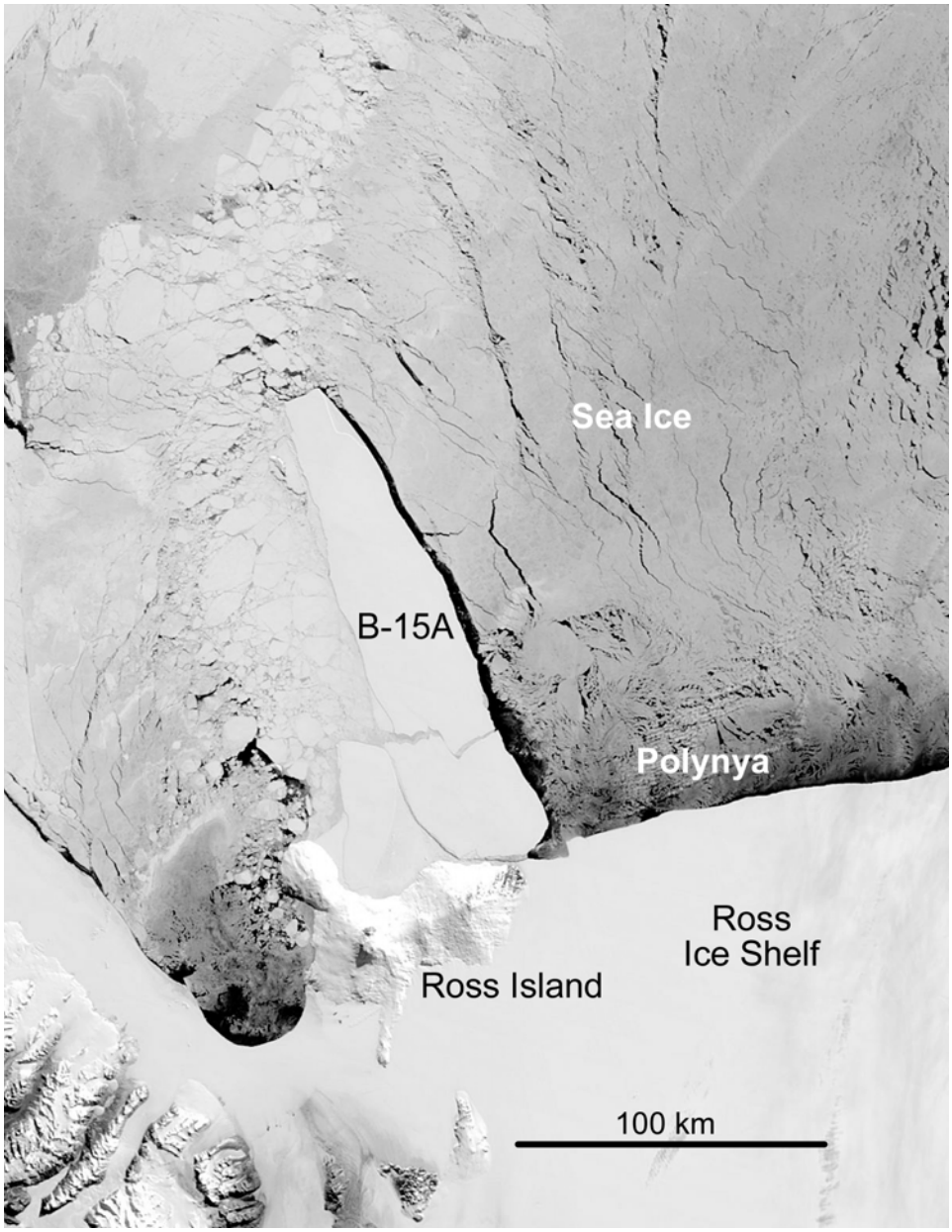

Figure 5.73. A 250-m resolution NASA EOS Terra MODIS image of the grounded iceberg B-15A in the Ross Sea, Antarctica, on October 26, 2003 (20 : 50 GMT). With an original area of ~11,000 km^2, B15 calved from the Ross Ice Shelf in March 2000. Iceberg B-15A subsequently fractured in early October 2003 (see Chapter 3 of Volume 2 of this book for further information).

Image courtesy of NASA (obtained from the NASA MODIS Rapidfire website at ⟨*http://rapidfire.sci.gsfc.nasa.gov/gallery/*⟩).

into newly forming ice in the shallow marginal seas north of Siberia. Ice dynamics and conditions are also an important determinant of habitat selection—e.g., by polar bears (*Ursus maritimus*) (Ferguson et al., 2000; Mauritzen et al., 2003; Stirling, 1997; Stirling et al., 2004) and ringed seals (*Phoca hispida*) (Barber and Iacozza, 2004), and determine both the foraging effort and diet of penguins (Ainley et al., 1998).

Until recently, our knowledge of sea ice motion was largely based upon data collected by satellite-tracked drifting buoys deployed on ice floes (Kottmeier et al., 1997) and even ice-beset ships such as Shackleton's ill-fated *Endurance* (Massom, 1992). This situation has changed dramatically, with a range of large-scale ice motion products now available from satellite data—e.g., high resolution (SAR) and low resolution (visible to TIR radiometers, passive-microwave radiometers, and radar scatterometers). Satellite-interrogated drifting ice buoys—e.g., by the Argos system onboard the TIROS/NOAA satellite series (Service Argos, 1996)—continue to play an important parallel role. Continuing coordinated international buoy programs are in operation in both the Arctic (⟨*http://iabp.apl.washington.edu/*⟩) and Antarctic (⟨*http://www.ipab.ac*⟩, and ⟨*http://www.antcrc.utas.edu.au/antcrc/buoys/buoys.html*⟩; Kottmeier et al., 1997; Vihma and Launiainen, 1993; Vihma et al., 2002). These have contributed a great deal to our understanding of pack ice drift behavior—e.g., Heil and Allison (1999). Data are also available from ⟨*http://nsidc.org/NASA/GUIDE/docs/dataset_documents/ipab_antarctic_drifting_buoy_data_set_document.gd.html*⟩. They provide accurate data with which to validate satellite retrievals (Heil et al., 2001b), with their data being increasingly assimilated into satellite ice motion estimates to improve the accuracy of the latter (Kwok, 2000). They also supply important information that cannot be measured by satellite sensors over sea ice—e.g., surface atmospheric pressure (Colony and Rigor, 1993) and wind speed and direction. These data are acquired in real time by the Global Telecommunications System (GTS) to play an important role in operational meteorological analyses. Modern autonomous "smart" buoys (Elder et al., 2002) also provide additional information on, for example, profiles of air, snow, ice and ocean temperatures, and snow accumulation, ice growth, and melt. With an even greater accuracy, GPS-tracked buoys are also used extensively in field experiments—e.g., as a means of determining the growth rate of sea ice advecting out of the Mertz Glacier polynya (Lytle et al., 2001), and to measure ice kinematics (Downer and Haskell, 2001; Leppäranta et al., 2001). Moreover, buoys serve as a useful data source during the summer melt period when satellite microwave techniques are largely inoperable (particularly in the Arctic—see below). They do, however, provide only a limited picture of the ice velocity field and its spatial derivatives. Moreover, while it has been possible to validate modeled fields of mean ice motion against drifting ice buoy and station trajectories (Meier et al., 2000; Thomas, 1999; Zhang et al., 2000), a similar validation of modeled ice deformation fields at small scales has not been feasible. For one thing, the spatio-temporal spacing of buoys is too great for such a task. Other limitations of buoys include their expense, the logistical difficulty of deployment, their sparse areal coverage, and their short operating lifetimes.

Here, we outline current techniques for deriving ice motion and deformation from sequential satellite images, based upon various feature-tracking and

cross-correlation techniques. All identify features in two or more sequential and co-registered images and measure their displacement over time. Computation of resultant ice velocity vectors is based on the pixel resolution and time interval between images, with techniques also differing in the degree of data filtering and post-processing involved. Satellite-derived motions represent the ensemble displacement, or average motion, of the tracked signature within the sensor's FOV. The temporal spacing of datapoints/images is an important issue in determining what scale of motion can be resolved. Obviously, the closer the spacing, the more realistic the representation of the actual velocity field. High-frequency ice motion driven by tidal, inertial, and synoptic-scale meteorological forcing, to which ice responds rapidly, can only be captured by satellite sea ice tracking on temporal scales of 12 hours or less (Drinkwater, 1998a). As Heil and Hibler (2002) showed in their modeling study, these high-frequency processes are in themselves important to the sea ice formation and melt cycle through their effect on opening and closing leads. These effects include tidal deformation processes (Hutchings et al., 2002). The scaling properties of sea ice dynamics and deformation are evaluated by Dempsey and Shen (2001), Marsan et al. (2004), and McNutt and Overland (2003). For a more detailed comparative review of satellite-derived ice motion techniques, see Maslanik et al. (1998b). Issues of accuracy are also evaluated by Heil et al. (2001b) and Lindsay (2002).

5.9.5.1 Medium-resolution visible to thermal infrared techniques

With its daily repeat coverage and overlap of passes at high latitudes, the AVHRR is well-suited to the measurement of ice motion in sequences of cloud-free imagery. The Maximum Cross Correlation (MCC) technique is a robust method that has been used to track recognizable ice features between pairs of channel-2 (under daylight conditions) and channel-4 (darkness) images (Emery et al., 1986, 1991b, 1995, 1997b; Fowler, 1995, 2003; Heacock et al., 1993; Maslanik et al., 1998b; Ninnis et al., 1986). The first step involves image navigation to a common map projection (see Rosborough et al., 1994 for details on the AVHRR navigation procedure). The algorithm then locates the maxima of two-dimensional cross-correlations in windowed portions of the images, which represent the endpoints of motion vectors that originate at the centre of the window in the search area. This results in an array of Lagrangian displacement vectors that represents the field of motion over the time interval between the two images. Cloud-covered areas and spurious correlations are subsequently filtered using a spatial coherence technique (Emery et al., 1991b). The magnitude of the ice velocities calculated by the MCC algorithm is set by both the size of this window and the time interval (Fowler, 2003; Scambos et al., 2002).

This technique has been used to produce the ice motion vectors included in the NOAA/NASA *AVHRR Polar Pathfinder 1.25-km Twice-daily EASE-grid Composites* dataset for both poles from August 1993 through December 1998 for the Northern Hemisphere, and April 1992 through January 1996 for the Southern Hemisphere (Scambos et al., 2002). These data, and excellent documentation, are

available from the NSIDC at ⟨*http://nsidc.org/data/docs/daac/nsidc0065_avhrr_1.25km.gd.htm*⟩. Information on accuracy is also provided. In a comparison with buoy data, Emery et al. (1991b) found the mean difference (bias accuracy) to be $0.71\,\mathrm{cm\,s^{-1}}$ in the x-direction, with a standard deviation of $0.62\,\mathrm{cm\,s^{-1}}$, with corresponding figures of $0.57\,\mathrm{cm\,s^{-1}}$ with a standard deviation of $\sim 0.51\,\mathrm{cm\,s^{-1}}$ in the y-direction. The bias for overall magnitude was about $1.0\,\mathrm{cm\,s^{-1}}$ with a standard deviation of $0.9\,\mathrm{cm\,s^{-1}}$. These differences are quite small (5 to 10%) compared with general ice velocities of 10 to $20\,\mathrm{cm\,s^{-1}}$, and demonstrate the validity of the MCC-derived ice velocities. Spatial correlation methods fall down, however, in regions where rapid changes occur in spectral and spatial characteristics on the pixel scale—e.g., in MIZs, where rapid floe rotation/deformation occurs (Emery et al., 1995). Moreover, persistent cloud cover can result in data gaps, particularly in MIZs and in summer.

In future, data from the NPP/NPOESS VIIRS (to be launched in 2006 as the follow-on to the AVHRR, OLS, and MODIS) will be used to operationally derive global ice edge motion, defined as the displacement of the edge (Appel et al., 2002). The proposed algorithm is again based on the application of the MCC technique to sequential cloud-free images, but this time for ice concentration rather than reflectance, radiance, or temperature, in order to maintain measurement consistency—i.e., Appel et al. (2002) argue that it represents a more stable property. In this case, the ice edge is taken to be the outer pack boundary represented by a VIIRS-derived ice concentration of 10%. It remains to be seen whether the use of concentration will yield accurate results during periods of intense freeze-up and melt. From 2009 onwards, VIIRS sensors will fly on satellites that are also equipped with the passive-microwave CMIS, enabling the production of complementary ice motion datasets.

5.9.5.2 Passive microwave techniques, and the measurement of ice-mass flux

Recent studies have demonstrated that reliable ice motion data can be derived from daily-averaged PMW T_B data under freezing conditions, to overcome the cloud limitation experienced by optical and TIR sensors. PMW-derived ice motions provide more frequent temporal sampling, better spatial coverage, and a longer period of coverage (1979 up to the present) than SAR, and more consistent coverage than the AVHRR and MODIS. Compared with SAR techniques (see below), data volume is small and the computation effort minimal. The precision of PMW-derived vectors is, however, less than that achievable using these other data sources, being limited by coarse spatial resolution. Moreover, reliable motions cannot presently be calculated in a consistent fashion during the late-spring through early-autumn period due to image de-correlation caused by surface melt effects—i.e., May to September for the Arctic (Maslanik et al., 1998b). This appears to be less of a problem in Antarctica (Heil et al., 2001b), where surface melt is less pronounced, although Antarctic sea ice presents a relatively homogeneous target for tracking. In addition, the impact of ubiquitous year-round floe flooding by seawater on motion retrieval accuracy is unknown.

Maslanik et al. (1998b) provided an in-depth assessment of techniques used. Two main automated motion-tracking routines have been developed for application to passive-microwave data:

- Methods based on identifying MCC between search areas in sequential images (Agnew et al., 1997; Drinkwater et al., 2001a; Fowler, 2003; Kwok et al., 1998b). This technique is similar to that applied to AVHRR time series.
- A wavelet method, which tracks the movement of particular wavelet-defined locations (features) over time (Liu and Cavalieri, 1998). This is in effect a bandpass filter with a threshold for feature detection.

The cross-correlation methods used by different groups differ mainly in terms of the degree of oversampling used, the type of ice vector filtering to remove spurious outliers, and the time interval between images used for the displacement calculations.

As noted by Maslanik et al. (1998b), each method also involves certain degrees of subjectivity, through the choice of statistical parameters or processing options and/or the selection of filtering criteria used. In all cases, the microwave "signature" that is identified and tracked over time comprises combinations of snow/ice microwave emissivity and ice concentration within the sensor field of view. The latter is ~14 km for the SSM/I 85-GHz channel and ~30 km for the 37-GHz channels of the SMMR and SSM/I, but mapped to grid cell sizes of 12.5 km and 25 km, respectively. Importantly, ice displacements can be reliably detected from 37-GHz data as well as 85-GHz data. While decreasing the resolution and precision of the motion product, this enables the time series to be extended back to 1979 through the use of Nimbus-7 SMMR data (85-GHz data are available from 1987 to the present only). Note that while SSM/I data are available on a daily basis, SMMR data were collected every other day. Kwok et al. (1998b) and Maslanik et al. (1998b) noted little difference between ice motions derived from V- or H-polarized data, or between using a single channel versus a combination of channels, although Agnew et al. (1997) suggested that H-polarization may be marginally preferable.

In addition to those outlined above, other factors affecting the accuracy of PMW-derived ice motions include:

- variable atmospheric conditions (columnar water content and cloud cover), particularly at 85 GHz. These effects tend to be more prevalent in Antarctica in general, and more serious in the Arctic during summer (Kwok et al., 1998b);
- modification of surface microwave signatures—e.g., due to snowfall, ridging, and flooding—thereby affecting the ability to track ice parcels. Some methods—e.g., Kwok et al. (1998b)—address both surface and weather effects by applying a filter; and
- rapid ice rotation and deformation, in regions such as the MIZ.

While the retrieval of vectors during late spring through late summer remains a problem (in the Arctic in particular), the wavelet approach, and perhaps improved filtering for the MCC method, may provide some useful data during this important period (Maslanik et al., 1998b). Maslanik et al. (1998b) found that basic error statistics among the different products, and derived by comparison with buoy data, are fairly similar and consistent overall. Generally, r.m.s. errors in velocity

estimates are at the sub-pixel scale (Kwok et al., 1998b). For the Kwok and Rothrock (1999) central Arctic study, standard deviations ranged from 4.4–6.7 km for 85-GHz data to 7.1–13.0 km for 37-GHz data for individual ice displacement vectors, as a result of the coarse spatial resolution. It is likely that improvements will occur with improved resolution AMSR data, as demonstrated in a study by Agnew et al. (2005) of sea ice transport through Baffin Bay/Labrador Sea and Fram Strait. Synoptic-scale patterns consistent with winds can be observed in motions sampled on intervals as fine as 24 hours, but the noise level of daily displacements is high. This noise can be effectively reduced through time averaging (Kwok et al., 1998b; Zhao et al., 2002), which produces useful mean fields and climatologies that portray both hemispheric patterns and regional variability (Figure 5.75, see color section). In a comparison of SSM/I- and buoy-derived ice drift data in the Weddell Sea, Drinkwater et al. (2001b) determined the r.m.s. error of the satellite product to be $\sim 8\,\mathrm{cm\,s^{-1}}$ for 1 day, reducing to $1.45\,\mathrm{cm\,s^{-1}}$, or $\sim 18\%$, for monthly mean velocities. Similar r.m.s. errors were found by Meier et al. (2000) and Heil et al. (2001b). Another study comparing satellite- and buoy-derived ice motion data in the Arctic is by Geiger et al. (2000).

Once again, most emphasis in algorithm development has been in the Arctic, and additional work is required to further assess performance in the Antarctic. While these data are attractive for assimilation into models, Maslanik et al. (1998b) suggested that more information is required on accuracies as a function of region, season, and ice conditions. Further refinement is required to improve motion retrievals in MIZs, and to investigate the use of orbital rather than daily-averaged T_B data. Moreover, Heil et al. (2001b) showed that it is crucial to determine the appropriate dimensions for the search and detection windows used in MCC methods. The use of higher resolution AMSR(-E) data, and NPOESS CMIS data from 2009, is expected to result in a significant improvement in the ice motion product.

There has been a recent healthy shift towards data fusion methods to merge or blend data or products from different sources to improve the accuracy of overall products. Issues remain, however, as to the best optimal interpolation procedure to use (Maslanik et al., 1998b). An example is given by Kwok (2000), who incorporated IABP buoy data into a time series of PMW-derived ice motion data (1978–1996) to detect and examine recent changes in sea ice motion in the Arctic Ocean associated with the North Atlantic Oscillation (NAO). The buoy data were incorporated to improve the accuracy of ice motion estimates, to produce 2-day motion fields as follows:

$$\hat{\boldsymbol{u}} = \sum_i \alpha_i u_i^{85\,\mathrm{GHz}} + \sum_j \beta_j u_j^{37\,\mathrm{GHz}} + \sum_k \gamma_k u_k^{buoy} \tag{5.51}$$

where u is ice motion and α, β, and γ are weighting coefficients determined by an optimal interpolation procedure (Colony and Thorndike, 1984). The resultant motion fields are sampled on a 100×100-km grid, with an expected average uncertainty of 1–2 km $\mathrm{day^{-1}}$ in interpolated estimates. The benefits of this approach are laid out in Drinkwater et al. (1999).

The ice motion datasets are being increasingly applied to a range of problems, including estimation of horizontal sea ice flux (note that the satellite measurement of ice thickness is covered in Section 5.9.6). Drinkwater et al. (2001a, b) combined several years of daily SSM/I ice drift data with ice draft measurements by moored Upward Looking Sonars (ULSs) into a time series of ice volume flux at points along a flux gate across the Weddell Sea, Antarctica. The ULS data were compared with contemporary ESCAT radar backscatter observations to obtain an empirical relationship between the rate of change of radar backscatter with incidence angle and ice thickness. Drinkwater et al. (2001b) then combined the resultant proxy ice thickness data with SSM/I-derived ice velocities to derive seasonally-varying estimates of net horizontal ice volume flux from 1992 to 1998, and showed that significant interannual variability occurs in the flux expressed as freshwater transport. Time series of SSM/I-derived ice motions and concentrations have also been used by Pilskaln et al. (2004) in support of an analysis of seasonal biogeochemical particle fluxes captured in time series sediment traps within the Seasonal Sea Ice Zone (SSIZ) of the Southern Indian Ocean. Secondary flux peaks in midwinter and in early spring were suggestive of small-scale, sea ice breakup events and the spring retreat of seasonal ice, respectively.

Monitoring of ice motion together with ice concentration and thickness provides a means of estimating ice mass, and thus freshwater, transport between ocean basins. Significant recent changes observed by Kwok (2000), and which impact the regional and total Arctic Ocean sea ice mass balance, include: a weakening of the Beaufort-Gyre (a major ocean/ice circulation feature in the Arctic Ocean); an enhanced eastward export of sea ice from the Laptev Sea; a weakening of the Transpolar Drift Stream; a reduction in sea ice extent in the Nordic Seas; an increase in ice import from the Kara/Barents Seas; and an increase in ice export from the Arctic Ocean to the North Atlantic via Fram Strait. The latter was examined in more detail by Kwok and Rothrock (1999), combining the same passive-microwave-derived ice motion data with ice thickness values from Vinje et al. (1998). According to Aagaard and Carmack (1989), ice flux through Fram Strait is the largest single component of the GIN Seas freshwater balance. Variability in this flux is of key importance in terms of its impact on the episodic freshening of surface waters in the Labrador and Greenland Seas, which in turn affects global thermohaline circulation (Dickson et al., 1988, 2003). While the role of this flux is well-established, its magnitude is poorly quantified. Kwok and Rothrock (1999) found that the NAO index explains ~74% of variance of the winter area flux, with an upward trend in the ice area flux over the 18-year period and a variation by a factor of 1.6 (see also Hilmer and Jung, 2000; Vinje et al., 1998). A sustained positive phase of the NAO in the late-1980s and early-1990s is linked to the recent decrease in sea-level pressure in the central Arctic reported by Walsh et al. (1996). In a follow-on study, Kwok et al. (2004a) analysed ice export estimates in Fram Strait from 1978 to 2002 and, over a 9-year record, the associated variability in the upward-looking sonar-derived thickness distributions of the Fram Strait. Correlation of winter ice area export with the NAO index remains high, while significant decreasing trends are apparent in the mean ice thickness of 0.45 m overall and 0.23 m over the winter months (December through March). Correspondingly,

the mode of multiyear ice thickness exhibits an overall decrease of 0.55 m and a winter decrease of 0.42 m. Further work by Cavalieri (2002) revealed a link between ice export and the atmospheric planetary wave phase. A major source of uncertainty in these and other estimates of sea ice flux results from uncertainty in lateral thickness profiles across flux gates (Vinje et al., 1998).

Monthly averages are again well-suited to the construction of ice motion anomaly maps, which are an extremely useful means of highlighting change in regional and hemispheric ice drift characteristics, thereby gaining insight into changes in large-scale atmospheric (and oceanic) circulation and on a scale that is comparable with present models. As with ice concentration and extent, these anomaly maps are typically derived from monthly means, given the high variability in daily maps. An example of a combined ice motion and concentration anomaly map is given in Figure 5.76 (see color section). This shows the major impact on the ice drift and concentration regimes of an anomalous shift in the regional climatological pattern of atmospheric circulation. Note that this change led to a major clearout of thick ice from the region to the east of the grounded bergs discussed earlier, and also to the east of the Balleny Islands. Both regions usually form traps for sea ice advecting in the opposite direction. Note the reversal in ice drift conditions compared with those 3 months earlier and shown in Figure 5.75 (which portrays the climatological norm).

5.9.5.3 Polar Pathfinder composite dataset

Ice motion data from the AVHRR, SMMR, SSM/I, and buoys (within the IABP) have been combined to produce the *Polar Pathfinder Daily 25 km EASE-grid Sea Ice Motion Vectors* dataset (Fowler, 2003; ⟨*http://nsidc.org/data/docs/daac/nsidc0116_icemotion.gd.html*⟩). An example of a daily image from the Arctic is given in Figure 5.77. Daily gridded fields were produced from the satellite data by using the MCC technique (Emery et al., 1997b) and smoothing and filtering routines discussed in Fowler (1995). To ascertain accuracy, Fowler (2003) interpolated several years of vectors to the same grid but without using the buoy data. The mean difference between the interpolated u components and the buoy vectors was $0.1\,\mathrm{cm\,s^{-1}}$ with an r.m.s. error of $3.364\,\mathrm{cm\,s^{-1}}$. The mean for the v component was $0.4\,\mathrm{cm\,s^{-1}}$ (r.m.s. error of $3.397\,\mathrm{cm\,s^{-1}}$). The composite ice motion product is available for both hemispheres, covering the period November 1978 to March 2003. Gridded motion fields (including browse images) are also available for annual, monthly, and weekly means, as well as means for the entire time series (see Figure 5.78). Data sources are:

- AVHRR channel-2 and -4 data interpolated to a 5-km resolution EASE-grid. Channel 4 was employed throughout the year, but it is not as useful during melt periods when the ice surface and water temperatures are similar. Channel 2 is only useful during sunlit periods in the late spring, summer, and early autumn.
- Nimbus-7 SMMR Pathfinder T_Bs at 37 GHz (25-km gridded resolution), with full coverage available only every 2 days, and DMSP SSM/I daily polar gridded T_Bs at 37 GHz (25-km resolution) and 85 GHz (12.5-km resolution), both V-

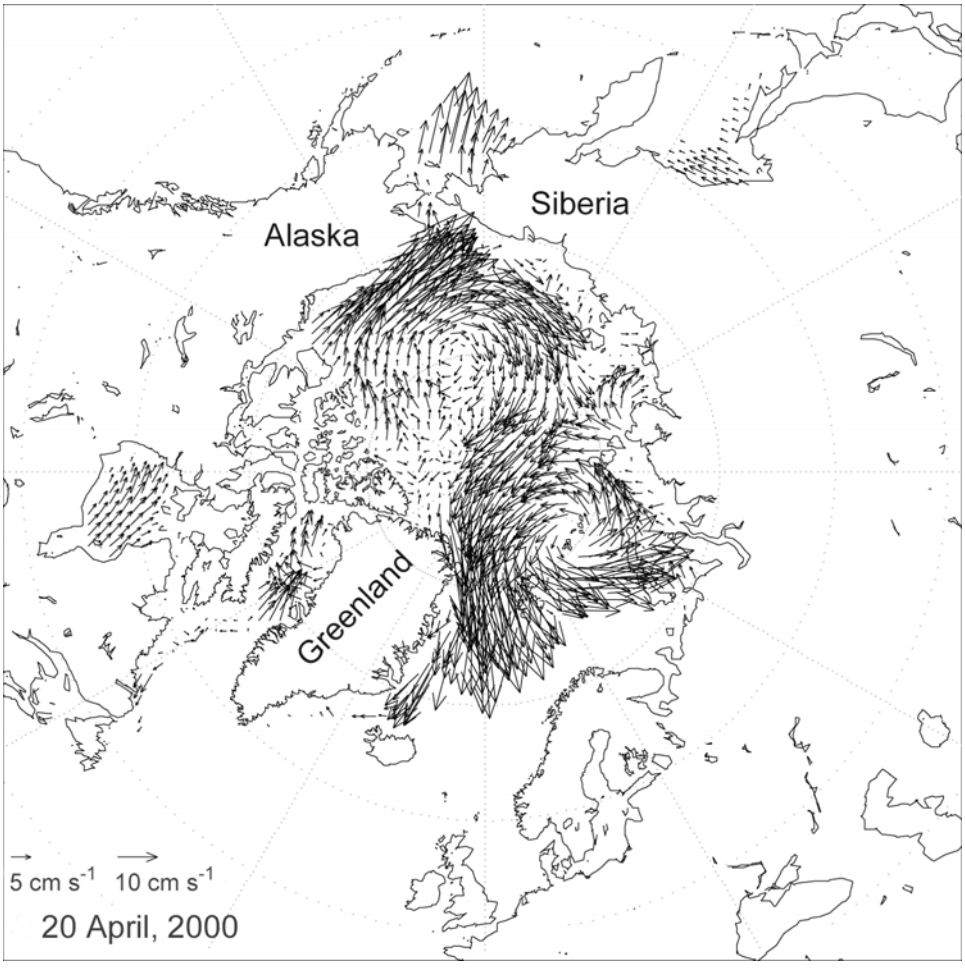

Figure 5.77. An example of a daily composite ice motion vector map from the NSIDC, for the Arctic for April 20, 2000. The map was created by optimal interpolation of daily gridded ice motion fields from the AVHRR, SSM/I, and IABP buoy data. In this case, every fourth vector is plotted.

From Fowler (2003). Reprinted with permission of NSIDC.

and H-polarization. Accuracies determined by comparisons with buoy data are given by Fowler (2003).

The composite ice motion maps in Figures 5.77 and 5.78 clearly show the large-scale patterns of mean ice drift in both polar regions in response to patterns of atmospheric circulation. In the Arctic, the climatological surface atmospheric pressure pattern creates two dominant features in the large-scale ocean surface and thus sea ice circulation—namely, the Beaufort Gyre (an anticyclonic circulation

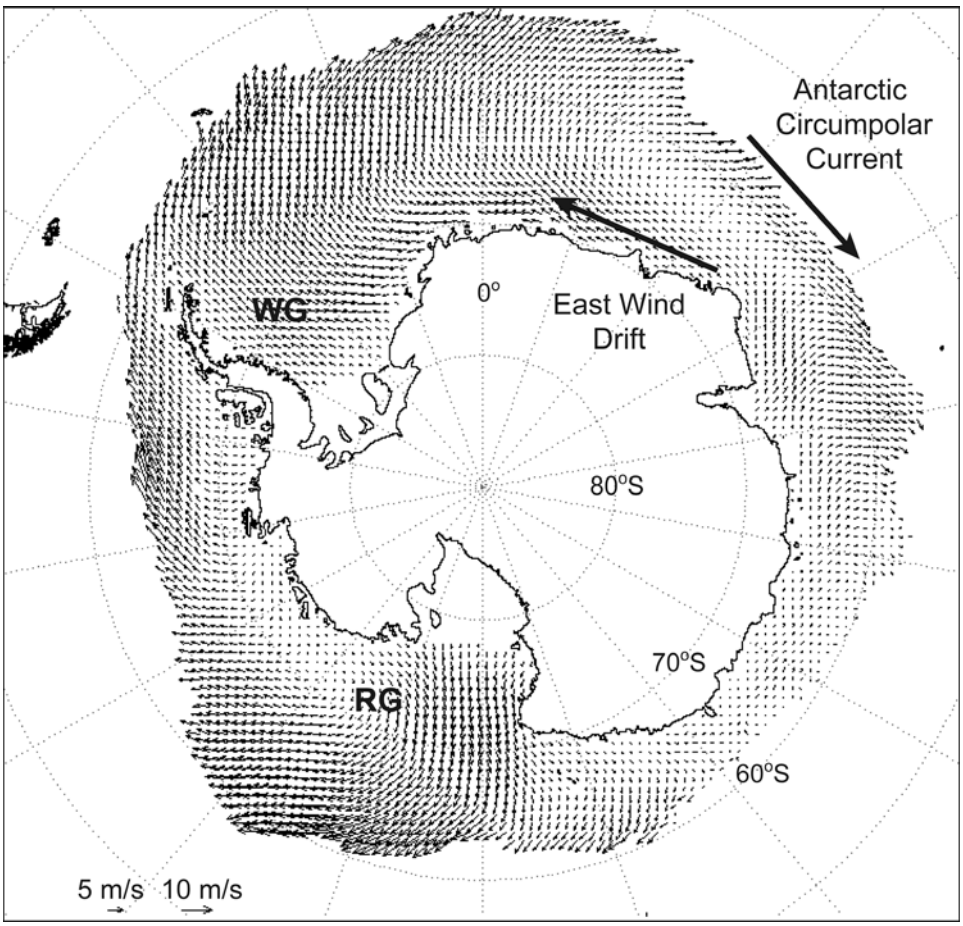

Figure 5.78. Map of the mean sea ice motion in the Antarctic in winter based on satellite observations from 1979 to 2003. The map was created by optimal interpolation of daily gridded ice motion fields from the AVHRR and SSM/I data, with every fourth vector plotted. From Fowler (2003). Reprinted with permission of NSIDC. WG = Weddell Gyre and RG = Ross Gyre.

in the Canadian Basin) and the Transpolar Drift. The latter involves a general drift from eastern Siberia to and through Fram Strait. As the Arctic Ocean is surrounded by land masses, internal ice stresses can be very large. This results in widespread ice deformation and greatly reduces ice speed in certain regions—e.g., north of Greenland and the Canadian Arctic Archipelago. Images such as this have helped to detect and monitor high degrees of variability from the mean motion in response to anomalous patterns of atmospheric circulation associated with, for example, the Arctic Oscillation (see Section 5.5).

The mean pattern (climatic mean) of sea ice drift in the Southern Ocean, as shown in Figure 5.78, is dominated by two features in ocean surface circulation—

namely, a zone of prevailing westerly (eastward) flow within the ACC and a zone of easterly (westward) flow within the near-coastal East Wind Drift. These two regimes, which reflect the prevailing wind fields, are approximately separated by the Antarctic Divergence. This is a region of ocean upwelling driven by the strong prevailing easterly winds to the south and westerlies to the north. Atmospheric circulation is itself dominated by broad-scale features in the climatological pressure field (King and Turner, 1997). These are a high-pressure system over the high continental plateau of the East Antarctic Ice Sheet, surrounded by a ring of low-pressure systems (cells) situated between 60 and 70°S and known as the Circumpolar Trough. Semi-permanent and intense low-pressure systems are encountered over the Ross and Weddell Seas and off East Antarctica in winter. The tendency of the ice to drift slightly to the left of the westerlies (due to the Coriolis Force)—i.e., to the north—results in a typically divergent (more open) ice cover and a general northward expansion of the sea ice area (with the surface air temperature also playing a major seasonal role) (Gordon, 1981). Major gyres are also apparent in the Ross and Weddell Seas. Although these gyres are not closed, and the ice cannot recirculate for years (as it does in the Beaufort Gyre) (Massom, 1992), they have an important impact on the thickness, deformation, age, and distribution of Antarctic sea ice in the two regions. As noted in Section 5.5, seasonal and longer term oscillations have recently been observed in these atmospheric pressure patterns, with major ramifications for the sea ice cover and climate.

5.9.5.4 Atlas of Antarctic Sea Ice Drift

Another extremely useful research tool has recently come online—namely, the digital *Atlas of Antarctic Sea Ice Drift* (Schmitt et al., 2004). This project has compiled data on ice drift derived from both satellite SSM/I data and satellite-tracked drifting buoy data from the International Program for Antarctic Buoys (IPAB). The overall aim is to provide a comprehensive view of sea ice motion around Antarctica as a reference for climate and ocean modeling. It also provides statistics on the state of sea ice cover for research, weather-forecasting models and ship-routing purposes. Data are available from ⟨*http://imkhp7.physik.uni-karlsruhe.de/~eisatlas/HTML/eisatlas_download.htm*⟩ in graphical representations involving various combinations of sea ice variables, periods, and years (dating back to 1979), commonly geo-referenced in a Geographic Information System (GIS). They also comprise ice concentrations from SSM/I and weather data from the NCEP/NCAR Reanalysis dataset. Examples of data from this source are given in Figure 5.79 (see color section).

The following digital data products have been calculated and can be accessed online in different temporal averaged resolutions and combinations:

- *Ice velocity*: gridded fields of SSM/I optimal interpolated mean ice drift velocity, illustrated with drift arrows.
- *Variance*: same fields for ice drift variance with overlaying covariance ellipses.
- *Anomaly*: anomaly fields, which show the difference of 1 month's mean compared with the monthly mean of all available years.

- *Buoy drift*: for all monthly means, buoy drift vectors and covariance ellipses are included in the vector fields when and where buoy data are available. Points where buoy data are included in the optimal interpolation of satellite drift are highlighted.
- *Kinematic parameters*: Differential Kinematic Parameters (DKPs)—e.g., divergence, vorticity, and shear—calculated from the ice motion vector (see Section 5.9.5.7).
- *Atmospheric pressure*: combined fields of gridded NCEP surface pressure with isobars and SSM/I ice drift vectors.
- *Temperature*: gridded NCEP temperature fields with 10-m model wind.
- *Ice concentration*: derived from SSM/I data with 10% isolines and drift vectors superimposed.

Please consult Schmitt et al. (2004) for detailed information on the datasets, data preparation methods, and error sources/estimates.

5.9.5.5 Radar scatterometer techniques

With passive-microwave radiometers, radar scatterometers are an important source of data with which to estimate hemispheric-scale ice motion on a routine daily basis. Although scatterometry shares some of the limitations of passive-microwave data, notably a low spatial resolution (nominally 25–50 km) and problems under melt conditions, it can obtain more useful data through thick clouds. Meier and Vermeychuk (2003) showed that the two datasets provide complementary information. Once again, the retrieval of ice motion maps from sequential scatterometer data is based on MCC techniques (Long and Drinkwater, 1999) and wavelet transform techniques (Liu and Cavalieri, 1998; Liu et al., 1998, 1999; Zhao and Liu, 2001; Zhao et al., 1998, 2002). Applied to the Arctic, these techniques are based on the large microwave backscatter contrast between first-year and multiyear ice. As noted previously, Antarctic sea ice is in general a more difficult target to track, due to the relative lack of contrast in the backscatter characteristics of first-year and multiyear ice and its higher degree of dynamism (whereby parcels of ice drift rapidly and even rotate over intervals between image acquisitions). Further work, however, showed that radar techniques originally designed and tuned for Arctic conditions could be adapted for application to Antarctica (Drinkwater, 1998b; Drinkwater and Kottmeier, 1994). Long and Drinkwater (1999) evaluated different techniques to track sea ice using ADEOS NSCAT Ku-band data in both hemispheres, some of which used enhanced-resolution SIRF data from the Scatterometer Climate Pathfinder (SCP) project at Brigham Young University (Long et al., 2001; ⟨*www.scp.byu.edu*⟩).

Figure 5.80 shows a map of mean daily Arctic sea ice drift derived from wavelet analysis of NSCAT data (Zhao and Liu, 2001), with black arrows indicating the coincident motion derived from IABP buoys (⟨*http://iabp.apl.washington.edu/data.html*⟩). Empty areas signify regions with no suitable template matching. A comparison is made in this figure with similarly derived sea ice drift results from contemporary 85-GHz SSM/I data at 12.5-km resolution (Figure 5.80b), showing

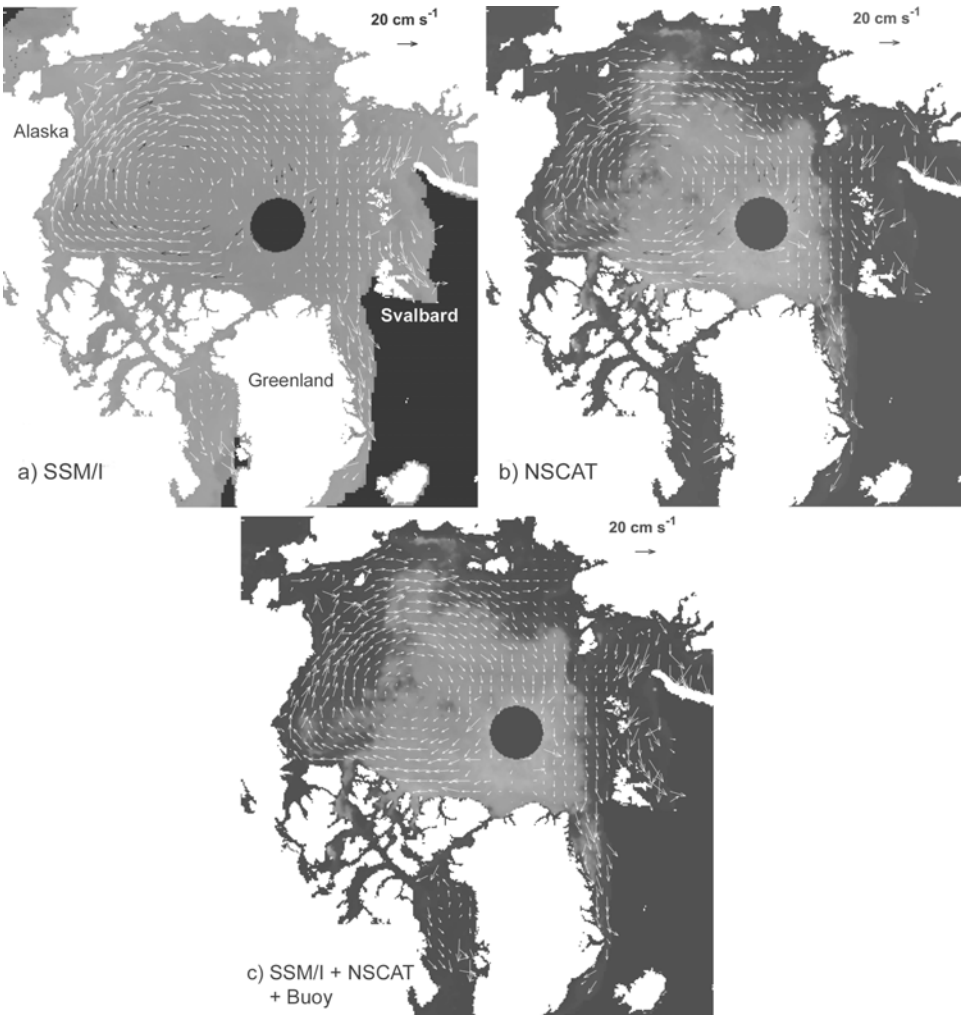

Figure 5.80. Daily sea ice drift maps of the Arctic for December 18, 1996 derived from wavelet analysis of (a) SSM/I 85-GHz radiance data, with coincident IABP drifting buoy velocities marked as black arrows; and (b) ADEOS NSCAT data with a grid cell size of 100×100 km. Thin white arrows denote ice velocities derived from wavelet analysis, while thicker arrows indicate buoy velocities. (c) A map of sea ice motion constructed from merged NSCAT, SSM/I, and buoy data for the same day.

consistency between the two datasets. Improved accuracy is derived when the two products are merged with buoy data to form a composite ice motion map by data fusion techniques, as shown in Figure 5.80c. This offers more complete coverage than is possible with the individual datasets alone. According to this study and Liu

and Cavalieri (1998), Liu et al. (1998), and Long and Drinkwater (1999), these calibrated/validated results indicate that the merged daily ice motion product is of sufficient accuracy for identification of large-scale sea ice dynamics and even assimilation into coupled ocean–ice numerical models. These important products will be enhanced with the availability of improved MetOp-1 ASCAT (Advanced SCATterometer) (launch 2005) and NPOESS CMIS data later this decade.

Working in Antarctica, Long and Drinkwater (1999) found that most of the sea ice zone may be tracked using NSCAT Ku-band data even during the period of austral spring–summer melt onset, when ERS C-band scatterometer techniques largely break down. Moreover, consistent vector retrievals are possible using NSCAT data during strong cyclone activity, which has a marked impact on the accuracy of motion retrievals from passive-microwave data. Zhao et al. (2002) applied the wavelet transform method to enhanced resolution (4.45 km) QuikSCAT data from the SCP project and SSM/I 85-GHz data, and showed good quantitative agreement between the two derived motion datasets and coincident buoy data, both in terms of speed (r.m.s. difference $<3\,\mathrm{cm\,s^{-1}}$) and direction (r.m.s. difference $\sim 30^{\circ}$). Once again, they showed that more complete coverage is possible when these comparable datasets are merged. Zhao et al. (2002) further suggested that such merged datasets are suitable for the computation of ice deformation. Once again, however, the scatterometer method and combined methods perform poorly in the outer pack, where brash ice and wave-fractured floes have image characteristics that make automated tracking difficult (Long and Drinkwater, 1999). Moreover, the accuracy of the Arctic motion product deteriorates in summer (at least from mid-June to September: Zhao et al., 2002) due to surface melt effects.

The moderate-resolution techniques outlined above provide excellent coverage, but at the expense of a relatively high level of uncertainty given the low resolution of the data (Holt and Kwok, 2003). Given these attributes, the data are best suited to the study of large-scale patterns of ice advection/circulation (Emery et al., 1997a; Kwok, 2000) and ice export (Kwok and Rothrock, 1999; Martin and Augstein, 2000). Measurement of small-scale processes, such as those associated with the opening and closing of individual leads, requires high-resolution data. Such data have been available since 1978 from satellite SAR sensors.

5.9.5.6 SAR techniques

Ice motion fields derived from sequential SAR images are again based upon tracking the displacement of ice parcels through time, using MCC and wavelet transform techniques. As with the scatterometer, the approach relies upon the microwave backscatter characteristics of the ice parcels remaining coherent over the time interval between image acquisitions. Observations are largely weather-independent, and at a high spatial resolution of 100 m. The precision is higher than that achievable using the other data sources outlined above, but spatial coverage is limited by the relatively narrow swath width and the temporal resolution is of the order of days. For SAR, automated sea ice-motion-tracking algorithms based on wavelet analysis have been developed by Liu and Peng (1998) and Liu et al. (1997a, 1998), while

MCC algorithms are described by Collins and Emery (1988), Curlander et al. (1985), Drinkwater (1997), Drinkwater and Kottmeier (1994), Fily and Rothrock (1987, 1990), Hall and Rothrock (1981), Holt et al. (1992), Kwok et al. (1990), Li et al. (1998), McConnell et al. (1991), Stern et al. (1995), and Sun (1996), for example. Although initially developed for application to data from narrow-swath and fixed incidence angle first-generation SARs onboard Seasat, ERS-1 and -2, and to a lesser extent JERS-1 (see ⟨*http://www.eorc.jaxa.jp/EORC/Gallery/Arctic_regions/arc_01.html*⟩), cross-correlation techniques have since been successfully adapted for application to wider swath Radarsat-1 ScanSAR data. Accuracies in general again fall down under melt conditions due to difficulties in ice displacement tracking under low-contrast backscatter conditions, and year-round in the MIZ due to the unsuitable rapidity of ice displacement (Peddada and Chang, 1996). Moreover, the lower backscatter contrast between ice types in Antarctica makes tracking more difficult, but not impossible (Drinkwater, 1998a, b). The availability of polarimetric SAR data may alleviate this problem, given its ability to improve ice-type discrimination (see Section 5.9.7). In general, longer wavelength SARs—i.e., at L- and C-band—are preferred for sea ice tracking. In particular, C-band is preferred due to the higher contrast (in the Arctic) between first-year and multiyear ice and wind-roughened openwater at this frequency, which improves feature tracking (Holt and Kwok, 2003).

Wilson et al. (2001b) used Radarsat-1 ScanSAR Wide imagery to derive ice kinematics in the North Water Polynya and surrounding pack ice region, applying the automated ice-tracking algorithm "Tracker" used operationally by the Canadian Ice Service (Heacock et al., 1993). An example of an ice motion map from this study is shown in Figure 5.81. In this case, analysis of the ice motion data provided information about polynya formation, maintenance, and disintegration. Georeferencing errors in image time series, which contribute to errors in the derived ice motion measurements, can be minimized by using known coastal positions as ground control points if possible.

The RGPS was designed specifically to exploit the new wide-swath capabilities of Radarsat (Kwok, 1998; Kwok et al., 1995a: ⟨*http://www.radar.jpl.nas.gov/rgps/radarsat.html*⟩), and routinely computes ice motion on a Lagrangian grid of the entire Arctic Basin from sequential composite ScanSAR image swath maps acquired as a "weekly snapshot" of basin-wide ice conditions (Drinkwater et al., 2001a). The data are processed to a spatial resolution of $\sim 100 \times 100$ m, calibrated, and archived at the Alaska Satellite Facility or ASF (⟨*http://asf.alaska.edu*⟩). While the nominal repeat cycle for Radarsat-1 is 24 days, orbital convergence towards the poles results in near-repeat coverage of the high latitudes at 3- to 7-day intervals (Kwok et al., 1999a). Each grid cell, of which there are ~70,000 for the Arctic Basin, initially comprises a $10 \times 10\,\text{km}^2$ element (apart from near the ice margins where the cell size is 25×25 km). Ice displacement is determined using a maximum cross-correlation technique (Fily and Rothrock, 1990; Kwok, 1998; Kwok et al., 1995a), with the cells being tracked in a Lagrangian fashion. Lindsay (2002) and Lindsay and Stern (2003) assessed this product. As noted earlier, a major current deficiency is that no RGPS-type system is in operation in Antarctica. Failing the establishment of

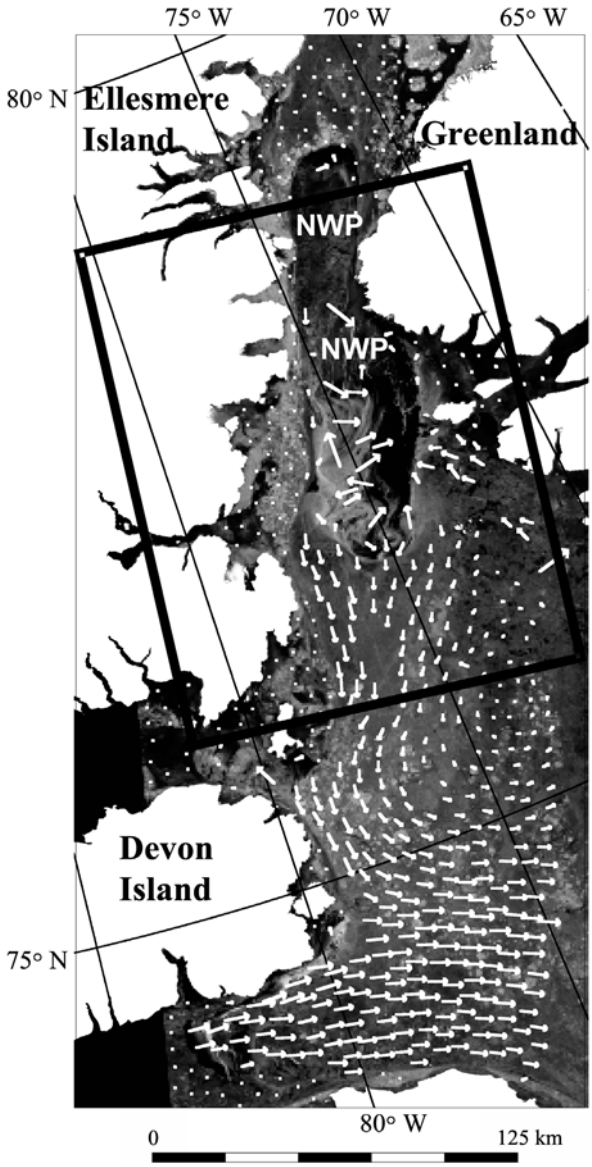

Figure 5.81. A Radarsat ScanSAR Wide image (100-m resolution) from April 13, 1998 (12 : 02 GMT) of the Smith Sound/North Water Polynya region between NW Greenland and Ellesmere Island, with ice motion vectors overlaid. In this example, the vector arrows denote net ice displacement over a 24-hour period. The polynya is the dark oblong area (NWP) in the upper part of the image. It is largely devoid of ice motion vectors as the main ice cover with the polynya is frazil ice, which is a difficult target to track in satellite data time series.

From Wilson et al. (2001b). Radarsat imagery © Canadian Space Agency 1998. Reprinted with permission of the International Glaciological Society (IGS).

an Antarctic RGPS, Stern (1998) suggested that an equivalent "Antarctic snapshot" capability could be implemented with the lower resolution global monitoring mode of Envisat-1 ASAR (1-km resolution, 400-km swath width), to provide large-scale ice motion products.

The RGPS builds upon an automatic ice-tracking algorithm for processing ERS-1 and -2 SAR data at the ASF (Kwok et al., 1990). Launched in July 1991, ERS-1 provided coverage up to 85° latitude. For its first 2 years, ERS-1 provided 3-day repeat coverage of high latitudes during its exact 3-day repeat cycle and the 35-day repeat cycle, which contained a drifting 3-day sub-cycle. Both ERS-1 and -2 collected C-band data over a 100-km swath at an incidence angle of ~23°. The ASF Geophysical Processor System (GPS—not to be confused with Global Positioning System) tracking procedure uses cross-correlation and feature-tracking techniques to routinely produce ice vector and displacement maps on a regular 5-km grid (Kwok and Cunningham, 1991). The derivation of intermediate-scale ice deformation products from ERS data is described by Li et al. (1995, 1998). For feature tracking, C-band data are preferable to L-band data. At C-band, the radar contrast between first-year and multiyear ice and wind-roughened openwater in leads and polynyas is relatively high. Incidentally, Ikeda and Tang (1992) used ice motion fields derived from satellite SAR and drifting ice beacon data as a proxy means of detecting and measuring ocean surface currents in data-sparse regions of the Labrador Current. This requires the accurate removal of the direct wind-driven component from the ice motion field. Before moving on, it should be noted that the potential may exist in future to accurately measure sea ice motion interferometrically using a closely spaced along-track configuration of SARs, or the innovative split antenna mode of TerraSAR-X, for example. Please see Chapter 1 of Volume 2 of this book for detailed information on SAR interferometry.

5.9.5.7 Ice deformation and kinematics

As the ice velocity field is spatially discontinuous, spatial scale is a key concept in the computation of ice deformation (Lindsay et al., 2003; Thorndike, 1986). Recent developments in Lagrangian ice tracking using time series of high-resolution satellite SAR images enable regular and precise quantification of differential ice kinematics and therefore the opening and closing of the sea ice pack, unaffected by cloud cover and darkness (Drinkwater et al., 2001a; Kwok et al., 1995a). The RGPS motion-tracking procedure, which is outlined by Kwok (1998) and Kwok et al. (1995a), produces gridded fields of cell area and four components of the velocity gradient—i.e., $\left(\frac{\partial u}{\partial x}, \frac{\partial u}{\partial y}, \frac{\partial v}{\partial x}, \frac{\partial v}{\partial y}\right)$—the latter from an approximation of the line integral around the cell boundary. Area changes and the strain rates of the cells are determined at each observation of the locations of the four corners of each cell. Deformation and rotation are then computed from these quantities as Dynamic Kinematic Parameters (DKPs) (Crane and Wadhams, 1996; Massom, 1992; Wadhams et al., 1989). The constituent DKPs of divergence (D), shearing rate of ice drift (SR, consisting of shear deformation rate S and normal deformation rate

N), and drift vorticity (V) are derived from the two-dimensional strain components—i.e., $\dot{\varepsilon}_x, \dot{\varepsilon}_y, \dot{\varepsilon}_{xy}, \dot{\varepsilon}_{yx}$—and the rotation component $\dot{\omega}$, where D equals the first invariant of the strain-rate tensor. These quantities are given as:

$$D = \frac{\partial u}{\partial x} + \frac{\partial v}{\partial y} \tag{5.52}$$

$$SR = \sqrt{\left(\frac{\partial u}{\partial x} - \frac{\partial v}{\partial y}\right)^2 + \left(\frac{\partial v}{\partial x} + \frac{\partial u}{\partial y}\right)^2} \tag{5.53}$$

$$S = \frac{\partial u}{\partial y} + \frac{\partial v}{\partial x} = 2\dot{\varepsilon}_{xy} \tag{5.54}$$

$$N = \frac{\partial u}{\partial x} - \frac{\partial v}{\partial y} = \dot{\varepsilon}_x - \dot{\varepsilon}_y \tag{5.55}$$

and

$$V = \frac{\partial v}{\partial x} - \frac{\partial u}{\partial y} = 2\dot{\omega} \tag{5.56}$$

where u and v are the displacements in the x- and y-directions, respectively, assuming a unit interval between the image pair acquisition times.

The divergence of a two-dimensional vector field of sea ice motion describes the relative change of an area within an enveloping curve (Schmitt et al., 2004). For D, a positive value indicates a divergent ice motion field (leading to the opening of leads), while a negative value signifies a convergent field (involving the closing of leads and possibly larger internal ice stress). Shear describes changes in shape, involving two components in the direction of mean ice motion and also perpendicular to it. It follows that the *total deformation* is given by $[D^2 + S^2 + N^2]^{1/2}$, while V defines the rotational component of the sea ice velocity field. It describes changes in the orientation of the enveloping curve, and has been found to be related to the vorticity of the geostrophic wind (Kottmeier and Sellmann, 1996). Further details relating to the RGPS measurements are given by Lindsay et al. (2003) and Stern and Moritz (2002). In their validation of RGPS products, Lindsay and Stern (2003) found a strong squared correlation of 0.996 between displacements derived from RGPS and drifting Argos buoy data, and an absolute tracking error of $\leq$286 m in RGPS data. The combined error in the deformation was 3.5% for individual 10-km cells, reducing to 0.43–0.02% with averaging over 16 to 1,000 cells. General error sources in deformation estimates carried out on a grid basis include (i) nonlinearity of deformed grid boundaries, (ii) complex and variable sampling (Lindsay et al., 2003; Marsan et al., 2004), and (iii) mislocation of tiepoints (Fily and Rothrock, 1990; Li et al., 1995, 1998; Stern et al., 1993). Regarding (i), the exclusion of highly distorted cells may result in certain RGPS estimates of deformation rate being biased (Lindsay et al., 2003).

With these deficiencies in mind, this unique dataset has a number of important applications. Importantly, it has enabled comparison of measured and modeled deformation rates over a wide range of scales, and over all seasons, for the first

time (Kwok, 2001; Lindsay et al., 2003; Maslowski and Lipscomb, 2003). These data are also well-suited to assimilation into various models (including ice-forecasting models), and incorporation into process studies and operational ice analyses (covered later in Section 5.9.17) (Holt and Kwok, 2003). Along with ice concentration data, time series of satellite-derived ice motion and ice flux data are being extensively used in research into the linkages between recent changes in sea ice behavior and modes of large-scale atmospheric circulation (Kwok and Rothrock, 1999). Time series of small-scale deformation derived from RGPS analyses have provided an unprecedented basin-scale view of the lengthscale of the lead patterns over the ice cover, the persistence of these linear features, and the response of these patterns to wind forcing (Kwok, 2002a). Marsan et al. (2004) used RGPS data products to compute the deformation of the sea ice on spatial scales from 10 to 500 km, and found a power law relationship between the deformation rate and the spatial scale, with an exponent of about $-1/5$ in autumn, winter, and spring. In summer, when the ice is in near free drift, the exponent is more negative and the deformation rate is higher. Power law distributions are associated with scale invariance. Further work on the spatial dependence of Arctic sea ice deformation using RGPS data was conducted by Marsan et al. (2004).

An example of RGPS output is shown in Figure 5.82 (color section), depicting the results of ice tracking over a 1-week period in December 1996. Data have been acquired and processed by the RGPS in this way since November 1996 for the Arctic Ocean (Kwok et al., 1999b). Taking the process a step further, ice thickness distributions are routinely computed from these data, in a manner discussed in Section 5.9.6.

Analysis of Radarsat ScanSAR Wide imagery of the high Arctic acquired several times a day by the RGPS, and at a sampling frequency near the orbital period of $\sim$101 minutes, enabled Kwok et al. (2003a) to detect high-frequency sea ice motion and evaluate its impact on Arctic Ocean ice dynamics in winter. The new data provided evidence of oscillating ice motion and deformation at length scales of $\geq$10 km, that can add up to an estimated 0.1 m of ice thickness over each winter period. High-frequency ice deformation around the inertial period—i.e., at timescales of $\sim$12 hours—is a ubiquitous feature of relative mesoscale sea ice motion in both the Arctic and Antarctic in winter (Geiger et al., 1998a, b; Heil and Hibler, 2002), in spite of the strength of the pack at this time. This motion typically results in a pulsating opening and closing of the ice pack even under winter high-ice-strength conditions, and is thought to greatly modify ocean–atmosphere heat exchange and make a major contribution to the ice mass budget (Heil and Hibler, 2002).

The exceptional Radarsat ScanSAR Wide high-resolution dataset is also enabling the testing of improved and more realistic rheological formulations in models of sea ice dynamics (Kwok and Holt, 1999; Richter-Menge et al., 2002; Stern et al., 1995). Referring back to Section 5.6.2, theories of internal ice stress, expressed as a constitutive law describing relationships between ice deformation rates/strain and stress, are used in sea ice dynamics models to parameterize the resistance of the pack to deformation. Modern models incorporate advanced elastic–viscous–plastic formulations (Hunke and Dukowicz, 1997) for efficient use

on high-performance computing facilities. For a comparison of different climate model ice rheologies, see Kreyscher et al. (2000). Typically, the stress in such formulations is taken to depend on both the state of deformation or strain rate of the pack and on its material properties as they relate to ice-packing densities and thickness distributions (Coon, 1980; Hibler, 1980; Leppäranta, 1998b, 2005; Pritchard, 1980, 1988). Ice deformation and advection are strongly affected by the large-scale mechanical behavior of the pack, and model performance is dependent on an effective parameterization of ice rheology (Ip, 1993; Ip et al., 1991). By providing views of Arctic sea ice motion and deformation in unprecedented detail, RGPS data are allowing the testing of new high-resolution coupled ice–ocean models (resolution $\sim$10 km) which incorporate anisotropic failure and flow characteristics (Hibler, 2001; Hutchings and Hibler, 2002a, b; Kwok, 2001). Anisotropic fracture mechanics refers to patterns of ice deformation that are characterized by narrow zones of failure with preferred orientations between rigid aggregates of ice (Coon et al., 1998; Hibler and Hutchings, 2002; Hibler and Schulson, 2000; Pritchard, 1998; Wang et al., 2003b) (Figure 5.83, see color section). Further research is required, and is underway, to determine which constitutive law provides the best fit with observations (Lindsay et al., 2003), whether hemisphere-/region-specific laws are required, and to better understand an anisotropic ice cover in terms of modeled mass and surface heat balance (Bamber and Kwok, 2004). Similar research in Antarctica is again limited by the lack of RGPS-like measurements.

In their estimation of DKPs from Antarctic ice drift vectors derived from drifting buoy and SSM/I data for the *Atlas of Antarctic Sea Ice Drift* dataset (see Section 5.9.5.4), Schmitt et al. (2004) chose ∂x and ∂y to be 600 km, in order to suppress the effects of the noise errors of u and v on the derivatives. This distance approximates correlation lengths of ice motion derived empirically in the Southern Ocean (Kottmeier et al., 1992; Vihma et al., 1996). Due to the large correlation lengths, spatial gradients of ice drift obtained from SSM/I are able to reflect meaningful vorticity and divergence on these scales. While smaller scale DKPs are important in analyses of lead and polynya formation, they cannot be obtained reliably from SSM/I-based ice drift. Note again that DKP data in the *Atlas of Antarctic Sea Ice Drift* dataset are available from ⟨*http://imkhp7.physik.uni-karlsruhe.de/~eisatlas/HTML/eisatlas_download.html*⟩.

5.9.6 Sea ice thickness and its distribution

An emerging and very important aspect of satellite remote sensing is the development of techniques to measure sea ice thickness. While the extent, concentration, and motion of sea ice can be measured and monitored reasonably well using satellites, the ultimate variable required to assess whether the global sea ice cover is shrinking or growing is ice volume—i.e., the product of ice concentration, extent, and thickness (Haas, 2003). While consistent satellite-derived ice concentration and extent data provide a two-dimensional description of global sea ice over a relatively long time series and to a reasonable accuracy, comparable large-scale information is lacking on its thickness distribution $g(h)$—see (5.4). Better understanding of the

processes that determine ice thickness distribution, particularly deformational mechanisms such as rafting and ridging, is needed to improve sea ice models and the representation of sea ice in coupled models.

While empirical relationships exist between sea ice thickness and SAR backscatter (and passive-microwave emissivity) (Kerman, 1998; Wadhams and Comiso, 1992; Zabel et al., 1996), for example, these data cannot be used alone to infer the complete shape of the ice thickness PDF (Probability Density Function) (Wadhams, 2004). An accurate estimation of regional to hemispheric $g(h)$ is critical to the calculation of areally averaged albedo, surface temperature, compressive strength, and deformation, as well as the estimation of regional fluxes of heat, mass, freshwater, and salt (Allison et al., 2001; Kwok et al., 1999b; Schramm et al., 1997a). The theory described earlier in Section 5.6.2.1, to determine changes in $g(h)$ (Thorndike et al., 1975), is an integral part of sea ice models, yet involves assumptions that are largely based on conjecture (ACSYS, 2003b), with ice thickness and its spatial and temporal variability being poorly represented (Morales Maqueda and Fichefet, 1996). The current lack of knowledge represents a major deficiency in our ability to accurately model current, hindcast, and future thickness distributions, and to validate these model simulations (Fichefet and Morales Maqueda, 1997; Lemke et al., 1990; Timmermann et al., 2004; Wu and Budd, 1998). As such, the accurate large-scale measurement of sea ice thickness, and its spatial and temporal variability, is of a high priority to validate and improve model simulations (Leppäranta, 1998b), and represents something of a "holy grail" in polar research.

Attention has been focused on this issue by recent observations that Arctic Ocean sea ice may be thinning at an alarming rate, based upon upward-looking sonar profiling along repeat submarine transects. Comparing ice draft data acquired by submarine sonar during the SCientific ICe EXpeditions (SCICEX) project in 1993–1997 with data from cruises over the period 1958–1976, Rothrock et al. (1999, 2003) observed a decrease of $\sim$1.3 m (or 40%) in mean ice draft at the end of the melt season in deep-water regions of the Arctic Ocean. Similar findings have emerged from the study of Wadhams and Davis (2000). In their analysis of submarine data from 1976 to 1994 in the section from Alaska to the North Pole, Tucker et al. (2001) showed an abrupt apparent thinning between the mid-1980s and the early-1990s, but virtually no change around the North Pole. Similar findings have also been published by Shy and Walsh (1996) and Winsor (2001). Tucker et al. (2001) further found a correspondence between sea ice thickness in the Beaufort Gyre region and the NAO, with relatively thick ice corresponding to a low NAO index and vice versa. An overarching issue is that uncertainties inherent to these analyses, and introduced by the sparse data coverage and large interannual variability, may explain the observed thinning (Laxon et al., 2002). Major discrepancies once again exist between different observational and model analyses. Model simulations of recent thickness change either show a more modest decrease—of $\sim$4% per decade (Hilmer and Lemke, 2000)—or no significant decrease at all (Polyakov and Johnson, 2000). Again, differences in model predictions are thought to result from uncertainties in the way that models represent the physics controlling ice thickness (Chapman et al., 1994; Shy et al., 2000). Indeed, it is far from clear whether

observed changes in regional thickness result from (i) enhanced melt due to changes in thermodynamic forcing (thermal or radiative), and/or (ii) changes in ice redistribution patterns in response to changes in dynamic forcing—i.e., the compensation of thinning in one region by thickening in another, adjacent region (Hilmer and Lemke, 2000; Laxon et al., 2003a, b; Steele and Flato, 2000). A detailed reanalysis of available submarine and modeled Arctic ice thickness data revealed that the latter may be the case, with high interannual variability also undermining the unambiguous inference of trends from sonar transect data (Holloway and Sou, 2002), although changes in the melt regime have also been observed (see Section 5.5). In addition, recent model simulations suggest that cyclical changes in Arctic ice thickness occur on decadal timescales (Battisti et al., 1997; Hilmer and Lemke, 2000; Polyakov and Johnson, 2000), in response to changes in wind and ocean stresses (Chapman et al., 1994; Deser et al., 2000; Köberle and Gerdes, 2003; Serreze et al., 2000; Zhang et al., 2000). This is clearly a complex picture.

The need for satellite remote-sensing methods to provide large-scale, consistent, and systematic estimates of ice thickness is paramount. Our current state of knowledge is based upon a number of disparate techniques which all have inherent weaknesses as well as strengths (Laxon et al., 2002; Wadhams, 2004). These can be briefly summarized as:

- *Ice-Profiling Sonars (IPSs) attached to submarines*. Coverage is sparse and sporadic, and is lacking from the Eastern Arctic and Canadian Shelf regions and the entire Southern Ocean—the latter due to both remoteness and the requirement of the Antarctic Treaty that all military vessels used in Antarctica be made available for international inspection (Wadhams, 2004).
- *Coordinated moored IPS programs* in both the Arctic and Antarctic. These provide measurements of the thickness of ice drifting across the sensor (Drucker et al., 2003; Fukamachi et al., 2003; Harms et al., 2001; Melling and Riedel, 1995; Strass, 1998; Strass and Fahrbach, 1998; Vinje et al., 1998). They are also equipped with a Doppler capability to estimate ice velocity, enabling estimates of ice export (transport rates) from, for example, the Arctic Basin via Fram Strait (Vinje, 2001b: ⟨*http://www.nopolar.no/ADACIT/*⟩). Measurements are, however, limited to a very small instrument footprint; the bias, precision, and accuracy of the draft measurements are poorly known; and the instruments are expensive to deploy and recover, with high losses to iceberg collisions. For information on the Antarctic moored IPS program, known as the Antarctic Sea Ice Thickness Project (AnSITP), in operation since 1990, please see ⟨*http://www.awi-bremerhaven.de/Research/IntCoop/Oce/ansitp.html*⟩, while data are available from ⟨*http://nsidec.org/data/g01359.html*⟩.
- *IPSs mounted on AUVs* have the potential to provide useful measurements in areas of interest (Clarke, 2003), and in the Antarctic in particular (Wadhams, 2004), but only have a maximum range of a few hundred kilometers (Griffiths, 2003).
- *Ice drilling* provides a very accurate estimate of local ice thickness characteristics (Eicken and Lange, 1989b; Haas and Eicken, 2001; Lange and Eicken, 1991; Tin

and Jeffries, 2001; Tin et al., 2003; Worby et al., 1996), but on the scale of individual floes, and specifically those that are safe to stand on.

- *Standardized visual (hourly) observations from ships* offer fairly broad-scale, but non-instantaneous, coverage and are reasonably accurate (Worby and Allison, 1999; Worby et al., 1998), but are limited to transit routes and as such tend to be biased towards thinner ice.
- *Airborne laser profilometry* (scanning or single-beam) provides a direct measurement of sea ice freeboard height, which may be converted into sea ice thickness by making assumptions about ice, water and snow density, and snow thickness (Comiso et al., 1991; Dierking, 1995; Forsberg et al., 2003; Keller et al., 2004; Ishizu et al., 1999; Wadhams, 2004).
- *Helicopter- and shipborne Electro Magnetic Induction (EMI)* (Eicken et al., 2001b; Haas, 1997, 1998; Haas et al., 1997; Multala et al., 1996; Prinsenberg et al., 1996; Worby et al., 1999). This technique (at frequencies of tens of Hz) exploits the marked difference in the electrical conductivities of sea ice and seawater to detect the ice–water interface, is typically used in concert with a laser altimeter (Forsberg et al., 2004), and requires knowledge of the ratio of snow to ice thickness. This has become a standard *in situ* measurement technique in recent years, but accuracy diminishes over thick ice and with increasing sensor distance from the ice surface (Holt and Kwok, 2003).

While providing important information, these techniques are logistically expensive, variable in accuracy, temporally and spatially limited in coverage, and are not carried out in a systematic repetitive fashion. As such, they are largely inadequate for monitoring interannual variability, detecting trends or validating model results (Hilmer and Lemke, 2000; Laxon et al., 2002; McLaren et al., 1992, 1994; Steele and Flato, 2000). The only viable means of obtaining the long-term, consistent, basin-wide observations required to develop a climatology of Arctic and particularly Antarctic sea ice is satellite remote sensing. This, however, represents a major challenge, due to the complexity and nature of sea ice as a remote-sensing target. For example, radar "sounding" of ice thickness from space has not been possible to date due in large part to the extremely lossy nature of sea ice, with the high brine content largely preventing the propagation of EM waves through this media. In effect, current spaceborne systems do not unambiguously "see" the lower ice surface (base), but rather sense either the surface or the volume within the uppermost few tens of centimeters of the ice. Recent technological advances, combined with the high priority of measuring large-scale ice thickness, have, however, led to the development of a number of promising techniques exploiting data from a range of different satellite sensors. These include psuedo-direct measurements by spaceborne laser and radar altimeters, and indirect measurement using passive-microwave, SAR, and visible to TIR sensors. The latter involves (i) the qualitative inference of thickness by image classification into thickness classes based on the WMO classification (WMO, 1970), and (ii) the incorporation of sequential satellite data into dynamic and/or thermodynamic sea ice models in order to estimate ice growth rates and concomitant thickness distributions. Here,

we briefly outline these techniques, and discuss the potential impact of CryoSat—a new satellite technology that represents the first ever sensor designed specifically to measure sea ice thickness, and IceSat.

5.9.6.1 Satellite radar altimetry

A new technique has been developed to estimate the thickness of Arctic ice thicker than ~1 m from direct measurements of sea ice freeboard using data from the 13.8-GHz radar altimeters onboard the ERS-1 and -2 satellites (Laxon et al., 2003a, b; Peacock et al., 1998). Radar echoes are individually analyzed to distinguish those emanating from areas of new ice/openwater from those from consolidated first-year and multiyear ice, with the former characterized by predominantly specular returns. Corrections for orbits, atmospheric delay, and tidal effects are then applied to determine the elevation of openwater/new ice and ice floes (Peacock and Laxon, 2004). It follows that the ice elevation above water, or freeboard, is the ice elevation minus the reference (open-water) elevation, integrated over the 1-km sensor footprint. Estimating ice thickness from these data requires knowledge of a number of parameters, including the depth within the snow plus ice layer from which the measured echoes are backscattered. Work by Beaven et al. (1995) suggests that the reflection at 13.4 GHz at normal incidence is from the snow/ice interface, implying that the ERS altimeters provide a measure of sea ice freeboard. Accurate knowledge of the location of the scattering centre relative to the snow/ice interface is a key issue, with freeboard measurement errors being magnified when applied to thickness measurement (given that only ~10% of free-floating ice is above the waterline). Laxon et al. (2003a, b) converted these data to estimates of area-averaged sea ice thickness by assuming that the ice is in hydrostatic equilibrium, then using fixed densities for seawater (1,023.9 $\mathrm{kg\,m^{-3}}$) and sea ice (915.1 $\mathrm{kg\,m^{-3}}$) from Wadhams et al. (1992), plus a monthly climatology of snow density and depth given by Warren et al. (1999). The estimated uncertainty in density values used (Wadhams et al., 1992) results in an uncertainty of ±11 cm in mean ice thickness (Laxon et al., 2003a, b). Using information from Radionov et al. (1996), Laxon et al. (2003a, b) determined a further uncertainty of ±6–9 cm related to interannual variability in snow loading. Note that mean snow densities reported from Antarctic cruises by Massom et al. (2001a) vary from 290 to 390 $\mathrm{kg\,m^{-3}}$.

Laxon et al. (2003a, b) and Peacock et al. (1998) estimated the overall uncertainty to be ~0.5 m for a single radar pulse, determined by comparison with submarine and moored IPS measurements, with contributions from a number of sources in addition to those outlined above. One relates to uncertainties in spacecraft orbital parameters, and variable atmospheric attenuation effects on the radar signal (including ionospheric effects). Moreover, as the radar pulse has a surface footprint of ~1 km, more information is collected from floes of this size or greater, leading to a bias in freeboard estimates if the thickness distribution of this floe size is different from that in general (Laxon et al., 2002). Additional uncertainty arises in thin-ice regions, due to the difficulty of distinguishing between reflections from thin ice and open water. As a result, this technique is best applied to regions of thick consolidated

ice, and may not be widely applicable to the relatively thin, more divergent first-year sea ice in Antarctica (Potter et al., 2002). Moreover, a better understanding of the relationship between floe size distribution and floe thickness is needed to interpret the altimeter data (Laxon et al., 2002). Another source of uncertainty relates to inadequate knowledge of snow thickness and density—i.e., thick snow cover can depress the ice surface, making the ice appear thinner in the altimeter data (Laxon et al., 2002). This problem may potentially be alleviated by incorporating new snow thickness information from the AMSR sensors (see Section 5.9.8), although these data are collected over a significantly larger footprint. The use of a fixed snow density value is complicated by the fact that snow density changes with metamorphism over time, or the addition of new snowfall (Massom et al., 2001a; Sturm et al., 1998, 2002a). Additional uncertainty may arise from flooding of the snow/ice interface, which is a widespread but poorly parameterized phenomenon in the Southern Ocean, due to the combined effects of generally thinner ice cover and high precipitation rates (Massom et al., 2001a). An overall consideration is that hemispheric maps of ice thickness derived from radar altimeter data require measurements collected over a month, over which time ice advection and deformation can alter the characteristics of ice within a given grid cell (Bamber and Kwok, 2004).

In spite of these limitations, this work has enabled the generation of monthly mean maps of wintertime (October–March) ice thickness over more than 50% of the perennial sea ice region of Arctic Ocean, or an area of $3.08 \times 10^6\,\mathrm{km}^2$ up to a maximum latitude of 81.5°N (determined by satellite orbital inclinations), and for the period 1993–2001 (Laxon et al., 2003a, b). In effect, this represents the first opportunity to study both the seasonal and interannual variability of thick sea ice thickness on a basinwide scale. The map of mean winter sea ice thickness for the 8-year period is shown in Figure 5.84 (see color section). Laxon et al. (2003a, b) investigated interannual variability by first subtracting the mean thickness from individual measurements, then averaging the residual thickness over each winter after applying a seasonal correction. Analysis of the resultant annual ice thickness anomaly maps reveals a high-frequency interannual variability in mean Arctic ice thickness, with changes in sea ice mass of up to 16% occurring within 1 year. According to Laxon et al. (2003a, b), this variability is driven more by recent changes in the amount and length of the summer melt season, as observed by Smith (1998a) and discussed in Section 5.9.15, rather than any changes in dynamic forcing and their effect on large-scale ice circulation/drift patterns—i.e., the change in ice thickness from spring to autumn, caused by ice melt in summer, is highly variable and appears to be a strong controller of ice thickness in the subsequent winter. The observed interannual variability is at both a higher frequency and greater amplitude than that simulated by regional models (Laxon et al., 2003a, b). Moreover, the addition of data from Envisat (Benveniste et al., 2002) and CryoSat (Drinkwater et al., in press) is expected to extend and improve this important time series. Launched in March 2002, Envisat's advanced Radar Altimeter (RA-2) has a special tracking mode and an improved vertical resolution with which to measure topographic features such as ice edges and sea ice thickness,

and is designed to overcome problems encountered over sea ice by ERS altimeters. In all cases, further validation of the error sources and magnitudes outlined above is, however, essential.

Other work by Mooney et al. (2000) investigated the use of ice thickness estimates from the ERS-1 and -2 radar altimeters, combined with satellite-derived ice velocity and concentration data, to determine ice volume and freshwater export values through Fram Strait. Such an approach is an important alternative to the spatially limited method using moored IPS data (Vinje et al., 1998), and complements SAR studies—e.g., Kwok and Rothrock (1999) and Kwok et al. (2004a)—but remains difficult to validate. It once again, however, illustrates the importance of synergistic analysis of available and complementary data.

5.9.6.2 CryoSat

A number of major new technological developments are occurring in response to the challenge of measuring ice thickness from space. The most promising is the Ku-band (2.2-cm wavelength) SIRAL, to be launched onboard ESA's CryoSat in 2004/5 (⟨*http://www.esa.int/ livingplanet/cryosat*⟩). In fact, SIRAL is the first spaceborne sensor specifically designed to measure sea ice thickness and its interannual variability, and will do so over a nominal 3-year lifetime (Drinkwater et al., in press; ESA, 2001, 2003; ESA and UCL, 2001). It is designed to systematically measure the freeboard of thick multiyear ice in the central Arctic, to a maximum latitude of 88°. As noted above, sea ice thickness can be estimated from these measurements by applying a priori ice density and snow cover thickness and density estimates, under the assumption that the ice is in isostatic equilibrium. It appears that, for dry snow, the radar echo is predominantly from the underlying saline ice surface (Laxon et al., 2003a, b). The scientific rationale is to gain accurate measurements of ice volume, with a view to detecting and monitoring change through time in order to assess the observational and modeling discrepancies discussed above, and in the light of apparent recent changes in both ice thickness and extent (see Section 5.5).

Based on the heritage of the altimeters onboard the TOPEX/Poseidon (launched in 1992) and Jason-1 (launched December 2001) missions, the new SIRAL sensor combines conventional pulse-limited altimeter hardware (Raney, 1998; Zelli, 1998) with novel synthetic aperture and interferometric signal processing to yield measurements at a higher along-track spatial resolution compared with conventional radar altimeters—e.g., ERS-2 (1995–2002) and Envisat (Drinkwater et al., in press; Wingham, 1999; Wingham et al., 2004). The concept is illustrated in Figure 5.85. Conventional pulse-limited altimeters transmit radar pulses separated by intervals of time that are sufficiently long (typically $\sim$500 μs) to ensure that the received signals (echoes) are uncorrelated. Signal averaging then enables reduction of fading noise. The pulse interval on SIRAL is only 50 μs. Although this results in correlation of return echoes, the bursts are processed by "aperture synthesis" techniques (Drinkwater et al., in press; Raney, 1998). The much-improved along-track resolution in SAR mode—i.e., 250 m—enables improved discrimination between ice floe surfaces

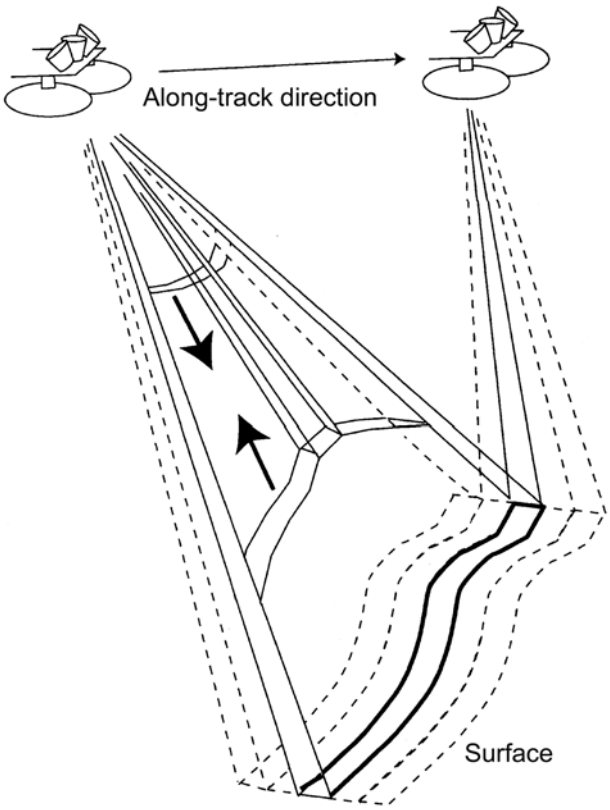

Figure 5.85. Schematic illustration of the concept of the CryoSat SIRAL altimeter instrument, which is (a) to use beam forming (Raney, 1998) in the along-track direction to improve on the signal-to-noise ratio (SNR) and pulse-limited resolution, while (b) using across-track interferometry in regions of undulating terrain (e.g., ice sheet margins) to determine the across-track source of the scattered energy. With SIRAL, coherent processing is used to narrow the directional gain of a normal incidence pulse-limited altimeter determined by its antenna in the along-track direction. Following processing, the "effective" illumination of the surface is the product of the antenna gain and that of the "beam" formed by the processing, with the net effect that the altimeter effectively illuminates a narrow across-track strip (the solid black line). A second antenna arranged in the across-track direction, and separated by a baseline of 1 m, enables determination of the across-track direction of the echo from the strip through cross-track interferometry (see Chapter 2 of Volume 2 of this book for a description of the latter). More than one "look" at the same surface strip is possible due to the along-track motion of the satellite, and statistical fluctuations of the echoes arising from the strip may be reduced through summation. Looks are data segments representing the application of pulse compression processing over only a part of the synthetic aperture. In practice, multiple beams are formed at each satellite location (a few of these are indicated by dashed lines), and the multiple looks at a particular strip are formed by selecting a different beam from each satellite location.

From Wingham et al. (2004). Reprinted with permission of IEEE. © 2005 IEEE.

(characterized by low backscatter) and intervening high-backscatter open ocean surfaces in leads (Laxon et al., 2003a, b). Ice surface topography is referenced to the ice-free ocean surface in leads. An essential element of such measurements is again precise knowledge of platform orientation and orbital position, which in this case is achieved by use of startrackers, a Laser Retro-Reflector (LRR) and a Doppler Orbitography and Radio-positioning Integrated by Satellite (DORIS) receiver mounted on the satellite.

CryoSat has the potential to greatly expand the spatial extent of the current sea ice thickness database and monitor changes in Arctic multiyear ice thickness. Similar uncertainties apply as they do to conventional altimetry measurements (see above), including the effect of radar penetration into multiyear ice. The requirement to measure ice freeboard to an accuracy of a few centimeters presents a challenge, given that uncertainties can be fairly large. These relate to variable snow and ice density, snow loading, ice surface topography, the preferential sampling of large floes, the different nature of ocean and ice echoes, and air–snow scattering (Haas, 2003; Wingham et al., 2001). It is anticipated that such measurements will be particularly powerful when combined with models. The predictive capability of both prognostic and thermodynamic-dynamics models has improved with the assimilation of realistic forcing parameters. The assimilation of satellite-derived and buoy velocities, for example, has been shown by Richter-Menge et al. (2002) to improve the correlation between modeled mean Arctic ice thickness and submarine sonar-derived mean thickness. Further improvements in model forcing and physics are required. Whether CryoSat produces useful thickness measurements of generally thinner Antarctic sea ice remains to be seen, although thicker regions of multiyear ice do occur—e.g., in the western Weddell Sea. Another potential application is the measurement of fast ice thickness. Once again, validation is of key importance, and is underway in a coordinated ESA program (Haas, 2003; Wingham, 2004).

5.9.6.3 Laser altimetry

Launched in January 2003, the GLAS on NASA's ICESat is potentially another major source of sea ice thickness information under clear-sky conditions. Although the primary objective of GLAS is to measure changes in ice sheet elevation (see Chapter 3 of Volume 2 of this book), it was also designed with the measurement of sea ice thickness in mind (Zwally et al., 2002b). With a pulse rate of $40\,s^{-1}$ and a beamwidth of $\sim$110 μrad, the 1,064-nm ICESat laser (GLAS) samples the surface within ellipsoidal footprints of $\sim$70 m in diameter with an alongtrack spacing of 170 m, and from an orbital inclination of 94°—i.e., to a maximum latitude of 86° (Zwally et al., 2002b). As such, surface measurements are provided at lengthscales equal to or above the spatial dimension of the footprint—i.e., $\sim$70 m. This is a substantial improvement over the $\sim$1.2-km footprint of the radar altimeters onboard ERS and Envisat, for example. Moreover, the uncertainty of variable penetration depth of radar signals into the snow/ice mass, depending upon conditions, does not apply for laser altimeters. Reflection of laser pulses occurs from the approximate surface itself, given the very small penetration depth due to the

shortwavelength radiation transmitted. A major disadvantage of laser altimeters compared with radar altimeters is that they cannot penetrate cloud cover. Other error sources are discussed in Zwally et al. (2002b), and include uncertainties in satellite radial orbit determination and atmospheric effects (attenuation and forward scattering).

Recent work by Kwok et al. (2004b) provided a first demonstration of the utility of spaceborne laser altimetry in estimating sea ice thickness in the Arctic. As with the radar altimeter technique outlined in Section 5.9.6.1, the approach relies upon the accurate measurement of ice freeboard (i.e., snow cover plus sea ice height above sea level) and its conversion to ice thickness h (based on the assumption of hydrostatic equilibrium and knowledge of snow cover thickness and density). Figure 5.86 (see color section) shows two local profiles of ice freeboard and draft estimated along two 160-km ICESat tracks, superimposed on near-coincident Radarsat ScanSAR images. One is from an area north of Ellesmere Island (Figure 5.86a) while the other is from an area in the East Siberian Sea close to the Siberian coast (Figure 5.86f). An important first step in determining freeboard from ICESat elevations (shown in Figures 5.86c and 5.86h) is to estimate the adjacent (local) sea level by identifying segments along-track with known thickness—i.e., thin ice or open water in leads. This information is essential as a reference due to large uncertainties in sea surface topography. In Figures 5.86c and 5.86h, the local minima and relatively flat areas along the ICESat profiles are indicative of areas of thinner ice or open water. These same areas are associated with low values in the coincident laser reflectivity profiles shown in Figures 5.86d and 5.86i. Note that reflectivity in this study is not a calibrated quantity because the GLAS detector saturation and atmospheric attenuation correction algorithms were not finalized, otherwise reflectivity would serve as an ideal indicator of open water/thin ice present. The approach adopted by Kwok et al. (2004b) is to use near-coincident Radarsat SAR imagery at approximately the same spatial resolution ($\sim$150 m) to examine leads in along-track ICESat segments. The age and thickness of ice in recently opened leads was determined from sequential SAR imagery using the ice growth model technique outlined in Section 5.9.6.4 and in Kwok and Cunningham (2002). The two pairs of Radarsat images shown in Figures 5.86b and 5.86g are separated by $<$5 days. In Figure 5.86b, for example, six leads that opened in the period between image acquisitions are apparent. The freeboard thickness values determined in the leads in this fashion are then used as references to level the ICESat elevation profiles. The resultant freeboard profiles are shown in Figures 5.86c and 5.86h. The estimated precision of the elevation measurements is $\sim$2 cm for regions of relatively flat ice.

As the laser returns from ice floes are from approximately the air/snow interface, with minimal penetration, snow depth h_S and density plus ice density must be accounted for in the conversion of observed freeboard to h. Uncertainty in these parameters represents the largest source of uncertainty in the computation of h. Due to a lack of suitable coincident data, Kwok et al. (2004b) derived snow thickness information from the snow climatology of Warren et al. (1999), making an assumption about snow density. They further used a sigmoidal function (to prevent snow depth from attaining values greater than the freeboard) where snow depth depends

on ice thickness (see the inset plot in Figure 5.86h). The resultant GLAS-derived sea ice thickness profiles are given in Figures 5.86c and 5.86h, with the associated thickness distributions and mean ice thickness estimates (of 3.9 m and 2.7 m) for the two areas being shown in Figures 5.86e and 5.86j. Also shown are the results of an analysis to test the sensitivity of mean ice thickness to changes in snow depth, in this case by 10 cm. This caused a change of ± 0.5 m and ± 0.25 m in the estimate of mean ice thickness, whereby decreasing/increasing the snow depth led to an increase/decrease in the mean ice thickness. This effect is most pronounced over thicker ice.

An important additional advantage of incorporating Radarsat data is that it provides a spatial context for interpretation of the ICESat elevation profiles. For example, the dominance of high radar backscatter in Figure 5.86b suggests that the primary ice type in this area is thick and rough multiyear ice. The area in Figure 5.86g, on the other hand, contains a mixture of multiyear and thinner/smoother first-year ice (lower backscatter). This results in higher variability in the GLAS relative reflectivity in Figure 5.86g. The extraction of useful surface roughness information from these data will be discussed in Section 5.9.9.

Zwally et al. (2004) further demonstrated the capability of ICESat to measure the mean surface elevation over 70-m footprints spaced at 170 m with a range precision of <3 cm to detect the freeboard height. They constructed Probability Density Functions (PDFs) of freeboard heights using data within 25 km of each measurement point along-track, fitting single or double dual-sigma Gaussians to each PDF to derive an ocean reference level. The dual-sigma Gaussian accounts for the typical asymmetry of the distributions, while the double Gaussian accounts for the bimodal distributions that occur in regions of mixed first-year and multiyear ice. This methodology is based on the likelihood that at least 1 to 2% open water and/or thin ice is present within each 50-km segment and/or the inclusion of sufficient information in the PDF to allow extrapolation to the reference level. Arctic sea ice thickness is then calculated using the snow cover climatology of Warren et al. (1999) and estimates of snow density. Resultant maps of sea ice thickness show similarities to those from satellite radar altimetry, as produced by Laxon et al. (2003b). Significant interannual variations are noted in the spatial distributions for the austral winters (February/March) of 2003 and 2004. In 2003, the multiyear ice pack extended farther southward in the direction of 45°E than normal. In the following year, the region of thick ice typical of the Canadian Arctic was more compacted than it was in 2003, with a larger area of thinner ice in the Beaufort and Chukchi Seas—the regions where the summer ice cover has been rapidly decreasing in recent years. In an exciting development, sea ice freeboard height distributions have been derived over Antarctica from ICESat data collected over distances of 50 km; these have been converted to maps of average freeboard thickness and sea ice thickness (Jay Zwally of NASA, pers. commun., October 2004). In this case, snow thickness information is derived from the standard AMSR-E product, as discussed in Section 5.9.8 (note that these data are not available for the Arctic).

From these emerging results, it appears that the ICESat dataset represents a significant advancement in the observation of Arctic sea ice freeboard, providing a dataset that is highly complementary to that of CryoSat. Once again, further

calibration and validation are essential. Particularly promising in this respect would be the combination of coincident ICESat/CryoSat measurement of ice freeboard with bottom-side measurement by long-range AUVs (Griffiths, 2003). As with CryoSat, it remains to be seen whether similar results can be achieved by ICESat over the generally thinner Antarctic sea ice cover, although initial results are highly encouraging (Yi and Zwally, 2005). Work also lies ahead to minimize uncertainty in snow thickness distribution, and its seasonal and spatial variability. The new satellite passive-microwave-derived snow thickness dataset from AMSR (see Section 5.9.8) may again prove to be useful in this respect, as may improved modeled estimates of precipitation, although both are at a low spatial resolution. Another error source relates to uncertainty in the estimation of the local sea level references necessary for accurate freeboard determination. This may again be minimized once calibrated GLAS reflectance data become available.

Due to the shorter than anticipated operating lifetime of ICESat's three lasers (Shuman, 2004), periods of data collection are limited to about 33 days each, for an expected total of about eight periods over 3 years instead of the planned continuous operation for 3 to 5 years (Kwok et al., 2004b). Level-2 ICESat sea ice roughness data from both hemispheres, codenamed GLA13, have been available from March 12, 2003 onwards from the NSIDC via NASA's EOS Data Gateway (⟨*http://nsidc.org/data/gla13.html*⟩). Freeboard height distributions over Arctic and Antarctic sea ice are derived over distances of ~50 km and converted into maps of average freeboard and sea ice thickness. Information on the data, and data analysis tools, are available from ⟨*http://nsidc.org/data/docs/glas_icesat_11_12_global_ altimetry.gd.html*⟩.

5.9.6.4 SAR—sea ice thickness from kinematics

A key aspect of SAR is its ability to provide ice kinematics products (Section 5.9.5.6) with which to better understand spatio-temporal variability in ice drift and opening and closing of the ice cover in response to momentum transfer (Drinkwater, 1995a). The routine processing of Radarsat ScanSAR data by the RGPS has, for the first time, enabled the quasi-operational estimate of ice motion, deformation, age, and thickness (of ice thinner than ~2 m) over the entire Arctic Ocean basin, and at a high spatial resolution of 100 m (Kwok, 1998; Kwok and Holt, 1999; Kwok et al., 1995a, 1999b). The technique uses repeat observations of Lagrangian elements or cells of sea ice in sequential 3-day repeat SAR imagery to estimate ice age and thickness (Kwok et al., 1999a, b). The deformation and thickness scheme is initiated at the start of each autumnal freezeup by covering the entire Arctic Ocean with 10×10-km cells (apart from 25×25-km cells towards the ice margins)—in a manner described earlier—and is run for the entire growth season. As no parameterization for melt is included, application is for winter only. The time-dependent drift and deformation of these polygonal ice areas are computed from the motion of their vertices, obtained by tracking common features in time-sequential SAR imagery (Kwok and Holt, 1999; Kwok et al., 1995a). The age histogram of newly formed ice within a given cell is then computed from the temporal record of the cell's change in area (see Figure 5.82). In other words, the sea ice age histogram specifies fractional area

coverage by newly formed ice of different ages. With each new satellite observation, the RGPS interprets a positive change in area as the creation of an area of open water by divergence and/or shear. An assumption is then made that ice growth occurs immediately, and this is modeled by applying a simple empirical ice growth formula (driven by air temperature). The growth rate and incremental increase in thickness between each weekly timestep is therefore controlled by simple ice dynamics. The uncertainty in ice age within this area depends on the time interval between observations (Kwok et al., 1999a, b). With convergence—i.e., a negative change in grid cell area—on the other hand, the thinnest/youngest component of the thickness/age distribution is assumed to have ridged and thickened according to model physics. The overall ice thickness distribution is then adjusted by redistributing that area of ridged thin ice into a separate thickness category in the age histogram (Drinkwater et al., 2001a). Ice age distribution is subsequently converted to a thickness distribution using a simple empirical ice growth formula, whereby growth rate is approximated as a function of the number of Freezing Degree Days (FDDs) associated with each age category and derived from 2-m air temperature data. This is accomplished using Lebedev's parameterization for ice thickness h (Lebedev, 1968; Maykut, 1986):

$$h = 1.33F^{0.58} \tag{5.57}$$

where F is the accumulated FDD of that category (Kwok et al., 1999a, b) and is given by:

$$F = \int_0^t (T_f - T_a)\, dt \tag{5.58}$$

where t is time, T_f is the freezing temperature of seawater, and T_a is the surface air temperature at 2 m from the IABP-POLES (NASA EOS POLES program) dataset (Yu and Lindsay, 2003). Note that the empirical relationship between h and F describes ice growth under an average rate of snow accumulation in the Russian sector of the Arctic Ocean, and that snow depth is not explicitly expressed in (5.40).

In addition to thermodynamic growth, the RGPS algorithm also accounts for the dynamic process of ridging, which redistributes the thinnest ice classes into thicker thickness categories (i.e., ice volume is conserved: Kwok et al., 1999a, b). By the approach used, three ice types are allowed to ridge: (i) the newest ice in a cell, (ii) the once ridged ice, and (iii) ice present at the time of cell creation. Following Parmeter and Coon (1972), all ridged ice is assumed to be $k = 5$ times its original thickness. If an area A is lost during ice convergence, then the ridged ice will occupy an area of $A(k-1)$. For each ice category, A is recalculated based on the amount of surface area lost to ridging (Kwok and Cunningham, 2002). All ice (including the ridged) then continues to grow according to (5.40).

In this manner, the volume of seasonal ice created and ice volume transferred into ridges can be computed from the ice thickness estimates. Indeed, the routine 3-day mapping of the ice cover by Radarsat has provided an unprecedented estimate of the seasonal ice production in the central Arctic for entire growth seasons over a 4-year period. Kwok (2002a) observed considerable differences in RGPS data in

total seasonal ice volume in the western Arctic between the winters of 1996/7 and 1997/8, which he attributed to changes in ice motion fields. Although the results are limited to the young/thin end of the ice age/thickness spectrum, this range is critical in that it dominates regional rates of turbulent heat flux between ocean and atmospheric, ice growth, and salt flux to the ocean (Maykut, 1978, 1986). In fact, RGPS products are invaluable as a means of developing much-improved estimates of area-weighted ocean–ice–atmosphere heat fluxes and salt fluxes (Drinkwater et al., 2001a). An example of results is given in Figure 5.87 (see color section), showing quantitative estimates of the evolving thickness distributions for thin and ridged ice in the Arctic Ocean for December 22, 1996. The close relationship between fracturing and ridging can be seen in Figures 5.82 and 5.87. Such information again provides additional insight into the mechanical "strength" of the pack, and its evolution. Of exciting potential in terms of characterizing time-varying changes in the ice volume of the Arctic Ocean is the synergistic merging of RGPS observations of ice kinematics and ice freeboard observations by CryoSat and ICESat (Holt and Kwok, 2003).

Thickness estimates produced by the RGPS remain difficult to validate. Potential error sources include uncertainties in computing areal changes (Lindsay and Stern, 2003), ridging assumptions, air temperatures, snow accumulation, and 3-day sampling (Kwok and Cunningham, 2002). Regarding the latter, recent work has shown that considerable deformational activity can occur at sub-daily timescales—i.e., around the inertial and tidal periods (Heil and Hibler, 2002). Kwok and Cunningham (2002) discounted uncertainty in area changes and the ridging parameterization as being major sources of error. Lindsay and Stern (2003) carried out an evaluation of the RGPS, finding reasonable agreement between retrievals of Arctic thin ice distributions by RGPS and AVHRR techniques (see below), but a large uncertainty in both methods. This uncertainty relates to the critical dependence of the methods on assumptions adopted for the thickness and density of the snow cover. Accurate ice tracking by the RGPS is also not possible during the summer melt period. Moreover, errors in divergence calculations are large in regions of high ice deformation such as coastal MIZs, and these are unfortunately areas of high ice growth. Yu and Lindsay (2003) also pointed out that, due to unpredictable backscatter variability soon after the autumnal onset of freezing, the RGPS cannot provide useful information in September and October—i.e., when thin ice growth is most vigorous. Once again, the lack of an RGPS-type system in Antarctica is a major deficiency. Although surface meltponds are absent from Antarctic sea ice, the latter is, however, characterized by a lower range (contrast) of microwave signatures overall and is more dynamic than its central Arctic counterpart, making it a more difficult target to track. Moreover, the widespread occurrence of flooding on Antarctic ice may further diminish the backscatter contrast between different ice types. The polarimetric and multi-polarization capabilities of the PALSAR and ASAR should enable improved discrimination of surface types (see below) and, potentially, improved tracking of Antarctic sea ice for ice deformation and thickness estimates. In the meantime, the establishment of an RGPS for Antarctic sea ice research is a high priority.

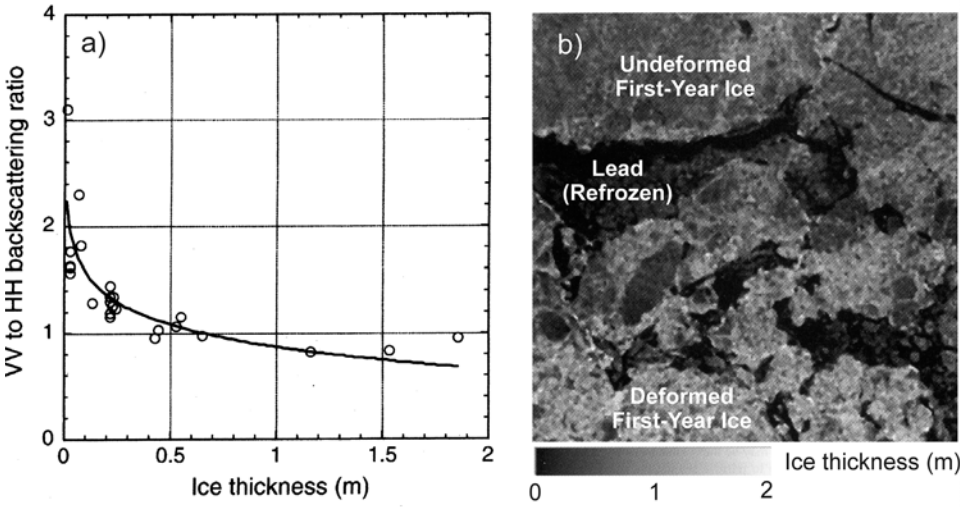

Figure 5.88. (a) An example of the relationship between sea ice thickness in the Sea of Okhotsk and the co-polarization power ratio $\gamma_{HH/VV}$ derived from measurements by the Japanese L-band Pi-SAR aircraft system. The thickness estimates are based on data from a moored ice-profiling sonar, with an associated Acoustic Doppler Current Profiler (ADCP) providing coincident information on ocean currents from which ice drift velocity could be derived. (b) An example of a map of ice thickness, derived from Pi-SAR data using (5.59). The sides of the image are 3×3 km.

From Wakabayashi et al. (2004). Reprinted with permission of IEEE. © 2005 IEEE.

5.9.6.5 SAR—sea ice thickness from polarimetry

New research in the Sea of Okhotsk, Japan, has shown the potential of polarimetric SAR[8] as a means of estimating sea ice thickness based on its dielectric properties at the relatively long wavelength (i.e., ~23 cm) of L-band (Matsuoka et al., 2001, 2002; Wakabayashi et al., 2001, 2004). Note that SAR polarimetry is covered in more detail in Section 5.9.7.3.2. Using fully polarimetric measurements acquired by the Japanese aircraft L-band Pi-SAR system, Wakabayashi et al. (2004), for example, found a relatively high correlation between sea ice thickness and the co- (like) polarization power ratio $\gamma_{HH/VV}$ for high-incidence angles. This is shown in Figure 5.88a. In this case, the correlation coefficient is 0.83. Based on the regression model fit as a logarithmic function in Figure 5.88a, Wakabayashi et al. (2004) developed the following empirical relationship between

[8] A multi-polarization SAR is a radar capable of acquiring more than one independent polarization measurement, either simultaneously or separately. SAR polarimetry refers to the science and techniques involved in the analysis of the polarimetric properties of EM waves and the scatterers of these waves.

ice thickness h and $\gamma_{HH/VV}$:

$$h = \exp\left(\frac{0.87 - [\gamma_{HH/VV}]}{0.71}\right) \tag{5.59}$$

Preliminary results, over a 3×3-km area of the Sea of Okhotsk and based on Pi-SAR measurements, are shown in Figure 5.88b. Although qualitative agreement is apparent between thickness and ice type, further studies are required where ground truth data are available.

Given that Pi-SAR instrument characteristics are similar to those of the ALOS PALSAR (see Wakabayashi et al., 2004 for a comparison), it follows that the latter shows promise as a means of estimating ice thickness over larger areas. As Wakabayashi et al. (2004) note, however, this application may be limited by the operational workload of ALOS. They also discuss other caveats, including the current lack of independent data for validation. Wider application is also unknown. Unfortunately, similar aircraft measurements are largely lacking from Antarctica.

5.9.6.6 Visible and thermal infrared techniques—estimating "thermal ice thickness"

An alternative and highly promising avenue is to combine satellite visible (VIS) and TIR data with models to estimate ice thickness. Groves and Stringer (1991) and Yu and Rothrock (1996), for example, combined NOAA AVHRR data with thermodynamic ice growth models to quantitatively estimate Arctic thin ice and its thickness distribution, again during the cold season (see also Lindsay and Rothrock, 1995). As stressed earlier, while thin-ice and open-water areas contained within leads and polynyas generally account for only a small fraction of the pack surface area, they make a highly disproportionate contribution to the overall turbulent heat (and moisture/gas) exchange between ocean and atmosphere, and of the opposite sign to that over thick ice (Maykut, 1982). Groves and Stringer (1991) used TIR imagery with models to estimate sea ice thickness in a coastal polynya in the Chukchi Sea, while Yu and Rothrock (1996) also derived coincident surface albedo (α) from clear-sky AVHRR VIS data for incorporation into their model. This approach is based upon the relationship between the surface physical skin temperature *IST* and albedo α of thin ice and its thickness (methods for deriving *IST* and α from satellite data are covered in Sections 5.9.11 and 5.9.13, respectively). It combined satellite data with a one-dimensional thermodynamic sea ice model (Maykut and Untersteiner, 1971) based on the surface energy balance equation (5.1) to estimate ice thickness h for each cloud-free AVHRR pixel, where ice thicker than 5 cm is assumed to have a uniform snow cover of thickness h_S. Yu and Lindsay (2003) factored in h_S by applying an empirical relationship between h_S and h, as proposed by Doronin (1971). The inputs are used to solve (5.1) for h for each pixel, to convert the *IST* field to an ice thickness map. The pixels in each scene are then summed to estimate the thickness distribution of sea ice up to $\sim$1 m thick. The results are shown in Figure 5.89 (see color section). Yu et al. (2001) examined the aggregate properties of Arctic thin ice using this algorithm, including brine flux,

ice growth, and compressive ice strength. With a strong dependence on ice thickness, these parameters exhibited large temporal and spatial variations. For a detailed description of the AVHRR model, and the assumptions therein (including a linear temperature profile in the snow, a constant water temperature of -1.8°C, and rapid growth of young ice), please refer to Yu and Rothrock (1996) and Yu and Lindsay (2003). Note that pixels at scan angles of $>45^{\circ}$ are rejected to minimize atmospheric attenuation and retain adequate ground resolution.

The current limitations to this technique were evaluated by Yu and Rothrock (1996) and Yu and Lindsay (2003). Even a thin snow cover can undermine the estimation of ice thickness from satellite TIR data by obscuring the relationship between ice thickness and skin surface temperature. Studies such as this typically derive snow depth information from empirical relationships between snow and ice thickness—e.g., Doronin (1971). This introduces considerable uncertainty into ice thickness calculations, which represents a significant source of error that is currently difficult to quantify. Although at a coarse spatial resolution of 12.5 km, the new AMSR-E snow thickness product may improve the algorithm performance by supplying improved estimates of snow thickness and its temporal variability over large areas. According to Yu and Rothrock (1996), downward longwave radiation is another major source of uncertainty. Incomplete cloud masking can also affect the accurate retrieval of surface temperature and albedo (see Sections 5.9.11 and 5.9.13), with sub-pixel, thin, and low-level clouds being a source of uncertainty. Even under clear-sky conditions, "diamond dust" in the lower atmosphere can influence the ability of the AVHRR to detect surface features such as leads (Key et al., 1994a), with the minimum detectable lead width being 400–700 m if the ice crystal layer optical depth is 0.6 (Stone and Key, 1993). Underestimates of thin-ice fraction result from the presence of narrow leads that are unresolved at the 1–4-km resolution of the AVHRR. See Key (1993, 1994) and Key et al. (1993, 1994b) for an analysis of lead resolving as a function of sensor field of view and implications for large-scale heat flux estimates. Other error sources relate to uncertainties in the parameterizations of sensible heat flux and downward longwave radiation in winter, and solar radiation and surface albedo in spring. Indeed, visible and near IR-channel data are unobtainable during periods of polar darkness.

Comparison of AVHRR-derived thicknesses with ice-profiling sonar measurements suggests that seasonal and regional variations in thin-ice distribution can be resolved to a reasonable accuracy using this method, providing a climatology with which to test models. The accuracy is reported to be $\sim$50%, while uncertainty in the cumulative thickness distribution ranges from $\sim$3% for ice $<$20 cm thick to $\sim$9% for ice with a thickness of $\sim$1 m (Yu and Rothrock, 1996). It is expected that accuracy will be increased by using improved data from MODIS and similar advanced sensors—e.g., AATSR, MERIS and VIIRS. An extension to this technique could potentially enable the estimation of salt flux rates (Yu and Rothrock, 1996). In their comparative study of the AVHRR and RGPS thin-ice thickness retrieval algorithms, Yu and Lindsay (2003) found that the finer spatial resolution of Radarsat results in the detection of more thin ice, while the RGPS may underestimate thin-ice production due to the 3-day sampling interval. The AVHRR offers wider coverage

with a higher temporal resolution. In spite of inherent biases, the correlation between the two estimates of h was high—up to 0.6 m. Note that while the RGPS includes both undeformed and ridged ice in the thin-ice thickness distribution—i.e., it parameterizes thermodynamic and dynamic growth—these classes are inseparable in the AVHRR TIR scheme. They concluded that a combination of the two complementary datasets could offer improved coverage and estimates of thin-ice thickness in the Arctic Basin, an approach that would be particularly beneficial in coastal and ice margin regions.

Drucker et al. (2003) adapted and applied the above technique to define a clear-sky "thermal ice thickness" in the St. Lawrence Island polynya (Bering Sea), adding meteorological observations to AVHRR-derived surface temperatures and a heat flux model (after Martin et al., 1998). Referring back to (5.1), and based on the assumption that the conductive heat flux through the ice F_c is a linear function of the temperature difference across the ice (and that the latter is thin), this gives:

$$F_c = \frac{k_i(IST - T_O)}{h_T} \tag{5.60}$$

where $k_i = 2.03\,\mathrm{W\,m^{-1}\,K^{-1}}$ is the thermal conductivity of sea ice, IST is the AVHRR-derived ice skin surface temperature (see Section 5.9.11), $T_O = -1.8^{\circ}\mathrm{C}$ is the ocean surface temperature, and h_T is the derived ice thickness. If the ice surface is not melting and is free of snow, then $F_c = F_T$, where F_T is the total heat flux at the ice surface (Martin et al., 1998), and (5.60) can be solved for h_T as follows:

$$h_T = \frac{k_i(IST - T_O)}{F_T} \tag{5.61}$$

Time series examples of resultant ice thickness maps are given in Figure 5.90 (see color section). AVHRR-derived thicknesses agree with ULS-derived thicknesses to within the observational uncertainty for smooth and lightly ridged ice. It is again anticipated that the application of this technique to MODIS data will yield improved results, given their improved geolocation, and higher spectral and spatial resolution.

These techniques illustrate the considerable benefits to be gained by combining satellite data with a model, in this case to derive thickness distributions of thin sea ice. As with the RGPS technique, long time series of such data would contribute to an improved understanding of not only regional sea ice heat and mass balance but also brine rejection rates to the underlying ocean and their impact on large-scale ocean circulation. A deficiency of both these and the RGPS technique when applied to Antarctica is that neither account for ice thickening by snow/ice formation, which as we have seen is a ubiquitous process in the Southern Hemisphere and one that may increase in importance under a global-warming scenario (Eicken and Lemke, 2001; Wu et al., 1999b). Moreover, ocean heat flux—the term F_w in (5.1)—is not included, yet as we have seen plays an important and regionally variable role in limiting the Antarctic ice thermodynamic equilibrium thickness (Lytle and Ackley, 1996; Lytle et al., 2000). It was pointed out earlier that ocean heat flux may also become a more important factor in the Arctic if current trends continue (Martinson et al., 2000).

5.9.6.7. Inference of ice thickness using passive-microwave radiometry

Efforts have been made in the Arctic to detect regions of thin sea ice using satellite passive-microwave data, based upon the correlation between initial ice growth and increasing T_B (Eppler et al., 1992; Grenfell and Comiso, 1986). Wensnahan et al. (1993), for example, applied an empirical equation employing principal component analysis to SSM/I data from the Bering Sea. Cavalieri (1994) adapted the NT algorithm to differentiate new (thickness $\leq$0.1 m), young (0.1–0.3 m), and first-year ($\geq$0.3 m) ice types within the seasonal ice zone, at the SSM/I spatial resolution of 25×25 km. This work is based on the relationship between decreasing PR and ice thickening, and was adapted by Kimura and Wakatsuchi (1999) and Martin et al. (1998) for application in the Sea of Okhotsk, with the latter study detecting new-ice production and polynyas. Tateyama et al. (2000) further developed an improved resolution algorithm—i.e., 12.5×12.5 km and known as S/KIT—to classify new, young, first-year, and fast ice, again for application in the Sea of Okhotsk. Ice thickness categories are in this case based on the radiometric properties of sea ice at 37 and 85 GHz, using the ratio of T_Bs from the vertically polarized channels—i.e., the ice thickness parameter is $R_{37V/85V}$. According to Tateyama et al. (2000), the 85V channel is most suitable for detecting sea ice thickness, as the dynamic range of the T_B of snow-covered thick ice increases with increasing frequency. Following Tateyama and Enomoto (2000, 2001), ice thickness h is calculated as:

$$h = h_0 + h_C(R_{37V/85V} - R_H) \tag{5.62}$$

where h_0 is the minimum thickness of each ice type (determined from shipborne measurements), h_C is a constant calculated by dividing the range in thickness by $R_{37V/85V}$ (maximum) minus the threshold values R_H of each ice type. Tateyama and Enomoto (2001) combined the S/KIT ice classification algorithm with ice concentrations from the NT algorithm (Cavalieri, 1994) to determine the volume of sea ice in the Sea of Okhotsk from 1992 to 1999. The results are shown in Figure 5.91. Note the strong correlation between ice volume and the "Cold Air Mass Index", or the accumulated daily average air temperature at 700-hPa height from December to April off the northeast coast of the Kamchatka Peninsula, where air temperature is largely affected by the Aleutian Low Pressure system. Small ice volumes tended to occur when the Aleutian Low was strong and air temperatures were low. Please see Tateyama and Enomoto (2001) for further details and a discussion of error sources.

This method was further tested and developed by Tateyama et al. (2002), again in the Sea of Okhotsk. They carried out multiple regression analysis to combine the attributes of the PR and $R_{37V/85V}$ techniques, resulting in an improved formula for estimating ice thickness h (in cm) from SSM/I brightness temperature data:

$$h = -537.33 \cdot PR + 83.88 \cdot R_{37V/85H} - 6.91 \tag{5.63}$$

where PR uses 19-GHz data and is:

$$PR = \frac{(T_{B19V} - T_{B19H})}{(T_{B19V} + T_{B19H})} \tag{5.64}$$

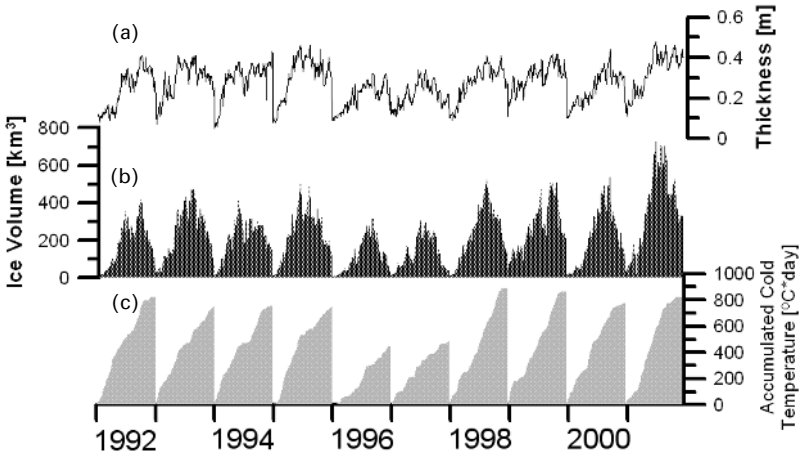

Figure 5.91. Time series of (a) ice thickness and (b) ice volume in the Sea of Okhotsk (7-day running mean), both derived from DMSP SSM/I data, compared with (c) the Cold Air Mass Index at 57.5°N, 167.5°E, derived from National Centers for Environmental Prediction/National Center for Atmospheric Research (NCEP/NCAR) reanalysis data, during the boreal winters (December–April) of 1991/2–2001/2.

Modified from Tateyama and Enomoto (2001). Reprinted with permission of the International Glaciological Society (IGS). © 2005 IGS.

Threshold values of PR and $R_{37V/85H}$ as a function of ice type—i.e., thickness range—for the Sea of Okhotsk are given in Tateyama et al. (2002, table 2).

While promising, particularly in the light of the availability of new improved data with the launches of the Aqua AMSR-E and ADEOS-II AMSR, the wider applicability of the above techniques is uncertain, and requires further work towards verification. Sources of uncertainty include the sensitivity of 85-GHz data to atmospheric contamination and changes in surface and snow properties and snowmelt, compared with lower frequencies.

5.9.6.8 Low-frequency passive-microwave radiometry

Of potential importance are a series of low-frequency passive-microwave radiometer missions. The first, namely the Soil Moisture and Ocean Salinity mission (SMOS), will be launched in 2007 (⟨*http://www.esa.int/livingplanet/smos*⟩). This satellite will carry a 1.4-GHz (L-band) multi-angular sensor operating at dual polarization, and based on new aperture synthesis technology (Kerr et al., 2000; Silvestrin et al., 2001). Aperture synthesis is an interferometric technique in which the correlation between pairs of small antennae and signal processing are used to achieve the spatial resolution of a single large antenna, thereby enabling the launch of longwavelength passive-microwave sensors (Le Vine et al., 2004). While SMOS, as its name suggests, is not specifically designed for sea ice applications, it could yield information on large-scale ice thickness integrated over its coarse (50 km) FOV. Such a sensor has never before been launched in space. Theory indicates that it may be possible to

determine the thickness of a slab of sea ice when it approximates the wavelength of the radiometer—i.e., 21.4 cm for the 1.4-GHz instrument (Comiso, 1996). In reality, and as a result of the complexity of sea ice, the monotonic increase in emissivity with thickness, as predicted by theory, may not necessarily always hold in reality—i.e., it depends on complex interactions of factors other than ice thickness. However, *in situ* observations in the Antarctic by Menasi et al. (1993) suggest that a relationship does exist between the microwave emissivity of sea ice measured at low frequency and its thickness, up to a thickness of ~0.8 m at which point the emissivity saturates.

The very coarse resolution of this sensor limits it to global applications. Moreover, considerable uncertainties in accuracy may remain due to the complexity of the combined sea ice/snow substrate as a microwave target. Once again, it remains to be seen whether useful information can be retrieved from these data. Given the very coarse resolution of the product, its validation will present a considerable challenge. A similar L-band (1.413 GHz) sensor will be launched onboard the joint U.S. (NASA) and Argentinian Aquarius mission in 2008 (see ⟨*http://essp.gsfc.nasa.gov/aquarius/index.html*⟩ for specifications), with an 8-day orbital repeat cycle over a 3-year lifetime (resolution 100 km across a 300-km swath width). Aquarius will also carry a 1.2-GHz radar scatterometer to correct for open ocean surface roughness effects on sea surface salinity. A similar instrument will be launched onboard NASA's HYDROsphere State (HYDROS) mission in 2010, the main aim of which is to measure global soil moisture and land surface freeze–thaw activity (Entekhabi et al., 2004; Long et al., 2005; ⟨*http://hydros.gsfc.nasa.gov/*⟩). This is an L-band combined active–passive system operating over a wide swath of 1,000 km at a constant look angle of 39°. The radar will operate at 1.26 GHz (VV-, HH-, and HV-pol), and at a spatial resolution of 3 and 10 km. The passive-microwave radiometer, on the other hand, will operate at 1.41 GHz (H-, V-, and U-pol) with a coarse spatial resolution of 40 km. The revisit interval is 1–3 days.

In summary, all of the different techniques outlined above have their own strengths and weaknesses, and yield different yet complementary quantities. Whereas the radar and laser altimeter techniques measure thick (high-freeboard) ice but exclude areas of open water/new ice, the SAR and visible to TIR-type techniques are limited to the measurement of thin ice only. Neither can offer useful measurement in the MIZ. Measurements from IPSs mounted on moorings and submarines, on the other hand, cover the full range of ice thickness distribution. This suggests that optimal results will come from the combined use of several different methods rather than from single sources alone. To reiterate, care should also be taken in the interpretation of time series of satellite-derived ice thickness data from a given region for the purposes of calculation of mass balance and its monitoring over time. For example, thinning can result not only from ice melt but also advection—either of thin ice into, or thick ice out of, a given region. As such, any interpretation or forecast of thickness distribution changes in terms of climate change and/or variability must account for both thermodynamic and dynamic processes (Haas, 2003). It is noted that efforts are being made to develop low-frequency radar systems for measuring sea ice thickness from helicopters and ultimately fixed-wing aircraft. By performing EM simulations using sea ice core

data from both polar regions, Ramasami et al. (2003) determined that a radar system operating in the frequency range of 50–250 MHz (VHF) is required to measure thick first-year or multiyear ice thickness (0.5–4 m) in the Arctic, while a 300–1,300-MHz frequency range (UHF) is needed for measurements of thin Arctic sea ice and Antarctic sea ice in general (0.5–2.0 m). They developed a radar system to operate over both frequency ranges. Initial field trials at Barrow, Alaska, and East Antarctica yielded accurate measurements. Significant technological challenges remain before such systems can successfully provide accurate data from space.

5.9.7 Sea-ice-type discrimination (classification)

An alternative method of deriving ice thickness information from satellite data is to classify the ice in terms of its stage of development (age)—i.e., based upon the WMO Sea Ice Nomenclature (WMO, 1970)—then use this information as a coarse proxy measure of thickness. By this means, it is possible to infer a range of ice thicknesses (including ice-free ocean) from which regional-scale variability in the ice thickness distribution can be estimated. While not as accurate as the direct measurement of thickness, this approach provides valuable broad-scale information where direct measurements are lacking. In the operational sense, this approach has also been extensively used to produce regional and hemispheric ice charts, by means of the visual (manual) interpretation of satellite data at visible to TIR wavelengths—e.g., DMSP OLS and NOAA AVHRR (Dedrick et al., 2001; Partington et al., 2003). Such charts, which are based upon ice concentration and extent information from passive-microwave sensors, have been produced by the U.S. National Ice Center, for example, since the 1970s (⟨*http://www.natice.noaa.gov/*⟩). Latterly, these charts also include ice-type information from SAR data (particularly from Radarsat in ScanSAR mode). See Section 5.9.17 for further information on operational applications of satellite remote sensing.

5.9.7.1 Passive-microwave techniques

We saw in the last section how efforts are being made to map thin-ice distribution from passive-microwave data. Here, we examine the most fundamental large-scale discrimination—namely, that of first-year and multiyear ice in the Arctic. This simple distinction can be used as a proxy, although rather crude, indicator of ice thickness. These ice types can be readily distinguished and mapped using multichannel passive-microwave data as they have different radiometric properties during the winter when their microwave signatures remain relatively stable (Comiso, 1990; Eppler et al., 1992; Johannessen et al., 1999; Kwok et al., 1996). Increased knowledge of the thickness distribution of the perennial pack is required to understand mass volume and the portion of the thickness regime that might be changing (Holt and Kwok, 2003).

Two separate approaches have been adopted in the use of passive-microwave data alone to estimate Arctic multiyear ice extent, concentration, and trends, as evaluated by Belchansky et al. (2004a). The first uses linear combinations of

brightness temperatures from the 18-, 19-, and 37-GHz channels, and requires tiepoints to guide discrimination of multiyear, first-year, and openwater signatures. Examples are the NASA Team (NT) algorithm (Gloersen and Cavalieri, 1986) and the NORSEX algorithm (Svendsen et al., 1983). Recall from Section 5.7.3 that, as sea ice ages, its microwave backscatter and radiative (emissive) properties change. In the Arctic, the emissivity of multiyear ice is significantly lower than that of first-year ice due to the reduction of dielectric loss by desalination through time (Grenfell, 1992) (see Section 5.7.1). This frequency-dependent change in ε, with a decreasing contrast between first-year and multiyear ice with increasing wavelength, is exploited to discriminate multiyear from first-year ice (Belchansky et al., 2004a; Comiso, 1990; Gloersen et al., 1992; Lomax et al., 1995). The main drawback of the tiepoint approach is that poorly understood and unaccounted for spatio-temporal variations occur in the emissivity of multiyear ice that undermine the use of static sets of tiepoints (Bechansky et al., 2004a; Kwok et al., 1996). The alternative approach to mapping multiyear ice with passive-microwave data is based upon the simple assumption that the total sea ice remaining at the end of each summer melt season is, by definition, second-year or multiyear ice (Comiso, 1990). The principal advantage of this approach is that it foregoes the need to classify ice types. It is, however, limited to a single observation each year. Other strengths and weaknesses are evaluated by Kwok et al. (1996).

An example of monthly averaged Arctic multiyear ice concentration maps derived from SSM/I data is given in Figure 5.92 (see color section). These were created from SSM/I data by applying the NT algorithm using the spectral gradient ratio at 37 and 19 GHz and the polarization ratio at 19 GHz (Cavalieri et al., 1984). Recalling (5.26) and (5.27) and using the relationships $T_B = C_{OW}T_{OW} + C_{FY}T_{FY} + C_{MY}T_{MY}$ (5.65) and $C_{OW} + C_{FY} + C_{MY} = 1$ (5.66), the fractional coverage of open water (C_{OW}), first-year ice (C_{FY}), and multiyear ice (C_{MY}) can be solved. Unfortunately, ice-type retrievals from satellite passive-microwave data have proved to be unreliable at times (Comiso, 1986; Kwok and Comiso, 1998; Thomas, 1993). Shortcomings include a discrepancy between winter and summer estimates of the multiyear ice fraction, apparently due to spatio-temporal variations in the assumed ice-type signatures. Model results and observations suggest that passive-microwave estimates of multiyear ice fraction could have uncertainties and biases of $\sim$20% (Kwok and Comiso, 1998; Thomas and Rothrock, 1993).

The discrimination of multiyear and first-year ice is not possible in the Arctic during the spring–summer melt period, when an increase in snow liquid water content and extensive meltpond coverage drastically change the microwave emissivity of the sea ice cover (Comiso et al., 1984; Carsey, 1985; Grenfell and Lohanick, 1985; Kwok et al., 1996; Lohanick, 1990, 1993). This has the net effect of masking age-related differences in the underlying ice signatures. Multiyear ice discrimination is also difficult throughout the year in Antarctica, due to its non-unique emissivity (Gloersen et al., 1992) (for reasons outlined in Section 5.7). Moreover, passive-microwave-derived results are somewhat limited by uncertainties associated with the mixing of ice types within the large sensor footprint and

variability in ice-type emissivity. See Kwok et al. (1996) for additional discussion of uncertainties. These authors concluded that the multiyear estimates provided in this fashion are consistently lower than those from coincident SAR data. Improved classification may be achievable using the new polarimetric capabilities of WindSat (see Section 5.8.1), compared with the SSM/I and AMSR sensors. As we will see in Section 5.9.7.4, improved mapping of Arctic multiyear ice is afforded by combining passive-microwave with active microwave data in a neural network analysis (Belchansky et al., 2004a).

5.9.7.2 Passive microwave mapping of large-scale ice-type regimes

Massom et al. (1999) developed a scheme to classify the Antarctic ice cover in terms of its constituent large-scale sea ice-type regimes from SSM/I T_B data. In short, this was accomplished by carrying out a cluster analysis on the multi-frequency data, to infer information on large-scale spatial (and temporal) variability in ice type based on unique surface emissivity characteristics (ice and snow cover combined) as a function of frequency and polarization. Maps of sea-ice-type regimes were created for the same study region, based upon results from a 1995 East Antarctic field experiment. By this technique, Massom et al. (1999) were able to identify, for example, the boundary or zone separating the MIZ (comprising small wet floes) and the inner pack (larger floes with a drier snow cover, due to minimal wave/swell effects). While the results were reasonable when compared with coincident *in situ* and ERS SAR observations, it remains to be seen whether the technique is robust enough to produce consistent results over longer time periods and larger areas. If so, this information is highly complementary to the coincident maps of ice concentration and snow thickness (produced using a subset of the same data), and may prove useful as a further source of information with which to validate and improve models (which are at a similar spatial resolution). Moreover, the earlier study used SSM/I 12.5–25-km data; incorporation of improved resolution (6.25 km) data from the high-frequency AMSR-E channels should improve the technique. An example of an iterative approach to sea ice classification using multi-sensor data, including SSM/I data, is given by Remund et al. (2000)—see Section 5.9.7.4.

5.9.7.3 SAR techniques

5.9.7.3.1 Conventional SAR

Other studies have exploited calibrated SAR data to gain high-resolution information on ice-type distributions—e.g., Fetterer et al. (1994), Hauser et al. (2002), Kwok et al. (1992a, b); Lythe et al. (1999). With its ability to penetrate polar clouds and darkness and measure the radar backscatter characteristics of the surface, SAR is potentially well-suited to the classification of component sea ice types within a given scene and at a high resolution of 25–100 m. A key factor here is the frequency dependence of the penetration depth through the snow cover into the ice and the backscatter (Drinkwater, 1995a). Recalling Section 5.7, the measured

backscatter intensity depends upon (i) the dielectric properties of the surface types and their relative concentrations within the sensor FOV, and (ii) their surface roughness characteristics. Ice-type mapping with SAR depends on the discrimination of surface versus volume scattering, surface roughness characteristics, and large-scale deformation and ice structures. Sea ice surface roughness and dielectric properties (linked to surface and volume scattering) change as the ice ages. For first-year ice, the relatively high salinity largely prevents radar penetration (at shorter wavelengths—e.g., C-band) and surface roughness-dependent scattering dominates the observed backscatter (Kwok and Cunningham, 1992; Onstott and Shuchman, 2004). Vant et al. (1978) show that the penetration depth at X-band ($\lambda = 3$ cm) for first-year ice with a bulk salinity of 7–8 p.s.u. at a temperature of $-5°$C is only 2–4 cm (with a dielectric loss of $\sim$150 dB m^{-1}). For Arctic multiyear ice, on the other hand, the low salinity in the ice freeboard enables significant microwave penetration into the ice under dry snow conditions, and the observed backscatter is dominated by volume scattering (from dielectric discontinuities or discrete scatterers such as gas bubbles) at radar frequencies of C-band and higher. A key factor here is that the bubble/void dimensions are within an order of magnitude of the radar wavelength—i.e., $\sim$3 and 6 cm—at X- and C-band, respectively (Onstott and Shuchman, 2004). Radars operating at L-band (23-cm wavelength) are less sensitive to small-scale surface roughness, and penetrate much deeper into the sea ice. As a result, the volume scattering largely emanates from internal ice inhomogeneities to yield information more on the morphology and structure (mechanical deformation features) of the ice (Drinkwater, 1995a; Drinkwater et al., 1991). As a result, the backscatter signatures of first-year and multiyear ice are similar at L-band. A system with multi-frequency imaging capabilities would yield complementary information on ice type and structures. The surface morphology is also different for multiyear ice in the Arctic, being heavily weathered with ridges rounded, compared with the more angular characteristics of first-year ice.

Under cold, dry conditions (and in the Arctic), backscatter at C- and X-band is dominated by surface scattering by small-scale surface roughness features for new and first-year ice, and by near-surface volume scattering for Arctic multiyear ice (see Section 5.7.1 for more details). As a result, reasonable backscatter separation is generally achievable for Arctic sea ice types at C- to Ku-band frequencies under freezing conditions (Onstott and Shuchman, 2004) (Figure 5.93a). The snow cover at this time is dry and largely transparent to the radar waves at higher frequencies—i.e., C- and X-band (Drinkwater, 1995a)—although the presence of icy layers and crystal enlargement by metamorphism affect the backscatter contribution. In winter, Arctic multiyear ice has a stable signature that contrasts (by 2–4 dB at C-band) with that of first-year ice (Fetterer et al., 1994; Kwok and Cunningham, 1994a, b), and represents a significantly brighter target. Note that this contrast is not as apparent for Antarctic sea ice. Morris et al. (1998), for example, observed in ERS-1 (C-band, VV-pol) SAR data that (i) values of σ^0 for Antarctic (Bellingshausen Sea) multiyear ice in the austral winter are similar to those in the Arctic, but higher in the Antarctic in summer; (ii) similar winter backscatter signatures for multiyear and thick first-year ice; and (iii) the largest contrast in Antarctic backscatter signatures is between

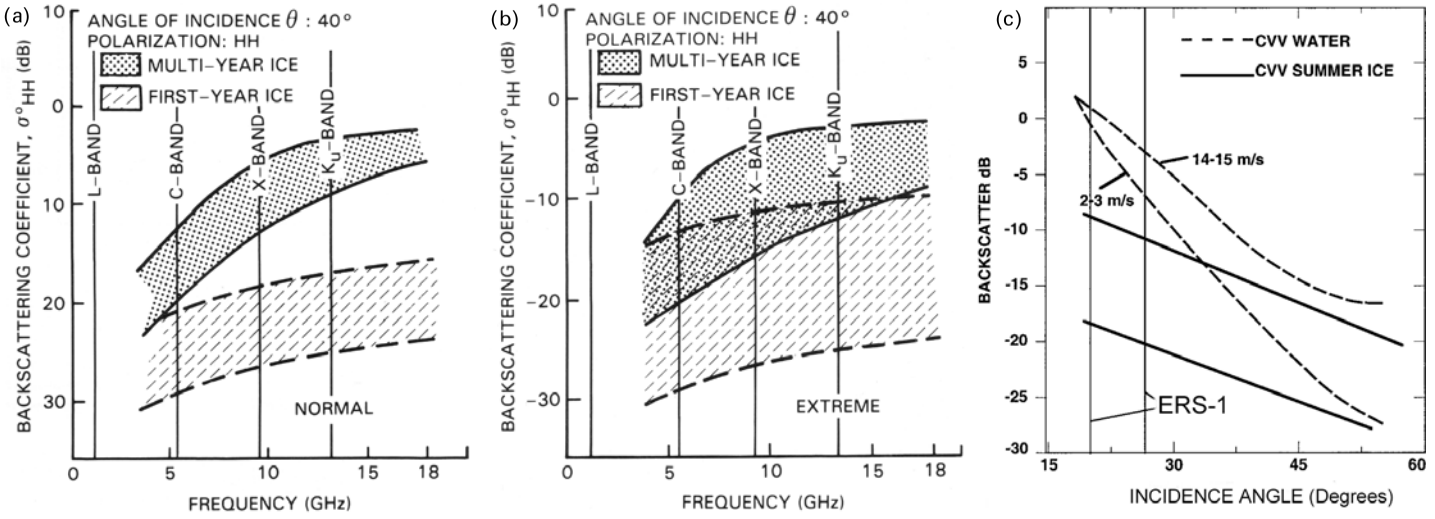

Figure 5.93. Frequency dependence, determined theoretically, of the σ^0 of Arctic first-year and multiyear ice at an incidence angle of 40° and under (a) normal/winter and (b) extreme/summer melt conditions. (c) Schematic plot of the summer dependence of the radar backscatter of the Arctic Ocean measured at C-band and VV-polarization. Solid lines delimit the approximate range for consolidated sea ice (using data from Barber et al., 1995; Comiso and Kwok, 1996; Onstott, 1992; Winebrenner et al., 1994, 1996), while the dashed lines show the equivalent values for ice-free ocean (from Stoffelen and Anderson, 1997).

Parts (a) and (b) from Kim (1984); and (c) from Holt and Martin (2001). Part (c) copyright 2001 American Geophysical Union. Reproduced by permission of American Geophysical Union.

new/young ice and older thicker ice types. Similar findings are given by Drinkwater and Liu (2000).

During the late-spring to summer melt period, the appearance of freewater in the snow volume has the net effect of transforming the snow into an opaque filter to microwaves. Under wet conditions, surface and volume scattering from the snow cover become the dominant backscatter mechanism, effectively masking the backscatter contrasts between the underlying ice types—e.g., Arctic multiyear and first-year ice—as shown in Figure 5.93b (Barber et al., 1995; Beavan and Gogineni, 1994; Comiso and Kwok, 1996; Winebrenner et al., 1994, 1996). This impact is greatest at higher frequencies (Hallikainen and Winebrenner, 1992), with Drinkwater et al. (1991) postulating that L-band may be the optimal frequency for discriminating between thick and thin ice over the seasonal melt period due to its reduced absorption loss compared with X- and C-bands.

Figure 5.93c is a schematic of incidence angle dependence in summer of both Arctic sea ice and open ocean at C-band (VV-pol). Over the 20–26° range of the ERS SARs, σ^0 lies between -10 and -17 dB for Arctic summer ice (Holt and Martin, 2001). Variability is due to (i) changes in meltpond distribution and characteristics (Barber et al., 1995; Comiso and Kwok, 1996), and (ii) rapid temperature fluctuations (particularly in late summer) (Nghiem et al., 1998; Winebrenner et al., 1996). Note that 2–3 m s^{-1} is the wind speed threshold above which Bragg scattering waves occur on open water (Holt and Martin, 2001). The decrease in backscatter with increasing incidence angle is apparent in Figure 5.93c, with a steeper slope for open water. Note that different relationships again prevail in Antarctica, due to a relative lack of surface melt in the austral summer. Morris et al. (1998), for example, observed that relatively little variability in σ^0 occurs in Antarctica over summer and winter. However, Drinkwater (1998b) noted that scattering coefficients for the various sea ice types in the Weddell Sea tend to converge during the transition from winter to summer towards values of about -7.5 dB, a signature that is similar to that of second-year and multiyear ice in winter. This appears to be driven by enhanced flooding as the ice temperature increases and surface melt takes place. A key factor is that summer surface melting is short-lived in Antarctica, with little meltpond formation and associated downward freshwater percolation to desalinate the surviving ice. In the Antarctic summer, the backscatter response is largely characterized by fluctuations in σ^0 that are correlated with melt and refreeze cycles associated with the passage of storms (Drinkwater and Liu, 2000; Drinkwater and Lytle, 1997).

Recall from Section 5.7 that σ^0 is also determined by frequency, polarization, and incidence angle. A good deal of research has been carried out to determine the optimum combination of sensor parameters for ice-type classification. Indeed, this is now a key consideration, given the emergence of multi-polarization and polarimetric SARs in space. To date, this work has largely taken place under controlled conditions (Swift et al., 1992), or has focused mainly on the Arctic, using modeling techniques and *in situ* and aircraft observations (often in concert with satellite measurements)—e.g., Kim et al. (1985a), Onstott et al. (1979, 1982, 1998), Onstott and Shuchman (1990), Perovich et al. (1998b). This research has contributed

to the development of techniques using both SARs and scatterometers to classify ice type and to characterize the electrical and physical properties that control backscatter levels (Onstott, 1992; Onstott and Shuchman, 2004). Excellent reviews are available on (i) the relative strengths and limitations of different system parameters—i.e., frequencies, polarizations, and incidence angles (Kim et al., 1985a; Onstott, 1992); (ii) the contribution of various sea ice geophysical parameters to the backscatter signature (Ulaby et al., 1986a); and (iii) issues of seasonality and the evolution of the microwave signature (Drinkwater, 1995a; Livingstone et al., 1987a, b). Please see Kwok and Cunningham (1994a) for information on the spectral characteristics of Arctic sea ice at C-band. Other excellent reviews tie this material together for both polar regions—e.g., Drinkwater (1995a, b, 1998a), Livingstone (1994), Onstott and Shuchman (2004), Rignot and Drinkwater (1994), and all relevant papers in Carsey (1992) and Tsatsoulis and Kwok (1998a).

Studies using mainly ERS SAR data have evaluated differences in backscatter as a function of ice type. In the Arctic, these have looked at both winter (Kwok and Cunningham, 1994b; Fetterer et al., 1994; Steffen and Heinrichs, 1994) and spring through autumn conditions (Barber et al., 1995; Winebrenner et al., 1994, 1996), while Drinkwater (1995a, 1998a, b) evaluated Antarctic ice types. The latter study noted the following backscatter statistics from ERS-1 C-band data (23° incidence angle) as a function of ice type in the Weddell Sea in winter: (i) smooth first-year ice: mean -15.5 to -16.1 ± 1.0 dB; (ii) rough first-year ice: mean -9.5 to -10.1 ± 1.8 dB; and second-year and multiyear ice: mean -5.7 to -6.8 ± 2.3 dB. Shuchman et al. (2004) noted that the dynamic range separating Antarctic first-year and multiyear ice in winter is $\sim$2–3 dB greater than that for similar ice forms in the Arctic, and is attributable to a thicker Antarctic snow layer, greater surface roughness, and the widespread contribution of surface flooding.

An example of the polarization- and frequency-dependent behavior of freezing Arctic sea ice is given in Figure 5.94. In this example, the ice-type information is weak at the shortest wavelength with the smallest penetration depth—i.e., P-band ($\lambda = \sim 60$ cm) (Onstott and Shuchman, 2004). Backscatter at this frequency is dominated by surface topography in the form of pressure ridges. Floe boundary delineation in this case is best achieved at VV-polarization, while HV-polarization is best for surface roughness detection. At L-band (the longest wavelength used in current satellite SAR systems—e.g., JERS-1 and ALOS), the overall information content is intermediate between that of P- and C-band. Again, ice-type and floe boundary discrimination is best achieved at VV-polarization, while optimal surface topographic information comes from the HV-channel. Due to its longer wavelength and greater penetration depth, L-band provides more information on the morphological characteristics of the ice (the bright streaks representing ridges and fractures). This frequency generally provides poorer discrimination of first-year and multiyear ice as the wavelength ($\sim$24 cm) is significantly greater than the size of discrete volume scatterers within the ice—i.e., gas bubbles have a typical diameter of $\sim$1 mm. It can be seen that the best ice-type discrimination is accomplished at C-band—e.g., ERS, Envisat and Radarsat (as the wavelength is equivalent to scatterer dimensions within the ice)—but at the expense of diminished surface roughness

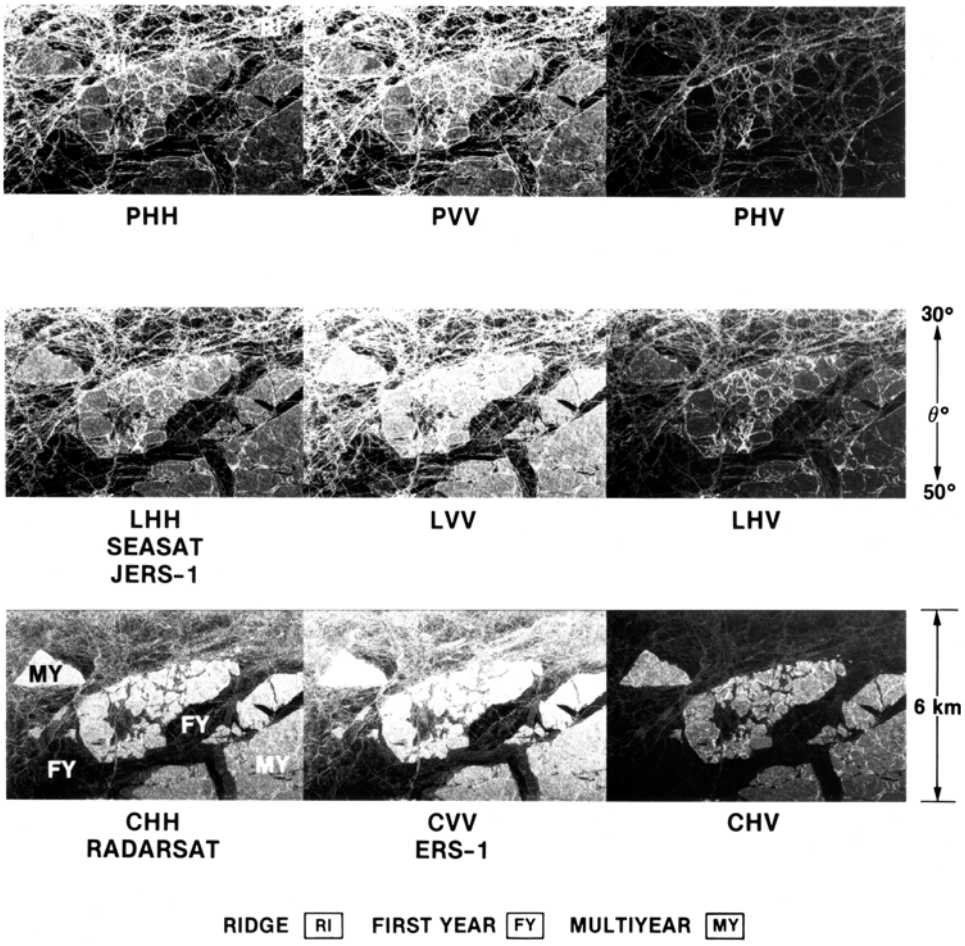

Figure 5.94. Sea ice in the Beaufort Sea imaged simultaneously at P-band ($\lambda = 60$ cm), L-band ($\lambda = 25$ cm), and C-band ($\lambda = 5$ cm) by the NASA JPL AIRSAR (AIRborne SAR) on March 11, 1988. The dominant ice types are first-year (marked FY) and multiyear (MY).
Courtesy of Ben Holt (NASA Jet Propulsion Laboratory).

information. Note that the optimum polarization for ice-type discrimination is now HH or HV. The detection of multiyear ice is best achieved in cross-polarization data, which Flett (2003) and Onstott and Shuchman (2004) attributed to a reduction in the effects of large- and small-scale surface roughness. It is probable that the upcoming TerraSAR-X X-band SAR (frequency 9.65 GHz), to be launched in April 2006, will yield signatures intermediate between those at P- and C-band, and will be useful for ice-type discrimination. Regarding incidence angle, it generally appears that $<35^\circ$ is optimal for discriminating water, first-year ice, and multiyear ice. Recall that the SARs operated at $<35^\circ$ on JERS-1 and 23° on ERS-1 and -2, while those onboard

Radarsat-1 and Envisat-1 are flexible over the range of 15–50° and 14–45°, respectively.

Following Shuchman et al. (2004) and Onstott (1992, 2004) and others, the following general summary relationships are given as guidance for single-frequency and single-polarization systems (polarimetric relationships are given in the next section):

- Ice discrimination is better at C-band than L-band, with X-band producing similar results (to C-band).
- Discrimination drops off at higher frequencies, particularly under melt conditions.
- Superior ice/water discrimination is achieved for C-band systems with HH-polarization compared with VV-polarization at intermediate incidence angles—e.g., 25–35° for Radarsat-1 (Flett, 2003)—in order to minimize ocean clutter (van der Sanden and Ross, 2001).
- While the above is generally the case, clear ice edge detection by HH-polarization SARs can be affected in the near range—i.e., at steep incidence angles—by contamination of a scene by varying sea surface signatures (Flett, 2003).
- For distinguishing between first-year ice and open ocean near the ice edge under calm/light wind conditions, HH-polarization at large incidence angles is preferable. For high winds, on the other hand, VV-polarization is better for distinguishing most sea ice types from open water over a large incidence angle range, apart from multiyear ice at large incidence angles (Nghiem, 2004; Nghiem and Bertoia, 2001).
- In their comparison of C-band ERS (VV-pol) and Radarsat-1 (HH-pol) data, Dokken et al. (2000a) established that VV-polarization is preferred for thin-ice discrimination, while HH-polarization is most useful for ice/open-water discrimination—i.e., ice concentration calculations.
- The optimum incidence angle range for ice-type discrimination is 20–70°, depending on polarization and ice type.
- The wide incidence angle range of ScanSAR data—e.g., 20–49° for the Radarsat-1 ScanSAR Wide mode—results in an across-swath variability in ice signatures (Flett, 2003).

Clearly, further research is necessary to determine optimal viewing and polarization combinations for different conditions (see also Section 5.9.7.3.1). The availability of Alternating Polarization Mode data from the Envisat ASAR provides a unique opportunity to test these issues and explore HH versus VV over a wide range of incidence angles (covered by the seven Envisat sub-swaths), albeit over narrow swaths of <100 km.

Factors complicating unambiguous ice-type discrimination from single-frequency SAR data include:

- Wetness in the snow due to flooding (Drinkwater and Lytle, 1997) and the wicking of brine by the snow (Massom et al., 2001a).

- Multiplicative speckle noise, although this can be minimized by pixel averaging and/or filtering (Curlander and McDonough, 1991; Lee et al., 1994).
- Similarity in the backscatter signatures of multiyear and pancake ice (Drinkwater, 1998a, b).
- Variations in snow/ice temperature and surface salinity result in large dielectric fluctuations (Barber et al., 1992; Nghiem et al., 1998; Shokr and Barber, 1994).
- Even when dry, the snow cover can make a variable and at times significant backscatter contribution as it evolves and metamorphoses (Barber et al., 1998a).
- Ephemeral warm-air incursions across the Antarctic pack in winter (Massom et al., 1997) can have a significant impact on the microwave backscattering characteristics of sea ice via their effect in changing ice and snow cover characteristics (Drinkwater et al., 1995).
- The sensitivity at all times of year of open-water returns—i.e., within leads and polynyas—to wind speed (Fetterer et al., 1994; Steffen and Heinrichs, 1994). Such regions exhibit a wide range of returns, from approximately -20 to -5 dB, which often overlap with signatures from all ice types (Soh et al., 1998). In summer, however, the contrast between openwater under windy conditions (at >-8 dB with a wind speed of $>5\,\mathrm{m\,s^{-1}}$) and ice (<-12 dB) is at its maximum compared with other seasons.
- Extensive coverage of frost flowers on snow-free ice in its early stages of growth can represent a rough surface at shorter wavelengths—e.g., C-band (Nghiem et al., 1997a; Onstott, 1992; Ulander et al., 1995). Frost flowers are strongly backscattering at C-band and higher wavelengths due to both surface roughness and their high salinity (to 150 p.s.u.: Drinkwater and Crocker, 1988), which causes them to be highly reflective to radar energy. This can diminish the backscatter contrast between thin ice and thicker first-year ice, and can even create a backscatter similar to that of multiyear ice in the Arctic (Steffen and Heinrichs, 1994). This effect is diminished at L-band (Drinkwater et al., 1991; Flett, 2003).

Once again, the above relationships are mainly for Arctic sea ice. Similar information is largely lacking from Antarctica, as relatively few studies have been carried out in Antarctica (Drinkwater, 1998a, b; Morris et al., 1998).

Ambiguities in σ^0 combined with overlap of ice-type backscatter distributions largely undermine the use of simple thresholding techniques assigning unique backscatter ranges to different ice classes. This is particularly true for thinner (younger) ice types. In SAR imagery, both tonal and textural information are available for the discrimination of different sea-ice-type classes, and are important in the automated or semi-automated interpretation of digital satellite imagery (Barber et al., 1993; Ulaby et al., 1986b). Automation is desirable for operational applications (Bertoia et al., 1998, 2004; Shuchman and Flett, 2003). Tone is created by point measurements of σ^0, and is predominantly a function of the size interrelationships between the scattering elements within an individual pixel and the radar wavelength (Barber and LeDrew, 1991). Texture is the spatial variation of tonal elements (gray levels) as a function of scale (Chou et al., 1994; Clausi, 2002;

Haralick et al., 1973; Ulaby et al., 1986b). Sea ice classification using SAR tonal statistical distributions has been examined by Smith et al. (1995b), for example. Other workers have performed image texture analysis to exploit the spatially dependent class characteristics present, using either a supervised classification—e.g., Barber and LeDrew (1991), Burns and Lyzenga (1984), Clausi (2002), Shokr (1991), Soh and Tsatsoulis (1999a), and Wackerman et al. (2003)—or unsupervised techniques (Clausi and Yue, 2004; Soh and Tsatsoulis, 1998, 1999b). Knowledge-based classification systems will become increasingly important (Soh et al., 2004). SAR data are well-suited to the application of neural network techniques to extract ice-type information (Silveira et al., 1994). Kern et al. (2003) used the co-occurrence probabilities method of texture analysis (Haralick et al., 1973) combined with a supervised neural network to classify surface types in ERS-2 SAR images in the Greenland Sea in spring. The neural network was trained and tested with five classes manually selected for each SAR orbit used—namely, open water, grease ice, first-year ice, level, and brash ice regions. Kaleschke and Kern (2002) devised a semi-automated scheme for ERS SAR classification using image processing, neural network analysis, and optimal data fusion (with SSM/I data). Aimed at improved classification of the Arctic MIZ, this technique identified open water, first-year, multiyear, new, and brash ice. Other potentially useful methods for improving the automated classification of single-channel SAR data include dynamic thresholding (Haverkamp et al., 1995; Wackerman et al., 1988) and expert systems (Haverkamp et al., 1995; McAvoy and Krakowski, 1989). Universal classification schemes such as those outlined above are possible due to the high level of inter-image calibration with modern SAR data. So far, however, no universally applicable automated classification scheme has been developed. In all cases, difficulties arise with single-frequency/single-polarization systems in the automated classification of new, young, and first-year ice types (Shuchman and Flett, 2003), and for all ice types during the summer melt period.

An automated Arctic ice classification scheme for routine application to ERS SAR data was developed within the NASA GPS at the ASF (Fetterer et al., 1994; Kwok et al., 1992a, b), which is the precursor of the RGPS. This assigns individual image pixels to one of four classes, employing a maximum-likelihood method and a lookup table of the expected mean and standard deviation of ice-type-specific backscatter values. These classes are new ice/open water, smooth first-year ice, rough (deformed) first-year ice, and multiyear ice. The resultant image product comprises pixels with numbers assigned according to the appropriate ice class. The classification is carried out on geo-coded, low-resolution (100 m) images, mapped to the standard SSM/I polar stereographic projection with each scene covering an area of 100×100 km. See Stern et al. (1995) for an application of this product to the determination of open-water production in central Arctic pack ice, and the parameterization of lead activity with a view to improving model representations of ice rheology.

In addition to providing estimates of the thickness distribution of thin ice in the Arctic Ocean (see Section 5.9.6.4), the RGPS also makes a routine estimate of the multiyear ice fraction in the Arctic Ocean from time series of calibrated Radarsat

ScanSAR data, at a resolution of 100 m (Kwok et al., 1995a, 1999a, b). In short, an independent estimate of the multiyear fraction within each 10×10-km grid cell is derived from the backscatter intensity of each SAR sample. The algorithm combines a maximum-likelihood classifier with a lookup table of expected backscatter characteristics to assign an image pixel to one of two classes—namely, multiyear and first-year ice (Kwok et al., 1999a). By definition, the area of multiyear ice fraction within a given cell remains constant through the winter, and anomalous spikes are filtered out. These data are available from November 1996 onwards, and are archived at the ASF and available through NASA's EOS DAAC system (⟨*http://www.asf. alaska.edu*⟩).

A major deficiency in sea ice classification using conventional single-frequency and single-polarization SAR data, and passive-microwave data, is overlap between the backscatter signature of ice-type classes, and poor discrimination between new ice and open water due to the variability in microwave backscatter and emissivity signatures of thin ice (Drinkwater et al., 1992; Kwok et al., 1998a). As we have seen, the early growth phase of ice, and its distribution, is critically important in controlling the intensity of heat, salt, and vapor fluxes at the polar ocean surface. This is a key area where multi-polarization measurements can make a major contribution.

5.9.7.3.2 SAR polarimetry for sea ice classification

Referring back to Section 5.8.2.1, a recent major development, and one that promises to greatly enhance sea ice classification from space, is the emergence of multi-polarization and fully polarimetric (quad-pol) spaceborne SAR systems. In this section, we briefly review the theory behind radar polarimetry, and evaluate recent results. Due to the fact that this is an emerging field, with the first satellite quad-pol system (ALOS PALSAR) being launched in 2006, the results are largely based on analyses using limited laboratory (Kwok et al., 1998a; Nghiem et al., 1997b), *in situ* and airborne data almost exclusively from the Arctic (Drinkwater et al., 2001a; Nghiem et al., 1995b), together with limited spaceborne data from the non-polar-orbiting SIR-C mission (Eriksson et al., 1998). These, however, paint an exciting if somewhat complex picture. It should be noted that polarimetric coverage is generally limited to narrow swaths, and is therefore unsuitable for basinwide applications.

While conventional radar systems have provided measurements of the scattering characteristics of sea ice as a function of frequency, incidence angle θ_i, and fixed polarization, radar polarimetry enables simultaneous observation of radar backscatter from a target surface at a number of different polarizations. As already discussed, a system is said to be fully (or quad) polarized if it simultaneously measures all combinations of linear polarizations—i.e., VV, VH, HH, and HV. Emerging spaceborne systems—e.g., Envisat ASAR, ALOS PALSAR, TerraSAR-X/-L, and Radarsat-2—can not only receive both the transmission polarization and its orthogonal, but also have polarimetric capability, whereby phase differences between different polarizations are also recorded. As a result, the unknown

complex scattered EM vector is sampled in two orthogonal directions, enabling complete characterization of the backscattered field (Boerner et al., 1998; Cloude, 2004; Drinkwater, 1990; Drinkwater et al., 1992; Hajnsek et al., 2003; Touzi et al., 2004; Ulaby and Elachi, 1990). As such, fully polarimetric SAR data contain more information than single-channel data about microwave ice-scattering processes. This provides the potential for much-improved discrimination of different ice types (Kwok et al., 1991; Nghiem and Bertoia, 2001; Rignot and Drinkwater, 1994). In particular, an improved estimation of open water and thin-ice fraction is expected. This is based upon the large difference in the dielectric properties of ice and open water, combined with the polarization sensitivity of σ^0 from a rough surface (Drinkwater et al., 1992). While the current Envisat ASAR has a user-specified alternating polarization capability—i.e., it cannot simultaneously measure all of the polarization combinations—the other SAR missions mentioned above have full polarimetric capability.

A fully polarimetric radar operating at a given frequency measures the complete scattering matrix for each pixel within an image (Ulaby and Elachi, 1990). In this case, the primary means of describing how a target surface scatters EM energy is given by the scattering matrix, from which other forms of polarimetric information can be derived—e.g., polarization signatures and synthesized images. The scattering matrix $\bar{\bar{\boldsymbol{S}}}$ is the basic single-look representation of the polarimetric data, and comprises four elements:

$$\bar{\bar{\boldsymbol{S}}} = \begin{bmatrix} |S_{\mathrm{HH}}| & |S_{\mathrm{HV}}| \\ |S_{\mathrm{VH}}| & |S_{\mathrm{VV}}| \end{bmatrix} \tag{5.67}$$

where $|S_{tr}|$ is a complex number representation of both the phase and amplitude of the radar return transmitted at polarization t and received at polarization r, where V and H are vertical and horizontal polarization, respectively (Drinkwater et al., 1992; Rignot and Drinkwater, 1994). Each element of the complex scattering matrix is a function of both frequency and radar illumination and scattering angles. The measurement of the relative phase as well as amplitude between channels is a key feature of polarimetric SARs.

The power and flexibility of SAR polarimetry as a classification tool emanates from the fact that, if a scattering matrix is known, then the target response to any combination of transmitted (incident) and received polarizations can be determined. This is referred to as polarization synthesis, and by this process images can be constructed to improve discrimination of surface features—e.g., new (thin) sea ice types. While different combinations of scattering mechanisms may yield identical polarization responses, additional polarization information improves our ability to solve for the dielectric properties of the main scatterers of sea ice and also its geometric structure (Drinkwater et al., 1991, 1992). One way that polarization synthesis can be performed is by the conversion of the scattering matrix $\bar{\bar{\boldsymbol{S}}}$ to the Stokes matrix (see below), then post- and pre-multiplying the matrix by the unit Stokes vector which represents the polarizations of interest of the receive and transmit antennae, respectively. An alternative processing step produces SAR data in "cross-product" format. By the latter, the cross-products $\langle S_{tr} S^*_{t'r'} \rangle$ are stored for

each pixel, where t, r, t', and r' denote H and V, * denotes the complex conjugate, and $\langle\cdot\rangle$ indicates ensemble (spatial) averaging over several (i.e., four) contiguous elements (Rignot and Drinkwater, 1994). The latter is known as *multi-look processing*.

Convenient forms for representing the elements of $\bar{\bar{\boldsymbol{S}}}$ in terms of SAR-recorded complex polarimetric backscattering information are the covariance matrix $\bar{\bar{\boldsymbol{C}}}$ and the Stokes matrix $\bar{\bar{\boldsymbol{M}}}$ (Ulaby and Elachi, 1990). Both consist of linear combinations of the cross-products of the four elements in $\bar{\bar{\boldsymbol{S}}}$, and fully describe the scattering properties of the target (Drinkwater and Kwok, 1991; Drinkwater et al., 1992; Kwok et al., 1995b; Zebker and van Zyl, 1990; van Zyl and Zebker, 1990; van Zyl et al., 1990). Following Drinkwater et al. (1992), the covariance matrix $\bar{\bar{\boldsymbol{C}}}$ is given by:

$$\bar{\bar{\boldsymbol{C}}} = \begin{vmatrix} \langle S_{\mathrm{HH}} S_{\mathrm{HH}}^* \rangle & \langle S_{\mathrm{HH}} S_{\mathrm{HV}}^* \rangle & \langle S_{\mathrm{HH}} S_{\mathrm{VV}}^* \rangle \\ \langle S_{\mathrm{HV}} S_{\mathrm{HH}}^* \rangle & \langle S_{\mathrm{HV}} S_{\mathrm{HV}}^* \rangle & \langle S_{\mathrm{HV}} S_{\mathrm{VV}}^* \rangle \\ \langle S_{\mathrm{VV}} S_{\mathrm{HH}}^* \rangle & \langle S_{\mathrm{VV}} S_{\mathrm{HV}}^* \rangle & \langle S_{\mathrm{VV}} S_{\mathrm{VV}}^* \rangle \end{vmatrix} \tag{5.68}$$

The covariance matrix, which fully characterizes the polarimetric scattering properties of a distributed scattering target—e.g., sea ice—is a convenient way of representing averages of polarimetric data, and minimizes the effect of speckle (Askne, 2003). Due to the latter, analysis of SAR data of distributed targets is more properly carried out in terms of area averages rather than by means of single-resolution cells. Note that an alternative to the covariance matrix is the *coherency matrix*.

Although 16 cross-products exist for each pixel, most are of second-order magnitude for most natural targets (Nghiem et al., 1995a, b). In effect, complete characterization of the polarimetric characteristics of polar surfaces can be achieved using the remaining four cross-products or, equivalently, the following five real numbers:

$$\sigma_{\mathrm{HH}} = \langle S_{\mathrm{HH}} S_{\mathrm{HH}}^* \rangle \tag{5.69}$$

$$\sigma_{\mathrm{HV}} = \langle S_{\mathrm{HV}} S_{\mathrm{HV}}^* \rangle \tag{5.70}$$

$$\sigma_{\mathrm{VV}} = \langle S_{\mathrm{VV}} S_{\mathrm{VV}}^* \rangle \tag{5.71}$$

$$\rho_{\mathrm{HHVV}^*} = \left| \frac{\langle S_{\mathrm{HH}} S_{\mathrm{VV}}^* \rangle}{\sqrt{\langle S_{\mathrm{HH}} S_{\mathrm{HH}}^* \rangle \langle S_{\mathrm{VV}} S_{\mathrm{VV}}^* \rangle}} \right| \tag{5.72}$$

$$\phi_{\mathrm{HHVV}^*} = \angle(\langle S_{\mathrm{HH}} S_{\mathrm{VV}}^* \rangle) \tag{5.73}$$

where σ is the radar backscatter intensity normalized by the projected area of the pixel, ρ_{HHVV^*} is the complex correlation coefficient between co-polarized elements of $\bar{\bar{\boldsymbol{C}}}$, and ϕ_{HHVV^*} is the phase difference between channels HH and VV, and $\angle(x)$ denotes the phase of the complex number x (Kwok et al., 1998a; Rignot and Drinkwater, 1994).

Polarimetric SAR data are particularly powerful in that they can be used to generate a variety of output products. These include multi-polarization intensity images, whereby images acquired with various combinations of transmit and

receive polarizations can be singly displayed or combined as ratios or false color composites to highlight subtle detail not apparent in conventional single-channel SAR data. Moreover, the complex polarimetric SAR data can be used, by polarization signatures, to create polarimetric (polarization) signatures and parameters for use in interpreting and understanding scattering mechanisms for selected classes of targets. The polarization signature of a target is a three-dimensional (geometric) graphical method of representing the response of a target (i.e., the backscattered power received) as a function of both incident and back-scattered polarizations in terms of their orientation and ellipticity. Polarization signatures generated from the scattering matrix are a useful tool enabling interpretation of the scattering properties of the target sea ice type, which in turn leads to improved understanding of the scattering mechanisms, roughness, and polarization dependence for that particular ice type.

In addition, a number of polarimetric discriminants are generally derived by polarimetric decomposition techniques to characterize the polarimetric signature of different sea ice types for sea ice classification purposes. Target decomposition enables improved physical interpretation of the target with respect to scattering mechanisms (Cloude and Pottier, 1997). The term "polarimetric discriminant" refers here to combinations of elements of the covariance matrix $\bar{\bar{C}}$ and describes the polarimetric response (see Drinkwater et al., 1992 for a more in-depth treatment). Note that, although they can be computed for each sample in a polarimetric SAR image, they are more often averaged over groups of samples to reduce noise effects. Polarimetric discriminants that have been used to classify sea ice include:

- The *total power (span)* of the scattered field—i.e., the total power received by the four channels of a fully polarimetric radar—where:

$$Span = \langle S_{HH}S_{HH}^{*}\rangle + \langle S_{VH}S_{VH}^{*}\rangle + \langle S_{HV}S_{HV}^{*}\rangle + \langle S_{VV}S_{VV}^{*}\rangle \tag{5.74}$$

  (Israelsson and Askne, 1991). This reduces signal variance, and improves feature delineation.
- The *co- (like-) polarization power ratio* $\gamma_{HH/VV}$, or the ratio between co-polarized elements of $\bar{\bar{C}}$, where:

$$\gamma_{HH/VV} = \frac{\langle S_{HH}S_{HH}^{*}\rangle}{\langle S_{VV}S_{VV}^{*}\rangle} \tag{5.75}$$

  The co-polarization ratio is useful for separating open water from a range of thin-ice types (Scheuchl et al., 2001), and for separating Arctic multiyear ice from rough thin ice and open water (Thomsen et al., 1998a, b). For snow-free new or young ice, $\gamma_{VV/HH}$ increases with incidence angle θ_i at a rate that depends on the complex dielectric constant of the ice; this relationship holds for P- and L-bands, but only for very smooth surfaces at C-band (Winebrenner, 1990). Its value is largely determined by the ice dielectric constant, and will be greatest for open water and/or new (thin) ice, while first-year and multiyear ice have values of $\sim$1 (Askne, 2003; Onstott and Shuchman, 2004). The use of ratios here and

below quantifies the difference in power between polarizations and characterizes the full polarization signature (Drinkwater et al., 1992).

- The *cross-polarization (cross-pol) ratio* $\gamma_{\mathrm{HV/VV}}$, where:

$$\gamma_{\mathrm{HV/VV}} = \frac{\langle S_{\mathrm{HV}} S_{\mathrm{HV}}^{*} \rangle}{\langle S_{\mathrm{HH}} S_{\mathrm{HH}}^{*} \rangle} \tag{5.76}$$

This provides a relative measure of volume scattering (HV) versus surface scattering (HH), with the different scattering mechanisms providing input for improved ice classification schemes (Drinkwater et al., 1991, 1992). Initial results from the Arctic using data from the Envisat ASAR AP mode suggest that the availability of cross-pol data will improve the discrimination of ice and open water under more exteme conditions (De Abreu et al., 2003). The ice edge detection capability is confirmed for C-band data by Scheuchl et al. (2001).

- The *depolarization ratio* γ_{depol}, defined as the ratio of cross-pol to both co-polarized channels, and given as:

$$\gamma_{depol} = \frac{2\langle S_{\mathrm{HV}} S_{\mathrm{HV}}^{*} \rangle}{\langle S_{\mathrm{HH}} S_{\mathrm{HH}}^{*} \rangle + \langle S_{\mathrm{VV}} S_{\mathrm{VV}}^{*} \rangle} \tag{5.77}$$

This gives an estimate of the amount of depolarization caused by the scatterers (Askne, 2003), and aids the discrimination of ice type (age). New ice is characterized by the lowest value, with multiyear ice having a high ratio and first-year ice an intermediate value (Onstott and Shuchman, 2004).

- The *co-pol correlation coefficient*, $\rho_{\mathrm{HHVV}^{*}}$, given in (5.72). The utility of $\rho_{\mathrm{HHVV}^{*}}$ in sea ice research has yet to be determined (Onstott and Shuchman, 2004), although it may prove useful in the discrimination of Arctic first-year and multiyear ice (Drinkwater et al., 1992).

- *Co-polarization phase difference*, specifically between the phase at HH- and VV-polarizations (or co-polarized phase), and retrieved from $\bar{\bar{C}}$ as follows:

$$\phi_{\mathrm{HH\text{-}VV}} = \tan^{-1}\left[\frac{(\mathrm{Im}\langle S_{\mathrm{HH}} S_{\mathrm{VV}}^{*} \rangle)}{(\mathrm{Re}\langle S_{\mathrm{HH}} S_{\mathrm{VV}}^{*} \rangle)}\right] \tag{5.78}$$

where Im and Re denote the imaginary and real parts, respectively. As it characterizes the number of bounces experienced by an EM wave during reflection, the co-polarized phase difference is useful in pixel classification. This discriminant is again useful in separating open water from ice, with the value being determined by the magnitudes of both the ice and water dielectric constants (Drinkwater et al., 1992; Onstott and Shuchman, 2004). In effect, the magnitude of HH–VV-correlation yields the variation of scattering mechanisms, with low values indicating a large mix of different scatterers (Askne, 2003). The smallest difference occurs for multiyear ice, and the largest for new (thin) ice. Work by Thomsen et al. (1998a, b) and Winebrenner et al. (1995), the former at C-band and the latter at L-band (wavelength 24 cm), showed this discriminant to be particularly promising for the classification and proxy thickness estimation of thin-ice types—i.e., $<\sim$0.3 m. Indeed, results from Winebrenner et al. (1995) and

Kwok et al. (1998a) showed a relationship between the co-polarized phase at L-band and the thickness of undeformed ice in the range 0–0.5 m, through a coherent interaction mechanism involving interactions from ice layer interfaces. Working in Antarctica, Winebrenner (1996) observed negative co-polarized phase values for new ice and positive values for adjacent thicker ice (again at L-band). Kwok et al. (1998a) concluded that it is essential to better understand co-polarized signature variation physically in order to infer ice thickness from observations, due to the apparent non-monotonic relationship. Laboratory C-band measurements further showed the value to be largest for bare ice and less for ice covered with low-density frost flowers (Kwok et al., 1998a).

For a more detailed treatment of polarimetric definitions and discriminants, please see Kong (1990) and Ulaby and Elachi (1990), and Drinkwater et al. (1992) for their application to sea ice.

The interpretation of sea ice polarimetric signatures requires detailed knowledge of the relationship between the EM scattering effects of sea ice's structural and physical properties. This provides a means of inferring enhanced information on sea ice properties from polarimetric signatures via their influence on the EM scattering properties of the ice. Nghiem et al. (1995a, c) developed a theoretical model to relate sea ice and snow processes and characteristics to polarimetric signatures, by calculating effective permittivities and backscattering covariance matrices at microwave frequencies. Given the complexity of the data and sea ice, such models are a key step in relating observed polarimetric backscattering signatures to the structural, physical, and EM properties of the ice. Aircraft systems, such as the Danish Centre for Remote Sensing's EMISAR (⟨*http://www.emi.dtu.dk/research/DCRS/Emisar/emisar.html*⟩) and NASA Jet Propulsion Laboratory's (JPL) polarimetric AIRSAR (airborne SAR) system (⟨*http://airsar.jpl.nasa.gov/*⟩), have been used to examine polarimetric scattering signatures of Arctic sea ice at different incidence angles (20–50°) (Dierking et al., 2004; Drinkwater et al., 1992; Nghiem et al., 1995b; Winebrenner et al., 1995). These data have been analyzed to determine the characteristics (i.e., relative and absolute backscatter at different polarizations) of sea ice signatures as a function of ice type. Moreover, aircraft measurements using the Japanese L-band Pi-SAR system have investigated ice thickness relationships in the Sea of Okhotsk (Matsuoka et al., 2001, 2002; Wakabayashi et al., 2001, 2004). Wakabayashi et al. (2004), for example, found a relatively high correlation between sea ice thickness and $\gamma_{HH/VV}$ for high-incidence angles at L-band (Figure 5.88).

Results from a number of sources, both new and dating back two decades, underline the great potential of both alternating and full polarization techniques when applied to sea ice. Although significant challenges remain before the full potential of these exciting techniques is realized, not least in interpretation of the signals over Antarctic sea ice, a number of relationships are becoming apparent that may aid the user in choosing the optimal polarization combination for a given application. Work by Dierking and Askne (1998) and Dierking et al. (2003) in the Greenland, Beaufort, and Baltic Seas showed that, at C- and L-band, the following

polarimetric parameters were identified as having the biggest potential for sea ice classification: γ_{depol}, $\gamma_{HH/VV}$, $\phi_{HH\text{-}VV}$, and the V-backscatter coefficient σ°_{HV}. Scheuchl et al. (2001) further found that σ°_{HV} at C-band is well-suited to ice edge detection (at steep θ_is), and is largely unaffected by wind in open-water regions, while σ°_{HH} data are preferred at shallower θ_is and for Arctic ice-type discrimination. Moreover, it appears that σ°_{HV} provides improved information on ice structure and topography (at least for the Arctic), and has some utility in enhancing the discrimination of smooth and deformed ice (van der Sanden and Ross, 2001). Working in the low-salinity Baltic Sea, Mäkynen and Hallikainen (2004) found VH-polarization at C-band and an incidence angle of 45° to provide reasonable ice-type discrimination accuracy. While backscatter from first-year ice is primarily a function of surface roughness, which has a minimal depolarizing effect, that from Arctic multiyear ice is largely a function of air bubbles within the ice volume, which depolarize the incident radar wave (van der Sanden and Ross, 2001). As a result, improved discrimination of Arctic first-year and multiyear ice is possible using cross-pol data compared with like-pol data (Onstott, 1992), as noted previously. As shown by Flett (2003) and illustrated in Figure 5.95, this approach could be particularly useful as a means of maximizing the discrimination of these two primary ice types in regions of highly deformed ice, where ridging typically leads to confusing bright signatures in like-pol data.

The extraordinary complementary information obtainable using the different polarimetric discriminants is again shown in Figure 5.96 (see color section), from the Greenland Sea. A large lead is prominent, and Dierking et al. (2003) interpreted the dark areas within the lead as frazil/grease ice and the bluish areas as wind-roughened open water. Contrasts are enhanced for certain features but decreased for others in the co-polarization and depolarization images (Figures 5.96b and c). Regions of thin ice (thickness range 20–40 cm) stand out most strongly, as bright patches, in the phase difference image (Figure 5.96d). Thin ice–open water discrimination is possible as the signature of open water ($\phi_{HH\text{-}VV} \approx 0$) differs from that of thin ice ($\phi_{HH\text{-}VV} > 0$) (Dierking et al., 2003).

The following broad conclusions can be drawn. For the Envisat ASAR, the AP mode may be useful in aiding the discrimination of (i) thin smooth ice (or new ice) and seasonal ice, and (ii) MIZ ice types (brash and pancakes) and other ice forms (M. Drinkwater, pers. commun., 2003). Different polarization combinations are suitable for different locations/conditions, although coverage is limited to narrow swaths of <100 km. The co-polarization ratio HH/VV may be more suitable for near-coastal situations in that it shows promise for distinguishing undeformed ice of different ages in polynya growth situations—i.e., it is sensitive to ice age/stage of growth—and provides the best distinction between thin and new ice types and openwater (Drinkwater et al., 1991; Thomsen et al., 1998a, b; van der Sanden and Ross, 2001). The VV/HV-ratio, on the other hand, may be more suited to MIZ applications in that it enables enhanced discrimination of rough deformed ice. Moreover, cross-pol contributions—i.e., for VV/HV- or HH/HV-ratio images—are more dominant for rough ice in the off-nadir than the near-nadir beams—i.e., higher incidence beams are preferred for co-polarization/cross-polarization

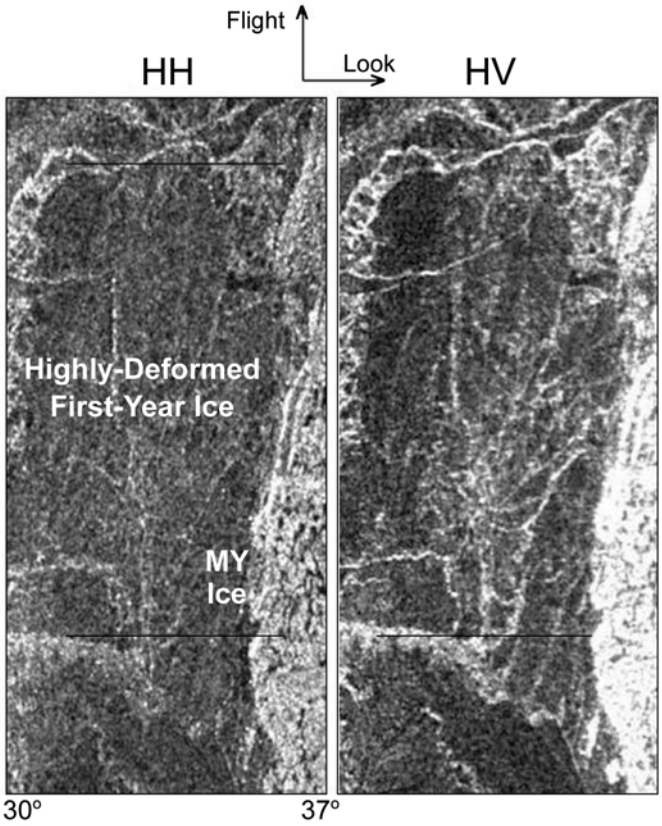

Figure 5.95. An airborne CV-580 SAR (C-band) image of a mix of undeformed and highly deformed (rubble field) first-year ice (the left side of each frame) and multiyear ice (the right side) acquired near Resolute Bay, Canada, on May 3, 1993 at (a) HH-pol and (b) HV-pol. The contrast between the two ice types is significantly clearer in the cross-pol image—i.e., up to 9 dB compared with <3 dB for the like-pol channel data. The spatial resolution of the original data is 6 m (seven looks).
From Flett (2003).

ratios. The HH/VV-ratio has the potential to improve the discrimination of Arctic multiyear from first-year ice, as the depolarized response of multiyear ice is strong whereas that of first-year ice is not (van der Sanden and Ross, 2001). The sea ice applications potential of Radarsat-2 is reviewed by Flett (2003), van der Sanden and Ross (2001), and Scheuchl et al. (2004a). Working with C-band SIR-C data in the Weddell Sea (Antarctica), Eriksson et al. (1998) achieved good thin-ice separation using the co-polarization ratio with one or the other of the like-pol channels—i.e., VV or HH. Thomsen et al. (1998a, b) further concluded that detailed information on scattering mechanism symmetries can be exploited to separate congelation and frazil ice in newly formed leads and openwater (see also Drinkwater et al., 1991).

Considerable effort is going into the development of ice classification algorithms for application to polarimetric SAR. These exploit both SAR phase and magnitude information. To date, sea ice classification of aircraft polarimetric SAR data has been carried out using four different approaches—namely, (i) maximum a posteriori using the covariance matrix (Rignot and Drinkwater, 1992; Rignot et al., 1992); (ii) the unsupervised Wishart classifier (a Bayesian minimum-distance classifier based on the complex probability (Wishart) distribution of the coherency matrix), and based on entropy, anisotropy, and α-angle decompositions (Ferro-Famil et al., 2001; Rodrigues et al., 2003; Scheuchl et al., 2001, 2002a, b, 2003); (iii) hierarchical or knowledge-based (Dierking et al., 2003; Skriver et al., 2003); and (iv) neural networks (Hara et al., 1995; Huynh et al., 1995; Kwok et al., 1995b). Please see these references for algorithm details.

As stated above, one approach to extracting additional information from fully polarimetric data is to perform an eigenvalue decomposition of the coherency matrix (Cloude and Pottier, 1996). By this means, the eigenvectors can be interpreted as scattering mechanisms and the corresponding eigenvalues as their relative strength (Scheuchl et al., 2001). Using this information, the target can be described using three physically based, rotation-invariant parameters—namely, entropy H, anisotropy A, and α-angle (Cloude and Pottier, 1997; Freeman and Durden, 1998; Wakabayashi et al., 2004). The entropy is defined by the eigenvalues and describes the randomness of the scattering. A value of $H = 0$ indicates a single scattering mechanism—i.e., isotropy—while $H = 1$ indicates a completely random mixture of scattering mechanisms with equal probability—i.e., a completely depolarizing target (Scheuchl et al., 2001). The anisotropy A represents the relative powers of the second and third eigenvalues, and is sensitive to surface roughness, while the α-angle represents an average dominant scattering mechanism. The α-angle (mean scattering angle) is derived using eigenvectors and eigenvalues, indicates the "type" of the mean scattering process, and ranges from 0° (surface scattering) to 90° (dihedral scattering) (Cloude et al., 1999). The result of the $H/A/\alpha$ classification is then typically used to initialize a Wishart classifier.

Rodrigues et al. (2003) showed that the contrast between ice and water is fairly pronounced in entropy imagery at L-band and anisotropy at C-band (in the Arctic). The relatively strong contrast in the entropy image at C-band (Scheuchl et al., 2001) is shown in Figure 5.97. Working with aircraft Pi-SAR L-band data in the Sea of Okhotsk (Japan), Wakabayashi et al. (2004) showed that the entropy of open water is consistently the lowest value at all incidence angles, due to the low-depolarization characteristics of openwater. Dierking et al. (2003) favored a hierarchical classification scheme as it enables consideration of existing knowledge (modeled and empirical) about sea ice signature dependencies. Statistical methods can then be used to determine decision boundaries at individual levels in the hierarchy, enabling adaptation to region and season. Based upon their classification of these and images from the other two study regions (which produced an estimated accuracy of up to 90%), and results from other studies, Dierking et al. (2003) came up with a list of radar parameters for both C- and L-band that are optimal for a given classification task (Table 5.6). Dierking et al. (2004) provided further information

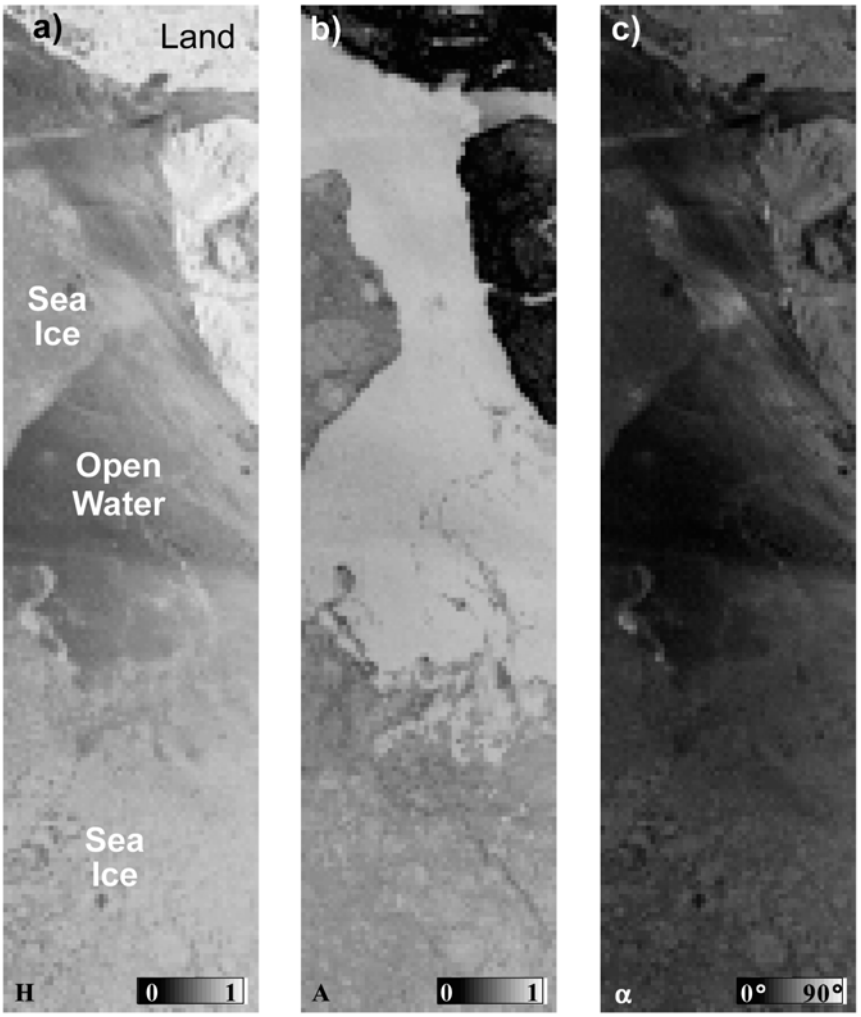

Figure 5.97. Coincident images of (a) entropy H, (b) anisotropy A, and (c) α-angle for first-year sea ice conditions in the Labrador Sea off the coast of Newfoundland (Canada). These images were derived from fully polarimetric C-band SAR data acquired during the Shuttle Imaging Radar-C (SIR-C) mission on April 18, 1994. Incidence angles range from 26° to 31°. In this case, surface melt conditions make the SAR scene difficult for sea ice detection and classification, particularly at steep SAR incidence angles.

From Scheuchl et al. (2001). Reprinted with permission of IEEE. © 2005 IEEE.

on the ability of radar polarimetry to provide improved discrimination (classification) of sea ice, including decision rules for the classification of Beaufort Sea ice at both C- and L-band.

While the prospect of more accurate and detailed sea ice classification is an exciting one, fully automated algorithms for application with polarimetric SAR

Table 5.6. Optimal radar parameters for a given classification task, based on C- and L-band data from a given Arctic region. See also Figure 5.96 and the accompanying discussion above.

Classification task	Band	Parameter	Region
Level FY ice versus level MY ice	C	σ°_{VV} or σ°_{HH}, σ°_{HV}	Beaufort Sea
Level ice (>0.3 m) versus deformed/ridged ice (FY, MY)	C	σ°_{VV} or σ°_{HH}, σ°_{HV}	Beaufort Sea, Baltic Sea
Thin ice (<0.3 m) versus	C	σ°_{VV} and σ°_{HH}, ϕ°_{HH-VV}	Greenland Sea
thicker ice versus open water.	L	σ°_{VV} or σ°_{HH}, ϕ°_{HV}, ϕ°_{HH-VV}	Beaufort Sea

From Dierking et al. (2003). FY = first-year and MY = multiyear.

data have so far proved to be too inaccurate or inconsistent for operational use. A number of factors currently stand in the way of the routine and unambiguous classification of sea ice with polarimetric SAR. These include system calibration difficulties and uncertainties, measurement noise, imprecise understanding of scattering mechanisms as a function of sea ice/snowcover type and state, and the sheer complexity of different scattering mechanisms in any pixel or group of pixels. Accurate calibration is a critical requirement for polarimetric SARs, given that much of the information content is contained in the differences in phase angle and in the ratios of amplitudes between the backscattering in the four combinations of transmit–receive polarization. Adjustments are required to equalize the gains and phases such that they are representative of the true scattering of the target, to compensate for receiver noise, and to reduce the cross-talk. Inaccurate calibration results in misinterpretation of the scattering mechanisms to undermine the advantages of polarimetry. Calibration can be achieved by data analysis combined with radar system design (Drinkwater et al., 1992).

Unfortunately, cross-pol channel data, such as those from the Envisat ASAR and Radarsat-2 SAR, are affected by system noise. In their analysis of ASAR data in the Canadian Arctic, Scheuchl et al. (2004b) observed the dynamic range of the cross-pol backscatter to be only ~8 dB, compared with ~14 dB for the co-polarized data. In effect, the lower limit of the dynamic range of the cross-pol data is restricted by the sensor noise level. The same authors noted variations in HV across the ASAR IS4-mode swath of ASAR data, of 4 dB for openwater and 1.5 dB for first-year ice, which they attributed to variation of the Signal-to-Noise Ratio (SNR). Compared with the noise level, low cross-polarized backscatter from open water and smooth first-year ice affects both automated classification and visual analysis (Scheuchl et al., 2004b). These effects conspire to limit their utility for sea ice applications, including the discrimination of open water and new, thin areas and the distinction of ridging and ice topography (Flett, 2003). Indeed, it appears that proper adjustment of the gain settings of the sensor is required to ensure a good SNR where the observed signals are close to the noise floor.

While current polarimetric classification techniques have all produced promising results when applied to aircraft data, and not least in the improved classification of lead ice, their robustness remains unknown due to a lack of adequate independent

data. A number of conclusions can, however, be drawn from existing studies and the ESA POLInSAR 2003 Workshop (⟨*http://earth.esa.int/polinsar/se_seaice. html*⟩):

- While polarimetry does not greatly improve the classification of thicker ice types (Rignot and Drinkwater, 1994), it shows tremendous promise in the identification of the early stages of new (thin) ice formation and the discrimination of ice and open water in both polar regions (Dierking et al., 2003; Scheuchl et al., 2003; Skriver et al., 2003; Winebrenner, 1996; Winebrenner et al., 1995).
- The role of phase in polarimetric classification is unclear. Further work is essential to test the possible relationships between the phase difference and thin-ice thickness. In particular, challenges remain in the determination of which scattering mechanisms dominate for thin ice and which model is best suited to the retrieval of ice thickness from polarimetric SAR data.
- The optimal frequency for polarimetric classification remains unclear, and varies with application and region. Overall, L-band appears to be more effective for full polarimetric ice classification than C-band (Dierking et al., 2004; Rodrigues et al., 2003), although regional advantages exist in using C-band data and the latter appear to be preferable for the discrimination of first-year and multiyear ice. Rodrigues et al. (2003) separated ice into five major classes at L-band—namely, newly formed ice, first-year ice, multiyear ice, compressed ice, and ridged ice. Kwok et al. (1995b) determined that C-band polarimetric data are more sensitive to ice thickness for thin-ice types than L-band. In each case, automated classification is sensitive to incidence angle (Scheuchl et al., 2003).
- Alternating Polarization (AP) mode measurements—e.g., by the Envisat ASAR—enable improved classification compared with single-channel data. Initial results suggest an effective discriminatory capability between thick and thin ice. The example given in Figure 5.98 (see color section) also suggests that the Envisat ASAR AP mode enables improved discrimination of open water and sea ice under strong wind conditions (Hawkins et al., 2002), where ambiguous classifications typically occur using conventional single-channel SAR data. The exact overall advantages compared with conventional SAR measurement techniques are yet to be fully established, however.
- For operational applications, near-future spaceborne polarimetric operating modes are unlikely to supplant standard ScanSAR imaging due to swath width (coverage) limitations of polarimetric modes of operation and data interpretation complexity, but are likely to provide more precise information where required (Flett, 2003). The Radarsat-2, ALOS PALSAR, and TerraSAR-L and -X systems operate over swaths of ~20–70 km in full polarimetric (quad-pol) mode. As a result, data from different satellites operating in dual-polarization mode but collecting data closely spaced in time may prove to be more useful in the practical sense, especially when this involves a mix of different radar frequencies (Dierking et al., 2004).
- Multi-frequency is superior to single-frequency polarimetry. Scheuchl et al. (2003), for example, reported that a combination of P-, C-, and L-band is

particularly useful (Figure 5.99, see color section). While such multifrequency systems are not due to be launched in space in the near future, it may be possible to combine (collocate) coincident measurements from different satellites—e.g., Radarsat-2 and ALOS— or the planned tandem operation of TerraSAR-X and -L. Improved methods of data integration, fusion, and processing automation are a key factor here.

It is anticipated that more robust results will emerge from analysis of Envisat ASAR data and as fully polarimetric spaceborne systems come online. Clearly, considerable research lies ahead before we better understand polarimetric signatures, and their variation with ice type, to the level where we can fully exploit the full potential of these extraordinary remote-sensing tools. This is particularly true in Antarctica. Issues relating to polarimetric coherence and entropy are discussed by Cloude (2004). A number of polarimetry ''toolkits'' are available that provide sample datasets and functionality for simple analysis. These include Sigma-0, available through NASA's JPL, and ESA's PolSARpro (see below). A similar toolkit, called the ''Polarimetry Work Station'', is available from the Canada Centre for Remote Sensing.

Another recent development has been the melding of SAR polarimetry and interferometry, or Pol-InSAR, as discussed in Chapter 2 of Volume 2 of this book (Cloude and Papathanassiou, 1998; Cloude et al., 2001; Papathanassiou and Cloude, 2001). An excellent short tutorial on both SAR polarimetry and inteferometry is given by Cloude (2004). Again, this field is in the research and development stage at present, due to the current scarcity of suitable data. While considerable attention is being paid to applying Pol-InSAR to studies of tree height and biomass estimation (Cloude, 2004; Treuhaft and Siqueria, 2000), the technique also shows potential as a means of enhancing the discrimination of polar surface types, given that an advantage of this symbiosis is gaining the ability to more accurately separate surface and volume scattering effects and contributions. The exact benefits and optimal polarization combinations are, however, yet to be determined. Clearly, the emergence of suitable data from the Envisat ASAR, Radarsat-2, ALOS PALSAR, and TerraSAR-X/-L will enable development and testing of new algorithms. Improvements are required in our understanding of the interaction of polarized waves with snow and ice in order to exploit the full scientific potential of Pol-InSAR (Cloude, 2004). Complications remain in both polarimetry and Pol-InSAR regarding validation and calibration. Software known as PolSARpro has been developed by ESA as a tutorial in the field of polarimetry and interferometric polarimetric SAR data processing. This is available for free download on the Internet from the ESA Web portal (Earthnet) at ⟨*http://earth.esa.int/polsarpro*⟩.

5.9.7.4 Combined passive–active mapping of Arctic multiyear ice

Belchansky et al. (2004) took advantage of the complementary attributes of both passive- and active-microwave data to generate maps of Arctic multiyear sea ice concentration for January 1988–2001. For this, they applied a neural network analysis to brightness–temperature data from three DMSP SSM/I channels (19H,

19V, and 37V), with learning data being provided with coincident multiyear ice distributions derived from Okean SLR and ERS SAR data. These were chosen because of the relative stability of the radar backscatter signature in winter (Kwok et al., 1996). Improved and consistent separation of the ice classes resulted from simultaneous analysis of the passive- and active-microwave data. The resultant monthly-mean maps of multiyear sea ice concentration, and a map of the 14-year standard deviation, are shown in Figure 5.100 (see color section). These new results suggest that the Arctic multiyear ice area has decreased at a significant linear rate of -54.3×10^3 km^2 yr^{-1} (-1.4% yr^{-1}) over the period 1988–2001. The largest and most persistent decline, of 3.3% yr^{-1}, occurred in the southern Beaufort and Chukchi Seas. Belchansky et al. (2004a) attribute this to a weakening of the Beaufort Gyre in response to anomalies in cyclonic atmospheric circulation over the past decade (Drobot and Maslanik, 2003). Strong overriding associations are noted with changing patterns of atmospheric circulation, including the AO, through their controlling influence on both the thermodynamic and dynamic processes affecting changes in the Arctic perennial pack (Dumas et al., 2003; Zhang et al., 2000).

Belchansky et al. (2004a) also compared their neural network estimates of multiyear ice area with those derived with other passive-microwave algorithms—namely, the NASA Team multiyear algorithm and the NASA Bootstrap and Team algorithms. The results are shown in Figure 5.101. While all of the methods depicted similar long-term trends and interannual fluctuations—e.g., a major increase in 1997 associated with a short-term phase reversal in atmospheric circulation patterns (Dickson et al., 2000)—substantial differences are noted in the magnitudes. Belchansky et al. (2004a) attribute these differences to a number of factors, including the effects of ice export (Kwok and Rothrock, 1999; Vinje et al., 1998) and incorrect autumn assimilation of new ice (Comiso, 2002a), in addition to ice convergence, attenuation of brightness temperature, and/or methodological bias. Good robustness of the neural network approach is suggested by comparison of the results with coincident RGPS-derived maps of multiyear distribution, showing reasonable spatial coherence. The principal advantages of the neural network approach compared with the other passive-microwave techniques outlined in Section 5.9.7.1 are that: (a) it exploits the relative stability of active-microwave signatures, (b) it accommodates nonlinear relationships between the input and output variables (Kwok et al., 1996), (c) it can be adapted for application to other winter months to enable investigation of intra-seasonal dynamics, and (d) it is inherently calibrated to seasonal and regional variability by the use of representative learning data (Belchansky et al., 2004a). The comparative strengths and weaknesses of the different approaches are evaluated in detail by Belchansky et al. (2004a).

5.9.7.5 Radar scatterometer techniques

Another excellent source of information on sea ice type, and on a global scale comparable with that of passive-microwave data, is the satellite radar scatterometer dataset (Early and Long, 1997a, b; Grenfell et al., 1993; Hyyppä and Hallikainen, 1999; Lecomte et al., 1993; Long and Drinkwater, 1999; Long et al., 2001; Tonboe,

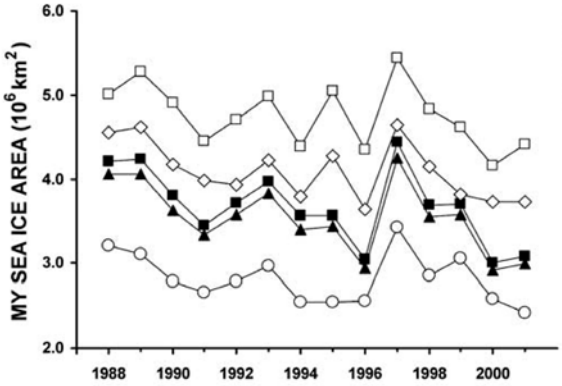

Figure 5.101. Estimates of annual mean Arctic multiyear sea ice area and linear trends (1988–2001) obtained by five different methods of SSM/I passive-microwave analysis. Previous-year total ice area minima are derived from the NASA Bootstrap and Team algorithms, and current-year January multiyear ice area estimates from the Okean-ERS neural network (NN), Okean neural network, and the NASA Team multiyear algorithm.

From Belchansky et al. (2004a). Copyright 2004 American Geophysical Union. Reproduced by permission of American Geophysical Union.

2001). Work by Drinkwater (1998a), Drinkwater et al. (1994), Gohin (1995), and Gohin and Cavanié (1994) demonstrated that the normalized backscatter from sea ice at 40° incidence (σ°_{40}) is sensitive to its physical, large-scale deformation, and surface roughness characteristics. Drinkwater (1998b) found that four main categories could be distinguished in Antarctica in ERS-1 ESCAT (C-band, VV-pol) data— namely, multiyear ice, deformed or rough first-year ice, smooth first-year ice, and nilas. Note that Antarctic multiyear ice classification is difficult using the previously mentioned techniques. Recalling Section 5.7.3, the factors affecting these signatures are surface roughness, ice salinity (dielectric properties), snowcover characteristics, and the distribution of inhomogeneities within the ice volume such as brine pockets and gas bubbles (Hosseinmostafa et al., 1995; Tucker et al., 1992; Yueh et al., 1997). All else being equal, the following relationships hold for Antarctic ice in winter (in the Weddell Sea in ESCAT data), where A and B refer to scatterometer data products described in Section 5.8.2.2—i.e., A is σ°_{40} and B is the slope of σ° versus incidence angle θ_i (Drinkwater, 1998b; Long and Drinkwater, 1999):

- Nilas (smooth ice, thickness <0.1 m)—very low A-values (range ~ -32.0 to -20 dB) and B-values (<0.25).
- Smooth first-year ice (thickness >0.5 m)—the relatively high salinity and absorptive loss result in medium to low A-values (~ -20.0 to -14.0 ± 1.5 dB)

and low B-values ($\sim$0.24). In their Arctic analysis of NSCAT Ku-band data, Yueh and Kwok (1998) observed typical values of <-14 dB.

- Rough first-year ice (heavily ridged)—high salinity and loss cause surface roughness to be the dominant scattering mechanism, leading to medium to high A-values (~-14.0 to -11.0 ±2.0 dB) and low B-values ($\sim$0.195).
- Multiyear ice—due to the relatively low salinity/absorptive loss and deformed surface, volume scattering as well as rough surface scattering contribute, resulting in high values for both A (~-11.0 to -6.0 ±3.0 dB) and B (~-0.15). Note that pancake ice gives a similar return (Drinkwater, 1998b). Yueh and Kwok (1998) found that the scattering contribution from multiyear ice volume, hummocky ice surfaces and ridges, and snow grains within a pixel of σ°_{40} data remained uniform (above -12 dB) under freezing conditions (in NSCAT data).
- Icebergs present a strong target, with mean values from ~-6.0 to 0.0 ±2.0 dB.

The values for Antarctic first-year and multiyear ice shown above are 2–3 dB higher than those in the Arctic, due to a thicker snow layer in Antarctica, rougher ice, and a contribution from flooding (Onstott, 2004).

Note again that enhanced-resolution data are available from the NASA Scatterometer Climate Record Pathfinder (SCP) at ⟨*http://www.scp.byu.edu/*⟩. Gohin and Maroni (1998) showed that for ERS C-band scatterometer data, σ° generally attains its maximum values in the MIZ, where the ice is highly fragmented and ridging and rafting predominates (Gohin and Maroni, 1998). However, high values are also characteristic of Arctic multiyear ice. As a result, they concluded that the unambiguous discrimination of ice types also requires use of the derivative of the backscatter as a function of incidence angle θ_i. The CERSAT ERS C-band sea ice dataset consists of backscatter at large and small incidence angles, plus the derivative of backscatter as a function of incidence angle. The key characteristics can be summarized as follows (Gohin and Maroni, 1998):

- the derivative at incidence angle 28° is used to distinguish open ocean from ice and/or marginal ice from multiyear ice (particularly in the Arctic);
- the backscatter coefficient at 50° is strongly sensitive to surface characteristics, and is particularly useful for distinguishing consolidated first-year ice from MIZ ice in Antarctica; and
- data at 40° are most suitable for distinguishing ice types within regions of consolidated pack, but less so in the MIZ, where the backscatter coefficients of openwater and sea ice overlap. These data are mainly used in the Arctic.

For further information on CERSAT ERS data, which are mapped to the standard NSIDC SSM/I grid for direct comparison with passive-microwave sea ice data, see Gohin and Maroni (1998).

Regarding NSCAT Ku-band data, each ice type exhibits characteristic scattering signatures (Remund and Long, 2003; Remund et al., 2000). Remund et al. (1998a, b) developed a four-dimensional feature classification scheme based on a k-means clustering approach to maximum-likelihood classification, for application with

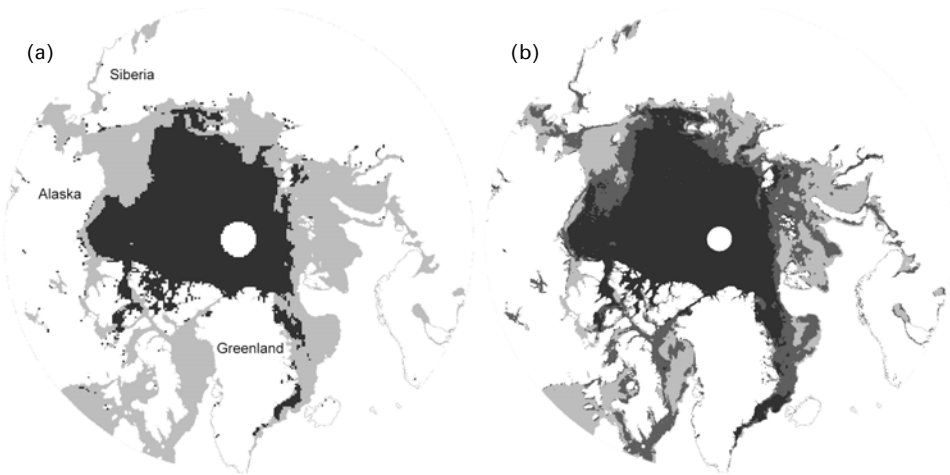

Figure 5.102. Classified Arctic images of (a) SSM/I ice concentration derived using the NASA Team algorithm where multiyear ice is set at concentrations $\geq$36%, and (b) NSCAT SIRF data using the *k*-means classifier. In (a) multiyear ice is black, and other ice medium gray. In (b) multiyear is also black, rough first-year medium gray, and smooth first-year light gray.
From Long and Drinkwater (1999). Reprinted with permission of IEEE. © 2005 IEEE.

enhanced-resolution (SIRF) *A*- and *B*-images from NSCAT. Preliminary results are shown in Figure 5.102, and demonstrate the applicability of NSCAT Ku-band data to large-scale classification. While no surface data are available to validate the Rough First Year (RFY), Smooth First Year (SFY) and nilas classes, the multiyear distributions in the NSCAT image (Figure 5.102b) are comparable with the NSIDC SSM/I-derived multiyear ice concentration images (thresholded at 36%) shown in Figure 5.102a.

Kwok (2004) demonstrates that a simple backscatter-based classification of QuikSCAT SeaWinds Ku-band (13.4 GHz) data can consistently delineate the daily coverage of the Perennial Ice Zone (PIZ), and determine its fraction in the Arctic Ocean in winter. This technique is based on the large backscatter contrast between the seasonal and perennial ice zones in the central Arctic, using a simple backscatter threshold. The effectiveness of this approach depends on the ice types present and the calibration acuracy of the instrument, which in this case is to better than $\pm$0.2 dB, and is season-dependent. It is undermined by significant variability in the backscatter signatures of both the seasonal and perennial sea ice zones from the boreal autumn through November, after which time the signature stabilizes. Kwok (2004) determines the ice regime threshold from QuikSCAT backscatter histograms, which are bimodal, refined using high-resolution Radarsat SAR data processed by the RGPS. From this analysis, Kwok (2004) found that, on average, the PIZ occupies 70% of the Arctic Ocean in October but a much smaller area at the end of May. Close correspondence is observed between coincident QuikSCAT and Radarsat estimates of perennial ice distributions. Through additional analysis of ice motion data derived from passive-microwave data, Kwok (2004) concluded

that this "loss" was mainly due to ice export, and to a lesser extent ice divergence. Considerable interannual variability is noted over the time period 1999 to 2003 (Figure 5.103, see color section). From this and other studies, it is apparent that scatterometers and passive-microwave radiometers yield highly complementary sea ice information.

While great advances are being made with data from individual sources, the future of operational remote sensing in particular lies in the powerful technique of data fusion (and assimilation). Grandell et al. (1999), for example, combined SSM/I with ERS-1 ESCAT data to retrieve sea ice information. In another example, and as part of the operational European Organisation for the Exploitation of Meteorological Satellites (EUMETSAT) Ocean and Sea Ice Satellite Application Facility project (O&SI SAF), Tonboe and Haarpaintner (2003) have further developed a supervised Bayesian classification method (Breivik et al., 2001) to combine AVHRR, SSM/I, and QuikSCAT SeaWinds data and produce a daily Arctic sea ice product (for an overview of sea ice products within the O&SI SAF, see Andersen et al., 2001 and Breivik et al., 2001). Such an approach is possible due to the real or near-real time availability of the data. For example, the QuikSCAT L2B BUFR data product (Leidner et al., 2000) is available from NOAA NESDIS $\sim$3 hours after the satellite overpass (Tonboe and Ezraty, 2002). The Bayesian classification technique requires a priori knowledge of the statistical distribution of the parameters (see Tonboe and Haarpaintner, 2003 for more details). The rationale is to exploit the complementary information derivable from each sensor—i.e., ice/water and ice-type discrimination from the scatterometer; ice concentration, type and ice/water discrimination from the SSM/I; and ice/water discrimination from the AVHRR. The resultant derived parameters are ice type, edge location, and concentration.

The scatterometer data, in this case from QuikSCAT SeaWinds, are particularly useful for ice-type discrimination—i.e., first-year versus multiyear ice (Ezraty and Cavanié, 1999a; Kwok, 2004; Remund and Long, 1999)—and ice edge detection (Haarpaintner et al., 2004). The frequency, polarization, and measurement geometry of SeaWinds combine to yield four main parameters that can be applied to an improved classification of sea ice—namely, (i) vertically polarized backscatter, (ii) horizontally polarized backscatter, (iii) the PR (the ratio of the difference over the sum of the backscatter at HH and VV) (Rignot and Drinkwater, 1994), and (iv) the daily standard deviation of the backscatter. For SeaWinds data, Tonboe and Haarpaintner (2003) found that the backscatter signature of first-year ice (~ -16 dB) is significantly lower than that of multiyear ice ($\sim$9 dB) under freezing conditions, while the mean PR is higher for first-year than multiyear ice—i.e., $\sim$0.23 versus $\sim$0.17. A complicating factor is that both the PR and backscatter are dependent on ice concentration, and it is therefore important to define classes relative to concentration. This results in two ice types (first-year and multiyear) at three ice concentration levels each (closed, medium, and open)—i.e., six discernible ice classes. Tonboe and Haarpaintner (2003) found that ice types cannot be unambiguously separated for concentrations of $<$30%, and in the boreal summer (June–August) due to surface melt. Moreover, high wind speeds (of $>15\,\mathrm{m\,s^{-1}}$) roughen the open-water surface to create an open-water signature that overlaps

with the two ice types. Voss et al. (2003) further combined QuikSCAT and SSM/I data with meteorological data to gain improved estimates of the areal extent of Arctic multiyear ice.

Another example of the potential importance of data fusion to operational sea ice classification is given by Remund et al. (2000). They demonstrated the power of a combined active–passive-microwave approach using 12 channels of overlapping Antarctic scatterometer data—i.e., from NSCAT and ERS-2—together with DMSP SSM/I data from 1996, and reconstructed into enhanced resolution imagery. The 12-dimensional dataset was linearly transformed by principal components analysis to reduce data noise and dimensionality. Subsequent steps involved iterative statistical data segmentation using maximum a posteriori and maximum-likelihood techniques. It appears that the algorithm differentiated Antarctic multiyear ice (PER), SFY, and RFY ice, pancake ice (PNC), icebergs (IB) and MIZ ice (Figure 5.104, see color section). Although these products are in need of validation, an encouraging factor is the temporal consistency. Such work points towards the future combination of MetOp-1 ASCAT data with those from SeaWinds and AMSR-E and/or NPOESS CMIS. These improved datasets should lead to enhanced products.

5.9.7.6 Visible to thermal infrared techniques

The basis of sea-ice-type discrimination using visible to TIR wavelength data is that different ice types exhibit different albedo and surface temperature characteristics, respectively, depending on ice thickness (Maykut, 1986) and snow cover absence/thickness (Allison et al., 1993; Grenfell and Maykut, 1977), which in turn depend on the ice developmental stage (age). While these relationships enable the differentiation of new/young ice from thicker first-year and multiyear ice, age classification is difficult for the thicker ice types, which are indistinguishable by their reflectance properties alone once they accumulate a snow cover thicker than a few centimeters (Brandt et al., 1999). Older ice does tend to be slightly colder in winter, enabling ice age classification using TIR data—e.g., as derived from AVHRR channel-4 ($\lambda = 10.3$–$11.3\,\mu m$) data in the Bering Sea by Massom and Comiso (1994). An example of a cloud-free AVHRR channel-4 image is shown in Figure 5.105. Note that this technique falls down in summer when little thermal contrast exists between ice types (and also between ice and open water). Multi-spectral sensors such as the DMSP OLS and NOAA AVHRR have been the mainstay of ice classification efforts (Fetterer and Hawkins, 1991; Gesell, 1989; Lythe et al., 1999; Massom and Comiso, 1994; Meier et al., 1997; Steffen et al., 1993; Welch et al., 1992; Zibordi and Meloni, 1991). Lindsay and Rothrock (1995) detected thin ice in Arctic leads in winter by its high thermal emission in AVHRR imagery. Zibordi and Van Woert (1993) further demonstrated the feasibility of mapping Antarctic sea ice using AVHRR data. Although severely limited by clouds, such data are of considerable importance as a complement to coarse-resolution microwave data and a means of interpreting the latter. Automated and semi-automated techniques have also been developed, such as the Australian Bureau of Meteorology IceMapper system, which was designed to

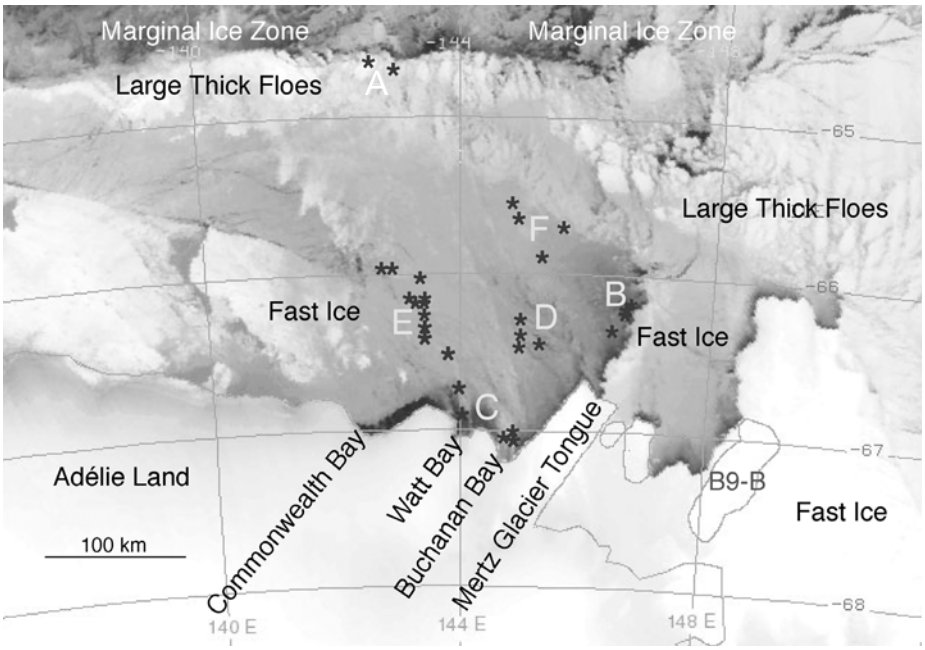

Figure 5.105. An example of a cloud-free NOAA AVHRR thermal infrared (channel 4) image from East Antarctica, showing complex pack and fast ice conditions in the vicinity of the Mertz Glacier Polynya. The image, with a resolution of ~1 km, was acquired at Casey Station on June 14, 1999. Under cold (freezing) conditions, the grayscale relates to the thickness of the sea ice and its snow cover (as marked); in this case, dark is thin (relatively warm) and light is thick (cold). Note the polynya to the west of Mertz Glacier Tongue. This and similar images were used to analyze the ice-type preference of crabeater seals (*Lobodon carcinophagus*), using contemporary sightings obtained during a research cruise of the R/V *Aurora Australis* and marked by stars and in groups marked A–F. Grounded iceberg B9-B is also marked.

From McMahon et al. (2002), after Massom et al. (2001b). Reprinted with permission of Cambridge University Press (CUP). © 2005 CUP.

interpret AVHRR scenes collected at Casey Base for operational and research purposes (Williams et al., 1997, 2002). McIntire and Simpson (2002) devised a scheme to classify Arctic sea ice, cloud, leads and water by applying neural networks to 1.6-μm data from Chinese Fengyun-1C satellite data.

Other studies have exploited cloud-free satellite high-resolution imagery to acquire detailed ice-type information over more limited scenes of ~200 km in diameter. Once again, ice classification is possible as the ice reflectance is related to its thickness for snow-free ice. Working in the Beaufort Sea with Landsat MSS data, Hall (1980) showed that it is possible to infer thickness up to 0.6 m and to an accuracy of ±0.05 m when climatologically derived ice growth rates are used in the calibration. Assuming that snow cover is not present on nilas and gray ice, reflectance values can be selected that correspond to open water, nilas, gray ice, gray–white ice, and thin, medium, and thick first-year ice (Comiso and Steffen, 2001). This

involves the accumulation of training datapoints for each category, which are then used to derive ice-type statistics—i.e., mean and standard deviations. The next step involves applying a maximum-likelihood classifier (Steffen and Schweiger, 1991), in which unclassified datapoints are assigned to the class to which they most likely belong (Comiso and Steffen, 2001). The latter used channel-4 (0.8–1.1 μm) data from the TM and MSS, as differences in the reflectance of open water and thin-ice types are greatest in the red and near-IR regions.

Once again, great benefits are to be gained by combining data from different sources, as illustrated in the discussion on polynyas (Section 5.9.4). Tateyama et al. (2002) combined AVHRR channels 1 (0.58–0.68 μm) and 2 (0.725–1.10 μm) to manually determine the extent of nilas in the Sea of Okhotsk. As many leads remained unresolved in these 1.1-km-resolution data, they also used imagery from the AVNIR onboard the Japanese ADEOS. This instrument had four channels operating between 0.42 and 0.89 μm, at a spatial resolution of 16 m. As such, it had similar capabilities to SPOT sensors. Steffen and Heinrichs (1994) merged Landsat TM data with ERS SAR data to improve the classification of thin-ice types. Such an approach provides only a qualitative measure of thin-ice distribution within given thickness ranges. Uncertainties are again introduced by the presence of unresolved leads, clouds, and atmospheric effects (Key, 1994; Key et al., 1993, 1994a; Stone and Key, 1993).

The recent trend towards the launch of sensors with enhanced spectral and radiometric resolutions is exciting from the perspective of sea ice classification. An example is the MERIS onboard Envisat. With 15 visible and near-IR spectral bands, programmable in position and width, coupled with a dual resolution of 300 m and 1,200 m and a global coverage every 3 days, this sensor has the potential to enhance the detection of regions of thin ice. The same applies to the EOS Terra and Aqua MODIS, with its 36 channels, 0.25-km resolution (at best), and improved onboard calibration. These sensors are providing superb imagery with potential for a more focused appraisal of surface types and conditions (Riggs et al., 1999, 2001).

A similar operational product was retrieved from data from the ADEOS-II GLI (2002–2003), using the CTSK1 algorithm (Stamnes, 1999a). In effect, this algorithm discriminates cloud/clear sky then classifies the clear pixels into six surface classes, including snow over sea ice, bare sea ice, and open ocean. Details of the 13 GLI channels used (covering the spectral range 0.38–12.5 μm) are given in Hori et al. (2001). In this algorithm, radiances in the visible and near-IR channels are converted to reflectances (R) by:

$$R = \frac{\pi I}{(F_0 \cos \theta_0)} \tag{5.79}$$

where I is the calibrated radiance of level-1b data, F_0 is the extra-terrestrial solar irradiance (Thekaekara, 1974), and θ_0 is the solar zenith angle. Cloud detection algorithms are outlined in Hori et al. (2001) and Stamnes (1999a).

Another emerging technology that shows great potential is near-simultaneous optical multi-angle remote sensing—e.g., the EOS Terra MISR. This sensor, which operates at four bands in the visible to near-IR, uniquely views the surface from

multiple angles across a 360-km swath and at a spatial resolution of 270 m. Initial investigations by Nolin et al. (2002) show that the MISR has great potential for distinguishing sea ice types on the basis of sub-pixel surface roughness characteristics, as well as reflectance and spectral properties. Preliminary work on sea ice in Hudson's Bay (Canadian Arctic) provided a whole spectrum of ice surface characteristics, where coincident nadir-viewing MODIS data could resolve only small differences in the variety of young-ice types. Nolin et al. (2002) further show that certain intermediate ice types that are not apparent in the SAR image are discernible in the MISR data (Figure 5.106, see color section). The MISR map in Figure 5.106b uses a statistical classification routine (called "ISODATA"). The five resultant classes of ice type were interpreted by comparison with the SAR image. The MISR measurements are also sensitive to surface roughness, but at a finer spatial scale. While older, rougher ice is largely backward-scattering to the MISR cameras (marked in blue), younger and smoother (less deformed) ice types are predominantly forward-scattering (marked red). Frost flowers represent a largely smooth target to the MISR visible band sensor and are mapped as forward-scattering. The remaining three classes have statistically distinct angular signatures and are intermediate within the forward/backward scattering continuum. Recent work carried out in East Antarctica may lead to improved interpretation of the information content in MISR data (Ted Scambos, NSIDC, pers. commun., 2003). Such data may be particularly powerful as a means of discriminating thin-ice types based on subtle differences in surface roughness when combined with polarimetric SAR data. To use the proverbial time-honored phrase, More Research Is Necessary (MRIN!).

From 2006, ice age (ice type) discrimination products will be operationally retrieved from the NPP/NPOESS VIIRS, using data from five channels centered on 0.64, 0.865, 10.76, 11.45, and 12.01 μm. Plans are for the algorithm to have three components (Appel et al., 2002), involving discrimination of:

- new/young ice from thicker first-year and multiyear ice in daytime by applying a reflectance threshold;
- new/young ice from thicker first-year and multiyear ice at nighttime (and in winter) by applying VIIRS ice surface temperature (*IST*) data (see Section 5.9.11) to an energy balance model (similar to that described in Section 5.9.6.5). Thin-ice thickness will be derived, using ancillary surface T_{air} and humidity, pressure, wind velocity, and snow depth data; and
- multiyear from first-year ice using a filtered distribution of *IST* (at nighttime) or ice reflectance (daytime), with identification of principal class-related peaks in probability densities and segmentation.

In all cases, the *IST* and surface reflectance data will be corrected for ice fraction using ice concentrations derived from the VIIRS. Snow depth is modeled as a function of snowfall history and ice thickness (age).

5.9.8 Snow cover thickness

We have seen how snow plays an immensely important role in modulating the exchange of energy and mass across the polar atmosphere–ice–ocean interaction

system, and also in the ecology of ice-covered oceans. A key determinant of this complex impact is the snow thickness, or snow depth, distribution. Poor current knowledge of this fundamental parameter once again engenders considerable uncertainty in model simulations and predictions, not least in the role of snow cover variability in the ice–albedo feedback mechanism and the insulative effect of snow on the ice thermodynamic growth rate. The overall impact of a projected increase in precipitation at high latitudes is unknown, given the competing effects of snow (Ledley, 1991; Schramm et al., 1997b). Moreover, while sea-ice-basal thermodynamic growth decreases with increasing snow thickness, snow makes a significant contribution to the overall sea ice mass balance in the Antarctic—in particular, through snow/ice formation (Eicken et al., 1994). In addition, snow has a major impact on the amount of PAR entering the ice and upper ocean (Perovich, 1996), and a thick snow cover acts to delay the melt season in certain regions (Eicken et al., 1995b). Together with accumulation rate, snow depth (h_S) is also an important variable in the ocean freshwater budget.

On the large scale, the snow thickness distribution depends on the age of the ice and climatological patterns of precipitation (P) and evaporation/ablation (E), where accumulation $= P - E$ (Budd et al., 1995). On localized scales, it is largely dominated by the horizontal redistribution of uncompacted snow by strong winds both during and after snowfall. This leads to both thinning of the snow cover by wind scouring, and the localized buildup (and erosion) of snow in the vicinity of point ice roughness features such as pressure ridges (Iacozza and Barber, 1999; Massom et al., 1997, 2001a; Sturm et al., 1998, 2002a). This in turn modifies the surface albedo (Brandt et al., 1999) and ice surface roughness (Sturm et al., 1998), with the latter affecting turbulent heat fluxes and the aerodynamic coupling between ice and atmosphere (Andreas, 1995; Steiner, 2001) (see Sections 5.6 and 5.9.9). Compared with changes in ice thickness, small changes in snow cover thickness h_S can have a disproportionately large impact on surface heat flux (Lytle et al., 2000). As such, modeling efforts should ideally include a wind redistribution parameter linked to ice surface roughness in the snow component.

Until recently, our knowledge of snow thickness distribution on sea ice was built entirely upon surface measurement compilations from short-thickness transects on individual ice floes or floe assemblages (Massom et al., 2001a; Sturm et al., 1998, 2002a), Russian ice stations in the Arctic (Warren et al., 1999), and standard hourly ice observations from the bridge of ships (Worby et al., 1998). While useful, all provide data which are too sparsely distributed to adequately resolve spatial and temporal variability in h_S, both of which are critically required by models to more accurately estimate surface energy balance variability and the ocean freshwater budget (Häkkinen, 1995; Marsland and Wolff, 1998), in addition to the contribution of snow/ice formation to overall mass balance (Wu et al., 1999b). Precipitation rate is also notoriously difficult to measure *in situ* in the sea ice zone (due to wind redistribution and ice motion), and rates derived from moisture fluxes in global atmospheric models are also unreliable over sea ice regions, although they are improving (Bromwich et al., 2004; Budd et al., 1995). Another factor affecting snow thickness distribution and ultimately the snow/ice mass budget is the loss of

an unknown proportion of the snow both into leads and by enhanced sublimation given the strong wind redistribution. The former constitutes a freshwater input into the ocean, while the latter entails a water vapor flux to the atmosphere. It follows that the impact of a possible increase in surface wind speed on snow redistribution and sublimation on sea ice is poorly understood. Given these factors, the remote measurement of snow thickness from space is an attractive proposition.

Fortunately, it has recently become possible to map large-scale snow depth h_S from satellite passive-microwave data (Arrigo et al., 1997, 1998a; Markus and Cavalieri, 1998). In fact, snow depth on sea ice is a new standard product from EOS Aqua AMSR-E data, at a spatial resolution of 12.5 km. Example maps are shown in Figure 5.107 (see color section). Importantly from a modeling perspective, it is simultaneously retrieved with coincident ice concentration and ice temperature products (see Sections 5.9.1 and 5.9.12). It is derived for both hemispheres using the algorithm described by Markus and Cavalieri (1998), but excluding the regions of Arctic perennial ice for the reasons outlined below. The technique was originally based upon regression analysis of coincident *in situ* snow depth measurements and SSM/I T_B data. Snow depth h_S (in centimeters) is determined from the spectral gradient ratio (GRV) of (T_B) data from the AMSR-E 18.7- and 36.5-GHz channels (V-pol) (Cavalieri and Comiso, 2000, 2004; Comiso et al., 2003a) as:

$$h_S = a_1 + a_2 GRV(\text{ice}) \tag{5.80}$$

where a_1 ($= -2.34$) and a_2 ($= -771$) are coefficients derived from the linear regression analysis, and GRV(ice) is the gradient ratio corrected for ice concentration C:

$$GRV(\text{ice}) = \frac{[T_B(36.5\text{V}) - T_B(18.7\text{V}) - k_1(1 - C)]}{[T_B(36.5\text{V}) + T_B(18.7\text{V}) - k_2(1 - C)]} \tag{5.81}$$

where $k_1 = [T_{BO}(36.5\text{V}) - T_{BO}(18.7\text{V})]$ and $k_2 = [T_{BO}(36.5\text{V}) + T_{BO}(18.7\text{V})]$ and C is derived from the same dataset by applying the NT2 algorithm (see Section 5.9.1). The open-water brightness temperatures T_{BO} are used as algorithm constraints, and represent mean values from ice-free regions. Vertical polarization channel data are used in preference to horizontal polarization due to their lower sensitivity to layering in the snow cover (Mätzler et al., 1984), a common feature of Antarctic (and Arctic) snow on sea ice (Granberg, 1998; Massom et al., 2001a; Sturm et al., 1998, 2002a). It can be seen from (5.81) that the performance of the snow depth algorithm depends on accurate knowledge of ice concentration. Please refer back to Section 5.9.1 for an assessment of error sources in AMSR ice concentration retrievals.

The new snow thickness algorithm is based on the enhanced scattering efficiency at 36.5 GHz compared with 18.7 GHz (Comiso et al., 2003a) and the assumption of an increase in microwave scattering with increasing snow depth (Chang et al., 1987). Due to the limited penetration depth of the microwave signal at these frequencies, the upper limit or saturation depth for snow depth retrievals is 0.5 m—i.e., snow thicknesses greater than this cannot be detected using the current algorithm. Moreover, snow depth retrievals are not carried out over regions of Arctic multiyear ice, as the microwave signature of the latter strongly resembles that of

snow on first-year ice (Cavalieri and Comiso, 2000; Comiso et al., 2003a). Both multiyear ice and deep snow on first-year ice create increasingly negative GRV-values. As a result, the algorithm is limited to seasonal ice zones and regions where the GRV-value exceeds -0.02, which corresponds to an estimated multi-year fraction of $<20\%$ (Cavalieri and Comiso, 2004). Moreover, the algorithm limits retrievals to overall ice concentrations of 20–100% due to a sensitivity to concentrations of $<20\%$. In effect, this excludes much of the MIZ. A limited comparison of snow depth distributions from ship measurements and from SSM/I snow depth retrievals in the Southern Ocean suggests that SSM/I retrievals underestimate *in situ* measurements by 3.5 cm and that the r.m.s. difference is about 4 cm (Markus and Cavalieri, 1998). This underestimate results from saturation depth limitations.

Sources of error in the retrieval of snow depth on sea ice include inherent errors in sea ice concentration retrieval, uncertainty in the linear relationship between snow depth and the AMSR-E T_Bs, and sensitivity to extreme weather effects. This algorithm can also only be applied under dry snow conditions. As stated earlier, the emissivity of the surface approaches unity under wet snow conditions, irrespective of frequency, and the gradient ratio approaches zero (Comiso et al., 2003a). This leads to a gross underestimate of snow depth. Another source of error occurs as a result of thaw–refreeze cycles, which result in a significant enlargement of snow grain size and a change in snow density (Colbeck, 1982; Massom et al., 2001a). This can occur on either diurnal or synoptic timescales, and causes a decrease in emissivity due to enhanced scattering within the snow (Barber et al., 1998a; Lohanick, 1990; Mätzler, 1998; Onstott et al., 1987). The effect increases with microwave frequency, with the resultant decrease in GRV leading to an underestimate of snow depth. This may be an issue not only during the spring–summer melt season but also at other times. In the Southern Ocean, synoptic warm-air incursions can bring about melt even in winter (Massom et al., 1997, 2003), typically followed by refreezing with a return to cold conditions. Such events can affect much of the sea ice zone, although they are more prevalent in the MIZ (Massom et al., 1997; Oelke, 1997; Sturm et al., 1998). Cyclical changes of this nature lead to large fluctuations in retrieved snow depths. Fortunately, melt–refreeze events can be identified as large variations in the T_B record (Stiles and Ulaby, 1980; Wankiewicz, 1993), and this information is used to flag pixels within which the daily variations in h_S are $>5\,\mathrm{cm\,d^{-1}}$ over a 5-day period. AMSR-E snow depth products are 5-day running averages, in order to minimize inherent uncertainties related to variability in weather, snowgrain size, and snow density (the latter also associated with temperature gradient metamorphism: Colbeck, 1982; Massom et al., 2001a; Sturm et al., 1998). The overall precision goal of the product is 5 cm or better (Cavalieri et al., 2002a; Comiso et al., 2003a, c). These data are available from the NSIDC (Cavalieri and Comiso, 2004; ⟨*http://nsidc.org*⟩).

In spite of these limitations, initial results are promising. Moreover, validation campaigns have taken place in both polar regions (Maslanik et al., 2001; Steffen, 2003; ⟨*http://eospso.gsfc.nasa.gov/validation*⟩), and are expected to result in error determination and fine-tuning of the coefficients in (5.59), and thus improved

algorithm performance and error determination. It is anticipated that future algorithm improvements will include the incorporation of snow grain size information and potentially 6.925-GHz and/or 10.65-GHz channel data, the latter to increase the snow depth retrieval limit beyond 0.5 m (due to the larger penetration depth). This would, however, degrade the spatial resolution. Data from the 89-GHz channel may also prove to be useful for thinner snow covers (Cavalieri et al., 1986; Comiso et al., 1989; Grenfell and Comiso, 1986), although atmospheric effects become more prominent at the higher frequency (St. Germain, 1994). In addition, WindSat provides another alternative source of brightness–temperature data at frequencies which are useful for snow thickness derivation, but with an additional polarimetric capability (see Section 5.8.1). It is again currently unknown whether this capability will lead to enhanced retrievals of h_S.

Looking into the future, measurements using radar data show some promise. Barber et al. (1998a) showed that, for a constant ice thickness, salinity, surface r.m.s., and correlation length, the complex permittivity of the snow/ice interface will be determined by h_S. They proposed that this information could be exploited to estimate snow thickness distributions from time series of radar-scattering data over first-year ice. In addition to the sea ice thickness-sounding radar mentioned in Section 5.9.6, scientists at the University of Kansas have developed a 2–8-GHz FMCW (Frequency Modulated Continuous Wave) radar to test the concept of measuring snow thickness over sea ice. A sledge-mounted prototype system was successfully tested on East Antarctic sea ice in October 2003 (Gogineni et al., 2003). The next step is to develop an airborne system. The launch of such sensors in space is some way off. In the meantime, however, snow thickness radar is playing an important role in the validation of the AMSR h_S product.

5.9.9 Ice/snow surface roughness characteristics

Earlier discussion highlighted surface roughness as a key determinant of backscatter intensity received by radar sensors (see Section 5.7). It also impacts the spectral reflectance and the angular distribution of reflected radiance measured by new-generation optical multi-angular sensors such as the Terra MISR (Nolin et al., 2002). In Section 5.9.7, we saw how small-scale surface roughness information could be inferred from MISR data. In this section, we examine the ways in which quantitative information on larger scale surface roughness features—e.g., pressure ridges—can be retrieved from satellite SAR and altimeter data.

On the basinwide scale, sea ice topography is characterized in coastal shear zones by rubble fields which cover a large proportion of the ice surface area, in the interior pack by pressure ridges of differing geometry and shape, and in the MIZ by the edge (freeboard) of ice floes (Birnbaum and Lüpkes, 2002). Ice surface roughness is closely linked to ice thickness distribution and ice drift, dynamics, and deformation (Weeks et al., 1989). Our incomplete knowledge of ridge geometry and distribution creates significant uncertainty in current mass balance estimates, given that a significant proportion of sea ice volume is contained in ridges (Worby et al., 1998). Improved statistical representations of

ridge size, shape, and spacing are required to account for this factor (Wadhams, 1994), and to enable more accurate estimates of ocean salt flux and ocean–atmosphere heat flux (Maykut, 1986; Mock et al., 1972). Such measurements are also essential to further examine recent submarine sonar observations of a sharp decrease in the number/concentration of deep pressure ridges in the Eurasian Basin of the Arctic Ocean (Wadhams and Davis, 2000), in parallel with the observed decrease in the fraction of multiyear ice. The cause of this decrease is subject to speculation, but may relate to changes in the regional ice dynamics regime, in this case over the period 1976–1996. Improved large-scale measurements are required of the frequency distributions of heights of pressure ridges and floe freeboards as well as ridge spacings and floe size distribution (see Section 5.9.10). Statistics of surface geometry are also required to improve model parameterization of the aerodynamic roughness of the pack—see (5.6)—which is a combination of skin and form drag, and for model validation (Harder and Lemke, 1994; Hibler et al., 1972; Steiner, 2001). This would result in improved model simulations of ice drift patterns and turbulent heat fluxes. Other key roughness impacts are on the mechanical strength of the pack and the bidirectional reflectance of the surface (Warren et al., 1998). Recent work by Tin and Jeffries (2001) suggests that a close relationship exists between Antarctic snow surface roughness and ice thickness/basal roughness, implying that information on the latter may be inferred from accurate surface roughness measurements. Ridges are also biologically important—e.g., as skylights for enhanced shortwave penetration and resting places for polar bears (*Ursus maritimus*). Recalling the previous section, surface roughness is a primary determinant of the snow thickness distribution. Last but not least, ice topography and deformation features pose a significant impediment and hazard to polar navigation (van der Sanden and Ross, 2001).

Once again, our current knowledge is largely based on *in situ* (e.g., by drilling) and airborne/shipborne measurements. While floe drilling provides high-resolution information (Adolphs, 1999; Tin and Jeffries, 2001), such information is spatially and temporally sparse. Other roughness estimates emanate from standard hourly ship observations of ridge height and spacing (Worby et al., 1998), although these tend to be biased by the tendency of ships to avoid deformed ice. The most accurate measurements to date have emanated from airborne laser altimetry surveys. Airborne laser altimetry has been used to measure ice freeboard (Ishizu et al., 1999) and the height and frequency distributions of pressure ridge sails and surface roughness features (Dierking, 1995; Garbrecht et al., 2002; Haas et al., 1999; Lewis et al., 1993; Mai et al., 1996). Another technique has been to use photoclinometric[9] analysis of shadows created by pressure ridges to determine their height and statistics in digital aerial photographs collected under sunny conditions—e.g., in East Antarctica (Lytle et al., 1998a). All of the above produce important data, but these are again sparsely distributed in space and time.

The measurement of sea ice surface elevation/topography from space has proved elusive. To date, SAR data, with their inherent sensitivity to surface roughness, have

[9] Photoclinomety (shape from shading) is an image-processing technique that uses differences in reflected sunlight as an indicator of surface roughness/slope..

been most extensively used for this purpose—e.g., Burns (1988), Johnston and Flett (2001). Where large-scale (meter-scale) surface roughness features occur—e.g., pressure ridges or rubble fields—their orientation is a determinant of radar backscatter intensity (see Section 5.7 for discussion of smaller scale roughness effects on radar backscatter). If the surface facets of ridges are oriented orthogonally towards the radar wave propagation direction, a strong dihedral backscatter results due to the wave reflection off adjacent, relatively smooth ice and into the rough ridge (Johansson and Askne, 1987; Manninen, 1996; Onstott, 1992; Onstott and Shuchman, 2004). The SAR backscatter from ridges exhibits a significant incidence angle and look angle dependence (Leppäranta and Thompson, 1989; Leppäranta et al., 1992). Weaker returns result from a ridge orientation which is parallel to the radar propagation direction, which leads to a limitation in the number of dihedral returns to the blocks comprising the ridge. Moreover, the volume-scattering signal of ridges also tends to be strong (Carlström, 1997; Carlström and Ulander, 1995), due to enhanced porosity and lower salinity thanks to gravity brine drainage (Onstott, 1992; Tucker et al., 1992). As such, ridges can be readily detected in SAR imagery as very bright targets—see Figure 5.94 (Haas et al., 1999). It should be noted that the roughness being measured is that of the ice, as dry snow under freezing conditions is largely transparent to microwaves at frequencies $\leq$C-band (Barber et al., 1998a). However, the snow becomes opaque when wet—i.e., during Arctic summer melt.

Haas et al. (1999) estimated spatial ridge frequencies from ERS C-band SAR backscatter signals (at 100-m resolution to reduce image speckle) of Antarctic sea ice in summer, using a neural network trained with coincident helicopter laser-profiling data. Pressure ridge frequencies ranged from 3 to 30 per kilometer. The results were promising, suggesting that more work is necessary to extend this method. Burns (1990) explored the use of L-band JERS-1 SAR data ($\lambda = 23.5$ cm, $\theta_i = 35^\circ$) to distinguish sea ice regions with different atmosphere drag characteristics. She used roughness statistics derived from several regions in a backscatter model to predict the radar return from surfaces with measured drag coefficients. Daida et al. (1996) developed a technique to extract low-contrast pressure ridge and rubble patterns from low-resolution ERS C-band SAR images of Arctic sea ice.

According to Askne and Johansson (1988) and Holt et al. (1990), sea ice ridges stand out most clearly at lower frequencies—i.e., C-band rather than X-band. Examination of Figure 5.94 shows that even longer wavelength (e.g., L-band) data are preferable for this application. While less effective at ice-type classification than C-band, L-band provides greater penetration into both first-year and multiyear ice, and provides enhanced information on large-scale fractures and deformation structures (even under melt conditions). It is often the case, however, that pressure ridges are difficult to distinguish from other bright features using automated image analysis techniques. This can be a particular problem outside the consolidated and relatively uniform central pack. Zhou and Li (2000a) developed a combined unsupervised/supervised classification technique to distinguish pressure ridges from surrounding first-year ice in the Ross Sea, Antarctica, based upon radar backscatter values in ERS-2 images with a pixel size of 100×100 m. The similarity between the

signatures of brash ice and pressure ridges at C-band necessitated the application of an object delineation method to depict ice floes as objects. This enabled the identification of high-backscattering features within floes as ice ridge pixels. Ridge concentration was then derived from SAR images and the statistics of coincident *in situ* ridge measurements. This supervised component is necessary due to the fact that, even if a bright pixel containing a ridge can be identified, the actual proportion occupied by the ridge is unknown (Vesecky et al., 1990). Results from the SAR-based analysis were similar to the lower end of the field-derived ridge statistics, suggesting that this is a promising method but in need of further development. Other work has investigated the retrieval of large-scale surface roughness information from scatterometer data using a Bayesian classification model (Similä et al., 2001).

As discussed earlier in Section 5.9.6, a product of RGPS gridded ice deformation and thickness measurement procedures is an estimate of the proportion of ridging of thin ice that has occurred since the annual initiation of the scheme on the first day of freezing (Holt and Kwok, 2003; Kwok et al., 1999a, b). This is not derived from a direct measure of surface roughness, but rather by monitoring the evolution of the ridging of thin ice due to convergence. This estimate is routinely made for each 10×10-km grid cell over a large proportion of the central Arctic Ocean, using time series of Radarsat ScanSAR data (Drinkwater et al., 2001a). An example map is given in Figure 5.87. Once again, these data are available from November 1996 onwards for the Arctic Ocean (Kwok et al., 1996). It is again anticipated that improved surface roughness information will emanate from satellite polarimetric data (see Section 5.9.7.3).

Once again, the advent of satellite polarimetric SAR shows considerable potential (Mäkynen and Hallikainen, 1998; van der Sanden and Ross, 2001). For example, cross-polarization channel data yield enhanced structural information and discrimination between smooth and deformed ice (Flett, 2003). This is primarily a function of the combined effects of multiple-reflection surface scattering and volume scattering in the ridges and their impact in enhancing cross-pol radar returns (Livingstone, 1994). Askne and Johansson (1988) also found that ridges should show up most clearly in cross-polarized data due to their anisotropic properties. This is not always the case, however, as shown in the example given in Figure 5.94. Clearly, further research is required to gain maximum benefit from polarimetric data applied to ice roughness studies.

A sensor that shows great promise in the measurement of surface roughness is the IceSat GLAS, described in Section 5.8. The main standard sea ice products from GLAS, and determined from the range data and waveform shapes, include surface roughness, elevation, and reflectivity (Zwally et al., 2002b). Note again that this roughness relates to the actual surface (or at least the skin surface)—i.e., the snow surface for snow-covered ice—given the negligible penetration depth of the optical beam. Kwok et al. (2004b) provided a first demonstration of the unique utility of ICESat-derived ice floe elevation for not only the estimation of sea ice thickness (see Section 5.9.6) but also the characterization of the roughness of the entire Arctic sea ice cover (to a maximum latitude of 86°). This was again achieved by analysis of the variability of successive elevation estimates along the altimeter track, and

at length scales at and above the spatial dimension of the laser footprint—i.e., ~70 m—separated by an along-track interval of 172 m. The retrieval precision was estimated to be ~2 cm over smooth ice. The authors concluded that smaller scale roughness estimates should be obtainable by broadening laser return waveforms as pulse saturation problems are resolved. Limitations include inability to penetrate cloud and coverage limited to narrow linear profiles.

The spatial distribution of GLAS-derived surface roughness for the Arctic Basin, over two 8-day periods, is shown in Figure 5.108a (see color section). The approximate range is from several centimeters (corresponding to the noise level of the retrieval process) to ~30 cm. An encouraging factor is that the spatial characteristics remained largely unchanged—i.e., consistent—between the two periods. As expected, the ice cover is roughest to the north of Greenland and Ellesmere Island (typically ~30 cm) and smoothest in the seasonal sea ice zone (~10 cm), with intermediate values over much of the central Arctic with multiyear ice cover. The spatial characteristics of the GLAS-derived roughness field are further examined by comparison with coincident Ku-band radar scatterometer data from QuikSCAT, shown in Figure 5.108b. The perennial and seasonal ice zones can be clearly delineated in the scatterometer maps, based upon differences in their backscatter characteristics—i.e., high backscatter from multiyear ice and lower backscatter from first-year ice (Kwok et al., 1999a). Another encouraging facet of this exciting new research is the strong correspondence between the changes in both laser-derived surface roughness and radar backscatter in the transition between these two distinct sea ice zones. This suggests that the new GLAS-derived surface roughness field could be potentially useful for better describing the spatially varying air/ice and ice/ocean drag coefficients used to calculate air–ice–ocean momentum exchanges. The level-2 sea ice altimetry product (GLA13), which is available from the NSIDC (⟨*http://nsidc.org/data/docs/daac/glas_ altimetry/gla13_records.html*⟩), contains the sea ice roughness (and freeboard) data calculated from algorithms fine-tuned for sea ice returns. It also includes the laser footprint reflectance, geolocation, and the instrument, atmospheric, and geodetic corrections used to correct range measurements. Parameters are at the full resolution of 40 samples per second, but only for locations within the ICESat sea ice mask. Large-scale measurement of sea ice elevation will, if accurate, also enable improved knowledge of the geoid in polar regions (Zwally et al., 2002b). The preliminary results presented in Section 5.9.6.3 further suggest that the combination of near-coincident ICESat and Radarsat data is potentially useful for understanding ridge statistics at the local scale. This is of major interest, given the challenge of deriving accurate large-scale ridge statistics from other satellite data.

5.9.10 Floe size distribution

Floe size distribution is another poorly quantified parameter, yet one that is again fundamentally important on a number of levels. With ice concentration and thickness, it has a direct impact on the vertical exchange of energy and momentum. Moreover, it affects ice melt in summer, with assemblages of small floes melting faster by the lateral melt of floe margins than large floes in an

equivalent ice/water concentration by virtue of their larger ratio of perimeter to upper-surface area (Holt and Martin, 2001; Holt and Rio, 1998; Maykut and Perovich, 1987; Steele, 1992). As such, the seasonal and regional description of floe size distribution is required to create a more complete picture of the upper-ocean heat budget in summer (Soh et al., 1998). Referring back to Section 5.9.6, a better understanding of the relationship between floe size distribution and floe thickness is needed to interpret ice thickness retrievals from satellite altimeter data. It is a determinant of ice mechanical strength, affecting the resistance of the pack to deformation, and ideally needs factoring into model ice rheologies. From an operational perspective, floe size affects polar ship navigation. It also has an impact on PAR levels in the upper ocean (Eicken, 1992) and the distribution of polar marine birds and mammals (Ferguson et al., 2000; McMahon et al., 2002; Mizuno et al., 2002).

Floes are formed by the fracturing of ice in the MIZ and adjacent to polynyas and large leads by waves and swell, and throughout the pack by thermal cracking, differential ice motion due to variable winds and ocean currents, and isostatic imbalances (Rothrock and Thorndike, 1984). The distribution of floe size is determined both by the characteristics of the external forcing and the strength and thickness of the ice. Floe size distribution combines with ice thickness to modify the wave/swell energy, which in turn modifies the ice (Fox and Haskell, 2001; Wadhams et al., 1988). Other processes affecting floe geometry include floe–floe collisions, and melting around floe perimeters. In the interior pack in winter, these processes tend to balance out, leading to the welding together of floes by freezing under relatively calm atmospheric conditions. Moreover, floe size is determined in certain regions, and most notably the MIZ, by not only destructive processes, whereby large floes are broken down into smaller floes, but also by constructive processes, an example being the growth of newly forming icefloes in the pancake cycle in response to interaction with waves and swell (Lange et al., 1989).

Theoretical considerations involving floe size and shape, the spatial arrangement of floes, and the abundance of floe size classes, are laid out in Rothrock and Thorndike (1984). Following these authors, floe size can be defined in a number of ways, including floe perimeter, its area, the diameter of the largest inscribed circle, or the mean of all diameters across the floe (termed the "mean caliper diameter"). Two approaches are generally used to analyze floe size distributions from floe size information derived from digital images—namely, (i) fractional area distribution and (ii) cumulative number density distribution (Burns et al., 1992; Lindsay and Rothrock, 1995; Paget et al., 2001; Rothrock and Thorndike, 1984). The first expresses the number of floes within a size range as a fraction of the total floe number within an image, while the number density distribution describes the area of all floes within a given size range as a fraction of the image area. Rothrock and Thorndike (1984) concluded that the cumulative number distribution $N(d)$, where d is the mean caliper diameter and N is the number of floes per unit area with diameters $> d$, is the most useful statistical descriptor of floe size.

Our current knowledge is again limited to a number of sparsely distributed measurements, largely based on standard observations from ship and more precise

analyses using airborne sensors. For example, Weeks et al. (1980) carried out an X-band SLR study of floe size/geometry (and roughness) in the Beaufort and Chukchi Seas. Paget et al. (2001) determined the floe size distribution of East Antarctic sea ice using digital aerial photographs, while Muramoto et al. (1993) made measurements using a shipborne video system. In general, the feedback nature of wave–ice interaction in the MIZ is reflected in the increase in mean floe size with increasing distance from ice edge—i.e., the open ocean (Fox and Haskell, 2001). Lytle et al. (1998b) examined this relationship in an analysis of digital aerial photography in East Antarctica, and showed how the gradation in floe size with distance from the ice edge affected the backscatter measured by ERS SAR. By this means, they were able to qualitatively segment the pack into zones of distinctive backscatter based on floe size. Although these data are useful, data quantifying the regional variability in floe size distribution and its evolution through the annual sea ice cycle are lacking.

The retrieval of floe size information from high-resolution satellite data represents an interesting and challenging image-processing problem. Primarily, the accurate determination of floe size depends upon the successful detection of individual floes in an image. This can be a difficult proposition, particularly for high-concentration ice covers where floes are closely packed and individual floe boundaries cannot always be unambiguously detected and delineated, as is often the case. Another potential error source results from the misinterpretation of ridge shadows as floe boundaries and, in places, the difficulty of estimating floe size for high-freeboard floes due to shadow effects. Techniques have been tested on a number of satellite datasets. Vinje (1977) used Landsat data to measure the size distribution of large floes ($>10 \times 10$ km) drifting through Fram Strait. Landsat data were also used by Banfield and Raftery (1992), while Burns et al. (1992) used AVHRR data (limited to a spatial resolution of $\sim$1 km at best). Most recent studies have used SAR data—e.g., Holt and Martin, 2001; Holt and Rio, 1998; Korsnes, 1993a, b; and Soh et al., 1998. The high spatial resolution required for floe size analysis rules out many satellite data sources. Even within SAR, subpixel-scale floes remain unresolved and unrepresented in distributions, leading to a bias towards larger size classes.

Some floe size algorithms are interactive, while others are automated or semi-automated (see Soh et al., 1998 for a review). One approach, using a local dynamic thresholding technique, has been applied to SAR data by Haverkamp et al. (1995) and Soh et al. (1998). The latter applied the "restricted growing concept" technique to Arctic summertime ERS C-band SAR data, using data sampled down to a pixel size of 100 m from the fine-resolution (25 m) original data in order to minimize image speckle interference effects. This technique establishes "separateness" among objects while preserving their original shapes and sizes. It consists of six stages—namely, (i) image enhancement, (ii) image segmentation (Haverkamp et al., 1995), (iii) floe extraction, (iv) filtering of floe shape (to remove insufficiently compact/irregularly shaped floes), (v) separation of open-water areas from the remainder of the ice cover not identified as floes, and (vi) computation of floe size distribution and coverage statistics. Results from the Beaufort and Chukchi Seas show that floe size distribution results are strongly dependent on environmental conditions in

summer. Although the backscatter signature of Arctic sea ice can fluctuate in an unstable manner in summer, as discussed in Section 5.7, Soh et al. (1998) showed that accurate segmentation is possible when the ice appears dark in SAR imagery due to surface wetness, and openwater in leads is bright—i.e., under moderately windy conditions—making floes readily identifiable. All SAR-based techniques are largely inoperable in the MIZ, due to extreme variations in backscatter from both ice and open water and the complex ice conditions (Soh et al., 1998). Another consideration is the decrease in backscatter contrast between ocean and ice at higher incidence angles. This technique was further developed by Holt and Martin (2001), and applied by them to ice in the western Arctic in summer (Figure 5.109, see color section). In the interior pack, Holt and Martin (2001) found that, for $d > 1\,\text{km}$, N decreased approximately as $d^{-\alpha}$, where α lay in the range of 1.8–2.9. Again, they found that the algorithm performs best under Arctic summer conditions when ice appears dark in SAR imagery due to surface melt, and when leads appear bright due to strong winds. Uncertainty is introduced under light-wind conditions, and due to air temperature fluctuations, leading to low-backscatter contrast and difficulty in delineating floe boundaries. See Holt and Martin (2001), Holt and Rio (1998), and Soh et al. (1998) for a detailed discussion of other caveats. Note that the satellite measurement of floe lateral melt rate remains impractical. Accurate estimates can only be achieved *in situ*—e.g., using photogrammetric techniques (Hall and Rothrock, 1987).

In principle, similar techniques are applicable to other high-resolution satellite imagery—e.g., from Landsat ETM+, AVNIR-2, Ikonos/Quickbird, and ASTER, although all are limited to narrow-swath coverage (particularly Quickbird and Ikonos) and cloud-free conditions. Wide-swath sensors are ruled out by their poor spatial resolution. Indeed, the large-scale measurement of floe size distribution from space represents a classic example of the current technological tradeoff between spatial resolution and swath width. At this point, ScanSAR sensors onboard Radarsat-1, Envisat, and in future Radarsat-2 and ALOS offer something of a compromise, with systems such as Radarsat-2 and TerraSAR-X/-L offering near meter-scale resolution data but over narrow swaths. It is also likely that the advent of polarimetric data and techniques will improve estimates of floe size (see Section 5.9.10). Clearly, much research and development again lies ahead.

5.9.11 Sea ice/snow skin surface temperature

Surface temperature is another fundamental yet poorly parameterized climate variable that can be obtained from space. In this section, we expand upon information provided in Chapter 4 by focusing on sea ice (ice sheet methods are discussed in Chapter 3 of Volume 2 of this book). Dependent upon conductive, radiative, and turbulent fluxes (Cheng et al., 2001; Guest and Davidson, 1994; Launiainen and Cheng, 1998; Overland and Guest, 1991), surface temperature drives the longwave radiation flux (5.1), controlling the balance between heat exchange with the atmosphere and conductive heat flux through the snow and ice layers (Maykut, 1982). Indeed, apart from shortwave radiative fluxes, all of the main

components of the heat exchange between the ice surface, ocean, and atmosphere are explicit functions of ice surface temperature. As such, it is closely allied with sea ice formation, state, and melt (see Section 5.9.15), and is therefore also intimately linked with surface albedo, which is covered in the next section. Such exchange has a deep-seated impact on global climate by controlling sea ice extent, thickness distribution, and mass balance. Accurate estimates of both the mean and variance are required to more realistically model the regional heat balance and ice growth and accompanying brine rejection rates. *In situ* measurements of snow and sea ice temperature are spatially and temporally sparse (Lindsay and Rothrock, 1994a; Massom et al., 2001a; Sturm et al., 1998, 2001, 2002a), and are inadequate for all but detailed case studies. Changes in large-scale surface temperature regimes may also be an important indicator of climate change/variability (Comiso, 2003a, c; Comiso et al., 2003a).

Referring back to Section 5.6.1, ice/snow surface temperature is controlled by the processes of vertical heat exchange, is dependent on conductive, turbulent, and radiative fluxes, and is strongly dependent on ice thickness. In the case of the ice surface, temperature also depends on the presence/absence and thickness of snow cover (Massom et al., 2001a; Sturm et al., 1998). For given atmospheric conditions, new or young ice has a warmer skin surface temperature than thicker snow-covered first-year and multiyear ice. This again provides a means of classifying ice types, as we will see. Factors affecting ice/snow surface and surface air temperature (T_{air}) variations over sea ice in winter, and their interrelationship, are discussed by Guest and Davidson (1994), Overland and Guest (1991), and Yu et al. (1995). Guest and Davidson (1994) showed that, due to the close relationship between T_{air} and ice/snow surface temperature, T_{air} fields can in principle be estimated from satellite-derived measurements of snow/ice surface temperature.

Here we outline the two temperature products that can currently be derived from satellite data. The first, which is covered in the next section, derives from passive-microwave data and relates to the temperature of the sea ice beneath the snow cover. The second product, discussed in this section, relates to the measurement of the surface "skin" temperature, and is determined from TIR data. This temperature, which we term *IST*, emanates from the upper microns of the snow/ice surface, due to the small penetration depth of radiation at TIR wavelengths. Referring back to Section 5.7.2 and (5.23), it can be seen that the retrieval of accurate *IST* values from space requires (i) a correction for atmospheric emission and absorption—mainly by water vapor, ozone (O_3), aerosols, and CO_2—and (ii) a precise knowledge of the surface emissivity and its angular dependence (given that the satellite sensor scan angle typically varies) (Stroeve et al., 1996). See Chapter 4 for more details on atmospheric contributions.

The snow/ice skin depth temperature *IST* can be derived from TIR measurements routinely acquired by satellite wide-swath, medium-resolution TIR radiometers—e.g., the NOAA AVHRR (Steffen, 1995), ERS ATSR and ATSR/2, Envisat AATSR and MERIS, and EOS Aqua and Terra MODIS. With its excellent polar coverage at a highest resolution of ~1 km (at nadir), the AVHRR has been a "workhorse" sensor of snow and ice skin temperature (and albedo) retrieval since

the late-1970s (Maslanik et al., 1998a; Steffen et al., 1993). With its dual-direction look capability, the ATSR and subsequent modified versions offer improved estimates of the atmospheric contribution to the observed surface signal, given their dual-direction look capability and higher radiometric precision (Shokr and Le, 1999). As noted preciously, the spatial and spectral resolutions of MODIS represent a substantial improvement over comparable systems in terms of sea ice detection and monitoring. These measurements will continue into the NPOESS era with the VIIRS. Details of the VIIRS *IST* algorithm are given by Sikorski et al. (2002).

5.9.11.1 The multi-channel approach

Two techniques are typically used to retrieve clear-sky *IST* maps from satellite TIR data, as is the case in ice sheet research (Chapter 3 of Volume 2 of this book). One is based on single-channel data only, while the second uses a multispectral approach. The latter uses the split-window channels—e.g., channels 4 (10.3–11.3 μm) and 5 (11.5–12.5 μm) for the NOAA AVHRR—to empirically correct for atmospheric water vapor attenuation effects, by exploiting the differential absorption characteristics in the two wavebands (Price, 1984). By this technique, an estimate is made of the surface temperature from the two brightness–temperature measurements. Underlying assumptions are that the linearity of the relationship results from linearization of the Planck function, and of linearity of the variation of atmospheric transmittance with column water vapor amount (Prata, 2002; Wan, 1999). In principle, this approach is similar to that used to routinely retrieve Sea Surface Temperatures (SSTs) outside the ice edge (Prabhakara et al., 1974), which relates satellite observations to *in situ* surface temperature observations via a regression model (Barton, 1992). As detailed *in situ* observations are largely lacking in sea ice zones, an alternative approach is typically used which models satellite sensor T_Bs or radiances by application of the radiative transfer equation. This ''forward model'' approach forms the foundation of current *IST* algorithms, such as that developed by Key and Haefliger (1992) for use in the central Arctic perennial pack. This multichannel algorithm uses empirical relationships to correct for atmospheric water vapor absorption, with coefficients being determined through a regression of surface temperatures against modeled T_Bs. Corrections are determined as a function of satellite viewing angle and for three different ''seasons''—namely, winter, ''transition'', and summer. Radiances in the AVHRR TIR channels are simulated by applying the LOWTRAN-7 radiative transfer model (Kneizys et al., 1988) to atmospheric humidity and temperature profiles collected from a Soviet drifting ice station near the North Pole, incorporating built-in profiles of aerosols and trace gases and modeled angular emissivities. Appropriate sensor response functions are applied to the calculated radiances, which were then converted to T_Bs by inverting the Planck function at the channel central wavelength appropriate for the temperature range 230–270 K (Kidwell, 2000).

Although the emissivity of snow (and sea ice) is closer to unity and less variable at TIR than at microwavelengths, it varies with sensor scan angle and represents an error source if not accounted for. The cross-track scan angle for the AVHRR is

Table 5.7. Angular emissivities of snow modeled at the wavelengths of AVHRR channels 4 (10.3–11.3 μm) and 5 (11.5–12.5 μm) for the NOAA 7 satellite. Emissivity is unitless.

Sensor scan (°)	Channel-4 emissivity	Channel-5 emissivity
0	0.9988	0.9961
10	0.9987	0.9958
20	0.9984	0.9949
30	0.9977	0.9933
40	0.9968	0.9908
50	0.9955	0.9872

From Key and Haefliger (1992), after Dozier and Warren (1982).

$\pm 55.4^\circ$ from nadir, creating a 2,900-km-wide data swath (Cracknell, 1997; Kidwell, 2000). Key and Haefliger (1992) and Key et al. (1997) made the assumption that the surface is snow-covered, and modeled the directional TIR emissivities for snow using the method of Dozier and Warren (1982). These were then integrated with the satellite-specific response function for each AVHRR TIR channel to obtain a wavelength-integrated emissivity. The resultant angular emissivities are given in Table 5.7. At AVHRR wavelengths, ε is largely insensitive to snowgrain size, snow liquid water content (at least up to 20% of the total particle volume), and temperature over the range typically encountered (Dozier and Warren, 1982; Key and Haefliger, 1992). Subsequent experiments suggest a greater dependence on grain size and packing fraction (Salisbury et al., 1994), with a decrease in ε with increasing grain size, but that angular effects dominate (Wald, 1994).

By incorporating a more extensive atmospheric dataset and making other improvements, Key et al. (1997) refined the technique described above for wider application, including marginal Arctic seas and the Antarctic sea ice zone. The improved Key et al. (1997) AVHRR *IST* algorithm again uses T_B data from channels 4 (T_4) and 5 (T_5), and incorporates the satellite scan angle θ (0–55°) to correct for variable atmospheric pathlength. The *IST* (in K) is:

$$IST + a + bT_4 + c(T_4 - T_5) + d[(T_4 - T_5)(\sec\theta - 1)] \tag{5.82}$$

where regression coefficients a, b, c, and d are derived for three temperature ranges—i.e., $T_4 < 240$ K, 240 K $< T_4 <$ 260 K, and $T_4 > 260$ K—to enable greater flexibility in accounting for seasonal variations in surface and atmospheric conditions appropriate for the region for which they are developed. Satellite-specific values for the AVHRR coefficients (for NOAA 7, 9, 11, and 12) are given for the Arctic and Antarctic in Key et al. (1997, tables 2 and 3, respectively). Although circumpolar, the Antarctic atmospheric data used to develop this algorithm are largely from coastal and near-coastal locations—i.e., the Antarctic Radiosonde Data Set (Connolley and King, 1993). As such, further refinement may be necessary to account for atmospheric effects further to the north, particularly in view of the fact that the Antarctic pack extends equatorward as far as ~56°S in certain

locations, and is therefore strongly affected by relatively warm and moist maritime air masses (Massom et al., 1997).

Due to a lack of adequate information, the effects of surface topography, snow age, and wind on ε are not incorporated into the model, although they may be important. Key et al. (1997) attempted, however, to account for the effect of widespread seasonal surface meltponding on the TIR emissivity of Arctic sea ice, by assuming that a mixture of snow/ice and ponds is present when the temperature is above melting point. They then determined ε as a weighted sum of freshwater and snow emissivities, where the weights are 0.2 for water and 0.8 for snow. Key et al. (1997) concluded that this is an approximation of reality only. More work is necessary to further refine the *IST* algorithm by accounting for, or at least minimizing, these and other uncertainty effects. Moreover, unresolved Ice Crystal Precipitation—ICP, "diamond dust"—often occurs within the low-level temperature inversion layer (Intrieri and Shupe, 2004; Kahl et al., 1992), and can introduce a warm bias into *IST* retrievals (Yu and Lindsay, 2003; Yu et al., 1995). Key and Haefliger (1992) showed that ICP with an optical depth of 0.34, and not detected as cloud, would lead to an error of $\sim$4 K in *IST* retrieval. Changes in ozone concentration from the mean standard profile constitute another error source. In spite of these uncertainties, algorithm performance is reasonable, with estimated accuracies of 0.3–2.1 K (Key et al., 1997; Perovich et al., 1997). This compares with estimated seasonally dependent accuracies of 1–4 K for the earlier Key and Haefliger (1992) technique (Key et al., 1994a; Yu et al., 1995). Such accuracies are sufficient for most climate process studies (Key et al., 1997), but further validation together with algorithm refinement is necessary to reduce uncertainty.

Three clear-sky *IST* datasets (including time of acquisition) have been produced by the NOAA/NASA AVHRR Polar Pathfinder Project (Hutchinson and Scambos, 1997; Maslanik et al., 1998a), by applying the Key et al. (1997) algorithm. These are:

- Twice-daily, 1.25-km EASE-grid data, composited onto two grids per day based on common local solar times and scan angle. Data are available from August 1993 through December 1998 for the Northern Hemisphere, and April 1992 through January 1996 for the Southern Hemisphere (Scambos et al., 2002).
- Twice-daily, 5-km EASE-grid composites, from July 1981 through August 1998 (Fowler et al., 2002a).
- Twice-daily, 25-km EASE-grid composites (coverage as above). These values are generated by subsampling the 5-km grids (Fowler et al., 2002b).

These datasets are available, for the regions poleward of 48.4°N and 53.2°S, from the NSIDC (⟨*http://nsidc.org*⟩). Excellent documentation is also given online.

The Key et al. (1997) algorithm has also been adapted for application to ERS-1 ATSR data, using the channels centered at $\sim$11 and 12 μm (Stroeve et al., 1996). This instrument differs from the AVHRR in that it views the same ground location from two different angles—i.e., forward at 55°, and at nadir. It is these two angles that are used in the *IST* algorithm (the ATSR also scans across-track from 0° to $\sim$22°). The resolution varies from 1×1 km (at nadir) to 1.5×2 km (forward view) across a 500-km swath width (ESA, 1991; Prata, 2002). Importantly, dual-angle systems

Table 5.8. Angular emissivities of snow modeled for the ERS-1 ATSR thermal infrared channels. Emissivity is unitless.

Sensor scan (°)	Channel-4 emissivity	Channel-5 emissivity
0	0.9984	0.9960
5	0.9984	0.9959
10	0.9983	0.9957
15	0.9981	0.9953
20	0.9978	0.9947
55	0.9931	0.9845

From Stroeve et al. (1996).

represent a significant improvement over conventional single-angle sensors such as the AVHRR in their ability to account for variations in atmospheric absorption due to different concentrations in all absorbing species, by virtue of not requiring that the absorptions remain in proportion (Stroeve et al., 1996). Although the multi-wavelength-only approach is effective at determining the effects of varying water vapor amounts, it is insensitive to the effects of atmospheric constituents—e.g., CO_2, O_3, and aerosols (Stroeve et al., 1996). Further discussion of high-latitude atmospheric corrections is given by Bamber and Harris (1994). The ATSR *IST* algorithm is given as:

$$IST = a + bT_{3,nadir} + cT_{3,forward} + dT_{3,nadir} + eT_{4,forward} \tag{5.83}$$

where coefficients a to e are obtained from a linear regression of satellite T_Bs and the surface temperature, T_3 and T_4 are the T_Bs (in K) of the two ATSR split-window channels centered on 11 and 12 μm, respectively, and the subscripts refer to the viewing angles (Key et al., 1997; Stroeve et al., 1996). Satellite-specific values for the ATSR regression coefficients a to e are given for both the Arctic and Antarctic in Key et al. (1997, table 4). Angular-wavelength-integrated emissivities of snow for the ATSR TIR channels are given in Table 5.8. With its improved dual-direction look capability, the ERS-1 ATSR and future versions exhibit smaller r.m.s. errors than the AVHRR, especially at higher temperatures (Key et al., 1997). This ATSR algorithm can be adapted for use with the ATSR/2 onboard ERS-2 and the AATSR on Envisat (Prata, 2002).

The AVHRR-based technique outlined earlier has also been adapted for application to MODIS data (Hall et al., 2004a). The MODIS instrument represents a major advance in that it can achieve a specified calibration accuracy of better than 1% absolute for the TIR bands, by viewing cold space and a full aperture blackbody before and after viewing the Earth scene (Wan, 1999). With its onboard calibration, high radiometric resolution, and global coverage, MODIS is expected to deliver improved snow/ice skin surface temperature information. For MODIS, the Key et al. (1997) AVHRR equation (5.82) has been adapted for use with channel-31 (10.78–11.28 μm) and -32 (11.77–12.27 μm) data. Daily 1-km and 4-km-resolution gridded and swath data at a resolution of 1 km are available from the NSIDC

DAAC at ⟨*http://nsidc.org/data/modis/*⟩ (Hall et al., 2004b). Data availability is from late 2000 onwards. An example of a MODIS *IST* product (MOD29), from the Fram Strait region of NE Greenland, is shown in Figure 5.110 (see color section). The main limitation on the MODIS *IST* product is unresolved fog or thin clouds (Hall et al., 2004a). Under totally clear-sky conditions, the accuracy (r.m.s. error) is of the order of 1.2–1.3 K (Hall et al., 2004a). With both the MODIS and AMSR-E onboard the Aqua satellite, it is possible to derive simultaneous information on both *IST* and ice temperature for the first time from space (see Section 5.9.12). Note that the possible incorporation of data from the 3.7- and 3.9-μm MODIS channels (20 and 21) is being investigated with a view to improving the *IST* product (Hall et al., 2004a). Validation of these new products is continuing in both the Antarctic and Arctic (Cavalieri et al., 2002a). The *IST* time series will continue with the launch of the VIIRS on the NPP mission in 2006 and subsequently on NPOESS-1 in 2009. The VIIRS *IST* algorithm is based upon the split-window approach and builds upon the AVHRR and MODIS heritage (Sikorsky et al., 2002). The scientific objective of VIIRS *IST* retrievals is to provide improved measures of regional and global fields.

It has been noted that the approach outlined above tends to underestimate the temperature of areas of open water within the pack by being tuned for snow surfaces (Lindsay and Rothrock, 1993). Maslanik and Key (1993) addressed this issue by incorporating concurrent passive-microwave data from the DMSP SSM/I to adjust the AVHRR-derived FOV *IST*s for SSM/I-derived ice concentration to retrieve ice-only skin surface temperature T_{ice}:

$$T_{ice} = [IST - T_{ocean}(1 - C_{tot})]/C_{tot} \tag{5.84}$$

where T_{ocean} is the physical temperature of freezing ice-free ocean (taken to be 271.2 K), and C_{tot} is the total ice concentration. While their results appeared reasonable compared with climatological averages, the absolute accuracy remains undetermined.

5.9.11.2 The single-channel approach

The second, simpler approach derives clear-sky *IST* from single-channel data alone—e.g., from channel 4 of the AVHRR (Comiso 2000, 2003c), or earlier data from the 11.5-μm channel of the Nimbus-7 Temperature Humidity Infrared Radiometer (THIR) at a spatial resolution of 6.7 km (Comiso, 1983). The AVHRR channel 4 is generally chosen in preference to channel 5 due to its lower sensitivity to atmospheric water vapor absorption (Ouaidrari et al., 2002; Price, 1984). This technique is based upon the assumption that, during the cold season, the atmospheric contribution (attenuation) is generally minimal due to the low water vapor content in polar atmospheres at low temperatures (Yu et al., 1995). With this assumption, (5.23) is reduced to:

$$I(T_B) = \varepsilon I_{sfc}(IST) \tag{5.85}$$

Under such conditions, and using a surface emissivity that is close to unity, the T_B measured at 11 μm is a reasonable approximation of the *IST* (Yu et al., 1995; Yu and Rothrock, 1996). This difference increases significantly under summer melt conditions—e.g., to 3 K (Key et al., 1997). Key et al. (1997) further showed that using channel-4 data alone, the effect of not including an angular dependence of emissivity on *IST*-retrieval accuracy is generally small compared with atmospheric effects. While the assumption of a cold, dry atmosphere is reasonable at certain times and in certain regions, it may not hold for peripheral Arctic seas and the Antarctic seasonal sea ice zone (Massom et al., 1997, 1998a). Comiso (2000) estimated errors to be ~2–3 K in Antarctica. In their comparison of *IST* retrievals from different techniques with field observations, Yu et al. (1995) indeed concluded that multi-channel (i.e., split-window) algorithms are generally more accurate in seasonal sea ice zones.

Error sources common to all techniques, both single- and multi-channel, are (i) uncertainties in the atmospheric correction, and (ii) sensor performance. Regarding the former, accuracy is affected by the presence of undetected and subpixel-scale clouds, and our limited knowledge of the spatiotemporal variability of atmospheric humidity, temperature, and aerosol fields used as input for radiative transfer models (Key et al., 1997; Yu et al., 1995). While the split-window approach accounts for atmospheric humidity and temperature, it does not incorporate corrections for the variable aerosol and diamond dust content of the polar atmosphere. Moreover, variability in surface angular emissivity also contributes to the overall uncertainty, with the effect of changes in snowgrain size being greatest at 12 μm (Stroeve et al., 1996). Stroeve et al. (1996) suggest that—for the ATSR, for example—surface emissivity should be known to within 0.1% to obtain a surface temperature retrieval accuracy of 0.1 K. The effect of surface melt requires further investigation. Major constraints on algorithm performance are instrument Noise Equivalent Difference Temperature (NEΔT) for each band, instrument calibration (Key and Haefliger, 1992), and the availability and quality of the surface calibration/validation observations. These issues become particularly important (for all datasets) when comparing, or creating time series from, data from different satellites and/or sensors.

5.9.11.3 Recent results

Products from these *IST* algorithms have been applied to studies of surface characteristics, heat balance, and climate variability. As discussed in Section 5.9.6, satellite-derived *IST* data have been combined with thermodynamic ice growth models to estimate Arctic thin-ice thickness distribution during the cold season (Groves and Stringer, 1991; Yu and Rothrock, 1996). While there are issues with inter-satellite calibration due to changes in sensor characteristics and orbital drift (which have been addressed by the AVHRR Polar Pathfinder Program: Maslanik et al., 1998a), satellite-derived surface temperature (and albedo) records are well-suited to trend analysis and are an important tool in the study of climate change and feedback mechanisms (Comiso, 2003c; Maslanik and Key, 1993). Indeed, they

represent the only continuous and synoptic observation of surface temperature in polar regions (Comiso, 2000).

A number of recent studies have combined AVHRR-derived *IST* estimates with ice concentration/extent and ancillary data to examine change in ice distribution and causal effects. An example of the type of product used is shown in Figure 5.111 (see color section)—a series of monthly mean anomaly maps of the Arctic for September over the period 1981–1999 (Comiso et al., 2003b). The maps were created by taking the difference of each September mean and the mean of all of the September values over the entire period (the mean *IST* map for 1981–1999 is also shown). This dataset corresponds to the ice concentration anomaly maps in Figure 5.37 discussed earlier (in Section 5.9.1.2.4). Compared with the sea ice temperature product discussed in the next section, the *IST* product also extends to adjacent terrestrial and ice sheet surfaces. Atypical warm areas are defined here by warm colors (i.e., yellow, red, purple), while cold anomalies are colored gray through green to blue. A predominance of anomalously warm temperatures is apparent for the 1990s, in particular, corresponding in part to regions of anomalously low ice concentrations (Figure 5.37). Comiso et al. (2003b) provided in-depth analysis of the role of changes in mean atmospheric circulation patterns on the observed changes in *IST* and ice distribution.

Comiso (2003b) carried out a study for the entire Arctic, using cloud-free AVHRR data for the period 1981–2001. Updated seasonal trend maps from these data, extended to 2003, are shown in Figure 5.112 (see color section). These illustrate positive trends in spring through autumn, but a negative trend in winter. Based upon a linear regression analysis of NOAA AVHRR-derived TIR data over the period 1981–2003 (Comiso and Parkinson, 2004), it appears that the mean surface temperture north of latitude 60°N has increased at a rate of ~0.54°C per decade over sea ice. By comparison, coincident net warming of 0.85°C and 0.79°C per decade occurred over Greenland and North America, respectively, while Eurasia cooled by ~0.14°C per decade. The uncertainty is $\sim \pm 0.2$°C per decade in each case. Figure 5.113 (see color section) shows the 22-year dataset split into two 11-year subsets, with a difference map. The latter shows that the surface temperature for the period 1992–2003 was warmer over most regions than the preceding period (1981–1992), except in parts of Russia. Over the entire 22-year satellite record and north of 60°N, the net warming trend also exhibited a considerable seasonal variability, ranging from 0.25°C per decade in summer to 0.84°C per decade in spring. Comiso (2003b) concluded that the substantial increase in the rate of Arctic warming may be associated with the recent change in phase of the AO (see Section 5.5) that has been linked to increasing greenhouse gas concentrations in the atmosphere. Comiso and Parkinson (2004) further attributed the anisotropic patterns in warming/cooling in Figure 5.112c to similar patterns in atmospheric circulation related to periodic changes from cyclonic to anticyclonic modes. Further analysis by Comiso and Parkinson (2004) revealed a lengthening of the Arctic sea ice melt season of ~3 days per decade. This and other studies underline the importance of satellites as a means of extending the relatively sparse *in situ* temperature dataset—e.g., of Jones et al. (1999).

In a similar study, Comiso (2000) combined AVHRR data from 1979 to 1998 with *in situ* measurements to produce monthly mean *IST* maps of the Southern Ocean (and Antarctic Ice Sheet—see Chapter 3 of Volume 2 of this book). By comparing monthly mean anomaly maps of *IST* and ice concentration for all Julys from 1979 to 1998, Comiso (2000) showed that the northernmost locations of the Antarctic sea ice edge are closely associated with alternating warm and cold temperature anomalies around the continent. He surmised that the pattern of these anomalies is consistent with that of the ACW (White and Peterson, 1996), but with a predominantly mode-3 atmospheric wave pattern rather than the previously reported mode-2 wave pattern. Further analysis suggests that the ACW is not only an ice edge phenomenon but also propagates into the pack ice. Intriguingly, the Comiso (2000) study also indicated that the sea ice *IST* around Antarctica exhibited a slight cooling trend over the period 1979–1998. It also recommended the separate processing of descending (night) and ascending (day) passes. The subsequent averaging minimizes errors and uncertainties associated with surface variability—e.g., the rapid response of *IST* to short-term changes in radiative forcing—at the expense of errors in surface temperature associated with ice motion over the period of averaging.

King and Comiso (2003) combined satellite-derived data with meteorological data to assess the spatial coherence in interannual temperature trends in the Antarctic Peninsula, highlighting the regional temperature increase of 2–4°C over the past 50 years. Further research by Kwok and Comiso (2002b) used *IST* data from the Comiso (2000) study to examine connections between large-scale patterns of Antarctic *IST* variability and atmospheric circulation—i.e., the Southern Semi-annual Oscillation (Van den Broecke, 1998) and the Southern Hemisphere Annular Mode (SAM) (Thompson and Wallace, 2000)—in the satellite data record from 1982 to 1998. In the Pacific sector, positive temperature anomalies and ice edge retreat are linked to El Niño episodes, while positive polarities of the SAM are linked to cold anomalies over much of Antarctica (apart from the Antarctic Peninsula). Moreover, the 17-year record reveals an apparent warming trend over the sea ice zone. Such trends should be treated with caution, however, as *IST* retrievals are highly variable and dependent on ice concentration and ice and snowcover thickness (Kwok and Comiso, 2002b).

5.9.12 Sea ice temperature

In this section, we describe a different product, and one that has only recently become routinely available with the launch of the Aqua AMSR-E in 2002: sea ice physical temperature, or T_I. This differs from the TIR-derived *IST* product in that it is retrieved from passive-microwave data and therefore represents the physical temperature at some depth in the snow/ice mass, given the longer wavelength and greater penetration depth of the emitted radiation. Unlike *IST*, T_I is largely unaffected by cloud cover, but at the expense of a poorer resolution (i.e., 25 km in the case of the AMSR-E product). Importantly from a modeling perspective, T_I is a standard product that is routinely produced on a daily basis coincident with the

other AMSR-E sea ice products, most notably ice concentration (Section 5.9.1) and snow cover thickness (Section 5.9.8).

Sea ice physical temperature is another important climate variable and modeling parameter, and a major source of current uncertainty in heat flux and ice growth rate calculations. Temperature also affects ice microstructure and properties, by regulating the composition and salinity of the liquid phase (Weeks and Ackley, 1986) and the connectivity of the pore/brine channel pathways in sea ice to affect the mechanical strength of the ice (Cox and Weeks, 1975, 1983). The permeability of sea ice with a salinity of 5 p.s.u. increases dramatically when its temperature attains a value greater than about -5°C, enabling the transport of brine, seawater, biological material, nutrients, and heat through the ice mass (Golden et al., 1998c). This in turn affects the wetness and salinity of the lower layers of the snow cover, and therefore the optical and dielectric properties of the snow/ice layer. Prolonged ice surface warming beyond threshold values is accompanied both by a reduction in surface salinity (Eicken, 2003a) and the downward flushing of salt in the ice column by snow meltwater percolating through enlarged and interconnected brine drainage channels (Untersteiner, 1968). In the Arctic, this creates a strong contrast in the salinities and micro-structure of first-year ice and ice that has survived a summer melt period—i.e., second-year or multiyear ice.

While IST is strongly coupled to, and approximates, T_{air} (Guest and Davidson, 1994), T_I is highly dependent on snow properties and thickness (Section 5.7.3), and is poorly correlated with IST. In winter and for snow-covered sea ice, the snow/ice interface temperature is typically significantly warmer than that of the snow surface. Moreover, it responds relatively slowly to changes in T_{air} and IST (Massom et al., 1997), given the low thermal diffusivity of the snow cover (Sturm et al., 1998). While fluctuations of as much as 20°C can occur in T_{air} and thus IST over a few hours in the Antarctic sea ice zone in winter with the passage of storms, the temperature range at/below the ice surface is much smaller (Massom et al., 1997, 2001a). By combining the IST and T_I datasets and assuming that the vertical temperature gradient across the snow ∇T is linear, it may be possible to derive improved estimates of heat flux as well as information on variability in snow textural properties—something which is currently neglected in most models. Variability in ∇T affects snow texture by driving temperature–gradient metamorphism, with small crystals transforming into larger crystals under high temperature–gradient conditions, for example (Colbeck, 1982). In Antarctica and in winter, average values of ∇T typically exceed $-25^{\circ}\mathrm{C\,m^{-1}}$ (Massom et al., 2001a; Sturm et al., 1998), which is the approximate critical threshold for depth hoar growth (Akitaya, 1974; Marbouty, 1980). By this process, Sturm et al. (1998) showed that depth hoar comprised nearly twice as much of the snowpack in autumn than in winter in the Amundsen, Bellingshausen, and Ross Seas, due to the higher ∇T across a thinner snow cover in autumn. Such variability is of key importance in determining the bulk effective thermal conductivity of the snow layer, which is a function of density and micro-structure—i.e., grain size, porosity, grain type, and the degree of inter-granular bonding (Massom et al., 2001a; Sturm et al., 1997, 1998). These changes also impact the optical and microwave properties of the snow. Surface albedo, for

example, is sensitive to changes in snow grain size (see Section 5.7.2). Model performance has been shown to be sensitive to changes in snow properties (Fichefet et al., 2000; Wu et al., 1999b).

The theoretical basis of the new technique to derive the average ice physical temperature within each pixel, T_I, from AMSR-E data is given by Comiso et al. (2003a), and can be briefly summarized as follows. Referring back to Section 5.9.1, the final value of T_P, derived from (5.34) using vertically polarized 6.925-GHz data, represents an estimate of the emitting temperature within each data element. Using this information and the associated AMSR ice concentration product C_I, T_I is calculated from the mixing equation as:

$$T_I = \frac{[T_P - T_{BO}(1 - C_I)]}{C_I} \tag{5.86}$$

The value of T_I represents the physical temperature of the sea ice layer emitting most of the radiation at 6.925 GHz. This formulation is based on the assumption that for dry snow conditions, snow cover is transparent at this frequency and T_I in effect represents the snow/ice interface temperature for first-year ice, the surface of which is opaque due to its relatively high salinity (Comiso et al., 2003a). For less saline and thicker ice—e.g., Arctic multiyear ice—and possibly thick fast ice, the derived sea ice temperature represents a weighted average of the ice freeboard (the layer of ice above the water level).

Examples of monthly mean AMSR-E T_I maps of the Arctic and Antarctic are given in Figure 5.114 (see color section). The expected accuracy is ~4 K (Cavalieri et al., 2001), which is lower than that of modern *IST* products, and depends upon a number of error sources. These include inherent uncertainties in the retrieval of sea ice concentration (Section 5.9.1) and spatial and temporal variations in ice emissivity at 6.925 GHz from different ice types and surface characteristics (Cavalieri and Comiso, 2004). As with the AMSR-E snow cover thickness product, this is a new standard product. Once again, validation campaigns have been carried out, and results are still being formulated at the time of going to press. Daily ascending, descending, and average T_I data are routinely produced by the NSIDC, and are available for both polar regions for the period from February 18, 2004 and at a spatial resolution of 25 km (⟨*http://nsidc.org/data/aesi25.html*⟩; Cavalieri and Comiso, 2004). In addition, WindSat (see Section 5.8.1) provides another source of low-frequency brightness–temperature data that can be potentially used to retrieve T_I data.

5.9.13 Sea ice albedo

The reflectance of a surface is a measure of its ability to reflect incident energy, and is defined as the ratio of reflected to incident energy at a given wavelength or narrow waveband. While this can apply to all wavelengths, the shortwave spectral albedo α_λ is the ratio of exitance (radiant flux density leaving the surface in all directions per unit area and per unit time) to irradiance per unit wavelength over a certain spectral interval. This ratio is determined by the sum of scattering and specular reflection at

the surface plus absorption and scattering in the volume of the snow/ice (Perovich, 1996). The total (all-wavelength) α_t is the hemispheric reflectance of a given surface integrated over the complete sphere of all directions and the solar spectrum of $\sim$0.25–3.0 μm (Warren, 1982). It is a fundamental variable controlling the radiation budget of polar oceans—see (5.1) and Maykut (1986)—and thus a major component of the Earth–atmosphere energy balance (Barry, 1996; Grenfell et al., 1994b). Indeed, surface albedo and clouds are the two most important parameters modulating the Earth's climate. The planetary albedo is the ratio of reflected to incident solar radiation at the TOA, and is an important boundary condition that needs to be known accurately for the modeling of large-scale energy exchange between polar and mid-latitudes (Steffen, 1995).

The albedo of polar oceans is a key parameter in the global climate system, and one that is highly variable. Broadband albedo influences the system and defines the shortwave energy input into the surface, partitioning shortwave radiative energy between atmosphere and ice/ocean in a spectrally and directionally integrated form. The temporal and spatial as well as spectral and directional characteristics of the albedo of polar oceans change dramatically over the course of a year. They are affected not only by the presence or absence of ice but also by the structural and optical properties of the ice and snow cover where it is present. As a result of the large albedo contrast between open ocean and sea ice, and between various types of ice depending on thickness (age) and snow cover thickness, grain size, impurities, and degree of melt (Grenfell and Maykut, 1977; Warren, 1982), accurate large-scale estimates of spatio-temporal change in sea ice albedo are critical as they represent an important tuning parameter in GCMs and coupled ice–ocean–atmosphere models (Meehl and Washington, 1990). Inaccurate albedo estimates translate into large errors in computations of the surface energy balance (Maykut, 1986), and the performance of current models is largely hampered by a lack of adequate albedo data on sufficiently large regional and temporal scales. This is a major deficiency, given the current uncertainty in the dominant sea ice melt albedo feedback mechanism (Curry et al., 1995). In general, most models describe sea ice albedo as a function of fractional snow cover and surface temperature only (comparative details are given in Barry, 1996).

While *in situ* experiments provide important detailed information on surface albedo—e.g., during the Surface Heat and Energy Balance of the Arctic (SHEBA) experiment (Moritz et al., 1993; Perovich et al., 1999b, 2002a, b)—satellite remote sensing offers the only practical means of gaining near-instantaneous information over large remote areas and of capturing the considerable spatio-temporal changes involved (see also Section 4.6). When carefully processed, data from modern optical sensors such as the NOAA AVHRR can be used to derive both the surface and planetary albedo and the shortwave radiation balance under daylight conditions (see Chapter 4). Broadly speaking, the area-averaged surface albedo measured by a satellite varies not only with ice/snow conditions and type/thickness, as we saw in Section 5.7.2, but also with ice concentration, viewing and incidence angles, solar zenith angle, and atmospheric composition (Key et al., 2001a). Surface albedo measurement from space is limited by cloud cover and dependent on accurate

cloud masking. Large-scale area-averaged maps of Arctic Ocean sea ice albedo have also been produced from DMSP OLS data by Robinson et al. (1992). Here, however, we first concentrate on the more flexible AVHRR (Laine and Heikinheimo, 1996), then on its successor the Terra/Aqua MODIS. Comiso (2001) used a single-channel approach—i.e., channel 1—to derive monthly mean albedo composites for the Arctic Ocean, with averaging helping to minimize errors. Most workers, however, use multispectral techniques, to obtain a broadband albedo from narrowband spectral measurements—i.e., by typically carrying out a narrow-to-broadband conversion using a linear combination of the individual isotropic albedos of the visible and near-IR bands. To reiterate, broadband albedo is of major interest in that it characterizes the total energy reflected from the surface and is used in the radiative schemes of climate and other models. Algorithms to retrieve sea ice albedo from NOAA AVHRR channel-1 and -2 data under clear-sky conditions have been formulated by De Abreu et al. (1994), Nakagawa (1992), Lindsay and Rothrock (1993, 1994b), and for cloudy skies by Key et al. (2001a). Note that information on equivalent ice sheet algorithms is given in Chapter 3 of Volume 2 of this book.

An important consideration in the derivation of areally integrated surface albedos from satellite optical measurements is that, under clear-sky conditions, the reflected radiances may be distinctly anisotropic. This is due to the combined effects of the surface characteristics of the snow/ice, which act as non-Lambertian reflecting surfaces at shorter wavelengths that characterize solar irradiance and the strong, directly incident (rather than diffuse) component. Fortunately, deviations from the isotropic case can be described by the BRDF. Knowledge of the BRDF is also necessary because satellite sensors such as the AVHRR generally measure the surface reflectance over a limited number of angles, whereas the desired albedo quantity is generally defined as the reflectance of a given surface integrated with respect not only to wavelength (typically between 0.25 μm to 2.50 or 3.0 μm) but also angle—i.e., for all directions within a hemisphere above the surface (Barnsley et al., 1994; Roujean et al., 2004). The BRDF specifies the behavior of surface scattering as a function of illumination and viewing angles at a particular wavelength, and describes the angular distribution of radiation reflected by a given surface under any given illumination geometry and for all angles of exitance (Nicodemus et al., 1977). Albedo is thus derived by integration of the BRDF with respect to the angle of exitance and wavelength. The dependence of BRDF on surface roughness was discussed by Warren et al. (1998).

We first outline the steps involved in deriving directional–hemispherical broadband clear-sky albedos of sea ice from NOAA AVHRR measurements. Developing the work of De Abreu et al. (1994) and Lindsay and Rothrock (1993, 1994b), Key et al. (2001a) laid out the necessary processing sequence as follows:

(1) Normalization of channel-1 and -2 data with respect to the solar zenith angle.
(2) Cloud detection using reflectances at 0.9 and 3.7 μm and brightness–temperature differences at 11 and 12 μm. Key et al. (2001a) utilized the spectral threshold test method (Key, 2002). See Section 5.8.2.4.1 for information on cloud-masking techniques.

(3) Calibration of channel-1 (0.58–0.68 μm) and -2 (0.725–1.10 μm) data to TOA reflectances (Rao et al., 1993), with updates of satellite-specific and time-dependent calibration coefficients being available from NOAA at ⟨*http://psbsgi1.nesdis.noaa.gov:8080/EBB/ml/nica12.html*⟩. This converts radiance to reflectance.

(4) Conversion of narrowband reflectances in channels 1 and 2 to a TOA broadband (0.28–4.0 μm) reflectance. This step is necessary as broadband reflectance values are required by the subsequent anisotropic reflectance correction procedure (in the next step). Following Li and Leighton (1992), the narrow-to-broadband conversion is by:

$$\rho_{TOA} = a + b\rho_{1,TOA} + c\rho_{2,TOA} \tag{5.87}$$

where ρ_{TOA} is the broadband TOA reflectance, $\rho_{1,TOA}$ and ρ_{2TOA} are the channel-1 and -2 reflectances, respectively, and a, b, and c are regression coefficients. The latter are determined using the *Streamer* radiative transfer model (Key and Schweiger, 1998, 2000), incorporating the DISORT solver of Stamnes et al. (1988).

(5) Correction of the TOA broadband reflectance for anisotropy, to correct for the dependence of the surface reflectance on the satellite–surface–Sun geometry, using data from Suttles et al. (1988) and based upon Taylor and Stowe (1984):

$$\alpha_{TOA} = \frac{\rho_{TOA}}{f} \tag{5.88}$$

where α_{TOA} is the TOA albedo, ρ_{TOA} is the reflectance observed at the sensor (simulated in Step 4), and f is the *anisotropic reflectance factor* (defined as the bidirectional reflectance normalized relative to the hemispherical reflectance and characterized by the BRDF: Nicodemus et al., 1977; Warren, 1982; Perovich, 1994). Once again, this step is necessary because satellite sensors with a narrow FOV such as the AVHRR measure the surface reflectance at one or a few angles only (Barnsley et al., 1994), and snow and ice are non-Lambertian reflecting surfaces (Steffen, 1995). Issues relating to anisotropic effects and snow are discussed in Jin and Simpson (1999, 2000), Steffen (1987, 1997), and laid out in more detail in Chapter 3 of Volume 2 of this book.

(6) Conversion of the TOA broadband albedo to a surface, broadband clear-sky albedo:

$$\alpha_{TOA} = a + b\alpha_s \tag{5.89}$$

where α_s is the surface reflectance, and regression coefficients a and b are a function of aerosol amount, ozone content, water vapor, and solar zenith angle. The coefficients, which were derived using a radiative transfer model for a range of illumination angles and surface and atmospheric conditions, are given in Key et al. (2001a, table 1). Alternatively, and if suitable input data are available, then the influence of the atmosphere on the radiation and its spectral signature can be assessed using radiative transfer models.

While the discussion above applies to the retrieval of surface albedo from satellite data under clear-sky conditions, further developments have been made by Key et al.

(2001a) to incorporate cloud effects in satellite retrievals. The impetus for this is the fact that clouds have a significant impact on snow and ice albedo (Grenfell and Perovich, 1984), and also that persistent cloud cover—e.g., typically 60–90% in the Arctic (Key et al., 2001b)—greatly limits the spatial coverage under clear-sky conditions alone. Cloud properties are strongly coupled to sea ice and open-water conditions, and to the planetary and surface albedos (Morales Maqueda et al., 2004). The impact of clouds on the surface broadband albedo is due to the fact that their absorptivity and thus transmittance varies as a function of wavelength in a manner that differs from that of the snow/ice surface (Key et al., 2001a). Due to selective absorption of the solar flux by clouds in near-IR wavelengths, and as ice/snow has a lower spectral albedo at these compared with visible wavelengths, the surface broadband albedo is greater under cloudy-than clear-sky conditions (Grenfell and Maykut, 1977; Grenfell and Perovich, 1984). See Chapter 4 for further discussion on the importance of clouds.

The new method of Key et al. (2001a) estimates the albedo of cloudy AVHRR pixels by interpolating the clear-sky albedo to cloudy regions, then adjusting them for cloud cover effects using satellite-derived estimates of cloud optical depth. The cloudy-sky broadband surface albedo $\alpha_{s,cld}$ is estimated as a function of the clear-sky albedo $\alpha_{s,clr}$, the solar zenith angle θ, and the cloud visible optical depth τ (unitless) as follows:

$$\alpha_{s,cld} = a + b_{s,clr} + c\ln(\tau + 1) + d\cos\theta \tag{5.90}$$

where a, b, c, and d are regression coefficients with values of $-0.049\,124\,3$, $1.067\,56$, $0.021\,707\,5$ and $0.017\,950\,5$, respectively. Please see the original reference for cloud optical depth information. Key et al. (2001a) reported that the clear- and cloudy-sky surface albedo for snow and sea ice can be obtained from space with an estimated uncertainty of $\sim$7% absolute for the High Arctic. They further concluded that a monthly clear-sky surface albedo climatology may be adjusted for clouds by incorporating an effect of $\sim$5% (a figure also determined by Grenfell and Perovich, 1984), while stressing that adjustments for cloud optical depth should ideally be performed with instantaneous retrievals. The overall accuracy of broadband albedo estimates is affected by uncertainties in corrections for atmospheric effects, TOA angular models (the anisotropic reflectance factor), instrumental calibration, sensor degradation (drift) with time, and cloud masking (De Abreu et al., 1994; Haefliger et al., 1993; Key et al., 2001a; Lindsay and Rothrock, 1994b; Steffen, 1995). See Key et al. (2001a) for a detailed assessment of error sources. Additional work is required to validate the algorithm in Antarctica, where different surface and atmospheric conditions prevail. Note that the coded procedures presented above are available online at: ⟨*http://stratus.ssec.wisc.edu*⟩, as part of the *Cloud and Surface Parameter Retrieval system* (*CASPR*) for polar AVHRR data (Key, 2002).

Taking a simpler approach, and making assumptions about surface anisotropy and aerosol effects, Comiso (2001) constructed annual mean albedo maps of the entire Arctic by taking albedo to be the reflectivity at $\sim$0.6 μm (AVHRR channel 1). The only correction was a normalization for solar zenith angle, after cloud masking. Anomaly maps for all years spanning the period 1987–1998, and

constructed by subtracting the climatology from the annual means, are shown in Figure 5.115 (see color section). This study compares these results with variability and trends in sea ice extent, cloud cover, and *IST*.

Once again, ice/snow surface broadband albedo and associated data products have been produced by the AVHRR Polar Pathfinder Project, as twice-daily EASE-grid composites at three resolutions (1.25 km, 5 km, and 25 km) and poleward of 48.4°N and 53.2°S. These are again available from the NSIDC at ⟨*http://nsidc.org*⟩ (Hutchinson and Scambos, 1997; Maslanik et al., 1998a), for the periods August 1993 to December 1998 for the Northern Hemisphere and April 1992 to January 1996 for the Southern Hemisphere for 1.25-km data, and July 1981 through August 1998 for 5- and 25-km data. For information on the algorithms used, data calibration, and data formats, see Fowler et al. (2002a, b) and Scambos et al. (2002).

With its higher spectral and spatial resolutions, the MODIS sensor onboard Terra and Aqua constitutes a significant improvement over the AVHRR in terms of albedo retrievals. Unlike the AVHRR, MODIS is equipped with onboard calibration, to an accuracy of 2% relative to the solar radiance (Guenther et al., 1998). An algorithm has been developed to produce daily clear-sky albedo estimates for areas determined to be sea ice by the MODIS ice classification algorithm—see Figure 5.57 (Hall et al., 2003; Klein, 2000; Klein and Stroeve, 2002). Further details are available at ⟨*http://nsidc.org/data/modis/*⟩. This algorithm builds upon techniques described above for the AVHRR (De Abreu et al., 1994; Schweiger et al., 1993) and also terrestrial snow and ice (Knap and Oerlemans, 1996; Stroeve et al., 1997). The standard 1-km resolution MODIS surface reflectance product, MOD09 (⟨*http://www.asd.ssc.nasa.gov/m2m/product_report.aspx?product_id=9*⟩), is derived routinely from band-1 to band-7 data and atmospherically corrected (Vermote and Vermeulen, 1999). MODIS data products are generally "stored" in granules, each derived from approximately 5 minutes of continuous instrument data in the Hierarchical Data Format for the Earth Observing System (HDF-EOS). Coincident atmospheric parameters, such as water vapor and ozone content, can be retrieved from MODIS MOD07_L2 products at a spatial resolution of 5 km and used with radiative transfer models to provide atmospheric correction (Zhou and Li, 2003). As measurements are made over a wide range of incidence angles and in a large number of spectral bands, both atmospheric conditions and surface anisotropy can be more accurately derived, leading to more accurate retrieval of surface albedo. Indeed, BRDF is a standard product derived from MODIS (product code MOD43B—see Strahler et al., 2003). The MODIS albedo algorithm uses a model of the BRDF of snow to account for anisotropic surface scattering effects, again based upon the DISORT model of Stamnes et al. (1988), and incorporates the known optical properties of snow. Further background information on the requisite correction for surface anisotropic effects in MODIS data by determining the surface BRDF is provided by Strahler et al. (1999, 2003) and Zhou and Li (1999, 2000b). As is generally the case, a difficulty exists in the comparison of fine-scale surface measurements with coarser resolution satellite data for validation purposes. In an attempt to overcome this, Zhou and Li (2003) developed a sub-pixel correction method in their

comparison of *in situ* and MODIS-derived spectral reflectances of Antarctic sea ice and snow cover.

The direct-beam directional hemispherical (or black-sky) albedo can be calculated by integration of the BRDF for a particular illumination geometry, while the completely diffuse bi-hemispherical (or white-sky) albedo can be derived through integration of the BRDF for the entire viewing and solar hemisphere (Strahler et al., 2003). Actual albedos under given illumination and atmospheric conditions can be estimated as a function of the diffuse skylight and a proportion between the black- and white-sky albedos. MODIS-derived products include white-sky albedos and black-sky albedos (at local solar noon) as both spectral and broadband quantities (Strahler et al., 2003).

Envisat's MERIS is a similar sensor to MODIS in terms of its spatial resolution, spectral characteristics in the visible to near-IR, and swath width. It can measure areally averaged spatial and temporal patterns of reflectance magnitude. Directional factors cannot, however, be derived from MERIS data alone in the way that they can from MODIS data, due to the limited observational frequency and angular range of the former. A possibility exists, though, to convert MERIS reflectances to usable albedos using directional factors derived from coincident MODIS or Terra MISR multi-angular observations.

New multi-angle spectro-radiometers such as the ASTER and MISR (Wanner et al., 1997) also show great potential as a means of deriving refined surface albedos by enabling a more complete characterization of the BRDF (Stroeve and Nolin, 2002). The key here is again improved information on the angular relationships to help account for anisotropic scattering effects from snow and ice, as well as more accurate correction for atmospheric effects. For the MISR as for the MODIS, the generation of the BRDF is a major element in the derivation of albedo as it quantitatively specifies the behavior of surface scattering as a function of viewing and illumination angles at a given wavelength (Li, 2000; Warren et al., 1998). See Diner et al. (1999b) for information on the theoretical basis of the MISR albedo algorithm. Information on MISR cloud detection and classification methods is given by Diner et al. (1999c). See Chapter 3 of Volume 2 of this book for further discussion of albedo measurement by MISR.

Adopting a different approach, Lindsay (2001a) inferred Arctic sea ice albedo from thin-ice thickness measurements derived from Radarsat ScanSAR data processed by the RGPS (as discussed earlier). This was achieved by parameterizing the albedo based on ice thickness for first-year ice (following Ebert and Curry, 1993), and using the snow depth climatology of Warren et al. (1999). Results are shown in Figure 5.116. The largest error source here was the rate of snow accumulation on new ice. Barber et al. (1998b) also examined the prediction of shortwave albedo from σ^0, exploiting regression analysis between Arctic multiyear ice σ^0 and albedo. Further work by Hanesiak et al. (2001), in the Canadian Arctic, demonstrated that the inversion of surface albedo from Radarsat-1 SAR imagery over smooth first-year ice is possible throughout the melt season. The same authors then ingested the SAR-derived surface albedo into a thermodynamic sea ice model to improve sea ice simulations and to better predict the timing of the seasonal breakup of first-year ice.

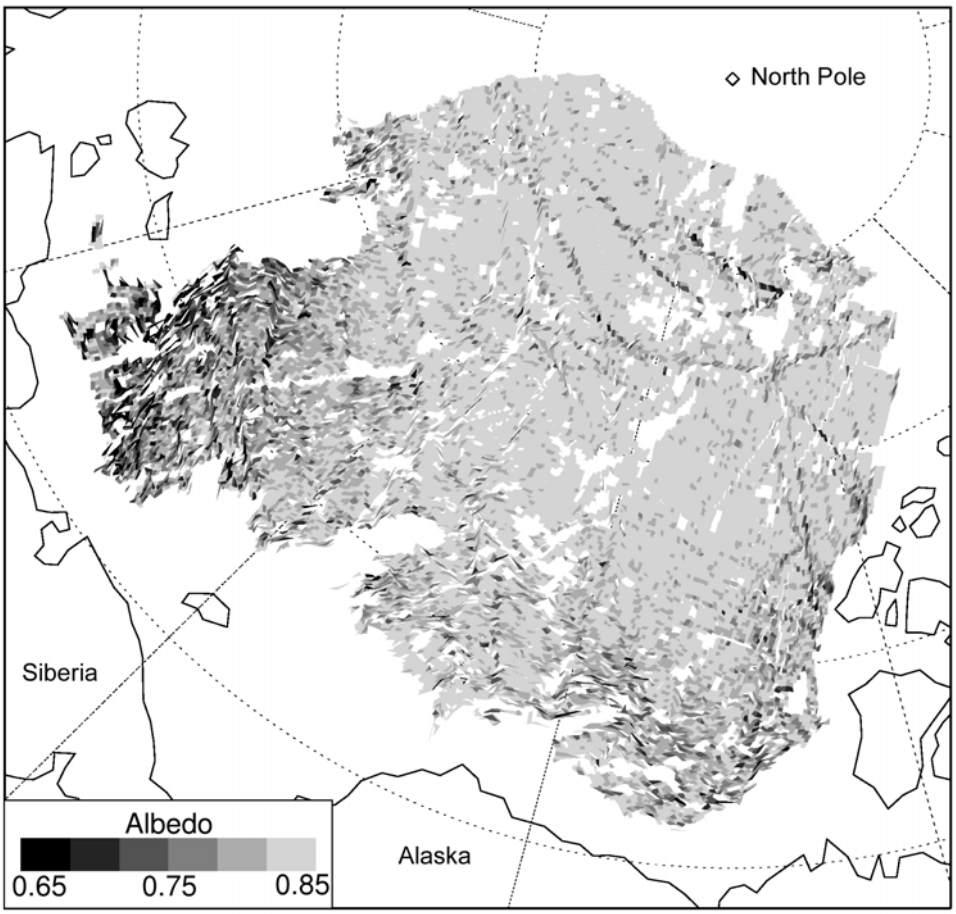

Figure 5.116. Map of the mean surface albedo for each RGPS cell for the Beaufort and Chukchi Seas (Arctic Ocean), April 20, 1997. The positions of the points are final locations after 160 days of drift (tracking), and 25,000 cells are plotted. The mean albedo was 0.79 (standard deviation 0.04).

From Lindsay (2001a). Reprinted with permission of the International Glaciological Society (IGS). © 2005 IGS.

Using a different approach again, Fetterer and Untersteiner (1998a) made estimates of Arctic sea ice surface albedo in summer from estimates of the aerial coverage of meltponds derived from uncalibrated, high-resolution, classified National Technical Means (NTM) satellite visible data. These data were collected at 1-m resolution, over a narrow (10 km) swath. Based upon Langleben (1971), they used a simple linear relationship between pond area and albedo, expressed as:

$$\text{Albedo} = 0.56 - (0.56 - 0.22)P \tag{5.91}$$

where P is the percentage coverage of ponds, 0.56 is the average albedo of melting old ice, and 0.22 is an average meltpond albedo. These are band-integrated values

(0.4 to 1.0 μm) for clear-sky conditions, taken from Grenfell and Maykut (1977). Errors in estimates of floe albedo are compounded by errors in assumed ice and pond albedo plus errors in estimates of pond coverage (Fetterer and Untersteiner, 1998a). For example, pond albedo can vary with the cyclical freeze–thaw patterns that can occur. Previous discussion has stressed the importance of meltpond formation and evolution in the Arctic surface energy budget in summer (Eicken et al., 2001a; Morassutti and LeDrew, 1996; Romanov, 1992). Recent observations are of a seasonal reduction in large-scale ice albedo from >0.8 to <0.55 which is largely driven by meltpond formation—i.e., the albedo of bare ice and open water remains relatively stable throughout summer (Eicken et al., 2001a). Furthermore, the seasonal evolution of ice albedo is intimately linked to changes in ice hydrology, with meltpond depth and coverage changing in response to changes in ice permeability (Eicken et al., 2001a). Such methods show promise, and could be extended using ultra-high-resolution data from new commercial satellites such as Ikonos and QuickBird. Once again, these data are limited to very-narrow-swath coverage. Note that meltponds are discussed further in Section 5.9.15.

5.9.14 Snow surface grain size and impurities

In the previous section and Section 5.7.2, we saw how snow surface grain size and the mass fraction of impurities in the snow have a first-order effect on the surface broadband albedo (Warren, 1982; Warren and Clarke, 1986). The larger the snow grain size and the mass fraction of impurities, the lower the albedos in the near-IR and visible regions, respectively (Warren and Wiscombe, 1980; Wiscombe and Warren, 1980). Surface grain size also provides proxy information on the physical and thermal characteritics of the surface. Specifically, current techniques use a radiative transfer model to relate imaging spectrometer data collected at a strong ice absorption feature centered at $\lambda = 1.03\,\mu m$ (see Section 5.7.1) to the optically equivalent grain size.

Snow surface grain size and impurities were measured operationally, and globally every 4 to 16 days, for the first time from space using the GLI onboard ADEOS-II (from 2002–2003) (Nakajima et al., 1998). The algorithm used (CTSK2b1) is described in Hori et al. (2001) and Stamnes (1999b). It uses reflectance values from two channels, in the visible (0.460 μm) and near-IR (0.865 μm)—the first sensitive to the mass fraction of impurities and the second to the effect of snow grain size on albedo. For a given sensor FOV, satellite-observed reflectances are compared with simulated reflectances calculated as functions of various mass fractions of snow impurities—nine classes from 0.02 to 2.5 parts per million by weight (p.p.m.w.)—and snow grain sizes—six classes from 50 to 2,000 μm—using a bilinear interpolation scheme. These were calculated with the radiative transfer model based on the DISORT multiple scattering algorithm which accounts for the BRDF of the snow surface (Stamnes et al., 1988), and stored in lookup tables. This simulates the actual reflectance properties of the snow surface. Corrections are made for atmospheric and aerosol effects. By this method, the combination of both snow parameters is determined that provides reflectances closest to those observed.

As grain size retrieval is based on Mie scattering theory—i.e., snow cover composed of spherical ice particles—the retrieved surface grain size refers to optically equivalent spherical grain radius (in μm) rather than physical grain size (Nussenzveig and Wiscombe, 1980; Wiscombe, 1980). The impurity product is defined as the mass fraction of impurities optically equivalent to carbon soot in p.p.m.w. Results are shown in Figure 5.117 (see color section). Error sources include uncertainties in atmospheric and aerosol corrections, the presence of subpixel-scale clouds and incomplete cloud masking, and incomplete knowledge of surface roughness and the BRDF (see Warren et al., 1998). Another ambiguity arises from the fact that natural snow grains are seldom spherical. Moreover, work by Aoki et al. (2000) suggested that the optically equivalent grain size providing the simulated snow albedo best matched to the observed albedo is closer to the narrower dimension of broken crystals and the branch width of new-snow dendrites rather than the physical size of each crystal. It should be noted that the crystal shape and size of new snow depends upon the atmospheric conditions during snowfall, and that subsequent eolian redistribution plays a major role in mechanically breaking down and altering the crystal structure of the surface snow cover (Massom et al., 2001a; Sturm et al., 1998). In spite of these limitations, reasonable results have been achieved (Hori et al., 2001).

5.9.15 Detection of ice/snow melt and refreezing

Over Arctic sea ice, the seasonal transition from a highly reflective dry snow cover to an absorptive wet snow cover, and the subsequent evolution of the surface composition, plays an important role in the temperature–melt–albedo feedback mechanism (Perovich, 2003). Melting snow decreases the surface albedo, leading to additional energy absorption, warmer air temperatures, and consequently additional snow melt (Curry et al., 2001). Different melt processes and patterns occur in Antarctica, with a lack of meltponds (see Section 5.6.1.3). Of major recent concern is uncertainty as to whether large-scale patterns of seasonal ice melt are changing, and whether the patterns contain any signals related to warming (Anderson and Drobot, 2001a; Drinkwater and Liu, 2000; Drobot and Anderson, 2001a). The regional-to-hemispheric patterns of ice decay and retreat are difficult to model accurately, again due to the complexity and temporal–regional variability of the processes involved and their intimate links to environmental conditions. In this section, we assess ways in which satellites are making a major contribution by enabling the detection and monitoring of:

- the timing and progression of annual surface melt onset;
- the timing and progression of the subsequent autumnal freezeup;
- from the above, the melt season length; and
- meltpond distribution.

Recalling Section 5.7.2, the appearance of water in snow cover does not have an effect on its reflectance *per se* in the optical region. It does, however, have a major

indirect impact by causing the grains to cluster, thereby increasing the effective snow grain size (Colbeck, 1979). This effect is greatest in the near-IR, and minimal at visible wavelengths (given the relative insensitivity of directional–hemispherical reflectance R_S at the latter to grain size). A number of studies have exploited the change in surface albedo related to surface melt in order to monitor the onset and progression of the latter across the Arctic Ocean in satellite broadband visible and near-IR data from the DMSP OLS and NOAA AVHRR (Robinson et al., 1992; Scharfen et al., 1987). Melt season duration plays a central role in the overall sea ice mass balance (Zhang et al., 2000). Sea ice ablation and meltpond formation can be detected as a decrease in reflectance at 0.6 to 0.8 μm, with a consistent decrease to ~1.6 μm. Working in the Canadian Arctic, De Abreu et al. (2001) found that a number of distinct melt stages—including winter, snow melt, ponding, drainage, and rotten ice—were of sufficient magnitude in their optical signatures that they could be detected in time series of AVHRR channel-1 and -2 TOA reflectances. According to Hyvärinen and Lammasniemi (1987), the potential exists to further exploit new high-spectral-resolution reflectance measurements collected at 1.03, 1.26, and 1.37 μm, such as those from hyperspectral sensors and spectrometers like Hyperion and MODIS, to detect the presence of liquid water. The need for cloud-free conditions is a major restrictive factor for optical methods, given the general increase in high-latitude cloudiness in spring–summer. More effective are time series of satellite microwave data, both active and passive, as discussed below, although these cannot detect all stages of seasonal melt (De Abreu et al., 2001). Having said this, correlations between melt/refreeze reflectance and microwave signatures suggest that combining the different data may improve the information obtainable, given the complementary nature of the information.

5.9.15.1 Passive-microwave methods

In the Arctic, melt onset entails a key transitional stage in the energy balance, marking a major decline in surface albedo and an associated increase in surface energy. We saw in Section 5.7 how initial melt in the Arctic in late spring to summer leads to the sudden appearance of liquid water within the snow cover matrix, which is closely linked to air temperature. When snow contains ~3% liquid water by volume, it becomes opaque and the surface emissivity approaches unity—i.e., it acts radiometrically like a blackbody and there is a sudden increase in brightness temperature. This provides a means of detecting and mapping the onset and progression of annual surface melt on a basinwide scale using time series of daily satellite passive-microwave T_Bs (Anderson, 1987, 1997; Smith, 1998b). The abrupt increase in T_B associated with melt is frequency- and polarization-dependent. Lower frequency channels—e.g., 19.3 GHz for the SSM/I and 18.0 GHz for the SMMR—are more responsive to snowmelt onset than are higher frequencies—e.g., 37.0 GHz—due primarily to the change in emission depth associated with melt. Moreover, higher frequency data are more affected by atmospheric water vapor effects in summer.

Using the Advanced Horizontal Range Algorithm (AHRA), Anderson and Drobot (2002) calculated the melt onset date by monitoring the difference between the T_Bs at 18 GHz (SMMR) or 19 GHz (SSM/I) and 37 GHz, all at horizontal polarization (which is most sensitive to snow melt effects). This approach was also used by Forster et al. (2001). When melt occurs, this difference changes from positive to near-zero or negative. Passive-microwave-derived estimates of snow Melt Onset (MO) dates have been produced in this fashion over Arctic sea ice for the period 1979–1999 (Anderson and Drobot, 2001a; Drobot and Anderson, 2001a, b, c). #Figure 5.118# (see color section) presents a 20-year mean melt onset map derived from these data (Anderson and Drobot, 2002), together with maps of the standard deviation and melt onset trend. This shows a spatial melt pattern that is approximately radial in nature, beginning along the southern ice edges and progressing northward.

Strong regional differences are also apparent in MO variability over the 20-year period (Anderson and Drobot, 2001a, 2002). The range in MO at a given location (Figure 5.118), defined as the difference between the latest and earliest melt dates, follows a distinct geographic pattern. Although most locations in the Arctic Basin exhibit a range of 1–2 months, that in the more southerly latitudes—e.g., in Hudson Bay and along the continental coastlines—often exceeds 2 months. Anderson and Drobot (2002) suggested that the lower variability in the central Arctic implies that the annual MO date is predominantly determined by the springtime transition in incoming solar radiation, while the larger variability in marginal seas implies that synoptic atmospheric conditions play a more significant role in influencing the MO date. The one-standard deviation map (Figure 5.118b) displays a similar pattern to the range map. Further analysis revealed apparent trends towards an earlier MO in several Arctic regions (Anderson and Drobot, 2002). These patterns are consistent with trends towards warmer surface air temperatures and increased cloud cover noted in other analyses (Dickson, 1999; Rigor et al., 2000). Annual MO dates derived from these data, from 1979 and mapped to a polar stereographic grid at a 25-km resolution, are available from the NSIDC at ⟨*http://nsidc.org/data/nsidc-0105.html*⟩ (Anderson and Drobot, 2001b; Drobot and Anderson, 2001c, d). Value-added products derived from these data are also available, including mean MO date, latest (maximum) and earliest (minimum) MO dates, range of MO dates, standard deviation of MO date, and an MO date trend analysis. Little similar work has been carried out using these techniques in Antarctica.

Another significant change occurs in the observed T_B at the end of the melt season—i.e., in autumn—when freezing conditions dry the snow to significantly lower sea ice emissivity. This change, which is typically less abrupt than the seasonal melt onset, enables detection and mapping of the onset of seasonal refreezing and its progression in the satellite time series. This in turn allows estimates to be made of the Melt Season Length (MSL) at given locations. As with ice extent and ice season length, MSL exhibits considerable interannual variability. Smith (1998a) determined the onset of freeze-up from Nimbus-7 SMMR and DMSP SSM/I data (1979–1998) to be late August, giving a mean MSL of 75 days over a range of 57 days (1979) to 81 days (1998), and found a significant increasing trend of

5.3 days (8%) per decade in MSL over a large proportion of the perennial Arctic pack. Using the same, but shorter—i.e., 1979–1986—dataset, Parkinson (1992) noted a lengthening of the sea ice season in the western Arctic—similar to findings in IABP temperature data by Rigor et al. (2000)—but a shortening in the Eastern Hemisphere. Rigor et al. (2000) attributed these trends to changes in patterns of atmospheric circulation, including the AO (Maslanik et al., 1996; Thompson and Wallace, 1998; Walsh et al., 1996).

Belchansky et al. (2004b) investigated Arctic sea ice melt and freeze onset dates, and melt season durations, for the period 1979–2001, using coincident SSM/I and IABP surface air temperature data (Rigor et al., 2000) and SMMR- and SSM/I-derived ice concentration and T_B data. The melt algorithm used was an enhanced version of the AHRA. Hemispheric melt duration varied from a 104-day minimum in 1983 and 1996 to a 124-day maximum in 1989, with ranges in the duration being largest in peripheral seas. Melt behavior was found to be correlated with the seasonal strength of the AO. Following high-index AO winters (January–March), spring melt tended to be earlier and autumn freeze later, leading to longer melt season durations (Figure 5.119, see color section). The largest increases in melt duration were observed in the eastern Siberian Arctic, coincident with cyclonic low pressure and ice motion anomalies associated with high-index AO phases. Decreasing correlations between consecutive year maps of melt onset in annual ice during 1979–2001 indicated increasing spatial variability and unpredictability in melt distributions from one year to the next. Despite recent declines in the winter AO index, recent melt distributions did not show evidence of re-establishing spatial patterns similar to those observed during the 1979–1988 low-index AO period. Recent freeze distributions have become increasingly similar to those observed during 1979–1988, suggesting a recurrent spatial pattern of freeze chronology under low-index AO conditions. Relationships between changes in Arctic mean melt onset, freeze onset, melt season, and anomalies in atmospheric circulation are illustrated in Figure 5.120 (see color section). This shows that the 1979–1988 low-index AO period was characterized by dominant anticyclonic conditions, which correspond to less variable melt durations in both annual and perennial ice. This example again illustrates the benefits of combining datasets to gain a better understanding of the complex interactions between sea ice and the climate system.

Enomoto et al. (2002) combined satellite (passive-microwave and ADEOS AVNIR visible), meteorological, and *in situ* observations to analyze interannual variability in patterns of surface melt and breakup of multiyear fast ice in Lützow-Holm Bay, East Antarctica. While individual melt features were resolved in the AVNIR imagery, the authors used the gradient ratio of the H-polarization 18-/19-GHz and 37-GHz channels of the SMMR and SSM/I to detect the melt duration in summer from 1978/9 to 1998/9. Enomoto et al. (2002) highlighted a number of strong relationships, including long melting periods prior to large breakups. Given the narrow coastal extent of fast ice, such studies will benefit from improved higher resolution data from the AMSR and future passive-microwave sensors.

5.9.15.2 SAR methods

Unfortunately, passive-microwave techniques are prone to contamination by atmospheric water vapor effects in summer, particularly at shorter wavelengths (frequencies of $\geq$37 GHz). Satellite microwave radar data from both SAR and scatterometer systems provide a viable alternative for melt detection, yielding complementary results that are less prone to atmospheric water vapor contamination effects in summer. Again referring back to Section 5.7, the appearance of even a small amount of free water (>3% by volume) in the snow cover leads to high dielectric loss, thereby increasing the snow absorption coefficient and dramatically affecting its reflectivity (Beavan and Gogineni, 1994; Onstott and Gogineni, 1985; Rott et al., 1988). This has the net effect of causing an abrupt decrease in σ^0 (Barber et al., 1998a; Onstott, 1992; Shokr and Barber, 1994)—e.g., of 4–6 dB for ERS C-band VV-polarization data (Winebrenner et al., 1994)—to enable MO detection and large-scale mapping of its progression. Jeffries et al. (1997b) observed a close correlation between large-scale sea ice backscatter behavior and air temperature in the Arctic Ocean from spring to autumn. Given this sensitivity, variability in freeze-up onset and length of the annual melt season may also be a bellwether of climate change/variability. A review of the effects of both melt and freeze-up processes on microwave signatures is given by Gogineni et al. (1992).

As noted earlier, the onset of melt transforms the snow into an opaque filter to microwaves to effectively mask the volume-scattering signature of the underlying sea ice. As a result, the melt onset signature tends to be stronger for Arctic multiyear than first-year ice, due to the greater effective contrast with the pre-melt signature for the former (Winebrenner et al., 1998). Winebrenner et al. (1998) suggested that improved estimates of snow melt extent on Arctic first-year ice should be possible using shorter wavelength (higher frequency) measurements from radar scatterometers operating at Ku-band—e.g., 14.6 GHz for the Seasat SASS and 14.0 GHz for ADEOS NSCAT.

Changes related to the subsequent autumnal freeze-up of ice surviving the summer melt can similarly be detected via their impact on surface dielectric and scattering properties (Carsey, 1985; Gogineni et al., 1992; Winebrenner et al., 1996). Winebrenner et al. (1996) also showed that a recovery of σ^0 to its pre-melt value (approximately -9 dB) occurred in ERS-1 data within a week of continuously sub-freezing air temperatures. Other studies using ERS-1 SAR data to examine the onset of freeze-up include that of Schwartz et al. (1994). As such, SAR (and scatterometer) data are well-suited to the measurement of MSL and its variability at given locations.

Once again, the advent of ScanSAR technology has made a major contribution by enabling wider coverage and more effective monitoring. Work by De Abreu et al. (2001) found Radarsat-1 ScanSAR data to be an effective means of identifying the "winter" and snowmelt stages of melt in the Canadian Arctic. The meltponding stage, on the other hand, is more susceptible to misidentification due to the high sensitivity of observed water backscatter to wind-induced roughness. Hanesiak et al. (2001) further integrated Radarsat-derived meltpond information

with a thermodynamic sea ice model to show the key effect of meltponding on the seasonal ablation and breakup of first-year ice in the Canadian Arctic.

Routine estimates of the dates of autumn freeze-up and spring melt over the entire Arctic Ocean Basin are now derived from time series of calibrated 100-m-resolution Radarsat-1 ScanSAR C-band (HH-pol) data processed by the RGPS (Kwok et al., 1999a, b). This is achieved through the detection of significant changes in the evolving radar backscatter record stored within each 10×10-km Lagrangian grid cell (Winebrenner et al., 1998). Kwok et al. (2003b) created melt onset maps of the entire Arctic sea ice zone using Radarsat-1 data. The same work found that the melt signal in RGPS data is also clearly detectable in backscatter changes not only over multiyear but also first-year ice, and mixtures of the two. Comparison with temperature data from IABP buoys showed that the melt onset timing estimated from the RGPS data was within 1–2 days of the timing of the zero-degree crossing of surface air temperature records. Further comparison of these results with passive-microwave data revealed that onset date estimates using the latter appear to be biased towards a later stage of melt. Repeat coverage is on a 3-day basis in the central Arctic with RGPS. Beyond this, coverage is limited by the narrow swath of SARs compared with alternative methods using radar scatterometers (see below). This is a major limitation to large-scale systematic coverage of Antarctica.

5.9.15.3 Radar scatterometer techniques

Although their spatial resolution is significantly lower than that of SARs, radar scatterometers are better suited to studies of the regional to hemispheric patterns of melt/freezeup and seasonal transitions in these patterns (Cavanié, 1998; Drinkwater and Carsey, 1991; Forster et al., 2001; Long and Drinkwater, 1999; Winebrenner et al., 1998). Their strength lies in their large-scale coverage (over a wide swath), day–night and all-weather operation, routine availability, and long time series (see Section 5.8.2.2). At the start of the melt season, the mean 40° incidence-angle-normalized backscatter coefficient σ^0 (σ^0_{40}) derived from ERS-1/-2 and ADEOS (NSCAT) scatterometer data is highly sensitive to abrupt changes in surface reflectivity related to the appearance of freewater in snow cover. As with the SAR techniques above, the subsequent autumnal freeze-up is also apparent as an abrupt increase in σ^0_{40}, enabling estimation of MSL. This application is once again greatly facilitated by the availability of enhanced resolution scatterometer data (see Section 5.8.2.2).

Drinkwater and Liu (2000) used time series of σ^0_{40} data from ERS and NSCAT to detect large-scale patterns of Antarctic sea ice surface melt and characterize its spatial and temporal variability. In their study, they combined collocated scatterometer data with Radarsat SAR and DMSP SSM/I data to determine the effects of the Antarctic surface melt progression on measured values of σ^0 and T_B, respectively. They developed a technique to map interannual variations in the circumpolar onset of the summer melt season and the cumulative number of melt days, applying it to data from 1992–1998. An example, showing results from both

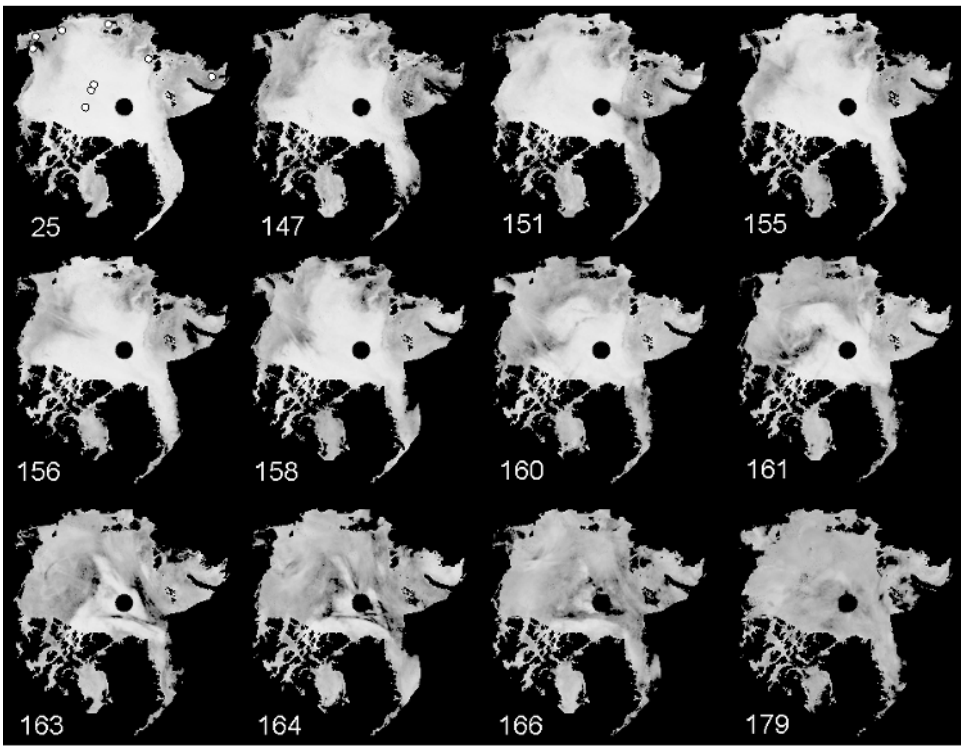

Figure 5.122. A time series of daily images of ADEOS NSCAT σ^0_{40} data of the Arctic sea ice cover acquired through the spring of 1997, clearly showing the spatio-temporal decrease in normalized backscatter with the progression of snowmelt onset. The numbers signify days of the year.

From Forster et al. (2001). Reprinted with permission of the International Glaciological Society (IGS). © 2005 IGS.

polar regions, is given in Figure 5.121 (see color section). These results indicate that the seasonal surface melt of Antarctic sea ice is relatively short-lived compared with the Arctic. In an earlier ERS study, Drinkwater et al. (1994) noted that freeze-up was characterized by only a slight decrease in σ^0_{40}, but a pronounced change in the gradient of backscattering with incidence angle B (see Section 5.8.2.2).

Forster et al. (2001) developed an Arctic melt detection algorithm using a smoothed derivative of NSCAT Ku-band σ^0_{40} data (VV-pol) with a minimum threshold to capture the spatio-temporal characteristics of the abrupt decrease in backscatter associated with the onset of melt. Following Drinkwater (1998a), this approach is used to minimize the problem of large differences between the initial backscatter values of Arctic first-year and multiyear ice. Time series of daily images such as those in Figure 5.122 show the dramatic and spatially cohesive nature of the springtime transformation over the entire Arctic sea ice cover. The map of snowmelt onset dates derived from these 1997 data is given in Figure 5.123, and shows that the occurence of the absolute timing of melt is mostly between days 140 and 173 and is

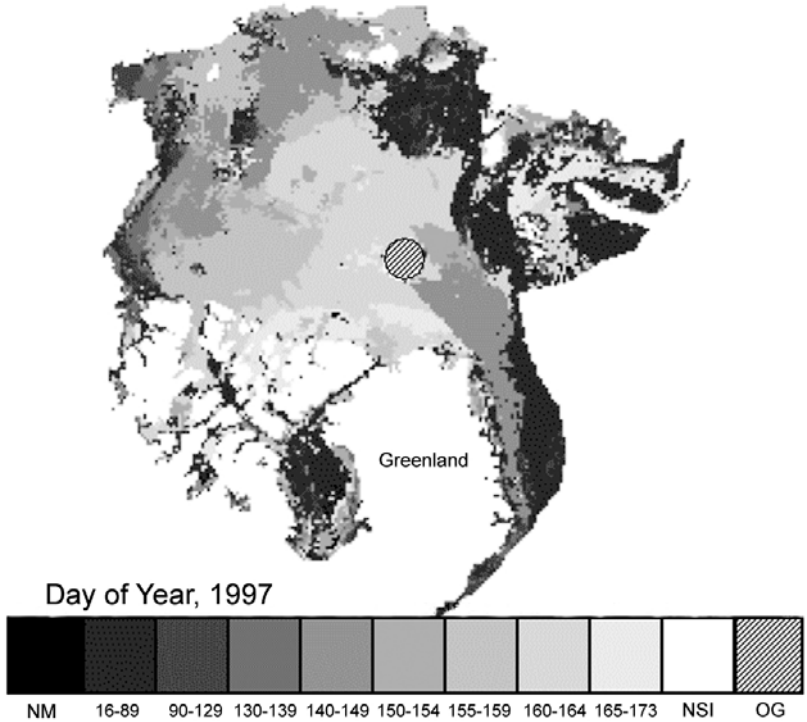

Figure 5.123. A map of NSCAT-derived melt onset dates across the Arctic sea ice zone in 2001, derived from the algorithm of Drinkwater (1998a) and Forster et al. (2001).

NM = no melt, NSI = no sea ice, and OG = orbital gap. From Forster et al. (2001). Reprinted with permission of the International Glaciological Society (IGS). © 2005 IGS.

reasonable. An AHRA-derived map of contemporary SSM/I melt onset timing showed similar trends, but melt occurred 1–10 days earlier in most locations in the NSCAT estimates. Forster et al. (2001) attributed this to differences in both the response of the passive and active systems and the assumptions inherent to the algorithms regarding the speed of melt and occurrence of post-melt freeze/thaw cycles.

The NSCAT algorithm has some difficulty in detecting melt onset dates for some Arctic first-year sea ice zones, due to their low pre-melt (initial) backscatter. Frey et al. (2003) further assessed this approach, using near-daily time series of σ^0_{40} data from ERS-1 to analyze local and regional patterns in, and controls on, the formation, melt onset, and decay of coastal first-year ice in the Eurasian Arctic from 1991 to 1999. They again concluded that this technique is again most effectively applied to regions of Arctic multiyear ice, where melt onset is detected as a sudden decrease in backscatter (Forster et al., 2001; Long and Drinkwater, 1999; Winebrenner et al., 1994, 1998; Yueh and Kwok, 1998) whereas an increase in backscatter can occur on first-year ice (Forster et al., 2001). In an attempt to overcome this source of ambiguity, Frey et al. (2003) exploited the backscatter–incidence angle relationship B to discriminate the presence of first-year ice, an

approach also used by Grandell et al. (1999) and Remund et al. (2000). By this method, Frey et al. (2003) were able to determine strong regional patterns in both the seasonal duration of the ice melt season and the date of melt onset, with a maximum in the Barents and Kara Seas and decreasing with distance eastwards. They concluded that inflowing rivers exert a considerable influence, with earlier formation (by about 4 days) and melt (by about 17 days) in sea ice adjacent to river mouths.

Encouragingly, comparable and complementary results have emerged using the different data sources/techniques outlined above, lending confidence to the techniques (many of which are new or emerging). Frey et al. (2003) found that annual melt onset typically occurs in June. Using ERS-1 SAR data for 1992, Winebrenner et al. (1994) found that melt advanced northwards across the Beaufort Sea over a 1-week period in mid-June. Similar results were attained by Yueh and Kwok (1998) using NSCAT data. In their analysis of snow melt progression via the albedo change detected in cloud-free DMSP OLS visible to near-IR channel data (1975–1988), Robinson et al. (1992) found that melt begins in the Chukchi and Beaufort Seas in late May and in the East Siberian and Laptev Seas in mid-June, before advancing to the central Arctic by late June. Smith (1998a) observed similar patterns in SMMR and SSM/I time series (1979–1996). Such findings show close correspondence with melt observations inferred from temperature data from the IABP (Rigor et al., 2000).

Challenges and uncertainties remain, however, not least due to our limited understanding of the physics underlying the observations (Winebrenner et al., 1998). This is particularly true in Antarctica. Issues remain regarding the probable impact of flooding related to snow loading on melt detection accuracy using microwave techniques (both active and passive). Working in the Weddell Sea, Drinkwater and Lytle (1997) noted that the saline slush comprised a layer characterized by high permittivity and enhanced values of σ^0_{40} (VV-pol) measured by the ERS-1 scatterometer. If such signatures can be unambiguously separated from those due to melt, then satellite microwave sensors may provide an invaluable means of mapping the distribution of surface flooding, leading to improved estimates of the overall contribution of snow/ice formation to the mass balance of Antarctic sea ice. Clearly, such work would benefit from the incorporation of additional information—e.g., from meteorological analyses. Another interesting and poorly understood factor is that ephemeral melt can even occur in winter in Antarctica, related to synoptic-scale incursions of midlatitude warm air across the sea ice zone (Massom et al., 1997). This could again possibly be detected in scatterometer time series, given their excellent temporal resolution.

5.9.15.4 Meltpond distribution

Meltponds play a key role in the energy balance of the Arctic Ocean in summer. They significantly reduce the albedo to increase the amount of solar radiation absorbed by the ice and accelerate seasonal sea ice melt. While programs such as SHEBA (Perovich et al., 1999a, b) have made a major contribution towards improving our understanding of meltpond formation and evolution (Eicken et al.,

2001a; Morassutti and LeDrew, 1996), information on the large-scale areal coverage of meltponds is required to understand the large-scale surface energy balance in summer—a critical need in the light of recent observations of change outlined in Section 5.5. This is again a challenging proposition, given that although meltponds cover extensive areas overall, they individually comprise fine-scale features some meters to tens of meters across. As such, they are largely unresolved by medium- to coarse-resolution satellite sensors. Aerial surveys have made a telling contribution (El Naggar et al., 1998; Perovich et al., 2002a; Tschudi et al., 1997, 2001), but are spatially and temporally limited. In response to this need, and in order to extend the SHEBA surface measurements, Fetterer and Untersteiner (1998a, b) used high-resolution ($\sim$1 m, scene 14×40 km) de-classified U.S. military reconnaissance (National Technical Means, NTM) satellite optical imagery to develop a dataset of meltpond statistics in the Beaufort Sea sector of the Arctic Ocean (Figure 5.124). Dataset details are given by Fetterer (2004). Further work on subsequent imagery developed a supervised maximum-likelihood classification scheme to detect individual ponds, using GIS software (NSIDC, 2000). The high-resolution satellite imagery was used to produce 10-km $\times$ 10-km surface-type maps (images in which pixels are classed as open water, ice, or pond), accompanying tables of pond statistics for cloud-free 500-m $\times$ 500-m cells, and files of pond sizes in each individual cell (see Figure 5.124d–e). Pond statistics—i.e., the number of ponds, percentage of area covered by ponds, and size of ponds—were computed for each cell. Resultant files were manually edited to remove spurious or cloud-contaminated cells. By this technique, pond coverage was estimated to range from 15% at freeze-up to 30–40% at the start of melt. Fetterer and Untersteiner (1998b) estimated errors in the estimate of pond coverage to be 5% absolute, resulting from the presence of unresolved ponds and overlap in class distributions. Using data such as these, it is in principle possible to improve the parameterization of regional Arctic sea ice albedo in summer in GCMs. These models typically do not treat the effect of meltpond formation and variability on albedo specifically. Instead, they tend to parameterize albedo over sea ice as a function of ice surface temperature and snow accumulation (Barry, 1996; Curry et al., 2001). SHEBA Reconnaissance Imagery are available for the period August 1997 to September 1998 from ⟨*http://nsidc.org/data/sheba_ntm/imagery.html*⟩ (NSIDC, 2000).

We saw earlier how ponding also reduces the accuracy of Arctic sea ice geophysical parameter products retrieved from satellite microwave data in summer. Passive-microwave ice concentration techniques cannot, for example, differentiate between ponds and true open water, leading to substantial errors in estimates of ice concentration (Cavalieri et al., 1984; Fetterer and Untersteiner, 1998b). Fetterer and Untersteiner (1998b), however, argued that accurate knowledge of meltpond fraction derived from NTM imagery may be used to reclassify the ponded ice area and lead to more accurate determinations of ice concentrations in summer. Similarly, Markus and Dokken (2002) developed a technique using Landsat 7 ETM+ spectral information to classify summer Arctic sea ice characteristics, including the open water fraction, white (snow-covered) ice, wet ice, and meltponds. Markus et al. (2002) refined this technique in a study in

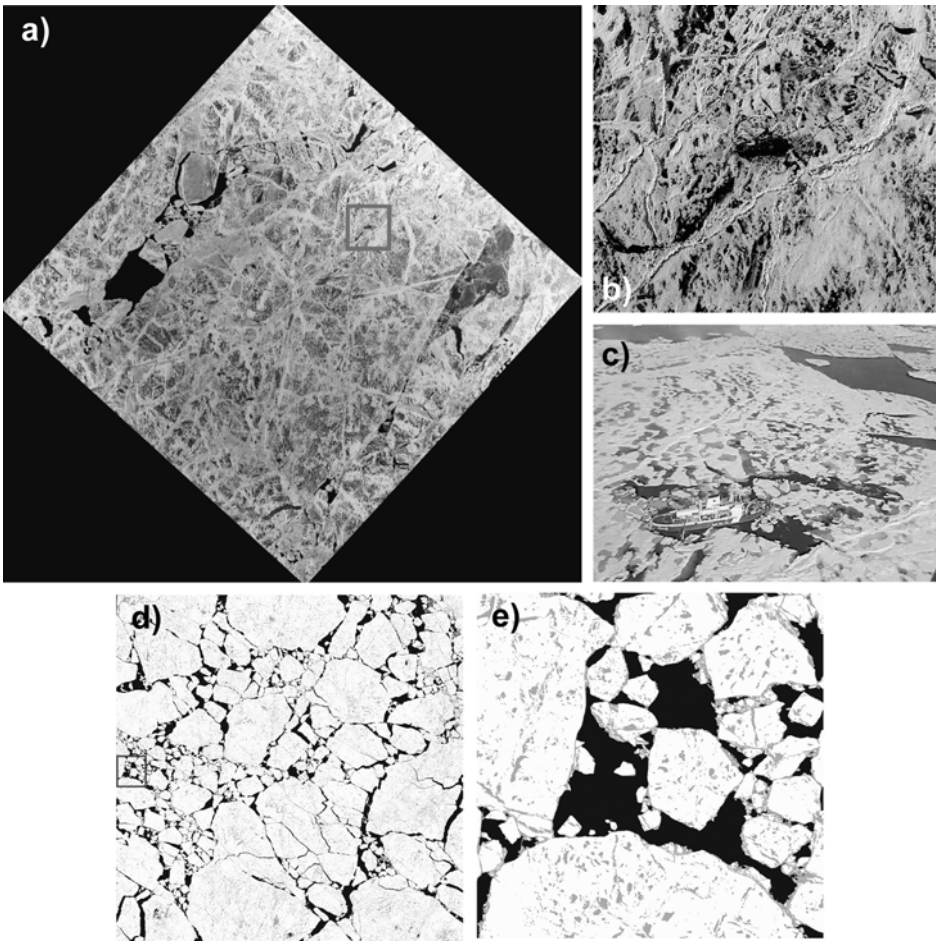

Figure 5.124. (a) U.S. military reconnaissance satellite image of sea ice in the Arctic Ocean from June 18, 1998 (the image strip is ~7.8 km across). The square marks the location of the Canadian icebreaker *CCGS Des Groseilliers* (length ~100 m). (b) A close-up view of the square. The ship is ~100 m long, and the dark regions are meltponds, as shown in the oblique aerial photograph from August 3, 1998 in (c). (d) Detail of a surface-type map. The image at upper right shows the 10-km^2 surface-type product. Open water is dark, ice is light, and ponds are gray. (e) Image of an area corresponding to the box in (d) and showing a higher level of detail, with meltponds clearly visible.

Parts (a)–(c) courtesy of Sylvie Lemelin (Canadian Coast Guard), from ⟨*http://nsidc.org/data/sheba_ntm/imagery.html*⟩. Parts (d) and (e) after Fetterer (2004), imagery courtesy of Florence Fetterer and Nancy Geiger Wooten (NSIDC).

Baffin Bay. They found that many meltponds were smaller than a Landsat pixel (resolution of 30 m), and that the Landsat classification scheme therefore underestimated meltpond fraction. With the aid of airborne high-resolution video images, they developed a technique to more accurately calculate the fractions of

open water, unponded ice, and ponded or wet ice from satellite data (Figure 5.125, see color section). A study by Markus et al. (2003) followed this up; a schematic of their Landsat analysis method is shown in Figure 5.126. It may be that ultra-high-resolution data from commercial satellites such as Ikonos and Quickbird can make a contribution under cloud-free conditions, although they are collected over a very narrow swath (~10–20 km) and large-scale coverage would be expensive.

Tschudi et al. (2005) further demonstrated how spectral radiance observations from the MODIS sensors onboard EOS Aqua and Terra can be used to estimate Arctic meltpond fraction and characterize its evolution. In particular, they used the MOD09 product from the MODIS Land Group dataset. This is an estimate of surface reflectance for several MODIS bands, produced by applying MODIS-derived corrections for atmospheric gases, water vapor, and aerosols together with

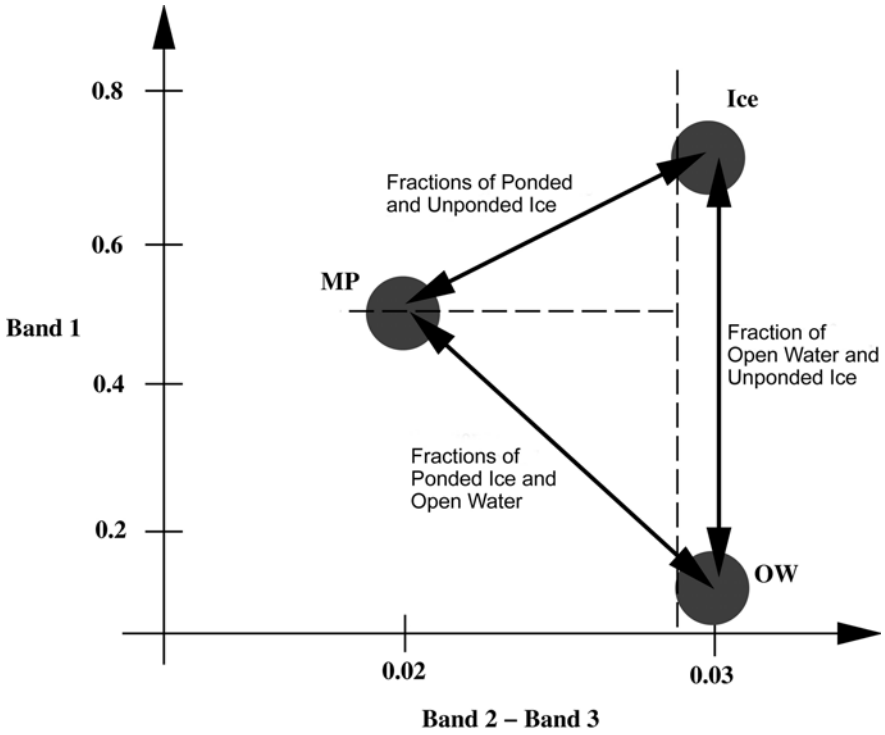

Figure 5.126. Schematic of the Landsat analysis method to derive the meltpond fraction of Arctic sea ice from Landsat ETM+ band-1 (0.450–0.515 μm), -2 (0.525–0.605 μm), and -3 (0.630–0.690 μm) data, at a spatial resolution of 30 m. Gray circles indicate the tiepoints, determined by comparison with coincident digital video data, for open water (OW), ice (Ice), and ponded ice (MP). The domain is divided into three regions (separated by dashed lines) that are analyzed separately. Fractions for each surface type are calculated by the relative distance between tiepoints.

From Markus et al. (2003). Reprinted with permission from Elsevier Publishing.

BRDF and cirrus clouds (Vermote and Vermeulen, 1999). Meltpond fraction is derived from the relationship:

$$\left[\sum a_i \alpha_i = \mathrm{R}\right]_j, \sum a_i = 1 \tag{5.92}$$

where R is the reflectance value for each MODIS pixel over band j; a_i is the area covered by meltponds, bare ice, or open water ($i = 1$, 2, or 3); and α_i is the reflectance for each surface type over band j. Tschudi et al. (2005) solve (5.92) for a_i using reflectance values for the different surface types measured *in situ* (Perovich et al., 2001), and the MODIS-derived reflectance R, to derive a unique meltpond fractional coverage per pixel. Results were compared with meltpond-areal fractions estimated from coincident digital photographs acquired by Aerosonde UAVs. While some discrepancies occur, there is general agreement between the two mean coverage estimates.

Jeffries et al. (1997b) adopted a different approach again. They developed a model to calculate meltpond fraction on Arctic Ocean multiyear ice using ERS C-band (VV-pol) SAR backscatter variability. This is based upon the assumptions that meltpond backscatter remains relatively stable and that bare ice has a constant and strong backscatter coefficient throughout summer. From this analysis, they estimated that the derived meltpond fraction varied between 60% early in the pond season to 10% at the end of summer. The uncertainty remains high, however, and further development is necessary—e.g., to better understand and model observed variability in summer backscatter. Earlier work by Holt and Digby (1985) showed that meltpond drainage in late summer leads to a granular and highly porous ice surface, resulting in an increase in radar backscatter that can be detected in time series of satellite SAR data. Radarsat data processed by the RGPS would be useful in this respect when combined with large-scale satellite-derived albedo data, given the importance of meltpond drainage in the seasonal evolution of Arctic sea ice albedo (Eicken et al., 2001a). This also gives information on the timing of pulses of freshwater entering the upper ocean—another important variable that may exhibit substantial interannual variability in response to changing climatological conditions.

The upcoming ESA Soil Moisture and Ocean Salinity mission (SMOS) L-band passive-microwave sensor is sensitive to ocean salinity. As such, it has the potential to distinguish between Arctic meltponds and the higher salinity seawater between floes, albeit at a poor spatial resolution of 50 km. This could prove useful in helping to improve Arctic sea ice concentration retrievals from SSM/I and AMSR(-E) data during the summer melt season, when ice concentration can be underestimated by up to 20% due to the presence of meltponds (Section 5.9.1). Further work is required to investigate the emissivity of sea ice at L-band under various weather and seasonal conditions as a function of both sea ice and sensor parameters. Additional information on the radiative and microwave scattering properties of meltponds is given by Barber and Yackel (1999).

5.9.16 Wave–ice interaction, and ice edge processes

Ice edge regions, or Marginal Ice Zones (MIZs), in which the ice cover interacts with the open ocean and wave–ice interaction is a dominant process, are important on a number of levels (Squire, 1998). The location and characteristics of these complex zones exhibit considerable variability, on synoptic through seasonal to interannual scales. They are characterized by intense ice–ocean–atmosphere interactions and at times enhanced biological activity—e.g., ice edge phytoplankton blooms—which are again highly variable. On the mesoscale, these interactions are associated with horizontal processes which transport ice or water masses across oceanic frontal zones, which are often associated with eddy activity (Johannessen et al., 1992, 1998). Indeed, MIZs impact regional oceanic and atmospheric circulation patterns, affecting the genesis of local and regional weather patterns (Overland and Pease, 1982).

Surface waves propagating into a sea ice cover from the open ocean, or from within extensive areas of open water within the pack—e.g., large leads and polynyas—have a major direct impact on the ice through the transfer of momentum and energy, and an indirect impact on surface energy budget. This can cause ice motion, compression (deformation and thickening), breakup due to floe collisions and flexing to play a fundamental role in determining floe size distribution (Wadhams, 1986). Indeed, waves play a central role in the formation, evolution, concentration, and destruction of sea ice over vast areas of the outer pack, or MIZ, yet are typically neglected in coupled sea ice models and GCMs. Under freezing conditions, they create a turbulent environment suitable for rapid pancake ice formation (Lange et al., 1989; Shen et al., 2001), leading to rapid ice edge advance in Antarctica in particular (Massom, 1992). Wave overwashing of floes can also lead to snow removal and ice surface wetting and salination (Massom et al., 2001a). This also has a first-order impact on the surface microwave signature, leading to a significant underestimate of ice concentration derived from satellite passive-microwave data (Massom et al., 1999). In summer, surface wetting and wave-induced floe breakdown play a major role in seasonal ice meltback by enhancing surface and lateral melt, respectively (see Section 5.6.1.3). Waves also affect the formation and dynamics of ice edge bands and the location and characteristics of the ice edge (Wadhams, 1986). Ice banding and streamer formation have been examined in Antarctica by Ishida et al. (1999) using Marine Observation Satellite (MOS)-1/-1b Multispectral Electronic Self-Scanning Radiometer (MESSR) data (resolution $\sim$50 m, scene dimension 100×100 km) received at Syowa Station. Launched in February 1990, the MOS-1b MESSR operated in four spectral bands (0.51–0.59, 0.61–0.69, 0.72–0.80, and 0.80–1.10 μm), with a revisit interval of 17 days. In addition, waves play a major role in the breakup of fast ice, particularly in summer when the protective pack ice has diminished (Chung and Fox, 2001; Langhorne et al., 2001; Squire et al., 1995).

Complex feedback interactions occur between ice covers and penetrating ocean swell fields. As swell propagates into the sea ice zone, the higher frequencies are attenuated by stress and friction from the ice, while lower frequency components

penetrate for distances which are directly proportional to the decrease in frequency and until they are damped to the stage where they have little effect (Wadhams, 1986; Wadhams et al., 1988). Through scattering the energy of incoming waves, the MIZ effectively shields the interior pack ice regions. Wave/swell propagation affects, and is affected by, the concentration and thickness and floe-size distributions of the ice cover (Squire and Dixon, 2003; Wadhams et al., 1988). In general, the feedback nature of wave–ice interaction in the MIZ manifests itself as a simultaneous lengthening of both the mean floe size and the dominant ocean wave length with increasing distance from the open ocean (Fox and Haskell, 2001). Although wave–ice interaction processes are largely concentrated in the outer 50–200 km of the pack—i.e., within the MIZ—swell can at times propagate vast distances into the interior pack and beyond. One such instance, reported by Squire et al. (1986) and analyzed by Liu and Mollo-Christensen (1988), greatly changed the surface roughness, wetness, and floe size characteristics over a wide swath of the eastern Weddell Sea in winter as far south as ~560 km from the ice edge. In this example, wave amplitudes and periods of ~1 m and 18 s, respectively, were observed in 90–100% concentrations of highly deformed, thick first-year ice. The anomalously low wavelengths were observed to lengthen with progressive ice deformation and breakup, before approaching values more typically observed in a uniform ice cover of moderate thickness or in a deep ice-free ocean. Similar events have been noted in the Sea of Okhotsk by Marko (2003) and in East Antarctica by Massom et al. (1999), who observed that resultant ice surface flooding caused an abrupt brightness–temperature increase in SSM/I data. The wider occurrence of such events is unknown. Morris et al. (1998) observed waves in ERS-1 imagery 270–400 km inside the Bellingshausen Sea ice edge. Wave–ice interaction also contributes to the breakup of fast ice (Langhorne et al., 2001), particularly during the spring–summer when the surrounding protective pack ice cover is no longer present. Overall, developing an improved understanding of the interaction between waves and sea ice is critical to climate and global ocean modeling. For more detailed information on the physics of wave–ice interaction, see Chung and Fox (2001), Langhorne et al. (1998, 2001), Squire (1995), Squire et al. (1995), and Wadhams (1986, 2000), as well as Meylan et al. (1997) for discussion of the parameterization of waves in dynamical models of MIZs.

Most satellite observations of ocean waves in sea ice have been carried out using SAR data. With their high resolution and sensitivity to surface roughness, satellite SARs are uniquely well-suited to the study of wave–ice interaction processes and ocean–ice interaction features in the MIZ, including detection of wave fragmentation of ice and the determination of the dominant wavelength through spectral analysis of intensity images (Lehner et al., 1997; Liu, 1995; Liu and Peng, 1993a, b, c; Liu et al., 1993, 1994; Schmidt and Heygster, 1997; Wadhams and Holt, 1991). An example is shown in Figure 5.127. A major advantage in using SAR over ice edge zones and MIZs is that the latter are invariably cloud-covered, and SAR can also resolve the complex morphological characteristics associated with these regions. Estimates can be made from SAR imagery of the spatial variability of the wave (and current) field through spectral analysis combined with wave–ice interaction models (Liu and

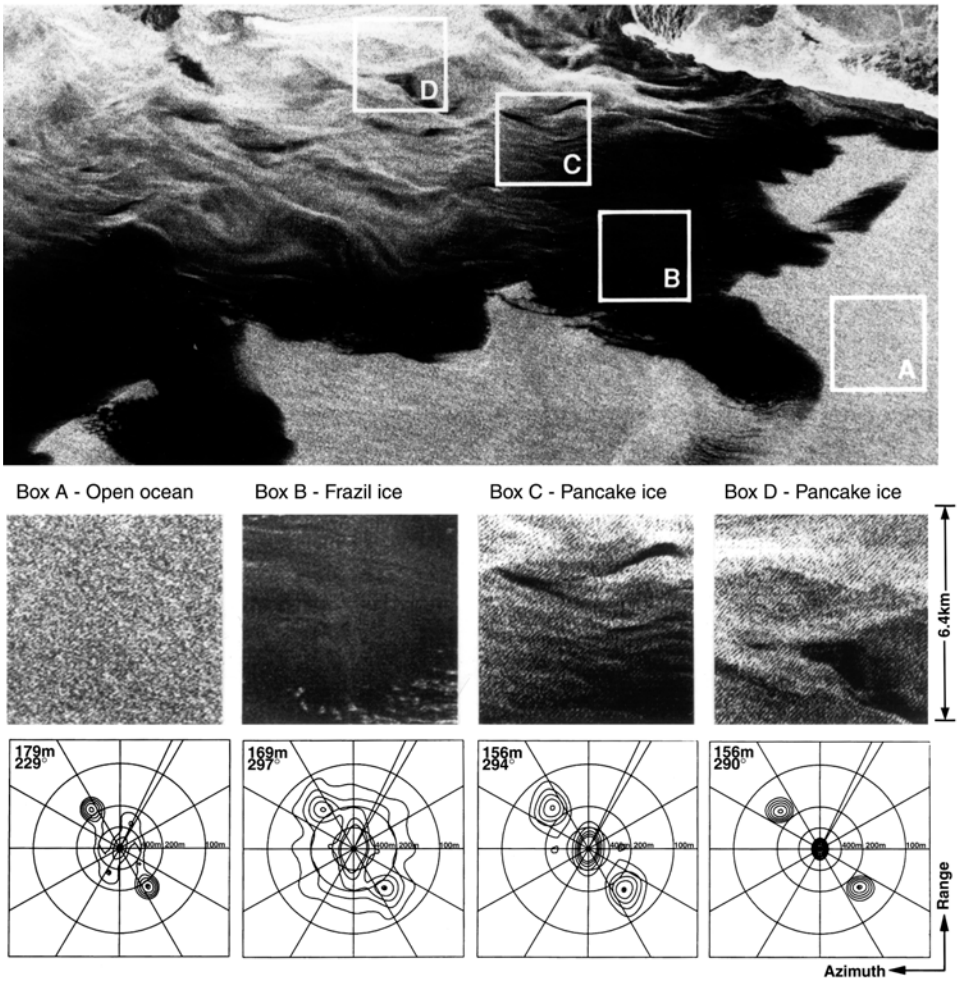

Figure 5.127. Use of Seasat L-band SAR data to study and model the propagation of ocean waves in pancake/frazil ice in the Chukchi Sea. The lower boxes show directional wave spectra derived from the SAR data.

From Wadhams and Holt (1991). Copyright 1991 American Geophysical Union. Reproduced by permission of American Geophysical Union.

Mollo-Christensen, 1988; Liu et al., 1991a, b; Liu et al., 1992; Liu and Peng, 1994, 1998). Such models parameterize both wave and ice characteristics to predict wave attenuation, dispersion, and refraction. SAR-derived estimates of directional wave spectra within a sea ice cover provide an important means with which to test and improve theories of wave attenuation and examine the impact of wave dispersion and direction (Larouche and Cariou, 1992). Schulz-Stellenfleth and Lehner (2002) studied wave damping observed in ERS-2 SAR scenes of the Bering and Weddell Seas using a technique originally developed by Kerbaol et al. (1998) for wind

estimation. Lyzenga et al. (1985) examined radar-imaging mechanisms of waves relating to the reduction of high-frequency waves and the effects of velocity bunching.

Wave–ice interaction information derived from SAR data has also been used to infer ice thickness. Wadhams and Holt (1991) detected the propagation of gravity waves through fields on pancake and frazil ice, then used this information to extract estimates of the thickness of these two ice types. In an Arctic study, Shuchman et al. (1994) similarly demonstrated that reasonable thickness estimates could be obtained from observing gravity wave propagation into the ice. Wadhams et al. (2002) used ERS-2 SAR data to spectrally analyze the wavelengths and propagation vectors of the dominant ocean wave "species" entering fields of frazil–pancake ice from the open ocean, with a view to inferring information on ice thickness (see Wadhams et al., 1999). They applied the technique to East Greenland and Antarctica.

SAR data have been applied to the detection and interpretation of mesoscale ice edge fronts, banding, and eddies, by combined analysis with models of surface effects associated with atmospheric instability due to upwelling, grease ice formation, and wave–current interaction (Liu and Peng, 1993a, b, c; Liu et al., 1994). The level of ice edge detail, and its temporal variability, that can be retrieved from high-resolution SAR data is apparent in Figure 5.128. Based on SAR-derived wave and current inputs, together with wind data, two-dimensional coupled ice–ocean interaction models can be used to predict ice edge (and ocean) dynamics. Ice edge eddies play a prominent role in the control of ice edge location and the distribution of momentum, heat, and mass, and may affect ice melt/loss by transporting ice into warmer waters (Johannessen et al., 1994b, 1995a; Liu and Peng, 1998). Such processes are also likely to be of biological significance through their impact on phytoplankton blooms. In their wavelet analyses using ERS SAR data, Liu and Peng (1993a) and Liu et al. (1994) found the typical diameter of eddies to be 20–40 km, with rotation speeds of up to $0.4\,\mathrm{m\,s^{-1}}$ (fast eddy!). Other satellite studies of ice edge eddies are by Fukamachi et al. (1998) and Wakatsuchi et al. (1990). Shuchman et al. (1993, 2004) provide further information on SAR ice edge and eddy detection, while Johannessen et al. (1992) and Shuchman et al. (2004) developed a conceptual model for SAR measurement in the MIZ. The physical and EM properties of sea ice formed in an ocean–wave environment are evaluated by Onstott et al. (1998). In future, additional complementary information will be provided by special wave-mode data from TerraSAR-L (Zink, 2003). This mode is similar to those on Envisat and ERS.

Recent work has also shown the efficacy of spaceborne SAR as a means of gaining improved operational estimates of wind speed and direction in coastal open ocean regions (Pichel and Clemente-Colón, 2000). Furevik et al. (2002) demonstrated the applicability to Arctic MIZs, where wind speed and direction play a major role in determining ice compactness and ice edge location. They further showed that wind fields could be measured within leads in this fashion. An example retrieval, from the Barents Sea, is given in Figure 5.129 (see color section). With further validation, such methods could make a significant contribution to improving our understanding of atmosphere–ice–ocean processes in these key and highly dynamic regions.

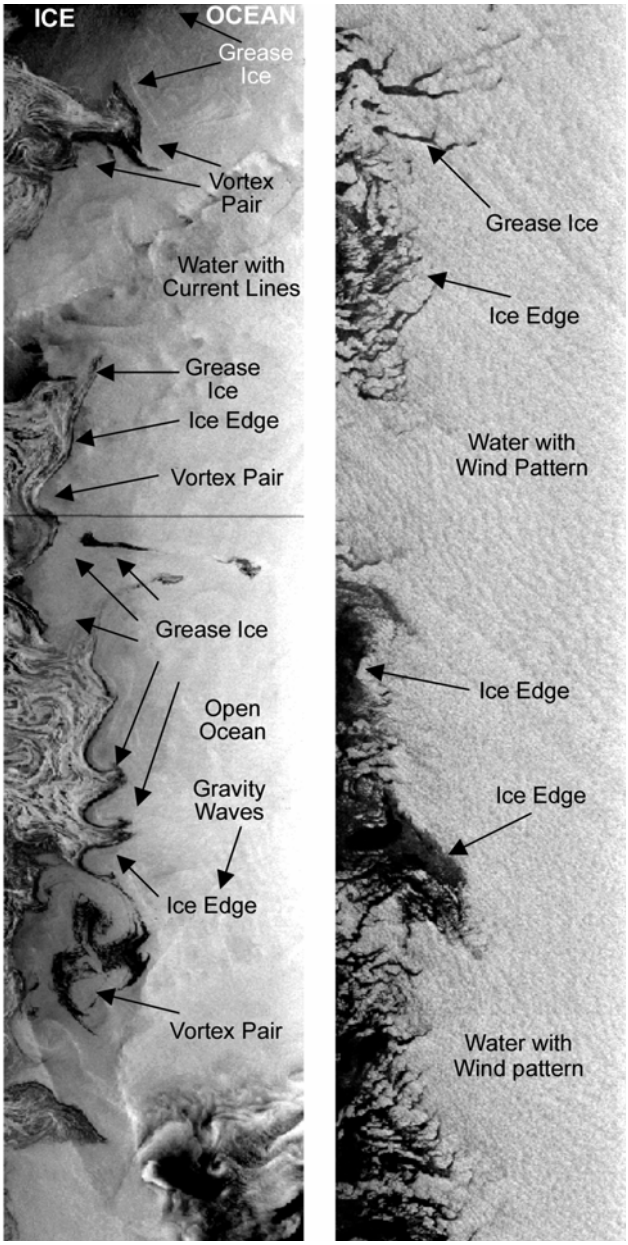

Figure 5.128. ERS-1 SAR image strips from (a) January 13, 1992 and (b) January 16, 1992, showing rapid ice edge variability in the Greenland Sea–Fram Strait region as a result of strong off-ice winds. Dominant features are marked. Note the immense detail not only in the sea ice but also in the ocean, with ocean current boundaries and waves identifiable.

From Shuchman et al. (2004). Reprinted with permission of the National Oceanographic and Atmospheric Administration (NOAA).

5.9.17 Operational ice observation, analysis, and forecasting

An important application of satellite remote sensing is in the provision of timely sea ice and iceberg information to high-latitude shipping and marine operations (DMSG, 2000). Indeed, satellite observations are the primary data source used by operational national ice centers. For information on the latter, please see Bertoia et al. (1998, 2004) and consult ⟨*http://www.aari.nw.ru/gdsidb/gdsidb_2.html*⟩. The NOAA AVHRR and DMSP OLS sensors have long been important workhorses of operational analyses, along with passive-microwave data. Passive-microwave ice concentrations are routinely incorporated in near-real time into operational sea ice analyses (Grumbine, 1996). An evaluation of SSM/I ice concentration algorithms used operationally by the U.S. NIC is given by Meier et al. (2001). Moreover, sea ice extent information from radar scatterometers such as QuikSCAT, as well as wind speed and direction off the ice edge, are now routinely used in operational analyses, again taking advantage of their excellent all-weather, day–night coverage. Operational agencies also use MODIS data (Flett, 2003). For further information on sea ice products from the U.S. National/Navy Ice Center, please see ⟨*http://www.natice.noaa.gov/*⟩, while in-depth information on the operational use of satellite data by the Canadian Ice Service (CIS) is covered by Flett (2003) and Ou (2004). Weekly ice charts digitized by the center and covering the period 1972 to 1994 are available for the Arctic (Dedrick et al., 2001). A subset of archived CIS ice charts for Canadian Arctic waters are also available online from ⟨*http://ice-glaces.ec.gc.ca/App/WsvPageDsp.cfm/*⟩ (see also Agnew and Howell, 2002, 2003; and CIS, 2002). Moreover, a historical ice chart archive for the Arctic, and produced by ACSYS (Løyning and Dick, 2003), has recently been made available at ⟨*http://acsys.npolar.no/ahica/intro.htm*⟩. The reader is encouraged to also consult Vinje (2001a), and also the International Ice Charting Working Group website at ⟨*http://nsidc.org/noaa/iicwg*⟩.

Table 5.9 provides a summary of the spatial and temporal nature of ice information requirements, in this case as defined by the CIS (Flett, 2003). These requirements are separated into tactical and strategic scales. The former refers to the level of information and detail required to support daily operations and ship navigation in ice. Strategic, on the other hand, refers to the level required for less immediate operations, including the preparation of daily ice analysis charts for the CIS (see below).

Latterly, SAR data have been increasingly used in operational analyses (Bertoia et al., 1998, 2004; Clemente-Colón et al., 2003; Flett, 2003; Gill, 2001; Gill et al., 2000; Pichel et al., 2003; Sephton and Partington, 1998; Wohl, 1995). In fact, SAR is the remote-sensing instrument of choice for ice monitoring due to its all-weather, day–night, and high-resolution capability. SAR imagery has been incorporated into NIC ice analyses since ERS-1 data became routinely available in 1992, and currently accounts for >20% of input into Northern Hemisphere NIC analyses (Bertoia et al., 2004; Clemente-Colón et al., 2003). Once again, operational ice analysis has been revolutionized by the availability of wide-swath ScanSAR data (Flett, 2003; Ramsay et al., 1998). According to Flett (2003), Radarsat-1 ScanSAR Wide imagery is the preferred source of information for the CIS due to its wide coverage over a 500-km

Table 5.9. A summary of the spatial and temporal sea ice information requirements as defined by the Canadian Ice Service for the Canadian Arctic.

Ice information requirement		Primary			Secondary					Iceberg
		Ice/water boundary or Ice edge	Ice concentration	Stage of development (e.g. new, thin, first-year, and multi-year ice)	Presence and location of leads (open water)	Ice thickness	Ice topography and roughness	Ice decay state (or, more specifically, Ice strength)	Snow properties (e.g. thickness; also wetness, density)	Iceberg detection
Spatial resolution	strategic	5 km	+/- 10% requires resolution < 100 m	50-100 m	50-100 m similar to ice concentration	5 km for average thickness over an area to +/- 20 % of total thickness	< 50 m to determine extent of ridging; need average ridge heights to within +/- 20 %	20 km for average strength over an area to +/- 20% of total strength	5 km for average snow depth to +/- 20 %	< 50 m
	tactical	<1 km	+/- 5 % requires resolution < 25 m	<20 m	<20 m	< 100 m to determine average and maximum thickness (including rafting) over an area to +/- 10% of total thickness	< 10 m to determine mean and maximum ridge heights to within +/- 10 %	5 km for average strength over an area to +/- 10% of total strength	1 km for average snow depth to +/- 10 %	<5 m
Temporal resolution	strategic	daily	daily	daily	daily	2x/week	daily	weekly	weekly	daily
	tactical	6 hours	6 hours	6 hours	6 hours	daily	6 hours	daily	daily	hourly
Description		In case of a diffuse ice edge, the CIS defines the ice/water boundry as 10% ice concentration	Percentage of ice covered area. Ice concentration is a key parameter in the WMO egg code	Ice classes are defined by WMO	Leads and polynyas	Important for navigation and/or loads on structures (Remark: Rafts show double or more the average floe thickness)	Presence, location and height of ridges Roughness indicated by concentration of ridges (in % or in number per unit area) – ridge density plus average height (or total thickness) of ridges	Identification of melt onset and ponding	To determine hull friction for ship resistance – also important for ice strength	Detection and tracking, possibly classification of type

From Flett (2003).

swath and because HH-polarization typically provides superior ice–water discrimination at intermediate incidence angles—e.g., of 25–35°—compared with VV-polarization. Having said this, Envisat ASAR data have also been extensively used by the CIS since the summer of 2003 (Flett, 2003). Radarsat-1 ScanSAR Wide B images of the Alaska region are received by NIC within <3 hours of acquisition by the ASF (Fairbanks, Alaska), through an agreement between the Canadian Space Agency (CSA), NOAA, and NASA (Bertoia et al., 1998). Although manual or semi-automated techniques remain the primary mode of operational analysis at this stage, considerable development is taking place in the field of automation in response to the immense data volume (Bertoia et al., 1998, 2004; Sephton and Partington, 1998), with expert systems, data fusion, and image segmentation techniques emerging (Bertoia et al., 1998; Clausi, 2002; Partington, 2000; Partington et al., 1999; Soh and Tsatsoulis, 1998, 1999b; Soh et al., 2004). Such data and techniques have greatly improved the quality of the operational product. For example, much safer estimates of ice edge location have been provided for crab fishermen in the Bering Sea, compared with previous estimates using visible to TIR data that were seriously hampered by cloud cover (Bertoia et al., 2004 estimated that cloud cover is present at or near the ice edge for ~70% of the time).

Improved high-resolution information on ice type and concentration is also possible with SAR, together with enhanced pressure ridge and iceberg detection (see Chapter 3 of Volume 2 of this book). A wealth of information on the U.S. and Canadian Ice Services, and their use of satellite data, is given in ⟨*http://www.natice.noaa.gov*⟩ and ⟨*http://ice-glaces.ec.gc.ca*⟩, respectively. An example of an operational CIS chart derived from Radarsat imagery in near-real time is shown in Figure 5.130 (see color section). Satellite-based ice charts are also produced for Greenland waters by the Danish Meteorological Institute, using methods described in Gill (2001) and Gill et al. (2000). Amongst other services, an operational system called ICEWATCH has been established as a joint venture of ESA and the Russian Space Agency (RKA) to operationally monitor sea ice conditions in the Northern Sea Route using ERS and Okean SLR radar data (Johannessen et al., 1997). In spite of the advances outlined above, robust automated ice classification remains an elusive goal of operational ice agencies, and is still in the research and development domain (Flett, 2003).

An important issue concerns the continued routine availability of wide-swath SAR after the demise of Radarsat-1, given that Radarsat-2 is ostensibly a commercial satellite (Staples et al., 2004). An agreement between JAXA (NASDA), NOAA, and the ASF to create an ALOS PALSAR data reception and processing node at the ASF may ensure continuation of such input. As such, agencies are gearing up to the inclusion of new-generation polarimetric SAR data, with its ability to improve sea ice classification (see Section 5.9.7.3). New ALOS PALSAR data will also be used for operational analyses of the Sea of Okhotsk in Japan, where the Japan Coast Guard plans frequent sea ice observations using the low-resolution ScanSAR mode (Rosenqvist et al., 2003). However, while the high-resolution operating modes of PALSAR and the Envisat ASAR offer selective and alternating polarization capabilities, these modes are limited to operational use by narrow swath widths—

e.g., 70 km for PALSAR (Flett, 2003). Radarsat-2, on the other hand, will provide selective polarization in ScanSAR mode (500-km swath), offering like- and cross-polarization data over a large area that is well-suited to operational applications (Scheuchl et al., 2004a). Indeed, improved operational information on ice–water discrimination and ice surface roughness characteristics are expected to emanate from the availability of cross-polarized SAR data. Significant challenges remain, however, before systems such as Radarsat-2 can be exploited operationally to their full potential (Ramsay et al., 2004). These include the handling of increased volumes of multi-channel data, detailed acquisition planning, and integration with other spaceborne SAR data—e.g., from Envisat. It should be noted that Radarsat-3, with a launch planned in 2007, will not be a commercial satellite.

The European ICEMON (Sea ICE MONitoring in the Polar Regions) initiative (see Section 5.9.17.1) is making extensive use of 150- to 300-m-resolution wide-swath SAR images from Envisat or Radarsat-1 to produce high-resolution icecharts of the Russian and European Arctic (⟨*http://www.icemon.org*⟩). Ice edge information from QuikSCAT data is also incorporated. These charts, which are produced by the Norwegian Meteorological Institute and are based on manual analysis by an experienced ice analyst, represent a significant improvement over operational ice charts based on passive-microwave data. The latter are useful in providing the regional- to hemispheric-scale picture, but are limited by their low resolution and ambiguities in coastal regions.

Polar navigation has also benefited in a direct fashion from recent technological advances and data availability—e.g., Vainio et al. (2000). Today's modern ice-breakers are equipped with both sophisticated GPS-based navigation systems and satellite L-/S-band data reception facilities, enabling the downloading of key information on sea ice and meteorological conditions in real time. Typical data downloaded by ships include DMSP SSM/I and OLS data, and NOAA AVHRR and TOVS. Having access to such information has revolutionized navigation in polar oceans, with immense savings in fuel bills as a result. It also enables flexibility in the planning and execution of scientific experiments within the sea ice zone. Note that the downloading of data from the more sophisticated and higher data rate sensors such as SAR, MODIS, and, in future, the NPOESS suite, requires a larger X-band antenna. This requires a stable platform, and as such is best deployed on land rather than at sea. Note that the operational agencies also plan to use TerraSAR data in future (Flett, 2003).

5.9.17.1 Assimilation of satellite data into models

Last but not least, an exciting emerging trend is the assimilation of satellite data into sea-ice-forecasting and prediction models, both for research and operational purposes. The latter application has been aided by the rapid processing and routine operational delivery of satellite-derived sea ice products to users (Bertoia et al., 1998, 2004; Dulière and Fichefet, 2004; Lieser and Lemke, 2002; Lindsay, 2001b; Partington and Steffen, 1998; Roberts et al., 2004; Rothrock and Thomas, 1992; Thomas and Rothrock, 1993). For example, operational agencies are making

increasing use of new ice-forecasting models based on the assimilation of satellite passive-microwave data, thereby diminishing the need for empirical observations for forecasting purposes (Partington and Steffen, 1998). The NIC, for example, has developed the Polar Ice Prediction System (PIPS) to carry out ice-operational forecasts by ingesting a variety of satellite data in near-real time, including DMSP SSM/I and Quikscat radar scatterometer data (⟨*http://science.natice.noaa.gov/scienceDisplay.htm*⟩; Bertoia et al., 2004; Van Woert et al., 2001b). Another system has been designed to nowcast/forecast ice conditions in the Beaufort Sea in support of a response to possible oil spills (Wang et al., 2003a). Thomas et al. (1996) proposed a scheme for assimilating satellite-derived ice concentration data into an Arctic sea ice mass balance model. Data assimilation methods will allow the improved models and new observations to be used to better determine the past, current, and future state of the marine cryosphere. Weaver et al. (2000) discussed the current status of data assimilation in sea ice monitoring, and the potential benefits of combining satellite data—e.g., ice concentration, thickness, motion, and deformation—and ice models (Figure 5.131). The consensus is that this approach will greatly enhance model performance and change detection, while relying on rigorous error analysis, and is cost-effective (Randall et al., 1998). The effective assimilation of different satellite datastreams into models remains a challenging task, but shows enormous potential.

Zhang et al. (2003) investigated the effects of assimilating IABP buoy and satellite SSM/I (85 GHz) ice motion data on the simulation of Arctic sea ice motion and thickness, aided by submarine observations for model validation. They found that assimilating the motion data significantly improved modeled ice motion, reducing the error to $0.04\,\mathrm{m\,s^{-1}}$ from $0.07\,\mathrm{m\,s^{-1}}$ and increasing the correlation with observations to 0.90 from 0.66. Assimilation leads to more robust ice motion with substantially reduced stoppage, which in turn leads to strengthened ice outflow at Fram Strait and enhanced ice deformation. Assimilation also significantly alters the spatial distribution of the icemass and brings the modeled ice thickness into better agreement with the thickness observed in four recent submarine cruises. While buoy data are most effective in reducing model errors because of their small measurement error, SSM/I data provide more complete spatial coverage. Zhang et al. (2003) conclude that the assimilation of both buoy and SSM/I data combines their individual advantages, resulting in the best overall model performance in simulating both ice motion and ice thickness. Meier and Maslanik (2001) further demonstrated the immense potential of data assimilation. By combining ice motions observed by buoys and SSM/I data with those from a model, they substantially reduced errors in estimates of motion and derived products of ice convergence and ice volume export, in this case through Fram Strait (Figure 5.132).

Other initiatives include ICEMON and the Northern View, which are services within the joint ESA–European Commission Global Monitoring for Environment and Security (GMES) consortium (⟨*http://earth.esa.int/gmes*⟩). The Northern View is an ice and Arctic monitoring service led by the Canadian Centre for Cold Ocean Resources Engineering (C-CORE) in Newfoundland (⟨*http://www.northview.org*⟩).

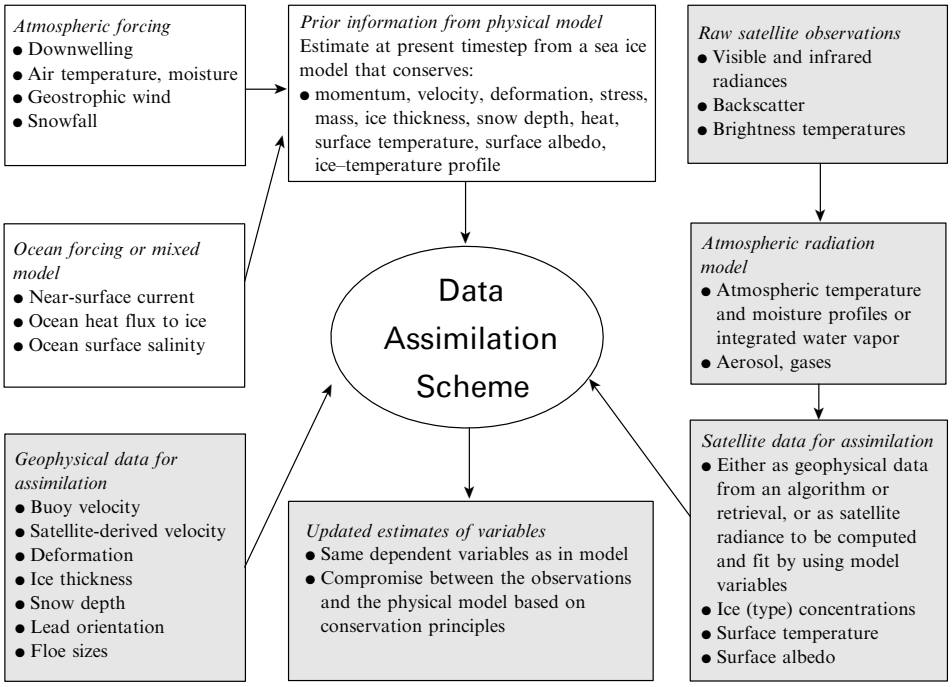

Figure 5.131. A possible framework for a sea ice data assimilation scheme. Fainter boxes represent the traditional sea ice model with forcing, while the heavier boxes involve data assimilation.

From Weaver et al. (2000). Reprinted with permission from the International Glaciological Society (IGS). © 2005 IGS.

The ICEMON program has the overall objective of implementing a coherent European operational monitoring system for high latitudes, consisting of sea ice, oceanographic, and meteorological components (⟨*http://www.icemon.org*⟩). In this way, an information service is provided for climate, environment, marine safety, and resource management. This has made, or will make, extensive use of Envisat Global Monitoring Mode (GMM) imagery and data from the NOAA AVHRR, DMSP SSM/I, ADEOS and QuikScat SeaWinds, Aqua AMSR-E and ADEOS AMSR, and in future from the MetOp ASCAT (launch 2005) and the Japanese GCOM-B1 SeaWinds (launch 2010). Importantly, these sources will provide a steady stream of low-cost operational data for the next decade or so and beyond. The ICEMON project makes extensive use of Envisat GMM data, producing range-normalized mosaics on a daily basis (Figure 5.133a). These data routinely cover significant areas of the Arctic every day without the need for product scheduling, and do so on a 1- or 2-km-resolution grid. An experimental automatic 2-day Arctic sea-ice-tracking procedure is also carried out on Envisat GMM ASAR data. The grid resolution used is 50 km (25×2 km), with coverage being limited to the area covered on each of the 3 days for which the data are used (days 1, 2, and 3)—

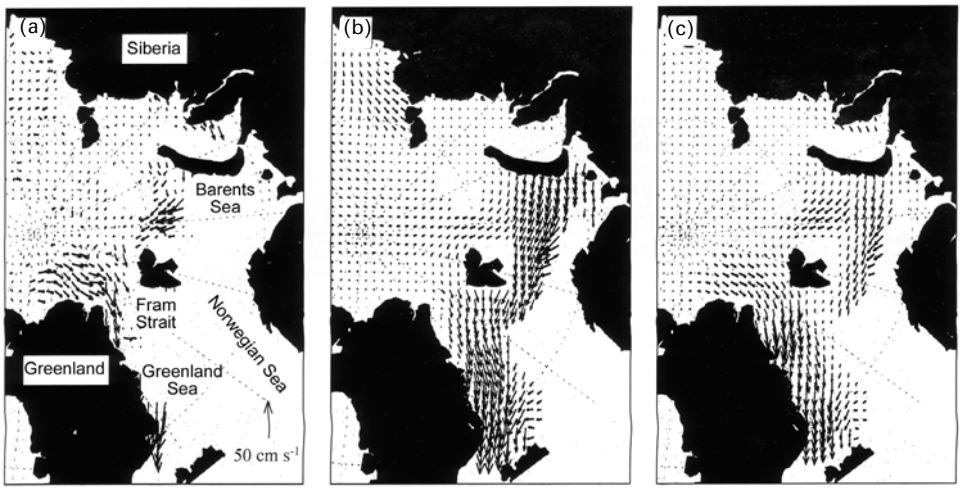

Figure 5.132. Ice motion in the eastern Arctic on March 18, 1993 derived from (a) SSM/I 85-GHz data (12.5-km resolution), (b) a sea ice model, and (c) the data assimilation.

From Meier and Maslanik (2001). Reprinted with permission from the International Glaciological Society (IGS). © 2005, IGS.

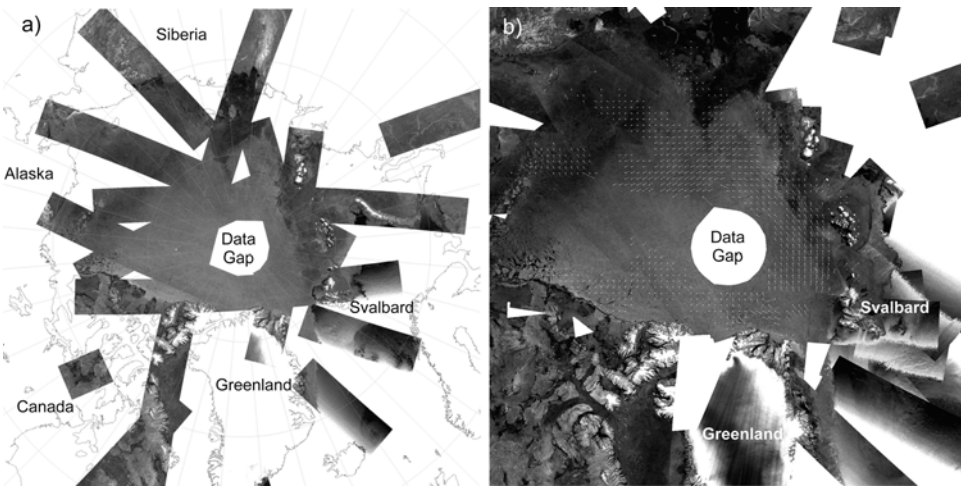

Figure 5.133. (a) A range-normalized daily composite mosaic of Envisat ASAR data over the Arctic on January 8, 2005. (b) An experimental Envisat ASAR-derived ice motion product from Christmas Day (2004), with a grid size of 50 km superimposed on the SAR amplitude image (2-km resolution). These images were derived from Envisat ASAR Global Monitoring Mode data (swathwidth 420 km, resolution 1 km) produced for the European ICEMON project (⟨*http://www.icemon.org*⟩) by Vexcel UK Limited and the Norwegian Meteorological Institute.

©ESA 2005. Reprinted with permission from ESA.

i.e., covering the 2-day ice drift from day 1 to day 3. An example is shown in Figure 5.133b.

Key inputs to the ICEMON project also include climatic data and weather data from surface observations, forecasts, and models, and ice thickness measurements from moored ice-profiling sonars—e.g., in Fram Strait—enabling the monitoring of horizontal ice flux rates. According to the ICEMON initiative, ice models are not only important as input to numerical weather prediction models, but also represent the future of operational ice charting (when assimilating satellite data). Information on the various constituent models of ICEMON is given at ⟨*http://www.icemon. org*⟩. An important aspect of such models is hindcast capability.

5.10 REFERENCES

Aagaard, K. and E. C. Carmack (1989). The role of sea ice and other fresh water in the Arctic circulation. *Journal of Geophysical Research*, **94**(C10), 14485–14498.

Aagaard, K. and E. C. Carmack (1994). The Arctic Ocean and climate: A perspective. In: O. M. Johannessen, R. D. Muench, and J. E. Overland (eds.), *The Polar Oceans and Their Role in Shaping the Global Environment*. American Geophysical Union, Washington, DC, pp. 5–20.

Aagaard, K., L. K. Coachman, and E. Carmack (1981). On the halocline of the Arctic Ocean. *Deep-Sea Research-A*, **28**, 529–545.

Aagaard, K., E. Fahrbach, J. Meincke, and J. H. Swift (1991). Saline outflow from the Arctic Ocean: Its contribution to the deep waters of the Greenland, Norwegian, and Iceland Seas. *Journal of Geophysical Research*, **96**(C11), 20433–20442.

Aagaard, K., D. Darby, K. Falkner, G. Flato, J. Grebmeier, C. Measures, and J. Walsh (1999). *Marine Science in the Arctic: A Strategy*. Arctic Research Consortium of the United States (ARCUS), Fairbanks, AK, 84 pp, available at ⟨*http://www.arcus.org/Marine_Science/plan.html*⟩.

Ackerman, S., K. Strabala, P. Menzel, R. Frey, C. Moeller, L. Gumley, B. Baum, C. Schaaf, and G. Riggs (1997). *Discriminating Clear Sky from Clouds (Cloud Mask Retrieval Algorithm): Theoretical Basis Document* (ATBD-MOD-06). NASA Goddard Space Flight Center, Greenbelt, MD, 32 pp.

Ackerman, S. A., K. I. Strabala, W. P. Menzel, R. A. Frey, C. C. Moeller, and L. E. Gumley (1998). Discriminating clear sky from clouds with MODIS. *Journal of Geophysical Research*, **103**(D24), 32141–32157.

Ackley, S. F. (1996). Sea ice. *Encyclopaedia of Applied Physics*. VCH, New York, pp. 81–103.

Ackley, S. F. and C. W. Sullivan (1994). Physical controls on the development and characteristics of Antarctic sea ice biological communities: A review and synthesis. *Deep-Sea Research*, **41**(10), 1583–1604.

Ackley, S. F., P. Wadhams, J. C. Comiso, and A. P. Worby (2003). Decadal decrease of Antarctic sea ice extent inferred from whaling records revisited on the basis of historical and modern sea ice records. *Polar Research*, **22**(1), 19–25.

ACIA (Arctic Climate Assessment) (2004). *Impacts of a Warming Arctic*. Cambridge University Press, Cambridge, UK, 139 pp.

ACSYS (2003a). *ACSYS Rationale*. Available online at ⟨*http://www.nopolar.no/acsys/rationale*⟩.

ACSYS (2003b). *Implementation and Achievements: Arctic Sea-Ice Program*. Available online at ⟨*http://www.nopolar.no/acysys/impplan/seaice.htm*⟩.

Adolphs, U. (1998). Ice thickness variability, isostatic balance and potential for snow ice formation on icefloes in the south polar Pacific Ocean. *Journal of Geophysical Research*, **103**(C11), 24675–24691.

Adolphs, U. (1999). Roughness variability of sea ice and snow cover thickness profiles in the Ross, Amundsen, and Bellingshausen Seas. *Journal of Geophysical Research*, **104**(C6), 13577–13591.

Adolphs, U. and C. Wendler (1995). A pilot study on the interactions between katabatic winds and polynyas at the Adélie Coast, eastern Antarctica. *Antarctic Science*, **7**, 307–314.

Agnew, T. A. and S. Howell (2002). Comparison of digitized Canadian ice charts and passive-microwave sea-ice concentrations. *Procedures of the International Geoscience and Remote Sensing Symposium, July 24–28, Toronto*.

Agnew, T. A. and S. Howell (2003). The use of operational ice charts for evaluating passive microwave ice concentration data. *Atmosphere–Ocean*, **41**(4), 317–331.

Agnew, T.A., H. Le, and T. Hirose (1997). Estimation of large scale sea ice motion from SSM/I 85.5 GHz Imagery. *Annals of Glaciology*, **25**, 305–311.

Agnew, T.A., H. Le, and M. Shokr (1999). Characteristics of large winter leads over the Arctic Basin from 85.5 GHz DMSP SSM/I and NOAA/AVHRR imagery. *Canadian Journal of Remote Sensing*, **25**(1), 12–20.

Agnew, T. A., B. T. Alt, R. De Abreu, and S. Jeffers (2001). The loss of decade old sea ice plugs in the Canadian Arctic Islands. *6th Conference on Polar Meteorology and Oceanography, San Diego, May 14–18* (extended abstracts). American Meteorological Society, Boston, pp. 9–12.

Agnew, T. A., J. Vandeweghe, and P. Yu (2005). Estimating sea-ice transport using the Advanced Sensor Microwave Imager (AMSR). *Proceedings of 8th Conference on Polar Meteorology and Oceanography, San Diego, January 8–14*.

Ainley, D. G. (2002). *The Adélie Penguin: Bellwether of Climate Change*. Columbia University Press, New York, 416 pp.

Ainley, D. G. and D. P. DeMaster (1990). The upper trophic levels in polar marine ecosystems. In: W. O. Smith Jr. (ed.), *Polar Oceanography, Part B: Chemistry, Biology, and Geology*. Academic Press, New York, pp. 599–630.

Ainley, D. G. and S. S. Jacobs (1981). Seabird affinities for ocean and ice boundaries in the Antarctic. *Deep-Sea Research*, **28A**, 1173–1185.

Ainley, D. G., P. R. Wilson, K. J. Barton, G. Ballard, N. Nur, and B. Karl (1998). Diet and foraging effort of Adélie penguins in relation to pack-ice conditions in the southern Ross Sea. *Polar Biology*, **20**, 311–319.

Ainley, D. G., C. T. Tynan, and I. Stirling (2003). Sea ice: A critical habitat for polar marine mammals and birds. In: D. Thomas and G. Dieckmann (eds.), *Sea Ice: An Introduction to its Physics, Biology, Chemistry and Geology*. Blackwell Science, Oxford, UK, pp. 240–266.

Ainley, D. G., E. D. Clarke, K. Arrigo, W. R. Fraser, A. Kato, K. J. Barton, and P. R. Wilson (2005). Decadal-scale changes in the climate and biota of the Pacific sector of the Southern Ocean, 1950s to the 1990s. *Antarctic Science*, **17**(2), 171–182.

Akitaya, E. (1974). Studies on depth hoar. *Contributions from the Institute of Low Temperature Science, Series A*, No. 26, 67 pp.

Alam, A. and J. Curry (1995). Lead-induced atmospheric circulations. *Journal of Geophysical Research*, **100**, 4643–4651.

Alam, A. and J. Curry (1998). Evolution of new ice and turbulent fluxes over freezing winter leads. *Journal of Geophysical Research*, **103**, 15783–15802.

Alexander, M. A., U. S. Bhatt, J. E. Walsh, M. S. Timlin, J. S. Miller, and J. D. Scott (2004). The atmospheric response to realistic Arctic sea ice anomalies in an AGCM during winter. *Journal of Climate*, **17**, 890–905.

Alexander, V. (1980). Interrelationships between seasonal sea ice and biological regimes. *Cold Regions Science and Technology*, **2**, 157–178.

Alexandrov, V. Yu., T. Martin, J. Kolatschek, H. Eicken, M. Kreyscher, and A. Makshtas (2000). Sea-ice circulation in the Laptev Sea and ice export to the Arctic Ocean: Results from satellite remote sensing and numerical modelling. *Journal of Geophysical Research*, **105**(C7), 17143–17159.

Alfultis, M. A. and S. Martin (1987). Satellite passive microwave studies of the Sea of Okhotsk ice cover and its relation to oceanic processes, 1978–1982. *Journal of Geophysical Research*, **92**(C12), 13013–13028.

Allison, I. (1997). Physical processes determining the Antarctic sea ice environment. *Australian Journal of Physics*, **50**, 759–771.

Allison, I., R. E. Brandt, and S. G. Warren (1993). East Antarctic sea ice: Albedo, thickness distribution, and snow cover. *Journal of Geophysical Research*, **98**(C7), 12417–12429.

Allison, I., R. G. Barry, and B. E. Goodman (2001). *Climate and Cryosphere (CLIC) Project. Science and Co-ordination Plan, Version 1* (WCRP-114, WMO/TD 1053. World Meteorological Organization, Geneva.

Ancel, A., G. L. Kooyman, P. J. Ponganis, J.-P. Gendner, J. Lignon, X. Mestre, N. Huin, P. H. Thorson, P. Robisson, and Y. Le Maho (1992). Foraging behaviour of emperor penguins as a resource detector in winter and summer. *Nature*, **360**(6402), 336–339.

Andersen, S., L.-A. Breivik, S. Eastwood, O. Godøy, H. Schyberg, and R. Tonboe (2001). Sea ice products from the O&SI SAF. *Proceedings of 2001 Eumetsat Meteorological Satellite Data Users' Conference*.

Anderson, L. G. and S. Kaltin (2001). Carbon fluxes in the Arctic Ocean: Potential impact by climate change. *Polar Research*, **20**(2), 225–232.

Anderson, L. G., K. Olsson, and M. Chierici (1998a). A carbon budget for the Arctic Ocean. *Global Biogeochemical Cycles*, **12**, 455–465.

Anderson, L. G., K. Olsson, E. P. Jones, M. Chierici, and A. Fransson (1998b). Anthropogenic carbon dioxide in the Arctic Ocean: Inventory and sinks. *Journal of Geophysical Research*, **103**, 27707–27716.

Anderson, L. G., E. P. Jones, and B. Rudels (1999). Ventilation of the Arctic Ocean estimated by a plume entrainment model constrained by CFCs. *Journal of Geophysical Research*, **104**, 13423–13429.

Anderson, M. (1987). The onset of spring melt in first-year ice regions of the Arctic as determined from Scanning Multichannel Microwave Radiometer Data for 1979 and 1980. *Journal of Geophysical Research*, **92**(C12), 13153–13163.

Anderson, M. R. (1997). Determination of a melt onset date for Arctic sea ice regions using passive microwave data. *Annals of Glaciology*, **25**, 382–387.

Anderson, M. R. and S. D. Drobot (2001a). Spatial and temporal variability in snowmelt onset over Arctic sea ice. *Annals of Glaciology*, **33**, 74–78.

Anderson, M. R. and S. D. Drobot (2001b). A new data set for monitoring snowmelt onset over Arctic sea ice. *6th Conference on Polar Meteorology and Oceanography*. American Meteorological Society, San Diego, pp. 1–15.

Anderson, M. R. and S. D. Drobot (2002). *Arctic Ocean Snow Melt Onset Dates Derived from Passive Microwave: A New Data Set* (NSIDC Glaciological Data Report GD-30). National Snow and Ice Data Center, Boulder, CO, pp. 13–17.

Andreas, E. L. (1980). Estimation of the heat and mass fluxes over Arctic leads. *Monthly Weather Review*, **108,** 2057–2063.

Andreas, E. L. (1995). Air-sea drag coefficients in the western Weddell Sea: 2. A model based on form drag and drifting snow. *Journal of Geophysical Research*, **100**, 4833–4843.

Andreas, E. L., (1998). The atmospheric boundary layer over polar marine surfaces. In: M. Leppäranta (ed.), *Physics of Ice-Covered Seas* (Vol. 2). Helsinki University Press, pp. 715–773.

Andreas, E. L. and S. F. Ackley (1981). On the difference in ablation seasons of Arctic and Antarctic sea-ice. *Journal of Atmospheric Science*, **39**, 440–447.

Andreas, E. L. and B. A. Cash (1999). Convective heat transfer over wintertime leads and polynyas. *Journal of Geophysical Research*, **104**, 25721–25734.

Andreas, E. L. and K. J. Claffey (1995). Air-ice drag coefficients in the western Weddell Sea: 1. Values deduced from profile measurements. *Journal of Geophysical Research*, **100**(C3), 4821–4831.

Andreas, E. L. and B. Murphy (1986). Bulk transfer coefficients for heat and momentum over leads and polynyas. *Journal of Physical Oceanography*, **16**(11), 1875–1883.

Andreas, E. L., C. A. Paulson, R. M. Williams, R. W. Lindsay, and J. A. Businger (1979). The turbulent heat flux from Arctic leads. *Journal of Boundary Layer Meteorology*, **17**, 57–91.

Andreas, E.L., M. A. Lange, S. F. Ackley, and P. Wadhams (1993). Roughness of Weddell Sea ice and estimates of the air-ice drag coefficient. *Journal of Geophysical Research*, **98**(C7), 12439–12452.

Aoki, T., T. Aoki, M. Fukabori, A. Hachikubo, Y. Tachibana, and F. Nishio (2000). Effects of snow physical parameters on spectral albedo and bidirectional reflectance of snow surface. *Journal of Geophysical Research*, **105**, 10219–10236.

Appel, I., K. A. Jensen, and W. Emery (2002). *Sea Ice Age/Edge Motion, Visible/Infrared Imager/Radiometer Suite Algorithm Theoretical Basis Document* (Version 5.1, April, SBRS Document Y2409). Raytheon Systems Company, Lanham, MD.

Arbetter, T. E. and A. Lynch (2002). *On the Relationship between Atmospheric Circulation and the Cosmonaut Sea Polynya* (Glaciological Data Report GD-30). National Snow and Ice Data Center, Boulder, CO, 52 pp.

Arbetter, T., A. Lynch, and D. Bailey (2004). Relationship between synoptic forcing and polynya formation in the Cosmonaut Sea: 1. Polynya climatology. *Journal of Geophysical Research*, **109**(C4), DOI: 10.1029/2003JC001837.

Arcone, S. A., A. J. Gow, and S. G. McGrew (1986). Structure and dielectric properties at 4.8 and 9.5 GHz of saline ice. *Journal of Geophysical Research*, **91**(C12), 14281–14303.

Armand, L. K. (2000). An ocean of ice: Advances in the estimation of past sea ice in the Southern Ocean. *Geological Society of America Today*, **10**(3), 1–7.

Armand, L. K. and A. Leventer (2003). Palaeo sea ice distribution: Its reconstruction and significance. In: D. Thomas and G. Dieckmann (eds.), *Sea Ice: An Introduction to Its Physics, Biology, Chemistry and Geology*. Blackwell Science, Oxford, pp. 333–372.

Armstrong, R. L. and M. J. Brodzik (1995). An Earth-gridded SSM/I data set for cryospheric studies and global change monitoring. *Advances in Space Research*, **16**(10), 155–163.

Armstrong, R. L., A. Chang, A. Rango, and E. Josberger (1993). Snow depth and grain-size relationships with relevance for passive microwave studies. *Annals of Glaciology*, **17**, 171–176.

Armstrong, T., B. Roberts, and C. Swithinbank (1973). *Illustrated Glossary of Snow and Ice*. Scott Polar Research Institute, University of Cambridge, UK, 69 pp.

Arrigo, K. R. (2000). Satellite observations of the Ross Sea polynya system. *American Geophysical Union Ocean Sciences Meeting* (Abstract OS11K-09).

Arrigo, K. R. (2003). Primary production in sea ice. In: D. N. Thomas and G. S. Dieckmann (eds.), *Sea Ice: An Introduction to Its Physics, Chemistry, Biology and Geology*. Blackwell Science, Oxford, UK, pp. 143–183.

Arrigo, K. R. and C. R. McClain (1994). Spring phytoplankton production in the western Ross Sea. *Science*, **265**, 261–263.

Arrigo, K. R. and C. W. Sullivan (1994). A high resolution bio-optical model of micro-algal growth: Tests using sea ice algal community time series data. *Limnology and Oceanography*, **39**, 609–631.

Arrigo, K. R. and D. N. Thomas (2004). Large scale importance of sea ice biology in the Southern Ocean. *Antarctic Science*, **16**(4), 471–486.

Arrigo, K. R. and G. L. van Dijken (2003a). Phytoplankton dynamics within 37 Antarctic coastal polynyas. *Journal of Geophysical Research*, **108**(C8), 3271, DOI: 10.1029/2002JC001739.

Arrigo, K. R. and G. L. van Dijken (2003b). Impact of iceberg C-19 on Ross Sea primary production. *Geophysical Research Letters*, **30**(16), 1836, DOI: 10.1029/2003GL017721.

Arrigo, K. R. and G. L. van Dijken (2004). Annual cycles of sea ice and phytoplankton in Cape Bathurst polynya, southeastern Beaufort Sea, Canadian Arctic. *Geophysical Research Letters*, **31**, L08304, DOI: 10.1029/2003GL018978.

Arrigo, K. R., C. W. Sullivan, and J. N. Kremer (1991). A bio-optical model of Antarctic sea ice. *Journal of Geophysical Research*, **96**, 10581–10592.

Arrigo, K. R., J. N. Kremer, and C. W. Sullivan (1993). A simulated Antarctic fast-ice ecosystem. *Journal of Geophysical Research*, **98**(C4), 6929–6946.

Arrigo, K. R., M. P. Lizotte, D. L. Worthen, P. Dixon, and G. Dieckmann (1997). Primary production in Antarctic sea ice. *Science*, **276**, 394–397.

Arrigo, K. R., D. L. Worthen, P. Dixon, and M. P. Lizotte (1998a). Primary productivity of near surface communities within Antarctic pack ice. In: M. P. Lizotte and K. R. Arrigo (eds.), *Antarctic Sea Ice: Biological Processes, Interactions, and Variability* (Antarctic Research Series No. 73). American Geophysical Union, Washington, D.C., pp. 23–43.

Arrigo, K. R., A. M. Weiss, and W. O. Smith Jr. (1998b). Physical forcing of phytoplankton dynamics in the western Ross Sea. *Journal of Geophysical Research*, **103**, 1007–1021.

Arrigo, K. R., D. L. Worthen, A. Schnell, and M. P. Lizotte (1998c). Primary production in Southern Ocean waters. *Journal of Geophysical Research*, **103C**, 15587–15600.

Arrigo, K. R., D. H. Robinson, D. L. Worthen, R. B. Dunbar, G. R. DiTullio, M. Van Woert, and M. P. Lizotte (1999). Phytoplankton community structure and the drawdown of nutrients and CO_2 in the Southern Ocean. *Science*, **283**, 365–367.

Arrigo, K. R., G. L. van Dijken, D. G. Ainley, and M. A. Fahnestock (2002). Ecological impact of a large Antarctic iceberg, *Geophysical Research Letters*, **29**(7), DOI: 10.1029/2001GL014160.

Arslan, A. N., Wang, H., Pulliainen, J., and M. Hallikainen (2001). Effective permittivity of wet snow using strong fluctuation theory. *Progress in Electromagnetics Research*, **31**, 279–296.

Arya, S. P. S. (1975). A drag-partition theory for determining the large-scale roughness parameter and wind stress on Arctic pack ice. *Journal of Geophysical Research*, **80**, 3447–3454.

Askne, J. (ed.) (2003). *Remote Sensing Using Microwaves*. Department of Radio and Space Science, Chalmers University of Technology, Göteborg, Sweden.

Askne, J. and R. Johansson (1988). Ice ridge observations by means of SAR. *Proceedings of IGARSS '88 Symposium, September 13–16* (ESA SP-284, IEEE 88CH$_2$497-6, 801–803). ESA, Noordwijk, The Netherlands.

Asmus, K. (2003). Russian environmental satellites: Current status and development perspectives. *17th Plenary Meeting of the Committee on Earth Observation Satellites (CEOS), November 19–20, Colorado Springs, Colorado* (Report 19.5, 13 pp.).

Asrar, G. (ed.) (1989). *Theory and Applications of Optical Remote Sensing*. John Wiley & Sons, New York, 752 pp.

Atkinson, A., V. Siegel, E. Pakhomov, and P. Rothery (2004). Long-term decline in krill stock and increase in salps within the Southern Ocean. *Nature*, **432**, 100–103, DOI: 10.1038/nature0299.

Attema, E. and P. Lecomte (1998). The ERS-1 and ERS-2 wind scatterometers, system performance and data products. *Proceedings of IGARSS '98, Seattle, Washington*, pp. 1967–1969.

Attema, E., Y.-L. Desnos, and G. Duchossiois (2000). Synthetic aperture radar in Europe: ERS, Envisat, and beyond. *John Hopkins APL Technical Digest*, **21**(1), 155–161.

Baba, K. and M. Wakatsuchi (2001). Eastward propagation of the intraseasonal variability of sea ice concentration and the atmospheric field in the marginal ice zone in the Antarctic. *Geophysical Research Letters*, **28**, 3669–3672.

Babko, O., D. A. Rothrock, and G. A. Maykut (2002). Role of rafting in the mechanical redistribution of ice thickness. *Journal of Geophysical Research*, **107**(C8), DOI: 10.1029/1999JC000190.

Backhaus, J. O., H. Fohrmann, J. Kämpf, and A. Rubino (1997). Formation and export of water masses produced in Arctic shelf polynyas: Process studies of oceanic convection. *ICES Journal of Marine Science*, **54**, 366–382.

Badgley, F. I. (1966). Heat budget at the surface of the Arctic Ocean. *Proceedings of Symposium on Arctic Heat Budget and Atmospheric Circulation* (RM-5233-NSF). Rand Corporation, Santa Monica, CA, pp. 267–278.

Bailey, D. A. and A. H. Lynch (2000a). Development of an Antarctic regional climate system model: Part I. Sea ice and large-scale circulation. *Journal of Climate*, **13**(8), 1337–1350.

Bailey, D. A. and A. H. Lynch (2000b). Development of an Antarctic regional climate system model: Part II. Station validation and surface energy balance. *Journal of Climate*, **13**(8), 1351–1361.

Bailey, D. A., T. E. Arbetter, and A. H. Lynch (2001). Atmospheric forcing of the Cosmonaut Sea Polynya. *6th Conference on Polar Meteorology and Oceanography, San Diego, May 14–18* (extended abstracts). American Meteorological Society, Boston, MA, pp. J21–J22.

Baines, P. G. and S. Condie (1998). Observations and modelling of Antarctic downslope flows: A review. In: S. S. Jacobs and R. F. Weiss (eds.), *Ocean, Ice and Atmosphere: Interactions at the Antarctic Continental Margin* (AGU Antarctic Research Series No. 75). American Geophysical Union, Washington, DC, pp. 29–49.

Bamber, J. (1994). Ice sheet altimeter processing scheme. *International Journal of Remote Sensing*, **15**, 925–938.

Bamber, J. and A. R. Harris (1994). The atmospheric correction for satellite infrared radiometer data in polar regions. *Geophysical Research Letters*, **21**, 2111–2114.

Bamber, J. and R. Kwok (2004). Measurement techniques. In: J. Bamber and A. Payne (eds.), *Mass Balance of the Cryosphere*. Cambridge University Press, Cambridge, UK, pp. 59–116.

Bamler, R., M. Eineder, B. Kampes, H. Runge, and N. Adam (2003). SRTM and beyond: Current situation and new developments in spaceborne SAR and InSAR. *Proceedings of the ISPRS Workshop on High Resolution Mapping from Space, 6–8 October, Hannover*. Institut für Photogrammetrie und GeoInformation, Universität Hannover, Germany, 7 pp.

Banfield, J. D. and A. E. Raftery (1992). Ice floe identification in satellite images using mathematical morphology and clustering about principal curves. *Journal of the American Statistical Association*, **87**(417), 7–16.

Banke, E. G. and S. D. Smith (1973). Wind stress on Arctic sea ice. *Journal of Geophysical Research*, **78**, 7871–7882.

Banke, E. G., S. D. Smith, and R. J. Anderson (1980). Drag coefficients at AIDJEX. In: R. S. Pritchard (ed.), *Sea Ice Processes and Models*. University of Washington Press, Seattle, WA, pp. 430–442.

Barber, D. G. and J. Iacozza (2004). Historical analysis of sea ice conditions in the M'Clintock Channel and the Gulf of Boothia, Nunavut: Implications for Ringed Seal and Polar Bear habitat. *Arctic*, **126**(1), 1–14.

Barber, D. G. and E. F. LeDrew (1991). SAR sea ice discrimination using texture statistics: A multivariate approach. *IEEE Transactions on Geoscience and Remote Sensing*, **57**(4), 385–395.

Barber, D. G. and J. Yackel (1999). The physical, radiative and microwave scattering characteristics of melt ponds on Arctic landfast sea ice. *International Journal of Remote Sensing*, **20**(10), 2069–2090.

Barber, D. G., E. F. LeDrew, D. G. Flett, M. Shokr, and J. Falkingham (1992). Seasonal and diurnal variations in SAR signatures of sea ice. *IEEE Transactions on Geoscience and Remote Sensing*, **30**(3), 638–642.

Barber, D. G., M. E. Shokr, R. A. Fernandes, E. D. Soulis, D. G. Flett, and E. F. LeDrew (1993). A comparison of second-order classifiers for SAR sea ice discrimination. *Photogrammetric Engineering and Remote Sensing*, **59**(9), 1397–1408.

Barber, D. G., T. N. Papakyriakou, E. F. LeDrew, and M. E. Shokr (1995). An examination of the relationship between the spring period evolution of the scattering coefficient and energy fluxes over landfast sea ice. *International Journal of Remote Sensing*, **16**, 3343–3363.

Barber, D. G., A. K. Fung, T. C. Grenfell, S. V. Nghiem, R. G. Onstott, V. Lytle, D. K. Perovich, and A. J. Gow (1998a). The role of snow on microwave emission and scattering over first-year sea ice. *IEEE Transactions on Geoscience and Remote Sensing*, **36**(5), 1750–1763.

Barber, D. G., A. Thomas, and T. N. Papakyriakou (1998b). Role of SAR in surface energy flux measurements over sea ice. In: C. Tsatsoulis and R. Kwok (eds.), *Analysis of SAR Data of the Polar Oceans: Recent Advances*. Springer-Verlag, Berlin, pp. 35–67.

Barber, D., R. Marsden, P. Minnett, G. Ingram, and L. Fortier (2001a). Physical processes within the North Water (NOW) Polynya. *Atmosphere–Ocean*, **39**, 163–166.

Barber, D., R. Marsden, and P. Minnett (eds.) (2001b). The International North Water (NOW) Polynya Study. *Atmosphere–Ocean*, **39** (special issue), 163–359.

Barber, D., J. Hanesiak, W. Chan, and J. Piwowar (2001c). Sea-ice and meteorological conditions in Northern Baffin Bay and the North Water Polynya between 1979 and 1996. *Atmosphere–Ocean*, **39**, 343–359.

Bareiss, J., H. Eicken, A. Helbig, and T. Martin (1999). Impact of river discharge and regional climatology on the decay of sea ice in the Laptev Sea during spring and early summer. *Arctic, Antarctic, and Alpine Research*, **31**, 214–229.

Barnsley, M. J., A. H. Strahler, K. P. Morris, and J.-P. Muller (1994). Sampling the surface Bidirectional Reflectance Distribution Function (BRDF): 1. Evaluation of current and future satellite sensors. *Remote Sensing Reviews*, **8**, 271–311.

Barry, R. G. (1996). The parameterization of surface albedo for sea ice and its snow cover. *Progress in Physical Geography*, **20**, 61–77.

Barry, R. G. (1997). Cryospheric data for model validations: Requirements and status. *Annals of Glaciology*, **25**, 371–375.

Barry, R. G. and R. Chorley (2003). *Atmosphere, Weather and Climate* (8th edn.). Routledge, London, 421 pp.

Barry, R. G. and J. R. Key (1994). Observational studies of Arctic ocean ice–atmosphere interactions. *Polar Geography and Geology*, **8**, 1–14.

Barry, R. G. and J. A. Maslanik (1989). Arctic sea ice characteristics and associated atmosphere–ice interactions. *Geojournal*, **18**, 5–44.

Barry, R. G., M. C. Serreze, J. A. Maslanik, and R. H. Preller (1993a). The Arctic Sea ice-climate system: Observations and modeling. *Reviews of Geophysics*, **31**(4), 397–422.

Barry, R. G., J. Maslanik, K. Steffen, R. L. Weaver, V. Troisi, D. J. Cavalieri, and S. Martin (1993b). Advances in sea ice research based on remotely-sensed passive microwave data. *Oceanography*, **6**, 5–13.

Barry, R. G., B. Goodison, I. Allison, C. Dick, and V. Ryabinin (2004). The World Climate Research Programme (WCRP) Climate and Cryosphere Project (CLIC): A global initiative. *European Geosciences Union First General Assembly, April 25–30, Nice, France* (Abstract 00134).

Barton, I. J. (1992). Satellite-derived sea surface temperatures: A comparison between operational, theoretical, and experimental algorithms. *Journal of Applied Meteorology*, **31**, 433–442.

Basharinov, A. E. and A. S. Gurvich (1970). Studies of the Earth's microwave emission and that of the atmosphere using the Kosmos-243 satellite (in Russian). *Vestnik AN SSSR*, **N10**, 37–42.

Bates, N. R., D. A. Hansell, C. A. Carlson, and L. I. Gordon (1998). Distribution of CO_2 species, estimates of net community production, and air-sea CO_2 exchange in the Ross Sea polynya. *Journal of Geophysical Research*, **103**, 2883–2896.

Battisti, D. S., C. M. Bitz, and R. E. Moritz (1997). Do general circulation models underestimate the natural variability in the Arctic climate. *Journal of Climate*, **10**, 1909–1920.

Beavan, S. G. and S. P. Gogineni (1994). Shipborne radar backscatter measurements from Arctic sea ice during the fall freeze-up. *Remote Sensing Reviews*, **9**, 3–25.

Beavan, S. G. and S. P. Gogineni (1998). Fusion of satellite SAR with passive microwave data for sea ice remote sensing. In: C. Tsatsoulis and R. Kwok (eds.), *Analysis of SAR Data of the Polar Oceans*. Springer-Verlag, Berlin, pp. 91–109.

Beckmann, A. and R. Timmermann (2001). Circumpolar influences on the Weddell Sea: Indication of an Antarctic circumpolar coastal wave. *Journal of Climate*, **14**, 3785–3792.

Bedritsky, A. I., V. V. Asmus, and A. B. Uspensky (1999). Current and future Russian meteorological satellite systems and their applications. *Proceedings of EUMETSAT Meteorological Satellite Data User's Conference, September 6–10, Copenhagen,* pp. 17–23.

Bélanger, S. and P. Larouche (2001). Satellite observations of the North Water polynya phytoplankton biomass: Potential impacts of an Arctic warming. *International*

Polynya Symposium, September, Quebec (abstract). Available online at ⟨*http://www.fsg.ulaval.ca/giroq/now/IPS2001/ips2001.htm*⟩.

Belchansky, G. I. and D. C. Douglas (2000). Classification methods for monitoring Arctic sea-ice using passive/active two-channel data. *Remote Sensing of Environment*, **73**(3), 307–322.

Belchansky, G. I. and D. C. Douglas (2002). Seasonal comparisons of sea ice concentration estimates derived from SSM/I, Okean and Radarsat data. *Remote Sensing of Environment*, **81**(1), 67–81.

Belchansky, G. I., D. C. Douglas, I. V. Alpatsky, and N. G. Platonov (2004a). Spatial and temporal multiyear sea ice distributions in the Arctic: A neural network analysis of SSM/I data, 1988–2001. *Journal of Geophysical Research*, **109**, C10017, DOI: 10.1029/2004JC002388.

Belchansky, G. I., D. C. Douglas, and N. G. Platonov (2004b). Duration of the Arctic sea ice melt season: Regional and interannual variability, 1979–2001. *Journal of Climate*, **17**(1), 67–80.

Bengtsson, L., V. A. Semenov, and O. M. Johannessen (2004). The early twentieth-century warming in the Arctic: A possible mechanism. *Journal of Climate*, **17**, 4045–4057.

Benveniste, J. (ed.) (2002). *Envisat RA2/MWR Product Handbook* (ESA Document PO-TN-ESR-RA-0050, Version 1.2). Available online at ⟨*http://wwwcpg.mssl.ucl.ac.uk/RA2_Handbook/concepts/ra2/ra2-mwr-PH.html*⟩.

Benveniste, J., M. Roca, S. Baker, D. Wingham, S. Laxon, O.-Z. Zanife, B. Legresy, and F. Rémy (2002). Envisat radar altimetry products for cryospheric studies. *EGS XXVII General Assembly, April 21–26, Nice, France* (Abstract 06093).

Berque, J., D. Lubin, and R. C. J. Somerville (2004). Infrared radiative properties of the Antarctic Plateau from AVHRR data: Part I. Effect of the snow surface. *Journal of Applied Meteorology*, **43**, 350–362.

Bertoia, C., J. Falkingham, and F. Fetterer (1998). Polar SAR data for operational sea ice mapping. In: C. Tsatsoulis and R. Kwok (eds.), *Recent Advances in the Analysis of SAR Data of the Polar Oceans*. Springer-Verlag, Berlin, pp. 201–234.

Bertoia, C., M. Manore, H. S. Andersen, C. O'Connors, K. Q. Hansen, and C. Evanego (2004). Synthetic aperture radar for operational ice observation and analysis at the U.S., Canadian, and Danish National Ice Centers. In: C. R. Jackson and J. R. Apel (eds.), *Synthetic Aperture Radar Marine Users Manual*. National Oceanic and Atmospheric Administration, Washington, DC, pp. 417–442.

Bi, D., W. F. Budd, A. C. Hirst, and X. Wu (2001). Collapse and reorganisation of Southern Ocean overturning under global warming in a coupled model. *Geophysical Research Letters*, **28**(20), 3927–3930.

Biggs, N. R. T. and A. J. Willmott (2001). A steady-state coupled ocean-polynya flux model of the North Water, Baffin Bay. *Geophysical and Astrophysical Fluid Dynamics*, **95**, 1–29.

Biggs, N. R. T., M. A. Morales Maqueda, and A. J. Willmott (2000). Polynya flux model solutions incorporating a parameterisation for the collection thickness of consolidated new ice. *Journal of Fluid Mechanics*, **408**, 179–204.

Bilello, M. (1980). Decay patterns of fast sea ice in Canada and Alaska. In: R. S. Pritchard (ed.), *Sea Ice Processes and Models*. University of Washington Press, Seattle, WA, pp. 313–326.

Bindoff, N. L. and T. J. McDougall (2000) Decadal changes along an Indian Ocean section at 32°S and their interpretation. *Journal of Physical Oceanography*, **30**(6), 1207–1222.

Bindoff, N. L., S. R. Rintoul, and R. Massom (2000). Bottom water formation and polynyas in Adélie Land, Antarctica. *Papers and Proceedings of the Royal Society of Tasmania*, **133**(3), 51–56.

Bindoff, N. L., G. D. Williams, and I. Allison (2001). Sea-ice growth and water-mass modification in the Mertz Glacier polynya, East Antarctica, during winter. *Annals of Glaciology*, **33**, 399–406.

Binyala, V., S. V. Oberoi, and K. S. Rao (2003). *Detection and Analysis of Growth of Sea Ice Using MSMR Brightness Temperature Data: Map India*. Available online at ⟨*http://www.gisdevelopment.net/application/nrm/ocean/mi03170.htm*⟩.

Birnbaum, G. and C. Lüpkes (2002). A new parameterisation of surface drag in the marginal sea ice zone. *Tellus*, **54A**, 107–123.

Bitz, C. M., M. M. Holland, M. Eby, and A. J. Weaver (2001). Simulating the ice-thickness distribution in a coupled climate model. *Journal of Geophysical Research*, **106**, 2441–2463.

Bjørgo, E., O. M. Johannessen, and M. W. Miles (1997). Analysis of merged SMMR-SSM/I time series of Arctic and Antarctic sea ice parameters 1978–1995. *Geophysical Research Letters*, **24**(4), 413–416.

Björk, G., J. Soderkvist, P. Winsor, A. Nikolopoulos, and M. Steele (2002). Return of the cold halocline layer to the Amundsen Basin of the Arctic Ocean: Implications for the sea ice mass balance. *Geophysical Research Letters*, **29**(11), 1513.

Bobylev, L. P., K. Kondratyev, and O. M. Johannessen (2004). *Arctic Environmental Variability in the Context of Global Change*. Springer-Verlag, Berlin, 500 pp.

Boerner, W.-M., H. Mott, E. Luneburg, C. Livingston, B. Brisco, R. J. Brown, J. S. Paterson, S. R. Cloude, E. Krogager, J. S. Lee et al. (1998). Polarimetry in remote sensing: Basic and applied concepts. In: F. M. Henderson and A. J. Lewis (eds.), *Manual of Remote Sensing* (3rd edn.). John Wiley & Sons, New York, pp. 271–357.

Bohm, E., T. S. Hopkins, and P. J. Minnett (1997). Passive microwave observations of the Northeast Water Polynya interannual variability: 1978–1994. *Journal of Marine Systems*, **10**, 87–98.

Bohren, C. F. and Barkstrom, B. R. (1974), Theory of the optical properties of snow. *Journal of Geophysical Research*, **79**, 4527–4535.

Bohren, C. F. and R. L. Beschta (1979). Snowpack albedo and snow density. *Cold Regions Science and Technology*, **1**, 47–50.

Bolsenga, S. J. (1983). Spectral reflectances of snow and fresh-water ice from 340 through 1100 nm. *Journal of Glaciology*, **29**(102), 296–305.

Bornemann, H., M. Kreyscher, S. Ramdohr, T. Martin, A. Carlini, L. Sellmann, and J. Plötz (2000). Southern elephant seal movements and Antarctic sea ice. *Antarctic Science*, **12**(1), 3–15.

Boyd, I. L., A. Kato, and Y. Ropert-Coudert (2004). Bio-logging science: Sensing beyond the boundaries. *Memoirs of National Institute of Polar Research*, **58** (special issue), 1–14.

Brandon, M. A. and P. Wadhams (1999). The near surface hydrography beneath the Odden ice tongue. *Deep-Sea Research II*, **46**, 1301–1318.

Brandt, R. E. and Warren, S. G. (1993). Solar-heating rates and temperature profiles in Antarctic snow and ice. *Journal of Glaciology*, **39**, 99–110.

Brandt, R. E., C. S. Roessler, and S. G. Warren (1999). Spectral albedo, absorptance, and transmittance in Antarctic sea ice. *Proceedings of 5th Conference on Polar Meteorology and Oceanography*, American Meteorological Society, Boston, MA, pp. 456–459.

Breivik, L.-A., S. Eastwood, Ø. Godøy, H. Schyberg, S. Andersen, and R. Tonboe (2001). Sea ice products for EUMETSAT satellite application facility. *Canadian Journal of Remote Sensing*, **27**(5), 403–409.

Breon, F. M., J. C. Buriez, P. Couvert, P. Y. Deschamps, J. L. Deuze, M. Herman, P. Goloub, M. Leroy, A. Lifermann, C. Moulin et al. (2002). Scientific results from the POLarization and Directionality of the Earth's Reflectances (POLDER). *Advances in Space Research*, **30**(11), 2383–2386.

Brierley, A. S. and D. N. Thomas (2002). Ecology of Southern Ocean pack ice. *Advances in Marine Ecology*, 2002, **43**, 171–276.

Brierley, A. S., P. G. Fernandes, M. A. Brandon, N. W. Armstrong, S. D. McPhail, P. Steveson, M. Pebody, J. Perrett, M. Squires, D.G. Bone, and G. Griffiths (2002). Antarctic krill under sea ice: Elevated abundance in a narrow band just south of ice edge. *Science*, **295**, 1890–1892.

Brigham, L. W. (1991). *The Soviet Maritime Arctic*. Belhaven Press, London; Scott Polar Research Institute, University of Cambridge, 336 pp.

Brigham, L. W., M. S. Timlin, and J. E. Walsh (2003). Arctic sea ice changes and future access for marine navigation. *Proceedings of 7th Conference on Polar Meteorology and Oceanography and Joint Symposium on High-Latitude Climate Variations, May 12–16, Hyannis, MA* (Paper P1.40). American Meteorological Society, Boston.

Broecker, W. S., S. L. Peacock, S. Walker, R. Weiss, E. Fahrbach, M. Schroeder, U. Mikolajewicz, C. Heinze, R. Key, T. H. Peng et al. (1998). How much deep water is formed in the Southern Ocean? *Journal of Physical Oceanography*, **103**, 15833–15843.

Bromwich, D. H. and G. K. Geer (1991). Satellite analyses of katabatic winds near Terra Nova Bay. *Antarctic Journal of the United States*, **26**, 268–271.

Bromwich, D. and D. D. Kurtz (1984). Katabatic wind forcing of the Terra Nova Bay polynya. *Journal of Geophysical Research*, **89**, 3561–3572.

Bromwich, D. H. and T. R. Parish (1998). Meteorology of the Antarctic. In: D. J. Karoly and D. G. Vincent (eds.), *Meteorology of the Southern Hemisphere*. American Meteorological Society, Boston, pp. 175–200.

Bromwich, D. H., J. F. Carrasco, Z. Liu, and R.-Y. Tzeng (1993). Hemispheric atmospheric variations and oceanographic impacts associated with katabatic surges across the Ross Ice Shelf, Antarctica. *Journal of Geophysical Research*, **98**, 13045–13062.

Bromwich, D., Z. Liu, A. N. Rogers, and M. L. Van Woert (1998). Winter atmospheric forcing of the Ross Sea Polynya. In: S. S. Jacobs and R. F. Weiss (eds.), *Ocean, Ice and Atmosphere: Interactions at the Antarctic Continental Margin* (AGU Antarctic Research Series No. 75). American Geophysical Union, Washington, DC, pp. 101–133.

Bromwich, D. H., Z. Guo, L. Bai, and Q-S. Chen (2004). Modeled Antarctic precipitation: Part I. Spatial and temporal variability. *Journal of Climate*, **17**(3), 427–447.

Brown, G. S. (1977). The average impulse response of a rough surface and its application. *IEEE Transactions on Antennas and Propagation*, **AP-25**, 67–74.

Brown, R. D. and P. Cote (1992). Interannual variability of landfast ice thickness in the Canadian High Arctic, 1950–1989. *Arctic*, **45**(3), 273–284.

Brown, R. G. B. and D. N. Nettleship (1981). The biological significance of polynyas to Arctic colonial seabirds. In: I. Stirling and H. Cleator (eds.), *Polynyas in the Canadian Arctic* (CWS Occasional Paper 45). Canadian Wildlife Service, Ottawa, pp. 59–66.

Buckley, F. S. E. and S. M. Mudge (2004). Dimethylsulphide and ocean–atmosphere interactions. *Chemistry and Ecology*, **20**(2), 73–95.

Buckley, R. G. and H. J. Trodahl (1987). Scattering and absorption of visible light by sea ice. *Nature*, **326**, 867–869.

Budd, W. F. (1991). Antarctica and global change. *Climate Change*, **18**(2-3), 271–299.

Budd, W. F., P. A. Reid, and L. J. Minty (1995). Antarctic moisture flux and net accumulation from global atmospheric analyses. *Annals of Glaciology*, **21**, 149–156.

Budd, W. F., X. Wu, and P. A. Reid (1997). Physical characteristics of the Antarctic sea-ice zone derived from modelling and observations. *Annals of Glaciology*, **25**, 1–7.

Budillon, G. and G. Spezie (2000). Thermohaline structure, and variability in the Terra Nova Bay polynya, Ross Sea. *Antarctic Science*, **16**, 493–508.

Budillon, G., G. Fusco, and G. Spezie (2000). A study of surface heat fluxes in the Ross Sea (Antarctica). *Antarctic Science*, **12**, 243–254.

Budillon, G., D. Flocco, S. Kern, and F. Napoli (2002). Observations on the opening and closure of the Ross Sea polynya in 1995–1999. *European Geophysical Society XXVII General Assembly, April 21–26, Nice, France* (Abstract 04598).

Buesseler, K. O., R. T. Barber, M.-L. Dickson, M. R. Hiscock, J. K. Moore, and R. Sambrotto (2003). The effect of marginal ice-edge dynamics on production and export in the Southern Ocean along 170°W. *Deep-Sea Research Part II*, **50**(3–4), 579–603.

Buffoni, G., A. Cappelletti, and P. Picco (2002). An investigation of thermohaline circulation in Terra Nova Bay polynya. *Antarctic Science*, **14**, 83–92.

Burckle, L. H. and R. Mortlock (1998). Sea-ice extent in the Southern Ocean during the Last Glacial Maximum: Another approach to the problem. *Annals of Glaciology*, **27**, 302–304.

Burns, B. A. (1988). SAR image statistics related to atmospheric drag over sea ice. *Proceedings of IGARSS '88 Symposium, Edinburgh, September 13–16* (ESA SP-284). ESA, Noordwijk, The Netherlands, pp. 409–412.

Burns, B. A. (1990). SAR image statistics related to atmospheric drag over sea ice. *IEEE Transactions on Geoscience and Remote Sensing*, **28**(2), 158–165.

Burns, B. A. and D. R. Lyzenga (1984). Textural analysis as a SAR classification tool. *Electromagnetics*, **4**, 309–322.

Burns, B. A., M. Schmidt-Gröttrup, and T. Viehoff (1992). Methods for digital analysis of AVHRR sea ice images. *IEEE Transactions on Geoscience and Remote Sensing*, **30**(3), 589–602.

Busalacchi, A. J. (2004). The role of the Southern Ocean in global processes: An Earth system science approach. *Antarctic Science*, **16**(4), 363–368.

Cai, W. J., P. H. Whetton, and D. J. Karoly (2003). The response of the Antactic Oscillation to increasing and stabilized atmospheric CO_2. *Journal of Climate*, **16**(10), 1525–1538.

Calvin, W. M., M. Milman, and H. H. Kieffer (2002). Reflectance of Antarctica from 3 to 5 μm: Discrimination of surface snow and cloud properties. *Annals of Glaciology*, **34**, 121–126.

Canadian Ice Service (2002). *MANICE: Manual of Standard Procedures for Observing and Reporting Ice Conditions* (9th edn.: Environment Canada). Canadian Ice Service, Ottawa, 130 pp.

Carleton, A. M. (1989). Antarctic sea-ice relationships with indices of the atmospheric circulation of the Southern Hemisphere. *Climate Dynamics*, **3**, 207–220.

Carleton, A. M. (2003). Atmospheric teleconnections involving the Southern Ocean. *Journal of Geophysical Research*, **108**(C1), DOI: 10.1029/2000JC000379.

Carlström, A. (1997). A microwave backscattering model for deformed first-year sea ice and comparisons with SAR data. *IEEE Transactions on Geoscience and Remote Sensing*, **35**, 378–391.

Carlström, A. and L. M. H. Ulander (1993). C-band backscatter signatures of old sea ice in the central Arctic during freeze-up. *IEEE Transactions on Geoscience and Remote Sensing*, **31**(4), 819–829.

Carlström, A. and L. M. H. Ulander (1995). Validation of backscatter models for level and deformed sea-ice in ERS-1 SAR images. *International Journal of Remote Sensing*, **16**, 3245–3266.

Carmack, E. C. (1986). Circulation and mixing in ice-covered waters. In: N. Untersteiner (ed.), *The Geophysics of Sea Ice* (NATO ASI B146). Plenum Press, pp. 641–712.

Carmack, E. C. (1990). Large scale physical oceanography of polar seas. In: W. O. Smith (ed.), *Polar Oceanography*. Academic Press, New York.., pp. 171–222.

Carsey, F. D. (1980). Microwave observation of the Weddell Polynya. *Monthly Weather Review*, **108**, 2032–2044.

Carsey, F. D. (1985). Summer Arctic sea ice character from satellite microwave data. *Journal of Geophysical Research*, **90**(C3), 5015–5034.

Carsey, F. D. (1986). Remote sensing as a research tool. In: N. Untersteiner (ed.), *The Geophysics of Sea Ice* ((.NATO ASI B146). Plenum Press, pp. 1021–1098.

Carsey, F. D. (ed.) (1992). *Microwave Remote Sensing of Sea Ice* (AGU Monograph No. 68). American Geophysical Union, Washington, DC, 462 pp.

Carsey, F. and G. Pihos (1989). Beaufort–Chukchi ice margin data from Seasat for ice conditions analogous to those of the Labrador Sea. *IEEE Transactions on Geoscience and Remote Sensing*, **27**, 41–551.

Carsey, F. D. and A. T. Roach (1994). Oceanic convection in the Greenland Sea Odden region as interpreted in satellite data. In: O. M. Johannessen, R. D. Muench, and J. E. Overland (eds.), *The Polar Oceans and Their Role in Shaping the Global Environment* (AGU Monograph No. 85). American Geophysical Union, Washington, DC, pp. 211–222.

Carsey, F. and H. J. Zwally (1986). Remote sensing as a research tool. In: N. Untersteiner (ed.), *The Geophysics of Sea Ice*. Plenum Press, New York, pp. 1021–1098.

Carsey, F. D., R. G. Barry, and W. F. Weeks (1992). Introduction. In: F. D. Carsey (ed.), *Microwave Remote Sensing of Sea Ice* (AGU Monograph No. 68). American Geophysical Union, Washington, DC, pp. 1–7.

Carsey, F., R. Harding, and C. Wales (1998). Alaska SAR Facility: The U.S. Science Center for sea ice SAR data. In: C. Tsatsoulis and R. Kwok (eds.), *Analysis of SAR Data of the Polar Oceans*. Springer-Verlag, Berlin, pp. 189–200.

Carver, K. (ed.) (1989). *SAR: Synthetic Aperture Radar* (Earth Observing System Instrument Panel Report Volume IIf). NASA, Washington, DC, 233 pp.

Cattle, H., R. R. Dickson, A. L. Gordon, O. M. Johannessen, and C. Mauritzen (2001). High-latitude processes and the ice-covered ocean. In: N. R. Smith and C. J. Koblinsky (eds.), *Observing the Ocean in the 21st Century*. The Global Ocean Data Assimilation Experiment (GODAE) Project Office, Australian Bureau of Meteorology, Melbourne, pp. 486–508.

Cavalieri, D. J. (1992). The validation of geophysical parameters using multi-sensor data. In: F. D. Carsey (ed.), *Microwave Remote Sensing of Sea Ice* (AGU Monograph No. 68). American Geophysical Union, Washington, DC, pp. 233–242.

Cavalieri, D. J. (1994). A microwave technique for mapping thin ice. *Journal of Geophysical Research*, **99**, 12561–12572.

Cavalieri, D. J. (2002). A link between Fram Strait sea ice export and atmospheric planetary wave phase. *Geophysical Research Letters*, **29**(12), DOI: 10.1029/2002GL014684.

Cavalieri, D. and J. Comiso. 2000. *Algorithm Theoretical Basis Document for the AMSR-E Sea Ice Algorithm* (revised December 1). NASA Goddard Space Flight Center, Greenbelt, MD, 79 pp. Available online at ⟨*http://eospso.gsfc.nasa.gov/ftp_ATBD/REVIEW/AMSR/atbd-amsr-seaice.pdf*⟩.

Cavalieri, D. and J. Comiso (2004). *AMSR-E/Aqua Daily L3 12.5 km Tb, Sea Ice Concentration, and Snow Depth Polar Grids V001: March 2004* (digital media). National Snow and Ice Data Center, Boulder, CO.

Cavalieri, D. J. and S. Martin (1985). A passive microwave study of polynyas along the Antarctic Wilkes Land coast. In: S. Jacobs (ed.), *Oceanology of the Antarctic Continental Shelf* (AGU Antarctic Research Series No. 43). American Geophysical Union, Washington, DC, pp. 227–252.

Cavalieri, D. J. and S. Martin (1994). The contribution of Alaskan, Siberian, and Canadian coastal polynyas to the cold halo-cline layer of the Arctic Ocean. *Journal of Geophysical Research*, **99**, 18343–18362.

Cavalieri, D. J. and C. L. Parkinson (1981). Large-scale variations in observed Antarctic sea ice extent and associated atmospheric circulation. *Monthly Weather Review*, **109**, 2323–2336.

Cavalieri, D. J., P. Gloersen, and W. J. Campbell (1984). Determination of sea ice parameters with the Nimbus-7 SMMR. *Journal of Geophysical Research*, **89**(D4), 5335–5369.

Cavalieri, D. J., P. Gloersen, and T. T. Wilheit (1986). Aircraft and satellite passive microwave observations of the Bering Sea cover during MIZEX West. *IEEE Transactions on Geoscience and Remote Sensing*, **GE-24**, 368–377.

Cavalieri, D. J., B. A. Burns, and R. G. Onstott (1990). Investigation of the effects of summer melt in the calculation of ice concentration using active and passive microwave data. *Journal of Geophysical Research*, **95**(C4), 5359–5369.

Cavalieri, D. J., J. P. Crawford, M. R. Drinkwater, D. T. Eppler, L. D. Farmer, R. R. Jentz, and C. C. Wackerman (1991). Aircraft active and passive microwave validation of sea ice concentration from the Defense Meteorological Satellite Program Special Sensor Microwave/Imager. *Journal of Geophysical Research*, **96**(C12), 21989–22008.

Cavalieri, D. J., J. Crawford, M. Drinkwater, W. J. Emery, D. T. Eppler, L. D. Farmer, M. Goodberlet, R. Jentz, A. Milman, C. Morris et al. (1992). *NASA Sea Ice Validation Program for the DMSP SSM/I: Final Report* (NASA Technical Memo 104559). NASA Goddard Space Flight Center, Greenbelt, MD, 126 pp.

Cavalieri, D. J., K. M. St. Germain, and C. T. Swift (1995). Reduction of weather effects in the calculation of sea ice concentration with the DMSP SSM/I. *Journal of Glaciology*, **41**, 455–464.

Cavalieri, D. J., P. Gloersen, C. L. Parkinson, J. C. Comiso, and H. J. Zwally (1997). Observed hemispheric asymmetry in global sea ice changes. *Science*, **278**(5340), 1004–1106.

Cavalieri, D. J., C. L. Parkinson, P. Gloersen, J. C. Comiso, and H. J. Zwally (1999a). Deriving long-term time series of sea ice cover from satellite passive-microwave multisensor data sets. *Journal of Geophysical Research*, **104**(C7), 15803–15814.

Cavalieri, D., C. Parkinson, P. Gloerson, and H. J. Zwally (1999b, updated 2002). *Sea Ice Concentrations from Nimbus-7 SMMR and DMSP SSM/I Passive Microwave Data* (CD-ROM). National Snow and Ice Data Center, Boulder, CO.

Cavalieri, D. J., T. Markus, J. Maslanik, J. Stroeve, M. Sturm, and B. Walter (2001). *EOS Aqua AMSR-E Arctic Sea Ice Validation Plan*. NASA Goddard Space Flight Center, Greenbelt, MD, 28 pp.

Cavalieri, D. J., J. Maslanik, T. Markus, J. Stroeve, M. Sturm, J. Heinrichs, E. Kim, A. J. Gasiewski, and J. C. Comiso (2002a). EOS Aqua AMSR-E Arctic sea ice validation program. *Proceedings of International Society of Optical Engineering III*, *Hangzhou, China, October 23–27* (Abstract 4894), pp. 413–424.

Cavalieri, D., P. Gloerson, and J. Zwally (2002b). In: J. Maslanik and J. Stroeve (eds.), *Near Real-Time DMSP SSM/I Daily Polar Gridded Sea Ice Concentrations* (digital media, updated regularly). National Snow and Ice Data Center, Boulder, CO.

Cavalieri, D. J., C. L. Parkinson, and K. Y. Vinnikov (2003a). 30-year satellite record reveals contrasting Arctic and Antarctic decadal scale sea ice variability. *Geophysical Research Letters*, **30**(18), 1970, DOI: 10.1029/2003GL018031.

Cavalieri, D., P. Gloersen, and J. Zwally (2003b). In: J. Maslanik and J. Stroeve (eds.), *DMSP SSM/I Daily Polar Gridded Sea Ice Concentrations* (digital media, 1990, updated 2003). National Snow and Ice Data Center, Boulder, CO.

Cavanié, A. (1998). An empirical C-band backscatter melt over Arctic sea ice from ERS-1 AMI-wind data. *Proceedings of a Joint ESA–Eumetstat Workshop on Emerging Scatterometer Applications: From Research to Operations, October 5–7, 1998*. ESA, Noordwijk, The Netherlands, pp. 99–106.

Cavicchioli, R., K. S. Siddiqui, D. Andrews, and K. R. Sowers (2002). Low temperature extremophiles and their applications. *Current Opinion in Biotechnology*, **13**, 253–261.

Chang, C.-I. (2003). *Hyperspectral Imaging: Techniques for Spectral Detection and Classification*. Kluwer Academic, Amsterdam, 367 pp.

Chang, A. T. C., J. L. Foster, and D. K. Hall (1987). Nimbus-7 derived global snow cover parameters. *Annuals of Glaciology*, **9**, 39–44.

Chapman, D. C. (2000). The influence of an alongshelf current on the formation and offshore transport of dense water from a coastal polynya. *Journal of Geophysical Research*, **105**, 24007–24019.

Chapman, W. L. and J. E. Walsh (1993). Recent variations in sea ice and air temperature in high latitudes. *Bulletin of the American Meteorological Society*, **74**(1), 33–47.

Chapman, W. L., W. J. Welch, K. P. Bowman, J. Sacks, and J. E. Walsh (1994). Arctic sea ice variability: Model sensitivities and a multidecadal simulation. *Journal of Geophysical Research*, **99**(C1), 919–935.

Chelton, D. B., J. C. Ries, B. J. Haines, L.-L. Fu, and P. S. Callahan (2001). Satellite altimetry. In: L.-L. Fu and A. Cazenave (eds.), *Satellite Altimetry and the Earth Sciences: A Handbook for Techniques and Applications*. Academic Press, New York, pp. 1–131.

Chen, T. C. and M. C. Yen (1997). Inter-decadal variation of the Southern Hemisphere circulation. *Journal of Climate*, **10**, 805–812.

Cheng, B., J. Launiainen, T. Vihma, and J. Uotila (2001). Modelling sea-ice thermodynamics in BALTEX-BASIS. *Annals of Glaciology*, **33**, 243–247.

Cherny, I. V. and G. M. Chernyavsky (2001). Combined optical-microwave imager/sounder MTVZA-OK. *Proceedings of IGARSS '01, Sydney, 9–13 July*.

Cherny, I. V., G. M. Chernyavsky, and N. N. Gorobets (2002). Spaceborne Microwave Image/Sounder MTVZA. *Proceedings of 25th ESA Antenna Workshop on Satellite Antenna Technology, September 18–20, 2002*. ESTEC, Noordwijk, The Netherlands, pp. 523–527.

Cho, K., N. Sasaki, H. Shimoda, T. Sakata, and F. Nishio (1996). Evaluation and improvement of SSM/I sea ice concentration algorithms for the Sea of Okhotsk. *Journal of the Remote Sensing Society of Japan*, **16**(2), 47–58.

Chou, J. R., C. Weger, J. M. Ligtenberg, K.-S. Kuo, R. M. Welch, and P. Breeden (1994). Segmentation of polar scenes using multi-spectral texture measures and morphological filtering. *International Journal of Remote Sensing*, **15**(5), 1019–1036.

Choudhury, B. J. (1981), Radiative properties of snow for clear sky solar radiation. *Cold Regions Science and Technology*, **4**, 103–120.

Chung, H. and C. Fox (2001). Calculation of wave propagation into land-fast ice. *Annals of Glaciology*, **33**, 322–326.

Clarke, A. and C. M. Harris (2003). Polar marine ecosystems: Major threats and future change. *Environmental Conservation*, **30**, 1–25.

Clarke, A. D. and K. J. Noone (1985). Soot in the Arctic snowpack: A cause for perturbations in radiative transfer. *Atmosphere Environment*, **19**, 2045–2053.

Clarke, T. (2003). Oceanography: Robots in the deep. *Nature*, **421**, 468–470.

Clausi, D. A. (2002). An analysis of co-occurrence texture statistics as a function of grey level quantization. *Canadian Journal of Remote Sensing*, **28**(1), 45–62.

Clausi, D. A. and B. Yue (2004). Comparing co-occurrence probabilities and Markov random fields for texture analysis of SAR sea ice imagery. *IEEE Transactions on Geoscience and Remote Sensing*, **42**(1), 215–228.

Clemente-Colón, P., W. G. Pichel, D. Lamb, M. Van Woert, F. M. Monaldo, D. R. Thompson, and C. C. Wackerman (2003). Operational use of SAR-derived ocean products: Are we there yet? *2003 EUMETSAT Meteorological Satellite Conference*.

CLIVAR Scientific Steering Group (1995). *CLIVAR Science Plan: A Study of Climate Variability and Predictability* (WCRP-89). World Meteorological Organization, Geneva. Available online at ⟨*http://www.clivar.org/publications/other_pubs/splan/science_toc.html*⟩.

Cloude, S. R. (2004). Radar polarimetry and interferometry: A tutorial introduction. *IEEE Geoscience and Remote Sensing Society Newsletter*, **131**, 25–29.

Cloude, S. R. and K. P. Papathanassiou (1998). Polarimetric SAR interferometry. *IEEE Transactions on Geoscience and Remote Sensing*, **36**(5), 1551–1565.

Cloude, S. R. and E. Pottier (1996). A review of target decomposition theorem in radar polarimetry. *IEEE Transactions on Geoscience and Remote Sensing*, **34**, 498–518.

Cloude, S. R. and E. Pottier (1997). An entropy based classification scheme for land applications of polarimetric SAR. *IEEE Transactions on Geoscience and Remote Sensing*, **35**(1), 68–78.

Cloude, S. R., I. Hajnsek, and K. P. Papathanassiou (1999). An eigenvector method for the extraction of surface parameters in polarimetric SAR. *Proceedings of CEOS SAR Workshop, Toulouse* (ESA SP-450). ESA, Noordwijk, The Netherlands, pp. 693–698.

Cloude, S. R., K. P. Papathanassiou, and E. Pottier (2001). Radar polarimetry and polarimetric interferometry. *IEEE Transactions on Electronics*, **E84-C**(12), 1814–1822.

Colbeck, S. C. (1979). Grain clusters in wet snow. *Journal of Colloid and Interface Science*, **72**(3), 371–384.

Colbeck, S. C. (1982). An overview of seasonal snow metamorphism. *Reviews of Geophysics and Space Physics*, **20**(1), 45–61.

Colbeck, S., E. Akitaya, R. Armstrong, H. Gubler, J. Lafeuille, K. Lied, D. McClung, and E. Morris (1990). *International Classification for Seasonal Snow on the Ground*. International Commission for Snow and Ice (IAHS), World Data Center A for Glaciology, University of Colorado, Boulder, CO.

Colling, A. (ed.) (2001). *Ocean Circulation* (2nd edn.). Open University/Butterworth-Heinemann, Boston, 286 pp.

Collins, M. J. (1992). Information fusion in sea ice remote sensing. In: F. D. Carsey (ed.), *Microwave Remote Sensing of Sea Ice* (AGU Monograph 28). American Geophysical Union, Washington, DC, pp. 431–442.

Collins, M. J. and W. J. Emery (1988). A computational method for estimating sea ice motion in sequential Seasat synthetic aperture radar imagery by matched filtering. *Journal of Geophysical Research*, **93**(C8), 9241–9251.

Colony, R. L. and I. G. Rigor (1993). *International Arctic Ocean Buoy Program Data Report for 1 January 1992–31 December 1992* (APL-UW TM 29-93). Applied Physics Laboratory, University of Washington, Seattle, 215 pp.

Colony, R. and A. Thorndike (1984). An estimate of the mean field of Arctic sea ice motion. *Journal of Geophysical Research*, **89**(C6), 10623–10629.

Colwell, S. and J. Turner (2003). The relationship between Antarctic coastal temperatures and sea ice extent. In: *Preprints of the Joint Antarctic Automatic Weather Station Annual Meeting, Antarctic Meteorological Research Center Annual Meeting, and Antarctic Mesoscale Prediction System (AMPS) Users' Workshop, Madison, WI, June 13–26*.

Comiso, J. C. (1983). Sea ice microwave emissivities from satellite passive microwave and infrared observations. *Journal of Geophysical Research*, **88**, 7686–7704.

Comiso, J. C. (1985). Remote sensing of sea ice using multispectral microwave satellite data. In: H. H. Fleming and M. T. Chahine (eds.), *Advances in Remote Sensing Retrieval Methods*. A. Deepak, Hampton, VA, pp. 349–369.

Comiso, J. C. (1986). Characteristics of Arctic winter sea ice from satellite multispectral microwave observations. *Journal of Geophysical Research*, **91**(C1), 975–994.

Comiso, J. C. (1990). Arctic multiyear ice classification and summer ice cover using passive microwave satellite data. *Journal of Geophysical Research*, **95**(C8), 13411–13422.

Comiso, J. C. (1991). Satellite remote sensing of the polar oceans, *Journal of Marine Systems*, **2**, 395–434.

Comiso, J. C. (1994). Surface temperatures in the polar regions from Nimbus 7 Temperature Humidity Infrared Radiometer. *Journal of Geophysical Research*, **99**(C3), 5181–5200.

Comiso, J. C. (1995a). Satellite remote sensing of the Arctic Ocean and adjacent seas. In: W. O. Smith Jr. and J. M. Grebmeier (eds.), *Oceanography: Marginal Ice Zones and Continental Shelves*. American Geophysical Union, Washington, DC, pp. 97–129,

Comiso, J. C. (1995b). *SSM/I Concentrations Using the Bootstrap Algorithm* (NASA Reference Publication 1380). NASA, Washington, DC, 40 pp.

Comiso, J. (1996). Applications of a low-frequency microwave sensor for sea ice research. In: D. Burrage, G. Lagerloef, and R. Massom (eds.), *Remote Sensing of Sea Surface Salinity, Ice Cover and Soil Moisture* (report on a workshop during the American Geophysical Union Western Pacific Geophysical Meeting, July 22–27, Brisbane). Australian Institute of Marine Science, Townsville, pp. 8–10.

Comiso, J. C. (2000). Variability and trends in Antarctic surface temperatures from *in situ* and satellite infrared measurements. *Journal of Climate*, **13**(10), 1674–1696.

Comiso, J. C. (2001). Satellite-observed variability and trends in sea-ice extent, surface temperature, albedo and clouds in the Arctic. *Annals of Glaciology*, **33**, 457–473.

Comiso, J. C. (2002a). A rapidly declining perennial sea ice cover in the Arctic. *Geophysical Research Letters*, **29**(20), 1956, DOI: 10.1029/2002GL015650.

Comiso, J. C. (2002b). *Bootstrap Sea Ice Concentrations from Nimbus-7 SMMR and DMSP SSM/I* (digital media). National Snow and Ice Data Center, Boulder, CO.

Comiso, J. C. (2003a). Large-scale characteristics and variability of the global sea ice cover. In: D. Thomas and G. Dieckmann (eds.), *Sea Ice: An Introduction to Its Physics, Chemistry, Biology and Geology*, Blackwell Scientific, Oxford, UK, pp. 112–142.

Comiso, J. C. (2003b). Warming trends in the Arctic from clear sky satellite observations. *Journal of Climate*, **16**(21), 3498–3510.

Comiso, J. C. (2003c). Enhanced sea ice cover characterization from new passive-microwave systems. In: *EGS-AGU-EUG Joint Assembly, Nice, France, April 6-11* (Geophysical Research Abstracts No. 5, 07865). European Geophysical Society, Katlenburg-Lindau, Germany.

Comiso, J. C. and A. L. Gordon (1987). Recurring polynyas over the Cosmonaut Sea and Maud Rise. *Journal of Geophysical Research*, **92**(C3), 2819–2833.

Comiso, J. C. and A. L. Gordon (1998). Interannual variability in summer sea ice minimum, coastal polynyas and bottom water formation in the Weddell Sea. In: M. Jeffries (ed.), *Antarctic Sea Ice: Physical Processes, Interactions and Variability* (Antarctic Research Series No. 74). American Geophysical Union, Washington, D.C., pp. 293–315.

Comiso, J. C. and A. L. Gordon (1996). Cosmonaut polynya in the Southern Ocean: Structure and variability. *Journal of Geophysical Research*, **101**(C8), 18297–18313.

Comiso, J. C. and R. Kwok (1996). Surface and radiative characteristics of the summer Arctic sea ice cover from multi-sensor satellite observations. *Journal of Geophysical Research*, **101**(C12), 28397–28416.

Comiso, J. C. and C. L. Parkinson (2004). Satellite-observed changes in the Arctic. *Physics Today*, **57**(8), 38–44.

Comiso, J. C. and K. Steffen (2001). Studies of Antarctic sea ice concentrations from satellite observations and their applications. *Journal of Geophysical Research*, **106**(C12), 31361–31385.

Comiso, J. C. and C. W. Sullivan (1986). Satellite microwave and *in situ* observations of the Weddell Sea ice cover and its marginal ice zone. *Journal of Geophysical Research*, **91**(C8), 9663–9681.

Comiso, J. C. and H. J. Zwally (1982). Antarctic sea ice concentrations inferred from Nimbus-5 ESMR and Landsat imagery. *Journal of Geophysical Research*, **87**(C8), 5836–5844.

Comiso, J. C. and H. J. Zwally (1997). Temperature corrected Bootstrap algorithm. *IEEE IGARSS '97 Digest*, **3**, 857–861.

Comiso, J. C., S. F. Ackley, and A. L. Gordon (1984). Antarctic sea ice microwave signature and the correlation with in-situ ice observations. *Journal of Geophysical Research*, **89**(C1), 662–672.

Comiso, J. C., T. C. Grenfell, D. L. Bell, M. A. Lange, and S. F. Ackley (1989). Passive microwave *in situ* observations of winter Weddell Sea ice. *Journal of Geophysical Research*, **94**(C8), 10891–10905.

Comiso, J. C., N. G. Maynard, W. O. Smith Jr., and C. W. Sullivan (1990). Satellite ocean color studies of Antarctic ice edges in summer and autumn. *Journal of Geophysical Research*, **95**, 9481–9496.

Comiso, J. C., P. Wadhams, W. B. Krabill, R. N. Swift, J. P. Crawford, and W. B. Tucker III (1991). Top/bottom multi-sensor remote sensing of Arctic sea ice. *Journal of Geophysical Research*, **96**(C2), 2693–2711.

Comiso, J. C., T. C. Grenfell, M. Lange, A. W. Lohanick, R. K. Moore, and P. Wadhams (1992). Microwave remote sensing of the Southern Ocean ice cover. In: F. D. Carsey (ed.), *Microwave Remote Sensing of Sea Ice* (AGU Monograph No. 28). American Geophysical Union, Washington, DC, pp. 243–259.

Comiso, J. C., C. McClain, C. Sullivan, J. Ryan, and C. L. Leonard (1993). CZCS pigment concentrations in the Southern Ocean and their relationships to some geophysical parameters. *Journal of Geophysical Research*, **98**(C2), 2419–2451.

Comiso, J. C., D. J. Cavalieri, C. L. Parkinson, and P. Gloersen (1997). Passive microwave algorithm for sea ice concentration: A comparison of two techniques. *Remote Sensing of Environment*, **60**(3), 357–384.

Comiso, J. C., P. Wadhams, L. T. Pedersen, and R. A. Gersten (2001). Seasonal and interannual variability of the Odden ice, tongue and a study of environmental effects. *Journal of Geophysical Research*, **106**(C5), 9093–9116.

Comiso, J. C., D. J. Cavalieri, and T. Markus (2003a). Sea ice concentration, ice temperature, and snow depth, using AMSR-E data. *IEEE Transactions on Geoscience and Remote Sensing*, **41**(2), 243–252, 2003.

Comiso, J. C., J. Yang, S. Honjo, and R. A. Krishfield (2003b). The detection of change in the Arctic using satellite and buoy data. *Journal of Geophysical Research*, **108**(C12), 3384, DOI: 1029-2002jc001247.

Comiso, D. J., D. J. Cavalieri, E. Kim, A. Gasiewsky, K. Raney, R. Cahalan, W. Krabill, K. Steffen, R. Massom, and S. Jacobs (2003c). *Antarctic AMSR Validation Program*. NASA Goddard Space Flight Center, Greenbelt, MD.

Connolley, W. M. (2002). Long-term variation of the Antarctic Circumpolar Wave. *Journal of Geophysical Research*, **107**(C12), DOI: 10.1029/2000JC000380.

Connolley, W. M. and J. C. King (1993). Atmospheric water-vapour transport to Antarctica inferred from radiosonde data. *Quarterly Journal of the Royal Meteorological Society*, **119**, 325–342.

Constable, A. J., S. Nicol, and P. G. Strutton (2003). Southern Ocean productivity in relation to spatial and temporal variation in the physical environment. *Journal of Geophysical Research*, **108**(C4), 8079, DOI: 10.1029/2001JC001270.

Coon, M. D. (1980). A review of AIDJEX modeling. In: R. S. Pritchard (ed.), *Sea Ice Processes and Models*. University of Washington Press, Seattle, pp. 12–23.

Coon, M. D., G. S. Knoke, D. C. Echert, and R. S. Pritchard (1998). The architecture of an anisotropic elastic-plastic sea ice mechanics constitutive law. *Journal of Geophysical Research*, **103**(C10), 21915–21925.

Cox, G. F. N. and W. F. Weeks (1975). *Brine Drainage and Initial Salt Entrapment in Sodium Chloride Ice* (CRREL Research Report 354). U.S. Army Cold Regions Research and Engineering Laboratory, Hanover, NH.

Cox, G. F. N. and W. F. Weeks (1983). Equations for determining the gas and brine volumes in sea-ice samples. *Journal of Glaciology*, **29**, 306–316.

Cox, G. F. N. and W. F. Weeks (1988). Numerical simulations of the profile properties of undeformed first-year sea ice during the growth season. *Journal of Geophysical Research*, **93**, 12449–12460.

Cracknell, A. (1997). *The Advanced Very High Resolution Radiometer*. Taylor & Francis, London, 968 pp.

Cracknell, A. P. (ed.) (2001). *Remote Sensing and Climate Change: The Role of Earth Observation*. Springer/Praxis, Chichester, UK, 336 pp.

Crane, D. and P. Wadhams (1996). Sea-ice motion in the Weddell Sea from drifting-buoy and AVHRR data. *Journal of Glaciology*, **42**(141), 249–254.

Crane, R. G. and M. R. Anderson (1994). Springtime microwave emissivity changes in the southern Kara Sea. *Journal of Geophysical Research*, **99**, 14303–14309.

Crocker, G. B. and P. Wadhams (1989). Breakup of Antarctic fast ice. *Cold Regions Science and Technology*, **17**(1), 61–76.

Crosta, X., A. Sturm, L. Armand, and J.-J. Pichon (2004). Late Quaternary sea ice history in the Indian sector of the Southern Ocean as recorded by diatom assemblages. *Marine Micropaleontology*, **50**, 209-223.

Croxall, J. P. and S. Nicol (2004). Management of Southern Ocean fisheries: Global forces and future sustainability. *Antarctic Science*, **16**, 569–584.

Croxall, J. P., P. N. Trathan, and E. J. Murphy (2002). Environmental change and Antarctic seabird populations. *Science*, **297**(5586), 1510–1514.

Cunningham, S. A., S. G. Alderson, B. A. King, and M. A. Brandon (2003). Transport and variability of the Antarctic Circumpolar Current in Drake Passage. *Journal of Geophysical Research*, **108**(C5), 8084, DOI: 10.1029/2001JC001147.

Curlander, J. C. and R. N. McDonough (1991). *Synthetic Aperture Radar: Systems and Signal Processing*. John Wiley & Sons, New York.

Curlander, J. C., B. Holt, and K. J. Hussey (1985). Determination of sea ice motion using digital SAR imagery. *IEEE Journal of Oceanic Engineering*, **OE-10**(4), 358–367.

Curran, M. A. J. and G. B. Jones (2000). Dimethylsulphide in the Southern Ocean: Seasonality and flux. *Journal of Geophysical. Research*, **105**(D16), 20451–20459.

Curran, M. A. J., G. B. Jones, and H. Burton (1998). Spatial distribution of DMS and DMSP in the Australasian sector of the Southern Ocean. *Journal of Geophysical Research*, **103**(D13), 16677–16689.

Curran, M. A. J., T. D. van Ommen, V. I. Morgan, K. L. Phillips, and A. S. Palmer (2003). Ice core evidence for Antarctic sea ice decline since the 1950s. *Science*, **302**, 1203–1206.

Curry, J. A. and E. E. Ebert (1992). Annual cycle of radiation fluxes over the Arctic Ocean: Sensitivity to cloud optical properties. *Journal of Climate*, **5**, 1267–1280.

Curry, J. A., F. G. Meyer, L. F. Radke, C. A. Brock, and E. E. Ebert (1990). Occurrence and characteristics of lower tropospheric ice crystals in the Arctic. *International Journal of Climatology*, **10**(7), 749–764.

Curry, J. A., J. L. Schramm, and E. E. Ebert (1993). Impact of clouds on the surface radiation balance of the Arctic Ocean. *Meteorol. Atmosph. Phys.*, **51**, 197–217.

Curry, J. A., J. L. Schramm, and E. Ebert (1995). Sea ice-albedo climate feedback mechanism. *Journal of Climate*, **8**, 240–247.

Curry, J. A., W. B. Rossow, D. Randall, and J. E. Schramm (1996). Overview of Arctic cloud and radiation characteristics. *Journal of Climate*, **9**, 1731–1764.

Curry, J. A., J. L. Schramm, D. Perovich, and J. O. Pinto (2001). Application of SHEBA/FIRE data to evaluation of sea ice surface albedo parameterizations. *Journal of Geophysical Research*, **106**(D14), 15345–15355.

Curry, J. A., J. L. Schramm, A. Alam, R. Reeder, T. E. Arbetter, and P. Guest (2002). Evaluation of data sets used to force sea ice models in the Arctic Ocean. *Journal of Geophysical Research*, **107**(C8), DOI: 10.1029/2000JC000466.

Curry, J. A., J. Maslanik, G. Holland, and J. Pinto (2004). Applications of aerosondes in the Arctic. *Bulletin of the American Meteorological Society*, **85**(12), 1855–1861.

Daida, J. M., R. G. Onstott, T. F. Bersano-Begey, S. J. Ross, and J. F. Vesecky (1996). Ice roughness classification and ERS SAR imagery of Arctic sea ice: Evalution of feature-extraction algorithms by genetic programming. *Proceedings of IGARSS '96*. Institute of Electrical and Electronics Engineers, Washington, DC, pp. 1520–1522.

Dammert, P. B. G., M. Leppäranta, and J. Askne (1998). SAR interferometry over Baltic Sea ice. *International Journal of Remote Sensing*, **19**(16), 3019–3037.

Darby, M. S., A. J. Willmott, and T. A. Somerville (1995). On the influence of coastline orientation on the steady state width of a latent heat polynya. *Journal of Geophysical Research*, **100**(C7), 13625–13633.

Dare, R. A. and B. W. Atkinson (1999). Numerical modelling of atmospheric response to polynyas in the Southern Ocean sea ice zone. *Journal of Geophysical Research*, **104**, 16691–16708.

D'Asaro, E. A. (2003). Performance of autonomous Lagrangian floats. *Journal of Atmospheric and Oceanic Technology*, **20**, 896–911.

Davidson, A. T. and A. van der Heijden (2000). Exposure of natural Antarctic microbial communities to ambient UV radiation: Effects on bacterioplankton. *Aquatic Microbial Ecology*, **21**, 257–264.

Davis, N. (1996). The Arctic wasteland: A perspective on Arctic pollution. *Polar Record*, **32**(182), 237–248.

De Abreu, R. A., J. Key, J. A. Maslanik, M. C. Serreze, and E. F. LeDrew (1994). Comparison of *in situ* and AVHRR-derived surface broadband albedo over Arctic sea ice. *Arctic*, **47**(3), 288–297.

De Abreu, R. A., D. G. Barber, K. Misurak, and E. F. Le Drew (1995). Spectral albedo of snow-covered first-year and multiyear sea ice during spring melt. *Annals of Glaciology*, **21**, 337–342.

De Abreu, R., J. Yackel, D. Barber, and M. Arkett (2001). Operational satellite sensing of Arctic first-year sea ice melt. *Canadian Journal of Remote Sensing*, **27**(5), 487–501.

De Abreu R., D. Flett, B. Scheuchl, and B. Ramsay (2003). Operational sea ice monitoring with RADARSAT-2: A glimpse into the future. *Proceedings of IGARSS '03, Toulouse, France, July 21–25*.

Dean, K. G., W. J. Stringer, K. Ahlnäs, C. Searcy, and T. Weingartner (1994). The influence of river discharge on the thawing of sea ice, Mackenzie River Delta: Albedo and temperature analyses. *Polar Research*, **13**, 83–94.

Dedrick, K. R., K. Partington, M. Van Woert, C. A. Bertoia, and D. Benner (2001). U.S. National/Naval Ice Center digital sea ice data and climatology. *Canadian Journal of Remote Sensing*, **27**(5), 457–475.

de la Mare, W. K. (1997). Abrupt mid-twentieth century decline in Antarctic sea ice extent from whaling records. *Nature*, **389**, 57–60.

Deming, J., L. Fortier, and M. Fukuchi (2002). The International North Water Polynya Study (NOW): A brief overview. *Deep-Sea Research Part III*, **49**, 4887–4892.

Dempsey, J. and H. H. Shen (eds.) (2001). *Scaling Laws in Ice Mechanics and Dynamics*. Kluwer Academic, Dordrecht, The Netherlands, 484 pp.

Denoth A. (1989). Snow dielectric measurements. *Advances in Space Research*, **9**(1), 233–243.

Deser, C., J. E. Walsh, and M. S. Timlin (2000). Arctic sea ice variability in the context of recent atmospheric circulation trends. *Journal of Climate*, **13**(3), 617–633.

Deser, C., M. Holland, G. Reverdin, and M. Timlin (2002). Decadal variations in Labrador Sea ice cover and North Atlantic sea surface temperatures. *Journal of Geophysical Research*, **107**(C5), 3035, DOI: 10.1029/2000JC000683.

Dethleff, D. (1994). Polynyas as a possible source for enigmatic Bennett Island atmospheric plumes. In: O. M. Johannessen, R. D. Muench, and J. E. Overland (eds.), *The Polar Oceans and Their Role in Shaping the Global Environment*. American Geophysical Union, Washington, DC, pp. 475–483.

Dethleff, D., P. Loewe, and E. Kleine (1998). The Laptev Sea flaw lead: Detailed investigation on ice formation and export during 1991/1992 winter season. *Cold Regions Science and Technology*, **27**, 225–243.

Dickson, B. (1999). All change in the Arctic. *Nature*, **397**(6718), 389–391.

Dickson, R. R., J. Meincke, S.-A. Malmberg, and A. L. Lee (1988). The Great Salinity Anomaly in the northern North Atlantic 1968–1982. *Progress in Oceanography*, **20**, 103–151.

Dickson, R. R., T. J. Osborn, J. W. Hurrell, J. Meincke, J. Blindheim, B. Adlandsvik, T. Vinje, G. Alekseev, and W. Maslowski (2000). The Arctic Ocean response to the North Atlantic Oscillation. *Journal of Climate*, **13**, 2671–2696.

Dickson, R., I. Yashayaev, J. Meincke, B. Turrell, S. Dye, and J. Holfort (2002). Rapid freshening of the deep North Atlantic Ocean over the past four decades. *Nature*, **416**, 832.

Dickson, R. R., R. Curry, and I. Yashayaev (2003). Recent changes in the North Atlantic. *Philosophical Transactions of the Royal Society of London*, **A(361),** 1917–1934.

Dieckmann, G. and H. H. Hellmer (2003). The importance of sea ice: An overwiew. In: D. N. Thomas and G. S. Dieckmann (eds.), *Sea Ice: An Introduction to Its Physics, Biology, Chemistry and Geology*. Blackwell Scientific, Oxford, UK, pp. 1–21.

Dieckmann, G. S., H. Eicken, C. Haas, D. L. Garrison, M. Gleitz, M. Lange, E.-M. Nöthig, M. Spindler, C. W. Sullivan, D. N. Thomas, and J. Weissenberger (1998). A compilation of data on sea ice algal standing crop from the Bellingshausen, Amundsen, and Weddell Seas from 1983 to 1994. In: M. P. Lizotte and K. R. Arrigo (eds.), *Antarctic Sea Ice Biological Processes, Interactions and Variability* (AGU Antarctic Research Series No. 73). American Geophysical Union, Washington, DC, pp. 85–92.

Dierking, W. (1992). *Sensitivity Studies of Selected Theoretical Scattering Models with Applications to Radar Remote Sensing of Sea Ice* (Berichte aus dem Fachbereich Physik, Report 33). Alfred-Wegener-Institut für Polar- und Meeresforschung, Bremerhaven, Germany.

Dierking, W. (1995). Laser profiling of the ice surface topography during the Winter Weddell Gyre Study 1992. *Journal of Geophysical Research*, **100**(C3), 4807–4820.

Dierking, W. (2001). *Radar Signatures of Frazil and Pancake Ice: A Review* (Report R 695). Electromagnetic Systems, Technical University of Denmark, 50 pp.

Dierking, W. and J. Askne (1998). Polarimetric L- and C-band SAR signatures of Baltic sea ice observed during EMAC-95. In: P. Gudmandsen (ed.), *Future Trends in Remote Sensing*. Balkema, Rotterdam, pp. 329–336.

Dierking, W., A. Carlstrom, and L. M. H. Ulander (1997). The effect of inhomogeneous roughness on radar backscattering from slightly deformed sea ice. *IEEE Transactions on Geoscience and Remote Sensing*, **35**(1), 147–159.

Dierking, W., H. Skriver, and P. Gudmandsen (2003). SAR polarimetry for sea ice monitoring. In: *Proceedings of ESA Workshop, POLInSAR: Applications of SAR Polarimetry and Polarimetric Interferometry, January* (ESA SP-529). ESRIN, Frascati, Italy. Available online at ⟨*http://www.earth.esa.int/polinsar*⟩.

Dierking, W., H. Skriver, and P. Gudmandsen (2004). On the improvement of sea ice classification by means of radar polarimetry. In: R. Goossens (ed.), *Remote Sensing in Transition*. Millpress, Rotterdam, pp. 203–209.

Diner, D. J., J. C. Beckert, T. H. Reilly, C. J. Bruegge, J. E. Conel, R. Kahn, J. V. Martonchik, T. P. Ackerman, R. Davies, S. A. W. Gerstl et al. (1998). Multi-angle Imaging SpectroRadiometer (MISR) intrument description and experiment overview. *IEEE Transactions on Geoscience and Remote Sensing*, **36**, 1072–1087.

Diner, D., G. P. Asner, R. Davies, Y. Knyazikhin, J.-P. Muller, A. Nolin, B. Pinty, C. B. Schaaf, and J. Stroeve (1999a). New directions in Earth observing: Scientific applications of multi-angle remote sensing. *Bulletin of the American Meteorological Society*, **80**, 2209–2228.

Diner, D. J., R. Davies, T. Várnai, C. Moroney, C. Borel., S. A. W. Gerstl, and D. L. Nelson (1999b). *Earth Observing System MISR Level 2 Top-of-Atmosphere Albedo Algorithm Theoretical Basis* (JPL D-13401, Rev. D). Available online at ⟨*http://eospso.gsfc.nasa.gov/eos_ homepage/for_scientists/atbd/docs/MISR/atbd-misr-08.pdf*⟩.

Diner, D. J., R. Davies, L. Di Girolamo, A. Horvath, C. Moroney, J.-P. Muller, S. R. Paradise, D. Wenkert, and J. Zong (1999c). *Earth Observing System MISR Level 2 Cloud Detection and Classification Algorithm Theoretical Basis* (JPL D-13401, Rev. D). Available online at ⟨*http://eospso.gsfc.nasa.gov/eos_homepage/for_scientists/atbd/docs/MISR/atbd-misr-07.pdf*⟩.

DiTullio, G. R., J. Grebmeier, K. R. Arrigo, M. P. Lizotte, D. H. Robinson, A. Leventer, J. Barry, M. Van Woert, and R. B. Dunbar (2000). Rapid and early export of *Phaeocystis antarctica* blooms in the Ross Sea, Antarctica. *Nature*, **404**, 595–598.

Divine, D., R. Korsnes, and A. Makshtas (2003). Variability and climate sensitivity of fast ice extent in the north-eastern Kara Sea. *Polar Research*, **22**(1), 27–34.

Dmitrenko, I., J. A. Hölemann, K. Tyshko, V. Churun, S. Kirillov, and H. Kassens (2001). The Laptev Sea flaw polynya, Russian Arctic: Effects on the mesoscale hydrography. *Annals of Glaciology*, **33**, 373–376.

DMSG (2000). *Ice: Report of the Disaster Management Support Group (DMSG) of the Committee on Earth Observation Satellites (CEOS)*. Committee on Earth Observation Satellites, Tokyo, 24 pp.

Dokken, S. T., B. Hakansson, and J. Askne (2000a). Intercomparison of Arctic sea ice concentration using Radarsat, ERS, SSM/I and in-situ data. *Canadian Journal of Remote Sensing*, **26**(6), 521–536.

Dokken, S. T., P. Winsor, T. Markus, and J. Askne (2000b). SAR, SSMI and numerical model characterisation of Arctic Ocean coastal polynyas. *Proceedings of ERS-Envisat Symposium, Gothenburg, Sweden*.

Doronin, Y. P. (1971). *Thermal Interaction of the Atmosphere and the Hydrosphere in the Arctic*. Israel Program for Scientific Translations, Jerusalem, pp. 85.

Downer, J. and T. G. Haskell (2001). Ice-floe kinematics in the Ross Sea marginal ice zone using GPS and accelerometers. *Annals of Glaciology*, **33**, 345–349.

Dozier, J. (1989). Remote sensing of snow in visible and near-infrared wavelengths. In: G. Asrar (ed.), *Theory and Applications of Optical Remote Sensing*. John Wiley & Sons, New York, pp. 527–547.

Dozier, J. and T. Painter (2004). Multispectral and hyperspectral remote sensing of alpine snow properties. *Annual Review of Earth and Planetary Sciences*, **32**, 465–494.

Dozier, J. and S. G. Warren (1982). Effect of viewing angle on the infrared brightness temperature of snow. *Water Resources Research*, **18**(5), 1424–1434.

Dozier, J., S. R. Schneider, and D. F. McGinnis Jr. (1981). Effects of grain size and snowpack water equivalence on visible and near-infrared satellite observations of snow. *Water Resources Research*, **17**(4), 1213–1221.

Drinkwater, M. R. (1988). Important changes in microwave scattering properties of young snow-covered sea ice as indicated from dielectric modelling. *Proceedings of IGARSS '88 Symposium, Edinburgh, Scotland, September 13–16* (ESA SP-284). ESA, Noordwijk, The Netherlands, pp. 793–797.

Drinkwater, M. R. (1990). Multi-frequency imaging radar polarimetry of sea ice. In: T. K. S. Murthy, J. G. Paren, W. M. Sackinger and P. Wadhams (eds.), *Ice Technology for Polar Oceans*. Computational Mechanics Publications, Boston, pp. 365–376.

Drinkwater, M. R. (1991). Ku band airborne radar altimeter observations in marginal sea ice during the 1984 Marginal Ice Zone Experiment. *Journal of Geophysical Research*, **96**(C3), 4555–4572.

Drinkwater, M. R. (1995a). Airborne and satellite SAR investigations of sea-ice surface characteristics. In: M. Ikeda and F. W. Dobson (eds.), *Oceanographic Applications of Remote Sensing*. CRC Press, Boca Raton, FL, pp. 339–357.

Drinkwater, M. R. (1995b). Applications of SAR measurements in ocean–ice–atmosphere interaction studies. In: M. Ikeda and F. W. Dobson (eds.), *Oceanographic Applications of Remote Sensing*. CRC Press, Boca Raton, FL, pp. 391–406.

Drinkwater, M. R. (1997). Satellite microwave radar observations of climate-related sea-ice anomalies. In: *Proceedings of Workshop on Polar Processes in Global Climate, Cancun, Mexico, November 13–15, 1996*. American Meteorological Society, Boston, pp. 115–118.

Drinkwater, M. R. (1998a). Satellite microwave radar observations of Antarctic sea ice. In: C. Tsatsoulis and R. Kwok (eds.), *Analysis of SAR Data of the Polar Oceans*. Springer-Verlag, Berlin, pp. 145–187.

Drinkwater, M. R. (1998b). Active microwave remote sensing observations of Weddell Sea ice. In: M. O. Jeffries (ed.), *Antarctic Sea Ice Physical Processes, Interactions and Variability* (AGU Antarctic Research Series No. 74). American Geophysical Union, Washington, DC, pp. 187–212.

Drinkwater, M. R.,. and F. D. Carsey (1991). Observations of the late-summer to fall transition with the 14.6 GHz SEASAT scatterometer. *Proceedings of IGARSS '91 Symposium, Espoo, Finland, June 3–6* (Vol. 3), pp. 597–1600.

Drinkwater, M. R. and G. B. Crocker (1988). Modeling changes in the dielectric and scattering properties of young snow-covered sea ice at GHz frequencies. *Journal of Glaciology*, **34**(118), 274–282.

Drinkwater, M. R. and C. Kottmeier (1994). Satellite microwave radar- and buoy-tracked ice motion in the Weddell Sea during WWGS'92. *Proceedings of IGARSS '94, Pasadena, CA, August 8–12* (Vol. 1), pp. 153–155.

Drinkwater, M. R., and R. Kwok (1991). Stokes matrix statistics in sea ice polarimetric SAR images. *Proceedings of IGARSS '91, June 3–6, Espoo, Finland* (Vol. 1, IEEE Catalog #CH2971-0), pp. 99–102.

Drinkwater, M. R. and C. C. Lin (2000). Introduction to the special section on emerging scatterometer applications. *IEEE Transactions on Geoscience and Remote Sensing*, **38**(4), 1763–1764.

Drinkwater, M. R. and X. Liu (1997). Observing interannual variability in sea-ice dynamics using NSCAT. *Proceedings of NSCAT Science Team Workshop, Honolulu, Hawaii, January 23–24* (JPL technical publication). Jet Propulsion Laboratory, Pasadena, CA.

Drinkwater, M. R. and X. Liu (2000). Seasonal to interannual variability in Antarctic sea-ice surface melt. *IEEE Transactions on Geoscience and Remote Sensing*, **38**(4), 1827–1842.

Drinkwater, M. R. and V. I. Lytle (1997). ERS-1 radar and field-observed characteristics of autumn freeze-up in the Weddell Sea. *Journal of Geophysical Research*, **102**(C6), 12593–12608.

Drinkwater, M. R. and V. A. Squire (1989). C-band observations of marginal ice zone rheology in the Labrador Sea. *IEEE Transactions on Geoscience and Remote Sensing*, **27**(5), 522–534.

Drinkwater, M. R., R. Kwok, D. P. Winebrenner, and E. Rignot (1991). Multifrequency polarimetric synthetic aperture radar observations of sea ice. *Journal of Geophysical Research*, **96**(C11), 20679–20698.

Drinkwater, M. R., R. Kwok, E. Rignot, H. Israelsson, R. G. Onstott, and D. P. Winebrenner (1992). Potential application of polarimetry to the classification of sea ice. In: F. D. Carsey (ed.), *Microwave Remote Sensing of Sea Ice* (AGU Monograph No. 68). American Geophysical Union, Washington, DC, pp. 419–430.

Drinkwater, M. R., D. G. Long, and D. S. Early (1993). Enhanced resolution ERS-1 scatterometer imaging of Southern Ocean sea ice. *ESA Journal*, **17**(4), 307–322.

Drinkwater, M. R., D. S. Early, and D. G. Long (1994). ERS-1 investigations of Southern Ocean sea ice geophysics using combined Scatterometer and SAR images. *IGARSS '94, Pasadena, CA, August 8–12, International Geoscience and Remote Sensing Symposium. Surface and Atmospheric Remote Sensing: Technologies, Data Analysis and Interpretation* (Vol. 1), pp. 165–7.

Drinkwater, M. R., Hosseinmostafa, R., and P. Gogineni (1995). C-band backscatter measurements of winter sea ice in the Weddell Sea, Antarctica. *International Journal of Remote Sensing*, **16**(17), 3365–3389.

Drinkwater, M. R., X. Liu, and D. Low (1998a). Interannual variability in Weddell sea ice from ERS wind scatterometer. *Proceedings of IGARSS '98, Seattle, WA, July 6–10*, pp. 1982–1984.

Drinkwater, M. R., P. Wadhams, D. Low, and X. Liu (1998b). Interannual variability in Weddell Sea ice from ERS wind scatterometer. *Proceedings of a Joint ESA–Eumetsat Workshop on Emerging Scatterometer Applications: From Research to Operations, October 5–7*. ESA, Noordwijk, The Netherlands, pp. 119–123.

Drinkwater, M. R., X. Liu, J. Maslanik, and C. Fowler (1999). *Optimal Analysis Products Combining Buoy Trajectories and Satellite-Derived Ice-Drift Fields* (International Programme for Antarctic Buoys, IPAB Biennial Meeting Report, May 11–13, 1998, Naples, Italy, WCRP Report No. 5/1999). World Climate Research Program, Geneva, Switzerland, pp. 1–11.

Drinkwater, M. R., R. Kwok, J. A. Maslanik, C. W. Fowler, and C. A. Geiger (2001a). Quantifying surface fluxes in the ice-covered polar oceans using satellite microwave remote sensing data. In: N. R. Smith and C. J. Koblinsky (eds.), *Observing the Ocean in the 21st Century*. GODAE Project Office, Australian Bureau of Meteorology, Melbourne.

Drinkwater, M. R., X. Liu, and S. Harms (2001b). Combined satellite- and ULS-derived sea-ice flux in the Weddell Sea, Antarctica. *Annals of Glaciology*, **33**, 125–132.

Drinkwater, M. R., R. Francis, G. Ratier, and D. J. Wingham (in press). The European Space Agency's Earth Explorer Mission CryoSat: Measuring variability in the cryosphere. *Annals of Glaciology*, **39**.

Drobot, S. D. and M. R. Anderson. (2001a). Determination of snow melt onset dates over the Arctic sea ice using passive microwave data. *Journal of Geophysical Research*, **106**(D20), 24033–24050.

Drobot, S. D. and M. R. Anderson (2001b). Comparison of interannual snowmelt-onset dates with atmospheric conditions. *Annals of Glaciology*, **33**, 79–83.

Drobot, S. and M. Anderson (2001c). *Snow Melt Onset over Arctic Sea Ice from SMMR and SSM/I Brightness Temperatures* (digital media). National Snow and Ice Data Center, Boulder, CO.

Drobot, S. and M. A. Anderson (2001d). An improved method for determining snowmelt onset dates over Arctic sea ice using Scanning Multichannel Microwave Radiometer and Special Sensor Microwave/Imager data. *Journal of Geophysical Research*, **106**(D20), 24033–24049.

Drobot, S. D. and J. A. Maslanik (2003). Interannual variability in summer Beaufort Sea ice conditions: Relationship to winter and summer surface and atmospheric variability. *Journal of Geophysical Research*, **108**(C7), 3233, DOI: 10.1029/2002JC001537.

Drucker, R., S. Martin, and R. Moritz (2003). Observations of ice thickness and frazil ice in the St Lawrence Island polynya from satellite imagery, upward looking sonar, and salinity/temperature moorings. *Journal of Geophysical Research*, **108**(C5), 3149, DOI: 10.1029/2001JC001213.

Drue, C. and G. Heinemann (2004). High-resolution maps of the sea-ice concentration from MODIS satellite data. *Geophysical Research Letters*, **31**(20), L20403, DOI: 10.1029/2004GL020808.

Du, Q. and C.-I Chang (2004). Linear mixture analysis-based compression for hyperspectral image analysis. *IEEE Transactions on Geoscience and Remote Sensing*, **42**(4), 875–905.

Dukhovskoy, D. S., M. A. Johnson, and A. Proshutinsky (2004). Arctic decadal variability: An auto-oscillatory system of heat and fresh water exchange. *Geophysical Research Letters*, **31**(3), L03302, DOI: 10.1029/2003GL019023.

Dulière, V. and T. Fichefet (2004). On the assimilation of satellite data into sea-ice models. *EGS First General Assembly, 25–30 April, Nice, France* (Abstract 00509).

Dumas, J. A., G. M. Flato, and A. J. Weaver (2003). The impact of varying atmospheric forcing on the thickness of arctic multi-year sea ice. *Geophysical Research Letters*, **30**(18), 1918, DOI: 10.1029/2003GL017433.

Dunbar, M. J. (1981). Physical causes and biological significance of polynyas and other open water in sea ice. In: I. Stirling and H. Cleator (eds.), *Polynyas in the Canadian Arctic* (Vol. 1, Occasional Paper 45). Canadian Wildlife Service, Ottawa, pp. 29–43.

Dunbar, M. and M. J. Dunbar (1972). The history of the North Water. *Proceedings Royal Society of Edinburgh,* **72**, 231–241.

Dunbar, R. B., A. R. Leventer, and D. A. Mucciarone (1998). Water column sediment fluxes in the Ross Sea, Antarctica: Atmospheric and sea ice forcing. *Journal of Geophysical Research*, **103**, 30741–30759.

Early, D. S. and D. G. Long (1997a). Azimuthal modulation of C-band scatterometer sigma(0) over Southern Ocean sea ice. *IEEE Transactions on Geoscience and Remote Sensing*, **35**(5), 1201–1209.

Early, D. S. and D. G. Long (1997b). Ice classification in the Southern Ocean using ERS-1 scatterometer data. *IGARSS '97, International Geoscience and Remote Sensing Symposium, Singapore, August 4–8*, pp. 1844–1846.

Early, D. S. and D. G. Long (1998). Scatterometer resolution enhancement. *Proceedings of IGARSS '98, Seattle, WA, July 6–10*, pp. 1970–1972.

Early, D. S. and D. G. Long (2001). Image reconstruction and enhanced resolution imaging from irregular samples. *IEEE Transactions on Geoscience and Remote Sensing*, **39**(2), 291–302.

Ebert, E. E. (1989). Analysis of polar clouds from satellite imagery using pattern recognition and a statistical cloud analysis scheme. *Journal of Applied Meteorology*, **28**, 382–399.

Ebert, E. E. and J. A. Curry (1993). An intermediate one-dimensional thermodynamic sea ice model for investigating ice–atmosphere interactions. *Journal of Geophysical Research*, **98**(C6), 10085–10109.

Ebert, E. E., J. L. Schramm, and J. A. Curry (1995). Disposition of solar radiation in sea ice and the upper ocean. *Journal of Geophysical Research*, **100**, 15965–15975.

Edwards, R. (2000). Iron in modern and ancient East Antarctic snow: Implications for phytoplankton in the Southern Ocean. PhD thesis, University of Tasmania, Hobart, Tasmania, Australia.

Eicken, H. (1992). The role of sea ice in structuring Antarctic ecosystems. *Polar Biology*, **12**, 3–13.

Eicken, H. (1998). Factors determining microstructure, salinity and stable-isotope composition of Antarctic sea ice: Deriving modes and rates of ice growth in the Weddell Sea. In: M. O. Jeffries (ed.), *Antarctic Sea Ice Physical Processes, Interactions and Variability*. American Geophysical Union, Washington, DC, pp. 89–122.

Eicken, H. (2003a). From the microscopic to the macroscopic to the regional scale: Growth, microstructure and properties of sea ice. In: D. N. Thomas and G. S. Dieckmann (eds.), *Sea Ice: An Introduction to Its Physics, Biology, Chemistry and Geology*. Blackwell Scientific, London, pp. 22–81.

Eicken, H. (2003b). The role of Arctic sea ice in transporting and cycling terrestrial organic matter. In: R. Stein and R. W. Macdonald (eds.), *The Organic Carbon Cycle in the Arctic Ocean*. Springer-Verlag, Berlin, pp. 45–53.

Eicken, H. and M. A. Lange (1989a). Development and properties of sea ice in the coastal regime of the Southeastern Weddell Sea. *Journal of Geophysical Research*, **94**, 8193–8206.

Eicken, H. and M. A. Lange (1989b). Sea ice thickness data: The many vs the few. *Geophysical Research Letters*, **16**, 495–498.

Eicken, H. and P. Lemke (2001). The response of polar sea ice to climate variability and change. In: J. L. Lozán et al. (eds.), *Climate of the 21st Century: Changes and Risks*. Wissenschaftliche Auswertungen/GEO, Hamburg, pp. 206–211.

Eicken, H., M. A. Lange, H. W. Hubberten, and P. Wadhams (1994). Characteristics and distributions of snow and meteoric ice in the Weddell Sea and their contribution to the mass balance of sea ice. *Annales Geophysicae*, **12**(1), 80–93.

Eicken, H., T. Viehoff, T. Martin, J. Kolatschek, V. Alexandrov, and E. Reimnitz (1995a). Studies of clean and sediment-laden ice in the Laptev Sea. *Reports on Polar Research*, **176**, 62–70.

Eicken, H., H. Fischer, and P. Lemke (1995b). Effects of the snow cover on Antarctic sea ice and potential modulation of its response to climate change. *Annals of Glaciology*, **21**, 369–376.

Eicken, H., E. Reimnitz, V. Alexandrov, T. Martin, H. Kassens, and T. Viehoff (1997). Sea-ice processes in the Laptev Sea and their importance for sediment export. *Continental Shelf Research*, **17**(2), 205–233.

Eicken, H., J. Kolatschek, J. Freitag, F. Lindemann, H. Kassens, and I. Dmitrenko (2000). Identifying a major source area and constraints on entrainment for basin-scale sediment transport by Arctic sea ice. *Geophysical Research Letters*, **27**, 1919–1922.

Eicken, H., D. K. Perovich, and T. C. Grenfell (2001a). The role of melt ponds in the evolution of Arctic summer pack ice albedos. *AMS Sixth Meeting on Polar Meteorology and Oceanography, May* (Abstract 3A.2).

Eicken, H., W. B. Tucker III, and D. K. Perovich (2001b). Indirect measurements of the mass balance of summer Arctic sea ice with an electromagnetic induction technique. *Annals of Glaciology*, **33**, 194–200.

Elachi, C. (1988). *Spaceborne Radar Remote Sensing: Applications and Techniques*. Institute of Electrical and Electronics Engineers, New York, 255 pp.

Elder, B., K. Claffey, D. K. Perovich, and J. A. Richter-Menge (2002). Autonomous measurements of ice mass balance. In: *Monitoring an Evolving Cryosphere* (summary of the NSIDC Special Session at the American Geophysical Union Fall Meeting, December 10–14, Report GD-30). National Snow and Ice Data Center, Boulder, CO, pp. 56.

El Naggar, S., C. Garrity, and R. O. Ramseier (1998). The modeling of sea ice melt-water ponds for the High Arctic using an airborne linescan camera, and applied to Satellite Special Sensor Microwave/Imager (SSM/I). *International Journal of Remote Sensing*, **19**, 2373–2394.

Emery, W. J., A. C. Thomas, M. J. Collins, W. R. Crawford, and D. L. Mackas (1986). An objective procedure to compute advection from sequential infrared satellite images. *Journal of Geophysical Research*, **91**, 12865–12879.

Emery, W. J., J. Brown, and Z. P. Nowak (1989). AVHRR image navigation: Summary and review. *Photogrammetric Engineering and Remote Sensing*, **55**(8), 1175–1183.

Emery, W. J., M. Radebaugh, C. Fowler, D. Cavalieri, and K. Steffen (1991a). A comparison of sea ice parameters computed from Advanced Very High Resolution Radiometer and Landsat satellite imagery, and from airborne passive microwave radiometry. *Journal of Geophysical Research*, **96**(C12), 22075–22085.

Emery, W. J., C. W. Fowler, J. Hawkins, and R. H. Preller (1991b). Satellite image inferred sea ice motion in Fram Strait, the Greenland Sea and the Barents Sea. *Journal of Geophysical Research*, **96**(C3), 4751–4768. [Correction: Emery, W. J. et al. (1991b). Correction to Fram Strait satellite image-derived ice motions. *Journal of Geophysical Research*, **96**(C5), 8917–8920].

Emery, W. J., C. W. Fowler, and J. Maslanik (1994). Arctic sea ice concentrations from Special Sensor Microwave Imager and Advanced Very High Resolution Radiometer satellite data. *Journal of Geophysical Research*, **99**(C9), 18329–18342.

Emery, W. J., C. W. Fowler, and J. A. Maslanik (1995). Satellite remote sensing of ice motion. In: M. Ikeda and F.W. Dobson (eds.), *Oceanographic Applications of Remote Sensing*. CRC Press, Boca Raton, FL, pp. 367–379.

Emery, W. J., C. W. Fowler, and J. A. Maslanik (1997a). Satellite-derived maps of Arctic and Antarctic sea ice motion: 1998–1994. *Geophysical Research Letters*, **24**(8), 897–900.

Emery, W., C. Fowler, and J. Maslanik (1997b). New satellite-derived sea ice motion tracks Arctic contamination. *Marine Pollution Bulletin*, **35**(7-12), 345–352.

Engelsen, O., H. Hop, E. N. Hegseth, E. Hansen, and S. Falk-Petersen (2004). Deriving phytoplankton biomass in the marginal ice zone from satellite observable parameters. *International Journal of Remote Sensing*, **25**(7-8), 1453–1457.

Enomoto, H. and A. Ohmura (1990). The influences of atmospheric half-yearly cycle on sea ice extent in the Antarctic. *Journal of Geophysical Research*, **95**, 9497–9511.

Enomoto, H., F. Nishio, H. Warashina, and S. Ushio (2002). Satellite observation of melting and break-up of fast ice in Lützow-Holm Bay, East Antarctica. *Polar Meteorology and Glaciology*, **16**, 1–14.

Entekhabi, D., E. G. Njoku, P. Houser, M. Spencer, T. Doiron, Y. Kim, J. Smith, R. Girard, S. Belair, W. Crow et al. (2004). The Hydrosphere State (HYDROS) satellite mission: An Earth system Pathfinder for global mapping of soil mositure and land freeze/thaw. *IEEE Transactions on Geoscience and Remote Sensing*, **42**(10), 2184–2195.

Eppler, D. T., L. D. Farmer, A. W. Lohanick, M. A. Anderson, D. Cavalieri, J. Comiso, P. Gloersen, C. Garrity, T. C. Grenfell, M. Hallikainen et al. (1992). Passive microwave signatures of sea ice. In: F. D. Carsey (ed.), *Microwave Remote Sensing of Sea Ice* (AGU Monograph No. 68). American Geophysical Union, Washington, DC, pp. 47–71.

Eriksson, L., M. R. Drinkwater, B. Holt, E. Valjavek, and O. Nortier (1998). SIR-C polarimetric radar results from the Weddell Sea. *Proceedings of IGARSS '98, Seattle, Washington, July 6–10* (Vol. 4, IEEE Catalog #98CH36174), pp. 2222–2224.

ESA (1991) *European Remote Sensing Satellite-ERS-1 Data Book: A Summary of the Technical Elements of the ERS-1 Spacecraft and Its Payload, April* (Report No. ESA BR-75). ESA, Paris.

ESA (2001). *CryoSat Mission and Data Description* (CS-RP-ESA-SY-0059). ESA, Noordwijk, The Netherlands.

ESA (2003). *CryoSat Science Report* (ESA SP-1272). ESA, Noordwijk, The Netherlands.

ESA and UCL (2001). *CryoSat Calibration and Validation Concept* (CS-PL-UCL-SY-0004). ESA, Noordwijk, The Netherlands.

Evans, D. L. and J. Plaut (1996). *Science Results from the Spaceborne Imaging Radar-C/X-Band Synthetic Aperture Radar (SIR-C/X-SAR)* (Report NAS 1.26:206707). National Academy of Sciences, Washington, D.C., 271 pp.

Everett, J. T. and B. B. Fitzharris (eds.) (2001). The Arctic and Antarctic. In: R. T. Watson, M. C. Zinyowera, and R. H. Moss (eds.), *The Regional Impacts of Climate Change: An Assessment of Vulnerability* (IPCC Special Repor). Intergovernmental Panel on Climate Change, UNEP-WMO, Cambridge University Press, Cambridge, UK, 527 pp.

Ezraty, R. and A. Cavanié (1999a). Intercomparison of backscatter maps over Arctic sea ice from NSCAT and the ERS scatterometer. *Journal of Geophysical Research*, **104**(C5), 11471–11483.

Ezraty, R. and A. Cavanié (1999b). Construction and evaluation of 12.5 km grid NSCAT backscatter maps over Arctic sea ice. *IEEE Transactions on Geoscience and Remote Sensing*, **37**(3), 1685–1697.

Ezraty, R. and J. F. Poillé (2001). *SeaWinds on QuikSCAT Polar Sea Ice Grids: User Manual* (Convection Report 5, V1.1, August). Institut Français de Recherche pour l'Exploitation de la Mer, Brest, France. Available online at ⟨*http://www.ifremer.fr/cersat/activite/ceo/imsi/f4i_html/e_intro.htm*⟩.

Fahrbach, E., R. G. Peterson, G. Rohardt, P. Schlosser, and R. Bayer (1994). Suppression of bottom water formation in the southeastern Weddell Sea. *Deep-Sea Research*, **41**, 389–411.

Fahrbach, E., M. Hoppema, G. Rohardt, M. Shröder, and A. Wisotzki (2004). Decadal-scale variations in the deep Weddell Sea. *Ocean Dynamics*, **54**, 77–91.

Falk, K., G. Gilchrist, K. Hobson, S. Benvenuti, and C. Egevang (2001). Breeding ecology of seabirds indicate contrasting foraging conditions between the eastern and western sectors of the NOW polynya. *International Polynya Symposium, September 9–13, Quebec City, Canada* (abstract). Available online at ⟨*www.fsg.ulaval.ca/giroq/now/IPS2001/ips2001.htm*⟩.

Falk-Petersen, S., H. Hop, W. P. Budgell, E. N. Hegseth, R. Korsnes, T. B. Løyning, J. B. Ørback, T. Kawamura, and K. Shirasawa (2000). Physical and ecological processes in the marginal ice zone of the northern Barents Sea during the summer melt period. *Journal of Marine Systems*, **27**, 131–159.

Fedak, M. A. (2004). Marine mammals as platforms for oceanographic sampling: A "win/win" situation for biology and operational oceanography. *Memoirs of the National Institute of Polar Research*, **58**, 133–147.

Fedotov, V. I., N. V. Cherapanov, and K. P. Tyshko (1998). Some features of the growth, structure and metamorphism of East Antarctic landfast sea ice. In: M. O. Jeffries (ed.), *Antarctic Sea Ice Physical Processes, Interactions and Variability* (AGU Antarctic Research Series No. 74). American Geophysical Union, Washington, DC, pp. 343–254.

Ferguson, S. H., M. K. Taylor, and F. Messier (2000). Influence of sea ice dynamics on habitat selection by polar bears. *Ecology*, **81**, 761–772.

Ferraro, R. R., F. Weng, N. C. Grody, I. Guch, C. Dean, C. Kongoli, H. Meng, P. Pellegrino, and L. Zhao (2002). NOAA satellite-derived hydrological products prove their worth. *EOS, Transactions of the American Geophysical Union*, **83**, 429–437.

Ferro-Famil, L., E. Pottier, and J. S. Lee (2001). Unsupervised classification of multi-frequency and fully polarimetric SAR images based on the H/A/Alpha-Wishart classifier. *IEEE Transactions on Geoscience and Remote Sensing*, **39**(11), 23332–23342.

Fett, R. W., R. E. Englebretson, and S. D. Burk (1997). Techniques for analyzing lead condition in visible, infrared and microwave satellite imagery. *Journal of Geophysical Research*, **102**, 13657–13671.

Fetterer, F. (2004). *Sea Ice Surface Characteristics from High Resolution Reconnaissance Imagery* (digital media). National Snow and Ice Data Center, Boulder, CO. Available at ⟨*http://nsidc.org/research/seaice_surface/*⟩.

Fetterer, F. M. and J. D. Hawkins (1991). *An AVHRR Data Set for Arctic Leads* (ARI Technical Note No. 118). U.S. Naval Oceanographic and Atmospheric Research Laboratory, Stennis Space Center, MI.

Fetterer, F. and K. Knowles (2002). *Sea Ice Index* (digital media). National Snow and Ice Data Center, Boulder, CO.

Fetterer, F. and V. Troisi (1997). *AARI 10-day Arctic Ocean EASE-Grid Sea-ice Observations* (digital media). National Snow and Ice Data Center, Boulder, CO.

Fetterer, F. and N. Untersteiner (1998a). Melt pond coverage statistics from classified satellite data. *International Geoscience and Remote Sensing Symposium IGARSS '98, Seattle, WA* (CD-ROM, IEEE 97CH36174).

Fetterer, F. and N. Untersteiner (1998b). Observations of melt ponds on Arctic sea ice. *Journal of Geophysical Research*, **103**(C11), 24821–24835.

Fetterer, F., M. R. Drinkwater, K. Jezek, S. Laxon, R. Onstott, and L. Ulander (1992). Sea ice altimetry. In: F. D. Carsey (ed.), *Microwave Remote Sensing of Sea Ice* (AGUl Monograph No. 28). American Geophysical Union, Washington, DC, pp. 111–135.

Fetterer, F. M., Gineris, D. J., and R. Kwok (1994). Sea ice type maps from Alaska Synthetic Aperture Radar Facility imagery: An assessment. *Journal of Geophysical Research*, **99**(C11), 22443–22458.

Fetterer, F., D. Gineris, and C. C. Wackerman (1998). Validating a scatterometer wind algorithm for ERS-1 SAR. *IEEE Transactions on Geoscience and Remote Sensing*, **36**(2), 479–492.

Fichefet, T. and M. A. Morales Maqueda (1997). Sensitivity of a global sea ice model to the treatment of ice thermodynamics and dynamics. *Journal of Geophysical Research*, **102**(C6), 12609–12646.

Fichefet, T. and M. A. Morales Maqueda (1999). Modelling the influence of snow accumulation and snow-ice formation on the seasonal cycle of the Antarctic sea-ice cover. *Climate Dynamics*, **15**, 251–268.

Fichefet T., B. Tartinville, and H. Goosse (2000). Sensitivity of the Antarctic sea-ice to the thermal conductivity of snow. *Geophysical Research Letters*, **27**(3), 401–404.

Fichefet, T., H. Goosse, and M. A. Morales Maqueda (2003a). A hindcast simulation of Arctic and Antarctic sea ice variability, 1955–2001. *Polar Research*, **22**(1), 91–98.

Fichefet, T., B. Tartinville, and H. Goosse (2003b). Antarctic sea ice variability during 1958–1999: A simulation with a global ice–ocean model. *Journal of Geophysical Research*, **108**(C3), DOI: 10.1029/2001JC001148.

Field, C. B. and M. R. Raupach (2004). *The Global Carbon Cycle: Integrating Humans, Climate, and the Natural World*. Island Press, Washington, DC.

Figa-Saldaña, J., J. J. W. Wilson, E. Attema, R. Gelsthorpe, M. R. Drinkwater, and A. Stoffelen (2002). The advanced scatterometer (ASCAT) on the Meteorological Operational (MetOp) platform: A follow on for European wind scatterometers. *Canadian Journal of Remote Sensing*, **28**(3), 404–412.

Fily, M. and D. A. Rothrock (1987). Sea ice tracking by nested correlations. *IEEE Transactions on Geoscience and Remote Sensing*, **25**(5), 570–580.

Fily, M. and D. A. Rothrock (1990). Opening and closing of sea ice leads: Digital measurements from synthetic aperture radar. *Journal of Geophysical Research*, **95**(C1), 789–796.

Fitzharris, B. (ed.) (1996). The cryosphere: Changes and their impacts. *Climate Change 1995, Impacts, Adaptations and Mitigation of Climate Change: Scientific–Technical Analyses*. Cambridge University Press, Cambridge, UK, pp. 241–265.

Flato, G. M. (2004). Sea-ice modelling. In: J. Bamber and A. Payne (eds.), *Mass Balance of the Cryosphere*. Cambridge University Press, Cambridge, UK, pp. 367–392.

Flato, G. M. and R. D. Brown (1996). Variability and climate sensitivity of landfast Arctic sea ice. *Journal of Geophysical Research*, **101**(C10), 25767–25777.

Flato, G. M. and W. D. Hibler III (1991). An initial numerical investigation of the extent of sea-ice ridging. *Annals of Glaciology*, **15**, 31–36.

Flato, G. M. and W. D. Hibler III (1995). Ridging and strength in modeling the thickness distribution of Arctic sea ice. *Journal of Geophysical Research*, **100**, 18611–18626.

Flato, G. M. and D. Ramsden (1997). Sensitivity of an atmospheric general circulation model to the parameterization of leads in sea ice. *Annals of Glaciology*, **25**, 96–101.

Flett, D. (2003). Operational use of SAR at the Canadian Ice Service: Present operations and a look into the future. *Proceedings of 2nd Workshop on Coastal and Marine Applications of SAR, September 8–12, 2003, Svalbard, Norway*.

Foldvik, A. and T. Gammelsrød (1988). Notes on Southern-Ocean hydrography, sea-ice and bottom water formation. *Palaeogeography, Palaeoclimatology, Palaeoecology*, **67**, 3–17.

Foldvik, A., Gammelsrød, T., Østerhus, S., Fahrbach, E., Rohardt, G., Schröder, M., Nicholls, K. W., Padman, L., and Woodgate, R. A.(2004). Ice shelf water overflow and bottom water formation in the southern Weddell Sea, *Journal of Geophysical Research*, **109**, C0201, DOI: 10.1029/2003JC002008.

Folland, C. K., T. K. Karl, J. R. Christy, R. A. Clarke, G. V. Gruza, J. Jouzel, M. E. Mann, J. Oerlemans, M. J. Salinger, and S.-W. Wang (2001. Observed climate variability and change. In: J. T. Houghton et al. (eds.), *Climate Change 2001: The Scientific Basis* (contribution of Working Group I to the Third Assessment Report of the Intergovernmental Panel on Climate Change). Cambridge University Press, Cambridge, UK, pp. 99–181.

Follows, M. and T. Oguz (2004). *The Ocean Carbon Cycle and Climate*. Kluwer Academic, The Netherlands, 395 pp.

Forsberg, R., S. M. Hvidegård, and K. Keller (2003). Airborne lidar measurement of sea-ice thickness. *Geophysical Research Abstracts*, **5**, 09612.

Forsberg, R., S. M. Hvidegård, K. Keller, C. Haas, A. Pfaffling, and J. Lieser (2004). Sea-ice thickness from airborne measurements: A comparison of laser altimetry and EM thickness measurements. *EGS First General Assembly, April 25–30, Nice, France* (Abstract 03606).

Forster, R. R., D. G. Long, K. C. Jezek, S. D. Drobot, and M. R. Anderson (2001). The onset of Arctic sea-ice snowmelt as detected with passive- and active-microwave remote sensing. *Annals of Glaciology*, **33**, 85–93.

Foster, J. L., D. K. Hall, and A. T. C. Chang (1987). Remote sensing of snow. *EOS Transactions of the American Geophysical Union*, **68**, 681–684.

Fournier-Sicre, A., T. Suslova, and A. Krasnov (2003). Sich-1M: A Russian–Ukrainian project. *ESA News from Moscow*, **9** (special issue, 7 July), 24–25.

Fowler, C. W. (1995). Ice motion derived from satellite remote sensing. PhD thesis, Aerospace Engineering Sciences Department, University of Colorado.

Fowler, C. (2003). *Polar Pathfinder Daily 25 km EASE–Grid Sea Ice Motion Vectors* (digital media). National Snow and Ice Data Center, Boulder, CO.

Fowler, C. W., W. J. Emery, and J. A. Maslanik (2001). Twenty-three years of Antarctic sea ice motion from microwave satellite imagery. *Proceedings of International Geoscience and Remote Sensing Symposium IGARSS '01, July 9–13, Sydney* (Vol. 1), pp. 157–159

Fowler, C., J. Maslanik, T. Haran, T. Scambos, J. Key, and W. Emery (2002a). *AVHRR Polar Pathfinder Twice-daily 5 km EASE–Grid Composites* (digital media). National Snow and Ice Data Center, Boulder, CO.

Fowler, C., J. Maslanik, T. Haran, T. Scambos, J. Key, and W. Emery. 2002b. *AVHRR Polar Pathfinder Twice-daily 25 km EASE–Grid Composites* (digital media). National Snow and Ice Data Center, Boulder, CO.

Fox, C. and T. G. Haskell (2001). Ocean wave speed in the Antarctic marginal ice zone. *Annals of Glaciology*, **33**, 350–354.

François, R, M. A. Altabet, E.-F. Yu, D. Sigman, M. P. Bacon, M. Frank, G. Bohrmann, G. Bareille, and L. D. Labeyrie (1997). Contribution of Southern Ocean surface water stratification to low atmospheric CO_2 concentrations during the last glacial period. *Nature*, **389**, 929–935.

Fraser, W. R. and D. G. Ainley (1986). Ice edges and seabird occurrence in Antarctica. *BioScience*, **36**(4), 258–263.

Fraser, W. R. and W. Z. Trivelpiece (1996). Factors controlling the distribution of seabirds: Winter–summer heterogeneity in the distribution of Adélie penguin populations. In: R. M. Ross, E. Hofmann, and L. B. Quetin (eds.), *Foundations for Ecological Research West of the Antarctic Peninsula* (AGU Antarctic Research Series No. 70). American Geophysical Union, Washington, DC, pp. 257–272.

Fraser, W. R., W. Z. Trivelpiece, D. G. Ainley, and S. W. Trivelpiece (1992). Increases in Antarctic penguin populations: Reduced competition with whales or a loss of sea ice due to environmental warming? *Polar Biology*, **11**, 525–531.

Frazer, T. K., L. B. Quetin, and R. M. Ross (1997). Abundance and distribution of larval krill, *Euphausia superba*, associated with annual sea ice in winter. In: B. Battaglia, J. Valencia, and D. W. H. Walton (eds.), *Antarctic Communities*. Cambridge University Press, Cambridge, U.K., pp. 107–111.

Freeman, A. and S. L. Durden (1998). A three-component scattering model for polarimetric SAR. *IEEE Transactions on Geoscience and Remote Sensing*, **36**, 963–973.

Frey, K. E., L. C. Smith, and D. E. Alsdorf (2003). Controls on Eurasian coastal sea ice formation, melt onset and decay from ERS scatterometry: Regional contrasts and effects of river influx. *International Journal of Remote Sensing*, DOI: 10.1080/0143116031000101684, 1–33.

Frezzotti, M., A. Cimbelli, and J. G. Ferrigno (1998). Ice-front and iceberg behaviour along Oates and George V coasts, Antarctica, 1912–96. *Annals of Glaciology*, **27**, 643–650.

Fritsen, C. H. and C. W. Sullivan (1999). Distributions and dynamics of microbial communities in the pack ice of the western Weddell Sea. In: B. Battaglia, J. Valencia, and D. W. H. Walton (eds.), *Proceedings of SCAR VI Biology Symposium, London*. Cambridge University Press, Cambridge, UK, pp. 1–20.

Fritsen, C. H., S. F. Ackley, J. N. Kremer, and C. W. Sullivan (1998). Flood–freeze cycles and micro-algal dynamics in Antarctic Pack Ice. In: M. P. Lizotte and K. R. Arrigo (eds), *Antarctic Sea Ice: Biological Processes, Interactions, and Variability* (Antarctic Research Series). American Geophysical Union, Washington, D.C., pp. 711–721.

Fritsen, C. H., S. L. Coale, D. R Neenan, A. H. Gibson, and D. L. Garrison (2001). Biomass, production and microhabitat characteristics near the freeboard of icefloes in the Ross Sea during the austral summer. *Annals of Glaciology*, **33**, 280–286.

Fu, L.-L. and A. Cazenave (eds.) (2001). *Satellite Altimetry and Earth Sciences* (International Geophysics Series No. 69). Academic Press, San Diego.

Fu, L.-L. and B. Holt (1982). *Seasat Views Oceans and Sea Ice with Synthetic Aperture Radar* (NASA JPL Publication 81–120). Jet Propulsion Laboratory, Pasadena, CA.

Fuhrhop, R., T. C. Grenfell, G. Heygster, K.-P. Johnsen, P. Schlossel, M. Schrader, and C. Simmer (1998). A combined radiative transfer model for sea ice, open ocean, and atmosphere. *Radio Science*, **33**, 303–316.

Fukamachi, Y., K. I. Ohshima, and T. Ishikawa (1998). Mesoscale ice features in the summer marginal ice zone off East Queen Maud Land observed in NOAA AVHRR imagery. In: M. O. Jeffries (ed.), *Antarctic Sea Ice Physical Processes, Interactions and Variability* (AGU Antarctic Research Series No. 74). American Geophysical Union, Washington, DC, pp. 317–323.

Fukamachi Y., M. Wakatsuchi, K. Taira, S. Kitagawa, S. Ushio, A. Takahashi, K. Oikawa, T. Furukawa, H. Yori-taka, M. Fukuchi et al. (2000). Seasonal variability of bottom water properties off Adélie Land, Antarctica. *Journal of Geophysical Research*, **105**, 6531–6540.

Fukamachi, Y., G. Mizuta, Ohshima, K. I., Melling, H., Fissel, D., and Wakatsuchi, M. (2003). Variability of sea-ice draft off Hokkaido in the Sea of Okhotsk revealed by a moored ice-profiling sonar in winter of 1999. *Geophysical Research Letters*, DOI: 10.1029/2002GL016197.

Fung, A. K. (1994). *Microwave Scattering and Emission Models and Their Applications*. Artech House, Norwood, MA.

Fung, A. K. and H. J. Eom (1982). Application of a combined rough surface volume scattering theory of sea ice and snow. *IEEE Transactions on Geoscience and Remote Sensing*, **20**, 528–536.

Furevik, B. R., O. M. Johannessen, and A. D. Sandvik (2002). SAR-retrieved wind in polar regions: Comparison with *in situ* data and atmospheric model output. *IEEE Transactions on Geoscience and Remote Sensing*, **40**(8), 1720–1732.

Fyfe, J. C., G. J. Boer, and G. M. Flato (1999). The Arctic and Antarctic Oscillations and their projected changes under global warming. *Geophysical Research Letters*, **26**(11), 1601–1604.

Gaiser, P. W., K. M. St. Germain, E. M. Twarog, G. A. Poe, W. Purdy, D. Richardson, W. Grossman, W. Linwood Jones, D. Spencer, G. Golba et al. (2004). The WindSat Spaceborne Polarimetric Microwave Radiometer: Sensor description and early performance. *IEEE Transactions on Geoscience and Remote Sensing*, **42**(11), 2347–2361.

Gallée, H. (1997). Air–sea interactions over Terra Nova Bay during winter: Simulation with a coupled atmosphere–polynya model. *Journal of Geophysical Research*, **102**, 13835–13849.

Gao, B.-O, P. Yang, and R.-R. Li (2003). Detection of high clouds in polar regions during the daytime using the MODIS 1.375-μm channel. *IEEE Transactions on Geoscience and Remote Sensing*, **41**(2), 474–481.

Garbrecht, T., C. Lüpkes, E. Augstein, and C. Wamser (1999). The influence of a sea ice ridge on low-level air flow. *Journal of Geophysical Research*, **104**(D20), 24449–24507.

Garbrecht, T., C. Lüpkes, J. Hartmann, and M. Wolff (2002). Atmospheric drag coefficients over sea ice: A validation of a parameterisation concept. *Tellus*, **A54**(2), 205–219.

Garrison, D. L. (1991). Antarctic sea ice biota. *American Zoologist*, **31**, 17–33.

Garrison, D.L. and S. Mathot (1996). Pelagic and sea ice microbial communities. In: R. M. Ross, E. E. Hofmann, and L. B. Quetin (eds.), *Foundations for Ecological Research West*

of the Antarctic Peninsula (AGU Antarctic Research Series No. 70). American Geophysical Union, Washington, DC, pp. 155–172.

Garrity, C. (1992). Characterization of snow on floating ice and case studies of brightness temperature changes during the onset of melt. In: F. D. Carsey (ed.), *Microwave Remote Sensing of Sea Ice* (AGU Monograph Series No. 68). American Geophysical Union, Washington, DC, pp. 313–326.

Gates, W. L., A. Henderson-Sellers, G. J. Boer, C. K. Folland, A. Kitoh, B. J. McAvaney, F. Semazzi, N. Smith, A. J. Weaver, and Q-C. Zeng (1996). Climate models: Evaluation. In: J. T. Houghton, L. G. Meira Filho, B. A. Cullander, N. Harris, A. Kattenberg, and K. Maskell (eds.), *Climate Change 1995: The Science of Climate Change*. Cambridge University Press, Cambridge, UK, pp. 233–284.

Gawarkiewicz, G. and D. C. Chapman (1995). A numerical study of dense water formation and transport on a shallow, sloping continental shelf. *Journal of Geophysical Research*, **100**, 4489–4507.

Gearheard, S. F. (2004). *When the Weather is Uggianaqtuq: Inuit Observations of Environmental Change* (CD-ROM). Available online from ⟨*http://nsidc.org/data/arcss122.html*⟩.

Geiger, C. A., S. F. Ackley, and W. D. Hibler III (1998a). Sea ice drift and deformation processes in the western Weddell Sea. In: M. O. Jeffries (ed.), *Antarctic Sea Ice Physical Processes, Interactions and Variability* (AGU Antarctic Research Series No. 74). American Geophysical Union, Washington, DC, pp. 141–160.

Geiger, C. A., W. D. Hibler III, and S. Ackley (1998b). Large-scale sea ice drift and deformation: Comparison between models and observations in the western Weddell Sea during 1992. *Journal of Geophysical Research*, **103**(C10), 21893–21913.

Geiger, C. A., Y. Zhao, A. K. Liu, and S. Häkkinen (2000). Large-scale comparison between buoy and SSM/I drift and deformation in the Eurasian Basin during winter 1992–1993. *Journal of Geophysical Research*, **105**, 3357–3368.

Gerdes, R. and C. Köberle (2002). Arctic fresh water export and Atlantic circulation. *EGS XXVII General Assembly*, *April 21–26, Nice, France* (Abstract 00639).

Gesell, G. (1989). An algorithm for snow and ice detection using AVHRR data: An extension of the APOLLO software package. *International Journal of Remote Sensing*, **10**, 897–905.

Gilchrist, H. G., G. J. Robertson, K. Hobson, and J. R. Lovvorn (2001). Ecology of common eider ducks wintering at polynyas in the Belcher Islands: Constraints imposed by ice and tidal currents. *International Polynya Symposium*, *September 9–13, Quebec City, Canada* (abstract). Available online at ⟨*www.fsg.ulaval.ca/giroq/now/IPS2001/ips2001.htm*⟩.

Giles, B., V. I. Lytle, and R. A. Massom (in preparation). Fast ice extent around East Antarctica using synthetic aperture radar images.

Gill, R. S. (2001). Operational detection of sea ice edges and icebergs using SAR. *Canadian Journal of Remote Sensing*, **27**(5), 411–432.

Gill, R. S. and H. Valeur (1996). *Evaluation of the Radarsat Imagery for the Operational Mapping of Sea Ice around Greenland* (Scientific Report 96–9). Danish Meteorological Institute, Copenhagen, 98 pp.

Gill, R. S., M. K. Rosengreen, and H. Valeur (2000). Operational ice mapping with Radarsat for ship navigation in Greenland waters. *Canadian Journal of Remote Sensing*, **26**(2), 121–132.

Gille, S. T. (2002). Warming of the Southern Ocean since the 1950s. *Science*, **295**(5558), 1275–1277.

Gillett, N. P. and D. W. J. Thompson (2003). Simulation of recent Southern Hemisphere climate change. *Science*, **302**(5643), 273–275.

Gillett, N. P., M. R. Allen, R. E. McDonald, C. A. Senior, D. T. Shindell, and G. A. Schmidt (2002). How linear is the Arctic Oscillation response to greenhouse gases? *Journal of Geophysical Research*, **107**, DOI: 10.1029/2001JD000589.

Giraldez, A. E. (2003). SAOCOM-1 Argentina L-band SAR mission overview. *Proceedings of 2nd Workshop on Coastal and Marine Applications of SAR*, *September 8–12, Svalbard, Norway*. Available online at ⟨*http://earth.esa.int/workshops/cmasar_2003/papers/E27gira.pdf*⟩.

Gladyshev, S., S. Martin, S. Riser, and A. Figurkin (2000). Dense water production on the northern Okhotsk shelves: Comparison of ship-based spring–summer observations for 1996 and 1997 with satellite observations. *Journal of Geophysical Research*, **105**, 26281–26299.

Glendening, J. W. (1995). Horizontally integrated atmospheric heat flux from an Arctic lead. *Journal of Geophysical Research*, **100**, 4613–4621.

Glendening, J. W. and S. D. Burk (1992). Turbulent transport from an Arctic lead: A large-eddy simulation. *Boundary Layer Meteorology,* **59**, 315–339.

Gloersen, P. (1995). Modulation of hemispheric sea-ice cover by ENSO events. *Nature*, **373**, 503–504.

Gloersen, P. and F. T. Barath (1977). A scanning multichannel microwave radiometer for Nimbus G and Seasat A. *IEEE Journal of Oceanic Engineering*, **OE-2**, 172–178.

Gloersen P. and Campbell W. J. (1991). Recent variations in Arctic and Antarctic sea-ice covers. *Nature*, **352**, 33–36.

Gloersen, P. and D. J. Cavalieri (1986). Reduction of weather effects in the calculation of sea ice concentration from microwave radiances. *Journal of Geophysical Research*, **91**, 3913–3919.

Gloersen, P. and N. Huang (1998). In search of an elusive Antarctic circumpolar wave in sea ice extents: 1978–1996. *International Symposium on Polar Aspects of Global Change*, *August 24–28, Tromsø, Norway* (abstract).

Gloersen, P. and A. Mernicky (1998). Oscillatory behaviour in Antarctic sea ice concentrations. In: M. O. Jeffries (ed.), *Antarctic Sea Ice Physical Processes, Interactions and Variability* (AGU Antarctic Research Series No. 74). American Geophysical Union, Washington, DC, pp. 161–171.

Gloersen, P. and V. Salomonson (1975). Satellites: New global observing techniques for ice and snow. *Journal of Glaciology*, **15**(73), 373–389.

Gloersen, P. and W. B. White (2001). Re-establishing the circumpolar wave in sea ice around Antarctica from one winter to the next. *Journal of Geophysical Research*, **106**(C3), 4391–4395.

Gloersen, P., T. C. Chang, T. T. Wilheit, and W. J. Campbell (1974). Polar sea ice observations by means of microwave radiometry. In: H. S. Santeford and J. L. Smith (eds.), *Advanced Concepts and Techniques in the Study of Snow and Ice*. National Academy of Science, Washington, DC, pp. 541–550.

Gloersen, P., W. J. Campbell, D. J. Cavalieri, J. G. Comiso, C. L. Parkinson, and H. J. Zwally (1992). *Arctic and Antarctic Sea Ice, 1978–1987: Satellite Passive-microwave Observations and Analysis* (NASA Special Publication SP-511). NASA Goddard Space Flight Center, Greenbelt, MD, 290 pp.

Gloersen, P., J. Yu, and E. Mollo-Christensen (1996). Oscillatory behavior in Arctic sea ice concentrations. *Journal of Geophysical Research*, **101**(C3), 6641–6650.

Gloersen, P., C. L. Parkinson, D. J. Cavalieri, J. C. Comiso, and H. J. Zwally (1999). Spatial distribution of trends and seasonality in the hemisphere sea ice covers: 1978–1996. *Journal of Geophysical Research*, **104**(C9), 20827–20835.

Godfred-Spenning, C. R. and I. Simmonds (1996) An analysis of Antarctic sea-ice and extratropical cyclone associations. *International Journal of Climatology*, **16**, 1315–1332.

Godfrey, J. S. and S. R. Rintoul (1998). The role of the oceans in Southern Hemisphere climate. In: D. J. Karoly and D. G. Vincent (eds.), *Meteorology of the Southern Hemisphere*. American Meteorological Society, Boston, pp. 283–306.

Goetz, A. F. H. (ed.) (1987). *HIRIS. High-Resolution Imaging Spectrometer: Science Opportunities for the 1990s* (Earth Observing System Instrument Panel Report Volume IIc). NASA, Washington, DC, 74 pp.

Gogineni, S. P., R. K. Moore, T. C. Grenfell, D. G. Barber, S. Digby, and M. Drinkwater (1992). The effects of freeze-up and melt processes on microwave signatures. In: F. D. Carsey (ed.), *Microwave Remote Sensing of Sea Ice* (AGU Monograph No. 68). American Geophysical Union, Washington, DC, pp. 329–341.

Gogineni, S., K. Wong, K. Sudarsan, P. Kanagaratnam, T. Markus, and V. Lytle (2003). An ultra-wideband radar for measurements of snow thickness over sea ice. *Proceedings of IGARSS '03, Toulouse, France, July 21–25* (Volume 4), pp. 2802–2804.

Gohin, F. (1995). Some active and passive microwave signatures of Antarctic sea-ice from midwinter to spring 1991. *International Journal of Remote Sensing*, **16**(11), 2031–2054.

Gohin, F. and A. Cavanié (1994). A first try at identification of sea ice using the three-beam scatterometer of ERS-1. *International Journal of Remote Sensing*, **15**(6), 1221–1228.

Gohin, F. and C. Maroni (1998). *ERS Scatterometer Polar Sea Ice Grids Manual*. IFREMER/CERSAT Technical Report C2-MUT-W-03-IF V2.0. IFREMER/CERSAT, Plouzané, France, 42 pp.

Gohin, F., A. Cavanié, and R. Ezraty (1998). Evolution of the passive and active microwave signatures of a large sea ice feature during its $2\frac{1}{2}$-year drift through the Arctic Ocean. *Journal of Geophysical Research*, **103**(C4), 8177–8189.

Golden, K. M. (2001). Brine percolation and transport properties of sea ice. *Annals of Glaciology*, **33**, 28–36.

Golden, K. M., D. Borup, M. Cheney, E. Cherkaeva, M. S. Dawson, K. H. Ding, A. K. Fung, D. Isaacson, S. A. Johnson, A. K. Jordan et al. (1998a). Inverse electromagnetic scattering models for sea ice. *IEEE Transactions on Geoscience and Remote Sensing*, **36**, 1675–1704.

Golden, K. M., M. Cheney, K. H. Ding, A. K. Fung, T. C. Grenfell, D. Isaacson, J. A. Kong, S. V. Nghiem, J. Sylvester, and D. P. Winebrenner (1998b). Forward electromagnetic scattering models for sea ice. *IEEE Transactions on Geoscience and Remote Sensing*, **36**(5), 1655–1674.

Golden, K. M., S. F. Ackley, and V. I. Lytle (1998c). The percolation phase transition in sea ice. *Science*, **282**, 2238–2241.

Golovin, P. N. (2002). Thermohaline variability and convective gravity currents in the region of coastal polynyas in the Laptev Sea. *Oceanology*, **42**, 162–173.

Gong, D. and S. Wang (1999). Definition of Antarctic oscillation index. *Geophysical Research Letters*, **26**, 459–462.

Goodison, B. E., R. D. Brown, and R. G. Crane (eds.) (1999). Cryospheric systems. In: M. D. King (ed.), *EOS Science Plan: The State of Science in the EOS Program* (NASA NP-1998-12-069-GSFC). NASA Goddard Space Flight Center, Greenbelt, MD, pp. 261–307.

Goosse, H. and T. Fichefet (1999). Importance of ice–ocean interactions for the global ocean circulation: A model study. *Journal of Geophysical Research*, **104**, 23337–23355.

Goosse, H., F. M. Selten, R. J. Haarsma, and J. D. Opsteegh (2001). Decadal variability in high northern latitudes as simulated by an intermediate-complexity climate model. *Annals of Glaciology*, **33**, 525–532.

Gordon, A. L. (1981). Seasonality of Southern Ocean sea ice. *Journal of Geophysical Research*, **86**, 4193–4197.

Gordon, A. L. (1982). Weddell deep water variability. *Journal of Marine Research,* **40**, 199–217.

Gordon, A. L. (1998). Western Weddell Sea thermohaline stratification. In: S. Jacobs and R. Weiss (eds.), *Interactions at the Antarctic Continental Margins* (AGU Antarctic Research Series No. 75). American Geophysical Union, Washington, DC, pp. 215–240.

Gordon, A. L. and J. C. Comiso (1988). Polynyas in the Southern Ocean. *Scientific American*, **258**, 90–97.

Gordon, A. L. and B. A. Huber (1990). Southern Ocean winter mixed layer. *Journal of Geophysical Research*, **95**(C7), 11655–11672.

Gordon, A., B. Huber, H. Hellmer, and A. Field (1993). Deep and bottom water of the Weddell Sea's western rim. *Science*, **262**, 95–97.

Gordon, A. L., M. Mensch, Z. Q. Dong, W. M. Smethie, and J. de Bettencourt (2000). Deep and bottom water of the Bransfield Strait eastern and central basins. *Journal of Geophysical Research*, **105**, 11337–11346.

Gordon, H. B. and S. P. O'Farrell (1997). Transient climate change in the CSIRO coupled model with dynamic sea ice. *Monthly Weather Review*, **125**(5), 875–907.

Gow, A. J., S. F. Ackley, W. F. Weeks, and J. W. Govoni (1982). Physical and structural characteristics of Antarctic sea ice. *Annals of Glaciology*, **3**, 113–117.

Granberg, H. (1998). Snow cover on sea ice. In: M. Leppäranta (ed.), *Physics of Ice-Covered Seas*. Helsinki University Press, Helsinki, pp. 605–649.

Grandell, J., J. Pallonen, M. Hallikainen, and M. Toikka (1993). Scatterometer measurements of Arctic sea ice at C-band. *International Geoscience and Remote Sensing Symposium (IGARSS '93)* (Volume 2), pp. 853–854.

Grandell, J., J. A. Johannessen, and M. T. Hallikainen (1999). Development of a synergetic sea ice retrieval method for the ERS-1 AMI wind scatterometer and SSM/I radiometer. *IEEE Transactions on Geoscience and Remote Sensing*, **37**(2), 668–679.

Grebmeier, J. M. and L. W. Cooper (1995). Influence of the St Lawrence-Island Polynya upon the Bering Sea benthos. *Journal of Geophysical Research*, **100**, 4439–4460.

Grenfell, T. C. (1979). The effects of ice thickness on the exchange of solar radiation over the polar oceans. *Journal of Glaciology*, **22**, 305–320.

Grenfell, T. C. (1983). A theoretical model of the optical properties of sea ice in the visible and near infrared. *Journal of Geophysical Research*, **88**, 9723–9735.

Grenfell, T. C. (1991). A radiative transfer model for sea ice with vertical structure variations. *Journal of Geophysical Research*, **96**, 16991–17001.

Grenfell, T. C. (1992). Surface-based passive microwave studies of multiyear sea ice. *Journal of Geophysical Research*, **97**(C3), 3485–3501.

Grenfell, T. C. and J. C. Comiso (1986). Multifrequency passive microwave observations of first–year sea ice grown in a tank. *IEEE Transactions on Geoscience and Remote Sensing*, **24**, 826–831.

Grenfell, T. C. and A. W. Lohanick (1985). Temporal variations of the microwave signature of sea ice during the late spring and early summer near Maud Bay, NWT. *Journal of Geophysical Research*, **90**(C3), 5063–5074.

Grenfell, T. C. and G. A. Maykut (1977). The optical properties of ice and snow in the Arctic basin. *Journal of Glaciology*, **18**(80), 445–463.

Grenfell, T. C. and D. K. Perovich (1981). Radiation absorption coefficients of polycrystalline ice from 400–1400 nm. *Journal of Geophysical Research*, **86**, 7447–7450.

Grenfell, T. C. and D. K. Perovich (1984). Spectral albedoes of sea ice and incident solar radiation in the southern Beaufort Sea. *Journal of Geophysical Research*, **89**, 3573–3580.

Grenfell, T. C. and S. G. Warren (1999). Representation of a non-spherical ice particle by a collection of independent spheres for scattering and absorption of radiation. *Journal of Geophysical Research*, **104**, 31697–31709.

Grenfell, T. C., D. K. Perovich, and J. A. Ogren (1981). Spectral albedos of an alpine snowpack. *Cold Regions Science and Technology*, **4**, 121–127.

Grenfell, T. C., D. L. Cavalieri, J. C. Comiso, M. R. Drinkwater, R. G. Onstott, I. Rubinstein, K. Steffen, and D. P. Winebrenner (1992). Considerations for microwave remote sensing of thin sea ice. In: F. D. Carsey (ed.), *Microwave Remote Sensing of Sea Ice* (AGU Monograph Series No. 68). American Geophysical Union, Washington, DC, pp. 291–301.

Grenfell, T. C., J. C. Comiso, M. A. Lange, H. Eicken, and M. R. Wensnahan (1994a). Passive microwave observations of the Weddell Sea during austral winter and early spring. *Journal of Geophysical Research*, **99**(C5), 9995–10010.

Grenfell, T. C., S. G. Warren, and P. C. Mullen (1994b). Reflection of solar radiation by the Antarctic snow surface at ultraviolet, visible, and near-infrared wavelengths. *Journal of Geophysical Research*, **99**, 18669–18684.

Grenfell, T. C., D. G. Barber, and A. K. Fung (1998). Evolution of electromagnetic signatures of sea ice from initial formation to the establishment of thick first-year ice. *IEEE Transactions on Geoscience and Remote Sensing*, **36**(5), 1642–1654.

Grenfell, T. C., B. Light, and M. Sturm (2002). Spatial distribution and radiative effects of soot in the snow and sea ice during the SHEBA experiment. *Journal of Geophysical Research*, **107**(C10), 8032, DOI 10.1029/2002JC000414).

Griffiths, G. (ed.) (2003). *The Technology and Applications of Autonomous Underwater Vehicles*. Taylor & Francis, London.

Griggs, M. (1968). Emissivities of natural surfaces in the 8- to 14-micron spectral region. *Journal of Geophysical Research*, **73**, 7545–7551.

Grody, N., J. Zhao, R. Ferraro, F. Weng, and R. Boers (2001). Determination of precipitable water and cloud liquid water over ocean from the NOAA 15 Advanced Microwave Sounding Unit. *Journal of Geophysical Research*, **106**, 2943–2953.

Groves, J. E. and W. J. Stringer (1991). The use of AVHRR TIR imagery to determine sea ice thickness within the Chukchi polynya. *Arctic*, **44**, 130–139.

Grumbine, R. W. (1991). A model of the formation of High Salinity Shelf Water on polar continental shelves. *Journal of Geophysical Research*, **96**, 22049–22062.

Grumbine, R. W. (1996). *Automated Passive Microwave Sea Ie Concentration Analysis at NCEP* (NOAA Technical Note No. 120). National Oceanic and Atmospheric Administration, National Oceanic and Atmospheric Administration, Camp Springs, MD, 13 pp.

Gudmandsen, P. (ed.) (1998). *Proceedings,. EARSeL Symposium 1997: Future Trends in Remote Sensing*. A. A. Balkema, Rotterdam.

Guenther, B., G. D. Godden, X. Xiong, E. J. Knight, S.-Y. Qiu, H. Montgomery, M. M. Hopkins, M. G. Khayat, and Z. Hao (1998). Prelaunch algorithm and data format for the Level 1 calibration products for the EOS-AM1 Moderate Resolution Imaging

Spectroradiometer (MODIS). *IEEE Transactions on Geoscience and Remote Sensing*, **36**, 1142–1151.

Guest, P. S. and K. L. Davidson (1987). The effect of observed ice conditions on the drag coefficient in the summer East Greenland Sea marginal ice zone. *Journal of Geophysical Research*, **92**, 6943–6954.

Guest, P. S. and K. L. Davidson (1991). The aerodynamic roughness of different types of sea ice. *Journal of Geophysical Research*, **96**(C3), 4709–4721.

Guest, P. S. and K. L. Davidson (1994). Factors affecting variations of snow surface temperature and air temperature over sea ice in winter. In: O. M. Johannessen, R. D. Muench, and J. E. Overland (eds), *The Polar Oceans and Their Role in Shaping the Global Evironment: The Nansen Centennial Volume* (AGU Monograph No. 85). American Geophysical Union, Washington, DC, pp. 435–442.

Guinet, C. (2004). Predator and öceanographer, elephant seals in the Southern Ocean. *ARGOS Forum*, **10**, 8–13.

Günther, S. and G. S. Dieckmann (2001). Vertical zonation and community transition of sea-ice diatoms in fast ice and platelet layer, Weddell Sea, Antarctica. *Annals of Glaciology*, **33**, 287–296.

Haak, H., J. Jungclaus, U. Mikolajewicz, and M. Latif (2003). Formation and propagation of great salinity anomalies. *Geophysical Research Letters,* **30**(9), DOI: 10.1029/2003GL017065.

Haapala, J. (2000). On the modelling of the ice thickness redistribution. *Journal of Glaciology*, **46**(154), 427–437.

Haarpaintner, J. (1999). The Storfjorden Polynya: ERS-2 SAR observations and overview. *Polar Research*, **18**, 175–182.

Haarpaintner, J., J. G. Gascard, and P. M. Haugan (2001a). Ice production and brine formation in Storfjorden, Svalbard. *Journal of Geophysical Research*, **106**, 14001–14013.

Haarpaintner, J., P. M. Haugan, and J.–C. Gascard (2001b). Interannual variability of the Storfjorden (Svalbard) ice cover and ice production observed by ERS-2 SAR. *Annals of Glaciology*, **33**, 430–436.

Haarpaintner, J., R. T. Tonboe, D. G. Long, and M. L. Van Woert (2004). Automatic detection and validity of the sea–ice edge: An application of enhanced–resolution QuikScat/SeaWinds data. *IEEE Transactions on Geoscience and Remote Sensing*, **42**(7), 1433–1443.

Haas, C. (1997). Comparison of sea-ice thickness measurements under summer and winter conditions in the Arctic using a small electromagnetic induction device. *Geophysics*, **62**, 749–757.

Haas, C. (1998). Evaluation of ship-based electromagnetic–inductive thickness measurements of summer sea-ice in the Bellingshausen and Amundsen Sea. *Cold Regions Science and Technology*, **27**(1), 1–16.

Haas, C. (2001). The seasonal cycle of ERS scatterometer signatures over perennial Antarctic sea ice and associated surface ice properties and processes. *Annals of Glaciology*, **33**, 69–73.

Haas, C. (2002). Validation of CryoSat sea-ice products: Instruments and methods. *Proceedings of IGARSS '02, Toronto, June 24–28*. Institute of Electrical and Electronics Engineers, New York, pp. 1753–1755.

Haas, C. (2003). Dynamics versus thermodynamics: The sea-ice thickness distribution. In: D. N. Thomas and G. S. Dieckmann (eds.), *Sea Ice:An Introduction to its Physics, Biology, Chemistry and Geology*. Blackwell Scientific, Oxford, UK, pp. 82–111.

Haas, C. and H. Eicken (2001). Interannual variability of summer sea ice thickness in the Siberian and central Arctic under different atmospheric circulation regimes. *Journal of Geophysical Research*, **106**(C3), 4449–4462.

Haas, C., S. Gerland, H. Eicken, and H. Miller (1997). Comparison of sea-ice thickness measurements under summer and winter conditions in the Arctic using a small electromagnetic induction device. *Geophysics*, **62**(3), 749–757.

Haas, C, Q. Liu, and T. Martin (1999). Retrieval of Antarctic sea-ice pressure ridge frequencies from ERS SAR imagery by means of in-situ laser profiling and usage of a neural network. *International Journal of Remote Sensing*, **20**(15–16), 3111–3123.

Haas, C., D. N. Thomas, and J. Bareis (2001). Surface properties and processes of perennial Antarctic sea ice in summer. *Journal of Glaciology*, **47**, 623–625.

Haefliger, M., K. Steffen, and C. W. Fowler (1993). AVHRR surface temperature narrowband albedo comparison with ground measurements for the Greenland Ice Sheet. *Annals of Glaciology*, **17**, 49–54.

Hagolle, O., J.-M. Nicolas, B. Fougnie, and F. Cabot (2004). Absolute calibration of vegetation derived from an interband method based on the sun glint over ocean. *IEEE Transactions on Geoscience and Remote Sensing*, **42**(7), 1472–1481.

Hajnsek, I., E. Pottier, and S. R. Cloude (2003). Inversion of surface parameters from polarimetric SAR. *IEEE Transactions on Geoscience and Remote Sensing*, **41**(4), 727–744.

Häkkinen, S. (1990). Models and their applications in polar oceanography. In: W. Smith (ed.), *Polar Oceanography: Part A. Physical Science*. Academic Press, New York, pp. 335–384.

Häkkinen, S. (1993). An Arctic source for the Great Salinity Anomaly: A simulation of the Arctic ice–ocean system for 1955–1975. *Journal of Geophysical Research*, **98**, 16397–16410.

Häkkinen, S. (1995). Seasonal simulation of the Southern Ocean coupled ice–ocean system. *Journal of Geophysical Research*, **100**, 22733–22748.

Häkkinen, S. (2000). Decadal air–sea interaction in the North Atlantic based on observations and modeling results. *Journal of Climate*, **13**(6), 1195–1219.

Häkkinen, S. and Mellor, G. L. (1992). Modeling the seasonal variability of a coupled Arctic ice–ocean system. *Journal of Geophysical Research*, **97**, 20285–20304.

Hale, G. M. and M. R. Querry (1973). Optical constants of water in the 200-nm to 200-μm wavelength region. *Applied Optics*, **12**, 555–563.

Hall, A. and M. Visbeck (2002). Forcing of ocean and sea ice variability by the Southern Hemisphere annular mode. *Journal of Climate*, **15**(21), 3043–3057.

Hall, D. K. (1998). Remote sensing of snow and ice using imaging radar. In: F. M. Henderson and A. J. Lewis (eds.), *Principles and Applications of Imaging Radar (Manual of Remote Sensing, Vol. 2)*. John Wiley & Sons, New York, pp. 677–703.

Hall, D. K. and J. Martinec (1985). *Remote Sensing of Snow and Ice*. Chapman & Hall, New York, 189 pp.

Hall, D. K., G. A. Riggs, and V. V. Salomonson (2001). *Algorithm Theoretical Basis Document (ATBD) for the MODIS snow-, lake ice- and sea ice-mapping algorithms*. NASA Goddard Space Flight Center, Greenbelt, MD. Available online at ⟨*http://modis-snow-ice.gsfc.nasa.gov/atbd.html*⟩.

Hall, D. K., Salomonson, V. V., Riggs, G. A., and A. G. Klein (2003). Snow and ice products from the Moderate Resolution Imaging Spectroradiometer. *Proceedings of 69th Annual American Society for Photogrammetry and Remote Sensing (ASPRS 2003) Conference, Anchorage, Alaska, May 5–9*.

Hall, D. K., J. Key, K. A. Casey, G. A. Riggs, and D. Cavalieri (2004a). Sea ice surface temperature product from MODIS. *IEEE Transactions on Geoscience and Remote Sensing*, **42**(5), 1076–1087.

Hall, D. K., G. A. Riggs, and V. V. Salomonson (2004b). *MODIS/Aqua Sea Ice Extent and IST Daily L3 Global 4km EASE–Grid Day V004, February* (digital media). National Snow and Ice Data Center, Boulder, CO.

Hall, D. K., G. A. Riggs, and V. V. Salomonson (in press). MODIS snow and sea ice products. In: J. Qu (ed.), *Earth Science Satellite Remote Sensing: Volume I. Science and Instruments*. Springer-Verlag, New York.

Hall, R. T. (1980). AIDJEX modeling group studies involving remote sensing data. In: R. S. Pritchard (ed.), *Sea Ice Processes and Models*. University of Washington Press, Seattle, pp. 151–162.

Hall, R. T. and D. A. Rothrock (1981). Sea ice displacement from Seasat synthetic aperture radar. *Journal of Geophysical Research*, **86**(C11), 11078–11082.

Hall, R. T. and D. A. Rothrock (1987). Photogrammetric observations of the lateral melt of sea icefloes. *Journal of Geophysical Research*, **92**(C7), 7045–7048.

Hallikainen, M. (1977). *Dielectric Properties of NaCl Ice at 16 GHz* (Report S-1107). Helsinki University of Technology, Radio Laboratory, Espoo, Finland, 37 pp.

Hallikainen, M. T. (1983). A new low-salinity model for UHF radiometry. *International Journal of Remote Sensing*, **4**, 655–681.

Hallikainen, M. (1992). Microwave remote sensing of low-salinity sea ice. In: F. D. Carsey (ed.), *Microwave Remote Sensing of Sea Ice*. American Geophysical Union, Washington, DC, pp. 361–373.

Hallikainen, M. and D. P. Winebrenner (1992). The physical basis for sea ice remote sensing. In: F. D. Carsey (ed.), *Microwave Remote Sensing of Sea Ice*. American Geophysical Union, Washington, DC, pp. 29–46.

Hallikainen M., F. T. Ulaby, and M. Abdelrazik (1986). Dielectric properties of snow in the 3 to 37 GHz Range. *IEEE Transactions on Antennas and Propagation*, **AP–34**(11), 1329–1339.

Hallikainen, M. T., M. Toikka, and J. Hyyppä (1988). Microwave dielectric properties of low-salinity sea ice. *Proceedings of IGARSS '88*, pp. 419–420.

Hamazaki, T. (1999). Overview of the Advanced Land Observing Satellite (ALOS): Its mission requirements, sensors, and a satellite system. *ISPRS Joint Workshop "Sensors and Mapping from Space 1999", September 27–30*. International Society for Photogrammetry and Remote Sensing, Hanover, Germany.

Hammill, M. O. and T. G. Smith (1989). Factors affecting the distribution and abundance of ringed seal structures in Barrow Strait, Northwest Territories. *Canadian Journal of Zoology*, **67**, 2212–2219.

Hanafin, J. A. and P. J. Minnett (2001). Cloud forcing of surface radiation in the North Water Polynya during NOW'98. *Atmosphere–Ocean*, **39**, 239–255.

Hanesiak. J. M., J. J. Yackel, and D. G. Barber (2001). Effect of melt ponds on first-year sea ice ablation: Integration of Radarsat-1 and thermodynamic modelling. *Canadian Journal of Remote Sensing*, **27**(5), 433–442.

Hanna, E. (2001). Anomalous peak in Antarctic sea-ice area, winter 1998, coincident with ENSO. *Geophysical Research Letters*, **28**, 1595–1598.

Hanna, E. and J. Bamber (2001). Derivation and optimization of a new Antarctic sea-ice record. *International Journal of Remote Sensing*, **22**(1), 113–139.

Hara, Y., R. G. Atkins, R. T. Shin, J. A. Kong, S. H. Yueh, and R. Kwok (1995). Application of neural networks for sea ice classification in polarimetric SAR images. *IEEE Transactions on Geoscience and Remote Sensing*, **33**(3), 740–748.

Haralick, R. M., K. Shanmugan, and I. Dinstein (1973). Textural features for image classification. *IEEE Transactions in Systems, Man and Cybernetics*, **6**, 610–621.

Harangozo, S. A. (1997). Atmospheric meridional circulation impacts on contrasting winter sea ice extent in two years in the Pacific sector of the Southern Ocean. *Tellus, Series A*, **49**, 388–400.

Harder, M. and P. Lemke (1994). Modelling the extent of sea ice ridging in the Weddell Sea. In: O. M. Johannessen, R. D. Muench, and J. E. Overland (eds.), *The Polar Oceans and Their Role in Shaping the Global Environment* (AGU Monograph No. 85). American Geophysical Union, Washington, DC, pp. 187–197.

Harder, M., P. Lemke, and M. Hilmer (1998). Simulation of sea ice transport through Fram Strait: Natural variability and sensitivity to forcing. *Journal of Geophysical Research*, **103**, 5595–5606.

Harms, S., E. Fahrbach, and V. H. Strass (2001). Sea ice transports in the Weddell Sea. *Journal of Geophysical Research*, **106**(C5), 9057–9074.

Hastings, D. A. (1998). *The Advanced Very High Resolution Radiometer (AVHRR): Overview*. NOAA National Data Center, NGDC, Boulder, CO (last modified on Thursday, May 28, 1998). Available online at ⟨*http://www.ngdc.noaa.gov*⟩.

Hastings, D. A. and W. J. Emery (1992). The Advanced Very High Resolution Radiometer (AVHRR): A brief reference guide. *Photogrammetric Engineering and Remote Sensing*, **58**(8), 1183–1188.

Haugan, P. M. and R. Skogseth (2003). Polynya model parameters related to observations from Storfjorden. *Geophysical Research Abstracts*, **5**, 11760.

Hauser, A., M. Lythe, and G. Wendler (2002). Sea-ice conditions in the Ross Sea during spring 1996 as observed on SAR and AVHRR imagery. *Atmosphere–Ocean*, **40**(3), 281–292.

Haverkamp, D., L.-K. Soh, and C. Tsatsoulis (1995). A comprehensive, automated approach to determining sea ice thickness from SAR data. *IEEE Transactions on Geoscience and Remote Sensing*, **33**(1), 45–56.

Hawkins, J. D. and M. Lybanon (1989). Geosat altimeter sea ice mapping. *IEEE Journal of Ocean Engineering*, **14**(2), 139–148.

Hawkins, R. K., J. Wolfe, J. Princz, T. I. Lukowski, D. Geudtner, K. P. Murnaghan, A. Wind, A. L. Gray, P. W. Vachon, R. Touzi et al. (2002). Verification of Alternating Polarization products. *Proceedings of the Envisat Calibration Review, September 9–13* (ESA SP-520). ESA/ESTEC, Noordwijk, The Netherlands, 10 pp.

Haykin, S., E. O. Lewis, R. K. Raney, and J. R. Rossiter (1994). *Remote Sensing of Sea Ice and Icebergs*. John Wiley & Sons, New York, 686 pp.

Heacock, T., T. Hirose, F. Lee, M. Manore, and B. Ramsay (1993). Sea ice tracking on the east coast of Canada using NOAA AVHRR imagery. *Annals of Glaciology*, **17**, 405–413.

Heil, P. (2001). Relationship between fast ice and local meteorological conditions at Davis Station, East Antarctica: A case study. *6th Conference on Polar Meteorology and Oceanography, San Diego, May 14–18* (extended abstracts). American Meteorological Society, Boston, pp. 25–28.

Heil, P. and I. Allison (1999). The pattern and variability of Antarctic sea-ice drift in the Indian Ocean and western Pacific sectors. *Journal of Geophysical Research*, **104**(C7), 15789–15802.

Heil, P. and W. D. Hibler III (2002). Modeling the high-frequency component of Arctic sea ice drift and deformation. *Journal of Physical Oceanography*, **32**(11), 3039–3057.

Heil, P., I. Allison, and V. I. Lytle (1996). Seasonal and interannual variations of the oceanic heat flux under a landfast Antarctic sea ice cover. *Journal of Geophysical Research*, **101**(C11), 25741–25752.

Heil, P., I. Allison, and V.I. Lytle (2001a). Effect of high-frequency deformation on the sea-ice thickness. In: J. P. Dempsey and H. H. Shen (eds.), *IUTAM Symposium on Scaling Laws in Ice Mechanics and Ice Dynamics* (Solid Mechanics and Its Applications No. 94). Kluwer Academic, Boston, pp. 417–426.

Heil, P., C. W. Fowler, J. A. Maslanik, W. J. Emery, and I. Allison (2001b). A comparison of East Antarctic sea-ice motion derived using drifting buoys and remote sensing. *Annals of Glaciology*, **33**, 139–144.

Hellmer, H. H. (2004). Impact of Antarctic ice shelf melting on sea ice and deep ocean properties, *Geophysical Research Letters*, **31**(10), L10307, DOI: 10.1029/2004GL019506.

Hewison, T. J., N. Selbach, G. Heygster, J. P. Taylor, and A. J. McGrath (2002). Airborne measurements of Arctic sea ice, glacier and snow emissivity at 24–183 GHz. *Proceedings of the International Geoscience and Remote Sensing Symposium, IGARSS '02*, Vol. 5, pp. 2851–2855.

Hibler, W. D. III (1979). A dynamic–thermodynamic sea ice model. *Journal of Physical Oceanography*, **9**, 815–846.

Hibler, W.D. III (1980). Modeling a variable thickness sea ice cover. *Monthly Weather Review*, **108,** 1943–1973.

Hibler, W. D. III (1986). Ice dynamics. In: N. Untersteiner (ed.), *The Geophysics of Sea Ice*. Plenum Press, New York, pp. 577–640.

Hibler, W. D. III (1989). Arctic ice–ocean dynamics. In: Y. Hermann (ed.), *The Arctic Seas: Climatology, Oceanography, Geology, and Biology*. Van Nostrand Reinhold, New York, pp. 47–92.

Hibler, W. D. III (2001). Modeling the formation and evolution of oriented fractures in sea ice. *Annals of Glaciology*, **33**, 157–164.

Hibler, W. D. III (2004). Modelling the dynamic response of sea ice. In: J. Bamber and A. Payne (eds), *Mass Balance of the Cryosphere*. Cambridge University Press, Cambridge, UK, pp. 227–336.

Hibler, W. D. III and J. Hutchings (2002). On simulating oriented failure zones in sea ice velocity fields. *EGS XXVII General Assembly, April 21–26, Nice, France* (Abstract 02041).

Hibler, W. D. III and E. Schulson (2000). On modeling the anisotropic failure and low of flawed sea ice. *Journal of Geophysical Research*, **105**(C7), 17105–17120.

Hibler, W. D. III, W. F. Weeks, and S. J. Mock (1972). Statistical aspects of sea ice ridge distributions. *Journal of Geophysical Research*, **77**, 5954–5970.

Hill, K. (2000). *AVHRR Processing System* (Antarctic CRC Research Report 16). Antarctic Cooperative Research Centre, Hobart, Australia.

Hilmer, M. and T. Jung (2000). Evidence of a recent change in the link between the North Atlantic Oscillation and Arctic sea ice export. *Geophysical Research Letters*, **27**(7), 989–992.

Hilmer, M., M. Harder, and P. Lemke (1998). Sea ice transport: A highly variable link between Arctic and North Atlantic. *Geophysical Research Letters*, **25**, 3359–3362.

Hilmer, S. and P. Lemke (2000). On the decrease of Arctic sea ice volume. *Geophysical Research Letters*, **27**(22), 3751–3754.

Hirst, A. C. (1999). The Southern Ocean response to global warming in the CSIRO coupled ocean–atmosphere model. *Environmental Modelling and Software*, **14**, 227–241.

Hobbs, P.V. (1974). *Ice Physics*. Clarendon Press, Oxford, UK, 836 pp.

Hofmann, E. E. and E. J. Murphy (2004). Advection, krill, and Antarctic marine ecosystems. *Antarctic Science*, **16**, 487–499.

Hofmann, E. E., J. M. Klinck, D. P. Costa, K. L. Daly, J. J. Torres, and W. R. Fraser (2002). U.S. Southern Ocean Global Ocean Ecosystems Dynamics Program. *Oceanography*, **15**(2), 64–74.

Holland, D. M. (2001a). Transient sea-ice polynya forced by oceanic flow variability. *Progress in Oceanography*, **48**, 403–460.

Holland, D. M. (2001b). Explaining the Weddell Polynya: A large ocean eddy shed at Maud Rise. *Science*, **292**, 1697–1700.

Holland, G. H., P. J. Webster, J. A. Curry, G. Tyrell, D. Gauntlett, G. Brett, J. Becker, R. Hoag, and W. Vaglienti (2001). The Aerosonde robotic aircraft: A new paradigm for environmental observations. *Bulletin of the American Meteorological Society*, **82**(5), 889–901.

Holland, M. M. and C. M. Bitz (2003). Polar amplification of climate change in coupled models. *Climate Dynamics*, **21**, 221–232, DOI: 10.1007/s00382-003-0332-6.

Holland, M. M., J. A. Curry, and J. L. Schramm (1997a). Modeling the thermodynamics of a sea ice thickness distribution: 2. Sea ice/ocean interactions. *Journal of Geophysical Research*, **102**, 23093–23107.

Holland, M. M., J. L. Schramm, and J. A. Curry (1997b). Thermodynamic feedback processes in a single–column sea-ice–ocean model. *Annals of Glaciology*, **25**, 327–332.

Hollinger, J. P., R. Lo, and G. Poe (1987). *Special Sensor Microwave/Imager User's Guide*. U.S. Naval Research Laboratory, Washington, DC.

Hollinger, J. P., J. L. Pierce, and G. A. Poe (1990). SSM/I instrument evaluation. *IEEE Transactions on Geoscience and Remote Sensing*, **28**(5), 781–790.

Holloway, G. and T. Sou (2002). Has Arctic sea ice rapidly thinned? *Journal of Climate*, 15691–15701.

Holman, J. P. (2002). *Heat Transfer* (9th edn.). McGraw-Hill, New York, 665 pp.

Holt, B. and S. A. Digby (1985). Processes and imagery on fast first-year sea ice during the ice melt season. *Journal of Geophysical Research*, **90**(C3), 45035–45044.

Holt, B. and R. Kwok (2003). Sea ice geophysical measurements from Seasat to the present, with an emphasis on ice motion: A brief review and a look ahead. *Proceedings of 2nd Workshop on Coastal and Marine Applications of SAR (CMASAR), Svalbard, Norway, September 8–12*. Available online at ⟨*http://earth.esa.int/symposia/cmasar_2003/*⟩.

Holt, B. and S. Martin (2001). The effect of a storm on the 1992 summer sea ice cover of the Beaufort, Chukchi, and East Siberian Seas. *Journal of Geophysical Research*, **106**(C1), 1017–1032.

Holt, B. and M.-H. Rio (1998). SAR studies of sea ice: Distribution of floe size. In: R. A. Brown (ed.), *Remote Sensing of the Pacific Ocean by Satellites*. Earth Ocean and Space, New South Wales, Australia, pp. 134–144.

Holt, B., J. Crawford, and F. Carsey (1990). Characteristics of sea ice during the Arctic winter using multifrequency aircraft radar imagery. In: S. F. Ackley and W. F. Weeks (eds.), *Sea Ice Properties and Processes* (CRREL Monograph 90-1). U.S. Army Cold Regions Research and Engineering Laboratory, Hanover, NH, pp. 224.

Holt, B., D. A. Rothrock, and R. Kwok (1992). Determination of sea ice motion from satellite images. In: F. D. Carsey (ed.), *Microwave Remote Sensing of Sea Ice* (AGU Monograph No. 28). American Geophysical Union, Washington, DC, pp. 343–353.

Holt, B., S. Martin, R. Kwok, and R. Drucker (2003). A new look at Arctic polynyas with multi-sensor satellite data. *SEARCH Open Science Meeting, October 27, 2003, Seattle, Washington* (abstract). Available online at ⟨*http://siempre.arcus.org/4DACTION/wi_pos_displayAbstract/7/724*⟩.

Honjo, S. (2004). Particle export and the biological pump in the Southern Ocean. *Antarctic Science*, **16**, 501–516.

Hooker, S. B., W. E. Esaias, G. C. Feldman, W. W. Gregg, and C. R. McClain (1992). *An Overview of SeaWiFS and Ocean Colour* (NASA Technical Memorandum 104566). NASA Goddard Space Flight Center, Greenbelt, MD, 24 pp.

Hopkins, M. A. (1996). On the mesoscale interaction of lead ice and floes. *Journal of Geophysical Research*, **101**, 18315–18326.

Hoppema, M. (2004a). Weddell Sea is a globally significant contributor to deep-sea sequestration of natural carbon dioxide. *Deep-Sea Research I*, **51**, 1169–1177, DOI: 10.1016/j.dsr.2004.02.011.

Hoppema, M. (2004b). Weddell Sea turned from source to sink for atmospheric CO_2 between pre–industrial time and present. *Global and Planetary Change*, **40**, 219–231, DOI: 10.1016/j.gloplacha.2003.08.001.

Hori, M., T. Aoki, K. Stamnes, B. Chen, and W. Lei (2001). Preliminary validation of the GLI cryosphere algorithms with MODIS daytime data. *Polar Meteorology and Glaciology*, **15**, 1–20.

Horner, R. A. (1985). *Sea Ice Biota*. CRC Press, Boca Raton, FL, 215 pp.

Horner, R., S. F. Ackley, G. S. Dieckmann, B. Gulliksen, T. Hoshai, L. Legendre, I. A. Melnikov, W. S. Reeburgh, M. Spindler, and C. S. Sullivan (1992). Ecology of sea ice biota: 1. Habitat, terminology and methodology. *Polar Biology*, **12**, 417–427.

Hosseinmostafa, A. R., V. I. Lytle, K. C. Jezek, S. P. Gogineni, S. F. Ackley, and R. K. Moore (1995). Comparison of radar backscatter from Antarctic and Arctic Sea ice. *Journal of Electromagnetic Waves and Their Application*, **9**(3), 421–438.

Houghton, J. T., Y. Ding, D. J. Griggs, M. Noguer, P. J. van der Linden, and D. Xiaosu (eds.) (2001). *IPCC Report on Climate Change 2001: The Scientific Basis* (contribution of Working Group 1 to the Third Assessment Report of the Intergovernmental Panel on Climate Change). Cambridge University Press, New York, 881 pp.

Howell, S. E. L., J. J. Yackel, R. De Abreu, T. Geldsetzer, and C. Breneman (2005). On the utility of SeaWinds/QuikSCAT data for the estimation of the thermodynamic state of first-year sea ice. *IEEE Transactions on Geoscience and Remote Sensing*, **43**(6), 1338–1350.

Huixing, G., Z. Qinbo, and W. Chuijin (1999). The FY-1C meteorological satellite and its remote sensor. *Proceedings of Asian Conference on Remote Sensing, Hong Kong, November 22–25*, pp. 1253–1257.

Hunewinkel, T., T. Markus, and G. C. Heygster (1998). Improved determination of the sea ice edge with SSM/I data for small-scale analysis. *IEEE Transactions on Geoscience and Remote Sensing*, **36(5)**, 1795–1808.

Hunke, E. C. and S. F. Ackley (2001). A numerical investigation of the 1997–1998 Ronne Polynya. *Journal of Geophysical Research*, **106**, 22373–22382.

Hunke, E. C. and J. K. Dukowicz (1997). An elastic–viscous–plastic model for sea ice dynamics. *Journal of Physical Oceanography*, **27**, 1849–1867.

Hunt, B. G., H. B. Gordon, and H. L. Davies (1995). The impact of the greenhouse effect on sea-ice characteristics and snow accumulation in the polar regions. *International Journal of Climatology*, **15**(1), 3–23.

Huntington, H. P. (2000). Native observations capture impacts of sea ice changes. *Witness the Arctic*, **8**(1), 1–2.

Hurrell, J. W. (1995). Decadal trends in the North Atlantic oscillation: Regional temperature and precipitation. *Science*, **269**, 676–679.

Hurrell, J. W. and H. van Loon (1994). A modulation of the atmospheric annual cycle in the Southern Hemisphere. *Tellus*, **46A**, 325–338.

Hurrell, J. W. and H. van Loon (1997). Decadal variations in climate associated with the North Atlantic Oscillation. *Climatic Change*, **36**, 301–306.

Hurrell, J. W., Y. Kushnir, G. Ottersen, and M. Visbeck (eds.) (2003). *The North Atlantic Oscillation* (AGU Monograph No. 134). American Geophysical Union, Washington, DC, 279 pp.

Hutchings, J. K. and W. D. Hibler III (2002a). Investigating the SAR ice deformation product in validation of sea ice rheology models: Monitoring an evolving cryosphere. *NSIDC Special Session at the American Geophysical Union Fall Meeting, December 10–14, 2001* (Summary of Report GD-30). National Snow and Ice Data Center, Boulder, CO, pp. 61–62.

Hutchings, J. and W. D. Hibler III (2002b). Validating sea ice plastic models with SAR data: How well do isotropic models reproduce observed failure zones? *EGS XXVII General Assembly, April 21–26, Nice, France* (Paper EGS02-A-01980).

Hutchings, J. K., P. Heil, and W. D. Hibler (2002). Effect of tides on sea ice deformation and growth rate. *EGS XXVII General Assembly, April 21–26, Nice, France* (Abstract 02037).

Hutchinson, T. A. and T. A. Scambos (1997). High-resolution polar climate parameters derived from 1-km AVHRR data. *Proceedings of 8th Symposium on Global Climate Change Studies*. American Meteorological Society, Long Beach, CA, pp. 284–289.

Huynh, D. D., S. H. Yueh, S. V. Nghiem, and R. Kwok (1995). *Computing Thickness of Sea Ice from Polarimetric SAR Data: Application of Neural Network for Retrieving Sea Ice Thickness from Model-generated Polarimetric Scattering Coefficients* (JPL New Technology Report, July, NPO-19343). Jet Propulsion Laboratory, Pasadena, CA, 2 pp.

Hyvärinen, T. and J. Lammasniemi (1987). Infrared measurement of free-water content and grain size of snow. *Optical Engineering*, **26**, 342–348.

Hyyppa, J. and M. Hallikainen (1992). Classification of low-salinity sea ice types by ranging scatterometer. *International Journal of Remote Sensing*, **13**(13), 2399–2413.

Iacozza, J. and D. G. Barber (1999). An examination of the distribution of snow on sea ice. *Atmosphere–Ocean*, **37**(1), 21–51.

Ikeda, M. and F. Dobson (eds.) (1995). *Oceanographic Application of Remote Sensing*. CRC Press, New York, 512 pp.

Ikeda, M. and C. L. Tang (1992). Detection of the Labrador Current using ice-floe movement in synthetic aperture radar imagery and ice beacon trajectories. *Atmosphere–Ocean*, **30**, 223–245.

Ingram, R. G., J. Bâcle, D. G. Barber, Y. Gratton, and H. Melling (2002). An overview of physical processes in the North Water. *Deep-Sea Research II*, **49**, 4893–4906.

Ingram, W. J., C. A. Wilson, and J. F. B. Mitchell (1989). Modeling climate change: An assessment of sea ice surface albedo feedbacks. *Journal of Geophysical Research*, **94**, 8690–8622.

Intrieri, J. M. and M. D. Shupe (2004). Characteristics and radiative properties of diamond dust over the Western Arctic Ocean region. *Journal of Climate*, **17**, 2953–2960.

Ip, C. F. (1993). Numerical investigation of different rheologies on sea-ice dynamics. Ph.D. thesis, Dartmouth College, Hanover, NH, 242 pp.

Ip, C. F., W. D. Hibler III, and G. M. Flato (1991). On the effect of rheology on seasonal sea-ice simulations. *Annals of Glaciology*, **15**, 17–25.

Isaacs, R. G. and J. C. Barnes (1987). Intercomparison of cloud imagery from DMSP OLS, NOAA AVHRR, GOES VISSR and Landsat MSS. *Journal of Atmospheric and Oceanic Technology*, **4**, 647–667.

Ishida, K., K. I. Ohshima, T. Yamanouchi, and H. Kanzawa (1999). MOS–1/1b MESSR observations of the Antarctic sea ice: Ice bands and streamers. *Journal of Oceanography*, **55**(417), 417–426.

Ishikawa, T., J. Ukita, K. I. Ohshima, M. Wakatsuchi, T. Yamanouchi, and N. Ono (1996). Coastal polynyas off East Queen Maud Land observed from NOAA AVHRR data. *Journal of Oceanography*, **52**, 389–398.

Ishizu, M., K. Mizutani, and T. Itabe (1999). Airborne freeboard measurements of sea ice and lake ice at the Sea of Okhotsk coast in 1993–95 by a laser altimeter. *International Journal of Remote Sensing*, **20**(12), 2461–2476.

Israelsson, H. and J. Askne (1991). Analysis of polarimetric SAR observations of sea ice. *Proceedings of IGARSS '91, Espoo, Finland*. Institute of Electrical and Electronics Engineers, New York, pp. 89–92.

Ito, H. (1985). Decay of the sea ice in the North Water area: Observation of ice cover in Landsat images. *Journal of Geophysical Research*, **90**, 8102–8110.

Jacka, T. H. and W. F. Budd (1998). Detection of temperature and sea-ice extent changes in the Antarctic and Southern Ocean, 1949–96. *Annals of Glaciology*, **27**, 553–559.

Jacobs, S. (2004). Bottom water production and its links with the thermohaline circulation. *Antarctic Science*, **16**(4), 427–437.

Jacobs, S. S. and J. C. Comiso (1989). Sea ice and oceanic processes on the Ross Sea continental shelf. *Journal of Geophysical Research*, **94**(C12), 18195–18211.

Jacobs, S. S. and J. C. Comiso (1993). A recent sea-ice retreat west of the Antarctic Peninsula. *Geophysical Research Letters*, **20**(12), 1171–1174.

Jacobs, S. S. and J. C. Comiso (1997). A climate anomaly in the Amundsen and Bellingshausen Seas. *Journal of Climate*, **10**(4), 697–711.

Jacobs, S. S. and C. F. Giulivi (1998). Interannual ocean and sea ice variability in the Ross Sea. In: S. S. Jacobs and R. F. Weiss (eds.), *Ocean, Ice and Atmosphere: Interactions at the Antarctic Continental Margin* (AGU Antarctic Research Series No. 75). American Geophysical Union, Washington, DC, pp. 135–150.

Jacobs, S. S. and R. F. Weiss (eds.) (1998). *Ocean, Ice and Atmosphere: Interactions at the Antarctic Continental Margin* (AGU Antarctic Research Series No. 75). Arnerican Geophysical Union, Washington, DC, 382 pp.

Jacobs, S. S., C. F. Guilivi, and A. A. Mele (2002). Freshening of the Ross Sea during the late 20th Century. *Science*, **297**(5580), 386–389.

Jeffers, S., T. A. Agnew, B. T. Alt, R. De Abreu, and S. McCourt (2001). Investigating the anomalous sea-ice conditions in the Canadian High Arctic (Queen Elizabeth Islands) during summer 1998. *Annals of Glaciology*, **33**, 507–512.

Jeffries, M. O. (ed.) (1998). *Sea Ice: Physical Processes, Interactions and Variability* (AGU Antarctic Research Series No. 74). American Geophysical Union, Washington, DC, 407 pp

Jeffries, M. O. and U. Adolphs (1997). Early winter snow and ice thickness distribution, ice structure and development of the western Ross Sea pack ice between the ice edge and the Ross Ice Shelf. *Antarctic Science*, **9**, 188–200.

Jeffries, M. O., A. P. Worby, K. Morris, and W. Weeks (1994). Late winter sea ice properties and growth processes in the Bellingshausen and Amundsen Seas. *Antarctic Journal of the United States*, **29**(1), 11–13.

Jeffries, M. O., A. P. Worby, W. F. Weeks, and K. Morris (1997a). Seasonal variations in the properties, and structural and composition of sea ice and snow cover in the Bellingshausen and Amundsen Seas, Antarctica. *Journal of Glaciology*, **43**(143), 138–151.

Jeffries, M. O., K. Schwartz, and S. Li (1997b). Arctic summer sea-ice SAR signatures, melt-season characteristics, and melt-pond fractions. *Polar Record*, **33**(185), 101–112.

Jeffries, M., S. Li, R. A. Jaña, H. R. Krouse, and B. Hurst-Cushing (1998). Late-winter first-year ice floe thickness variability, seawater flooding and snow ice formation in the Amundsen and Ross Seas. In: M. Jeffries (ed.), *Antarctic Sea Ice: Physical Processes, Interactions and Variability* (AGU Antarctic Research Series No. 74). American Geophysical Union, Washington, DC, pp. 69–87.

Jeffries, M. O., H. R. Krouse, B. Hurst-Cushing, and T. Maksym (2001). Snow-ice accretion and snow-cover depletion on Antarctic first-year sea-ice floes. *Annals of Glaciology*, **33**, 51–60.

Jensen, J. R. (2000). *Remote Sensing of the Environment: An Earth Resource Perspective*. Prentice Hall, Upper Saddle River, NJ, 544 pp.

Jensen, J. R. (2004). *Introductory Digital Image Processing: A Remote Sensing Perspective* (3rd edn.). Prentice Hall, Upper Saddle River, NJ, 526 pp.

Jezek, K. C., D. Perovich, K. M. Golden, C. Luther, D. G. Barber, P. Gogineni, T. Grenfell, A. Jordan, C. Mobley, S. Nghiem et al. (1998). A broad spectral, interdisciplinary investigation of the electromagnetic properties of sea ice. *IEEE Transactions on Geoscience and Remote Sensing*, **36**(5), 1633–1641.

Jianping, X. and W. Caiying (2000). The Chinese meteorological satellite programs. *Proceedings of 2000 EUMETSAT Meteorological Satellite Data Users' Conference, Bologna, Italy, May 29–June 2*, pp. 168–173.

Jin, Z. and J. J. Simpson (1999). Bidirectional anisotropic reflectance of snow and sea ice in AVHRR channel 1 and 2 spectral regions: Part I. Theoretical analysis. *IEEE Transactions on Geoscience and Remote Sensing*, **37**(1), 543–554.

Jin, Z. and J. J. Simpson (2000). Bidirectional anisotropic reflectance of snow and sea ice in AVHRR channel 1 and 2 spectral regions: Part II. Correction applied to imagery of snow on sea ice. *IEEE Transactions on Geoscience and Remote Sensing*, **38**, 999–1015.

Joffre, S. M. (1983). Determining the form drag contribution to the total stress of the atmospheric flow over ridged sea ice. *Journal of Geophysical Research*, **88**, 4524–4530.

Johannessen, O. M. and M. W. Miles (2000). Arctic sea ice and climate change: Will the ice disappear in this century? *Science Progress*, **83**(3), 209–222.

Johannessen, O. M., W. J. Campbell, R. Shuchman, S. Sandven, P. Gloersen, E. G. Jospberger, J. A. Johannessen, and P. M. Haugan (1992). Microwave study programs of air–ice–ocean interactive processes in the seasonal ice zone of the Greenland and Barents Seas. In: F. Carsey (ed.), *Microwave Remote Sensing of Sea Ice* (AGU Monograph No. 68). American Geophysical Union, Washington, DC, pp. 261–289.

Johannessen, O. M., R. D. Muench, and J. E. Overland (1994a). *The Polar Oceans and Their Role in Shaping the Global Environment* (AGU Monograph No. 85). American Geophysical Union, Washington, DC, 540 pp.

Johannessen, O. M., S. Sandven, W. P. Budgell, J. A. Johannessen, and R. A. Shuchman (1994b). Observation and simulation of ice tongues and vortex pairs in the marginal ice zone. In: O. M. Johannessen, R. D. Muench, and J. E. Overland (eds.), *The Polar*

Oceans and Their Role in Shaping the Global Environment (AGU Monograph No. 85). American Geophysical Union, Washington, DC, pp. 109–136.

Johannessen, J. A., G. Digranes, H. Espedal, O. M. Johannessen, P. Samuel, D. Browne, and P. Vachon (1994c). *ERS-1 SAR Ocean Feature Catalogue* (ESA Report SP-1174). ESA, Noordwijk, The Netherlands.

Johannessen, O. M., M. Miles, and E. Bjorgo (1995a). The Arctic's shrinking sea ice. *Nature*, **376**, 126–127.

Johannessen, J. A., R. A. Shuchman, and O. M. Johannessen (1995b). Synthetic aperture radar on ERS-1. In: M. Ikeda and F. W. Dobson (eds), *Oceanographic Applications of Remote Sensing*. CRC Press, Boca Raton, FL, pp. 27–44.

Johannessen, O. M., S. Sandven, L. H. Pettersson, K. Kloster, T. Hamre, and J. Solhaug (1997). ICEWATCH: Real-time sea ice monitoring of the Northern Sea Route using satellite SAR technology. *The 3rd ERS Symposium: Space at the Service of Our Environment, 14–21 March*. ESA, Noordwijk, The Netherlands

Johannessen, J. A., P. Janssen, J. F. Minster, I. Robinson, D. Rothrock, and P. W. Vachon (eds.) (1998). Advances in oceanography and sea ice research using ERS observations. *ournal of Geophysical Research*, **103** (special issue), 7753–8214.

Johannessen, O. M., E. V. Shalina, and M. W. Miles (1999). Satellite evidence for an Arctic sea ice cover in transformation. *Science*, **286**(5446), 1937–1939.

Johannessen, O. M., L. Bengtsson, M. W. Miles, S. I. Kuzmina, V. A. Semenov, G. V. Alekseev, A. P. Nagurnyi, V. F. Zakharov, L. P. Bobylev, L. H. Pettersson et al. (2004). Arctic climate change: Observed and modelled temperature and sea ice variability. *Tellus*, **56A**(4), 328–341.

Johansson, R. and J. Askne (1987). Modelling of radar backscattering from low-salinity ice with ridges. *International Journal of Remote Sensing*, **8**, 1667–1677.

Johnson, G. C. and A. H. Orsi (1997). Southwest Pacific thermohaline changes between 1968/9 and 1990/1. *Journal of Climate*, **10**, 306–316.

Johnson, M. A., A. Y. Proshutinsky, and I. V. Polyakov (1999). Atmospheric patterns forcing two regimes of Arctic circulation: A return to anticyclonic conditions? *Geophysical Research Letters*, **26**, 1621–1624.

Johnston, M. and D. Flett (2001). First-year ridges in Radarsat ScanSAR imagery: Influence of incidence angle and feature orientation. *Proceedings of International Symposium on Remote Sensing in Glaciology, 4–8 June, College Park, Maryland*. International Glaciological Society, Cambridge, U.K.

Jones, P. D., M. New, D. E. Parker, S. Martin, and I. G. Rigor (1999). Surface air temperature and its changes over the past 150 years. *Review of Geophysics,* **37**(2), 173–199.

Joughin, I. R., D. B. Percival, and D. P. Winebrenner (1993). Maximum likelihood estimation of K distribution parameters for SAR data. *IEEE Transactions on Geoscience and Remote Sensing*, **31**(5), 989–999.

JPL (2001). *QuikSCAT Science Data User's Manual, Version 2.2* (JPL D-18053). Jet Propulsion Laboratory, Pasadena, CA.

Kahl, J. D., M. C. Serreze, and R. C. Schnell (1992). Low-level tropospheric temperature inversions in the Canadian Arctic. *Atmosphere–Ocean*, **30**, 511–529.

Kaleschke, L. and S. Kern (2002). ERS-2 SAR image analysis for sea ice classification in the marginal ice zone. *Proceedings of IGARSS '02, Toronto, Ontario, June 24–28*.

Kaleschke, L., G. Heygster, C. Lupkes, A. Bochert, J. Hartmann, J. Haarpaintner, and T. Vihma (2001). SSM/1 sea ice remote sensing for mesoscale ocean–atmosphere interaction analysis. *Canadian Journal of Remote Sensing*, **27**(5), 526–537.

Kalnay, E., M. Kanamitsu, R. Kistler, W. Collins, D. Deaven, L. Gandin, M. Iredell, S. Saha, G. White, J. Woollen et al. (1996). The NCEP/NCAR 40-year reanalysis project. *Bulletin of the American Meteorological Society*, **77**, 437–471.

Karcher, M. J., R. Gerdes, F. Kauker, and C. Köberle (2003). Arctic warming: Evolution and spreading of the 1990s warm event in the Nordic seas and the Arctic Ocean. *Journal of Geophysical Research*, **108**(C2), 3034, DOI: 10.1029/2001JC001265.

Kärkäs, E., H. B. Granberg, K. Kanto, K. Rasmus, C. Lavoie, and M. Leppäranta (2002). Physical properties of the seasonal snow cover in Dronning Maud Land, East Antarctica. *Annals of Glaciology*, **34**, 89–94.

Karoly, D. J. (1990). The role of transient eddies in low frequency zonal variations of the Southern Hemisphere circulation. *Tellus*, **42A**, 41–50.

Karoly, D. J. and D. G. Vincent (eds.) (1998). *Meteorology of the Southern Hemisphere*. American Meteorological Society, Boston, 410 pp.

Kasamatsu, F., P. Ensor, and G. G. Joyce (1998). Clustering and aggregations of minke whales in Antarctic feeding grounds. *Marine Ecology Progress Series*, **168**, 1–11.

Katsaros, K. and R. A. Brown (1991). Legacy of the SEASAT mission for studies of the atmosphere and air–sea-ice interactions. *Bulletin of the American Meteorological Society*, **72**(7), 967–981.

Kattenberg, A., F. Giorgi, H. Grassl, G. A. Meehl, J. F. B. Mitchell, R. J. Stouffer, T. Tokioka, A. J. Weaver, and T. M. L. Wigley (1996). Climate models: Projections of future climate. In: J. T. Houghton, L. G. Miera Filho, B. A. Callander, N. Harris, A. Kattenberg and K. Maskell (eds.), *Climate Change 1995*. Cambridge University Press, Cambridge, UK, pp. 285–357.

Kaufman, Y. J. (1989). The atmospheric effect on remote sensing and its correction. In: G. Asrar (ed.), *Theory and Applications of Optical Remote Sensing* (Wiley Series in Remote Sensing). John Wiley & Sons, pp. 336–429.

Kauker, F., R. Gerdes, M. Karcher, C. Köberle, and J. L. Lieser (2003). Variability of Arctic and North Atlantic sea ice: A combined analysis of model results and observations from 1978 to 2001. *Journal of Geophysical Research*, **108**(C6), 3182, DOI: 10.1029/2002JC001573.

Kaupp, V. and B. Holt (1998). The Alaska SAR Facility: An overview and key geophysical applications. *Proceedings of IGARSS '98, Seattle, Washington*.

Kawamura, T., K. I. Ohshima, T. Takizawa, and S. Ushio (1997). Physical, structural and isotropic characteristics and growth process on fast ice in Lützow-Holm Bay, Antarctica. *Journal of Geophysical Research*, **102**, 3345–3355.

Kawanishi, T., T. Sezai, Y. Ito, K. Imaoka, T. Takeshima, Y. Ishido, A. Shibata, M. Miura, H. Inahata, and R. W. Spencer (2003). The Advanced Microwave Scanning Radiometer for the Earth Observing System (AMSR-E): NASDA's contribution to the EOS for global energy and water cycle studies. *IEEE Transactions of Geoscience and Remote Sensing*, **GE-41**(2), 184–194.

Keeling, R. F. and B. B. Stephens (2001). Antarctic sea ice and the control of Pleistocene climate instability. *Paleoceanography*, **16**(1), 112–131.

Keller, K., S. M. Hvidegaard, and R. Forsberg (2004). Airborne laser measurements of sea-ice freeboard in the polar sea. *EGS 1st General Assembly, April 25–30, Nice, France* (Abstract 03396).

Kerbaol, V., B. Chapron, and P. W. Vachon (1998). Analysis of ERS-1/2 synthetic aperture radar wave mode imagettes. *Journal of Geophysical Research*, **103**(C4), 7833–7846.

Kerman, B. R. (1998). On the relationship of pack ice thickness to the length of connectivity trees in SAR imagery. In: H. T. Shen (ed.), *Ice in Surface Waters* (Vol. 2). Clarkson University, Potsdam, New York.

Kern, S. (2001). A new algorithm to retrieve the sea ice concentration using weather-corrected 85 GHz SSM/1 measurements. PhD thesis, Department of Physics and Electrical Engineering, University Bremen, Bremen, Germany.

Kern, S. (2004). A new method for medium-resolution sea ice analysis using weather-influence corrected Special Sensor Microwave/Imager 85 GHz data. *International Journal of Remote Sensing*, **25**(21), 4555–4582.

Kern, S. and G. Heygster (2001). Sea-ice concentration retrieval in the Antarctic based on the SSM/1 85.5 GHz polarisation. *Annals of Glaciology*, **33**, 109–114.

Kern, S., L. Kaleschke, and D. A. Clausi (2003). A comparison of two 85-GHz SSM/I ice concentration algorithms with AVHRR and ERS–2 SAR imagery. *Transactions on Geoscience and Remote Sensing*, **41**(10), 2294–2305.

Kerr, Y. H., J. Font, P. Waldteufel, and M. Berger (2000). The Soil Moisture and Ocean Salinity Mission: SMOS. *ESA Earth Observation Quarterly*, **66**, 18–25.

Key, E., P. Minnett, and C. Ananasso (2001b). Variations in cloud forcing in western Arctic polynyas. *International Polynya Symposium, September 9–13, Quebec* (abstract). Available online at ⟨*www.fsg.ulaval.ca/giroq/now/IPS2001/ips2001.htm*⟩.

Key, J. (1993). Estimating the area fraction of geophysical fields from measurements along a transect. *IEEE Transactions on Geoscience and Remote Sensing*, **31**.

Key, J. (1994). The area coverage of geophysical fields as a function of sensor field-of-view. *Remote Sensing of Environment*, **48**(3), 339–346.

Key, J. (2002). *The Cloud and Surface Parameter Retrieval (CASPR) System User's Guide*. Cooperative Institute for Meteorological Satellite Studies, University of Wisconsin, 61 pp. Available online at ⟨*http://stratus.sec.wisc.edu/cspr/caspr.html*⟩.

Key, J. and R. G. Barry (1989). Cloud cover analysis with Arctic AVHRR: Part 1. Cloud detection. *Journal of Geophysical Research*, **94**, 18521–18535.

Key, J. and M. Haefliger (1992). Arctic ice surface temperature retrieval from AVHRR thermal channels. *Journal of Geophysical Research*, **97**(D5), 5885–5893.

Key, J. and A. J. Schweiger (1998). Tools for atmospheric radiative transfer: Streamer and Fluxnet. *Computers and Geosciences*, **24**, 443–451.

Key, J. R. and A. J. Schweiger (2000). *Streamer User's Guide, Version 72*. Cooperative Institute for Meteorological Satellite Studies, University of Wisconsin, Madison, WI.

Key, J., R. Stone, J. Maslanik, and E. Ellefsen (1993). The detectability of sea ice leads in satellite data as a function of atmospheric conditions and measurement scale. *Annals of Glaciology*, **17**, 227–232.

Key, J., J. A. Maslanik, T. Papakyriakou, M. C. Serreze, and A. J. Schweiger (1994a). On the validation of satellite-derived sea ice surface temperature. *Arctic*, **47**, 280–287.

Key, J., J. A. Maslanik, and E. Ellefsen (1994b). The effects of sensor field-of-view on the geometrical characteristics of sea ice leads and implications for large-area heat flux estimates. *Remote Sensing of Environment*, **48**(3), 347–357.

Key, J., J. Collins, C. Fowler, and R. Stone (1997). High-latitude surface temperature estimates from thermal satellite data. *Remote Sensing of Environment*, **61**, 302–309.

Key, J. R., X. Wang, J. C. Stroeve, and C. Fowler (2001). Estimating the cloudy-sky albedo of sea ice and snow from space. *Journal of Geophysical Research*, **106**(D12), 12489–12497.

Keys, H. J. R., S. S. Jacobs, and D. Barnett (1990). The calving and drift of iceberg B-9 in the Ross Sea, Antarctica. *Antarctic Science*, **2**, 243–257.

Kidder, S. Q. and T. H. Vonder Haar (1995). *Satellite Meteorology: An Introduction*. Academic Press, San Diego, 466 pp.

Kidder, S. Q. and H. Wu (1984). Dramatic contrast between low clouds and snow cover in daytime 3.7 μm imagery. *Monthly Weather Review*, **112**, 2345–2346.

Kidson, J. W. (1988). Interannual variations in Southern Hemisphere circulation. *Journal of Climate*, **1**(12), 1177–1198.

Kidson, J. W. (1999). Principal modes of Southern Hemisphere low-frequency variability obtained from NCEP-NCAR reanalyses. *Journal of Climate*, **12**, 2808–2830.

Kidwell, K. (2000). *NOAA KLM User's Guide* (revised edn.). National Environmental Satellite Data Information Services (NESDIS), National Climatic Data Center, Boulder, CO. Available at ⟨*www2.ncdc.noaa.gov/docs/klm/index.htm*⟩.

Kim, Y. S. (1984). Theoretical and experimental study of radar backscatter from sea ice. PhD dissertation, University of Kansas, Lawrence, KS.

Kim, Y. S., R. K. Moore, and R. G. Onstott (1984). *Theoretical and Experimental Study of Radar Backscatter from Sea Ice* (Report #RSL TR 331-37). University of Kansas Lawrence, KS, 168 pp.

Kim, Y. S., R. K. Moore, R. G. Onstott, and S. Gogineni (1985a). Towards identification of optimum radar parameters for sea ice monitoring. *Journal of Glaciology*, **31**(109), 214–219.

Kim, Y. S., R. G. Onstott, and R. K. Moore (1985b). The effect of a snow cover on microwave backscatter from sea ice. *IEEE Journal of Oceanic Engineering*, **9**, 383–388.

Kimura, N. and M. Wakatsuchi (1999). Processes controlling the advance and retreat of sea ice in the Sea of Okhotsk. *Journal of Geophysical Research*, **104**(C5), 11137–11150.

Kimura, N. and M. Wakatsuchi (2001). Mechanisms for the variation of sea-ice extent in the Northern Hemisphere. *Journal of Geophysical Research*, **106**(C12), 31319–31332.

Kimura, N. and M. Wakatsuchi (2004). Increase and decrease of sea ice area in the Sea of Okhotsk: Ice production in coastal polynyas and dynamic thickening in convergence zones. *Journal of Geophysical Research*, **109**, C09S03, DOI: 10.1029/2003JC001901.

King, E. A. (2003). *Polar-orbiting Operational Environmental Satellites: Future Directions* (report). CSIRO Earth Observation Centre, Canberra, 10 pp. Available online at ⟨*http://www.cossa.csiro.au/reports/king/eking_miami02.pdf*⟩.

King, J. C. and J. C. Comiso (2003). The spatial coherence of interannual temperature trends in the Antarctic Peninsula. *Geophysical Research Letters*, **30**(2), 1040, DOI: 10.1029/2002GL015580.

King, J. C. and J. Turner (1997). *Antarctic Meteorology and Climatology*. Cambridge University Press, New York, 409 pp.

King, J. C., J. Turner, G. J. Marshall, W. M. Connolley, and T. A. Lachlan–Cope (2003a). *Antarctic Peninsula Climate Variability and Its Causes as Revealed by Instrumental Records* (AGU Antarctic Research Series No. 79). American Geophysical Union, Washington, DC, pp. 17–30.

King, M. D., J. Closs, S. Spangler, and R. Greenstone (2003b). *EOS Data Products Handbook* (Vol. 1, NP-2003-4-544-GSFC). NASA Goddard Space Flight Center, Greenbelt, MD.

Kirkwood, R. and Robertson, G. (1997) Seasonal change in the foraging ecology of emperor penguins on the Mawson Coast, Antarctica. *Marine Ecology Progress Series*, **156**, 205–223

Klein, A. G. (2000). Development of a prototype snow albedo algorithm for the NASA MODIS instrument. *57th Annual Eastern Snow Conference, Syracuse, New York, May 17–19*.

Klein, A. G. and J. Stroeve (2002). Development and validation of a snow albedo algorithm for the MODIS instrument. *Annals of Glaciology*, **34**, 45–52.

Knap, W. H. and J. Oerlemans (1996). The surface albedo of the Greenland Ice Sheet: Satellite-derived and *in situ* measurements in the Søndre Strømfjord area during the 1991 melt season. *Journal of Glaciology*, **42**, 364–374.

Kneizys, F. X., E. P. Shettle, L. W. Abreu, J. H. Chetwynd, G. P. Anderson, W. O. Gallery, J. E. A. Selby, and S. A. Clough (1988). *Users Guide to LOWTRAN 7* (AFGL-TR-88-0177, Environmental Research Paper 1010). USAF Geophysics Laboratory, Hanscom AFB, MA, 137 pp.

Köberle, C. and R. Gerdes (2003). Mechanisms determining the variability of Arctic sea ice conditions and export. *Journal of Climate*, **16**(17), 2843–2858.

Koerner, R. M. (1973). The mass balance of sea ice in the Arctic Ocean. *Journal of Glaciology*, **12**(65), 173–185.

Koh, G. (1992). Dielectric properties of ice and snow at 26.5 to 40 GHz. *Proceedings of IGARSS '92*, pp. 820–822.

Komuro, Y. and H. Hasumi (2003). Effects of surface freshwater flux induced by sea ice transport on the global thermohaline circulation. *Journal of Geophysical Research*, **108**(C2), 3047, DOI: 10.1029/2002JC001476.

Kondo, J. and H. Yamazawa (1986). Measurement of snow surface emissivity. *Boundary-Layer Meteorology*, **71**, 288–299.

Kondratyev, K. Ya. and V. V. Melentyev (1994). Microwave remote sensing of the snow and ice cover: The Russian experience. In: O. M. Johannessen, R. D. Muench, and J. E. Overland (eds.), *The Polar Oceans and Their Role in Shaping the Global Environment* (AGU Monograph No. 85). American Geophysical Union, Washington, DC, pp. 497–504.

Kondratyev, K. Y., O. M. Johannessen, and V. V. Melentyev (1996). *High Latitude Climate and Remote Sensing*. Wiley/Praxis, Chichester, UK, 208 pp.

Kong, J. A. (ed.) (1990). *Polarimetric Remote Sensing: Progress in Electromagnetic Research* (Vol. 3). Elsevier Science, New York, 520 pp.

Kong, J. A. (2000). *Electromagnetic Wave Theory*. EMW Publishing, Cambridge, MA, 1007 pp.

Kooyman, G. L. and J. Burns (1999). Weddell seal versus emperor penguin: Boss of the Ross Sea. *American Zoologist*, **39**, 9–19.

Korsnes, R. (1993a). Quantitative analysis of sea ice remote sensing imagery. *International Journal of Remote Sensing*, **14**(2), 295–311.

Korsnes, R. (1993b). A mathematical approach to the segmentation of sea-ice SAR. *International Journal of Remote Sensing*, **14**(2), 313–332.

Koshlyakov, M. N. and R. Y. Tarakanov (2003). Antarctic Bottom Water in the Pacific sector of the Southern Ocean. *Oceanology*, **43**(1), 1–15.

Kottmeier, C. and D. Engelbart (1992). Generation and atmospheric heat exchange of coastal polynyas in the Weddell Sea. *Boundary-Layer Meteorology*, **60**(3), 207–234.

Kottmeier C. and L. Sellmann (1996). Atmospheric and oceanic forcing of Weddell Sea ice motion. *Journal of Geophysical Research*, **101**(C9), 20809–20824.

Kottmeier, C., J. Olf, W. Frieden, and R. Roth (1992). Wind Forcing and Ice Motion in the Weddell Sea. *Journal of Geophysical Research*, **97**(D18), 20373–20383.

Kottmeier, C., S. Ackley, E. Andreas, D. Crane, H. Hoeber, J. Kong, J. Launinien, D. Limbert, D. Martinson, R. Roth et al. (1997). *Wind, Temperature and Ice Motion Statistics in the Weddell Sea* (a compilation based on data from drifting buoys, vessels,

and operational weather analyses, WMO/TD 797). International Programme for Antarctic Buoys, World Climate Research Programme, Geneva, 48 pp.

Kouraev, A. V., F. Papa, P. I. Buhrizin, Z. Cazenave, J.-F. Cretaux, J. Dozortseva, and F. Rémy (2003). Ice cover variability in the Caspian and Aral seas from active and passive microwave data. *Polar Research*, **22**(1), 43–50.

Kovacs, A. and M. Mellor (1974). Sea ice morphology and ice as a geological agent in the southern Beaufort Sea. In: J. C. Reed and J. F. Sater (eds.), *The Coast and Shelf of the Beaufort Sea*. Arctic Institute of North America, Calgary, Canada, pp. 113–161.

Kowalik, Z. and A. Proshutinsky (1994). The Arctic Ocean tides. In O. M. Johannessen, R. D. Muench, and J. E. Overland (eds.), *The Polar Oceans and Their Role in Shaping the Global Environment* (AGU Monograph No. 85). American Geophysical Union, Washington, DC, pp. 137–158.

Kozo, T. L., L. D. Farmer, and J. P. Welsh (1990). *Wind-generated Polynyas off the Coasts of the Bering Sea Islands* (CRREL Monograph 90-1). U.S. Army Cold Regions Research and Engineering Laboratory, Hannover, NH, pp. 126–132.

Krajick, K. (2001). Arctic life, on thin ice. *Science*, **291**, 424–425.

Kramer, H. J. (2002). *Observation of the Earth and Its Environment: Survey of Missions and Sensors* (4th edn.). Springer-Verlag, New York, 1514 pp.

Krembs, C., H. Eicken, K. Junge, and J. Deming (2002). High concentrations of exopolymeric substances in Arctic winter sea ice: Implications for the polar ocean carbon cycle and cryoprotection of diatoms. *Deep-Sea Research*, **49**(12), 2163–2181.

Kreyscher, M., Harder, M., and Lemke, P. (1997). First results of the Sea Ice Model Intercomparison Project (SIMIP). *Annals of Glaciology*, **25**, 8–11.

Kreyscher, M., M. Harder, T. Markus, P. Lemke, G. Flato, and M. Gregory (2000). Results of the Sea Ice Model Intercomparison Project: Evaluation of sea ice rheology schemes for use in climate simulations. *Journal of Geophysical Research*, **105**(C5), 11299–11320.

Kurtz, D. D. and D. H. Bromwich (1985). *A Recurring, Atmospherically Forced Polynya in Terra Nova Bay* (AGU Antarctic Research Series No. 43). American Geophysical Union, Washington, DC, pp. 177–201.

Kummerow, C. (1993). On the accuracy of the Eddington approximation for radiative transfer in the microwave frequencies. *Journal of Geophysical Research*, **98**, 2757–2765.

Kwok, R. (1998). The Radarsat Geophysical Processor System. In: C. Tsatsoulis and R. Kwok (eds.), *Analysis of SAR Data of the Polar Oceans: Recent Advances*. Springer-Verlag, Berlin, pp. 235–258.

Kwok, R. (2000). Recent changes in Arctic Ocean sea ice motion associated with the North Atlantic Oscillation. *Geophysical Research Letters*, **27**(6), 775–778.

Kwok, R. (2001). Deformation of the Arctic Ocean sea ice cover: November 1996 through April 1997. In: J. Dempsey and H. H. Shen (eds.), *Scaling Laws in Ice Mechanics and Dynamics*. Kluwer Academic, Dordrecht, The Netherlands, pp. 315–323.

Kwok, R. (2002a). Sea ice concentration estimates from satellite passive microwave radiometry and openings from SAR ice motion. *Geophysical Research Letters*, **29**(9), 1311, DOI: 10.1029/202GL014787.

Kwok, R. (2002b). Arctic sea-ice area and volume production: 1996/97 versus 1997/98. *Annals of Glaciology*, **34**, 147–153.

Kwok, R. (2002c). Sea ice deformation, growth, and thickness from small-scale ice motion. *EGS XXVII General Assembly, April 21–26, 2002, Nice, France* (Abstract 00787).

Kwok, R. (2004). Annual cycles of multiyear sea ice coverage of the Arctic Ocean: 1999–2003. *Journal of Geophysical Research*, **109**, C11004, DOI: 10.1029/2003JC002238.

Kwok, R. and J. C. Comiso (1998). The perennial ice cover of the Beaufort Sea from active and passive microwave observations. *Annals of Glaciology*, **25**, 376–381.

Kwok, R. and J. C. Comiso (2002a). Southern Ocean climate and sea ice anomalies associated with the Southern Oscillation. *Journal of Climate*, **15**(5), 487–501.

Kwok, R. and J. C. Comiso (2002b). Spatial patterns of variability in Antarctic surface temperature: Connections to the Southern Hemisphere Annular Mode and the Southern Oscillation. *Geophysical Research Letters*, **29**, DOI: 10.1029/2002GL015415.

Kwok, R. and G. Cunningham (1991). *Alaska SAR Facility Geophysical Processor System Data User's Handbook* (JPL D-9526). Jet Propulsion Laboratory, Pasadena, CA, 70 pp.

Kwok, R. and G. F. Cunningham (1992). Backscatter characteristics of the winter sea ice cover in the Beaufort Sea. *Journal of Geophysical Research*, **99**(C4), 7787–7803.

Kwok, R. and G. F. Cunningham (1994a). Backscatter characteristics of the winter ice cover in the Beaufort Sea. *Journal of Geophysical Research*, **99**(C4), 7787–7802.

Kwok, R. and G. F. Cunningham (1994b). Use of time series SAR data to resolve ice type ambiguities in newly-opened leads. *Proceedings of International Geoscience and Remote Sensing Symposium, Pasadena, CA, August 8–12, 1994* (Vol. 2). Institute of Electrical and Electronics Engineers, Piscataway, NJ, pp. 1024–1026.

Kwok, R. and G. F. Cunningham (2000). *Radarsat Geophysical Processor System Data User's Handbook (Version 1.0)* (JPL D-19149). Jet Propulsion Laboratory, Pasadena, CA.

Kwok, R. and G. F. Cunningham (2002). Seasonal ice area and volume production of the Arctic Ocean: November 1996 through April 1997. *Journal of Geophysical Research*, **107**(C10), 8038, DOI: 10.1029/2000JC000469.

Kwok, R. and B. Holt (1999). Sea ice thickness from kinematics. *CEOS SAR Workshop, Toulouse, October 26–29* (ESA-CNES). Available online at ⟨*http://www.estec.esa.nl/ceos99/papers/*⟩.

Kwok, R. and D. A. Rothrock (1999). Variability of Fram Strait ice flux and North Atlantic Oscillation. *Journal of Geophysical Research*, **104**(C3), 5177–5189.

Kwok, R., J. C. Curlander, R. McConnell, and S. S. Pang (1990). An ice-motion tracking system at the Alaska SAR Facility. *IEEE Journal of Oceanic Engineering,* **15**(1), 44–54.

Kwok, R., M. R. Drinkwater, A. Pang, and E. Rignot (1991). Characterization and classification of sea ice in polarimetric SAR data. *Proceedings of IGARSS '91, June 3–6, Espoo, Finland* (Vol. 1, IEEE Catalog #CH2971–0).

Kwok, R., G. Cunningham, and B. Holt (1992a). An approach to identification of sea ice types from spaceborne SAR data. In: F. Carsey (ed.), *Microwave Remote Sensing of Sea Ice* (AGU Monograph Series No. 68). American Geophysical Union, Washington, DC, pp. 355–360.

Kwok, R., E. Rignot, B. Holt, and R. G. Onstott (1992b). Identification of sea ice types in spaceborne synthetic aperture radar data. *Journal of Geophysical Research*, **97**(C2), 2391–2402.

Kwok, R., D. A. Rothrock, H. L. Stern, and G. F. Cunningham (1995a). Determination of the age distribution of sea ice from Lagrangian observations of ice motion. *IEEE Transactions on Geoscience and Remote Sensing*, **33**(2), 392–400.

Kwok, R., S. V. Nghiem, S. H. Yueh, and D. D. Huynh (1995b). Retrieval of thin ice thickness from multifrequency polarimetric SAR data. *Remote Sensing of Environment*, **51**(3), 361–374.

Kwok, R., J. C. Comiso, and G. F. Cunningham (1996). Seasonal characteristics of the perennial ice cover of the Beaufort Sea. *Journal of Geophysical Research*, **101**(C12), 28417–28439.

Kwok, R., S. V. Nghiem, S. Martin, D. P. Winebrenner, A. J. Gow, D. P. Perovich, C. T. Swift, D. G. Barber, K. M. Golden, and E. J. Knapp (1998a). Laboratory measurements of sea ice: Connections to microwave remote sensing. *IEEE Transactions on Geoscience and Remote Sensing*, **36**(5), 1716–1730.

Kwok, R., A. Schweiger, D. A. Rothrock, S. Pang, and C. Kottmeier (1998b). Sea ice motion from satellite passive microwave imagery assessed with ERS SAR and buoy motions. *Journal of Geophysical Research*, **103**(C4), 8191–8214.

Kwok, R., G. F. Cunningham, and S. Yueh (1999a). Area balance of the Arctic Ocean perennial ice zone: October 1996–April 1997. *Journal of Geophysical Research*, **104**(C11), 25747–25759.

Kwok, R., G. F. Cunningham, N. LaBelle-Hamer, B. Holt, and D. Rothrock (1999b). Ice thickness from high-resolution radar imagery. *EOS, Transactions of American Geophysical Union*, **80**(42), 495–497.

Kwok, R., G. F. Cunningham, and D. Nguyen (2000). *Alaska SAR Facility Radarsat Geophysical Processor System: Product Specification (Version 2.0)* (JPL D-13448). Jet Propulsion Laboratory, Pasadena, CA.

Kwok, R., G. F. Cunningham, and W. D. Hibler III (2003a). Sub-daily sea ice motion and deformation from Radarsat observations. *Geophysical Research Letters*, **30**(23), 2218, DOI: 10.1029/2003GL018723.

Kwok, R., G. F. Cunningham, and S. V. Nghiem (2003b). A study of the onset of melt over the Arctic Ocean in Radarsat synthetic aperture radar imagery. *Journal of Geophysical Research*, **108**(C11), 3363, DOI: 10.1029/2002JC001363.

Kwok, R., G. F. Cunningham, and S. S. Pang (2004a). Fram Strait sea ice outflow. *Journal of Geophysical Research*, **109**, C01009, DOI: 10.1029/2003JC001785.

Kwok, R., H. J. Zwally, and D. Yi (2004b). ICESat observations of Arctic sea ice: A first look. *Geophysical Research Letters*, **31**, L16401, DOI: 10.1029/2004GL020309.

Landsat Project Science Office (2003). *Landsat 7 Science Data Users Handbook*. Available online at ⟨*http://ltpwww.gsfc.nasa.gov/IAS/handbook/handbook_toc.html*⟩.

Laine, V. and M. Heikinheimo (1996). Estimation of surface albedo from NOAA AVHRR data in high latitudes. *Tellus*, **48A**(3), 424–441.

Lange, M. A. (2002). Sea ice contamination: A review. In: V. Squire and P. Langhorne (eds.), *Ice in the Environment: Proceedings of 16th International Symposium on Ice, Dunedin, New Zealand, December 2–6* (Vol. 3). International Association for Hydraulic Research, Ecole Polytechnique Fédérale, Lausanne, Switzerland/University of Otago, Dunedin, New Zealand, pp. 152–162,

Lange, M. A. and H. Eicken (1991). The sea ice thickness distribution in the northwestern Weddell Sea. *Journal of Geophysical Research*, **96**(C3), 4821–4837.

Lange, M. A., S. F. Ackley, P. Wadhams, G. Dieckmann, and H. Eicken (1989). Development of sea ice in the Weddell Sea. *Annals of Glaciology*, **12**, 92–96.

Lange, M. A., P. Schlosser, S. F. Ackley, P. Wadhams, and G. S. Dieckmann (1990). ^{18}O concentrations in sea ice of the Weddell Sea, Antarctica. *Journal of Glaciology*, **36**(124), 315–323.

Langhorne, P. J., V. A. Squire, C. Fox, and T. G. Haskell (1998). Breakup of sea ice by ocean waves. *Annals of Glaciology*, **27**, 438–442.

Langhorne, P., V. A. Squire, C. Fox, and T. G. Haskell (2001). Lifetime estimation for a landfast ice sheet subjected to ocean swell. *Annals of Glaciology*, **33**, 333–338.

Langleben, M. P. (1971). Albedo of melting sea ice in the southern Beaufort Sea. *Journal of Glaciology*, **10**(58), 101–104.

Larouche, P. and C. Cariou (1992). Directional wave spectra estimation in a marginal ice zone using linear prediction. *Journal of Physical Oceanography*, **22,** 196–206.

Launiainen, J. and B. Cheng (1998). Modelling of ice thermodynamics in natural water bodies. *Cold Regions Science and Technology*, **27**, 153–178.

Launiainen, J. and T. Vihma (1994). On the surface heat fluxes in the Weddell Sea. In: O. M. Johannessen, R. D. Muench, and J. E. Overland (eds.), *Polar Oceans and Their Role in Shaping the Global Environment* (AGU Monograph Series No. 85). American Geophysical Union, Washington, DC, pp. 399–419.

Launiainen, J. and T. Vihma (eds.) (2001). *BALTEX–BASIS Final Report* 2001 (Publication 19). International BALTEX Secretariat, Geesthacht, Germany.

Laur, H. and S. T. Dokken (1997). Observation of large scale features with ERS SAR browse images. *Earth Observation Quarterly*, **55**, 1–5.

Laur, H., P. Bally, P. Meadows, J. Sanchez, B. Schaettler, E. Lopinto, and D. Esteban (1998). *ERS SAR Calibration Derivation of the Backscattering Coefficient Sigma-nought in ESA ERS SAR PRI Products* (Doc. No. ES-TN-RS-PM-HL09 7, September). ESA, Noordwijk, The Netherlands.

Laxon, S. W. C. (1989). Satellite radar altimetry over sea ice. Ph.D. thesis, Mullard Space Science Laboratory, University College, London, 246 pp.

Laxon, S. W. (1990). Seasonal and inter-annual variations in Antarctic sea ice extent as mapped by radar altimetry. *Geophysical Research Letters*, **17**, 1553–1556.

Laxon, S. W. (1994a). Sea ice altimeter processing scheme at the EODC. *International Journal of Remote Sensing*, **15**(4), 915–924.

Laxon, S. (1994b). Sea ice extent mapping using the ERS-1 radar altimeter. *EARSeL Advances in Remote Sensing*, **3**(2), 112–116.

Laxon, S., P. Wadhams, C. Dick, and K. Steffen (2002). *Recent Variations in Arctic Sea Ice Thickness* (report to the Arctic Ocean Sciences Board by ACSYS/CliC Observation Products Panel, IACPO Informal Report 7). World Climate Research Programme, Geneva, Switzerland.

Laxon, S., C. Dick, K. Steffen, and P. Wadhams (2003a). Trends and variability in Arctic sea-ice thickness. *ACSYS/CliC Ice and Climate News*, **4**, 5–6.

Laxon, S., N. Peacock, and D. Smith (2003b). High interannual variability of sea ice thickness in the Arctic region. *Nature*, **425**, 947–950, DOI: 10.1038/nature02050.

Laxon, S., O. Johannessen, M. Miles, P. Wadhams, and J. E. Walsh (2004). Sea-ice observations. In: J. Bamber and A. Payne (eds.), *Mass Balance of the Cryosphere*. Cambridge University Press, Cambridge, UK, pp. 337–366.

Lazzara, M. A., L. M. Keller, C. R. Stearns, J. E. Thom, and G. A. Wiedner (2003). Antarctic satellite meteorology: Applications for weather forecasting. *Monthly Weather Review*, **131**(2), 371–383.

Lebedev, L. (1968). Maximum size of a wind-generated lead during sea freezing. *Oceanology*, **8**, 313–318.

Lecomte, P., A. Cavanié, and F. Gohin (1993). Recognition of sea ice zones using ERS-1 scatterometer data. *Proceedings of IGARSS '93*, pp. 855–857.

Ledley, T. S. (1988). A coupled energy balance climate–sea ice model: Impact of sea ice and leads on climate. *Journal of Geophysical Research*, **93**(D12), 15919–15932.

Ledley, T. S. (1991). Snow on sea ice: Competing effects in shaping climate. *Journal of Geophysical Research*, **96**, 17195–17208.

Ledley, T. S. (1993). Variations in snow on sea ice: A mechanism for producing climate variations. *Journal of Geophysical Research*, **98**(D6), 10401–10410.

Lee, J. S., I. Jurkevich, P. Dewaele, P. Wambacq, and A. Oosterlinck (1994). Speckle filtering of synthetic aperture radar images: A review. *Remote Sensing Reviews*, **8**(4), 313–340.

Lee, T. F., S. Atwater, and C. Samuels (1993). *Sea Ice Edge Enhancement Using Polar-Orbiting Environmental Satellite Data* (AMS Notes, September). American Meteorological Society, Boston, pp. 369–377.

Legendre, L., S. F. Ackley, G. S. Dieckmann, B. Gullicksen, R. Homer, T. Hoshiai, I. A. Melnikov, W. S. Reeburgh, M. Spindler, and C. W. Sullivan (1992). Ecology of sea ice biota: 2. Global significance. *Polar Biology*, **12**, 429–444.

Legrésy, B. and F. Rémy (1997). Altimetric observations of surface characteristics of the Antarctic Ice Sheet. *Journal of Glaciology*, **43**(144), 265–275.

Lehner, S., J. Schulz–Stellenfleth, and R. Bamler (1997). Estimation of wind, wave and ice parameters at the ice boundary by using active microwave systems of the ERS satellites. *Proceedings of 3rd ERS Symposium: Space at the Service of Our Environment*. ESA/ESTEC, Florence, Italy, pp. 943–948.

Lehner, S., J. Horstmann, and J. Schulz-Stellenfleth (2004). TerraSAR-X for oceanography: Mission overview. *Proceedings of IGARSS '04, Anchorage, AK, September 20–24*.

Lei, G.-T., R. K. Moore, and S. P. Gogineni (1988). *Investigation of Radar Backscattering from Second-year Sea Ice* (RSL Technical Report 3311-7). Radar Systems and Remote Sensing Laboratory, University of Kansas.

Leidner, S. M., R. N. Hoffman, and J. Augenbaum (2000). *SeaWinds Scatterometer Real-time BUFR Geophysical Data Product, Users Guide, v. 2.3.0*. National Oceanic and Atmospheric Administration/National Environmental Satellite, Data and Information Service, Silver Spring, MD.

Lemke, P., W. B. Owens, and W. D. Hibler III (1990). A coupled sea ice–mixed layer–pycnocline model for the Weddell Sea. *Journal of Geophysical Research*, **95**(C6), 9513–9525.

Lemke, P., W. D. Hibler III, G. M. Flato, M. Harder, and M. Kreyscher (1997). On the improvement of sea-ice models for climate simulations: The Sea-Ice Model Intercomparison Project. *Annals of Glaciology*, **25**, 183–187.

Lemke, P., M. Harder, and M. Hilmer (2000). The response of Arctic sea ice to global change. *Climate Change*, **46**, 277–287.

Leppäranta, M. (ed.) (1998a). *Physics of Ice-covered Seas* (Vols. 1 and 2). Helsinki University Printing House, Helsinki.

Leppäranta, M. (ed.) (1998b). The dynamics of sea ice. *Physics of Ice-covered Seas* (Vol. 1). Helsinki University Printing House, Helsinki, pp. 305–342.

Leppäranta, M. (2005). *The Drift of Sea Ice*. Springer-Praxis, Chichester, UK, 272 pp.

Leppäranta, M. and T. Thompson (1989). BEPERS-88 sea ice remote sensing with synthetic aperture radar in the Baltic Sea. *EOS, Transactions of the American Geophysical Union*, **70**(28), 698–699, 708–709.

Leppäranta, M., R. Kuittinen, and J. Askne (1992). BEPERS Pilot-Study: An experiment with X–band synthetic aperture radar over Baltic Sea ice. *Journal of Glaciology*, **38**(128), 23–35.

Leppäranta, M., Z. Zhanghai, J. Haapala, and T. Stipa (2001). Sea-ice kinematics measured with GPS drifters. *Annals of Glaciology*, **33**, 151–156.

Leventer, A. (2003). Particulate flux from sea ice in polar waters. In: D. Thomas and G. S. Dieckmann (eds.), *Sea Ice: An Introduction to Its Physics, Chemistry, Biology and Geology*. Blackwell Science, Oxford, UK, pp. 303–332.

Le Vine, D. M., M. Kao, A. B. Tanner, C. T. Swift, and A. Griffis (1990). Initial results in the development of a synthetic aperture microwave radiometer. *IEEE Transactions on Geoscience and Remote Sensing*, **28**, 614–619.

Le Vine, D., C. Koblinsky, F. Pellerano, G. Lagerloef, Y. Chao, S. Yueh, and W. Wilson (2004). A sensor to measure salinity in the open ocean from space. *International Journal of Remote Sensing*, **25**(7–8), 1313–1318.

Levrini, G. and G. Brooker (2001). EnviView: A gateway to access the Envisat data products. *ESA Earth Observation Quarterly*, **68**, 8–11.

Lewis, E. L., E. P. Jones, P. Lemke, T. D. Prowse, and P. Wadhams (2000). *The Freshwater Budget of the Arctic Ocean*, Kluwer Academic, Dordrecht, The Netherlands, 644 pp.

Lewis, E. O., C. E. Livingstone, C. Garrity, and J. R. Rossiter (1994). Properties of snow and ice. In: S. Haykin, E. O. Lewis, R. K. Raney and J. R. Rossiter (eds.), *Remote Sensing of Sea Ice and Icebergs*. John Wiley & Sons, New York, pp. 21–96.

Lewis, J. E., M. Leppäranta, and H. B. Granberg (1993). Statistical properties of sea ice surface topography in the Baltic Sea. *Tellus*, **45A**, 127–142.

Li, S. (2000). Polar environments assessment by remote sensing. In: R. A. Meyers (ed.), *Encyclopedia of Analytical Chemistry*. John Wiley & Sons, Chichester, UK, pp. 8660–8679.

Li, Z. and H. G. Leighton (1992). Narrowband to broadband conversion with spatially autocorrelated reflectance measurements. *Journal of Applied Meteorology*, **31**, 421–432.

Li, S., Z. Cheng, and W. F. Weeks (1995). A grid-based algorithm for the extraction of intermediate-scale sea-ice deformation descriptors from SAR ice motion products. *International Journal of Remote Sensing*, **16**(17), 3267–3286.

Li, S., L. Shapiro, L. McNutt, and A. Jeffers (1996). Applications of satellite radar interferometry to the detection of sea ice deformation. *Journal of the Remote Sensing Society of Japan*, **16**(2), 67–77.

Li, S., Z. Cheng, and W. F. Weeks (1998). Extraction of intermediate scale sea ice deformation parameters from SAR ice motion products. In: C. Tsatsoulis and R. Kwok (eds.), *Analysis of SAR Data of the Polar Oceans: Recent Advances*. Springer-Verlag, Berlin, pp. 69–90.

Lieser, J. L. and P. Lemke (2002). A sea ice forecast model for the Arctic Ocean. *Ice in the Environment: Proceedings of 16th International Symposium on Ice* (Vol. II), pp. 439–444.

Light, B. (2001). Observations and modeling of structural–optical properties in first-year sea ice. *6th Conference on Polar Meteorology and Oceanography, San Diego, May 14–18* (extended abstracts). American Meteorological Society, Boston, pp. 205–208.

Light, B., H. Eicken, G. A. Maykut, and T. C. Grenfell (1998). The effect of included particulates on the optical properties of sea ice. *Journal of Geophysical Research*, **103**(C12), 27739–27752.

Light, B., G. A. Maykut, and T. C. Grenfell (2003a). Effects of temperature on the microstructure of first-year Arctic sea ice. *Journal of Geophysical Research*, **108**(C2), 3051, DOI: 10.1029/2001JC000887.

Light, B., T. C. Grenfell, and D. K. Perovich (2003b). Transmission of solar radiation by a summer sea ice cover. *Proceedings of 7th Conference on Polar Meteorology and Oceanography and Joint Symposium on High–latitude Climate Variations, May 12–16, Hyannis, MA*. American Meteorological Society, Boston, p. 1.14.

Lindsay, R. W. (2001a). Arctic sea-ice albedo derived from RGPS-based ice-thickness estimates. *Annals of Glaciology*, **33**, 225–229.

Lindsay, R. W. (2001b). Assimilation of ice thickness information into a sea ice model. *6th Conference on Polar Meteorology and Oceanography, San Diego, May 14–18* (extended abstracts). American Meteorological Society, Boston, pp. 219–222.

Lindsay, R. W. (2002). Ice deformation near SHEBA. *Journal of Geophysical Research*, **107**(C10), 8042, DOI: 10.1029/2000JC000445.

Lindsay, R. W. and D. Rothrock (1993). The calculation of surface temperature and albedo of Arctic sea ice from AVHRR. *Annals of Glaciology*, **17**, 391–397.

Lindsay, R. and D. A. Rothrock (1994a). Arctic sea ice surface temperature from AVHRR. *Journal of Climate*, **7**, 174–183.

Lindsay, R. W. and D. A. Rothrock (1994b). Arctic sea ice albedo from AVHRR. *Journal of Climate*, **7**, 1737–1749.

Lindsay, R. and D. A. Rothrock (1995). Arctic sea ice leads from Advanced Very High Resolution Radiometer images. *Journal of Geophysical Research*, **100**(C3), 4533–4544.

Lindsay, R. W. and H. L. Stern (2003). The Radarsat Geophysical Processor System: Quality of sea ice trajectory and deformation estimates. *Journal of Atmospheric and Oceanic Technology*, **20**(9), 1333–1347.

Lindsay, R. W., J. Zhang, and D. A. Rothrock (2003). Sea-ice deformation rates from satellite measurements and in a model. *Atmosphere–Ocean*, **41**(1), 35–47.

Lipscomb, W. H. (2001). Remapping the thickness distribution in sea ice models. *Journal of Geophysical Research*, **106**, 13989–14000.

Lisitzin, A. P. (2003). *Sea-ice and Iceberg Sedimentation in the Ocean, Recent and Past*. Springer-Verlag, Berlin, 564 pp.

Liss, P. S., A. L. Chuck, S. M. Turner, and A. J. Watson (2004a). Air–sea gas exchange in Antarctic waters. *Antarctic Science*, **16**, 517–529.

Liss, P., P. Boyd, E. Cortijo, K. Denman, B. Huebert, T. Jickells, T. Johannesssen, G. Komen, D. Kumar, P. Matrai et al. (2004b). *The Surface Ocean–Lower Atmosphere Study (SOLAS): Science Plan and Implementation Strategy* (IGBP Report 50). International Geosphere–Biosphere Programme, Stockholm, 89 pp.

Liu, A. K. (1995). Study of waves in ice-covered ocean using SAR. In: M. Ikeda and F. Dobson (ed.), *Oceanographic Application of Remote Sensing*. CRC Press, New York, pp. 397–404.

Liu, A. K. and D. J. Cavalieri (1998). On sea ice drift from the wavelet analysis of the Defense Meteorological Satellite Program (DMSP) Special Sensor Microwave Imager (SSM/I) data. *International Journal of Remote Sensing*, **19**(7), 1415–1423.

Liu, A. K. and E. Mollo-Christensen (1988). Wave propagation in a solid pack ice. *Journal of Physical Oceanography*, **18**, 1702–1712.

Liu, A. K. and C. Y. Peng (1993a). Marginal ice zone study using SAR. In: I. S. F. Jones, R. W. Stewart and Y. Sugimori (eds.), *Satellite Remote Sensing of Oceanic Environment*. Seibutsu Kenkyusha, Tokyo, pp. 341–348.

Liu, A. K. and C. Y. Peng (1993b). Synthetic aperture radar for ocean applications. *Proceedings of Symposium on Remote Sensing in Environmental Research and Global Change: Environment '93, Hong Kong*, pp. 167–182.

Liu, A. K. and C. Y. Peng (1993c). Ocean–ice interaction in the marginal ice zone. *Proceedings of 2nd ERS-1 Symposium, Hamburg, Germany, October 11–14* (ESA SP-361). ESA, Noordwijk, The Netherlands, pp. 317–322.

Liu, A. K. and C. Y. Peng (1998). Wavelet analysis of SAR images in the marginal ice zone. In: C. Tsatsoulis and R. Kwok (eds.), *Analysis of SAR Data of the Polar Oceans*. Springer-Verlag, Berlin, pp. 111–128.

Liu, A. K., B. Holt, and P. W. Vachon (1991a). Wave propagation in the marginal ice zone: Model predictions and comparisons with buoy and SAR data. *Journal of Geophysical Research*, **96**(C3), 4605–4621.

Liu, A. K., B. Holt, P. W. Vachon, and C. Y. Peng (1991b). Observations of wave refraction at an ice edge by synthetic aperture radar. *Journal of Geophysical Research*, **96**(C3), 4803–4808.

Liu, A. K., P. W. Vachon, C. Y. Peng, and A. S. Bhogal (1992). Wave attenuation in the marginal ice zone during LIMEX. *Atmosphere–Ocean*, **30**(2), 192–206.

Liu, A. K., S. Häkkinen, and C. Y. Peng (1993). Wave effects on ocean–ice interaction in the marginal ice zone. *Journal of Geophysical Research*, **98**, 10025–10036.

Liu, A. K., C. Y. Peng, and T. J. Weingartner (1994). Ocean–ice interaction in the marginal ice zone using SAR. *Journal of Geophysical Research*, **99**, 22391–22400.

Liu, A. K., S. Martin, and R. Kwok (1997a). Tracking of ice edge and ice floes by wavelet analysis of SAR images. *Journal of Atmospheric and Oceanic Technology*, **14**, 1187–1198.

Liu, A. K., C. Y. Peng, and Y. S. Chang (1997b). Wavelet analysis of satellite images for coastal watch. *IEEE Journal of Ocean Engineering*, **22**, 9–17.

Liu, A. K., Y. Zhao, and W. T. Liu (1998). Sea ice motion derived from satellite agrees with buoy observations. *EOS, Transactions of the American Geophysical Union*, **79**, 353–359.

Liu, A., Y. Zhao, and S. Y. Wu (1999). Arctic sea ice drift from wavelet analysis of NSCAT and SSM/I data. *Journal of Geophysical Research*, **104**(C5), 11529–11538.

Liu, J., D. G. Martinson, X. Yuan, and D. Rind (2002a). Evaluating simulated Antarctic sea ice variability and its global teleconnections in global climate models. *International Journal of Climatology*, **22**(8), 885–900.

Liu, J., X. Yuan, D. Rind, and D. G. Martinson (2002b). Mechanism study of the ENSO and southern high latitude climate teleconnections. *Geophysical Research Letters*, **29**(14), 1679, DOI: 1029/2002GL015143.

Liu, J., J. A. Curry, and D. G. Martinson (2004a). Interpretation of recent Antarctic sea ice variability. *Geophysical Research Letters*, **31**, L02205, DOI: 10.1029/2003GL018732.

Liu, Y., J. Key, R. Frey, S. Ackerman, and W. P. Menzel (2004b). Nighttime polar cloud detection with MODIS. *Journal of Applied Meteorology*, **92**, 181–194.

Livingstone, C. E. (1994). Synthetic aperture radar images of sea ice. In: S. Haykin, E. O. Lewis, R. K. Raney and J. R. Rossiter (eds.), *Remote Sensing of Sea Ice and Icebergs*. John Wiley & Sons, New York, pp. 540–569.

Livingstone, C. E., R. G. Onstott, L. D. Arsenault, A. L. Gray, and K. P. Singh (1987a). Microwave sea ice signatures near the onset of melt. *IEEE Transactions on Geoscience and Remote Sensing*, **25**(2), 159–173.

Livingstone, C., K. Singh, and L. Gray (1987b). Seasonal and regional variations of active/passive microwave signatures of sea ice. *IEEE Transactions on Geosciences and Remote Sensing*, **25**(2), 159–172.

Lizotte, M. P. (2001). The contributions of sea ice algae to Antarctic marine primary production. *American Zoologist*, **41**(1), 57–73.

Lizotte, M. P. and K. R. Arrigo (editors) (1998). *Antarctic Sea Ice: Biological Processes, Interactions, and Variability* (AGU Antarctic Research Series 73). American Geophysical Union, Washington, DC.

Loeb, V., V. Siegel, and O. Holm-Hansen (1997). Effects of sea-ice extent and salp or krill dominance on the Antarctic food web. *Nature*, **387**, 897–900.

Lohanick, A. W. (1990). *Some Observations of Established Snow on Saline Ice and Their Relevance to Microwave Remote Sensing* (CRREL Monograph 90–1). U.S. Army Cold Regions Research and Engineering Laboratory, Hanover, NH, pp. 61–67.

Lohanick, A. W. (1993). Microwave brightness temperatures of laboratory-grown undeformed first-year ice with an evolving snow cover. *Journal of Geophysical Research*, **98**(C3), 4667–4674.

Lomax, A. S., D. Lubin, and R. H. Whritner (1995). The potential of interpreting total and multiyear ice concentration in SSM/I 85.5 GHz imagery. *Remote Sensing of Environment*, **54**(1), 13–26.

Long, D. G. (2003). Reconstruction and resolution enhancement techniques for microwave sensors. In: C. H. Chen (ed.), *Frontiers of Remote Sensing Information Processing*, World Scientific, Hackensack, NJ, pp. 255–281.

Long, D. G. and M. R. Drinkwater (1999). Cryosphere applications of NSCAT data. *IEEE Transactions Geoscience and Remote Sensing*, **37**(3), 1671–1684.

Long, D. G. and D. Early (1993). Sea ice observed at enhanced resolution by spaceborne scatterometers. *OCEANS '93: Engineering in Harmony with Ocean Proceedings* (Vol. 3), pp. 137–142.

Long, D. G., P. J. Hardin, and P. T. Whiting (1993). Resolution enhancement of spaceborne scatterometer data. *IEEE Transactions on Geoscience and Remote Sensing*, **31**(3), 700–715.

Long, D. G., M. R. Drinkwater, B. Holt, S. Saatchi, and C. Bertoia (2001). Global ice and land climate studies using scatterometer image data. *EOS, Transactions of the American Geophysical Union*, **82**(43), 503 [includes the EOS Electronic Supplement, which is available online at ⟨*http://www.agu.org/eos_elec/010126e.html*⟩].

Long, D. G., M. W. Spencer, and E. G. Njoku (2005). Spatial resolution and processing tradeoffs for HYDROS: Application of reconstruction and resolution enhancement techniques. *IEEE Transactions on Geoscience and Remote Sensing*, **43**(1), 3–12.

Louet, J. (2001). The Envisat mission and system. *ESA Bulletin*, **106**, 11–25.

Løyning, T. and C. Dick (2003). ACSYS Historical Ice Chart Archive. *ACSYS/CliC Ice and Climate News*, **4**, 7–8.

Luar, H. (1992). *Derivation of Backscatter Coefficient* σ^0 *in ERS–1: SAR.PRI Products*. ESA, Noordwijk, The Netherlands, 16 pp.

Lubin, D. and E. Morrow (1998). Evaluation of an AVHRR cloud detection and classification method over the central Arctic Ocean. *Journal of Applied Meteorology*, **37**(2), 166–183.

Lubin, D., P. Ricchiazzi, C. Gauthier, and R. H. Whritner (1994). A method for mapping Antarctic surface ultraviolet radiation using multispectral satellite imagery. In: C. S. Weiler and P. A. Penhale (eds.), *Ultraviolet Radition in Antarctica: Measurements and Biological Effects* (AGU Antarctic Research Series No. 62). American Geophysical Union, Washingon, DC., pp. 53–82.

Lubin, D., C. Garrity, R. Ramseier, and R. H. Whritner (1997). Total sea ice concentration retrieval from the SSM/1 85.5 GHz channels during arctic summer. *Remote Sensing of Environment*, **62**, 63–76.

Luscombe, A. and A. Thomson (2001). Radarsat-2 calibration: Proposed targets and techniques. *Proceedings of IGARSS '01, July 9–13, Sydney, Australia*, Vol. 1, pp. 496–498.

Lynch, A. H., J. A. Maslanik, and W. Wu (2001). Mechanisms in the development of anomalous sea ice extent in the western Arctic: A case study. *Journal of Geophysical Research*, **106**(D22), 28097–28106.

Lynch, A. H., J. A. Curry, R. D. Brunner, and J. A. Maslanik (2004). Toward an integrated assessment of the impacts of extreme wind events on Barrow, Alaska. *Bulletin of the American Meteorological Society*, **85**(2), 209–221.

Lythe, M., A. Hauser, and G. Wendler (1999). Classifiction of sea ice types in the Ross Sea, Antarctica from SAR and AVHRR imagery. *International Journal of Remote Sensing*, **20**(15&16), 3073–3085.

Lytle, V. I. and S. F. Ackley (1991). Sea ice ridging in the eastern Weddell Sea. *Journal of Geophysical Research*, **96**, 18411–18416.

Lytle, V. I. and S. F. Ackley (1996). Heat flux through sea ice in the western Weddell Sea: Convective and conductive processes. *Journal of Geophysical Research*, **101**, 8853–8868.

Lytle, V. I., A. P. Worby, and R. A. Massom (1998a). Sea ice ridge heights in East Antarctica. *Annals of Glaciology*, **27**, 449–454.

Lytle, V. I., R. A. Massom, A. P. Worby, and I. Allison (1998b). Floe sizes in the East Antarctic sea ice zone estimated using combined SAR and field data. In: *3rd ERS Symposium, Florence, Italy, March 1997* (ESA Publication SP–414, No. 3). ESA/ESTEC, Noordwijk, The Netherlands, pp. 931–936.

Lytle, V. I., R. Massom, N. Bindoff, A. Worby, and I. Allison (2000). Wintertime heat flux to the underside of East Antarctic pack ice. *Journal of Geophysical Research*, **105**(C12), 28759–28769.

Lytle, V. I., A. P. Worby, R. A. Massom, M. Paget, I. Allison, X. Wu, and A. Roberts (2001). Ice formation in the Mertz Glacier polynya, East Antarctica, during winter. *Annals of Glaciology*, **33**, 368–372.

Lyzenga, D. R., R. A. Shuchman, J. D. Lyden, and C. L. Rufenach (1985). SAR imaging of waves in water and ice: Evidence for velocity bunching. *Journal of Geophysical Research*, **90**, 1031–1036.

Macdonald, R. A. (1995a). Corona: Success for space reconnaissance. A look into the cold war and a revolution in intelligence. *Photogrammetric Engineering and Remote Sensing,* **61**, 321–325.

MacDonald, R. A. (1995b). Opening the Cold War sky to the public: Declassifying satellite reconnaissance imagery. *Photogrammetric Engineering and Remote Sensing*, **61**(4), 380–390.

Macdonald, R. W. and M. C. O'Brien (2001). The Beaufort Shelf–The Bathurst polynya: Small is beautiful. *International Polynya Symposium, September 9–13, Quebec City, Canada* (abstract). Available online at ⟨*www.fsg.ulaval.ca/giroq/now/IPS2001/ips2001.htm*⟩.

Macdonald, R. W, E. C. Carmack, F. A. McLaughlin, K. K. Falkner, and J. H. Swift (1999). Connections among ice, runoff, and atmospheric forcing in the Beaufort Gyre. *Geophysical Research Letters*, **26**, 2223–2226.

Magnuson, J. J., D. M. Robinson, R. H. Wynne, B. J. Benson, D. M. Livingstone, T. Arai, R. A. Assel, R. D. Barry, V. Card, E. Kuusisto et al. (2000). Historical trends in lake and river ice cover in the Northern Hemisphere. *Science*, **289**, 1743–1746.

Mahmood, A., J. P. Crawford, R. Michaud, and K. C. Jezek (1998). Mapping the world with remote sensing. *EOS, Transactions of the American Geophysical Union*, **79**, 17–23.

Mahoney, A., H. Eicken, D. Norton, L. Shapiro, T. Grenfell, D. Perovich, J. Richter-Menge, and D. Perovich (2002). Revisiting the fast-ice regimes of the Chuckchi and Beaufort Seas 25 years on. In: *Monitoring an Evolving Cryosphere: the NSIDC Special Session at the American Geophysical Union Fall Meeting, December 10–14* (summary of Report GD-30). National Snow and Ice Data Center, Boulder, CO, pp. 69.

Mai, S., C. Wamser, and C. Kottmeier (1996). Geometric and aerodynamic roughness of sea ice. *Boundary-layer Meteorology*, **77**, 233–248.

Maiden, M., R. Thomas, R. G. Barry, R. Armstrong, M. J. Brodzik, A. Brenner, A. C. Fowler, W. Emery, J. Francis, D. Hancock et al. (1996). The Polar Pathfinders: Data

products and science plans. *EOS, Short Article and Electronic Journal Publications*, **78**(5), 52. Available online at ⟨*http://www.agu.org/eos_elec/96149e.html*⟩

Mailhot, J., A. Tremblay, S. Belair, I. Gultepe, and G. A. Isaac (2002). Mesoscale simulation of surface fluxes and boundary layer clouds associated with a Beaufort Sea polynya. *Journal of Geophysical Research*, **107**(C10), 8031, DOI: 10.1029/2000JC000429.

Mäkynen, M. and M. Hallikainen (1998). C-band backscattering signatures of Baltic sea ice. *International Proceedings of IGARSS '98: Sensing and Managing the Environment, Seattle, Washington, July 6–10*.

Mäkynen, M. and M. Hallikainen (2004). Investigation of C- and X-band backscattering signatures of Baltic sea ice. *International Journal of Remote Sensing*, **25**(11), 2061–2086.

Makshtas, A. P., E. L. Andreas, P. N. Svyashchennikov, and V. F. Timachev (1999). Accounting for clouds in sea ice models. *Atmospheric Research*, **52**, 77–113.

Makshtas, A. P., S. V. Shoutilin, and E. L. Andreas (2003). Possible dynamic and thermal causes for the recent decrease in sea ice in the Arctic Basin. *Journal of Geophysical Research*, **108**(C7), 3232, DOI: 10.1029/2001JC000878.

Maksym, T. and M. O. Jeffries (2001). Phase and compositional evolution of the flooded layer during snow–ice formation on Antarctic sea ice. *Annals of Glaciology*, **33**, 37–44.

Manabe, S. and R. J. Stouffer (1993). Century-scale effects of increased atmospheric CO_2 on the ocean–atmosphere system. *Nature*, **364**(6434), 215–218.

Manabe, S., R. J. Stouffer, M. J. Spelman, and K. Bryan (1991). Transient responses of a coupled ocean–atmosphere model to gradual changes of atmospheric CO_2: Part I. Annual mean response. *Journal of Climate*, **4**, 785–818.

Manabe, S., M. J. Spelman, and R. J. Stouffer (1992). Transient responses of a coupled ocean–atmosphere model to gradual changes of atmospheric CO_2: Part II. Seasonal response. *Journal of Climate*, **5**(2), 105–126.

Manninen, T. (1996). Surface morphology and backscattering of ridge sails in the Baltic Sea. *Journal of Glaciology*, **42**, 141–156.

Marbouty, D. (1980). An experimental study of temperature–gradient metamorphism. *Journal of Glaciology*, **26**(94), 303–312.

Marko, J. R. (2003). Observations and analyses of an intense waves-in-ice event in the Sea of Okhotsk. *Journal of Geophysical Research*, **108**(C9), 3296, DOI: 10.1029/2001JC001214.

Markus, T. and B. A. Burns (1995). Method to estimate sub-pixel scale coastal polynyas with satellite passive microwave data. *Journal of Geophysical Research*, **100**(C3), 4473–4487.

Markus, T. and D. J. Cavalieri (1998). Snow depth distribution over sea ice in the Southern Ocean from satellite passive microwave data. In: M. Jeffries (ed.), *Antarctic Sea Ice: Physical Processes, Interactions and Variability* (AGU Antarctic Research Series No. 74). American Geophysical Union, Washington, DC, pp. 19–39.

Markus, T. and D. J. Cavalieri (2000). An enhancement of the NASA Team sea ice algorithm. *IEEE Transactions on Geoscience and Remote Sensing*, **38**(3), 1387–1398.

Markus, T. and S. T. Dokken (2002). Evaluation of late summer passive microwave Arctic sea ice retrievals. *IEEE Transactions on Geoscience and Remote Sensing*, **40**(2), 348–356.

Markus, T., C. Kottmeier, and E. Fahrbach (1998). Ice formation in coastal polynyas in the Weddell Sea and their impact on oceanic salinity. In: M. Jeffries (ed.), *Antarctic Sea Ice: Physical Processes, Interactions and Variability* (AGU Antarctic Research Series No. 74). American Geophysical Union, Washington, DC, pp. 273–292.

Markus, T., D. J. Cavalieri, and A. Ivanoff (2002). The potential of using Landsat 7 ETM+ for the classification of sea-ice surface conditions during summer. *Annals of Glaciology*, **34**, 415–419.

Markus, T., D. J. Cavalieri, M. A. Tschudi, and A. Ivanoff (2003). Comparison of aerial video and Landsat 7 data over ponded sea ice. *Remote Sensing of Environment*, **86**, 458–469.

Marsan, D., H. Stern, R. Lindsay, and J. Weiss (2004). Scale dependence and localization of the deformation of Arctic Sea Ice. *Physical Review Letters*, **93**(17), 178–501.

Marshall, G. J., P. A. Stott, J. Turner, W. M. Connolley, J. C. King, and T. A. Lachlan-Cope (2004). Causes of exceptional atmospheric circulation changes in the Southern Hemisphere. *Geophysical Research Letters*, **31**, L14205, DOI: 10.1029/2004GL019952.

Marsland. S. and J.-O. Wolff (1998). East Antarctic seasonal sea-ice and ocean stability: A model study. *Annals of Glaciology*, **27**, 477–482.

Marsland, S., N. Bindoff, G. Williams, and W. Budd (2001). Hamburg Ocean Primitive Equation Model study of the Mertz Glacier polynya. *International Polynya Symposium, September 9–13, Quebec* (abstract). Available online at ⟨*www.fsg.ulaval.ca/giroq/now/IPS2001/ips2001.htm*⟩.

Marsland, S. J., N. L. Bindoff, G. D. Williams, and W. F. Budd (2004). Modelling water mass formation in the Mertz Glacier Polynya and Adélie Depression, East Antarctica. *Journal of Geophysical Research*, **109**, C11003, DOI: 10.1029/2004JC002441.

Martin, S. (2002). Polynyas. In: J. H. Steele, K. K. Turekian and S. A. Thorpe (eds.), *Encyclopedia of Ocean Sciences*. Academic Press, London, pp. 2241–2247.

Martin, S. (2004). *An Introduction to Ocean Remote Sensing*. Cambridge University Press, Cambridge, UK, 454 pp.

Martin, S. and Cavalieri, D. J. (1989). Contributions of the Siberian shelf polynyas to the Arctic Ocean intermediate and deep water. *Journal of Geophysical Research*, **94**(12), 12725–12738.

Martin, S. and R. Drucker (1997). The effect of possible Taylor columns on the summer ice retreat in the Chukchi Sea. *Journal of Geophysical Research*, **102**, 10473–10482.

Martin, S. and P. Kaufman (1981). A field and laboratory study of wave damping by grease ice. *Journal of Glaciology*, **27**, 283–313.

Martin, S. and E. A. Muñoz (1997). Properties of the Arctic 2-m air temperature for 1979–present derived from a new gridded data set. *Journal of Climate*, **10**(6), 1428–1440.

Martin, S., P. Kauffman, and C. Parkinson (1983). The movement and decay of ice edge bands in the winter Bering Sea. *Journal of Geophysical Research*, **88**, 2803–2812.

Martin, S., K. Steffen, J. Comiso, D. Cavalieri, M. R. Drinkwater, and B. Holt (1992). Microwave remote sensing of polynyas. In: F. D. Carsey (ed.), *Microwave Remote Sensing of Sea Ice*. American Geophysical Union, Washington, DC, pp. 303–311.

Martin, S., Y. Yu, and R. Drucker (1996). The temperature dependence of frost flower growth on laboratory sea ice and the effect of the flowers on the infrared observations of the surface. *Journal of Geophysical Research*, **101**, 12111–12125.

Martin, S., E. Muñoz, and R. Drucker (1997). Recent observations of a spring–summer warming over the Arctic Ocean. *Geophysical Research Letters*, **24**, 1259–1262.

Martin, S., R. Drucker, and K. Yamashita (1998). The production of ice and dense shelf water in the Okhotsk Sea polynyas. *Journal of Geophysical Research*, **103**, 27771–27782.

Martin, S., R. Drucker, and H. Stern (2000). A satellite and meteorological study of the Bering Sea, St Lawrence Island polynya. *AGU Ocean Sciences Meeting* (Abstract OS11K-01).

Martin, S., R. Drucker, R. Kwok, and B. Holt (2004). Estimation of thin ice thickness and heat flux for the Chukchi Sea Alaskan coast polynya from Special Sensor Microwave/Imager data, 1990–2001. *Journal of Geophysical Research*, **109**, C10012, DOI: 10.1029/2004JC002428.

Martin, T. and E. Augstein (2000). Large-scale drift of Arctic sea ice retrieved from passive microwave satellite data. *Journal of Geophysical Research*, **105**(C4), 8775–8788.

Martinson, D. G. (1990). Evolution of the Southern Ocean winter mixing layer and sea ice: Open ocean deepwater formation and ventilation. *Journal of Geophysical Research*, **95**, 11641–11654.

Martinson, D. G. (1991). Open ocean convection in the Southern Ocean. In: P. C. Chu and J. C. Gascard (eds.), *Deep Convection and Deep Water Formation in the Oceans*. Elsevier Science, North-Holland, pp. 37–52.

Martinson, D. G. (1993). Ocean heat and seasonal sea ice thickness in the Southern Ocean. In: W. R. Peltier (ed.), *Ice in the Climate System*. Springer-Verlag, Berlin, pp. 597–609.

Martinson, D. G. and R. A. Iannuzzi (1998). Antarctic ocean–ice interaction: Implications from ocean bulk property distributions in the Weddell Gyre. In: M. Jeffries (ed.), *Antarctic Sea Ice Physical Processes, Interactions and Variability* (AGU Antarctic Research Series No. 74). American Geophysical Union, Washington, DC, pp. 243–271.

Martinson, D. G. and C. Wamser (1990). Ice drift and momentum exchange in winter Antarctic pack ice. *Journal of Geophysical Research*, **95**(C2), 1741–1755.

Martinson, D. G., P. D. Killworth, and A. L. Gordon (1981). A convective model for the Weddell polynya. *Journal of Physical Oceanography*, **11**, 466–488.

Martinson, D. G., K. Bryan, M. Ghil, M. M. Hall, T. R. Karl, E. S. Sarachik, S. Sorooshian, and L. D. Talley (eds.) (1995). *The Natural Variability of the Climate System on Decade-to-Century Time Scales*. National Academy Press, Washington, DC, 630 pp.

Martinson, D. G., M. Steele, and R. D. Muench (2000). Loss of the cold halocline and Arctic Ocean heat fluxes. *XXV General Assembly of the European Geophysical Society, Nice, France, April 25–29* (abstract). European Geophysical Society, Katlenburg-Lindau, Germany.

Maslanik, J. A. (1992). Effects of weather on the retrieval of sea ice concentration and ice type from passive microwave data. *International Journal of Remote Sensing*, **13**(1), 37–54.

Maslanik, J. and J. Key (1993). Comparison and integration of ice-pack temperatures derived from AVHRR and passive microwave imagery. *Annals of Glaciology*, **17**, 372–378.

Maslanik, J. A. and J. Key (1995). Fetch and stability sensitivity in large-area estimates of turbulent heat flux over sea ice. *Journal of Geophysical Research*, **100**(C3), 4573–4584.

Maslanik, J. A., M. C. Serreze, and R. G. Barry (1996). Recent decreases in Arctic summer ice cover and linkages to atmospheric circulation anomalies. *Geophysical Research Letters*, **23**(13), 1677–1680.

Maslanik, J., C. Fowler, J. Key, T. Scambos, T. Hutchinson, and W. Emery (1998a). AVHRR-based Polar Pathfinder products for modeling applications. *Annals of Glaciology*, **25**, 388–392.

Maslanik, J., T. Agnew, M. Drinkwater, W. Emery, C. Fowler, R. Kwok, and A. Liu (1998b). *Summary of Ice-motion Mapping Using Passive Microwave Data* (Special Publication 8). National Snow and Ice Data Center, Boulder, CO.

Maslanik, J. A., M. C. Serreze, and T. Agnew (1999). On the record reduction in 1998 Western Arctic sea ice cover. *Geophysical Research Letters*, **26**(13), 1905–1908.

Maslanik, J., J. Stroeve, T. Markus, M. Sturm, and J. Heinrichs (2001). *Validation of AMSR-E Polar Ocean Products Using a Combination of Modeling and Field Observations*. University of Colorado, Boulder, CO.

Maslowski, W. and W. H. Lipscomb (2003). High resolution simulations of Arctic sea ice, 1979–1993. *Polar Research*, **22**(1), 67–74.

Maslowski, W., B. Newton, P. Schlosser, A. Semtner, and D. Martinson (2000). Modelling recent climate variability in the Arctic Ocean. *Geophysical Research Letters*, **27**(22), 3743–3746.

Maslowski, W., D. C. Marble, W. Walczowski, and A. Semtner (2001). On the large-scale shifts in Arctic Ocean and sea-ice conditions during 1979–1998. *Annals of Glaciology*, **33**, 545–550.

Masonis, S. J. and S. G. Warren (2001). Gain of the AVHRR visible channel as tracked using bidirectional reflectance of Antarctic and Greenland snow. *International Journal of Remote Sensing,* **22**(8), 1495–1520.

Massom, R. A. (1988). The biological significance of open water within the sea ice covers of the polar regions. *Endeavour, New Series*, **12**(1), 21–27.

Massom, R. (1991). *Satellite Remote Sensing of Polar Regions: Applications, Limitations and Data Availability*. Belhaven Press, London/Lewis Publishers (CRC Press), Boca Raton, FL, pp. 307.

Massom, R. A. (1992). Observing the advection of sea ice in the Weddell Sea using buoy and satellite passive microwave data. *Journal of Geophysical Research*, **97**(C10), 15559–15572.

Massom, R. (1995). Satellite remote sensing of polar snow and ice: Present status and future directions. *Polar Record*, **31**(177), 99–114.

Massom, R. (2002). Fun without touching: Satellite remote sensing of sea ice. *Australian Antarctic Magazine*, **4.**

Massom, R. A. (2003). Recent iceberg calving events in the Ninnis Glacier region, East Antarctica. *Antarctic Science*, **15**(2), 303–313.

Massom, R. A. and J. C. Comiso (1994). The classification of Arctic sea ice types and the determination of surface temperature using Advanced Very High Resolution Radiometer data. *Journal of Geophysical Research*, **99**(C3), 5201–5218.

Massom, R. A., M. R. Drinkwater, and C. Haas (1997). Winter snow cover on sea ice in the Weddell Sea. *Journal of Geophysical Research*, **102**(C1), 1101–1117.

Massom, R. A., V. I. Lytle, A. P. Worby, and I. Allison (1998a). Winter snow cover variability on East Antarctic sea ice. *Journal of Geophysical Research*, **103**(C11), 24837–24855.

Massom, R. A., P. T. Harris, K. J. Michael, and M. J. Potter (1998b). The distribution and formative processes of latent heat polynyas in East Antarctica. *Annals of Glaciology*, **27**, 420–426.

Massom, R. A., J. C. Comiso, A. P. Worby, V. I. Lytle, and L. Stock (1999). Regional classes of sea ice cover in the East Antarctic pack from satellite and *in situ* data during the winter time period. *Remote Sensing of Environment*, **68**(C1), 61–76.

Massom, R. A., H. Eicken, C. Haas, M. O. Jeffries, M. R. Drinkwater, M. Sturm, A. P. Worby, X. Wu, V. I. Lytle, S. Ushio et al. (2001a). Snow on Antarctic sea ice. *Reviews of Geophysics*, **39**(3), 413–445.

Massom, R. A., K. L. Hill, V. I. Lytle, A. P. Worby, M. J. Paget, and I. Allison (2001b). Effects of regional fast-ice and iceberg distributions on the behaviour of the Mertz Glacier polynya, East Antarctica. *Annals of Glaciology*, **33**, 391–398.

Massom, R. A., K. Jacka, M. J. Pook, C. Fowler, N. Adams, and N. Bindoff (2003). An anomalous late-season change in the regional sea ice regime in the vicinity of the Mertz Glacier Polynya, East Antarctica. *Journal of Geophysical Research*, **108**(C7), 3212, DOI: 10.1029/2002JC001354.

Massom, R., S. E. Stammerjohn, R. C. Smith, M. J. Pook, R. Iannuzzi, N. Adams, D. Martinson, M. Vernet, L. Quetin, R. Ross et al. (in press). Extreme anomalous atmospheric circulation in the West Antarctic Peninsula region in austral spring and summer 2001/2, and its profound impact on sea ice and biota. *Journal of Climate*.

Matear, R. J. (2001). Effects of eddy parameterizations and numerical advection schemes on ocean ventilation and anthropogenic carbon dioxide uptake of an ocean general circulation model. *Ocean Modelling*, **3**, 217–248.

Matear, R. and A. C. Hirst (1999). Climate change feedback on the future oceanic CO_2 uptake. *Tellus*, **51**(3), 722–733.

Matsuoka, T., S. Fujita, and S. Mae (1996). Effect of temperature on dielectric properties of ice in the range 5–39 GHz. *Journal of Applied Physics*, **80**(10), 2344–2348.

Matsuoka, T., S. Fujita, S. Morishima, and S. Mae (1997). Precise measurement of dielectric anisotropy in ice Ih at 38 GHz. *Journal of Applied Physics*, **81**(5), 5884–5888.

Matsuoka, T., S. Uratsuka, M. Satake, T. Kobayashi, A. Nadai, T. Umehara, H. Maeno, H. Wakabayashi, K. Nakamura, and F. Nishio (2001). CRL/NASDA airborne SAR (Pi-SAR) observations of sea ice in the Sea of Okhotsk. *Annals of Glaciology*, **33**, 115–119.

Matsuoka, T., S. Uratsuka, M. Satake, A. Nadai, T. Umehara, H. Maeno, H. Wakabyashi, F. Nishio, and Y. Fukamachi (2002). Deriving sea-ice thickness and ice types in the Sea of Okhotsk using dual-frequency airborne SAR (Pi-SAR) data. *Annals of Glaciology*, **34**, 429–434.

Mätzler, C. (1985). *Interaction of Microwaves with Natural Snow Cover* (Habilitationsschrift 152). lnstitute of Applied Physics, University of Bern, Bern, Switzerland, 148 pp.

Mätzler, C. (1996). Microwave permittivity of dry snow. *IEEE Transactions on Geoscience and Remote Sensing*, **34**(2), 573–581.

Mätzler, C. (1998). Microwave properties of snow and ice. In: B. Schmitt, C. De Bergh, and M. Festou (eds.), *Solar System Ices*, pp. 241–257, Kluwer Academic, Dordrecht, The Netherlands.

Mätzler, C. (2001). Applications of SMOS over terrestrial ice and snow. *3rd SMOS Workshop, DLR, Oberpfaffenhofen, Germany, December 10–12*. ESA, Noordwijk, The Netherlands.

Mätzler, C. and U. Wegmüller (1987). Dielectric properties of freshwater ice at microwave frequencies. *Journal of Physics D, Applied Physics*, **20**, 1623–1630

Mätzler, C., R. O. Ramseier, and E. Svendsen (1984). Polarisation effects in sea-ice signatures. *IEEE Journal of Oceanic Engineering*, **OE–9**(5), 333–338.

Mätzler, C., A. Wiesmann, J. Pulliainen, and M. Hallikainen (2000). Development of microwave emission models of snowpacks. *IEEE Geoscience and Remote Sensing Society Newsletter*, **115**, 18–25.

Mauritzen, C. and S. Häkkinen (1997). Influence of sea ice on thermohaline circulation in the Arctic–North Atlantic Ocean. *Geophysical Research Letters*, **24**(24), 3257–3260.

Mauritzen, M., S. E. Belikov, A. N. Boltunov, A. E. Derocher, E. Hansen, R. A. Ims, Ø. Wiig, and N. Yoccoz (2003). Functional responses in polar bear habitat selection. *Oikos*, **100**, 112–124.

Mawson, D. (1915). *The Home of the Blizzard; Being the Story of the Australasian Antarctic Expedition 1911–1914*. Heinemann, London, 438 pp.

Maykut, G. A. (1978). Energy exchange over young sea ice in the central Arctic. *Journal of Geophysical Research*, **83**(C7), 3646–3658.

Maykut, G. A. (1982). Large-scale heat exchange and ice production in the central Arctic. *Journal of Geophysical Research*, **87**(C10), 7971–7984.

Maykut, G. A. (1985). The ice environment. In: R. A. Horner (ed.), *Sea Ice Biota*. CRC Press, Boca Raton, FL, pp. 21–82.

Maykut, G. A. (1986). The surface heat and mass balance. In: N. Untersteiner (ed.), *The Geophysics of Sea Ice* (Series B: Physics Vol. 146). Plenum Press, New York, pp. 395–463.

Maykut, G. A. and M. G. McPhee (1995). Solar heating of the Arctic mixed layer. *Journal of Geophysical Research*, **100**, 24691–24703.

Maykut, G. A. and D. K. Perovich (1987). The role of shortwave radiation in the summer decay of a sea ice cover. *Journal of Geophysical Research*, **92**(C7), 7032–7044.

Maykut, G. A. and N. Untersteiner (1971). Some results from a time-dependent thermodynamic model of sea ice. *Journal of Geophysical Research*, **76**(6), 1550–1575.

McAvoy, J. C. and E. M. Krakowski (1989). A knowledge based system for the interpretation of sea ice. *Proceedings of IGARSS '89, July 10–14, Vancouver, Canada*, pp. 844–847.

McClain, C. R., G. C. Feldman, and S. B. Hooker (2004). An overview of the SeaWiFS project and strategies for producing a climate research quality global ocean bio-optical time series. *Deep-Sea Research II*, **51**, 5–42.

McConnell, R., R. Kwok, J. C. Curlander, W. Kober, and S. S. Pang (1991). Y–S correlation and dynamic time warping: Two methods for tracking ice floes in SAR images. *IEEE Transactions on Geoscience and Remote Sensing*, **29**(6), 1004–1012.

McIntire, T. J. and J. J. Simpson (2002). Arctic sea ice, cloud, water and lead classification using neural networks and 1.6-μm data. *IEEE Transactions on Geoscience and Remote Sensing*, **40**(9), 1956–1972.

McLaren, A. S., J. E. Walsh, R. H. Bourke, R. L. Weaver, and W. Wittmann (1992). Variability in sea-ice thickness over the North Pole from 1977 to 1990. *Nature*, **358**(6383), 224–226.

McLaren, A. S., R. H. Bourke, J. E. Walsh, and R. L. Weaver, (1994). Variability in sea-ice thickness over the North Pole from 1958 to 1992. In: O. M. Johannessen, R. D. Muench, and J. E. Overland (eds.), *The Polar Oceans and Their Role in Shaping the Global Environment*. American Geophysical Union, Washington, DC, pp. 363–371.

McMahon, C., M. Hindell, A. Dorr, and R. A. Massom (2002). Winter distribution and abundance of crabeater seals off George V Land, East Antarctica. *Antarctic Science*, **14**(2), 128–133.

McMinn, A., C. Ashworth, and K. G. Ryan (2000). In situ primary production of an Antarctic fast ice bottom algal community. *Aquatic Microbial Ecology*, **21**, 177–185.

McNeil, B. I., B. Tilbrook, and R. J. Matear (2001). The storage and uptake of anthropogenic carbon dioxide in the Southern Ocean south of Australia between 1968 and 1996. *Journal of Geophysical Research*, **106**, 31431–31445.

McNeil, B. I., R. J. Matear, J. L. Bullister, R. M. Key, and J. L. Sarmiento (2003). Anthropogenic CO_2 uptake by the oceans using the global chorofluorocarbon dataset. *Science*, **299**, 235–299.

McNutt, S. L. and J. E. Overland (2003). Spatial hierarchy in Arctic sea ice dynamics. *Tellus*, **55A**, 181–191.

McPhee, M. (1978). A simulation of inertial oscillation in drifting pack ice. *Dynamics of Atmosphere and Oceans*, **2**, 107–122.

McPhee, M. G. (1992). Turbulent heat flux in the upper ocean under sea ice. *Journal of Geophysical Research*, **97**(C4), 5365–5379.

McPhee, M. G. (2002). Turbulent stress at the ice/ocean interface and bottom surface hydraulic roughness during the SHEBA drift. *Journal of Geophysical Research*, **107**(C10), 8037, DOI: 10.1029/2000JC000633.

McPhee, M. G. and D. G. Martinson (1994). Turbulent mixing under drifting pack ice in the Weddell Sea. *Science*, **263**, 218–221.

McPhee, M. G., T. P. Stanton, J. H. Morison, and D. G. Martinson (1998). Freshening of the upper ocean in the central Arctic: Is perennial sea ice disappearing? *Geophysical Research Letters*, **25**, 1729–1732.

McPhee, M. G., C. Kottmeier, and J. H. Morison (1999). Ocean heat flux in the central Weddell Sea during winter. *Journal of Physical Oceanography*, **29**, 1166–1179.

Meehl, G. A. and W. M. Washington (1990). CO_2 climate sensitivity and snow–sea–ice albedo parameterization in an atmospheric GCM coupled to a mixed-layer ocean model. *Climate Change*, **16**, 283–306.

Meehl, G. A., J. W. Hurrell, and H. van Loon (1998). A modulation of the mechanism of the semiannual oscillation in the Southern Hemisphere. *Tellus*, **50A**, 442–450.

Meehl, G. A., W. D. Collins, B. A. Boville, J. T. Kiehl, T. M. L. Wigley, and J. M. Arblaster (2000). Response of the ncar climate system model to increased CO_2 and the role of physical processes. *Journal of Climate*, **13**, 1879–1898.

Meier, W. N. (2005). Comparison of passive microwave ice concentration with AVHRR imagery in Arctic peripheral seas. *IEEE Transactions on Geoscience and Remote Sensing*, **43**(6), 1324–1337.

Meier, W. N. and J. A. Maslanik (2001). Synoptic-scale ice-motion case-studies using assimilated motion fields. *Annals of Glaciology*, **33**, 145–150.

Meier, W. N. and T. Vermeychuk (2003). Sea ice motion products from microwave imagery. *Proceedings of 7th Conference on Polar Meteorology and Oceanography and Joint Symposium on High-Latitude Climate Variations, May 12–16, Hyannis, MA* (Abstract P12.8). American Meteorological Society, Boston.

Meier, W., J. Maslanik, and J. Key (1997). Multiparameter AVHRR-derived products for Arctic climate studies. *Earth Interactions*, **1**, 5.

Meier, W. N., J. A. Maslanik, and C. W. Fowler (2000). Error analysis and assimilation of remotely sensed ice motion with an Arctic sea ice model. *Journal of Geophysical Research*, **105**(C2), 3339–3356.

Meier, W. N., M. L. Van Woert, and C. Bertoia (2001). Evaluation of operational SSM/I ice-concentration algorithms. *Annals of Glaciology*, **33**, 102–108.

Melling, H. (1998). Detection of features in first-year pack ice by synthetic aperture radar (SAR). *International Journal of Remote Sensing*, **19**, 1223–1249.

Melling, H. and D. A. Riedel (1995). The underside topography of sea-ice over the continental-shelf of the Beaufort Sea in the winter of 1990. *Journal of Geophysical Research*, **100**(C7), 13641–13653.

Menasi, J., C. Swift, K. St. Germain, J. Comiso, and A. Lohanick (1993). Passive microwave measurement of sea ice thickness. *Journal of Geophysical Research*, **98**(C12), 22569–22578.

Menendez, C. G., V. Serafini, and H. Le Treut (1999a). The storm tracks and energy cycle of the Southern Hemisphere: Sensitivity to sea-ice boundary conditions. *Annals of Geophysics*, **17**(11), 1478–1492.

Menendez, C. G., V. Serafini, and H. Le Treut (1999b). The effect of sea ice on the transient atmospheric eddies of the Southern Hemisphere. *Climate Dynamics*, **15**(9), 659–671.

Meylan, M. H., V. A. Squire, and C. Fox (1997). Toward realism in modeling ocean wave behavior in marginal ice zones. *Journal of Geophysical Research*, **102**, 9029–9049.

Miller, L. A., P. L. Yager, K. A. Erickson, J. Bâcle, J. K. Cochran, M.-È. Garneau, M. Gosselin, D. J. Hirschberg, B. Klein, B. LeBlanc et al. (2002). Carbon distributions and fluxes in the North Water, northern Baffin Bay, 1998 and 1999. *Deep-Sea Research II*, **49**, 5151–5170.

Minnett, P. J., F. Bignami, E. Böhm, P. S. Galbraith, P. Gudmandsen, T. S. Hopkins, R. G. Ingram, M. A. Johnson, H. I. Niebauer, R. O. Ramseier et al. (1997). A summary of the formation and seasonal progression of the Northeast Water Polynya. *Journal of Marine Systems*, 1079–1085.

Mizuno, A. W., A. Wada, T. Ishinazaka, K. Hattori, Y. Watanabe, and N. Ohtaishi (2002). Distribution and abundance of spotted seals *Phoca largha* and ribbon seals *Phoca fasciata* in the southern Sea of Okhotsk. *Ecological Research*, **17**(1), 79, DOI: 10.1046/j.1440–1703.2002.00464.

Mobley, C. D., G. F. Cota, T. C. Grenfell, R. A. Maffione, W. S. Pegau, and D. K. Perovich (1998). Modeling light propagation in sea ice. *IEEE Transactions on Geoscience and Remote Sensing*, **36**(5), 1743–1749.

Mock, S. J., A. D. Hartwell, and W. D. Hibler III (1972). Spatial aspects of pressure ridge statistics. *Journal of Geophysical Research*, **77**, 5945–5953.

Mooney, A., S. Laxon, and N. Peacock (2000). New estimates of the fresh water flux through the Fram Strait using satellite derived ice thickness. *XXV General Assembly of the European Geophysical Society, Nice, France, April 25–29* (abstract). European Geophysical Society, Katlenburg-Lindau, Germany.

Moore, G. W. K., K. Alverson, and I. A. Renfrew (2002). A reconstruction of the air–sea interaction associated with the Weddell Polynya. *Journal of Physical Oceanography*, **32**, 1685–1698.

Moore, J. C. and S. Fujita (1993). Dielectric properties of ice containing acid and salt impurities at microwave and LF frequencies. *Journal of Geophysical Research*, **98**, 9769–9780.

Moore, R. K. and M. R. Abbott (2000). Phytoplankton chlorophyll distributions and primary production in the Southern Ocean. *Journal of Geophysical Research*, **105**(C12), 28709–28722.

Moore, R. K. and W. L. Jones (2004). Satellite scatterometer wind vector measurements: The legacy of the Seasat satellite scatterometer. *IEEE Geoscience and Remote Sensing Society Newsletter*, **132**, 18–32.

Morales Maqueda, M. A. and T. Fichefet (1996). A case for including more complete representations of sea ice processes in numerical climate models. *Proceedings of Workshop on Polar Processes in Global Climate, November 13–15, Cancun, Mexico*. American Meteorological Society, Boston, pp. 77–80.

Morales Maqueda, M. A., A. J. Wilmott, and N. R. T. Biggs (2004). Polynya dynamics: A review of observations and modeling. *Reviews of Geophysics*, **42**, DOI: 10.1029/2002RG000116.

Morassutti, M. P. and E. F. LeDrew (1996). Albedo and depth of melt ponds on sea ice. *International Journal of Climate*, **16**, 817–838.

Moreira, A. (2003). TerraSAR–X upgrade to a fully polarimetric imaging mode. *Proceedings of ESA Workshop, POLInSAR: Applications of SAR Polarimetry and Polarimetric Interferometry, ESRIN, Frascati, Italy, January 14–16* (ESA SP-529). Available online at ⟨*http://www.earth.esa.int/polinsar*⟩.

Morena, L. C., K. V. James, and J. Beck (2004). An introduction to the Radarsat-2 mission. *Canadian Journal of Remote Sensing*, **30**(3), 221–234.

Morison, J. H., M. G. McPhee, T. B. Curtin, and C. A. Paulson (1992). The oceanography of winter leads. *Journal of Geophysical Research*, **97**(C7), 11199–11218.

Morison, J. H., M. Steele, and R. Andersen (1998). Hydrography of the upper Arctic Ocean measured from the nuclear submarine USS Pargo. *Deep-sea Research I*, **45**(1), 15–38.

Morison, J. H., K. Aagaard, and M. Steele (2000). Recent environmental changes in the Arctic: A review. *Arctic*, **53**, 359–371.

Morison, J., V. Alexander, L. Codispoti, T. Delworth, B. Dickson, H. Eicken, J. Grebmeier, J. Kruse, J. Overland, J. Overpeck et al. (2001). *SEARCH: Study of Environmental*

Arctic Change Science Plan. Arctic Research Consortium of the United States, Fairbanks, AL.

Morison, J. H., K. Aagaard, K. K. Falkner, K. Hatakeyama, R. Moritz, J. E. Overland, D. Perovich, K. Shimada, M. Steele, T. Takizawa et al. (2002). North Pole Environmental Observatory delivers early results. *EOS, Transactions of the American Geophysical Union*, **83**(33), 357, 360–361.

Moritz, R. E. and D. K. Perovich (1996). *SHEBA: A Research Program on the Surface Heat Budget of the Arctic Ocean Science Plan* (ARCSS/OAII Report 5). University of Washington, Seattle, 64 pp.

Moritz, R. E., K. Aagaard, D. J. Baker, L. A. Codispoti, S. L. Smith, W. O. Smith, R. C. Tipper, and J. E. Walsh (eds.) (1990). *Arctic System Science: Ocean–Atmosphere–Ice Interactions, UCLA Lake Arrowhead Conference Center, March 12–16* (report). Joint Oceanographic Institutions, Washington, DC, 132 pp.

Moritz, R. E., J. A. Curry, N. Untersteiner, and A. S. Thorndike (1993). *Prospectus: Surface Heat Budget of the Arctic Ocean* (NSF-ARCSS OAII Technical Report 3). SHEBA Project Office, Polar Science Center, Applied Physics Laboratory, University of Washington, Seattle, 33 pp.

Moritz, R. E., C. M. Bitz, and E. J. Steig (2002). Dynamics of recent climate change in the Arctic. *Science*, **297**, 1497–1502.

Morris, K., M. O. Jeffries, and S. Li (1998). Sea ice characteristics and seasonal variability of ERS-1 backscatter in the Bellingshausen Sea. In: M. O. Jeffries (ed.), *Antarctic Sea Ice Physical Processes, Interactions and Variability* (AGU Antarctic Research Series No. 74). American Geophysical Union, Washington, DC, pp. 213–242.

Morris, K., S. Li, and M. Jeffries (1999). Meso- and micro-scale sea-ice motion in the East Siberian Sea as determined from ERS-1 SAR data. *Journal of Glaciology*, **45**(150), 370–383.

Muench, R. D., J. H. Morison, L. Padman, D. G. Martinson, P. Schlosser, B. Huber, and R. Hohmann (2001). Maud Rise revisited. *Journal of Geophysical Research*, **106**, 2423–2440.

Muench, R. D. and H. H. Hellmer (2002). Deep Ocean Ventilation Through Antarctic Intermediate Layers (DOVETAIL). *Deep-sea Research II*, **49**(21, special issue), 4711–4886.

Multala, J., H. Hautaniemi, M. Oksama, M. Leppäranta, J. Haapala, A. Herlevi, K. Riska, and M. Lensu (1996). An airborne electromagnetic system on a fixed wing aircraft for sea ice thickness mapping. *Cold Regions Science and Technology*, **24**, 355–373.

Muramoto, K.-I., K. Matsura, and T. Endoh (1993). Measuring sea-ice concentration and floe-size distribution by image processing. *Annals of Glaciology*, **18**, 33–38.

Murphy, E. J., A. Clarke, C. Symon, and J. J. Priddle (1995). Temporal variation in Antarctic sea-ice: Analysis of a long term fast-ice record from the South Orkney Islands. *Deep-sea Research I*, **42**(7), 1045–1062.

Murphy, E. J., D. J. Morris, J. L. Watkins, and J. Priddle (1988). Scales of interaction between Antarctic krill and the environment. In: D. Sahrhage (ed.), *Antarctic Ocean and Resources Variability*. Springer, Berlin, pp. 120–130.

Murray, R. J. and I. Simmonds (1995). Responses of climate and cyclones to reductions in Arctic winter sea ice. *Journal of Geophysical Research*, **100**, 4791–4806.

Mysak, L. A. (1999). Inter-decadal variability at northern latitudes. In: A. Navarra (ed.), *Beyond El Niño: Decadal and Inter-decadal Climate Variability*. Springer-Verlag, New York, pp. 1–24.

Mysak, L. and S. Venegas (1998). Decadal climate oscillations in the Arctic: A new feedback loop for atmospheric–ice–ocean interactions. *Geophysical Research Letters*, **25**, 3607–3610.

Mysak, L. A., R. G. Ingram, J. Wang, and A. van der Baaren (1996). The anomalous sea-ice extent in Hudson Bay, Baffin Bay and the Labrador Sea during three simultaneous NAO and ENSO episodes of 1972/73, 1982/83 and 1991/92. *Atmosphere–Ocean*, **34**, 313–343.

Naderi, F. M., M. H. Freilich, and D. G. Long (1991). Spaceborne radar measurement of wind velocity over the ocean: An overview of the NSCAT scatterometer system. *Proceedings of the IEEE*, **79**(6), 850–866.

Naito, Y. (ed.) (2004). Bio-logging science. *Memoirs of the National Institute of Polar Research*, **58** (special issue), 250 pp.

Nakagawa, K. (1992). Estimation of surface albedo distribution in the Lützow-Holm Bay and its neighbourhood with NOAA/AVHRR data. *Proceedings of NIPR Symposium on Polar Meteorology and Glaciology* (Vol. 6), pp. 1–15.

Nakajima, T. Y., T. Nakajima, M. Nakajima, H. Fukushima, M. Kuji, A. Uchiyama, and M. Kishino (1998). Optimization of the Advanced Earth Observing Satellite II Global Imager channels by use of radiative transfer equations. *Applied Optics*, **37**, 3149–3163.

Nansen, F. (ed.) (1902). The oceanography of the North Polar basin. *The Norwegian North Polar Expedition, 1893–1896: Scientific Results* (Vol. 3). Longmans, Green & Co., 422 pp.

Narayanan, M. S. and A. Sarkar (2001). *Observations of Marine Atmosphere from Indian Oceansat–1*. Available online at ⟨*http://meghatropiques.lmd.polytechnique.fr/documents/workshop2/proc_s5p01.pdf*⟩.

NASA (1987). *HIRIS: High-Resolution Imaging Spectrometer: Science Opportunities for the 1990s* (Instrument Panel Report, NASA Earth Observation System, Vol. HC). NASA, Washington, DC, 74 pp.

NASDA (2003). *AMSR–E Data User's Handbook* (NCX–030021, September). National Space Development Agency of Japan, Tokyo.

National Research Council (1998). *Review of NASA's Distributed Active Archive Centers*. National Academy Press, Washington, DC.

Nghiem, S. V. (2004). On the use of Envisat ASAR for remote sensing of sea ice. *Envisat Symposium, September 6–10, Salzburg, Austria* (abstract).

Nghiem, S. V. and C. Bertoia (2001). Study of multi-polarisation C-band backscatter signatures for Arctic sea ice mapping with future satellite SAR. *Canadian Journal of Remote Sensing*, **27**(5), 387–401.

Nghiem, S. V., R. Kwok, S. H. Yueh, and M. R. Drinkwater. (1995a). Polarimetric signatures of sea ice: 1. Theoretical model. *Journal of Geophysical Research*, **100**(C7), 13665–13679.

Nghiem, S. V., R. Kwok, S. H. Yueh, and M. R. Drinkwater (1995b). Polarimetric signatures of sea ice: 2. Experimental observations. *Journal of Geophysical Research*, **100**(C7), 13681–13698.

Nghiem, S. V., R. Kwok, S. H. Yueh, J. A. Kong, M. A. Tassoudji, C. C. Hsu, and R. T. Shin (1995c). Polarimetric scattering from layered media with multiple species of scatterers. *Radio Science*, **30**(4), 835–852.

Nghiem, S. V., R. Kwok, J. A. Kong, R. T. Shin, S. A. Arcone, and A. J. Gow (1996). An electrothermodynamic model with distributed properties for effective permittivities of sea ice. *Radio Science*, **31**(2), 297–311.

Nghiem, S. V., S. Martin, D. K. Perovich, R. Kwok, R. Drucker, and A. J. Gow (1997a). A laboratory study of the effect of frost flowers on C band radar backscatter from sea ice. *Journal of Geophysical Research*, **102**(C2), 3357–3370.

Nghiem, S. V., R. Kwok, S. H. Yueh, A. J. Gow, D. K. Perovich, J. A. Kong, and C.-C. Hsu (1997b). Evolution of polarimetric signatures of thin saline ice under constant growth. *Radio Science*, **32**(1), 127–151.

Nghiem, S. V., R. Kwok, S. H. Yueh, A. J. Gow, D. K. Perovich, C.-C. Hsu, K.-H. Ding, J. A. Kong, and T. C. Grenfell (1998). Diurnal thermal cycling effects on microwave signatures of thin sea ice. *IEEE Transactions on Geoscience and Remote Sensing*, **36**(1), 111–124.

Nichols, D., J. Bowman, K. Sanderson, C. Nichols, T. Lewis, T. McMeekin, and P. D. Nichols (1999). Developments with Antarctic micro-organisms: Culture collections, bio-activity screening, taxonomy, PUFA production and cold adapted enzymes. *Current Opinion in Biotechnology*, **10**, 240–246.

Nichols, T., F. Berkes, D. Jolly, and N. B. Snow (2004). Climate change and sea ice: Local observations from the Canadian Western Arctic. *Arctic*, **126**(1), 68–79.

Nicol, S., T. Pauly, N. L. Bindoff, S. Wright, D. Thiele, G. W. Hosie, P. G. Strutton, and E. Woehler (2000). Ocean circulation off East Antarctica affects ecosystem structure and sea-ice extent. *Nature*, **406**, 504–507.

Nicodemus, F. E., J. C. Richmond, J. J. Hsia, I. W. Ginsberg, and T. Limperis (1977). *Geometrical considerations and nomenclature for reflectance* (U.S. NBS Monograph 160). Institute for Basic Standards, Washington, DC.

Niebauer, H. J. (1998). Variability in Bering Sea ice cover as affected by a regime shift in the north Pacific in the period 1947–1996. *Journal of Geophysical Research*, **103**(C12), 27717–27737.

Niebauer, H. J., N. A. Bond, L. P. Yakunin, and V. V. Plotnikov (1999). An update on the climatology and sea ice of the Bering Sea. In: T. R. Loughlin and K. Ohtani (eds.), *The Bering Sea: A Summary of Physical, Chemical and Biological Characteristics and a Synopsis of Research* (AK-SG-99-03). University of Alaska Sea Grant Press, Fairbanks, AL, pp. 29–60.

Nihashi, S. and K. I. Ohshima (2001). Relationship between ice decay and solar heating through open water in the Antarctic sea ice zone. *Journal of Geophysical Research*, **106**(C8), 16767–16782.

Ninnis, R. N., W. J. Emery, and M. J. Collins (1986). Automated extraction of sea ice motion from AVHRR imagery. *Journal of Geophysical Research*, **91**(C9), 10725–10734.

Njoku, E. G., B. Rague, and K. Fleming (1998). *Nimbus-7 SMMR Pathfinder Brightness Temperature Data* (Publication 98-4). Jet Propulsion Laboratory, Pasadena, CA.

Nolin, A. W. and J. Dozier (2000). A hyperspectral method for remotely sensing the grain size of snow. *Remote Sensing of Environment*, **74**, 207–216.

Nolin, A. W., F. M. Fetterer, and T. A. Scambos (2002). Surface roughness characterizations of sea ice and ice sheets: Case studies with MISR data. *IEEE Transactions on Geoscience and Remote Sensing*, **40**(7), pp. 1605–1615.

Nolin, A., R. L. Armstrong, and J. Maslanik (2003). *Near Real-Time SSM/I EASE–Grid Daily Global Ice Concentration and Snow Extent* (digital media, updated regularly). National Snow and Ice Data Center, Boulder, CO.

Noone, D. and I. Simmonds (2004). Sea ice control of water isotope transport to Antarctica and implications for ice core interpretation. *Journal of Geophysical Research*, **109**, D07105, DOI: 10.1029/2003JD004228.

Nöthig, E. M., U. Bathmann, J. Jennings, E. Fahrbach, R. Gradinger, L. Gordon, and R. Makarov (1991). Regional relationships between biological and hydrological properties in the Weddell Sea in late austral winter 1989. *Journal of Marine Chemistry*, **35**, 325–336.

NSIDC (2000). *SHEBA Reconnaissance Imagery Version 1.0* (digital media). National Snow and Ice Data Center, Boulder, CO.

NSIDC (1996). *DMSP SSM/I Brightness Temperatures and Sea Ice Concentration Grids for the Polar Regions: User's Guide* (CD–ROM, Special Report 1, January). Cooperative Institute for Research in Environmental Sciences, University of Colorado, Boulder, CO.

Nuñez, M., K. Michael, D. Turner, M. Wall, and C. Nilsson (1997). A satellite-based climatology of UV-B irradiance for Antarctic coastal regions. *International Journal of Climatology*, **17**, 1029–1054.

Nussenzveig, H. M. and W. J. Wiscombe (1980), Efficiency factors in Mie scattering. *Physical Review Letters*, **45**, 1490–1494.

OASIS (2004). *Science Plan for the Ocean–Atmosphere–Sea Ice–Snowpack (OASIS) Interactions Program, Version 2.2* (December). Dept. of Chemistry, Purdue University, IN.

O'Brien, H. W. and R. H. Munis (1975). *Red and Near-infrared Spectral Reflectance of Snow*. (Research Report 332). U.S. Army Cold Regions Research and Engineering Laboratory, Hanover, NH, 18 pp.

Oelke, C. (1997). Atmospheric signatures in sea-ice concentration estimates from passive microwaves: Modelled and observed. *International Journal of Remote Sensing*, **18**(5), 1113–1136.

O'Farrell, S. P. (1998). Investigation of the dynamic sea-ice component of a coupled atmosphere sea-ice general circulation model. *Journal of Geophysical Research*, **103**(C8), 15751–15782.

O'Farrell, S. P. and W. M. Connolley (1998). Comparison of warming trends predicted over the next century around Antarctica from two coupled models. *Annals of Glaciology*, **27**, 576–582.

Ohshima, K. I., K. Yoshida, H. Shimoda, M. Wakatsuchi, T. Endoh, and M. Fukuchi (1998). Relationship between the upper ocean and sea ice during the Antarctic melting season. *Journal of Geophysical Research*, **103**, 7601–7615.

Oke, P. R. and M. H. England (2004). On the oceanic response to changes in the latitude of the Southern Hemisphere sub-polar westerly winds. *Journal of Climate*, **17**, 1040–1054.

Olbers, D., D. Borowski, C. Volker, and J.-O. Wolff (2004). The dynamical balance, transport and circulation of the Antarctic Circumpolar Current. *Antarctic Science*, **16**, 439–470.

Olmsted, C. (1993). *Alaska SAR Facility Scientific SAR User's Guide* (ASF-SD-003). Alaska SAR Facility, Fairbanks, AL, 53 pp.

Onstott, R. G. (1992). SAR and scatterometer signatures of sea ice. In: F. D. Carsey (ed.), *Microwave Remote Sensing of Sea Ice* (AGU Monograph No. 68, American Geophysical Union, Washington, DC, pp. 73–104.

Onstott, R. G. (2004). Antarctic sea ice and icebergs. In: C. R. Jackson and J. R. Apel (eds.), *Synthetic Aperture Radar Marine User's Manual*. National Oceanic and Atmospheric Administration, Washington, DC.

Onstott, R. G. and S. P. Gogineni (1985). Active microwave measurements of Arctic sea ice under summer conditions. *Journal of Geophysical Research*, **90**(C3), 5035–5044.

Onstott, R. G. and R. A. Shuchman (1990). Comparison of SAR and scatterometer data collected during CEAREX. *Proceedings of IGARSS '90 Symposium, College Park, MD*. Institute of Electrical and Electronics Engineers, Piscataway, NJ, pp. 1513–1516.

Onstott, R. G. and R. A. Shuchman (2004). SAR measurements of sea ice. In: C. R. Jackson and J. R. Apel (eds.), *Synthetic Aperture Radar Marine User's Manual*. National Oceanic and Atmospheric Administration, Washington, DC, pp. 81–115.

Onstott, R. G., R. K. Moore, and W. F. Weeks (1979). Surface-based scatterometer results of Arctic sea ice. *IEEE Transactions on Geoscience and Electronics*, **17**, 78–85.

Onstott, R. G., S. Gogineni, and C. Delker (1982). Four years of low altitude sea ice broadband backscatter measurements. *IEEE Journal of Oceanic Engineering*, **7**, 44–50.

Onstott, R. G., T. C. Grenfell, C. Mätzler, C. A. Luther, and E. A. Svendsen (1987). Evolution of microwave sea ice signatures during early and mid summer in the marginal ice zone. *Journal of Geophysical Research*, **92**(C7), 6825–6835.

Onstott, R. G., P. Gogineni, A. J. Gow, T. C. Grenfell, K. C. Jezek, D. K. Perovich, and C. T. Swift (1998). Electromagnetic and physical properties of sea ice formed in the presence of wave action. *IEEE Transactions on Geoscience and Remote Sensing*, **36**, 1764–1783.

Oozeva, C., C. Noongwook, G. Noongwook, C. Alowa, and I. Krupnik (2004). *Watching Ice and Weather Our Way*. Arctic Studies Center, National Museum of Natural History, Smithsonian Institution and Savoonga Whaling Captains' Association, Savoonga, AK, 208 pp.

O'Reilly, J. E., S. Maritorena, B. G. Mitchell, D. A. Siegel, K. L. Carder, S. A. Garver, M. Kahru, and C. McClain (1998). Ocean color chlorophyll algorithms for SeaWiFS. *Journal of Geophysical Research*, **103**, 24937–24953.

Orr, J. C., E. Maier-Reimer, U. Mikolajewicz, P. Monfray, J. L. Sarmiento, J. R. Toggweiler, N. K. Taylor, J. Palmer, N. Gruber, C. Sambine et al. (2001). Estimate of anthropogenic carbon uptake from four three-dimensional global models. *Global Biogeochemical Cycles*, **15**, 43–60.

Orsi, A. H., T. Whitworth III, and W. D. Nowlin Jr. (1995). On the meridional extent and fronts of the Antarctic Circumpolar Current. *Deep-Sea Research*, **42**, 641–673.

Orsi, A. H., G. C. Johnson, and J. L. Bullister (1999). Circulation, mixing, and production of Antarctic Bottom Water. *Progress in Oceanography*, **43**, 55–109.

Ou, Z. (2004). An integrated spatial information system for ice service. *Proceedings of 20th ISPRS Congress, Istanbul, Turkey, July 12–23* (Commission 1). Available online from ⟨*http://www.isprs.org/istanbul2004/comm1/comm1.html*⟩.

Ouaidrari, H., S. N. Goward, K. P. Czajkowski, J. A. Sobrino, and E. Vermote (2002). Land surface temperature estimation from AVHRR TIR measurements: An assessment for the AVHRR Land Pathfinder II data set. *Remote Sensing of Environment*, **81**, 114–128.

Overland, J. E. (1985). Atmospheric boundary layer structure and drag coefficients over sea ice. *Journal of Geophysical Research*, **95**(C5), 9029–9049.

Overland J. E. and K. L. Davidson (1992). Geostrophic drag coefficients over sea ice. *Tellus*, **44**(A), 54–66.

Overland, J. E. and P. S. Guest (1991). The Arctic snow and air temperature budget over sea ice during winter, *Journal of Geophysical Research*, **96**, 4651–4662.

Overland, J. E. and C. H. Pease (1982). Cyclone climatology of the Bering Sea and its relation to sea ice extent. *Monthly Weather Review*, **110**, 5–13.

Overland, J. E., M. Wang, and N. A. Bond (2002). Recent temperature changes in the western Arctic during winter and spring. *Journal of Climate*, **15**, 1702–1716.

Paget, M. J., A. P. Worby, and K. J. Michael (2001). Determining the floe-size distribution of East Antarctic sea ice from digital aerial photographs. *Annals of Glaciology*, **33**, 94–100.

Palmisano, A. C. and D. L. Garrison (1993). Micro-organisms in Antarctic Sea Ice. In *Antarctic Microbiology*, edited by E. I. Friedmann. Wiley–Liss, New York, pp. 167–218.

Papathanassiou, K. P. and S. R. Cloude (2001). Single baseline polarimetric SAR interferometry. *IEEE Transactions on Geoscience and Remote Sensing*, **39**(11), 2352–2363.

Parish, T. R. and D. H. Bromwich (1987). The surface windfield over the Antarctic continent: A review. *Nature*, **328**(6125), 51–54.

Parkinson, C. L. (1983). On the development and cause of the Weddell Polynya in a sea ice simulation. *Journal of Physical Oceanography*, **13**(3), 501–511.

Parkinson, C. L. (1991). Interannual variability of the spatial distribution of sea ice in the north polar region. *Journal of Geophysical Research*, **96**(C3), 4791–4801.

Parkinson, C. L. (1992). Spatial patterns of increases and decreases in the length of the sea ice season in the North Polar region. *Journal of Geophysical Research*, **97**(C9), 14377–14388.

Parkinson, C. L. (1994). Spatial patterns in the length of the sea ice season in the Southern Ocean, 1979–1986. *Journal of Geophysical Research*, **99**, 16327–16339.

Parkinson, C. L. (1995). Recent sea-ice advances in Baffin Bay/Davis Strait and retreats in the Bellingshausen Sea. *Annals of Glaciology*, **21**, 348–352.

Parkinson, C. L. (1998). Length of the sea ice season in the Southern Ocean. In: M. O. Jeffries (ed.), *Antarctic Sea Ice Physical Processes, Interactions and Variability* (AGU Antarctic Research Series No. 74), Antarctic Geophysical Union, Washington, DC, pp. 173–186.

Parkinson, C. L. (2000a). Variability of Arctic sea ice: The view from space, an 18–year record. *Arctic*, **53**(4), 341–358.

Parkinson, C. L. (2000b). Recent trend reversals in Arctic sea ice extents: Possible connections to the North Atlantic Oscillation. *Polar Geography*, **24**, 1–12.

Parkinson, C. L. (2002). Trends in the length of the Southern Ocean sea-ice season, 1979–99. *Annals of Glaciology*, **34**, 435–440.

Parkinson, C. L. (2003). Aqua: An Earth-observing satellite mission to examine water and other climate variables. *IEEE Transactions on Geoscience and Remote Sensing*, **41**, 173–183.

Parkinson, C. L. (2004). Southern Ocean sea ice and its wider linkages: Insights revealed from models and observations. *Antarctic Science*, **16**, 387–400.

Parkinson, C. L. and D. J. Cavalieri (1989). Arctic sea ice 1973–1987: Seasonal, regional and interannual variability. *Journal of Geophysical Research*, **94**(C10), 14199–14223.

Parkinson, C. L. and D. J. Cavalieri (2002). A 21 year record of Arctic sea-ice extents and their regional, seasonal and monthly variability and trends. *Annals of Glaciology*, **34**, 441–446.

Parkinson, C. L. and P. Gloersen (1993). Global sea ice coverage. In: R. J. Gurney, J. L. Foster and C. L. Parkinson (eds.), *Atlas of Satellite Observations Related to Global Change*. Cambridge University Press, UK, pp. 371–383.

Parkinson, C. L. and R. Greenstone (2000). *EOS Data Products Handbook* (Vol. 2, NP-2000-5-055-GSFC). NASA Goddard Space Flight Center, Greenbelt, MD.

Parkinson, C. L. and W. M. Washington (1979). A large-scale numerical model of sea ice. *Journal of Geophysical Research*, **84**(C1), 311–337.

Parkinson, C. L., J. C. Comiso, H. J. Zwally, D. J. Cavalieri, P. Gloersen, and W. J. Campbell (1987). *Arctic Sea Ice, 1973–1976: Satellite Passive-Microwave Observations* (NASA SP-489). NASA, Washington, DC, 296 pp.

Parkinson, C. L., D. J. Cavalieri, P. Gloersen, H. J. Zwally, and J. C. Comiso (1999). Arctic sea ice extents, areas and trends, 1978–1996. *Journal of Geophysical Research*, **104**(C9), 20837–20856.

Parkinson, C. L., D. Rind, R. J. Healy, and D. G. Martinson (2001). The impact of sea ice concentration accuracies on climate model simulations with the GISS GCM. *Journal of Climate*, **14**, 2606–2623.

Parmeter, R. R. (1975). A model of simple rafting in sea ice. *Journal of Geophysical Research*, **80,** 1948–1952.

Parmeter, R. R. and M. Coon (1972). Model of pressure ridge formation in sea ice. *Journal of Geophysical Research*, **77**, 6565–6575.

Partington, K. (2000). A data fusion algorithm for mapping sea-ice concentration from Special Sensor Microwave/Imager data. *IEEE Transactions on Geoscience and Remote Sensing*, **38**(4), 1947–1958.

Partington, K. and C. Bertoia (1999). Evaluation of Special Sensor Microwave/Imager sea ice products. *Proceedings of International Geoscience and Remote Sensing Symposium, Hamburg, Germany, June 28–July 2* (CD-ROM).

Partington, K. and K. Steffen (1998). *National Ice Center Data Assimilation Plan* (National Ice Center white paper). Available online at ⟨*http://www.natice.noaa.gov*⟩.

Partington, K., M.-R. Keller, P. Seymour, and C. Bertoia (1999). Data fusion for use of passive microwave data in operational sea-ice monitoring. *Proceedings of International Geoscience and Remote Sensing Symposium, Hamburg, Germany, June 28–July 2* (CD-ROM).

Partington, K., T. Flynn, D. Lamb, C. Bertoia, and K. Dedrick (2003). Late twentieth century Northern Hemisphere sea-ice record from U.S. National Ice Center ice charts. *Journal of Geophysical Research*, **108**(C11), 3343. DOI: 10.1029/2002JC001623.

Paterson, J. S., B. Brisco, S. Argus, and G. Jones (1991). *In situ* measurements of micro-scale surface roughness of sea ice. *Arctic*, **44**(1), 140–146.

Peacock, N. R. and S. W. Laxon (2004). Sea surface height determination in the Arctic Ocean from ERS altimetry. *Journal of Geophysical Research*, **109**, C07001, DOI: 10.1029/2001JC001026.

Peacock, N. R., S. W. Laxon, R. Scharoo, W. Maslowski, and D. P. Winebrenner (1998). Geophysical signatures from precise altimetric height measurements in the Arctic Ocean. *Proceedings of IGARSS '98, July 6–10, Seattle* (Vol. **4,** 1964–1966).

Pease, C. H. (1987). The size of wind-driven coastal polynyas. *Journal of Geophysical Research*, **92**, 7049–7059.

Peddada, S. and T. Chang (1996). Bootstrap confidence region estimation of the motion of rigid bodies. *Journal of the American Statistical Association*, **91**(433), 231–241.

Peixoto, J. R. and A. H. Oort (1992). *Physics of Climate*. American Institute of Physics, New York, 520 pp.

Perovich, D. K. (1990a). Theoretical estimates of light reflection and transmission by spatially complex and temporally varying sea ice covers. *Journal of Geophysical Research*, **95**, 9557–9567.

Perovich, D. K. (1990b). The evolution of sea ice optical properties during fall freeze–up: Ocean Optics 10. *Proceedings of SPIE International Society of Optical Engineering*, **1302**, 520–531.

Perovich, D. K. (1994). Light reflection from sea ice during the onset of melt. *Journal of Geophysical Research*, **99**, 3351–3359.

Perovich, D. K. (1995). Observations of ultraviolet light reflection and transmission by first-year sea ice. *Geophysical Research Letters*, **22**(11), 1349–1352.

Perovich, D. K. (1996). *The Optical Properties of Sea Ice* (Report 96-1). U.S. Army Cold Regions Research and Engineering Laboratory (CRREL), Hanover, NH.

Perovich, D. K. (1998). Observations of the polarization of light reflected from sea ice. *Journal of Geophysical Research*, **103**, 5563–5575.

Perovich, D. K. (2003). Sunlight and sea ice: On the partitioning of solar radiation by a sea ice cover. *Proceedings of 7th Conference on Polar Meteorology and Oceanography and Joint Symposium on High-Latitude Climate Variations, May 12–16, Hyannis, MA* (P3.1). American Meteorological Society, Boston.

Perovich, D. K. and A. J. Gow (1991). A statistical description of microstructure of young ice. *Journal of Geophysical Research*, **96**(C9), 16943–16953.

Perovich, D. K. and A. J. Gow (1996). A quantitative description of sea ice inclusions. *Journal of Geophysical Research*, **101**, 18327–18343.

Perovich, D. K. and G. A. Maykut (1990). The treatment of shortwave radiation and open water in large-scale models of sea-ice decay. *Annals of Glaciology*, **14**, 242–246.

Perovich, D. K. and J. A. Richter-Menge (2000). Ice growth and solar heating in springtime lead. *Journal of Geophysical Research*, **105**, 6541–6548.

Perovich, D. K. and W. B. Tucker (1997). Arctic sea-ice conditions and the distribution of solar radiation during summer. *Annals of Glaciology*, **25**, 445–450.

Perovich, D. K., B. C. Elder, and J. A. Richter-Menge (1997). Observations of the annual cycle of sea ice temperature and mass balance. *Geophysical Research Letters*, **24**, 555–558.

Perovich, D. K., C. S. Roesler, and W. S. Pegau (1998a). Variability in Arctic sea ice optical properties. *Journal of Geophysical Research*, **103**(C1), 1193–1208.

Perovich, D. K., J. Longacre, D. G. Barber, R. A. Maffione, G. F. Cota, C. D. Mobley, A. J. Gow, R. G. Onstott, T. C. Grenfell, W. S. Pegau et al. (1998b). Field observations of the electromagnetic properties of first-year sea ice. *IEEE Transactions on Geoscience and Remote Sensing*, **36**, 1705–1715.

Perovich, D. K., T. C. Grenfell, B. Light, J. A. Richter-Menge, M. Sturm, W. B. Tucker III, H. Eicken, G. A. Maykut, and B. Elder (1999a). *SHEBA: Snow and Ice Studies* (CD-ROM). U.S. Army Cold Regions Research and Engineering Laboratory, Hanover, NH.

Perovich, D. K., E. L. Andreas, J. A. Curry, H. Eicken, C. W. Fairall, T. C. Grenfell, P. S. Guest, J. Interieri, D. Kadko, R. W. Lindsay et al. (1999b). Year on ice gives climate insights. *EOS, Transactions of the American Geophysical Union*, **80**, 481–486.

Perovich, D. K., J. A. Richter-Menge, and W. B. Tucker III (2001). Seasonal changes in Arctic sea ice morphology. *Annals of Glaciology*, **33**, 171–176.

Perovich, D. K., W. B. Tucker III, and K. A. Ligett (2002a). Aerial observations of the evolution of ice surface conditions during summer. *Journal of Geophysical Research*, **107**(C10), 8048, DOI: 10.1029/2000JC000449.

Perovich, D. K., T. C. Grenfell, B. Light, and P. V. Hobbs (2002b). Seasonal evolution of the albedo of multiyear Arctic sea ice. *Journal of Geophysical Research*, **107**(C10), 8044, DOI: 10.1029/2000JC000438.

Perovich D. K., T. C. Grenfell, J. A. Richter–Menge, B. Light, W. B. Tucker III, and H. Eicken (2003). Thin and thinner: Ice mass balance measurements during SHEBA. *Journal of Geophysical Research*, **108**(C3), DOI: 10.1029/2001JC001079.

Peterson, B. J., R. M. Holmes, J. W. McClelland, C. J. Vörösmarty, R. B. Lammers, A. I. Shiklomanov, and S. Rahmstorf (2002). Increasing Arctic river discharges: Responses and feedbacks to global climate change. *Science*, **298**, 2171–2173.

Pfirman, S., H. Eicken, D. Bauch, and W. F. Weeks (1995). Potential transport of radionuclides and other pollutants by Arctic sea ice. *Science of Total Environment*, **159**(2–3), 129–146.

Pichel, W. G. and P. Clemente-Colón (2000). NOAA CoastWatch SAR applications and demonstration. *Johns Hopkins APL Technical Digest*, **21**(1), 49–57.

Pichel, W. G., P. Clemente-Colón, C. Bertoia, M. Van Woert, C. C. Wackerman, F. Monaldo, D. R. Thompson, K. S. Friedman, and X. Li (2003). Routine production of SAR-derived ice and ocean products in the United States. *Proceedings of 2nd Workshop on Coastal and Marine Applications of SAR, September 8–12, Svalbard, Norway*. Available online at ⟨*http://earth.esa.int/workshops/cmasar_2003/*⟩.

Piepmeier, J. R. and A. J. Gasiewski (2001). Digital correlation polarimetry: Analysis and demonstration. *IEEE Transactions on Geoscience and Remote Sensing*, **39**, 2392–2410.

Pillsbury, R. D. and S. S. Jacobs (1985). Preliminary observation from long-term current meter moorings near the Ross Ice Shelf, Antarctica. In: S. S. Jacobs (ed.), *Oceanology of the Antarctic Continental Shelf* (Antarctic Research Series 43). American Geophysical Union, Washington, D.C., pp. 87-107.

Pilskaln, C. H., S. J. Manganini, T. W. Trull, L. Armand, W. Howard, V. L. Asper, and R. Massom (2004). Geochemical particle fluxes in the Southern Indian Ocean seasonal ice zone: Prydz Bay region, East Antarctica. *Deep Sea Research I*, **51**, 307–332, DOI: 10.1016/j.dsr.2003.10.010.

Pinto, J. O., J. A. Curry, and K. L. McInnes (1995). Atmospheric convective plumes emanating from leads: 1. Thermodynamic structure. *Journal of Geophysical Research*, **100**, 4621–4631.

Pinto, J. O., A. Alam, J. A. Maslanik, and J. A. Curry (2003). Characteristics and atmospheric footprint of springtime leads at SHEBA. *Journal of Geophysical Research*, **108**, DOI: 10.1029/2000JC000473.

Piwowar, J. M. and E. F. LeDrew (2001). On the autoregressive nature of Arctic sea ice concentrations. *Canadian Journal of Remote Sensing*, **27**(5), 517–525.

Polyakov, I. V. and M. A. Johnson (2000). Arctic decadal and interdecadal variability. *Geophysical Research Letters*, **27**(24), 4097–4100.

Polyakov, I. V., A. Y. Proshutinsky, and M. A. Johnson (1999). Seasonal cycles in two regimes of Arctic climate. *Journal of Geophysical Research*, **104**, 25761–25788.

Polyakov, I. V., G. V. Alekseev, R. V. Bekryaev, U. Bhatt, R. Colony, M. A. Johnson, V. P. Karklin, A. P. Makshtas, D. Walsh, and A. V. Yulin (2002). Observationally-based assessment of polar amplification of global warming. *Geophysical Research Letters*, **29**, 1878, DOI: 1029/2001GL011111.

Polyakov, I., G. V. Alekseev, R. V. Bekryaev, U. Bhatt, R. Colony, M. A. Johnson, V. P. Karklin, D. Walsh, and A. V. Yulin (2003). Long–term ice variability in Arctic marginal seas. *Journal of Climate*, **16,** 2078–2085.

Popov, A. V. and V. F. Romanov (2001). The Laptev Sea flaw polynyas in the climate system. *International Polynya Symposium, 9–13 September 2001, Quebec* (Abstract). Available online at ⟨*www.fsg.ulaval.ca/giroq/now/IPS2001/ips2001.htm*⟩.

Potter, M. J. (1995). An evaluation of polynyas in East Antarctica. BSc thesis, University of Tasmania, Australia.

Potter, R. C. H., S. W. Laxon, and N. Peacock (2002). Estimation of Antarctic sea ice thickness from satellite radar altimetry. *EGS XXVII General Assembly, April 21–26, Nice, France* (Paper EGS02-A-05827, OA6-1FR5P-026).

Powell, A. M. and P. A. Zuzolo (2000). The benefits of visual multi-source, multi-resolution data analysis and fusion. *16th International Conference on Interactive Information and Processing Systems (IIPS) for Meteorology, Oceanography, and Hydrology, January 9–14*. American Meteorological Society, Boston, pp. 132–135.

Prabhakara, C. P., G. Dalu, and V. G. Kunde (1974). Estimation of sea surface temperature from remote sensing in the 11–13 μm window region. *Journal of Geophysical Research*, **79**(33), 5039–5044.

Prata, A. (2002). *Land Surface Temperature Measurement from Space: AATSR Algorithm Theoretical Basis Document*. ESA, Noordwijk, The Netherlands, 34 pp. Available at ⟨*earth.esa.int/pub/ESA_DOC/LST–ATBD.pdf*⟩.

Prata, A. J., R. P. Cechet, I. J. Barton, and D. T. Llewellyn-Jones (1990). The Along-Track Scanning Radiometer for ERS-1: Scan geometry and data simulation. *IEEE Transactions on Geoscience and Remote Sensing*, **28**, 3–13.

Price, J. C. (1984). Land surface temperature measurements from the split-window channels of the NOAA-7 Advanced Very High Resolution Radiometer. *Journal of Geophysical Research*, **89**, 7231–7237.

Prinsenberg, S. J., I. K. Peterson, and S. Holladay (1996). Comparison of airborne electromagnetic ice thickness data with NOAA/AVHRR and ERS-1/SAR images. *Atmosphere–Ocean*, **34**(1), 185–205.

Pritchard, R. S. (ed.) (1980). *Sea Ice Processes and Models* (proceedings of Arctic Ice Dynamics Joint Experiment—AIDJEX), University of Washington Press, Seattle.

Pritchard, R. S (1988). Mathematical characteristics of sea ice dynamics models. *Journal of Geophysical Research*, **93**, 15609–15618.

Pritchard, R. S. (1998). Ice conditions in an anisotropic sea ice dynamics model. *International Journal of Offshore and Polar Engineering*, **8**, 9–15.

Pritchard, R. S. (2001). Sea ice dynamics models. In: J. Dempsey and H. H. Shen (eds.), *Scaling Laws in Ice Mechanics and Dynamics*. Kluwer Academic, Dordrecht, The Netherlands, pp. 265–288.

Proshutinsky, A. Y. and M. A. Johnson (1997). Two circulation regimes of the wind–driven Arctic Ocean. *Journal of Geophysical Research*, **102**, 12493–12514.

Proshutinsky, A., M. Steele, J. Zhang, G. Holloway, N. Steiner, S. Häkkinen, D. M. Holland, R. Gerdes, C. Koeberle, M. Karcher et al. (2001). Multinational effort studies differences among Arctic Ocean models. *EOS*, **82**(51), 637–644.

Proshutinsky, A., R. H. Bourke, and F. A. McLaughlin (2002). The role of the Beaufort Gyre in Arctic climate variability: Seasonal to decadal climate scales. *Geophysical Research Letters*, **29**, 2100–2105.

Proshutinsky, A., A. Plueddemann, J. Toole and R. Krishfield (2004). Ice-based observatories: A strategy for improved understanding of the Arctic atmosphere–ice–ocean environment within the context of an Integrated Arctic Observing System. *International Workshop Sponsored by the National Science Foundation, Woods Hole Oceanographic Institution, June 28–30, Woods Hole, MA* (report), 65 pp. Available online at ⟨*http://www.whoi.edu/science/PO/arcticgroup/projects/ipworkshop_report.html*⟩.

Quetin, L. B., R. M. Ross, T. K. Frazer, and K. L. Haberman (1996). Factors affecting distribution and abundance of zooplankton, with an emphasis on Antarctic krill, *Euphausia superba*. In: R. M. Ross, E. E. Hofinann, and L. B. Quetin (eds.), *Foundations for Ecological Research West of the Antarctic Peninsula* (AGU Antarctic Research Series No. 70). American Geophysical Union, Washington, DC, pp. 357–371.

Quilfen, Y. (1997). High-resolution scatterometry in preparation for the AScat instrument. *3rd ERS Symposium on Space at the Service of Our Environment, March 3, Florence, Italy* (ESA Vol. 414, No. 3). ESA, Noordwijk, The Netherlands, pp. 1233–1238,

Quilfen, Y., B. Chapron, T. Elfouhaily, K. Katsaros, J. Tournadre, and B. Chapron (1998). Observation of tropical cyclones by high-resolution scatterometry. *Journal of Geophysical Research*, **103**, 7767–7786.

Radionov, V. F., N. N. Bryazgin, and Y. I. Aleksandrov (1996). *The Snow Cover of the Arctic Basin*. Gidrometeoizdat, Moscow, 102 pp. [in Russian]. English translation available from Polar Science Center, University of Washington, Seattle, WA as Technical Report APL-UW TR 9701.

Ramasami, V., S. Gogineni, B. Holt, P. Kanagaratnam, K. Gurumoorthy, S. K. Namburi, J. Henslee, A. Mahoney, D. Braaten, and V. Lytle (2003). A low frequency wideband depth sounder for sea ice. *Proceedings of IGARSS '03, Toulouse, France, July 21–25* (Vol. 4). Institute of Electrical and Electronics Engineers, Piscataway, NJ, pp. 2811–2813.

Ramsay, B., M. J. Manore, L. Weir, K. Wilson, and D. Bradley (1998). Use of Radarsat data in the Canadian Ice Service. *Canadian Journal of Remote Sensing*, **24**(1), 36–42.

Ramsay, B., D. Flett, M. Manore, and R. De Abreu (2001). Radarsat-1 for sea ice monitoring in Canada. *Proceedings of IGARSS '01, Sydney, Australia, July*.

Ramsay, B., D. Flett, H. S. Andersen, R. Gill, S. Nghiem, and C. Bertoia (2004). Preparation for the operational use of Radarsat-2 for ice monitoring. *Canadian Journal of Remote Sensing*, **30**(3), 415–423.

Ramseier, R., I. G. Rubinstein, and A. F. Davies (1988). *Operational Evaluation of Special Sensor Microwave/Imager by the Atmospheric Environment Service, Centre for Research in Experimental Space Science, York University, North York, Ontario* (report). Centre for Research in Experimental Space Science, AES, York University, North York, Ontario.

Randall, D., J. Curry, D. Battisti, G. Flato, R. Grumbine, S. Häkkinen, D. Martinson, R. Preller, J. Walsh, and J. Weatherly (1998). Status and outlook for large-scale modeling of atmosphere–ice–ocean interactions in the Arctic. *Bulletin of American Meteorological Society,* **79**, 197–219.

Raney, R. K. (1998). The delay Doppler radar altimeter. *IEEE Transactions on Geoscience and Remote Sensing*, **36**(5), 1578–1588.

Rao, C. R. N., J. Chen, F. W. Staylor, P. Abel, Y. J. Kaufman, E. Vermote, W. R. Rossow, and C. L. Brest (1993). *Degradation of the Visible and Near-infrared Channels of the Advanced Very High Resolution Radiometer on the NOAA-9 Spacecraft: Assessment and Recommendations for Corrections* (NOAA Technical Report NESDIS 70). Department of Commerce, Washington, D.C.

Raphael, M. N. (2003). Impact of observed sea-ice concentration on the Southern Hemisphere extratropical atmospheric circulation in summer. *Journal of Geophysical Research*, **108**(D22), 4687, DOI: 10.1029/2002JD003308.

Rapley, C., R. Bell, I. Allison, R. Bindschadler, G. Casassa, S. Chown, G. Duhaime, V. Kotlyakov, M. Kuhn, O. Orheim, P. C. Pandey, H. K. Petersen, H. Schalke, W. Janoschek, E. Sarukhanian, and Z. Zhang (2004). A Framework for the International Polar Year 2007–2008. *International Council for Science*, 38 pp.

Raschke, E. (1987). *International Satellite Cloud Climatology Project (ISCCP) Workshop on Cloud Algorithms in the Polar Regions* (Report WMO/TD-170). World Meteorological Organization, Geneva, 77 pp.

Rees, W. G. (1993). Infrared emissivity of Arctic winter snow. *International Journal of Remote Sensing*, **14**, 3069–3073.

Rees, W. G. (2001). *Physical Principles of Remote Sensing* (2nd edn.). Cambridge University Press, Cambridge, UK, 372 pp.

Rees, W. G. and S. P. James (1992). Angular variation of the infrared emissivity of ice and water surfaces. *International Journal of Remote Sensing*, **13**, 2873–2886.

Reijnders, P. J. H., J. Plötz, J. Zegers, and M. Gräfe (1990). Breeding biology of Weddell seals (*Leptonychotes weddellii*) at Drescher Inlet, Riiser Larsen Ice Shelf, Antarctica. *Polar Biology*, **10**, 301–306.

Reimnitz, E., H. Kassens, and H. Eicken (1995a). Sediment transport by Laptev Sea ice. *Reports on Polar Research*, **176**, 71–77.

Reimnitz, E., H. Eicken, T. Martin (1995b). Multi-year fast ice along the Taymyr Peninsula, Siberia. *Arctic*, **48**, 359–367.

Remund, Q. P. and D. G. Long (1999). Sea ice extent mapping using Ku-band scatterometer data. *Journal of Geophysical Research*, **104**(C5), 11515–11527.

Remund, Q. P. and D. G. Long (2003). Large-scale inverse Ku-band backscatter modeling of sea ice. *IEEE Transactions on Geoscience and Remote Sensing*, **41**(8), 1821–1832.

Remund, Q. P., D. G. Long, and M. R. Drinkwater (1998a). Polar sea ice classification using enhanced resolution NSCAT data. *Proceedings of IGARSS '98 Symposium, Seattle, July 6–10*, pp. 1976–1978.

Remund, Q. P. and D. G. Long (1998b). Sea ice mapping algorithm for QuikSCAT and SeaWinds. *Proceedings of IGARSS '98, Seattle, July 6–10*, pp. 1686–1688.

Remund, Q. P., D. G. Long, and M. R. Drinkwater (2000). An iterative approach to multi-sensor sea ice classification. *IEEE Transactions on Geoscience and Remote Sensing*, **38**(4), 1843–1856.

Renfrew, I. A., J. C. King, and T. Markus (2002). Coastal polynyas in the southern Weddell Sea: Variability in the surface energy budget. *Journal of Geophysical Research*, **107**(C6), 3063, DOI: 10.1029/2000JC000720.

Renwick, J. A. (2002). Southern hemisphere circulation and relations with sea ice and sea surface temperature. *Journal of Climate*, **15**, 3058–3068.

Ribic, C. A., D. G. Ainley, and W. R. Fraser (1991). Habitat selection by marine mammals in the marginal ice zone. *Antarctic Science*, **3**, 181–186.

Richter-Menge, J. A., D. K. Perovich, and W. S. Pegau (2001). Summer ice dynamics during SHEBA and its effect on the ocean heat content. *Annals of Glaciology*, **33,** 201–206.

Richter-Menge, J., S. L. McNutt, J. E. Overland, and R. Kwok (2002). Relating Arctic pack ice stress and deformation under winter conditions. *Journal of Geophysical Research*, **107**, DOI: 10.1029/2000JC000477.

Riggs, G. A., D. K. Hall, and S. A. Ackerman (1999). Sea ice extent and classification mapping with the Moderate Resolution Imaging Spectroradiometer airborne simulator. *Remote Sensing of Environment*, **68**, 152–163.

Riggs, G., D. K. Hall, and J. Key (2001). Initial evaluation of MODIS sea ice observations. *58th Eastern Snow Conference, May 15–17, Ottawa.*

Riggs, G. A., D. K. Hall, and V. V. Salomonson (2003). *MODIS Sea Ice Products User's Guide* (February 2003). Available online at ⟨*http://modis–snow–ice.gsfc.nasa.gov/siugkc.html*⟩.

Rignot, E. and M. R. Drinkwater (1992). On the application of polarimetric radar observations for sea ice classification. *Proceedings of IGARSS '92 Symposium* (Vol. 1), pp. 576–578.

Rignot, E. and M. R. Drinkwater (1994). Winter sea ice mapping from multi-parameter synthetic aperture radar data. *Journal of Glaciology*, **40**(134), 31–45.

Rignot, E., R. Chellappa, and P. Dubois (1992). Unsupervised segmentation of polarimetric SAR data using the covariance matrix. *IEEE Transactions on Geoscience and Remote Sensing*, **30**(4), 697–705.

Rigor, I. G. and R. L. Colony (1997). Sea-ice production and transport of pollutants in the Laptev Sea, 1979–1993. *Science of Total Environment*, **202**, 89–110.

Rigor, I. G., R. L. Colony, and S. Martin (2000). Variations in surface air temperature observations in the Arctic 1979–97. *Journal of Climate*, **13**, 896–914.

Rigor, I. G., J. M. Wallace, and R. L. Colony (2002). Response of sea ice to the Arctic Oscillation. *Journal of Climate*, **15**, 2648–2663.

Rind, D. (2001). *El Niños and La Niñas Rearrange Antarctic Sea Ice*. Available online at ⟨*http://www.giss.nasa.gov/research/intro/rind_01/*⟩.

Rind, D. R., R. Healy, C. Parkinson, and D. Martinson (1995). The role of sea ice in $2 \times CO_2$ climate modelling sensitivity: I. The total influence of sea ice thickness and extent. *Journal of Climate*, **8**, 449–463.

Rind, D., R. Healy, C. Parkinson, and D. G. Martinson (1997). The role of sea ice in $2 \times CO_2$ climate model sensitivity: Part II. Hemispheric dependencies. *Geophysical Research Letters*, **24**(12), 1491–1494.

Rind, D., M. Chandler, J. Lerner, D. G. Martinson, and X. Yuan (2001). The climate response to basin-specific changes in latitudinal temperature gradients and the implications for sea ice variability. *Journal of Geophysical Research*, **106**(D17), 20161–20173.

Rintoul, S. R. (1998). On the origin and influence of Adélie Land Bottom Water. In: S. Jacobs and R. Weiss (eds.), *Ocean, Ice and the Atmosphere: Interactions at the Antarctic Continental Margin* (AGU Antarctic Research Series No. 75). American Geophysical Union, Washington, DC, pp. 151–171.

Rintoul, S. R. (2000). Southern Ocean currents and climate. *Papers and Proceedings of the Royal Society of Tasmania*, **133**, 41–50.

Rintoul, S. and J. Church (2002). The Southern Ocean's global reach: A crucial cog in Earth's heat engine. *Australian Antarctic Magazine*, **4**, 2–4.

Rintoul, S. R. and S. Sokolov (2001). Baroclinic transport variability of the Antarctic Circumpolar Current south of Australia (WOCE repeat section SR3). *Journal of Geophysical Research*, **106**, 2795–2814.

Rintoul, S. R., J. Church, S. Wijffels, E. Fahrbach, M. Garcia, A. Gordon, B. King, R. Morrow, A. Orsi, and K. Speer (2001a). Monitoring and understanding Southern Ocean variability and its impact on climate. In: N. R. Smith and C. J. Koblinsky (eds.), *Observing the Ocean in the 21st Century*. GODAE Project Office, Australian Bureau of Meteorology, Melbourne, pp. 486–508.

Rintoul, S. R., C. Hughes, and D. Olbers (2001b). The Antarctic Circumpolar System. In: G. Siedler, J. Church, and J. Gould (eds.)), *Ocean Circulation and Climate*, Academic Press, New York, pp. 271–302.

Roberts, A., I. Allison, and V. I. Lytle (2001). Sensible- and latent-heat estimates over the Mertz Glacier polynya, East Antarctica, from in-flight measurements. *Annals of Glaciology*, **33**, 377–384.

Roberts, A., P. Heil, W. F. Budd, and R. Hughes (2004). Medium range numerical prediction of Antarctic sea ice. *EGS 1st General Assembly, April 25–30, Nice, France* (Abstract 05531).

Robertson, R., M. Visbeck, A. L. Gordon, and E. Fahrbach (2002). Long-term temperature trends in the deep waters of the Weddell Sea. *Deep-Sea Research II*, **49**(21), 4791–4806.

Robinson, D. A., M. C. Serreze, R. G. Barry, G. Scharfen, and G. Kukla (1992). Large-scale patterns and variability of snowmelt and parameterised surface albedo in the Arctic basin. *Journal of Climate*, **5**(10), 1109–1119.

Robinson, I. S. (2004). *Measuring the Oceans from Space: The Principles and Methods of Satellite Oceanography*. Springer-Praxis, Chichester, UK, 669 pp.

Rodrigues, A., D. Corr, K. Partington, E. Pottier, and L. Ferro-Famil (2003). Unsupervised Wishart classifications of sea ice using entropy, alpha and anisotropy decompositions.

Proceedings of ESA Workshop, POLInSAR: Applications of SAR Polarimetry and Polarimetric Interferometry, ESRIN, Frascati, Italy, January 14–16 (ESA SP-529). Available online at ⟨*http://www.earth.esa.int/polinsar*⟩.

Roessler, C. and R. Iturriaga (1994). Absorption properties of marine-derived material in Arctic sea ice. *Proceedings of SPIE Ocean Optics XII*, **2258**, 933–944.

Romanov, I. P. (1992). *The Ice Cover of the Arctic Basin*. Arctic and Antarctic Research Institute, St. Petersburg, 211 pp. [in Russian].

Ropelewski, C. F. (1983). Spatial and temporal variations in Antarctic sea-ice (1973–1983). *Journal of Climatology and Applied Meteorology*, **22**, 470–473.

Rosborough, G. W., D. G. Baldwin, and W. J. Emery (1994). Precise AVHRR image navigation. *IEEE Transactions on Geoscience and Remote Sensing*, **32**(3), 644–657.

Rosenqvist, A., D. Ichitsubo, Y. Osawa. A. Matsumoto, N. Ito, and T. Hamazaki (2003). A brief overview of the Advanced Land Observing Satellite (ALOS) and its potential for marine applications. *Proceedings of 2nd Workshop on Coastal and Marine Applications of SAR (CMASAR), September 8–12, Svalbard, Norway*.

Ross, R. M., E. E. Hofmann, and L. B. Quetin (eds.) (1996). *Foundations for Ecological Research West of the Antarctic Peninsula* (AGU Antarctic Research Series No. 70). American Geophysical Union, Washington, DC.

Rossow, W. B. and R. A. Schiffer (1999). Advances in understanding clouds from ISCCP. *Bulletin of the American Meteorological Society*, **80**, 2261–2287.

Rothrock, D. A. (1986). Ice thickness distribution: Measurement and theory. In: N. Untersteiner (ed.), *The Geophysics of Sea Ice: B. Physics*. Plenum Press, New York, pp. 551–575.

Rothrock, D. A. and D. R. Thomas (1992). Ice modeling and data assimilation with the Kalman smoother. In: F. D. Carsey (ed.), *Microwave Remote Sensing of Sea Ice*. American Geophysical Union, Washington, DC, pp. 405–418.

Rothrock, D. A. and A. S. Thorndike (1984). Measuring the sea ice floe size distribution. *Journal of Geophysical Research*, **89**(C4), 6477–6486.

Rothrock, D. A., Y. Yu, and G. A. Maykut (1999). Thinning of the Arctic sea-ice cover. *Geophysical Research Letters*, **26**(23), 3469–3472.

Rothrock, D. A., J. Zhang, and Y. Yu (2003). The Arctic ice thickness anomaly of the 1990s: A consistent view from observations and models. *Journal of Geophysical Research*, **108**(C3), 3083, DOI: 10.1029/2001JC001208.

Rott, H., C. Mätzler, D. Strohl, S. Bruzzi, and K. B. Lenhart (1988). *Study on SAR Land Applications for Snow and Glacier Monitoring* (Technical Report 6618/85/F/FL (SC)). European Space Agency, Noordwijk, The Netherlands, 186 pp.

Rott, H., T. Nagler, and R. Scheiber (2003). Snow mass retrieval by means of SAR interferometry. *Proceedings of FRINGE 2003 Workshop, Frascati, Italy, December 1–5* (ESA SP-550).

Roujean, J.-L., C. B. Schaaf, and W. Lucht (2004). Fundamentals of bi-directional reflectance and BRDF modeling. In: M. von Schoenmark, B. Geiger, and H. P. Roeser (eds.), *Reflective Properties of Vegetation and Soil*. Wissenshaft und Technik Verlag, Berlin, pp. 105–120.

Rudels, B., L. G. Anderson, and E. P. Jones (1996). Formation and evolution of the surface mixed layer and halocline of the Arctic Ocean. *Journal of Geophysical Research*, **101**(C4), 8807–8821.

Rudnick, D. L. and M. J. Perry (eds.) (2003). *ALPS: Autonomous and Lagrangian Platforms and Sensors: Report of Workshop, March 31–April 2, La Jolla, California*, 64 pp. Available online at ⟨*www.geo-prose.com/ALPS*⟩.

Ruf, C. S., C. T. Swift, A. B. Tanner, and D. M. LeVine (1998). Interferometeric synthetic aperture microwave radiometry for the remote sensing of the Earth. *IEEE Transactions on Geoscience and Remote Sensing*, **26**, 597–611.

Rum, G. (2003). COSMO-SkyMed: Mission definition and main applications and products. *Proceedings of ESA Workshop, POLInSAR—Applications of SAR Polarimetry and Polarimetric Interferometry, ESRIN, Frascati, Italy, January 14–16* (ESA SP-529). Available online at ⟨*http://www.earth.esa.int/polinsar*⟩.

Ruskai, M. B., G. Beylkin, R. Coifman, I. Daubechies, S. Mallat, Y. Meyer, and L. Raphael (1992). *Wavelets and Their Applications*. Jones & Bartlett, Boston, MA, 474 pp.

Sabine, C. L., R. A. Feely, N. Gruber, R. M. Key, K. Lee, J. L. Bullister, R. Wanninkhof, C. S. Wong, D. W. R. Wallace, B. Tilbrook et al. (2004). The oceanic sink for anthropogenic CO_2. *Science*, **305**, 367–371.

St. Germain, K. M. (1994). A two-phase algorithm to correct for atmospheric effects on the 85 GHz channels of the SSM/I in the Arctic region. *Proceedings of International Geoscience and Remote Sensing Symposium IGARSS '94, Pasadena, California* (Vol. I), pp. 67–69.

St. Germain, K. M., G. A. Poe, and P. W. Gaiser (2002). Polarimetric emission model of the sea at microwave frequencies and comparison with measurements. *Progress in Electromagnetic Research*, **37**, 2–32.

Saitoh, S. (1995). AVHRR on NOAA. In: M. Ikeda and F. W. Dobson (eds.), *Oceanographic Application of Remote Sensing*. CRC Press, Boca Raton, FL, pp. 407–417.

Salisbury, J. W., D. M. D'Aria, and A. Wald (1994). Measurements of TIR spectral reflectance of frost, snow and ice. *Journal of Geophysical Research*, **99**, 24235–24240.

Sakellariou, N. K., H. G. Leighton, and Z. Li (1993). Identification of clear and cloudy pixels at high latitudes from AVHRR radiances. *International Journal of Remote Sensing*, **14**, 2005–2024.

Sandven, S., O. M. Johannessen, M. W. Miles, L. H. Pettersson, and K. Kloster (1999). Barents Sea seasonal ice zone features and processes from ERS-1 SAR: Seasonal Ice Zone Experiment 1992. *Journal of Geophysical Research*, **104**, 15843–15857.

Sandven, S., K. Kloster, H. Tangen, T. Andreasssen, H. Goodwin, and K. Partington (2003). Sea ice mapping using Envisat ASAR wideswath images. *Proceedings of 2nd Workshop on Coastal and Marine Applications of SAR (CMASAR), September 8–12, Svalbard, Norway*.

Sarmiento, J. L., Hughes, T. M. C., Stouffer, R. J., and Manabe, S. (1998). Simulated response of the ocean carbon cycle to anthropogenic climate warming. *Nature*, **393**, 245–249.

Sarmiento, J. L., N. Gruber, M. A. Brzezinski, and J. P. Dunne (2004). High-latitude controls of thermocline nutrients and low latitude biological productivity. *Nature*, **427**, 56–60.

Savage, G., J. Priddle, L. C. Gilpin, U. Bathmann, E. J. Murphy, N. J. P. Owens, R. T. Pollard, D. R. Turner, C. Veth, and P. Boyd (1996). An assessment of the role of the marginal ice zone in the carbon cycle of the Southern Ocean. *Antarctic Science*, **8**, 349–358.

Scambos, T., T. Haran, C. Fowler, J. Maslanik, J. Key, and W. Emery (2002). *AVHRR Polar Pathfinder Twice-daily 1.25 km EASE–Grid Composites* (digital media). National Snow and Ice Data Center, Boulder, CO.

SCAR (1993). *The Role of the Antarctic in Global Change: An International Plan for a Regional Research Programme*. Scientific Committee on Antarctic Research, Cambridge, UK.

Scharfen, G., R. G. Barry, D. A. Robinson, G. Kukla, and M. C. Serreze (1987). Large-scale patterns of snow melt on Arctic sea ice mapped from meteorological satellite data. *Annals of Glaciology*, **9**, 200–205.

Schauer, U. (1995). The release of brine-enriched shelf water from Storfjord into the Norwegian Sea. *Journal of Geophysical Research*, **100**(C8), 16015–16028.

Schauer, U. and E. Fahrbach (1999). A dense bottom water plume in the western Barents Sea: Downstream modification and interannual variability. *Deep Sea Research I*, **46**, 2095–2108.

Scheuchl, B., R. Caves, I. Cumming, and G. Staples (2001). Automated sea ice classification using spaceborne polarimetric SAR data. *Proceedings of IGARSS '01, July 9–13, Sydney*.

Scheuchl, B., I. Hajnsek, and I. Cumming (2002a). Sea ice classification using multi-frequency polarimetric SAR data. *Proceedings of IGARSS '02, Toronto, June*.

Scheuchl, B., I. Hajnsek, and I. Cumming (2002b). Model-based classification of polarimetric SAR sea ice data. *Proceedings of IGARSS '02, Toronto, June*.

Scheuchl, B., I. Hajnsek, and I. Cumming (2003). Classification strategies for polarimetric SAR sea ice data. *Proceedings of ESA Workshop, POLInSAR: Applications of SAR Polarimetry and Polarimetric Interferometry, ESRIN, Frascati, Italy, January 14–16* (ESA SP-529). Available online at ⟨*http://www.earth.esa.int/polinsar*⟩.

Scheuchl, B., R. Caves, D. Flett, R. De Abreu, M. Arkett, and I. Cumming (2004a). The potential of cross-polarization information for operational sea ice monitoring. *Proceedings of ESA Envisat 2004, Salzburg, Austria, September 6–10*. Available online at ⟨*http://sar.ece.ubc.ca/papers/ENVISAT_Symp_2004.pdf*⟩.

Scheuchl, B., D. Flett, R. Caves, and I. Cumming (2004b). Potential of Radarsat-2 data for operational sea ice monitoring. *Canadian Journal of Remote Sensing*, **30**(3), 448–461.

Schledermann, P. (1980). Polynyas and prehistoric settlement patterns. *Arctic*, **33**(2), 292–302.

Schlosser, E. (1988). Optical studies of Antarctic sea ice. *Cold Regions Science and Technology*, **15**, 289–293.

Schmidt, G. A. and J. E. Hansen (1999). Role of sea ice in global change pondered. *EOS, Transactions of American Geophysical Union*, **80**, 317–339.

Schmidt, R. and G. Heygster (1997). Use of ocean wave imaging to detect the marginal ice zone in ERS-SAR images. *Proceedings of 3rd ERS Symposium: Space at the Service of Our Environment, Florence, Italy* (ESA SP-414).

Schmitt, C., Ch. Kottmeier, S. Wassermann, and M. Drinkwater (2004). *Atlas of Antarctic Sea Ice Drift*. Available online at ⟨*http://imkhp7.physik.uni-karlsruhe.de/~eisatlas*⟩.

Schnack-Schiel, S. B. (2003). The macrobiology of sea ice. In: D. N. Thomas and G. S. Dieckmann (eds.), *Sea Ice: An Introduction to Its Physics, Biology, Chemistry, and Geology*. Blackwell Science, Oxford, U.K., pp. 211–239.

Schramm, J. L., M. M. Holland, J. A. Curry, and E. E. Ebert (1997a). Modeling the thermodynamics of a sea ice thickness distribution: 1. Sensitivity to ice thickness resolution. *Journal of Geophysical Research*, **102**, 23079–23091.

Schramm, J. L., M. M. Holland, and J. A. Curry (1997b). The effects of snowfall on a snow–ice-thickness distribution. *Annals of Glaciology*, **25**, 287–291.

Schulson, E. M., D. Iliescu, and C. E. Renshaw (1999). On the initiation of shear faults during brittle compressive failure: A new mechanism. *Journal of Geophysical Research*, **104**(B1), 695–705.

Schulz-Stellenfleth, J. and S. Lehner (2002). Spaceborne synthetic aperture radar observations of ocean waves traveling into sea ice. *Journal of Geophysical Research*, **107**(C8), DOI: 10.1029/2001jc000837.

Schumacher, J. D., K. Aagaard, C. H. Pease, and R. B. Tripp (1983). Effects of a shelf polynya on flow and water properties in the northern Bering Sea. *Journal of Geophysical Research*, **88**, 2723–2732.

Schwartz, K., M. O. Jeffries, and S. Li (1994). Using ERS–1 data to monitor the state of the Arctic Ocean sea ice surface between spring and autumn, 1992. *IGARSS '94 Symposium, August 8–12 Pasadena, CA* (Vol. III). Institute of Electrical and Electronics Engineers, Piscataway, NJ, pp. 1759–1762.

Schweiger, A. J. (2004). Changes in seasonal cloud cover over the Arctic seas from satellite and surface observations. *Geophysical Research Letters*, **31**, L12207. DOI: 10.1029/2004GL020067.

Schweiger, A. J., M. C. Serreze, and J. R. Key (1993). Arctic sea ice albedo: A comparison of two satellite–derived datasets. *Geophysical Research Letters*, **20**, 41–44.

Schweiger, A. J., R. W. Lindsay, J. R. Key, and J. A. Francis (1999). Arctic clouds in multiyear satellite data sets. *Geophysical Research Letters*, **26**(13), 1845–1848.

Schwerdtfeger, P. (1963). The thermal properties of sea ice. *Journal of Glaciology*, **4**(36), 789–807.

Scorer, R. S. (1989). Cloud reflectance variations in channels-3. *International Journal of Remote Sensing*, **10**, 675–686.

Searcy, C., K. Dean, and W. Stringer (1996). A river-coastal sea ice interaction model: Mackenzie River Delta. *Journal of Geophysical Research*, **101**, 8885–8894.

Sedwick, P. N. and G. R. DiTullio (1997). Regulation of algal blooms in Antarctic shelf waters by the release of iron from melting sea ice. *Geophysical Research Letters*, **24**, 2515–2518.

Seibel, B. A. and H. M. Dierssen (2003). Cascading trophic impacts of reduced biomass in the Ross Sea, Antarctica: Just the tip of the iceberg. *Biological Bulletin*, **205**, 93–97.

Semiletov, I., A. Makshtas, S.-I. Akasofu, and E. Andreas (2004). Atmospheric CO_2 balance: The role of Arctic sea ice. *Geophysical Research Letters*, **32**, L05121, DOI: 10.1029/2003GL017996.

Semtner, A. J. (1976). A model for the thermodynamic growth of sea ice in numerical investigation of climate. *Journal of Physical Oceanography*, **6**(3), 379–389.

Sephton, A. J. and K. C. Partington (1998). In: C. Tsatsoulis and R. Kwok (eds.), *Analysis of SAR Data of the Polar Oceans*. Springer-Verlag, Berlin, pp. 259–280.

Serreze, M. (2003). Arctic climate. In: J. R. Holton, J. A. Curry, and J. A. Pyle (eds.), *Encyclopedia of Atmospheric Sciences*. Academic Press, New York, pp. 146–154.

Serreze, M. C., R. G. Barry, and A. S. McLaren (1989). Seasonal variations of ice motion and effects on sea ice concentration in the Canada Basin. *Journal of Geophysical Research*, **94**(C8), 10955–10970.

Serreze, M. C., J. A. Maslanik, J. R. Key, R. F. Kokaly, and D. A. Robinson (1995). Diagnosis of the record minimum in Arctic sea ice area during 1990 and associated snow cover extremes. *Geophysical Research Letters*, **22**(16), 2183–2186.

Serreze, M. C., J. E. Walsh, F. S. Chapin III, T. Osterkamp, M. Dyurgerov, V. Romanovsky, W. C. Oechel, J. Morison, T. Zhang, and R. G. Barry (2000). Observational evidence of recent change in the northern high latitude environment. *Climatic Change*, **46**, 159–207.

Serreze, M. C., J. A. Maslanik, T. A. Scambos, F. Fetterer, J. Stroeve, K. Knowles, C. Fowler, S. Drobot, R. G. Barry, and T. M. Haran (2003). A record minimum Arctic sea ice extent and area in 2002. *Geophysical Research Letters*, **30**(3), 1110, DOI: 10.1029/2002GL016406.

Service Argos (1996). *User Manual*. Service Argos, Washington, DC, pp. 176.

Shapiro, I., R. Colony, and T. Vinje (2003). April sea ice extent in the Barents Sea, 1850–2001. *Polar Research*, **22**(1), 5–10.

Shen, H. H. and V. A. Squire (1998). Wave damping in compact pancake ice fields due to interactions between pancakes. In: M. O. Jeffries (ed.), *Antarctic Sea Ice Physical*

Processes, Interactions and Variability (AGU Antarctic Research Series No. 74). American Geophysical Union, Washington, DC, pp. 317–323.

Shen, H. H., S. F. Ackley, and M. A. Hopkins (2001). A conceptual model for pancake-ice formation in a wave field. *Annals of Glaciology*, **33**, 325–341.

Sheng, Y., L. C. Smith, K. E. Frey, and D. E. Alsdorf (2002). A high temporal resolution data set of ERS scatterometer radar backscatter for research in Arctic and sub-Arctic regions. *Polar Record*, **38**(205), 115–120.

Shi, J. and J. Dozier (1995). Inferring snow wetness using C-band data from SIR-C's polarimetric synthetic aperture radar. *IEEE Transactions on Geoscience and Remote Sensing*, **33**(4), 905–914.

Shine, K. P. and R. G. Crane (1984). The sensitivity of a one-dimensional thermodynamic sea ice model to changes in cloudiness. *Journal of Geophysical Research*, **89**, 10615–10622.

Shine, K. P., A. H. Henderson-Sellers, and R. G. Barry (1984). Albedo–climate feedback: The importance of cloud and cryosphere variability. In: A. L. Berger and C. Nicolis (eds.), *New Perspectives in Climate Modelling*. Elsevier, Amsterdam, pp. 135–155.

Shirasaki, K., H. Enomoto, K. Tateyama, H. Warashina, and A. Watanabe (1998). Observation of sea ice conditions using visible and near-infrared channels in MOS–1/MESSR and ADEOS/AVNIR. *Polar Meteorology and Glaciology*, **12**, 86–96.

Shokr, M. E. (1991). Evaluation of second-order texture parameters for sea ice classification from radar images. *Journal of Geophysical Research*, **C6**, 10625–10640.

Shokr, M. and T. Agnew (1999). Sea ice parameters retrieval using synergistic observations from SSM/I 85.5 GHz and AVHRR. *Proceedings of International Geoscience and Remote Sensing Symposium (IGARSS '99), June 28–July 2, Hamburg, Germany*.

Shokr, M. E. and D. G. Barber (1994). Temporal evolution of physical and dielectric properties of sea ice and snow during the early melt season: Observations from SIMS '90 experiment. *Journal of Glaciology*, **40**(134), 16–30.

Shokr, M. and H. Le (1999). Animation and stereo products from ATSR to support operational and climatic monitoring of Arctic sea ice. *Proceedings of International Workshop on Applications of the ERS Along Track Scanning Radiometer, June 23–25, ESA/ESRIN, Frascati, Italy*.

Shuchman, R. A. and D. G. Flett (2003). SAR measurements of sea ice parameters: Sea ice session overview paper. *Proceedings of 2nd Workshop on Coastal and Marine Applications of SAR (CMASAR), Svalbard, Norway, September 8–12*. Available online at ⟨*http://earth.esa.int/symposia/cmasar_2003/*⟩.

Shuchman, R. A. and R. G. Onstott (1990). Remote sensing of the polar oceans. In: W. O. Smith Jr. (ed.), *Polar Oceanography: Part A. Physical Science*. Academic Press, New York, pp. 123–169.

Shuchman, R. A., O. Johannessen, S. Sandven, E. A. Ericson, L. Pettersson, K. Kloster, C. C. Wackerman, and R. G. Onstott (1993). Marginal ice zone signatures observed by the ERS-1 SAR during SIZEX '92. *International Geoscience and Remote Sensing Symposium (IGARSS '93): Better Understanding of Earth Environment* (Vol. 2), pp. 641–646.

Shuchman, R. A., C. Rufenach, and O. M. Johannessen (1994). Extraction of marginal ice zone thickness using gravity wave imagery. *Journal of Geophysical Research*, **99**(C1), 901–918.

Shuchman, R. A., R. G. Onstott, O. M. Johannessen, S. Sandven, and J. A. Johannessen (2004). Processes at the ice edge: The Arctic. In: C. R. Jackson and J. R. Apel (eds.), *Synthetic Aperture Radar Marine User's Manual*. National Oceanic and Atmospheric Administration, Washington, DC, pp. 373–395.

Shuman, C. A. (2004). ICESat's first year of measurements over the polar ice sheets. *EOS, Transactions of the American Geophysical Union*, **85**(17), Joint Assembly Supplement, Abstract C42A-01.

Shy, T. L. and J. E. Walsh (1996). North Pole ice thickness and association with ice motion history. *Geophysical Research Letters*, **23**(21), 2975–2978.

Shy, T. L., J. E. Walsh, W. L. Chapman, A. H. Lynch, and D. A. Bailey (2000). Sea-ice model validation using submarine measurements of ice draft. *Annals of Glaciology*, **31**, 307–312.

Siedler, G., J. Church, and J. Gould (eds.) (2001). *Ocean Circulation and Climate*. Academic Press, New York, 715 pp.

Siegel, V. and V. Loeb (1995). Recruitment of Antarctic krill (*Euphausia superba*) and possible causes for its variability. *Marine Ecology Progress Series*, **123**(1–3), 45–56.

Sigman, D. M., S. L. Jaccard, and G. H. Haug (2004). Polar ocean stratification in a cold climate. *Nature*, **428**(6978), 31–32.

Signorini, S. R. and D. J. Cavalieri (2002). Modeling dense water production and salt transport from Alaskan coastal polynyas. *Journal of Geophysical Research*, **107**(C9), DOI: 10.1029/2000JC000491.

Sikorski, R. J., K. A. Jensen, and W. Emery (2002). *Ice Surface Temperature: Visible/Infrared Imager/Radiometer Suite Algorithm Theoretical Basis Document, Version 5* (March SBRS Document Y2405). Raytheon Systems, Lanham, MD, 49 pp. Available online at ⟨*http://www.ipo.noaa.gov/Library/viirs_NDX.html*⟩.

Silveira, P. E., M. Van Dyne, and C. Tsatsoulis (1994). Feature matching from SAR Arctic data using neural networks. *Proceedings of IGARSS '94, August 8–12, Pasadena, California.*

Silvestrin, P., M. Berger, Y. H. Kerr, and J. Font (2001). ESA's second Earth Explorer opportunity mission: The Soil Moisture and Ocean Salinity mission—SMOS. *IEEE Geoscience and Remote Sensing Newsletter*, **118**, 11–14.

Similä, M., E. Arjas, M. Mäkynen, and M. Hallikainen (2001). Bayesian classification model for sea ice roughness from scatterometer data. *IEEE Transactions on Geoscience and Remote Sensing*, **39**, 1586–1595.

Simmonds, I. (2003). Modes of atmospheric variability over the Southern Ocean. *Journal of Geophysical Research*, **108**(C4), DOI: 10.1029/2000JC000542.

Simmonds, I. and W. F. Budd (1990). A simple parameterization of ice leads in a general circulation model, and the sensitivity of climate to change in Antarctic ice concentration. *Annals of Glaciology*, **14**, 266–269.

Simmonds, I. and W. F. Budd (1991). Sensitivity of the Southern Hemisphere circulation to leads in the Antarctic pack ice. *Quarterly Journal of the Royal Meteorological Society*, **117**, 1003–1024.

Simmonds I. and T. H. Jacka (1995). Relationships between the interannual variability of Antarctic sea ice and the Southern Oscillation. *Journal of Climate*, **8**, 637–647.

Simmonds, I. and J. C. King (2004). Global and hemispheric climate variations affecting the Southern Ocean. *Antarctic Science*, **16**, 401–413.

Simmonds, I., A. Rafter, T. Cowan, A. B. Watkins, and K. Keay (in press). Large-scale vertical momentum, kinetic energy and moisture fluxes in the Antarctic sea ice region. *Boundary-layer Meteorology*.

Simpson, J. J. and R. H. Keller (1995). An improved fuzzy logic segmentation of sea ice, clouds, and ocean in remotely sensed arctic imagery. *Remote Sensing of Environment*, **54**, 290–312.

Simpson, J. J. and S. R. Yhann (1994). Reduction of noise in AVHRR channel 3 data with minimum distortion. *IEEE Transactions on Geoscience and Remote Sensing*, **32**, 315–328.

Skriver, H., W. Dierking, P. Gudmandsen, T. Le Toan, A. Moreira, K. Papathanassiou, and S. Quegan (2003). Applications of synthetic aperture radar polarimetry. *Proceedings of ESA Workshop, POLInSAR: Applications of SAR Polarimetry and Polarimetric Interferometry, ESRIN, Frascati, Italy, January 14–16* (ESA SP-529). Available online at ⟨*http://www.earth.esa.int/polinsar*⟩.

Slater, P. N. (1980). *Remote Sensing, Optics and Optical Systems*. Addison-Wesley, Reading, MA, 575 pp.

Smetacek, V., P. Assmy, and J. Henjes (2004). The role of grazing in structuring Southern Ocean pelagic ecosystems and biogeochemical cycles. *Antarctic Science*, **16**, 541–558.

Smith, D. M. (1996). Extraction of winter sea ice concentration in the Greenland and Barents Seas from SSM/I data. *International Journal of Remote Sensing*, **17**(13), 2625–2646.

Smith, D. M. (1998a). Recent increase in the length of the melt season of perennial Arctic sea ice. *Geophysical Research Letters*, **25**, 655–658.

Smith, D. M. (1998b). Observation of perennial Arctic sea ice melt and freeze-up using passive microwave data. *Journal of Geophysical Research*, **103**, 27753–27769.

Smith, D. M., E. C. Barrett, and J. C. Scott (1995b). Sea-ice type classification from ERS-1 SAR data based on grey level and texture information. *Polar Record*, **31**(177), 135–146.

Smith, R. C. and S. E. Stammerjohn (2001). Variations of surface air temperature and sea-ice extent in the western Antarctic Peninsula region. *Annals of Glaciology*, **33**, 493–500.

Smith, R. C., B. B. Prezelin, K. S. Baker, R. R. Bidigare, N. P. Boucher, T. Coley, D. Karentz, S. MacIntyre, H. A. Matlick, D. Menziez et al. (1992). Ozone depletion: Ultraviolet radiation and phytoplankton biology in Antarctic waters. *Science*, **255**, 952–959.

Smith, R. C., K. Baker, W. Fraser, E. Hofmann, D. Karl, J. Klinck, L. Quetin, B. Prézelin, R. Ross, W. Trivelpiece et al. (1995a). The Palmer LTER: A long-term ecological research program at Palmer Station, Antarctica. *Oceanography*, **8(3)**, 77–86.

Smith, R. C, S. E Stammerjohn, and K. S Baker (1996). Surface air temperature variations in the western Antarctic peninsula region. In: R. M. Ross, E. E. Hofmann and L. B. Quetin (eds.), *Foundations for Ecological Research West of the Antarctic Peninsula* (AGU Antarctic Research Series No. 70). American Geophysical Union, Washington, DC, pp. 105–121.

Smith, R. C., K. S. Baker, and S. E. Stammerjohn (1998a). Exploring sea ice indexes for polar ecosystem studies. *BioScience*, **48**, 83–93.

Smith, R. C., K. S. Baker, M. L. Byers, and S. E. Stammerjohn (1998b). Primary productivity of the Palmer Long Term Ecological Research Area and the Southern Ocean. *Journal of Marine Systems*, **17**(1–4), 245–259.

Smith, R. C., D. Ainley, K. Baker, E. Domack, S. Emslie, B. Fraser, J. Kennett, A. Leventer, E. Mosley-Thompson, S. Stammerjohn et al. (1999). Marine ecosystem sensitivity to climate change: Historical observations and paleoecological records reveal ecological transitions in the Antarctic Peninsula region. *Bioscience*, **49**, 393–404.

Smith, R. C., K. S. Baker, H. M. Dierssen, S. E. Stammerjohn, and M. Vernet (2001). Variability of primary production in an Antarctic marine ecosystem as estimated using a multi-scale sampling strategy. *American Zoologist*, **41**, 40–56.

Smith, R. C., W. R. Fraser, S. E. Stammerjohn, and M. Vernet (2003a). Palmer Long-Term Ecological Research on the Antarctic marine ecosystem. In: E. W. Domack, A. Leventer, A. Burnett, P. Convey, M. Kirby, and R. Bindschadler (eds.), *Antarctic Peninsula*

Climate Variability: Historical and Paleoenvironmental Perspectives (AGU Antarctic Research Series No. 79). American Geophysical Union, Washington, DC, pp. 131–144.

Smith, R. C., W. R. Fraser, and S. E. Stammerjohn (2003b). Climate variability and ecological response of the marine ecosystem in the Western Antarctic Peninsula (WAP) region. In: D. Greenland, D. G. Goodin, and R. C. Smith (eds.), *Climate Variability and Ecosystem Response at Long-Term Ecological Research (LTER) Sites*. Oxford University Press, New York, pp. 158–173.

Smith, R. C., X. J. Yuan, J. Liu, D. G. Martinson, and S. E. Stammerjohn (2003c). The quasi-quintennial time scale climate variability and ecological response. In: D. Greenland, D. Goodin, and R. C. Smith (eds.), *Climate Variability and Ecological Response*. Oxford University Press, Oxford, UK, pp. 196–206.

Smith, S. D., R. D. Muench, and C. H. Pease (1990). Polynyas and leads: An overview of physical processes and environment. *Journal of Geophysical Research*, **95**, 9461–9479.

Smith, W. O. Jr. (ed.) (1990). *Polar Oceanography: Part A. Physical Science*. Academic Press, New York, 406 pp.

Smith, W. O. Jr. and R. F. Anderson (eds.) (2003). U.S. Southern Ocean JGOFS Program (AESOPS): Part III. *Deep-Sea Research II*, **50**(3–4), Special Issue.

Smith, W. O. Jr. and L. I. Gordon (1997). Hyperproductivity of the Ross Sea (Antarctica) polynya during austral spring. *Geophysical Research Letters*, **24**, 233–236.

Smith, W. O. Jr. and J. M. Grebmeier (1995). *Arctic Oceanography: Marginal Ice Zones and Continental Shelves* (AGU Coastal and Estuarine Studies No. 49). American Geophysical Union, Washington, DC, 287 pp.

Smith, W. O. Jr. and C. Lancelot (2004). Bottom-up versus top-down control in plankton of the Southern Ocean. *Antarctic Science*, **16**, 531–539.

Smith, W. O. Jr. and D. M. Nelson (1985). Phytoplankton bloom produced by a receding ice edge in the Ross Sea: Spatial coherence with the density field. *Science*, **227**, 163–166.

Smith, W. O. Jr. and D. M. Nelson (1986). Importance of ice edge phytoplankton production in the Southern Ocean. *BioScience*, **36**, 251–257.

Smith, W. O. Jr. and E. Sakshaug (1990). Polar phytoplankton. In: W. O. Smith Jr. (ed.), *Polar Oceanography: Part B. Chemistry, Biology, and Geology*. Academic Press, San Diego, pp. 477–525.

Smith, W. O. Jr., N. K. Keene, and J. C. Comiso (1988). Interannual variability in estimated productivity of the Antarctic marginal ice zone. In: D. Sahrhage (ed.), *Antarctic Ocean and Resources Variability*. Springer-Verlag, Berlin, pp. 131–139.

Soh, L.-K. and C. Tsatsoulis (1998). Automated sea ice segmentation (ASIS). *Proceedings of IGARSS '98, Seattle* (Vol. 2), pp. 586–588.

Soh, L.-K., and C. Tsatsoulis (1999a). Texture analysis of SAR sea ice imagery using gray level co-occurence matrices. *IEEE Transactions on Geoscience and Remote Sensing*, **37**(2), 780–795.

Soh, L.-K. and C. Tsatsoulis (1999b). Unsupervised segmentation of ERS and Radarsat sea ice images using using multi-resolution peak detection and aggregated population equalization. *International Journal of Remote Sensing*, **20**(15–16), 3087–3109.

Soh, L.-K., C. Tsatsoulis, and B. Holt (1998). Identifying ice floes and computing ice floe distributions in SAR images. In: C. Tsatsoulis and R. Kwok (eds), *Analysis of SAR Data of the Polar Oceans*. Springer-Verlag, Berlin, pp. 9–34.

Soh, L.-K., C. Tsatsoulis, D. Gineris, and C. Bertoia (2004). ARKTOS: An intelligent system for SAR sea ice image classification. *IEEE Transactions on Geoscience and Remote Sensing*, **42**(1), 229–248.

SooHoo, J. B., A. C. Palmisano, S. T. Kottmeier, M. P. Lizotte, S. L. SooHoo, and C. W. Sullivan (1987). Spectral light absorption and quantum yield of photosynthesis in sea ice microalgae and a bloom of *Phaeocystis pouchetii* from McMurdo Sound, Antarctica. *Marine Ecology Progress Series*, **39**, 175–189.

Speer, K., S. R. Rintoul, and B. Sloyan (2000). The diabatic Deacon cell. *Journal of Physical Oceanography*, **30**, 3212–3222.

Spencer, M. W., C. L. Wu, and D. G. Long (2000). Improved resolution backscatter measurements with the SeaWinds pencil-beam scatterometer. *IEEE Transactions on Geoscience and Remote Sensing*, **38**, 89–104.

Spezie, G. and G. M. R. Manzella (eds.) (1999). *Oceanography of the Ross Sea, Antarctica*. Springer-Verlag, New York, 286 pp.

Spindler, M. (1990). A comparison of Arctic and Antarctic sea ice and the effects of different properties on sea ice biota. In: U. Bleil and J. Thiede (eds.), *Geological History of the Polar Oceans: Arctic versus Antarctic*. Kluwer Academic, Dordrecht, The Netherlands, pp. 173–186.

Squire, V. A. (1995). Geophysical and oceanographic information in the marginal ice zone from ocean wave measurements. *Journal of Geophysical Research*, **100**, 997–998.

Squire, V. A. (1998). The marginal ice zone. In: M. Leppäranta (ed.), *Physics of Ice-covered Seas* (Vol. 1). Helsinki University Printing House, Helsinki, pp. 381–446.

Squire, V. A. and T. W. Dixon (2003). How a region of cracked sea ice affects ice-coupled wave propagation. *Annals of Glaciology*, **33**, 327–332.

Squire, V. A., P. Wadhams, and S. C. Moore (1986). Surface gravity wave processes in the winter Weddell Sea. *EOS, Transactions of the American Geophysical Union*, **67**(44), 1005.

Squire, V. A., J. P. Dugan, P. Wadhams, P. J. Rottier, and A. K. Liu (1995). Of ocean waves and sea ice. *Annual Revue of Fluid Mechanics*, **27**, 115–168.

Stammerjohn, S. E. and R. C. Smith (1996). Spatial and temporal variability of western Antarctic Peninsula sea ice coverage. In: R. M. Ross, E. E. Hofmann and L. B. Quetin (eds.), *Foundations for Ecological Research West of the Antarctic Peninsula* (AGU Antarctic Research Series No. 70). American Geophysical Union, Washington, DC, pp. 81–104.

Stammerjohn, S. E. and R. C. Smith (1997). Opposing Southern Ocean climate patterns as revealed by trends in regional sea ice coverage. *Climatic Change*, **37**(4), 617–639.

Stammerjohn, S. E., M. R. Drinkwater, R. C. Smith, and X. Liu (2003). Ice–atmosphere interactions during sea-ice advance and retreat in the western Antarctic Peninsula region. *Journal of Geophysical Research*, **108**(C10), 27–1, 3329, DOI: 10.1029/2002JC001543.

Stamnes, K. (1999a). *Cloud Detection on Snow/Sea Ice (CTSK1)* (draft algorithm description, NASDA Internal Document 3.4.1). NASDA, Tokyo, pp. 1–28.

Stamnes, K. (1999b). *Snow Grain Size/Impurities (CTSK2b1)* (draft algorithm description, NASDA Internal Document 3.4.2). NASDA, Tokyo, pp. 1–27.

Stamnes, K., S.-C. Tsay, W. Wiscombe, and K. Jayaweera (1988). Numerically stable algorithm for discrete-ordinate-method radiative transfer in multiple scattering and emitting layered media. *Applied Optics*, **27**, 2502–2509.

Staples, G. (2003). Radarsat-2 mission update and applications overview. *Proceedings of ESA Workshop, POLInSAR: Applications of SAR Polarimetry and Polarimetric Interferometry, ESRIN, Frascati, Italy, January 14–16* (ESA SP-529). Available online at ⟨*http://www.earth.esa.int/polinsar*⟩.

Staples, G., J. Hornsby, W. Branson, K. O'Neill, and P. Rolland (2004). Turning the scientifically possible into the operationally practical: Radarsat-2 commercialization plan. *Canadian Journal of Remote Sensing*, **30**(3), 408–414.

Steele, M. (1992). Sea ice melting and floe geometry in a simple ice-ocean model. *Journal of Geophysical Research*, **97**(C11), 17729–17738.

Steele, M. and T. Boyd (1998). Retreat of the cold halocline layer in the Arctic Ocean. *Journal of Geophysical Research*, **103**(55), 10419–10435.

Steele, M. and G. M. Flato (2000). Sea ice growth, melt and modelling: A survey. In: E. L. Lewis (ed.), *The Freshwater Budget of the Arctic Ocean* (NATO Science Series No. 70). NATO, La Spezia, Italy, pp. 549–587.

Steele, M., J. H. Morison, and T. B. Curtin (1995). Halocline water formation in the Barents Sea. *Journal of Geophysical Research*, **100**(C1), 881–894.

Steele, M., D. Thomas, D. Rothrock, and S. Martin (1996). A simple model study of the Arctic Ocean freshwater balance, 1979–1985. *Journal of Geophysical Research*, **101**, 20833–20848.

Steffen, K. (1986). Atlas of sea ice types, deformation processes and openings in sea ice. *Zürcher Geographische Schriften*, **20**, 55.

Steffen, K. (1987). Bidirectional reflectance of snow at 500–600 nm, large scale effects of seasonal snow cover. *Proceedings of the IAHS*, **166**, 415–425.

Steffen, K. (1995). AVHRR applications for ice surface studies. In: M. Ikeda and F. Dobson (eds.), *Oceanographic Application of Remote Sensing*. CRC Press, New York, pp. 307–320.

Steffen, K. (1997). Effect of solar zenith angle on snow anisotropic reflectance. In: W. L. Smith and K. Stamnes (eds.), *IRS'96: Current Problems in Atmospheric Radiation, Proceedings of International Radiation Symposium, Fairbanks, AK, August 19–24, 1996*. A. Deepak, Hampton, VA, pp. 41–44.

Steffen, K. (1999). *Aerosol, Cloud, Climate Interactions* (NASA Report). NASA, Washington, D.C., pp.10.

Steffen, K. (2003). Validation of AMSR sea-ice products in the Bellingshausen Sea, Antarctica. *ACSYS/CliC Ice and Climate News*, **4**, 10–11.

Steffen, K. and J. Heinrichs (1994). Feasibility of sea-ice typing with synthetic aperture radar (SAR): Merging of Landsat Thematic Mapper and ERS-1 SAR imagery. *Journal of Geophysical Research*, **99**(C11), 22413–22424.

Steffen K. and J. M. Maslanik (1988). Comparison of Nimbus 7 Scanning Multichannel Microwave Radiometer radiance and derived sea ice concentration with Landsat imagery for the North Water area of Baffin Bay. *Journal of Geophysical Research*, **93**(C9), 10769–10781.

Steffen, K. and A. J. Schweiger (1990). A multi-sensor approach to sea ice classification for the validation of DMSP SSM/I passive microwave derived sea ice products. *Photogrammetric Engineering and Remote Sensing*, **56**(1), 75–82.

Steffen, K. and A. Schweiger (1991). NASA Team algorithm for sea ice concentration retrieval from Defense Meteorological Satellite Program Special Sensor Microwave/Imager: Comparison with Landsat satellite imagery. *Journal of Geophysical Research*, **96**(C12), 21971–21987.

Steffen, K., J. Key, D. Cavalieri, J. Comiso, P. Gloersen, K. S. Germain, and I. Rubinstein (1992). Microwave remote sensing of sea ice. In: F. D. Carsey (ed.), *The Estimation of Geophysical Parameters Using Passive Microwave Algorithms in Microwave Remote Sensing of Sea Ice*. American Geophysical Union, Washington, DC, pp. 201–231.

Steffen, K., R. Bindschadler, C. Casassa, J. Comiso, D. Eppler, F. Fetterer, J. Hawkins, J. Key, D. Rothrock, R. Thomas, R. Weaver, and R. Welch (1993). Snow and ice applications of AVHRR in polar regions: Report of a workshop held in Boulder, Colorado, May 20, 1992. *Annals of Glaciology*, **17**, 1–16.

Stein, R. and R. W. Macdonald (eds.) (2003). *The Organic Carbon Cycle in the Arctic Ocean*. Springer-Verlag, Berlin, 363 pp.

Steiner, N. (2001). Introduction of variable drag coefficients into sea-ice models. *Annals of Glaciology*, **33**, 181–186.

Stern, H. L. (ed.) (1998). *The Critical Role of SAR in Earth System Science* (a white paper). Alaska SAR Facility User Working Group, Alaska SAR Facility, Fairbanks, AK.

Stern, H. L. and R. E. Moritz (2002). Sea ice kinematics and surface properties from Radarsat SAR during the SHEBA drift. *Journal of Geophysical Research*, **107**(C10), DOI: 10.1029/2000JC000472.

Stern, H. L., R. Kwok, S. Li, and M. Milkovich (1993). Ice motion validation team report. In: R. Kwok and G. Cunningham (eds.), *Alaska SAR Facility Geophysical Processor System Data User's Handbook,Version 2.0* (JPL Document D-9526). Jet Propulsion Laboratory, Pasadena, CA, pp. 101–108.

Stern, H. L., D. A. Rothrock, and R. Kwok (1995). Open water production in Arctic sea ice: Satellite measurements and model parameterizations. *Journal of Geophysical Research*, **100**(C10), 20601–20612.

Stewart, F. J. and C. H. Fritsen (2004). Bacteria–algae relationships in Antarctic sea ice. *Antarctic Science*, **16**(2), 143–156.

Stewart, R. H. (1985). *Methods of Satellite Oceanography*. University of California Press, Berkeley, 360 pp.

Stierle, A. P. and H. Eicken (2002). Sedimentary inclusions in Alaskan coastal sea ice: Small-scale distribution, interannual variability and entrainment requirements. *Arctic and Antarctic Alpine Research*, **34**(4), 103–114.

Stiles, W. H. and F. T. Ulaby (1980). The active and passive microwave response to snow parameters. 1: Wetness. *Journal of Geophysical Research*, **85**(C2), 1037–1044.

Stirling, I. (1980). The biological significance of polynyas in the Canadian Arctic. *Arctic*, **33**, 303–315.

Stirling, I. (1997). The importance of polynyas, ice edges and leads to marine mammals and birds. *Journal of Marine Systems*, **10**, 9–21.

Stirling, I., and H. Cleator (eds.) (1981). *Polynyas in the Canadian Arctic* (Vol. 1, CWS Occasional Paper 45). Canadian Wildlife Service, Ottawa, 70 pp.

Stirling, I. and A. E. Derocher (1993). Possible impacts of climate warming on polar bears. *Arctic*, **46**, 240–245.

Stirling, I., N. J. Lunn, J. Iacozza, C. Elliott, and M. Obbard (2004). Polar bear distribution and abundance on the south–western Hudson Bay coast during open water season, in relation to population trends and annual ice patterns. *Arctic*, **126**(1), 15–26.

Stoffelen, A. and D. Anderson (1997). Scatterometer data interpretation: Derivation of the transfer function CM0D4. *Journal of Geophysical Research*, **102**, 5767–5780.

Stogryn, A. (1971). Equations for calculating the dielectric constant of saline water. *IEEE Transactions in Microwave Theory and Techniques*, **19**, 733–736.

Stogryn, A. and G. J. Desargant (1985). The dielectric properties of brine in sea ice at microwave frequencies. *IEEE Transactions on Antennas and Propagation*, **AP-33**(5), 523–532.

Stoll, M. H. C., H. Thomas, H. J. W. de Baar, I. Zondervan, E. de Jong, U. V. Bathmann, and E. Fahrbach (2002). Biological versus physical processes as drivers of large oscillations

of the air–sea CO_2 flux in the Antarctic Marginal Ice Zone during summer. *Deep-sea Research I*, **49**, 1651–1667.

Stone, R. (1998). Variations in western Arctic temperatures in response to cloud radiative and synoptic-scale influences. *Journal of Geophysical Research*, **102**(D18), 21769–21776.

Stone, R. and J. Key (1993). The detectability of winter sea ice leads in thermal satellite data under varying atmospheric conditions. *Journal of Geophysical Research*, **98**(C7), 12469–12482.

Stössel, A., J. M. Oberhuber, and E. Maier-Reimer (1996). On the representation of sea ice in global ocean general circulation models. *Journal of Geophysical Research*, **101**, 18193–18212.

Strahler, A. H., W. Lucht, C. B. Schaaf, T. Tsang, F. Gao, X. Li, J.-P. Muller, P. Lewis, and M. P. Barnsley (1999). *Algorithm Theoretical Basis Document, MODIS Product ID: MOD34 (MODIS BRDF/Albedo), Version 5.0*. NASA, Washington, DC.

Strahler, A. H., C. B. Schaaf, J.-P. Muller, F. Gao, X. Li, M. P. Barnsley, P. Lewis, and W. Lucht (2003). *MODIS BRDF/Albedo Product (MOD43B) User's Guide*. NASA, Washington, DC. Available online at ⟨*http://geography.bu.edu/brdf/userguide/index.html*⟩.

Strass, V. H. (1998). Measuring sea ice draft and coverage with moored upward looking sonars. *Deep-Sea Research I*, **45**, 795–818.

Strass, V. H. and E. Fahrbach (1998). Temporal and regional variation of sea ice draft and coverage in the Weddell Sea obtained from Upward Looking Sonars. In: M. O. Jeffries (ed.), *Antarctic Sea Ice: Physical Processes, Interactions and Variability* (AGU Antarctic Research Series No. 74). American Geophysical Union, Washington, DC, pp. 123–139.

Stringer, W. J. and J. E. Groves (1991). Location and areal extent of polynyas in the Bering and Chukchi Seas. *Arctic*, **44**, 164–171.

Stroeve, J. (1998). *Impact of Various Processing Options on SSM/I-derived Brightness Temperatures* (NSIDC Special Report 7). National Snow and Ice Data Center, University of Colorado, Boulder, CO. Available online at ⟨*http://nsidc.org/pubs/special/7/*⟩.

Stroeve, J. C. and A. W. Nolin (2002). New methods to infer snow albedo from the MISR instrument with applications to the Greenland Ice Sheet. *IEEE Transactions on Geoscience and Remote Sensing*, **40**(7), 1616–1625.

Stroeve, J. and J. Smith (2001). *Comparison of Near Real-time DMSP SSM/I Daily Polar Gridded Products and SSM/I Polar Gridded Products*(NSIDC Special Publication 10). National Snow and Ice Data Center, Boulder, CO. Available online at ⟨*http://nsidc.org/NASA/GUIDE/SSMI/special_publication10.pdf*⟩.

Stroeve, J., M. Haefliger, and K. Steffen (1996). Surface temperature from ERS-1 ATSR infrared thermal satellite data in polar regions. *Journal of Applied Meteorology*, **35**(8), 1231–1239.

Stroeve, J., A. Nolin, and K. Steffen (1997). Comparison of AVHRR-derived and *in situ* surface albedo over the Greenland Ice Sheet. *Remote Sensing of Environment*, **62**, 262–276.

Stroeve, J., J. Maslanik, and X. Li (1998). An intercomparison of DMSP F11- and F13-derived sea ice products. *Remote Sensing of Environment*, **64**, 132–152.

Stroeve, J. C., M. C. Serreze, F. Fetterer, T. Arbetter, W. Meier, J. Maslanik, and K. Knowles (2005). Tracking the Arctic's shrinking ice cover: Another extreme September minimum in 2004. *Geophysical Research Letters*, **32**, L04501, DOI: 10.1029/2004GL021810.

Sturm, M. (2002). Snow cover. *The Encyclopedia of Atmospheric Sciences*. Academic Press, New York.

Sturm, M., J. Holmgren, M. Konig, and K. Morris (1997). The thermal conductivity of seasonal snow. *Journal of Glaciology*, **43**(143), 26–41.

Sturm, M., K. Morris, and R. Massom (1998). The winter snow cover of the West Antarctic pack ice: Its spatial and temporal variability. In: M. O. Jeffries (ed.), *Antarctic Sea Ice Physical Processes, Interactions and Variability* (AGU Antarctic Research Series No. 74). American Geophysical Union, Washington, DC, pp. 1–18.

Sturm, M., J. Holmgren, and D. K. Perovich (2001). Spatial variations in the winter heat flux at SHEBA: Estimates from snow–ice interface temperatures. *Annals of Glaciology*, **33**, 213–220.

Sturm, M., J. Holmgren, and D. K. Perovich (2002a). Winter snow cover on the sea ice of the Arctic Ocean at the Surface Heat Budget of the Arctic Ocean (SHEBA): Temporal evolution and spatial variability. *Journal of Geophysical Research*, **107**(C10), 8047, DOI: 10.1029/2000JC000400.

Sturm, M., D. K. Perovich, and J. Holmgren (2002b). Thermal conductivity and heat transfer through the snow and ice of the Beaufort Sea. *Journal of Geophysical Research*, **107**(C21), 8043, DOI: 10.1029/2000JC000409.

Sullivan, C. W., K. R. Arrigo, C. R. McClain, J. C. Comiso, and J. Firestone (1993). Distributions of phytoplankton blooms in the Southern Ocean. *Science*, **262**, 1832–1837.

Sun, Y. (1996). Automatic ice motion retrieval from ERS-1 SAR images using the optical flow method. *International Journal of Remote Sensing*, **17**(1), 2059–2087.

Suttles, J. T., R. N. Green, P. Minnis, G. L. Smith, W. F. Staylor, B. A. Wielicki, I. J. Walker, D. F. Young, V. R. Taylor, and L. L. Stowe (1988). *Angular Radiation Models for Earth–Atmosphere Systems. Volume I: Shortwave Radiation* (NASA RP-1184). NASA, Washington, D.C., 147 pp.

Svendsen, E., K. Kloster, B. Farrelly, O. M. Johannessen, J. A. Johannessen, W. J. Campbell, P. Gloersen, D. Cavalieri, and C. Mätzler (1983). Norwegian Remote Sensing Experiment: Evaluation of the Nimbus 7 Scanning Multichannel Microwave Radiometer for sea ice research. *Journal of Geophysical Research*, **88**, 2781–2991.

Svendsen, E., C. Mätzler, and T. C. Grenfell (1987). A model for retrieving total sea ice concentration from a spaceborne dual-polarized passive microwave instrument operating near 90 GHz. *International Journal of Remote Sensing*, **8**, 1479–1487.

Swadling, K. M., A. D. McPhee, and A. McMinn (2000). Spatial distribution of copepods in fast ice of eastern Antarctica. *Polar Bioscience*, **13**, 55–65.

Swift, C. T. (1999). Seasat scatterometer observations of sea ice. *IEEE Transactions on Geoscience and Remote Sensing*, **37**(2), 716–723.

Swift, C. T. and D. J. Cavalieri (1985). Passive microwave remote sensing for sea ice research. *EOS, Transactions of the American Geophysical Union*, **66**(49), 1210–1212.

Swift, C. T., L. S. Fedor, and R. O. Ramseier (1985). An algorithm to measure sea ice concentration with microwave radiometers. *Journal of Geophysical Research*, **90**, 1087–1099.

Swift, C. T., K. St. Germain, K. C. Jezek, S. P. Gogineni, A. J. Gow, D. K. Perovich, T. C. Grenfell, and R. G. Onstott (1992). Laboratory investigations of the electromagnetic properties of artificial sea ice: The passive microwave signatures of sea ice. In: F. D. Carsey (ed.), *Microwave Remote Sensing of Sea Ice* (AGU Monograph Series No. 68). American Geophysical Union, Washington, DC, pp. 177–200.

Swift, J. H., E. P. Jones, K. Aagaard, E. C. Carmack, M. Hingston, R. W. Macdonald, F. A. McLaughlin, and R. G. Perkin (1997). Waters of the Makarov and Canada basins. *Deep-sea Research II*, **44**, 1503–1529.

Takizawa, T., K. I. Ohshima, S. Ushio, T. Kawamura, and H. Enomoto (1994). Temperature structure and characteristics appearing on SSM/I images of the Cosmonaut Sea, Antarctica. *Annals of Glaciology*, **20**, 298–306.

Tateyama, K. and H. Enomoto (2000). Estimation of the volume of sea ice cover in the Sea of Okhotsk and related atmospheric conditions for 1991/92–1998/99 winters. *Polar Meteorology and Glaciology*, **14**, 58–67.

Tateyama, K. and H. Enomoto (2001). Observation of sea ice thickness fluctuation in the seasonal ice covered area during 1992–1999 winters. *Annals of Glaciology*, **33**, 449–456.

Tateyama, K., H. Enomoto, S. Takahashi, K. Shirsaki, K. Hyakutake, and F. Nishio (2000). New passive microwave remote sensing technique for sea ice in the Sea of Okhotsk using 85-GHz channel of DMSP SSM/I. *Bulletin of Glaciological Research*, **17**, 23–30.

Tateyama, K., H. Enomoto, T. Toyota, and S. Uto (2002). Sea ice thickness estimated from passive microwave radiometers. *Polar Meteorology and Glaciology*, **16**, 15–31.

Taylor, V. R. and L. L. Stowe (1984). Reflectance characteristics of uniform Earth and cloud surfaces derived from Nimbus-7 ERB. *Journal of Geophysical Research*, **89**, 4981–4996.

Thekaekara, M. P. (1974). Extraterrestrial solar spectrum, 3000–6100 Å at 1-Å intervals. *Applied Optics*, **13**, 518–522.

Thiele, D. and P. C. Gill (1999). Cetacean observations during a winter voyage into Antarctic sea ice south of Australia. *Antarctic Science*, **11**(1), 48–53.

Thomas, D. N. and G. S. Dieckmann (eds.) (2003). *Sea Ice: An Introduction to Its Physics, Chemistry, Biology and Geology*. Blackwell Scientific, Oxford, UK, 424 pp.

Thomas, D. N. and S. Papadimitriou (2003). Biogeochemistry of sea ice. In: D. N. Thomas and G. S. Dieckmann (eds.), *Sea Ice: An Introduction to Its Physics, Biology, Chemistry and Geology*. Blackwell Scientific, Oxford, UK, pp. 267–302.

Thomas, D. N., R. J. Lara, H. Eicken, G. Kattner, and A. Skoog (1995). Dissolved organic matter in Arctic multi-year sea ice during winter: Major components and relationship to ice characteristics. *Polar Biology*, **15**, 477–483.

Thomas, D. R. (1993). Arctic sea ice signatures for passive microwave algorithms. *Journal of Geophysical Research*, **98**(C6), 10037–10052.

Thomas, D. R. (1999). The quality of sea ice velocity estimates. *Journal of Geophysical Research*, **104**(C6), 13627–13655.

Thomas, D. R. and D. A. Rothrock (1993). The Arctic Ocean ice balance: A Kalman smoother estimate. *Journal of Geophysical Research*, **98**(C6), 10053–10067.

Thomas, D. R., S. Martin, D. Rothrock, and M. Steele (1996). Assimilating satellite concentration data into an Arctic sea ice mass balance model, 1979–1985. *Journal of Geophysical Research*, **101**(C9), 20849–20868.

Thomas, I. L. and P. J. Minnett (1986). An introductory review of the measurement of ocean surface wind vectors with a satellite radar scatterometer. *International Journal of Remote Sensing*, **7**(3), 309–323.

Thomas, R. H. (1995). *Polar Research from Satellites*. Joint Oceanographic Institutions, Washington, DC, 91 pp.

Thompson, D. W. J. and S. Solomon (2002). Interpretation of recent Southern Hemisphere climate change. *Science*, **296**(5569), 895–899.

Thompson, D. W. J. and J. M. Wallace (1998). The Arctic Oscillation signature in the wintertime geopotential height and temperature fields. *Geophysical Research Letters*, **25**, 1297–1300.

Thompson, D. W. J. and J. M. Wallace (2000). Annular modes in extra-tropical circulation: Part I. Month-to-month variability. *Journal of Climate*, **13**, 1000–1016.

Thomsen, B. B., S. V. Nghiem, and R. Kwok (1998a). Polarimetric C-band SAR observations of sea ice in the Greenland Sea. *Proceedings of IGARSS '98, Seattle,* pp. 2502–2504.

Thomsen, B. B., L. T. Pedersen, H. Skriver, and W. Dierking (1998b). Polarimetric EMISAR observations of sea ice in the Greenland Sea. In: P. Gudmandsen (ed.), *Future Trends in Remote Sensing*. Balkema, Rotterdam, pp. 345–351.

Thorndike, A. S. (1986). Kinematics of sea ice. In: N. Untersteiner (ed.), *The Geophysics of Sea Ice* (NATO ASI Ser. B, No. 146). Plenum Press, New York, pp. 489–550.

Thorndike, A. S. and R. Colony (1982). Sea ice motion in response to geostrophic winds. *Journal of Geophysical Research*, **87**(C8), 5845–5852.

Thorndike, A. S., D. S. Rothrock, G. A. Maykut, and R. Colony (1975). The thickness distribution of sea ice. *Journal of Geophysical Research*, **80**(33), 4501–4513.

Thorndike, A. S., C. Parkinson, and D. A. Rothrock (eds.) (1992). *Report of the Sea Ice Thickness Workshop, November 19–21, 1991, New Carrolton, MD*. Polar Science Center, University of Washington, Seattle, 41 pp.

Tilzer, M. M., B. von Bodungen, and V. Smetacek (1985). Light-dependence of phytoplankton photosynthesis in the Antarctic Ocean: Implications for regulating productivity. In: W. R. Siegfried, P. R. Condy and R. M. Laws (eds.), *Antarctic Nutrient Cycles and Food Webs*. Springer-Verlag, Berlin, pp. 60–69.

Timmermann, R., A. Beckmann, and H. H. Helmer (2001). The role of sea ice in the freshwater budget of the Weddell Sea, Antarctica. *Annals of Glaciology*, **33**, 419–424.

Timmermann, R., H. Goosse, G. Madec, T. Fichefet, C. Ethe, and V. Dulière (2004). On the representation of high latitude processes in the ORCALIM global coupled sea ice–ocean model. *Ocean Modelling*, **8**, 175–2001.

Tin, T. and M. O. Jeffries (2001). Sea ice thickness and roughness in the Ross Sea, Antarctica. *Annals of Glaciology*, **33**, 187–193.

Tin, T., M. O. Jeffries, M. Lensu, and J. Tuhkuri (2003). Estimating the thickness of ridged sea ice from ship observations in the Ross Sea. *Antarctic Science*, **15**(1), 47–54.

Tiuri, M., A. Sihvola, E. Nyfors, and M. Hallikainen (1984). The complex dielectric constant of snow at microwave frequencies. *IEEE Journal of Oceanic Engineering*, **9**(5), 377–382.

Tison, J.-L., R. D. Lorrain, A. Bouzette, M. Dini, A. Bondesan, and M. Stiévenard (1998). Linking landfast sea ice variability to marine ice accretion at Hells Gate Ice Shelf, Ross Sea. In: M. O. Jeffries (ed.), *Antarctic Sea Ice: Physical Processes, Interactions and Variability* (AGU Antarctic Research Series No. 74). American Geophysical Union, Washington, DC, pp. 375–407.

Tjuata, S., A. K. Fung, and M. Dawson (1993). An analysis of scattering and emission from sea ice. *Remote Sensing Review*, **7**, 83–106.

Tjuata, S., A. K. Fung, and J. C. Comiso (1995). Effects of snow cover on sea ice emission. *IEEE IGARSS '95 Digest*, **1**, 697–699.

Tomczak, M. and J. S. Godfrey (2003). *Regional Oceanography: An Introduction* (2nd edn.). Daya, New Delhi, 390 pp.

Tonboe, R. (2001). QuikSCAT: SeaWinds scatterometer observations of sea ice types around Greenland. *Proceedings of SPIE 2001 8th International Symposium on Remote Sensing, Toulouse, France*.

Tonboe, R. and R. Ezraty (2002). Monitoring of new-ice in Greenland waters. *Proceedings of IGARSS '02, Toronto*.

Tonboe, R. and J. Haarpaintner (2003). *Implementation of QuikScat SeaWinds Data in the EUMETSAT Ocean and Sea Ice Product* (Technical Report 03–13). Danish Meteorological Institute, Copenhagen, 41 pp.

Toudal, L. and M. D. Coon (2001). Interannual variability of the sea-ice-induced salt flux in the Greenland Sea. *Annals of Glaciology*, **33**, 385–390.

Toudal, L., K. Q. Hansen, H. Valeur, P. Wadhams, E. Aldworth, and J. C. Comiso (1999). Mapping of ice in the Odden by satellite and airborne remote sensing. *Deep-sea Research II*, **46**(6–7), 1255–1274.

Toutin, T. and P. Cheng (2002). QuickBird: A milestone for high resolution mapping. *Earth Observation Magazine*, **11**(4), 14–18.

Touzi, R., W. M. Boerner, J. S. Lee, and E. Lueneburg (2004). A review of polarimetry in the context of synthetic aperture radar: Concepts and information extraction. *Canadian Journal of Remote Sensing*, **30**(3), 380–407.

Tremblay, L.-B. and L. A. Mysak (1998). On the origin and evolution of sea-ice anomalies in the Beaufort–Chukchi Sea. *Climate Dynamics*, **14**, 451–460.

Treuhaft, R. N. and P. Siqueria (2000). Vertical structure of vegetated land surfaces from interferometric and polarimetric radar. *Radio Science*, **35**(1), 141–177.

Trevena, A. J., G. B. Jones, S. W. Wright, and R. L. Van Den Enden (2003). Profiles of dimethylsulphoniopropionate (DMSP), algal pigments, nutrients, and salinity in the fast ice of Prydz Bay, Antarctica. *Journal of Geophysical Research*, **108**(C5), 3145, DOI: 10.1029/2002JC001369.

Trodahl, H. J., R. G. Buckley, and M. Vignaux (1989). Anisotropic light radiance in and under sea ice. *Cold Regions Science and Technology*, **16**, 305–308.

Trull, T., R. Matear, and B. Tilbrook (2002). The Southern Ocean and the carbon cycle: Unfinished business. *Australian Antarctic Magazine*, **4**, 6–8.

Tsai, W., J. E. Graf, C. Winn, J. N. Huddleston, S. Dunbar, M. H. Freilich, F. J. Wentz , D. G. Long, and W. L. Jones (1999). Post-launch sensor verification and calibration of the NASA Scatterometer. *IEEE Transactions on Geoscience and Remote Sensing*, **GE-37**(3), 1517–1542.

Tsatsoulis, C. and R. Kwok (eds.) (1998a). *Analysis of SAR Data of the Polar Oceans: Recent Advances*. Springer-Verlag, Berlin, 290 pp.

Tsatsoulis, C. and R. Kwok (eds.) (1998b). Recent advances in the analysis of SAR data of the polar oceans. *Analysis of SAR Data of the Polar Oceans: Recent Advances*. Springer-Verlag, Berlin, pp. 3–8.

Tschudi, M. A., J. A. Maslanik, and J. A. Curry (1997). Determination of areal surface feature coverage in the Beaufort Sea using aircraft video data. *Annals of Glaciology*, **25**, 434–438.

Tschudi, M. A., J. A. Curry, and J. A. Maslanik (2001). Airborne observations of summertime surface features and their effect on surface albedo during FIRE/SHEBA. *Journal of Geophysical Research*, **106**, 15335–15344.

Tschudi, M. A., J. Maslanik, and D. K. Perovich (2005). Melt pond coverage on Arctic sea ice from MODIS. *Proceedings of 8th Conference on Polar Meteorology and Oceanography, San Diego, California, January 8–14*.

Tucker, W. B., A. J. Gow, and W. F. Weeks (1987). Physical properties of summer sea ice in the Fram Strait. *Journal of Geophysical Research*, **92**, 6787–6803.

Tucker, W. B., D. K. Perovich, A. J. Gow, W. F. Weeks, and M. R. Drinkwater (1992). Physical properties of sea ice relevant to remote sensing. In: F. D. Carsey (ed.), *Microwave Remote Sensing of Sea Ice* (AGU Monograph No. 28). American Geophysical Union, Washington, DC, pp. 9–28.

Tucker, W. B., A. J. Gow, D. A. Meese, and H. W. Bosworth (1999). Physical characteristics of summer sea ice across the Arctic Ocean. *Journal of Geophysical Research*, **104**, 1489–1504.

Tucker, W. B., J. W. Weatherly, D. T. Eppler, L. D. Farmer, and D. L. Bentley (2001). Evidence for rapid thinning of sea ice in the western Arctic Ocean at the end of the 1980s. *Geophysical Research Letters*, **28**(14), 2851–2854.

Turner, J. (2004). The El Niño–Southern Oscillation and Antarctica. *International Journal of Climatology*, **24**, 1–31.

Turner, J. and S. Pendlebury (2004). *The International Antarctic Weather Forecasting Handbook*. British Antarctic Survey, Cambidge, UK, 663 pp. Available at ⟨*http://www.nerc-bas.ac.uk/public/icd/jtu/ftpinst.html*⟩.

Turner, S. M., P. D. Nightingale, W. Broadgate, and P. S. Liss (1995). The distribution of dimethyl sulfide and dimethylsulfonioproprionate in the Antarctic waters and sea ice. *Deep-sea Research I*, **42**, 1059–1080.

Turner, J., S. R. Colwell, G. J. Marshall, T. A. Lachlan-Cope, A. M. Carleton, P. D. Jones, V. Lagun, P. A. Reid, and S. Iagovkina (2005). Antarctic climate change during the last 50 years. *International Journal of Climatology*, **25**, 279–294.

Tynan, C. T. (1998). Ecological importance of the southern boundary of the Antarctic Circumpolar Current. *Nature*, **392**, 708–710.

Tynan, C. T. and D. P. DeMaster (1997). Observations and predictions of Arctic climatic change: Potential effects on marine mammals. *Arctic*, **50**(4), 308–322.

Ulaby, F. T. and C. Elachi (1990). *Radar Polarimetry for Geoscience Applications*. Artech House, Dedham, MA, 364 pp.

Ulaby, F. T., R. K. Moore, and A. K. Fung (1981). *Microwave Remote Sensing Active and Passive: Volume I. Microwave Remote Sensing Fundamentals and Radiometry*. Addison-Wesley, Reading, MA, 456 pp.

Ulaby, F. T., R. K. Moore, and A. K. Fung (1982). *Microwave Remote Sensing: Active and Passive: Volume II. Radar Remote Sensing and Surface Scattering and Emission Theory*. Addison-Wesley, Reading, MA, 609 pp.

Ulaby, F. T., R. K. Moore, and A. K. Fung (1986a). *Microwave Remote Sensing: Active and Passive: Vol. III. Volume Scattering and Emission Theory, Advanced Systems and Applications*. Artech House, Dedham, MA, 1100 pp.

Ulaby, F. T., F. Kouyate, B. Brisco, and T. H. Lee Williams (1986b). Textural information in SAR images. *IEEE Transactions on Geoscience and Remote Sensing*, **24**(2), 235–245.

Ulander, L. M. H. (1987). Interpretation of Seasat radar-altimeter data over sea ice using near-simultaneous SAR imagery. *International Journal of Remote Sensing*, **8**(11), 1679–1686.

Ulander, L. M. H., A. Carlström, and J. Askne (1995). Effect of frost flowers, rough saline snow and slush on ERS-1 SAR backscatter of the Arctic sea ice. *International Journal of Remote Sensing*, **16**, 3287–3305.

Untersteiner, N. (1961). On the mass and heat budget of Arctic sea ice. *Archiv für Meteorologie, Geophysiks und Bioklimatologie*, A, **12**, 151–182.

Untersteiner, N. (1968). Natural desalination and equilibrium salinity profile of perennial sea ice. *Journal of Geophysical Research*, **73**(4), 1251–1257.

Untersteiner, N. (ed.) (1986) *The Geophysics of Sea Ice*. Plenum Press, New York, 1,196 pp.

Untersteiner, N. and E. Carmack (1990). *Arctic Sea Ice, Freshwater and Global Ocean Climate: Some Possible Connections* (appendix, report of the 4th Session). WMO Working Group on Sea Ice and Climate, World Meteorological Organization, Geneva..

Uotila, J., T. Vihma, and J. Launiainen (2000). Response of the Weddell Sea pack ice to wind forcing, *Journal of Geophysical Research*, **105**(C1), 1135–1152.

Ushio, S. and M. Wakatsuchi (1993). A laboratory study on supercooling and frazil ice production processes in winter coastal polynyas. *Journal of Geophysical Research*, **98**, 20321–20328.

Ushio, S., T. Takizawa, K. I. Ohshima, and T. Kawamura (1999). Ice production and deep-water entrainment in shelf break polynya off Enderby Land, Antarctica. *Journal of Geophysical Research*, **104**, 29771–29780.

Ussher, S. J., E. P. Achterberg, and P. J. Worsfold (2004). Marine biogeochemistry of iron. *Environmental Chemistry*, **1**, 67–80.

Uttal, T., J. A. Curry, M. G. McPhee, D. K. Perovich, R. E. Moritz, J. A. Maslanik, P. S. Guest, H. L. Stern, J. A. Moore, R. Turenne et al. (2002). Surface heat budget of the Arctic Ocean. *Bulletin of the American Meteorological Society*, **83**(2), 255–276.

Vainio, J., M. Similä, and H. Gronvall (2000). Operational use of Radarsat SAR data as aid to winter navigation in the Baltic Sea. *Canadian Journal of Remote Sensing*, **26**, 314–317.

Van den Broecke, M. R. (1998). The semiannual oscillation and Antarctic climate: Part 2. Recent changes. *Antarctic Science*, **10**, 184–191.

van der Sanden, J. J. and S. G. Ross (eds.) (2001). *Applications Potential of Radarsat-2: A Preview* (report prepared for the Canadian Space Agency). Natural Resources Canada and Canada Centre for Remote Sensing, Ottawa, 117 pp.

van Loon, H. (1967). The half yearly oscillations in middle and high southern latitudes and the coreless winter. *Journal of Atmospheric Science*, **24**, 472–486.

van Loon, H. and D. J. Shea (1985). The Southern Oscillation: Part IV. The precursors south of 15°S to the extremes of the oscillation. *Monthly Weather Review*, **113,** 2063–2074.

Van Woert, M. (1999a). Wintertime dynamics of the Terra Nova Bay polynya. *Journal of Geophysical Research*, **104C**, 7753–7769.

Van Woert, M. L. (1999b). The wintertime expansion and contraction of the Terra Nova Bay polynya. In: G. Spezie and G. M. R. Manzella (eds.), *Oceanography of the Ross Sea, Antarctica*. Springer-Verlag, Berlin, pp. 145–164.

Van Woert, M. L., W. N. Meier, C.-Z. Zou, A. Archer, A. Pellegrini, P. Grigoni, and C. Bertoia (2001a). Satellite observations of upper-ocean currents in Terra Nova Bay, Antarctica. *Annals of Glaciology*, **33**, 407–412.

Van Woert, M. L., W. N. Meier, C.-Z. Zou, J. A. Beesley, and P. D. Hovey (2001b). Satellite validation of the May 2000 sea ice concentration fields from the Polar Ice Prediction System. *Canadian Journal of Remote Sensing*, **27**(5), 443–456.

van Zyl, J. J. and H. A. Zebker (1990). Imaging radar polarimetry. In: J. A. Kong (ed.), *Polarimetric Remote Sensing, Progress in Electromagnetic Research* (Vol. 3). Elsevier Science, New York, 520 pp.

van Zyl, J., H. Zebker, and C. Elachi (1987). Imaging radar polarisation signatures: Theory and observation. *Radio Science*, **22**(4), 529–543.

van Zyl, J. J., H. A. Zebker, and C. Elachi (1990). Polarimetric SAR applications. In: F. T. Ulaby and C. Elachi (eds.), *Radar Polarimetry for Geoscience Applications*. Artech House, Norwood, NJ, pp. 315–360

Vant, M. R., R. B. Gray, R. O. Ramseier, and V. Makios (1974). Dielectric properties of fresh sea ice at 10 and 35 GHz. *Journal of Applied Physics*, **45**, 4712–4717.

Vant, M. R., R. O. Ramseier, and V. Makios (1978). The complex dielectric constant of sea ice at frequencies in the range 0.1–40 GHz. *Journal of Applied Physics*, **49**(3), 1264–1280.

Vaughan, D. G., G. J. Marshall, W. M. Connolley, J. C. King, and R. Mulvaney (2001). Devil in the detail. *Science*, **293**, 1777–1779.

Vaughan, D. G., G. J. Marshall, W. M. Connolley, C. Parkinson, R. Mulvaney, D. A. Hodgson, J. C. King, C. J. Pudsey, and J. Turner (2003). Recent rapid regional climate warming on the Antarctic Peninsula. *Climatic Change*, **60**(3), 243–274.

Vavrus, S. and S. P. Harrison (2003). The impact of sea-ice dynamics on the Arctic climate system. *Climate Dynamics*, **20**, 741–757.

Venegas, S. A. and M. R. Drinkwater (2001). Sea ice, atmosphere and upper ocean variability in the Weddell Sea, Antarctica. *Journal of Geophysical Research*, **106**, 16747–16765.

Venegas, S. A., M. R. Drinkwater, and G. Shaffer (2001). Coupled oscillations in Antarctic sea ice and atmosphere in the South Pacific Sector. *Geophysical Research Letters*, **28**(17), 3301–3304.

Vermote, E. and A. Vermeulen (1999). *Atmospheric Correction Algorithm: Spectral Reflectances (MOD09), ATBD Version 4.0*. Available online at ⟨*http://modis.gsfc. nasa.gov/data/atbd/atbd_mod08.pdf*⟩.

Vernet, M., E. A. Brody, O. Holm-Hansen, and B. G. Mitchell (1994). The response of Antarctic phytoplankton to ultraviolet radiation: Absorption, photosynthesis, and taxonomic composition. In: C. S. Weiler and P. A. Penhale (eds.), *Ultraviolet Radition in Antarctica: Measurements and Biological Effects* (AGU Antarctic Research Series No. 62). American Geophysical Union, Washingon, DC, pp. 143–158.

Vesecky, J. F., M. P. Smith, and R. Samadani (1990). Extraction of lead and ridge characteristics from SAR images of sea ice. *IEEE Transactions on Geoscience and Remote Sensing*, **28(4)**, 740–744.

Vihma, T. and J. Launiainen (1993). Ice drift in the Weddell Sea in 1990–1991 as tracked by a satellite buoy. *Journal of Geophysical Research*, **98**, 14471–14485.

Vihma, T., J. Uotila, B. Cheng, and J. Launiainen (2002). Surface heat budget over the Weddell Sea: Buoy results and model comparisons. *Journal of Geophysical Research*, **107**(C2), 3013, DOI: 10.1029/2000JC000372, 2002.

Vihma, T., J. Hartmann, and C. Lüpkes (2003). A case study of on-ice air flow over the marginal sea-ice zone. *Boundary-layer Meteorology*, **107**, 189–217.

Vihma, T., J. Launiainen, and J. Uotila (1996). Weddell Sea ice drift: Kinematics and wind forcing. *Journal of Geophysical Research*, **101**(C8), 18279–18296.

Vinje, T. E. (1977). *Sea Ice Studies in the Spitsbergen–Greenland Area* (NTIS Landsat Report E77-10206). National Technical Information Service, Springfield, VA.

Vinje, T. (2001a). Anomalies and trends of sea ice extent and atmospheric circulation in the Nordic seas during the period 1864–1998. *Journal of Climate*, **14**(3), 255–267.

Vinje, T. (2001b). Fram Strait ice fluxes and atmospheric circulation 1959–2000. *Journal of Climate*, **14**, 3508–3517.

Vinje, T. and O. Finnekåsa (1986). The ice transport through Fram Strait. *Norsk Polarinstitut Skrifter*, **186**, 1–39.

Vinje, T., N. Nordlund, and Å. Kvambekk (1998). Monitoring ice thickness in the Fram Strait. *Journal of Geophysical Research*, **103**(C5), 10437–10449.

Vinnikov, K. Y., A. Robock, R. J. Stouffer, J. E. Walsh, C. L. Parkinson, D. J. Cavalieri, J. F. B. Mitshell, D. Garrett, and V. F. Zakharov (1999). Global warming and Northern Hemisphere sea ice extent. *Science*, **286**(5446), 1934–1937.

Vinnikov, K. Y., A. Robock, D. J. Cavalieri, and C. L. Parkinson (2002). Analysis of seasonal cycles in climatic trends with application to satellite observations of sea ice extent. *Geophysical Research Letters*, **29**(9), DOI: 10.1029/2001GL014481.

Voss, S., G. Heygster, and R. Ezraty (2003). Improving sea ice type discrimination by the simultaneous use of SSM/I and scatterometer data. *Polar Research*, **22**(1), 35–42.

Vyas, N. K., M. K. Dash, S. M. Bhandari, N. Khare, A. Mitra, and P. C. Pandey (2003). On the secular trends in sea ice extent over the Antarctic region based on OCEANSAT-1 MSMR observations. *International Journal of Remote Sensing*, **24**(11), 2277–2287.

Wackerman, C., R. R. Jentz, and R. A. Shuchman (1988). Sea ice type classification of SAR imagery. *Proceedings of IGARSS '88, September 12–16, Edinburgh,* pp. 425–428.

Wackerman, C., W. G. Pichel, and P. Clemente-Colón (2003). Automated location of ice regions in Radarsat SAR imagery. *Proceedings of 2nd Workshop on Coastal and Marine Applications of SAR, September 8–12, Svalbard, Norway*. Available online at ⟨*http://earth.esa.int/workshops/cmasar_2003/papers/E18wack(1.1.1).pdf*⟩.

Wadhams, P. (1986). The Seasonal Ice Zone. In: N. Untersteiner (ed.), *The Geophysics of Sea Ice*. Plenum Press, New York, pp. 825–991.

Wadhams, P. (1994). Sea ice thickness changes and their relation to climate. In: O. M. Johannessen, R. D. Muench, and J. E. Overland (eds.), *The Polar Oceans and Their Role in Shaping the Global Environment* (AGU Monograph No. 85). American Geophysical Union, Washington, DC, pp. 337–361.

Wadhams, P. (2000). *Ice in the Ocean*. Gordon & Breech, London, 364 pp.

Wadhams, P. (2004). In situ measurement techniques: Sea ice. In: J. Bamber and A. Payne (eds.), *Mass Balance of the Cryosphere*. Cambridge University Press, Cambridge, UK, pp. 43–58

Wadhams, P. and J. C. Comiso (1992). The ice thickness distribution inferred using remote sensing techniques. In: F. Carsey (ed,), *Microwave Remote Sensing of Sea Ice* (AGU Monograph No. 68). American Geophysical Union, Washington, DC, pp. 375–383.

Wadhams, P. and N. R. Davis (2000). Further evidence of ice thinning in the Arctic Ocean. *Geophysical Research Letters*, **27**(24), 3973–3975.

Wadhams, P. and N. R. Davis (2001). Arctic sea-ice morphological characteristics in summer 1996. *Annals of Glaciology*, **33**, 165–170.

Wadhams, P. and B. Holt (1991). Waves in frazil and pancake ice and their detection in Seasat synthetic aperture radar imagery. *Journal of Geophysical Research*, **96**(C5), 8835–8852.

Wadhams, P., M. A. Lange, and S. F. Ackley (1987). The ice thickness distribution across the Atlantic sector of the Antarctic ocean in mid-winter. *Journal of Geophysical Research*, **92**(C13), 14535–14552.

Wadhams, P., V. A. Squire, D. J. Goodman, A. M. Cowan, and S. C. Moore (1988). The attenuation rates of ocean waves in the marginal ice zone. *Journal of Geophysical Research*, **93**, 6799–6818.

Wadhams, P., C. B. Sear, D. R. Crane, M. A. Rowe, S. J. Morrison, and D. W. S. Limbert (1989). Basin-scale ice motion and deformation in the Weddell Sea during winter. *Annals of Glaciology*, **12**, 178–186.

Wadhams, P., W. B. Tucker III, W. B. Krabill, R. N. Swift, J. C. Comiso, and N. R. Davis (1992). Relationship between sea ice freeboard and draft in the Arctic basin, and implications for ice thickness monitoring. *Journal of Geophysical Research*, **97**(C12), 20325–20334.

Wadhams, P., F. Parmiggiani, G. de Carolis, and M. Tadross (1999). Mapping the thickness of pancake ice using ocean wave dispersion in SAR imagery. In: G. Spezie and G. M. R. Manzella (eds.), *Oceanography of the Ross Sea, Antarctica*. Springer-Verlag, New York, pp. 17–34.

Wadhams, P., F. Parmiggiani, and G. de Carolis (2002). The use of SAR to measure ocean wave dispersion in frazil-pancake icefields. *Journal of Physical Oceanography*, **32**(6), 1721–1746.

Wakabayashi, H., T. Matsuoka, K. Nakamura, and F. Nishio (2001). CRL/NASDA airborne SAR (Pi-SAR) observations of sea ice in the Sea of Okhotsk. *Annals of Glaciology*, **33**, 120–124.

Wakabayashi, H., T. Matsuoka, K. Nakamura, and F. Nishio (2004). Polarimetric characteristics of sea ice in the Sea of Okhotsk observed by airborne L-band SAR. *IEEE Transactions on Geoscience and Remote Sensing*, **42**(11), 115–119.

Wakatsuchi, M., S. Martin, and E. Munoz (1990). Satellite and oceanographic observations of large-scale ice-edge eddies in the Kuril Basin region of the Okhotsk Sea. *Annals of Glaciology*, **14**, 360–362.

Wald, A. (1994). Modeling thermal infrared (2–14 μm) reflectance spectra of frost and snow. *Journal of Geophysical Research*, **99**, 24241–24250.

Walker, N. P. (1997). Limitations on the possible resolution enhancement of ERS-1 scatterometer images. *IEEE Transactions on Geoscience and Remote Sensing*, **35**(1), 196–198.

Walkington, I. A. and A. J. Willmott (2004). A coastal polynya flux model incorporating ice concentration. *European Geoscience Union 1st General Assembly, April 25–30, Nice, France* (Abstract EGU04-A-03478).

Walsh, J. E. and M. S. Timlin (2003). Northern Hemisphere sea ice simulations by global climate models. *Polar Research*, **22**(1), 75–82.

Walsh, J. E., W. L. Chapman, and T. L. Shy (1996). Recent decrease of sea level pressure in the central Arctic. *Journal of Climate*, **9**, 480–485.

Walsh, J. E., J. Curry, M. Fahnestock, M. C. Kennicutt II, A. D. McGuire, W. B. Rossow, M. Steele, C. J. Vorosmarty, R. Wharton, C. Elfring et al. (2000). *Enhancing NASA's Contributions to Polar Science*. National Academy Press, Washington, DC.

Walter, B. A. (1989). A study of the planetary boundary layer over the polynya downwind of St. Lawrence Island in the Bering Sea using aircraft data. *Boundary-Layer Meteorology*, **48**, 255–282.

Wan, Z. (1999). *MODIS Land–Surface Temperature Algorithm Theoretical Basis Document (LST ATBD), Version 3.3, April*. Available online at ⟨*modis.gsfc.nasa.gov/data/atbd/atbd_mod11.pdf*⟩.

Wang, H., J. Pulliainen, and M. Hallikainen (2000). Application of strong fluctuation theory to microwave emission from dry snow. *Progress in Electromagnetics Research*, **29**, 39–55.

Wang, J. and M. Ikeda (2001). Arctic sea-ice oscillation: Regional and seasonal perspectives. *Annals of Glaciology*, **33**, 481–492.

Wang, J., M. Jin, M. Ikeda, K. Shimada, and J. Takahashi (2003a). *A Nowcast/Forecast Model for the Beaufort Sea Ice–Ocean–Oil Spill System* (Annual Rep. 9). U.S. Dept. of the Interior, Minerals Management Service, Alaska OCS Region, Anchorage, pp. 19–31.

Wang, J., R. Kwok, F. J. Saucier, J. Hutchings, M. Ikeda, W. Hibler III, J. Haapala, M. D. Coon, H. E. M. Meier, H. Eicken et al. (2003b). Working toward improved small-scale sea ice–ocean modeling in the Arctic Seas. *EOS, Transactions of the American Geophysical Union*, **84**(34), 325, 329–330.

Wang, X. and J. R. Key (2003). Recent trends in Arctic surface, cloud, and radiation properties from space. *Science*, **299**(5613), 1725–1728.

Wankiewicz, A. (1993). Multi-temporal microwave satellite observations of snowpacks. *Annals of Glaciology*, **17**, 155–160.

Wanner, W., A. Strahler, B. Hu, P. Lewis, J.-P. Muller, X. Li, C. Barker-Schaaf, and M. Barnsley (1997). Global retrieval of BRDF and albedo over land from EOS

MODIS and MISR data: Theory and algorithm. *Journal of Geophysical Research*, **102**, 17143–17162.

Warren, S. G. (1982). Optical properties of snow. *Reviews of Geophysics and Space Physics*, **20**(1), 67–89.

Warren, S. G. (1984). Optical constants of ice from the ultraviolet to the microwave. *Applied Optics*, **23**, 1206–1225.

Warren, S. G. and A. D. Clarke (1986). Soot from Arctic haze: Radiative effects on the Arctic snowpack. *Glaciological Data*, **18**, 73–77.

Warren, S. G. and W. J. Wiscombe (1980). A model for the spectral albedo of snow: II. Snow containing atmospheric aerosols. *Journal of Atmospheric Science*, **37**(12), 2734–2745.

Warren, S. G., C. S. Roesler, and R. E. Brandt (1997). Solar radiation processes in the East Antarctic sea ice zone. *Antarctic Journal of the United States*, **32**(5), 185–187.

Warren, S. G., R. E. Brandt, and P. O. Hinton (1998). Effect of surface roughness on bidirectional reflectance of Antarctic snow. *Journal of Geophysical Research*, **103**(E11), 25789–25807.

Warren, S. G., I. G. Rigor, N. Untersteiner, V. F. Radionov, N. N. Bryazgin, Y. I. Aleksandrov, and R. Colony (1999). Snow depth on Arctic sea ice. *Journal of Climate*, **12**(6), 1814–1829.

Watkins, A. B. and I. Simmonds (2000). Current trends in Antarctic sea ice: The 1990s' impact on a short climatology. *Journal of Climate*, **13**(24), 4441–4451.

WCRP (1998). *Arctic Climate System Study (ACSYS)* (summary report of the Sixth Session of the WCRP ACSYS Scientific Steering Group, WCRP Informal Report No. 8/1998, Appendix F: WCRP Satellite Data Requirements). World Climate Research Programme, Geneva, Switzerland

WCRP (1999). Hydrological cycle in the Arctic region. *ACSYS Implementation and Achievements* (revised draft). Available online at ⟨*www.npolar.no/acsys/impplan/index.htm*⟩.

Weatherly, J. W. (2004). Sensitivity of Antarctic precipitation to sea ice concentrations in a general circulation model. *Journal of Climate*, **17**(16), 3214–3223.

Weaver, A. J., C. M. Bitz, A. F. Fanning, and M. M. Holland (1999). Thermohaline circulation: High-latitude phenomena and the difference between the Pacific and Atlantic. *Annual Review of Earth and Planetary Sciences*, **27**, 231–285.

Weaver, R. L. S., K. Steffen, J. Heinrichs, J. A. Maslanik, and G. M. Flato (2000). Data assimilation in sea-ice monitoring. *Annals of Glaciology*, **31**, 327–332.

Weeks, W. F. (1976). Sea ice conditions in the Arctic. *AIDJEX Bulletin*, **34**, 173–205.

Weeks, W. F. (1998). Growth conditions and the structure and properties of sea ice. In: M. Leppäranta (ed.), *Physics of Ice-covered Seas* (Vol. 1). University of Helsinki, pp. 25–104.

Weeks, W. F. and S. F. Ackley (1986). The growth, structure, and properties of sea ice. In: N. Untersteiner (ed.), *The Geophysics of Sea Ice*. Plenum Press, New York, pp. 9–164.

Weeks, W. F., W. B. Tucker, M. Frank, and S. Fungcharoen (1980). Characterization of surface roughness and floe geometry of sea ice over the continental shelves of the Beaufort and Chukchi Seas. In: R. S. Pritchard (ed.), *Sea Ice Processes and Models*. University of Washington Press, Seattle.

Weeks, W. F., S. F. Ackley, and J. Govoni (1989). Sea ice ridging in the Ross Sea, Antarctica, as compared with sites in the Arctic. *Journal of Geophysical Research*, **94**, 4984–4988.

Wefelmeier, C. and D. Etling (1991). The influence of sea ice distribution on the atmosphere boundary layer, *Zeitung Meteorologie*, **41**, 333–342.

Weiler, C. S. and P. A. Penhale (eds.) (1994). *Ultraviolet Radiation in Antarctica: Measurements and Biological Effects* (Antarctic Research Series 62). American Geophysical Union, Washingon, D.C., 257 pp.

Weingartner, T. J., D. J. Cavalieri, K. Aagaard, and Y. Sasaki (1998). Circulation, dense water formation, and outflow on the northeast Chukchi shelf. *Journal of Geophysical Research*, **103**, 7647–7661.

Welch, R. M., S. K. Sengupta, A. K. Goroch, P. Rabindra, N. Rangaraj, and M. S. Navar (1992). Polar cloud and surface classification using AVHRR imagery: An intercomparison of methods. *Journal of Applied Meteorology*, **31**, 405–420.

Welch, R. M., R. E. Feind, T. A. Berendes, D. E. Lloyd, and A. M. Logar (1996). *The ASTER Polar Cloud Mask Algorithm* (theoretical basis document). Jet Propulsion Laboratory, Pasadena, CA.

Wendler, G., D. Gilmore, and J. Curtis (1997). On the formation of coastal polynyas in the area of Commonwealth Bay, Eastern Antarctica. *Atmospheric Research*, **45**, 55–75.

Wensnahan, M., G. A. Maykut, T. C. Grenfell, and D. P. Winebrenner (1993). Passive microwave remote sensing of thin sea ice using principal component analysis. *Journal of Geophysical Research*, **98**(C7), 12453–12468.

Werner, M. (2000). Shuttle Radar Topography Mission (SRTM): Mission overview. *Proceedings of EUSAR 2000, Munich, Germany*.

Wettlaufer, J. S. (1999). Crystal growth, surface phase transitions and thermo-molecular pressure. In: J. S. Wettlaufer, J. G. Dash, and N. Untersteiner (eds.), *Ice Physics and the Natural Environment*. Springer-Verlag, New York, pp. 39–68.

White, W. B. and R. Peterson (1996). An Antarctic circumpolar wave in surface pressure, wind, temperature, and sea ice extent. *Nature*, **380**(6576), 699–702.

White, W. B., C. Shyh-Chin, R. J. Allan, and R. C. Stone (2002). Positive feedbacks between the Antarctic Circumpolar Wave and the global El Niño–Southern Oscillation Wave. *Journal of Geophysical Research*, **107**(C10), DOI: 10.1029/2000JC000581.

White, W. B., P. Gloersen, and I. Simmonds (2004). Tropospheric response in the Antarctic Circumpolar Wave along the sea ice edge around Antarctica. *Journal of Climate*, **17**(4), 2765–2779.

Wienecke, B. (2002). Hard times for Ross Sea penguins. *Australian Antarctic Magazine*, **3**, 36–37.

Wienecke, B. C. and G. Robertson (1997) Foraging space of emperor penguins *Aptenodytes forsteri* in Antarctic shelf waters in winter. *Marine Ecology Progress Series*, **159**, 249–263

Williams, G. D. and N. L. Bindoff (2003). Wintertime oceanography of the Adélie Depression. *Deep-sea Research II*, **50**(8–9), 1373–1392.

Williams, R. N., P. Crowther, and S. F. Pendlebury (1997). Design and development of an operational sea ice mapping system for meteorological applications in the Antarctic. *International Geoscience and Remote Sensing Symposium, Singapore, August 3–8, IGARSS '97* (Vol. 4). Institute of Electrical and Electronics Engineers, Piscataway, NJ, pp. 1689–1691.

Williams, R. N., K. J. Michael, S. Pendlebury, and P. Crowther (2002). An automated image analysis system for determining sea-ice concentration and cloud cover from AVHRR images of the Antarctic. *International Journal of Remote Sensing*, **23**(4), 611–625.

Wilson, K. J., D. J. King, and D. G. Barber (2001b). A case study in tracking 1998 polynya ice dynamics in Smith Sound, North Water polynya region, Canadian Arctic, using RADARSAT-1 data. *Annals of Glaciology*, **33**, 413–418.

Wilson, P. R., D. G. Ainley, N. Nur, S. S. Jacobs, K. J. Barton, G. Ballard, and J. C. Comiso (2001a). Adélie penguin population change in the Pacific sector of Antarctica: Relation to sea-ice extent and the Antarctic Circumpolar Current. *Marine Ecology-Progress Series*, **213**, 301–309.

Winebrenner, D. P. (1990). Accuracy of thin ice/open water classification using multi-polarisation SAR. *Proceedings of IGARSS '90 Symposium* (Vol. 1). Institute of Electrical and Electronics Engineers, Piscataway, NJ, pp. 2237–2240.

Winebrenner, D. P. (1996). Polarimetric backscatter at 23 cm wavelength from Antarctic lead ice and estimation of ice thickness. *Proceedings of IGARSS '96 Symposium*, Vol. 2, pp. 941–943.

Winebrenner, D. P., J. Bredow, M. R. Drinkwater, A. K. Fung, S. P. Gogineni, A. J. Gow, T. C. Grenfell, H. C. Han, J. K. Lee, J. A. Kong et al. (1992). Microwave sea ice signature modeling. In: F. D. Carsey (ed.), *Microwave Remote Sensing of Sea Ice* (AGU Monograph Series No. 68). American Geophysical Union, Washington, DC, pp. 137–175.

Winebrenner, D. P., E. D. Nelson, R. Colony, and R. D. West (1994). Observation of melt onset on multiyear Arctic sea ice using the ERS-1 synthetic aperture radar. *Journal of Geophysical Research*, **99**(C11), 22425–22441.

Winebrenner, D. P., L. D. Farmer, and L. R. Joughin (1995). On the response of polarimetric synthetic aperture radar signatures at 24-cm wavelength to sea ice thickness in Arctic leads. *Radio Science*, **30**(2), 373–402.

Winebrenner, D. P., B. Holt, and E. D. Nelson (1996). Observations of autumn freeze-up in the Beaufort and Chukchi Seas using ERS-1 synthetic aperture radar. *Journal of Geophysical Research*, **101**(C7), 16401–16419.

Winebrenner, D. P., D. G. Long, and B. Holt (1998). Mapping the progression of melt onset and freeze-up on Arctic sea ice using SAR and scatterometry. In: C. Tsatsoulis and R. Kwok (eds.), *Analysis of SAR Data of the Polar Oceans: Recent Advances*. Springer-Verlag, Berlin, pp. 129–144.

Wingham, D. J. (1999). The first of ESA's first opportunity missions: CryoSat. *ESA Earth Observation Quarterly*, **63**, 21–24.

Wingham, D. J. (2004). Validation of Cryosat ice mass fluxes. *EGS 1st General Assembly, April 25–30, Nice, France* (Abstract 03531).

Wingham, D. J., R. Forsberg, S. Laxon, P. Lemke, H. Miller, K. Raney, S. Sandven, R. Scharroo, P. Vincent, and H. Rebhan (2001). *CryoSat Calibration and Validation Concept* (ESA Document CS-PL-UCL-SY-0004). ESA, Noordwijk, The Netherlands, 91 pp.

Wingham, D. J., L. Phalippou, C. Mavrocordatos, and D. Wallis (2004). The mean echo and echo cross-product from a beamforming interferometric altimeter and their application to elevation measurements. *IEEE Transactions on Geoscience and Remote Sensing*, **42**(10), 2305–2323.

Winsor, P. (2001). Arctic sea ice thickness remained constant during the 1990s. *Geophysical Research Letters*, **28**(6), 1039–1041.

Winsor, P. and G. Björk (2000). Polynya activity in the Arctic Ocean from 1958 to 1997. *Journal of Geophysical Research*, **105**(C4), 8789–8803.

Winsor, P. and G. Björk (2000). Polynya activity in the Arctic Ocean from 1958 to 1997. *Journal of Geophysical Research*, **105**, 8789–8803.

Winsor, P. and D. C. Chapman (2002). Distribution and interannual variability of dense water production from coastal polynyas on the Chukchi Shelf. *Journal of Geophysical Research*, **107**(C7), DOI: 10.1029/2001JC000984.

Wiscombe, W. J. (1980). Improved Mie scattering algorithms. *Applied Optics*, **19**(9), 1505–1509.

Wiscombe, W. J. and S. G. Warren (1980). A model for the spectral albedo of snow: I. Pure snow. *Journal of Atmospheric Sciences*, **37**, 2712–2733.

Wismann, V. (1998). Monitoring the Earth with spaceborne scatterometers. *Proceedings of the 32nd ESLAB Symposium*m 15–18 September (ESA Publication Division SP-423). ESA/ESTEC, Noordwijk, The Netherlands, pp. 189–199.

WMO (1970). *The WMO Sea-Ice Nomenclature: Terminology, Codes and Illustrated Glossary* (WMO/OMM/BMO 259, TP 145). World Meteorological Organization, Geneva.

Wohl, G. (1995). Operational sea ice classification from synthetic aperture radar imagery. *Photogrammetric Engineering and Remote Sensing*, **61**(12), 1455–1462.

Wolfe, W. L. and G. L. Zissis (1989). *The Infrared Handbook*. IRIA Center, Environmental Research Institute of Michigan, Ann Arbor, MI, 1668 pp.

Wolff, E., A. M. Rankin, and R. Röthlisberger (2003). An ice core indicator of Antarctic sea ice production? *Geophysical Research Letters*, **30**, 2158, DOI: 10.1029/2003GL018454.

Wong, A., N. L. Bindoff, and J. A. Church (1999). Large-scale freshening of intermediate waters in the Pacific and Indian Oceans. *Nature*, **400**, 440–443.

Worby, A. P. and I. Allison (1999). *A Ship-based Technique for Observing Antarctic Sea Ice: Part I. Observational Techniques and Results* (Report 15). University of Tasmania, Antarctic Cooperative Research Center, 63 pp.

Worby, A. P. and J. C. Comiso (2004). Studies of the Antarctic sea ice edge and ice extent from satellite and ship observations. *Remote Sensing of Environment*, **92**, 98–111.

Worby, A. P., M. O. Jeffries, W. Weeks, K. Morris, and R. Jana (1996). The thickness distribution of sea ice and snow cover during late winter in the Bellingshausen and Amundsen Seas, Antarctica. *Journal of Geophysical Research*, **101**(C12), 28441–28455.

Worby, A. P., R. A. Massom, I. Allison, V. I. Lytle, and P. Heil (1998). East Antarctic sea ice: A review of its structure, properties and drift. In: M. O. Jeffries (ed.), *Antarctic Sea Ice Physical Processes, Interactions and Variability* (AGU Antarctic Research Series No. 74). American Geophysical Union, Washington, DC, pp. 41–68.

Worby, A. P., P. Griffin, V. I. Lytle, and R. A. Massom (1999). On the use of electromagnetic induction sounding to determine winter and spring sea ice thickness in the Antarctic. *Cold Regions Science and Technology*, **29**(1), 49–58.

Wu, P., R. Wood, and P. Stott, (2004). Does the recent freshening trend in the North Atlantic indicate a weakening thermohaline circulation? *Geophysical Research Letters*, **31**(2), L02301, DOI: 10.1029/2003GL018584.

Wu, X. and W. F. Budd (1998). Modelling global warming and Antarctic sea ice changes over the past century. *Annals of Glaciology*, **27**, 413–419.

Wu, X., I. Simmonds, and W. F. Budd (1997). Modeling of Antarctic sea ice in a general circulation model. *Journal of Climate*, **10**(4), 593–609.

Wu, X., W. F. Budd, and T. H. Jacka (1999a). Simulations of Southern Hemisphere warming and Antarctic sea-ice changes using global climate models. *Annals of Glaciology*, **29**, 61–65.

Wu, X., W. F. Budd, V. I. Lytle, and R. A. Massom (1999b). The effect of snow on Antarctic sea ice simulations in a coupled atmosphere–sea ice model. *Climate Dynamics*, **15**, 127–143.

Wu, X., W. F. Budd, A. P. Worby, and I. Allison (2001). Sensitivity of the Antarctic sea-ice distribution to oceanic heat flux in a coupled atmosphere-sea-ice model. *Annals of Glaciology*, **33**, 577–584.

Wu, X., W. F. Budd, and I. Allison (2003). Modelling the impacts of persistent Antarctic polynyas with an atmosphere–sea-ice general circulation model. *Deep-Sea Research II*, **50**(8–9), 1357–1372, DOI: 10.1016/S0967-0645(03)00072-9.

Yager, P. L., D. W. R. Wallace, K. M. Johnson, W. O. Smith Jr., P. J. Minnett, and J. W. Deming (1995). The Northeast Water Polynya as an atmospheric CO_2 sink: A seasonal rectification hypothesis. *Journal of Geophysical Research*, **100**, 4389–4398.

Yamaguchi, Y., A. B. Kahle, H. Tsu, T. Kawakami, and M. Pniel (1998). Overview of the Advanced Spaceborne Thermal Emission and Reflection Radiometer (ASTER). *IEEE Transactions on Geoscience and Remote Sensing*, **36**(4), 1062–1071.

Yamaguchi, Y., H. Fujisada, A. B. Kahle, H. Tsu, M. Kato, H. Watanabe, I. Sato, and M. Kudoh (2001). ASTER instrument performance, operational status, and application to Earth sciences. *Proceedings of IGARSS 2001*, pp. 1215–1216.

Yamanouchi, T. and S. Kawaguchi (1992). Cloud distribution in the Antarctic from AVHRR and radiation measurements at the ground. *International Journal of Remote Sensing*, **13**, 111–117.

Yamanouchi, T. and K. Seko (1992). *Antarctica from NOAA Satellites: Clouds, Ice and Snow*. National Institute of Polar Research, Tokyo, 91 pp.

Yamanouchi, T., K. Suzuki, and S. Kawaguchi (1987). Detection of clouds in Antarctica from infrared multispectral data of AVHRR. *Journal of Meteorological Society of Japan*, **65**, 949–962.

Yamanouchi, T., N. Hirasawa, G. Kadosaki, and M. Hayashi (2000). Evaluation of AVHRR cloud detection at Dome Fuji Station, Antarctica. *Polar Meteorology and Glaciology*, **14**, 110–116.

Yen, Y.-C. (1981). *Review of Thermal Properties of Snow, Ice and Sea Ice* (CRREL Report 81–10). U.S. Army Cold Regions Research and Engineering Laboratory, Hanover, NH.

Yi, D. and H. J. Zwally (2005). Comparing CryoSat, ICESat, and AMSR-E measurements over Antarctic sea ice. *Proceedings of the CryoSat 2005 Workshop, March 8–10*. ESA ESRIN, Frascati, Italy.

Yoder, J. A. (ed.) (1999). *Status and Plans for Satellite Ocean-colour Missions: Considerations for Complementary Missions* (IOCCG Report No. 2). International Ocean-Colour Coordinating Group, Dartmouth, Canada, 43 pp.

Young, N. W. (2001). An iceberg the size of Jamaica! *Australian Antarctic Magazine*, **1**, 24–25.

Yu, Y. L. (1996). Regional Arctic ice thickness and brine flux from AVHRR. PhD thesis, University of Washington, Seattle, 142 pp.

Yu, Y. and R. W. Lindsay (2003). Comparisons of thin ice fractions estimated from RGPS and AVHRR. *Journal of Geophysical Research*, **108**(C12), 3387, DOI: 10.1029/2002JC001319.

Yu, Y. and D. A. Rothrock (1996). Thin ice thickness from satellite thermal imagery. *Journal of Geophysical Research*, **101**(C10), 25753–25766.

Yu, Y., D. A. Rothrock, and R. W. Lindsay (1995). Accuracy of sea ice temperature derived from the Advanced Very High Resolution Radiometer. *Journal of Geophysical Research*, **100**, 4525–4532.

Yu, Y., D. A. Rothrock, and J. Zhang (2001). Thin ice impacts on surface salt flux and ice strength: Inferences from AVHRR. *Journal of Geophysical Research*, **106**, 13975–13988.

Yuan, X. (2004). ENSO-related impacts on Antarctic sea ice: A synthesis of phenomenon and mechanisms. *Antarctic Science*, **16**, 415–425.

Yuan, X. and D. G. Martinson (2000). Antarctic sea ice variability and its global connectivity. *Journal of Climate*, **13**, 1697–1717.

Yuan, X. and D. G. Martinson (2001). The Antarctic Dipole and its predictability. *Geophysical Research Letters*, **28**(18), 3609–3612.

Yuan, X., D. G. Martinson, and X. Liu (1999). Effect of air–sea-ice interaction on winter 1996 Southern Ocean subpolar storm distributions. *Journal of Geophysical Research*, **104**(D2), 1991–2007.

Yueh, S. H. and R. Kwok (1998). Arctic sea ice extent and melt onset from NSCAT observations. *Geophysical Research Letters*, **25**(23), 4369–4372.

Yueh, S. H., R. Kwok, S.-H. Lou, and W.-Y. Tsai (1997). Sea ice identification using dual-polarized Ku-band scatterometer data. *IEEE Transactions on Geoscience and Remote Sensing*, **35**(3), 560–569.

Yueh, S. H., R. Kwok, S. V. Nghiem, and R. West (1998). Change monitoring of Antarctic sea ice using NSCAT dual-polarized backscatter measurements. *International Geoscience and Remote Sensing Symposium, Seattle, WA, July 6–10, IGARSS '98* (Vol. 4). Institute of Electrical and Electronics Engineers, Piscataway, NJ, pp. 2228–2230.

Zabel, I. H. H., K. C. Jezek, S. P. Gogineni, and P. Kanagaratnam (1996). Search for proxy indicators of young sea ice thickness. *Journal of Geophysical Research*, **101**(C3), 6697–6709.

Zebker, H. A. and J. J. van Zyl (1990). Imaging radar polarimetry: A review. *Proceedings of the IEEE*, **79**(11), 1583–1606.

Zeebe, R., H. Eicken, D. Robinson, G. Dieckmann, and D. Wolf-Gladrow (1996). Modeling the heating and melting of sea ice through light absorption by microalgae. *Journal of Geophysical Research*, **111**(C1), 1163–1182.

Zelli, C. (1998). *High Spatial Resolution Radar Altimeter: Payload Options Definition* (Issue 2, ESA Contract Report TNO/RAS/0041/ALS). ESA, Noordwijk, The Netherlands.

Zhang, J., D. A. Rothrock, and M. Steele (1998a). Warming of the Arctic Ocean by a strengthened Atlantic inflow: Model results. *Geophysical Research Letters*, **25**(10), 1745–1748.

Zhang, J., W. D. Hibler III, M. Steele, and D. A. Rothrock (1998b). Arctic ice–ocean modeling with and without climate restoring. *Journal of Physical Oceanography*, **28**, 191–217.

Zhang, J., D. A. Rothrock, and M. Steele (2000). Recent changes in Arctic sea ice: The interplay between ice dynamics and thermodynamics. *Journal of Climate*, **13**(17), 3099–3114.

Zhang, J., D. Thomas, D. A. Rothrock, R. W. Lindsay, Y. Yu, and R. Kwok (2003). Assimilation of ice motion observations and comparisons with submarine ice thickness data. *Journal of Geophysical Research*, **108**(C6), 3170, DOI: 10.1029/2001JC001041.

Zhang, X., J. E. Walsh, J. Zhang, U. S. Bhatt, and M. Ikeda (2004). Climatology and interannual variability of Arctic cyclone activity: 1948–2002. *Journal of Climate*, **17**, 2300–2317.

Zhang, Y. and A. J. Semtner (2001). The Antarctic Circumcolar Wave in a global, high-resolution, coupled ice-ocean model. *Annals of Glaciology*, **33**, 539–544.

Zhao, Y. and A. K. Liu (2001), Principal-component analysis of sea-ice motion from satellite data. *Annals of Glaciology*, **33**, 133–138.

Zhao, L. and F. Weng (2002). Retrieval of ice cloud parameters using the Advanced Microwave Sounding Unit (AMSU). *Journal of Applied Meteorology*, **41**, 384–395.

Zhao, Y., A. K. Liu, and C. A. Geiger (1998). Arctic sea ice motion from wavelet analysis of SSM/I data. *Journal of Advanced Marine Science and Technology Society,* **4**(2), 313–322.

Zhao, Y., A. K. Liu, and D. G. Long (2002). Validation of sea ice motion from QuikSCAT with those from SSM/I and buoys. *IEEE Transactions on Geoscience and Remote Sensing*, **40**(6), 1241–1246.

Zhou, G., O. Baysal, and P. Kauffmann (2002). Current status and future tendency of sensors in Earth observing satellites. *Proceedings of the Pecora 15/Land Satellite Information IV/ISPRS Commission I/FIEOS*.

Zhou, X. and S. Li (1999). Summer and winter snow and sea ice surface spectral directional reflectance and albedo measured in the Ross Sea. *IGARSS '99* (Vol. I), pp. 104–106.

Zhou, X. and S. Li (2000a). Concentration determination of sea ice pressure ridge in the Ross Sea based on radar backscatter and object delineation methods. *Proceedings of IGARSS '00, Taking the Pulse of the Planet: The Role of Remote Sensing in Managing the Environment, Hawaii, July 24–28*. Institute of Electrical and Electronics Engineers, Piscataway, NJ, pp. 1323–1325.

Zhou, X. and S. Li (2000b). Measurement of BRDF of snow and sea ice in the Ross and Amundsen Seas by the visible and near-infrared channels of MODIS. *Proceedings of IGARSS '00, Taking the Pulse of the Planet: The Role of Remote Sensing in Managing the Environment, Hawaii, July 24–28*. Institute of Electrical and Electronics Engineers, Piscataway, NJ, pp. 1567–1569.

Zhou, X. and S. Li (2003). Comparison between *in situ* and MODIS-derived spectral reflectances of snow and sea ice in the Amundsen Sea, Antarctica. *International Journal of Remote Sensing*, **24**(24), 5011–5032.

Zhou, X., S. Li, and K. Morris (2001). Measurement of all-wave and spectral albedos of snow-covered summer sea ice in the Ross Sea, Antarctica. *Annals of Glaciology*, **33**, 267–274.

Zibordi, G. and G. P. Meloni (1991). Classification of Antarctic surfaces using AVHRR data: A multispectral approach. *Antarctic Science*, **3**, 333–338.

Zibordi, G. and M. Van Woert (1993). Antarctic sea ice mapping using the AVHRR. *Remote Sensing of Environment*, **45**, 155–163.

Zibordi, G., M. Van Woert, G. P. Meloni, and I. Canossi (1995). Intercomparison of sea ice concentration from SSM/1 and AVHRR data of the Ross Sea. *Remote Sensing of Environment*, **53**, 145–152.

Zink, M. (2003). The TerraSAR–L Interferometric Mission objectives. *Proceedings of the ESA Fringe '03 Workshop, December 1–5, 2003, ESA ESRIN*. Available online at ⟨*http://earth.esa.int/workshops/fringe03/*⟩.

Zink, M., C. Buck, J.-L. Suchail, R. Torres, A. Bellini, J. Closa, Y.-L. Desnos, and B. Rosich (2001). The radar imaging instrument and its applications: ASAR. *ESA Bulletin*, **106**, 46–55.

Zubov, N. N. (1943). *L'dy Arktiki (Arctic Ice)* (Technical Report AFGL-TR-79-0034, 1979, U.S. Air Force Geophysical Laboratory, Hanscom Air Force Base, MA). Izdatel'stvo Glavsevmorputi, Moscow, 491 pp.

Zwally, H. J. (2004a). Advances in measuring Antarctic sea-ice thickness and ice-sheet elevations with ICESat laser altimetry. *The XXVIII SCAR and COMNAP XVI Meeting, Bremen, Germany, July 25–31* (Abstract Volume). Alfred-Wegener-Stiftung, Berlin, pp. 86.

Zwally, H. J. (2004b). IceSat's measurements of ice sheet elevation changes and sea ice thickness distributions. *European Geosciences Union 1st General Assembly, April 25–30, Nice, France* (Abstract EGU04-A-06648).

Zwally, H. J., J. C. Comiso, C. L. Parkinson, W. J. Campbell, F. D. Carsey, and P. Gloersen (1983). *Antarctic Sea Ice 1973–1976 from Satellite Passive Microwave Observations* (NASA SP-459). NASA, Washington, DC, 206 pp.

Zwally, H. J., J. C. Comiso, and A. L. Gordon (1985). Antarctic offshore leads and polynyas and oceanographic effects. In: S. Jacobs (ed.), *Oceanology of the Antarctic Continental Shelf* (AGU Antarctic Research Series No. 43). American Geophysical Union, Washington, DC, pp. 203–226.

Zwally, H. J., J. A. Major, A. C. Brenner, and R. A. Bindschadler (1987). Ice measurements by Geosat radar altimetry. *Johns Hopkins APL Technical Digest*, **8**(2), 251–254.

Zwally, H. J., J. C. Comiso, C. L. Parkinson, D. J. Cavalieri, and P. Gloersen (2002a). Variability of Antarctic sea ice 1979–1998. *Journal of Geophysical Research*, **107**(C5), 3041, DOI: 10.1029/2000JC000733.

Zwally, H. J., B. Schutz, W. Abdalati, J. Abshire, C. Bentley, A. Brenner, J. Bufton, J. Dezio, D. Hancock, D. Harding et al. (2002b). ICESat's laser measurements of polar ice, atmosphere, ocean, and land. *Journal of Geodynamics*, **34**, 405–445.

Zwally, H. J., D. Yi, J. Saba, and S. W. Laxon (2004). Mapping Arctic sea-ice freeboard-height distributions and ice thicknesses with ICESat. *EOS, Transactions of the AGU*, **85**(47), Fall Meeting Supplement, Abstract C22A-05.

Appendix

Parameters of synthetic aperture radar missions

As discussed in Chapters 1 and 5, Synthetic Aperture Radar (SAR) is perhaps the single most powerful tool for high-latitude remote sensing, by virtue of its ability to map surface features at high spatial resolution in all weather. This appendix tabulates the instrumental parameters of the major polar-orbiting SAR sensors since 1978, and illustrates the steady increase in capabilities.

Table A.1. Frequency and wavelength of IEEE (Institute of Electrical and Electronics Engineers) radar band designation.

Band	*Frequency* (GHz)	*Wavelength* (cm)
P-Band	0.3–1	30–100
L-Band	1–2	15.0–30.0
S-Band	2–4	7.5–15.0
C-Band	4–8	3.75–7.5
X-Band	8–12	2.5–3.75
Ku-Band	12–18	1.67–2.5
K-Band	18–27	1.11–1.67
Ka-Band	27–40	0.75–1.11

Table A.2. The NASA Seasat SAR.

Parameters	*Seasat SAR*
Mission month	July–October
Mission year	1978
Altitude (km)	800
Orbital inclination	108°
Frequency (GHz)	1.28
Polarization	HH
Swathwidth (km)	100
Azimuth (AZ) resolution (m)	25 (4-look)
Range (RG) resolution (m)	25
Peak power (kW)	1
Bandwidth (MHz)	19

Table A.3. The Japan Aerospace Exploration Agency (JAXA) Japanese Earth Resources Satellite-1 (JERS-1) SAR.

Parameters	*JERS-1 SAR*
Launch date	11 February 1992
Operation end date	12 October 1998
Altitude (km)	570
Orbital inclination	98°
Orbital period (minutes)	96
Repeat cycle (days)	44
Local time at descending node	10 : 30–11 : 00 AM
SAR observation frequency (GHz)	1.3 (L-band)
Bandwidth (MHz)	15
Polarization	HH
Resolution (m)	18 (3-look)
Nadir angle	35°
Swathwidth (km)	75

Table A.4. The European Space Agency (ESA) Advanced Microwave Instrument (AMI) aboard the Earth Remote Sensing satellites (ERS-1, ERS-2).

Parameters	*AMI aboard ERS-1 and ERS-2*
Launch dates (ERS-1, ERS-2)	17 July 1991, 21 April 1995
Operation end date (ERS-1)	10 March 2000
Altitude (km)	785
Orbital inclination	98.5°
Orbital period (minutes)	100
Repeat cycle (days)	35
Local time at descending node	10 : 30 AM
SAR observation frequency (GHz)	5.3 (C-band)
Bandwidth (MHz)	15.55
Polarization	VV
Resolution, alongtrack (m)	6–30
Resolution, acrosstrack (m)	26.3
Nadir angle	23°
Swath .width (km)	102.5

Table A.5. The Canadian Space Agency RADARSAT-1 SAR (Luscombe et al., 1993[1]).

Parameters	*RADARSAT-1 SAR*
Launch date	4 November 1995
Altitude (km)	798 km
Orbital inclination	98.6°
Orbital period (minutes)	100.7
Repeat cycle (days)	24
Local time at ascending node	18 : 00 ± 00 : 15
SAR observation frequency (GHz)	5.3 (C-band)
Bandwidth (MHz)	11.6, 17.3, or 30.0
Polarization	HH

RADARSAT-1 SAR imaging modes:

Mode	*Nominal resolution* (m)	*Number of beams* (km)	*Swathwidth*	*Nadir angle* (°)
Fine	8	15	45	37–47
Standard	30	7	100	20-49
Wide	30	3	150	20–45
ScanSAR Narrow	50	2	300	20–49
ScanSAR Wide	100	2	500	20–49
Extended High	18–27	3	75	52–58
Extended Low	30	1	170	10–22

[1] Luscombe, A. P., I. Ferguson, N. Shepherd, D. G. Zimcik, and P. Naraine, (1993). The RADARSAT synthetic aperture radar development. *Canadian Journal of Remote Sensing*, **19**(4), 298–310.

Table A.6. The ESA Environmental Satellite (ENVISAT) Advanced Synthetic Aperture Radar (ASAR).

Parameters	*ENVISAT ASAR*
Launch date	1 March 2002
Altitude (km)	800 km
Orbital inclination	98.55°
Orbital period (min)	100.6
Repeat cycle (days)	35
Local time at descending node	10 : 00 AM
SAR observation frequency (GHz)	5.33 (C-band)
Polarization	VV, HH, or cross (HH&HV or VV&VH)

ENVISAT ASAR imaging modes:

Mode	*Polarization*	*Resolution* (m)	*Swathwidth* (km)	*Characteristics*
Image Mode (IM)	VV or HH	30	58–109	7 selectable swaths
Alternating Polarization (AP) mode	HH/VV, HH/HV, or VV/VH	30	58–109	2 co-registered images per acquisition in 1 of 7 selectable swaths; radiometric resolution reduced as compared with IM
Wide Swath (WS)	VV or HH	150	405×405	ScanSAR mode
Global Monitoring (GM)	VV or HH	1000	405×405	ScanSAR mode
Wave Mode (WM)	VV or HH	30	5×5 or 5×10 vignettes	Vignettes are acquired at regular intervals alongtrack, and are converted to wave spectra for ocean monitoring

Table A.7. Canadian Space Agency RADARSAT-2 SAR.

Parameters	*RADARSAT-2 SAR*
Launch date	Mid-2005
Altitude (km)	798 km
Orbital inclination	98.6°
Orbital period (min)	100.7
Repeat cycle (days)	24
Local time at ascending node	18 : 00
SAR observation frequency (GHz)	5.405 (C-band)
Polarization	HH, VV, HV, VH

RADARSAT-2 imaging modes:

Polarization	*Beam mode*	*Resolution RG × AZI* (m)	*Swathwidth* (km)
Selective single	Ultra-fine	3 × 3	20
Transmit H or V	Multi-look fine	11 × 9	50
Receive H or V			
Polarimetric	Fine Quad-Pol	11 × 9	25
Transmit H and V on alternate pulses	Standard Quad-Pol	25 × 28	25
Receive H and V on every pulse			
Selective polarization	Standard	25 × 28	100
Transmit H or V	Wide	25 × 28	150
Receive H or V or (H and V)	Low incidence	40 × 28	170
	High incidence	20 × 28	70
	Fine	10 × 9	50
	ScanSAR Wide	100 × 100	500
	ScanSAR Narrow	50 × 50	300

Courtesy Canadian Space Agency.

Table A.8. JAXA Advanced Land-Observing Satellite (ALOS) Phased-Array-type L-band Synthetic Aperture Radar (PALSAR).

Parameters	*PALSAR*
Launch date	Mid-2005
Altitude (km)	691.65
Orbital inclination	98.16°
Repeat cycle (days)	46 days (2 days for side-cycle instruments)
Local time at descending node	10 : 30 AM
SAR observation frequency (GHz)	1.27 (L-band)
Polarization	Single, dual, quad-polarization

PALSAR imaging modes:

Mode:	*High resolution*		*Direct downlink*	*ScanSAR*	*Polarimetry*
	Single-pol	*Dual-pol*			
Polarization	HH or VV	HH/HV or VV/VH	HH or VV	HH or VV	HH/HV + VV/VH
Nadir angle (°)	8–60 (39 typical)	8–60 (39 typical)	8–60 (39 typical)	18–43	8–30 (24 typical)
Resolution (m)	7–44 (10 at 39°)	14–88 (20 at 39°)	14–88 (20 at 39°)	100 (multilook)	24–89 (30 at 24°)
Swathwidth	40–70	40–70	40–70	250–350	20–65

Courtesy A. Rosenqvist, JAXA.

Table A.9. The ESA TerraSAR-L.

Parameters	*TerraSAR-L*
Launch date	2008
Altitude (km)	630
Repeat cycle (days)	14
Local time at ascending node	18 : 00
SAR observation frequency (GHz)	1.258 (L-band)
Polarization	Single, dual, quad-polarization

TerraSAR-L imaging modes:

Mode	*Nadir angle* (°)	*Resolution* $RG \times AZI$ (m)	*Swathwidth* (km)
Quad Polarization	20–36	9×5	40
Dual Polarization	20–45	9×5	70
Single Polarization	20–45	5×5	70
ScanSAR Dual-Pol	20–45	50×50	>200
ScanSAR Single-Pol	20–45	20×5	>200
Wave mode	20–45	9×5	20

Courtesy M. Zink, ESA-ESTEC.

Table A.10. The DLR TerraSAR-X.

Parameters	*TerraSAR-X*
Launch date	April 2006
Altitude (km)	514
Orbital inclination	97.44°
Repeat cycle (days)	11
Local time at ascending node	18 : 00
SAR observation frequency (GHz)	9.65 (X-band)
Polarization	Single, dual, quad-polarization

TerraSAR-X imaging modes:

Mode	*Coverage RG x AZI* (km)	*Resolution RG x AZI* (m)	*Polarization*	*Nadir angle range* (degrees)
HR Spotlight	10×5	$(1.5–3.5) \times 1.0$	Single, Dual, Quad	20–55
Spotlight	10×10	$(1.5–2.3) \times 2.0$	Single, Dual, Quad	20–55
StripMap	$30 \times \leq 1{,}650$	$(1.7–3.5) \times 3.0$	Single	20–45
Polarimetric StripMap	$15 \times \leq 1{,}650$	$(1.7–3.5) \times 6.0$	Dual, Quad	20–45
ScanSAR	$100 \times \leq 1{,}650$	$(1.7–3.5) \times 16.0$	Single, Dual, Quad	20–45
Experimental 300-MHz Spotlight	10×5	$(0.6–1.5) \times 1.0$	Single, Dual, Quad	20–55
Experimental dual-receive StripMap	$30 \times \leq 1{,}650$	$(1.7–3.5) \times 1.5$	Single, Dual, Quad	20–45

Courtesy S. Lehner, DLR.

Index

A-train, NASA constellation 52, 411
AARC 44, 58
AATSR 54, 414, 416, 523, 572, 576
Absorptance 87, 366
Absorption
  coefficient 103, 362
  correction for atmospheric 258, 367, 416
  cross section 76, 88, 144, 163–164
  definition 74–80
  retrieval (POAM) 166
  shortwave 275–276
Adams, John Quincy 7, 8, 10, 13, 19
ACIA 328, 332, 334
Acoustic doppler current profiler 521
ACSYS 332, 334, 342, 508, 609
Active Polarization Ratio (APR) 457–459
ADEOS, JAXA spacecraft 45, 97, 119, 144, 400, 411, 465, 499–500, 559, 594–597, 614
ADEOS–II, JAXA spacecraft 42, 45, 381, 400, 411, 419, 423–424, 427, 432, 434, 526, 559, 590
Adding–doubling method 90
Advanced Horizontal Range Algorithm (AHRA) 593–594, 598
Aerial photography 565
Aerosol 40, 50, 159, 165–166, 173, 277, 279– 282, 367, 415
  accumulation mode 281
  coarse mode 281
  chemical composition 281
  deposition on sea ice 350
  direct shortwave effect 277, 280
  direct longwave effect 280
  extinction 88, 89, 163, 167–168, 172, 258, 260
  indirect effects 50, 51, 280
  optical depth 166–167, 265–268
  scattering 82
  semi-direct effect 280
  stratospheric 141, 169, 171
  vertical distribution 405
Aerosonde 314, 603
Air Force Geophysics Laboratory (U.S.) 90
AIRS 47, 123, 249
AIRSAR 535, 544
Alaska Satellite Facility (ASF) 390, 397–399, 502, 504, 539, 611
Albedo
  definition 71, 358, 582–583
  ocean 362
  planetary 53, 583
  satellite imagery display 73
  satellite measurement of 582–590
  sea ice 181, 214, 237, 250, 255–256, 362–363
  shortwave 274, 583
  snow surface 250–251, 254–255
  surface 36, 53, 92, 193–194, 205, 235, 237,

Albedo (*cont.*)
249–265, 270–271, 344, 417, 420, 468, 522, 561, 592
Aleutian low 452, 525
Algal blooms 453
ALI 51, 420
Almaz, Russian spacecraft series 389
Along-track scanning direction 92, 514–516
ALOS, JAXA spacecraft 56, 392, 394, 399, 419, 437–438, 460, 463, 479, 522, 534, 539, 550–551, 571, 611
American Geophysical Union 198
Amery Ice Shelf 42, 198
AMI 389, 399
AMPS 200–201
AMRC 43, 58, 196–197, 200
AMSR 381, 424, 427, 434, 457, 475, 480, 493, 512, 526, 530, 564, 594, 614
AMSR bootstrap algorithm (ABA) 427–428
AMSR sea ice concentration algorithms 426–434
AMSR-E 48, 381, 417, 423, 427–432, 434, 444, 456, 475, 481, 493, 512, 523, 526, 530, 557, 562–563, 580–582, 603
AMSU 47, 381, 417, 433–434
Amundsen, Roald 36
Amundsen Sea 205, 446–447, 455, 581
ANARE 195
Annawan, U.S. merchant brig 9
Angular dependence model 72
Angular second moment 222
Anisotropic reflectance factor 71, 257–258, 585–586
Anisotropy 547–548, 585
Antarctic Bottom Water 336, 338, 471–472, 480, 486
Antarctic Circumpolar Current (ACC) 320, 322, 329, 451, 497–498
Antarctic Circumpolar Wave (ACW) 338, 451, 580
Antarctic food web (foodchain) 179–180, 329
Antarctic Oscillation 339, 436
Antarctic Peninsula 5, 9, 24, 26, 173, 181–182, 184, 195, 203–205, 294, 337, 340–341, 446, 448, 450, 452, 455, 580
Antarctica and the Global Climate System (AGCS) 342
Antenna 116
Apodization function 126–127
APT telemetry 409
Aqua, NASA spacecraft 42, 46, 50, 179, 212, 410–411, 423, 427, 434, 461, 476, 526, 559, 562, 572, 580, 584, 602, 614
Aquarius, NASA and Argentinian spacecraft 527
Aral Sea 310
Arctic marine system 316
Arctic Ocean Section, Canada/U.S. expedition 226
Arctic Oscillation (AO) 46, 194, 335–336, 339, 451, 493, 552, 579, 594
Argentine Islands Station, Antarctica 139
Argos telemetry 197, 489, 505
Argument of perigee 65
ARM program, U.S. Department of Energy 293–294
Artist algorithm 424
ASAR 54, 390–393, 398, 463–464, 504, 520, 536, 539, 540, 545, 549–551, 610–611, 614–615
ASCAT 55, 400, 501, 557, 614
Ascending node 64, 66, 410
ASPeCt 342
Asymmetry factor 83, 228, 235, 281
ASTER 47, 415–416, 418–419, 571, 588
Atlantic Water 333
Atlas of Antarctic Sea Ice Drift 498–499, 507
ATMOS 159
Atmospheric correction 416, 572, 590
Atmospheric sounding 44, 120, 126, 160, 210
ATSR(/2) 414–416, 572–573, 575–576, 578
Aura, NASA spacecraft 48, 49, 66, 144, 411
Aurora Australis, Australian icebreaker 57, 558
Augsburg College 196
Australian Bureau of Meteorology 557
Automated Geophysical Observatory (AGO) 196, 201
Automatic weather stations 195–199, 201–202, 314
Autonomous underwater vehicle (AUV) 453, 509, 518
Autosub 346, 453
AVHRR 42, 44, 53, 54, 57, 73, 93, 94, 97, 108, 112, 113, 134, 173, 175, 176, 200,

201–203, 208, 212, 217–219, 221, 223–224, 226, 229, 230–232, 234–242, 255, 257–261, 267–270, 284, 288, 335, 392, 407–409, 411, 414–416, 435, 439–443, 445, 454, 461, 465–466, 471, 476, 478–481, 484–485, 490–492, 495–497, 520, 522–524, 556–559, 570, 572–580, 583–585–587, 592, 609, 612, 614
AVNIR(–2) 56, 394, 419, 465, 559, 571, 594
AWiFS 419

Backscatter coefficient (*see* Microwave)
Backscatter UltraViolet (BUV sensor) 44
Baffin Bay 470, 493, 601
Balleny Islands 495
Baltic Sea 310, 544
Band gap 99, 103, 116
Bandwidth, detector 104, 105, 128
Banks, Sir Joseph 8
Barents Sea 452, 454, 544–545, 599
Barrow 466
Bayesian classifier 214–215, 217, 224, 547, 567
Bayesian statistics 285
Beamsplitter 123–124
Beaufort Gyre 333, 335, 451, 494, 496–497, 508, 552
Beaufort High 451
Beaufort Sea 245–246, 294, 3143, 336, 445, 450, 455, 470, 517, 535, 544, 548, 549, 552, 558, 570, 589, 599–600, 612
Beer's (Bouger's) law 80, 84, 163
Bellingshausen Sea 195, 205, 436, 446–448, 455, 531, 581, 605
Bellingshausen, Thaddeus von 6, 36
Bering Sea 333, 442, 452, 455, 467–468, 525, 557, 606, 610
Bering Strait 321, 442
Bering, Vitus 442
BEST 343
Bidirectional reflectance distribution function (BRDF) 71–74, 240–241, 252, 257, 262, 274, 417, 584–585, 587–588, 590–591, 603
Biogeochemical cycling 324–325, 327–328, 330, 468–469, 494
Biotechnology 331
Black Sea 310
Blackbody 86, 366, 433, 592
Blackbody calibration source 109, 110, 217, 240
Blaze, of grating 122
Bolometer 98
Bootstrap algorithm 423–427, 552
Bootstrap Basic Algorithm (BBA) 423, 427–428
Bottom Water (*see also* Antarctic Bottom Water) 325, 328, 336, 338, 468
Bowtie imaging configuration 95, 97
Bragg scattering waves 533
Brash ice (*see* Sea ice)
Brewer–Dobson circulation 137–138
Brigham Young University 458–459
Brightness temperature 87, 114, 117, 173, 175, 217–220, 230–232, 237, 285, 287–289, 366–367, 369, 371, 423–424, 426–431, 444, 456, 495, 525, 563–564, 573, 592–594, 596
Brine rejection 468, 479–482
Bristol algorithm 423
British Antarctic Survey 138–139, 151–153, 195, 196, 294
Buoys, drifting 489
Byrd Polar Research Center 204
Byrd, Richard 2

C, programming language 59
CALIOP 52
CALIPSO, NASA spacecraft 52, 282, 411
Cal/Val (AES-York) algorithm 423
Canadian Arctic Archipelago 321, 497
Canadian Basin 497
Canadian Ice Service 502, 609–610
Canadian Space Agency (CSA) 610
Cape Hudson 486
Carbon cycle 327, 330, 337, 453
CASES 342
Casey Station, Antarctica 557
Caspian Sea 310
CASPR 230, 586
CAST, Chinese Academy for Space Technology 57
Catalytic cycles (ozone destruction) 134–137
CEAREX drift group 286–290
Centre for Cold Ocean Resources Engineering (C-CORE) 614

CERES 46, 53, 110, 262
CERSAT 402, 554
Chapman, Sydney 134
Charge-coupled device (CCD) 101–103, 105, 106, 110
Chile 9, 10, 24
Chlorofluorocarbons (CFCs) 133, 136–138
Chlorophyll 56, 119, 182–183, 453–454, 482
Chukchi Sea 442, 455, 481, 517, 552, 570, 589, 599, 606
Circumpolar Deep Water 471
Circumpolar Trough 498
Circumpolar vortex, Antarctic 338
CLAES 178
Clear sky precipitation (*see* Diamond dust)
CLIC 342–343
Climate warming 1, 46, 133, 193–195, 290, 335, 337, 341, 349, 468
CLIVAR 315, 338, 342
ClO (chlorine monoxide) 128–129, 141, 178
Cloud amount (fraction) 227, 243, 264–266, 270, 272, 290
  base height 248
  clearing 285
  detection and classification 213–226, 289, 414, 559, 584, 588
  droplet size distribution 227–228, 245
  effect (CE) 275
  effective radius 51, 220, 228, 235–246, 248–249
  excess absorption 293
  emissivity 211, 217, 220, 280
  forcing 264, 270, 272, 468
  ice water content 247
  ice water, optical properties 200, 220
  liquid water 173, 233, 424
  liquid water asymmetry factor 83
  liquid water content 51, 57, 227–228, 244–246, 248, 265
  liquid water extinction, microwave 115
  masking 214, 219, 414–415, 420, 440, 462, 523, 584, 586, 588
  optical depth 181, 194, 201, 227–228, 235–244, 265–266, 586
  particle size 40, 52, 249
  susceptibility 280
  temperature 213, 220, 238
  thermodynamic phase 52, 194, 227–228, 230–235, 287
  tropospheric cirrus 173, 175, 243–244, 414
  vertical inhomogeneity 243
Cloud–radiation feedback 46, 194
CloudSat, NASA spacecraft 50, 411
CMIS 53, 381–382, 491, 493, 501, 557
CNES, Centre National d'Etudes Spatiales 56, 405, 411
CO_2 40, 48, 78, 154, 176, 210, 283, 286, 324, 327–329, 336–337, 342, 367, 469
CO_2-slicing 120, 154, 210–211, 248, 286
Coarse mode 281
Coherency matrix 541, 547–548
Cold halocline layer (CHL) 334
Columbia, NASA space shuttle 53
Commonwealth Bay 477
Community climate model (CCM), NCAR 277–279
Congelation ice (*see* Sea ice)
Congress, U.S. 5–11, 13, 17
Contrast 222
Cook Ice Shelf 486
Cook, James 8, 12
Coriolis, U.S. Navy spacecraft 382
Coriolis force 355
Corona, U.S. spy satellite series 413
COSMO-SkyMed, European spacecraft program 397
Couthouy, James 15, 16, 23, 24, 37
Covariance matrix 541
Crabeater seal 558
CrIS 53–54
Crosstrack scanning direction 92, 93, 96, 217, 411, 417, 419, 433
Cryogenic cooling 100
CryoSat, ESA spacecraft 312, 405, 511–515, 517–18, 520
CRYSYS 342
CTD data 346
CTSK1
algorithm 559
Curtis–Godson approximation 164
Cyclogenesis 201, 205, 332
CZCS 45, 182–183, 410, 454, 484

DAAC 57–58, 398–399, 426, 461, 539
Dana, James Dwight 15, 19, 21, 23, 24, 37, 38
Danish Center for Remote Sensing 544
Danish Meteorological Institute 611

Dark current 105, 111
Darwin, Charles 12, 38
Deep Water 325, 327, 334, 338, 468
de Gerlache, Adrien 36
Defense Intelligence Satellite Program, U.S 413
Delta–Eddington approximation 89
Democratic–Republican party (U.S. history) 7, 8, 17
Denitrification 143, 178
Density, sea water 511
Depletion region 100
Descending node 64, 66, 159, 410
Des Groseilliers, Canadian Coast Guard icebreaker 57, 294, 601
Detectivity, specific 106, 107
Diamond dust 261, 415, 523, 575, 578
Dickerson, Mahlon 13–18, 21, 38
Dielectric constant, definition 370
Dielectric constant, water 373
Dielectric loss noise 105
Differential absorption spectroscopy 138, 140, 144, 151, 156, 159
Differential kinematic parameters (*see* Sea ice, kinematics)
Diffraction limit 93
Diffuser 110
Dimethylsulfide (DMS) 331
Dimethylsulfoniopropionate (DMSP) 331
Dirac delta function 70
Directional hemispherical reflectance, of snow 360
Directivity 117, 119
Discrete dipole approximation 92, 229
Discrete ordinates method 90, 236, 360
DISORT radiative transfer model 90, 360, 587, 590
DKPs 504, 507
DLR, German aerospace agency 55
DMSP, U.S. satellite series 44, 45, 53, 94, 97, 200, 209, 251, 311, 381, 417, 423, 426, 439, 446, 449, 454, 456– 457, 465, 471, 473, 475, 480, 495, 526, 551, 557, 577, 592–593, 596, 599, 609, 612, 614
DNA damage 180
Dobson spectrophotometer 138, 144, 151–152
Dobson unit 134
Doppler broadening lineshape 79
DORIS 54, 515
DSCOVR, NASA spacecraft 52, 53, 62, 144
Dumont D'Urville, Jules-Sébastien-César 16, 17, 19, 24, 26, 32, 33, 36
Dwell time (integration time) 93
Dynamic range, detector 101, 104
Dynode 101

EarlyBird 419
Earth location (navigation) 98, 490
Earth Observation Research Center (JAXA) 58, 411
Earth Observing System (EOS) 2, 42, 44–53, 57–58, 66, 97, 116, 123, 294, 381, 398, 406, 410, 413, 415, 417, 426, 434, 488, 539, 562, 602
Earth Probe, NASA spacecraft 144–145, 148
Earth Science Enterprise, NASA 153
Earthnet, ESA 551
EASE–Grid 408, 495, 575, 587
East Siberian Sea 516, 599
East Wind Drift 465, 484, 497–498
Eccentric anomaly 63
Echelle spectrograph 122
ECMWF 198, 435, 445
Eddington approximation 89
e-folding distance 361
Eigenvalue decomposition 547
Eights, James 8, 9, 15, 19
El Niño–Southern Oscillation (ENSO) 46, 195, 198, 204, 329, 338, 436, 447, 451–452, 580
Eld, Henry 27, 28, 29
Electromagnetic induction (EMI) 510
Electromagnetic radiation 39, 40, 41, 67, 116, 331, 383
Electromagnetic spectrum 39, 41, 108, 357–358, 361
Ellesmere Island 503, 516
EMISAR 544
Emissivity 87, 115, 211, 249–250, 254, 260, 263, 280, 287, 288, 345, 366–368, 376, 384, 424, 429–430, 433, 574, 576
Empirical orthogonal function (EOF) 335
Entrance slit 120–121, 126
Endurance, HMS 489
Entropy 222, 547, 551

Envisat, ESA spacecraft (*see also* ASAR) 42, 45, 54, 97, 126, 387, 390–391, 393, 398, 403–406, 412, 416, 438, 460, 463, 479, 504, 513, 515, 534, 536, 540, 545, 549–550, 559, 607, 610–611, 614–615
EO-1, NASA spacecraft 51, 120, 420
EOSDIS 57, 59
EPIC 52, 144
Equatorial coordinate system 64
Equinox 64
Equivalent blackbody temperature 88, 107, 109
ERB, NASA spacecraft 45
ERBE, NASA sensor and constellation 72, 262, 274–279
Erebus, HMS 26, 34
EROS Data Center, U.S. Geological Survey 413
EROS-A1 419
Error propagation 264–265
ERS-1, ESA spacecraft 42, 45, 54, 387, 388–390, 398–400, 403, 405–406, 416, 460, 461, 463, 465, 478–479, 502, 504, 511, 513, 530, 531, 534, 553, 556, 575–576, 595–596, 598–599, 605, 608–609
ERS-2, ESA spacecraft 45, 54, 388, 399–400, 405–406, 414, 416, 437, 461, 465, 479, 502, 504, 511, 513, 538, 557, 566, 596, 606–607
ERTS-1, NASA spacecraft 42
ESA Earth Observation User Service Portal 58
ESCAT 399–402, 494, 553, 556
ESMR 310, 380–381, 423, 426, 443–444
ETM+ 51, 97, 414, 417–418, 463, 571, 600, 602
EUMETSAT 556
Eurasian Basin 334, 565
European Space Agency (ESA) 54–55, 58, 179, 390, 400, 405, 513, 603, 611, 613
Excitance, radiant 69
Exploring Expedition, United States (1838–42) 2, 7–39
Exponential sum fitting of transmissions 91
External mixture 281

Fanning, Edmund 5, 6, 7, 9, 15
Faraday Station, Antarctica 340
Fast Atmosphere Signature Code (FASCOD) 90, 91
Fast ice (*see* Sea ice)
Feature space 215
Feature vector 225
Feautrier method 90
Fengyun (FY-), CAST spacecraft series 57, 408–409, 414, 439, 558
Field of view (FOV) 39, 93, 96, 110, 160, 164–165, 415, 426, 490, 523, 526, 531, 577, 585, 590
Figures of merit, detector 103
Finnish Meteorological Institute 48
Firn 348
First year ice (*see* Sea ice)
Flaw leads (*see* Sea ice)
Floes (*see* Sea ice)
Flux (irradiance)
  broadband 69
  definition 68, 365
  downwelling 68, 262, 344, 347
  extraterrestrial solar 68, 70, 73, 85–86, 146, 223, 257, 263, 559
  incident on detector 104
  isotropic net 68, 262–270
  upwelling 68, 262, 344
Flying Fish, USS 21, 24–26, 32, 33, 36
FORTRAN, programming language 59, 90, 152, 229
Focal plane 116, 120
Fourier Transform Infrared (FTIR) 49, 55, 123–127, 227, 248, 250, 280, 294
Fram Strait 321–322, 333, 335, 493–494, 497, 513, 570, 608, 614
Frazil ice (*see* Sea ice)
Freeboard (*see* Sea ice)
Frequency-modulated continuous wave radar 564
Frequency response, detector 104
Freshwater budget (fluxes) 325–326, 334, 336, 341
Fresnel diffraction theory 117
Frost flowers 375, 537
Full width at half maximum (FWHM) 159–160

Gain, detector 101
Gas correlation spectroscopy 283
Generation–recombination noise 105

Geolocation (navigation) 98, 408
Geographic Iinformation Ssystem (GIS) 498, 600
Geophysical Processor System (GPS) 504, 538
Geophysical Research Letters 140
Geostationary satellites 314
Glacier tongue 325, 558
GLAS 39, 49, 52, 405–406, 515–518, 567–568
GLI 56, 411, 415, 559, 590
Global area coverage (GAC) 226, 407
Global Change Master Directory 57
Global Climate Model (GCM) 193, 195, 228, 264, 277, 293, 332, 336, 340, 469, 583, 600, 604
Global Monitoring Mode (GMM, Envisat ASAR) 392–393, 614–615
Global Positioning System (GPS) 611
Global Telecommunications System (GTS) 489
Global warming (*see* Climate warming)
Global Weather Center (U.S. Air Force) 148
GLOBEC 343
GOES 200, 210, 211
Golay cell 98
GOME 123
Gradient ratio (GR) 424, 431–432, 562–563
Grating 120–122
Gray, Asa 15, 21, 23, 24
Graybody 366
Gray level difference vector 222–223
Grease ice (*see* Sea ice)
Great Salinity Anomaly 336
Greenhouse effect 264
Greenhouse gases and related warming 328, 332, 336–337
Greenland Ice Sheet 46, 112, 205, 214, 217, 255, 259
Greenland–Iceland–Norwegian (GIN) Seas 326, 494
Greenland Sea 544, 545, 549, 608
Ground instantaneous field of view (GIFOV) 93, 96, 97, 119, 120, 144, 207, 210, 213, 217, 220, 274, 283
Gulf of St. Lawrence 310
Hale, Horatio 15, 19, 21, 23
Half Power Beam Width 117
Halley Bay Station, Antarctica 138–139
Halocline 325, 336, 468, 472
HALOE 159
Healy, USCGC (icebreaker) 57
Helmholtz principle of reciprocity 70
Henry, Joseph 38
Hero, U.S. merchant sloop 5
Herring bone contamination (AVHRR channel 3) 414
Heterodyning 128
Heterodyne radiometer 120
Heterogeneous chemistry 133, 141–143, 179
Hierarchical data format (HDF) 59, 587
HIRDLS 48
HIRS 44, 53, 54
HIRS/2 154–156, 210, 212, 283–289
HITRAN 90
Hobart (Australia) 33, 34
Home of the Blizzard, Mawson 477
Horizontal field of view (HFOV) 159
HRPT telemetry 53, 57, 407, 409
HRV 463
HSB 47
Hudson Bay 560, 593
Hudson, William L. 24–25, 27–31, 33, 37
Hue–lightness–saturation technique 478–479
Hydrologic cycle 46, 315
HYDROS 527
Hyperion 51, 120, 420, 592
Hyperspectral imaging 51, 120, 312, 420, 592

IABP–POLES 519
IAnZone 342
Ice–albedo feedback 46, 193–194, 332, 342, 583, 591
Iceberg B-15 486–487
Iceberg B-15A 487, 488
Iceberg B9-B 477, 486, 558
Iceberg C-19 487
Iceberg detection 406, 421, 484–487, 554, 557, 610
Icebergs, grounded 462, 465, 477, 484, 495
Ice-profiling sonar, moored (IPS, *see also* Submarine sonar) 356, 509, 513, 527, 614

Ice sheet elevation 50
Ice sheet, radar altimeter waveform 404
Icecolors, USAP research cruise 181, 184
Icemap algorithm, MODIS 461
IceMapper algorithm 557
ICEMON 611, 613–615
ICESat, NASA spacecraft 39, 43, 49, 50, 51, 282, 405–406, 515–518, 520, 567–568
Icewatch 611
IDL™ programming language 58
Ikonos 417, 419, 571, 590, 602
Indian Remote Sensing (IRS-), ISRO spacecraft series 56, 382, 418
Indian Space Research Organisation (ISRO) 56–57, 419
Indium gallium arsenide (InGaAs) 100, 103, 104
INDOEX, international experiment 280, 293
Injection noise 106
Insolation 40
Instantaneous field of view (IFOV) 93, 94, 110, 116, 150, 156, 428
Integrating sphere 111
Integration time 93
Intensity, radar backscatter 541
Intensity, specific (of radiation; radiance) 66, 69, 70, 71, 73, 74, 80, 84, 88, 89, 111, 114, 120, 123, 146–149, 154, 164–165, 211, 220– 221, 223, 237, 256–257, 262, 285, 365–367, 430–431, 439, 453, 559, 564
Interferogram 125–126, 464
Interferometer 120, 123
Intermediate frequency (IF) 128–129
Internal mixture 281
International Programme for Antarctic Buoys 489, 498
International Arctic Buoy Program (IABP) 460, 489, 493, 495–496, 498–500, 519, 594, 596, 599, 612
International Geophysical Year 138
International Polynya Symposium 469–470
Inuit communities 332, 462, 469
Inverse centimeters 67
Irradiance (*see* Flux)
IRIS 126
IRS, Indian satellite series 418–419
ISCCP 112, 148, 213–214
Isotropic intensity 69

Jackson, Andrew 7, 9, 10, 11, 13, 17
Japan Coast Guard 611
Jason-1 513
JAXA, Japan Aerospace Exploration Agency 56, 58, 392, 399, 411, 424, 427, 432, 611
JERS-1, JAXA spacecraft 56, 388–389, 399, 437, 465, 502, 534–535, 566
JGOFS 328
Johnson, Walter 15, 18
Johnson (Nyquist) noise 105
Jones, Thomas Ap Catesby 11, 13, 16, 18, 19

k-distribution method 91
Kamchatka Peninsula 525
Kara Sea 465, 599
Katabatic winds 2, 198, 199, 205–207, 209, 467
Kepler
  auxiliary circle 63
  laws of planetary motion 63
Key, Jeffrey 91, 212, 230
Kirchhoff's law 87, 366
Klimat 409
Knowledge-based classification 538
Kosmos, Russian spacecraft series 310, 389
Krill, Antarctic 180, 330, 341, 452–453
L'Astrolabe, French Navy corvette 16
Labrador Current 504
Labrador Sea 493, 548
Lagrange-1 (L1) point 52, 62
Lagrangian analysis 178–179
Lagrangian displacement vectors 490
Lagrangian ice tracking 504
Lambertian surface 70, 73, 111, 236, 240, 461
Landsat 1, NASA spacecraft 42
Landsat 7, NASA spacecraft 51, 66, 110, 414, 417–418, 600
Landsat Multispectral Scanner (MSS) 44, 94, 97, 101, 251, 439, 558–559, 570
Landsat Enhanced Thematic Mapper (ETM+) 51, 97, 414, 417–418, 463, 571, 600–602

Landsat Thematic Mapper (TM) 44, 93, 95, 96, 251, 414, 417, 463, 559
Laptev Sea 463, 494, 599
Larsen-B Ice Shelf 43
Laser altimetry 50, 515–518, 565
Laser profilometry 510
Laser Retro-Reflector (LRR) 515
Latent heat 326
Law Dome, East Antarctic Ice Sheet 337
Lazarev Sea 475
Leads (*see* Sea ice)
Lidar 39, 49, 50, 141, 233, 294, 411
Limb darkening 165
Limb inversion 167–168
Line-by-line radiative transfer calculation 89, 126, 155–156
Line-By-Line Radiative Transfer Model (LBLRTM) 90
Line of nodes 64
Line of sight (LOS) 159–161, 163–165
Line scanner imaging configuration 93, 97, 98
Line shape factor 78, 79
Liou, Kuo-Nan 92
LISS–I, II, III 418–419
LLLS 409
Local area coverage (LAC) 226, 407–408
Local thermodynamic equilibrium (LTE) 87
Longwave radiation 41, 53, 61, 98, 227, 262–266, 269–270, 275–276, 278–281, 290, 344–345, 523
Lorentz profile 78
LOWTRAN radiative transfer model 90–91, 260–261, 573
LTER 343, 455
Lützow-Holm Bay 465, 594

Macedonian, USS 13, 18, 21
Main lobe, antenna 116
Marie Byrd Land 205
Marine Observation Satellite (MOS-1/-1b), JAXA spacecraft 418, 604
Marginal ice zone (MIZ, *see* Sea ice)
Mass absorption coefficient 78–80
Mawson, Sir Douglas 2, 477
Maximum Cross-Correlation (MCC) technique 490, 491, 492–493, 495, 499, 501–502
Maximum likelihood classification 538
McIDAS^{TM} satellite data-processing software 59, 98
McMurdo Sound 487
McMurdo Station, Antarctica 44, 58, 142, 180, 196, 200, 248
Mean anomaly 63
Mean motion constant 63
Meltponds (*see* Sea ice)
Melville, Herman 9
Mercury cadmium telluride (HgCdTe) 100, 102, 106, 107, 110, 123
MERIS 54, 392, 411–412, 484, 523, 559, 572, 588
Mertz Glacier 413, 465, 467, 484–485, 558
Mesoscale cyclones (see polar lows)
MESSR 604
Meteor, Russian spacecraft series 55, 144, 381–382, 409–410
Methanesulfonic acid (MSA) 337
MetOp, ESA spacecraft series 54–55, 400, 409, 434, 501, 557, 614
Michelson interferometer 123–124, 126
Microwave active (radar) 116, 368, 370, 385, 407, 527–528
  backscatter, seasonal evolution 377
  backscatter coefficient 370–371, 375, 378, 400–402, 437–438, 459, 595–599
  bands 357
  liquid water extinction 115
  loss tangent 371–372
  passive 116, 311–312, 368, 380–385, 407, 421–422, 426, 434, 436, 440–441, 443, 445, 450–452, 456, 481, 489, 499, 501, 551–553, 555, 580, 600
  passive, advantages and disadvantages 383–384
  passive, low frequency 526–528
  passive, sensor data availability 426
  passive, sensor frequencies 423–424, 428
  passive techniques, melt and refreezing 592–594
  passive techniques, sea ice 422–436
  passive techniques, sea ice classification 528–530
  passive techniques, sea ice motion 491–495
  passive techniques, sea ice thickness 525–526
  polarization (*see* Polarization)
  radar, low-frequency 527–528

Microwave active (radar) (*cont.*)
radiometry 112–119
signature, seasonal dependence 376
volume scattering 372–373
zenith opacity 114
Middle-infrared (mid-IR) 39, 89, 90, 100, 107, 109, 110, 116, 154–157, 173, 176, 205–207, 210, 213, 217, 220–221, 227, 229, 248–249, 254, 280, 283, 286, 288, 358
Mie theory 81, 88, 89, 91, 163, 172, 235, 361, 591
MIPAS 54, 126
Mirage (looming, towering) 35
Mirny, Russian Navy frigate 6
Mission to Planet Earth (NASA) 153
MISR 47, 415–419, 464, 560, 564, 588
Mixed layer 325
MLS 48, 127–129, 178
MODIS 46, 51, 110, 176, 201, 212–213, 234, 239, 244, 255, 257, 392, 410–411, 414–415, 417, 419, 439, 441–442, 461–462, 466, 476, 481, 484, 486, 488, 491, 523–524, 559–560, 572–573, 576–577, 584, 587–588, 592, 602–603, 609, 612
MODTRAN 90
Modulation transfer function 93
Monochromatic radiation 66, 85, 101, 108, 123, 124, 148, 163
Monochromatic calculations 89, 89, 147, 162
Monochromator 111, 146
Monte Carlo simulations 92
Montreal Protocol 49, 133, 138
MOPITT 47
MOS 418
MPLNET 294
MR-900B 409
MR-2000M 409
MSMR 56–57, 382, 418, 444
MSPPS 434
MSS (*see* Landsat MSS)
MSU 283–286, 288, 290
MSU-E 410
MSU-MR 409
MTVZA 381–382
Multiangle optical remote sensing 416–417, 559–560
MVISR 57, 408, 414
MWR 54, 403, 405
Myriade, French satellite series 411

N-values (TOMS algorithm) 147–151
Nansen, Fridtjof 2
Narrow-to-broadband conversion 259, 585
NASA Bootstrap (NB) algorithm 423, 446, 552–553
NASA Goddard Institute for Space Studies 112
NASA Goddard Space Flight Center 52, 90, 91, 294
NASA Jet Propulsion Laboratory 56, 544
NASA Langley Atmospheric Sciences Data Center 416
NASA Team (NT) algorithm 423–424, 426–427, 431, 435, 449, 456, 525, 529, 552–553
NASA Team 2 (NT2) algorithm 425, 427, 430–433, 562
NASDA, *see* JAXA
Nathaniel B. Palmer, USAP icebreaker 57
National Center for Atmospheric Research (U.S.) 200, 436, 448
National Center for Environmental Prediction (U.S.) 198, 201, 212, 291, 436, 448, 498–499, 526
National Ice Center (U.S. Navy) 423, 443, 528, 609, 610, 612
National Institute for Standards and Technology 53, 110, 111, 240
National Ozone Expeditions, U.S. 140
National Technical Means, US satellite series 589–590, 600
Nature magazine 153
Naval Research Laboratory, U.S 159, 382
Navy, France 16, 33
Navy, Royal (U.K.) 12
Navy, United States 7, 10, 12, 13, 15–21, 24
NCEP/NCAR Reanalysis dataset 436, 498, 526
Near-infrared (near-IR) 39, 51, 89, 100, 103, 107, 112, 116, 213, 221, 227, 229, 235, 254, 264, 274, 358–359, 361–362, 406, 408, 410–412, 414, 418–419, 439, 442, 461, 523, 559, 584, 586, 590, 592, 599
NEMS 128

Nephanalysis 214
NESDIS (NOAA) 434, 556
Netherlands Agency for Aerospace Programs 48
Neural network 215–217, 439, 538, 551, 553, 558
Nilas (*see* Sea ice)
Nimbus, NASA spacecraft series 42, 128
Nimbus 4 45, 126
Nimbus 5 310, 380, 423, 426
Nimbus 7 42, 45, 55, 144, 182, 410, 417, 423, 426, 444, 446, 449, 454, 484, 492, 577
NISTAR 53
Nitrogen, odd 134–135, 137
NO_2 160, 163, 167–169
NOAA 611
NOAA Polar Orbiter spacecraft 42, 53, 92, 93, 112, 154, 156, 197, 200, 217, 284, 407, 409, 433–434
Noise-equivalent power (NEP) 106
Noise-equivalent spectral radiance (NER) 106, 107
Noise-equivalent temperature difference (NEΔT) 107, 578
Nordic Seas 333, 494
Normalized difference sea ice index (NDSI) 461
NORSEX algorithm 423, 456, 529
Northern annular mode 194, 270, 274
North Atlantic Oscillation (NOA) 46, 194, 335, 452, 493–494, 508
North Pole Environmental Observatory 346–347
Northern annular mode 194, 270, 274
Northern Sea Route 409, 611
Northern View 613
Norwegian Meteorological Institute 459
NPOESS, US satellite series 53–54, 55, 144, 381–382, 397, 405, 407, 411–413, 484, 491, 493, 501, 557, 560, 573, 577, 612
NRTSI 426, 435–436, 441, 448
NSCAT 400–401, 457–458, 499–501, 554–555, 557, 595–599
NSIDC 58, 406, 408, 410, 426, 428, 432, 435, 443, 448– 450, 461, 491, 495, 496, 518, 554, 560, 563, 568, 575–576, 582, 593, 600
OC4v4 algorithm (ocean color) 482
OCM 56, 418
OCTS 56, 411
Occultation, solar absorptive 157, 159–173, 176
OLS 44, 53, 94, 97, 201, 206, 209, 251, 288, 409, 439, 457, 465, 471, 475, 491, 557, 584, 592, 599, 609
OMI 48, 144
OMPS 53
Ocean color remote sensing 45, 51, 56, 182–183, 410–411, 421, 453– 454, 482–484
Ocean emissivity, microwave 384, 429
Ocean heat flux 345–346
Ocean, radar altimeter waveform 404
Ocean wind roughening 424, 437–438
Oceansat-1 418–419
Okean, Russian spacecraft series 55, 381, 385–386, 465, 552–553, 611
OLS 44, 53, 94, 97, 201, 206, 209, 251, 288, 409, 439, 457, 465, 471, 475, 491, 528, 557, 584, 592, 599, 609
OMI 48, 144
OMPS 53
Optical depth 80, 84–86, 90, 148, 163–164, 166–167, 181, 194, 201, 227–228, 235–244, 265–268, 361
Orbit
  elliptical 62–63
  geostationary 62, 200, 207
  halo 52
  low earth (LEO) 62, 64
  polar (high inclination) 43, 61, 62, 65, 207
  prograde 64
  retrograde 64
  Sun-synchronous 65, 66, 144, 146, 159, 162
Orbital
  eccentricity 62, 66
  elements, classical 65, 98
  inclination 64, 66, 396
  period 63, 396–397
  plane 64, 65
  precession 65, 66
Orbiting Carbon Observatory, NASA spacecraft 411
OrbView-2 410
Orders of spectra 121

Ozone
  9.6-micron band emission 154–156
  absorption cross section 76, 77, 80, 86, 91, 144
  catalytic cycles (destruction) 134–137
  Chappuis bands 77, 159, 164
  climatology (global) 134–135
  column abundance 48, 52, 53, 146–150, 154–158, 168, 258–259, 265–268, 367
  depletion (Antarctic, ozone "hole") 1, 129, 133, 138–143, 151–153, 179–184, 195, 294
  depletion (Arctic) 133, 177–179
  depletion (gas phase) 138, 141, 152
  depletion (global) formation in stratosphere 74–75
  Hartley bands 120
  Huggins bands 77, 120
  recovery 49, 138, 179
  retrieval, infrared 153–157
  vertical profile 129, 136, 140–141, 146–147, 168

P-n junction 99, 100
Pacific decadal oscillation 452
Pack ice (*see* Sea ice)
Palmer LTER (*see* LTER)
Palmer, Nathaniel B. 5, 6, 9
Palmer Station, Antarctica 44, 58, 180, 181, 248
PALSAR 46, 56, 392, 394, 398, 419, 463–464, 520, 522, 539, 550, 611
PAN 418, 419
Pancake ice (*see* Sea ice)
Panchromatic band 417–419
PARASOL 52, 411
Parker, Eugene N. 152
Passive microwave (*see* Microwave, passive)
Path difference, interferometer 124
Peacock, USS 8, 10, 24–32, 36
Peale, Titian R. 8, 15, 23
Penguin, U.S. merchant schooner 9
Penguins
  Adélie 340, 448, 484, 487
  chinstrap 340
  diet and foraging 489
  emperor 330, 463, 487
  polynyas and 469
Perigee 62, 64
Permittivity 370–371, 373
Phase function
  definition 80
  Henyey–Greenstein 82–83, 89
  ice particles 82
  practical modeling 89
  Rayleigh scattering 81, 88
Photocathode 100, 101, 116
Photoclinometry 565
Photoconductive mode 99, 100
Photodissociation 74, 75, 88, 134, 143
Photoelectric effect (photoemission) 100, 116
Photoemissive mode 99, 100
Photoionization 74
Photomultiplier tube (PMT) 101, 123, 146
Photon detectors 98, 99
Photosynthetically active radiation (PAR) 180–181, 182, 184, 330–331, 350, 561
Photovoltaic mode 99, 100
Phytoplankton 56, 180, 182, 330, 340, 453–454, 469, 483–484, 487, 604
Pickering, Charles 15, 23
Pioneer, USS 13–15, 21
Pi–SAR 521, 544, 547
Pixel 103
Planck function 86–88, 109, 116, 154, 155, 223, 365–367, 573
Plane-parallel approximation 84, 88, 227, 244
POAM 157–169, 171–174, 176–177
POES 53, 407
Poinsett, Joel 19, 21
Polar bear 350, 489, 565
Polar coordinate system 67–68
Polar Ice Prediction System (PIPS) 612
Polar lows 199, 201–205, 435
Polar mesospheric clouds (PMCs) 176–177
Polar MM5 200–202
Polar pathfinder composite dataset 495–498
Polar Pathfinder Program 58, 282–293, 312, 408, 490, 495–496, 575, 578, 587
Polar Sea, USCGC (icebreaker) 57
Polar Star, USCGC (icebreaker) 57
Polar stratospheric clouds (PSCs) 50, 141–143, 156, 157, 168–176, 178
Polar vortex 143, 152, 178, 180, 181
Polarimetric SAR (*see* Synthetic Aperture Radar polarimetry)

Polarimetric microwave radiometer 382
Polarization
  alternating mode 390–391
  by PSCs 141
  definition 119, 380, 542
  discriminants 542–543
  lidar 233–234
  linear modes (HH, VV, HV, VH) 45, 380, 393, 536, 539
  multi-polarization 390
  of passive microwave sensor frequencies 423–425, 428–431, 433, 492, 527, 562
  ratio (PR) 424–425, 431, 444, 457, 459, 482, 525– 526, 556
  sea ice emissivity 384
  Stokes matrix 540–541
  Stokes vector 383
Polarstern, German icebreaker 57
Poleward transport 325
POLDER 52, 56, 119, 411
Pollutant entrainment and transport 327, 463, 487–488
PolSARpro software 551
Polynya 319, 324, 334, 386, 421, 425, 440, 465, 466–487, 522, 569, 604
  Amundsen Sea 483
  Antarctic coastal map 473
  as polar oasis 468–469
  attributes 467
  Bathurst Island 470
  biological significance 468–469
  Cape Hudson 472
  Cosmonaut Sea 469, 471
  "deepwater" 467
  extent 470–479
  flaw 467
  impact of icebergs 484–487
  Kashevarov Bank 471
  latent heat 467
Mertz Glacier 465, 467, 469–470, 472, 477, 485– 486, 489, 558
  models 470, 474–475, 481
  North-East Water 470, 478
  North Water 468, 470, 476, 478, 484, 502, 503
  Odden/Nordbukta system 471
  Pine Island Bay 483
  Polynya Signature Simulation Method (PSSM) 474–475, 478, 482
  primary production in 475, 482–484
  Prydz Bay 483
  Ronne Ice Shelf 483
  Ross Ice Shelf 471, 487
  Ross Sea 474–475, 483
  sensible heat 467
  "shelfwater" 467
  Siberian Shelf 468
  signature simulation method 474–475, 478, 482
  St. Lawrence Island 467, 478, 480–481, 524
  Terra Nova Bay 471, 479–480
  themes in current research 469–470
  Weddell 471
Polynya Signature Simulation Method (PSSM) 474–475, 478, 482
Porpoise, USS 13, 18, 21, 24, 27, 32
Potential well diagram 75
Power pattern, antenna 117–118
Precipitable water 265–268, 272
Pressure ridge (*see* Sea ice)
Primary production 46, 179–182, 184, 329, 341, 421, 453– 454, 469, 482–484, 487
Prince Olav Coast 465
Principal component analysis (PCA) 172–173
PRISM 56
Probability density function 225, 353, 508, 517
Pulse-limited footprint 403
Pure oxygen atmosphere 74–75, 134
Pushbroom scanner configuration 96, 97, 110
Pycnocline 336
Pyroelectric detector 98

Quantum efficiency 103
Quantum noise 105
QuickBird 417, 419, 571, 590
Quickscat (*see also* SeaWinds) 45, 400, 402, 417, 419, 457–459, 481, 501, 555–556, 568, 590, 602, 609, 611–612, 614

Radar (*see* microwave, active)
Radar Altimeter-2 (RA-2) 403–404, 512
Radar altimetry 50, 380, 385, 402–406, 421, 460– 461, 511–513, 564

Radar altimetry, waveforms 404
Radar scatterometry 380, 385, 399–402, 421, 457–460, 459, 499–501, 552–557, 596–599, 612
Radarsat–1, CSA spacecraft 42, 55, 389–390, 394–395, 398, 437–438, 460, 476, 502, 516–517, 536, 571, 588, 595–596, 609, 611
Radarsat-2, CSA spacecraft 55, 394–396, 437–438, 460, 464, 479, 539, 546, 549, 551, 571, 611
Radarsat-3, CSA spacecraft 395, 611
Radarsat Geophysical Processor System (RGPS) 397–398, 437, 502, 504–507, 518–520, 523–524, 538, 552, 555, 567, 588–589, 596, 603
Radiance (*see* Intensity)
Radiation budget 226, 228, 262–282, 583
Radiative transfer equation 84–86, 88–92, 154, 155, 369
Radio frequency (RF) 116, 127
Radiometric calibration 109–112, 146, 217, 237, 240–242, 388
Radiometric resolution 312
Radiometric units 92, 110
Radiosonde data 574
Rafting (*see* Sea ice)
RAR (*see* Real-Aperture Radar)
Rawinsonde data correction 260–261
Rayleigh–Jeans approximation 87–88, 114, 117, 369
Rayleigh's criterion 121, 378
Rayleigh scattering cross section 81, 88
READER 315
Readout noise 105
Real-Aperture Radar 385
Reanalysis, meteorological 179, 436, 448, 498
Refraction, atmospheric 35, 162
Refractive index ice versus water 119, 229, 235, 246, 359
PSC constituents 171
Relative azimuth 70, 72
Reflectance 39, 69, 70, 73, 148–149, 223, 231–232, 236, 255, 358–359, 366, 414, 559–560, 592, 603
Relief, USS 21, 23, 24, 28, 37
Reservoir compounds 137, 141–143
Resolute Bay, Canada 546
Resolving power
  grating 122–123
  interferometer 125–126
Resourcesat 419
Response function, interferometer 126–127
Response time, detector 100
Responsivity, spectral 103, 104, 108, 109, 111, 162, 260
Resurs, Russian spacecraft series 410
Reynolds, Jeremiah (journalist) 5–12, 15–17, 19, 21, 33, 37, 38
Reynolds, William (midshipman) 27, 30, 39
Right ascension of the ascending node 64
Ringed seal 350, 489
Root mean square (RMS) error 267, 576
Ross Ice Shelf 34, 198, 206–208, 475, 486–488
Ross Island 487
Ross, James Clark 26, 32, 34–36
Ross Sea 182, 200, 446, 455, 466, 480, 486–488, 498, 566, 581
Rotational transition 76, 116
Royal Society, Transactions 6
Russian Hydrometeorological Centre 381
Russian Space Agency (RKA) 55–56, 611

SAGE 157, 171, 282
Salinity 46, 317–318, 320, 333, 336, 375, 426, 487, 537, 553–554, 581
Salps 452
SAM II 157, 169–171
SAOCOM 397
SASS 400
Sastrugi 355
Satellite sensor classes 420–421
Saturation, detector 104
SBDART radiative transfer model 91
SCAR 314, 328, 342
SCARA–B 262
Scattering
  conservative (elastic) 81, 88
  cross-section 80, 85, 163
  matrix 45, 540
  Mie (particle) 40
  non-conservative (inelastic) 82, 85
  non-selective (wavelength-independent) 40
  Raman 148
  Rayleigh (molecular) 40, 81, 84–86, 148, 159, 163, 166–168, 258

Scatterometer Climate record Pathfinder (SCP) 401, 499, 501, 554
Scatterometer Image Reconstruction with Filtering (SIRF) algorithm 400–401, 499, 555
SCIAMACHY 54
SCICEX, U.S. Navy field program 508
Science magazine 153
Scott Base, Antarctica 196
Scott, Robert Falcon 2
Scripps Institution of Oceanography 44, 52, 53
Sea Gull, USS 21, 24, 26
Sea ice
  absorption coefficient 362
  advection 354–356
  albedo 181, 214, 237, 250, 255–256, 324, 347, 362–363, 522, 600
  albedo, effect of cloud cover 364, 586
  albedo, effect of snow cover 362–363
  albedo, remote sensing 582–590
  algae 341, 453
  Arctic 309
  basal melt 350–352
  biology 315
  brash ice 320, 501, 566
  classification 316–321, 421, 510, 528
  classification, passive microwave 528–530
  classification, radar scatterometry 552–557
  classification, SAR 530–539
  classification, SAR polarimetry 539–551, 611
  classification, visible/thermal imager 557–560
  columnar 323
  concentration 421–428, 430, 433–435, 439–441, 446, 449, 451, 499, 556, 577
  concentration, anomalies and trends 434–436
  concentration retrieval, error sources 425–426, 432
  congelation 317
  constitutive law (*see* Sea ice, rheology)
  deformation 354–356, 489, 497, 504–507, 518, 564, 604–605
  density 345, 511
  dielectric constant 370, 373
  divergence 504–507
  drag coefficients 355
  drift 317, 325, 352, 354–356, 487, 497–499, 564
  drilling 509
  dynamics 313, 343, 352, 354–356, 487–507
  ecological significance 315, 328–331, 340–341, 463
  edge 425, 453–454, 460
  edge, Antarctic 180, 330, 337, 453
  edge, Arctic 310, 452, 457
  edge characteristics 421, 443
  edge, general definition 456
  edge location 320, 456–457, 556, 607
  edge processes, remote sensing 604–608
  elevation 568
  emissivity, microwave 384, 424, 426, 429, 433, 527
  extent 309–311, 333, 443–462
  fast ice 319, 389, 406, 442, 462–466, 484, 594
  first year 251, 318, 322, 363, 371–372, 376–378, 383–384, 424, 431, 449, 517, 529, 531, 535, 543, 545–546, 548–550, 553–558, 560, 588
  first year, rough versus smooth 555, 557
  flaw leads 319, 462–463, 468
  floes 319, 345, 389, 406, 438, 466, 487, 501, 511–512, 534, 564–565, 567, 590, 604–605
  floe size distribution, remote sensing 568–571
  flooding 349, 364, 425–426, 433, 491, 599, 605
  forecasting and prediction models 612–615
  formation processes 316–321, 467
  frazil 317, 322, 472, 481, 545, 607
  freeboard 403, 516–517, 564–565
  freezing degree days (FDDs) 519
  global areal exent 309–310, 450
  grease ice 317, 363, 438, 545, 607
  inertial motion/deformation 506–507
  information sources 314–315
  kinematics 487–507, 518–520
  leads 317, 330, 354, 386, 437–438, 440, 467, 469, 490, 523, 559
  marginal ice zone (MIZ) 252, 320, 341, 425, 438, 443, 451, 454– 455, 458, 491, 493, 502, 520, 527, 530, 538, 545, 554, 557, 563–564, 569–571, 604–605, 607
  mass flux 494–495, 513, 614–615

Sea ice (*cont.*)
melt and refreezing, remote sensing 425, 591–603
melt cycle 490, 533
melt periods 461
melt processes 350–352, 421, 425, 437, 468
melt season 440, 579, 593–594, 595–596
meltponds 250, 252, 259, 322, 351, 364, 375, 421, 433–434, 438, 529, 533, 589–590, 595
meltpond distribution, remote sensing 599–603
meteoric 349
microwave backscatter 379, 530–534
microwave backscatter coefficient 377, 388, 531–533, 537, 553
microwave penetration depth 371–372
microwave properties 368–380
microwave properties, seasonality 376
modeling 340, 355–356, 469, 506, 520, 588
motion 335, 406, 421, 458, 487–507
motion anomaly maps 495
multiyear 318, 333, 372, 376–378, 383–384, 424, 431, 449, 515, 517, 529–530, 531, 533, 535, 537, 542–543, 545–546, 549–554, 557, 560, 581, 594
multiyear ice area 333, 449, 529–530, 551–553
nilas 317, 363, 439, 553, 558–559
normal deformation 504–507
old 318, 560
operational observation of 609–612
optical properties 358–364
pack ice 319, 406, 421, 465–467, 487, 605
palaeorecords 310
pancake 317, 537, 554, 557, 604, 607
perennial ice zone (PIZ) 555
permeability 581
polar contrasts 321–323
polynya (*see* Polynya)
pressure ridge 318, 353–354, 378, 386, 534, 564–566, 610
production 479–482
radar altimeter waveform 404
radar backscatter 377–378
rafting 318
rheology 356, 506–507
season length 333, 454–456
seasonal sea ice zone (SSIZ) 494
second-year 318, 533, 581
shear deformation 504–507
shear zone 319, 354
shipborne observations 510
skin surface temperature (IST), remote sensing 522, 524, 560, 571–580
snowcover 324, 347–350
snowcover thickness, remote sensing 512
strength 356
surface melt 433, 450
surface roughness 377–379, 405, 421, 437, 517, 518, 531, 547, 561
surface roughness, remote sensing 377–379, 564–568
surface temperature 345, 367, 421, 426–429, 461, 478, 495, 522, 524, 560
surface wetness 425
temperature, remote sensing 580–582
terminology 316–317
thermal conductivity 324, 345, 524, 581
"thermal ice thickness" 524
thermodynamics 343–344
thickness 313, 333, 335, 352–354, 363, 389, 405, 421, 426, 449, 450–451, 479–480, 484, 487, 494, 507–528, 550, 564, 607
thickness distribution 352–354, 507–528
thickness, from visible/thermal imagers 522–525
thickness from kinematics 518–521
thickness, from passive microwave data 525–526
thickness, in situ information sources 494, 509–510
total deformation 505
trends in extent 444–451
velocity field 487, 498
velocity vectors 489
vorticity, drift 504–507
wave–ice interaction, remote sensing 604–608
whaling/sealing records 310, 337
young 318, 363, 425, 533, 542, 557, 560
Sea Lion algorithm 424, 474
Sea of Okhotsk 310, 424, 471, 521, 525–526, 544, 605, 611

Seals
  ringed 350
  southern elephant 347
  Weddell 463
SEARCH 334
Seasat L-band mission 386, 389, 502
Seasat-A scatterometer (SASS) 400–401, 457, 595
Sea surface temperature (SST) 57, 454, 461, 573
SeaSpace Corporation 59, 98
SeaStar, NASA spacecraft 51, 410
SeaWiFS 45, 51, 97, 110, 182–183, 410, 454, 482–484, 486
SeaWinds (*see also* QuikScat) 400–402, 417, 459, 556–557, 614
Search array 209
Sediments 255–256, 315, 323, 327, 487–488
Sediment traps 494
Semi-Annual Oscillation (SAO) 338, 580
Semiconductors 99, 100, 102
Sensible heat 326
Seraph, U.S. merchant brig 9
Shackleton, Ernest 2, 36, 489
Shear zone (*see* Sea ice)
SHEBA, Arctic Canada/U.S. experiment 233–234, 250–253, 259, 290, 292– 294, 583, 599–600
Shirase, Japanese icebreaker 57
Shortwave radiation 39, 61, 68, 85, 98, 110, 193–194, 244, 255, 261–266, 269, 274–276, 278–281, 344–345, 347, 351, 358, 364, 419, 468
Shot noise 105
Shuttle Imaging Radar (SIR-C) 395, 539, 546, 548
Shuttle Radar Topography Mission (SRTM) 395
Sica 437
SICH-1M, Russian–Ukrainian satellite 3, 82, 418
Side lobe, antenna 117
Side-Looking Radar (SLR) 55, 385, 552, 611
Sigma-O software 551
Signal–to–noise ratio (SNR) 93, 94, 96, 100, 106, 108, 146, 157, 213, 230, 235, 274, 284, 412, 514, 549
Silicon detector 100, 102–104, 106, 107
Single scattering albedo 82–83, 85–86, 228, 232, 281
Siple Coast 207, 217
SIRAL 405, 513–514
S/KIT algorithm 525
Skill score 214, 226
Slit function 123
SLR (*see* Side-Looking Radar)
SME 176
Smithsonian Institution 38
SMMR 42, 45, 381, 417, 423–424, 426, 428, 432, 435–436, 443–444, 446–449, 482, 492, 495, 592–593–594, 599
SMOS 526–527, 603
Snow
  accumulation rate 519
  albedo 254–255, 322, 347, 349, 358, 591
  density 424, 511, 563
  depth (thickness) 428, 516, 522–523, 560
  dielectric constant 373–374
  emissivity 217–218, 368, 433, 574, 576
  grain size 254–255, 358, 360–361, 373, 406, 420–421, 424, 563, 578
  grain size, remote sensing 590–591
  impurity content 421
  impurity content, remote sensing 590–591
  layering 424
  liquid water content 529, 592
  melt 434, 563
  melt and refreezing, remote sensing 591–603
  melt onset 593, 596–599
  melt season length (MSL) 593–596
  metamorphism 348, 360, 581
  microwave backscatter 379
  microwave backscatter coefficient 375
  microwave penetration depth 374
  optical depth 361
  optical properties 358–364
  penetration depth 572
  properties on sea ice 318, 321, 324
  radiative transfer modeling 230, 241, 251, 360
  reflectance 358, 360
  role in sea ice growth/decay 347–352
  skin surface temperature (IST), remote sensing 571–580
  thermal conductivity 348–349
  thickness, remote sensing 560–564

Snow (*cont.*)
transmittance 359
vertical profile 348
wetness 363–364, 373–375
wetness, effect on backscatter 373–375
wetness, effect on emissivity 433, 536
wicking of brine 536
Snow/ice 349–350, 524, 599
SO_2 150–151
Solar constant 263
Solar zenith angle 68, 70, 72, 73, 92, 223, 236, 239, 242, 259–260, 265, 408, 559, 586
SOLAS 328
Solid angle 67, 116
SOLSTICE 148
Soot 323
South Pole 16, 73, 180, 248, 254, 274–276, 294
Southern Annular Mode (SAM) 339, 580
Southern Ocean, recent changes 338
Southern Oscillation Index (SOI) 198–199, 436
Space Shuttle, NASA 29, 45, 395
Spatial coherence technique 220–221, 490
Spatial resolution 312
Speckle noise 537
Spectral inversion 167
Spectral resolution 312
Spectralon™ 110
Spectrometer, dispersing 120–123
Spectroscopy, imaging (see Hyperspectral imaging) Specular reflector 70, 378
SPOT, French spacecraft/sensor program 96, 97, 159, 161, 409, 414, 417–418, 420, 463, 559
SSM/I 45, 53, 184, 311, 381, 383, 417, 423–426, 428, 432–436, 441, 443, 446–449, 454, 456–457, 459–460, 472–474, 478, 480–484, 486, 492–500, 507, 525–526, 529–530, 538, 551, 554–557, 563, 577, 593–594, 596, 598–599, 603, 605, 609, 612–613
SSMIS 381–382
SSM/T 53, 382
SSU 283
Stamnes, Knut 90, 182
Stearns, Charles 195
Stefan–Boltzmann law 87, 345, 366
Stokes matrix (*see* Polarization)
Stokes vector (*see* Polarization)
Strain rate tensor 505
Streamer, radiative transfer model 91, 230
Submarine sonar 333, 356, 508–509, 511
Subsatellite point 64
Surface energy balance 344–347
Superheterodyne receiver (radiometer) 127
Sydney, Australia 26, 27, 30, 33, 34,
Symmes, John Cleves 2, 3, 4, 5, 6, 21
Synthetic aperture radar (SAR) 42, 45, 55, 56, 310, 379–380, 385, 386–399, 402, 405, 417, 419, 421–422, 433, 436–439, 456, 463, 474, 476, 478, 480, 484–485, 489, 491, 501, 513, 530–552, 559, 564–567, 570–571, 588, 595–596, 599, 603, 605–612
calibration 549
co-pol corrleation coefficient 543
co-polarization phase difference 543
co-polarization power ratio 542, 545–546
cross-polarization phase difference 543, 545
depolarization ratio 543, 545
ERS 377–378
Interferometric 45, 464, 504
measurement of sea ice extent 457–460
multilook processing 541
polarimetry 45, 379–380, 392–397, 438–439, 460, 479, 520, 521–522
polarimetry, utility for ice classification 550, 611
polarimetry, total power 542
Pol-InSAR 550–551
scanning configuration 387
ScanSAR 388–392, 394–397, 437–438, 460, 463, 476–478, 486, 502–503, 506–507, 516, 518, 536, 539, 550, 567, 571, 588, 595–596, 609–611
single polarization, interpretation 388
techniques, melt and refreezing 595–596
techniques, sea ice 436–439
techniques, sea ice classification 530–551, 611
techniques, sea ice motion/kinematics 501–504, 518–519
techniques, sea ice thickness 518–522
Syowa Station, Antarctica 138, 275–276, 465, 604

Tangent point 157, 162
Target array 209
Teleconnections 327, 338–339, 451
Telemetry, satellite 92, 98
Temperature, ice-free freezing ocean 577
Temperature profile-weighting function 210–211
Temperature, surface 249, 260–261, 266–268, 270–271, 288–290, 335, 423, 435, 440, 461
Temperature, surface, trends 579–580
Temperature, surface air (2m) 519, 581, 594
TeraScan™ satellite data-processing software 59, 98, 157
TeraVision™ satellite data-processing software 59, 98, 157
Terra, NASA spacecraft 42, 46, 212, 410, 415–417, 461, 463, 466, 476, 488, 559, 564, 572, 584, 588, 602
TerraSAR-L 55, 395–397, 438, 539, 550–551, 571, 607
TerraSAR-X 55, 387, 395–397, 438, 504, 535, 539, 550–551, 571
Terror, HMS 26, 34
TES 49
Texture recognition 221, 537–538
Thermal detectors 98
Thermal infrared (TIR) 310, 335, 345, 364, 367–368, 375, 380, 406, 409, 414–418, 421–422, 439–440, 461–462, 463, 465–466, 474, 476, 484–485, 489, 491, 510, 522–524, 557, 579, 610
Thermohaline circulation of the ocean 325, 334, 342, 468, 470
THIR 577
Throughput, optical 106
Tidal effects 490
Tiepoint 424–425, 428–429, 439–440, 529
TIGR dataset 285
TIROS 42, 407
TOMS 42, 44, 66, 101, 123, 138–140, 143–153, 156, 158, 162, 181, 184
TOPEX/Poseidon 513
TOVS 154, 156–158, 213, 283–286, 289–291, 612
Tracker algorithm (Canadian Ice Service) 502–503
Training data 214, 223
Transantarctic mountains 207–208
Transfer noise 105
Transmittance 154–156, 163–164, 166, 210, 285, 359, 361, 364, 366
Transpolar Drift 321, 494, 497
Trend analysis, issues relating to 436, 450
TRMM, 47
True anomaly 62
Tsay, Si-Chee 90
Two-stream approximation 89, 90

UARS, NASA spacecraft 45, 48, 148, 178–180
UAV 314
Ultraviolet (UV) radiation 1, 41, 74, 89, 91, 123, 126, 138–139, 178–184, 330, 454
United Kingdom Meteorological Organization 178
United States Antarctic Program (USAP) 44, 57, 58, 180–181, 195, 200
United States Space Command 98
University of California, Los Angeles 92
Upward-Looking Sonar (ULS, *see also* Ice-Profiling Sonar) 494, 508
Ushuaia, Argentina 180
UV-A radiation 88
UV-B radiation 89, 138, 144, 178, 180–182, 184
UV-C radiation 74, 89, 137, 144
Van Buren, Martin 19
Vertical field of view (VFOV) 159, 164
Vibrational transition (mode) 76, 78, 162, 164
Vicarious calibration 112–113, 217, 242, 585
VIIRS 53, 234, 244, 411–412, 484, 491, 523, 560, 573, 577
Vincennes, USS 3, 21, 30–33, 35, 36, 37
VHRR 42
Voigt profile 79
Volume extinction coefficient 235, 281
Vostok, Russian Navy frigate 6
Vostok Station, Antarctica 254

Walden, Von P. 294
War of 1812 3, 11, 12
Warren, Stephen G. 251, 294

Water vapor 40, 48, 57, 116, 129, 153–155, 159, 162–164, 166, 176, 193–194, 199, 207, 227, 258–259, 285, 290–291, 324–325, 367, 423, 440, 592
Wave–ice interaction (*see* Sea ice edge processes)
Wavelength calibration 146
Wavelet analysis 437–438, 492, 499–501
Wavenumber 67
Weather filter 424, 431
Weddell, James 6, 17, 24
Weddell Sea 176, 182, 205, 323, 327, 338, 351–352, 436, 444, 446, 455, 472, 474–475, 480, 493–494, 498, 515, 533–534, 546, 599, 605–606
Weddell seals 463
Western Antarctic Peninsula (WAP) region 181–182, 341, 455
Whig party (U.S. history) 7, 9
Whiskbroom scanner 94, 97, 98
Whritner, Robert 53
Wide field sensor (WiFS) 418
Wien's displacement law 87, 366
Wilkes, Charles 12, 13, 15, 16, 18, 19, 21–27, 30–37, 58, 62, 151, 153, 283
WindSat, US satellite 382–383, 434, 582
Wind speed 57
Wind vectors 199, 207, 209–213
WINDII 176
Window, atmospheric 41, 119
  microwave 42, 116, 357
  middle-infrared 42, 116, 227, 229, 249, 280, 283, 286, 288, 358, 368
  near-infrared 42, 288, 358, 368
Wiscombe, Warren 91
Wisconsin, University of 43, 59, 195–197, 230
Wishart classifier 547
World Meteorological Organization (WMO) 316, 510

Zélée, French Navy corvette 17
Zooplankton 329, 452

Printing: Mercedes-Druck, Berlin
Binding: Stein+Lehmann, Berlin

Figure 1.10. NASA's Earth Observing System Aqua spacecraft.
Courtesy Goddard Space Flight Center.

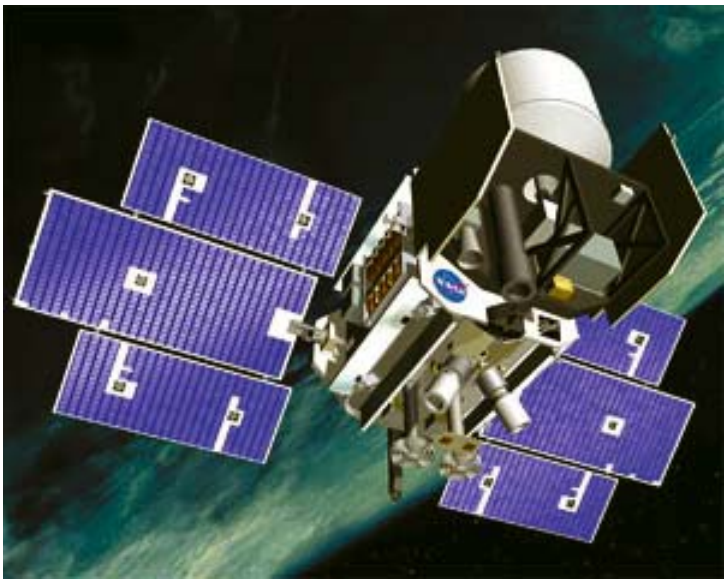

Figure 1.11. NASA's ICESat spacecraft.
Courtesy Goddard Space Flight Center.

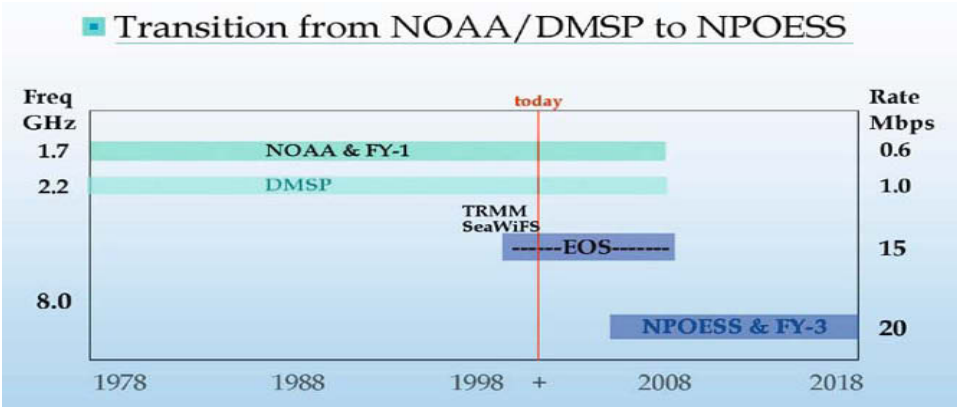

(a)

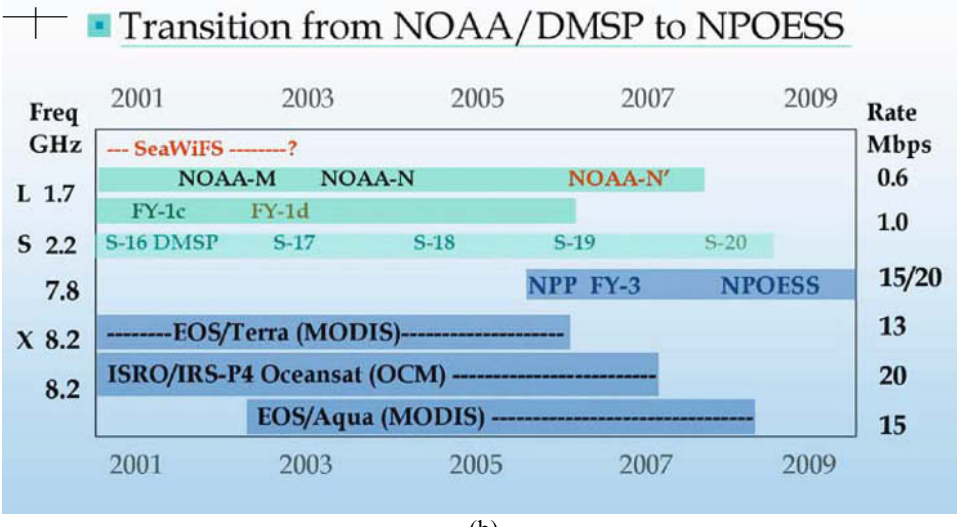

(b)

Figure 1.12. Timeline of the expected transition between "heritage" Earth remote-sensing missions and the new generation of remote sensors offering an order of magnitude more capability, and using high-density X-band telemetry.

Courtesy of Dr. Robert L. Bernstein, SeaSpace Corporation.

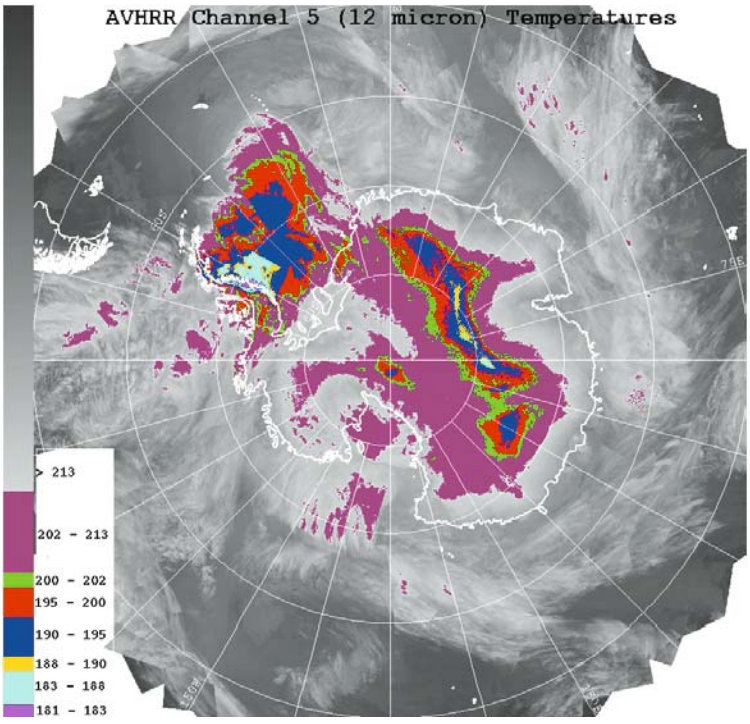

(a)

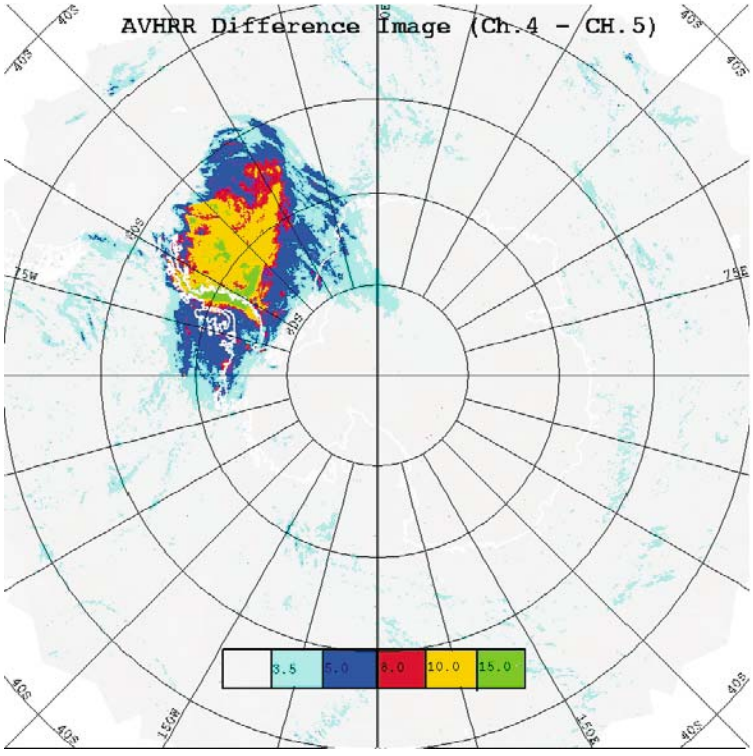

(b)

Figure 3.21. AVHRR composite image of Antarctica for August 31, 1992. Top: channel 5. Bottom: brightness temperature difference between channels 4 and 5, DT45; probable PSCs are color-coded red ($\Delta T_{45} > 5\,\mathrm{K}$), yellow ($\Delta T_{45} > 10\,\mathrm{K}$), and green ($\Delta T_{45} > 15\,\mathrm{K}$).

Courtesy Kathy Pagan, NASA Ames Research Center.

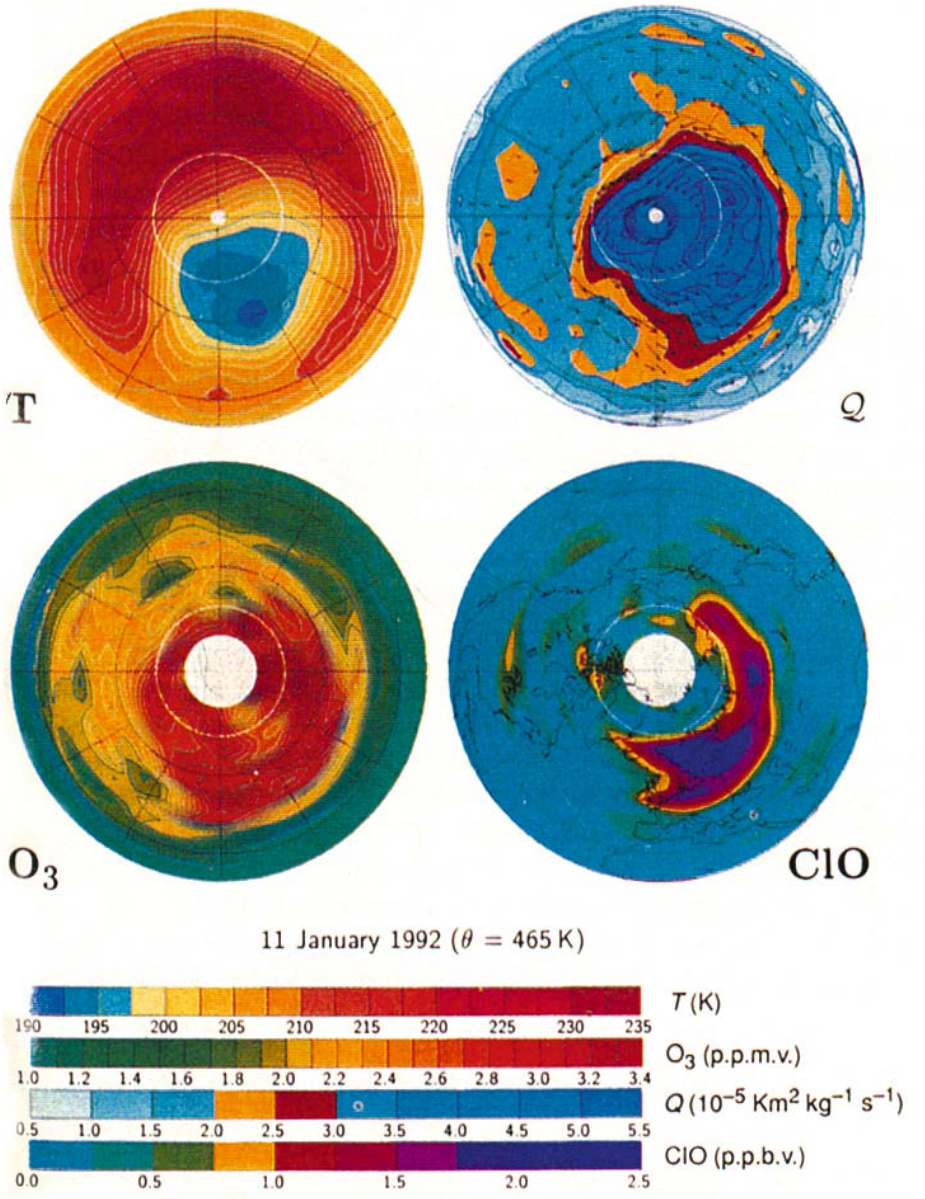

Figure 3.23. Examples of Microwave Limb Sounder (MLS) measurements during the 1992 Arctic winter. The upper panels show temperature and potential vorticity at the 465-K potential temperature altitude, derived from National Center for Environmental Prediction (NCEP) reanalysis data. The lower panels show ozone and ClO measured by MLS on January 11, 1992.

From Waters et al. (1993). Copyright 1993 *Nature* magazine.

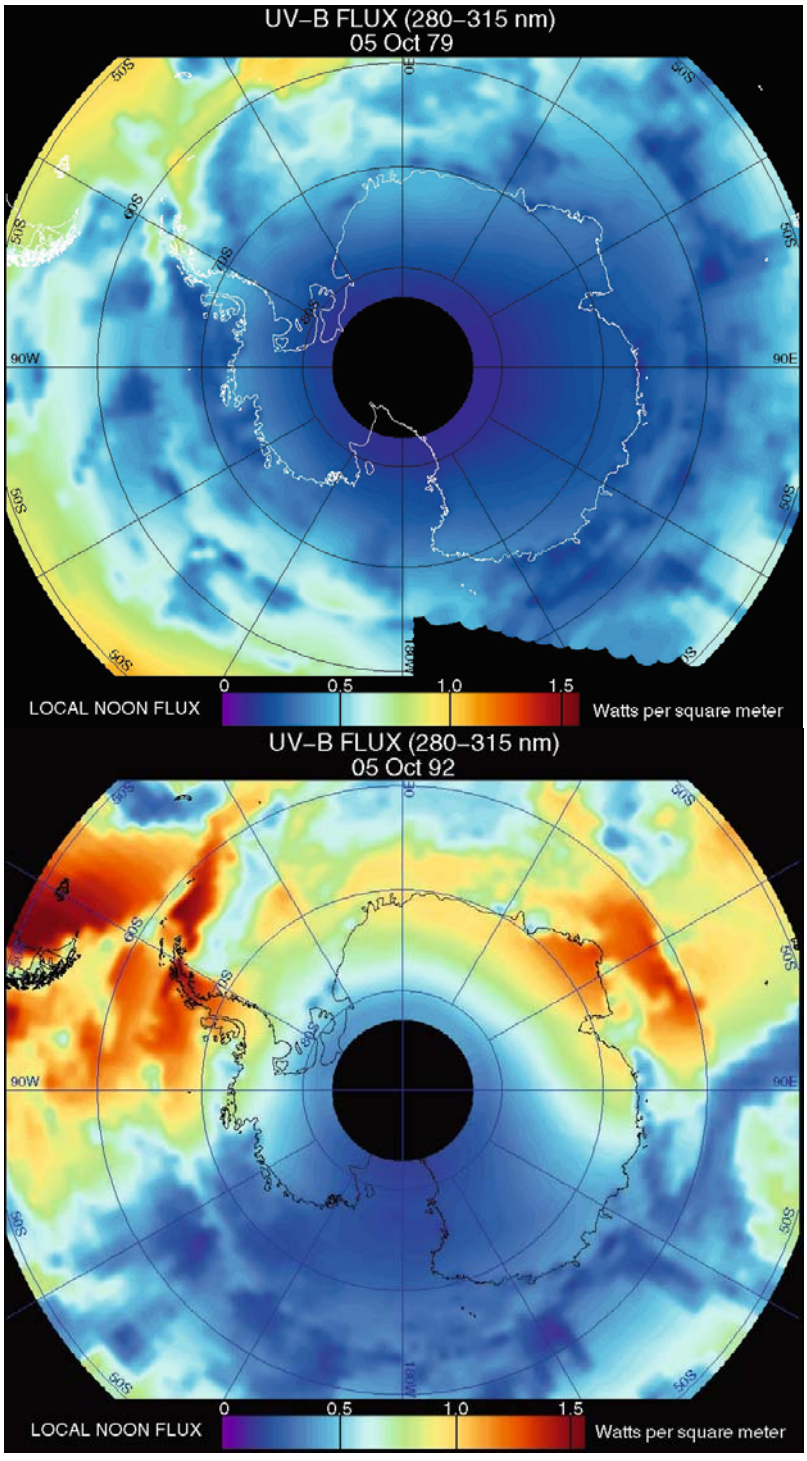

Figure 3.25. The local noon UV-B flux (integral 280–315 nm) reaching the Antarctic and Southern Ocean surface on October 5, 1979 (top) and 1992 (bottom), derived from a radiative transfer retrieval algorithm that uses TOMS data to specify total column ozone and cloud effective optical depth, and SSM/I data to specify sea ice concentration.

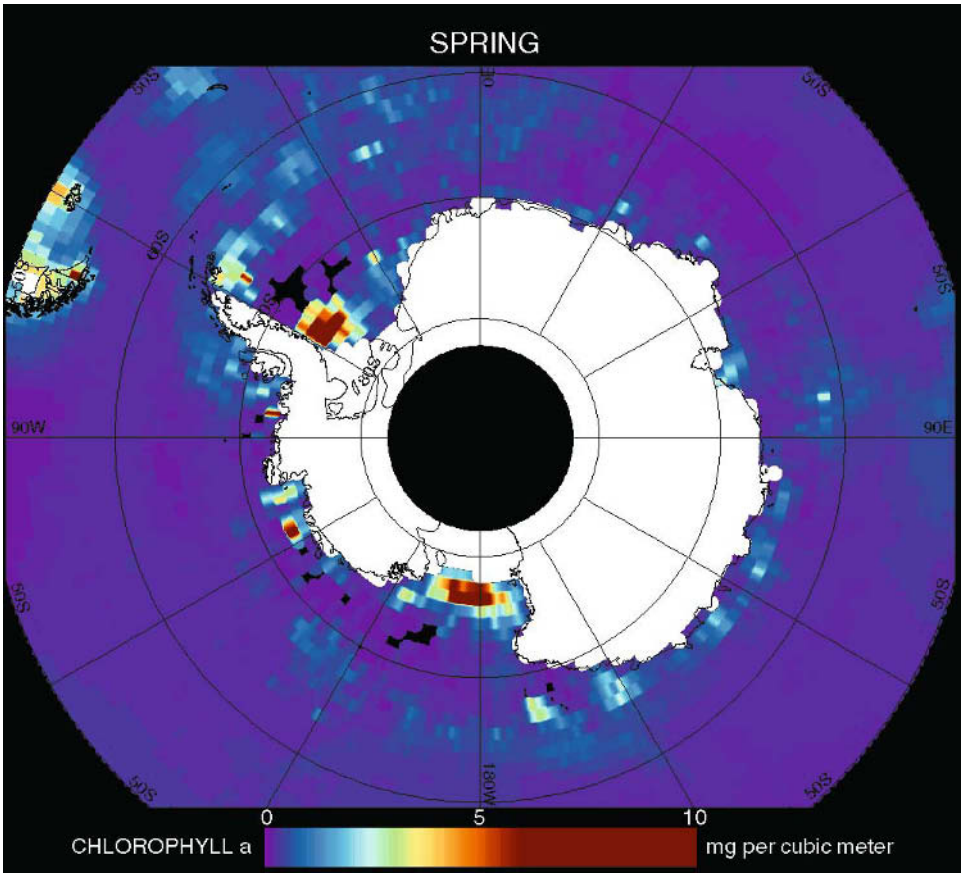

Figure 3.27. SeaWiFS-derived map of chl *a* surface biomass abundance throughout the Southern Ocean, averaged over all available austral spring (September–November) data.
Courtesy Gert van Dijken and Kevin Arrigo, Stanford University.

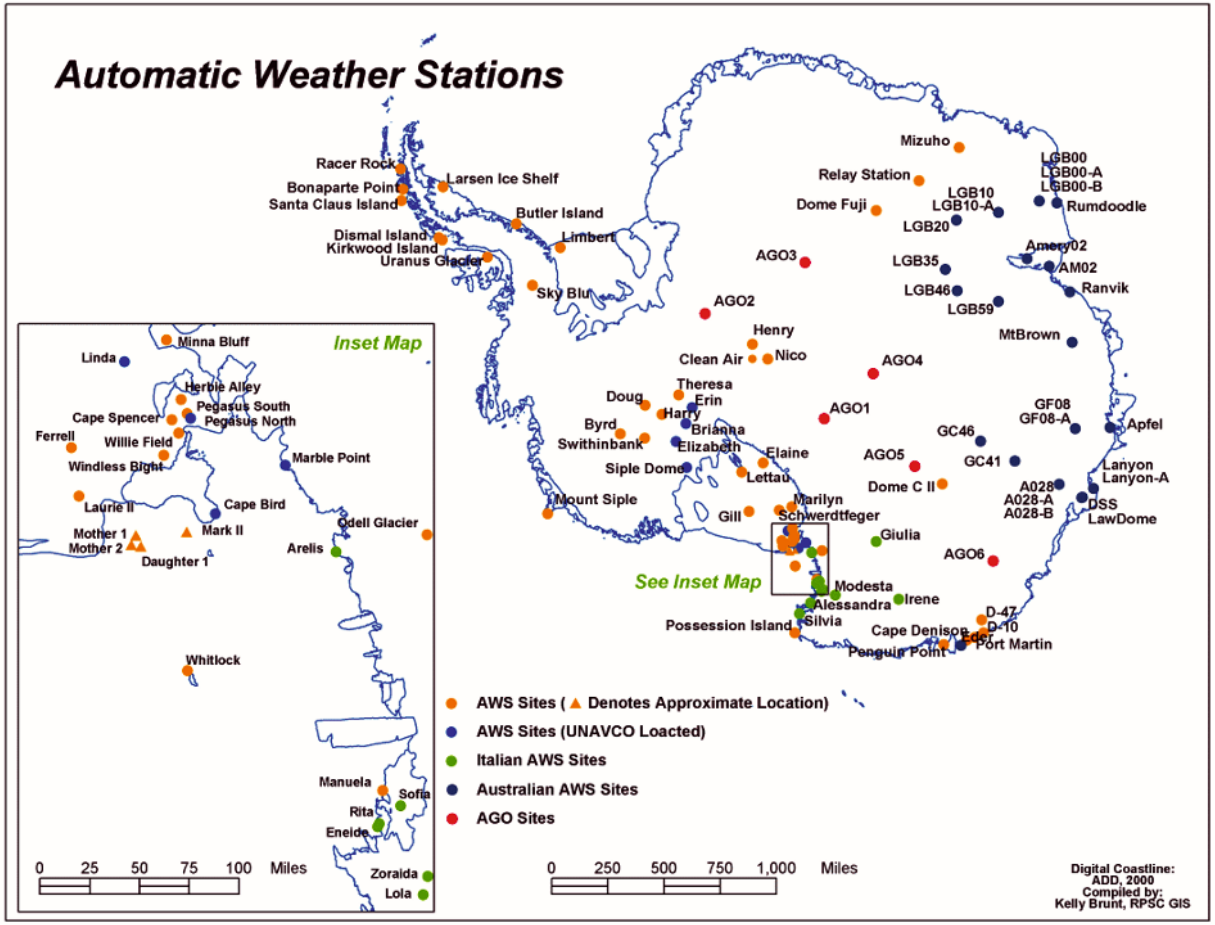

Figure 4.3. Location of Antarctic AWS sites as of 2002.
courtesy Matthew Lazzara and Shelley Knuth, University of Wisconsin.

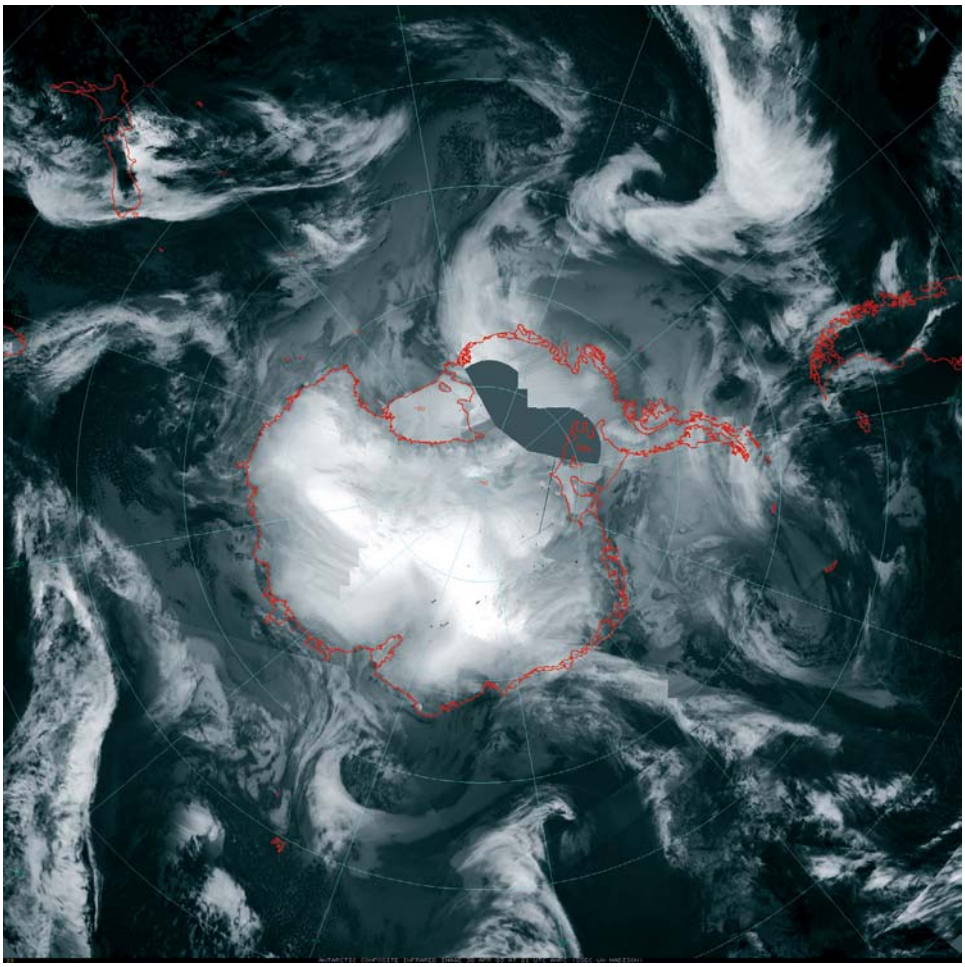

Figure 4.6. Composite of mid-IR imagery from AVHRR and GOES spacecraft covering nearly all of Antarctica and the Southern Ocean. These images are produced for 3-hour intervals by the AMRC.

Courtesy Matthew Lazzara and Shelley Knuth, University of Wisconsin.

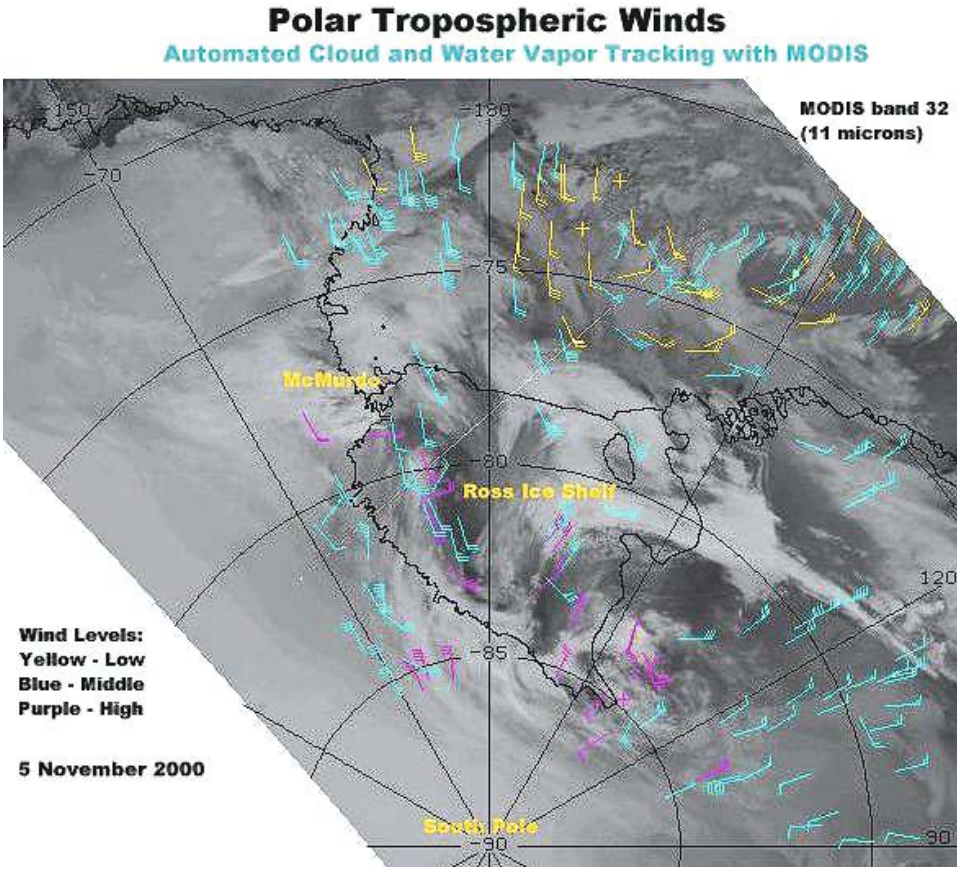

Figure 4.16. Example of wind vectors derived by applying an automated cloud tracking and CO_2-slicing algorithm to a sequence of MODIS images over Antarctica.

Courtesy Dr. Jeffrey Key, NOAA/NESDIS.

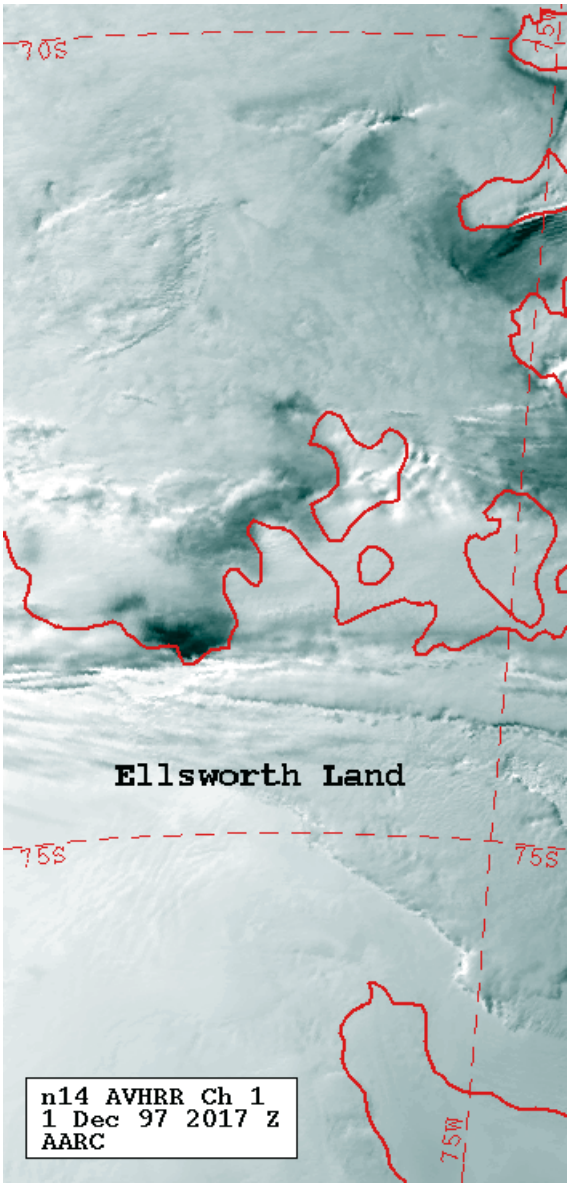

Figure 4.20. NOAA-14 AVHRR channel-1 image over part of West Antarctica at 20 : 17 UTC on December 1, 1997.

Data from the Arctic and Antarctic Research Center at the Scripps Institution of Oceanography.

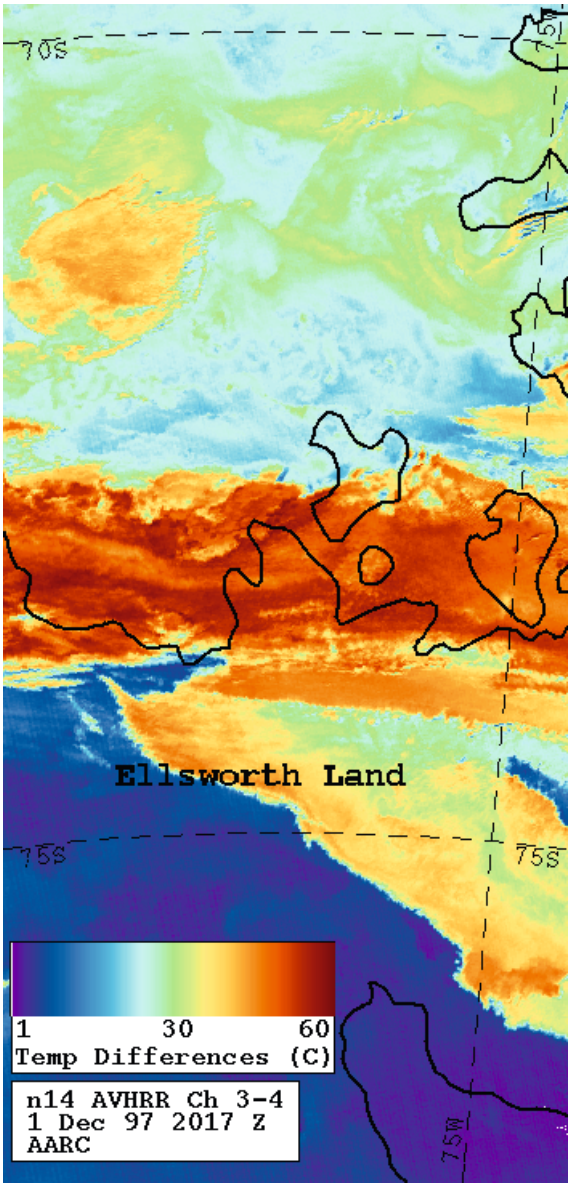

Figure 4.21. Image of the brightness temperature difference between channels 3 and 4, for the data of Figure 4.19.

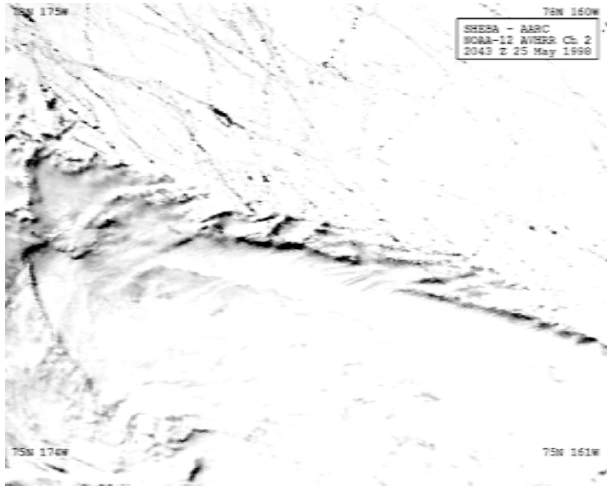
78N 175W
78N 160W
SHEBA - AARC
NOAA-12 AVHRR Ch 2
2043 Z 25 May 1998
75N 174W
75N 161W

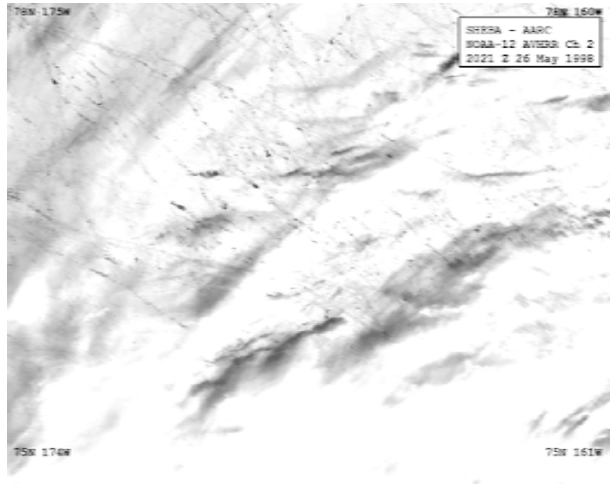
78N 175W
78N 160W
SHEBA - AARC
NOAA-12 AVHRR Ch 2
2021 Z 26 May 1998
75N 174W
75N 161W

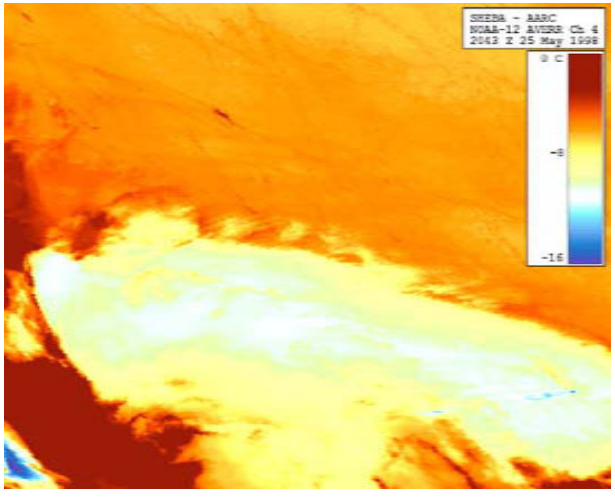
SHEBA - AARC
NOAA-12 AVHRR Ch 4
2043 Z 25 May 1998
0 C
-8
-16

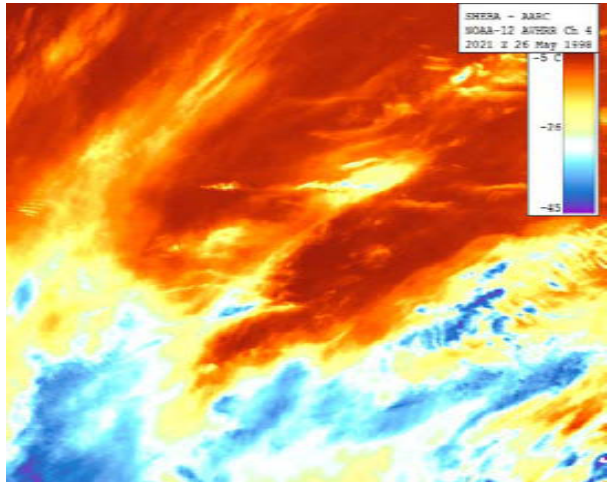
SHEBA - AARC
NOAA-12 AVHRR Ch 4
2021 Z 26 May 1998
-5 C
-26
-45

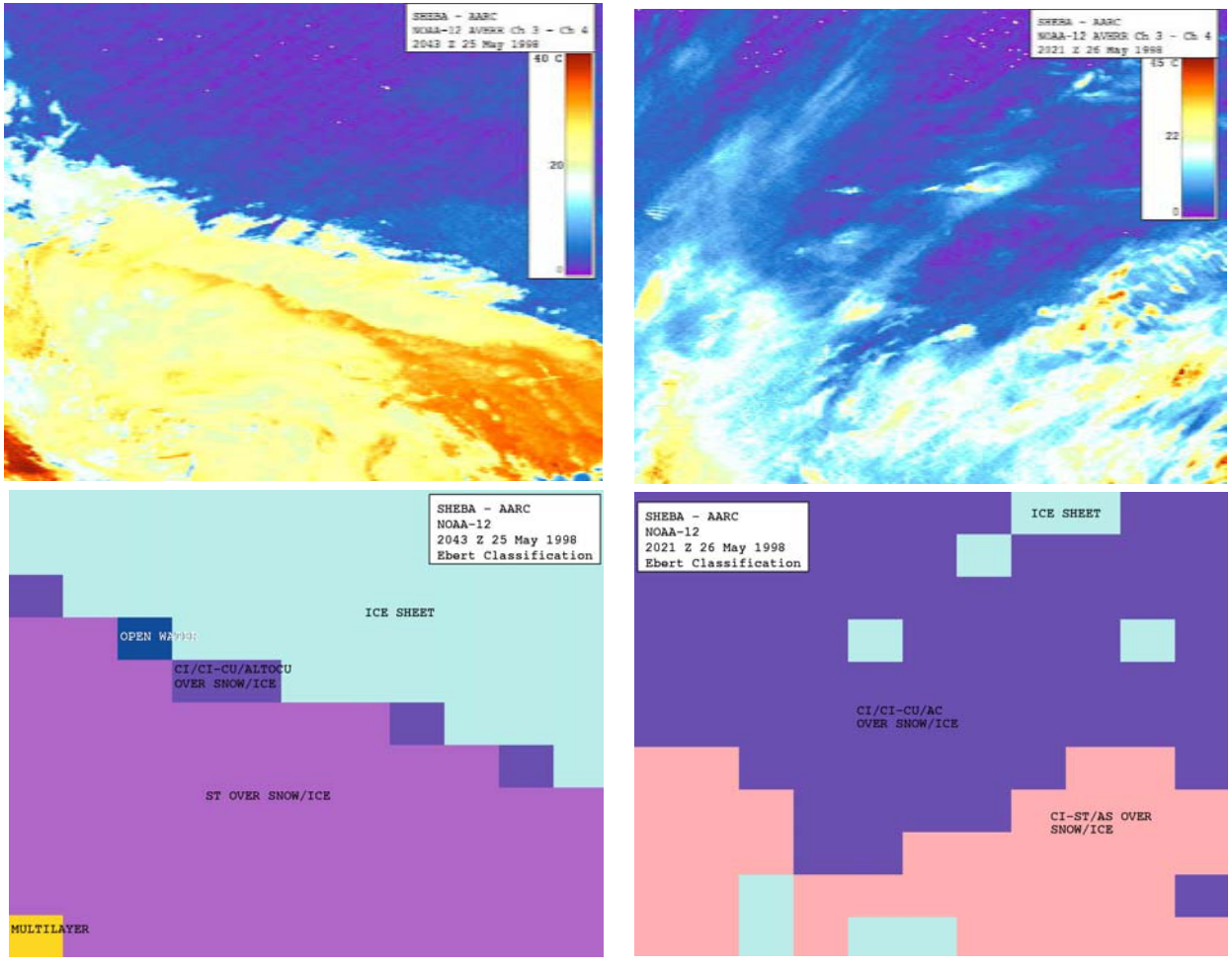

Figure 4.24. Demonstration of how the Ebert (1987) cloud classification scheme utilizes both textural and multispectral features to identify low clouds (left panels) and high clouds (right panels) in full-resolution (LAC) AVHRR images from the SHEBA field experiment (Perovich *et al.*, 1999; Uttal *et al.*, 2002). The top panels are the channel-1 images obtained on May 25 and 26, 1998, respectively. The next panels down show the corresponding mid-IR (channel 4) images, and the third panels down show the corresponding brightness temperature difference (channels 3 and 4) images. The bottom panels show the final classifications of 32×32-pixel cells.

Data from the Arctic and Antarctic Research Center at the Scripps Institution of Oceanography.

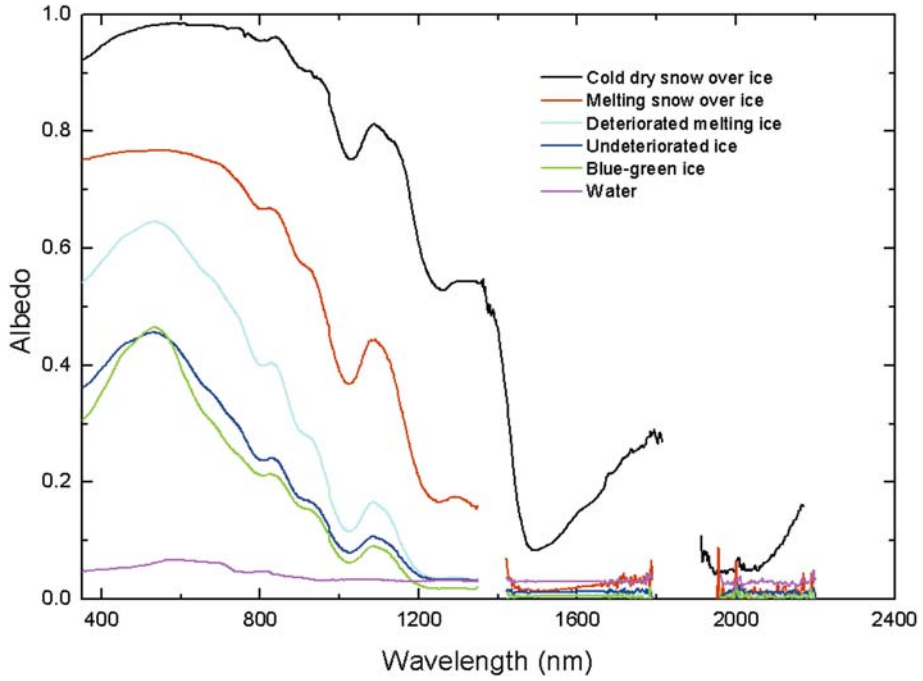

Figure 4.45. Evolution sequence of first-year ice albedo measured near Barrow, Alaska.
Data courtesy of Donald K. Perovich, U.S. Army Cold Regions Research and Engineering Laboratory.

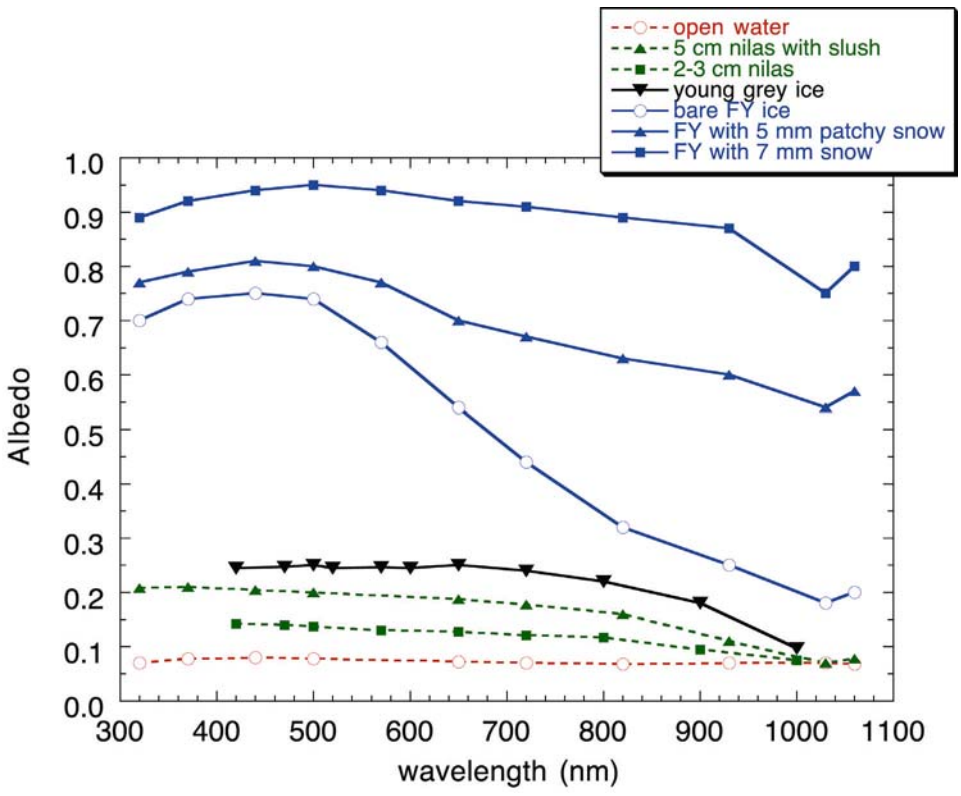

Figure 4.47. The spectral albedo of Antarctic sea ice in various stages of development.
As measured by Brandt et al. (1999).

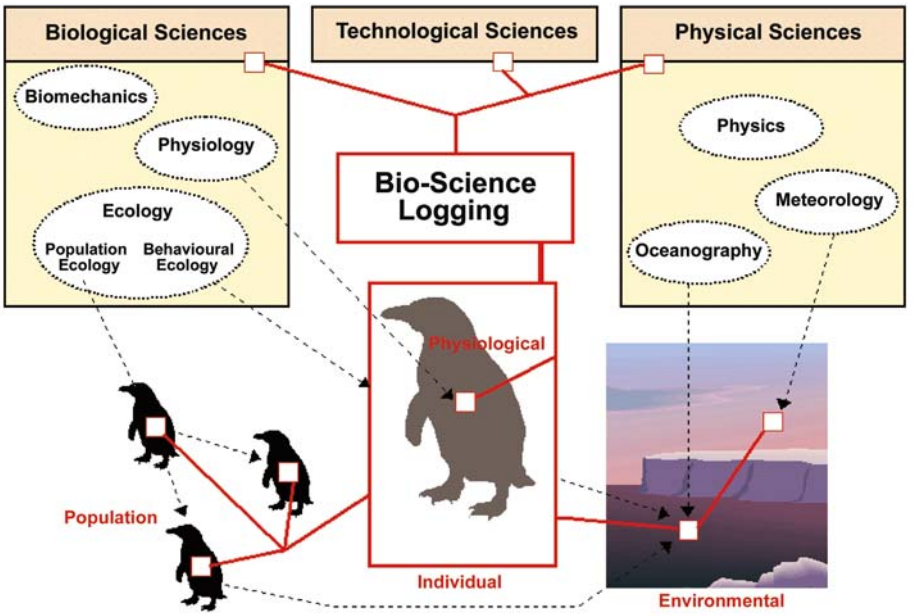

Figure 5.2. Schematic showing the network of information collected through bio-logging science (red connectors) that links the individual organism and its functions to the environment (biosphere, right and biotope, left). A similarity exists between the interface box used by bio-logging researchers to communicate with data loggers and bio-logging which is at the interface of biological, technical and physical sciences (yellow boxes).

From Boyd et al. (2004). Reprinted with permission of the Japan National Institute for Polar Research (NIPR). Copyright NIPR 2004.

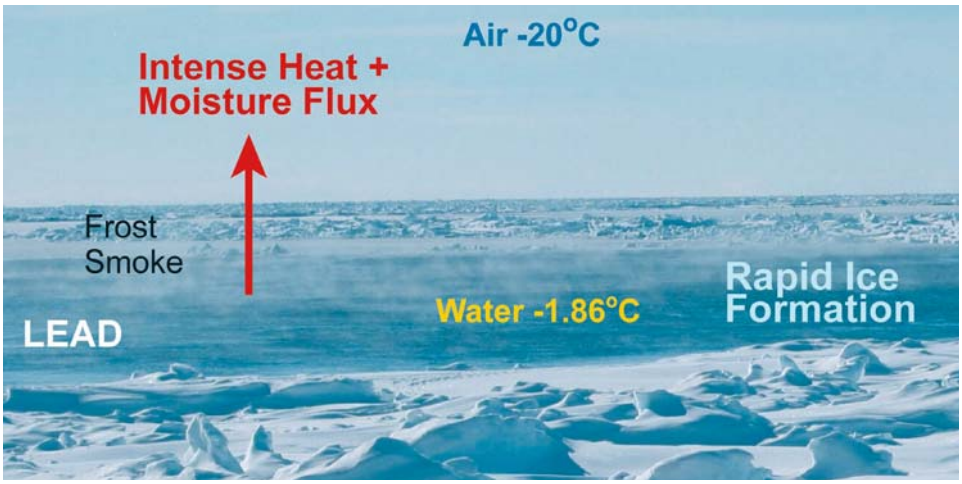

Figure 5.6. Photograph from the central section of the East Antarctic sea ice zone in winter showing the intense heat and water vapor loss that occurs from leads in the sea ice cover, where seawater with a temperature approximating -1.8°C is exposed to a significantly colder atmosphere. The steam emerging from the lead in the background is termed *frost smoke*. The ice cover comprises typical deformed first-year ice (foreground) with a thickness of $\sim$0.6 m in unridged areas and a snow cover of $\sim$0.1–0.3 m in thickness. Exchanges of heat, gases and momentum between the atmosphere and polar ocean are profoundly modified by the presence of a sea ice cover (Andreas and Cash, 1999; Maykut, 1986), as is the atmospheric boundary layer (Andreas, 1998). The magnitude of this modulation depends to a large extent on the thickness distribution of the sea ice and its snow cover. Note that while rapid rates of ice formation (and therefore brine rejection) occur in leads and polynyas, much slower rates occur on the base of existing thick floes.

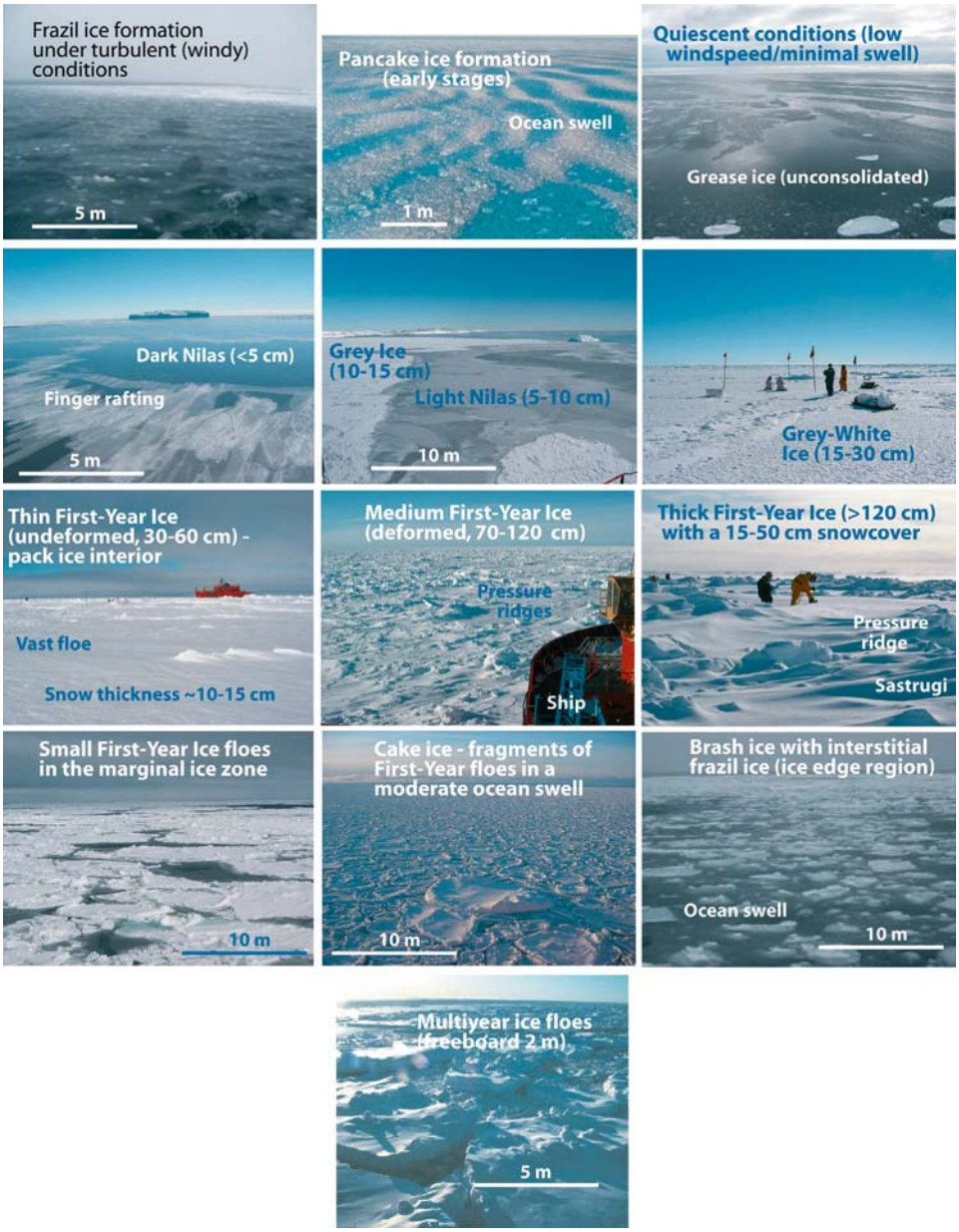

Figure 5.5. Photographs of different ice types and thicknesses for the Antarctic, with terminology based on the standard World Meteorological Organization sea ice classification (WMO, 1970). These photographs were taken in East Antarctica during the austral late autumn through early spring—i.e., during the freezing season. See Eicken (2003a) for photographs of Arctic sea ice types.

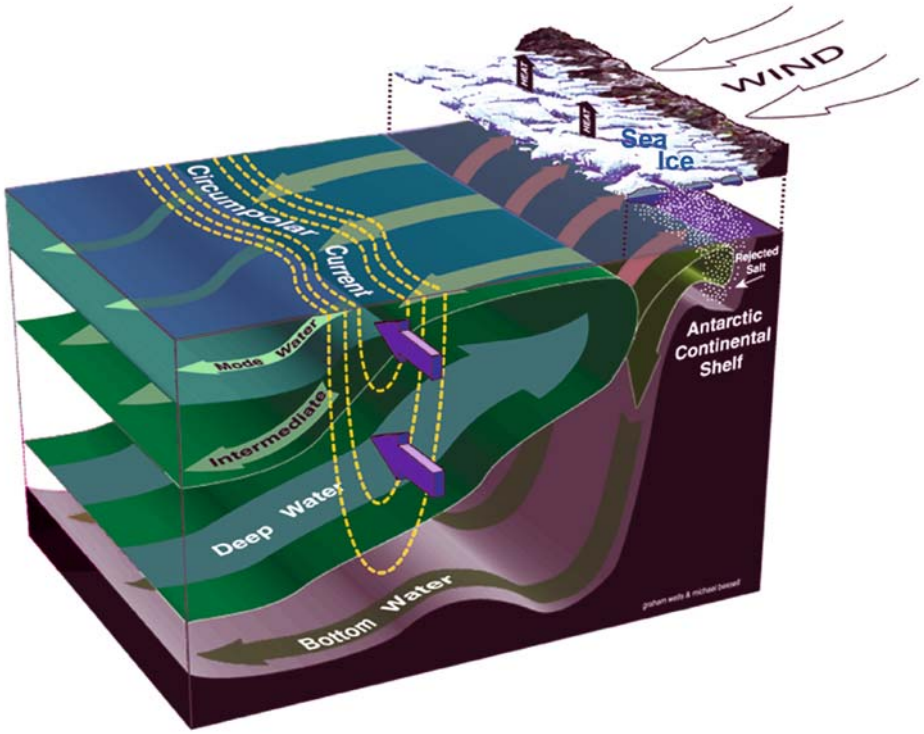

Figure 5.7. Schematic of the impact of intense atmosphere–ocean–sea ice interactions on watermass characteristics of the high-latitude Southern Ocean. Water mass transformations here form a crucial link in the global overturning circulation by connecting the intermerdiate and deep layers of the ocean (Rintoul, 2000; Speer et al., 2000; Rintoul et al., 2001b). Upwelling of deep water occurs to the surface south of the Antarctic Circumpolar Current (ACC). Part is freshened by melting sea ice and precipitation to become less dense (the addition of heat is also a factor), and flows equatorward and sinks as mode and intermediate Water. The remainder flows onto the continental shelf, where it is cooled through intense atmosphere–ocean–ice interactions and salt is added from brine rejected during sea ice formation. This denser water sinks and flows off the continental shelf and into the deep ocean to form Antarctic Bottom Water (Jacobs, 2004). This flows northwards in the abyssal ocean. By uniquely connecting the world's ocean basins, the ACC enables inter-basin exchange and a global-scale overturning circulation of watermasses to exist (Cunningham et al., 2003; Olbers et al., 2004; Rintoul and Sokolov, 2001). Heat transported by this overturning circulation is one of the main mechanisms by which the ocean influences the Earth's climate (Rintoul and Church, 2002). Climate models predict that such overturning circulation is sensitive in both hemispheres to climate change (Houghton et al., 2001).

From Rintoul and Church (2002), with the original figure created by Michael Bessell and Graham Wells. Copyright Commonwealth of Australia, reproduced by permission.

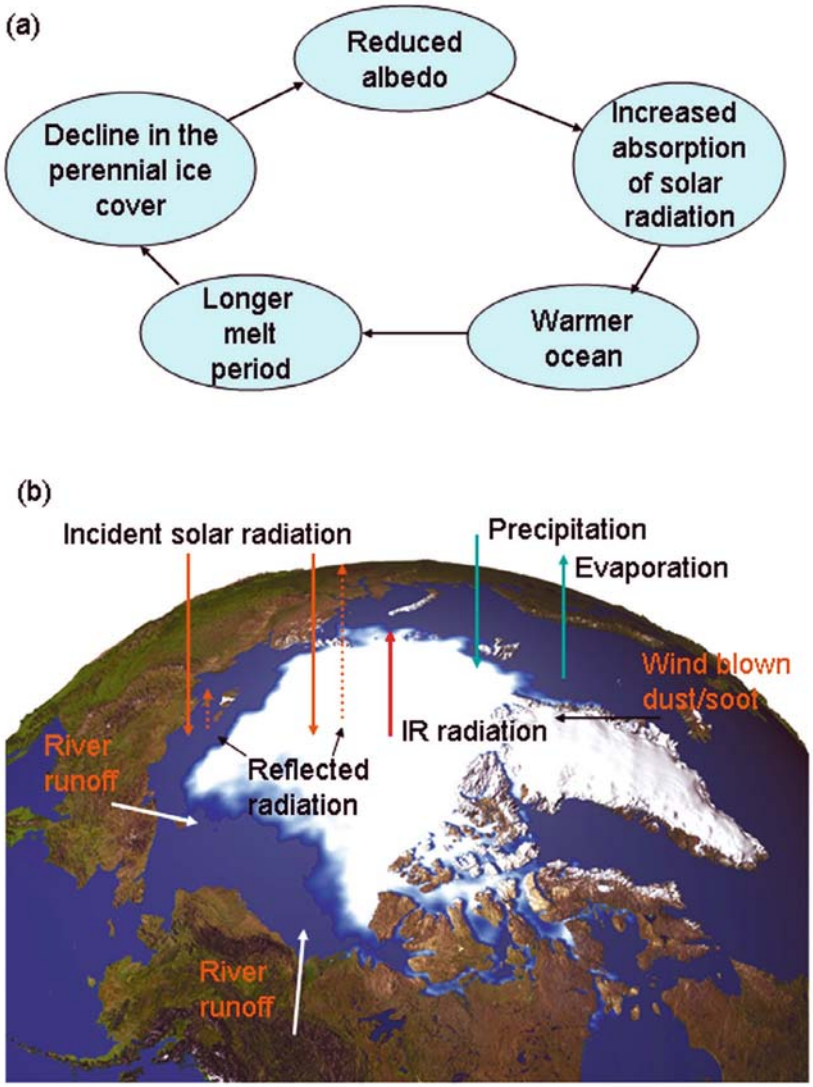

Figure 5.10. A schematic representation of (a) the sea ice albedo–ocean feedback loop, and (b) some of the key fluxes affecting the Arctic system, overlaying a satellite-derived ice concentration/extent map of the perennial ice cover at its summertime minimum in 2002. A major current concern is the impact of a recent decrease in the areal extent and thickness of Arctic perennial ice (see below) on further reduction of the ice cover. As is also the case in the Southern Ocean, the sea ice, ocean, and atmosphere of the Arctic are intimately interconnected. A change in one affects the others, to set up a feedback. In the case of the ice albedo–ocean feedback, a decrease in sea ice areal extent results in an increase in the solar flux into the upper ocean. This has the effect of warming its waters to further thin the ice and hasten its retreat. Moreover, regional warming would enhance surface melt to reduce the sea ice albedo and lead to enhanced melt.

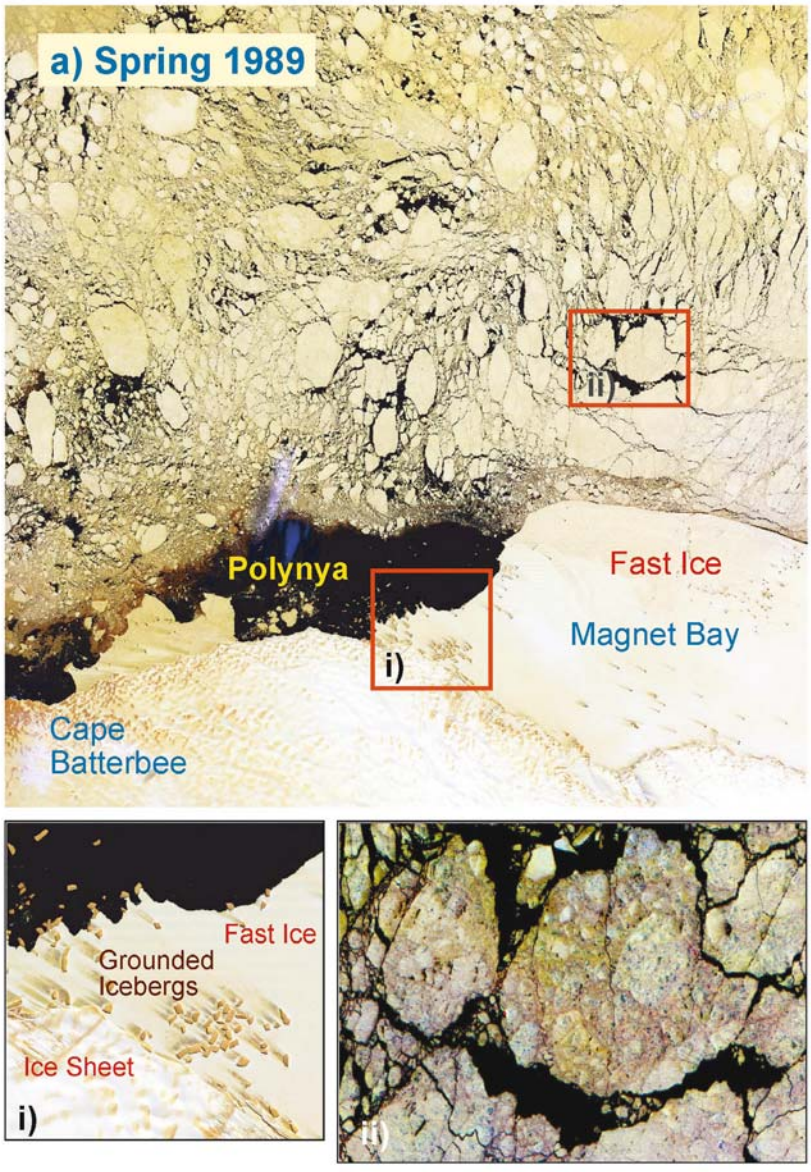

Figure 5.32a. Landsat Thematic Mapper (TM) image of coastal Antarctic sea ice conditions offshore from Cape Batterbee (~64.5°S, 55°E), from 27 March 1989. The main image dimensions are 184 × 185.2 km, with sub-scenes (i) and (ii) showing details of the pack and fast ice, respectively. Ice conditions early in the freeze-up season are dominated by young ice and a mixture of frazil, slush, and possibly pancake ice. The dynamic range is 8-bit—i.e., 256 gray levels per pixel. Sea ice features can be enhanced by combining data from channels 3 (0.62–0.69 μm), 4 (0.76–0.90 μm), and 5 (1.55–1.75 μm) to form a color composite image. The polynya in the foreground results from strong katabatic winds blowing offshore. Contrast stretching showed that the dark areas actually mainly comprise dark nilas. Also apparent is a large lens of fast ice in Magnet Bay, attached to numerous small icebergs (shown in detail in sub-image (i). Such imagery can, when cloud-free, greatly aid the validation of coarser resolution sea ice products—e.g., passive-microwave ice concentration data—and the interpretation of complex SAR data.

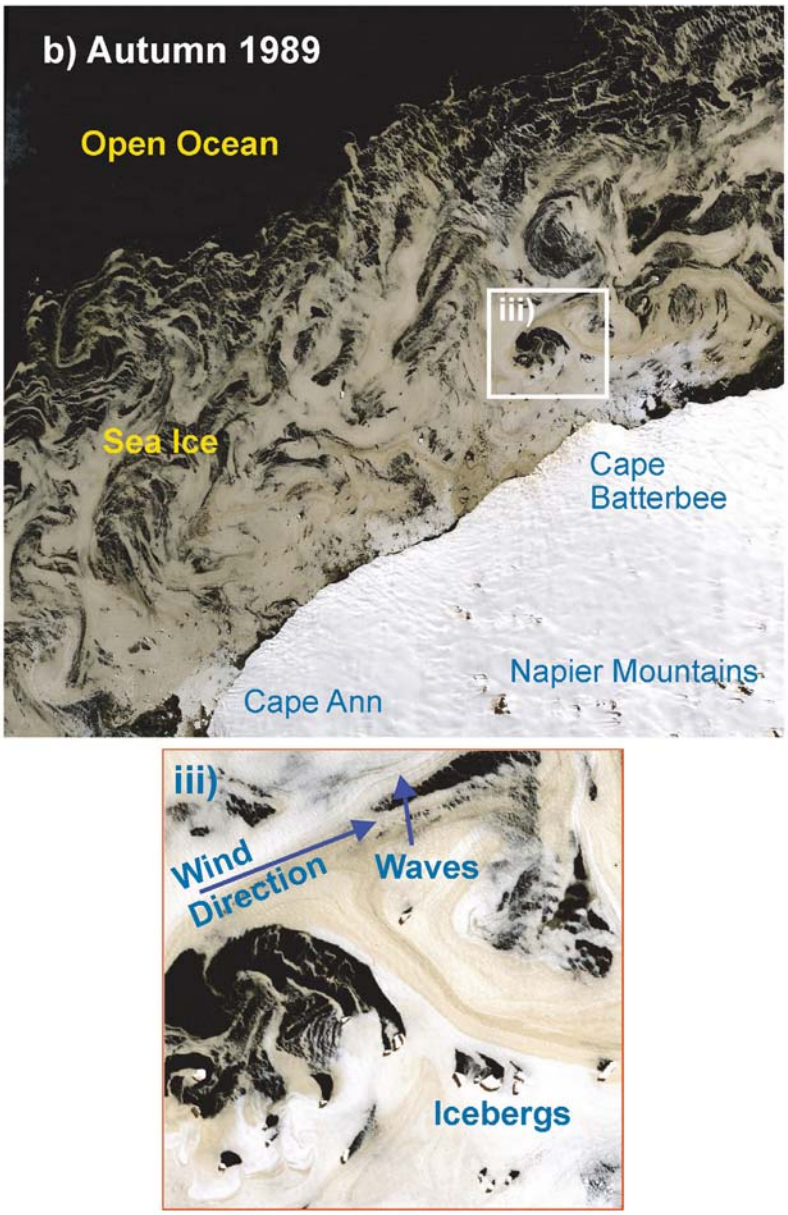

Figure 5.32b. Landsat Thematic Mapper (TM) image from approximately the same region as in Figure 32a but 8 months later (on November 24, 1989), and showing quite different sea ice conditions—i.e., a more diffuse ice cover comprising smaller floes. Note the complex eddy-like patterns traced by the unconsolidated ice, and the particularly diffuse nature of the outer pack (which comprises a series of bands). Ice interaction with numerous small icebergs is apparent (as dark dots) close to the ice sheet—see sub-image (iii).

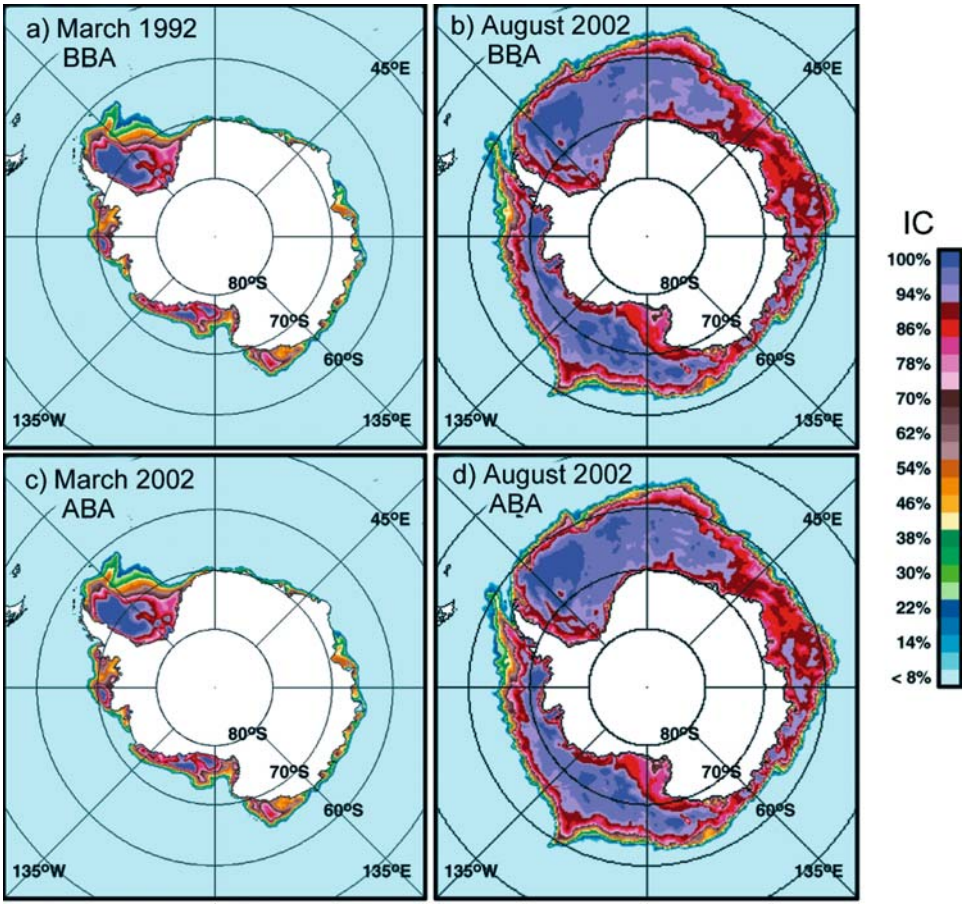

Figure 5.34. Color-coded BBA Antarctic ice concentration maps for (a) the austral summer (March 1992) and (b) winter (August 2002), and (c) and (d) equivalent maps derived using the ABA algorithm. That the two algorithms produce similar results suggests that the surface temperature effect on ice concentration retrieval accuracy using the BBA algorithm may be minimal. Note that ice concentrations are generally measurable down to 8%, below which it is not possible to discriminate between ice-covered areas and open water.

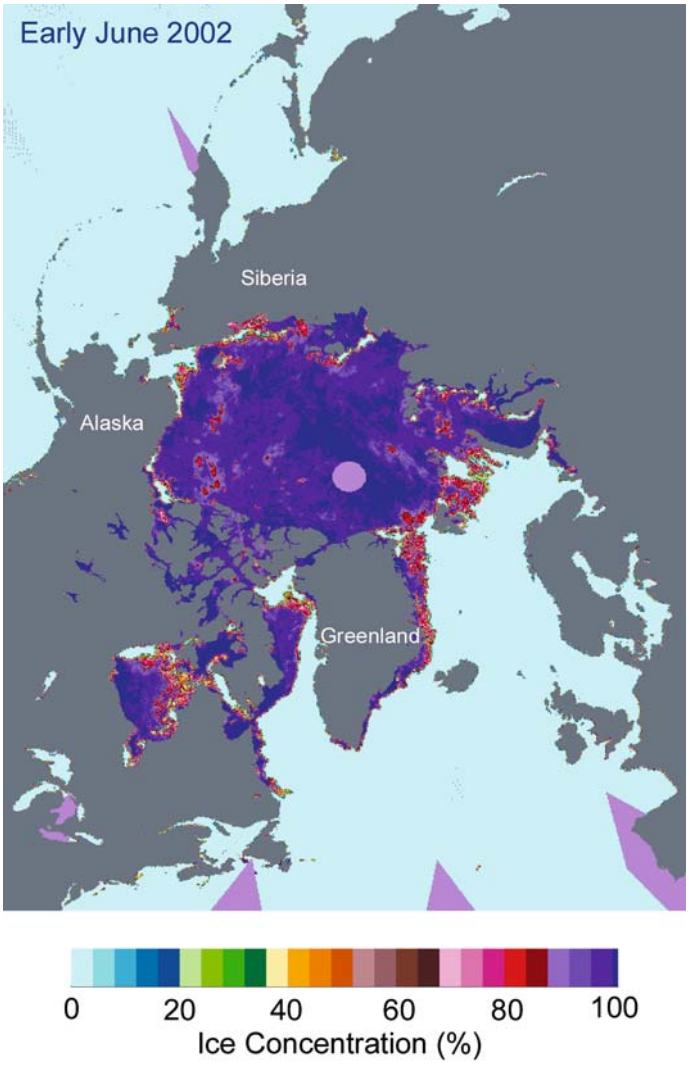

Figure 5.36. A daily map of Arctic sea ice concentration in early June 2002 retrieved from Aqua AMSR-E data using the NT2 algorithm.

From Comiso et al. (2003a). Reprinted with permission of the IEEE. © 2005 IEEE.

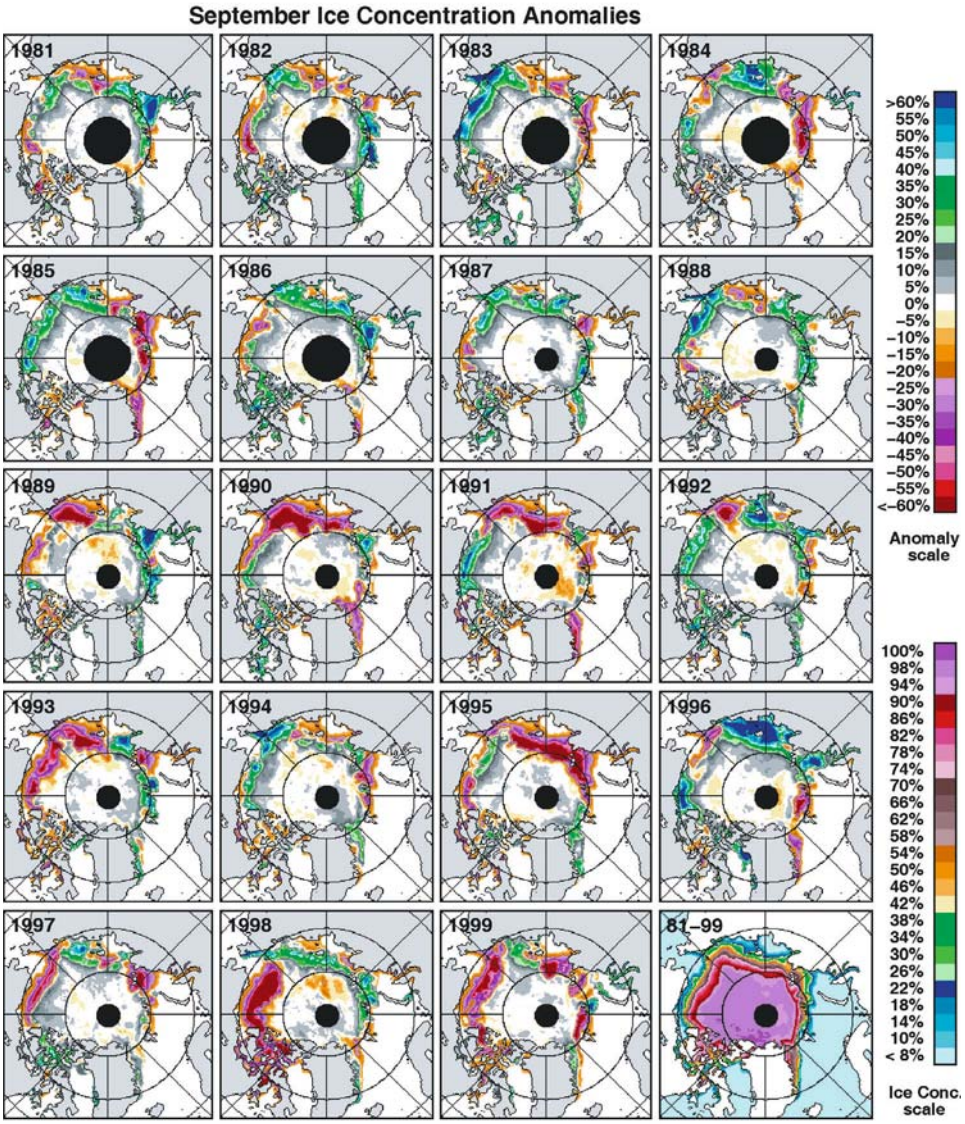

Figure 5.37. Color-coded monthly anomaly maps of Arctic ice concentration for each September (the annual ice minimum extent) from 1981 to 1999. The last image, labeled "81–89", is the mean of all September ice concentrations from 1981 to 1999. The ice concentration maps were created by applying the NASA Bootstrap algorithm (Comiso *et al.*, 1997) to Nimbus-7 SMMR and DMSP SSM/I T_B data, gridded to a 25-km resolution and polar stereographic projection and available from the NSIDC.

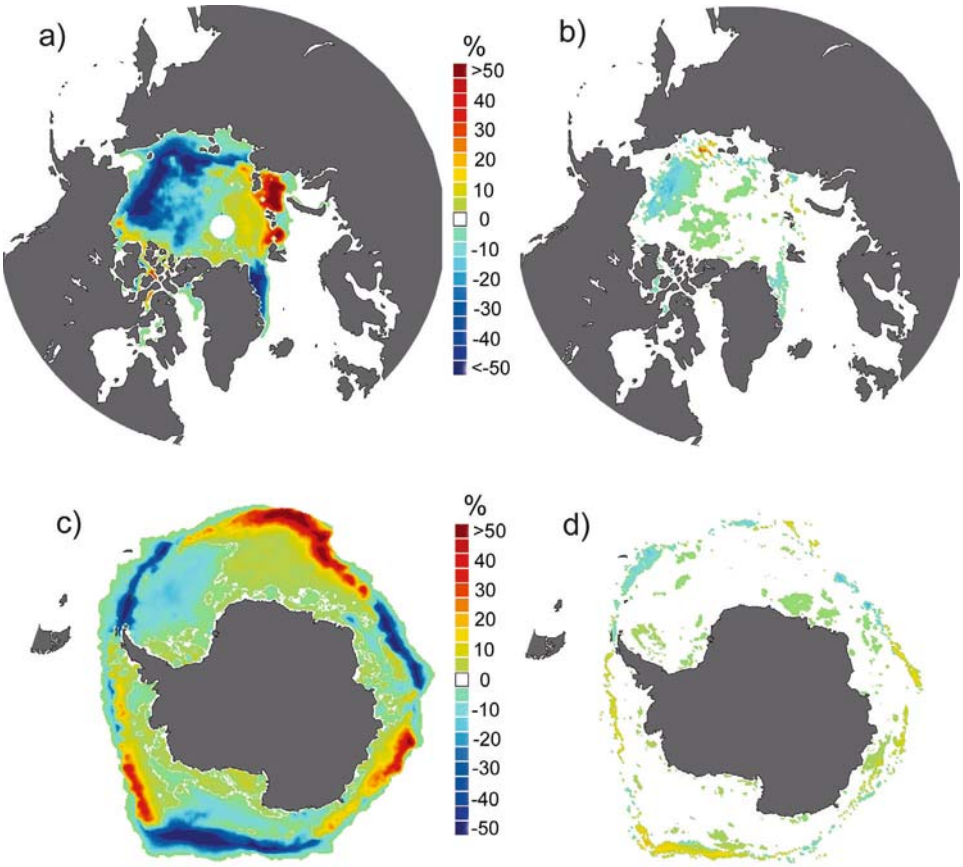

Figure 5.38. Maps of ice concentration anomalies in (a) the Arctic, and (c) the Antarctic for September 2003. Associated trends in ice concentration for the Arctic and Antarctic are shown in (b) and (d), respectively. In this example, the total anomaly for the Antarctic is $-0.4 \times 10^6\,\mathrm{km}^2$, while that for the Arctic is $-0.7 \times 10^6\,\mathrm{km}^2$. These images were obtained from the Sea Ice Index of the US National Snow and Ice Data Center (NSIDC), University of Colorado (⟨*http://nsidc.org/data/seaice_index/*⟩; Fetterer and Knowles, 2002).

Courtesy of Florence Fetterer (NSIDC), produced by Nancy Geiger Wooten and Ken Knowles (NSIDC).

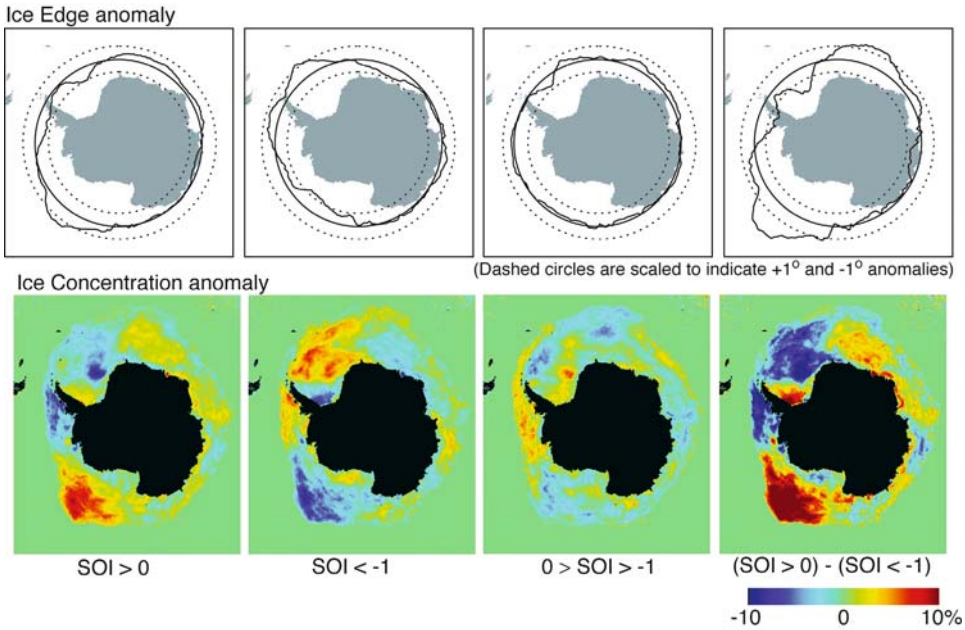

Figure 5.39. Composites of Antarctic ice edge/concentration anomalies for 1982 to 1998, derived from SMMR and SSM/I data during the three possible phases of the Southern Oscillation Index (SOI)—namely, $SOI > 0$, $0 \geq SOI \geq -1$, and $SOI < -1$—and also the difference between the two extremes—i.e., $SOI > 0$ and $SOI < -1$. The SOI is the difference in the standardized sea level pressures between Tahiti and Darwin. Large negative values are associated with intense ENSO episodes. The anomalies here are scaled to emphasize the spatial pattern. Dashed circles indicate $\pm 1^{\circ}$ anomalies in the ice edge location.

From Kwok and Comiso (2002a). Reproduced with permission of American Meteorological Society (AMS), © 2005 AMS.

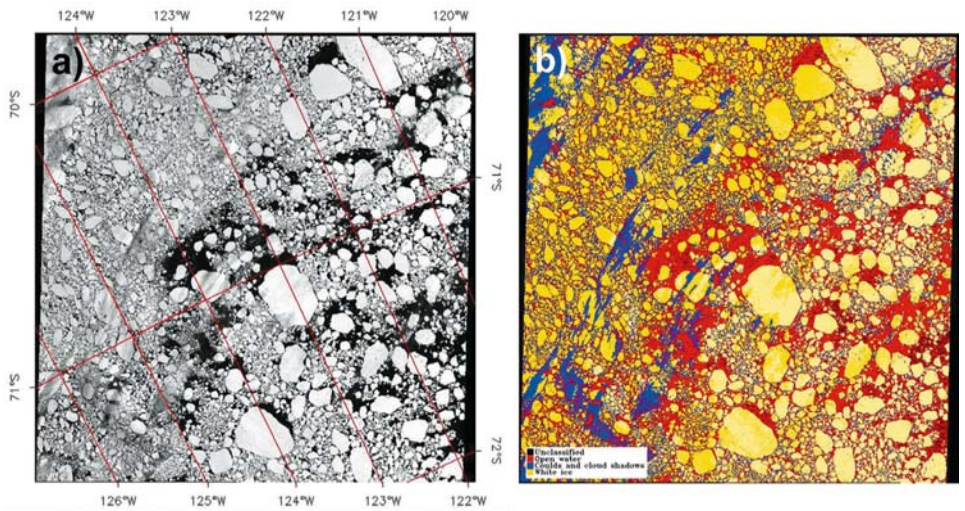

Figure 5.40. (a) A Landsat MSS scene (170×180 km) of sea ice in the Amundsen Sea, Antarctica in December 1990; and (b) the same image classified using the tiepoint method applied to channel-4 (0.8–1.1 μm) data. The IFOV is 30 m. White ice is yellow, open water red, and clouds and cloud shadows blue. Clouds (in blue) were detected using channel-2 (0.6–0.7 μm) and -4 data. In this particular case, the color-coded scene shows an averaged concentration of 85%—a value that was used by Comiso and Steffen (2001) to validate coincident ice concentration retrievals from SSM/I data using the NASA Bootstrap and Team algorithms. The latter yielded comparable concentration values of 90% and 83%, respectively.

From Comiso and Steffen (2001). Copyright 2001 American Geophysical Union. Reproduced by permission of American Geophysical Union.

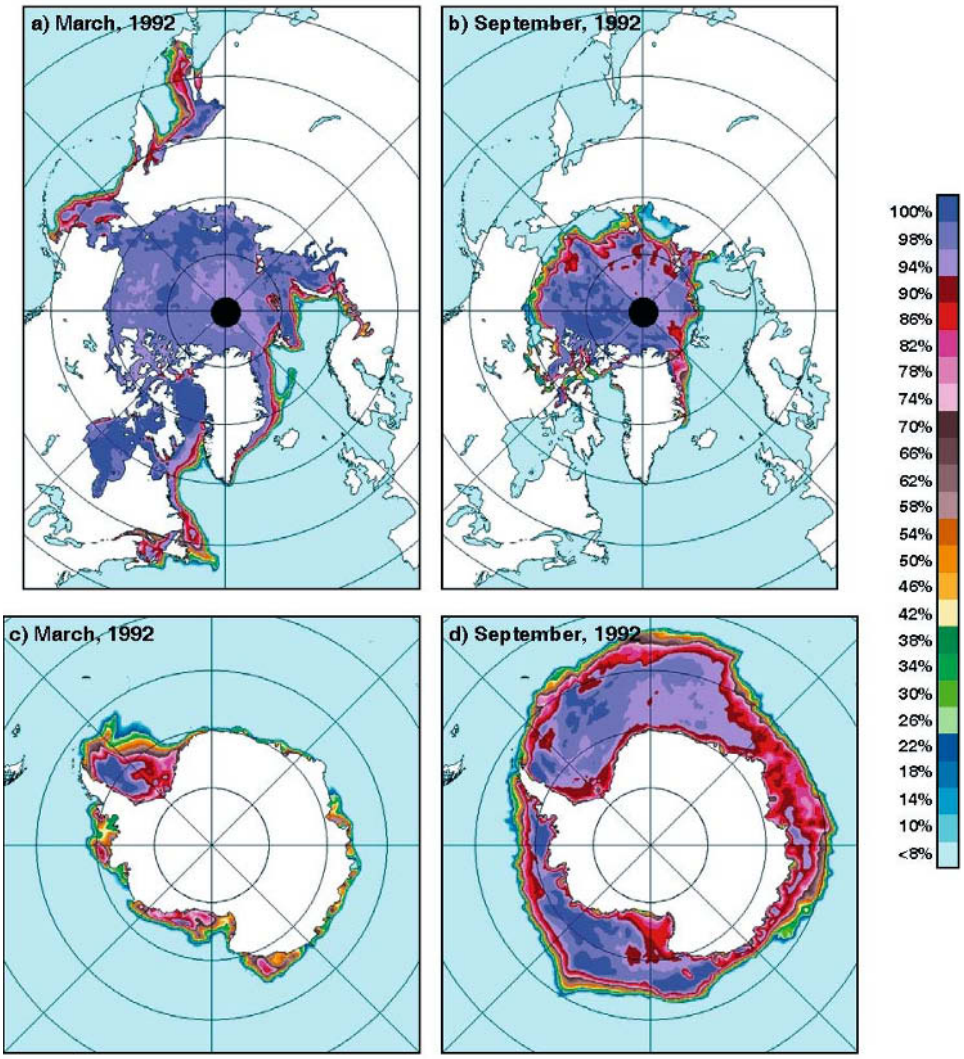

Figure 5.43. Maps of mean monthly sea ice concentration and extent from (a and b) the Arctic, and (c and d) the Antarctic, from March and September 1992. These images were derived from DMSP SSM/I brightness temperature data by applying the NASA Bootstrap algorithm (Comiso, 1995a).

Imagery courtesy of Joey Comiso (NASA Goddard Space Flight Center).

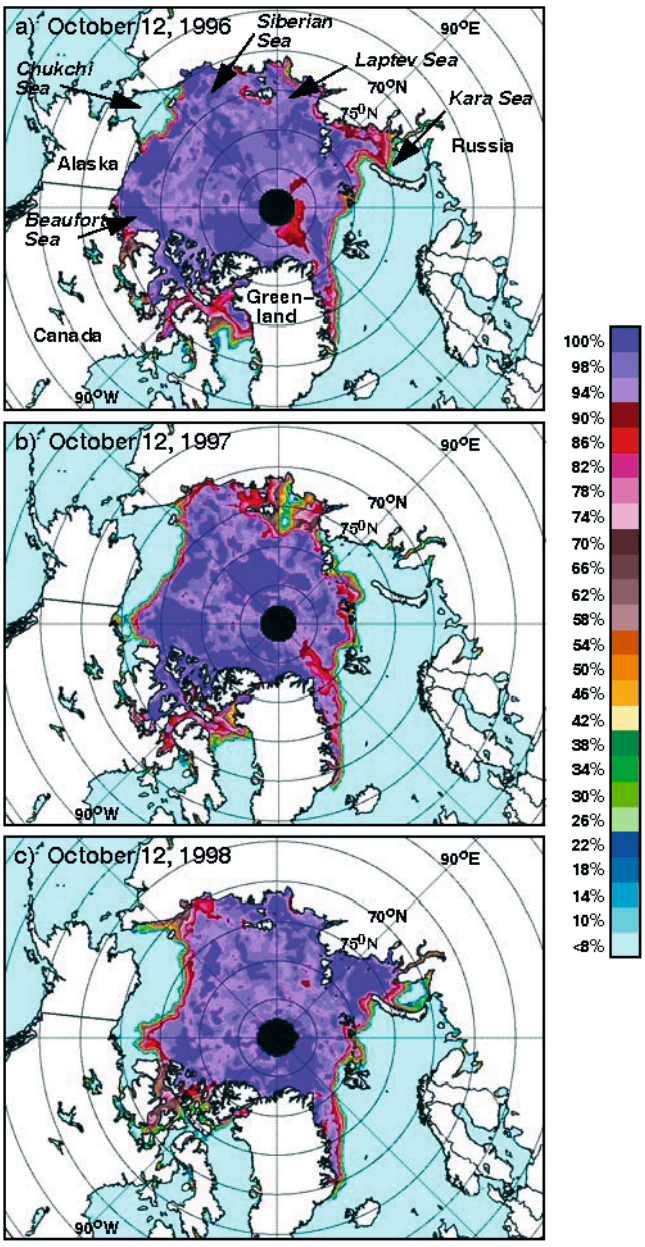

Figure 5.44. Color-coded, daily ice concentration maps of the Arctic from the approximate freezeup period, on October 12 in (a) 1996, (b) 1997, and (c) 1998. Note the extraordinary differences in sea ice extent in the Beaufort, Kara, and Chukchi Seas and the Canadian Arctic/West Greenland, in particular. The maps were created from SSM/I T_B data using the NASA Bootstrap algorithm (Comiso et al., 1997).

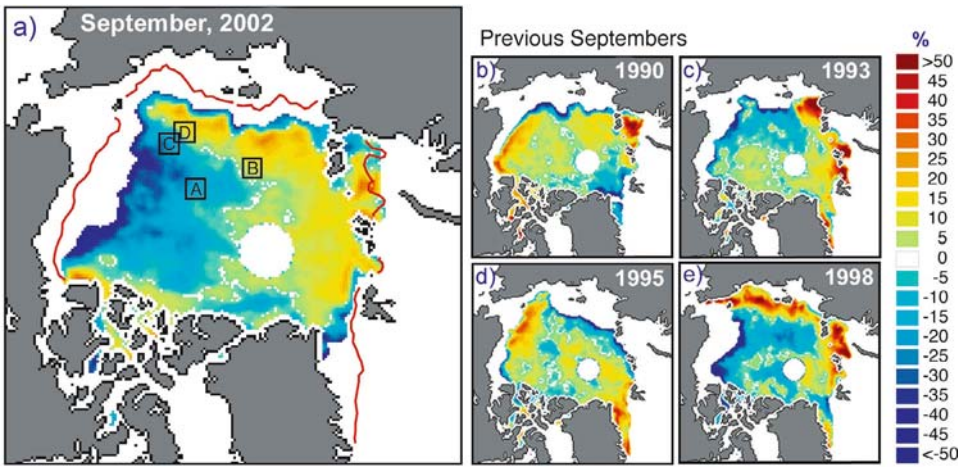

Figure 5.47. A map of monthly mean Arctic sea ice extent and concentration anomalies (in %) for September 2002 derived from near-real time SSM/I data and relative to NASA-Standard-Team-algorithm-derived mean values for the period 1988–2000. The median ice extent over the same period is indicated by the red line. The four boxes (A, B, C, and D) depict the MODIS validation areas shown in Figure 5.41. On the right are September sea ice extent and concentration anomalies for the four previous minimum-extent years: (b) 1990, (c) 1993, (d) 1995, and (e) 1998.

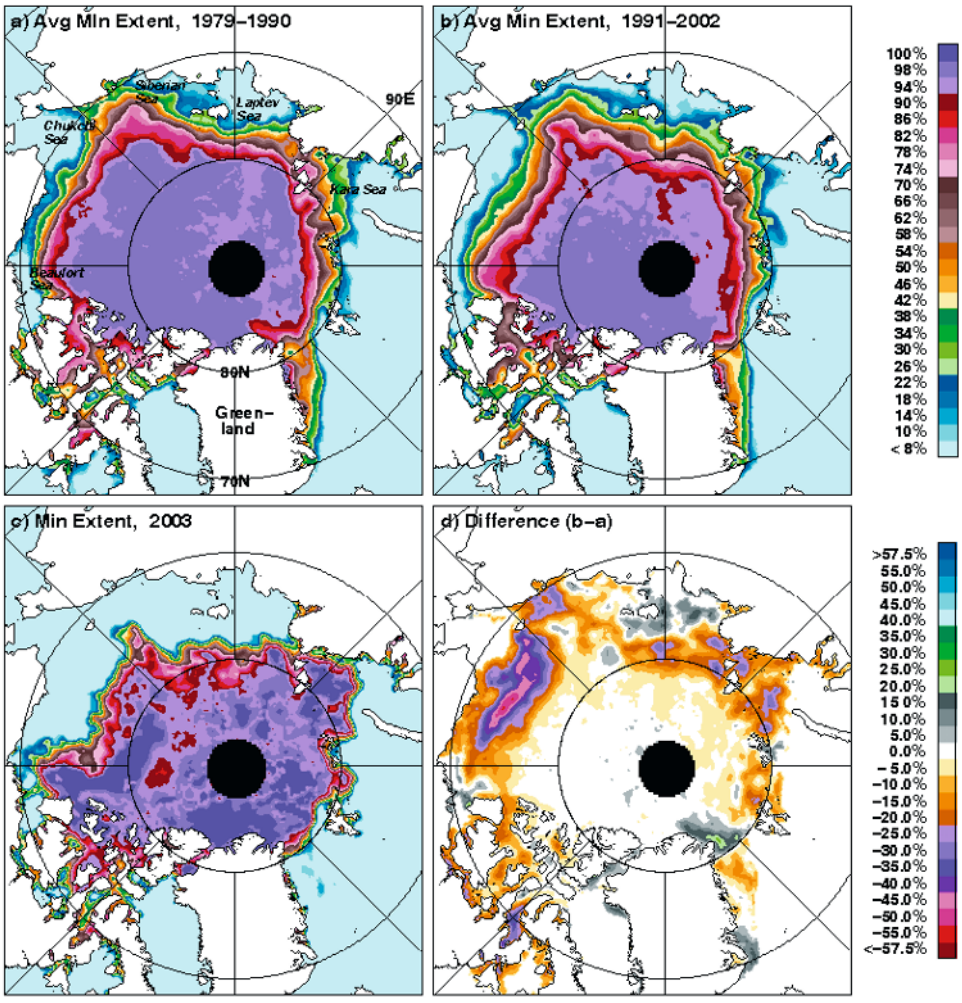

Figure 5.48. Maps of Arctic mimimum summertime sea ice concentration and extent derived from consistent processing of Nimbus-7 SMMR and DMSP SSM/I data. Panels (a) and (b) show the average minima recorded over the years 1979–1990 and 1991–2002, respectively. Panel (c) shows the extreme minimum recorded in 2003. Note that the ice concentration boundaries are sharper in (c) because averaging results in the blurring of ice motion effects. (d) The relative difference (b) minus (a), showing the change over time. This shows that the greatest reduction in sea ice has occurred in the Beaufort Sea region (north of Alaska). Such changes have far-reaching ramifications, as discussed in Section 5.4.

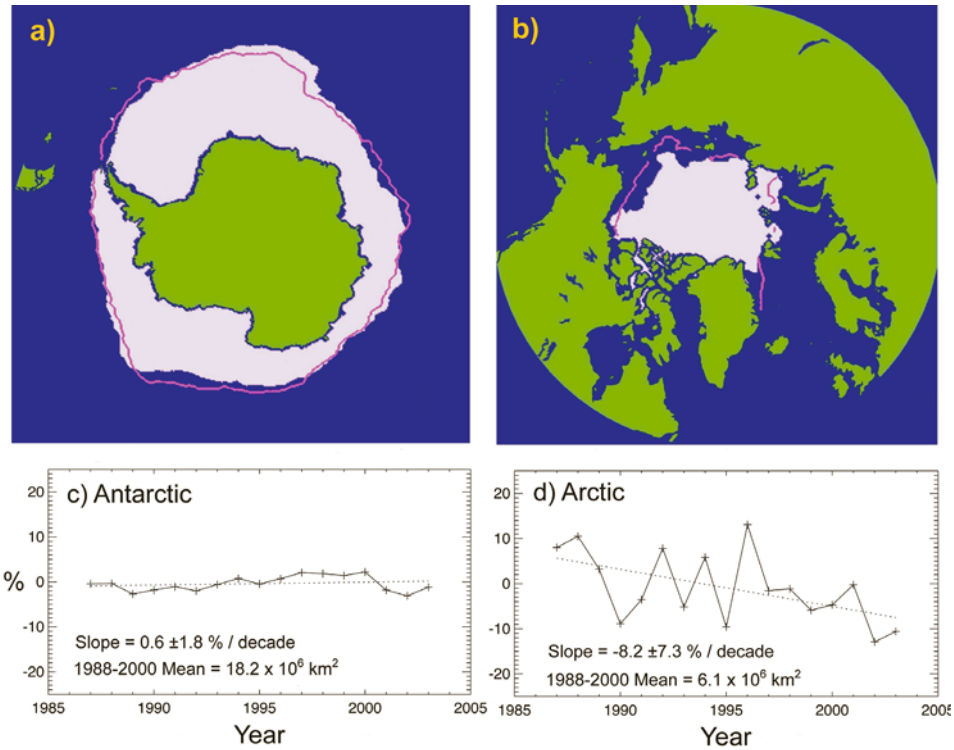

Figure 5.50. Maps of sea ice extent anomalies in (a) Southern Ocean, and (b) the Northern Hemisphere for September 2003—i.e., based upon the monthly mean compared with the mean September value from 1988–2000—with associated trend plots shown in (c) and (d), respectively. The purple line in (a) and (b) demarcates the median ice edge for September (based on monthly data from 1988–2000). The total extent in the Antarctic at this time was 18.0×10^6 km, and in the Arctic 5.4×10^6 km^2. These images were obtained from the Sea Ice Index of the US National Snow and Ice Data Center (NSIDC), University of Colorado (⟨*http://nsidc.org/data/seaice_index/*⟩; Fetterer and Knowles, 2002).

Courtesy of Florence Fetterer (NSIDC), produced by Nancy Geiger Wooten and Ken Knowles (NSIDC).

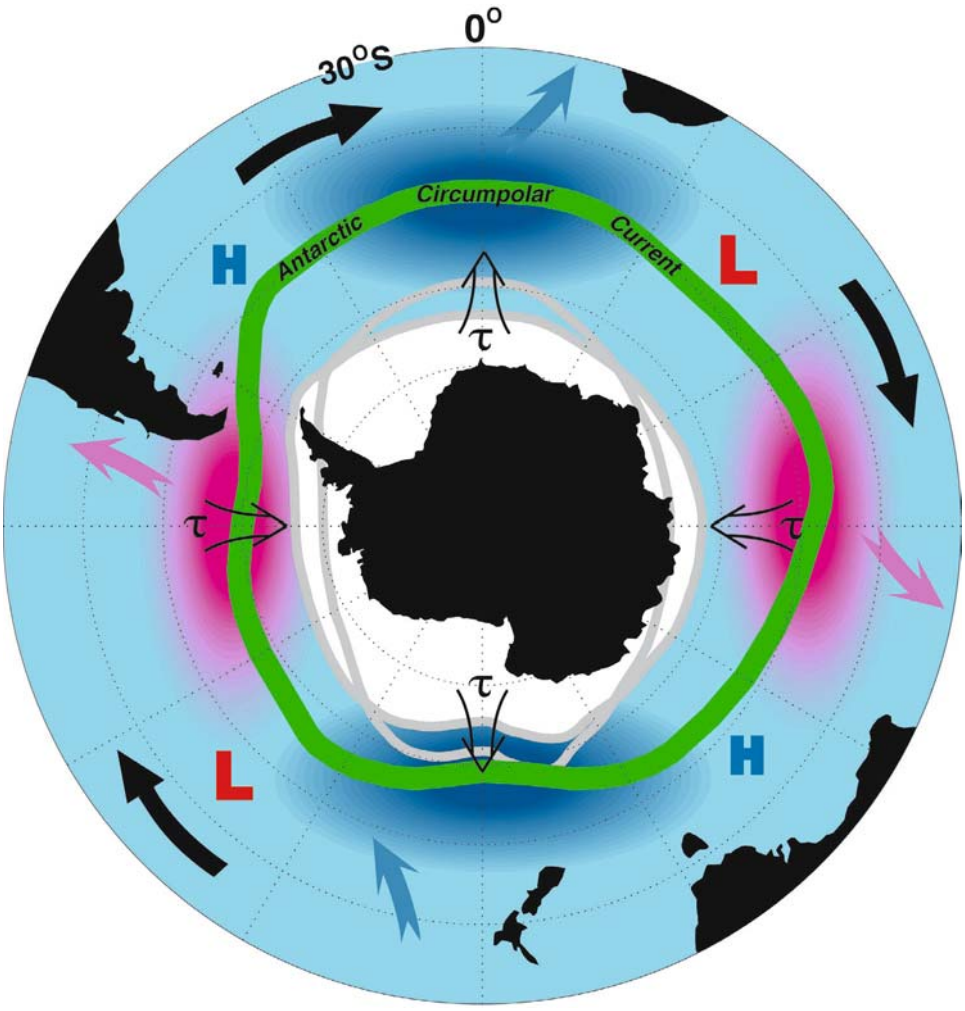

Figure 5.51. A simplified schematic summary of interannual variations in atmospheric sea level pressure (bold L = low and H = high), sea surface temperature (blue = relatively cold, red = warm), meridional wind stress (denoted by τ), and sea ice areal extent (gray lines), together with the mean course of the Antarctic Circumpolar Wave (green). Sea ice extent is based on an overall 13-year average derived from DMSP SSM/I data (1979–1991), with a 15% ice concentration threshold. Heavy black arrows depict the general eastward propagation of anomalies, while other arrows indicate apparent communications between the Antarctic Circumpolar Current and more northerly sub-tropical ocean gyres.

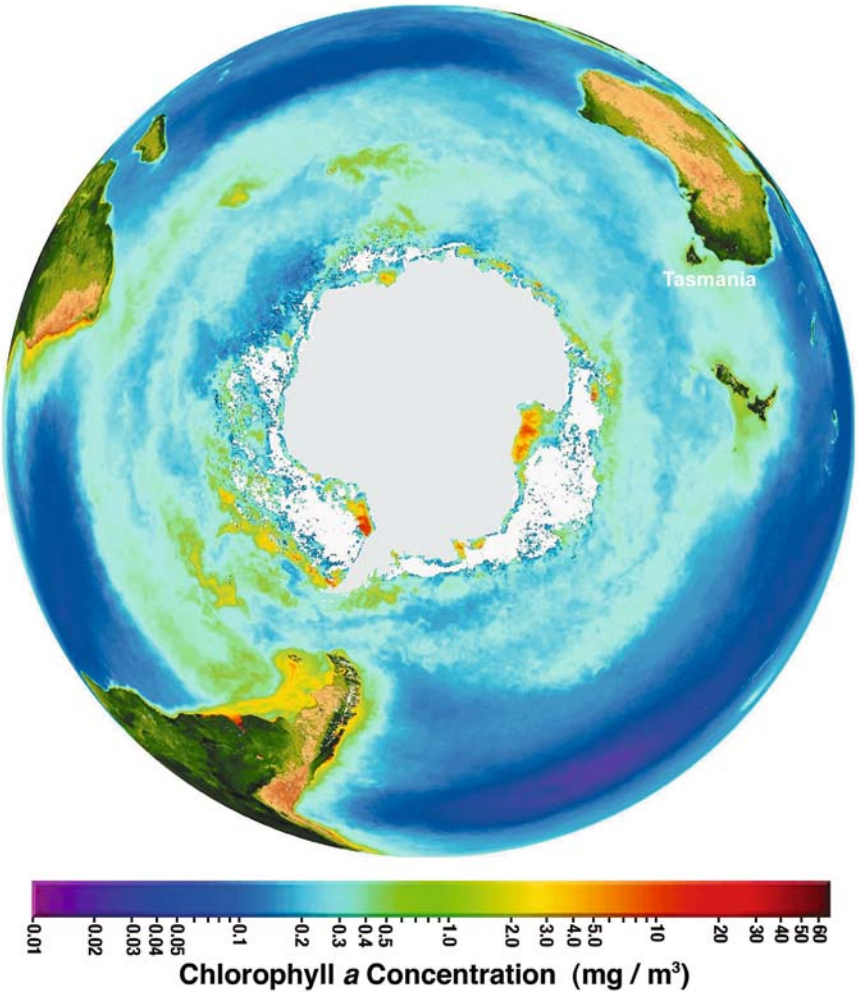

Figure 5.52. A composite ocean color image of the Southern Ocean produced from data from the SeaWiFS sensor onboard the SeaStar satellite, for the period September 1997 to August 2000. The color scale relates to chlorophyll *a* (phytoplankton) concentration in the ice-free ocean, with red being the highest concentration and blue the lowest. The ice sheet and sea ice are masked out in white. Note the very high values within polynya regions of the southern Weddell and Ross Seas.

From Massom (2002). Image courtesy of the SeaWiFS Project (⟨*http://seawifs.gsfc.nasa.gov/SEAWIFS.html*⟩), NASA/Goddard Space Flight Center and ORBIMAGE.

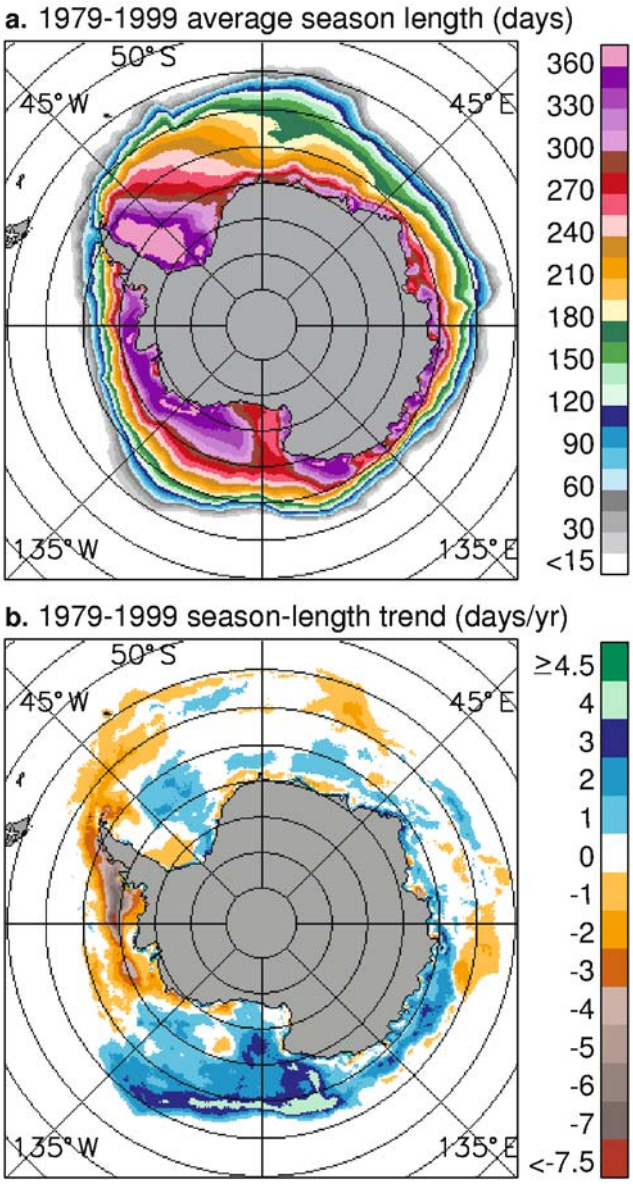

Figure 5.53. (a) Average length of the ice season (in days) for the period 1979 to 1999, using a 15% ice concentration cutoff; and (b) trends in the average ice season length over the same period and with the same concentration cutoff. The ice concentrations were derived from SMMR and SSM/I data using the NASA Team algorithm (Cavalieri et al., 1999b).

After Parkinson (2002). Courtesy of Claire Parkinson and Nick DiGirolamo (NASA Goddard Space Flight Center).

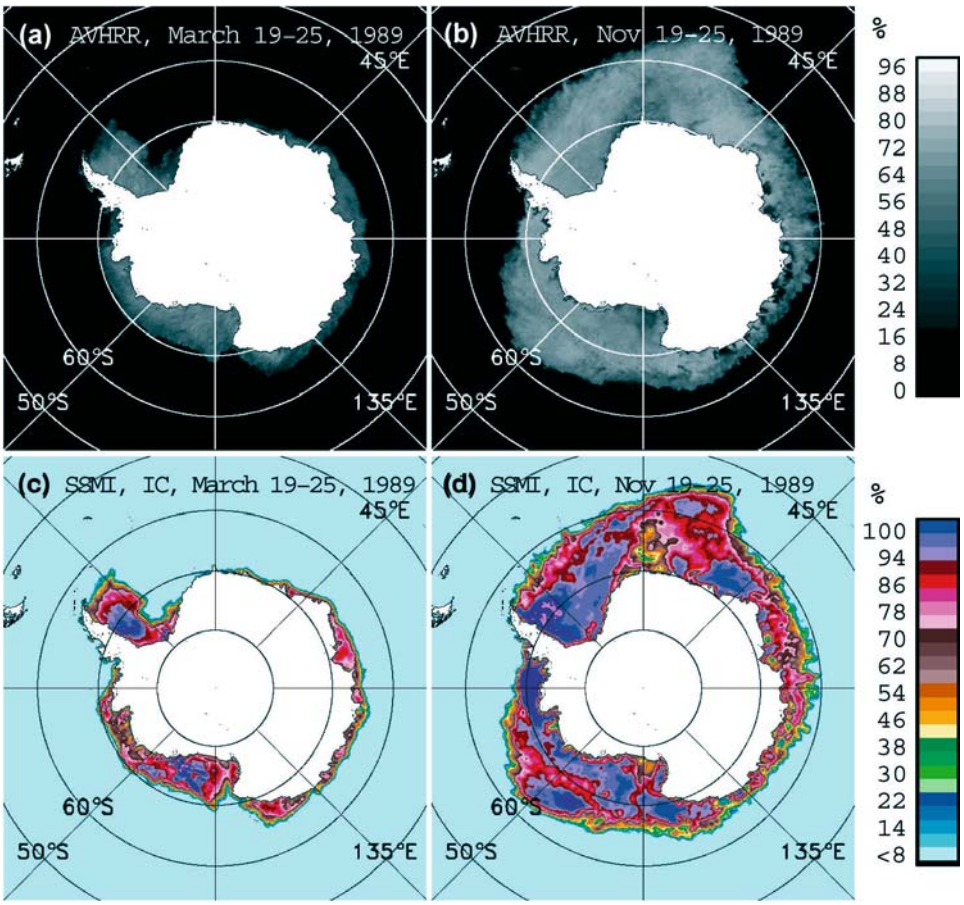

Figure 5.56. Maps of Antarctic sea ice derived from weekly averaged cloud-free AVHRR channel-1 (0.6 μm) global area coverage (4-km resolution) data from (a) late March 1989 and (b) late November 1989. (c) and (d) are corresponding maps of ice concentration/extent derived from DMSP SSM/I data. Note the polynyas along the East Antarctic coastline in (b).

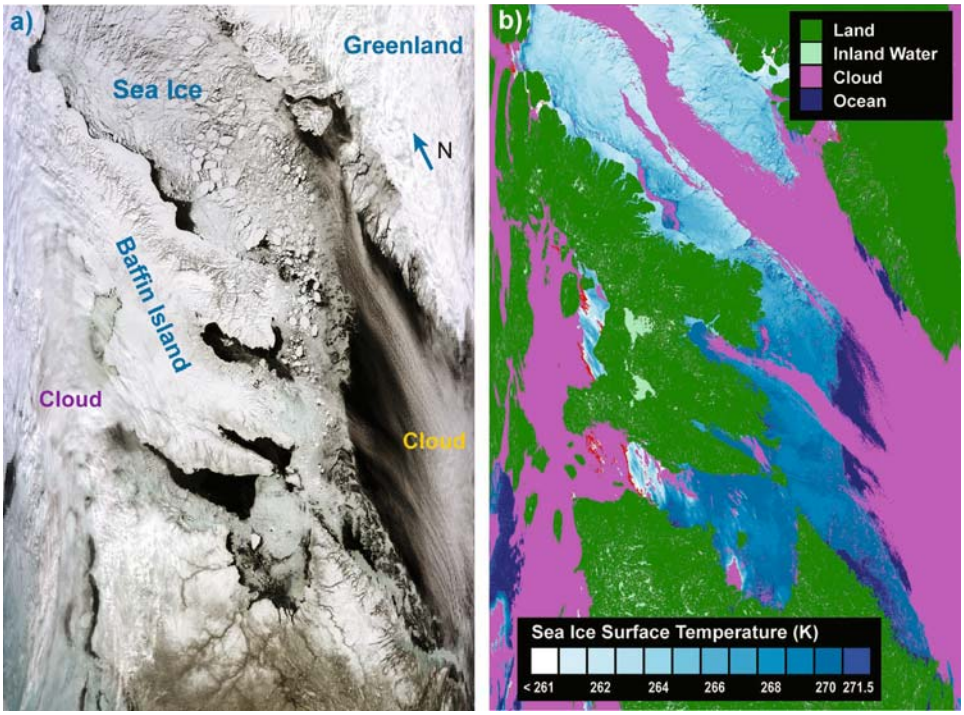

Figure 5.57. An example of MODIS sea ice image products produced by the NASA MODIS Project and archived at the U.S. National Snow and Ice Data Center, from the Baffin Bay region of the Eastern Arctic and acquired on May 5, 2001 (16 : 10 UTC)—the author's birthday!! (a) A 500-m-resolution true-color reflectance image derived from level-1b-calibrated visible band radiances from bands 1 (0.65 μm), 3 (0.47 μm), and 4 (0.55 μm). (b) The corresponding 1-km-resolution map of sea ice surface temperature (*IST*). The classification image (ice extent map), including cloud masking, is again a standard product derived from the MODIS/Terra Sea Ice Extent L2 Swath 1-km dataset (⟨*http://nsidc.org/data/mod29.html*⟩). Sea ice here is identified as any pixel with an *IST* of $\leq$271.5 K.

Images © NSIDC and NASA. Imagery courtesy of Dorothy Hall (NASA Goddard Space Flight Center), produced by Kimberley Casey (NASA Goddard Space Flight Center).

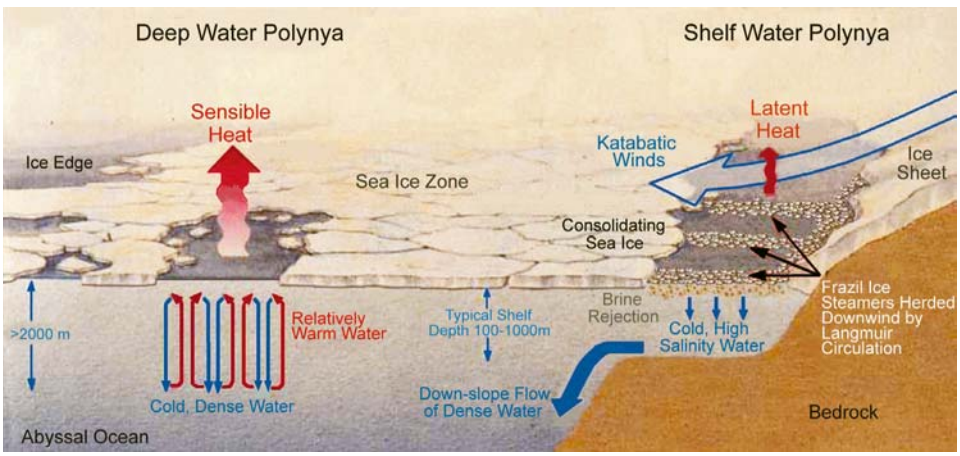

Figure 5.60. A schematic representation of physical processes occurring in, and responsible for, the formation of shelf-water and deep-water polynyas.

After Morales Maqueda *et al.* (2004), modified from Colling (2001). Copyright 2004 American Geophysical Union. Reproduced by permission of American Geophysical Union.

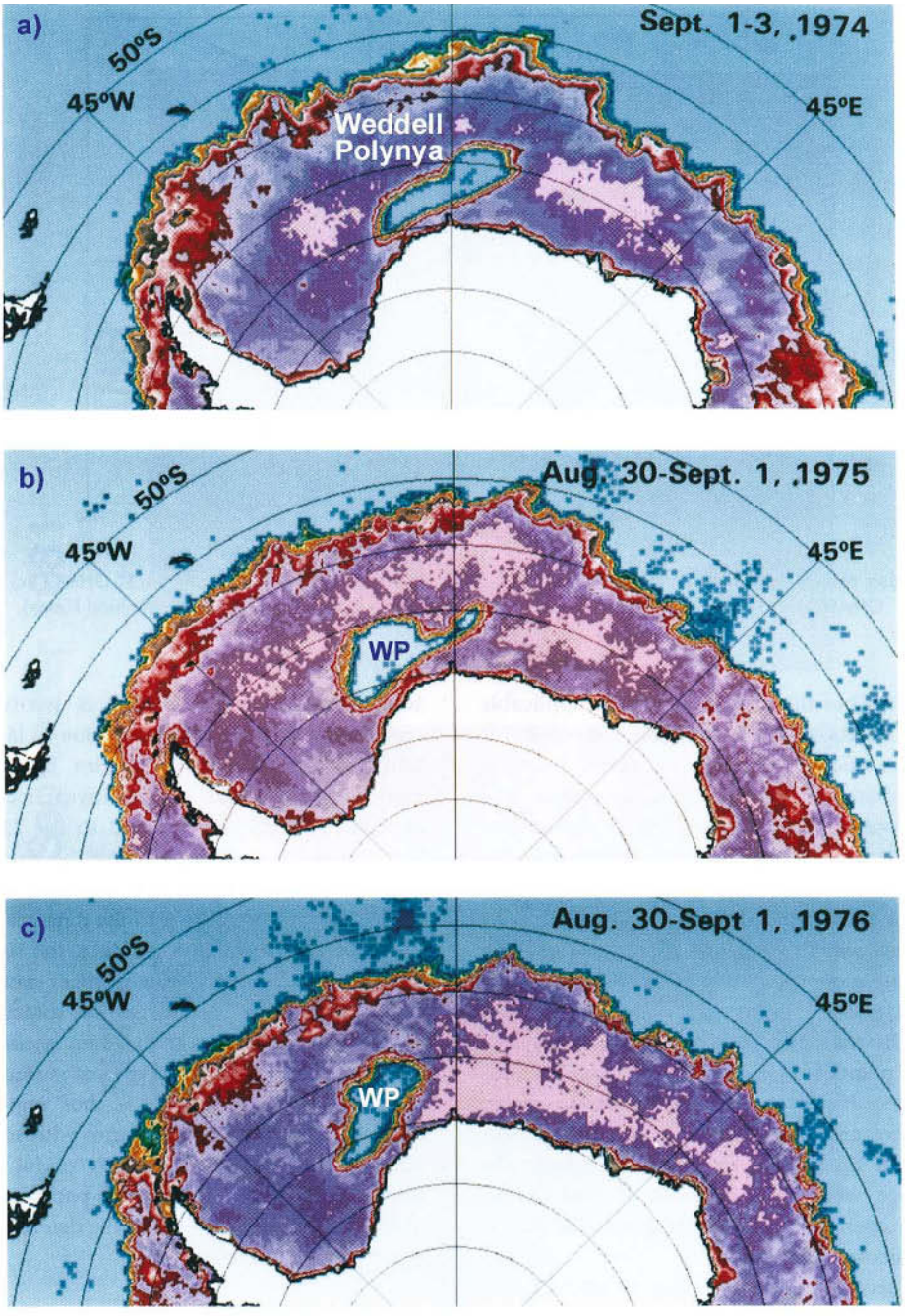

Figure 5.61. Passive-microwave 3-day composite ice concentration images derived from Nimbus-5 ESMR data showing the extraordinary Weddell Polynya (marked WP) that occurred in the winters of (a) 1974, (b) 1975, and (c) 1976. At its largest, the polynya measured $1{,}000 \times 350$ km.

From Gordon and Comiso (1988). Reproduced with permission of Dr. Joey Comiso (NASA Goddard Space Flight Center).

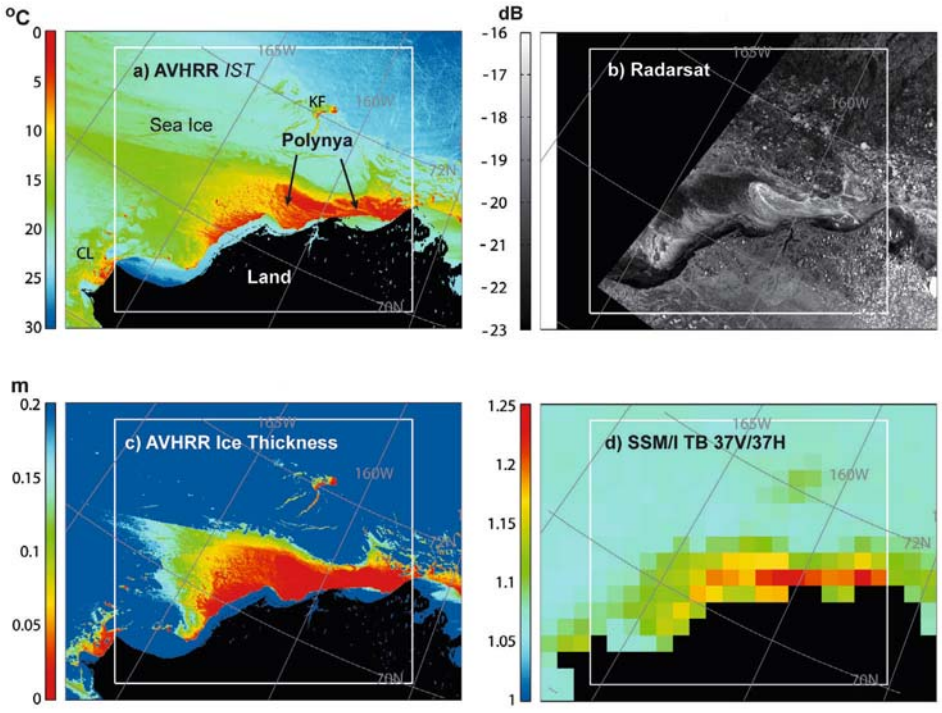

Figure 5.63. A comparison of imagery of the Chukchi polynya adjacent to the Chukchi Sea coast of Alaska collected on March 12, 2000, showing (a) an AVHRR-derived ice (skin) surface temperature image (see Section 5.9.11) at 16 : 44 GMT, (b) a Radarsat ScanSAR image at 16 : 59 GMT, (c) an AVHRR-derived ice thickness map (see Section 5.9.6.5) at 16 : 44 GMT, and (d) a daily averaged SSM/I 37 GHz V/H brightness–temperature map (resolution 25 km). Fog from open-water regions within polynyas is a limitation on the use of visible to thermal infrared imagery. In (c), the apparent area of thin ice extending northwestwards is in fact an ambiguous signal related to the presence of fog.

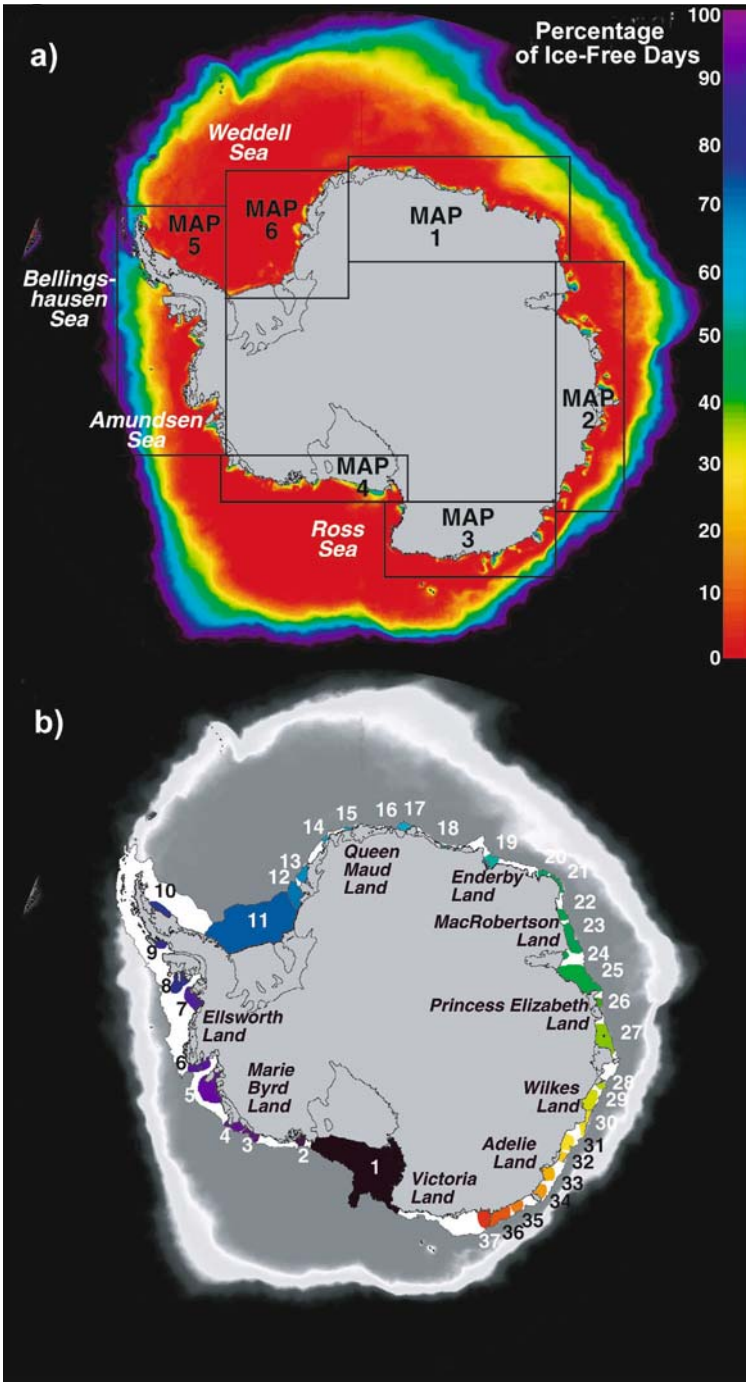

Figure 5.65. (a) A map of the percentage of ice-free days around Antarctica derived from SSM/I ice concentration data over the period 1997–2001, using data from only June to October each year. (b) 37 polynyas identified and numbered.

From Arrigo and van Dijken (2003a). Copyright 2003 American Geophysical Union. Reproduced by permission of American Geophysical Union.

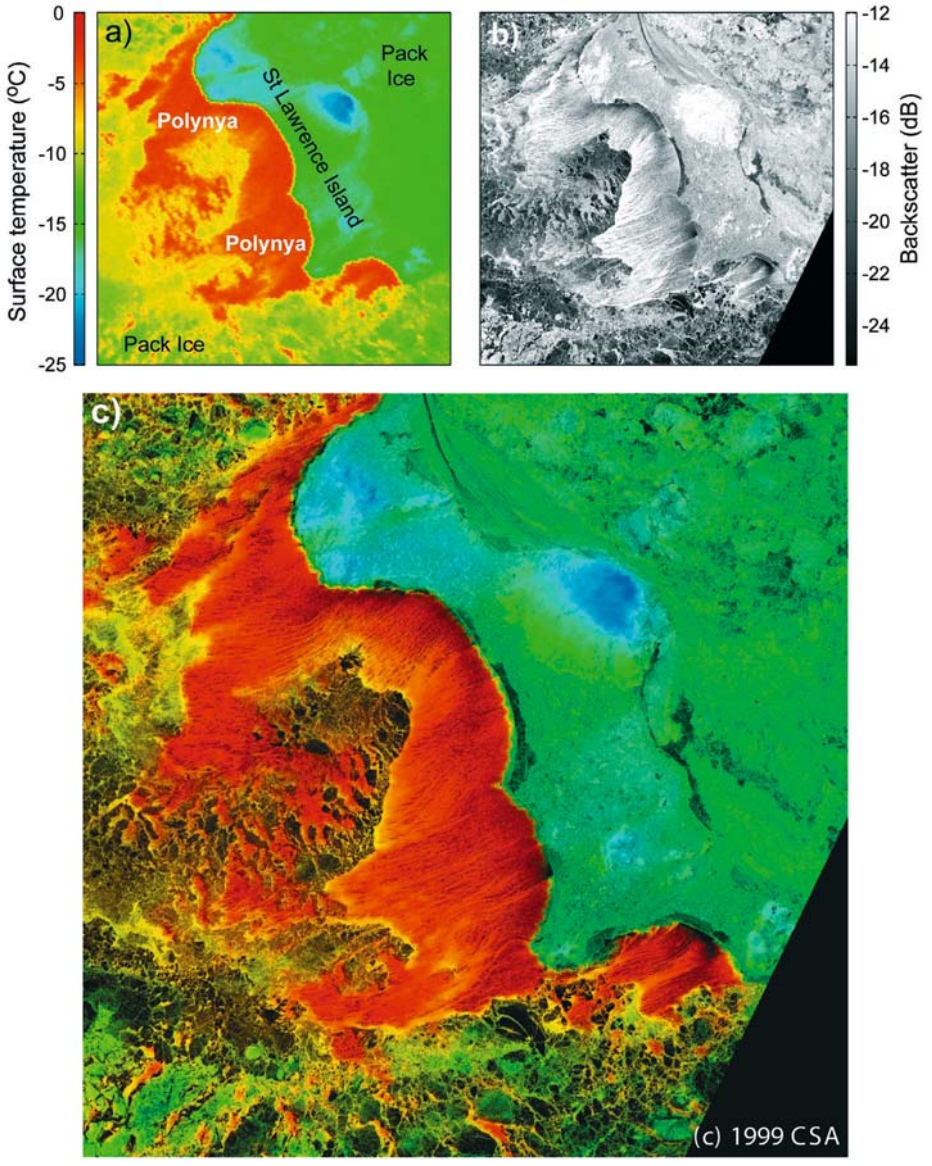

Figure 5.67. An HLS image of the St. Lawrence Island polynya region, from January 9, 1999, comprising coincident (a) NOAA AVHRR-derived skin surface temperature (*IST*) data and (b) radar backscatter data from Radarsat-1 in ScanSAR mode. The polynya shows up clearly on the leeward (downwind) side of the island as a warmer region in (a) and a brighter region in (b). The streaks within the polynya in the radar image (c) correspond to frazil ice streamers in the direction of the surface wind, with wind roughening of the surface contributing the higher backscatter.

Plate 21 from Martin (2004). Figure courtesy Robert Drucker and Seelye Martin (University of Washington), copyright Cambridge University Press, used with permission. Radarsat data copyright Canadian Space Agency/Agence Spatiale Canadienne 1999, processed and distributed by Radarsat International, used with permission.

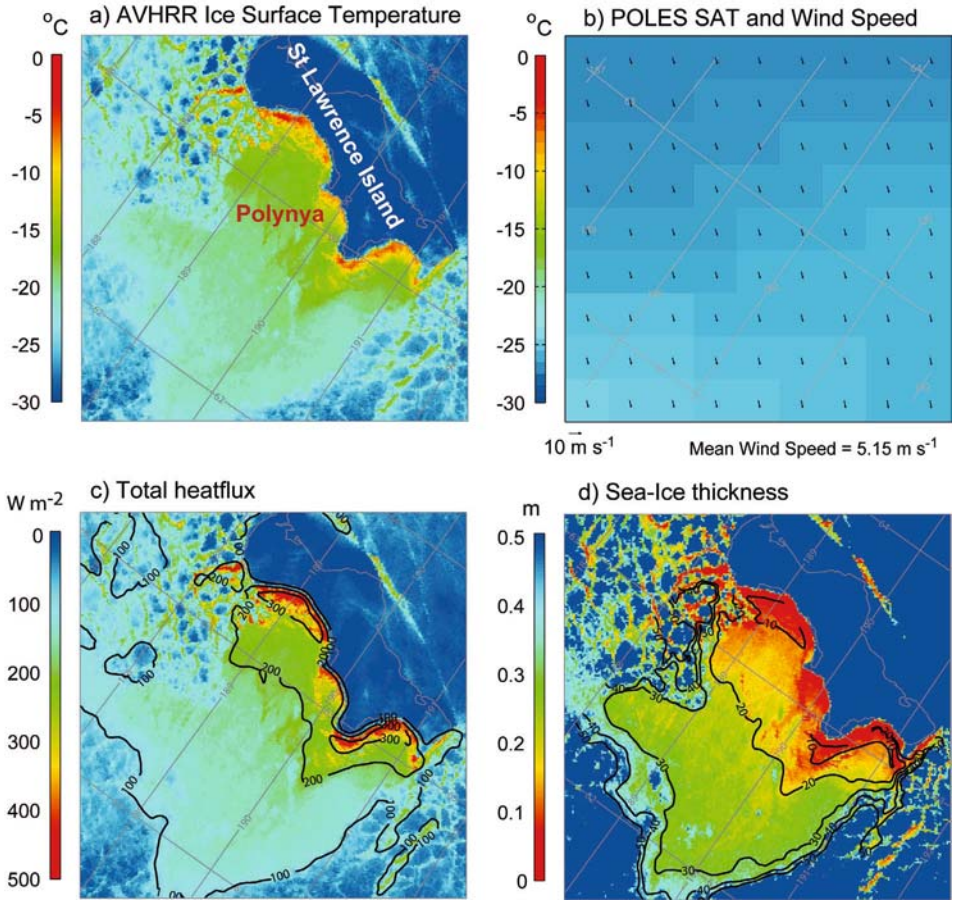

Figure 5.68. A sequence of geophysical products derived from cloud-free AVHRR imagery of the St. Lawrence Island polynya on February 6, 1999, and showing the calculation of (a) skin surface temperature at 04 : 10:58 GMT at a resolution of ~1 km (derived from channel-4 and -5 data using the technique outlined in Section 5.9.11.1); (b) surface air temperature (SAT) and wind speed derived from the POLES (Polar Exchange at the Sea Surface) dataset, (c) the total heat flux (using knowledge of *IST*, sea level pressure and surface air temperature and wind speed); and (d) thin-ice thickness (using the technique laid out in Section 5.9.6.5).

Courtesy of Robert Drucker (University of Washington), reproduced with permission.

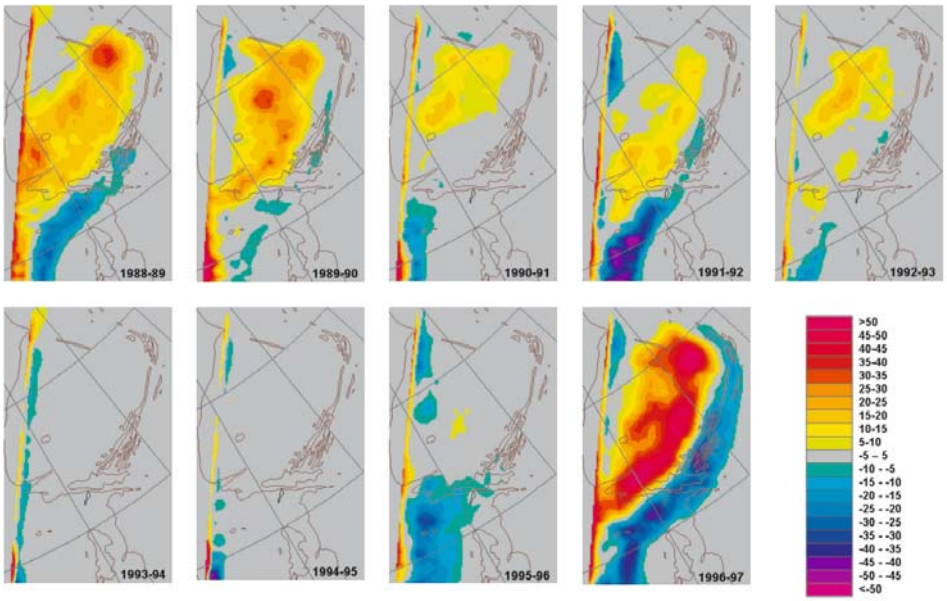

Figure 5.69. Net annual salt flux to the Odden region of the Greenland Sea for the period 1988–89 to 1996–97 and calculated from daily DMSP SSM/I sea ice concentration observations and European Centre for Medium-range Weather Forecasts (ECMWF) winds. Units are kg salt m^{-2}. Overlain are latitude and longitude grids with spacings of 5° and 20°, respectively, and the 2,000-m ocean depth contour.

From Toudal and Coon (2001). © 2005 International Glaciological Society (IGS), reproduced with permission.

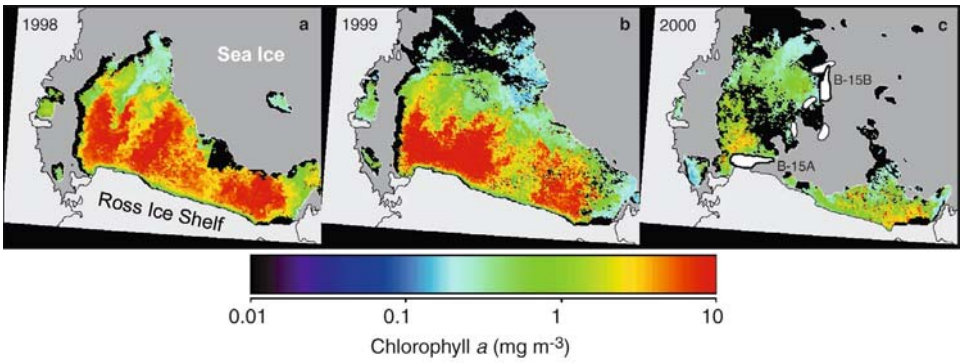

Figure 5.74. Mid-December distributions of sea ice (gray) from DMSP SSM/I and chlorophyll concentrations from SeaWiFS for (a) 1998, (b) 1999, and (c) 2000. Six fragments of iceberg B-15, detected in MODIS imagery, are shown in white in (c).

From Arrigo et al. (2002). Copyright 2002 American Geophysical Union. Reproduced by permission of American Geophysical Union.

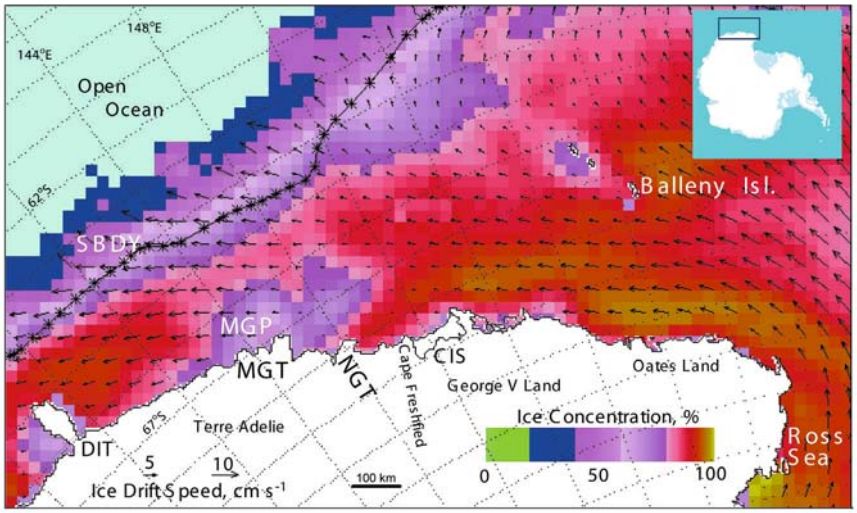

Figure 5.75. Map of monthly mean ice motion superimposed on a monthly mean map of ice concentration (both derived from SSM/I data) for the George V Land and Adélie Land coasts of Antarctica, July 1999. The line marked SBDY demarcates the southern boundary of the Antarctic Circumpolar Current (ACC), based upon Orsi et al. (1995), CIS is the Cook Ice Shelf, DIT the Dibble Iceberg Tongue, NGT the Ninnis Glacier Tongue, MGT the Mertz Glacier Tongue, and MGP the Mertz Glacier Polynya. Note the extensive nature of the polynya on the downwind (lee) side of the MGT and the grounded iceberg blocking features discussed in Section 5.9.4, and the pseudo-stationary ice region to the immediate east (corresponding to the thick-ice promontory in Figure 5.31).

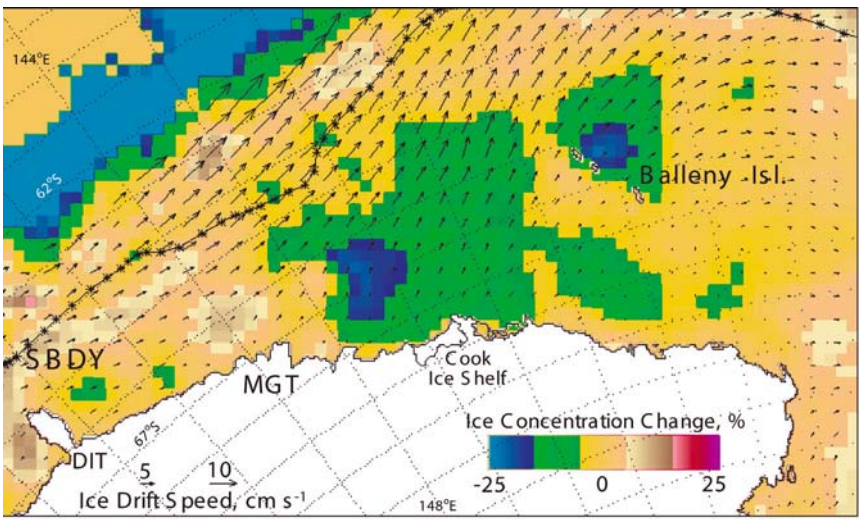

Figure 5.76. Map of anomalies in SSMR- and SSM/I-derived sea ice drift and sea ice concentration combined for October 1999, for the George V Land and Adélie Land coasts of Antarctica (equivalent to the region in Figure 5.75). The anomaly maps were created by subtracting the mean values for all Octobers over the period 1979 to 2000 from the mean map for October 1999. The line marked SBDY demarcates the southern boundary of the Antarctic Circumpolar Current (ACC), based upon Orsi et al. (1995), DIT is the Dibble Iceberg Tongue and MGT the Mertz Glacier Tongue.

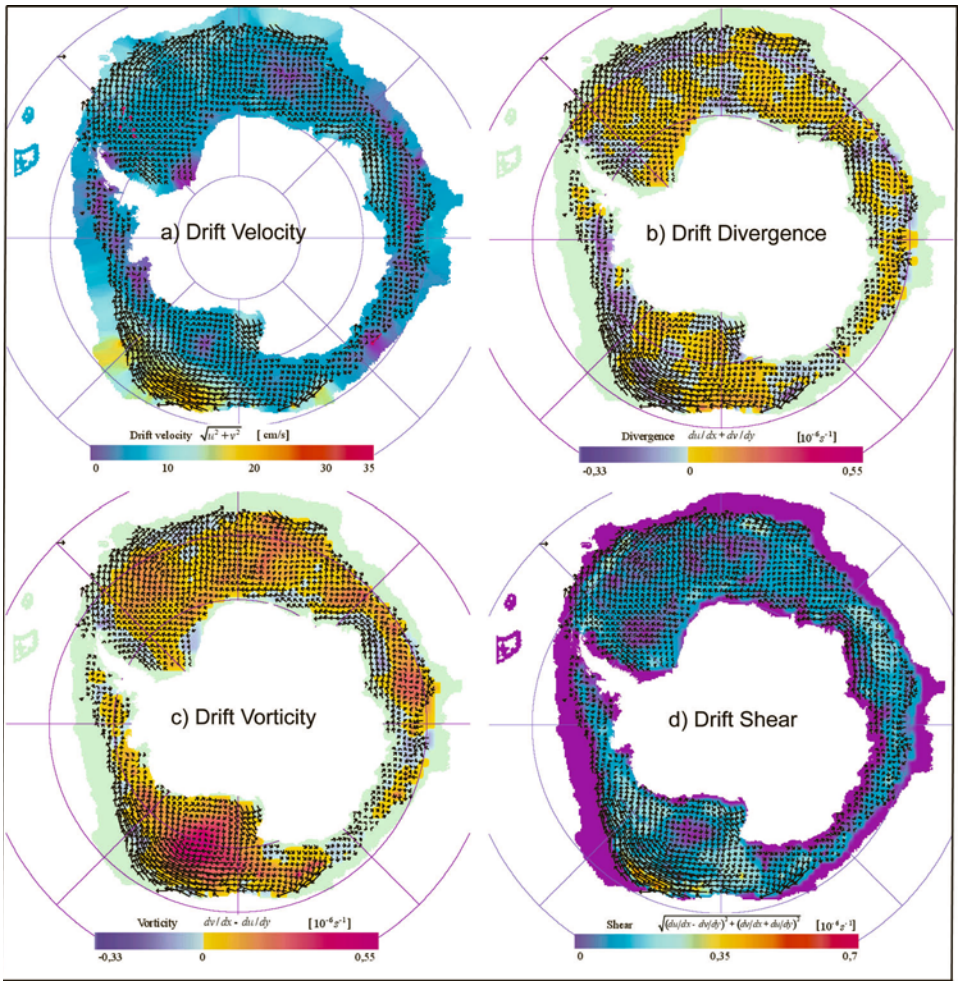

Figure 5.79. Monthly mean maps of Antarctic sea ice (a) drift velocity, (b) drift divergence, (c) drift vorticity, and (d) drift shear. The gridded fields represent optimal interpolations derived from DMSP SSM/I data.

These images were obtained from the online *Atlas of Antarctic Sea Ice Drift* (Schmitt et al., 2004). The work was performed at the Institut für Meteorologie und Klimaforschung, Universität Karlsruhe by funding of the Deutsche Forschungsgemeinschaft (DFG) Project Ko924/3-1. Published under ⟨*http://imkhp7.physik.uni-karlsruhe. de/∼eisatlas*⟩.

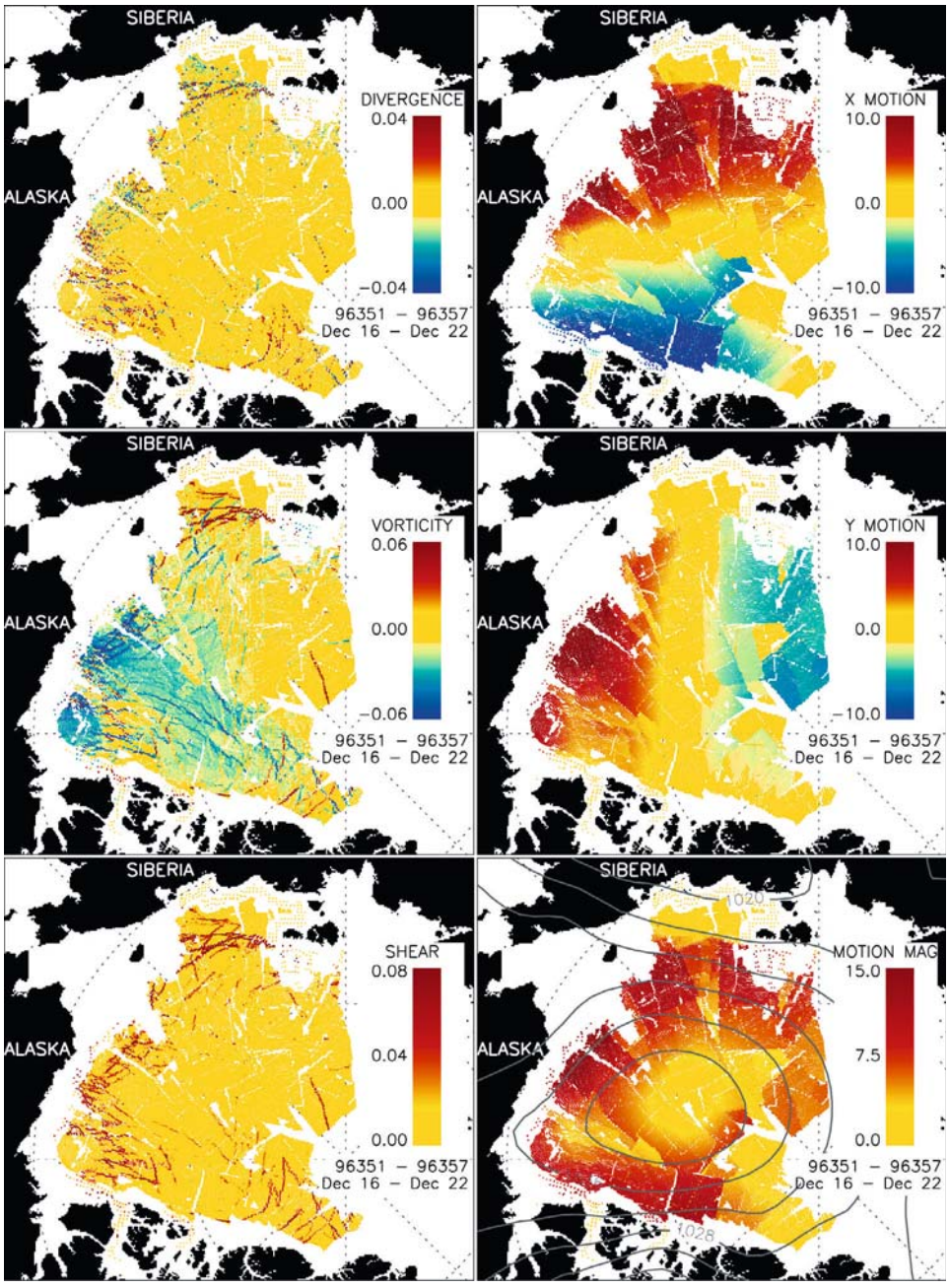

Figure 5.82. Ice divergence, vorticity, shear, and general ice motion for the central Arctic Basin from the period December 16 to 22, 1996 (images 96351–96357), derived from Radarsat ScanSAR data by the Radarsat Geophysical Processor System (RGPS).

From Drinkwater et al. (2001a). Radarsat data copyright Canadian Space Agency/Agence Spatiale Canadienne 1999, processed and distributed by Radarsat International, used with permission.

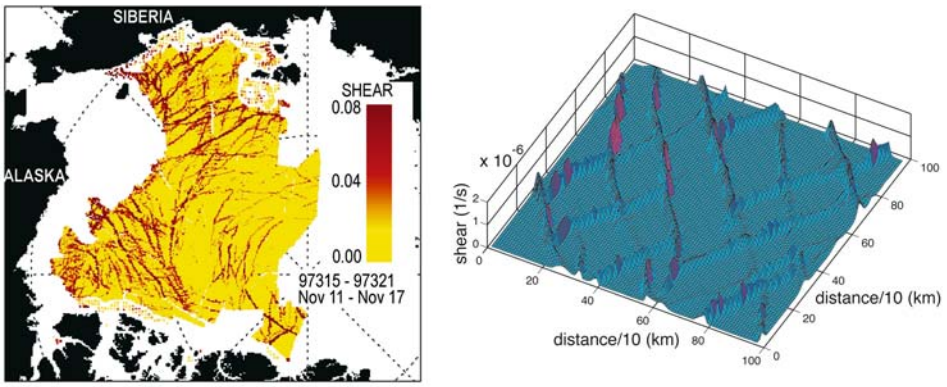

Figure 5.83. (a) Average shear deformation of Lagrangian elements, with dimensions of $\sim 10 \times 10$ km, over a 6-day period in the Arctic Ocean, based on small-scale ice motion data derived from the Radarsat Geophysical Processor System (RGPS). (b) Sea ice shear/fractures simulated with a viscous–plastic sea ice model and an isotropic rheology where spatial domain is discretized with a sufficiently high spatial resolution (10 km).

From Wang et al. (2003b). Copyright 2003 American Geophysical Union. Reproduced by permission of American Geophysical Union.

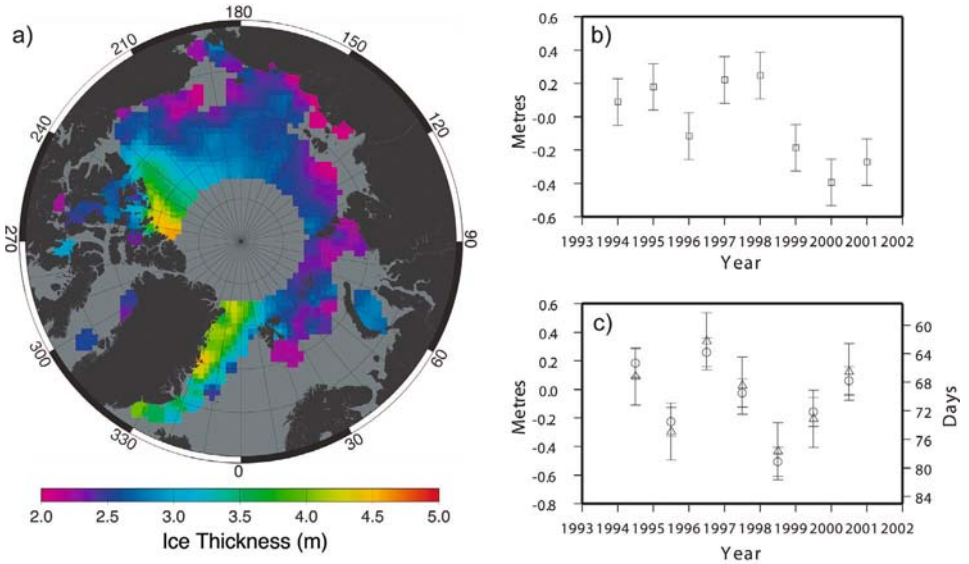

Figure 5.84. (a) Map of the average Arctic winter sea ice thickness from October 1993 to March 2001 derived from ERS-1 and -2 radar altimeter data, with a grid size of 100 km. Note that data are not available for the marginal ice zone, and the mean thickness in this case excludes thin ice (<0.5–1.0 m) and openwater. (b) Mean boreal winter (October to March) ice thickness anomaly for the period 1993–2001. The data show a spatial average of anomalies in ice thickness, obtained by subtracting the mean field—shown in (a)—from individual grids of average winter ice thickness. (c) Changes in ice thickness between consecutive winters (circles) and melt season length (triangles) during the intervening summer period, derived from passive-microwave observations (Smith, 1998a).

From Laxon et al. (2003a, b). Reproduced with permission of *Nature* magazine. © 2003 *Nature*.

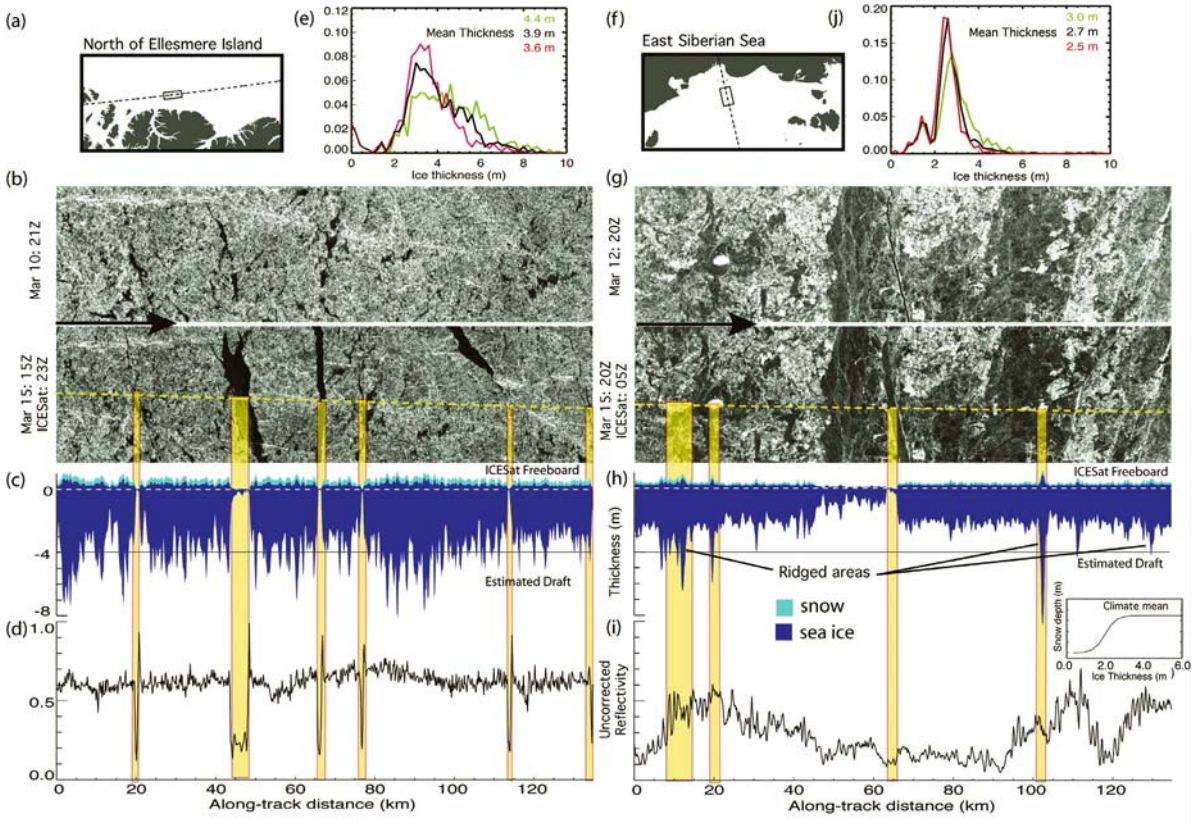

Figure 5.86. Two near-coincident ICESat GLAS and Radarsat SAR datasets from the regions of the Arctic Ocean marked in the small inset maps (a, f). The upper Radarsat SAR image in (b) is from March 10, 2003 (~21:00 GMT), while the lower image shows the same region 5 days later (on March 15 at ~15:00 GMT), with the ICESat GLAS groundtrack (at ~23:00 GMT) superimposed as a yellow dashed line (flight from left to right). In (g), the upper Radarsat SAR image is from 12 March (20:00 GMT), while the lower image is from 15 March (~15:00 GMT) with an ICESat groundtrack from ~05:00 GMT superimposed. (c, h) ICESat freeboard profile and estimated ice draft (snow = light blue, ice = dark blue). (d, i) Along-track profile of uncorrected GLAS reflectivity. "Overshoots" in the reflectivity profile in (d) are artefacts caused by saturation of the GLAS detector amplifier during transitions from dark-to-bright surfaces. (e, j) The estimated thickness distribution with three different snow cover thicknesses superimposed (red is the climatological mean +10 cm, black the mean, and green the mean −10 cm). The inset plot in (i) shows the sigmoidal function for applying snow depth. The vertical scale depends on the climatological snow depth at the geographic location of interest.

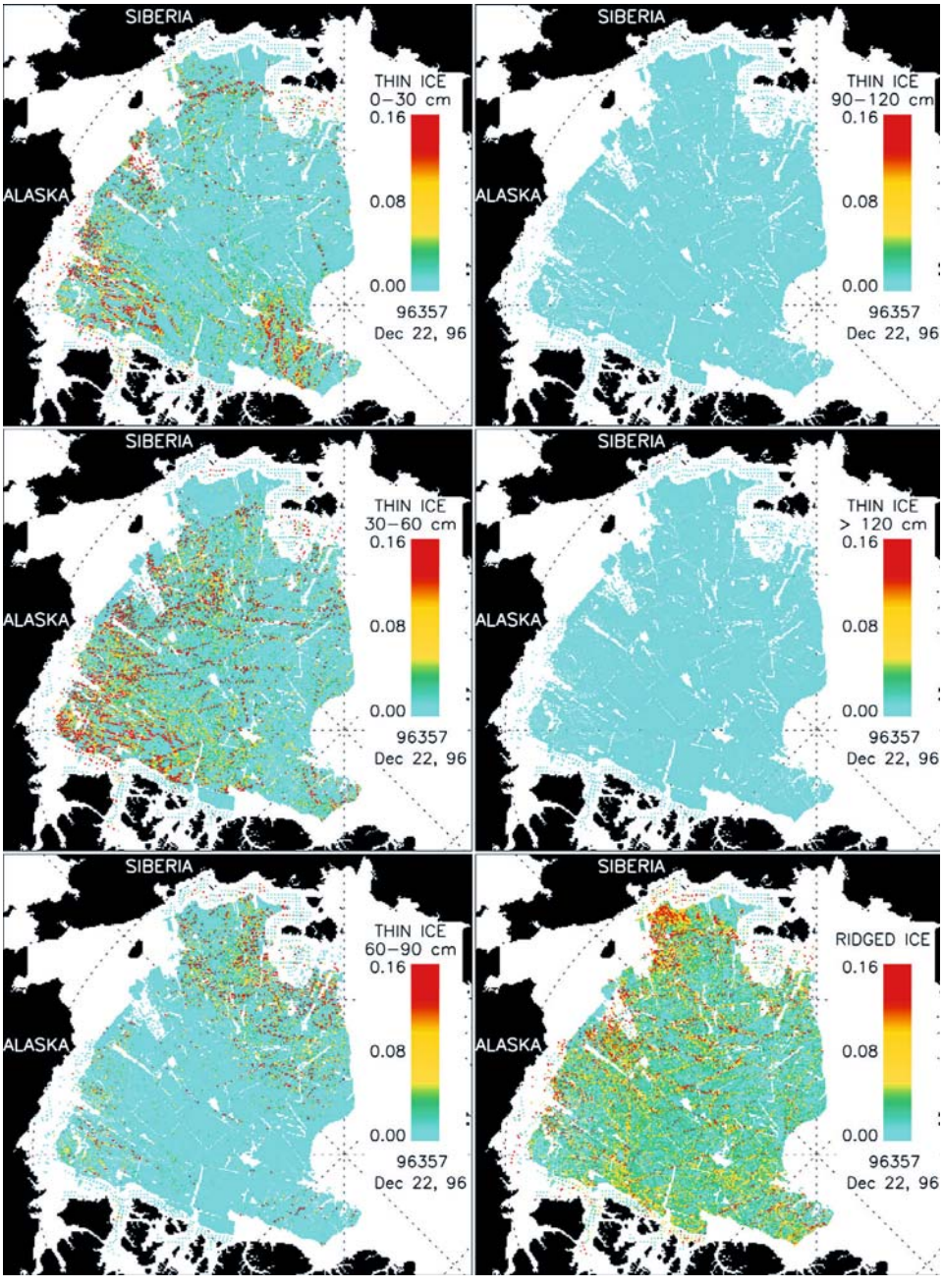

Figure 5.87. Ice thickness distributions over the Arctic Ocean basin on December 22, 1996 (image 96357), computed from Radarsat imagery for various thickness categories by the RGPS. Radarsat imagery,

From Drinkwater et al. (2001a). Radarsat data copyright Canadian Space Agency/Agence Spatiale Canadienne 2005, processed by Alaska Satellite Facility, reproduced with permission.

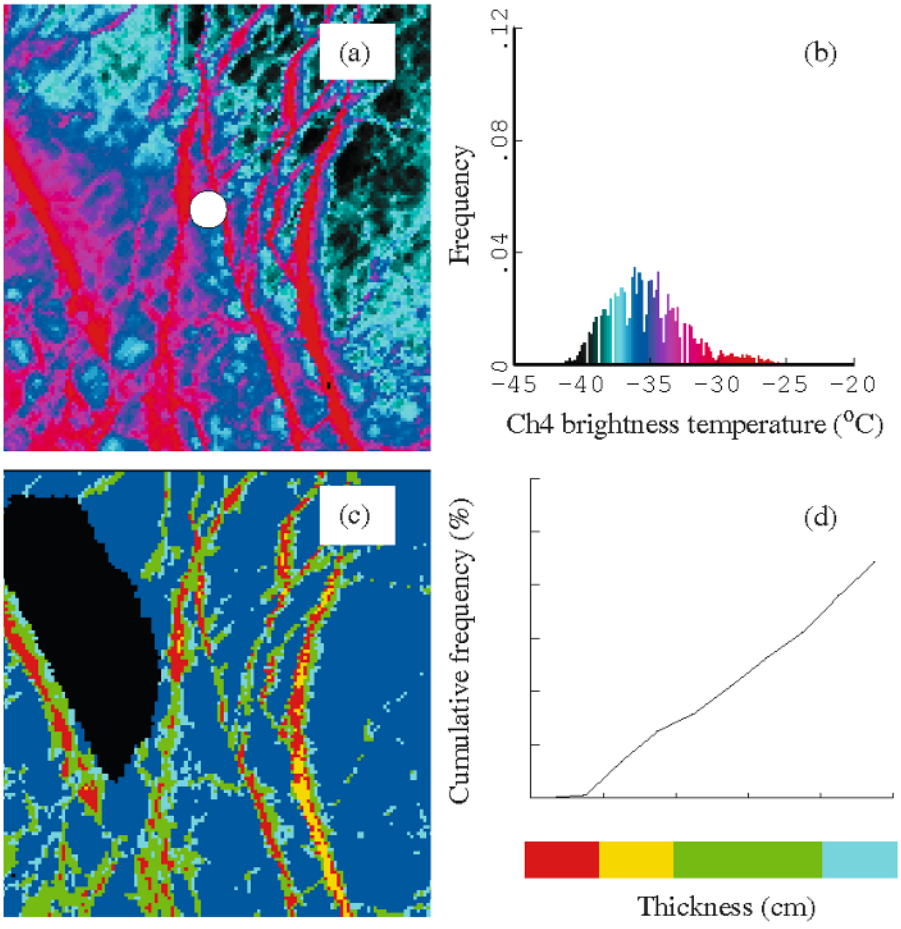

Figure 5.89. (a) AVHRR-derived *IST*, (b) its frequency distribution, (c) estimated ice thickness and (d) its cumulative distribution over a 150×150-km region of the Beaufort Sea on December 1, 1990. The white dot in (a) demarcates the location of a moored ice-profiling sensor used for validation, while the black patch in (c) represents a cloud-masked area.

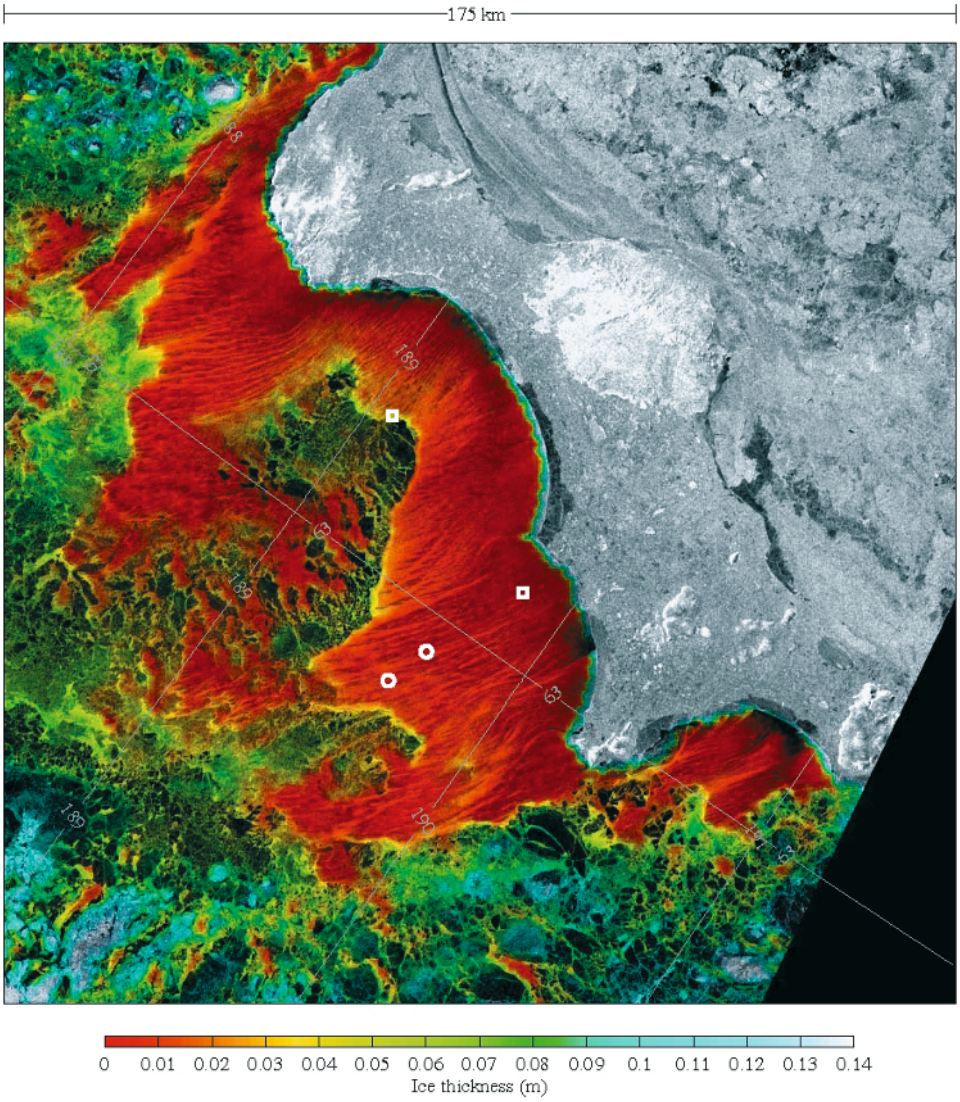

Figure 5.90. Composite image of AVHRR-derived ice thickness h_T superimposed on a near-simultaneous Radarsat C-band SAR data, for January 9, 1999. Colors correspond to thickness values in the scale, while the image texture and detail correspond to 200-m-resolution SAR backscatter. The circles and squares denote the locations of ULSs and SeaBird salinity/temperature sensors, respectively. See also Figure 5.68.

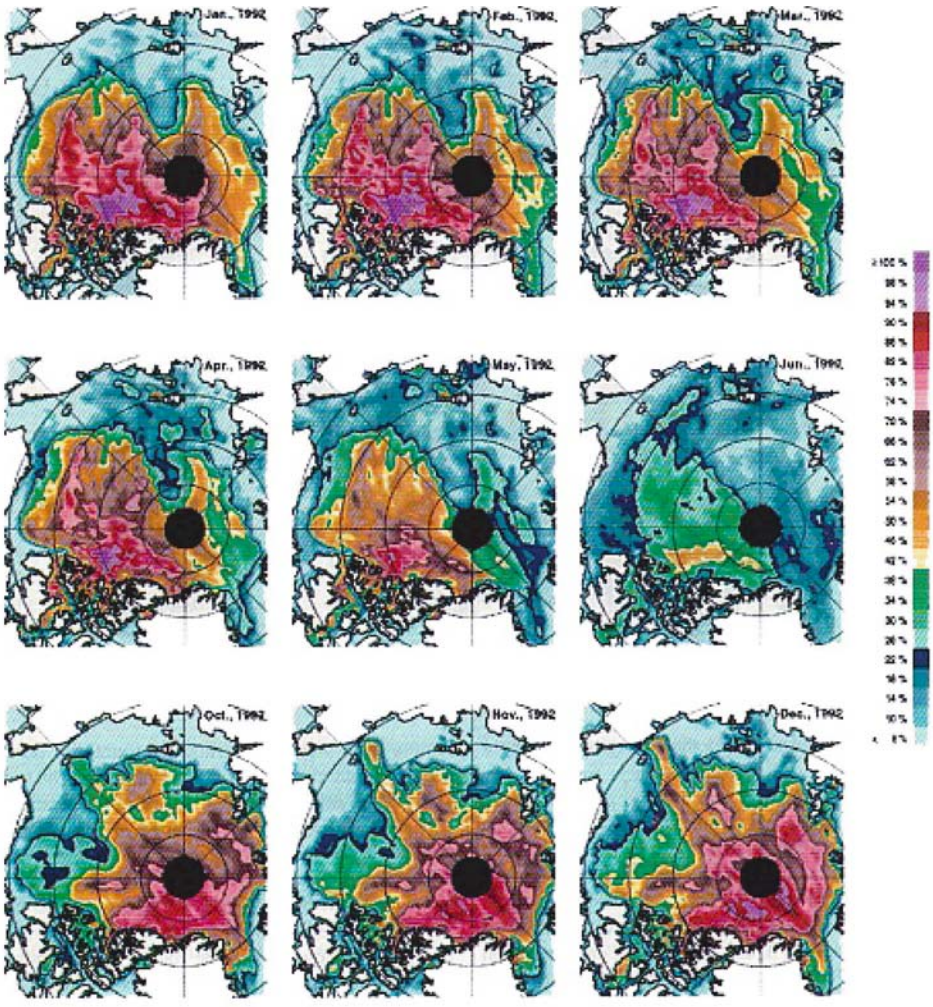

Figure 5.92. Monthly averaged maps of Arctic multiyear sea ice concentration, derived SSM/I data for 1992. Spatial resolution is 25 km.

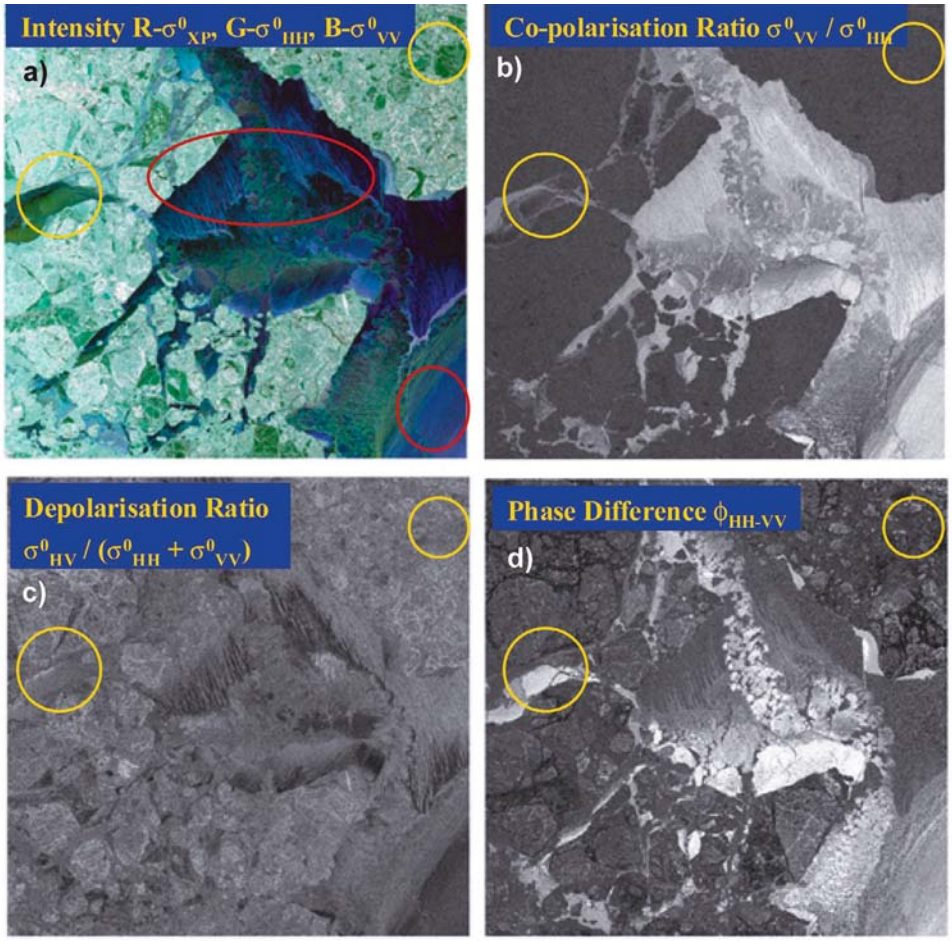

Figure 5.96. C-band images of sea ice in the Greenland Sea from March 24, 1995, recorded by the Danish aircraft EMISAR. (a) Intensity image; (b) co-polarization ratio; (c) depolarization ratio; and (d) the phase difference between the HH- and VV-pol channels. Each image is $\sim 12 \times 20$ km in dimension. The red ellipses and green arrows in (a) demarcate different signatures in the phase difference image (d). Image scaling is from black to white, and is from -6 to $+13$ dB for the co-pol ratio, -19 to -1 dB for the de-pol ratio, and -180 to $+180^\circ$ for the phase difference. Polarimetric parameters were computed on a pixel-by-pixel basis. The wind speed at the time of acquisition was $<12\,\mathrm{m\,s^{-1}}$, and the air temperature $\sim -20^\circ$C.

From Dierking et al. (2003).

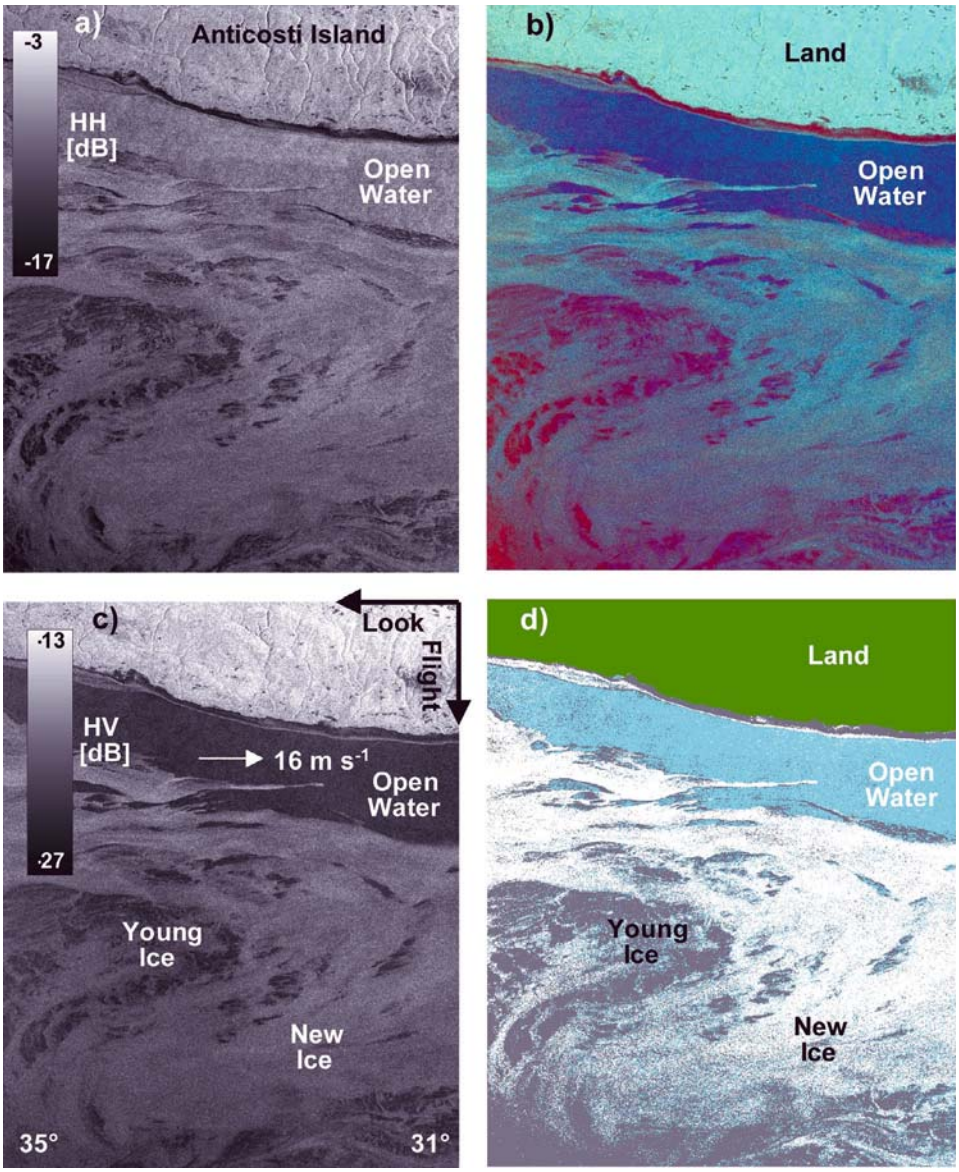

Figure 5.98. Envisat ASAR Alternating Polarisation (AP) mode scenes (beam IS4: 31–36° incidence) acquired on February 7, 2003 in the Gulf of St. Lawrence, Canada. (a) the HH-pol backscatter image; (b) a multi-pol, false-color RGB composite where red = HH/VV, blue = HH, and green = HV; (c) an HV backscatter image; and (d) a classified image based on the modified Wishart classification technique. These examples indicate improved discrimination of sea ice and open water using AP mode, in spite of strong wind conditions.

Courtesy Mark Drinkwater (ESA) based on Envisat results from Bernd Scheuchl (University of British Columbia). Image copyright European Space Agency (2003).

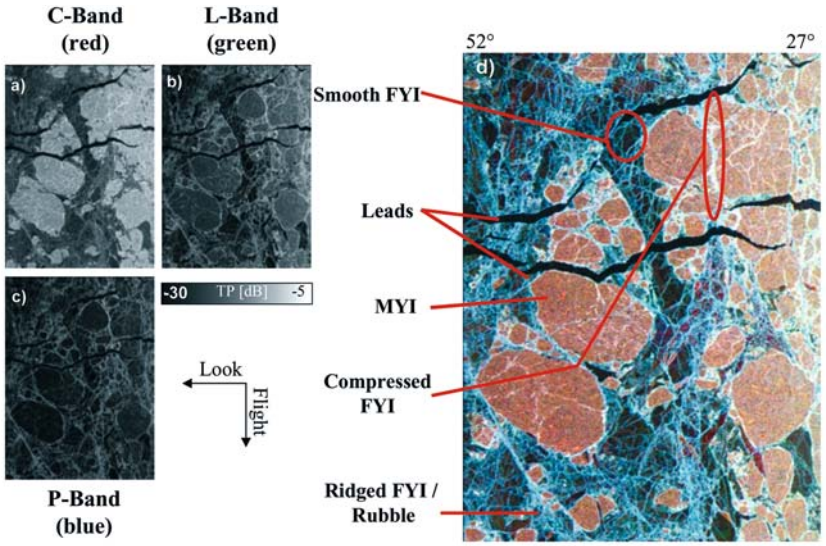

Figure 5.99. Total power images of data collected by the NASA JPL AIRSAR polarimetric SAR system in (a) C-band, (b) L-band, and (c) P-band. (d) A false-color composite of the three images (a to c). This scene was acquired on March 11, 1988, with center coordinates of 73.048°N and 142.285°W and incidence angles from 27° to 52°. The pixel spacing for the data is 6.7 m in slant range and 12.1 m in azimuth (four-look images). Additional averaging of 2×2 pixels was carried out prior to data analysis to reduce image speckle effects. Ice types present are marked on (d), according to the interpretation of Drinkwater et al. (1992). See Scheuchl et al. (2003) for a classification of sea ice in this scene based on the complex Wishart distribution of the coherency matrix.

From Scheuchl et al. (2003). Copyright European Space Agency 2005, reproduced with permission.

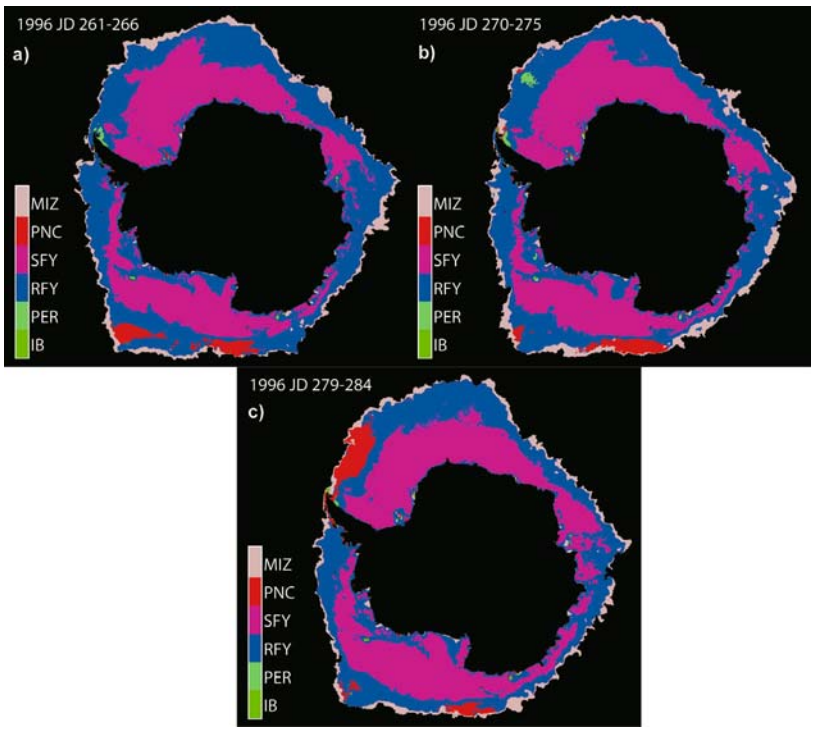

Figure 5.104. Maximum a posteriori ice classification of combined active–passive microwave image series from 1996 for (a) days 261–266, (b) 270–275, and (c) 279–284.

From Remund et al. (2000). © 2005 IEEE, reproduced with permission.

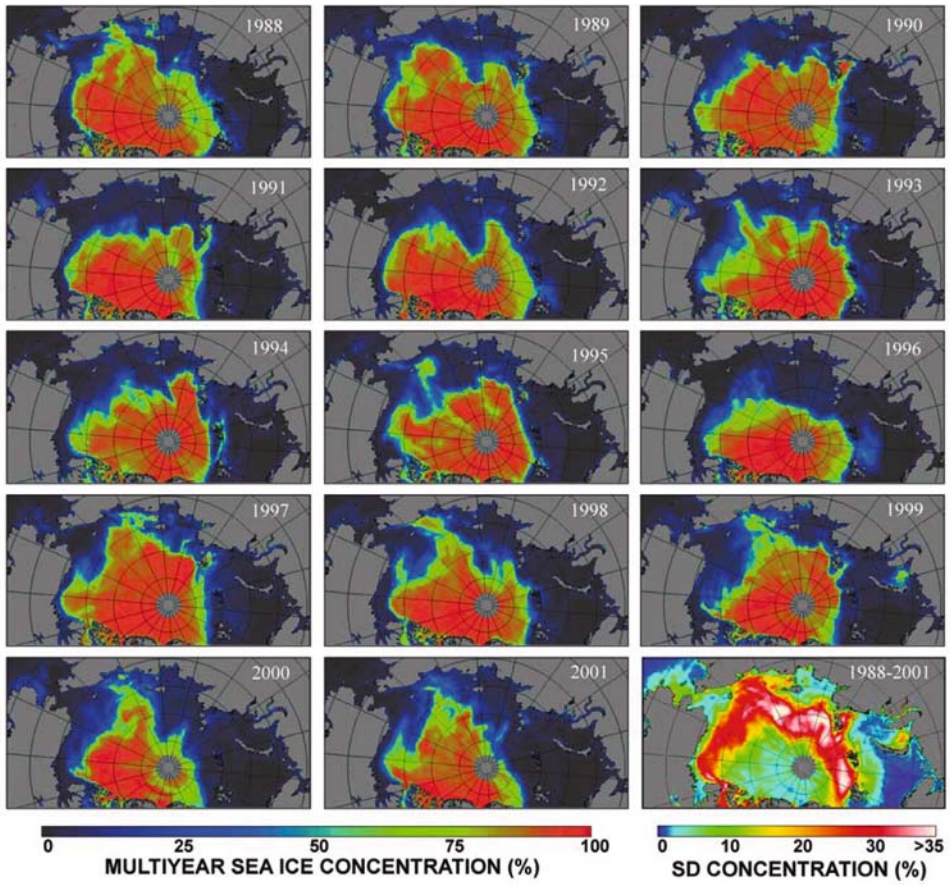

Figure 5.100. Maps of the January, mean, Arctic, multiyear sea ice concentration estimates for the period 1988–2001, based on neural network inversions of daily DMSP passive-microwave brightness–temperature data (19V, 19H, 37V). Learning data are derived from Okean Side-Looking Radar and ERS SAR data. The 14-year standard deviation is shown in the bottom right panel.

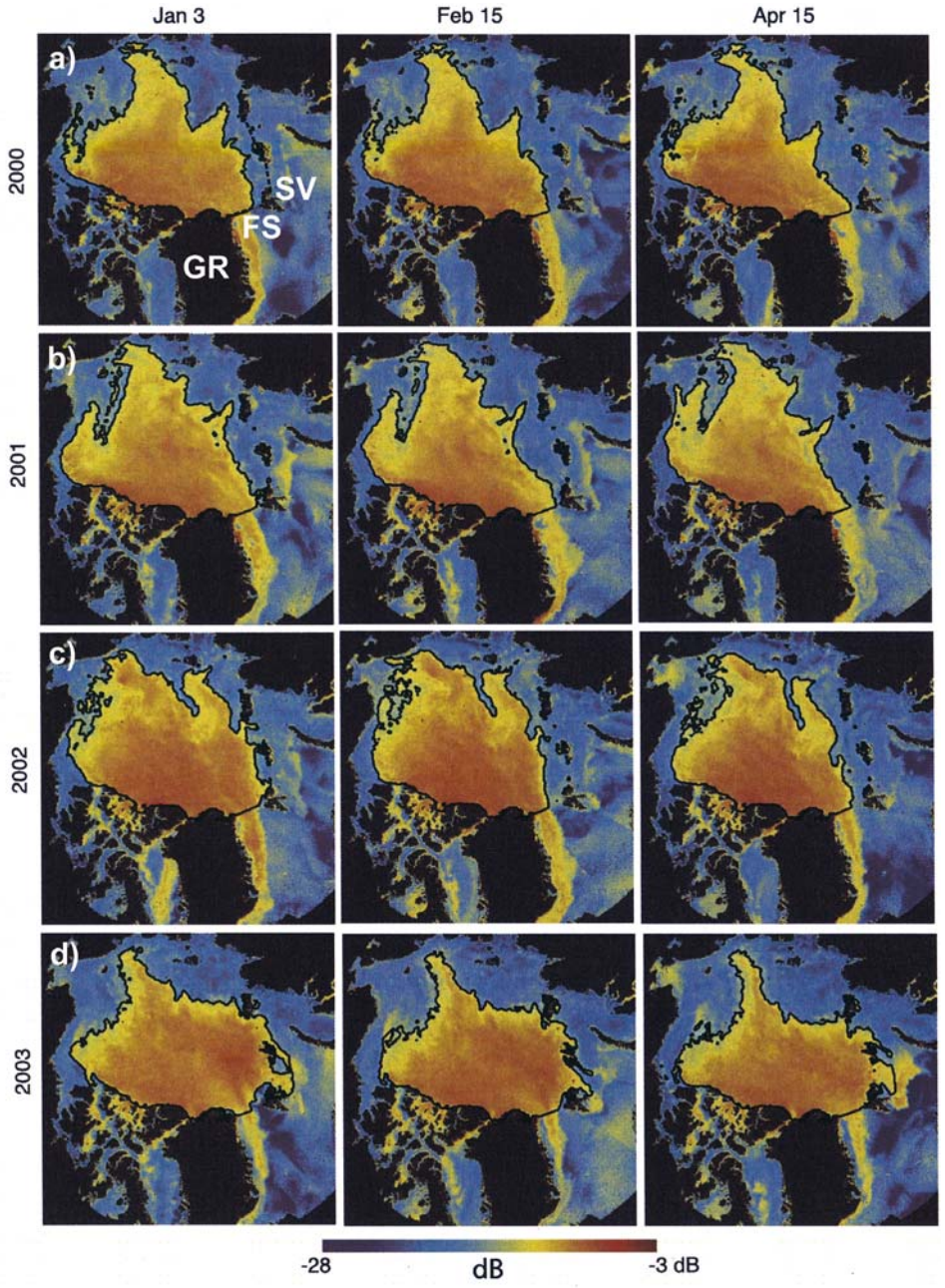

Figure 5.103. Daily Seawinds QuickSCAT VV-backscatter maps of the Arctic with boundaries of the perennial sea ice zone overlain for January 3, February 15, and April 15 for the years (a) 2000, (b) 2001, (c) 2002, and (d) 2003. GR is Greenland, SV is Svalbard, and FS is Fram Strait.

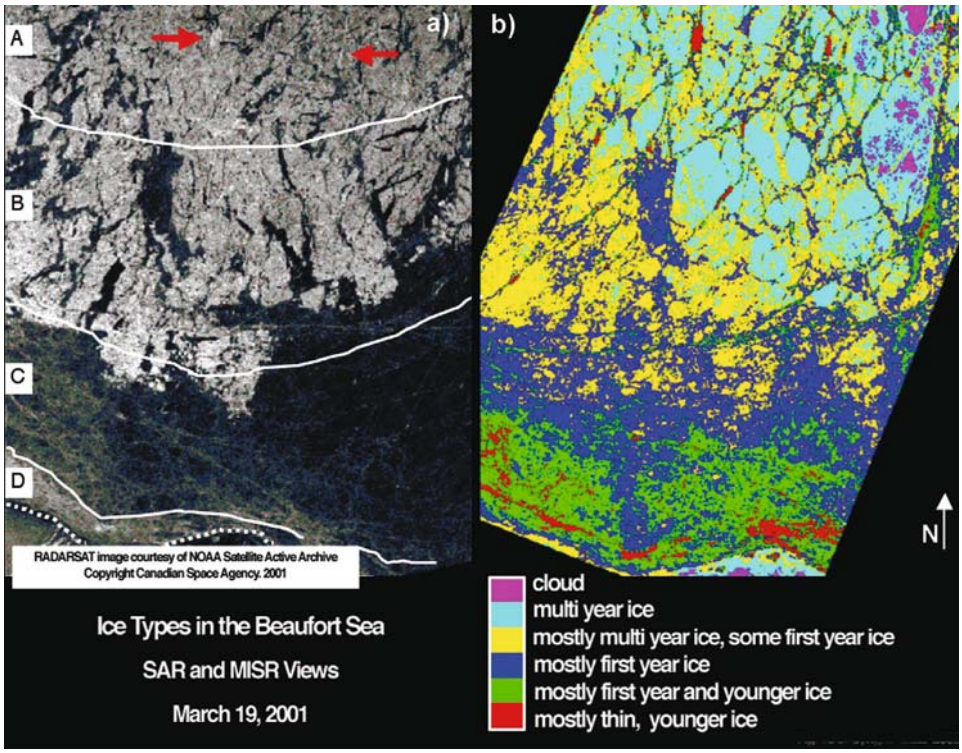

Figure 5.106. Maps of sea ice classification in coincident (a) Radarsat SAR and (b) EOS Terra MISR images in the Beaufort Sea on March 19, 2001. The images are 200 km across. In the SAR image, white lines delineate different sea ice zones, with regions of mostly multiyear ice (A) being separated from regions with large amounts of first-year and younger ice (B–D). Red arrows point to bright areas in which large, crystalline frost flowers have formed on young, thin ice. This has the effect of increasing the backscatter, causing this young ice type to exhibit an increased radar backscatter.

Image credit: NASA/GSFC/LaRC/JPL, MISR Team. Radarsat image courtesy NOAA Satellite Active Archive, © Canadian Space Agency 2001. From Nolin et al. (2002). Figure © IEEE 2002, reproduced with permission.

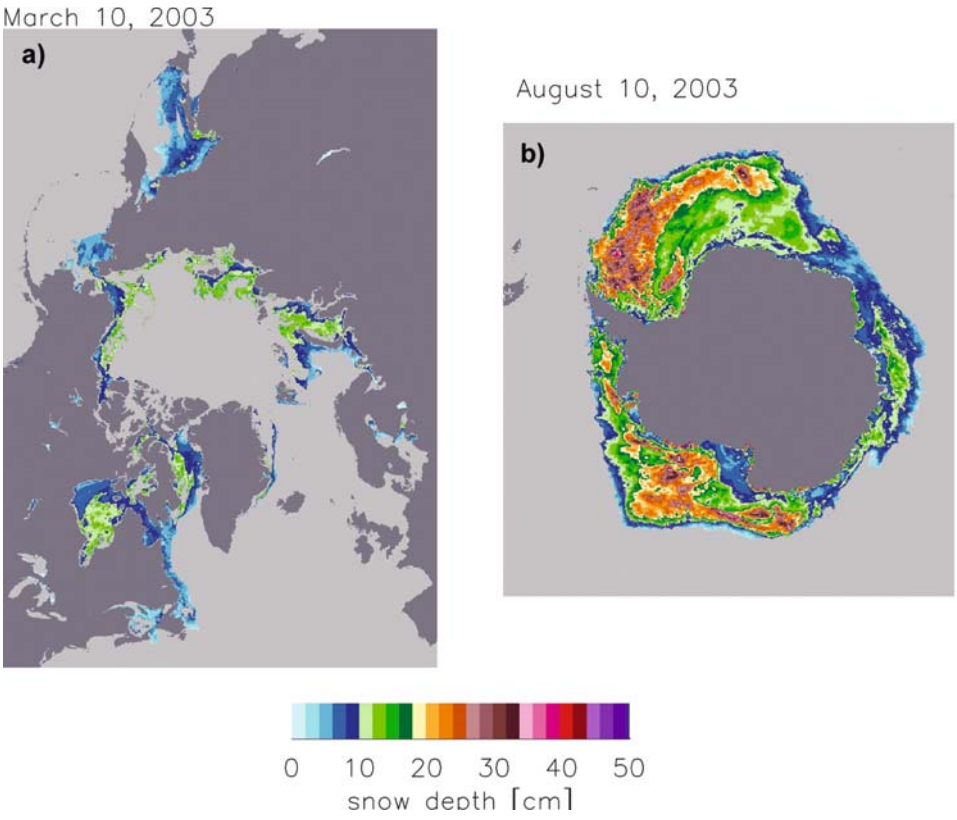

Figure 5.107. Maps of snow depth on sea ice for (a) the Arctic (on March 10, 2003), and (b) the Antarctic (on August 10, 2003), retrieved from AMSR-E brightness–temperature and derived ice concentration data. Note that this product cannot be retrieved over regions of Arctic perennial sea ice (see Figure 5.108).

Imagery courtesy Thorsten Markus (NASA Goddard Space Flight Center).

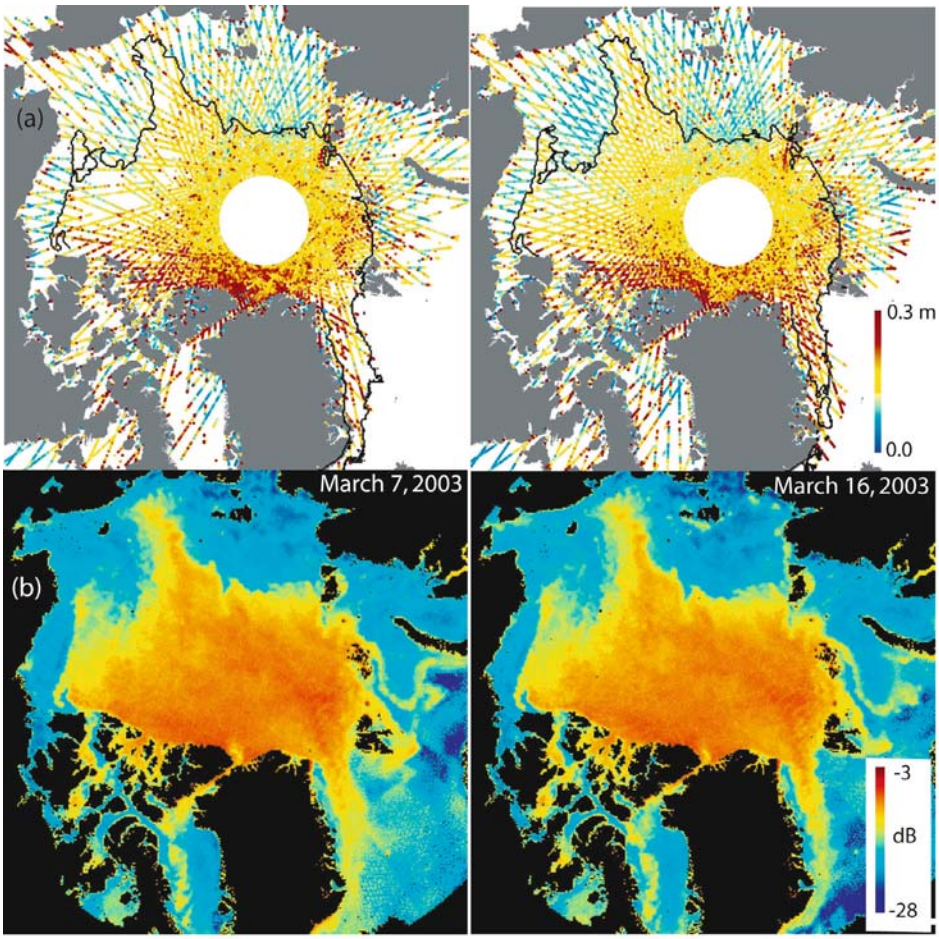

Figure 5.108. A map of the surface roughness of the Arctic sea ice cover at a 10-km length scale derived from ICESat elevations, compared with coincident QuikSCAT radar scatterometer backscatter data. The edge of the perennial ice zone, derived from the QuikSCAT data, is marked. (a) ICESat surface roughness composites from March 4–11 and March 12–20, 2003, with the edge of the perennial ice zone (derived from the QuikSCAT data) overlain. (b) Maps of QuikSCAT backscatter fields on March 7 and March 16, 2003.

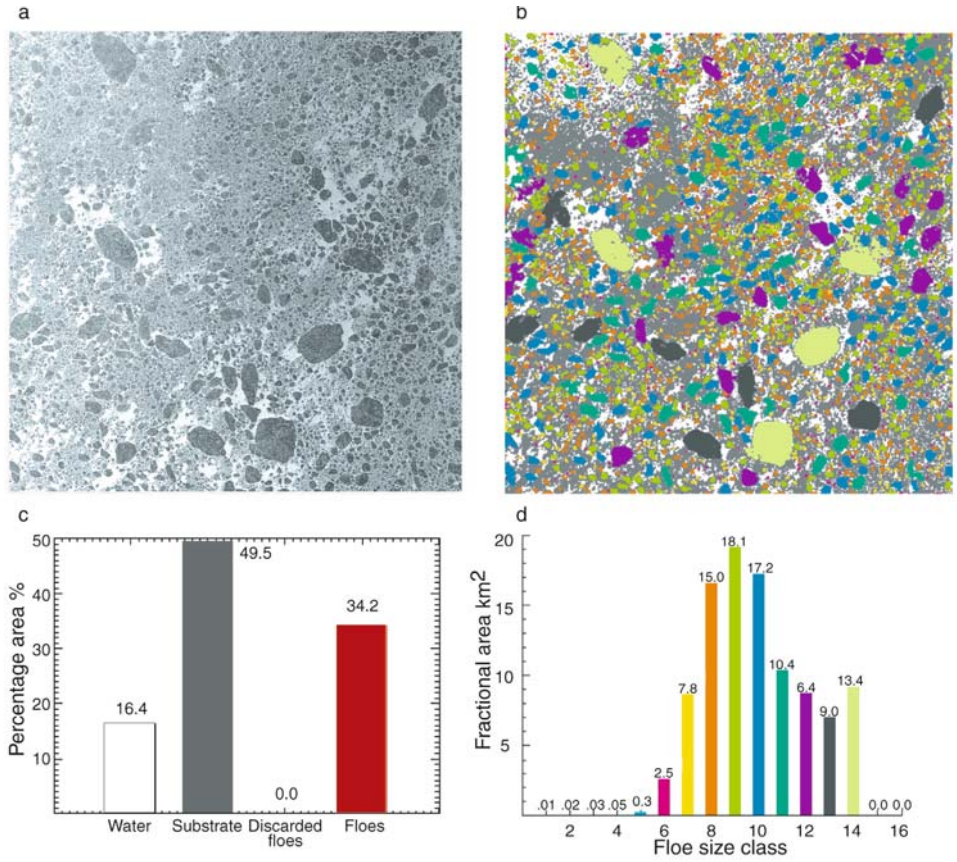

Figure 5.109. An illustration of the floe classification procedure, showing (a) an input ERS-1 SAR image (dimensions 100×100 km); (b) the output image showing the different floe-size classes (color-classified); (c) a histogram showing the percentage areal coverage of the four derived output classes; and (d) the fractional area (marked as percentages) covered by the different derived floe classes seen in (b). Note that the openwater fraction was determined using the technique described by Holt and Martin (2001) described in Section 5.9.1.

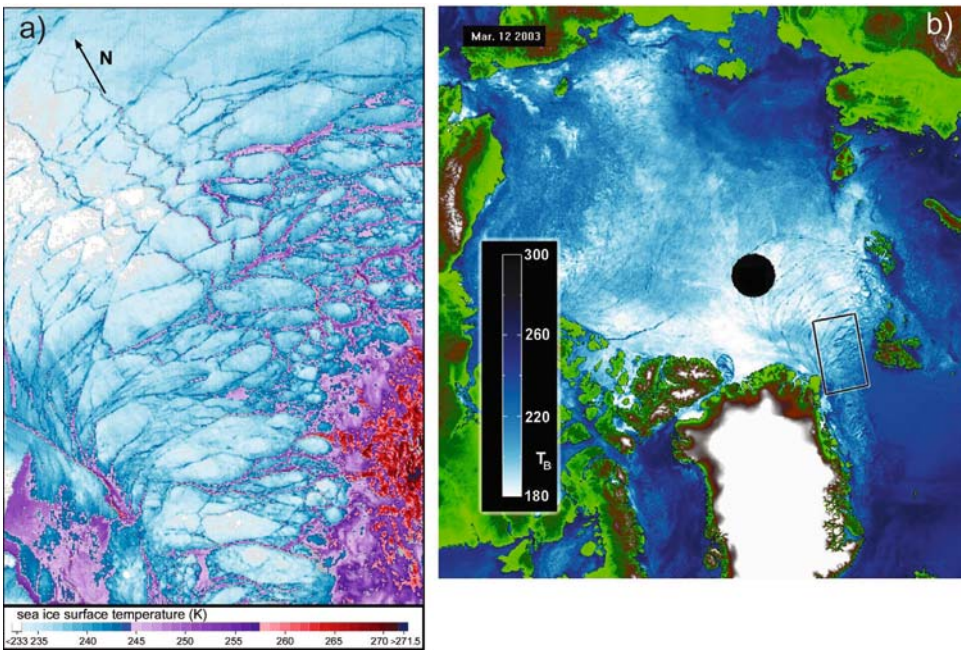

Figure 5.110. (a) An example of a cloud-free Terra MODIS ice surface temperature (*IST*) product (MOD29) derived from data collected on March 12, 2003 (18 : 45 GMT) in the Fram Strait region of the NE Greenland Sea. The approximate image center point is at 81.7°N, 1.0°E. The highest *IST*s, shown in red in the southern part of the scene, equate to a region of warmer or lower concentration/thin ice in the marginal ice zone. (b) An Aqua AMSR-E 89-GHz vertically polarized brightness temperature image of the Arctic from the same day, created by averaging several swaths of data and at a spatial resolution of 5 km. The rectangular red box demarcates the area shown in (a).

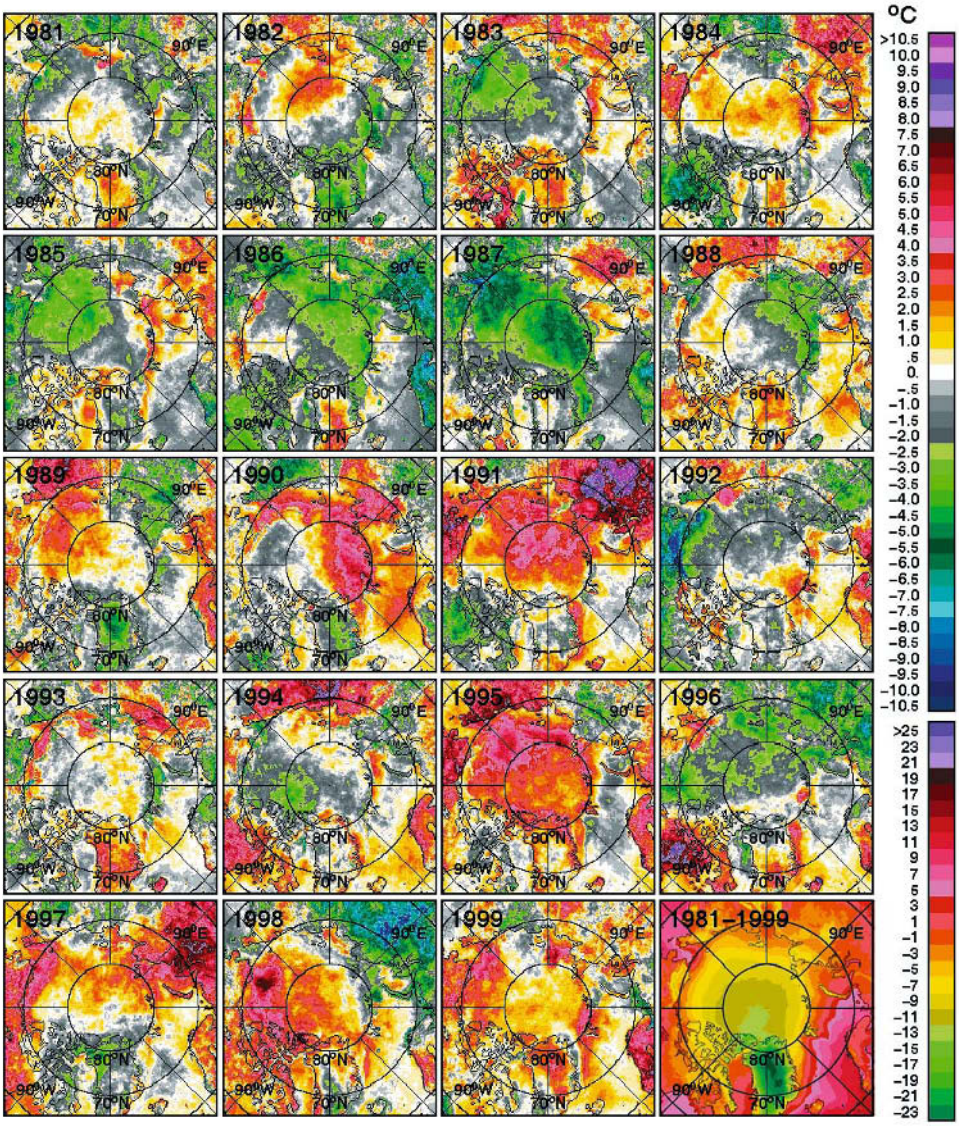

Figure 5.111. Mean monthly AVHRR-derived *IST* anomaly maps of the Arctic for all Septembers from 1981 to 1999. The image labeled "1981–1999" (bottom right) is the average of all September *IST* values from 1981 to 1999. The *IST* datasets are created from channel-4 Global Area Coverage (GAC) data using the single-channel technique outlined above. The data were subsampled to a grid size of 6.25×6.25 km, and mapped to the standard SSM/I polar stereographic grid to facilitate direct comparison with passive-microwave sea ice concentration data—e.g., those in Figure 5.37.

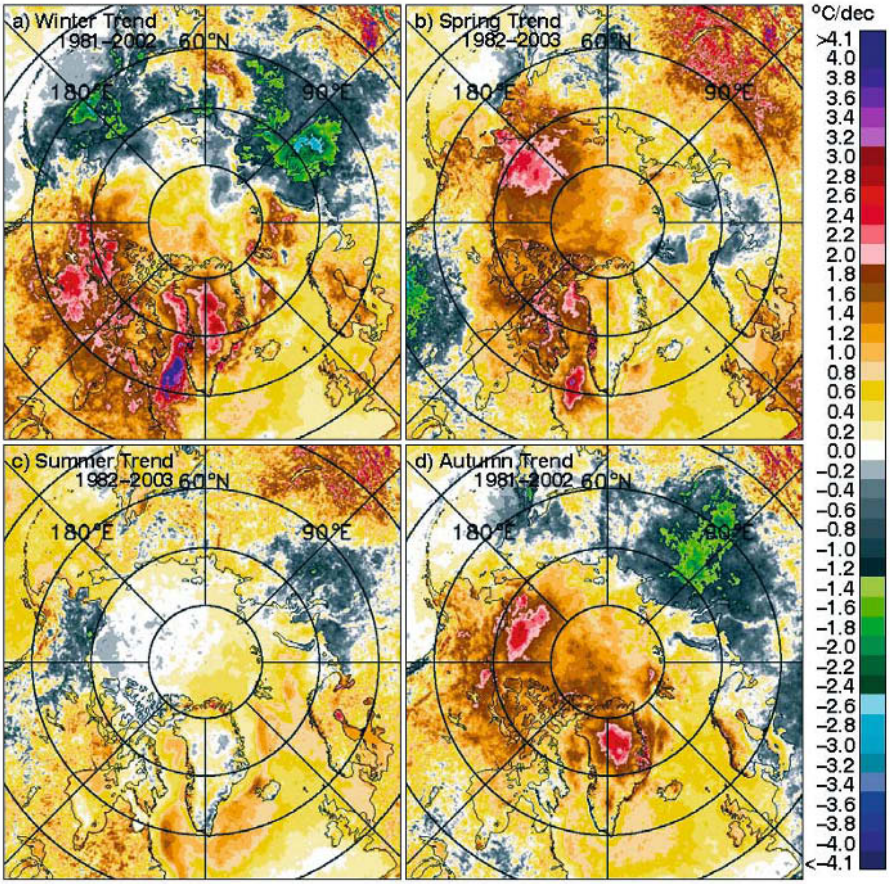

Figure 5.112. Color-coded *IST* trend maps derived from NOAA AVHRR data over the period 1981–2003 for the Arctic in (a) autumn (SON), (b) winter (DJF), (c) spring (MAM), and (d) summer (JJA). Trends were derived through linear regression of monthly anomalies in each data pixel, with anomalies being calculated by subtracting the monthly climatology from monthly values. This is an updated version of a figure in Comiso (2003b).

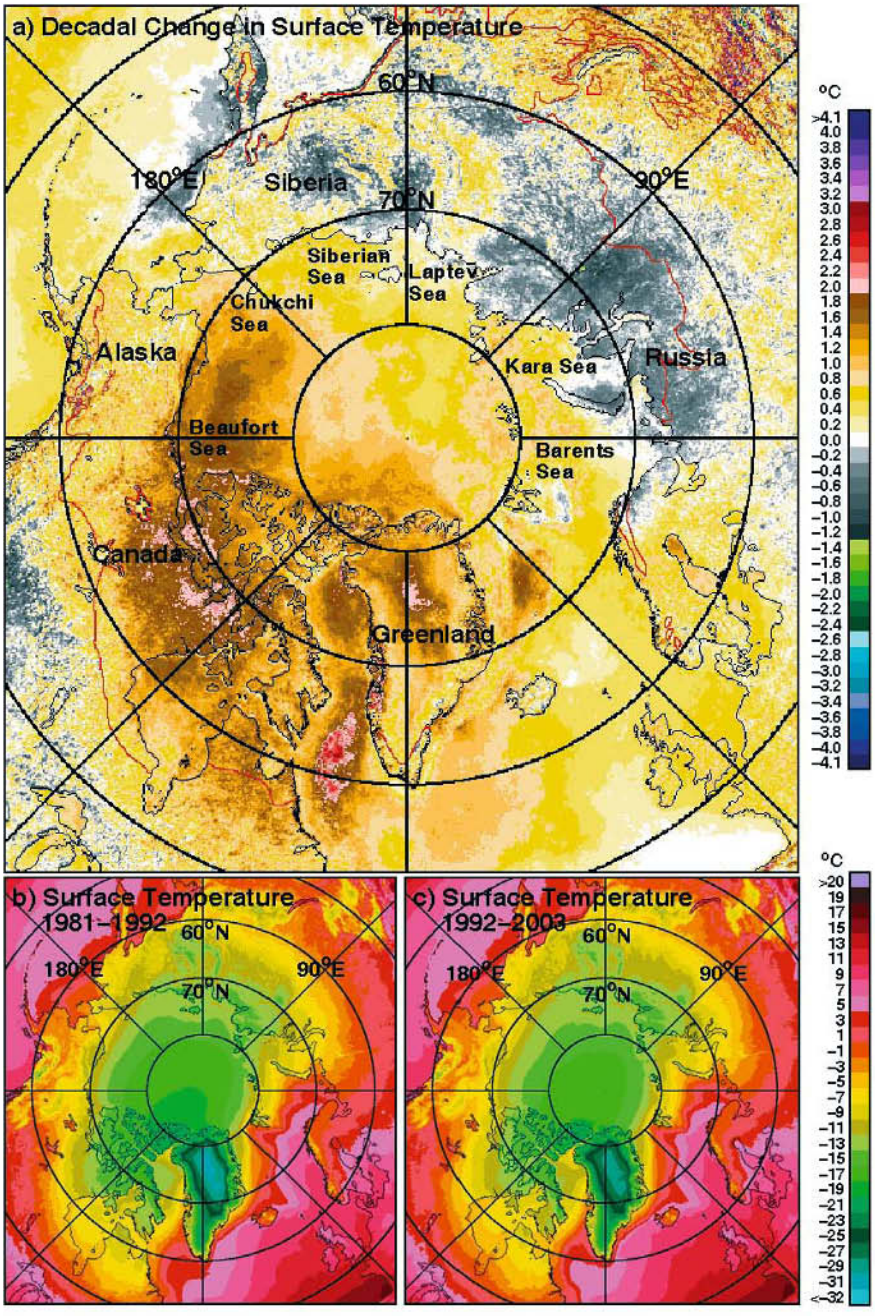

Figure 5.113. Color-coded maps of the NOAA AVHRR-derived mean surface temperature (*IST*) of the Arctic for the periods (b) August 1981 through July 1992, and (c) August 1992 through July 2003. (a) A difference map of *IST*, derived by subtracting (c) from (b). The red line in (a) demarcates the southern boundary of discontinuous permafrost.

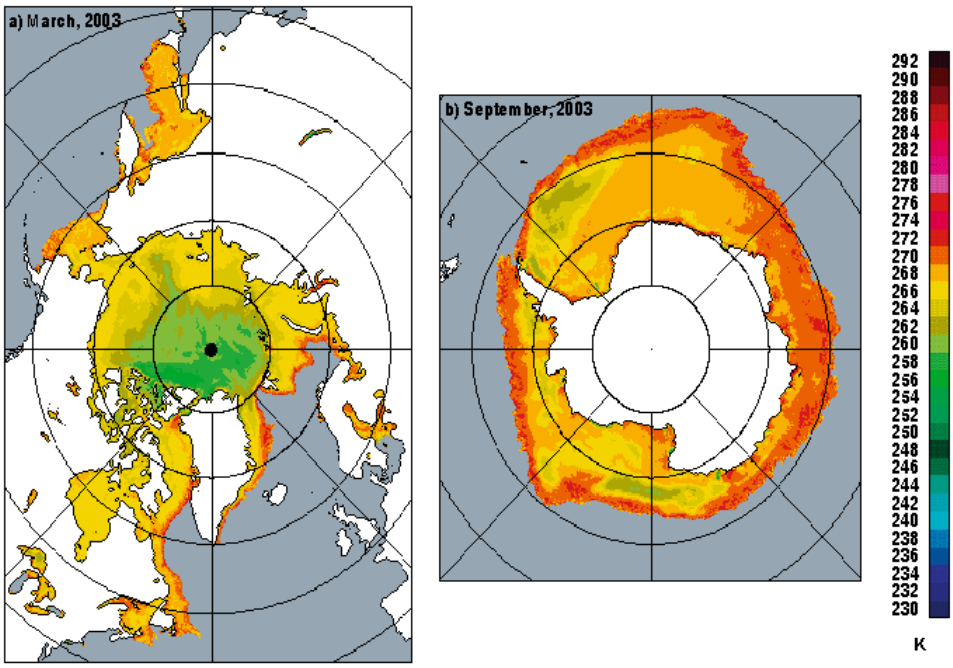

Figure 5.114. Monthly mean maps of T_I derived from AMSR-E brightness temperature data for (a) the Arctic in March 2003, and (b) the Antarctic in September 2003.

Courtesy of Joey Comiso (NASA Goddard Space Flight Center).

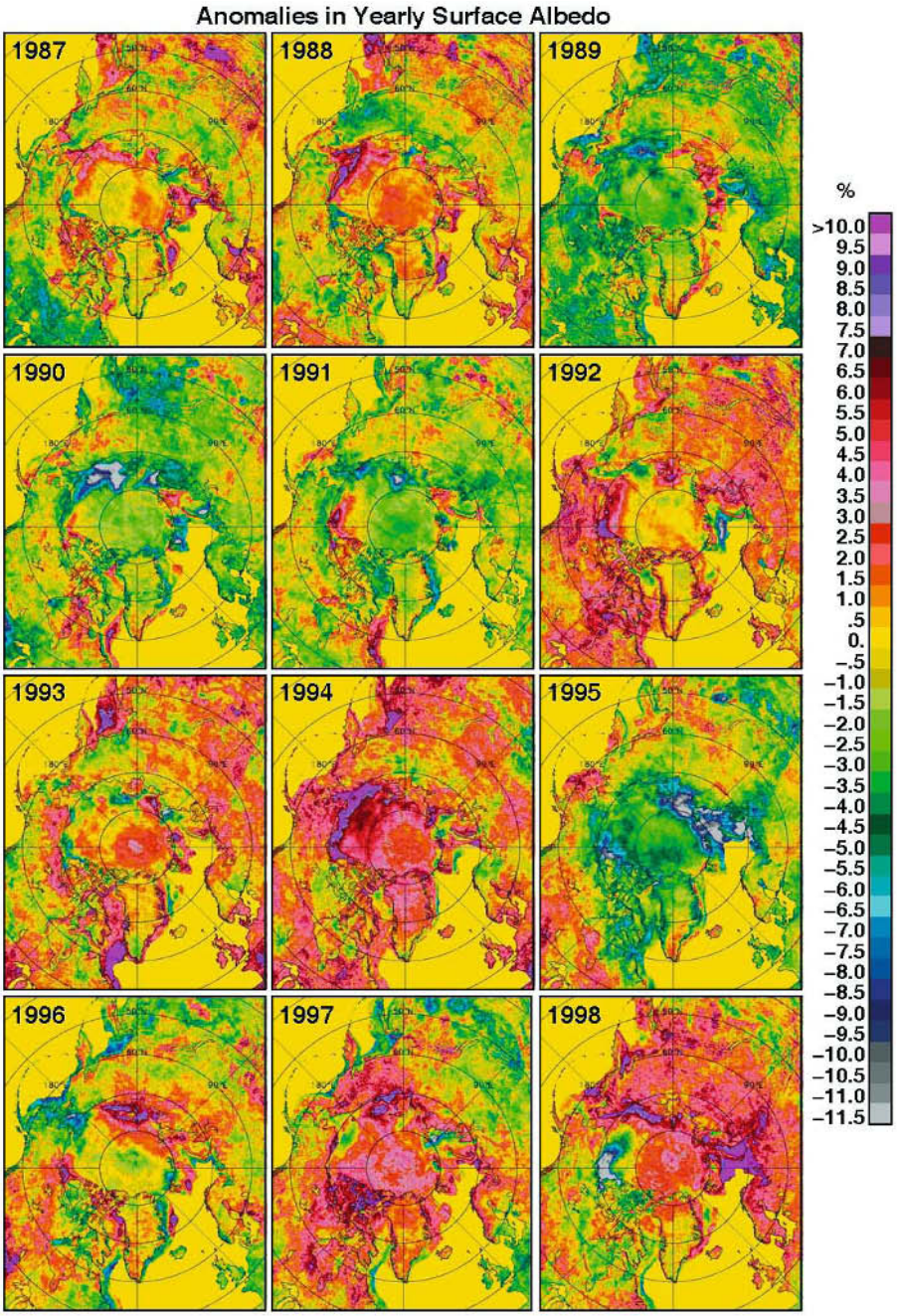

Figure 5.115. Color-coded anomaly maps of annual albedo in the Arctic from 1987- to 1998-derived AVHRR data. Note that incomplete coverage is available over 5 months of the year—i.e., in October to February in the Arctic.

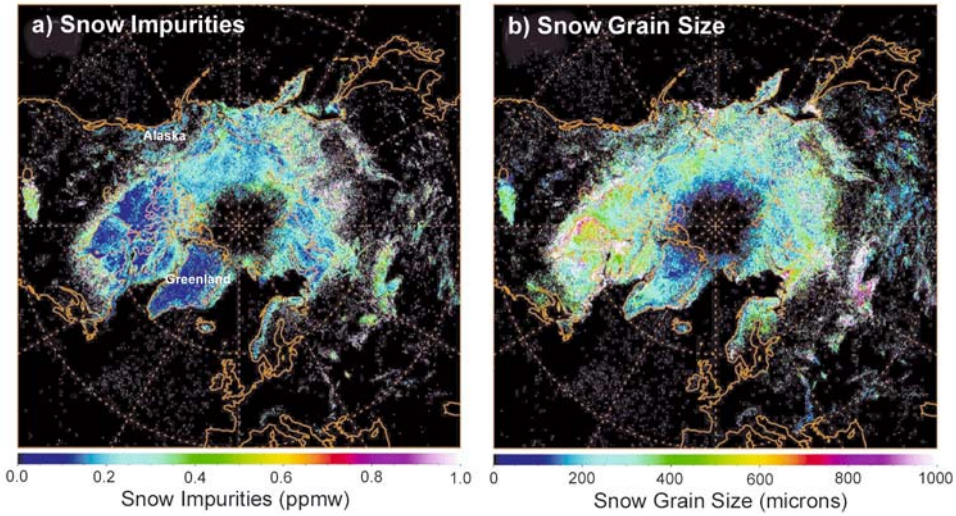

Figure 5.117. An example of snow/ice products from cloud-free ADEOS-II GLI imagery acquired from April 7 to May 7, 2003: (a) snow impurities, and (b) snow surface grain size. As discussed earlier, snow impurities are extensive in the Arctic, but much less so in Antarctica.

Courtesy of JAXA EORC (⟨*http://www.eorc.jaxa.jp*⟩). Reproduced with permission of JAXA.

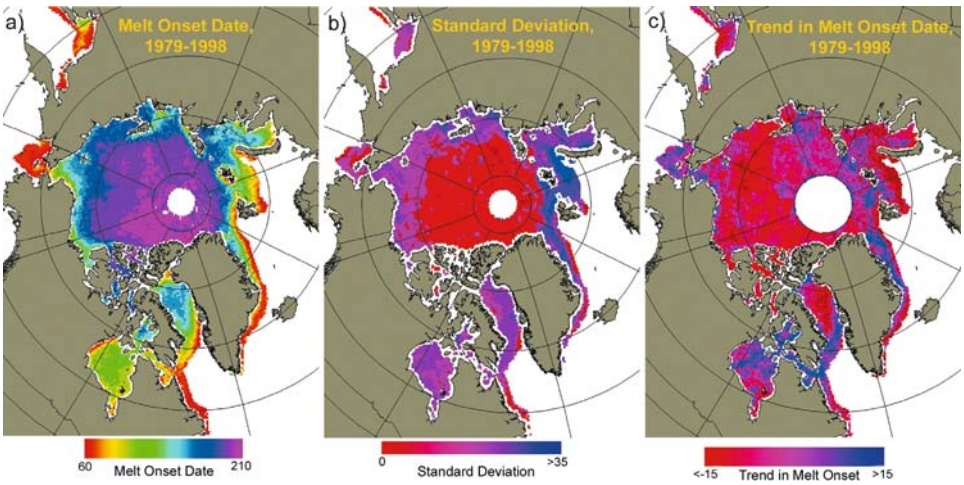

Figure 5.118. (a) Map of mean sea ice melt onset dates in the Arctic derived from passive-microwave satellite data, 1979–1998. Melt onset typically begins in March in the peripheral seas—e.g., the Bering Sea, the Sea of Okhotsk—and along the Labrador coast, and progresses radially northward over the next 4 months, with the latest average melt onset occurring in the Lincoln Sea north of Greenland, in accordance with the minimum in air temperatures located in that region. (b) Standard deviation in melt onset dates, 1979–1998. Interannual variability in melt onset in the Arctic Ocean typically ranges from 1 to 2 weeks, while variability in the peripheral seas is typically 3 to 4 weeks. (c) Linear trend per grid cell in the annual melt onset date, 1979–1998. Negative values indicate trends toward earlier melt onset. The results indicate that melt onset is occurring earlier over most of the Arctic Ocean and peripheral seas, particularly in the Beaufort/Chukchi Seas region.

Courtesy of Sheldon Drobot (Polar Research Board and Board on Atmospheric Sciences and Climate, The National Academies, Washington, DC). Reproduced with permission.

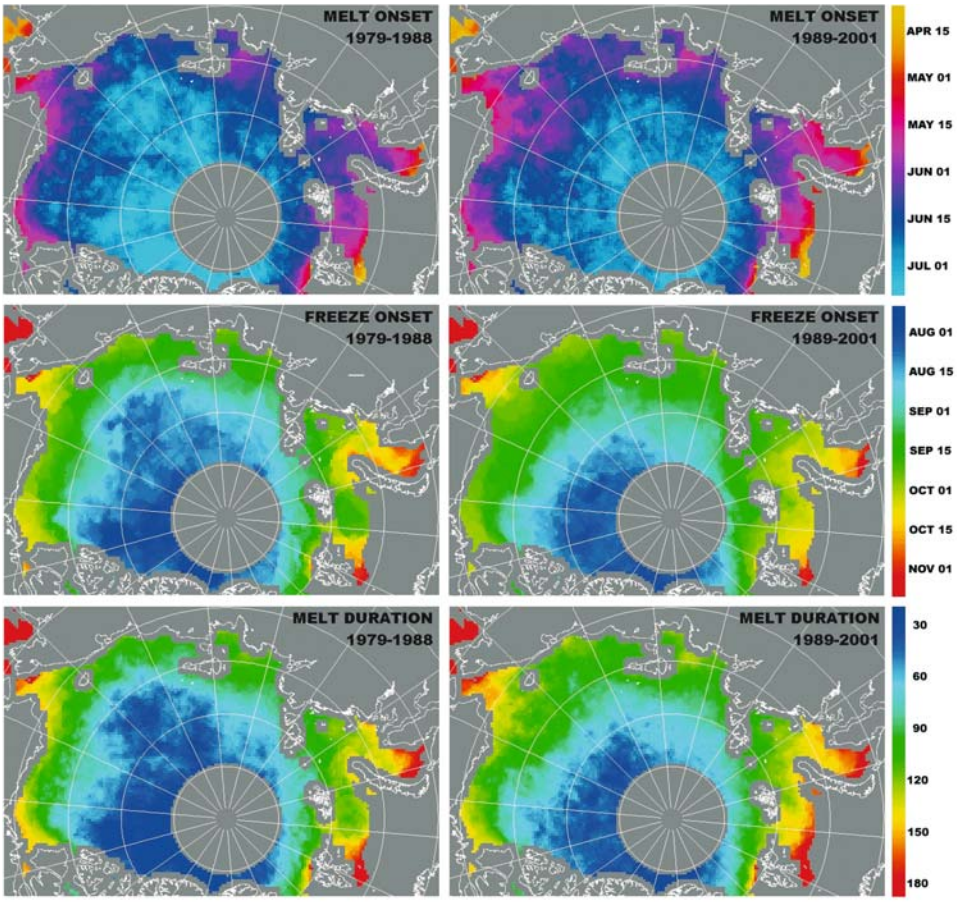

Figure 5.119. Maps of average sea ice melt onset date, freeze onset date, and melt season duration in the Arctic Ocean and surrounding seas during the low-index Arctic Oscillation (AO) period (1979–1988) and high-index AO period (1989–2001).

From Belchansky et al. (2004b).

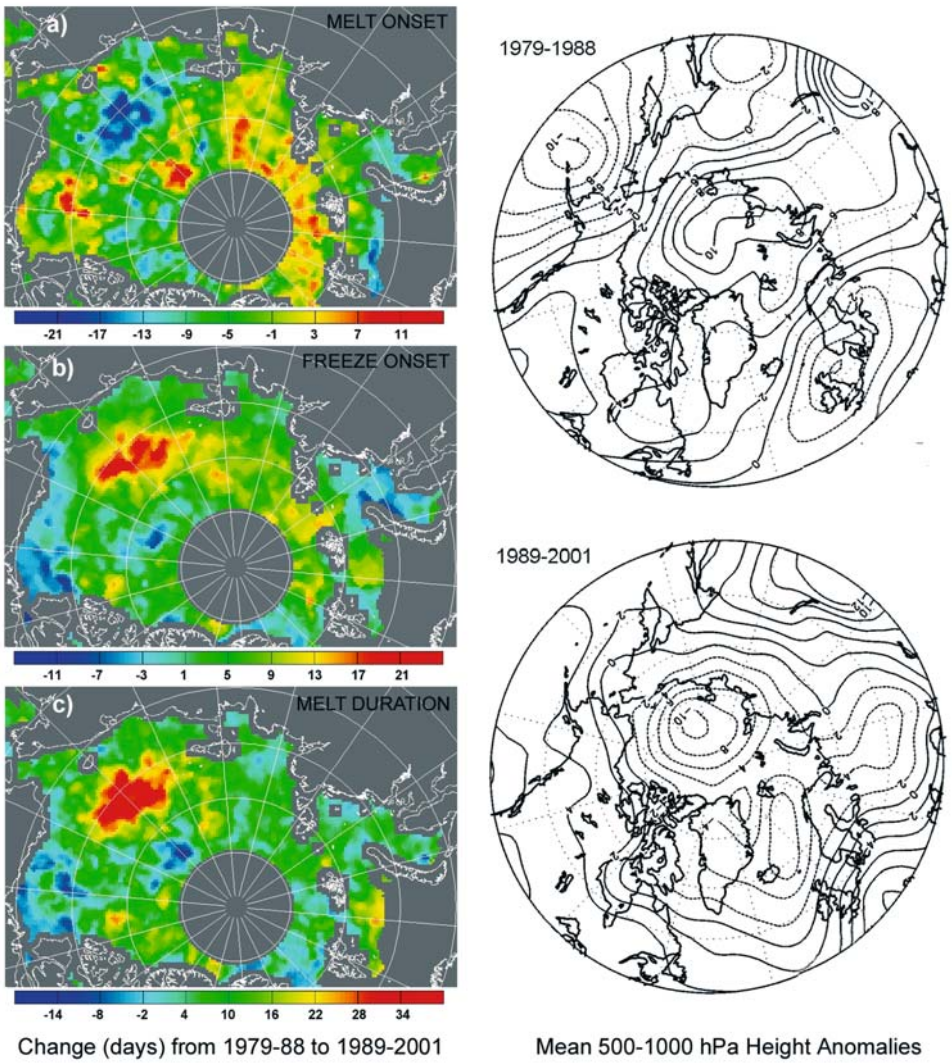

Figure 5.120. Change in the mean (a) melt onset, (b) freeze onset, (c) melt season duration (days), from 1979–1988 to 1989–2001. Averaged 500–1,000-hPa geopotential height anomalies for (d) the low-index Arctic Oscillation (AO) period (1979–1988) and (e) high-index AO period (1989–2001). Atmospheric anomaly figures were provided by the NOAA-CIRES Climate Diagnostocs Centre, Boulder, Colorado (available online at ⟨*http://www.cdc.noaa. gov/*⟩.

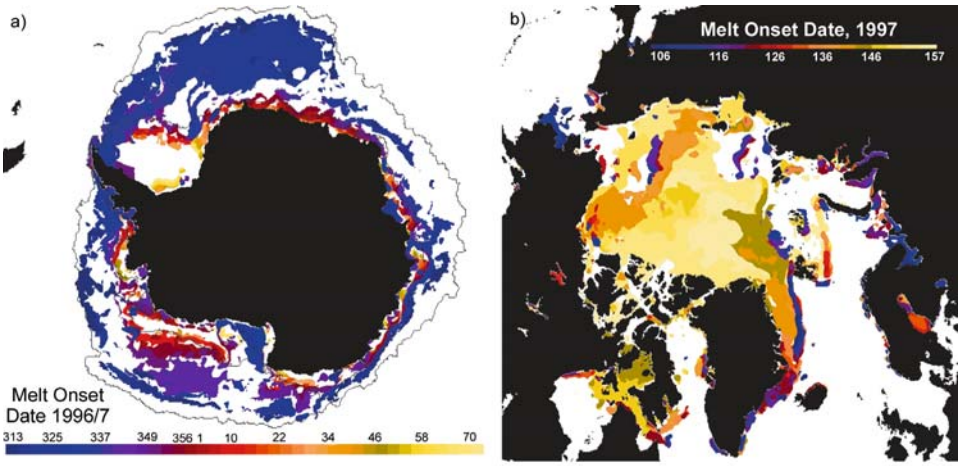

Figure 5.121. Maps of the sea ice melt onset dates for (a) Antarctica (1996/7 where day 313 is November 8 and day 70 is March 11), and (b) the Arctic (1997, where day 106 is April 16 and day 157 is June 6), derived from NSCAT data.

Part (a) from Drinkwater and Liu (2000), and part (b) courtesy Mark Drinkwater (ESA). Reproduced with permission of ESA.

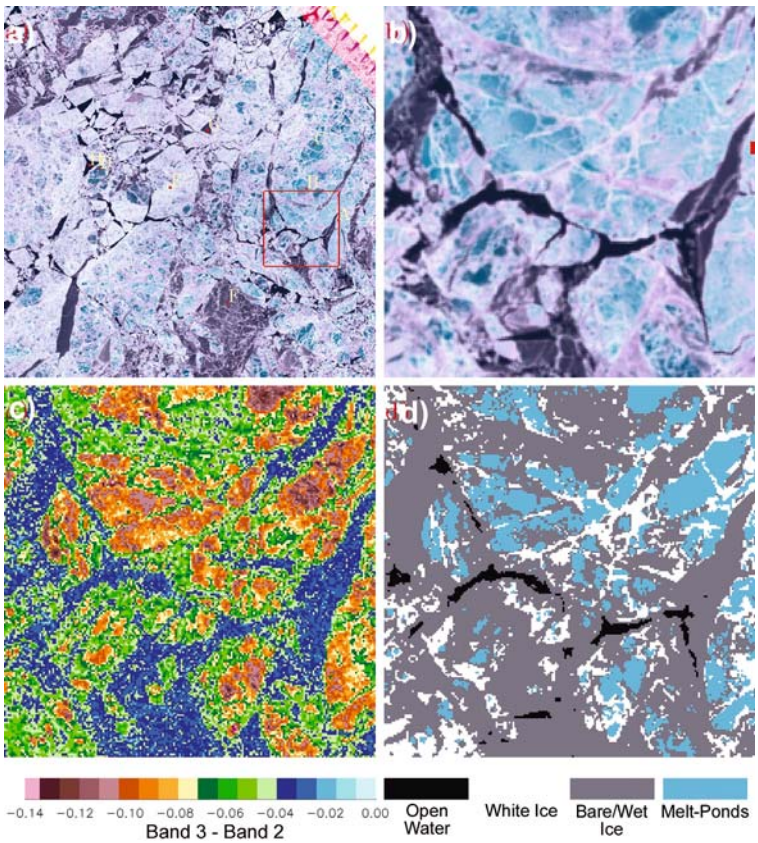

Figure 5.125. (a) A sub-scene (width 25 km) of a Landsat 7 ETM+ true-color image (bands 3, 2, and 1) of sea ice in Baffin Bay on June 26, 2000. (b) A "blowup" of the boxed region in (a). (c) Difference map of bands 3 and 2 for the area shown in (b). (d) Classified image of the same area.

From Markus et al. (2002). © 2005 International Glaciological Society, reproduced with permission.

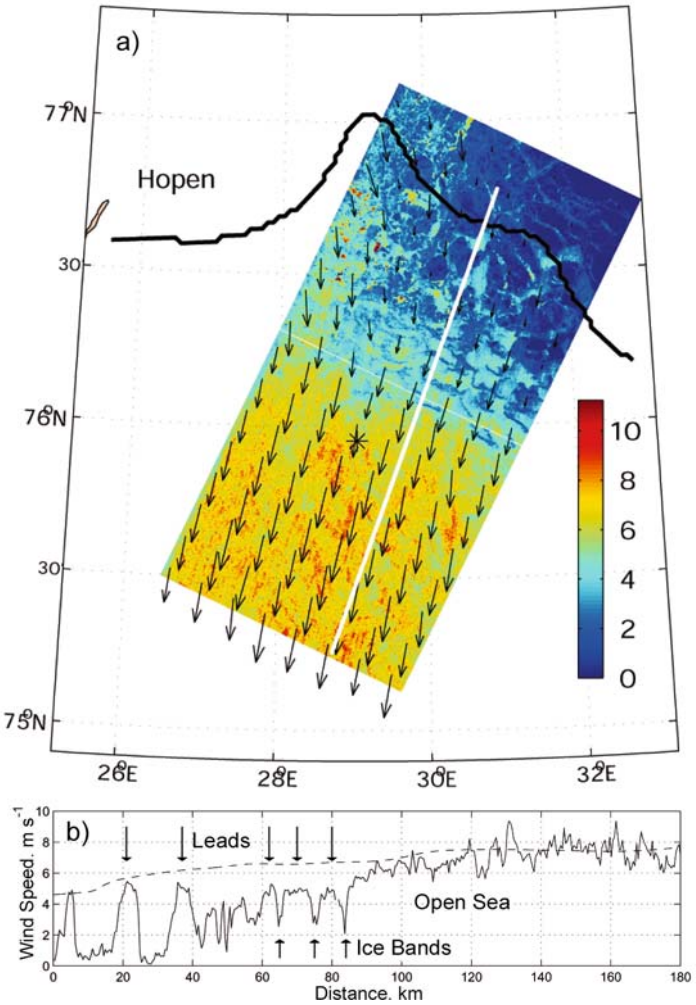

Figure 5.129. (a) A map of surface wind speed and direction retrieved from two ERS SAR scenes (100 km across) from the marginal ice zone (MIZ) in the Barents Sea, May 7, 1999 (10 : 08 UTC). Wind speeds were retrieved with a 400-m pixel size using the CMOD-IFR2 algorithm (Quilfen et al., 1998), with direction being derived from image spectra in 8×8 sub-images. The color bar is for wind speed (in $\mathrm{m\,s^{-1}}$). The lower scene is virtually ice-free, whereas the upper scene covers the MIZ, with closed pack to the north, some leads in the center, and ice bands in the south. Wind speeds of $<1\,\mathrm{m\,s^{-1}}$ (dark blue) equate to consolidated ice, and should be ignored. (b) A linear profile of the wind speed, along the bold white line in (a), running from north (left) to south (right). Arrows above the data indicate leads, while those below indicate ice bands.

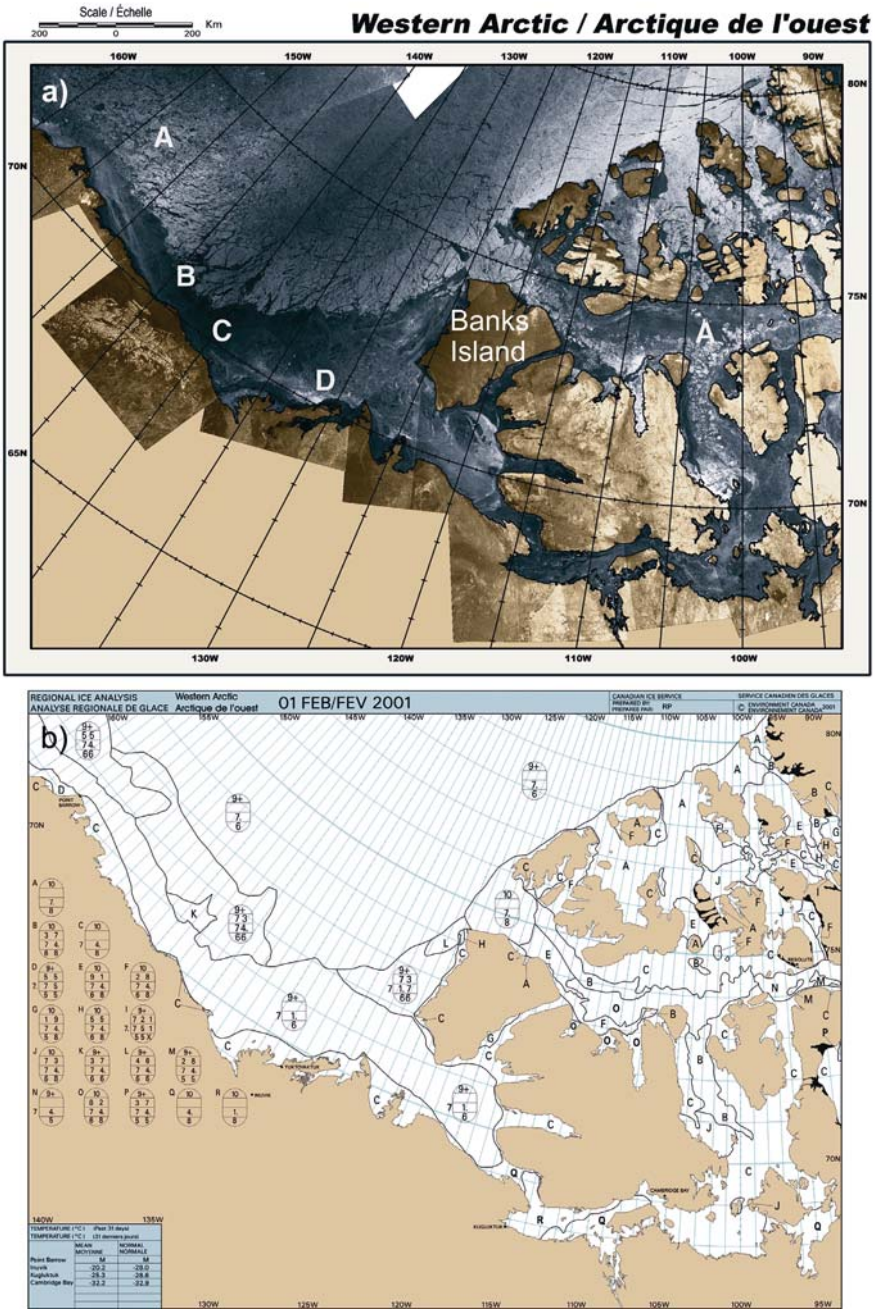

Figure 5.130. (a) Mosaic of Radarsat-1 ScanSAR Wide imagery from the Canadian Arctic, February 1–4 2001 (CSA, 2001). (b) The Regional Ice Analysis Chart derived by the Canadian Ice Service from (a). Radarsat-1 imagery is used operationally for daily ice mapping by the Canadian Ice Service of ice conditions in areas of active navigation, as well as for an annual Arctic Ice Atlas (see Ramsay et al., 2001). Ice analysts and forecasters now use sophisticated graphic workstations to analyse and integrate data from various sources to generate digital products and maps in a timely fashion (Ou, 2004).

From Bertoia et al. (2004). © 2005 National Oceanic and Atmospheric Administration, reprinted with permission.